NUREG/CP-0142
Vol. 2

Proceedings of the 7th International Meeting on Nuclear Reactor Thermal-Hydraulics NURETH-7

Sessions 6–11

Held at
Sheraton Hotel and Convention Center
Saratoga Springs, New York
September 10–15, 1995

Compiled by
R. C. Block, F. Feiner, ANS

Sponsored by
American Nuclear Society
American Institute of Chemical Engineers
American Society of Mechanical Engineers
Canadian Nuclear Society
European Nuclear Society
Atomic Energy Society of Japan
Japanese Society of Multiphase Flow
U.S. Nuclear Regulatory Commission

Proceedings prepared by
Northeastern New York Chapter
American Nuclear Society

AVAILABILITY NOTICE

Availability of Reference Materials Cited in NRC Publications

Most documents cited in NRC publications will be available from one of the following sources:

1. The NRC Public Document Room, 2120 L Street, NW., Lower Level, Washington, DC 20555-0001

2. The Superintendent of Documents, U.S. Government Printing Office, P. O. Box 37082, Washington, DC 20402-9328

3. The National Technical Information Service, Springfield, VA 22161-0002

Although the listing that follows represents the majority of documents cited in NRC publications, it is not intended to be exhaustive.

Referenced documents available for inspection and copying for a fee from the NRC Public Document Room include NRC correspondence and internal NRC memoranda; NRC bulletins, circulars, information notices, inspection and investigation notices; licensee event reports; vendor reports and correspondence; Commission papers; and applicant and licensee documents and correspondence.

The following documents in the NUREG series are available for purchase from the Government Printing Office: formal NRC staff and contractor reports, NRC-sponsored conference proceedings, international agreement reports, grantee reports, and NRC booklets and brochures. Also available are regulatory guides, NRC regulations in the *Code of Federal Regulations*, and *Nuclear Regulatory Commission Issuances*.

Documents available from the National Technical Information Service include NUREG-series reports and technical reports prepared by other Federal agencies and reports prepared by the Atomic Energy Commission, forerunner agency to the Nuclear Regulatory Commission.

Documents available from public and special technical libraries include all open literature items, such as books, journal articles, and transactions. *Federal Register* notices, Federal and State legislation, and congressional reports can usually be obtained from these libraries.

Documents such as theses, dissertations, foreign reports and translations, and non-NRC conference proceedings are available for purchase from the organization sponsoring the publication cited.

Single copies of NRC draft reports are available free, to the extent of supply, upon written request to the Office of Administration, Distribution and Mail Services Section, U.S. Nuclear Regulatory Commission, Washington, DC 20555-0001.

Copies of industry codes and standards used in a substantive manner in the NRC regulatory process are maintained at the NRC Library, Two White Flint North, 11545 Rockville Pike, Rockville, MD 20852-2738, for use by the public. Codes and standards are usually copyrighted and may be purchased from the originating organization or, if they are American National Standards, from the American National Standards Institute, 1430 Broadway, New York, NY 10018-3308.

NUREG/CP-0142
Vol. 2

Proceedings of the 7th International Meeting on Nuclear Reactor Thermal-Hydraulics NURETH-7

Sessions 6–11

Held at
Sheraton Hotel and Convention Center
Saratoga Springs, New York
September 10–15, 1995

Date Published: September 1995

Compiled by:
R. C. Block, F. Feiner, ANS

Sponsored by
American Nuclear Society
555 N. Kensington Avenue
La Grange Park, IL 60525

American Institute of Chemical Engineers
345 East 47th Street
New York, NY 10017-2392

American Society of Mechanical Engineers
345 East 47th Street
New York, NY 1007-2392

Canadian Nuclear Society
144 Font Street West
Suite 725
Toronto, Ontario, Canada M5J2L7

European Nuclear Society
Secretariat: Monbijoustrasse 5
P.O. Box 5032
CH-3001 Berne, Switzerland

Atomic Energy Society of Japan
No. 1-13, 1-chome
Shimbashi, Minato-ku
Tokyo 105, Japan

Japan Society of Multiphase Flow
Prof. Akimi Serizawa
Department of Nuclear Engineering
Yoshida, Sakyo, Kycto 606-01
Japan

Division of Systems Technology
Office of Nuclear Regulatory Research
U.S. Nuclear Regulatory Commission
Washington, DC 20555-0001

Proceedings prepared by
Northeastern New York Chapter
Amrican Nuclear Society

NUREG/CP-0142, Volume 2, has been reproduced from the best available copy.

ABSTRACT

Technical papers accepted for presentation at the Seventh International Topical Meeting on Nuclear Reactor Thermal-Hydraulics are included in the present Proceedings. Except for the invited papers in the plenary session, all other papers are contributed papers. The topics of the meeting encompass all major areas of nuclear thermal-hydraulics, including analytical and experimental works on the fundamental mechanisms of fluid flow and heat transfer, the development of advanced mathematical and numerical methods, and the application of advancements in the field in the development of novel reactor concepts. Because of the complex nature of nuclear reactors and power plants, several papers deal with the combined issues of thermal-hydraulics and reactor/power-plant safety, core neutronics and/or radiation.

The participation in the conference by the authors from several countries and four continents makes the Proceedings a comprehensive review of the recent progress in the field of nuclear reactor thermal-hydraulics worldwide.

PLANNING COMMITTEE MEMBERS

General Chairman: Richard T. Lahey, Jr.

Vice-Chairman: M. Richard Mendelson

Technical Program Chairman: Michael Z. Podowski

Registration: Thomas M. Sutton

Secretary: Ray G. Gamino

Finance: Hunter B. Currin

Fund Raising: Brian Bielecki and Norman Francis

Publications: Frank Feiner and Robert C. Block

Arrangements: Robert C. Rohr

Publicity: David F. McMullan

Special Events: Jeffrey G. Hoole

Spouse Events: Ann E. Kelly

SCIENTIFIC ADVISORY COMMITTEE

K. Akagawa	Japan
G.F. Hewitt	Great Britian
Y.Y. Hsu	R.C., Taiwan
J. H. Kim	USA
S. Levy	USA
F. Mayinger	Germany
G. Matsui	Japan
U. Mueller	Germany
V. Nakoriakov	Russia
R.I. Nigmatulin	Russia
W. Rohsenow	USA
T. Sakaguchi	Japan
V.E. Schrock	USA
N. Todreas	USA
L.S. Tong	USA

TECHNICAL PROGRAM COMMITTEE

M. Akiyama	Japan
K.H. Ardon	Great Britain
S. Antal	USA
M. Aritomi	Japan
B. Azzopardi	Great Britain
S. Banerjee	USA
F.R. Best	USA
B. Boyack	USA
N. Brauner	Israel
G.P. Celata	Italy
J.H. Cha	South Korea
A. Clausse	Argentina
M.L. Corradini	USA
J.M. Courtaud	France
M. Cumo	Italy
V.K. Dhir	USA
G.E. Dix	USA
J.J. Dorning, Jr.	USA
R.B. Duffey	USA
F. Eltawila	USA
M. Epstein	USA
M. Erdman	USA
S. Ettore	USA
W. Frid	Sweden
M. Golay	USA
Y.A. Hassan	USA
S. Sreepada	USA
A. Strupczewski	Poland
L. Szabados	Hungary
R. Taleyarkhan	USA
T.G. Theofanous	USA
R.E. Henry	USA
G. Hetsroni	Israel
L. Hochreiter	USA
M. Ishii	USA
H. Karwat	Germany
G. Kojasoy	USA
V.S. Krishnan	Canada
T. K. Larson	USA
H. Lemmonier	France
J. March-Leuba	USA
M. Merilo	USA
F. Moody	USA
H. Nariai	Japan
B. Nigmatulin	Russia
H. Ninokata	Japan
O. Nylund	Sweden
P.F. Peterson	USA
V. Ransom	USA
K. Rehme	Germany
D.S. Rowe	USA
Z. Rouhani	USA
K. Rust	Germany
B.R. Sehgal	Sweden
A. Serizawa	Japan
B.S. Shiralker	USA
L. Shotkin	USA
J. Weisman	USA
W. Wulff	USA
G. Yadigaroglu	SWITZERLAND
S.T. Yin	CANADA

SESSION ORGANIZERS

Almenas, K.
Aritomi, M.
Banerjee, S.
Baratta, A.J.
Best, F.R.
Boyack, B.
Brauner, N.
Catton, I.
Celata, G.P.
Cha, J.H.
Chabard, J.P.
Cheng, L.
Corradini, M.L.
Courtaud, J.M.
Dhir, V.K.
DiMarzo, M.
Dorning, Jr., J.J.
Eltawila, F.
Frid, W.
Golay, M.W.
Grand, D.
Groeneveld, D.C.
Hassan, Y.A.
Hodge, S.
Hochreiter, L.
Ishii, M.
Karwat, H.
Kojasoy, G.
Krishnan, V.S.
Kurul, N.
Larson, T.K.
Lemmonier, H.
March-Leuba, J.
McMullan, D.
Merilo, M.
Modro, M.
Moody, F.
Nariai, H.
Ninokata, H.
Nylund, O.
Peterson, P.F.
Pilch, M.M.
Ransom, V.H.
Rehme, I.K.
Rouhani, Z.
Rowe, D.S.
Serizawa, A.
Shotkin, L.
Sreepada, S.
Taleyarkhan, R.
Theofanous, T.G.
Todreas, N. E.
Weisman, J.
Wilson, G.
Wright, R.W.
Wulff, W.
Yadigaroglu, G.
Yin, S. T.
Yoder, G. L.

TABLE OF CONTENTS

VOLUME I

Plenary Session - NUCLEAR POWER REACTORS FOR THE 21st CENTURY

"Turning Points in Reactor Design"
E. Beckjord 1

"Resolution of Thermal-Hydraulic Safety and Licensing Issues for the System 80+"
F.L. Carpentino, S.E. Ritterbusch, R.E. Schneider and M.C. Jacob 21

"AP600 Design Certification Thermal Hydr· ·lics Testing and Analysis"
L.E. Hochreiter and E.J. Piplica 43

"Prospects for Bubble Fusion"
R.I. Nigmatulin and R.T. Lahey, Jr. 49

Session 1 - ADVANCES IN TWO-PHASE FLOW MODELING

"A Mechanistic Determination of Horizontal Flow Regime Boundaries Using Void Wave Celerity"
J.-W. Park 76

"A Criterion for the Onset of Slugging in Horizontal Stratified Air-Water Countercurrent Flow"
M.-H. Chun, H.-Y. Nam, B.-R. Lee and Y.-S. Kim 93

"Characterization of Non Equilibrium Effects on High Quality Critical Flows"
E. Camelo, H. Lemonnier, J. Ochterbeck and S. Selmer-Olsen 111

"Local Pressure Gradients Due to Incipience of Boiling in Subcooled Flows"
J. McDuffey and A. Ruggles 131

"Drift Flux Model as Approximation of Two Fluid Model for Two Phase Dispersed and Slug Flow in Tube"
R.I. Nigmatulin 141

"Development, Implementation and Assessment of Specific, Two-Fluid Closure Laws for Inverted-Annular Film-Boiling"
F. de Cachard 166

"Analytical Solution of Laminar-Laminar Stratified Two-Phase Flows with Curved Interfaces"
N. Brauner, Y. Rovinsky and D. Moalem Maron 192

"Velocity of Large Bubble in Liquid-Solid Mixture in a Vertical Tube"
H. Hamaguchi and T. Sakaguchi 212

"About the Statistical Description of Gas-Liquid Flows"
D. Sanz, G. Guido-Lavalle, P. Carrica and A. Clausse 231

"Entropy Analysis on Non-Equilibrium Two-Phase Flow Models"
H. Karwat and Y.Q Ruan 248

"A General Unified Non-Equilibrium Model for Predicting Saturated and Subcooled Critical Two-Phase Flow Rates Through Short and Long Tubes"
D.W.H. Fraser and A.H. Abdelmessih 264

"Predictions of Bubbly Flows in Vertical Pipes Using Two-Fluid Models in CFDS-Flow 3D Code"
A.O. Banas, M.B. Carver and D. Unrau 284

Session 2 - ADVANCES IN BOILING AND CONDENSATION HEAT TRANSFER

"Condensation During Gravity Driven ECC: Experiments with PACTEL"
R. Munther, H. Kalli and J. Kouhia 299

"An Investigation of Condensation From Steam-Gas Mixtures Flowing Downward Inside a Vertical Tube"
S.Z. Kuhn, V.E. Schrock and P.F. Peterson 312

"Study of Condensation Heat Transfer Following a Main Steam Line Break Inside Containment"
J.H. Cho, F.A. Elia, Jr. and D.J. Lischer 336

"Effect of Subcooling and Wall Thickness on Pool Boiling From Downward-Facing Curved Surfaces in Water"
M.S. El-Genk and A.G. Glebov 353

"Numerical Model of Condensation from Vapor-Gas Mixtures for Forced Down Flow Inside a Tube"
R.Y. Yuann, V.E. Schrock and X.M. Chen 377

"A Model for the Performance of a Vertical Tube Condenser in the Presence of Noncondensable Gases"
A. Dehbi and S. Guentay 402

"UPTF-TRAM Experiments for SBLOCA: Evaluation of Condensation Processes in TRAM Tests A6 and A7"
H.G. Sonnenburg, J. Tuunanen and V.V. Palazov 423

"Condensation Heat Transfer Coefficient with Noncondensible Gases for Heat Transfer in Thermal Hydraulic Codes"
S. Banerjee and Y.A. Hassan 434

Session 3 - EXPERIMENTAL METHODS AND INSTRUMENTATION

"Experimental Study of Horizontal Annular Channels Under Non-Developed Conditions"
G. Delgadino, J. Balino and P.M. Carrica 462

"Interfacial Shear Stress in Stratified Flow in a Horizontal Rectangular Duct"
C. Lorencez, M. Kawaji, A. Ousaka and Y. Murao 478

"Quenching Phenomena in Natural Circulation Loop"
H. Umekawa, M. Ozawa and N. Ishida 487

"Measurement of the Interaction Between the Flow and the Free Surface of a Liquid"
K. Okamoto, W.D. Schmidl, O.G. Philip and Y.A. Hassan 497

"The Use of Waveguide Acoustic Probes for Void Fraction Measurement in the Evaporator of BN-350-Type Reactor"
V. Melnikov and B. Nigmatulin 508

"Buoyancy-Driven Flow Excursions in Fuel Assemblies"
J.E. Laurinat, P.K. Paul and J.D. Menna 514

"An Experimental Investigation of the Post CHF Enhancement Factor for a Prototypical ITER Divertor Plate with Water Coolant"
T.D. Marshall, R.D. Watson, J.M. McDonald and D.L. Youchison 532

"Transient Pool Boiling Heat Transfer Due to Increasing Heat Inputs in Subcooled Water at High Pressures"
K. Fukuda, M. Shiotsu and A. Sakurai 554

"Cross-Sectional Void Fraction Distribution Measurements in a Vertical Annulus Two-Phase Flow by High Speed X-Ray Computed Tomography and Real-Time Neutron Radiography Techniques"
G.D. Harvel, K. Hori, K. Kawanishi and J.S. Chang 574

"Two-Phase Velocity Measurements Around Cylinders Using Particle Image Velocimetry"
Y.A. Hassan, O.G. Philip, W.D. Schmidl and K. Okamoto 591

"Characteristics of Turbulent Velocity and Temperature in a Wall Channel of a Heated Rod Bundle"
T. Krauss and L. Meyer 603

"The Coolability Limits of a Reactor Pressure Vessel Lower Head"
T.G. Theofanous and S. Syri 627

Session 4 - MULTIDIMENSIONAL FLOW AND HEAT TRANSFER PHENOMENA

"Numerical Simulation of Multidimensional Two-Phase Flow Based on Flux Vector Splitting"
H. Stadtke, G. Franchello and B. Worth 648

"CFD Simulation of Flow and Phase Distribution in Fuel Assemblies with Spacers"
H. Anglart, O. Nylund, N. Kurul and M.Z. Podowski 673

"Computational Fluid Dynamic Analysis of a Closure Head Penetration in a Pressurized Water Reactor"
D.R. Forsyth and R.E. Schwirian 696

"THEHYCO-3DT: Thermal Hydrodynamic Code for the 3 Dimensional Transient Calculation of Advanced LMFBR Core"
S.G. Vitruk, A.S. Korsun, P.A. Ushakov and B.N. Gabrianovich 711

"Transition to Chaos In a Square Enclosure Containing Internal Heat Sources"
A. Cihat Baytas 720

"ASTRID: a 3D Eulerian Software for Subcooled Boiling Modelling Comparison with Experimental Results in Tubes and Annuli"
E. Briere, D. Larrauri and J. Olive 736

"The Multi-Dimensional Module of CATHARE 2 Description and Applications"
F. Barre, I. Dor and C. Sun 750

Session 5 - CCFL AND FLOODING PHENOMENA

"Reflooding and Boil-Off Experiments in a VVER-440 Like Rod Bundle and Analysis with the Cathare Code"
V. Korteniemi, T. Haapalehto and M. Puustinen 770

"Counter-Current Flow in a Vertical to Horizontal Tube with Obstructions"
P. Tye, A. Matuszkiewicz, A. Teyssedou, A. Tapucu and W. Midvidy 781

"Flooding Characteristics of Gas-Liquid Two-Phase Flow in a Horizontal U Bend Pipe"
T. Sakaguchi, N. Nakamori, T. Ueno, J. Kodama, S. Hosokawa, H. Minagawa and Y. Fujii 804

"CCFL in Hot Legs and Steam Generators and Its Prediction with the Cathare Code"
G. Geffraye, P. Bazin, P. Pichon and A. Bengaouer 815

VOLUME II

Session 6 - NATURAL CIRCULATION AND/OR CONVECTION

"On Heat Transfer Characteristics of Real and Simulant Melt Pool Experiments"
T.N. Dinh, R.R. Nourgaliev and B.R. Sehgal 827

"Passive Decay Heat Removal by Natural Air Convection After Severe Accidents"
F.J. Erbacher, X. Cheng, H.J. Neitzel 846

"Natural Circulation in a VVER Geometry: Experiments with the PACTEL Facility and Cathare Simulation"
P. Raussi S. Kainulainen and J. Kouhia 854

"Parametric Numerical Investigation of Natural Convection in a Heat-Generating Fluid with Phase Transitions"
A.E. Aksenova, V.V. Chudanov, V.F. Strizhov and P.N. Vabishchevich 865

Session 7 - INSTABILITY MECHANISMS, WAVES, AND NONLINEAR DYNAMICS

"Geysering in Boiling Channels"
M. Aritomi, T. Takemoto, J-H Chiang, M. Mori and H. Tabata 875

"Two-Phase Flow Stability Structure in a Natural Circulation System"
Z. Zhou 888

"FIBWR2 Evaluation of Fuel Thermal Limits During Density Wave Oscillations in BWRs"
N. Nik, S.R. Rajan and M. Karasulu 911

"Density Wave Oscillations of a Boiling Natural Circulation Loop Induced by Flashing"
M. Furuya, F. Inada and A. Yasuo 923

"Rayleigh-Taylor Instability of Cylindrical Jets With Radial Motion"
X.M. Chen, V.E. Schrock and P.F. Peterson 933

"Two-Phase Flow Instabilities in Vertical Annular Channel"
I. Babelli, S. Nair and M. Ishii 947

"Problems in Experimental and Mathematical Investigations of the Accidental Thermohydraulic Processes in RBMK Nuclear Reactors"
B.I. Nigmatulin, L.K. Tikhonenko, V.N. Blinkov and A.J. Kramerov 967

"An Investigation of the Stability of a Boiling Water Reactor Under Natural Circulation Conditions Using TRAC-BF-1"
S. Lider, G.E. Robinson, A.J. Baratta and J.G. Refling 978

"Analysis of the Void Wave Propagations: Wave Number Independent Characteristics"
C.H. Song, H.C. No and M.K. Chung 986

"Modeling and Numerical Simulation of Oscillatory Two-Phase Flows with Application to Boiling Water Nuclear Reactors"
M. Rosa and M.Z. Podowski 1003

"Thermal-Hydraulic Instabilities in Pressure Tube Graphite-Moderated Boiling Water Reactors"
G. Tsiklauri and B. Schmitt 1022

"Dynamics of Shock Wave Propagation and Interphase Process in Liquid-Vapour Medium"
B.G. Pokusaev and N.A. Pribaturin 1032

Session 8 - TRANSIENT ANALYSIS AND SIMULATION

"Evaluation of a Main Steam Line Break With Induced, Multiple Tube Ruptures: A Comparison of NUREG 1477 (Draft) and Transient Methodologies - Palo Verde Nuclear Generating Station"
K.R. Parrish 1046

"Application of UPTF Data for Modeling Liquid Draindown in the Downcomer Region of a PWR Using RELAP5/MOD2-B&W"
G. Wissinger and J. Klingenfus 1069

"Plant Data Comparisons for Comanche Peak 1/2 Main Feedwater Pump Trip Transient"
W.J. Boatwright, W.G. Choe, D.W. Hiltbrand, C.V. DeVore and J.F. Harrison 1083

"RBMK-LOCA-Analyses with the ATHLET-Code"
A. Petry, A. Domoradov, A. Finjakin and A. Moskalev 1090

"Small-Break Loss of Coolant Accident in the Updated Pius 600 Advanced Reactor Design"
B. E. Boyack, J.L. Steiner, S.C. Harmony, H.J. Stumpf, and J.F. Lime 1100

"Simulation of a Beyond Design-Basis-Accident With RELAP5/MOD3.1"
J. Banati 1116

"Rapid Depressurization Event Analysis in BWR/6 Using RELAP5 and Contain"
A.K. Muftuoglu and M.A. Feltus 1127

"A Thermal-Hydraulic Code for Transient Analysis in a Channel with a Rod Bundle"
I.D. Khodjaev 1139

Session 9 - ADVANCED WATER REACTOR THERMAL-HYDRAULICS

"Analysis of an AP600 Intermediate Size Loss-Of-Coolant Accident"
B.E. Boyack and J.F. Lime 1153

"A Concept of JAERI Passive Safety Light Water Reactor System (JPSR)"
Y. Murao, F. Araya and T. Iwamura 1169

"Assessment of the Advantages of a Residual Heat Removal System Inside the Reactor Pressure Vessel"
G.M. Gautier 1196

"NRC Review of Passive Reactor Design Certification Testing Programs: Overview, Progress, and Regulatory Perspective"
A.E. Levin 1231

"Flooding of a Large, Passive, Pressure-Tube LWR"
P. Hejzlar, N.E. Todreas and M.J. Driscoll 1224

"SBWR PCCS Vent Phenomena and Suppression Pool Mixing"
P. Coddington and M. Andreani 1249

"Scaling for Integral Simulation of Thermalhydraulic Phenomena in SBWR During LOCA"
M. Ishii, S.T. Revankar, R. Dowlati, I. Babelli, W. Wang, H. Pokharna, M.L. Bertodano, V.H. Ransom, R. Viskanta and J.T. Han 1272

"A Practical View of the Insights from Scaling Thermal-Hydraulic Tests"
A.E. Levin and G.D. McPherson 1291

Session 10 - LIQUID-METAL-COOLED REACTOR THERMAL-HYDRAULICS

"Analysis of Overflow-Induced Sloshing in an Elastic-Wall Vessel Using Physical Component BFC Method"
D. Lu, A. Takizawa and S. Kondo 1302

"Study of Mixed Convective Flow Penetration into Subassembly from Reactor Hot Plenum in FBRs"
J. Kobayashi, H. Ohshima, H. Kamide and Y. Ieda 1313

"Large Eddy Simulation of Mixing Between Hot and Cold Sodium Flows-Comparison with Experiments"
J.P. Simoneau, H. Noe and B. Menant 1324

"Natural Convection Heat Transfer on Two Horizontal Cylinders in Liquid Sodium"
K. Hata, M. Shiotsu, Y. Takeuchi, K. Hama and A. Sakurai 1333

"Evaluation of Wrapper Tube Temperatures of Fast Neutron Reactors Using the Transcoeur-2 Code"
B. Valentin, G. Chaigne and P. Brun 1351

"Simulation of Decay Heat Removal by Natural Convection in a Pool Type Fast Reactor Model - RAMONA with Coupled 1D/2D Thermal Hydraulic Code System"
N. Kasinathan, A. Rajakumar, G. Vaidyanathan and S.C. Chetal 1361

"Conjugate Heat Transfer Analysis of Multiple Enclosures in Prototype Fast Breeder Reactor"
K. Velusamy, V. Balasubramaniam, G. Vaidyanathan and S.C. Chetal 1380

"Computational Modeling for Hexcan Failure Under Core Disruptive Accidental Conditions"
T. Sawada, H. Nimokata and A. Shimizu 1398

Session 11 - CONTAINMENT THERMAL-HYDRAULICS

"Investigations on Sump Cooling After Core Melt Down"
J.U. Knebel 1407

"Containment Atmosphere Response to External Sprays"
J. Green and K. Almenas 1418

"Modelling of Local Steam Condensation on Walls in Presence of Noncondensable Gases. Application to a LOCA Calculation in Reactor Containment Using the Multidimensional GEYSER/TONUS Code"
L.V. Benet, C. Caroli, P. Cornet, N. Coulon and J.P. Magnaud 1443

"The Modelling of Wall Condensation with Noncondensable Gases for the Containment Codes"
C. Leduc, P. Cost, V. Barthel and H. Deslandes 1456

"An Interpretation of Passive Containment Cooling Phenomena"
B.J. Chung and C.S. Kang 1477

"Detailed Thermal-Hydraulic Computation into a Containment Building"
A. Caruso, I. Flour, O. Simonin and C. Cherbonnel 1489

"Free Convective Condensation in a Vertical Enclosure"
R.J. Fox, P.F. Peterson, M.L. Corradini and A.P. Pernsteiner 1501

"Condensation in the Presence of Noncondensible Gases: AP600 Containment Simulation"
M. Anderson and M.L. Corradini 1519

"Hydrogen Behavior in Ice Condenser Containments"
P. Lundstrom, P. Gango, H. Tuomisto, O. Hongisto and T.G. Theofanous 1535

"Aerodynamics, Heat and Mass Transfer in Steam-Aerosol Turbulent Flows in Containment"
B.I. Nigmatulin, V.A. Pershukov, V.V. Ris, E.M. Smirnov, L.I. Zaichik, A.A. Vinberg, D.V. Sidenkov and V.A. Belov 1555

"GEYSER/TONUS: A Coupled Multi-D Lumped Parameter Code for Reactor Thermal Hydraulics Analysis in Case of Severe Accident"
M. Petit, M. Durin, and J. Gauvain 1574

VOLUME III

Session 12 - FUEL/COOLANT INTERACTION

"On The Constitutive Description of the Microinteractions Concept in Steam Explosions"
X. Chen, W.W. Yuen and T.G. Theofanous 1586

"Correlations Between the Disintegration of Melt and the Measured Impulses in Steam Explosions"
G. Frohlich, A. Linca and M. Schindler 1607

"Analysis of Supercritical Vapor Explosions Using Thermal Detonation Wave Theory"
B.I. Shamoun and M.L. Corradini 1637

"The Numerical Methods for the Development of the Mixture Region in the Vapor Explosion Simulations"
Y.H. Yang, H. Ohashi, M. Akiyama and T. Morii 1653

"Thermal-Hydraulic Behaviors of Vapor-Liquid Interface Due to Arrival of a Pressure Wave"
A. Inoue, Y. Fujii, M. Matsuzaki and M. Takahashi 1663

"Boiling Characteristics of Dilute Polymer Solutions and Implications for the Suppression of Vapor Explosions"
K.H. Bang and M.H. Kim 1677

"Experimental Investigation of 150-KG-Scale Corium Melt Jet Quenching In Water"
D. Magallon and H. Hohmann 1688

"FCI Experiments in the Corium/Water System"
I.K. Huhtiniemi, H. Hohmann and D. Magallon 1712

"Experimental Studies of Thermal and Chemical Interactions Between Oxide and Silicide Nuclear Fuels with Water"
A. Farahani and M.L. Corradini 1728

"The Effect of Constraint on Fuel-Coolant Interactions in a Confined Geometry"
H.S. Park and M.L. Corradini 1743

"The Mixing of Particle Clouds Plunging into Water"
S. Angelini, T.G. Theofanous and W.W. Yuen 1754

"Experimental Studies of Thermal and Chemical Interactions between Molten Aluminum and Water"
A.A. Farahani and M.L. Corradini 1779

Session 13 - THERMAL-HYRAULICS OF SEVERE ACCIDENTS

"Interaction Between the Radiative Flux Emitted by a Corium Melt and Aerosols from Corium/Concrete/Interaction"
M. Zabiego, G. Cognet and P. Henderson 1797

"Modeling of Heat and Mass Transfer Processes During Core Melt Discharge From a Reactor Pressure Vessel"
T.N. Dinh, V.A. Bui, R.R. Nourgaliev, T. Okkonen and B.R. Sehgal 1809

"Results of International Standard Problem No. 36 Severe Fuel Damage Experiment of a VVER Fuel Bundle at the CORA Facility"
M. Firnhaber, L. Yegorova, U. Brockmeir, S. Hagen, P. Hofmann and K. Trambauer 1830

"Oxidation During Reflood of Reactor Core with Melting Cladding"
L.J. Siefken, C.M. Allison, K.L. Davis and J.K. Hohorst 1851

"Crust Formation and Its Effect on the Molten Pool Coolability"
R.J. Park, S.J. Lee, S.K. Sim and K.J. Yoo 1863

"Simulation of the Thermalhydraulic Behavior of a Molten Core Within a Structure, with the Three Dimensions Three Components TOLBIAC Code"
B. Spindler, G.-M. Moreau and S. Pigny 1881

"The Modelling of Core Melting and In-Vessel Corium Relocation in the APRIL Code"
S.W. Kim, M.Z. Podowski, R.T. Lahey, Jr. and N. Kurul 1889

"CODE PACKAGE "SVECHA: Modeling of Core Degradation Phenomena at Severe Accidents"
M.S. Veshchunov, A.E. Kisselev, A.V. Palagin, A.V. Lemekha, A.M. Volchek, N.V. Yamshchikov, A.V. Boldyrev and A.I. Deryugin 1914

Session 14 - HEAT TRANSFER WITH PHASE CHANGE; APPLICATIONS TO SEVERE ACCIDENT SITUATIONS

"Experimental Simulation of Water Cooling of Corium Spread Over the Floor of BWR Containment"
F. Moraga, R.T. Lahey, Jr. and M.Z. Podowski 1930

"SULTAN TEST FACILITY Large Scale Vessel Coolability in Natural Convection at Low Pressure"
S. Rouge 1949

"An Integral Model for the Calculation of Heat Flux Distribution in a Pool With Internal Heat Generation"
J.M. Bonnet 1958

Session 15 - COMPUTATIONAL AND MATHEMATICAL MODELING

"Numerical Simulation of Stratified Shear Flow Using a Higher Order Taylor Series Expansion Method"
K. Iwashige and T. Ikeda 1972

"Application of an Analytical Method for Solution of Thermal Hydraulic Conservation Equations"
M. R. Fakory 1982

"Numerical Investigation of Heat Transfer in High-Temperature Gas-Cooled Reactors"
G. Chen and S. Anghaie 1997

"Development of a Graphical User Interface for the TRAC Plant/ Safety Analysis Code"
A.E. Kelly, C.K. Harkins and R.J. Smith 2003

"A Comparison of the Effect of the First and Second Upwind Schemes on the Predictions of the Modified RELAP5/MOD3"
G. Th. Analytis 2011

"Local Mesh Refinement for Incompressible Fluid Flow With Free Surfaces"
H. Teresaka, H. Kajiwara, K. Ogura, H. Ueda and A. Takizawa 2021

"Level Tracking in Detailed Reactor Simulations"
B. Aktas and J. Mahaffy 2035

"The Sensitivity Analysis by Adjoint Method for the Uncertainty Evaluation of the CATHARE-2 Code"
F. Barre, A. de Crecy and C. Perret 2045

Session 16 - MODEL & COMPUTER CODE VALIDATION & ASSESSMENT

"Development and Assessment of a Modified Version of RELAP5/MOD3"
G. Th. Analytis 2067

"A Study of the Dispersed Flow Interfacial Heat Transfer Model of RELAP5/MOD2.5 and RELAP5/MOD3"
M. Andreani, G.Th. Analytis and S.N. Aksan 2079

"Assessment of Computer Codes for VVER-440/213-Type Nuclear Power Plants"
L. Szabados, Gy. Ezsol and L. Perneczky 2102

"VIPRE Modeling of VVER-1000 Reactor Core for DNB Analyses"
Y. Sung, T.Q. Nguyen and J. Cizek 2112

"CATHARE2 Calculations of SPE4 Test Small Break LOCA on PMK Facility"
E. Laugier and J. Radet 2119

"Quantitative Code Accuracy Evaluation of ISP 33"
H. Kalli, A. Miettinen, H. Purhonen, F. D'Auria, M. Frogheri and M. Leonardi 2146

"FARO Base Case Post-Test Analysis by COMETA Code"
A. Annunziato and C. Addabbo 2159

"The Analysis of SCS Return Momentum Effect on the RCS Water Level During the Mid-Loop Operations"
J.K. Seo, J.Y. Yang, S.T. Hwang, and G.C. Park 2169

"An Assessment of RELAP5 MOD3.1.1 Condensation Heat Transfer Modeling with GIRAFFE Heat Transfer Tests"
B.D. Boyer, Y. Parlatan, G.C. Solvik and U.S. Rohatgi 2185

"ATHLET Validation Using Accident Management Experiments"
V. Teschendorff, H. Glaeser and F. Steinhoff 2203

"A Simple Modelling of Mass Diffusion Effects on Condensation with Noncondensable Gases for the Cathare Code"
P. Coste and D. Bestion 2222

"INJECT, and the Modeling of Waste Recycling Processes"
E. Gracyalny and M.L. Corradini 2240

"Some Thermohydraulics of Closure Head Adapters in a 3 Loop PWR"
F. Hofmann, O. Daubert, C. Bertrand, M. Hecker, F. Arnoux-Guisse and O. Bonnin 2250

"Analysis of a Small Break Loss-Of-Coolant Accident of Pressurized Water Reactor by APROS"
S. Al-Falahi, M. Hanninen and K. Porkholm 2263

"Evaluation and Assessment of Reflooding Models in RELAP5/MOD 2.5 and RELAP5/MOD3 Codes Using Lehigh University and PSI-Neptune Bundle Experimental Data"
M. Sencar and N. Aksan 2280

"Overview on CSNI Separate Effects Tests Validation Matrix"
N. Aksan, F. D'Auria, H. Glaeser, R. Pochard, C. Richards and A. Sjoberg 2303

"RELAP5 Analyses of Two Hypothetical Flow Reversal Events for the Advanced Neutron Source Reactor"
N.C.J. Chen, M.W. Wendel and G.L. Yoder 2335

"MELCOR Benchmarking Against Integral Severe Fuel Damage Tests"
I.K. Madni 2349

"Validation of the THIRMAL-1 Melt-Water Interaction Code"
C.C. Chu, J.J. Sienicki and B.W. Spencer 2359

"Experimental Assessment of Computer Codes Used for Safety Analysis of Integral Reactors"
A.A. Falkov, V.S. Kuul, O.B. Samoilov, A.N. Lepekhin and G.N. Polyansky 2384

"Assessment of the SE2-ANL Code Using EBR-II Temperature Measurements"
W.S. Yang and A.M. Yacout 2394

"RELAP5 Model to Simulate the Thermal-Hydraulic Effects of Grid Spacers and Cladding Rupture During Reflood"
C.K. Nithianandan, J.A. Klingenfus and S.S. Reilly 2410

"Validation of Advanced NSSS Simulator Model for Loss-of-Coolant Accidents"
S.P. Kao, S.K. Chang and H.C. Huang 2428

"Severe Accident Simulation at Olkiluoto"
H. Tirkkonen, T. Saarenpaa and L-C Po 2438

VOLUME IV

Session 17 - CHF MODELING AND PREDICTIONS

"The Sudden Coalescence Model of the Boiling Crisis"
P.M. Carrica and A. Clausse 2453

"Role of Heater Thermal Response in Reactor Thermal Limits During Oscillatory Two-Phase Flows"
A.E. Ruggles, A.D. Vasil'ev, N.W. Brown and M.W. Wendel 2470

"Methodology For the Study of the Boiling Crisis in a Nuclear Fuel Bundle"
F. de Crecy and D. Juhel 2480

"An Investigation of Transition Boiling Mechanisms of Subcooled Water Under Forced Convective Conditions"
K-W Lee and S-Y Lee 2489

"A Formal Approach For the Prediction of the Critical Heat Flux in Subcooled Water"
C. Lombardi 2506

"A Comparison of CHF Between Tubes and Annuli Under PWR Thermal Hydraulic Conditions"
C. Herer, A. Souyri and J. Garnier 2519

"New Model for Burnout Prediction in Channels of Various Cross Section"
V.P. Bobkov, N.V. Kozina, V.N. Vinogradov and O.A. Zyatnina 2539

"On the Look-Up Tables For the Critical Heat Flux in Tubes (History and Problems)"
P.L. Kirillov and I.P. Smogalev 2558

"A Comparison of Critical Heat Flux in Tubes and Bilaterally Heated Annuli"
S. Doerffer, D.C. Groeneveld and S.C. Cheng 2583

"Experience Using Individually Supplied Heater Rods in Critical Power Testing of Advanced BWR Fuel"
M. Majed, G. Norback, P. Wiman, G.I. Hadaller, R.C. Hayes and F. Stern 2608

"CHF Considerations for Highly Moderated 100% MOX Fueled PWRs"
D. Saphier and P. Raymond 2621

"General Correlation for Prediction of Critical Heat Flux Ratio in Water Cooled Channels"
R. Pernica and J. Cizek 2636

Session 18 - THERMAL-HYDRAULIC COUPLING IN REACTOR SYSTEMS

"A Study of the Effect of Space-Dependent Neutronics on Stochastically-Induced Bifurcations in BWR Dynamics(*)"
G. Th. Analytis 2654

"Analysis of the Return to Power Scenario Following a LBLOCA in a PWR"
R Macian T.N. Tyler and J.H. Mahaffy 2669

'Stability Analysis of BWR Nuclear-Coupled Thermal-Hydraulics Using a Simple Model"
A.A. Karve, Rizwan-uddin and J.J. Dorning 2677

"Coupled Calculation of the Radiological Release and the Thermal-Hydraulic Behaviour of a 3-Loop PWR After a SGTR by Means of the Code RELAP5"
W. Van Hove, K. Van Laeken, L. Bartsoen, B. Centner and L. Vanhoenacker 2704

Session 19 - SUBCHANNEL THERMAL-HYDRAULICS

"Analysis of Two-Phase Flow Inter-Subchannel Mass and Momentum Exchanges by the Two-Fluid Model Approach"
H. Ninokata, A. Deguchi and A. Kawahara 2721

"Large Scale Transport Across Narrow Gaps in Rod Bundles"
M.S. Guellouz and S. Tavoularis 2738

"Void Fraction Distribution in a Heated Rod Bundle Under Flow Stagnation Conditions"
V.A. Herrero, G. Guido-Lavalle and A. Clausse 2762

"Numerical Determination of the Lateral Loss Coefficients for Subchannel Analysis in Nuclear Fuel Bundles"
S. Kim and G-C Park 2773

Session 20 - THERMAL-HYDRAULICS OF REACTOR SYSTEMS AND COMPONENTS

"The Low-Power Low-Pressure Flow Resonance in a Natural Circulation Cooled BWR"
T.H.J.J. van der Hagen and A.J.C. Stekelenburg 2785

"Flow Characteristics of Korea Multi-Purpose Research Reactor"
H. Kim, H.T. Chae, B.J. Jun and J.B. Lee 2786

"Analysis of Steam Generator Loss-Of-Feedwater Experiments with APROS and RELAP5/MOD3.1 Computer Codes"
E. Virtanen, T. Haapalehto and J. Kouhia 2806

"Horizontal Steam Generator Thermal-Hydraulics"
O. Ubra and M. Doubek 2815

Session 21 - THERMAL-HYDRAULICS TEST FACILITIES

"ISP33 Standard Problem on the Pactel Facility"
H. Purhonen, J. Kouhia and H. Kalli 2834

"SPES-2, An Experimental Program to Support the AP600 Development"
M. Tarantini and C. Medich 2841

"PWR-Related Integral Safety Experiments in the PKL III Test Facility - SBLOCA Under Beyond-Design-Basis Accident Conditions"
P. Weber, K.J. Umminger and B. Schoen 2856

"SPES-2, AP600 Integral System Test S01007 2" CL to Core Make-Up Tank Pressure Balance Line Break"
M. Bacchiani, C. Medich, M. Rigamonti, O. Vescovi, A. Alemberti and L.E. Conway 2869

"Investigations on the Thermal-Hydraulics of a Natural Circulation Cooled BWR Fuel Assembly"
H.V. Kok, T.H.J.J. van der Hagen and R.F. Mudde 2884

"Physical Modelling of a Rapid Boron Dilution Transient"
N.G. Andersson, B. Hemstrom, R. Karlsson and S. Jacobson 2895

"Further Evaluation of the CSNI Separate Effect Test Activity"
F. D'Auria, S.N. Aksan, H. Glaeser, A. Sjoberg, R. Pochard and J. Lillington 2904

"Water Hammer Phenomena Occurring in Nuclear Power Installations While Filling Horizontal Pipe Containing Saturated Steam With Liquid"
Y.F. Selivanov, P.L. Kirillov and A.D. Yefanov 2916

Session 22 - THERMAL-HYDRAULICS AND SAFETY OF NONCOMMERCIAL REACTORS

"Natural Circulation Analysis for the Advanced Neutron Source Reactor Refueling Process II"
R.F. Tucker, S. Dasaradhi, Y. Elkassabgi and G.L. Yoder 2924

"Cold Source Vessel Development For the Advanced Neutron Source"
P.T. Williams and A.T. Lucas 2941

"Modeling and Analysis of Thermal-Hydraulic Response of U-Al Reactor Fuel Plates Under Transient Heatup Conditions"
S.N. Valenti, T. Fuketa, S.H. Kim, V. Georgevich, R.P. Taleyarkhan, K. Soyama, K. Ishijima and T. Kodaira 2957

"Study on Severe Accident Fuel Dispersion Behavior in the ANS Reactor at ORNL"
S.H. Kim, R.P. Taleyarkhan, S.N. Valenti, V. Georgevich and J. Y. Xiang 2977

"The Phebus FP Thermal-Hydraulic Analysis with MELCOR"
K. Akagane, Y. Kiso T. Fukahori and M. Yoshino 2994

"Flow Excursion Time Scales in the Advanced Neutron Source Reactor"
C.D. Sulfredge 3003

"Thermal-Hydraulics of Wave Propagation and Pressure Distribution Under Hypothetical Fuel-Coolant-Interaction Conditions in the ANS Reactor"
R.P. Taleyarkhan, V. Georgevich, S.N. Valenti and S.H. Kim 3028

"Modeling and Analysis Framework for Core Damage Propagation During Flow-Blockage Initiated Accidents in the ANS Reactor at ORNL"
S.H. Kim, R.P. Taleyarkhan, S.N. Valenti and V. Georgevich 3052

Session 23 - MIXING AND TURBULENCE

"Turbulent Mixed Convection in Vertical and Inclined Flat Channels with the Aiding Flows"
P. Poskas, J. Vilemas, E. Adomaitis, G. Bartkus 3073

"Mixing Phenomena of Interest to Boron Dilution During Small Break LOCAs in PWRs"
H.P. Nourbakhsh and Z. Cheng 3083

"Numerical Boron Mixing Studies for Loviisa Nuclear Power Plant "
P. Gango 3096

"Turbulence Prediction in Two-Dimensional Bundle Flows Using Large Eddy Simulation"
W.A. Ibrahim and Y.A. Hassan 3120

Session 24 - LOCAL FLOW AND HEAT TRANSFER PHENOMENA IN REACTOR CHANNELS

"Statistical Parameter Characteristics of Gas-Phase Fluctuations for Gas-Liquid Intermittent Flow
G. Matsui, H. Monji and M. Takaguchi 3142

"3-D Flow Analyses for Design of Nuclear Fuel Spacer"
Z. Karoutas, C-Y Gu and B. Scholin 3153

"Bubble Behaviour and Mean Diameter in Subcooled Flow Boiling"
O. Zeitoun and M. Shoukri 3175

"Correlation of Critical Heat Flux Data for Uniform Tubes"
T. Jafri, T.J. Dougherty and B.W. Yang 3197

* "A Model of Film Boiling in the Presence of Electric Fields"
P.M. Carrica, V. Masson, A. Clausse, P. DiMarco and W. Grassi 3218

** "A Simple Delay Model for Two-Phase Flow Dynamics"
A. Clausse, D.F. Delmastro and L.E. Juanico 3232

* Paper assigned to Session 14 in the Conference Program
** Paper assigned to Session 11-3 in the Conference Program

PREFACE

Welcome to Saratoga Springs, the place of the first of the NURETH meetings, held in 1980. Since this first meeting, the NURETH series have included: Santa Barbara, California in 1983, Newport, Rhode Island in 1985, Karlsruhe, Germany in 1989, Salt Lake City, Utah in 1992 and Grenoble, France in 1993. Now, after fifteen years, the seventh of the NURETH meetings is being held again in the birth place of the series.

As you probable know, the NURETH meetings have been initiated and sponsored or co-sponsored by the Thermal-Hydraulics Division of the American Nuclear Society. The TH Division has clearly become a leader in establishing and maintaining high technical standards regarding topical meetings in the field of nuclear thermal-hydraulics, paper acceptance criteria for such meetings, and promoting international cooperation and exchange. In particular, the papers accepted for presentation at NURETH-7 and published in these volumes have been thoroughly reviewed by leading experts in their respective fields. Their work, as well as the efforts of the session organizers, are the cornerstones of the high technical quality of this meeting.

The present conference has been organized by the Northeastern New York Section of the American Nuclear Society. In addition, the following organizations have agreed to join the ANS Thermal Hydraulics Division as co-sponsors of NURETH-7: American Institute of Chemical Engineers (AIChE), American Society of Mechanical Engineers (ASME), Canadian Nuclear Society (CNS), European Nuclear Society (ENS), Japanese Nuclear Society (JNS), Japanese Society of Multiphase Flow (JSMF) and the U.S. Nuclear Regulatory Commission.

Except for the invited papers in the plenary session, all the other papers are contributed. They have been divided into twenty-four major topics. These topics cover all major areas of nuclear thermal-hydraulics.

The theme of the NURETH-7 conference is ***Thermal-Hydraulics for the 21st Century***. This theme has been implemented in the program of the meeting through technical papers covering areas such as: progress in analytical and experimental work on the fundamentals of nuclear thermal-hydraulics, the development of advanced mathematical and numerical methods, and the application of advancements in the field in the development of novel reactor concepts. Because of the complex nature of nuclear reactors and power plants, several papers deal with the combined issues of thermal-hydraulics and reactor/power-plant safety, core neutronics and/or radiation.

I hope that both the conference participants and other future readers of this multi-volume edition of NURETH-7 Proceedings will find several new and innovative ideas as the results of the work by the authors representing an outstanding international community of experts from academia and industry.

On behalf of the organizing committee I invite you to actively participate in the conference and wish you a pleasant stay in Saratoga Springs.

Michael Z. Podowski
Technical Program Chairman

ACKNOWLEDGMENTS

The efforts of the authors of both invited and contributed papers included in this volume are gratefully acknowledged. Also acknowledged is the cooperation of the members of the Technical Program Committee and the Scientific Advisory Committee who helped to organize the technical program of the meeting and accomplish its scientific objectives. Special thanks are extended to the session organizers and paper reviewers.

Finally, appreciation is expressed to the U.S. Nuclear Regulatory Commission for their support of the publication of the Proceedings.

ON HEAT TRANSFER CHARACTERISTICS OF REAL AND SIMULANT MELT POOL EXPERIMENTS

T.N. Dinh, R.R. Nourgaliev and B.R. Sehgal

Royal Institute of Technology, Division of Nuclear Power Safety
Brinellvägen 60, 10044 STOCKHOLM, SWEDEN
Fax:(46) (8) 790-76-78, e-mail: nam@ne.kth.se

Abstract

The paper presents results of analytical studies of natural convection heat transfer in scaled and/or simulant melt pool experiments related to the PWR in-vessel melt retention issue. Specific reactor-scale effects of a large decay-heated core melt pool in the reactor pressure vessel lower plenum are first reviewed, and then the current analytical capability of describing physical processes under prototypical situations is examined. Experiments and experimental approaches are analysed by focusing on their ability to represent prototypical situations. Calculations are carried out in order to assess the significance of some selected effects, including variations in melt properties, pool geometry and heating conditions. Rayleigh numbers in the present analysis are limited to 10^{12}, where uncertainties in turbulence modeling are not overriding other uncertainties. The effects of fluid Prandtl number on heat transfer to the lowermost part of cooled pool walls are examined for square and semicircular cavities. Calculations are performed also to explore limitations of using side-wall heating and direct electrical heating in reproducing the physical picture of interest. Needs for further experimental and analytical efforts are discussed as well.

1 PHENOMENA AND MODELING

A large melt pool might form in the reactor core, in the lower plenum of the reactor pressure vessel, or in the containment, during a severe light water reactor accident. Most notably at the moment, the feasibility of external vessel flooding as a severe accident management measure, and the phenomena affecting the success in retaining molten core material inside the vessel, are under active study. For this case, the assessment of the potential for a vessel-coolant heat transfer crisis and a subsequent vessel failure requires knowledge of heat transfer from the melt pool to the vessel lower head wall. The local heat fluxes are of specific importance. Despite the fact that some experimental studies have been performed, it is not possible to experiment with the real situation involving large scales [1], different three-dimensional geometries of the reactor lower head and melt pool and real core melt properties (small Prandtl number, temperature-dependent properties, non-Newtonian fluid). In order to confirm the reactor applicability of the experimental results obtained with simulant materials in various lower head models, there is a clear need for *confirmatory experimental and analytical studies.*

The phenomenology of the issue involves a wide spectrum of physical processes. A comprehensive overview of reactor-specific features and related phenomena can be found in Ref.[1].

[1] The most important scaling criterion are the Rayleigh numbers (Ra), which are proportional to length scale (H) in power of 5, $Ra \propto H^5$.

Large uncertainties are associated with in-vessel accident progression and phenomena (volume and composition of core melt pools, stratification of melt, physico-chemistry of core melt-vessel interaction, late in-vessel water supply above the pools). The safety margins available, and thereby also the *acceptable* uncertainty level, depend strongly on the reactor design under consideration. A systematic approach to problem resolution by the ROAAM was presented in Ref.[2], analysing the effects of a metallic top layer, core melt natural convection heat transfer, thermal and mechanical behavior of vessel lower head, and ex-vessel boiling heat transfer.

Numerical studies of natural convection heat transfer in large self-heated liquid pools have been limited to the *two-dimensional* formulation [3],[4],[5],[6]. In addition, natural convection flows in internally heated cavities distinguish from external natural convection flows by consisting of unsteady multi-vortex flow fields in the region near the top wall and stably stratified layers near the bottom wall; see observations by the holographic interferometry in Refs.[3],[4]. Consequently, the fluid flow problems in question require the use of fine computational grids and mesh organization in such a way that locally significant flow variations are properly modeled. The physics and modeling aspects of turbulent convection in large volumetrically heated liquid pools are discussed in detail in Ref.[7]. Only a summary of computational modeling can be given here. Fig. 1 presents results of calculations performed by using different low-Reynolds-number (LRN) $k-\epsilon$ turbulence models for the upper surface of internally heated liquid pools with isothermal surfaces: a square slice in experiments of Steinberner and Reineke [4] and torospherical slices in the COPO experiments [8]. It can be seen that the laminar model is able to predict (with errors less than 25%) heat transfer rates up to the transition-to-turbulence region, i.e. $Ra \sim 10^{12}$ in square cavities. In addition, most of the well-known LRN $k-\epsilon$ turbulence models applied are capable of predicting heat fluxes to the pool's side walls due to the convection-dominated nature of descending flows along cooled vertical surfaces. However, these models fail in describing heat fluxes to the top and, also, to the bottom surface of the liquid pool. It was shown that the turbulent Prandtl number, Pr_t, and turbulent viscosity, ν_t, have to be re-formulated to take into account specific effects of turbulence generation in buoyancy-induced, strongly stably and unstably stratified flows in the lower and upper regions of the liquid pool, respectively [7]. Although some empirical correlations for Pr_t and ν_t (as functions of the local Richardson number) have been proposed to describe data of specific experiments, there exist no reliable methods to predict related reactor-scale processes. The resolution of the in-vessel melt retention issue, up to now, depends on experimental observations, data and correlations, and whether those are relevant to prototypical situations.

In the present paper, we consider natural convection heat transfer regimes, whose Rayleigh numbers are below 10^{12}. Experimental and analytical works have been indicating that internally heated liquid pools behave, in integral sense, in a quite similar way both at high Ra numbers and at low Ra numbers. In fact, the dimensionless heat transfer laws ($Nu_i = f(Ra)$) obtained at lower Rayleigh number were, with success, extended to higher Rayleigh numbers in square cavities and hemi- and torospherical pools [4], [8],[9],[10]. The differences are within the uncertainties. Thus, the trends observed at low Ra numbers may hold at higher Ra numbers also. That is why it is not irrelevant to establish the integral picture for $Ra = 10^{12}$, where the uncertainties of the turbulence model are not overriding other uncertainties. Also, since the real material tests have been and probably will continue to be performed at small scales with Rayleigh numbers limited to 10^{12}, it is crucial to assess their scaling and design effects (e.g., Lorentz force, side-wall heating, melt properties). Similar analyses have to be performed for higher Rayleigh number conditions ($10^{14} - 10^{16}$), after a reliable turbulence model has been developed and validated against the existing data base. In this context, one can utilize the computational approach that has been found suitable for low Rayleigh numbers.

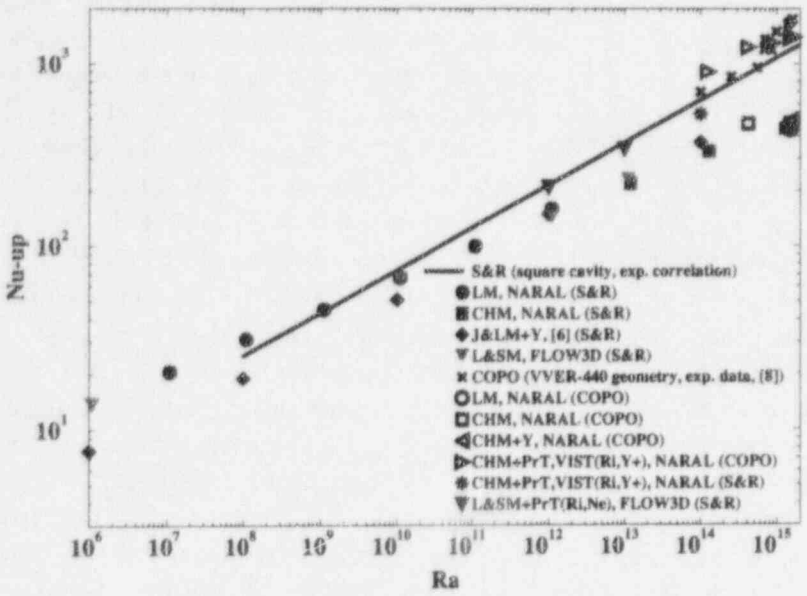

Figure 1: Calculational results vs. experiments for internally heated *water* pools.

2 POTENTIAL EFFECTS OF NON-PROTOTYPICAL CONDITIONS

Experimental investigations of heat transfer under conditions of interest might be classified into two main groups: (i) *simulant experiments* and (ii) *small-scale real material tests.*

In the past, simulant experiments of the first group were conducted at low Rayleigh numbers, except for the Steinberner and Reineke experiments in square cavities [4], where Ra numbers were up to $3 \cdot 10^{13}$. Related natural convection heat transfer experiments were carried out in internally heated fluid layers, square and semicircular cavities with isothermal walls (see e.g. Refs.[1],[9],[10], for relevant reviews). Even though several three-dimensional experimental studies have been performed, uniformity of volumetric heat generation rate and/or conditions of isothermally cooled top, side and bottom surfaces were not achieved in such experiments. From the *heat transfer* point of view, most experiments were two-dimensional, with adiabatic face and back surfaces. Since the previous simulant experiments are not necessarily - in every detail - representative of a molten corium in the pressure vessel bottom head, new simulant experiments have recently been pursued. Heat transfer data were obtained for high Rayleigh number conditions ($10^4 < Ra < 10^{16}$) in the two-dimensional torospherical slices of the COPO experiments [8] and in the three-dimensional hemispherical pool of the UCLA experiments [10]. Such simulant experiments employ water (Pr = 2.7-7.2) or Freon R-113 (Pr = 5.2-13) as working fluids. Some other simulants (salts, glass-type oxidic melts) have also been considered, yet such experiments have not been carried out so far. Also, there exist other uncertainties related to physical properties of core melts such as multi-component and non-Newtonial fluid behavior, and temperature dependence of core melt properties. Perhaps in future, when related core melt data and observations will become available, such effects could be accounted for in experimental modeling by selection of appropriate simulants. In general, simulant material experiments have

many advantages as they are inexpensive, easy in performance and can provide quantitative heat transfer data. In addition, the convection conditions can be made free of several potential distortions (Rayleigh numbers, geometry, heating methods), compared to reactor situations.

The second group is formed by small-scale experiments, employing various oxidic/metallic compositions of the prototypical core melt as the working fluid. Such experiments have a confirmatory character rather than providing data needed for natural convection heat transfer [1]. Earlier small-scale experiments using joule-heating of molten UO_2 at Argonne National Laboratory (ANL) had found higher downward heat fluxes than what had been predicted on the basis of correlations developed using low temperature simulant liquids [11], [12]. Explanations of such discrepancies were given to radiation properties of pure molten UO_2, Lorentz forces and heat generation in the lower crust. In contrast, enhanced upward heat flux was observed in in-core small-scale experiments with 5 kg molten UO_2 at Cadarache (France) [13]. Several mechanisms have been proposed to explain the data [13],[14]. Core melt experiments, as a rule, are small-scale and comprise significant distortions due to pool geometry and heating methods applied, not to mention the fact that such experiments can suffer from uncertainties in measurement and data reduction, definition of the real geometry of crust-surrounded melt pools, and knowledge of the high-temperature melt properties. Also, there are possibilities of gas gap formation between the top crust (anchored to the vessel wall) and free surface of small-scale melt pools. Concerning also other aspects than natural convection flows and heat transfer, there exist uncertainties in predicting the behavior of multi-component melt under high Ra number and low Ra number conditions [14]. While changing the physico-chemistry of core melt-vessel interaction by possible precipitation of the denser phase near cold boundaries, the low-Rayleigh-number natural convection would also promote component stratification and affect strength characteristics of the core melt crust.

Despite the potential problems, one has to acknowledge the importance of experiments with prototypical core melt, providing more confidence in the current understanding of the general physical picture. Even though there are no exist straight-forward methods to control important phenomena (such as non-Newtonian fluid behavior and temperature dependent properties, etc.) in experiments with prototypic core melts, their results are crucial to validate the simulant experiments. For example, sould the results from the real material experiments verify natural convection heat transfer correlations obtained in simulant, Newtonian fluid-experiments, one could conclude insignificance of such *specific* effects (non-Newtonian fluid, temperature-dependent properties) in reactor-scale melt pools, where Rayleigh numbers are higher and, therefore, turbulence dominates the flow behavior. In particular, such real material tests are to be performed in the RASPLAV program under the OECD/NEA sponsorship [15]. Oxidic/metallic core melts will be employed as working fluids in the small-scale natural convection heat transfer experiments (Ra numbers are limited to 10^{10}). The direct electrical heating and side-wall heating are being considered as methods for simulating decay power generation in core melts. Both a semicircular slice and a hemispherical pool are included as test sections. Several aspects determining the relevance and usefulness of such natural convection heat transfer experiments may be foreseen: the uniformity of power generation rate, the absence of gas gap formation and melt-vessel physico-chemical interaction during flow development and heating transients, the sufficiency of melt superheat over freezing point (to avoid mushy regime), the influence of secondary effects on natural convection flows and heat transfer (Lorentz force or side-wall heating, two-dimensionality of test sections).

It is clear from the above considerations that careful scaling and other design considerations are crucial for planning and analysis of the core melt tests, and to assess the applicability of simulant experiments to prototypical situations. In general, one has to consider three classes of

experimental scaling and design effects, caused by (1) *physical properties of working fluids*, (2) *geometrical peculiarities of liquid pools*, and (3) *boundary, heating and transient conditions*.

3 QUANTIFICATION OF SELECTED PHENOMENA

In this section, we discuss in more detail some *selected* experimental vs. reactor processes. Calculations have been performed to examine the effects of using simulant materials and small scales. However, since no well validated turbulence model for natural convection with high Rayleigh number is available, numerical studies are limited so far to the range of $Ra < 10^{12}$. The NARAL-2D program has been employed to produce most of the results presented in the paper. In the NARAL code, the set of mean flow equations in complex domains is solved by using the technique of two-dimensional algebraic coordinate transformation developed earlier and described elsewhere [16]. The control volume methodology and the SIMPLE solution procedure for pressure-linked equations [17] are adopted for numerical treatment. The dependent variables are the contravariant velocities, pressure and temperature. The NARAL code results have been compared to natural convection experiments of heat generating fluid (radioactive tritium) in closed vertical cylinders with Ra numbers ranging from 10^3 to 10^6, as well as experiments of the volumetrically heated semicircular cavity of Jahn and Reineke with Ra numbers up to $5 \cdot 10^{11}$ [3]. The NARAL model has successfully predicted the average Nu numbers on all isothermal walls of an internally heated square cavity for Ra numbers up to 10^{11}. Further, the calculated local heat fluxes are in good agreement with available experimental data [7]. A picture of the computational errors can be obtained from Figures 2,3 and 4, which present the calculational results of the average top, side and bottom Nusselt numbers in square cavities (water, aspect ratio 1:1). One can see that, for Rayleigh numbers up to 10^{12}, the discrepancies between the calculated results (*water* line, $Pr = 7$) and the experimental correlations are not larger than 25% for Nu_{up} or 12% for Nu_{sd} and Nu_{dn}. The general CFD program CFDS-FLOW3D [18] also has been used to calculate 3D flows when such computations are required. The laminar model of FLOW3D in semicircular cavities has been subjected to extended validation efforts [7]. Transient simulations are used in the computational modeling, and aspects of flow development and stabilization are taken into account as well.

3.1 Physical properties of working fluids

In a real reactor situation, some aspects of the melt properties might have a unique effect on natural convection heat transfer in a large melt pool. Firstly, the Prandtl number of the core melt can be much lower than that of simulant material used in experiments, which will lead, in the reactor case, to a thicker thermal boundary layer, smaller temperature gradients and less significant stratification effects. A separate reactor-specific consideration of the thermal and dynamic boundary layers is thus needed. Secondly, in near-wall (crust) regions the melt viscosity can change two or three orders of magnitude due to the melt temperature approaching the solidus point. This phenomenon causes an additional laminarization, makes the effect of unstable stratification less important and affects the heat flux distribution.

3.1.1 Fluid Prandtl number

In order to examine the effects of the fluid Prandtl number, we have carried out computations for natural convection heat transfer in **square cavities**. General tendencies were obtained by systematic examinations for $Pr = 0.08, 0.8, 1.2, 2$ and 7. The benchmark problem is the *water* ($Pr = 7$) experiments and experimental correlations (validated up to $Ra = 10^{14}$ and presented in the paper of Steinberner and Reineke [4]) in the range of the Rayleigh number from 10^6 to 10^{12}. In the same range of the Rayleigh number, computations were carried out for *core melt* pools, employing oxidic core melt (Corium-A, $Pr = 0.8$) and oxidic/metallic core melt (Corium-B, Corium-C, $Pr = 0.08$) as the working fluids. From the figures, one can see a good agreement of the calculated Nusselt numbers with experimental correlations obtained from water experiments. Also, for the range of applications, the experimental correlations, $Nu_{up} = f(Ra)$ and $Nu_{sd} = f(Ra)$, derived from the above-mentioned water experiments, are suitable for presenting calculated data for fluids with much lower Prandtl numbers [2]. Underpredictions (see Figs. 2,3) of *corium* curves compared to *water* curve are not more than 25%. More importantly, the curves do not diverge with increasing Rayleigh numbers. In contrast to this, significant effects of the fluid Prandtl number were observed for the bottom surface, Fig. 4. Higher Nusselt numbers to the bottom surface (as much as two times for $Ra = 10^{12}$) are related to both the physics of stably stratified layers in the lower region of the melt pool and to the decrease of heat fluxes to the top and side surfaces, which can affect the heat flux to the bottom surface through the energy balance. Since heat conduction is the dominant mechanism of heat transfer from strongly stably stratified layers to the bottom surface, a relative increase in heat conductivity due to decrease of the Prandtl number is able to intensify heat transfer rates to the bottom surface. This effect of stable stratification is defined here as the α-phenomenon. Another significant effect, named as the ν-phenomenon, was observed at peripheral regions, where boundary descending flows penetrate into the stably stratified layers. The lower are the viscosities ν of the fluid layers (i.e. fluid Prandtl numbers), the easier it is for descending flows to destabilize such layers, and the more heat is transferred to the bottom cooled wall. This physical picture can be seen in Fig. 5, depicting local Nusselt numbers for different Prandtl numbers. The higher are the Rayleigh numbers (due to higher coefficient of thermal expansion, for example), the stronger is the effect of stable stratification (Ri), and, therefore, the effect of the fluid Prandtl number. Most notably, the relationship between the Prandtl number and its effect (for the considered range of Pr 0.08-7) is not linear. A more or less sudden change is observed between $Pr = 0.5$-1.

Calculations have been performed also for **semicircular cavities** with Rayleigh numbers up to 10^{12}. Similarly, α and ν-phenomena were observed at the lowermost part of the semicircular cavity and at regions of interaction between descending flows and stably stratified layers (angle $\theta < 30^{\circ}$), respectively (see Figs. 6-7). Areas where α-phenomenon dominates are decreased wit' ncreasing Rayleigh number. For the bottom part of semicircular cavities ($\theta < 30^{\circ}$), the io between local Nusselt numbers calculated for $Pr = 7$ and $Pr = 0.6$ increases with inc. ıg Rayleigh number in the examined range of $Ra = 10^9 - 10^{12}$. Penetration of descending flow. :o the stably stratified layers in a melt pool with $Pr = 0.6$ can be seen from Fig. 8, depicting temperature field results calculated for $Ra = 10^{10}$. Calculations performed for the **torospherical slice cavity** have also confirmed the above observations for square and semicircular cavities. As can be foreseen, the α-phenomenon areas in torospherical cavity were larger than those of semicircular cavities. Also, the ν-phenomenon effects on the curved surface of the torospherical cavity are qualitatively similar to those of the semicircular cavity.

[2] For Corium-B and Corium-C, the fluid Prandtl numbers are the same, but corresponding values of kinematic viscosity, ν, and thermal diffusivity, α, of the fluids differ as much as three times. However, the Nusselt numbers are unchanged, indicating universality of the fluid Prandtl number for problems considered (see Figs. 2,3 and 4).

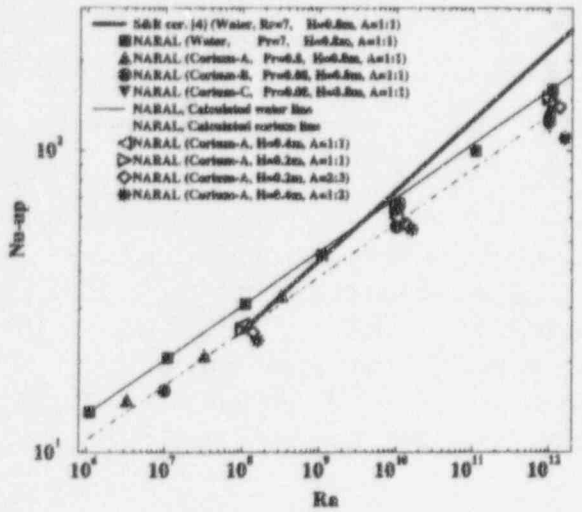

Figure 2: Effects of the fluid Prandtl number: the Nusselt number for the top surface of square cavity.

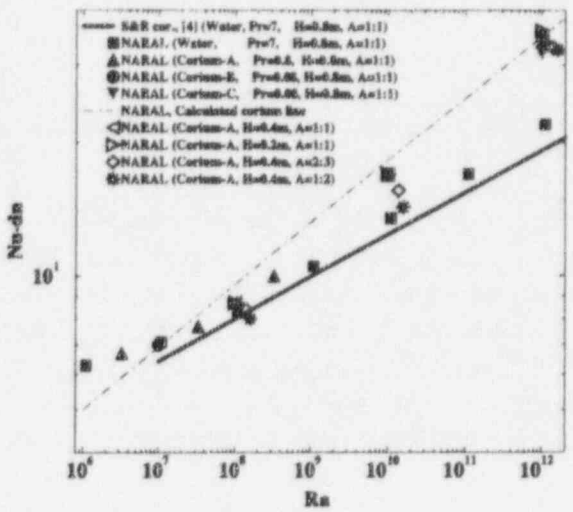

Figure 4: Effects of the fluid Prandtl number: the Nusselt number for the bottom surface of square cavity.

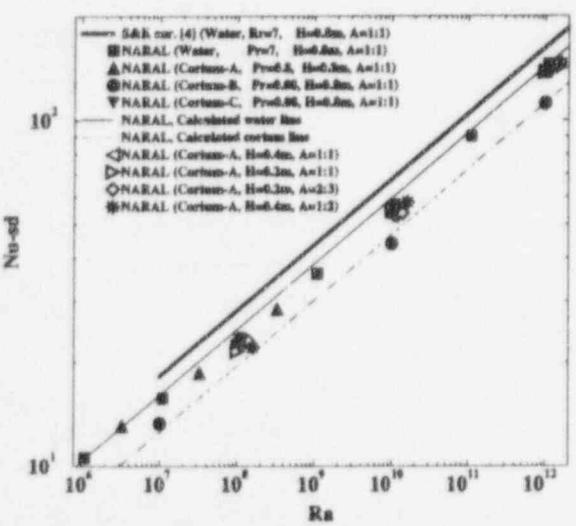

Figure 3: Effects of the fluid Prandtl number: the Nusselt number for the side-wall surface of square cavity.

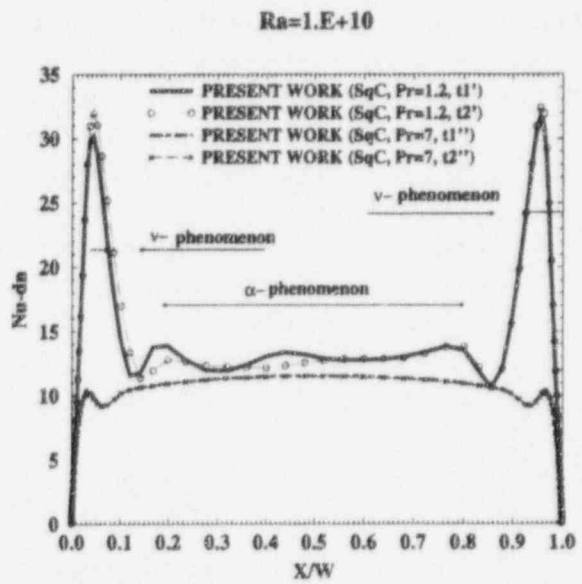

Figure 5: Local Nusselt numbers for the bottom surface of square cavity. Calculations for $Ra = 10^{10}$.

It can be concluded for the examined range of Rayleigh numbers that the relative effects of α-phenomenon on heat transfer characteristics are less than those of ν-phenomenon. Because no experimental data are available for low-Prandtl-number fluids typical for core melt, there are clear needs for well-defined core melt experiments and/or simulant experiments employing low-Prandtl-number fluids.

3.1.2 Temperature dependence of melt viscosity

In order to estimate the effects of temperature dependence of fluid viscosity, additional computations have been performed for a core melt, whose viscosity is considered to change drastically in the mushy region, ΔT_{mushy}, near the temperature, $T_{mp,f}$, of the freezing boundary of melt pools. This phenomenon is represented by the second term of correlation (1). Thus, the viscosity of Corium-D is changed to about 100 times higher in the temperature range of about 10K near the solidus point, $T_{mp,f} = 2850$K. The first term of correlation (1) is based on similar correlations that have been widely used in reactor safety studies; see e.g. [19].

$$\mu(T) = \mu_{liquid} + \mu_{mushy} = 1.675 \cdot 10^{-4} \cdot exp\left(\frac{9848}{T}\right) + 4.23 \cdot 10^{-1} \cdot exp(T_{mp,f} - T) \quad (1)$$

Table 1 presents the Nusselt numbers, Damköhler numbers and temperature range, ΔT_{max}, of melt pools for both constant and variant viscosities, μ. The Damköhler numbers as well as inverse temperature difference, $\frac{1}{\Delta T_{max}}$, represent level of mixing in liquid pools. Some decrease of the Nusselt numbers ($\sim 20\%$) can be seen for the case with lower melt superheats (larger height and lower heat generation rates for the same Ra number, $Ra = 10^{12}$). For *small-scale core melt experiments*, the calculational results indicate that low power generation rates, q_v, in cavities of height 0.2-0.4m (low-Rayleigh-number tests) lead to limited melt superheat above the solidus point, ΔT_{max}, creating large uncertainties in defining bulk viscosity and including significant effects of temperature dependence of melt properties. For *prototypical situations*, we feel that the effects of the temperature dependence of melt viscosity on thermal characteristics (Nu, Da) might have to be considered, should the temperature difference between the solidus and liquidus points (150-200K) be comparable to the temperature range of melt pools, ΔT_{max} (50-250K). Under high Rayleigh number conditions, very good mixing also could occur in the central region of internally heated liquid pools. Therefore, the effects of fluid viscosity are perhaps suppressed in boundary layers. Furthermore, decrease in heat transfer coefficient could be compensated by a corresponding increase in the driving pool temperature difference, leading to only minor viscosity-induced changes to heat flux distribution.

Table 1: Effects of temperature dependence of melt viscosity on the cavity walls Nusselt numbers.

N^o	Fluid	Pr	H, m	$\mu(T)$	Ra	Nu_{up}	Nu_{sd}	Nu_{dn}	Da	$\Delta T_{max}, K$
1	Corium-A	0.8	0.2	*const*	10^{12}	150	138	36	330	136
2	Corium-D	0.9	0.2	Eq.(1)	10^{12}	135	128	34	322	140
3	Corium-A	0.8	0.4	*const*	10^{12}	145	140	34	310	17
4	Corium-D	0.9	0.4	Eq.(1)	10^{12}	120	117	30	275	20

Certainly, similar analyses have to be carried out for reactor-scale Rayleigh-number regimes, as soon as a reliable method of computational modeling is available. Moreover, experiments are needed to examine effects of non-Newtonian fluids and to provide valuable data on natural convection heat transfer of fluids with temperature-dependent viscosity.

3.2 Geometrical effects

Figs. 2,3 and 4 present results of computations performed for Corium-A melt cavities with varying sizes and aspect ratios. For processes in square cavities of the same Rayleigh numbers, the Nusselt and Damköhler numbers remain unchanged for varying heights of cavity (H = 0.2, 0.4, 0.8m), implying that the Rayleigh number is the only representative dimensionless group of natural convection heat transfer, at least, for the fluids with constant physical properties. Small influence (20%) of the aspect ratio were found, when calculating processes in cavities with aspect (height-to-width) ratios 1:1, 2:3 and 1:2. The effects of the lower head geometry (forms, sizes) in molten corium-vessel interaction were estimated elsewhere by using the 2D transformation technique of the NARAL code developed for fluid flow and heat transfer in complex domains [16]. Putting together calculation results, recent experimental data from [8] and [10], and previous experiments in semicircular and square cavities, e.g. [3] and [4], one could imagine that the physics of natural convection heat transfer in internally heated liquid pools is not sensitive to the geometrical factors. In such a case, the relevant data base supporting modeling efforts is wider. However, experiments in liquid pools with representative geometry of reactor lower head are preferred to provide data on local heat flux distributions for reactor applications.

We want to point out that most of the experiments (except for [10]) and analyses performed so far are *two-dimensional*. Fig. 9 presents results of computations by the FLOW3D code [18] performed both two and three-dimensional formulation to investigate influence of three-dimensional slice cavities on heat transfer characteristics. The 3D results (Nu_{3D}) are compared to results of 2D calculations, which assume no flow effects of the adiabatic *face* and *back* walls of the slice cavity. For the case of $Ra = 10^7$ calculated, one can see a significant decrease in the Nusselt number to the *cooled* top and side-wall surfaces, when the slice thickness-to-height ratios of the slice cavities are decreased. It is due to the flow diminishing effects of the *face* and *back* walls. An analysis of calculated 3D flow fields for a number of processes up to $Ra = 10^{10}$ shows that there may exist also other physical mechanisms affecting flow fields of a multi-vortex structure. When narrowing the slice width, the buoyancy-induced vortexes could start interacting, which eventually intensifies the heat transfer rates. It is worth noting here that most slice experiments (low and high Rayleigh number) belong to the affected range of the slice thickness-to-height ratios, $\Delta x/H < 0.25$). The two-dimensional computational modeling is the other extra reason for unsatisfactory comparison between calculated results and data obtained from slice geometry experiments, causing thus additional difficulties in understanding the physics of the processes. However, calculated results, for the range of Rayleigh number up to 10^{12}, create a feeling that the effect of two-dimensionality is limited to 25%. Further 3D numerical studies are planned to assess the effects of two-dimensionality in higher Rayleigh number experiments. Also, three-dimensional experiments can be strongly recommended.

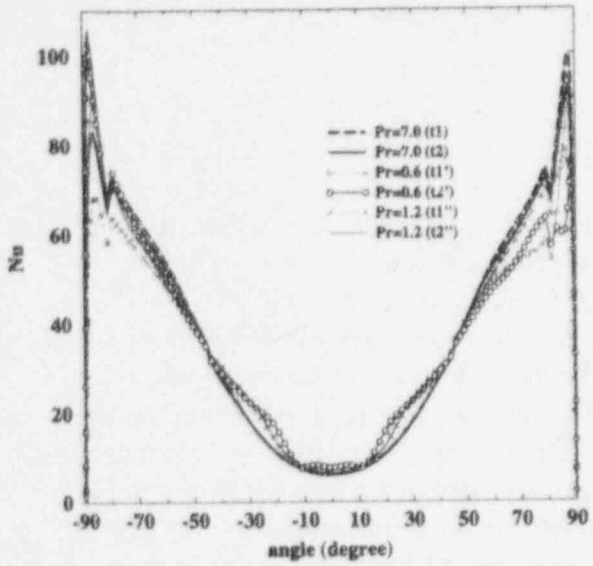

Figure 6: Local Nusselt numbers for the curved surface of semicircular cavity. Calculations for $Ra = 10^{10}$.

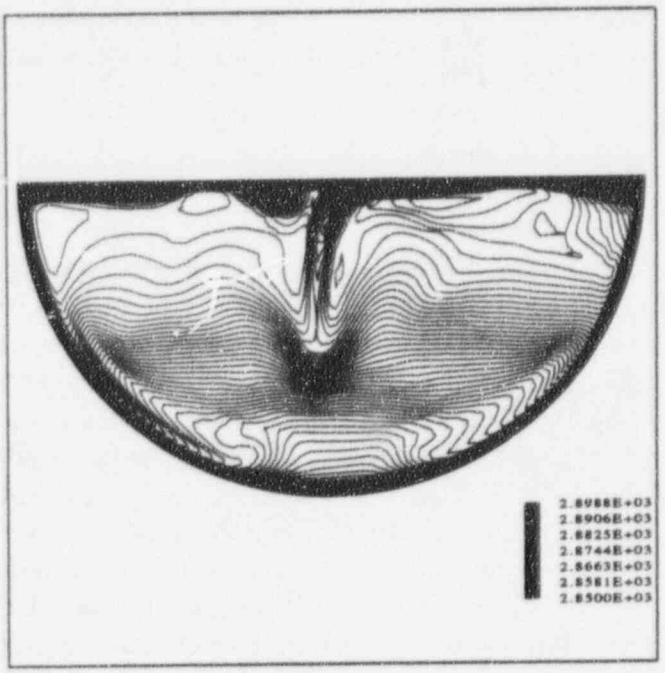

Figure 8: Temperature field in semicircular cavity. Calculation for $Ra = 10^{10}$, $Pr = 0.6$.

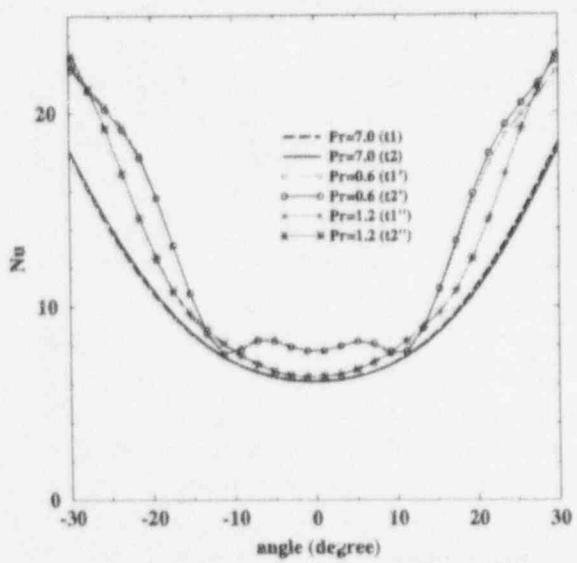

Figure 7: Local Nusselt numbers for the curved surface of semicircular cavity ($\theta < 30°$). Calculations for $Ra = 10^{10}$.

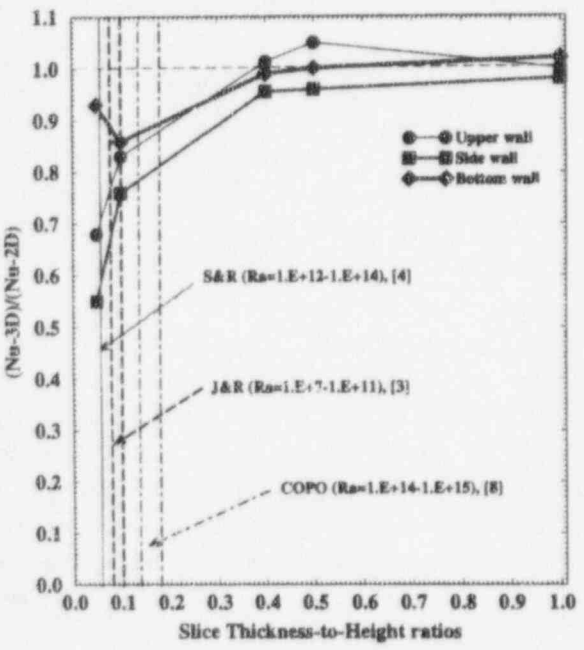

Figure 9: Effects of the three-dimensionality in slice experiments. Calculations for $Ra = 10^7$.

3.3 Boundary, transient and heating conditions

Up to now, no studies have been performed to provide a firm basis for designing experiments with prototypical core melts. Uncertainties and possible distortions may be caused by the boundary, transient and heating conditions of core melt pools. For example, the boundary temperature of a naturally convecting melt pool with freezing is yet to be quantified. An appearance of a gas gap due to anchored top crust in small-scale melt pools, and, therefore, reduced heat transfer rates from the free surface of the melt pool, has to be avoided. It is also known that the smaller is the Rayleigh number, the longer is the time period required for heating transients ($Fo \sim Ra^{-0.2}$) [20]. In this sense, one has to consider competing thermal-hydraulic and physico-chemical processes when planning small-scale core melt experiments. Such considerations are important to understand, interprete and analyse the experimental heat transfer data. In the present paper, we focus attention on effects of heating methods, which, in our opinion, are the dominant factors in designing small-scale core melt experiments.

3.3.1 Flow distortions by heating elements

A number of (electrical, microwave, etc.) methods have been proposed to simulate volumetric power generation in liquid (melt) pool. For high-temperature core melt experiments, the direct electrical heating by alternate currents, inductive heating, or using external and internal heaters, are considered as the most potential technical approaches.

Calculations have been performed for small-scale core melt experiments in slice geometry facilities, using side-wall heating elements. The idea is to examine distortions of flow fields (and heat transfer) due to power supply from the side (*face* and *back*) walls by comparing to the *equivalent-in-power*, $Q = q_v \cdot V = 2q_s \cdot S$, process with internal energy sources. Flow fields in the central planes of slices are shown in Fig. 10 for *internal* heating and in Fig. 11 for *side-wall* heating. It can be seen that flows are descending in the lower core region in case of side-wall heating, and rising in case of internal heating. Temperature fields are also different for two cases (Fig. 12 and Fig. 13). It is clear that the side-wall heating involves two-loop structures with convection-dominated heat transfer to the top and side cooled surfaces. When the slice is deep enough, the Nusselt number to the cooled bottom and side surfaces are similar to those of internal heating. For $Ra = 10^{10}$ and a slice thickness-to-height ratio is 1/4, the Nusselt number to the top surface of the side-wall heated cavity is as much as two times higher than that of an internally heated cavity.

Naturally, the use of an internally installed heating plate could also affect flow fields in the regions near the bottom surface by destroying the stably stratified layers. In this sense, the method of using heating rods has some advantages. Other effects on crust behavior due to its internal heating and heat fluxes from side walls were out of the current modeling efforts. In general, no straight-forward conclusion can be made about the capability of external heating methods or internal heating elements in physical simulation of *natural convection heat transfer in self-heated core melt pools*. The side-wall heating method can be employed in separate effects studies such as examination of downward heat fluxes. For instance, the ν-phenomenon of fluid Prandtl number effect might also be explored in the melt pool with side-wall heating. However, as it can be seen from Figs. 12-13, α-phenomenon would not be reproduced properly in the sidewall-heated melt pool, which involves less stratification in lower regions of the pool. One has to keep in mind the above analysed physical picture in two cases with internal heating and side-wall heating, when interpreting data obtained from the latter one.

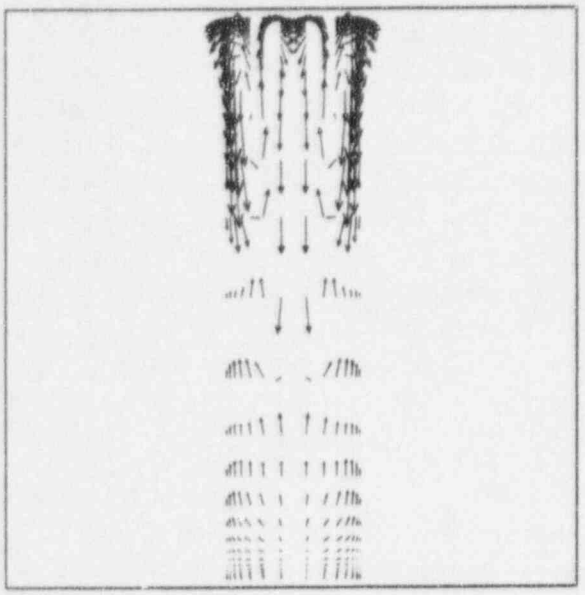

Figure 10: Flow fields in an internally heated core melt pool $Ra = 10^{10}$ (plane $y = W/2$).

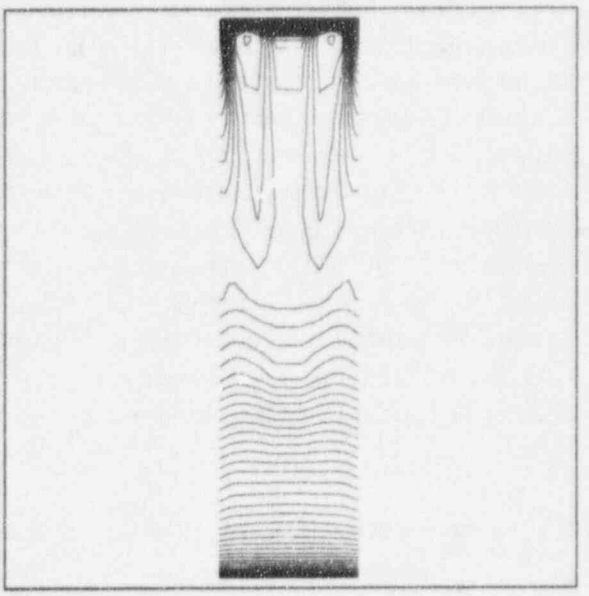

Figure 12: Temperature fields in an internally heated core melt pool $Ra = 10^{10}$ (plane $y = W/2$).

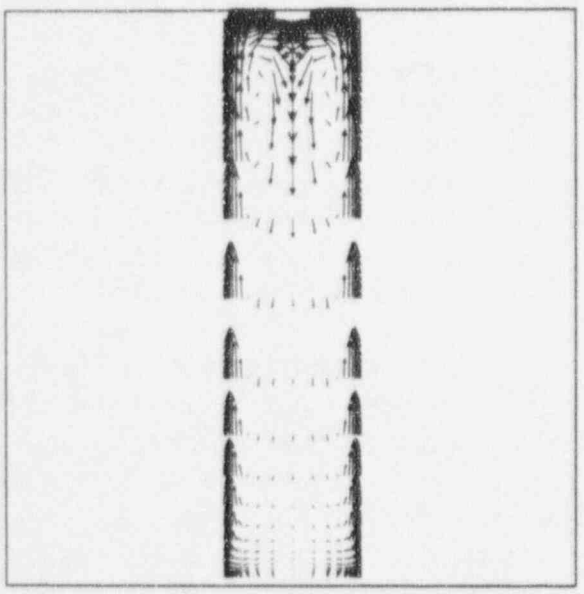

Figure 11: Flow fields in core melt pool with side-wall heating, equivalent to $Ra = 10^{10}$ (plane $y = W/2$).

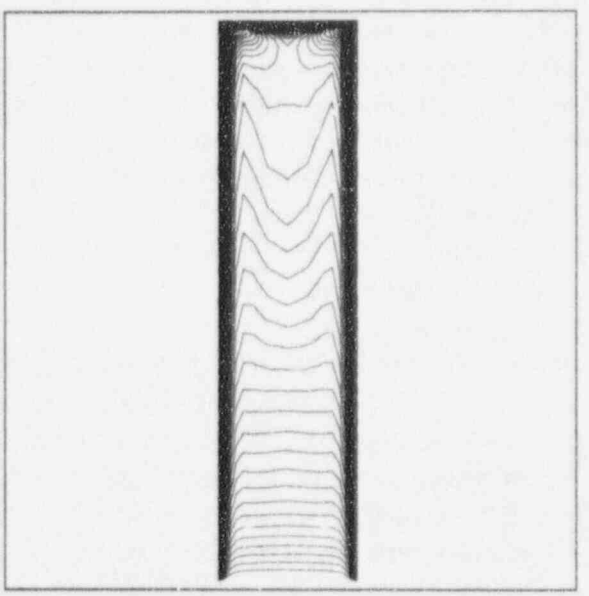

Figure 13: Temperature fields in core melt pool with side-wall heating, equivalent to $Ra = 10^{10}$ (plane $y = W/2$).

3.3.2 Flow distortions by electromagnetic forces

Direct electrical heating is a very useful method to provide internal power generation. At the same time, the electromagnetic field introduces additional body forces. Most notably, the ponderomotive force arises from current crossing magnetic field lines as

$$\mathbf{F} = \mathbf{J} \times \mathbf{B} \tag{2}$$

where $\mathbf{F}$ is the force (N/m^3), $\mathbf{J}$ is the current density (A/m^2), and $\mathbf{B}$ is the magnetic field density (Tesla). The magnetic flux density, $\mathbf{B}$, is calculated as follows

$$\mathbf{B} = \frac{\mu_m}{4\pi} \int \int_V \int \frac{\mathbf{J} \times \mathbf{r}}{r^2} dV \tag{3}$$

In this section, we limit our considerations to a case of a slice-geometry pool with side (*face* and *back*) walls serving as electrodes. An algorithm for calculating the space distribution of the electromagnetic force including those caused by the secondary currents has been developed. Effects of three-dimensionality of the magnetic field induced are assumed negligibly small in this scoping analysis. Then, the program calculates the magnetic flux density in arbitrary 2D domains [Eq.(3)], including square and semicircular cavities. It can be shown that analytical solutions (4) obtained for infinite cylinder can be used to describe the magnetic flux density in the infinite square slab with errors less than 12% for the important components.

$$B_y = -\mu_m \frac{J}{2} \Delta z; \qquad B_z = \mu_m \frac{J}{2} \Delta y \tag{4}$$

where $\Delta z, \Delta y$ are distances from the symmetry point (origin) of the magnetic field, $\mathbf{B}$. When experimenting with water or its salt solutions, the electromagnetic forces are negligibly small due to their electrical conductivities ($\sigma \sim 2 \cdot 10^{-4}\ \Omega^{-1}m^{-1}$ for distilled water and 10^{-2} $\Omega^{-1}m^{-1}$ for water salt solutions). Instead, electrical conductivity for representative core melts can range from 10^3 to $10^5\ \Omega^{-1}m^{-1}$ for oxidic ($UO_2 - ZrO_2$) core melt and metal-rich ($UO_2 - ZrO_2 - Zr - SS$) core melts, respectively. This necessitates an accurate analysis of the effects of the electromagnetic (Lorentz) force on natural convection flows and heat transfer. We are not aware of any previous work reporting modeling efforts under these conditions. From present analysis several notes can be made: (a) the Lorentz force is generated mostly by the externally applied electrical current; (b) the Lorentz force has maximum values at the boundary layers of liquid pools; (c) the *total* Lorentz force is always centrifugal, even though the electrical current is alternate. Assuming a joule-heating rate determined as $q_v = J^2/\sigma(T)$, from Eqs.(2,4) we have

$$F_{m,i} = \mu_m \frac{\sigma(T) q_v \Delta z_i}{2} \tag{5}$$

Further, we introduce the coefficient of thermal variation of electrical conductivity, β_σ, as follows

$$\beta_\sigma = -\frac{1}{\sigma}\frac{\partial \sigma}{\partial T} \tag{6}$$

Performing appropriate algebraic operations for pressure (P) and body forces in the Navier-Stokes equations by including the heat transfer solution-independent part of the electromagnetic body force into the static pressure, we have

$$\begin{aligned} F_i = F_{m,i} + \rho g_i - \frac{\partial P}{\partial z_i} &= \frac{\mu_m q_v \Delta z_i}{2}[\sigma_o - \beta_\sigma \sigma_o (T - T_o)] + g_i[\rho_o - \beta \rho_o (T - T_o)] - \frac{\partial P}{\partial z_i} \\ &= -\frac{\mu_m q_v \Delta z_i}{2}\beta_\sigma \sigma_o (T - T_o) - g_i \beta \rho_o (T - T_o) - [\frac{\partial P}{\partial z} - \frac{\mu_m q_v \Delta z_i}{2}\sigma_o - \rho_o g_i] \end{aligned} \tag{7}$$

Thus, real contributions of the electromagnetic forces on natural convection depend on *non-uniformity* of temperature field in melt pool and thermal variation of electrical conductivity. Eqs.(8-9) present the approximate formulas of electromagnetic forces acting on *natural convection flows* in square cavity.

$$F_{z,m} = -\frac{\mu_m q_v \Delta z}{2}\beta_\sigma \sigma (T - T_o) \tag{8}$$

$$F_{y,m} = -\frac{\mu_m q_v \Delta y}{2}\beta_\sigma \sigma (T - T_o) \tag{9}$$

As can be seen, the effects of the electromagnetic force depend on both electrical conductivity and its temperature variation. It is worth noting that there are large uncertainties in assessing β_σ for high-temperature core melts. However, we recognize the fact that β_σ is negative for oxidic melts and positive for metallic liquids. Therefore, the electromagnetic forces of interest are *centripetal* for *oxidic core melt* and *centrifugal* for *metal-rich oxidic core melt*. Probably, there are oxidic/metallic compositions with $\beta_\sigma \to 0$, which would, of course, be favourable for experiments considered. Order-of-magnitude analytical assessments of the electromagnetic force on natural convection flow fields and heat transfer performed show that (a) the electromagnetic force could become comparable with the inertia and buoyancy forces for metal-rich core melts; (b) the ratio between the magnetic Rayleigh number, Ra_m, and the buoyancy Rayleigh number, Ra, is linearly proportional to the power generation rate, q_v, and, therefore, increases with the Rayleigh number. For small size ($H = 0.4$m) core melt pools, the magnetic Rayleigh number can even be of the same order as the buoyancy Rayleigh number for $q_v = 1$ MW/m^3 for metal-rich corium. In order to demonstrate *phenomenological tendencies* of the electromagnetic influence on natural convection flows and heat transfer, we have performed computational modeling for *extreme, hypothetical* cases with the *negative* magnetic Rayleigh number (Fig. 15, $Ra_m = -10^{11}$) and the *positive* magnetic Rayleigh number (Fig. 16, $Ra_m = 10^{11}$), when the buoyancy Rayleigh number is 10^{10}. Comparing to flow field results for the case without influence of the electromagnetics (Fig. 14, $Ra = 10^{10}$), the centrifugal force of electromagnetics destroys the stable stratification in the lower region (Fig. 15), and by doing that intensifies heat fluxes. Inversely, the centripetal force stabilizes flows in the upper and side-wall regions and, therefore, significantly reduces heat transfer rates; see Table 2. Also, electromagnetic forces affect mixing levels in core melt pools. It can be seen by comparing temperature differences, ΔT_{max}, and Damköhler numbers for the three cases under consideration.

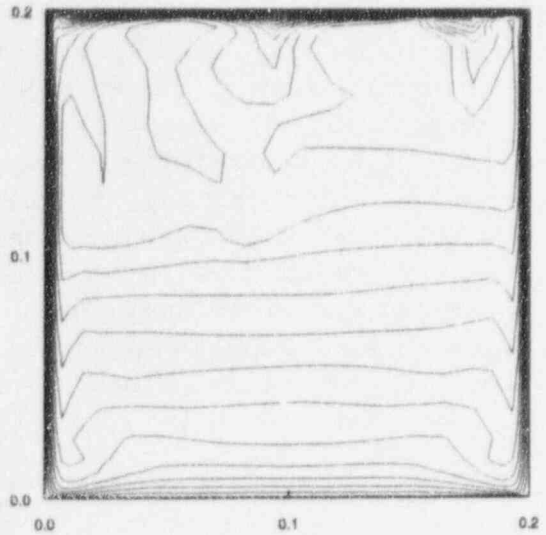

Figure 14: Temperature field in core melt pool $Ra = 10^{10}$, $\Delta T_{max} = 3.2$K.

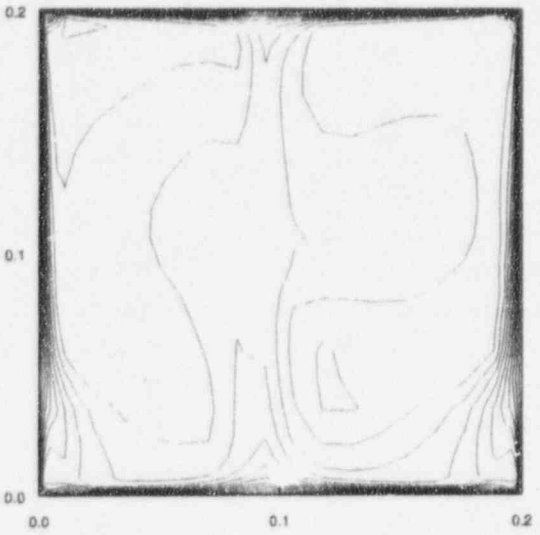

Figure 15: Temperature field in core melt pool with the negative magnetic Rayleigh number, $\Delta T_{max} = 2.2$K.

Table 2: The electromagnetic influence on heat transfer characteristics

Ra_m	0	-10^{11}	10^{11}
Ra	10^{10}	10^{10}	10^{10}
Nu_{up}	60	72	48.8
Nu_{sd}	53	58	13.6
Nu_{dn}	17	44.5	6.1
Da	130	185	26.3
ΔT_{max}, K	3.2	2.2	17

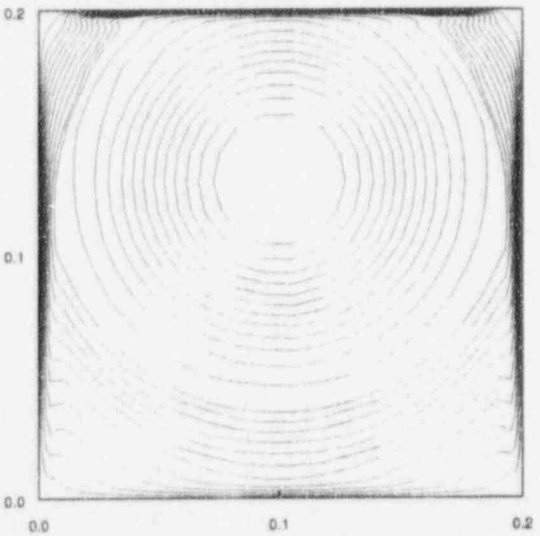

Figure 16: Temperature field in core melt pool with the positive magnetic Rayleigh number, $\Delta T_{max} = 17$K.

In the above considered case, the ratio between the magnetic Rayleigh number and buoyancy Rayleigh number was $Ra_m/Ra = 10$. Such ratios can be experienced at high (buoyancy) Rayleigh numbers, when large electrical currents are required and the corium is metal-rich. Nevertheless, our assessments allow us to conclude that from the electromagnetics point of view, there exist possibilities of having negligible effects of the electromagnetics for low-Rayleigh-number experiments. In such a case, the ratio Ra_m/Ra can even be less than 0.1 for oxidic core melt. As already mentioned, there exist large uncertainties in melt viscosity (ν) near the solidus point. In order to quantify the test regime, i.e. the Rayleigh number ($\sim \frac{1}{\nu}$), one has to operate the core melt experiments with sufficient melt superheat ($\Delta T_{max} > 30$K), providing representativity of experimental melt pools (compared to prototypical core melt pool with higher superheat). The melt superheats, ΔT_{max}, however, depend on the Rayleigh number ($\Delta T_{max} \sim q_v \cdot Ra^{-0.2} \sim Ra^{0.8}$). Due to such complications, the selection of test conditions and performance (based on extensive analysis of the results of 2D-3D computational modeling of convection in gravitational and electromagnetic fields) as well as improved data on thermo-physical and electrical properties of core melt, are required. For example, the quality of test facility design calculations and subsequent experiments would largely depend on whether uncertainties related to σ and β_σ for high temperature core melts can be reduced. Limiting values of buoyancy-induced Rayleigh numbers have to be determined by optimising height-to-power ratios.

4 CONCLUSION

As the in-vessel melt retention is becoming an important safety measure for some existing plants and for some advanced, medium-power light water reactor designs, care has to be taken when studying various phenomenological aspects relevant to issue resolution. The basic objective of the past and current experiments and analyses, related to the large core melt pools in the reactor vessel lower plenum, is to obtain insight into the physics of the heat transfer process under *prototypical conditions* of interest. The common approach is to conduct simulant material experiments and to generalize experimental data in the form of correlations, $Nu = f(Ra)$. In addition, small-scale core-melt experiments, as a rule, involve problems to demonstrate their relevance to reactor processes, due to applied heating methods, slice geometry of melt pools, low values of the Rayleigh number, and other measurement and test performance problems. Analytical and computational modeling has not, so far, been proved to be the reliable method to describe turbulent natural convection flows and heat transfer in large volumetrically heated liquid pools. Moreover, the set of identified, important physical phenomena and effects involved in melt pool thermal hydraulics requires separate effects analyses by experiments and/or modeling. Certainly, the highest priority has to be given to the phenomena, that could have the largest effect on heat fluxes imposed on melt pool boundaries.

In the paper, an overview was given of the scaling and other design effects of internally heated natural convection heat transfer experiments. The most reliable calculations performed have modeled relatively low-Rayleigh-number regimes (Ra up to 10^{12}). These are sufficient to predict thermal hydraulics in small-scale core melt experiments, and to assess sensitivity of heat fluxes to selected separate effects. However, for $Ra > 10^{12}$ there are several phenomena whose significance can only be judged. We have performed original computations for liquid pools with internal energy sources to quantify the general tendencies of the effects of various parameters. First, calculations performed for $Ra < 10^{12}$ in square and semicircular cavities indicated that descending boundary flows are able to penetrate into the bottom part of liquid pools with small fluid Prandtl numbers (Pr = 0.6-1.2), rendering thus conditions for destabilization of the lower fluid layers and, therefore, enhancing heat transfer to the lowermost part of cooled pool walls.

Further experimental and computational studies are needed to quantify this effect. Second, it was shown that effects of temperature dependence of physical properties have to be taken into account only when melt superheat over the melt solidus point is small which could be the case in small-scale core melt experiments. Thirdly, slice thickness-to-height ratios, $\Delta x/H$, more than 0.25 can be recommended for slice experiments in order to eliminate wall effects of face and back surfaces. Fourthly, the side-wall heating method would be useful for separate effects studies with prototypical core melts, should related design effects be accounted for in data processing and interpretation. Finally, it was shown that uncertainties in assessing effects of the Lorentz force are related to both electrical conductivities and their temperature variations. In order to achieve conditions where electromagnetic influence on natural convection flow and heat transfer is minor, the height-to-power and oxide-to-metal ratios have to be chosen by means of design calculations. For this purpose, an appropriate analysis method was developed in the paper.

ACKNOWLEDGEMENT

The authors would like to thank the reviewers who have provided detailed and constructive comments for the paper. Many thanks are due to Mr. Timo Okkonen of KTH for his interest and many useful discussions during the course of work that has been summarized in this paper.

NOMENCLATURE

Arabic letters

A	Aspect (heigh-to-width) ratio, $A = H/W$
Da	Damköhler number, $Da = \frac{q_v H^2}{\kappa \Delta T_{max}}$
Fo	Fourier number, $Fo = \frac{\alpha \Delta t}{H^2}$
g	Gravitational acceleration, m/s^2
H	Height of pools or cavities, m
Nu	Nusselt number, $Nu = \frac{q_s H}{\kappa \Delta T_{ave}}$
Pr	Prandtl number, $Pr = \nu/\alpha$
q_v	Volumetrical heat generation rate, W/m^3
r	Distance, m; Eq.(3)
Ra	Rayleigh number, $Ra = \frac{q_v H^5}{\alpha \kappa \nu} g\beta$
Ra_m	Magnetic Rayleigh number, $Ra_m = \frac{q_v H^5}{\alpha \kappa \nu} \frac{\mu_m q_v \beta_\sigma \sigma H}{\rho}$
T	Temperature, K
y, z	Horizontal and vertical coordinates, m
W	Width of pools or cavities, m

Greek letters

β	Thermal expansion coefficient , 1/K
κ	Heat conductivity , W/m·K
μ	Dynamic viscosity, Pa·s
μ_m	Magnetic permeability, $\sim 4\pi \text{x} 10^{-7}$ V-s^2/C-m
ν	Kinematic viscosity, m^2/s
ρ	Density, kg/m^3

Subscripts

dn	Bottom surface
i	i-direction
o	Referred value
sd	Side wall surface

up Upper surface

List of abbreviations

CHM	Chien model
CHM+PrT,VIST	Modified Chien model, using $Pr_t(Ri, y^+)$ and $\nu_t(Ri, y^+)$ [7]
CHM+Y	Chien model, including Yap term
COPO	Conditions of COPO experiments
FLOW3D	Calculations by using FLOW3D program
J&LM+Y	Jones and Launder model, including Yap term
J&R	Jahn and Reineke
LM	Laminar model
L&SM	Launder and Sharma model
L&SM+PrT(Ri,Ne)	Launder and Sharma model, using modified formula for Pr_t [7]
NARAL	The present work
S&R	Steinberner and Reineke

References

[1] T. Okkonen, "In-Vessel Core Debris Cooling Through External Flooding of the Reactor Pressure Vessel". An invited overview paper. *Proceedings of the OECD/CSNI/NEA Workshop on Large Molten Pool Heat Transfer*, Grenoble, France, March 9-11, 1994 (also OECD/NEA/CSNI/R(94)6 PWG4 Situation Report).

[2] T.G. Theofanous et al., "Experience from The First Two Integrated Approaches to In-Vessel Retention Through External Cooling", *Proceedings of the OECD/CSNI/NEA Workshop on Large Molten Pool Heat Transfer*, Grenoble, France, March 9-11, 1994.

[3] M. Jahn and H.H. Reineke, "Free Convection Heat Transfer with Internal Heat Sources: Calculations and Measurements", *Proceedings of the 5th Int. Heat Transfer Conference*, Tokyo, Japan (1974), Vol.3, paper NC-2.8.

[4] U. Steinberner and H.H. Reineke, "Turbulent Buoyancy Convection Heat Transfer with Internal Heat Sources" , *Proceedings of the 6th Int. Heat Transfer Conference*, Toronto, Canada (1978), Vol.2, pp.305-310.

[5] J.E. O'Brien and G.L Hawkes, "Thermal Analysis of a Reactor Lower Head with Core Relocation and External Boiling Heat Transfer", *AIChE Symposium Series*, No.283, Vol.87, 1991.

[6] K.M. Kelkar, K.K. Khankari, and S.V. Patankar, "*Computational Modeling of Turbulent Natural Convection in Flows Simulating Reactor Core Melt*", Final Report Submitted to Sandia National Laboratories, Albuquerque, December 1993.

[7] T.N. Dinh and R.R. Nourgaliev, "On Turbulence Modeling of Large Volumetrically Heated Liquid Pools", *Nuclear Engineering and Design*, 1995 (in press).

[8] O. Kymäläinen, H. Tuomisto, O. Hongisto, and T.G. Theofanous, "Heat Flux Distribution from a Volumetrically Heated Pool with High Rayleigh Number",

Proceedings of the 6th Int. Topical Meeting on Nuclear Reactor Thermal Hydraulics, NURETH-6, Grenoble, France, October 1993, pp.47-53.

[9] M. Sonnenkalb, "Summary of Previous German Activities and Status of GRS Program on In-Vessel Molten Pool Behavior and Ex-Vessel Coolability", *Proceedings of the OECD/CSNI/NEA Workshop on Large Molten Pool Heat Transfer*, Grenoble, France, March 9-11, 1994.

[10] F.J. Asfia and V.K. Dhir, "Natural Convection Heat Transfer in Volumetrically Heated Spherical Pools", *Proceedings of the OECD/CSNI/NEA Workshop on Large Molten Pool Heat Transfer*, Grenoble, France, March 9-11, 1994.

[11] L., Baker, Jr, et al., "Heat Removal From Molten Fuel Pools", *Proceedings of the International Meeting on Fast Reactor Safety and Related Physics*, Chicago, Illinois, October 5-8, 1976.

[12] R.P. Stein, L. Baker, Jr, W.H., Gunther, and C. Cook, "Heat Transfer from Internally Heated Molten UO_2 Pools", *Proceedings of the Fourth Post-Accident Heat Removal Information Exchange*, pp.1468-1472 (1979).

[13] G. Kevser, "The SCARABEE BF1 Experiment with a Molten UO_2 Pool and its Interpretation", *Proceedings of the OECD/CSNI/NEA Workshop on Large Molten Pool Heat Transfer*, Grenoble, France, March 9-11, 1994.

[14] B.D. Turland, "Debris Retention in the Lower Head of a PWR by Cavity Flooding", *Proceedings of the Workshop on Severe Accident Research in Japan, SARJ-94*, JEARI-memo 07-011, Tokyo, Japan, 1995.

[15] J. Royen, "OECD RASPLAV Project", *Proceedings of the 2nd CORVIS Task Force Meeting*, PSI, Switzerland, July 8-9, 1993.

[16] T.N. Dinh and A.A. Popov, "Molten Corium - Reactor Vessel Interaction: Scaling and Other Aspects", *ASME 1993 Winter Annual Meeting*. New Orleans, Louisiana, USA. December 1993. Section 14C: Advanced Nuclear Power Plants. ASME paper 93-WA/HT-81.

[17] S.V. Patankar, *"Numerical Heat Transfer and Fluid Flow"*, Hemisphere Publ.Corp., New York, 1980.

[18] *"CFDS-FLOW3D User Guide"*. Release 3.3. User Manual. AEA, UK. 1994.

[19] J.L.Rempe et al., *"Light Water Reactor Lower Head Failure Analysis"*. NUREG/CR-5642. USNRC. 1992.

[20] F.A., Kulacki, and A.A., Emara, "Steady and Transient Thermal Convection in a Fluid Layer with Uniform Volumetric Energy Sources", *Journal of Fluid Mechanics*, Vol.83, part 2, 1977, pp.375-395.

PASSIVE DECAY HEAT REMOVAL BY NATURAL AIR CONVECTION AFTER SEVERE ACCIDENTS

F.J. Erbacher*, X. Cheng**, H.J. Neitzel*

* Forschungszentrum Karlsruhe
Institut für Angewandte Thermo- und Fluiddynamik
Postfach 3640, D-76021 Karlsruhe

** Technische Universität Karlsruhe
Institut für Strömungslehre und Strömungsmaschinen
Postfach 6980, D-76128 Karlsruhe

ABSTRACT

The composite containment proposed by the Research Center Karlsruhe and the Technical University Karlsruhe is to cope with severe accidents. It pursues the goal to restrict the consequences of core meltdown accidents to the reactor plant. One essential of this new containment concept is its potential to remove the decay heat by natural air convection and thermal radiation in a passive way. To investigate the coolability of such a passive cooling system and the physical phenomena involved, experimental investigations are carried out at the PASCO test facility. Additionally, numerical calculations are performed by using different codes. A satisfying agreement between experimental data and numerical results is obtained.

1. INTRODUCTION

The Research Center Karlsruhe and the Technical University Karlsruhe have proposed a new containment concept for future pressurized water reactors [1]. The so called composite containment should ensure that it remains intact in severe core meltdown accidents and the decay heat can be removed in a passive way by natural air convection and thermal radiation.

The proposed containment shown in fig. 1 consists of an inner steel shell of approx. 60 m diameter and an outer concrete shell of approx. 2 m wall thickness. The annular gap of about 1 m width is bridged by longitudinal support ribs fixed in the concrete shell. The ribs are placed at intervals on the circumference with 50 cm spacings and transfer the load of the expanding and deflecting steel shell to the reinforced concrete wall (composite containment) in case of hydrogen detonation. With this concept the two individual containment shells of the present-day design remain essentially unchanged and the capability to withstand higher loads is achieved by the composite structure.

A core catcher is an integral part of this innovative design proposal. In a core meltdown accident the decay heat in the core melt converts cooling water into steam. The steam produced condenses on the internal structures and on the inner surface of the externally cooled steel shell. Reflux of the steam condensate to the core catcher establishes a passive self-circulating steam/water flow. The increase in the temperature of the steel shell results in natural convection of air in the individual chimneys formed by support ribs in the annular gap. Moreover, radiative heat transfer takes place between the steel shell, the support ribs and the concrete shell. Decay heat is thus removed by natural air convection and thermal radiation to

the ambient atmosphere in a passive way. The presence of the support ribs increases the total surface area and improves the radiative heat transfer. It was found that the radiative heat transfer enhances significantly the total heat transfer of the passive cooling system.

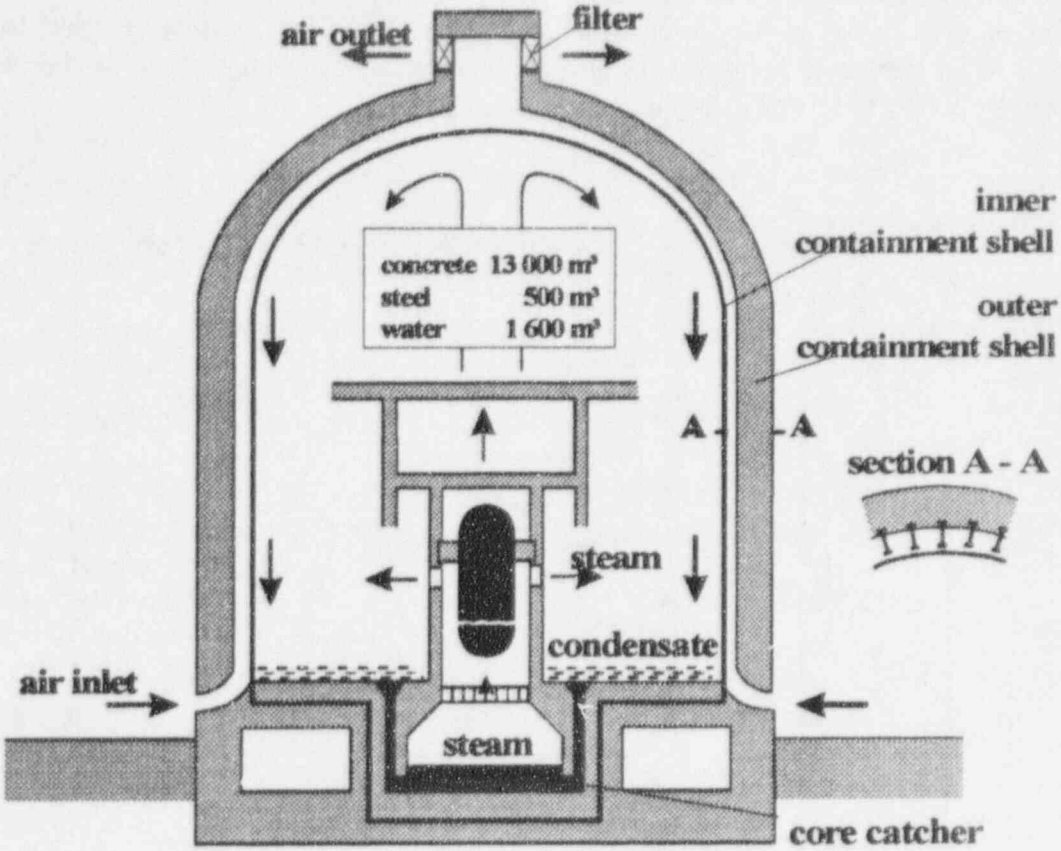

Fig.1: New containment concept - Composite containment

A survey of literature emphasizes the need of additional theoretical as well as experimental works concerning natural air convection under the given conditions: high Rayleigh-number, large channel geometries and strong interaction between convective and radiative heat transfer. To determine the coolability of such a passive cooling system and to study the physical phenomena involved, experimental investigations are performed in the PASCO (acronym for *pas*sive *co*ntainment cooling) test facility at the Institute of Applied Thermo- and Fluiddynamics of the Research Center Karlsruhe. In these experiments different effects, e.g. the effect of flow channel geometries and wall emissivity on heat transfer are studied. Moreover, generic informations and a broad data base will be provided for validation of advanced multi-dimensional computer codes, mainly in respect to modeling radiative heat transfer and turbulence.

In addition to experimental work, numerical simulations are carried out with a simplified one-dimensional code PASCO and an advanced three-dimensional code FLUTAN.

In the present paper the first experimental results are presented and compared with the numerical results obtained with the two different codes.

2. PASCO TEST FACILITY

The PASCO test facility shown in fig.2 simulates a cooling channel of the proposed containment. The test section consists of a one-sided, electrically heated vertical rectangular channel. The cross section of the test channel is 0.5 m x 1.0 m, it can be varied. The total heated height is 8 m, with four individually heatable zones. The channel is open to the atmosphere at its inlet and outlet. In the present experiments the temperature of the heated plates is controlled to be constant and uniform.

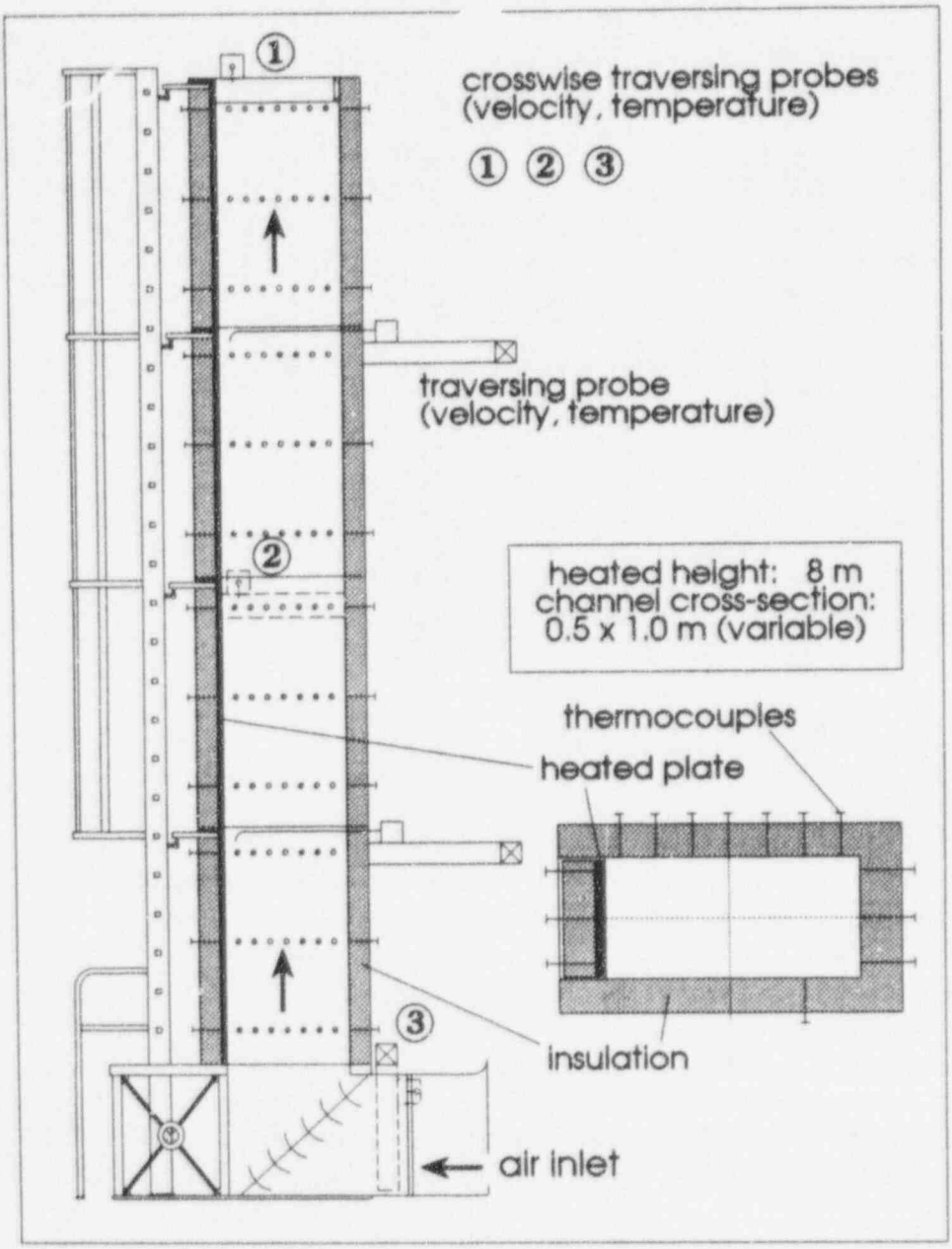

Fig.2: The PASCO test facility

The test facility is equipped among others with approx. 170 thermocouples to measure the distribution of wall temperatures. Traversing probes for recording the temperature and velocity of air are installed at five different elevations. Cross-wise traversing probes at the inlet, in the mid-plane and at the outlet measure the temperature- and velocity distributions over each

channel cross-section. Moreover, pressure at channel inlet, air humidity and heating power are recorded.

Experiments are performed at different values of heated wall temperature T_h, wall emissivity ε, heated height h and channel depth L. Table 1 summarizes the test parameters.

Table 1: Test parameters

Heated wall temperature T_h, ^{0}C	100 - 175
Wall emissivity ε	0.2 - 0.9
Heated height h, m	2.0 - 8.0
Channel depth L, m	0.25 - 1.0

3. EXPERIMENTAL RESULTS

Figure 3 shows the measured profiles of the air temperature and the air velocity at the channel outlet. The channel cross-section is 0.5m x 1.0m. In this experiment the heated wall temperature T_h is kept constant and equal to 150 ^{0}C. The air temperature at the channel inlet T_{in} is 20.3 ^{0}C and the average temperature of the ambient surroundings T_{am} is 22.7 ^{0}C. It can be seen in which way the profiles are affected by thermal radiation. A total heat power of 6.8 kW was transferred to air and the air mass flow is 0.54 kg/s. If the experimental results are extrapolated to reactor conditiions, a total decay heat of about 8 MW could be removed by the passive cooling system with natural air convection.

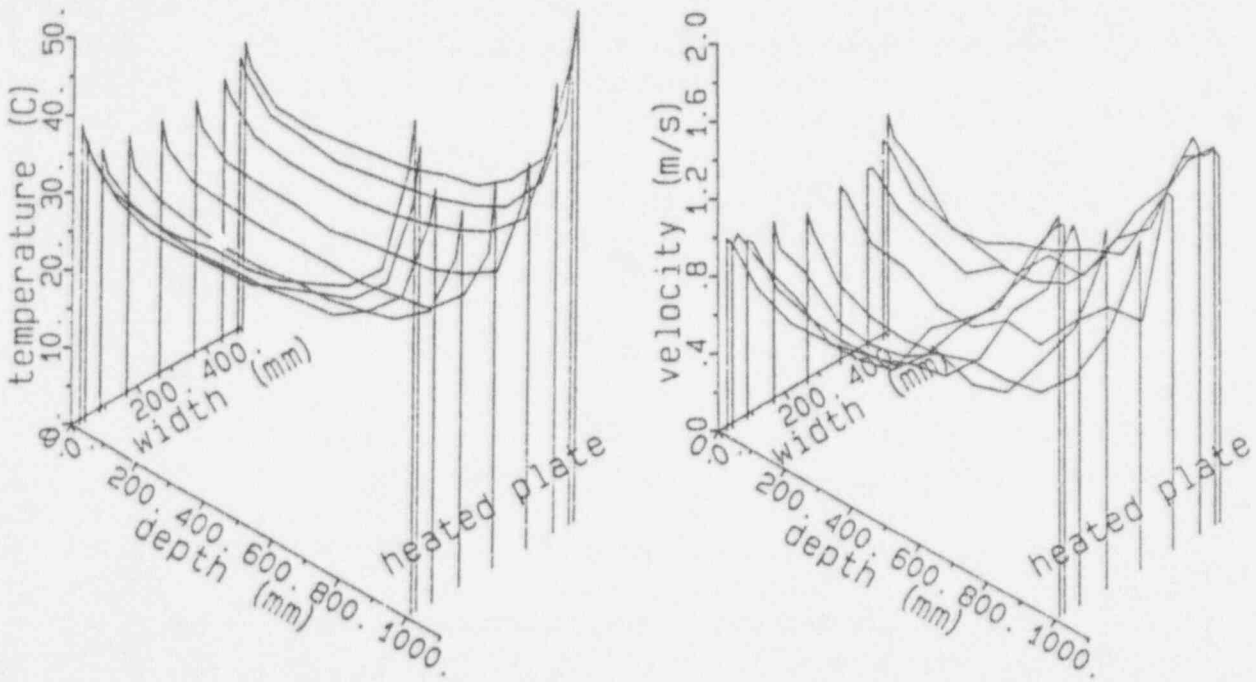

Fig.3: Measured temperature- and velocity profiles at the channel outlet
(T_h = 150 ^{0}C, T_{in} = 20.3 ^{0}C, T_{am} = 22.7 ^{0}C, ε = 0.9)

Table 2 shows the measured heat power and air mass flow at different experimental conditions. In all the experiments the wall emissivity is 0.9, the channel cross-section 0.5m x 1.0m and the heated height 8.0 m.

Table 2: Experimental results

Test number	M014	M018	M019	M022
Heated wall temperature T_h, ^{0}C	100	125	150	175
Inlet temperature of air T_{in}, ^{0}C	23.3	23.6	22.4	23.0
Ambient temperature T_{am}, ^{0}C	25.4	25.3	24.8	25.0
Transferred heat power, kW	3.33	4.79	6.58	8.23
Air mass flow, kg/s	0.34	0.41	0.44	0.54

4. NUMERICAL SIMULATIONS

For numerical simulations of the natural air convection in the PASCO test facility two different codes were used. The simplified one-dimensional code PASCO [2], [3] has been developed to predict the global thermal-hydraulics of the containment cooling and to assess the experimental data of the PASCO test facility. It is based on the heat balances at the individual walls and the one-dimensional enthalpy and momentum balances for the air. The heat transfer from the walls to the air is by natural convection. The following correlation

$$Nu = c\,Ra^{1/3} \qquad (1)$$

is used to calculate the heat transfer coefficient of natural convection, where Nu is the Nusselt number and Ra the Rayleigh number. The constant c has been determined for each individual walls. Between the individual walls of the chimney radiative heat transfer is taken into account.

The advanced three-dimensional code FLUTAN is an extended version of the COMMIX code [4], [5], which was developed at the Argonne National Laboratory. It is a finite-difference code for single-phase steady-state and transient analyses of single and multi-component systems in Cartesian or in cylindric coordinates. The FLUTAN code has been applied to many complex thermalhydraulic problems [6]. For the simulation of the turbulent flow in the PASCO test channel the standard k-ε turbulence model is used with logarithmic wall functions for the velocity and the temperature distribution near the wall. To extend the application of the FLUTAN code to the PASCO test channel, a thermal radiation model has been developed with the following main features [7]:

- Radiatively non-participating fluids, grey and diffuse surfaces.
- Net radiation method for enclosures.
- Analytical methods for view factor computation.
- Macro-element method for improving numerical efficiency.

Table 3 compares the measured results with the data calculated with two different codes.

Table 3: Comparison of the measured with the calculated results
(T_h = 150 ^{0}C, T_{in} = 20.3 ^{0}C, T_{am} = 22.7 ^{0}C, ε = 0.9)

Parameter	Measurement	PASCO code	FLUTAN code
Heat power, kW	6.8	6.8	8.1
Air mass flow, kg/s	0.54	0.52	0.40
Average temperature of the side wall, ^{0}C	47	62	47.6
Average temperature of the back wall, ^{0}C	50	64	48.1

The heat power and the air mass flow calculated by the PASCO code agree well with the measured data. The FLUTAN code reproduces accurately the average temperature of the side wall and the back wall. Nevertheless, large discrepancy is observed between the experimental and numerical (FLUTAN) results concerning the heat power and the air mass flow.

Figure 4 shows the distribution of air temperature and air velocity along the mid-line at the outlet cross-section as function of the distance from the heated plate.

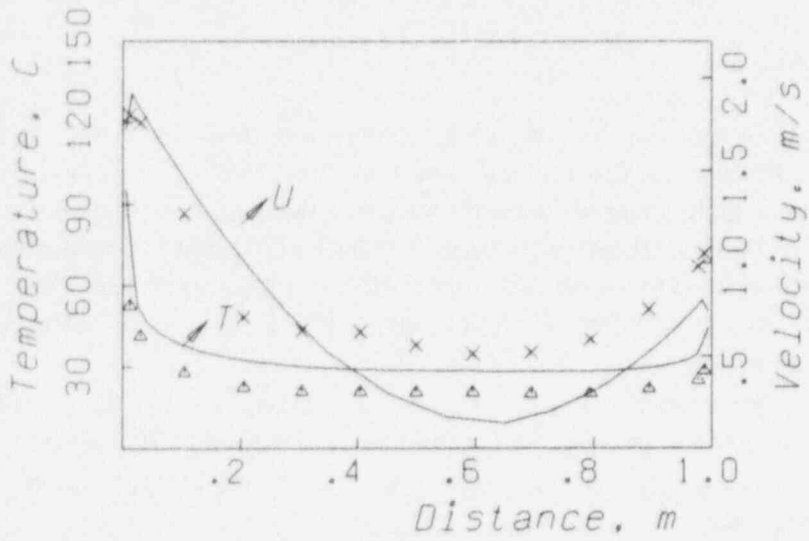

Fig.4: Measured and calculated distribution of air temperature and air velocity
Δ- temperature, x - velocity
(T_h = 150 °C, T_{in} = 20.3 °C, T_{am} = 22.7 °C, ε = 0.9)

The curves are the results calculated with the FLUTAN code and the symbols are the data obtained in the PASCO experiments. Qualitatively the calculated results agree well with the measured data. The quantitative discrepancy which is also evident from Table 3 emphasizes the need of improving turbulence-modeling in the FLUTAN code for turbulent natural convection.

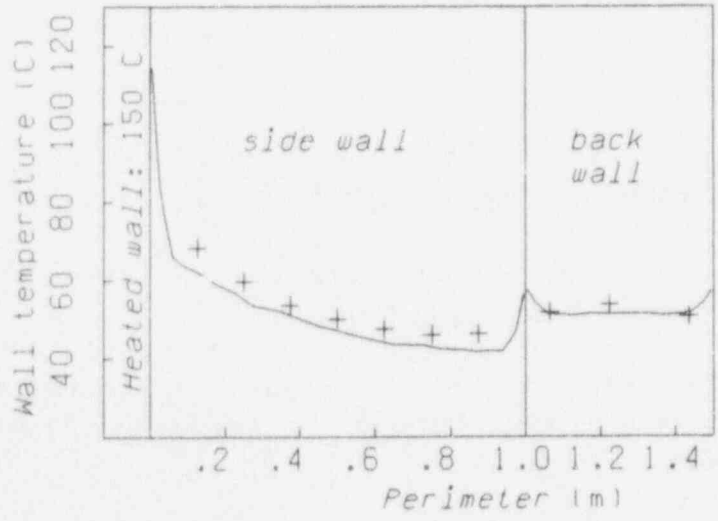

Figure 5. Temperature distribution on the side wall and on the back wall
curve: FLUTAN calculation, symbols: measurement
(T_h = 150 °C, T_{in} = 20.3 °C, T_{am} = 22.7 °C, ε = 0.9)

Figure 5 shows the temperature distribution on the side wall and on the back wall at the elevation 4.2 m. The curve presents the results calculated with the FLUTAN code and the symbols are the experimental data. A good agreement is found between the experimental and the calculated results. On the side wall the maximum temperature appears close to the heated wall. It decreaces rapidly with increasing distance from the heated wall. Toward the corner where the side wall connects the back wall the temperature increases again. On the back wall a similar distribution of wall temperature in the corner region is also obtained.

5. CONCLUSIONS

- Passive containment cooling by natural air convection and thermal radiation offers an innovative safety feature for future pressurized water reactors
- In the PASCO test facility the physical phenomena involved in natural air convection and thermal radiation under different conditions can be studied and a broad data base will be provided for further developing advanced multi-dimensional computer codes.
- At high wall emissivities thermal radiation contributes significantly to the total heat transfer by natural air convection.
- The codes used have achieved satisfying agreement with experiments. However, they showed also the need of improving the turbulence-modeling in natural air convection.
- Additional larger scale experiments must prove the containment coolability under all conceivable conditions.

Further research works are underway to develop a correlation of heat transfer coefficient of natural air convection in unsymmetrically heated, vertical channels.

ACKNOWLEDGEMENT

This work is partially supported by the 'Bundesministerium für Forschung und Technologie' under the Project Number 15NU0961.

REFERENCES

1. H.H. Hennies, G. Kessler, J. Eibl, "Improved Containment Concept for Future Pressurized Water Reactor", Int. Workshop on Safety of Nuclear Installations of the Next Generation and Beyond, Chicago, IL, USA, August 28-31 (1989)

2 H.J. Neitzel, "Abschätzung der Wärmeabfuhr durch Naturkonvektion bei einem alternativen Containmentkonzept", KfK 5005, Juni 1992

3 F.J. Erbacher, H.J. Neitzel, "Passive Containment Cooling by Natural Air Convection for Next Generation Light Water Reactors", Proc. of the NURETH-5, Salt Lake City, Utah, USA, September 21-24, 1992

4 V.L. Shah, et.al., "COMMIX-1B: A Three-Dimensional Transient Single-Phase Computer Program for Thermal Hydraulic Analysis of Single and Multicomponent Systems", NUREG/CR-4348 Vol.1, Argonne, Illinois, September 1985

5 H.B. Borgwaldt, "COMMIX-IB, a Robust Vectorized Poisson Solver Implemented in the COMMIX-2(V)", Proc. of the Int. Conference on Supercomputing in Nuclear Applications, Mito City, Ibaraki, Japan, 1990

6 D. Weinberg, K. Rust, H. Hoffmann, H.H. Frey, "Comparison of Code Predictions against Natural Convection Experiments", Natural Circulation Phenomena in Nuclear Reactor Systems: 1994 Int. Mechanical Engineering Congress and Exposition, Chicago, November 6-11, 1994

7 X. Cheng, F.J. Erbacher, H.J. Neitzel, "Thermal Radiation in a Passive Containment Cooling System by Natural Air Convection", Int. Symposium on Radiative Heat Transfer, Kusadasi, Turkey, 14-18 August, 1995

Natural Circulation in a VVER Reactor Geometry: Experiments With the PACTEL Facility and CATHARE Simulations

P. Raussi, S. Kainulainen
Lappeenranta University of Technology
PL 20, 53851, Lappeenranta, FINLAND

J. Kouhia
VTT Energy
PL 20, 53851, Lappeenranta, FINLAND

Abstract

There are some 40 reactors based on the VVER design in use. Database available for computer code assessment for VVER reactors is rather limited. Experiments were conducted to study natural circulation behaviour in the PACTEL facility, a medium-scale integral test loop patterned after VVER pressurized water reactors. Flow behaviour over a range of coolant inventories was studied with a small-break experiment. In the small-break experiments, flow stagnation and system repressurization were observed when the water level in the upper plenum fell below the entrances to the hot legs. The cause was attributed to the hot leg loop seals, which are a unique feature of the VVER geometry. At low primary inventories, core cooling was achieved through the boiler-condenser mode. The experiment was simulated using French thermalhydraulic system code CATHARE.

1. Introduction

Natural circulation is an important passive core cooling mechanism in nuclear power plants during both regular operations and transients. The efficiency and general behaviour of natural circulation cooling depends upon the nature of the fluid flow within the primary system, and this varies with coolant inventory. This dependence is of particular interest in a small-break loss of coolant accident (SBLOCA) scenario where core cooling could be required at substantially reduced inventories. Natural circulation experiments provide an opportunity to evaluate system cooling capabilities over a wide range of conditions, most notably the low inventory levels not typically experienced at a power plant.

Many test facilities have been constructed to study thermal hydraulic phenomena in western reactor geometries. PACTEL is a medium-scale integral test facility designed to simulate thermal hydraulic phenomena characteristic of the Soviet-designed VVER reactors, with particular attention to the versions used in Finland. The facility was constructed by the Technical

Research Centre of Finland and the Lappeenranta University of Technology as a part of their continuing reactor safety program.

Natural circulation is characterized by three distinct modes: single-phase flow for a near maximum primary inventory, two-phase circulation at intermediate inventories, and reflux condensation or a boiler-condenser mode at low inventories. Transitions between these flow types are usually relatively smooth. Very low mass flow rates are observed for the reflux condensation and boiler condenser modes, but energy transport is still sufficient to provide core cooling.

Thermal hydraulics experiments have been conducted with VVER-type test facilities, but these are limited to small-scale models. One such facility is REWET-III in Finland, a volumetrically scaled (1:2333), full height, single loop model. Natural circulation studies with rewet III have been discussed by Kervinen & al [1][2]. Another facility patterned after the VVER is PMK, located in Hungary. It is also a volumetrically scaled, single loop and full height model similar in size to REWET-III, but designed for full pressure and full scaled power. It has been used to study natural circulation and the effects of loop seal clearing on the core liquid level. Experiments showed that the transition between single and two-phase flow is not always smooth, with the nature of this transition depending upon the core power and mass inventory [3].

2. PACTEL facility

PACTEL is a volumetrically scaled (1:305), out of pile model of the two Russian designed VVER-440 pressurized water reactors used in Finland. The facility includes a pressurizer, high and low pressure emergency core cooling systems, and an accumulator (fig. 1). The peak operating pressures on the primary and secondary sides are 8 MPa and 4.6 MPa, respectively. The reactor vessel is simulated with a U-tube construction including separate downcomer and core sections. The core itself consists of 144 hexagonally arranged full height, electrically heated fuel rod simulators with a maximum total power output of 1 MW, or 22% of scaled full power. The fuel rod pitch (12.2 mm) and diameter (9.1 mm) are identical to those of the reference reactor.

Component heights and relative elevations correspond to those of the full scale reactor to match the natural circulation pressure heads in the reference system. The hot and cold leg elevations of the reference plant have been reproduced including the loop seals. The hot leg loop seals are a result of the steam generator locations, which are at roughly the same elevation as the hot leg connections to the upper plenum. The hot and cold leg connections to a steam generator are at the underside of each col-

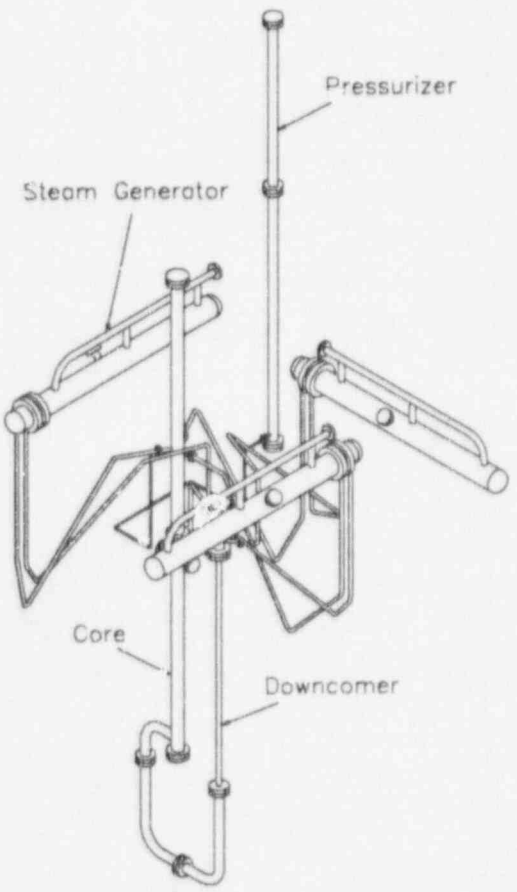

Fig. 1. PACTEL facility.

lector, thus a U-shaped pipe is necessary to complete the connection to the pressure vessel without sharp bends. The cold leg loop seals are formed by the elevation difference between the inlets and outlets of the reactor coolant pumps, just as in other PWRs.

Three coolant loops with double capacity steam generators are used to model the six loops found in the reference power plant. The U-tube lengths and diameters in the older PACTEL steam generators corresponded to those of the full scale models. The height of the tube bundle was only about 15 % of the height of the reference steam generator. To study the effect of the bundle height a new stem generator model have been installed to the facility. The bundle height is now 1.0 m (in the power plant 3.34 m). Secondary side steam production is vented through control valves directly to the atmosphere.

The horizontal orientation of the steam generators is one of the distinguishing features of the VVER design. One consequence of this geometry is a reduced driving head for natural circulation. Another notable feature is the relatively large secondary side water inventory, which tends to slow the progression of transients.

3. Natural circulation in the VVER geometry

Natural circulation experiments with the PACTEL facility have been analyzed by Lomperski and Kouhia [4]. The experiments demonstrated significant qualitative differences between natural circulation in VVER and typical PWR geometries.

Peak natural circulation mass flow rates observes in the single rather than two-phase flow regime. In the VVER geometry there is only a modest increase in the driving head associated with two-phase flow. Transition between single and two-phase flow was not smooth in most of the SBLOCA tests. The flow temporarily stagnated when the water level reached the hot leg entrances and did not resume until the loop seals cleared, fig 2. The loop seel cleared after the water level at the upstream side of the loop seal reached the bottom of the loop seal. In the experiments with three loops highly asymmetric behaviour was observed after two-phase flow was established. Two of the loop seals refilled after clearing, reducing flow and shifting the energy transport to the third loop.

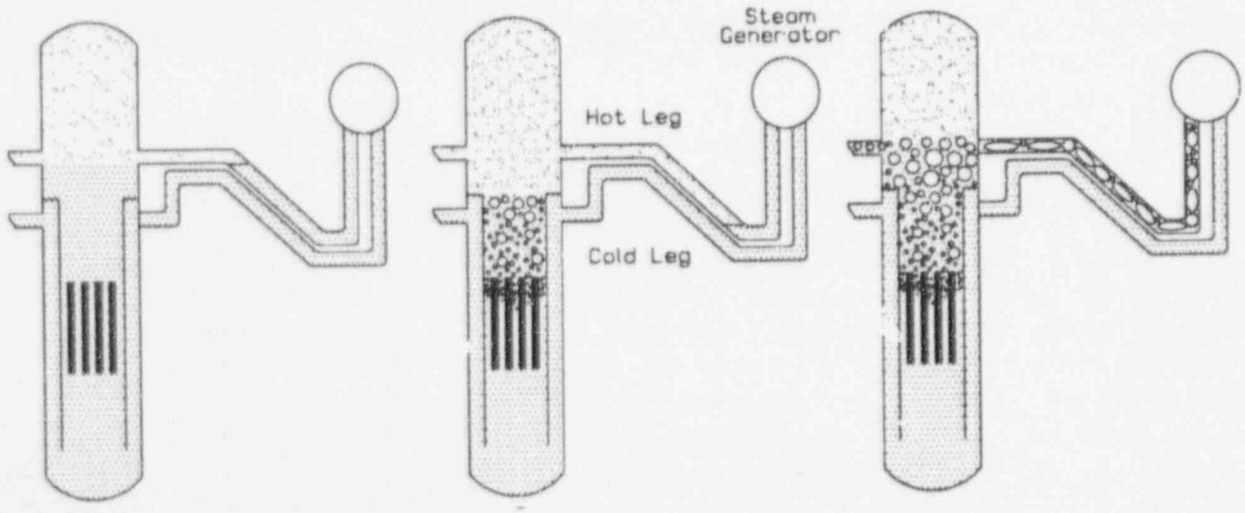

Fig. 2. Inventory distribution during (a) initial flow stagnation, (b) loop seal clearing, and (c) flow resumption.

Flow stagnation occurred near the same inventory regardless of the break size, though the duration was shortest for the largest break. Tests also showed how the pressurizer altered the transition between single and two-phase flow. When it remained connected to the rest of the primary, fluid flow in and out of the pressurizer resulted in large magnitude flow and pressure oscillations as the system inventory alternated between the regions of stagnant flow and steady two-phase flow.

Condensate flow from the steam generators to the downcomer was intermittent for the boiler-condenser mode. The steam generators retained significant amounts of coolant, with the downcomer flow surges comprising some 5-10% of the total inventory. The amount of water retained in the steam generators influences the core collapsed level, which in turn has a bearing on when the top of the core begins to dry out and overheat. It is clear that significant coolant holdup in the steam generators can shorten the elapsed time to core heatup in the event of a SBLOCA.

It was demonstrated that loop seal refilling occurs for low steam flow rates because of countercurrent flow in the upflow side of the hot leg. This behaviour points to the importance of using a multi-loop facility to investigate SBLOCAs in a VVER geometry. There will certainly be an interdependence between loop seal filling and the accompanying loss of flow in some loops, and flow behaviour in other loops. It is also conceivable that if the coolant inventory supporting two-phase flow were maintained for a long period, flow characteristics may continue to change as the core decay heat decreases and steam production drops.

4. Experiment description

The experiment (SBL-22) was performed to study natural circulation and the behaviour of the new steam generator model over a continuous range of primary side coolant inventories. To simplify the experiment only one of three primary loops was used in the test. The experiment has been made as simple as possible to establish a basic understanding of natural circulation flow behaviour in the PACTEL facility.

The experiment was started with a steady state period at the full water inventory. The primary circulation pump was stopped and the break was opened in the cold leg at 1000 s. At the same time the pressurizer was disconnected from the rest of the primary side. The break size was 0.04% of the PACTEL cold leg cross sectional area. The break size corresponds to 0.12%

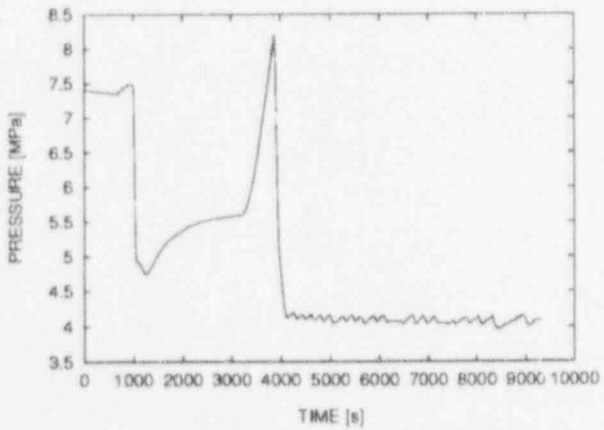

Fig. 3. Primary pressure in the SBLOCA experiment.

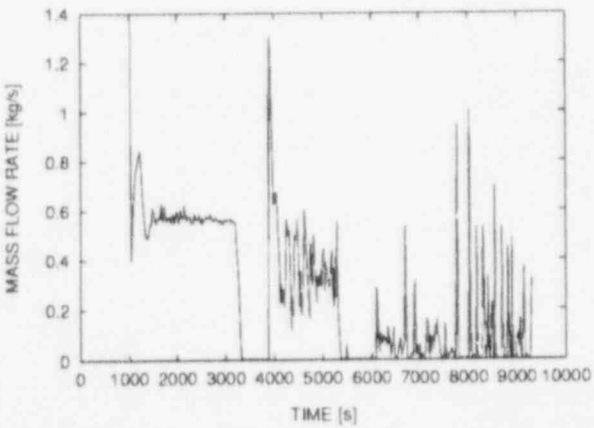

Fig. 4. Downcomer mass flow rate in the SBLOCA experiment.

of the scaled down cold leg area of the reference reactor. The core power during the entire experiment was 70 kW.

No other actions were taken during the experiment than maintaining the secondary side level through additions of the feed water. The test was terminated when the cladding temperatures started to rise at the top of the core. The measured primary pressure and the downcomer mass flow rate in the experiment are showed in Fig. 3 and 4.

Table 1. Heat transfer modes during the SBLOCA experiment.

time [s]	inventory [%]	mode
1000-3400	100-74	single-phase
3900-5300	67-56	two-phase
5300-9500	56-32	boiler-cond.

After opening the break valve at 1000 s, the primary pressure dropped until the hot leg saturation pressure was reached. The heat transfer mode from the primary to secondary side was single-phase natural circulation until the upper plenum collapsed level reached the hot leg pipe entrance and the loop flow stagnated at 3400 s. The energy transport from the core to the steam generator was lost and the primary pressure increased. The flow remained stagnant until the hot leg loop seal cleared at 3900 s. Since the pressurizer was disconnected there was only one flow stagnation and loop seal clearance controlled by the primary inventory.

After the loop seal opened two-phase mixture flowed to the steam generator and the system pressure started to decrease. Two-phase natural circulation continued until the boiler-condenser mode was established at 5300 s. Although the steam generator has been changed since the previous natural circulation test series, the overall behaviour of the loop has remained roughly the same. Table 1 summarises the different heat transfer modes.

After the primary circulation pump was stopped the flow reversed in the lower SG tube layers, because the density in the cold collector was somewhat higher than that in the hot collector. Fig. 5 shows the situation in the steam generator before the flow stagnation. The upper part of the tube bundle handled most of the heat transfer from the primary to secondary side.

During the stagnant flow period the temperature distribution in the primary side of the steam generator was almost uniform. When the loop seal cleared and the flow resumed there was liquid in the cold collector and two-phase mixture in the hot collector (Fig 6). That initiated again a reverse flow in the lower part of the tube bundle. The uppermost tubes handled most the of the heat transfer. After the loop seal clearance the manometric balance presented in fig. 2a

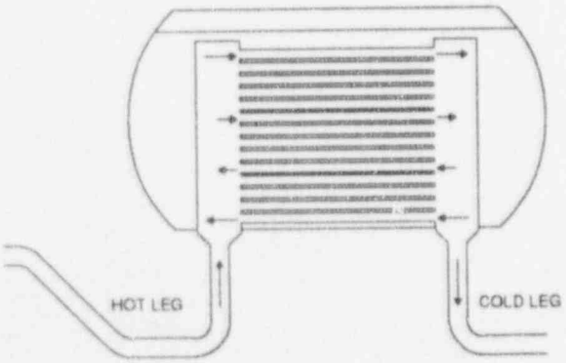

Fig. 5. Flow directions in the steam generator tubes during the single-phase flow.

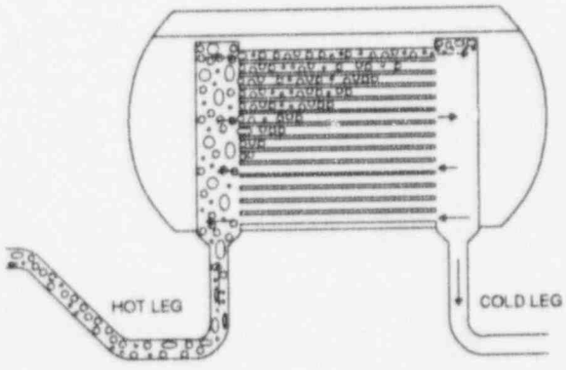

Fig. 6. Behaviour of the steam generator after the loop seal clearing.

was lost and the water level in the cold collector decreased as the level in the upper plenum increased.

Most of the steam went to the uppermost part of the tube bundle. There was clearly a liquid flow through the lower part of the tube bundle early in the two-phase region. However, that changed when the two-phase flow period advanced further. Towards the end of the two-phase flow stage the differential pressure over the tubes changed so that the pressure was higher in the hot collector than in the cold collector. There was no evidence of a constant reverse flow in any of the tubes, when the elapsed time was 4700 s from the beginning of the experiment. Temperature oscillations were observed in the lowest tube layer, which indicated that sometimes the flow direction was reversed, however.

In the boiler-condenser mode the mass flow rate was very low. Thus, the driving force for the flow from the hot to cold collector was weak. The cold collector was totally filled by steam when the boiler-condenser mode started. The flow from the heat exchange tubes to the cold leg was not continuous, but intermittent flow peaks were observed. These peaks were induced by the secondary side pressure fluctuations and the feed water injection.

Similar tests with the previous PACTEL steam generator show clearly that considerable amount of liquid can accumulate into the tubes during the boiler-condenser mode. The retaining water decreases the heat transfer before the tubes are emptied to the cold leg. That behaviour is not evident in this experiment. The reason is that the length of the tubes of the new steam generator construction is only third of the tube length of the previous steam generator. Experimental and analytical studies of horizontal steam generators have been presented in seminars held in Lappeenranta [5].

The cold leg loop seal caused flow peaks at the very end of the transient. When the level in the cold leg reached the bottom of the loop seal, steam flowed into the inclined part of the cold leg and rose to the pump. A new liquid level was formed and the coolant flowed from the cold leg side to the upper plenum to equalize the manometric balance of the loop.

5. CATHARE code

The CATHARE 2 code version V1.3E used for these calculations is a French system code developed by CEA, EDF & Framatome for the analysis of design basis accidents. It is based on a two-fluid 6 equation model expressing mass, momentum and energy conservation for each phase (gas and liquid). Additional mass equations are written in order to account for non-condensable gases. The numerical scheme is a finite difference method using staggered mesh and first order upwind differencing. The time discretization is fully implicit. Several modules are available to represent the different components of a circuit: 1-D pipe, 2-node volume and 1-node tee. The constitutive relations in the CATHARE code are either taken from the literature or original models developed from the analysis of a large experimental program associated to the code.

CATHARE assessments on VVER test facilities have been done calculating some tests performed on PACTEL (ISP33) and on PMK loops (SPE-1, SPE-2, SPE-3). Tests performed on IVO test rig have been used by CATHARE developers to propose a CCFL correlation at the upper tie plate. Test data of REWET-II reflooding experiments have also been used to assess CATHARE.

6. CATHARE model for PACTEL SBLOCA test

The 1-D pipe module was used for hot leg, cold leg, downcomer, lower plenum, core and core by-pass in the schematization of the PACTEL facility. Nine tubegroups were represented in the SGs primary side. For the secondary side, a vertical 1D element with nine meshes was used, each secondary mesh exchanging with a group of tubes. The 2-node volume module with a moving mixture level was used for the upper plenum, hot and cold SG collectors and the upper part of the downcomer. It allows the description of vertical stratification and phase separation effects at the junctions with pipes. The pressurizer was modelled with a boundary condition during steady state. The tee module (I-node module modelling phase separation in a tee junction) was used to connect the hot leg element to the pressure boundary. Leak flow has been given as a function of the primary pressure. Figure 7 presents the nodalization of the primary side.

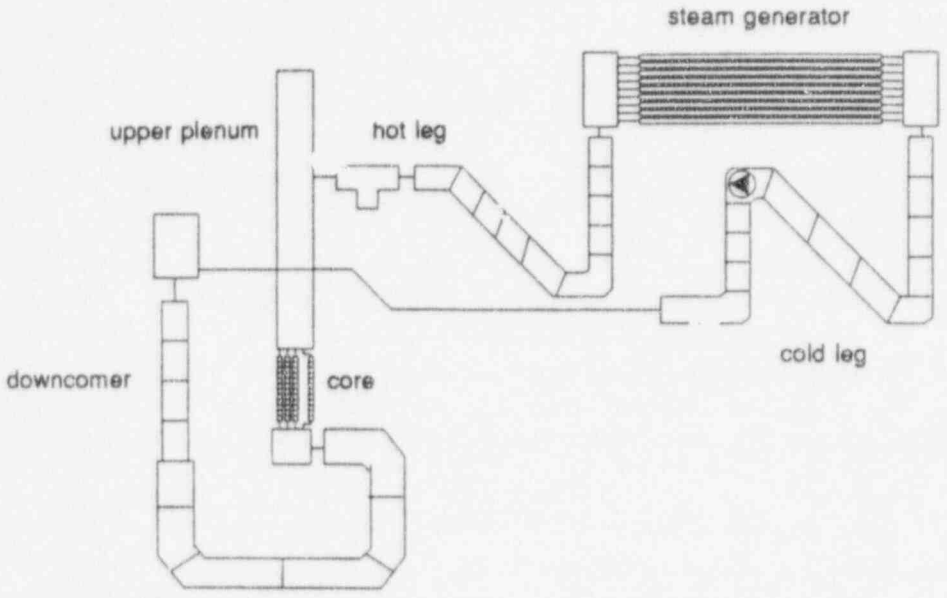

Fig. 7. Nodalization of the primary side.

7. Results of CATHARE calculation

The results of CATHARE simulation as well as the experimental results can be divided to five different period. The primary pressure and coolant mass flow during CATHARE simulation have been presented in figures 8 and 9. The same experiment have been calculated using RELAP5 and APROS codes by Riikonen & al [6]. Primary pressure and mass flow in RELAP and APROS simulations have been presented in figures 10 and 11. Periodical results of CATHARE simulation are:

1. **Steady state** (0-1000 s). The simulation starts with the calculation of a 1000 s steady state period. Code predicts the initial conditions of the transient reasonably well.

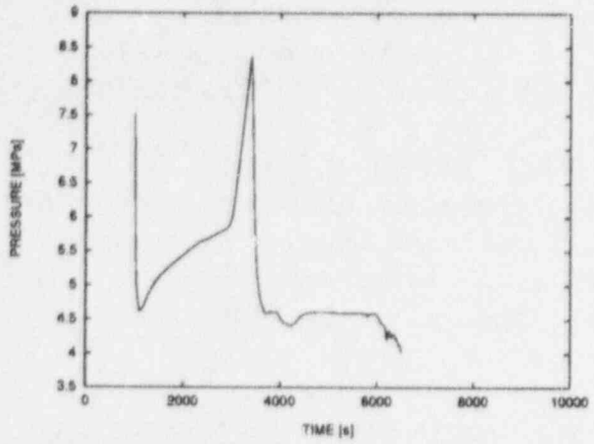

Fig. 9. Calculated primary mass flow rate, CATHARE simulation.

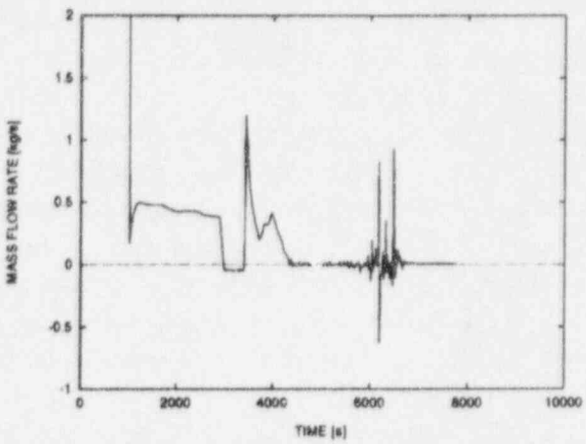

Fig. 9. Calculated primary mass flow rates, CATHARE simulation.

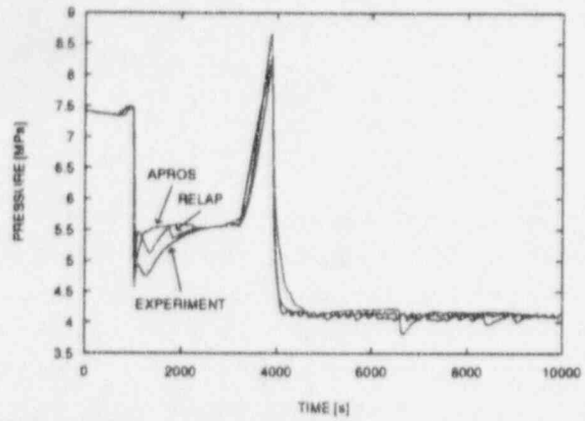

Fig. 10. Measured and calculated (RELAP5 and APROS) primary pressures.

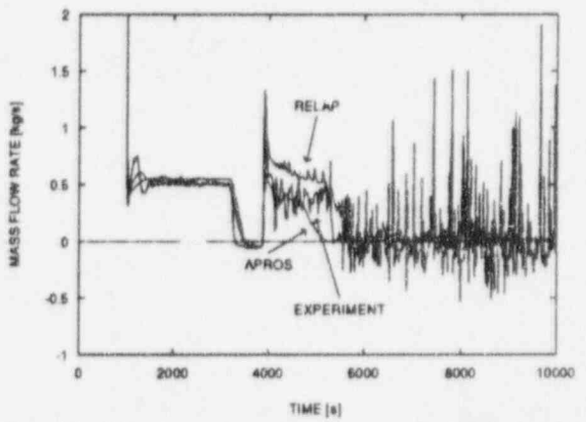

Fig. 11. Measured and calculated (RELAP5 and APROS) downcomer mass flow rates.

2. **One-phase natural circulation** (1000-3400 s in experiment) starts at 1000 s after the pressurizer is disconnected, the primary circulation pump is stopped and the cold leg break is opened. The rapid drop from the steady state pressure to the saturation pressure is predicted correctly. The downcomer mass flow rate is not correctly calculated immediately after the pump coast down and it takes about 100 s before the calculated mass flow agrees with the measured one. The pressure starts to increase again after the coast down. The pressure is controlled by the temperature of the steam at the upper plenum. This is predicted better in CATHARE calculations than in RELAP5 and APROS calculations.

After the pump has been stopped the flow reverses in the lower tube layers of the steam generator in calculation like in the experiment. In the uppermost tube layers the flow is to the normal direction. Also in the calculations most of the heat transfer from the primary to secondary side is handled by the upper part of the tube bundle.

3. **Flow stagnation** (3400-3900 s in experiment). A loss of loop flow occurs in the calculations at 3000 s. The core power was not transported to the secondary side and the pressure increased as in the experiment. The flow resumes in calculation at 3700 s. The simulation have relatively good agreement with the experiment.

4. **The two-phase natural circulation** (3900-5300 s in experiment) period is also shorter in the calculation (3700-4500 s) than in the experiment. The calculated and measured system pressures are in a good agreement during this period. In the end of the two phase flow period the primary pressure decreases near the secondary side pressure. Strong internal circulation in the primary side of the steam generator is predicted by the code early in the two-phase region. Later in the simulation there is no significant reverse flow in any of the steam generator tubes.

5. **The boiler-condenser** (after 5500 s in the experiment) mode energy transport begins earlier in the calculation than in the experiment (4500 s). During the boiler-condenser mode the code overestimates the primary pressure. The primary pressure stayed about 5 bar higher than measured pressure. The same finding have been reported in CATHARE analyses of the ISP-33 natural circulation experiment [7]. We have not been able to provide reason for the termination of the CATHARE simulation before the end of the experiment. RELAP5 and APROS gave better estimations for the boiler-condenser mode.

8. Conclusions

In the experiment natural circulation in the VVER geometry was studied during a small break LOCA. The experiment was analyzed with the CATHARE code. The code was able to predict the different natural circulation modes. In the single-phase period the downcomer mass flow rate and the flow stagnation were predicted well. The steam generator behaviour in single-phase natural circulation was simulated well. The flow reversing in the lower tube layers was clearly visible and the heat transfer distribution from the primary to secondary side was simulated satisfactory.

The time of transition from the two-phase flow mode to the boiler-condenser was too early. The verification of the calculated steam and water distributions in the two-phase and boiler-condenser mode is not possible, because the measured values are not available. Calculated primary pressure during boiler-condenser mode was not in good agreement with the measured one. The Reynolds numbers in the horizontal steam generator tubes are very low during the boiler-condenser mode and the flow is stratified. The condensation model used in the code was developed for the vertical pipes. Condensation models used for stratified flow conditions included to APROS and RELAP5 codes give better prediction.

References

[1]. T. Kervinen, O. Hongisto, Natural circulation experiments in the REWET-III facility, Proc. of the Int. ANS/ENS Topical Meeting on Thermal Reactor Safety (1986) pp. XVIII4.1-XVIII4.8.

[2]. T. Kervinen, H. Purhonen and H. Kalli, Oscillations of the natural circulation flow in small break conditions in the REWET-III facility, in: Natural Circulation, ASME FED-Vol. 61, HTD-Vol. 92, 1987, pp. 83-89.

[3]. I. Toth, Loop seal effects on core cooling in VVER-type reactors, Proc. of the Int. ENS/ANS Conf. on Thermal Reactor Safety, Avignon, NUCSAFE 88 Vol. 3, October 1988, pp. 1049-1058.

[4]. S. Lomperski, and J. Kouhia, Natural circulation experiments with the VVER geometry, Nuclear Engineering and Design, 147 (1994) 409-424.

[5]. Third International Seminar on Horizontal Steam Generators, October 18-20, 1994 Lappeenranta, Finland.

[6]. V. Riikonen, M. Puustinen, J. Kouhia, RELAP5/MOD3.1 and APROS (V2.1) analysis of the SBLOCA experiment with the new steam generator on the PACTEL facility. VTT, PROPA 10/94.

[7]. Purhonen, H., Kouhia, J., Holmström, H., OECD/NEA/CSNI international standard problem No.33. PACTEL natural circulation stepwise coolant inventory reduction experiment. Comparison Report. NEA/ CSNI/R(94) Parts I and II.

PARAMETRIC NUMERICAL INVESTIGATION OF NATURAL CONVECTION IN A HEAT-GENERATING FLUID WITH PHASE TRANSITIONS

A.E. Aksenova, V.V. Chudanov, V.F. Strizhov, P.N. Vabishchevich

Institute of Nuclear Safety Russian Ac.Sci.
52 B. Tulskaya, Moscow 113191, Russia
Fax: (095) 230-20-23

ABSTRACT — Unsteady natural convection of a heat-generating fluid with phase transitions in the enclosures of a square section with isothermal rigid walls is investigated numerically for a wide range of dimensionless parameters. The quasisteady state solutions of conjugate heat and mass transfer problem are compared with available experimental results. Correlation relations for heat flux distributions at the domain boundaries depending on Rayleigh and Ostrogradskii numbers are obtained. It is shown that generally heat transfer is governed both by natural circulation and crust formation phenomena. Results of this paper may be used for analysis of experiments with prototypic core materials.

1 INTRODUCTION

The need of parametric investigation of a heat-generating fluid with phase transitions results from the necessity to predict correctly the behaviour of a molten heat-generating corium for various hypothetical accident scenarios in a pressurized water reactor (PWR). As a result of such accident, it is possible accumulation volumes of corium both in-core and in the reactor vessel lower head.

Presence of the large amounts of corium masses in the reactor vessel lower head may lead to the vessel collapse and at the same time under specific cooling conditions the retention of the molten corium in the reactor vessel is possible. In this connection it is necessary to investigate the mechanisms of the heat transfer in corium on the basis of a more complete model accounting for both the buoyancy-driven flow and corium melting and solidification processes.

The process of corium heating in pressure vessel is defined by residual volumetric decay heating, which leads both to melting of the fuel and to the beginning of strongly vortical (turbulent) flow caused by buoyancy forces in the molten pool. In this case the main characteristics of the heat and mass transfer are governed by several processes, namely: processes of natural convection, cooling regimes of the fuel at the external boundaries, presence of solid phase near cooled surfaces, properties of both solid and liquid phases and the process duration. Thus, complete solution of the thermal corium/vessel interaction problem requires consideration of the conjugate heat and mass transfer problem.

Usually all processes are considered separately. Prediction of natural circulation and calculation of the local heat flux allows to determine crust thickness and melting through of the reactor vessel (see, for example, references [20, 21]). Most previously published numerical and experimental investigations [1] - [10] were devoted to investigation of natural convection in a heat-generating fluid. Water used a simulating liquid in these experiments. As a result of these investigations heat transfer was determined as a function of dimensionless Rayleigh and Prandtl numbers in a specified geometry. In the framework of severe accident simulation, when a large amount of solidified corium is being formed, it is important to take into account the dependence of heat transfer (average Nusselt number) on crust formation phenomenon. To characterize heat transfer accounting for crust it is proposed to use not only Rayleigh number but also Ostrogradskii number. The latter parameter may be defined as ratio of integral heat generation in whole volume to average heat flux through solid phase and may be considered like dimensionless

Table of Nomenclature

$\mathrm{Asp} = l/x$ -aspect ratio
$a = k/(\rho c_p)$ - thermal diffusivity [m^2s^{-1}]
$\mathrm{Bi} = (h\,l)/k$ - Biot number
c_p - specific heat [$Jkg^{-1}K^{-1}$]
$\mathbf{e} = (0,1)$ - vector, characterized of ejected force direction
g - gravitational acceleration [ms^{-2}]
h - heat transfer coefficient
k - thermal conductivity [$Wm^{-1}K^{-1}$]
l - cavity height
$Nu = -(grad\,u)$ - local modified Nusselt number
$\mathrm{Nu} = 1/l \int_l Nu/(u_{av})\,dl$ - average Nusselt number (or intensity heat transfer)
$\mathrm{Os} = (q\,l^2)/(k\,(u_\ell - u_w))$ - Ostrogradskii number
$\mathrm{Pr} = \nu/a$ - Prandtl number
q - rate of volumetric heat generation
$Q = \frac{1}{l} \int_l Nu\,dl$ - average heat flux
$\mathrm{Ra}_q = (\beta\,g\,q\,l^5)/(a\,\nu\,k)$ - modified Rayleigh number
$\mathrm{Ra}_u = (\beta\,g\,(u_\ell - u_w)\,l^3)/(a\,\nu)$ - Rayleigh number
$\mathrm{Ste} = \lambda/(c_p\,(u_s - u_\ell))$ - Stefan number

t - dirnensionless time
u - temperature
$u_{av} = 1/V \int_V u\,dV$ - average temperature
u_ℓ - temperature of phase changes
u_w - temperature of wall

$\mathbf{v} = (v_1, v_2)$ - vector of velocity
v_1 - dimensionless horizontal velocity
v_2 - dimensioniess vertical velocity
x - cavity width,$(x = l)$
x_1 - dimensionless horizontal coordinate
x_2 - dimensionless vertical coordinate

Greek symbols

β - coefficient of volume extension
δ - delta-function
λ - enthalpy of phase changes
ν - kinematic viscosity
ρ - density

Subscript

$_{av}$ - average
$_{dn}$ - lower surface
$_\ell$ - liquidus
$_q$ - flux
$_s$ - solidus
$_{sd}$ - lateral surface
$_w$ - wall
$_u$ - temperature
$_{up}$ - upper surface

temperature of phase transition.

Notice that with increasing of the Ostrogradskii number, the volume of the solid phase (crust) decreases, but with decreasing Ostrogradskii number, growth of the crusts is observed. While considering the results of works [1] - [10] from the point of view of natural convection in a molten heat-generating corium, which forms the crust near the cooling boundaries, it should be noted that main results of these works corresponds to limiting case under sufficiently large Ostrogradskii numbers ($\mathrm{Os} \geq 10^3$). On the other hand in the reactor case, namely during retention of corium in reactor vessel lower head, the estimations of characteristic Ostrogradskii numbers are given by range from 100 to 1000. Furthermore, the usage of the previous correlation relations [1] - [10] for studying molten corium behaviour in the reactor vessel lower head may be correct when the crust presence doesn't influence distribution of heat fluxes. In real conditions the presence of crusts may significantly influence distribution of heat flux through boundaries. All mentioned above indicate necessity of more detailed investigation of natural circulation in a heat generating fluid for wide range of Rayleigh and Ostrogradskii numbers.

This paper provides numerical investigation of natural convection problem in a heat-generating fluid with regard to corium melting and solidification processes. The main goal of these numerical investigations is an obtaining of new correlation relations for heat fluxes distribution at the square cavity boundaries depending on Rayleigh and Ostrogradskii numbers.

As a result of parametric investigation of natural convection problem in a heat-generating fluid with phase transitions new correlation relations for the basic thermal characteristics (Nusselt number at the upper, lateral and lower boundaries of considered domain) were developed for the range of Ostrogradskii numbers (40–1000) and Rayleigh numbers (10^8–10^{12}). The obtained results were presented both in the form of graphics and in functional form as:

$$\mathrm{Nu} = C1(\mathrm{Ra}) \cdot \mathrm{Os}^n, \quad \text{or} \quad \mathrm{Nu} = C2(\mathrm{Os}) \cdot \mathrm{Ra}^m,$$

$$10^8 \le \mathrm{Ra} \le 10^{12}, \quad 40 \le \mathrm{Os} \le 1000, \quad \mathrm{Pr} = 1, \quad \mathrm{Asp} = 1.$$

2 GOVERNING EQUATIONS

Two-dimensional natural convection problem of a heat-generating fluid with phase transitions is considered in a square cavity with all isothermal walls. Let $\Omega = \{x | x = (x_1, x_2), 0 < x_\alpha < a, \alpha = 1, 2\}$ is the domain in which the solution of the problem is searched. Let $S(t)$ be the phase change interface, for which the temperature $u(x,t)$ is fixed and equal to a constant temperature of phase change u_ℓ.

$$S(t) = \{x | x \in \Omega, u(x,t) = u_\ell\},$$

where $u_\ell = \mathrm{Os}^{-1}$. In this case, the phase change boundary $S(t)$ divides the domain Ω by two subdomains. The domain $D(t)$, where $D(t) = \{x | x \in \Omega, u(x,t) > u_\ell\}$, corresponds to the liquid phase of substance and other part $D_0 = \Omega \backslash D$ corresponds to the solid phase.

The above-mentioned processes are described by an energy equation and unsteady Navier-Stokes equations with Boussinesq approximation for buoyancy. In the temperature-vorticity-stream function formulation for the 2D case these equations may be written in the following dimensionless form:

$$\left(1 + \mathrm{Ste}\, \chi_{s\ell}\right) \left(\frac{\partial u}{\partial t} + (\mathbf{v}\nabla)\, u\right) = \frac{1}{\mathrm{Pr}} \Big(\sum_{\alpha=1}^{2} \frac{\partial^2 u}{\partial x_\alpha^2} + 1\Big), \quad x \in \Omega \tag{1}$$

$$\frac{\partial \omega}{\partial t} + (\mathbf{v}\nabla)\, \omega = \sum_{\alpha=1}^{2} \frac{\partial^2 \omega}{\partial x_\alpha^2} + \frac{\mathrm{Ra}_u\, \mathrm{Os}}{\mathrm{Pr}} \frac{\partial u}{\partial x_1}, \quad x \in D(t) \tag{2}$$

$$\sum_{\alpha=1}^{2} \frac{\partial^2 \psi}{\partial x_\alpha^2} = -\omega, \quad x \in D(t) \tag{3}$$

$$v_1 = \frac{\partial \psi}{\partial x_2}, \quad v_2 = -\frac{\partial \psi}{\partial x_1} \tag{4}$$

where u, ω, ψ, v_1 and v_2 stand are used for the dimensionless temperature, vorticity, stream function, horizontal and vertical velocity components, respectively, x_1, x_2 are dimensionless Cartesian coordinates and t is the dimensionless time.

$$\chi_{s\ell} = \begin{cases} 1, & u \in (u_s, u_\ell), \\ 0, & u \notin (u_s, u_\ell). \end{cases}$$

$\mathrm{Ste}[\lambda/(c\,(u_s - u_\ell))]$ is the Stefan number. $\mathrm{Os}[(q\,l^2)/(k\,(u_\ell - u_w))]$ is Ostrogradskii number. Dammköhler number is western analog of Ostrogradskii number. $\mathrm{Pr}[(\nu/a)]$ is the Prandtl number, $\mathrm{Ra}_u[(\beta\, g\, (u_\ell - u_w)\, l^3)/(a\,\nu)]$ is the Ravleigh number, based on the temperature difference. Equation (2) may be written in standard form as:

$$\frac{\partial \omega}{\partial t} + (\mathbf{v}\nabla)\omega = \sum_{\alpha=1}^{2} \frac{\partial^2 \omega}{\partial x_\alpha^2} + \frac{\mathrm{Ra}_q}{\mathrm{Pr}} \frac{\partial u}{\partial x_1}, \tag{5}$$

where $\mathrm{Ra}_q[(\beta\, g\, q\, l^5)/(a\,\nu\, k)]$ is modified Rayleigh number, based on the volumetric heat generation value. Uniformly distributed internal heat sources are considered in the problem. Normalization is done here using the cavity height l, the kinematic viscosity ν and the value ql^2/k, which is proportional to a temperature difference.

The equation system (1), (5), (3), (4) is closed by appropriate initial and boundary conditions.

no-slip, no-permeability conditions for the velocity vector:

$$\psi(x,t) = 0, \quad \frac{\partial \psi}{\partial n}(x,t) = 0, \quad x \in \partial D, \tag{6}$$

isothermal thermal conditions:

$$u(x,t) = 0, \quad x \in \partial\Omega. \tag{7}$$

The quiescent state $u = \omega = \psi = 0$ was used as the initial conditions for the time integration.

3 NUMERICAL METHOD

Different numerical approaches [11] are used to solve of solidification and melting problem. In this paper the method of fictitious domains with extension by lower coefficients [12] is used to obtain numerical solution of equations (1), (5), (3), (4) with boundary conditions (6) and (7) for calculation of flow field in variable domain $D(t)$. Numerical implementation of the operator-splitting scheme used in calculations is based on the solution of elliptic grid problems at every time-step. Boundary values of the vorticity are calculated using completely implicit approach. The scheme is unconditionally stable for linearized equations, i.e. time-step doesn't depend on a spatial grid and is evaluated only from the temporal accuracy constraint for the nonlinear phenomena considered. Convective terms are approximated using special second-order formulae based on the central differences. More details of this method are available in refs. [13, 14]. Reasonable agreement of calculated results with experimental [2, 8] and numerical-experimental [9, 10] works for different boundary conditions and geometries was obtained. Results of validation for natural convection problem of a heat-generating fluid for cylindrical and hemispherical enclosures are presented in proceedings 21th Water Reactor Safety Meeting (USA) [16] and 4th International Topical Meeting on Nuclear Thermal Hydraulics, Operations and Safety (Taiwan) [17]. Besides, numerical results concerning simulation of periodical natural convection in rectangular enclosures are published in [15].

4 RESULTS AND DISCUSSION

Numerical calculations for the natural convection problem of a heat-generating fluid with phase transitions in square cavity were conducted on a Sun 4/80 (Sparc Station 10) workstation. The analysis of influence of the basic parameters on features of the convective heat exchange in a closed square cavity has been performed for the following range of dimensionless parameter values: $10^8 \leq \mathrm{Ra} \leq 10^{12}$, $40 \leq \mathrm{Os} \leq 10^3$, $\mathrm{Ste} = 0$, $\mathrm{Pr} = 1$, $\mathrm{Asp} = 1$.

The range of Rayleigh numbers chosen for numerical investigation corresponds to unsteady laminar and transient to turbulent flow regimes [1](see table 1), that's why all calculations were conducted without any turbulent models.

Table 1:Heat transfer regimes ([1]).

Regimes	Ra
Conductive Regime	10^4
Laminar Convection	10^5–10^8
Periodic Flow	10^8–10^9
Transient to Turbulent Regime	10^{10}–10^{12}
Turbulent Regime	$> 10^{12}$

Ostrogradskii numbers for numerical predictions were chosen from the following range: $40 \leq \mathrm{Os} \leq 1000$. Ostrogradskii numbers from this range may correspond to different cases of severe accident and experiments with prototypic core materials. Let's consider two limiting cases:

- In the first one the molten pool consists of oxidic materials such as UO_2 and ZrO_2, having the low heat conductivity $\approx 3\ W/(mK)$. Let the characteristic size of the molten pool equals $\approx 2.5\ m$, the melting temperature of the molten pool is equal to $\approx 2800\ K$ and the boundary temperature is equal to $300\ K$. Such conditions correspond to large Ostrogradskii numbers ≈ 830.

- In the other limiting case, the molten pool consists from the homogeneous mixture of oxidic and metal materials having the high heat conductivity $\approx 10\ W/(mK)$. Assume that the characteristic size of the molten pool is equal to ($\approx 1\ m$) and the melting temperature and cooling temperatures are the some like in the first case. Such conditions correspond to small Ostrogradskii numbers ≈ 40.

The rate of volumetric heat generation both in the first and in the second cases was equal to $1\ W/(m^3)$.

Evolution of melting zone defined by Stefan number is not goal of investigation for this article, because the quasi steady state regime of flow is considered, therefore numerical predictions may be performed for the case $\mathrm{Ste} = 0$. Prandtl number was fixed in all calculations and equals unity.

While processing of the calculation results main attention have been given to such dimensionless parameters as intensity of heat transfer (local Nusselt number) at the lateral, upper and lower surfaces; volume of liquid phase. Since in process of achievement of quasisteady state solution indicated parameters were oscillating close to its average values, averaging of calculated values over sufficiently large time interval was performed.

While calculating the above-mentioned values numerical uncertainty due to oscillating regime of natural convection doesn't exceed 5% from its average values.

Calculation results presented below were made using grid 81×81 with finer meshes near interfaces which correspond to the mesh of 161×161 for Ostrogradskii number from the range $40 \leq \mathrm{Os} \leq 400$. For Ostrogradskii number from the range of $400 < \mathrm{Os} \leq 10^3$ were made using grid 81×81 with finer meshes near interfaces which correspond to the mesh of 321×321.

While verifying the program and the numerical method, Steinbrenner correlations [6] were used (see Fig.1).

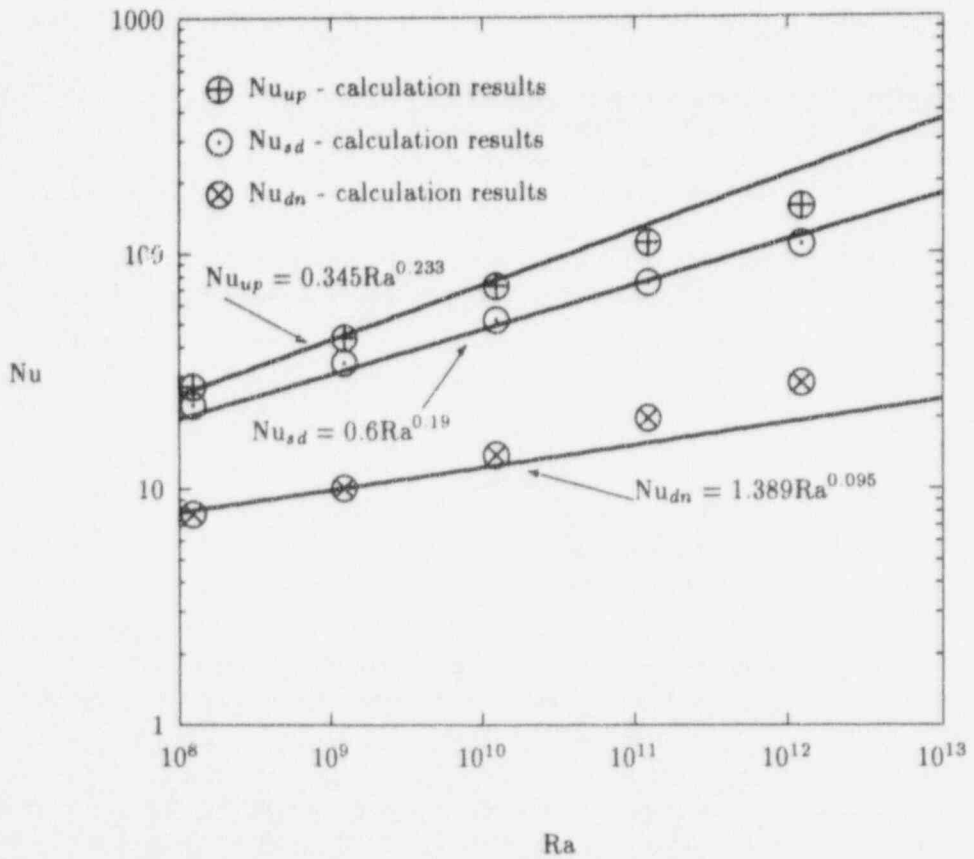

Fig.1: Comparison our predictions with Steinbrenner correlations.

On the Fig.1 Steinbrenner correlations for the case $Os = \infty$ are presented as solid lines. Our predictions for the case $Os = 1000$ are designated by signs and qualitative coincidence with Steinbrenner correlations. Notice that Nusselt numbers obtained in our predictions are calculated as ratio of average heat flux to average temperature in the whole domain, including both the liquid and solid phases. Whereas in Steinbrenner correlations Nusselt number is defined as ratio of average heat flux to the maximal liquid phase temperature only, this approach corresponds to investigation of problem under infinite of Ostrogradskii numbers. This fact does explain the difference between the experimental results and our predictions.

A comprehensive verification and validation of the program and numerical method on the problem of natural convection of a heat-generating fluid were performed in setting similar to [9, 10]. Good agreement (about 5% discrepancy) our predictions with results above-mentioned numerical-experimental works was obtained. A more full comparison of the predicted results was published in [16, 17]. Moreover tests have been performed on the conjugate heat transfer problem with moving boundary of the phase transition. A good agreement numerical results with experiment [18], in which the melting of the pure gallium is investigated, was achieved. Results of the calculations are presented in proceedings of the Workshop on Large Molten Pool Heat Transfer **OECD**[19].

4.1 Calculation results

Since of the relation of solid and liquid volumes may influence the intensity of a heat transfer towards vessel boundaries, investigation of the influence of Rayleigh and Ostrogradskii numbers on the behavior of the liquid phase fraction have been performed. The heat transfer regimes corresponding to Ostrogradskii numbers $40 < Os \leq 1000$, where the strongly nonlinear change of the volume of solid phase occurs, are investigated. Such regimes have the mixed conductive-convective character, therefore they are a greatest interest from the point of view of the natural convection simulation. Fig. 2 presents the variation of liquid phase volume in percent.

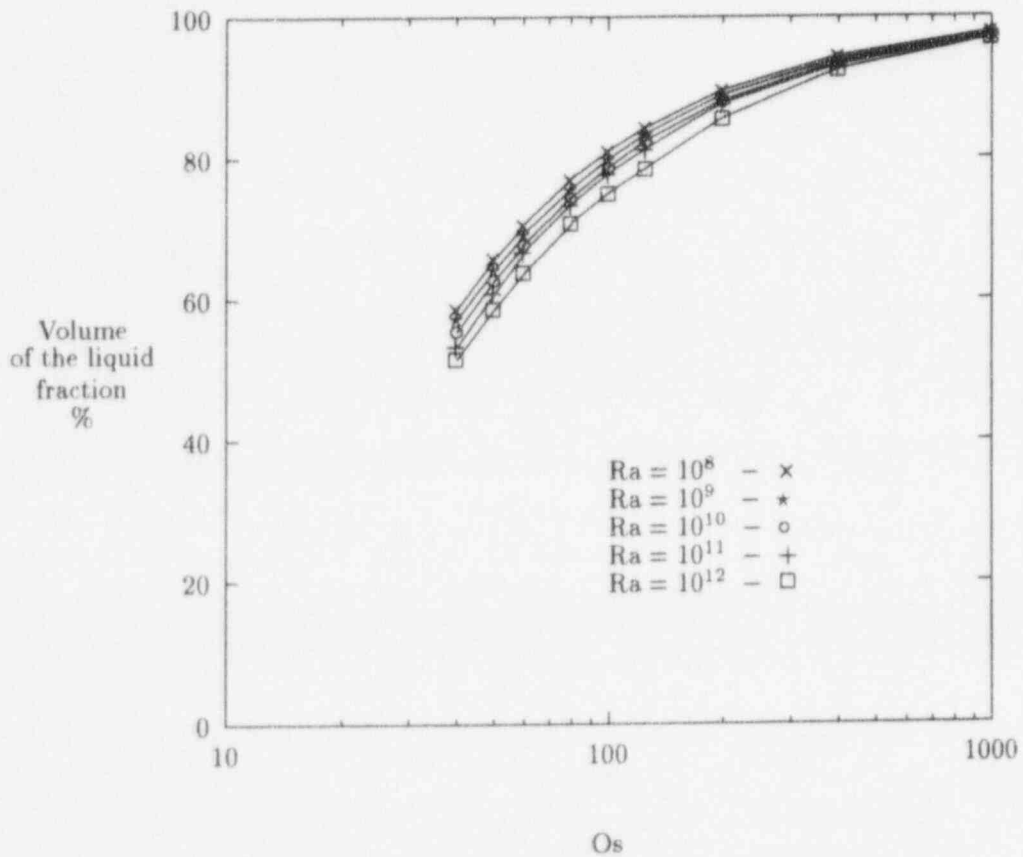

Fig.2: Volume of the liquid phase in percent.

Results of calculation show that small values of Ostrogradskii number ($40 \leq Os < 100$) correspond to small volume

of liquid phase. So in chosen range of Ostrogradskii number the volume of liquid phase was varied from 50 to 70 percent and hence the volume of solid phase was equal to 50, 30 percent. Thus the regime of the heat transfer in the square cavity under the small values of Ostrogradskii number has a heat conduction nature, mainly. At the same time for Ostrogradskii numbers ≥ 1000 convective processes begins to play dominating role in nature of heat transfer regime, because under the such values of Ostrogradskii number practically the whole domain is occupied by liquid phase. So for the case $\mathrm{Os} = 1000$ the volume of liquid phase reached $\approx$95–98% and consequently the solid phase no exceed 5%. The influence of Rayleigh number on the variation of liquid phase volume is less significantly than influence of Ostrogradskii number. Nevertheless, it should be noted that with increasing of Rayleigh number the liquid phase fraction decreases in the range of Ostrogradskii number $40 \leq \mathrm{Os} \leq 1000$.

In the framework of severe accident simulation it is necessary to know the distribution of heat flux on the corium/vessel interface boundary. Investigations of the influence of Ostrogradskii number at variation of average Nusselt number at the boundaries of square cavity were done in connection with above-mentioned problem. Fig.3 demonstrates the distribution of average Nusselt number for the different values of Rayleigh number on the upper wall. The intensity of heat transfer at the boundary of square enclosure becomes stronger with increasing of Ostrogradskii number. Initially this process is almost linear, but later with increasing of Ostrogradskii number passage to the more sloping region is being observed. The beginning of the sloping region could not be defined unambiguously, since with increasing of Rayleigh number shift of the left boundary of sloping region in the direction of the large Ostrogradskii numbers occurs.

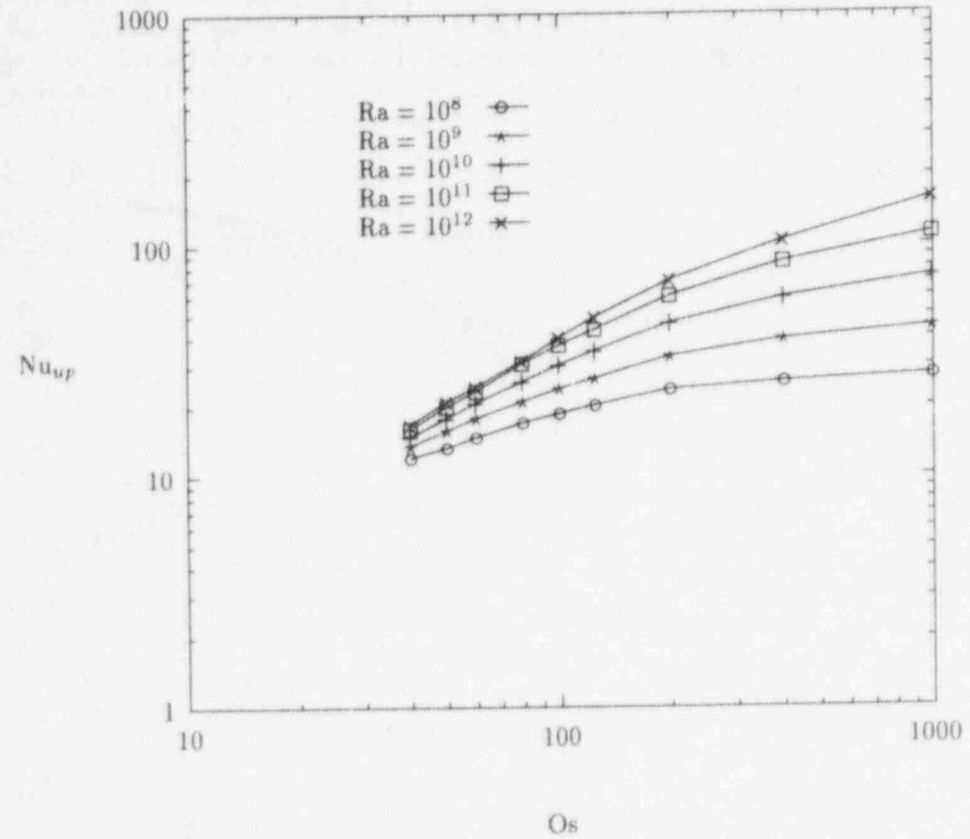

Fig.3: Average Nusselt number at the upper wall for the different Rayleigh numbers.

5 CORRELATION RELATIONS

As a result of parametric investigation of natural convection problem of a heat-generating fluid with phase transitions new correlation relations were developed. These relations connect basic dimensionless parameters of natural convection problem, Rayleigh number and Ostrogradskii number, with such characteristics of process of corium/vessel

interaction as intensity of heat transfer (Nu number) on the lateral, upper and lower surfaces of considered domain. Above-mentioned relations were received with help of linear regression method. Coefficients of straight line equation, connecting $log\,\mathrm{Nu}$ with $log\,\mathrm{Os}$ or $log\,\mathrm{Ra}$ are defined by means of method of least squares.

While obtaining correlations in the form of $\mathrm{Nu} = C \cdot \mathrm{Os}^n$ range of Ostrogradskii numbers was divided on the two following regions. The first region includes values from 40 to 200, in the second region values of Ostrogradskii number higher than 200 and interval 10^4 were included. Values of parameters C and n for the criteria dependencies $\mathrm{Nu}_{up}(\mathrm{Os})$, $\mathrm{Nu}_{sd}(\mathrm{Os})$, $\mathrm{Nu}_{dn}(\mathrm{Os})$ are given below in tables 2 and 3.

Table 2:Criteria dependencies $\mathrm{Nu}(\mathrm{Os})$ for the case $\mathrm{Os} \leq 200$.

$log\mathrm{Ra}$	$\mathrm{Nu} = C \cdot \mathrm{Os}^n$					
	up		sd		dn	
	C	n	C	n	C	n
8	2.036	0.475	2.436	0.391	5.568	0.079
9	1.460	0.602	1.754	0.505	4.449	0.162
10	1.013	0.731	1.352	0.593	3.479	0.246
11	0.757	0.836	1.045	0.671	2.769	0.322
12	0.708	0.864	0.860	0.735	2.341	0.373

Table 3:Criteria dependencies $\mathrm{Nu}(\mathrm{Os})$ for the case $\mathrm{Os} > 200$.

$log\mathrm{Ra}$	$\mathrm{Nu} = C \cdot \mathrm{Os}^n$					
	up		sd		dn	
	C	n	C	n	C	n
8	20.590	0.038	16.880	0.041	7.323	0.016
9	28.123	0.059	21.194	0.064	7.684	0.047
10	38.154	0.079	28.271	0.076	13.079	0.009
11	44.709	0.116	28.442	0.127	14.618	0.041
12	36.069	0.194	25.197	0.192	17.048	0.063

The graphs of Nusselt number, Nu, against Ostrogradskii number, Os, for Rayleigh number 10^{12} are shown in Fig.4. Correlations for the range of Ostrogradskii number $\mathrm{Os} \leq 200$ are presented as solid lines. The criteria dependencies for the range of Ostrogradskii number $\mathrm{Os} > 200$ are presented as dotted lines.

Dependencies in the form of $\mathrm{Nu} = C \cdot \mathrm{Ra}^n$ have been obtained for the range of Rayleigh numbers $10^8 \leq \mathrm{Ra} \leq 10^{12}$. In table 4 the values of parameters C and n for the criteria dependencies in the form of $\mathrm{Nu}_{up}(\mathrm{Ra})$, $\mathrm{Nu}_{sd}(\mathrm{Ra})$, $\mathrm{Nu}_{dn}(\mathrm{Ra})$ are shown. These relations correspond to reactor conditions, i.e. to values of Ostrogradskii number $\mathrm{Os} = 1000, 400$ and 200.

Table 4:Criteria dependencies $\mathrm{Nu}(\mathrm{Ra})$.

Os	$\mathrm{Nu} = C \cdot \mathrm{Ra}^n$					
	up		sd		dn	
	C	n	C	n	C	n
1000	0.800	0.193	0.990	0.170	0.587	0.140
400	1.544	0.155	1.920	0.130	0.921	0.117
200	2.665	0.121	3.120	0.090	1.693	0.086

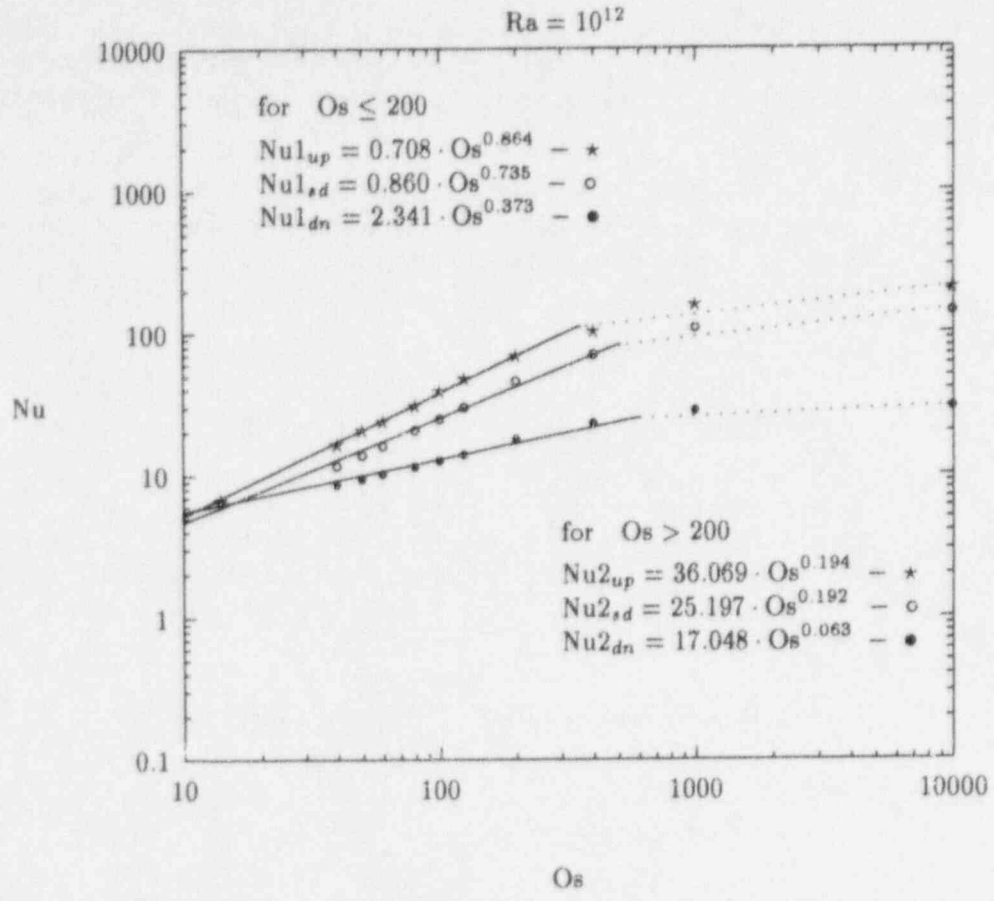

Fig.4: Correlation dependencies $\mathrm{Nu} = C \cdot \mathrm{Os}^n$ for Rayleigh number $\mathrm{Ra} = 10^{12}$.

The graphs of Nusselt number on the upper boundary, Nu_{up}, against Rayleigh number for Ostrogradskii numbers of 200,400,1000 are shown in Fig.5.

For comparison our predictions with experimental results the plot $\mathrm{Nu}_{up} = 0.345 \cdot \mathrm{Os}^{0.233}$, obtained by Steinbrenner [6] only for liquid phase ($\mathrm{Os} = \infty$) are shown in Fig.5. This plot are presented as dotted line.

CONCLUSIONS

1. In the framework of parametric numerical investigation of natural convection with phase transitions it is shown, that the heat and mass transfer is governed both by the natural circulation and crust formation phenomena;
2. New correlation relations for Nusselt numbers at the upper, lateral and lower boundaries of square cavity against Ostrogradskii number in the range of $40 \leq \mathrm{Os} \leq 1000$ for the different Rayleigh numbers were obtained;
3. New correlation relations for Nusselt numbers at the upper, lateral and lower boundaries of square cavity against Rayleigh number from 10^8 to 10^{12} for the Ostrogradskii numbers 200,400,1000 were obtained.

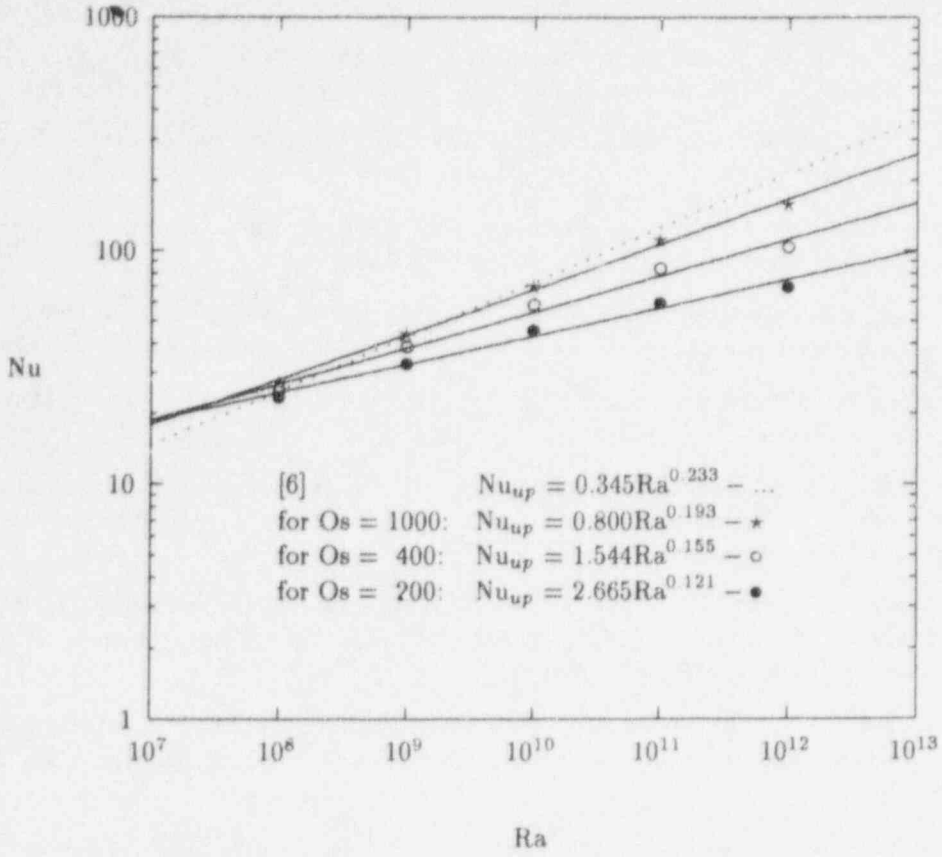

Fig 5: Correlation dependencies in the form of $\mathrm{Nu} = C \cdot \mathrm{Ra}^n$ for Ostrogradskii numbers $\mathrm{Os} = 200, 400, 1000$.

References

[1] K.M. Kelkar, R.C. Schmidt and S.V. Patankar, "Numerical analysis of laminar natural convection of an internally heated fluid in a hemispherical cavity," Proc.Int. Heat Transfer Conf., San Diego, 355-364 (1992).

[2] F.A. Kulacki and A.A. Emara, "Steady and transient convection in a fluid layer with uniform volumetric energy sources," J. Fluid Mech. 83, pt.2, 375–395 (1977).

[3] A.A. Emara and F.A. Kulacki, "A numerical investigation of thermal convection in a heat-generating fluid layer," ASME J. Heat Transfer 102, 531–537 (1980).

[4] F.X. Mayinger, M. Jahn, H.H. Reineke, and V. Steinbrenner, "Examination of Thermohydraulic Processes and Heat Transfer in a Core Melt, Federal Ministry for Research and Technology," Final Report BMFT RS 48/1, Institut fur Verfahrenstechnik der T.U., Hanover FRG, (in German), (1976).

[5] E.A. Kulacki, "Review and Evaluation of 'Examination of Thermohydraulic Processes and Heat Transfer in a Core Melt', by Mayinger, Jahn, Reineke, and Steinbrenner," Letter Report prepared for U.S.N.R.C. under contract AT(49-24)-0149, Mar.31 (1976).

[6] U. Steinbrenner, and H.H. Reineke, "Turbulent Buoyancy Convection Heat Transfer with Internal Heat Sources," Proc. 6th Int. Heat Transfer Conf., 2, 305-310 (1978).

[7] F.X. Mayinger, P. Fritz, H.H. Reineke, and et al., "Theoretical and Experimental Research on the Behavior of a Core Melt on Reactor Containment and on the Basement Concrete," Bunesministerium fuer Forschung und Technologie Report, FT-FB (RS 166-79-05), Bonn FRG, (in German) (1980).

[8] J.-H. Lee and R.J. Golstein, "An experimental study on natural convection heat transfer in an inclined square enclosure containing internal energy sources," ASME J. Heat Transfer 110, 345–349 (1988).

[9] M. Jahn and H.H. Reineke, "Free convection heat transfer with internal heat sources, calculations and measurements," Proc. 5th Int. Heat Transfer Conf., Tokyo, Japan, 74–78 (1974).

[10] H.-O. May, "A numerical study on natural convection in an inclined square enclosure containing internal heat sources," Int. J. Heat Mass Transfer 34, 919–928 (1991).

[11] A.A. Samarskii, P.N. Vabishchevich, O.P. Iliev and A.G. Churbanov, "Numerical simulation of convective/diffusion phase change problems - a review," Int. J. Heat Mass Transfer 36, No. 17, 4095–4106 (1993).

[12] P.N. Vabishchevich, Method of Fictitious Domains in Mathematical Physics, Moscow University publisher, Moscow (1991) (in Russian)

[13] P.N. Vabishchevich, M.M. Makarov, V.V. Chudanov, A.G. Churbanov, "Numerical simulation of convective flows in the stream function-vorticity-temperature formulation," Preprint of Institute for Mathematical Modelling, Russian Academy of Sciences, No.28 (1993) (in Russian).

[14] P.N. Vabishchevich, M.M. Makarov, A.G. Popkov, V.V. Chudanov, A.G. Churbanov, "Numerical solution of hydrodynamics problems in the stream function-vorticity formulation," Preprint of Institute for Mathematical Modelling, Russian Academy of Sciences, No.22 (1993) (in Russian).

[15] A.G. Churbanov, P.N. Vabishchevich, V.V. Chudanov, and V.F. Strizhov, "A numerical study of natural convection of a heat-generating fluid in rectangular enclosures," Int. J. Heat Mass Transfer 37, No. 18, 2969–2984 (1994).

[16] V.V. Chudanov, A.G. Churbanov, V.F. Strizhov and P.N. Vabischevich, "Current status and validation of RASPLAV code," Proc. 21st Water Reactor Safety Meeting, Washington, USA (1993).

[17] L.A. Bolshov, R.V. Arutyunyan, V.V. Chudanov, and et al., "Numerical study of natural convection of a heat-generating fluid in nuclear reactor safety problems,"
Proc. 4th International Topical Meeting on Nuclear Thermal Hydraulics, Operations and Safety, Taipei, Taiwan (1994).

[18] V. Voller and C. Swaminathan, "Fixed grid solution of phase change problems,"
J. of Theoretical and Applied Mechanics 2, Year XXIII, Sofia, 30-40 (1992).

[19] A.E. Aksenova, V.V. Chudanov, A.G. Churbanov, and et al., "Molten Pool Behavior in the Lower Head," Proc. of the Workshop on Large Molten Pool Heat Transfer, France, 321–345 (1994).

[20] J.E. O'Brien and G.L. Hawks, "Thermal Analysis of a Reactor Lower Head with Core Relocation and External Boiling Heat Transfer", Heat Transfer-Minneapolis, AIChE Symposium Series 97, No. 283, 159-168 (1991).

[21] T.G. Theofanous, Sanna Syri, Tony Salmassi, and et. al., "Critical heat flux through curved, downward facing, thick walls," Proc. of the Workshop on Large Molten Pool Heat Transfer, France, 409–428 (1994).

GEYSERING IN BOILING CHANNELS

Masanori ARITOMI and *Takatoshi TAKEMOTO*
Tokyo Institute of Technology, 2-12-1 Ohokayama, Meguro-ku, Tokyo, 152 Japan
TEL +81-3-5734-3063, FAX +81-3-5734-2959

Jing-Hsien CHIANG
Japan NUS Corporation Limited, 3-9-15 Kaigan, Minato-ku, Tokyo, 108 Japan
TEL +81-3-5540-1865, FAX +81-3-5540-1869

Michitsugu MORI
Tokyo Electric Power Company, 1-1-3 Uchisaiwai-cho, Chiyoda-ku, Tokyo, 100 Japan
TEL +81-45-585-6933, FAX +81-45-585-8943

and

Hiroaki TABATA
Japan Atomic Power Company, 1-6-1 Ohtemachi, Chiyoda-ku, Tokyo, 100 Japan
TEL +81-3-3201-6631, FAX +81-3-3212-5720

ABSTRACT

A concept of natural circulation BWRs such as the SBWR has been proposed and seems to be promising in that the primary cooling system can be simplified. The authors have been investigating thermo-hydraulic instabilities which may appear during the start-up in natural circulation BWRs. In our previous works, geysering was investigated in parallel boiling channels for both natural and forced circulations, and its driving mechanism and the effect of system pressure on geysering occurrence were made clear. In this paper, geysering is investigated in a vertical column and a U-shaped vertical column heated in the lower parts. It is clarified from the results that the occurrence mechanism of geysering and the dependence of system pressure on geysering occurrence coincide between parallel boiling channels in circulation systems and vertical columns in non-circulation systems.

1. INTRODUCTION

Many concepts have been proposed for the next generation LWRs in which passive and simplified safety functions are actively introduced. A concept of natural circulation BWRs, e.g. the SBWR[1], has been proposed as one such case. It seems to be promising in that the primary cooling system can be simplified but simultaneously it also brings some disadvantages. Aritomi et al. provided a discussion concerning advantages and disadvantages on eliminating recirculation pumps[2]. From the consideration, it was clear that establishment of a rational start-up procedure is one of the most important problems in achieving natural circulation BWRs because they have to be heated by fission energy from start-up under low temperature and pressure conditions. Thermo-hydraulic instability was experienced during start-up in thermal natural circulation boilers using fossil fuel. Although there were no published papers about this instability, it was estimated that the instability might be a kind of geysering. In thermal natural circulation boilers, flow instability during the start-up is not a significant problem, so long as the dryout phenomenon, which induces heat transfer tube

failure, can be avoided. This countermeasure was worked out: The output from burners was decreased down to a partial load of about 25% which did not induce the dryout phenomenon and was then increased up to the rate power after the pressure in the steam header reached up to about 0.3MPa. On the other hand, if thermo-hydraulic instabilities were to occur during start-up in natural circulation BWRs, they would hamper their operation for raising power output because void fraction fluctuation in the reactor core would oscillate the reactivity.

The authors have also been investigating thermo-hydraulics during start-up in natural circulation BWRs simulating both normal and abnormal start-up conditions. It was found from the results that three kinds of thermo-hydraulic instabilities may occur according to reactor configuration and start-up procedure[2]; (1) out-of-phase geysering induced by condensation of a large bubble, (2) in-phase natural circulation instability induced by hydrostatic head fluctuation in steam separators and (3) out-of-phase density wave instability.

Thermo-hydraulic instabilities in boiling two-phase flow have been investigated for a long time. Boure, Bergles and Tong[3] and Aritomi[4] have reviewed previous works and classified instabilities into their driving mechanisms. Lahey and Drew[5] reviewed a number of reports concerning thermo-hydraulic instabilities in BWRs. Since the density wave instability has been investigated by many researchers, its driving mechanism has been understood and analytical methods have been established. In contrast with this, the geysering and natural circulation oscillation have not been investigated extensively.

Griffith is believed to have been the first to have investigated geysering[6]. He presented an aspect of geysering induced in the case where liquid in a vertical column with a closed end was heated near the bottom. Nakanishi et al. investigated geysering in a single channel under forced circulation conditions and found that geysering was only generated at velocities lower than 0.02m/s[7]. However, our study indicated that geysering appeared in velocities up to about 0.2m/s[2]. Geysering in parallel channels has never been understood well enough to design a way to prevent it from occurrence. The authors have been investigating geysering in twin parallel boiling channels under both natural and forced circulation conditions and proposed its driving mechanism[8]. In order to verify the proposed driving mechanism, the effect of subcooling in the outlet plenum on its occurrence was also investigated in twin parallel boiling channels under forced circulation[9].

Next, by considering our proposed driving mechanisms of geysering and natural circulation oscillation, it was inferred that an increase in the system pressure would suppress these instabilities. This inference was experimentally confirmed[10],[11]. Based on our proposed driving mechanism of geysering, it is inferred that geysering occurs most readily in twin channels and geysering may be not induced in natural circulation BWRs where there are many fuel assemblies. Geysering was, however, induced in the thermal boilers which had many heat transfer tubes. Finally, geysering was experimentally investigated in three and four parallel channels with the same thermo-hydraulic conditions under both natural and forced circulation conditions and the results were compared with those in twin channels in order to examine the effect of the number of channels on its stability map[12]. In addition, the experiments were also carried out for the heated lengths different in each channel to investigate how power distribution in the core influences the occurrence of geysering[12].

In this paper, geysering is investigated in a vertical column with its closed bottom and a U-shaped vertical column heated in the lower parts which are non-circulation systems with the aim of verifying the generality of the driving mechanism of geysering proposed for parallel boiling channels. Although it was clarified from our previous works[10],[11] that an increase in the system pressure prevents geysering from occurrence, the system pressure, at which geysering is prevented from occurrence, could not be clarified, because the experiments could not be performed at a pressure more than 0.2MPa due to the structure of the experimental apparatus. The U-shaped vertical is designed so as the experiments can be carried out up to 1MPa. The dependence of system pressure on geysering occurrence was investigated in the U-shaped vertical column and the results are compared with those obtained in parallel boiling

channels.

2. EXPERIMENTAL APPARATUS

A schematic diagram of an experimental apparatus is shown in **Fig.1**, which was composed of an upper tank and a test channel. Water was used as a work fluid. Vapor generated in the test section was liquefied by a condenser installed in the upper tank, and water temperature in the upper tank was monitored with a CA thermocouple and regulated by a subcooler and cartridge heaters installed therein. Pyrex glass viewing windows were attached on the side walls of the upper tank to monitor the water level and to observe phenomenon at the exit of the test channel. The upper tank, except for the observation windows, was covered with enough thermal insulator to restrain heat loss. The experimental apparatus was designed to withstand pressures up to 1MPa in order to study the dependence of system pressure on the stability flow map of geysering. A pressure regulation system, which consisted of a compressor, a pressure regulation valve and a relief valve, was installed in the upper tank. The system pressure was regulated by feeding pressurized air to the upper tank and by releasing it to the atmosphere through the relief valve.

Geysering was investigated experimentally in two kinds of test columns. One was a U-shaped vertical column composed of two vertical channels whose bottoms were connected. The circulation rate was measured by an orifice flowmeter installed in the connection. The other was a vertical column similar to Griffith's work[6]. In this case, a vertical column was detached from the U-shaped channel. The vertical part in each test section was an annular channel, and the inner rod was made of a cartridge heater (10mm O.D.), installed concentrically in the test section made of Pyrex glass (22mm I.D.) and heated by a AC current. The effectively heated length of the inner rod was 150mm, which was located near the bottom. The differential pressure between the bottom of each channel and the upper tank was measured by a differential pressure transducer. The heat loss from the test section was obtained in advance: Heat input of the heater, at which water temperature in the test channel was kept constant, was measured.

The experimental conditions are tabulated in **Table 1**.

3. DRIVING MECHANISM OF GEYSERING IN A VERTICAL COLUMN AND A U-SHAPED VERTICAL COLUMN

3.1 Results in a Vertical Column

At first, geysering was investigated experimentally in a vertical column similar to Griffith's work. Four kinds of flow pattern were observed with an increase in heat input; ① natural convection, ② geysering with periodicity, ③ geysering without periodicity and ④ stable two-phase flow, as a typical flow pattern map is shown in **Fig.2**.

In a natural convection region, heated water flows up along the heater wall and lower temperature water flows down along the outer wall. Hot water coming up is mixed complexly with cold water in a non-heated riser as secondary flow is induced, and thus the heat added in the heated section is transferred into water in the upper tank. With increasing heat flux, subcooled boiling is induced, water in the non-heated riser is heated and a slug bubble is formed quickly. **Figure 3** illustrates typical measurements and sketches of observation. The slug bubble grows absorbing small bubbles coming up, and void fraction in the channel increases. A decrease in the hydrostatic head enhances vaporization in the heated section. Immediately after the slug bubble arrives at the exit of the channel, it is mixed with subcooled water and is rapidly condensed and vanishes. If the non-heated riser is long enough, subcooled water reentering from the upper tank cannot reach the heated section and saturated

boiling always occurs. Consequently, superheated water does not exist but water temperature fluctuates as a change in the saturated temperature equivalent to a change in the hydrostatic head. Since the slug bubble is formed periodically, geysering appears with the periodicity. Since the vaporization rate increases as the heat flux increases, the feature of slug bubble formation becomes complex and irregular, that is, two slug bubbles may exist simultaneously in the non-heated riser. As a result, condensation frequency of a slug bubble varies and geysering appears without the periodicity. Typical measurements and sketches of observation are shown in **Fig.4**. With further increasing the heat flux, stable churn turbulent or annular mist flow appears in the riser and the differential pressure between the bottom of the channel and the upper tank scarcely fluctuates as shown in **Fig.5**.

Figure 6 shows typical results of amplitudes of differential pressure between the bottom of the channel and the upper tank. The amplitude is made dimensionless by the hydrostatic head in the channel filled with water. The amplitude increases with an increase in heat flux in the region where geysering is periodically induced, but is almost kept constant in the region where geysering without the periodicity occurs. For stable two-phase flow, differential pressure fluctuation becomes smaller.

Next, the effect of the water level on the flow stability map of periodical geysering was investigated to understand whether slug bubble condensation is indispensable for geysering to occur or not. The experimental results are demonstrated in **Fig.7**. If the water level above the exit of the channel is deep enough to condense a slug bubble rapidly, it does not influence the flow stability map of periodical geysering. With decreasing the water level, even if water in the upper tank is subcooled enough for bubble condensation, a slug bubble cannot condense perfectly but flows out through the free surface to a gas space, because water near the exit of the channel does not circulate enough and is heated up. The disappearance rate of a slug bubble in the test channel becomes longer, and thus another slug bubble is formed in the non-heated riser before a slug bubble disappears. The periodicity of geysering occurrence results in vanishing. It is seen from the experimental results that geysering is induced periodically in a vertical column under the following conditions:

Water in the upper tank is subcooled enough to condense rapidly a slug bubble. In a vertical column with a long non-heated riser located above the heated section and a narrow cross section, subcooled water reentering from the upper tank does not arrive at the heated section and boiling always occurs therein. Superheated water is not observed in the heated section under the conditions where geysering appears.

The existence of superheated liquid is not, therefore, an indispensable condition for geysering to occur.

3.2 Results in a U-shaped Vertical Column

In boiling circulation systems, the feature of geysering in parallel channels is different from that in a single channel because of difference in the freedom of flow rate distribution. Hence, the test section was remodeled from a vertical column to a U-shaped vertical column which consisted of two vertical columns and had two heated sections.

As heat fluxes increases equally in two columns, five kinds of flow pattern regions were observed; ① natural convection, ② geysering with periodicity, ③ stable boiling natural circulation, ④ density wave instability and ⑤ stable boiling natural circulation, as is shown on the typical flow pattern map in **Fig.8**.

In a natural convection region, heated water flows up along each heater wall and lower temperature water flows down along each outer wall. This phenomenon is the same feature as in a vertical column, and circulation between both vertical columns is not observed.

With increasing heat fluxes in both columns, subcooled boiling is induced, water temperature in the non-heated riser rises and a slug bubble is formed soon in a column (Column A). **Figure 9** shows typical measurements. The slug bubble grows absorbing small

bubbles coming up, and void fraction in the channel increases. A decrease in the hydrostatic head enhances vaporization in the heated section. Immediately after the slug bubble arrives at the exit of the channel, it is mixed with subcooled water and is rapidly condensed and vanishes. Then, subcooled water reenters from the upper tank to the other column (Column B). If the non-heated riser is long enough, subcooled water in the upper tank cannot reach the heated section of Channel B. At the next stage, a slug bubble is formed in Column B. These phenomena repeat periodically and alternatively in both columns. Namely, the flow direction alternates such as U-shaped manometer oscillation; from Column A to Column B and from Column B to Column A. This is the feature of geysering induced in a U-shaped vertical column.

As heat fluxes further increases, the plural slug bubbles appear in the non-heated riser. The circulation rate is increased intermittently by condensing the plural slug bubbles within a short period. Consequently, boiling natural circulation is induced at a steady state. In this case, the flow direction is fixed, that is, one column is a riser, and the other column is a downcomer whose heated section plays only a role of a preheater. In the present test section, flow direction is settled at random: Column A is sometimes a riser and Column B is sometimes a riser.

With a further increase in heat flux of both columns, density wave instability is induced, which oscillates round a constant natural circulation rate as shown in **Fig.10**. With further increasing heat fluxes, density wave instability is suppressed and stable boiling natural circulation appears again.

It is seen from **Fig.8** that the subcooling in the upper tank influences the region where density wave instability occurs, but that the region where geysering is induced is almost independent of it. In the regions where geysering and density wave instability occur, the characteristics of flow oscillation were investigated experimentally in reference to subcooling in the upper tank. **Figure 11** shows periods of flow oscillation for both geysering and density wave instability. In a U-shaped vertical column, since geysering behaves as a U-shaped manometer oscillation, all heated water does not flow out but the heated water equivalent to the volume, which flows out due to the formation of a large bubble, only replaces subcooled water reentering from the upper tank. Consequently, the subcooling in the upper tank does not affect directly the water temperature in the heated section. On the other hand, since natural circulation always occurs while density wave instability is induced, subcooled water in the upper tank is always fed to the heated section. Since the time delay for boiling is dependent on the subcooling, the period is influenced by it.

Figure 12 shows the amplitude of flow oscillation related to geysering. As the subcooling in the upper tank decreases or the heat flux increases, the amplitude becomes greater. An increase in the heat flux enlarges vaporization rate, so a larger slug bubble is formed in the non-heated riser. Since a decrease in the subcooling raises water temperature in the non-heated riser, a larger slug bubble is formed therein. An increase in the volume of a slug bubble increases the volumetric condensation rate and results in greater amplitude. An increase in the amplitude enhances the volume of subcooled water reentering from the upper tank to the column and the mixing rate of heated water and subcooled water. Consequently, since water temperature becomes lower with increasing the amplitude, time delay for boiling is almost constant even for an increase in the heat flux within the experimental conditions in this work, so the periods scarcely are independent of the heat flux.

If input powers of both heaters are different, the column with higher heat flux is a riser and the other column is a downcomer. Then, stable boiling natural circulation is induced and geysering does not appear. Once stable boiling natural circulation is formed, even if the input powers where geysering appears are regulated equally in both columns, geysering is not induced. Hence, geysering in a U-shaped vertical column is induced with a delicate balance.

From the results, the phenomenological mechanism of geysering induced in a U-shaped vertical column is postulated as follows:

At a low feat flux, small bubbles generated in saturated or subcooled boiling coalesce, and a large bubble covering the whole channel is formed in Column A. The formation of a large bubble increases void fraction in the riser and reduces the hydrostatic head. A decrease in the saturated temperature enhances vaporization in the heated section. The large bubble grows absorbing many small bubbles with higher drift velocity. When the large bubble reaches the upper tank, it is mixed with subcooled water therein, is rapidly condensed and vanishes. Consequently, the pressure is rapidly decreased, a rising flow rate is increased in the column and subcooled water reenters from the upper tank to the other channel (Column B). If the non-heated riser is long enough, reentering subcooled water cannot reach the heated section and hot water in the non-heated riser flows into the heated section. Both heated sections are filled with liquid, and a non-boiling condition is restored for a while. A large bubble is formed in the heated section of Column B where higher temperature fluid is reentered. It is the feature of geysering in a U-shaped vertical column that these phenomena appear periodically and alternatively in both columns.

To verify this phenomenological postulate, the effect of non-heated riser length on the flow stability map of geysering was investigated experimentally and the results are shown in **Fig.13**. In the case that the non-heated riser is short enough for subcooled water to reenter from the upper tank to the heated section, the unstable region where geysering is induced becomes narrower as for both heat flux and the subcooling in the upper tank. A slug bubble is condensed in Column A. The subcooled water reenters to Column B while being mixed with the heated water in the non-heated riser and reaches the heated section if the volumetric condensation rate is high enough. Water temperature in Column B is lower than that in Column A, and thus at the next stage, boiling occurs first in Column A and natural circulation is induced. If the non-heated riser is long enough for the reentering subcooled water not to arrive at the heated section, the flow stability map of geysering is almost independent of the non-heated riser length.

4. EFFECT OF SYSTEM PRESSURE ON GEYSERING OCCURRENCE

It was clarified from our previous works that an increase in the system pressure prevents geysering from occurrence. Since the experiments could not be performed at the pressure more than 0.2MPa because of the structure of the experimental apparatus, the system pressure preventing geysering from occurrence could not be clarified quantitatively. The effect of the system pressure on geysering occurrence was, therefore, investigated in a U-shaped vertical column.

Figure 14 demonstrates the experimental results of the dependence of the system pressure on the flow stability map of geysering in a U-shaped vertical column. The lower limits of heat flux where geysering appears are independent of the system pressure. On the other hand, the upper limits of heat flux decreases with an increase in the system pressure: Geysering wanting the periodicity is irregularly induced at 0.3MPa and geysering is prevented from occurrence at a pressure more than 0.3MPa. Typical measurements of geysering wanting the periodicity are demonstrated in **Fig.15**. **Figure 16** shows the dependence of the system pressure on amplitudes of flow oscillation for periodical geysering. The amplitude of flow oscillation increases slightly at the same heat flux with an increase in the system pressure. The periods are almost independent of the system pressure and heat flux similar to the results shown in **Fig.11**. The following insights are seen from our observation:

(1) The volume of a slug bubble generated at low heat flux becomes slightly greater with an increase in the system pressure, because of lower drift velocity of a slug bubble.
(2) As the system pressure increases, the upper volume limit of a slug bubble decreases and the plural slug bubbles are readily generated in the non-heated riser.
(3) When the plural slug bubbles appear in one column, subcooled water reenters continuously from the upper tank to the other column. Consequently, natural circulation is induced at

a steady state and geysering is suppressed from occurrence.

Let us compare the flow stability maps of geysering obtained in a U-shaped vertical column and in parallel boiling channels for natural circulation. Since the cross sections of flow channels are different from each test section, the volumetric heat generation rate is introduced in this paper. A result comparing the stability maps is illustrated in **Fig.17**. The following insights are seen from the figure:

(1) The stability maps agrees between both experimental apparatus even if their configuration are remarkably different: A U-shaped vertical column is a non-circulation system and the parallel boiling channels is a circulation system.

(2) The upper limit of the system pressure where geysering is induced is about 0.3MPa.

From the results mentioned above, the driving mechanism of geysering induced in parallel boiling channels and a U-shaped boiling channels, which have a freedom of flow direction, can be explained as follows:

When subcooled boiling is induced, a large bubble covering the whole channel is formed in the non-heated riser located in the downstream of the heated section if velocity is low enough. Then, the growth of a large bubble decreases the hydrostatic head, decreases the saturated temperature and results in enhancement of vaporization in this channel. When the large bubble reaches the outlet plenum, if water therein is subcooled, it is rapidly condensed and vanishes. The pressure is rapidly decreased and high rising flow is induced in the channel. Consequently, in parallel boiling channel systems, if the volumetric condensation rate of the large bubble is great enough, flow reversal or an almost stagnant condition is induced in the other channels. In a U-shaped boiling channel system, subcooled water reenters in the other channel. At the next stage, a large bubble is formed in the channel where the highest temperature water exists. In U-shaped boiling channel systems, if water temperature in the channel where the large bubble was formed and condensed is higher than that in the other channel, natural circulation is induced at a steady state, and if it is lower, geysering occurs since a large bubble is formed in the other channel.

Therefore, the following condition is indispensable to induced geysering: (1) Circulation rate is low enough to generate a large bubble covering the whole channel, and (2) water in the outlet plenum is subcooled enough to condense the large bubble rapidly.

An increase in the system pressure suppresses a large bubble from formation and results in preventing geysering from occurrence.

5. CONCLUSIONS

Geysering was investigated experimentally in a vertical column and a U-shaped vertical column heated in the lower parts. The results were compared with those which had been obtained in parallel boiling channels for natural circulation. The following insights were clarified:

(1) In a vertical column, geysering is induced periodically under the following condition: Water in the upper tank is subcooled enough for condensing rapidly a slug bubble. In a vertical column with a long non-heated riser located above the heated section and a narrow cross section, subcooled water reentering from the upper tank does not arrive at the heated section and boiling always occurs therein. Superheated water is not observed in the heated section under the conditions where geysering appears. Therefore, the existence of superheated liquid is not required for geysering to occur.

(2) In a U-shaped vertical column with short heated sections and long non-heated risers, geysering is induced periodically and alternatively in both channels like U-shaped manometer oscillation for low heat input, that is, the average circulation rate is almost zero. With an increase in heat input, natural circulation is steadily induced. The flow direction is random. The heated section in the downcomer plays a role of a preheater.

As heat input further increases, the density wave instability appears.

(3) The driving mechanism of geysering in a U-shaped vertical column is the same as that in parallel boiling channels under circulation conditions.

(4) As for the effect of system pressure on geysering occurrence, rearranging the heat input in the term of calorific power unit fluid volume, the flow stability map for a U-shaped vertical column is identical to that in parallel boiling channels under natural circulation conditions. Geysering is not induced at pressures higher than about 0.3MPa.

This work has been carried out in boiling channels with simple configuration as a fundamental study. Hence, the flow stability map and boundaries derived experimentally in this work cannot be applied to full scale BWR prototypes, so that it is recognized that scaling-cum-dimensional testings would need to be conducted to establish their foundation.

This work was performed in the Tokyo Institute of Technology in collaboration with the Tokyo Electric Power Company and the Japan Atomic Power Company.

REFERENCE

[1] J.D.Duncan. SBWR, A Simplified Boiling Water Reactor, *Nucl. Engrg. Des.*, **109** 73-77 (1988).

[2] M.Aritomi, J.H.Chiang, T.Nakahashi, M.Wataru and M.Mori, Fundamental Study on Thermo-Hydraulics during Start-up in Natural Circulation Boiling Water Reactors, (I) Thermo-Hydraulic Instabilities, *J. Nucl. Sci. Technol.*, **29** (1992) 631-641.

[3] J.A.Boure, A.E.Bergles and S.L.Tong, Review of Two-Phase Flow Instability, *Nucl. Engrg. Des.*, **25**, (1973) 165-192.

[4] M.Aritomi, Handbook of Two-Phase Flow; 6. Flow Stability, *Corona Co.*, (1989.5) 171-205 (in Japanese).

[5] R.T.Lahey,Jr. and D.A.Drew, An Assessment of the Literature Related to LWR Instability Model, *NUREG/CR-1414* (1980).

[6] P.Griffith, Geysering in Liquid-Filled Lines, *ASME Paper 62-HT-39* (1962).

[7] S.Nakanishi, S.Ishigai, M.Ozawa, Y.Mizuta and H.Tarui, Flow Instability in Boiling Channels (2nd Report, Geysering), *Trans. JSME,* **44** (1978) 4252-4262 (in Japanese).

[8] M.Aritomi, J.H.Chiang and M.Mori, Fundamental Studies on Safety-Related Thermo-Hydraulics of Natural Circulation Boiling Parallel Channel Flow Systems under Startup Conditions (Mechanism of Geysering in Parallel Channels), *Nuclear Safety,* **33** (1992) 170-182.

[9] M.Aritomi, J.H.Chiang and M.Mori, Geysering in Parallel Boiling Channels, *Nucl. Engrg. Des.*, **141** (1993) 111-121.

[10] J.H.Chiang, M.Aritomi, R.Inoue and M.Mori, Thermo- Hydraulics during Start-up in Natural Circulation Boiling Water Reactors, *Nucl. Engrg. Des.* **146** (1994) 241-252.

[11] J.H.Chiang, M.Aritomi, M.Mori and M.Higuchi, Fundamental Study on Thermo-Hydraulics during Start-up in Natural Circulation Boiling Water Reactors, (III) Effect of System Pressure on Geysering and Natural Circulation Oscillation, *J. Nucl. Sci. Technol.*, **31** (1994) 883-893.

[12] M.Aritomi, J.H.Chiang, T.Ishikawa, M.Mori and H.Tabata, Thermo-Hydraulic Instabilities during Start-Up in Natural Circulation Boiling Water Reactors (Effect of the Number of Channels on Flow Instabilities), *Proc. 1st Germany-Japanese Symposium on Multi-Phase Flow,* Karlsruhe, *KfK 5389* (1994.8) 285-299.

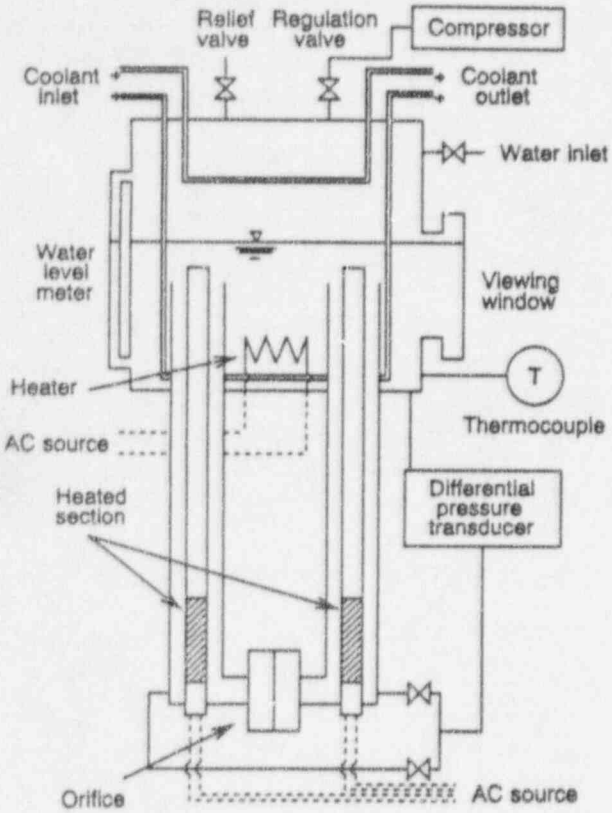

Fig.1 Experimental apparatus of a U-shaped vertical column

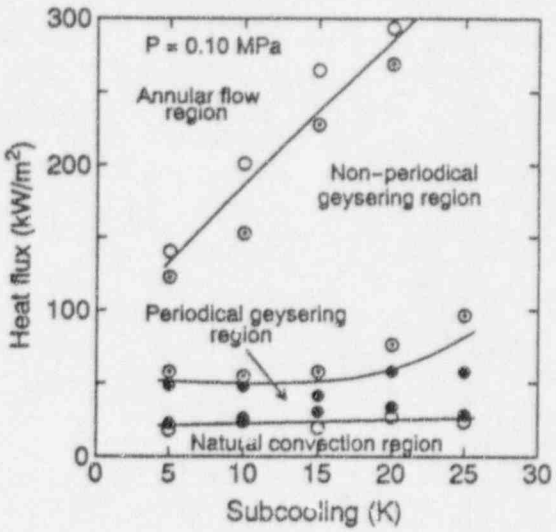

Fig.2 Flow stability map in a vertical column

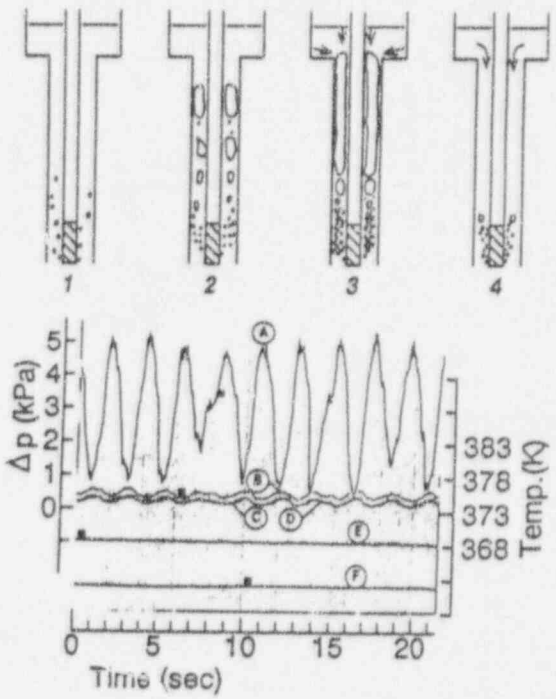

Ⓐ : Differential pressure between the bottom of a column and the upper tank
Ⓑ ~ Ⓓ : Water temperature in the heated region
Ⓔ : Water temperature in the upper tank
Ⓕ : Heat flux

Fig.3 Typical measurements and sketches of periodical geysering

Table 1 Experimental conditions

Pressure in the upper tank	0.1 - 0.5MPa
Subcooling in the upper tank	5 - 25K
Heat Flux	0 - 300kW/m^2
Heated length	150mm
Non-heated riser length	260, 610, 960mm

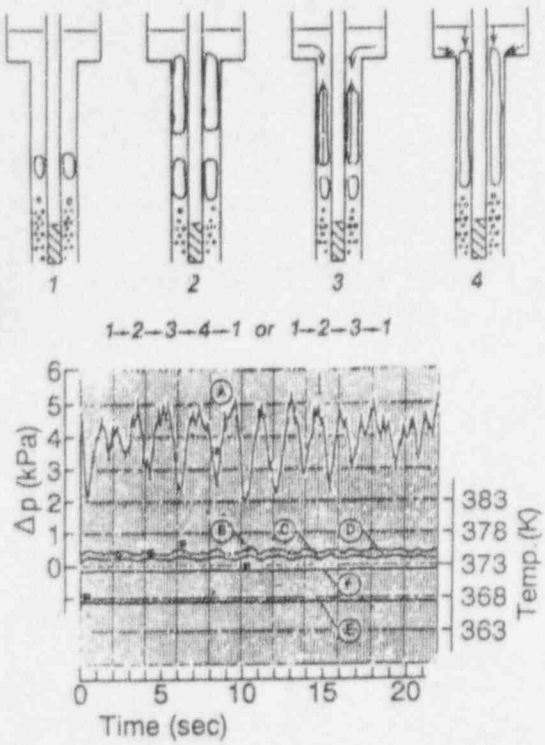

Ⓐ : Differential pressure between the bottom of a column and the upper tank
Ⓑ ~ Ⓓ : Water temperature in the heated region
Ⓔ : Water temperature in the upper tank
Ⓕ : Heat flux

Fig.4 Typical measurements and sketches of non-periodical geysering

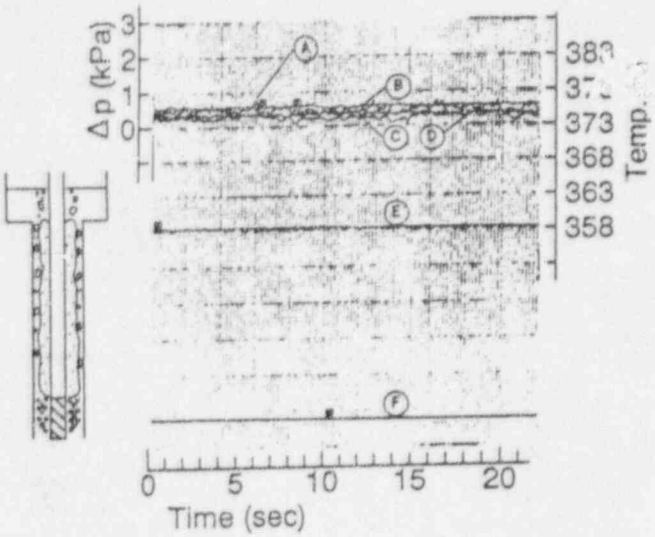

Ⓐ : Differential pressure between the bottom of a column and the upper tank
Ⓑ ~ Ⓓ : Water temperature in the heated region
Ⓔ : Water temperature in the upper tank
Ⓕ : Heat flux

Fig.5 Typical measurements and sketches of annular mist flow

① : Natural convection region
② : Periodical geysering region
③ : Non-periodical geysering region
④ : Stable abbular mist flow region

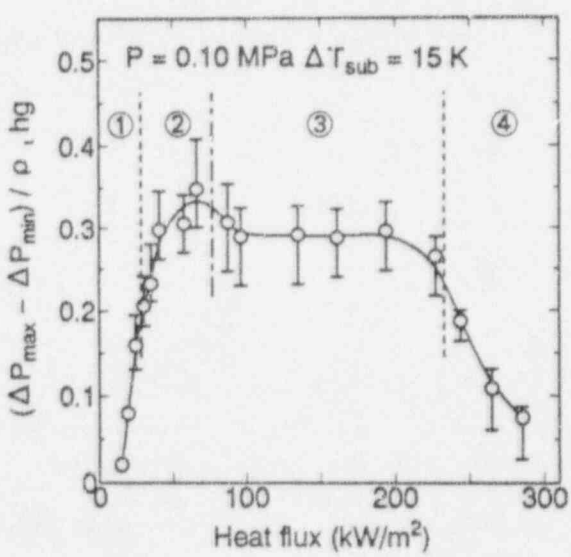

Fig.6 Amplitude of differential pressure between the bottom of the channel and the upper tank

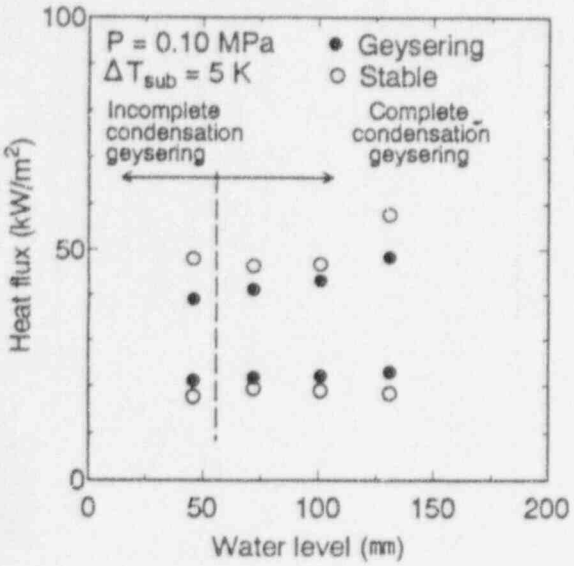

Fig.7 The flow stability map of periodical geysering in reference to water level

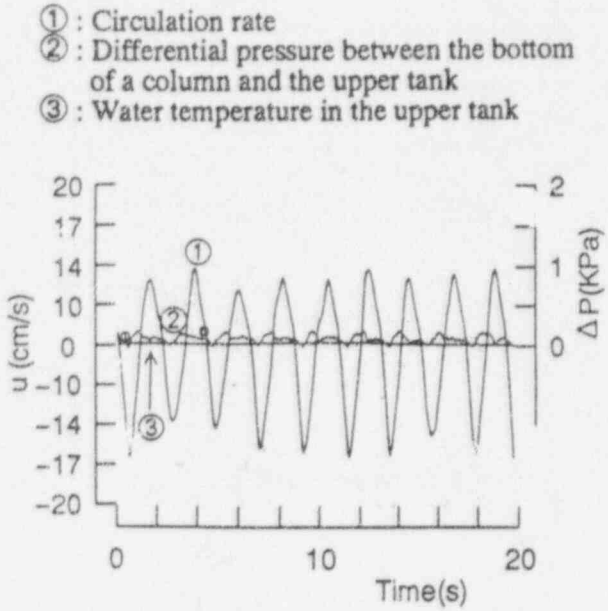

Fig.9 Typical measurements of geysering in a U-shaped vertical column

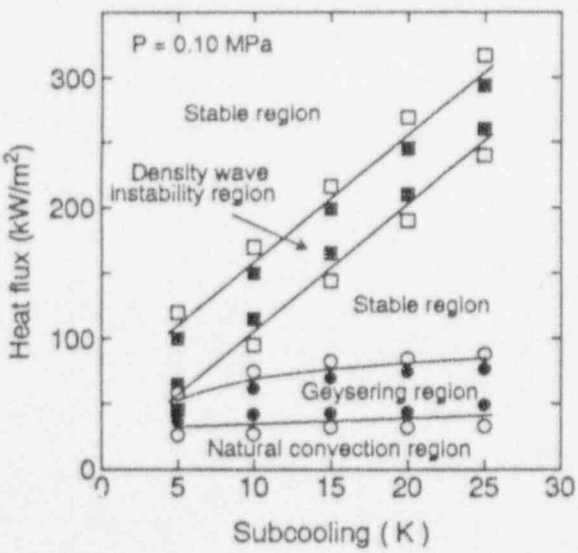

Fig.8 Flow stability map in a U-shaped vertical column

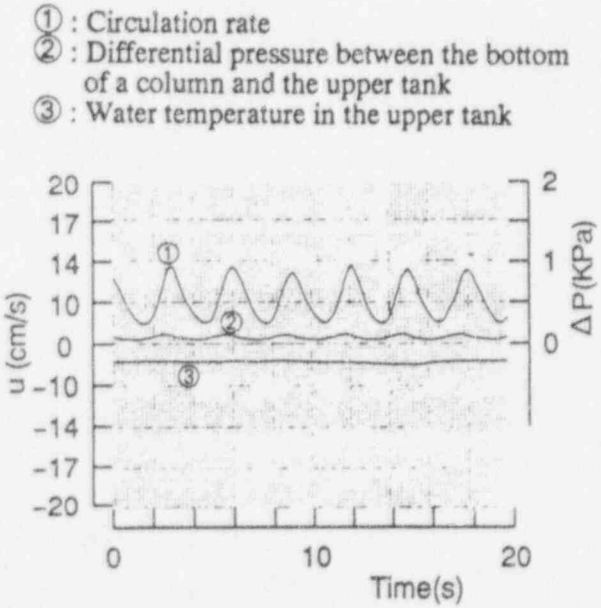

Fig.10 Typical measurements of density wave instability in a U-shaped vertical column

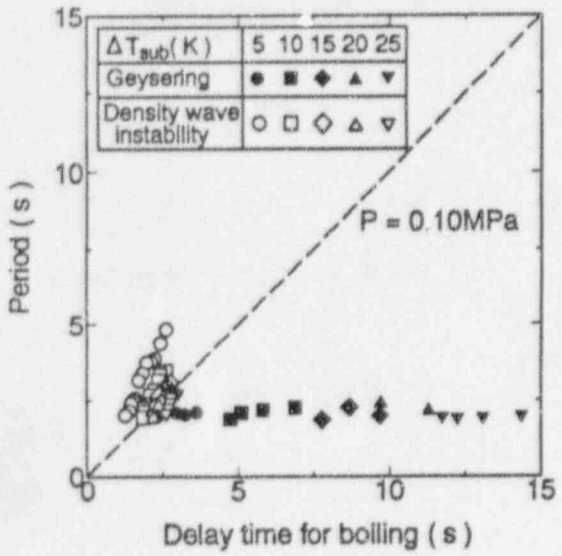

Fig.11 Periods of geysering and density wave instability in a U-shaped vertical column

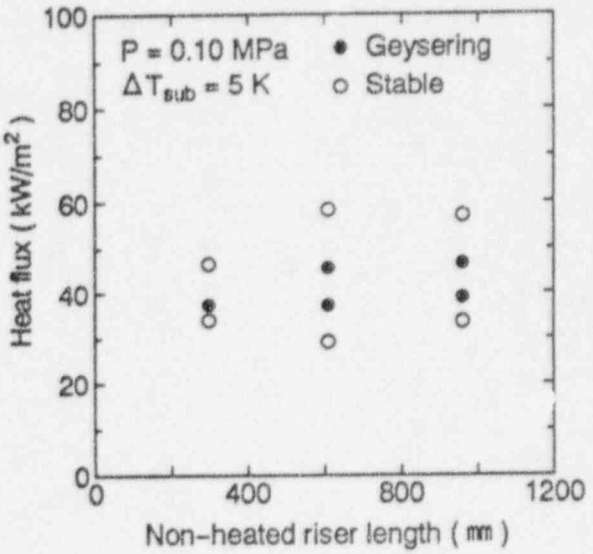

Fig.13 The effect of non-heated riser length on flow stability map of geysering

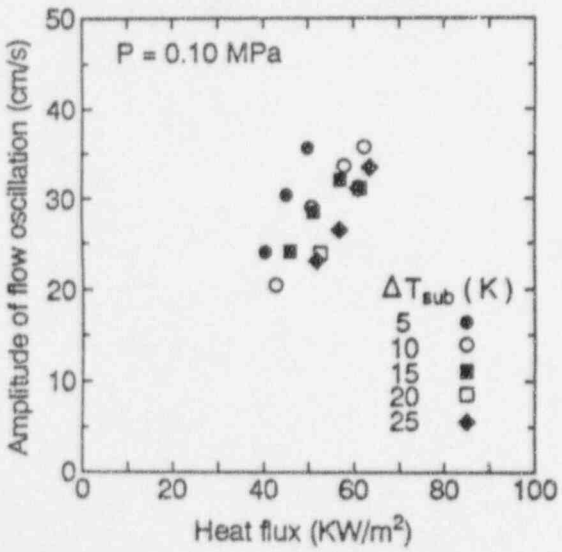

Fig.12 Flow oscillation amplitudes of geysering in a U-shaped vertical column

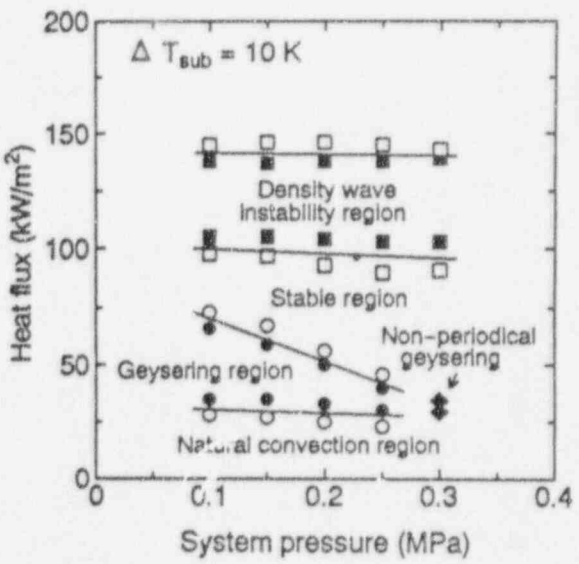

Fig.14 The effect of system pressure on flow stability map of geysering in a U-shaped vertical column

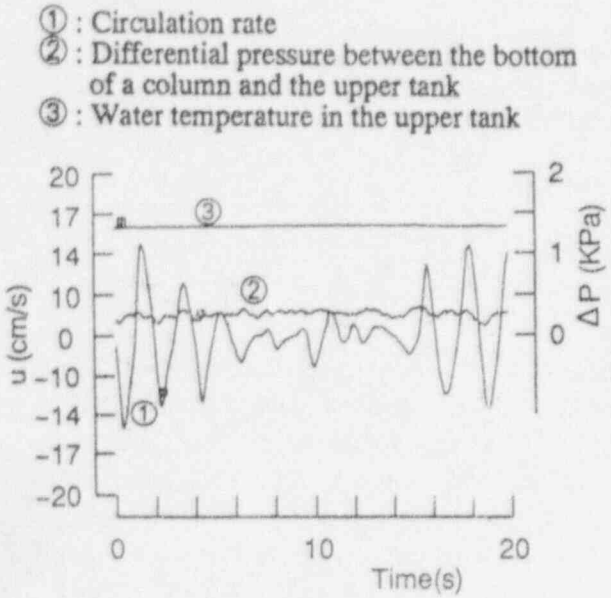

Fig.15 Typical measurements of geysering wanting the periodicity in a U-shaped vertical column

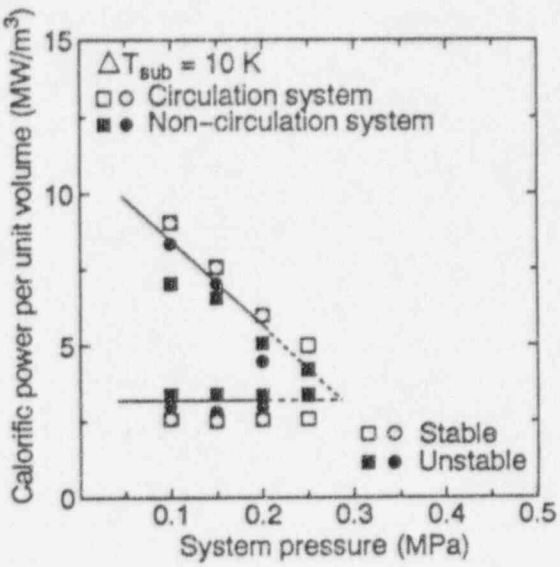

Fig.17 Comparison of the effect of system pressure on flow stability of geysering between parallel boiling channels and a U-shaped column

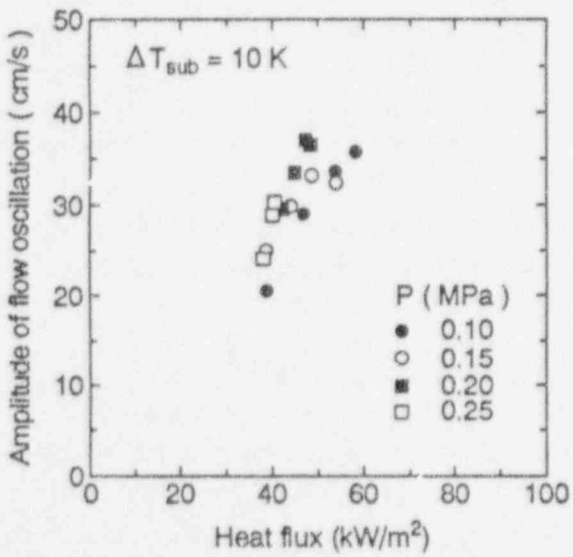

Fig.16 Flow oscillation amplitudes of geysering in a U-shaped vertical column in reference to system pressure

Two-Phase Flow Stability Structure in a Natural Circulation System

Zhiwei Zhou *
Nuclear Engineering Laboratory
Swiss Federal Institute of Technology at Zurich (ETHZ)
ETH Zentrum, CH-8092 Zurich, Switzerland

ABSTRACT

The present study[1] reports a numerical analysis of two-phase flow stability structures in a natural circulation system with two parallel, heated channels. The numerical model is derived, based on the Galerkin moving nodal method. This analysis is related to some design options applicable to integral heating reactors with a slightly-boiling operation mode, and is also of general interest to similar facilities. The options include: (1) Symmetric heating and throttling; (2) Asymmetric heating and symmetric throttling; (3) Asymmetric heating and throttling. The oscillation modes for these variants are discussed. Comparisons with the data from the INET two-phase flow stability experiment have qualitatively validated the present analysis.

INTRODUCTION

Two-phase flow density-wave oscillations (DWOs) in natural circulation systems are of particular importance in the design of integral heating reactors (Wang et al. [1], Wu et al. [2]) . This type of reactor is designed for low-pressure operation, and the so-called *low-quality DWOs* may occur in some circumstances. Since Russian scientists proposed the conceptual design of the AST-500, an integral, slightly-boiling heating reactor (Zaval'skii et al. [3]), the development of the relevant technologies in a number of countries (e.g Wang et al. [1], Burgsmueller et al. [4] and Goetzman et al. [5]) has demanded the better understanding of these special types of instabilities in real engineering systems.

The studies concerning DWOs before 1980 concentrated mainly on the high-quality DWOs relating to BWRs and other industrial boiling systems. Many analysis tools and methods were developed and validated, either by comparing with the experimental data, or by being applied to the design of some prototype facilities. The achievements of the high-quality DWOs analysis have been reviewed by Bouré et al. [6], Bergles [7], Yadigaroglu [8] and Lahey and Podowski [9]. From a stability experiment, Fukuda and Kobori [10] classified DWOs into two types, namely *the gravitational pressure drop dominated* and *the frictional pressure drop dominated* instabilities. These two types exactly correspond to the low-quality and the high-quality DWOs discussed in the present paper. They also found that the low-quality DWOs would more easily occur in a natural circulation system. Recent experimental investigations, reported by Chiang and Aritomi [11] (where they named as *"natural circulation oscillation"*) and Kyung and Lee [12], have confirmed the classification of Fukuda and Kobori. In fact, the analysis of the low-quality DWOs

*Previous address: Institute of Nuclear Energy Technology (INET), Tsinghua University, Beijing 100084, China.
[1]Paper submitted to NURETH-7, Saratoga Spring, New York, September 10-15, 1995

did not attain real engineering importance until a few years ago when the research and development of integral heating reactors, and other passive safety systems, accelerated.

Although the general mechanisms of DWOs have been well understood for sometime, and many tools and methods have been developed, the complex interactions of different oscillation modes in a natural circulation system with parallel heated channels still maintain some research interest. Thus, not only is the validation of some general, thermal-hydraulic codes still necessary, but also fundamental studies are needed for gaining insight and confidence in low-pressure applications.

The 5-MW prototype heating reactor NHR-5 (Fig. 1, Wang et al. [1]) at the INET of Tsinghua University in Beijing, has run successfully for several years. Currently, the NHR-5 is licensed to run in a natural circulation PWR mode. The operational experience gained has proven that the associate technologies of the NHR-5 are very safe and reliable.

However, it appears that a number of thermal-hydraulic problems related to the *slightly-boiling* operation mode remain unsolved. Among these, two-phase flow instabilities are still interesting topics, especially during the start-up stage and power reduction transients.

An experiment, namely the INET-PSI stability experiment, from which the reference data for the NHR-5 design were produced was carried out co-operatively by the INET and the Paul Scherrer Institute (PSI) Switzerland (Fig. 2, Wu et al. [2]). This facility was a natural-circulation system with two parallel, heated channels and was used as an out-of-core hydraulic simulation system for the NHR-5. The oscillations have been detected in the range of $x_e < 0.01$ and $p < 20bar$ with the periods of seconds.

Some parallel theoretical studies have also been undertaken by Gao et al. [13], Brunet et al. [14], Zhou and Yadigaroglu [15] and Zhou and Heusser [16]. Recently, Zhang et al. [17] reported a numerical simulation using the RETRAN02 code, which showed that the low-quality DWOs may possibly take place in integral heating reactors working in the PWR mode during a heat-sink-loss accident. The studies mentioned above indicate that the existing methods and tools, previously developed for analyzing high-quality DWOs can be extended to the analysis of low-quality DWOs.

The above-mentioned theoretical investigations and numerical simulations concerning low-quality DWOs have concentrated on finding stability boundaries, mostly for single-loop systems. The nonlinear characteristics of this type of DWO, especially in a complex system with parallel, heated channels, have not been thoroughly investigated.

Generally, the low-quality DWOs may be induced either in a single-loop or in a complex natural circulation system, either with or without power feedback, and either at a fixed power level or during a power transient. The present study is a numerical investigation of the low-quality DWOs applied to the INET experimental facility with two parallel heated channels. The present work differs from previous studies in aiming at the stability structures in this natural circulation system.

MATHEMATICAL MODELING

The numerical simulation model of the system is shown in Fig. 3. The mathematical system is derived from 1-D homogeneous equilibrium conservation equations for mass, momentum and energy as follows.

(a) Single-Phase Region

$$\dot{M} = (A\rho_f u) = C_1(t) \tag{1}$$

$$-\frac{\partial p}{\partial z} = \frac{f\rho_f u^2}{2D} + \frac{\partial \rho_f u}{\partial t} - \rho_f g \mathbf{e_g} \cdot \mathbf{e_s} + \sum_j K_j \delta(z - L_j) \frac{\rho_f u^2}{2} \tag{2}$$

$$\frac{\partial h}{\partial t} + u\frac{\partial h}{\partial z} = \frac{q'' P_H}{\rho_f A_H} \tag{3}$$

(b) Two-Phase Region

$$\frac{\partial \rho}{\partial t} + \frac{\partial}{\partial z}(\rho u) = 0.0 \tag{4}$$

$$-\frac{\partial p}{\partial z} = \frac{f\rho u^2}{2D} + \frac{\partial \rho u}{\partial t} + \frac{\partial}{\partial z}\left(\rho u^2\right) - \rho g \mathbf{e_g} \cdot \mathbf{e_s} + K_e \delta(z - L_H) \frac{\rho_e u_e^2}{2} \tag{5}$$

$$\frac{\partial \rho h}{\partial t} + \frac{\partial}{\partial z}(\rho u h) = \frac{q'' P_H}{A_H} \tag{6}$$

the equation of state gives:

$$\rho = \begin{cases} \rho_f & h < h_f(p_0) \\ \frac{1}{v_f + \frac{v_{fg}}{h_{fg}}(h - h_f)} & h > h_f(p_0) \end{cases} \tag{7}$$

The basic assumptions embedded in the present mathematical model include:

- the system pressure at which all thermodynamic properties are evaluated is constant;
- the flow in the system is 1-D, and both phases are incompressible fluids and homogeneously flow with the same cross-sectional velocity;
- the enthalpy distribution is linear, and the two phases are locally in thermal equilibrium;
- the heat flux on the wall is assumed constant and no power feedback is involved.

It is worth while to discuss the considerations of adopting the above assumptions for simplifying the mathematical system and for processing reliable numerical solutions, but with the main physical features remaining intact. It has been known [18] that 1-D model is generally inadequate to represent the effect of subcooled boiling for high frequency (> 1 Hz) stability analysis. The characteristic frequency in the present study is fairly below 1 Hz, thus 1-D subcoold boiling model should be valid. However, the RETRAN02 code simulation carried out by Gao et al. [19] has shown that the flow dynamics with a number of 1-D subcooled boiling models did not produce significantly different results to that with only the equilibrium assumption for the same system, under the similar operation conditions, but in the single-loop mode. We believe that the relatively large ratio of the riser length to the heater length of the INET experimental facility has diminished the influence of subcooled boiling. It might have stronger effect to the flow instabilities if such a ratio were small. Thus, thermodynamic equilibrium assumption is a trade-off between simplicity and perfection. It is suitable for the present study based on the confidences established from the past experiences when NHR-5 heating reactor was developed.

It has been also well-known [8] that DWOs are dominated only by the dynamic feedback mechanism among the perturbations of mass flow rate, flow enthalpy, two-phase density (or quality) and pressure

drops in the two-phase flow system. A dozens of parameters, such as phase slip factor (or drift-flux velocity), heat transfer coefficient, subcooled boiling, wall thermal capacity etc., may influence the details of flow stability, such as oscillation frequency, amplitude etc., but not the driving mechanism. The most adequate assumptions for simplifying physical system should be delineated as those under which the corresponding mathematical system becomes as simple as possible, the irrelevant and non-significant effects are eliminated, and the relevant and important effects are kept as much as possible aiming at the purpose of the analysis. The present study intends to investigate the mechanisms of the low-quality DWOs in a complicated natural circulation system and to gain insights and experiences of developing next generation of passively safe nuclear heating reactors. The assumptions listed above are believed to be fairly adequate for such purposes.

The system is divided into a number of control volumes as shown in Fig. 3. According to the above assumptions, the conservation equations are converted into a set of ordinary differential equations using the Galerkin-based moving nodal method and the Leibniz's rule of integration for the heated section, but with the fixed nodal method for the other components. The details of this model have been described by Lahey [20] for a single-loop natural circulation system, thus only the final form of the converted, ordinary differential equations, and the boundary conditions relating to the parallel channels, will be described.

The integral of the energy equation in the single-phase region in j-th heated channel gives

$$\frac{dL_{i,j}}{dt} = 2u_{in,j} - \frac{dL_{i-1,j}}{dt} - 2N_s \left(\frac{q'' P_H}{A_H \rho_f \Delta h_{sub}} \right)_j (L_{i,j} - L_{i-1,j}) \qquad (i = 1, N_s; j = 1, 2) \tag{8}$$

The integral of the mass conservation equation yields

$$\frac{dM_{ch,j}}{dt} = A_{H,j}(\rho_f u_{in,j} - \rho_{e,j} u_{e,j}) \qquad (j = 1, 2) \tag{9}$$

The assumed linear enthalpy profile in the two-phase flow region leads to

$$M_{ch,j} = \int_0^{L_H} \rho dz = \rho_f \lambda_j A_{H,j} + A_{H,j} \rho_f (L_{H,j} - \lambda_j) \frac{ln(\rho_f / \rho_{e,j})}{\rho_f / \rho_{e,j} - 1} \qquad (j = 1, 2) \tag{10}$$

which relates the fluid mass in the heated section j with the exit density.

The combination of the mass and energy equations in the two-phase flow region defines a velocity equation:

$$\frac{\partial u_j}{\partial z} = \Omega_j = \left(\frac{q'' P_H v_{fg}}{A_H \rho_f h_{fg}} \right)_j \qquad (j = 1, 2) \tag{11}$$

whose integration along the channel is

$$u_j(z, t) = u_{in,j} + \Omega_j (z - \lambda_j) \qquad (j = 1, 2) \tag{12}$$

Moreover, the integral form of the mass conservation for each segment in a riser is

$$\frac{dM_{r,j}}{dt} = A_{H,j} u_{e,j} (\rho_{r-1,j} - \rho_{r,j}) \qquad (r = 1, N_R; j = 1, 2) \tag{13}$$

The fine meshes used for the adiabatic risers justify the use of a linear density profile. The analogue to the heated section by using a linear profile of the enthalpy along the adiabatic riser proposed by Lahey [20] is not used, so that

$$M_{r,j} = \frac{A_{R,j} L_{R,j}}{2N_{R,j}} (\rho_{r,j} + \rho_{r-1,j}) \qquad (r = 1, N_R; j = 1, 2) \tag{14}$$

Equations (8), (9) and (13) define $2 \times (1 + N_s + N_R)$ system of first-order, differential equations, while equations (10) and (14) provide $2 \times (1 + N_R)$ supplementary algebraic relations. Meanwhile, the mathematical system has a total of $2 \times (3 + N_s + 2N_R)$ unknowns ($L_{i,j}$, $M_{ch,j}$, $M_{r,j}$, $u_{in,j}$, $\rho_{e,j}$, $\rho_{r,j}$). Hence, two additional equations are needed to close the system: these are the imposed boundary conditions.

The boundary conditions include the two pressure drop balances for the channels. Another unknown u_d, the velocity in the downcomer is, however, introduced. The integral of the momentum equation along each loop yields

$$\Delta p_d + \Delta p_j = 0 \qquad (j = 1, 2) \tag{15}$$

where Δp_d and Δp_j are pressure drops along the downcomer and the channel j, respectively. All acceleration terms are included implicitly in the pressure drop expressions for simplicity. Comparing to that given by Rizwan-uddin and Dorning [21], in which they separated the acceleration term from the total pressure drop for each channel, the present expression is equivalent. Their emphasis may be more aimed at the imposed pressure drop or imposed inlet mass flow rate boundary conditions, however the present one is more at natural circulation loops.

The splitting of the downflow region into the two heated channels satisfies the condition:

$$u_d = \sum_{j=1}^{2} \left(\frac{A_{H,j}}{A_{loop}} \right) u_{in,j} \tag{16}$$

By eliminating u_d between Eqs. (15) and (16), and then substituting for the pressure-drop balances. Hence, a mathematic system with $2 \times (3 + N_s + 2N_R)$ equations is generated, and now the unknown numbers are matched. The final form of ODE system can be symbolically expressed as

$$\frac{d\mathbf{Y}}{dt} = \mathbf{F}(\mathbf{Y}, t) \tag{17}$$

in which $\mathbf{Y} = (L_{i,j}, M_{ch,j}, M_{r,j}, u_{in,j}, \rho_{e,j}, \rho_{r,j})$ is the unknown vector to be solved.

Equation (17) is solved numerically using the implicit Gear's algorithm encompassed in the well-known, ODE solver package LSODE (Hindmarsh [22]). The relative and absolute tolerances for controlling computational errors are set as $E_R = 10^{-6}$ and $E_A = 10^{-7}$, respectively. The numerical tests [16] have indicated that when $E_A < 10^{-6}$ and $E_R < 10^{-5}$, LSODE code can reliably solve the mathematical system modelling the limit cycle oscillatory flow in the physical system mentioned above. The time steps are automatically controlled by the code according to the error tolerances with the maximal time step $\Delta t_{max} = 0.05s$. Because the period of the expected flow oscillation has been known in the range of 1 to 20 seconds, the resolution defined by Δt_{max} has been proven quite satisfactory.

Numerical tests have demonstrated that the number of nodes used in the Galerkin-based nodal method does not significantly influence the results. The present node numbering ($N_s = 3$ and $N_R = 9$) is a suitable compromise between accuracy and efficiency.

RESULTS AND DISCUSSIONS

Proper thermal-hydraulic design is essential for optimizing the performance of the reactor core. The present paper analyzes the low-quality DWOs in the system shown in Fig. 3 for the following three cases: (1) Symmetrical heating and throttling; (2) Asymmetrical heating and symmetrical throttling; and (3) Asymmetrical heating and throttling. These three combinations are somehow related to the optimal design of the reactor core, once power distributions among the fuel assemblies are taken into account.

The nominal lengths of the heated section and the adiabatic riser of the INET experimental facility (see Fig. 2), L_H and L_R, are $0.58m$ and $3m$, respectively. The heating elements in the heated section of each channel are 4×4 electric rod bundle with the rod diameter $D_H = 10mm$ and the pitch size $S_H = 13.3mm$. The power distribution of the heated section is axially uniform. The nominal diameter of the riser D_R is $60mm$. Other detail geometric parameters of the facility have been encompassed in reference [2]. The numerical simulation system shown in Fig. 3 are designed to represent the INET experimental facility characterized by these main geometric parameters. The system pressure is also set at the same level as that of the experiment, i.e., $p = 15bar$.

The stability threshold for a given power level is obtained from the transient results, triggered by imposing a velocity perturbation to the corresponding steady-state solutions, or the *fixed points* of Eq. (17). The initial perturbation is given by

$$u_{in,2}(t) = \begin{cases} u_{in,2,0} & t < t_0 \\ u_{in,2,0} + \delta u_{in} & t = t_0 \end{cases} \tag{18}$$

Figure 4 depicts three typical results leading to self-sustained oscillations for the above three cases. From these examples, one can distinguish the corresponding dominant modes. In the case of *symmetrical heating and throttling* (Fig. 4(a)), the out-of-phase, equal-amplitude, limit-cycle oscillation is the dominant mode. For the latter two cases, the asymmetries have yielded fundamental changes in the oscillation modes of the parallel channel system in which channel 1 represents the high-power channel. Figure 4(b) indicates that the limit-cycle oscillation is still the dominant mode in the second case, with asymmetrical heating and symmetrical throttling. However, the amplitudes in both channels are different and the phase lag is no longer 180°, but less than 45°. The oscillation in the low-power channel is stronger than that in the high-power channel. The entire system oscillates more like the in-phase *loop oscillation* dominated by the low-power channel. The oscillation in the high-power channel exhibits slight nonlinear behavior. Figure 4(c) shows that the oscillation mode of the system with asymmetrical heating and throttling, is also limit-cycle. Unlike the previous cases, the phase lag of the oscillations in the two heated channels in this last case is quite close to 180°, but the oscillation in the high-power channel is stronger. The entire system oscillates more like the out-of-phase *parallel channel oscillation*, controlled by the high-power channel. The oscillation in the low-power channel displays obvious nonlinear behavior.

Generally, the basic oscillation modes in a natural circulation system with parallel, heated channels can be classified as the in-phase loop oscillation and the out-of-phase channel oscillation. The actual modes differs from one another only in the various combinations of these two basic modes. It has been known (e.g., [2] and [10]) that the low-quality DWOs are controlled by the change of gravitational pressure drops in the hot legs (including the heated sections and the risers), and balanced mainly by the inlet pressure drops. The higher the channel power, and the larger the inlet throttling, the more stable. The parallel-channel oscillation is more easily triggered than the loop oscillation. The mechanisms, and the key points for the above three modes, are addressed as follows.

In the first case, the two channels are identical so that the parallel-channel oscillation should be the

out-of-phase, equal-amplitude, limit-cycle oscillation. Because mass continuity can be preserved within the two hot legs in such a mode, the oscillations only involve the two hot legs, but not the common downcomer. The crucial point in designing a parallel-channel system, under similar conditions, is to avoid the out-of-phase, parallel-channel, limit-cycle oscillations. The fuel assemblies, with their connected risers at the same radial positions in a reactor core, may be similar to this case.

In the second case with $\frac{\dot{Q}_{1,0}}{\dot{Q}_{2,0}} = 1.44$, because the inlet pressure-drop coefficients are the same for both channels, the higher power level corresponds to a more stable flow. Thus, the low-power channel is more unstable, so that it is more *active* and dominates the oscillations in the entire system. The key criterion for designing a similar system, free from the low-quality DWOs, is to prevent the system from the oscillations referenced to the low-power level channel. The fuel assemblies at different radial positions in the reactor core may coincide with the situation.

It is interesting to explain the last case in more detail in order to gain insight into the optimal design of the reactor core. This situation occurs when the flow conditions are optimized by taking into account the power distribution among the fuel assemblies, with *equal exit quality* as a constraint. This constraint can be realised by suitably setting the inlet throttling according to the power of each channel, which leads to

$$x_{e,j} = \frac{h_{e,j} - h_{sat}}{h_{fg}} = \left(\frac{\dot{Q}}{\dot{M} h_{fg}}\right)_j - \frac{\Delta h_{sub}}{h_{fg}} \qquad (j = 1, 2) \tag{19}$$

Moreover, the pressure drops in all channels are the same, and can be approximated as

$$\Delta p_{in} \propto K_j u_{in,j}^2 \qquad (j = 1, 2) \tag{20}$$

The combination of the above two equations yields

$$\left(\frac{\dot{Q}_1}{\dot{Q}_2}\right) \approx \sqrt{\frac{K_2}{K_1}} \tag{21}$$

which can be used to select the inlet throttling, according to the power of each channel. The power ratio is set to 1.5 for the numerical calculation. The inlet throttling, K_1 and K_2, are set at 15 and 35, respectively, to obtain the average value 25, which is the nominal value when the system is operated as a single loop. In this example, the average levels of the boiling boundaries in the two heated channels are very close. The significant, unbalanced oscillation amplitudes imply that the oscillation in the downcomer is close to being *in-phase* with that in the high-power channel. The stabilizing effect of increasing the inlet throttling is stronger than that of increasing the power if the *equal exit quality* condition is enforced. This explains why the channel with low power is more stable than that with high power in the region where one would expect low power to be more unstable. The most important point, in optimizing the design of a low-quality, natural circulation system with parallel heated channels with *equal exit quality*, is that the inlet thresholds must be well paired with the channel powers. Protecting the system from the low-quality DWOs depends mainly on avoiding the oscillations referenced to the high power channel.

Figure 5 compares the stability thresholds predicted by the present study with data from the INET stability experiment, for the three above-mentioned set-ups. Fairly good agreement is achieved, although some slight differences remain. The comparisons validate the present model, relating to the stability threshold predictions for different set-ups. The comparisons cover a large interest region for the design of integral heating reactors, operating in the BWR mode.

Another way of investigating the stability structure of the natural circulation system is to study transient response of the system following a smooth exponential power transition with

$$\dot{Q}(t) = \begin{cases} \dot{Q}_0 & t \le t_0 \\ \dot{Q}_0 \left(1 \mp \alpha \left(1 - \exp\left[-\left(\frac{t-t_0}{\beta}\right)\right]\right)\right) & t \ge t_0 \end{cases} \tag{22}$$

which means that the system is run first at a specified power level $\dot{Q}_0$, and then a power transition is triggered at t_0. The parameters α and β are positive constants which serve to the power transition characteristics. During the resulting transient, all other parameters remain unchanged. The negative sign in the above equation corresponds to a power reduction and the positive sign to a power increase, respectively. In the present analysis, the parameters are chosen following ranges

$$0.1 \le \alpha \le 0.3 \qquad \text{and} \qquad 1.0 \le \beta \le 50.0 \tag{23}$$

Figures 6, 7 and 8 show results for the three cases mentioned above. In all three examples, the system is initially run either in the stable region and then with the power decreasing, enters the *unstable region*, as estimated by the stability threshold found from the analysis of the flow transient triggered by a velocity perturbation of equation (18), or *vice versa*. The results show that with slow power reduction (large β), the system moves to a stable configuration for all three cases, while with fast transitions, the system becomes unstable for the last two cases but remains stable for the first case. However, the power increase transients always lead the system to the stable region. Only if the power is well into the unstable region, does the slow transient induce oscillations in the system (see Fig. 9).

These results suggest the existence of a conditionally-stable region in which small perturbations will be damped, while large perturbations will trigger instabilities. A possible explanation of this conditionally-stable region is that there are only two basic modes for the low-quality DWOs: namely, the in-phase loop oscillation and the out-of-phase channel oscillation. The power level at the onset of the former always differs from that of the latter (at least for the cases discussed here). Real modes for different operational set-ups are combinations of these two basic modes. The reasoning is based on the fact that the pure loop oscillation can be triggered by a small perturbation, while the combined oscillation requires a finite perturbation to destroy *the equilibrium* conditions established when the system is in the absolute stable region (no matter how these equilibrium conditions are established). The results shown in Figs. 6 to 9 support this conjecture. The case of symmetrical heating and throttling is more clear as an example for detail discussion.

Figure 10 depicts the phase diagram of the system obtained by thoroughly analyzing the numerical results around the conditionally-stable region for the case of symmetrical heating and throttling. The conditional stable region is naturally partitioned by the onset point of the out-of-phase oscillation, A, the onset point of the pure in-phase loop oscillation, A' which may be fully shadowed by the parallel-channel oscillations and the surface of the unstable limit cycle corresponding to the minimum perturbation intensity required to trigger oscillations in this region. From Fig. 10, one finds that A corresponds to a complicated bifurcation, and A' to a subcritical bifurcation. The results also reveal that this conditionally-stable region is very narrow, thus a *relatively small* velocity perturbation in this region may yield strong oscillations. The results in Fig. 9 with a large power-level change in a slow-power reduction transition indicate that an in-phase oscillation has been triggered. The results in Figs. 6(c) and 6(d) present a striking contrast between a symmetrical transient and an asymmetrical transient. The former yields stable and the latter leads to unstable. These also lends support to the conjecture made above. The stability structures for other two cases are similar to the case of symmetrically heating and throttling. They differ from each other only in the system oscillation mode related to the corresponding set-up.

The comparisons with the three sets of experimental data from the INET facility strongly support the basic oscillation modes classification given in the present study. These data include: (1) the onset points of DWOs from *the single-loop* experiments; (2) the onset points of DWOs from *the parallel channel* experiments, with the cross-connection valve closed; (3) the onset points of DWOs from *the parallel channel* experiments, with the cross-connection valve open. The cross-connection is located above the heated section to connect both upflow risers. This connection actually results in the system being closer to one with two parallel heated sections, but with only one common riser. Because the heated sections are relatively short compared to the risers, one can expect that the system will be more like a *single-loop* system, but its volume is doubled if the cross-connection valve is open. Figure 11 shows the comparisons of these three sets of experimental data. A typical example of the experimental results is depicted in Fig. 12. The data is selected from the set of the experiment with symmetrical heating and throttling, and with the cross-conn· tion valve closed. The experimental number is B82909. The mode can be identified as the out-of-phase, equal-amplitude channel oscillation. The oscillation period is about 4 to 5 seconds which is very close to the transient time for the fluid particles to pass through the up-flow channel where the oscillation took place. This oscillation period has provided strong evidence to support the present study with the matter of naming this type of two-phase flow instabilities as the low-quality DWOs.

CONCLUSIONS

Two-phase flow instabilities in a low-quality, natural circulation system with two parallel-heated channels have been numerically studied. Different stability oscillation modes corresponding to different operational set-ups are distinguished. The present study has verified that the combination of the in-phase, loop oscillations and the out-of-phase, parallel-channel oscillations may lead to a complex flow stability structure for a complicated natural circulation system operating at low-quality and low-pressure conditions.

A quite narrow conditionally-stable region has been detected by analyzing numerical simulation results. The mechanism of this stability structure has been explained. The present study has also found that a smooth, power-reduction transient can lead the system from an unconditionally-stable region to a conditionally-stable region. This conditionally-stable region is quite sensitive to the flow perturbation. Any real engineering system, whose control safety is the main priority cannot be operated in such conditionally-stable regions.

The results of the present study emphasize the importance of carefully carrying out numerical analyses, especially when general codes are used to simulate the system stability characteristics during power transients. Rohatgi et al. [23] have also pointed out some new challenges on time-domain codes for DWOs analysis. Correctly understanding of the stability structure in the conditionally-stable region is essential for designing passive safe *Integral District Heating Reactors*. The significance of the present study is to point out that if only one transient mode is analyzed - either a power reduction or perturbation transient - the complete information concerning the stability structure may not be obtained.

ACKNOWLEDGMENT

This work was done in the Swiss Federal Institute of Technology in Zurich. The author is gratefully indebted to all colleagues in both the INET of Tsinghua University and the PSI for their enthusiastic supports; especially to Professor G. Yadigaroglu and Dr. J. Halin for their valuable discussions about physical and numerical problems.

NOMENCLATURE

A	cross-sectional flow area, m^2
e	unit vector of the flow path or of gravity
f	Darcy frictional factor
g	gravitational acceleration, ms^{-2}
h	specific enthalpy, J/kg
k	local pressure drop ceofficient
L	node location or the length of the flow section, m
M	channel or node mass, kg
N	node number
p	pressure, bar
P	heated or wetted perimeter, m
$q"$	heat flux, Wm^{-2}
$\dot{Q}$	heating power, W
t	time, s
T	temperature, ^oC
u	velocity, m/s
v	specific volume, m^3/kg
z	coordinate in hot leg, m

Greek Symbol

ρ	density, kg/m^3
λ	location of boiling boundary, m
δ	$\delta-$ function, $\delta(x) = 0.0$, if $x \neq 0.0$ and $\delta(x) = 1.0$, if $x = 0.0$
Δ	difference

Subscript

ch	channel
e	exit of the heated section
f	liquid phase
g	gravitational
loop	external loop
R	riser
s	single phase
sat	saturated
sub	subcooling

REFERENCES

1. D. Wang, C. Ma, D. Dong and J. Lin, "*Chinese Nuclear Heating Reactor and Demonstration Plant*," Nucl. Eng. and Des. 136, 91-98 (1992).

2. S. Wu, M. Yiao, D. Wang, E. Knoglinger, and K. Hofer, *"An Experimental Study on Hydrodynamic Stability of Low Quality Two-Phase Flow with Natural Circulation,"* in Experimental Heat Transfer, Fluid Mechanics and Thermodynamics, Eds. R. K. Shah, E. N. Ganic, K. T. Yang, Elsevier Publishing Co. Inc., 1120-1127 (1988).

3. V. P. Zaval'skii, L. L. Kobzar, P. A. Leppik, and V. V. Maimistov, *"Stability of the Coolant Circulation in a Model of the AST-500 Reactor ,"* Soviet Atomic Energy 55, 639-643 (1984) (Translated from Atomnaya Energiya, 55, 205-208 (1983)).

4. P. Burgsmueller, J. F. Jaeger, M. J. Klaentschi, W. Seifritz, F. Vuilleumier, and F. Wegmann, *"The Swiss Heating Reactor for District Heating of Small Communities,"* Nuclear Technology 79, 167-174 (1987).

5. C Goetzman, D. Bittermann, and A. Goebel, *"Design Principles of a Simple and Safe 200 - MW(thermal) Nuclear District Heating Plant,"* Nuclear Technology 79, 144-157 (1987).

6. J. A. Boure, A. E. Bergles, and L. S. Tong, *"Review of Two-Phase Flow Instability,"* Nuclear Engineering and Design 25, 165-192 (1973).

7. A. E. Berglers, *"Instabilities in Two-Phase Systems,"* in Two-Phase Flow and Heat Transfer in the Power and Process Industries, Eds. A. E. Bergles, J. G. Collier, J. M. Delhaye, G. F. Hewitt, and F. Mayinger, Hemisphere, New York City, New York (1981).

8. G. Yadigaroglu, *"Two-Phase Flow Instabilities and Propagation Phenomena,"* in Thermalhydraulics of Two-Phase Systems for Industrial Design and Nuclear Engineering, Eds. J. M. Delhaye, M. Giot, and M. T. Rietmuller, pp. 353 - 403, Hemisphere, New York City, New York(1981).

9. R. T. Lahey and M. Z. Podowski, *"On the Analysis of Various Instabilities in Two-Phase Flows,"* in Multiphase Science and Technology, Eds. G. J. Hewitt, J. M. Delhaye and N. Zuber, pp. 183 - 370, vol. 4, Hemisphere, New York City, New York(1989).

10. K. Fukuda and T. Kobori, *"Classification of Two-Phase Flow Instability by Density-Wave Oscillation Model,"* J. Nucl. Science Technology 16, 95-108 (1979).

11. J. H. Chiang, M. Aritomi and M. Mori, *"Fundamental Study on Thermo-Hydraulics during Start-Up in Natural Circulation Boiling Water Reactors, (II) - Natural Circulation Oscillation Induced by Hydrostatic Head Fluctuation,"* J. Nucl. Science and Technology 30, 203-211 (1993).

12. I. S. Kyung and S. Y. Lee, *"Experimental observations on flow characteristics in an open two-phase natural circulation loop,"* Nucl. Engineering and Des. 159, 163-176 (1994).

13. Z. Gao, J. Li, X. Chen, and Z. Zhang, *"Analysis of Stability in a Low Pressure, Low Quality and Two-Phase Flow with Natural Circulation,"* in Multiphase Flow and Heat Transfer, Eds. X. J. Chen, T. N. Veziroglu, and C. L. Tian, Hemisphere, New York City, New York, 505-514 (1991).

14. M. Brunet, E. Knoglinger, and M. A. Zimmerman, *"Time-Domain Analysis of Density-Wave Oscillations in a Natural Circulation Loop at Low Quality,"* Proc. of 6th International RETRAN meeting, (1989).

15. Z. Zhou and G. Yadigaroglu, *"Stability of Natural Circulation with Gravity-Induced Flashing,"* Transactions ANS 57, 379 - 381, (1988).

16. Z. Zhou and P. Heusser, *"Numerical Simulation of Two-Phase Flow Nonlinear Density-Wave Oscillations for a Natural Circulation Loop,"* Proc. of the 1991 European Simulation Multi-Conference, SCS Simulation Councils, Inc., 595-600 (1991),

17. Z. Zhang, Z. Gao, J. Li and Y. Wang, "*A Study of Two-Phase Flow Stability During the Accident of Nuclear Heating Reactors with Natural Circulation*," ASME publication, HTD 260, 59 - 64 (1993).

18. R. P. Roy and G. Yadigaroglu, "*An Investigation of Heat Transport in Oscillatory Turbulent Sub-cooled Flow*," J. Heat transfer 98, 630-637 (1976).

19. Z. Gao, D. Wang, Z. Zhang, J. Li, C. Gao and B. Xu, "*Theoretical Study of Two-Phase Density-Wave Instability*," Proceeding of the NURETH-6, Granoble, France, 277-285 (1993).

20. R. T. Lahey, Jr., "*An Application of Fractal and Chaos Theory in the Field of Two-Phase Flow and Heat Transfer*," Wärme-und Stoffübertragung 26, 351-363 (1991).

21. Rizwan-uddin and J. Dorning, "*Nonlinear Dynamics of Two-Phase Flow in Multiple Parallel Heated Channels*," ASME publication, HTD 197, 63-72 (1992).

22. A. C. Hindmarsh, "LSODE and LSODI, Two Initial Value Ordinary Differential Equation Solvers," ACM SIGNUM Newsl. 15, 10 (1980).

23. U. S. Rohatgi, L. Y. Neymotin and W. Wulff, "Assessment of ROMONA-3B Methodology with Oscillatory Flow Tests," Nuclear Engineering and Design 143, 69-82 (1993).

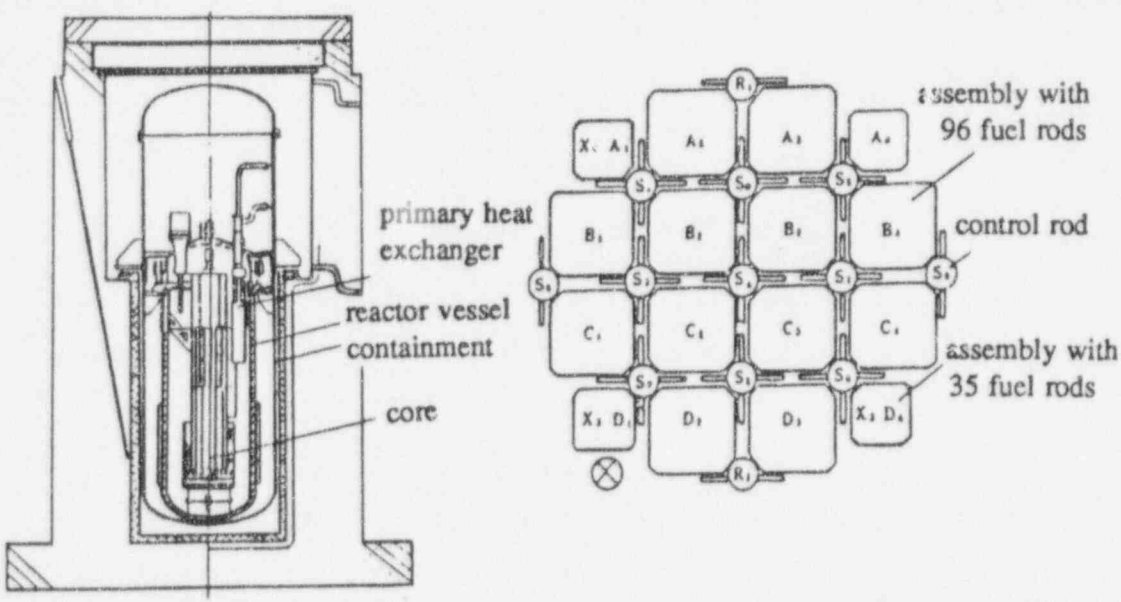

(a) sideview of reactor schemation (b) cross-section of reactor core

Figure 1: The NHR-5 heating reactor

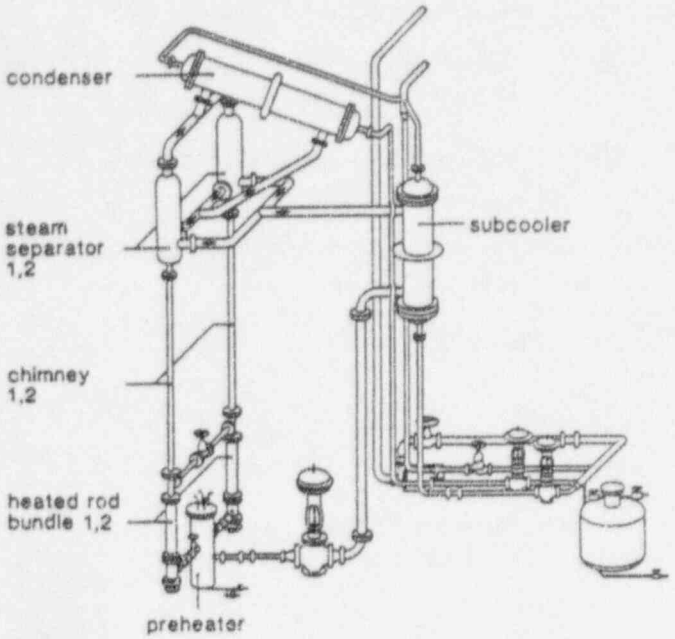

Figure 2: The INET experimental facility

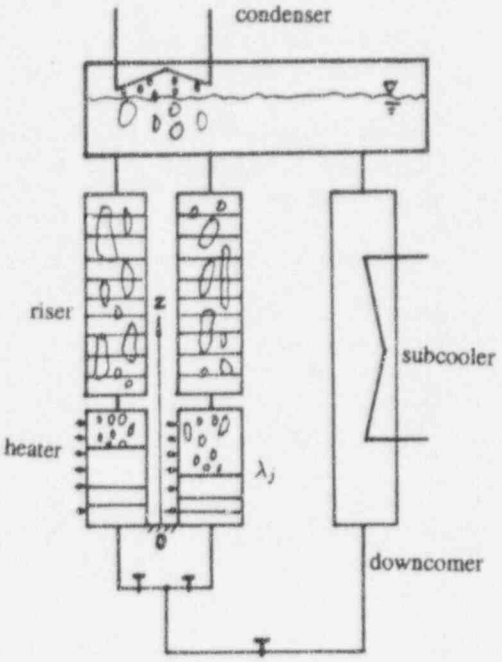

Figure 3: Numerical simulation model

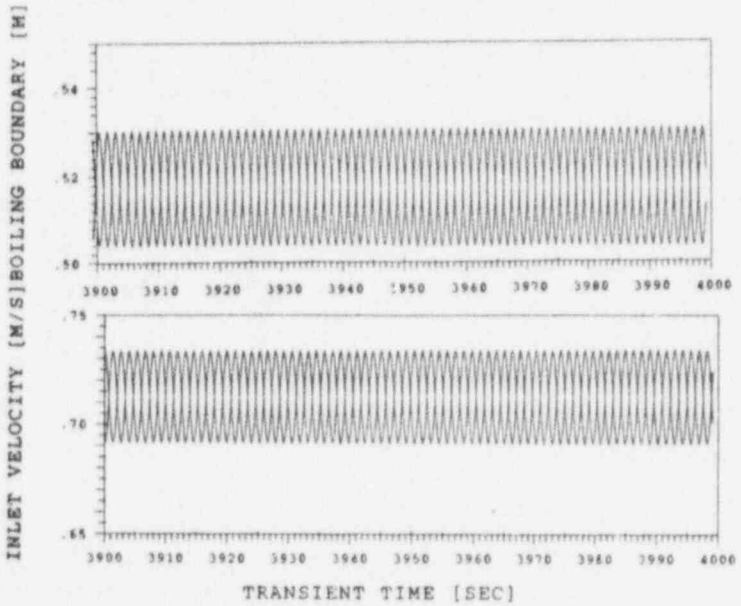

Figure 4(a): $\frac{Q_1}{Q_2} = \frac{72.5\text{kW}}{72.5\text{kW}}$, $\frac{K_1}{K_2} = \frac{25}{25}$, $\Delta T_{sub} = 14.0\text{K}$

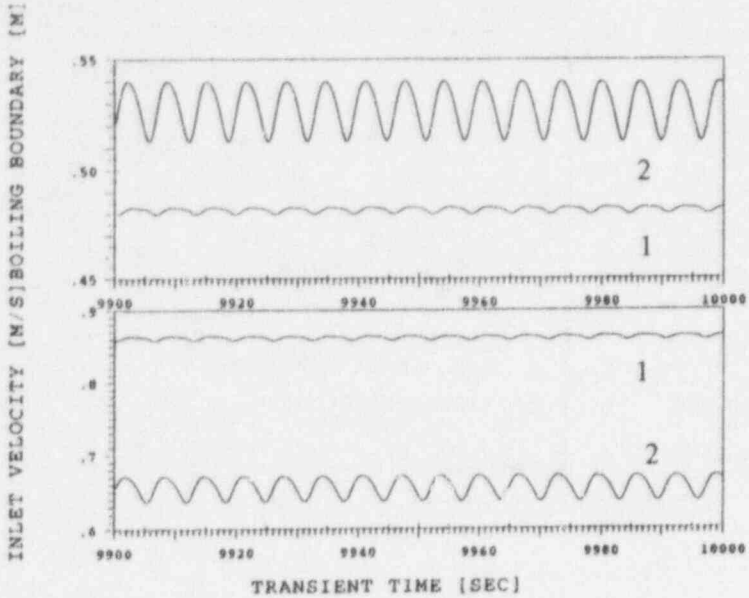

Figure 4(b): $\frac{\dot{Q}_1}{\dot{Q}_2} = \frac{100.8\text{kW}}{70\text{kW}}$, $\frac{K_1}{K_2} = \frac{25}{25}$, $\Delta T_{sub} = 15.2\text{K}$

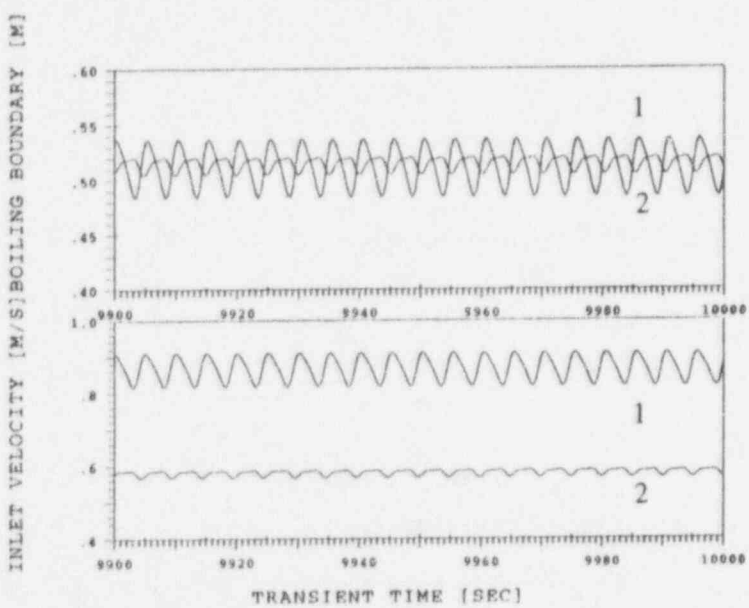

Figure 4(c): $\frac{\dot{Q}_1}{\dot{Q}_2} = \frac{75\text{kW}}{50\text{kW}}$, $\frac{K_1}{K_2} = \frac{15}{35}$, $\Delta T_{sub} = 13.5\text{K}$

Figure 4: Typical oscillation modes for three operational set-ups: $p = 15bar$, (a) symmetrical heating and throttling; (b) asymmetrical heating and symmetrical throttling; (c) asymmetrical heating and throttling; $\delta u_{in,2} = 10\% u_{in,2,0}$ for all three cases.

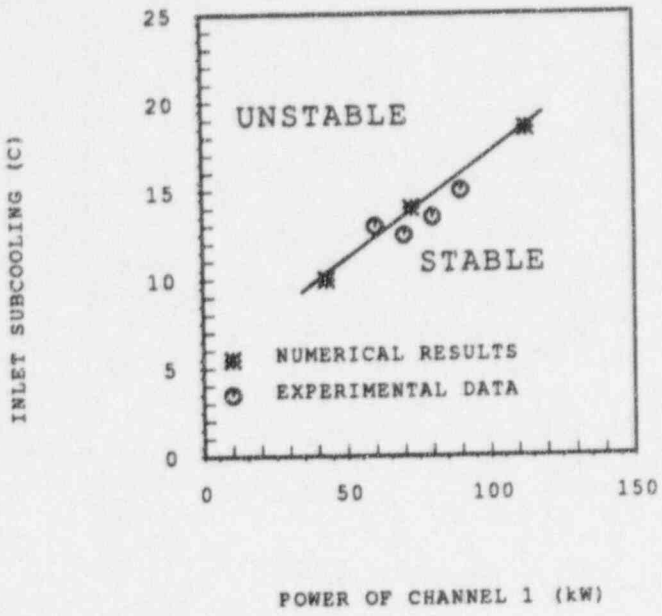

Figure 5(a): $\frac{\dot{Q}_1}{\dot{Q}_2} = 1$, $\frac{K_1}{K_2} = \frac{25}{25}$

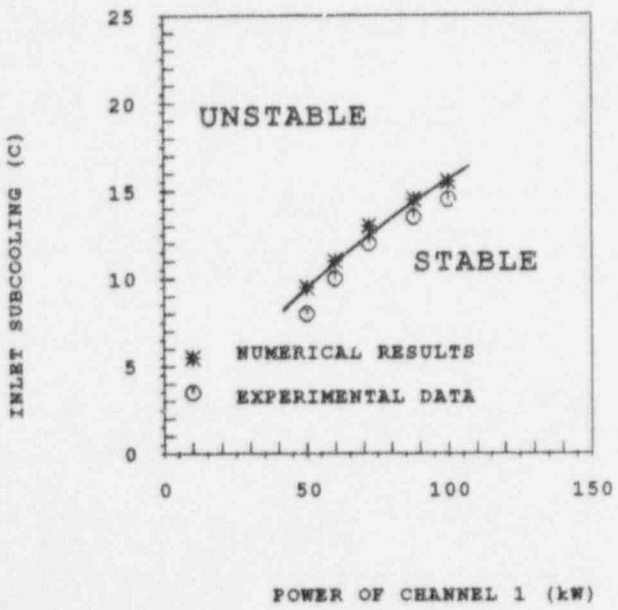

Figure 5(b): $\frac{\dot{Q}_1}{\dot{Q}_2} = 1.44$, $\frac{K_1}{K_2} = \frac{25}{25}$

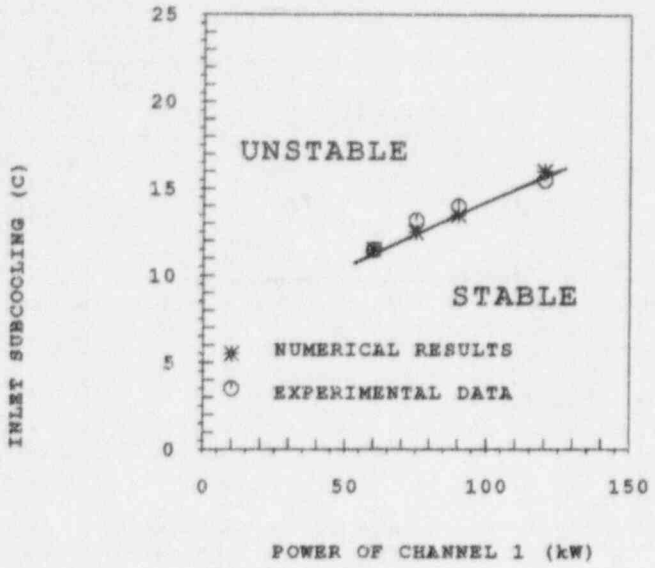

Figure 5(c): $\frac{\dot{Q}_1}{\dot{Q}_2} = 1.5$, $\frac{K_1}{K_2} = \frac{15}{35}$

Figure 5: Comparisons of the predicted DWOs onsets with INET experimental data: $p = 15bar$, (a) symmetrical heating and throttling; (b) asymmetrical heating and symmetrical throttling; (c) asymmetrical heating and throttling.

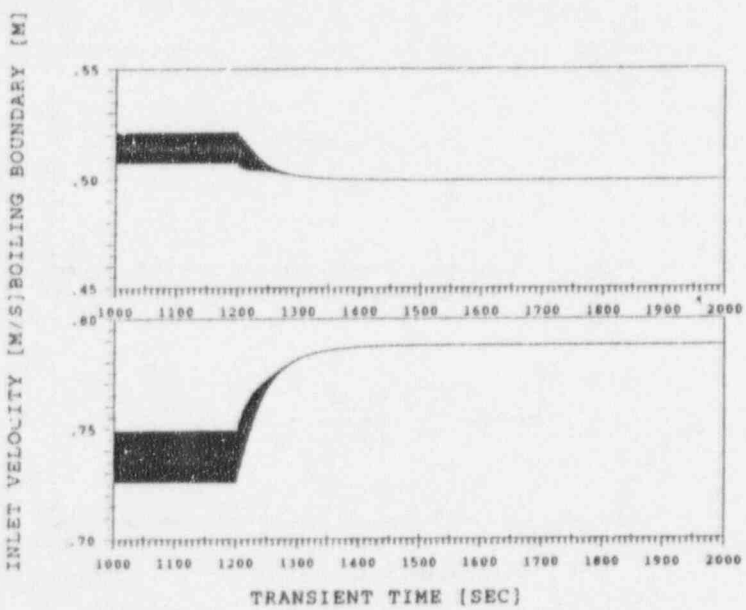

Figure 6(a): power increase to stable, $\dot{Q}_{j,0} = 80.0$kW, $\beta_j = 50$s, $\alpha = 0.1$

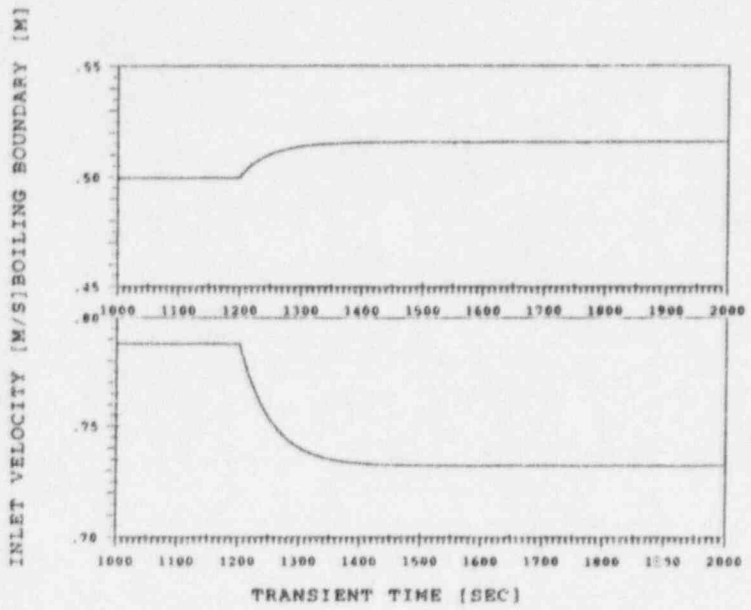

Figure 6(b): power reduction to stable, $\dot{Q}_{j,0} = 88.0$kW, $\beta_j = 50$s, $\alpha = 0.1$

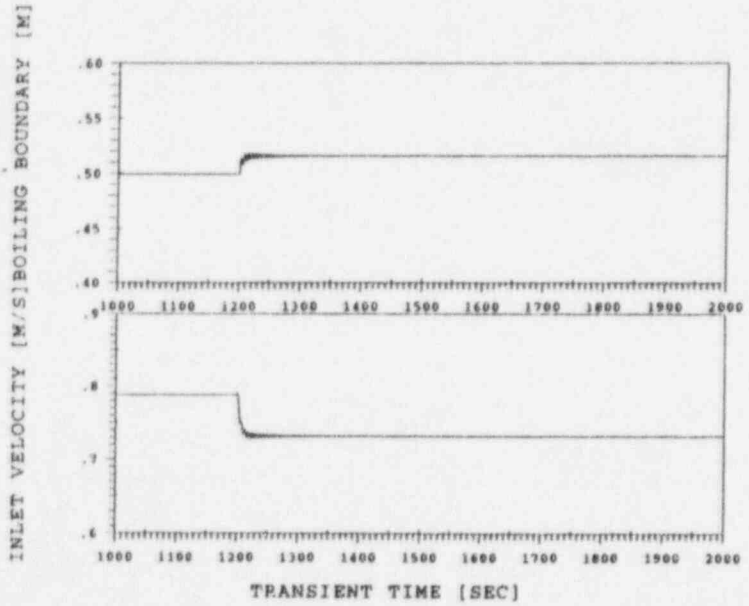

Figure 6(c): power reduction to stable, $\dot{Q}_{j,0} = 88.0$kW, $\beta_j = 5$s, $\alpha = 0.1$

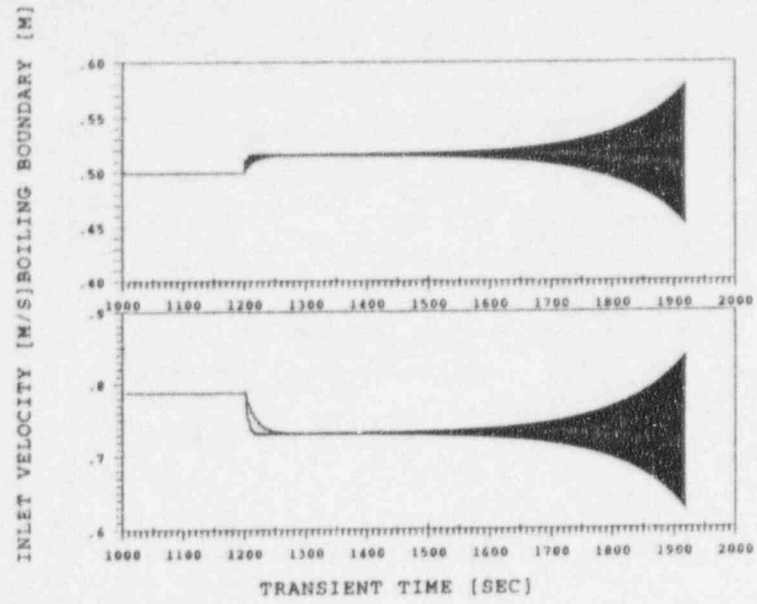

Figure 6(d): power reduction to unstable, $\dot{Q}_{j,0} = 88.0\text{kW}$, $\frac{\beta_1}{\beta_2} = \frac{58}{108}$, $\alpha = 0.1$

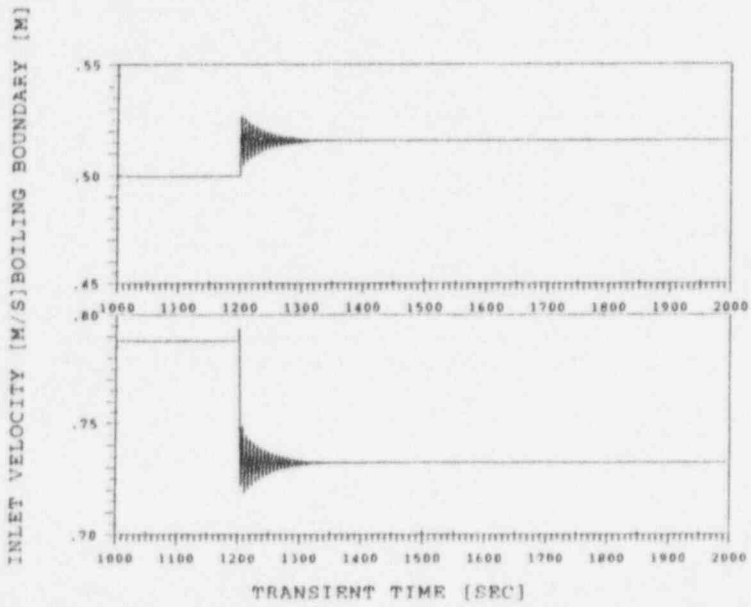

Figure 6(e): power reduction to stable, $\dot{Q}_{j,0} = 88.0\text{kW}$, $\beta_j = 1\text{s}$, $\alpha = 0.1$

Figure 6: Transient flow response to the power transition for the case of symmetrical heating and throttling, $p = 15bar$.

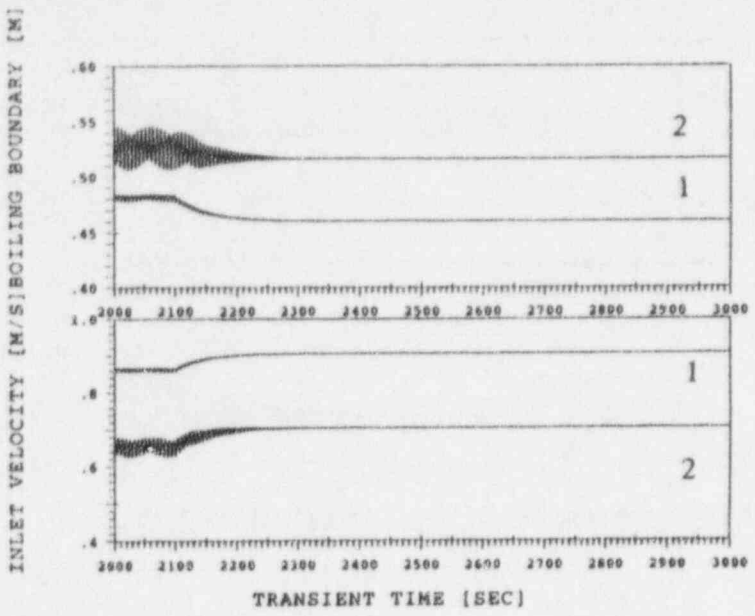

Figure 7(a): power increase to stable, $\frac{\dot{Q}_{1,0}}{\dot{Q}_{2,0}} = \frac{100.8\text{kW}}{70\text{kW}}$, $\beta_j = 50\text{s}$, $\alpha = 0.1$

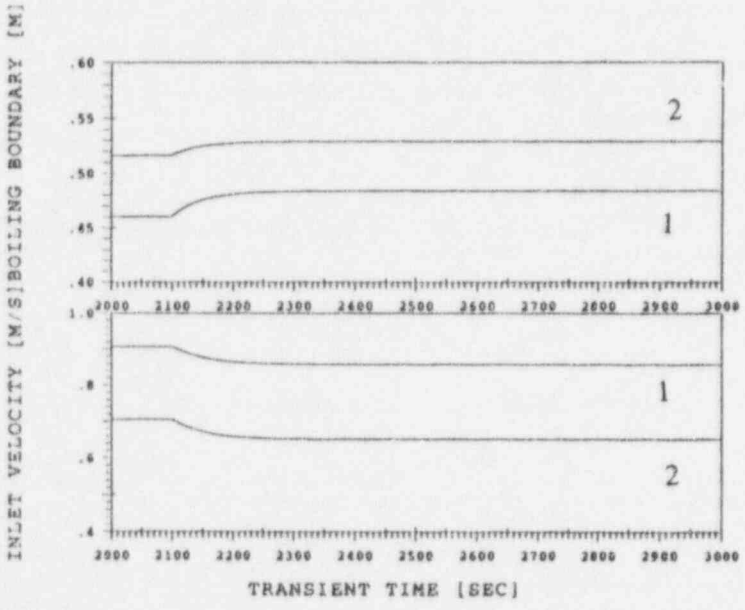

Figure 7(b): power reduction to stable, $\frac{\dot{Q}_{1,0}}{\dot{Q}_{2,0}} = \frac{110.88\text{kW}}{77\text{kW}}$, $\beta_j = 50\text{s}$, $\alpha = 0.1$

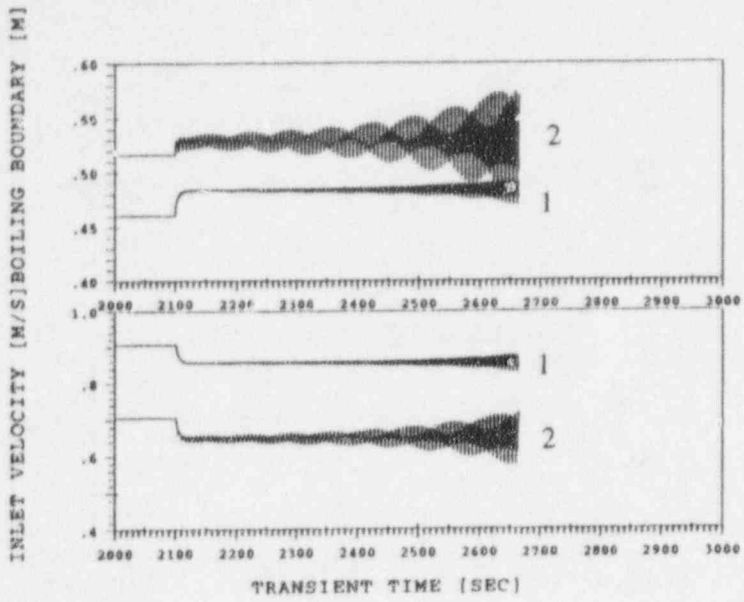

Figure 7(c): power reduction to unstable, $\frac{\dot{Q}_{1,0}}{\dot{Q}_{2,0}} = \frac{110.88\text{kW}}{77\text{kW}}$, $\beta_j = 5\text{s}$, $\alpha = 0.1$

Figure 7: Transient flow response to the power transition for the case of asymmetrical heating and symmetrical throttling, $\frac{K_1}{K_2} = \frac{25}{25}$, $p = 15bar$.

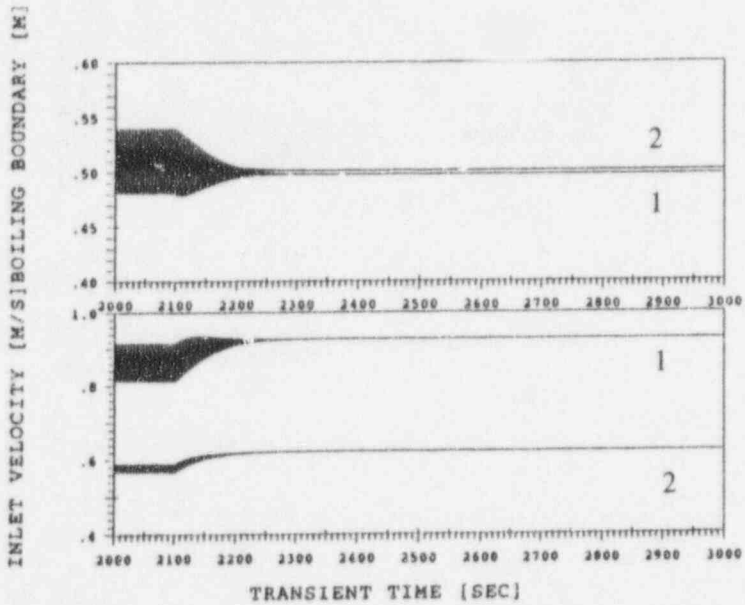

Figure 8(a): power increase to stable, $\frac{\dot{Q}_{1,0}}{\dot{Q}_{2,0}} = \frac{75\text{kW}}{50\text{kW}}$, $\beta_j = 50\text{s}$, $\alpha = 0.1$

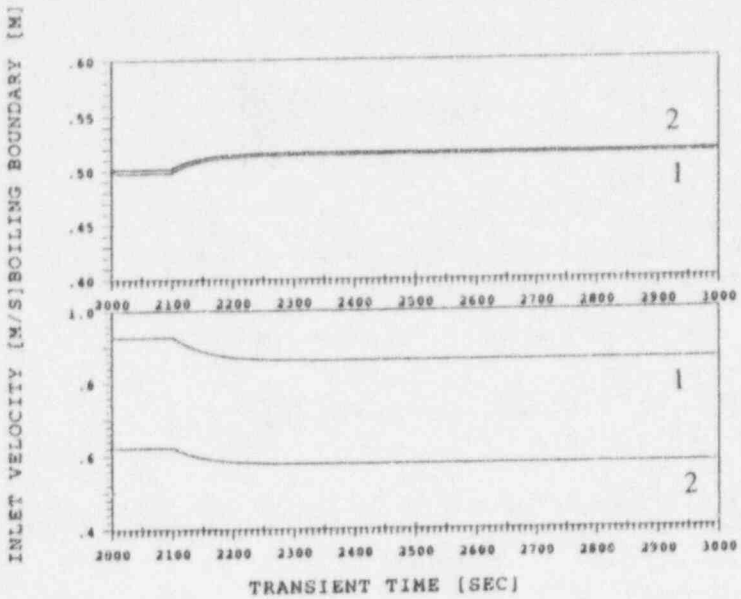

Figure 8(b): power reduction to stable, $\frac{\dot{Q}_{1,0}}{\dot{Q}_{2,0}} = \frac{82.5\text{kW}}{55\text{kW}}$, $\beta_j = 50\text{s}$, $\alpha = 0.1$

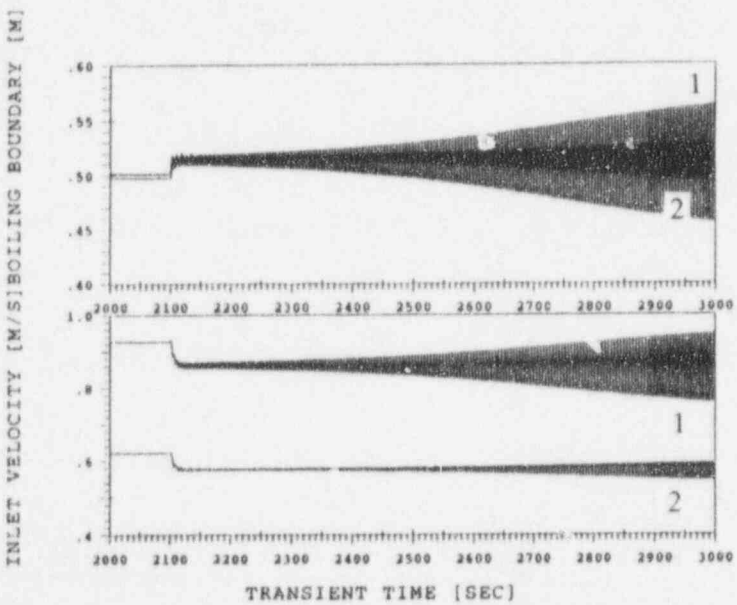

Figure 8(c): power reduction to unstable, $\frac{\dot{Q}_{1,0}}{\dot{Q}_{2,0}} = \frac{82.5\text{kW}}{55\text{kW}}$, $\beta_j = 5\text{s}$, $\alpha = 0.1$

Figure 8: Transient flow response to the power transition for the case of asymmetrical heating and throttling, $\frac{K_1}{K_2} = \frac{15}{35}$, $p = 15bar$.

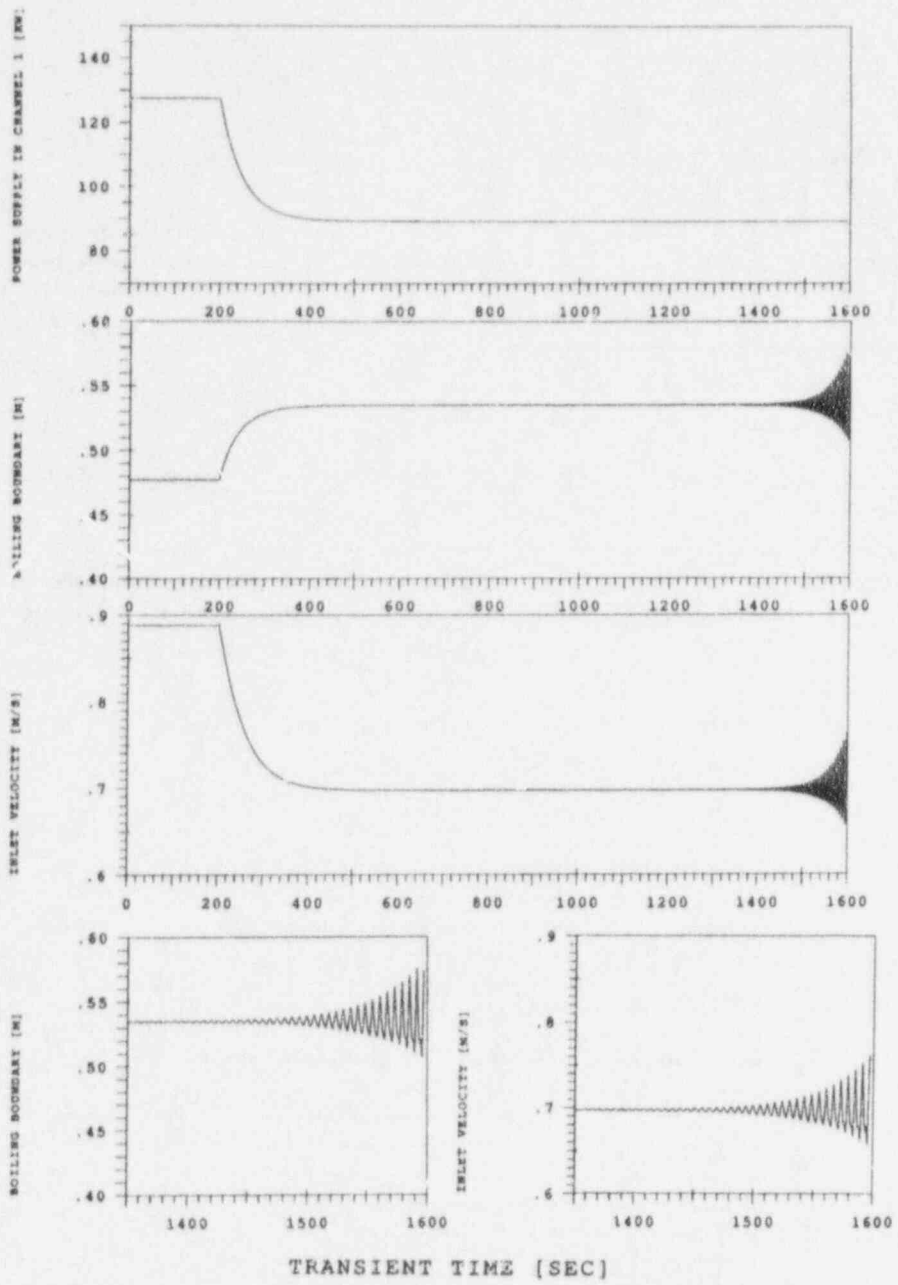

Figure 9: Details of in-phase loop oscillation following a power reduction transient, $p = 15bar$, $\dot{Q}_{j,0} = 127.577kW$, $K_j = 25$, $\Delta T_{in} = 18K$, $\beta_j = 50s$, $\alpha = 0.3$, power reduction to unstable.

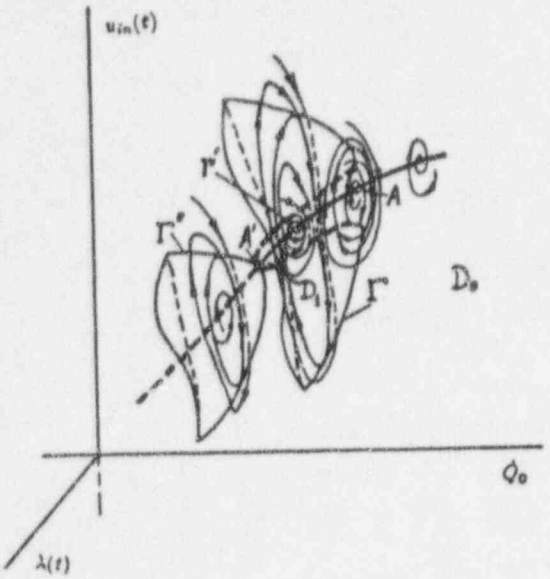

Figure 10: Stability structure in $u_{in} - \lambda - \dot{Q}$ phase diagram for the case of symmetrical heating and throttling.

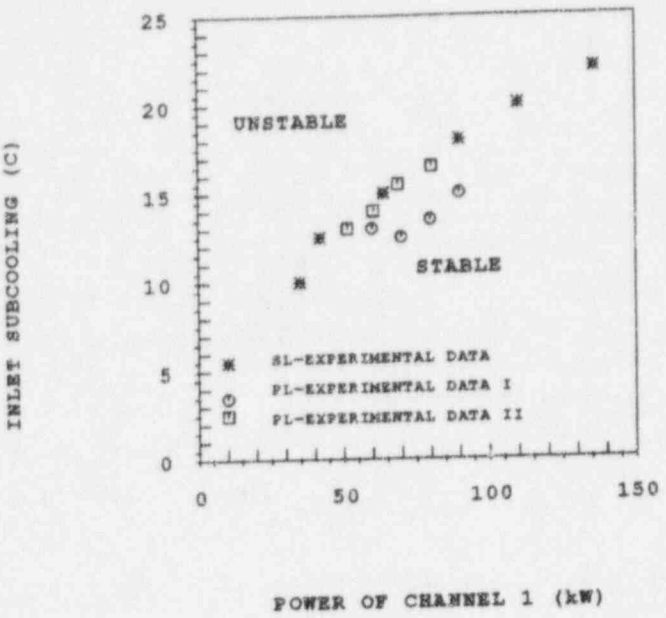

Figure 11: Comparisons of instability onsets among three sets of experimental data form the INET-PSI stability experiment, $p = 15bar$.

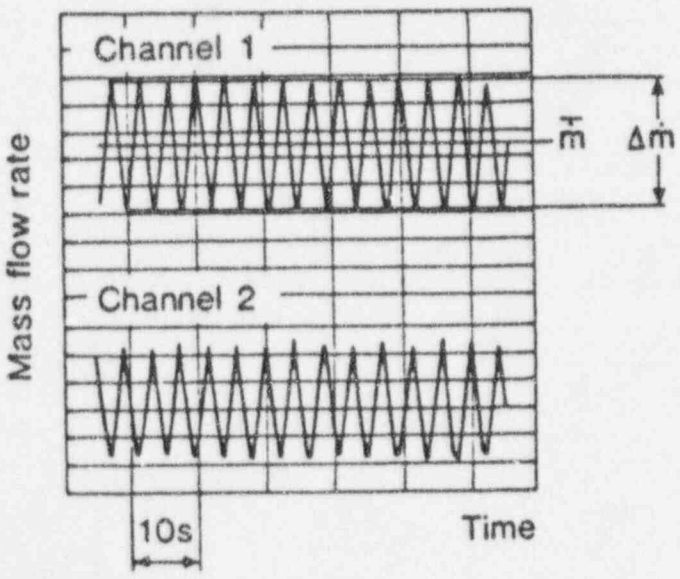

Figure 12: A typical example of experimental results from the INET-PSI stability experiment, $p = 15bar$, $\dot{Q}_{j,0} = 69kW$, $K_j = 27$, $\Delta T_{in} = 16K$, No. B82909.

FIBWR2 Evaluation of Fuel Thermal Limits During Density Wave Oscillations in BWRs

N. Nik, S. R. Rajan, M. Karasulu,
New York Power Authority, White Plains

ABSTRACT

Analyses were performed to evaluate hydraulic and thermal margin responses of three different BWR fuel designs subjected to the same periodic power/flow oscillations, such as those that might be exhibited during an instability event. The power/flow versus time information from the oscillations was used as a forcing function to calculate the hydraulic response and the MCPR performance of the limiting fuel bundles during the regional oscillations using the analytical code FIBWR2. The results of the calculations were used to determine the thermal margin variation as a function of oscillation magnitude.

1. INTRODUCTION

BWRs may experience instabilities due to the potential density wave oscillations which are characteristics of all two-phase flow systems. These instabilities, caused by time-lags in void propagation and characterized by a period related to the transit time of a fluid particle through the boiling channels, affect density and consequently cause mass flow rate to oscillate in the shrouded fuel bundles. The boiling channel can become unstable and sustain an oscillation with a constant pressure drop across the channel. In BWR's the oscillatory flow effect causes nuclear power generation to oscillate because of the tight void-reactivity nuclear feedback coupling of flow to power, especially under gravity driven or natural circulation. Sustained power oscillations (limit cycle) may violate the NRC's General Design Criteria 12 (GDC-12). Large oscillations may exceed thermal limits, leading to fuel damage.

In this study a fuel performance analysis was carried out using the transient code FIBWR2 [1], to evaluate the hydraulic behavior and thermal margin response of various fuel bundles during regional oscillations. The oscillations represented by FIBWR2 were based on supplied forcing functions [2] of variations in hot channel power and flow levels.

2. FIBWR2 CODE GENERAL DESCRIPTION AND QUALIFICATION

FIBWR2 is a transient multi-channel BWR core thermal-hydraulic analysis code that explicitly models all flow paths in a core and each individual bundle, with the bypass represented as a one dimensional hydraulic channel. The distinct features of FIBWR2 are:

- Transient multi-channel Critical Power Ratio (CPR) calculation.
- Modeling of axially varying flow geometries, i.e., partial length rods; and
- Detailed modeling of leakage paths, advance water tubes/channel box , and bypass flow.

FIBWR2 does not have the capability of predicting multi-dimensional BWR stability performance characteristics.

The thermal hydraulic and fuel heat transfer solution methods, correlations, and constitutive models used in FIBWR2 are comparable to those in other transient codes such as RETRAN [3], TRAC [4], RAMONA [5], and THERMIT2 [6].

Several aspects of the thermal hydraulic performance of a BWR can be evaluated using FIBWR2. A single assembly or a full core can be modeled and the thermal hydraulic response to transient inlet and outlet pressure boundary conditions can be determined. Two calculational methods are provided in the code. A total core pressure boundary condition can be imposed with assemblies in the core represented as groups of thermal-hydraulically similar parallel channels, and flow in each bundle calculated. Alternatively, a total inlet flow can be specified, with the code calculating channel flow splits and core pressure drop.

The fuel rod models used in FIBWR2 are: transient heat conduction through fuel pellet and cladding; the fuel-clad gap conductance; the fuel pellet radial power distribution; and the fuel and clad internal heat generation. In addition to these models, FIBWR2 uses temperature dependent fuel and clad material properties for transient calculations.

FIBWR2 has been qualified against an analytical flow decay solution; and against RETRAN02 calculated core transients including a core power spike, flow variation, and pressure ramp increase events [7].

3. CASES CONSIDERED

The fuel assemblies evaluated in this study were the 8x8, 9x9, and 10x10 designs. The 8x8 design is a 150-inch active fuel length assembly with seven spacers and one large water rod replacing four fuel rods. The 9x9 design has 146 inches of active fuel length with seven spacers, and contains two large water rods in place of seven fuel rods. The 10x10 design with 150-inches active fuel length also uses two large water rods replacing eight fuel rods and contains eight spacers. The 9x9 and 10x10 designs also use part length rods which are explicitly modeled with FIBWR2.

The fuel performance analysis was based on three sets of forcing functions of variations in hot channel power and flow levels representing three oscillation magnitudes, provided by the BWROG [2]. The first oscillation represents a "Caorso-type" event [8, 9] with 10% of rated peak-to-peak APRM. The second oscillation (Intermediate) is based on plant data with an APRM oscillation magnitude of 25% of rated. The third oscillation, an extrapolated case proportional to the first case, is used to simulate a large magnitude regional instabilities. The forcing functions are for the limit cycle oscillations (decay ratio = 1). Initial core conditions, applied to all three oscillations analyzed, are given in Table 1. These oscillation characteristics were applied to each fuel design identified above in conjunction with the inlet orificing and rated bundle powers of a representative mid-size BWR-4. The FIBWR2 analyses assumed a single bundle of each design representing a hot channel condition. Fuel channel nodalization includes 24 heated nodes, inlet orifice, upper and lower tie plates, and fuel rod spacers. Water rods are simulated as unheated rods.

4. THERMAL HYDRAULIC RESPONSE DURING OSCILLATIONS

Results of all oscillation cases for each fuel design are qualitatively similar. Figure 1 shows the typical nodal power and cladding surface heat flux response of the 8x8 design for the intermediate oscillation. Figure 2 shows mass flow rate variations at the bottom and top of the active fuel length for 8x8 fuel for the intermediate oscillation, illustrating the phase shift in the hydraulic response. The first few cycles were not plotted because they were not typical of the steady limit cycle response. Results for the "Caorso" and extrapolated oscillations for this 8x8 design differ from those shown in Figures 1 and 2 primarily in the magnitude of the flow response.

Figures 3 and 4 show comparisons of cladding surface heat flux response, and channel exit flows for the 8x8, 9x9, and 10x10 fuel designs, respectively, for the intermediate oscillation. The 10x10 design has the shortest thermal time constant, and exhibits the highest heat flux and largest flow oscillations compared to the 8x8 and 9x9 designs as shown in Figures 3 and 4.

5. THERMAL MARGIN DURING OSCILLATIONS

The thermal margin or critical power ratio was calculated by FIBWR2 for each fuel design with each input neutron power perturbation. The thermal margin is calculated using the GEXL correlation. Figure 5 compares MCPR behavior for the 8x8, 9x9, and 10x10 fuel designs for the same imposed power perturbation. As shown in Figure 5, 8x8 fuel has the highest MCPR during the limit cycle oscillation followed by 10x10 and 9x9 bundle designs.

These results have been combined to determine the hot channel delta-CPR/Initial CPR (ICPR) variation as a function of oscillation magnitude, as shown in Figure 6. Figure 6 shows that the 8x8 and 9x9 designs have more margin to the safety limit than 10x10 fuel. The calculated delta-CPR/ICPR for the 9x9 fuel is approximately the same as the 8x8 fuel at the lowest oscillation magnitude; and 0.06 and 0.08 higher at the intermediate and extrapolated magnitudes, respectively.

The resulting delta-CPR/ICPR characteristic as shown in Figure 6 can be applied to various initial conditions to estimate the minimum CPR for a given magnitude of oscillation. The initial (pre-oscillation) CPR, however, depends on a number of other parameters including plant operating state, margin to operating limits, and operating limit MCPR. For conditions following a recirculation pump runback or trip, the initial CPR will also depend on MCPR change as a function of flow and on the magnitude of the flow change. Hence a wide range of ICPRs is possible even for a given reactor.

6. SUMMARY AND CONCLUSION

Fuel thermal limits during BWR density wave oscillations for the regional oscillation mode (simulated by supplied forcing functions of variations in hot channel power and flow levels) were evaluated using the multi-channel thermal hydraulic transient code FIBWR2. For a given fuel design, i.e., 8x8, 9x9, or 10x10, the hydraulic response and the MCPR performance of the limiting bundles were investigated during limit cycle oscillations. For a particular fuel design, a representative relationship of delta-CPR/Initial CPRs (ICPR) and peak bundle oscillation magnitudes was examined. This is referred to by BWROG as the DIVOM (Delta CPR divided by the Initial CPR Versus the Oscillation Magnitude) curve.

The 10x10 fuel has less margin to the safety limit than either the 8x8 or 9x9 designs due to a shorter thermal time constant. A shorter time constant results in higher heat flux and flow oscillations for the same imposed power oscillation. The 9x9 fuel has a delta-CPR/ICPR performance that is approximately the same as that for the 8x8 fuel; and 0.06 and 0.08 lower at the intermediate and extrapolated oscillations, respectively.

7. REFERENCES

1. FIBWR2 Owner's Group; "FIBWR2: A Transient Flow Distribution Code for Boiling Water Reactor Cores, SCIE-COM-207-92", Dec. 1992.

2. Transmittal, Pfefferlen, H.C. (General Electric Company) to Nir, I (Middle South Utilities Company), OG9-228-54 "Information on Phase I Stability Analysis" March 2, 1989.

3. McFadden, J.H., et. al., "RETRAN-02: A Program for Transient Thermal - Hydraulic Analysis of Complex Fluid Flow Systems.", EPRI-NP-1850-CCM-5, Rev. 4, November 1988.

4. Taylor, D.D., et.al., "TRAC-BD1/MOD 1: An Advanced Best Estimate Computer Program for Boiling Water Reactor Transient Analysis", NUREG/CR-3633, April 1984.

5. Wulff, W., et. al., "A Description and Assessment of RAMMONA-3B Mod. 0 Cycle 4: A Computer Code with Three-Dimensional Neutron Kinetics for BWR System Transients," NUREG/CR-3664, January 1984.

6. Kelly, J.E., et. al., "THERMIT-2: A Two-Fluid Model for Light Water Reactor Subchannel Transients Analysis," Report No. MIT-EL-81-014, April 1981.

7. Gitnick, B.J., et. al., "Benchmarking of the FIBWR2 Transient BWR Core Hydraulic Code," Scientech, Inc. SCIE-COM-207-92, February 1993.

8. Takigawa, Y, "Caorso Limit Cycle Oscillation Analysis with Three-Dimensional Transient Code TOSDYN-2," Nuclear Technology, Vol. 79, November 1987.

9. Gialdi, E., et. al., "Core Stability in Operating BWR: Operational Experience, "Proceedings on Nuclear Energy", Volume 15, 1984.

TABLE 1

INITIAL / AVERAGE CORE CONDITIONS

PARAMETER	VALUE
Core Power	44.5% rated
Core Flow	29% rated
Inlet Temperature	537.8 K
Core Pressure	965.7 Psi
Hot Channel Inlet Flow	0.04165 Mlb/hr

HOT CHANNEL AXIAL POWER FACTORS

(Radial Peaking Factor = 1.4819)

	Node	APF
Bottom of Active Fuel (BAF)	1	.4841
	2	1.3334
	3	1.4364
	4	1.3877
	5	1.3737
	6	1.3571
	7	1.3200
	8	1.2590
	9	1.1987
	10	1.1505
	11	1.0959
	12	1.0424
	13	1.0060
	14	.9782
	15	.9649
	16	.9557
	17	.9454
	18	.9564
	19	.9228
	20	.8370
	21	.7259
	22	.5753
	23	.4688
Top of Active Fuel (TAF)	24	.2246

(1) Average power/flow condition for all cases were 44.5% / 29%.

(2) Peak oscillation magnitudes of 137, 274, and 356 percent rated are for "Caorso type", intermediate, and extrapolated oscillations given in Tables 2, 3, and 4.

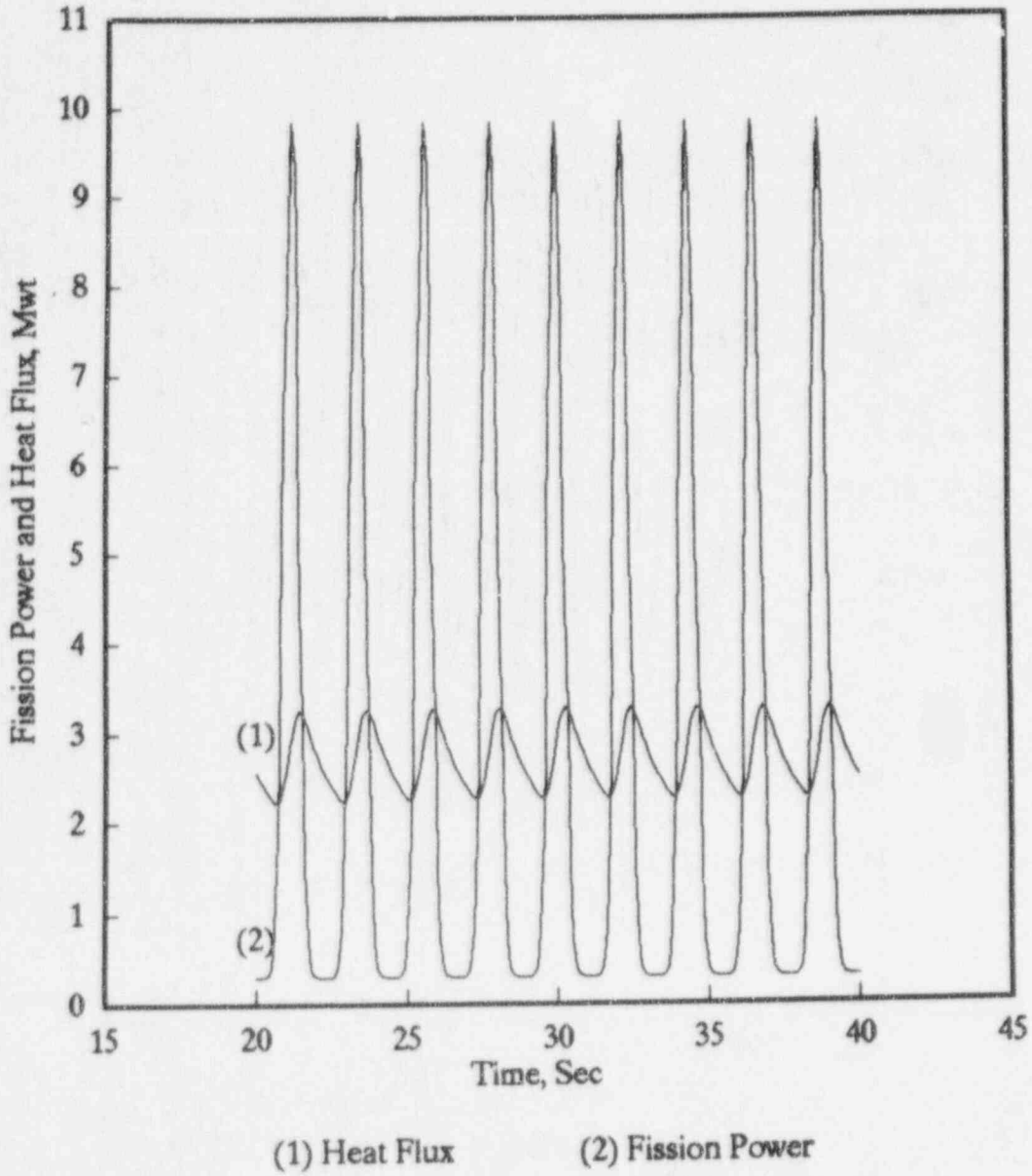

Figure 1: Fission Power and Cladding Heat Flux for 8x8 Fuel Intermediate Oscillation

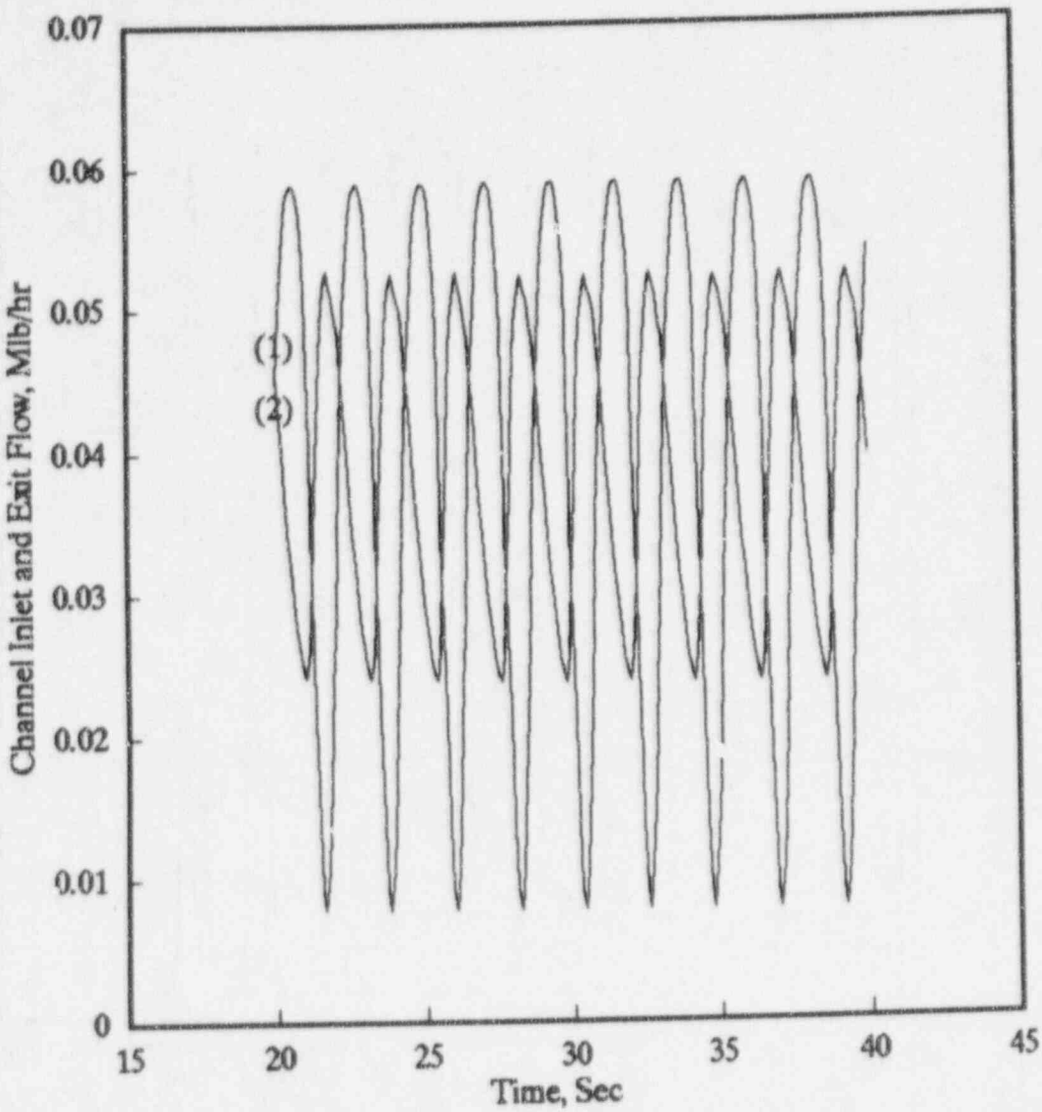

(1) Channel Inlet Flow (2) Channel Exit Flow

Figure 2: Channel Inlet and ExitFlow for 8x8 Fuel Intermediate Oscillation

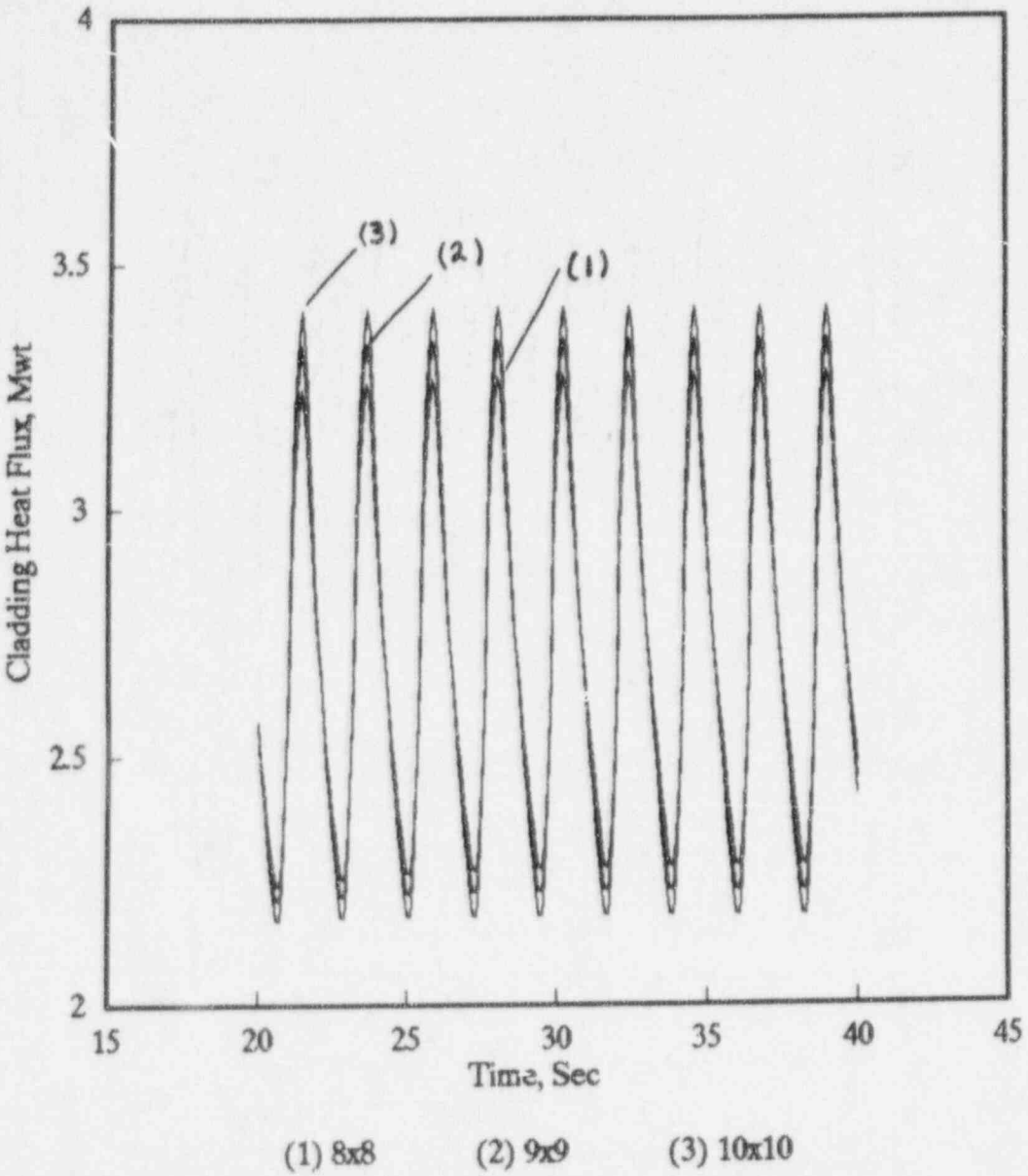

Figure 3: Cladding Heat Flux for 8x8,9x9, and 10x10 Fuels Intermediate Oscillation

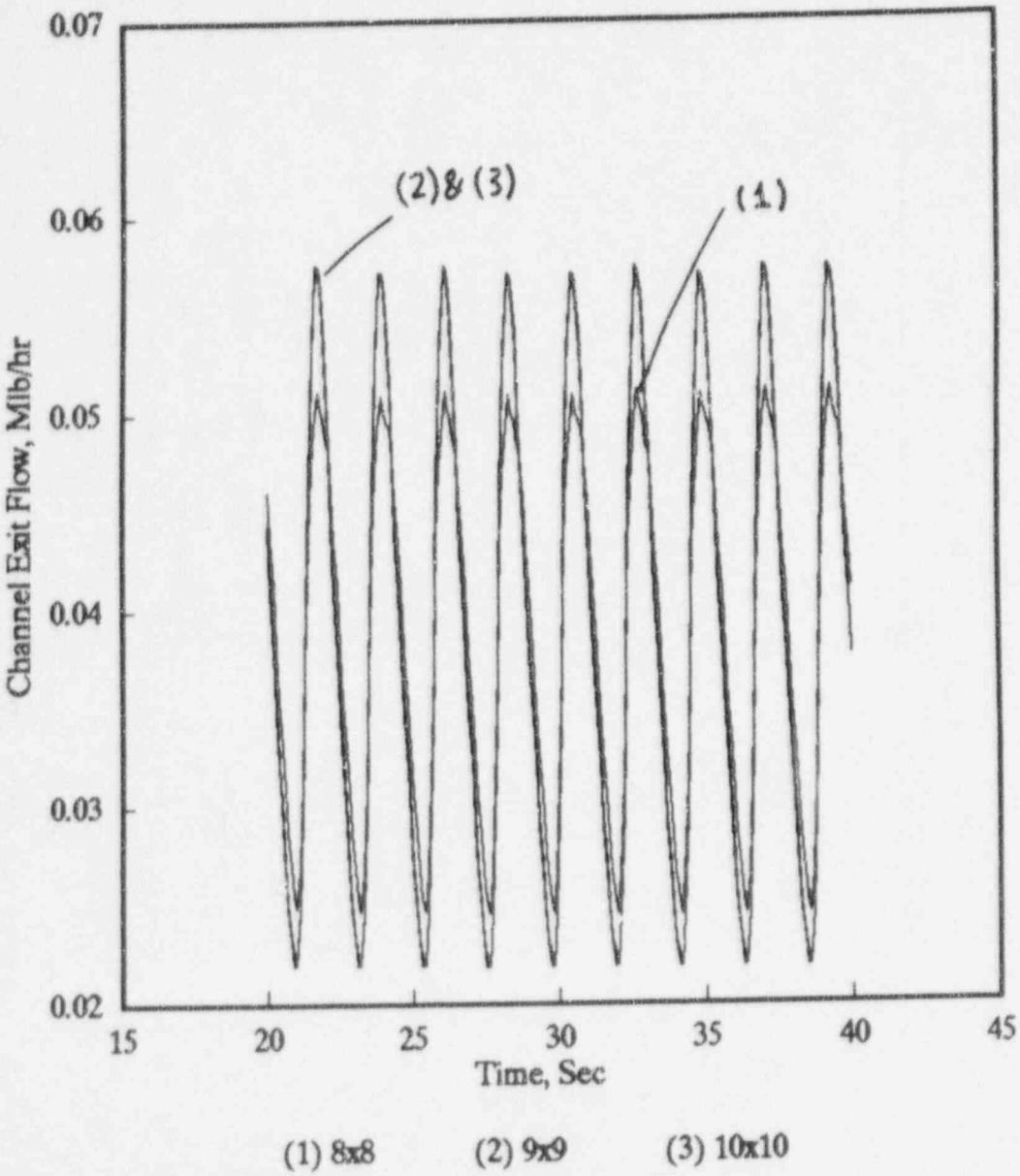

Figure 4: Channel Exit Flow for 8x8,9x9, and 10x10 Fuels Intermediate Oscillation

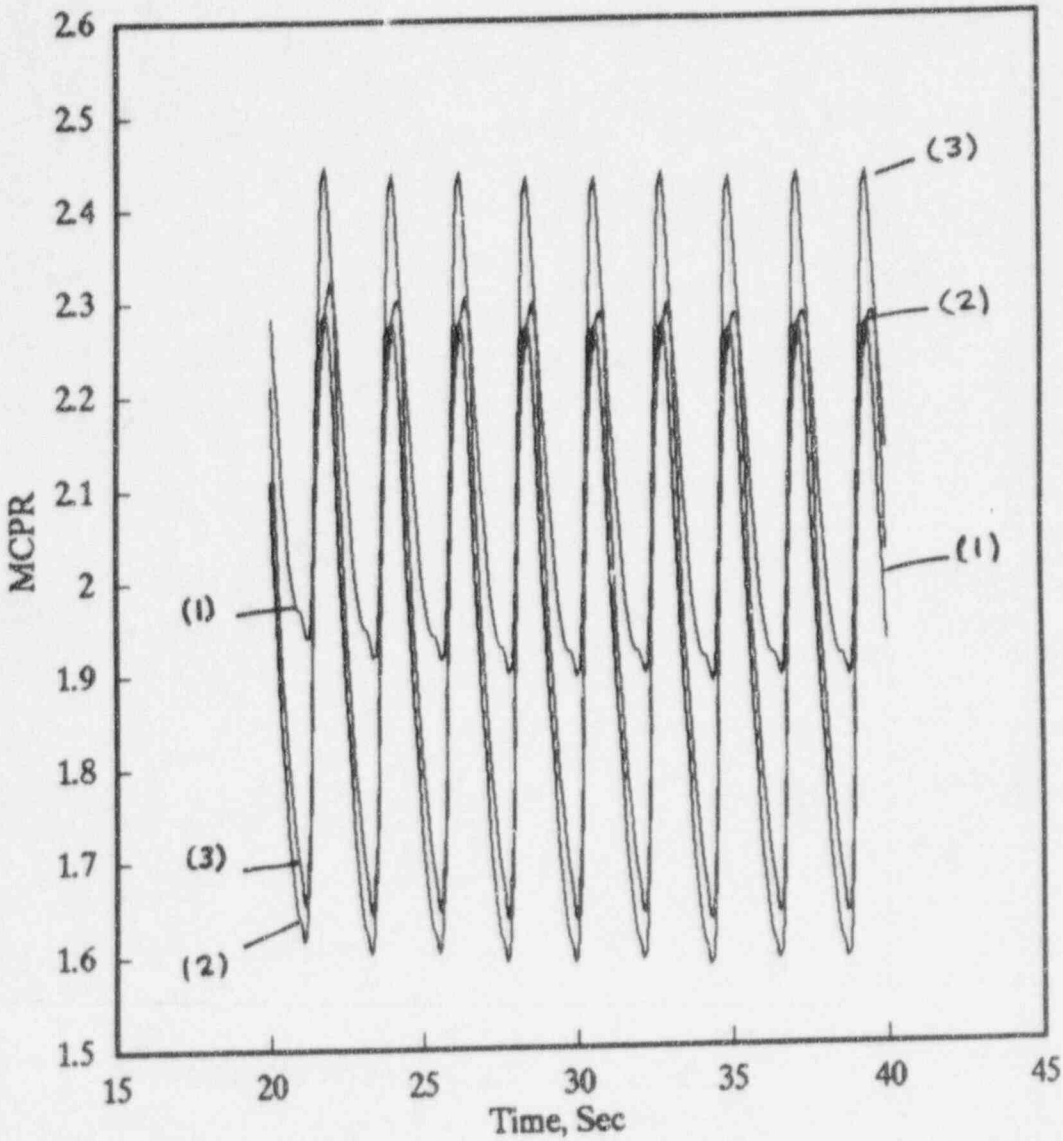

Figure 5: MCPR for 8x8, 9x9, and 10x10 Fuels Intermediate Oscillation

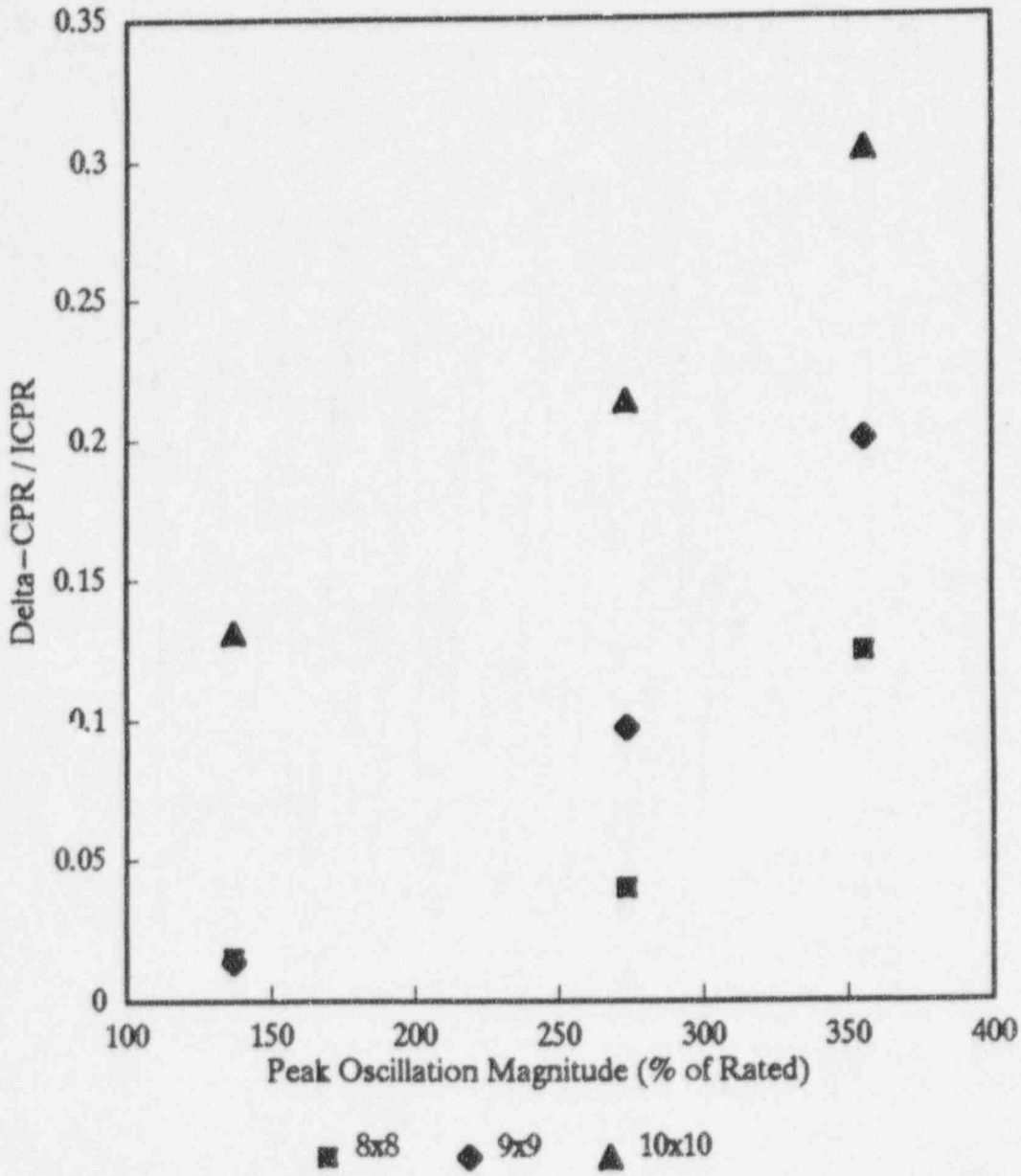

Figure 6: Thermal Margin Response During Regional Oscillation 560 Bundle Midsize Core (Orifice Diam. = 2.09 inch)

Density Wave Oscillations of a Boiling Natural Circulation Loop Induced by Flashing

Masahiro FURUYA, Fumio INADA and Akira YASUO

Central Research Institute of Electric Power Industry

11-1 Iwatokita 2-Chome, Komae-City, Tokyo 201, JAPAN

ABSTRACT

Experiments are conducted to investigate two-phase flow instabilities in a boiling natural circulation loop with a chimney due to flashing in the chimney at lower pressure. The test facility used in this experiment is designed to have non-dimensional values which are nearly equal to those of natural circulation BWR. Stability maps in reference to the heat flux, the inlet subcooling, the system pressure are presented. This instability is suggested to be density wave oscillations due to flashing in the chimney, and the differences from other phenomena such as flow pattern oscillations and geysering phenomena are discussed by investigating the dynamic characteristics, the oscillation period, and the transient flow pattern.

1 INTRODUCTION

Advanced Light Water Reactors (ALWRs) with simplified passive safety systems such as AP-600 and SBWR[1][2] are being developed in the USA and in other countries. In simplified BWRs, recirculation pumps installed in current BWRs are removed, and a chimney is installed on the core to increase the natural circulation flow rate. In natural circulation BWR, thermo-hydraulic stability at low pressure start up should be estimated while considering the flashing induced by the pressure drop in the channel and the chimney due to gravity head[3][4]. In this paper, thermo-hydraulic instability was investigated experimentally with a test loop in which the height of the test loop was comparable with that of natural circulation BWR, so that the nondimensional parameters to estimate thermo-hydraulic stability of reactors at low pressure start up were close to natural circulation BWR.

Several studies have addressed stability at low pressure start up of natural circulation BWR. Aritomi et al.[5]-[7] and Chiang et al.[8][9] conducted a basic study on the instabilities under the low pressure condition in a parallel channel natural circulation loop. They reported that three

types of instability, viz. geysering, natural circulation oscillations, and density wave oscillations could occur in their experiment, however, the effect of the flashing on the instabilities is not paid attention in their work.

Yokobori et al.[10] and Lin et al.[11] calculated the stability of natural circulation BWR during start-up using a TRAC code which is a time domain two-phase flow analysis code with a two-fluid model. Masuhara et al.[12] calculated the stability using a linear stability analysis code with a drift-flux model. Both results showed instability could not occur in natural circulation BWR during start-up. Yokobori, et al.[10] and Masuhara et al.[12] also conducted stability experiment using freon. However, the TRAC code analysis and the linear stability code analysis[12] were not evaluated using experimental data in relation to the stability at low pressure condition, and the experiment using freon can underestimate flashing induced by the pressure drop in the channel and the chimney due to gravity head because the change in saturation enthalpy of freon with pressure is much smaller than that of water.

The Dodewaard BWR station in the Netherlands, which is a natural circulation BWR with a chimney, is being operated now [13]. The claim is that instability can not occur during start-up. However, the composition of the Dodewaard reactor is not the same as that of natural circulation BWR because there are no separators in the Dodewaard reactor. It is not clear what type of instability is the most critical and whether or not operation condition of the natural circulation BWR is far from the unstable region.

Inada et al.[3][4] investigated the flow instabilities of a boiling natural circulation loop with a chimney with a small scale (1/6 of the representative natural circulation BWR in height) test apparatus and linear stability analysis using homogeneous two-phase flow model, and showed 'adiabatic flashing due to decrease in gravity head', hereinafter abbreviated "flashing", in the chimney takes important role on the instability. However, a test loop should be as tall as the representative natural circulation BWR to simulate the flashing effect in it. Further detail measurement systems are needed to confirm the characteristics and the mechanism of the instability.

To solve these issue in this study, the test facility was designed and constructed to have nondimensional parameters equal to those of natural circulation BWR for the thermo-hydraulic similarity. Parameters representing the flashing quantity, Froude number, pressure loss coefficients, etc. were derived[14] from the nondimensional form of the basic equations using drift-flux model for the boiling two phase flow system.

This paper presents the experimental results of the test facility to investigate two-phase flow instabilities in a boiling natural circulation loop with a chimney at lower pressures ranging from 0.1 to $0.5MPa$ and addresses the characteristics and mechanism of the instability as well as conditions where oscillations take place due to flashing in the chimney.

2 TEST FACILITY

Figure 1 is a schematic of the test facility. This loop consists of two channels, a chimney, an upperplenum, a downcommer, a subcooler, and a preheater. The channel length is $1.7m$ and the chimney length is $5.7m$, which are around 70% the values in a typical natural circulation BWR. A heater pin is installed into each channel concentricity. The test fluid is water.

This facility was designed and constructed to have nondimensional parameters equal to those of natural circulation BWR for the thermo-hydraulic similarity listed in **Table 1**. The flow rate which was necessary to calculate some of the nondimensional parameters was estimated using steady-state two-phase calculation code with a drift-flux model. We summarized the definitions and descriptions of the nondimensional parameters in a previous paper[14].

Table 1 Comparison of the Test Facility with natural circulation BWR

System Pressure	0.1MPa		0.5MPa	
Target	Reactor	Test Fac	Reactor	Test Fac
Froude Number	$1.1\cdot10^{-3}$	$7.6\cdot10^{-4}$	$1.1\cdot10^{-3}$	$7.4\cdot10^{-4}$
Friction Coef in the Channel	6.87	5.71	6.19	5.17
Orifice Coef at the Channel Inlet	10–50	30	10–50	30
Orifice Coef at the Chimney Exit (Separator Loss)	20–40	21	20–40	21
Phase Change Number	11.6	13.1	2.74	3.17
Subcool Number	8.98	8.98	2.11	2.11
Flashing Parameter	67	46	5.3	3.4
Ratio of Vapor Density to Liquid	$6.2\cdot10^{-4}$	$6.2\cdot10^{-4}$	$2.9\cdot10^{-3}$	$2.9\cdot10^{-3}$
Ratio of Vapor Density at the Channel Inlet to that at Chimney Exit	2.01	1.63	1.20	1.13
Nondimensional Downcommer Cross Sectional Area	1.05	1.11	1.05	1.11
Nondimensional Chimney Cross Sectional Area	2.59	2.47	2.59	2.47
Nondimensional Chimney Length	3.34	3.38	3.34	3.38
Nondimensional Drift Velocity	1.32	1.97	1.25	1.92

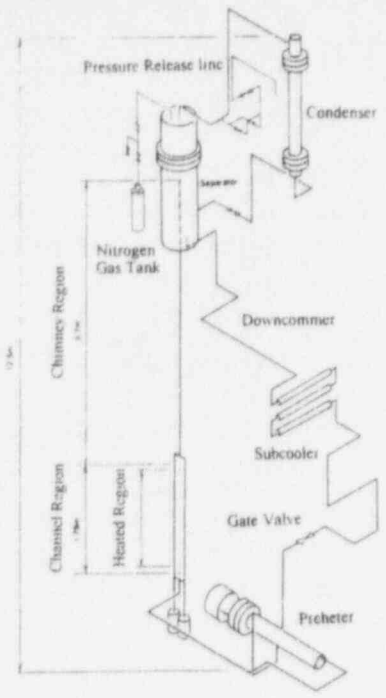

Fig.1 Schematic Diagram of the Test Facility

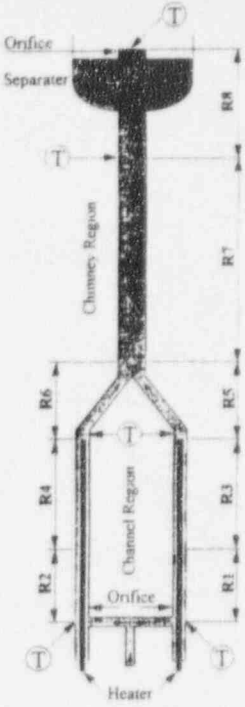

Fig.2 Region of Measurements

Although the value of the Froude number and flashing parameter of the test facility is around 70% of those of a typical natural circulation BWR, due to short height of the facility, the value of most of the parameters agree well.

The regions for differential pressure measurements and the locations for temperature measurements are shown in **Figure 2**. The condenser is not addressed in this experiment. When the system pressure is maintained at $0.1MPa$, experiments are carried out with the valve attached at the upper separator open. Otherwise, the separator dome is pressurized by injecting nitrogen to keep system pressure at a specific level. Results are obtained where the channel inlet temperature is raised by one or two degree Kelvin, when the system is confirmed to be in the steady-state after the heat flux at the channel and the system pressure are controlled and maintained at specific value under natural circulation.

3 RESULTS AND DISCUSSION

3.1 Representative Flow Oscillations

Figure 3 (a)-(d) show representative waves where P_s=$0.2MPa$ and q''=$53kW/m^2$. The void fraction is estimated from the differential pressure. The average and the r.m.s value over three cycles, when the flow is unstable (corresponding to Figures (b) and (c)), are tabulated in **Table 2** as well as the explanations of the legend used in Figure 3. All values of differential pressure and temperature remain constant (Figure (a), N_{sub}= 29.8) when boiling does not occur in the chimney. The values oscillate intermittently and periodically (Figure (b), N_{sub}= 23.6) when the channel inlet temperature, which only remains constant, exceeds a specific value due to pulsation of recirculation flow. Note that the time scale in Figure (b) is three times longer than those in the other figures. A further increase in the inlet temperature decreases the oscillation period so the wave resembles a sinusoidal curve (Figure (c), N_{sub}= -0.080; note that the nondimensional channel inlet subcooling, N_{sub}, is based on the saturation temperature in reference to the pressure in the separator dome, which can be a negative value.) It is clear that vapor developed in the middle of the chimney due to flashing and

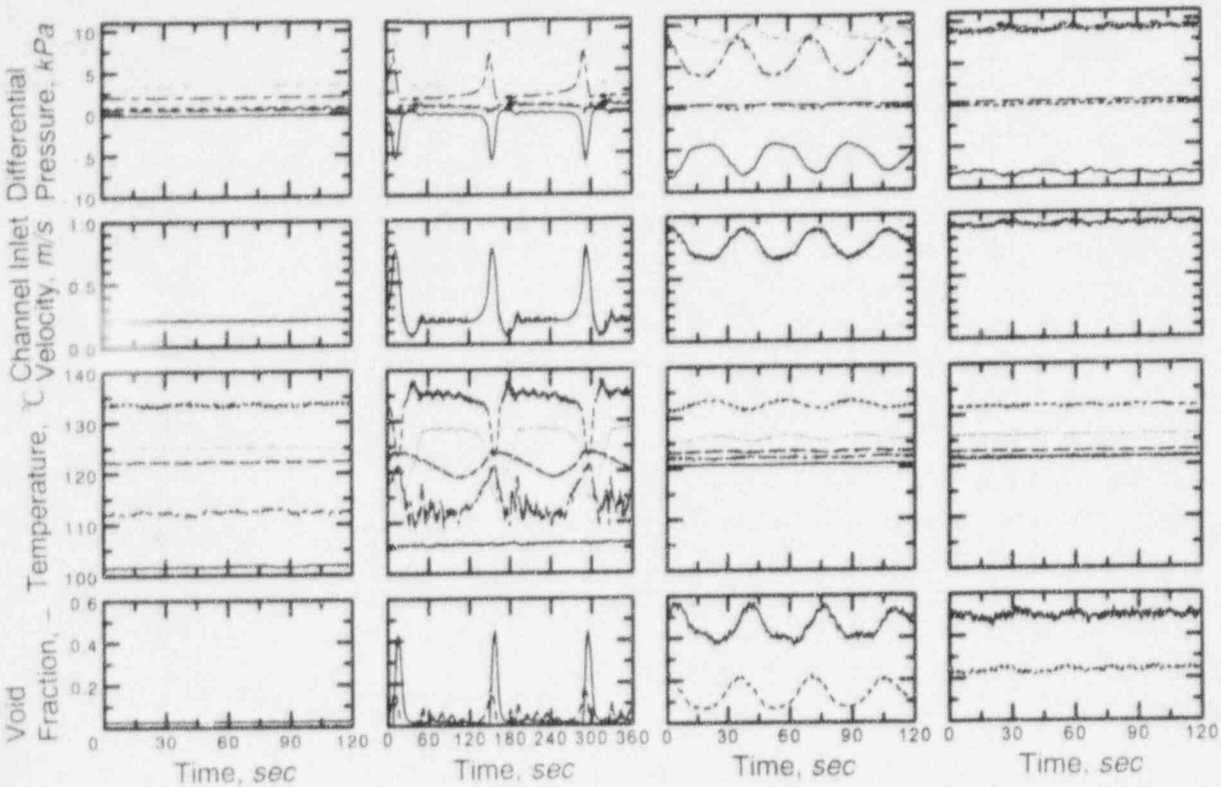

(a) Stable under Highly Subcooled Condition (N_{sub}=29.8)

(b) Intermittent Oscillations (N_{sub}=23.6)

(c) Sinuous Oscillations (N_{sub}=-0.080)

(d) Stable under Slightly Subcooled Condition (N_{sub}=-2.17)

Fig.3 Representative Waves in Various with Nondimensional Inlet Temperature (N_{sub}) where P_s=0.2MPa and q''=53kW/m^2

moved upward because the Figures (b) and (c) show a phase difference in the void fractions between R7 and R8. Moreover an increase in the inlet temperature reduces the amplitude of the flow rate, differential pressure, and temperature fluctuations (Figure (d), N_{sub}= -2.17), then flow is stabilized.

Most of the experiments are conducted with the inlet temperature increasing as described above, however, the stability boundaries agreed well with those obtained by decreasing the inlet temperature.

3.2 Effect of System Pressure on the Stability

Each condition invariance is classified and plotted in **Figure 4** with respect to heat flux and nondimensional inlet subcooling, where the system pressure is 0.2*MPa*. The solid line in the figure is a present correlation described later. The symbol ' • ' means stable condition; '◇' intermittent but periodic oscillations as shown in Figure 3(b); and '○', sinusoidal oscillations as shown in Figure 3(c).

Table 1 Legend Explanation of the Fig. 3 and Averge and r.m.s. Value

		(b)		(c)	
Legend	Property, *Unit*	Ave	r.m.s	Ave	r.m.s
	Diff. Pressure, *kPa*				
———	R1,2	-0.61	1.65	-5.93	0.887
·····	R3,4	0.75	0.31	0.15	0.140
– – – –	R5,6	0.66	0.28	0.37	0.025
– · – · –	R7	2.42	1.53	5.85	1.070
———	R8	3.71	1.51	8.76	0.442
	Temperature, ℃				
———	Channel Inlet	105.8	0.5	120.8	0.1
———	Channel Exit	124.8	10.2	126.1	0.6
– – – –	Chimney Middle	121.6	3.6	123.4	0.1
– · – · –	Chimney Exit	114.2	6.3	122.2	0.2
·····	Heater Surface	133.7	7.0	132.5	0.7
	Void Fraction, -				
– – – –	R3,4	0.002	0.007	0.000	0.000
– · – · –	R5,6	0.019	0.026	0.000	0.000
·····	R7	0.020	0.049	0.132	0.035
———	R8	0.048	0.120	0.452	0.038
———	Inlet Velocity, *m/s*	0.236	0.190	0.767	0.057
	System Pressure, *kPa*	201.9	1.92	203.3	0.21

The range of the unstable region during inlet subcooling increase with increasing heat flux. Intermittent oscillations occur in the higher subcooling, sinusoidal oscillations during the lower subcooling. Because the period and waveform of the oscillations change continuously with inlet subcooling, these differences are not clearly seen but depend on the length of time when the void fraction is very small (plateau shown in the Figure 3(b)).

Figure 5 is the stability map at system pressures of 0.1, 0.2, 0.35, and $0.5MPa$. It is apparent from this figure that increasing the system pressure reduces the range during subcooling where instability occurs. In fact, no instability was observed at $1MPa$ under the same experimental parameters as that at $0.5MPa$. This tendency was also reported by others[3][12].

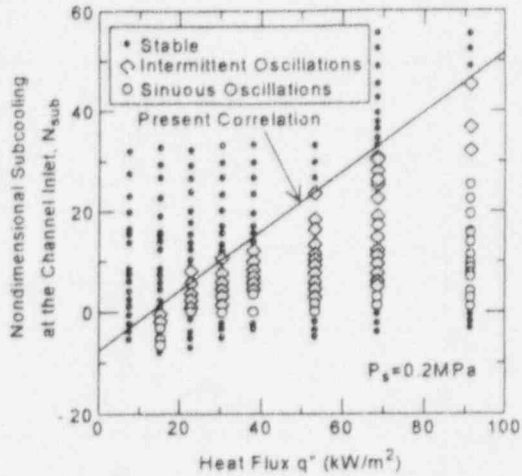

Fig. 4 Comparison of the Stability Boundaries Between Experiments and Present Correlation

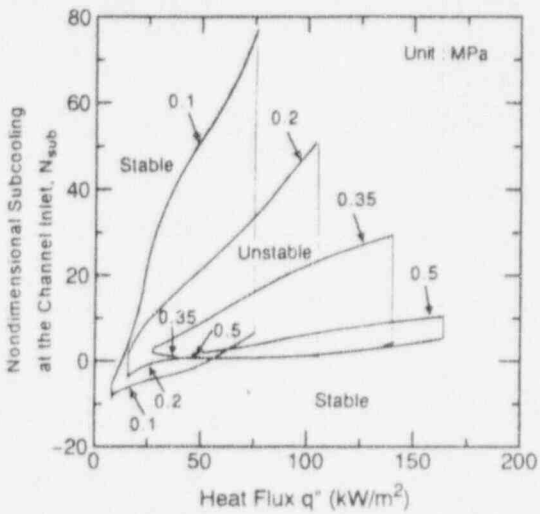

Fig. 5 Effect of System Pressure on the Stability Boundaries

3.3 Interaction between Channels

The test facility has two parallel channels to investigate the flow oscillations between channels. Those oscillations are not observed in these experimental series. Measured values of each channel are the same at any moment and location even where instability is taken place because that instability is driven by the void fluctuations due to the flashing in the chimney and boiling is not occurred in the channels.

4 MECHANISM OF THE INSTABILITIES

The types of the instabilities which we should consider[15] in this configuration of the facility are the flow pattern transition instability, geysering, natural circulation oscillations, and density wave oscillations. Acoustic oscillations are excluded because its mechanism is the resonance of pressure waves and its period is far smaller than that of oscillations in this experiment ranging from 13 to 250 seconds. If the flow excursion initiates dynamic interaction between the chimney and the separator dome, which has a compressive volume, pressure drop oscillations should be taken into consideration. However, the r.m.s. value of pressure at the separator dome is relatively small as tabulated in Table 2. Pressure drop oscillations are excluded in this reason.

4.1 Flow Pattern

Flow pattern transition instabilities have been postulated as occurring when the flow condition are close to the point of transition between bubbly flow and annular flow. Although this facility can simulate flashing phenomena, the chimney diameter of the facility is too small to simulate high quality flow pattern such as churn and annular flow.

In this section, the transient flow pattern is examined to make sure that the flow condition is not close to churn or annular flow and the flow pattern transition instability can be excluded from the main mechanism of the instability in this experiment. The Mishima-Ishii's diagram[16] was adopted to examine the flow pattern. Experimental data were plotted in **Figure 6** for about three cycles of oscillations at the upper part of the chimney, R8 (see Figure 2), under conditions of P_s=0.2MPa and q''=53kW/m^2. The slip velocity was calculated from the modified Bankoff correlation. Labels (b)-(d) are corresponding to those in Figure 3 (b)-(d). Experimental data do not appear in the figure due to the small void fraction under the highly subcooled condition.

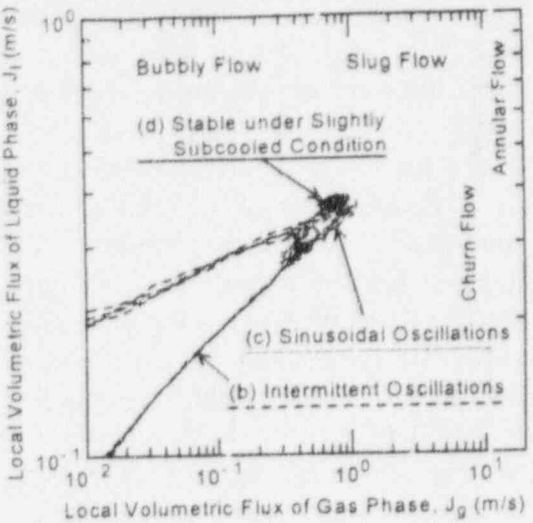

Fig. 6 Transient Flow Pattern in R8
(P_s=0.2MPa and q''=53kW/m²)

The flow pattern of intermittent oscillations ranges from liquid single phase flow to slug flow. That of sinusoidal, in oscillations which boiling always taken place in the chimney, is slug flow and the locus resembles an ellipse. Decreasing inlet subcooling reduces the area of the ellipse, then the flow becomes stable.

Flow pattern is checked for all condition in this experiment and found not to fall in or change to churn or annular flow with its characteristically lower pressure drop initiating flow pattern transition instability.

4.2 Consideration of the Instability Classification by the Oscillation Period

Geysering has been observed in a variety of closed end (or forced flow at small flow rate) vertical columns of liquid which are heated at the base. Its process breaks down into three processes, viz. boiling delay, condensation (or expulsion of vapor), and liquid returning[17]. It is also reported that the period of flow oscillation, τ_{fo}, is nearly equal to the boiling delay time, τ_{bd}, because the boiling delay time is much longer than that for the other two processes in most cases.

Since geysering has not yet been defined clearly for natural circulation flow in relation to density wave oscillations, we treat the characteristics of geysering in the natural circulation system as those in a closed end or forced circulation system ($\tau_{fo} \approx \tau_{bd}$). Boiling delay time is defined as the time required for the fluid having some degree of subcooling, $\Delta T_{sub,in}$, to be heated up to the saturation temperature based on the pressure at the channel inlet and is expressed by the following equation.

$$\tau_{bd} = \frac{\rho_f Cp_f \Delta T_{sub,in} A_c l_c}{q''} \quad (1)$$

The relationship between the boiling delay time and the flow oscillation period, τ_{fo}, is depicted in **Figure 7**. The properties of the density, ρ_f, and the specific heat capacity at the constant pressure, Cp_f, of water are based on the temperature at the channel inlet. A_c and l_c are the flow area and length of the heated section, respectively.

The oscillation period is one order of magnitude larger than the boiling delay time, and increases with increasing boiling delay time. This flow oscillation due to flashing is not geysering as defined above. The reasons are the flow rate is large enough to form a super-

heated layer of water and there is not enough subcooled water to condense large bubbles as shown in Figure 4.

In the boiling system under the condition of density wave oscillations, the oscillations are due to multiple regenerative feedback between the flow rate, vapor generation rate, and pressure drop. It is reported that the period is approximately one and a half to two times the time required for a fluid to travel through the channel[15].

Figure 8 illustrates the relationship between the flow oscillation period and the time required to pass through the chimney region, which is equal to a value of the volume divided by the average volumetric flow rate of the liquid. All (199 points of) data under unstable condition are correlated well in variance with system pressure, heat flux, and inlet subcooling. The oscillation period is nearly one and a half to two times the time required for a fluid to travel through the chimney region. As described above, temperature oscillations at the chimney inlet and outlet are out of phase (shifted by approximately 180 degree). Those two facts are practical characteristics of the density wave oscillations. As presented here intermittent (but periodical) and sinusoidal oscillations in this experiments, are both in the same category as density wave oscillations, because both data are correlated continuously in the same curve.

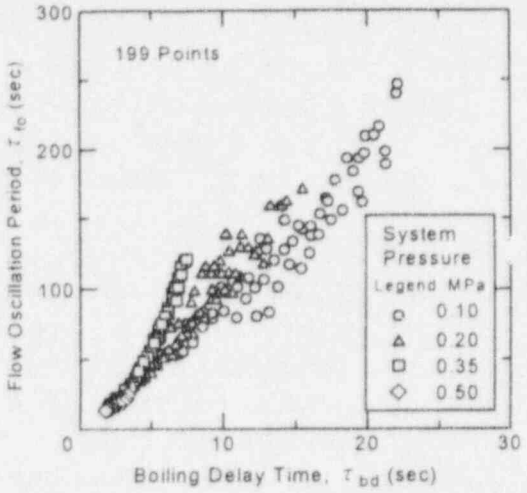

Fig. 7 Relation Between the Flow Oscillation Period and the Boiling Delay Time

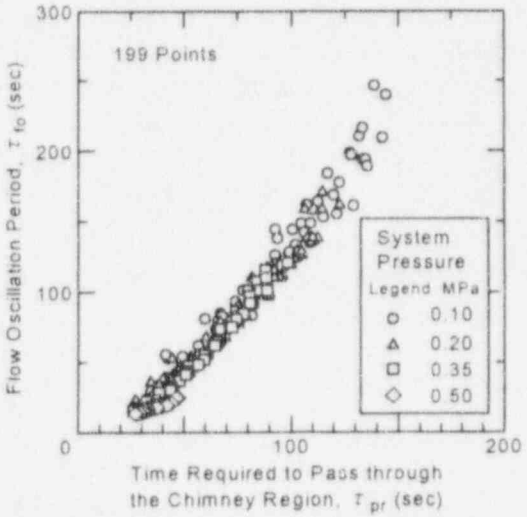

Fig. 8 Relation Between the Flow Oscillation Period and the Time Required to Pass through the Chimney Region

4.3 Driving Force for the Natural Circulation and Flow Rate

Chiang and Aritomi et al.[9] observed three different type of oscillations in their experiments; they are geysering, density wave oscillations, and natural circulation oscillations. They assume the following driving mechanism of natural circulation oscillations:

(1) Vapor accumulates in a non-heated pipe (connecting the outlet plenum to the separator tank, which consists of vertical and horizontal pipes in their apparatus), where the vaporization rate is insufficient.
(2) While bubbles coalesce with incoming vapor, the hydrostatic head decreases gradually.
(3) Accumulated vapor flows out and water is filled.
(4) The hydrostatic head increases and thus the circulation rate decrease (returning to process (1)).

These phenomena repeat periodically, as momentum energy is shifted quasi-statically by about 180 degree against the driving force of the circulation. There are no bent or horizontal pipes in the two phase section of our facility, where vapor tends to accumulate and the recirculation flow rate is so fast that vapor can not accumulate because of the long chimney, which is a vertical pipe. Natural circulation oscillations can not take place in the natural circulation BWR for the same reason, thermo-hydraulic similarity.

Dynamic characteristics are investigated for the response of the driving force of the circulation to momentum energy in order to clarify the differences with natural circulation oscillations. **Figure 9** illustrates the relationship of the driving force of the circulation, $(\rho_f - \rho_g) g \alpha_f V_r / A_r$, to the momentum energy, $\rho_f u_{in}^2 / 2$, where the system pressure is $0.2MPa$, the heat flux is $53kW/m^2$,and the subscript, r, denotes property at the chimney.

The average values are plotted in Figure 9(a). Those values are on the straight line that passes through the origin so the static characteristics are well correlated whether the flow condition is stable or unstable.

The trajectory is shown in Figure 9(b) for the representative intermittent and sinusoidal oscillations as shown in Figures 3(b) and (c). The trajectory moves on the straight line of static characteristics as illustrated in Figure 9(a). It becomes clear that vapor can not accumulate in the two phase section so that the response of driving force of the circulation to momentum energy is much fast. Again, the type of instability in this experiment is density wave oscillations rather than natural circulation oscillations in which the trajectory traces the ellipse in Figure 9(b).

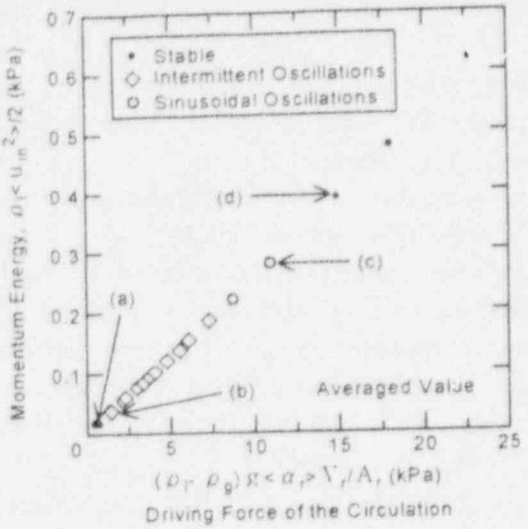

(a) Average Value

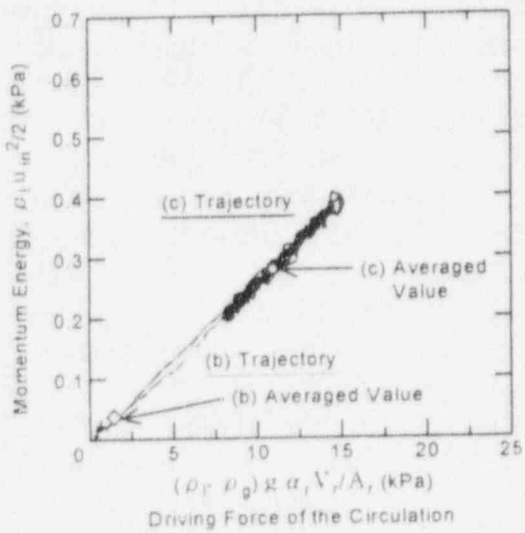

(b) Trajectory

Fig. 9 Relation Between Driving Force of the Circulation and Momentum energy *(P_s=0.2MPa and q''≒53kW/m²)*

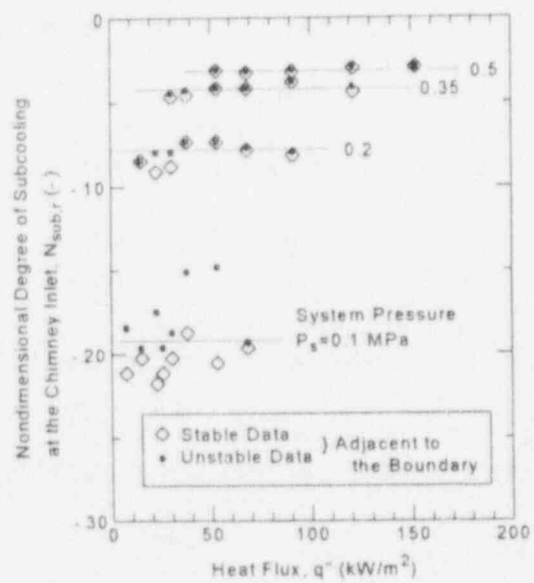

Fig. 10 Stability Boundaries under Higher Subcooling Condition

4.4 Stability Boundary at Higher Subcooling

Authors have presented experimental results on the stability boundary at lower subcooling and reported that it is predictable using a homogeneous model in which flashing is taken into account[3][4], however, it is important to quantitatively evaluate the stability

boundary at higher subcooling under practical startup condition of the natural circulation BWR[13].

Figure 10 shows stability boundaries under higher subcooling condition in degree of subcooling at the chimney inlet with respect to heat flux. Neighboring stable data were plotted as solid dots '●' and neighboring unstable data as '◇'. It is clear from the figure that the stability demarcation in chimney inlet subcooling is only a function of the system pressure where void fraction in the chimney is several per cent indicating that the flashing is starting in the chimney. Thus, the stability demarcation in the void fraction and recirculation flow rate are also only functions of the system pressure. Channel inlet subcooling at the demarcation is calculated by the chimney inlet subcooling and circulation flow rate at the demarcation and plotted as a solid line in Figure 4 with respect to heat flux. This correlation of stability boundary is in good agreement with the experimental one.

5 CONCLUSION

The following conclusions are drawn concerning the instability of the boiling natural circulation loop with a chimney induced by adiabatic flashing due to decrease in gravity head in the chimney under lower system pressure:

(1) The type of the instability that occurred in the experiments is suggested to be density wave oscillations due to flashing in the chimney and is different from the other instabilities such as geysering and flow pattern transient oscillations by investigating the dynamic characteristics, the oscillation period, and the transient flow pattern.
(2) Stability depends on the chimney inlet temperature. Thus if this temperature exceeds some value, instability is initiated where flashing is dominant in the chimney. Correlation for the stability demarcation at the higher inlet subcooling is derived using this value and is in good agreement with the experimental one.

Acknowledgments

Authors would like to thank Dr. H. T. Kim of GE Nuclear Energy for providing the design parameters of the natural circulation BWR and useful discussions.

Reference

[1] L. C. Hsu and L. C. Fennern , Int. Conf. Des. Safety of Adv. Nuc. Pow. Plants (ANP92) AESJ, **4**, 10(1992).
[2] B. S. Shiralkar *et al.*, Int Conf. Des. Safety of Adv. Nuc. Pow. Plants (ANP92) AESJ, **1**, 31(1992).
[3] F. Inada and A. Yasuo, Int. Conf. Des. Safety of ADV. Nuc. Pow. Plants, (ANP92) AESJ, **3**, 25(1992).
[4] F. Inada and T. Ohkawa, Int. Conf. New Trends in Nucl. Sys. Thermohydraulics, 187-193(1994).
[5] M. Aritomi *et al.*, Proc. 6th Nucl. Thermal Hydraulic, ANS Winter Meeting (1990).
[6] M. Aritomi *et al.*, 1st JSME/ASME Joint Int. Conf. on Nucl. Eng. (ICONE-1), **1**,87-94(1991).
[7] M. Aritomi *et al.*, Nucl. Safety, **33**, 170-182(1992).
[8] J. H. Chiang *et al.*, Proc. 5th Int. Topical Meeting on Reactor Thermal Hydraulics (NURETH-5), 119-126(1992).
[9] J. H. Chiang *et al.*, J. Nucl Sci. Tech., **30**, 203-211(1993).

[10] S. Yokobori *et al.*, Proc. 5th Int. Topical Meeting on Reactor Thermal Hydraulics (NURETH-5) (1992).
[11] J. H. Lin *et al.*, Proc. 2nd JSME/ASME Joint Int. Conf. on Nucl. Eng. (ICONE-2), **1**, 281-285(1993).
[12] Y. Masuhara *et al.*, 2nd ASME/JSME Joint Int. Conf. on Nucl. Eng. (ICONE-2), **1**, 135-141(1993).
[13] W. H. M. Nissen *et al.*, Int. Conf. Des. Safety of Adv. Nucl. Pow. Plants (ANP92) AESJ, **2**, 25(1992).
[14] F. Inada, M. Furuya, and A. Yasuo, 3rd ASME/JSME Joint Int. Conf. on Nucl. Eng. (ICONE-3), **1**, 173-178(1995).
[15] J. A. Bouré *et al.*, Nucl. Eng. Des., **25**, 165-192(1973).
[16] K. Mishima and M. Ishii, Int. J. Heat Mass Transfer, **27**, 5, 723-737(1984).
[17] S. Nakanishi, Trans. JSME, **44**, 388, 4252-4262(1978) (in Japanese).

Rayleigh-Taylor Instability of Cylindrical Jets with Radial Motion

Xiang M. Chen
GE Nuclear, M/C F21
P. O. Box 780
Wilmington, NC 28402

Virgil E. Schrock and Per F. Peterson
Department of Nuclear Engineering
University of California at Berkeley
Berkeley, CA 94720

Abstract

Rayleigh-Taylor instability of an interface between fluids with different densities subjected to accelleration normal to itself has interested researchers for almost a century. The classic analyses of a flat interface by Rayleigh and Taylor have shown that this type of instability depends on the direction of acceleration and the density differences of the two fluids. Plesset later analyzed the stability of a spherically symmetric flows (and a spherical interface) and concluded that the instability also depends on the velocity of the interface as well as the direction and magnitude of radial acceleration. The instability induced by radial motion in cylindrical systems seems to have been neglected by previous researchers. This paper analyzes the Rayleigh-Taylor type of instability for a cylindrical surface with radial motions. The results of the analysis show that, like the spherical case, the radial velocity also plays an important role. As an application, the example of a liquid jet surface in an Inertial Confinement Fusion (ICF) reactor design is analyzed.

1. Introduction

Rayleigh [1] and Taylor [2] showed that the stability of a flat interface between two fluids of different density is related to the direction of surface acceleration alone. For curved surfaces the criterion is a little more complicated due to the surface curvature. Plesset [3] analyzed the problem of a spherical surface in 1954. He found that the interfacial stability is related not only to the direction of acceleration but also to the surface velocity.

Though there has been interest in the stability of jets for a long time [4,5], our literature search indicated that the case of radial motion in cylindrical systems was not previously analyzed. Perhaps the isochoric heating problem arising in fusion reactor designs is the first example of this type of motion [6]. During the relaxation of internal pressure of a liquid jet, caused by absorption of a pulse of neutron energy, the cylindrical surface expands with very high velocity and acceleration/deceleration. The surface instability is important for the hydraulic integrity of the jet. Based on a mathematical approach similar to that used by Plesset, the stability conditions for a cylindrical interface flowing in the radial direction is derived in this study. The derivations in this paper are solely focused on the effects of the radial motion. The uniform axial velocity of the jets plays no role in Rayleigh-Taylor instability. The analysis is focused on the mechanism of the instability equation and therefore employs a simplified disturbance pattern with dependence only on the angular coordinate. A derivation for a more general three-dimensional disturbance is presented in the Appendix to this paper.

The stability criterion for cylindrical interfaces is then applied to the liquid jets in HYLIFE-II [7] -- an Inertial Confinement Fusion (ICF) reactor. Estimation of characteristic growth time of an unstable perturbation is also derived in order to provide insight into the possible modes of jet fragmentation.

2. Derivation of the Differential Equation for the Perturbation

Figure 1 displays the general configuration of the problem. Although the general perturbation may vary in both angular and axial directions, the derivation here will focus on the wave behavior in the angular direction only. The derivations in this section will be based on

incompressible flow equations. In reality, radial motion in a cylindrical body is usually induced by some compressibility of the fluid. In the case of the jets in the HYLIFE-II reactor [7], outward motion is induced by expansion within the rarefaction wave propagating into the liquid jets. However, it is still reasonable to use incompressible equations to analyze the perturbation at the interface of such flow. First of all, the compressibility shown by the fluid (especially liquid) concentrates in a very narrow zone which is known as the wave front. Previous calculations [6] have indicated that an incompressible model coupled with Joukowsky equation at the wave front to catch the velocity and pressure jump does a very good job in predicting the surface motion of the cylindrical jet surface. Once the wave front moves away, the local flow at the interface is basically "incompressible". Because of this, the assumption that the pressure follows the Bernoulli equation at the interface should also be reasonable. That is to say that, although the motion within the expansion wave does not follow incompressible flow theory, the Bernoulli equation should be applicable near the surface. For the same reason, the instability equations so derived can be used to predict the instability of surfaces of cylindrical bubbles produced by a submerged explosion as suggested by Plesset for a spherical bubble.

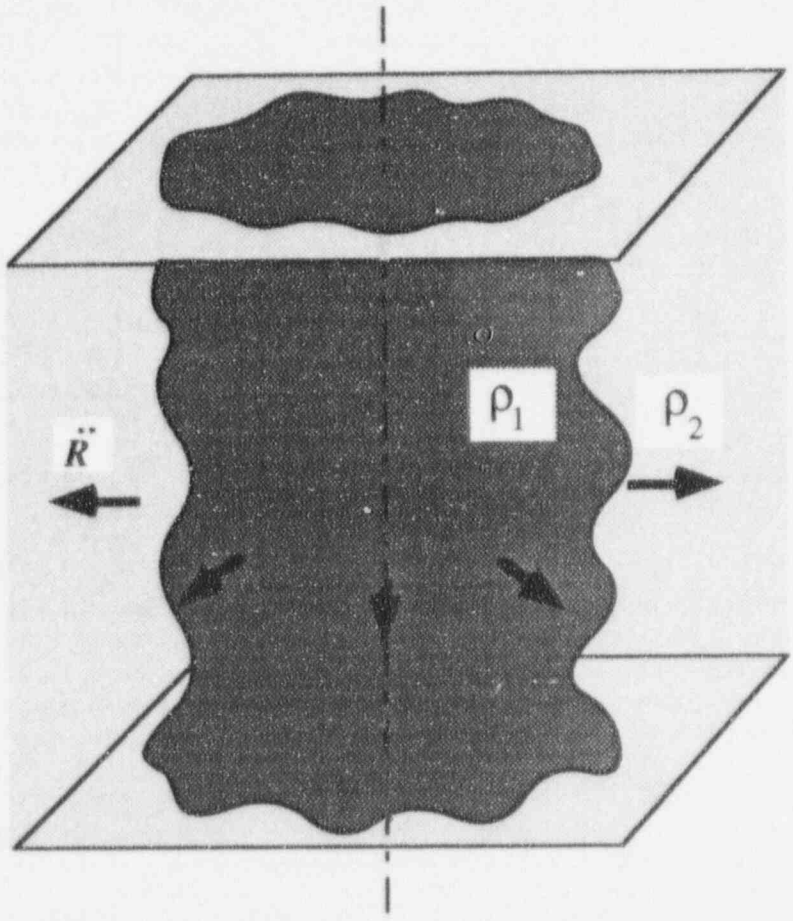

Fig. 1 A Perturbed Cylindrical Surface

In a cylindrical coordinate system with its origin at the center of cylinder, the flow potential for radially symmetric motion is

$$\varphi = -R\dot{R}\ln r \tag{1}$$

The radial velocity at the position r in the fluid is $-\partial\varphi/\partial r$. This potential, of course, implies a line source or sink at the origin according to whether the sign of surface velocity $\dot{R}$ is positive or negative.

We need to see now how a small distortion behaves with time. Let us consider then the radius as the combination of the mean value and the perturbation

$$r_s = R + a\cos n\theta \quad , \tag{2}$$

where a is a function of time and represents the half amplitude of the perturbation, which is very small compared to the radius R. One may notice that in writing the perturbation depending only on θ we have assumed a two-dimensional wave system (axially uniform).

For the first order analysis, the fluid velocity at the interface in the radial direction is

$$V = \dot{R} + \dot{a}\cos n\theta \tag{3}$$

If we consider a potential which corresponds to a disturbance which decreases away from the interface in both inward and outward directions, then we have the perturbed potential function as

$$\varphi_1 = -R\dot{R}\ln r + b_1 r^n \cos n\theta \quad , \qquad r < R, \tag{4}$$

$$\varphi_2 = -R\dot{R}\ln r + b_2 r^{-n} \cos n\theta \quad , \quad r > R \, . \tag{5}$$

Both potentials still satisfy the Laplace equation. The quantities b_1 and b_2 are determined by the requirement of continuity of velocity,

$$-\left(\frac{\partial\varphi_1}{\partial r}\right)_{r_s} = -\left(\frac{\partial\varphi_2}{\partial r}\right)_{r_s} = \dot{R} + \dot{a}\cos n\theta \quad , \tag{6}$$

with the result that

$$\varphi_1 = -R\dot{R}\ln r - \frac{r^n}{nR^{n-1}}\left(\dot{a} + a\frac{\dot{R}}{R}\right)\cos n\theta \tag{7}$$

$$\varphi_2 = -R\dot{R}\ln r + \frac{R^{n+1}}{nr^n}\left(\dot{a} + a\frac{\dot{R}}{R}\right)\cos n\theta \tag{8}$$

to first order.

For potential flow, the pressures on either side of the interface surface are related to potentials by the Bernoulli equations

$$p_1 = P_1(t) + \rho_1\left[\left(\frac{\partial \varphi_1}{\partial t}\right)_{r_s} - \frac{1}{2}(\nabla\varphi_1)_{r_s}^2\right] \quad , \tag{9}$$

$$p_2 = P_2(t) + \rho_2\left[\left(\frac{\partial \varphi_2}{\partial t}\right)_{r_s} - \frac{1}{2}(\nabla\varphi_2)_{r_s}^2\right] \quad . \tag{10}$$

Differentiating (7) and (8) and neglecting terms of order a^2, one has

$$\left(\frac{\partial \varphi_1}{\partial t}\right)_{r_s} = -\ln R\frac{d}{dt}(R\dot{R}) + \left\{-\frac{a}{R}\frac{d}{dt}(R\dot{R}) - \frac{R}{n}\ddot{a} + \frac{n-2}{n}\dot{a}\dot{R} - \frac{a\ddot{R}}{n} + a\frac{\dot{R}^2}{R}\right\}\cos n\theta \tag{11}$$

$$\left(\frac{\partial \varphi_2}{\partial t}\right)_{r_s} = -\ln R\frac{d}{dt}(R\dot{R}) + \left\{-\frac{a}{R}\frac{d}{dt}(R\dot{R}) + \frac{R}{n}\ddot{a} + \frac{n+2}{n}\dot{a}\dot{R} + \frac{a\ddot{R}}{n} + a\frac{\dot{R}^2}{R}\right\}\cos n\theta \tag{12}$$

$$(\nabla\varphi_1)_{r_s}^2 \approx (\nabla\varphi_2)_{r_s}^2 \approx V^2 \approx \dot{R}^2 + 2\dot{a}\dot{R}\cos n\theta \quad . \tag{13}$$

The pressures at a position the interface are connected by the relation

$$p_1 = p_2 - \sigma/R_1 \tag{14}$$

where R_1 is the principal radius of curvature of the interface (the other radius is infinity for the assumed disturbance) and σ is the surface tension. To first order, the curvature for the cylindrical case (Lamb [5], Sec. 173) is

$$\frac{1}{R_1} = \frac{1}{R} + \frac{a}{R^2}(n^2 - 1)\cos n\theta \quad , \tag{15}$$

so that across the interface

$$p_1 = p_2 + \sigma\left(\frac{1}{R} + \frac{a}{R^2}(n^2 - 1)\cos n\theta\right) \tag{16}$$

Substituting the expressions of p_1 and p_2 given by (9) and (10) respectively into (16) using the known functions of φ_1 and φ_2 from (11) to (13), one has the differential equation that describes the flow. One then can separate the terms which are independent of $\cos n\theta$ and give the equation of motion for the unperturbed interface:

$$R\ln R\frac{d^2R}{dt^2} + \left(\frac{1}{2} + \ln R\right)\dot{R}^2 = \frac{1}{\rho_1 - \rho_2}\left(P_1 - P_2 - \frac{\sigma}{R}\right) \quad , \tag{17}$$

where P_1 and P_2 are the time dependent boundary conditions on the Bernoulli equations. The

remaining terms, proportional to cos$n\theta$, give the differential equation for a:

$$\ddot{a} + 2\frac{\dot{R}}{R}\dot{a} + Aa = 0 \tag{18}$$

where

$$A = \frac{[\rho_1(n+1) - \rho_2(n-1)]\ddot{R} + \frac{n\sigma}{R^2}(n^2-1)}{(\rho_1+\rho_2)R} \quad . \tag{19}$$

Equation (18) involves a first-order term and its coefficients $\dot{R}/R$ and A are also time dependent. To simplify the relation, we consider the transformation of $\alpha=(R/R_0)a$, where the factor is the ratio of the current radius to initial radius. The disturbance equation for α then becomes

$$\ddot{\alpha} - G(t)\alpha = 0 \quad , \tag{20}$$

where

$$G(t) = \frac{[\rho_2 - \rho_1]n\ddot{R} - \frac{n\sigma}{R^2}(n^2-1)}{(\rho_1+\rho_2)R} \quad . \tag{21}$$

This is an interesting result since, unlike the spherical interface case, this $G(t)$ does not contain the surface velocity. The stability of a cylindrical interface obviously depends on the curvature, velocity and the acceleration of the interface, however, the surface velocity dependence is buried within the transformation of the dependent variable. In other words, all the effect of velocity is in the transformation factor (R/R_0). With the expression in (20) one can discuss the stability of the disturbance based on the sign of $G(t)$.

3. The Stability Conditions

The stability of a small disturbance on a cylindrical surface is determined by equation (18). If the solution $a(t)$ increases with time the surface is unstable, otherwise the surface is stable. At any moment, given data for the coefficients in equation (18), the tendency of the solution $a(t)$ can be evaluated. Equation (18) is satisfied by solutions of the form $a = a_o e^{kt}$. Substitution into equation(18) yields a quadratic algebraic equation for k. This leads immediately to the conclusion that when the the interfacial velocity is negative the interface is unstable because the equation will always have a positive root.

For the sake of a better physical picture, two special cases are further considered in the following. One may consider a general situation by integrating equation (20) once over time. It is easy to see that when $G(t)$ is positive α will have a positive growth rate, otherwise α is diminishing.

Case 1, $\sigma=0$; $\rho_1 >> \rho_2$:

This is a simplification of the case of a liquid cylinder with negligible surface tension. With the above assumptions, the function G can be simplified to

$$G(t) = \frac{-n\ddot{R}}{R} \tag{22}$$

Since n and R are always positive, $G(t)$ has the opposite sign of $\ddot{R}$. If the acceleration is pointing toward the heavier fluid ρ_1, the interface is unstable. Of course, the radius plays a role in $G(t)$ and we need also to note the effect of the transformation factor from a to α here. Obviously, the surface velocity, through (R_0/R), plays a role in the growth of the disturbance amplitude. For example, when $\dot{R}$ is positive, the real disturbance half amplitude $a = (R_0/R)\alpha$ could be diminishing even though α is growing slowly. The curvature of the surface affects the rate of growth but not the stability criterion in this specific case.

Case 2, σ=0; $\rho_1 << \rho_2$:

This corresponds to a cylindrical bubble in an infinite liquid with negligible surface tension. In this case

$$G = \frac{n\ddot{R}}{R} \quad . \tag{23}$$

The interface is stable when $\ddot{R}$ is negative.

Similar to the case of the spherical interface, the stability of the cylindrical interface depends on its acceleration, velocity and curvature. A positive velocity (expansion) is always a stabilizing factor. If the interface only accelerates mildly toward the heavier fluid, the expanding motion could make the interface stable. On the other hand, a negative velocity (contraction) tends to make the interface unstable. According to equation (18), if the coefficient A is negligibly small compared with $\dot{R}/R$, an integration over time gives an instability growth rate that increases exponentially with time. Even when the surface acceleration rate is positive the interface is still unstable due to the negative interface velocity.

In this section we have arbitrarily chosen to derive the instability equation for the surface disturbances having angular dependence only. This does not imply that the angularly dependent disturbance is less stable than the axially dependent one. Simplicity of the analysis is the motivation here. Doing the comparable derivation for a disturbance with both axial and angular dependence is a little more tedious. In that case the proper perturbation potential function which satisfies the cylindrical form of the Laplace equation is the product of modified Bessel functions of the first kind $I_n(\mu r)$, the $\cos n\theta$ and the cos[illegible,4]. The detailed derivation for such a disturbance equation is provided in the Appendix to this paper.

If the unstable modes have a very short wavelength compared to the radius of the interface the disturbances should have no orientation preference and should behave like the planar case. In neither case would the curvature of the surface be important. That is to say, disturbances with either axial or angular dependence have the same effects. But if the magnitude of the disturbance is appreciable relative to the interface radius, one must analyze the problem with the equations derived in the Appendix.

A summary of the stability conditions for the liquid cylinder and the clindrical bubble is given in Table 1.

Table 1. Stability Conditions for Cylindrical Interface with Radial Motion

Velocity $\dot{R}$	Acceleration $\ddot{R}$	Liquid Cylinder	Cylindrical Bubble
Positive	Positive	Stable	Conditionally Stable
Positive	Negative	Conditionally Stable	Stable
Negative	Positive	Unstable	Unstable
Negative	Negative	Unstable	Unstable

4. Application to the Relaxing Jets in the HYLIFE-II Reactor

One may have noticed that in deriving the disturbance equation (18) the effect of viscosity has been neglected. Scaling shows that the viscous damping is insignificant in the short-term. In this section the inviscid stability criterion will be applied to a Flibe jet of a HYLIFE-II reactor.

As shown by Chen et al.[6], after isochoric heating the surface of cylindrical jets first gains a positive velocity because of the large pressure difference across the interface initially and then decelerates as the expansion wave moves toward the center of the jet and a declining volume of liquid is expanding. Table 2 describes the conditions for a typical relaxing jet surface during the decelerating stage. The following assessments will be based on these parameters.

Table 2 Surface Parameters of an Example Relaxing Jet

Parameters		Value	
surface tension	σ	0.2	N/m
liquid density	ρ_1	1991.6	kg/m^3
ambient vapor density	ρ_2	10^{-3}	kg/m^3
surface radius	R	0.025	m
surface velocity	$\dot{R}$	20	m/s
surface acceleration rate	$\ddot{R}$	-10^6	m/s^2

4.1. The stability criterion under zero viscosity condition

There are seven independent parameters in equation (18). To discuss the effects of every parameter would be excessive. Let us consider only the parameters that are important in our application. During the pressure relaxation, the surface velocity of a jet is always positive unless

the jet does not break internally (in that case, the liquid jet will oscillate). The density inside the jet is much greater than the surrounding vapor ($\rho_1 >> \rho_2$). During the time that the rarefaction wave propagates inward, the variation of the radius is only a few percent, i.e., $R/R_0 \approx 1.0$. Thus we may approximate R as constant at the initial size of the Flibe jets. Now we can rewrite equation (21) as

$$G = -n\frac{\ddot{R}}{R} - n(n^2 - 1)\frac{\sigma}{R^3\rho_1} \quad . \tag{24}$$

When G is negative, the interface is stable. This will be the case when

$$\frac{\sigma}{\rho_1} \geq \frac{-1}{(n^2 - 1)} R^2\ddot{R} \quad . \tag{25}$$

One can see from equation (25) that it is possible to have a stable surface even when the $\ddot{R}$ is negative. Higher-order modes (greater n) are more likely to be stable. Smaller radius is also a stabilizing factor. Figure 2 plots the stability boundary based on equation (25) for different disturbance modes. A specific mode is stable if the combination of surface tension and acceleration fall above the boundary line for that mode. Figure 2 also marks the condition of the typical Flibe jet surface (from Table 2). With Flibe properties, if the deceleration rate is greater than $0.4\ m/s^2$ for $n = 2$ mode, the surface becomes unstable. According to the calculation by Chen et al.[6], the surface deceleration rate is as high as 10^6-$10^7\ m/s^2$. If we take the deceleration rate as 10^6, only perturbations with n greater 2945 are damped.

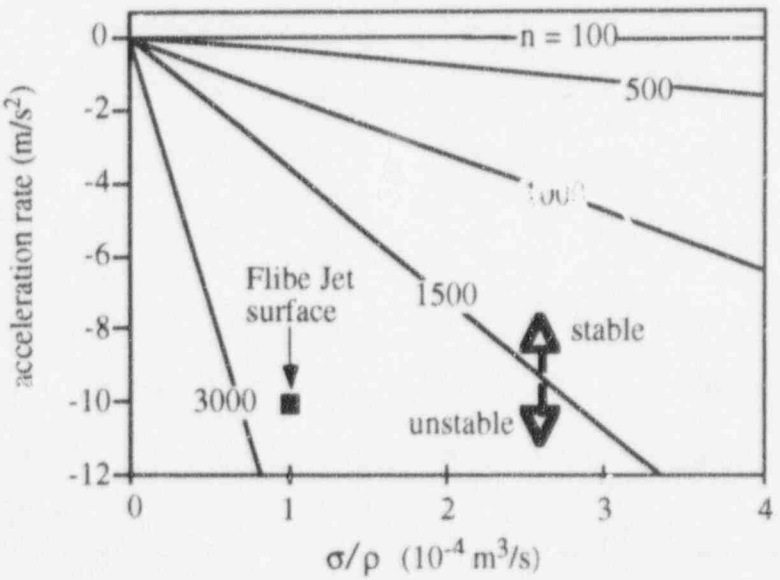

Fig. 2 The Stability of Different Disturbance Modes

4.2. Estimation of Characteristic Growth Time for the Instabilities

To accurately determine the growth of the instabilities non-linear analysis is generally necessary. For cylindrical jets the surface condition varies dynamically. However, from linear theory one may estimate the growth rate of the instability at the incipience of disturbance provided that the surface condition does not change too much within a short time. Taking a typical condition, one may conduct an estimation for the cylindrical Flibe jets as follows. Substituting the Flibe jets parameters from Table 2 into equation (18), one has

$$\ddot{a} + 1600\dot{a} + \left[-4\times 10^{7}(n+1) + 6.34n(n^{2}-1)\right]a = 0 \tag{26}$$

Seeking an exponential solution such as $a = a_0 e^{kt}$ of the differential equation, one may obtain two roots from the resulting algebraic equation as

$$k_{1,2} = \frac{-1600 \pm \sqrt{1600^{2} - \left[-4\times 10^{7}(n+1) + 6.34n(n^{2}+1)\right]}}{2} \quad . \tag{27}$$

When one of the roots is positive, a will grow. Further more, the larger the positive root, the greater the growth rate of a. The maximum can be found from

$$\frac{dk}{dn} = 0 \quad ,$$

or

$$-4\times 10^{7} + 6.34(3n^{2}-1) = 0 \quad . \tag{28}$$

Therefore, the fastest growing mode is that when n is approximately 1450. For this mode the positive root $k_1 \approx 1.95\times 10^{5}\ s^{-1}$. This gives $\tau \approx 5.12\times 10^{-6}\ s$, which is comparable with the relaxation time scale. Figure 3 displays the variation of the positive root versus n. As n increases, the root k_1 increases steadily to a maximum. Then as the third-order term in equation (27) becomes large the quantity inside the square root symbol decreases and eventually becomes negative. The modes with very large n will be stable. The most dangerous wavelength of the disturbance can also be estimated from the fastest growing mode as,

$$\lambda^{*} = 2\pi R/n \approx 1.08\times 10^{-4}\ m \quad .$$

The corresponding wavelength on a planar surface is $2\pi\sqrt{\dfrac{3\sigma}{(\rho_1-\rho_2)\ddot{R}}} = 1.09\times 10^{-4}\ m$. The size of this wavelength indicates that the unstable surface condition could result in generation of small droplets about $0.1\ mm$ in diameter. This small characteristic wavelength also confirms that the instability wave is indeed much smaller than the radius of cylindrical Flibe jets and the instability can be calculated accurately from the planar formula. Therefore, the growth of the instability modes will have no orientation preference and instability waves will emerge from the surface like fingers. On the other hand, since the characteristic growth time of the instability is not much shorter than the relaxation time span, it is unlikely that the surface instability will cause massive fragmentation of liquid jets into small droplets before the liquid jet undergoes fracture due to the internal tension.

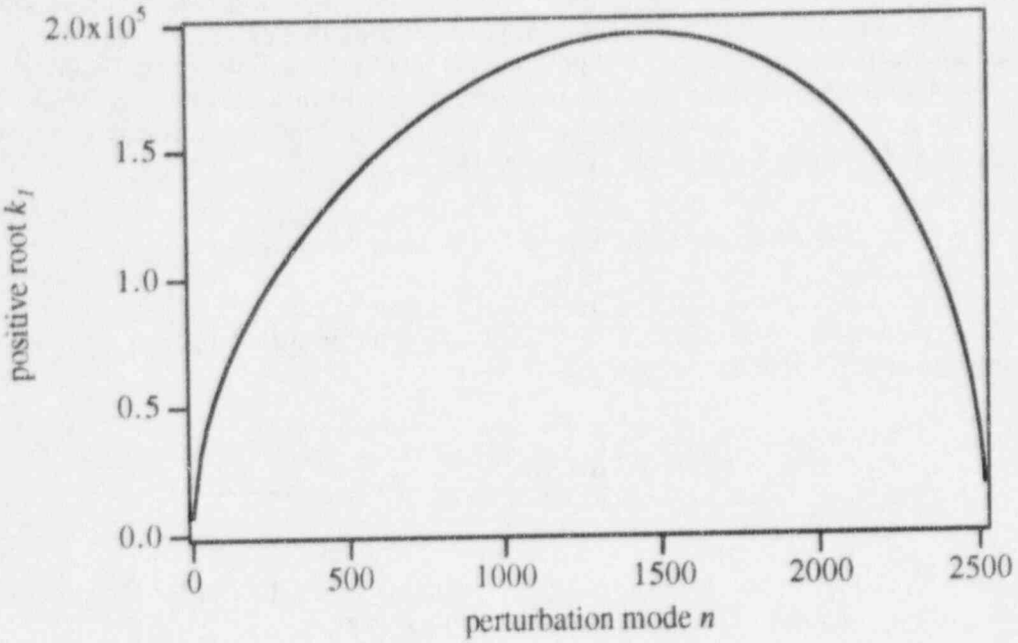

Fig. 3 The Instability Growth Constant for Different Modes

5. Reduction of the Cylindrical to Planar Case

It is worthwhile to show that when the radius goes to infinity the analysis here will generate the same stability criterion as for the plane surface. First of all, the linear term in equation (18) goes to zero as the denominator R becomes very large. In the quantity A the equivalent dimensional wave number for planar system is simply n/R ($=k$). For k to be finite, n will have to approach infinity as well. Thus, one can rewrite equation (19) as

$$A = k\frac{[\rho_1 - \rho_2]\ddot{R} + \sigma k^2}{(\rho_1 + \rho_2)} \tag{29}$$

When $(\rho_1 - \rho_2)\ddot{R}$ is negative and $k_c < \sqrt{\ddot{R}(\rho_2 - \rho_1)/\sigma}$ the interface is unstable. Take the derivative of A against k, one could also obtain the wave number of the fastest growing mode as

$$k^* = \sqrt{\frac{(\rho_1 - \rho_2)\ddot{R}}{3\sigma}} \tag{30}$$

which is identical to the result obtained by Taylor [2].

6. Conclusions

Similar to the spherical interface, the stability of the cylindrical interface depends also on the surface velocity. Unlike the planar interface which is always stable when the interface acceleration is pointing to the lighter fluid, a curved interface under similar acceleration can be unstable if the surface velocity is negative. This is because equation (18) will always have a

positive root if surface velocity is negative. On the other hand, positive surface velocity (expansion) could also help to stabilize a surface with a small acceleration pointing toward the heavier fluid. The derived perturbation equation (18) generates the same criterion as for the planar interface when radius approaches infinity.

For the HYLIFE-II application, the fastest growing instability has a very small wavelength. In the particular example listed in Table 1, the planar equation gives almost the identical result for fastest growing wavelength. The estimated growth time for the instability on the surface of the liquid jets in HYLIFE-II reactor is similar to the time of pressure relaxation. This means that massive fragmentation of jets due to this type of instability is unlikely. Tiny fingers may shed some fine drops but a cylindrical surface is likely to be restored when radial motion has subsided.

7. Nomenclature

Letters

A	disturbance wave function
a	magnitude of a small disturbance
G	time dependent coefficient in disturbance equation
k	wave numbers
n	wave mode
P, p	pressure
R	the outer radius of a jet; universal gas constant
r	coordinate in cylindrical and spherical geometry
$\dot{R}$	surface velocity
$\ddot{R}$	surface acceleration
R_1, R_2	principal curvature radii
t	time
V	velocity

Symbols

φ	velocity potential of an incompressible flow
θ	angle
λ	wave length
ρ	density; or relative density
σ	surface tension
τ	time scale
ω	wave frequency

superscription and subscription

o	initial state
s	surface values
$\dot{}$	first order time derivative
$\ddot{}$	second order time derivative

8. References

[1]. L. Rayleigh, "Investigation of the character of the equilibrium of an incompressible heavy fluid of variable density," Scientific Papers, Vol. II, 200-, Cambridge, England (1900).

[2]. G. I. Taylor, "The Instability of Liquid Surfaces When Accelerated in a Direction Perpendicular to Their Plane," Proc. Roy. Soc. (London), A201, 193-196 (1950).

[3]. M. S. Plesset, "On the Stability of Fluid Flows with Spherical Symmetry," Journal of

Applied Physics 25 96-98 (1954).
[4]. J. N. Anno, The Mechanics of Liquid Jets, D. C. Heath and Company, Lexington (1977).
[5]. H. Lamb, Hydrodynamics, Cambridge University Press, Cambridge (1932).
[6]. X. M. Chen, V. E. Schrock and P. F. Peterson, "The Hydraulic Analysis of Cylindrical Flibe Jets in a HYLIFE-II Reactor," Fusion Technology 21, 1531-1536 (1992).
[7]. R. W. Moir et al., "HYLIFE-II: A Molten-Salt Inertial Fusion Energy Power Plant Design--Final Report", Fusion Technology 25, 1-25 (1994).

Appendix The Perturbation Equation of Cylindrical Interface with Radial Motion when Disturbances with both Axial and Angular Dependence Exist

For the sake of simplicity, the derivation below is based on the assumption that the fluid density inside the jet is much higher than that outside. The general derivation should be very similar but involves two sets of flow potentials, one for each fluid. This effectively treats the pressure in the lighter fluid as constant.

Consider a surface perturbation of the form

$$r_s = R + a\cos m\theta \cos kz \tag{I-1}$$

to allow both angular and axial perturbations. We are seeking a velocity potential with a perturbation $\varphi = \varphi_0 + \varphi'$, where $\varphi_0 = w_0 z - R\dot{R}\ln r$, and φ' must also satisfy Laplace's equation

$$\frac{1}{r}\frac{\partial}{\partial r}\left(r\frac{\partial \varphi'}{\partial r}\right) + \frac{1}{r^2}\frac{\partial^2 \varphi'}{\partial \theta^2} + \frac{\partial^2 \varphi'}{\partial z^2} = 0 \tag{I-2}$$

Using the solution $\varphi' = f(r)\cos m\theta \cos kz$ direct substitution into equation (I-2) gives for $f(r)$

$$\frac{1}{r}\frac{\partial}{\partial r}\left(r\frac{\partial f(r)}{\partial r}\right) - \left(\frac{m^2}{r^2} + k^2\right) f(r) = 0 \tag{I-3}$$

Therefore $f(r)$ is the modified Bessel function of the first kind and of order m.

$$\varphi = w_0 z - R\dot{R}\ln r + \beta I_m(kr)\cos m\theta \cos kz \tag{I-4}$$

The variable β is determined by requiring radial velocity continuity at the jet surface, that is,

$$\begin{aligned} u_{r_s} = \dot{r}_s &= \dot{R} + \dot{a}\cos m\theta \cos kz \approx -\frac{\partial \varphi}{\partial r}\Big|_{r=R} \\ &= \dot{R} + \left[-a\frac{\dot{R}}{R} - \beta k I_m'(kR)\right]\cos m\theta \cos kz \end{aligned} \tag{I-5}$$

giving

$$\beta = -\frac{\dot{a}R + a\dot{R}}{kRI'_m(kR)} \tag{I-6}$$

so that

$$\varphi = w_0 z - R\dot{R}\ln r - \frac{\dot{a}R + a\dot{R}}{kRI'_m(kR)} I_m(kr)\cos m\theta \cos kz \quad . \tag{I-7}$$

The pressure in the inviscid jet is that due to surface tension

$$p = \sigma\left(\frac{1}{R_1} + \frac{1}{R_2}\right) \tag{I-8}$$

where R_1 and R_2 are the principal curvature radii. This gives

$$p = \frac{\sigma}{R} - \frac{a\sigma}{R^2}\left(1 - m^2 - k^2R^2\right)\cos m\theta \cos kz \tag{I-9}$$

Since the velocity w_0 does not effect the stability, it will be omitted for the following derivation. Using the Bernoulli integral,

$$p = P(t) + \rho\left[\left(\frac{\partial\varphi}{\partial t}\right)_{r_s} - \frac{1}{2}(\nabla\varphi)^2_{r_s}\right] \tag{I-10}$$

$P(t)$ is the constant from the spatial integration of the equation of motion which leads to the Bernoulli integral. The terms in the brackets in the above equation can be readily found to be

$$\begin{aligned}\left(\frac{\partial\varphi}{\partial t}\right)_{r_s} = &-\ln R\frac{d}{dt}\left(R^2\dot{R}\right) + \left\{-\frac{a}{R}\frac{d}{dt}\left(R\dot{R}\right) - \left[\ddot{a} + \frac{\ddot{R}}{R}a + \frac{\dot{R}\dot{a}}{R} - \frac{\dot{R}^2\alpha}{R^2}\right]\frac{I_m(kR)}{kI'_m(kR)}\right. \\ &\left. + \frac{\dot{a}R\dot{R} + a\dot{R}^2}{RI'^2_m} I'_m(kR)I_m(kR)\right\}\cos m\theta\cos kz\end{aligned} \tag{I-11}$$

$$(\nabla\varphi)^2_{r_s} = \dot{R}^2 + 2\dot{a}R\cos m\theta\cos kz \tag{I-12}$$

Substituting equation (I-11) and (I-12) into (I-10) and using (I-9), one can sort out the terms of the perturbations to obtain the following perturbation equation,

$$\ddot{a}+\dot{a}\left[\frac{\dot{R}}{R}-\frac{\dot{R}kI_m''}{I_m'}+\dot{R}\frac{kI_m'}{I_m}\right]+a\left\{\frac{kI_m'}{RI_m}\frac{d}{dt}\left(R\dot{R}\right)+\left(\frac{\ddot{R}}{R}-\frac{\dot{R}^2}{R^2}\right)\right.$$
$$\left.-\frac{\dot{R}^2kI_m''(kR)}{RI_m'}+(m^2+k^2R^2-1)\frac{\sigma}{\rho R^2}\frac{kI_m'}{I_m}\right\}=0 \qquad \text{(I-13)}$$

This is the full perturbation equation for an inviscid cylindrical interface with radial motion.

As did equation (18) (obtained from the simplified form of perturbation), equation (I-13) relates the growth of the disturbance to the radius, radial velocity and acceleration. No simple transformation can simplify this partial differential equation with time dependent coefficients. The acceleration effect should still be the major effect as its role in the equation is similar to that in equation 18. Numerical methods are necessary for solving this equation.

TWO-PHASE FLOW INSTABILITIES IN A VERTICAL ANNULAR CHANNEL

I. Babelli, S. Nair, and M. Ishii

Thermal-hydraulics and Reactor Safety Laboratory
1290 School of Nuclear Engineering, Purdue University
West Lafayette, Indiana 47907-1290

ABSTRACT

An experimental test facility was built to study two-phase flow instabilities in vertical annular channel with emphasis on downward flow under low pressure and low flow conditions. The specific geometry of the test section is similar to the fuel-target sub-channel of the Savannah River Site (SRS) Mark 22 fuel assembly.

Critical Heat Flux (CHF) was observed following flow excursion and flow reversal in the test section. Density wave instability was not recorded in this series of experimental runs. The results of this experimental study show that flow excursion is the dominant instability mode under low flow, low pressure, and down flow conditions. The onset of instability data are plotted on the subcooling-Zuber (phase change) numbers stability plane.

I. INTRODUCTION

Owing to the downward nature of the flow in the Savannah River Site (SRS) Mark 22 fuel assembly, two-phase flow instabilities are possible following a sudden reduction in the coolant flow rate (e.g. following a loss-of-pumping accident) [2]. Buoyancy force due to vapor which was generated by the reactor decay power, acts in the direction of destabilizing the system, possibly causing flow instabilities.

Hydrodynamically induced Critical Heat Flux (CHF) is encountered at powers less than those required for enthalpy burnout for down flow in parallel channels [2]. The low flow nature of this set of experiments makes for a complex phenomena of flow instabilities in the test section. This is due to the buoyancy force which plays a significant role in the case of downward, low pressure and low flow systems.

The body of the literature that addresses two-phase flow instabilities in down flow at low pressure and low flow conditions is very limited. Rush et al. [1] conducted a series of integral flow excursion experiments with SRS Mark 22 fuel assembly mockup. The experiments provided data on the onset, progression, and recovery from flow instability transients for the mockup. The authors do not present any quantification of the flow excursion instability as a design criteria. It also does not specify a region of stable operation.

Guerrero and Hart [2] conducted a series of experiments on an electrically heated assembly mockup of the SRS fuel assembly. They reported the onset of flow instability as that of initial flow fluctuations and sub-channel flow redistribution, followed by progressive sub-channel flow reversals and localized boiling, progressive channel reversal, and finally dryout in one channel. They observed a large margin between the point of initial flow instability and the point of dryout and thermal excursion. They correlated the instability data by using the Grashof number, the friction factor and the Reynolds number. The range of subcooling was very limited (two values of inlet subcooling were used) and no study of the effect of inlet and/or exit throttling was carried on.

The need for experimental studies on two-phase flow instabilities in down flow is evident. This paper presents original experimental data on downward two-phase flow excursion instability.

II. EXPERIMENTAL FACILITY

An experimental test facility was constructed to study two-phase flow instabilities at low flow and low pressure conditions for vertical down flow of Freon-113, as the test fluid. The annular geometry of the test section is designed to simulate the SRS (Savannah River Site) reactor Mark 22 assembly flow conditions, with provision made for down flow and up flow in the test section. A scaling study for simulating the heavy water reactor by Freon-113 was carried out [5]. The model geometry, working fluid, and the operating conditions were chosen with consideration to the cost effectiveness and scaling. The simulated loop correctly scales the Zuber (phase change), subcooling, and friction numbers. These ensure that the dynamic phenomena due to the void propagation, enthalpy waves, and pressure drop are simulated [5].

Central to the test facility, which consists mainly of delivery and recovery systems of the test fluid, Freon-113, in addition to various instrumentation to monitor and record the data, is the test section. It consists of a 1829 mm long, 19 mm ID beaded glass tube (fused with 25.4 mm conical tube at each end for assembling), and a cartridge type heater with 1829 mm heated length, 12 mm OD. Use is made of the transparent test section to investigate the hydrodynamic aspects of the two-phase flow instabilities.

A detailed description of the test facility, shown schematically in figure 1, is provided below:

1. Test section

The cartridge heater at the center of the test section is 2170 mm long, 12 mm OD with a maximum power of 6.72 kW. The heated length of the heater is 1829 mm long which is equal to the length of the beaded glass tube that makes the outer wall of the annular space of the test section with 19 mm ID. The annular gap throughout the heated section is 3.5 mm (except at the location of the spacer rings where it is 2.5 mm). The beaded glass tube is fused at both ends with 25.4 mm conical connectors for assembling with the rest of the loop.

Sixteen 0.21 mm OD K-type thermocouples are spot welded on the heater surface to monitor and record the surface temperature of the heater during the experimental runs. Each thermocouple is spot-welded to the heater surface and the junction is further covered with high-temperature thermally conductive cement to help fixing the thermocouples to heater surface. The thermocouples are equally spaced near the center of the heater but are more closely spaced near the two ends since dryout is expected more frequently near the outlet. The locations of the sixteen thermocouples are shown in figure 2. The azimuthal location of each thermocouple differs from the rest of the thermocouples with respect to the heater surface, in order to detect the CHF location as closely as possible. The azimuthal locations of the thermocouples are not shown, however, in figure 2.

Four spacer-rings are used to center the heater in the test section, as shown in figure 3. Use is made also of the spacer-rings to guide the thermocouple wires away from the heater surface such that the wires extend along the glass wall. Eight thermocouples are withdrawn from the top of the test section and the remaining eight are withdrawn from the bottom.

Two Teflon flanges are attached at both ends of the test section. Each flange has three side holes; two for thermocouples and one serves as pressure tap connection. The upper and lower plena are made of 50.8 mm Pyrex crosses. The connections to the test section and the delivery and recovery lines are made via 50.8 to 25.4 mm Pyrex reducers.

The test section is equipped with two flow resistance devices made of hard Teflon in the shape of a tapered plug as can be seen in figure 2. The degree of flow restriction is controlled by advancing or retracting the tapered plugs.

2. Freon delivery and recovery system

A 2 HP centrifugal pump, capable of delivering 9.15×10^{-3} m^3/s maximum flow rate and 20.4 m of maximum head, is used to supply Freon to the test section. The pump is installed at the lowest point of the test loop and a draining valve is attached to it. A by-pass line with a ball valve is connected to the inlet and outlet of the pump to regulate the

flow rate to the test section. Downstream of the pump, a pre-heater is installed to control the Freon temperature entering the test section. The 2 kW galvanized steel pre-heater can increase the Freon temperature, flowing at 0.3 m/s in a 25.4 mm diameter tube, by 10 C.

Downstream of the pre-heater the system branches into two: up-flow and down-flow branches. To direct the flow in either direction, a set of two valves (two sets are available) is closed which will force the Freon to flow, say, in the downward direction in the test section. The test section outlet, for both up and down flow cases, is connected to the inlet of a condenser which consists of double sets of coils submerged in a water bath. The outer set has 22 coils with 430 mm OD and 324 mm ID, and the inner set has 15 coils with 310 mm OD and 280 mm ID. The outlet of the condenser is connected to a sub-cooler which controls the Freon subcooling required for the experimental runs. The sub-cooler consists of a chest-type freezer with a bath of Ethylene Glycol in which a set of 17 coils with 430 mm OD and 324 mm ID is submerged. If no subcooling is desired, the Freon emerging from the condenser could be directed to by-pass the sub-cooler to the pump inlet.

A 25.4 mm ID by-pass tube is connected to the test section. The flow through the by-pass line is controlled by a ball valve and is measured by a turbine flow meter. Ten tubular band-type heaters of 495 W power each are mounted on the by-pass line and are used to match the temperature conditions of the flow inside the by-pass line with the temperature conditions inside the test section. The by-pass line isolates the flow disturbances and/or instabilities generated in the loop from the test section instabilities.

The test loop is supplemented with a 56.8×10^{-3} m^3 galvanized steel degassing tank located at the highest point of the test section. Two immersion heaters of 600 W power each are screwed at the bottom of the degassing tank which is equipped with a level gauge to monitor the Freon level inside the degassing tank. A condenser is attached to the degassing tank that utilizes water to cool a set of 28 coils with 63.5 mm OD and 50 mm ID. The degassing tank along with the heaters and the condenser could be used to regulate the pressure in the loop resembling a pressurizer in a reactor.

The loop has four relief valves that are connected to the test section lower plenum, the test section upper plenum, positive pressure line of the degassing tank, and to the negative pressure line of the degassing tank with cracking pressures of 206.8 kPa, 206.8 kPa, 20.7 kPa, and -6.9 kPa, respectively. The outlets of the relief lines are connected to a dump tank. The dump tank is equipped with a 6.9 kPa cracking pressure relief valve.

The Freon circulating through the loop is regularly filtered using a 25 micrometer pleated paper filter cartridge to trap any impurities or dirt that might exist in the Freon stream.

The test section assembly is encased in a box of transparent, anti-shattering Lexan sheet to provide protection for personnel and instrumentation against any possible breakage of the test section.

3. Instrumentation

The parameters that are monitored and recorded in this experiment are: temperature, pressure, flow rate, degree of flow restriction, and heaters' power. Data are measured and recorded via MetraByte's DAS-8PGA/EXP-16 data acquisition system, whereas Labtech Notebook software is used to manage and analyze the collected data. The DAS-8PGA/EXP-16 system contains the original eight analog input channels in the DAS-8PGA box, in addition to two EXP-16 multiplexer boxes with sixteen analog input channels in each box, variable gain setup switches, and cold junction sensing and compensation circuitry for direct temperature measurement using thermocouples. The sampling rate for all channels is 1 Hz and the duration of continuous sampling is 10 minutes. Description of the instrumentation is detailed in the subsections below:

1. The test section heater surface temperature is measured using sixteen 0.21 mm OD K-type thermocouples that are spot welded on the heater surface and are covered with high temperature thermally conductive cement. An ice box is installed to serve as a reference point for the heater thermocouples. If CHF occurs in a heat flux controlled experiment, the wall temperature rises sharply and may result in a burnout of the heater if the power is not tripped immediately. To avoid such a drastic deterioration in the surface temperature, a feedback control circuit is built with a solid state relay that cuts the power off the heater if the surface temperature exceeds 120 C at any point on the heater surface. The trip circuit will also cut the power off the heater if any of the thermocouples fails to function properly. The sixteen thermocouples are connected to the EXP-16 multiplexer box number 1 which has a set gain of 1000. The power to the heater could also be cut off manually using an on-off switch located on the electronic circuit box. Figure 2 shows the locations of the heater thermocouples. The power trip circuit was calibrated to trip the heater at a temperature of 120 C for each thermocouple using a known temperature source.

2. The temperature of the test fluid is monitored in several locations around the loop in order to establish the temperature conditions designated for the specific experimental run. The fluid temperature measurements are made with K-type thermocouples of 1.6 mm diameter, at nine locations in the test loop. The thermocouples are directly connected to EXP-16 multiplexer box number 0 set to a gain of 50 and taking advantage of the cold junction sensing and compensation circuitry. The location of each thermocouple is shown approximately in figure 1.

3. A turbine flow meter and a paddle wheel flow meter are installed in the loop to measure the flow rate of Freon at two locations.

A. Main flow meter: A paddle wheel flow meter which is located near the inlet to the pre-heater and is used to measure the flow rate in the loop with range of 2.84-283.9 x 10^{-3} m^3/s.

B. By-pass flow meter: A turbine flow meter which is located on the test section by-pass line and is used to measure the flow rate in the by-pass line with range of 2.84-28.4 x 10^{-3} m^3/s.

The turbine flow meter was calibrated by the manufacturer whereas the paddle wheel flow meter was calibrated on site. The output signals of the flow meters are directed to the DAS-8PGA box (with set gain of 1). Independent DC power supply is provided for each flow meter with an input voltage of 12 VDC.

4. Pressure measurements are made at five locations in the test loop. Three differential diaphragm-type pressure transducers are used to measure the pressure drop across the lower plenum, the test section and the upper plenum with ranges of 13.8 kPa, 35.4 kPa, and 35.4 kPa, respectively. Mating connectors are used to connect the pressure transducers to the carrier demodulator which is used to condition the pressure signals and hence to send them to DAS-8PGA data acquisition box (with set gain of 1). The three pressure transducers were calibrated on site.

The remaining two pressure measurements are made with absolute pressure gauges. The system pressure is measured at the lower plenum using a pressure gauge with range of 0-1379 kPa , whereas the degassing tank pressure is measured using a gauge with a range of 0-207 kPa. Both pressure gauges are fixed at the main control panel of the test loop.

III. TEST PROCEDURE

The manner in which the experiments were conducted is summarized below:

- Repeated filtering and degassing of the Freon-113 is carried on before conducting any test series.
- Inlet flow rate, inlet subcooling, and inlet flow restriction, and exit flow restriction are pre-determined.
- Heater is set at a pre-determined power level at which subcooled boiling is initiated in the test section.
- Heater power is increased by 100 W, and the coolant flow into the test section is maintained for several minutes until the temperature of the heater surface reaches steady state.
- Power is further increased until instability is encountered.
- Power, subcooling, inlet flow rate, inlet and exit restriction and system pressure are recorded for the specific run.
- Several runs are randomly repeated for repetition to ensure repeatability of data.

The raw data recorded by the data acquisition system are compiled to represent the instability plane in terms of the subcooling number vs. the Zuber (phase change) number.

IV. RESULTS AND DISCUSSION

1. Physical description of the instability

With increase in heater power, at constant inlet flow rate and temperature, subcooled boiling starts at the last third of the test section. The heater surface thermocouple junctions are the locations where nucleation starts. With further increase in power, the bubbles grow and start to detach from the heater surface and flow down stream to the exit of the test section. The increase in void generation will cause bubbles to coalesce into one, or several, small cap bubbles at the exit of the test section where the flow area is suddenly enlarged at the 25.4 mm conical section. Beyond certain void fraction in the test section, the flow will start to decelerate in the test section and accelerate in the bypass line. The increase in pressure drop along with the destabilizing buoyancy effect due to increase in the void content of the test section will retard the flow into the test section completely. At this point the, bubbles along the length of the test section will grow rapidly in size and flow reversal will occur in the test section. The ensuing flow pattern is of natural circulation between the test section and the bypass line, superimposed on the forced flow into the bypass from the pump. The bypass flow rate signal shows a higher flow rate than that of the main pump. This instability, which Guerrero and Hart [2] term as the first instability, is in fact the flow excursion instability. This experiment is conducted in a transparent test section which allows clear observation of the manner in which the system undergoes transition from low quality state to a high quality state, which clearly indicates flow excursion instability. Guerrero and Hart [2] relied on temperature records to infer the phenomena.

It is important to mention here that the flow excursion instability is not a local phenomenon but is system dependent. The effects of thermocouple wires, thermocouple junctions, and spacer rings are, therefore, limited to local phenomena. Examples of theses phenomena are:

- Thermocouple junctions provide excellent nucleation sites.
- Due to the relatively high thermal capacity of the spacer rings (made of brass), their locations are the last to be quenched after power trip.

No attempt was made, however, to study the local effects of the thermocouples or the spacer rings since they do not affect the stability of the system.

2. Output data

The raw data are collected and analyzed to obtain the instability boundaries. Figure 4.a shows the heater surface temperature at the inlet and exit of the test section for Run # 9 ($K_i = 0$). Figure 4.b shows the same information for Run # 46 ($K_i = 22$). Notice the temperature increase at both inlet and outlet. The increase of the inlet fluid temperature due to flow reversal is more pronounced since at the entrance to the test section, the fluid

is at its coldest condition. Also notice that the heater surface temperature for the case of higher inlet restriction was much higher indicating a more violent excursion, which was physically observed. Also notice that the system reached CHF during Run # 46.

Figures 5.a and 5.b show the main and bypass flow rates for Runs # 9 and 46, respectively. When the bypass flow rate exceeded the main flow rate, in Run # 9, this indicated that the flow excursion was followed by flow reversal. Flow reversal did not take place in Run # 46. The violent vaporization of the Freon in the test section prevented the bypass liquid from entering the test section which remained voided until the control circuit tripped the heater power following CHF.

Data on the inlet velocity into the test section, the inlet subcooling, the inlet and exit flow restriction, and the heater power are properly collected for each run and the subcooling number and phase change number were consequently calculated as can be seen from Table 1. The third column and the fifth column of Table 1 show the standard deviation of the test section inlet velocity and the inlet fluid temperature, respectively. The test section heater power (current x voltage) was digitally recorded.

The instability boundary is shown in figure 6. At high subcooling, the instability boundary lies to the left of the zero exit quality line. At low subcooling, the instability boundary crosses the zero exit quality line to the region of positive quality.

For a higher inlet flow restriction, $K_i = 22$, and at the region of high subcooling, the instability boundary lies further to the left of the zero exit quality line in comparison with the case of zero inlet flow restriction. At lower subcooling the instability boundary crosses the zero exit quality line to the region of positive quality similar to the case of zero inlet restriction.

We see from figure 6 that subcooled boiling plays an important role in two-phase flow instabilities for the down-flow case. This is evidenced by the experimental observation that at relatively high subcooling, the system undergoes unstable transition from low-quality state to high-quality state even though the exit quality is negative. This trend was reported by Guerrero and Hart [2]. At low inlet subcooling, the unstable transition occurs at a positive exit quality.

Similar to the results reported in [2], the flow in the test section and bypass undergoes re-distribution following the increase in void fraction and increase in pressure drop. This phenomena has to be accounted for when making an analytical predictions of the instability boundaries. Most instability predictions [3,4] assume, for simplicity, that a constant pressure drop boundary condition is applied to the physical system. The results of this paper support the results obtained by Guerrero and Hart [2] for the case of variable pressure drop at the boundaries.

V. CONCLUSIONS

Experimental data were obtained for flow excursion instability under low flow and low pressure for down flow conditions in an annular geometry. Flow excursion was the dominant instability mode for down flow conditions and density wave instability was not observed, in agreement with the predictions of Nair et al. [4].

For any single-phase heat transfer loop with parallel channels and downward flow orientation, the decrease of flow rate into the heated section (increase in Zuber number) will eventually bring the system closer towards the static instability domain. If the subsequent decrease in power (decay power as the case would be for nuclear reactor) is not adequate such that the Zuber number keeps on increasing, the system will become unstable and CHF is imminent.

The "First instability" reported by Guerrero and Hart [2] is in reality the flow excursion instability. The same trend of temperature and flow fluctuation was observed, in addition to the real transient from low quality to high quality state, i.e., flow excursion.

The transient is more violent for higher inlet restriction in down flow, with accompanying elevated heater surface temperature. CHF was not recorded at all for the case of zero inlet restriction, even at very low subcooling, whereas CHF was reached very quickly following flow excursion in the case of high inlet restriction (K_i = 22), for average to low subcooling.

Subcooled boiling is important in down flow instabilities, as can be seen from figure 6. The instability boundaries were shown to lie at the region of negative quality for both cases of inlet flow restriction. Inada and Yasuo [6] showed that subcooled boiling is also important in up flow. In fact, their data show that the unstable excursive transition from low-quality state to high-quality state occurs in the negative exit quality region.

It is further needed to quantify the instability boundaries with changes in exit restriction. An accurate modeling of the instabilities in down flow is needed in order to assess the region of instabilities. Any analytical model that attempts to predict the onset of flow excursion instability in low flow, low pressure, and down flow system needs to account for the effect of thermal non-equilibrium. The analytical models of Rohatgi and Duffey [3] and Nair et al. [4] do not account for the effect of thermal non-equilibrium.

NOMENCLATURE

A_c	Test section flow area (m^2)
i_{fg}	Latent heat of vaporization (J/kg)
$K_e = \frac{\Delta P_e}{\rho_f v_{in}^2}$	Exit flow restriction
$K_i = \frac{\Delta P_i}{\rho_f v_{in}^2}$	Inlet flow restriction
l	Heated length (m)
$N_{sub} = \frac{\Delta i_{sub}}{i_{fg}} \cdot \frac{\Delta \rho}{\rho_g}$	Subcooling number
$N_Z = \frac{q''_w \xi \, l}{A_c v_{in} i_{fg}} \cdot \frac{\Delta \rho}{\rho_g \rho_f}$	Zuber (phase change) number
q	Heater power (W)
q''_w	Wall heat flux (W/m^2)
v_{in}	Inlet velocity into the test section (m/s)
Δi_{sub}	Inlet subcooling (J/kg)
Δp_i	Inlet plenum pressure drop (Pa)
Δp_e	Exit plenum pressure drop (Pa)
$\Delta \rho = \rho_f - \rho_g$	Density difference (kg/m^3)
ρ_f	Liquid density (kg/m^3)
ρ_g	Vapor density (kg/m^3)
ξ	Heated perimeter (m)

REFERENCES

[1]. G.C. Rush, J.E. Blake, R.M. Privette, and C.A. Nash, "Flow Excursion Experiments with a Savannah River Mark 22 Fuel Assembly Mockup", WSRC-OS-90-66, February 1990.

[2]. H.N. Guerrero and C.M. Hart, "Flow Instability and Flow Reversal in Heated Annular Multichannels with Initial Downward Flow", AIChE Symposium Series, 295, vol. 89, pp. 98-104, 1993.

[3]. U.S. Rohatgi and R.B. Duffey, "Natural Circulation and Stability Limits in Advanced Plants: The Galilean Law", Proc. Int'l Conf. on New Trends in Nuclear System Thermohydraulics, vol. 1 "Primary and Secondary Thermohydraulics", May 30th-June 2nd, 1994-Pisa, Italy, pp. 177-185.

[4]. S. Nair, S. Lele, M. Ishii, and S.T. Revankar, "Analysis of Flow Instabilities and Their Role on Critical Heat Flux for Two-Phase Down Flow and Low Pressure Systems", Submitted for publication in the International Journal of Heat and Mass Transfer.

[5]. M. Ishii, S.T. Revankar, I. Babelli, and S. Lele, "Hydrodynamically Induced Dryout and Post-Dryout Important to Heavy Water Reactors - A Yearly Progress Report," Purdue University, School of Nuclear Engineering Report, PU NE-92/2.

[6]. F. Inada and Y. Yasuo, "The Boiling Flow Instability of Natural Circulation BWR with Chimney at Low Pressure Start-up," International Conference on Design and Safety of Advanced Nuclear Power Plants, Tokyo, Japan, October 25-29, 1992.

Table 1 Listing of experimental data

Run	Vin	σ	Tin	σ	q	Nsub	Nz	Inlet restri
#.	m/s	m/s	C	C	W			Ki
1	0.40	0.03	19.58	0.21	3549.00	39.91	38.97	0.00
2	0.36	0.03	7.76	0.26	3528.00	53.59	43.31	0.00
3	0.39	0.03	7.10	0.18	3570.00	54.34	41.06	0.00
4	0.60	0.04	29.29	0.82	2610.00	25.89	19.70	0.00
5	0.69	0.04	37.13	0.18	1875.00	15.42	12.61	0.00
6	0.62	0.03	23.83	0.26	3200.00	34.23	23.51	0.00
7	0.59	0.04	17.49	0.23	4255.00	39.81	32.64	0.00
8	0.50	0.04	16.87	0.28	3528.00	40.89	31.95	0.00
9	0.43	0.03	29.39	0.32	2346.00	24.98	24.76	0.00
10	0.37	0.03	0.65	0.25	4232.00	62.03	50.47	0.00
11	0.39	0.03	5.38	0.28	3652.00	55.71	41.59	0.00
12	0.40	0.04	26.92	0.47	2048.00	26.82	22.88	0.00
13	0.29	0.04	8.06	0.23	2946.90	53.71	44.43	0.00
14	0.31	0.04	12.80	0.44	2655.00	47.52	38.01	0.00
15	0.26	0.03	14.74	0.20	2453.14	44.66	40.62	0.00
16	0.29	0.03	5.28	0.24	3037.65	55.98	45.70	0.00
17	0.28	0.03	8.30	0.27	2804.60	51.82	44.86	0.00
18	0.27	0.03	11.29	0.29	2649.60	47.69	43.77	0.00
19	0.26	0.03	13.17	0.26	2523.50	45.06	40.46	0.00
20	0.28	0.03	14.34	0.26	2449.50	43.50	38.15	0.00
21	0.39	0.03	9.51	0.30	3764.65	51.12	42.80	0.00
22	0.37	0.04	24.09	0.26	2306.50	33.23	26.96	0.00
23	0.34	0.05	25.98	0.29	2182.40	30.71	28.11	0.00
24	0.33	0.03	27.44	0.27	2105.60	28.76	27.83	0.00
25	0.37	0.04	29.90	0.40	1855.50	25.61	22.28	0.00
26	0.44	0.04	30.48	0.49	1855.50	24.83	19.08	0.00
27	0.43	0.03	31.94	0.92	1786.30	23.00	19.11	0.00
28	0.57	0.04	34.14	0.42	2244.00	19.95	17.92	0.00
29	0.60	0.03	36.40	0.40	2050.84	16.93	15.42	0.00
30	0.62	0.04	38.50	0.55	1842.00	14.13	13.66	0.00
31	0.63	0.04	39.70	0.38	1741.45	12.52	12.73	0.00
32	0.61	0.04	40.68	0.32	1667.10	11.21	12.55	0.00
33	0.61	0.04	41.01	0.22	1648.30	10.91	12.59	0.00
34	0.30	0.02	11.02	0.26	2804.60	49.49	41.06	0.00
35	0.66	0.05	42.17	0.21	1250.73	9.23	10.33	0.00
36	0.69	0.04	43.50	0.25	1177.20	7.68	9.30	0.00
37	0.67	0.05	44.87	0.32	977.90	5.87	7.95	0.00
38	0.59	0.05	38.96	0.39	2108.80	13.90	14.92	22.00
39	0.51	0.02	36.41	0.31	1974.70	17.30	15.88	22.00
40	0.58	0.04	15.29	0.28	3195.72	45.63	30.03	22.00
41	0.57	0.03	11.81	0.28	3582.60	50.41	34.26	22.00
42	0.57	0.04	11.57	0.37	3781.85	50.73	36.16	22.00
43	0.62	0.04	9.13	0.42	3960.00	53.99	34.81	22.00
44	0.59	0.03	17.24	0.35	2952.60	43.16	27.28	22.00
45	0.56	0.04	19.78	0.37	2629.80	39.77	25.59	22.00
46	0.55	0.04	23.00	0.79	2267.56	34.95	22.47	22.00
47	0.55	0.05	25.93	0.41	1984.00	31.16	19.66	22.00
48	0.46	0.04	27.84	0.38	1849.50	28.61	21.72	22.00
49	0.48	0.04	29.72	0.24	1684.35	26.23	19.13	22.00
50	0.50	0.04	31.09	0.21	1568.88	24.41	17.10	22.00

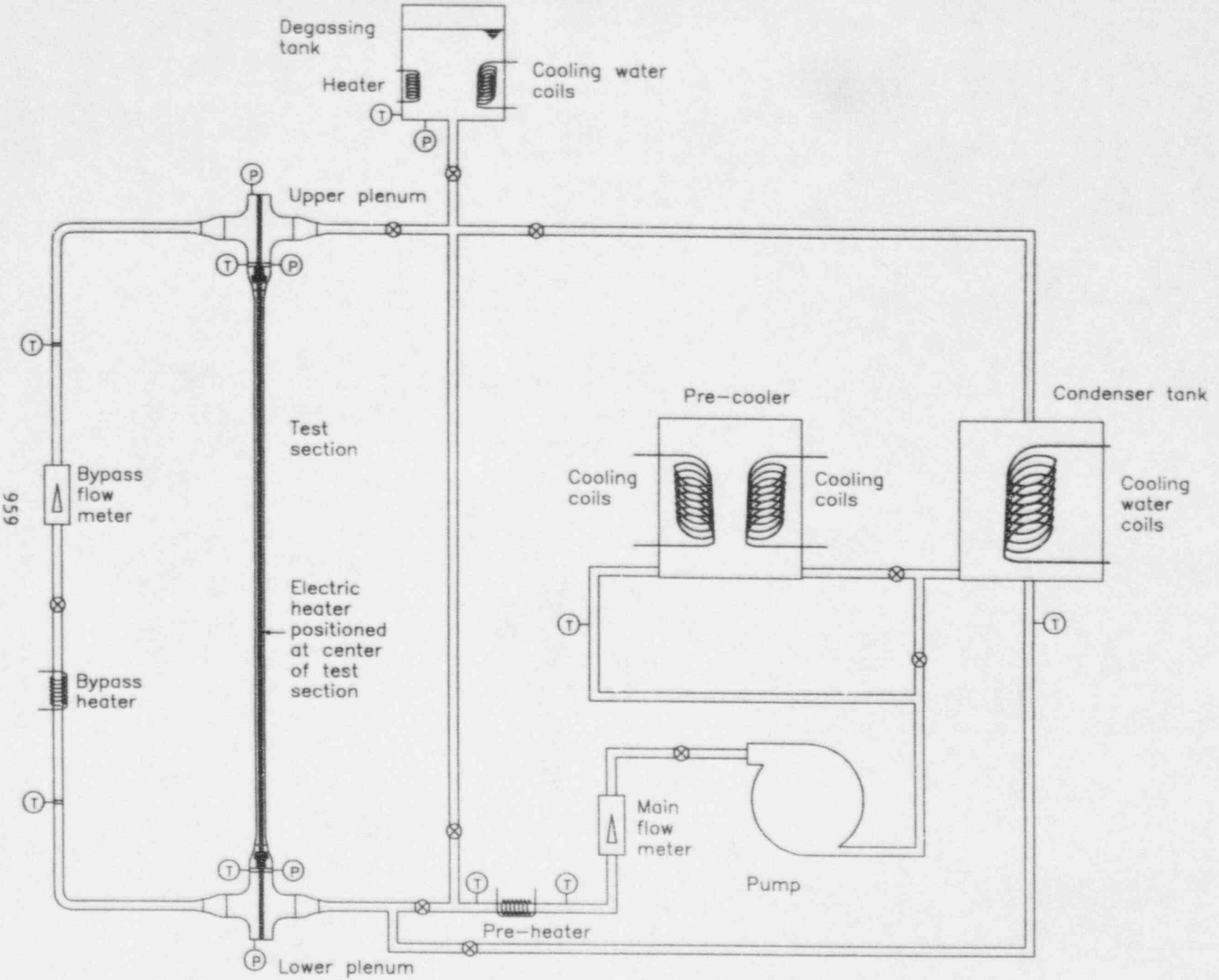

Figure 1. Schematic drawing of the test facility

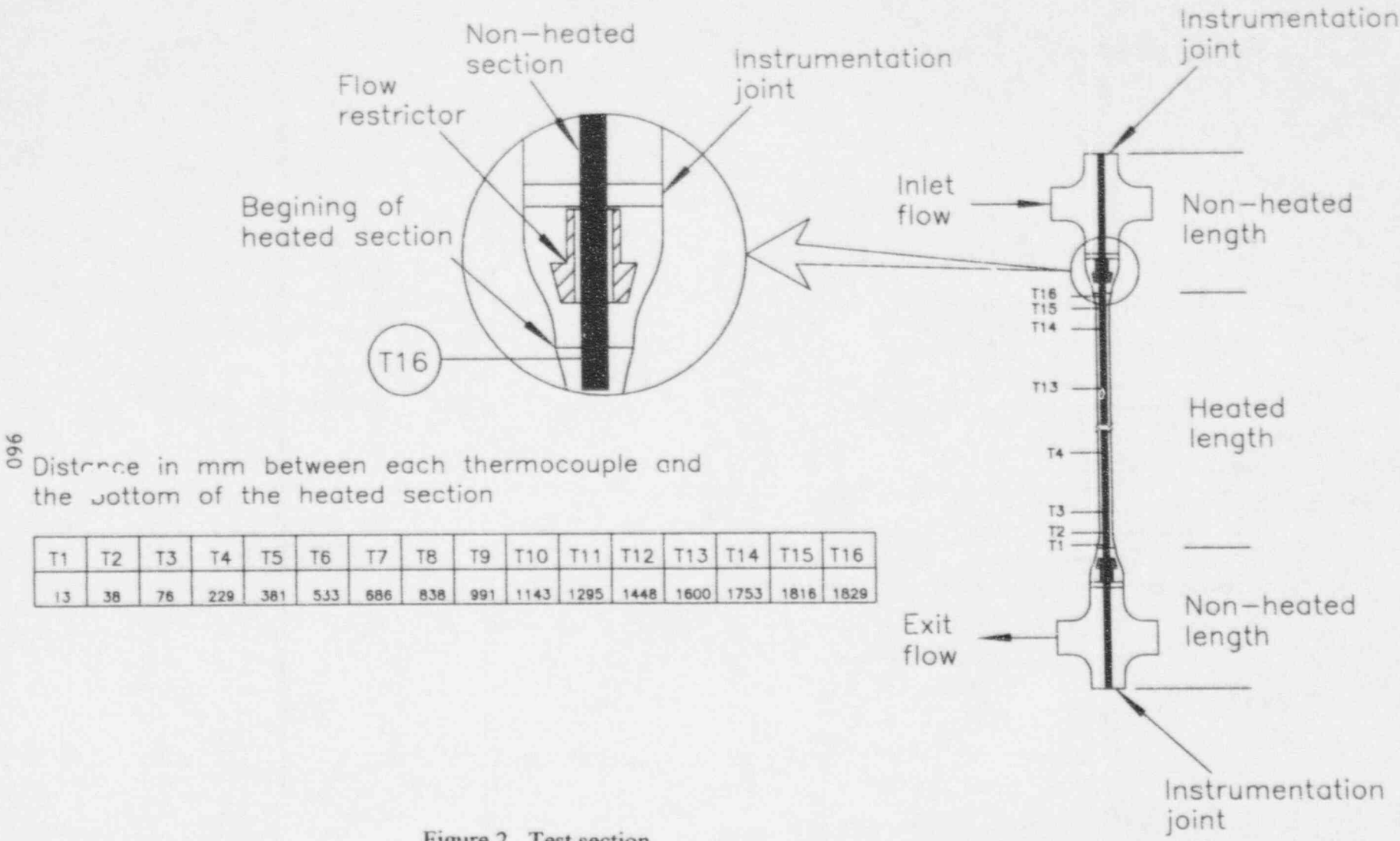

096

Distance in mm between each thermocouple and the bottom of the heated section

T1	T2	T3	T4	T5	T6	T7	T8	T9	T10	T11	T12	T13	T14	T15	T16
13	38	76	229	381	533	686	838	991	1143	1295	1448	1600	1753	1816	1829

Figure 2. Test section

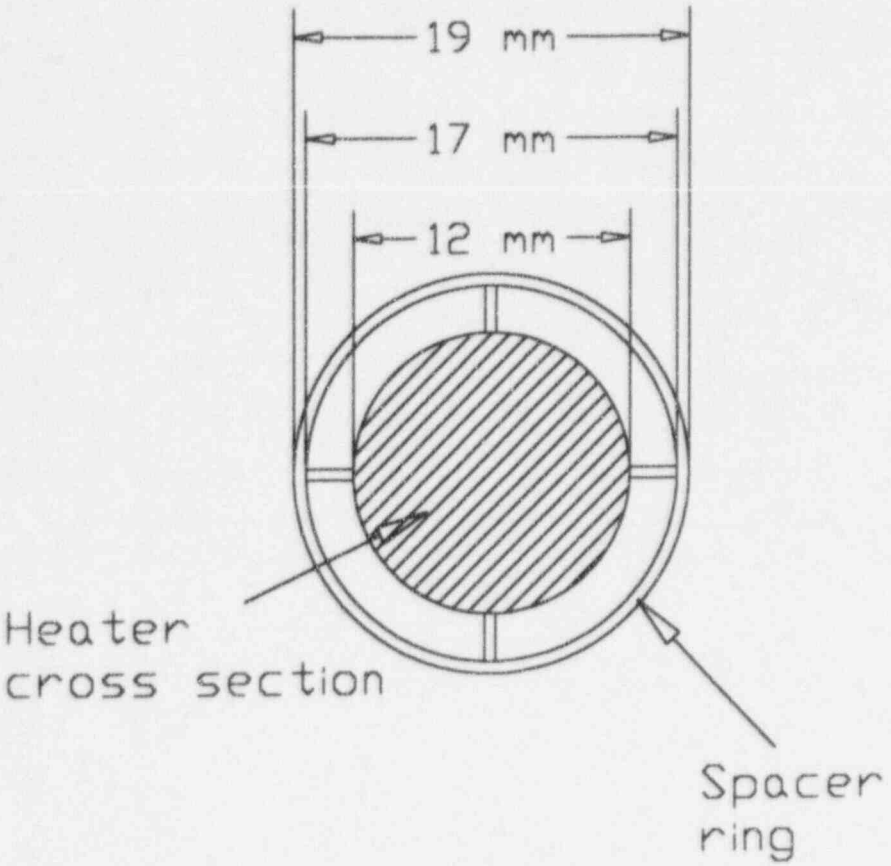

Figure 3 Schematic drawing of the spacer ring

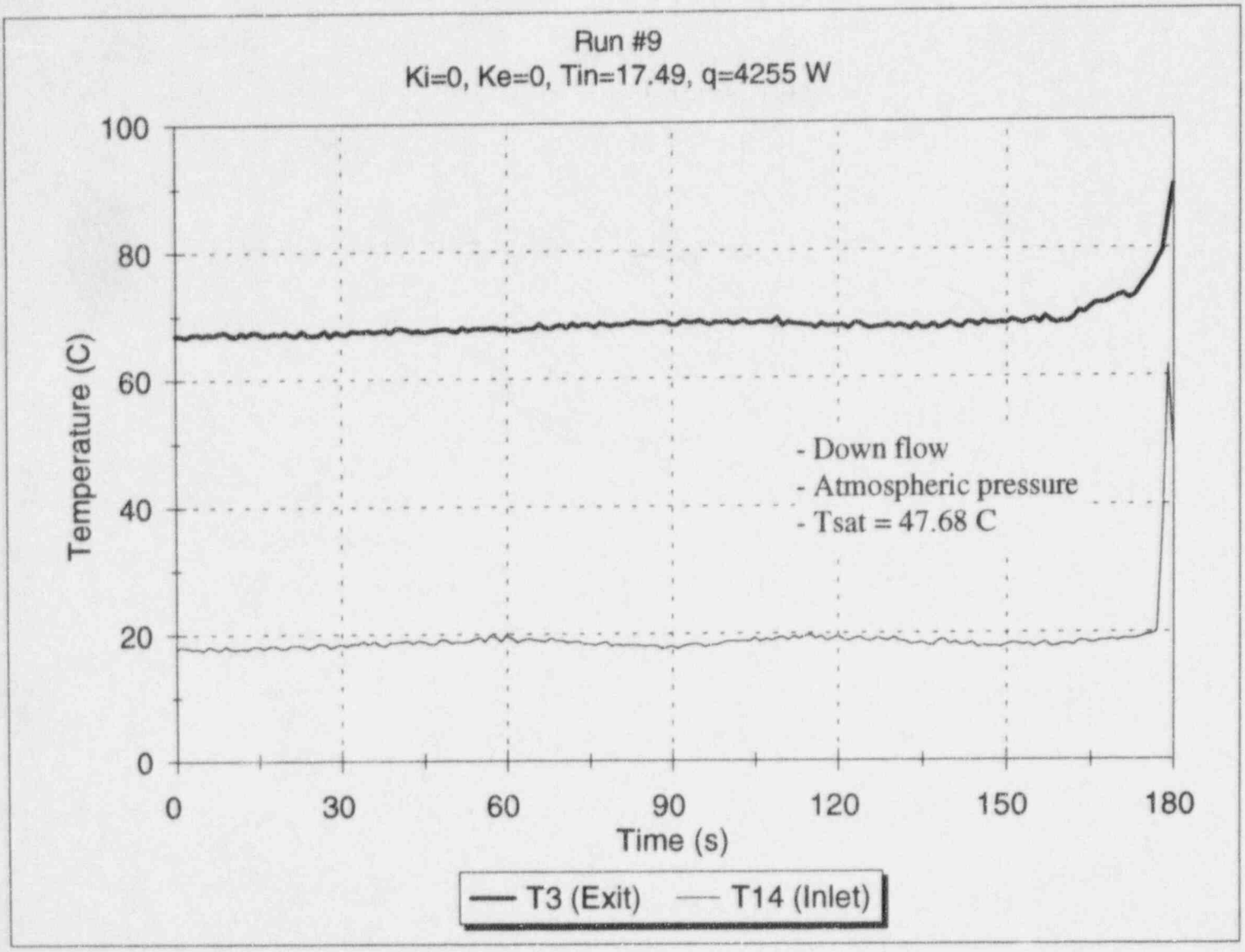

Figure 4.a Heater surface temperature at test section inlet and exit for Run # 9

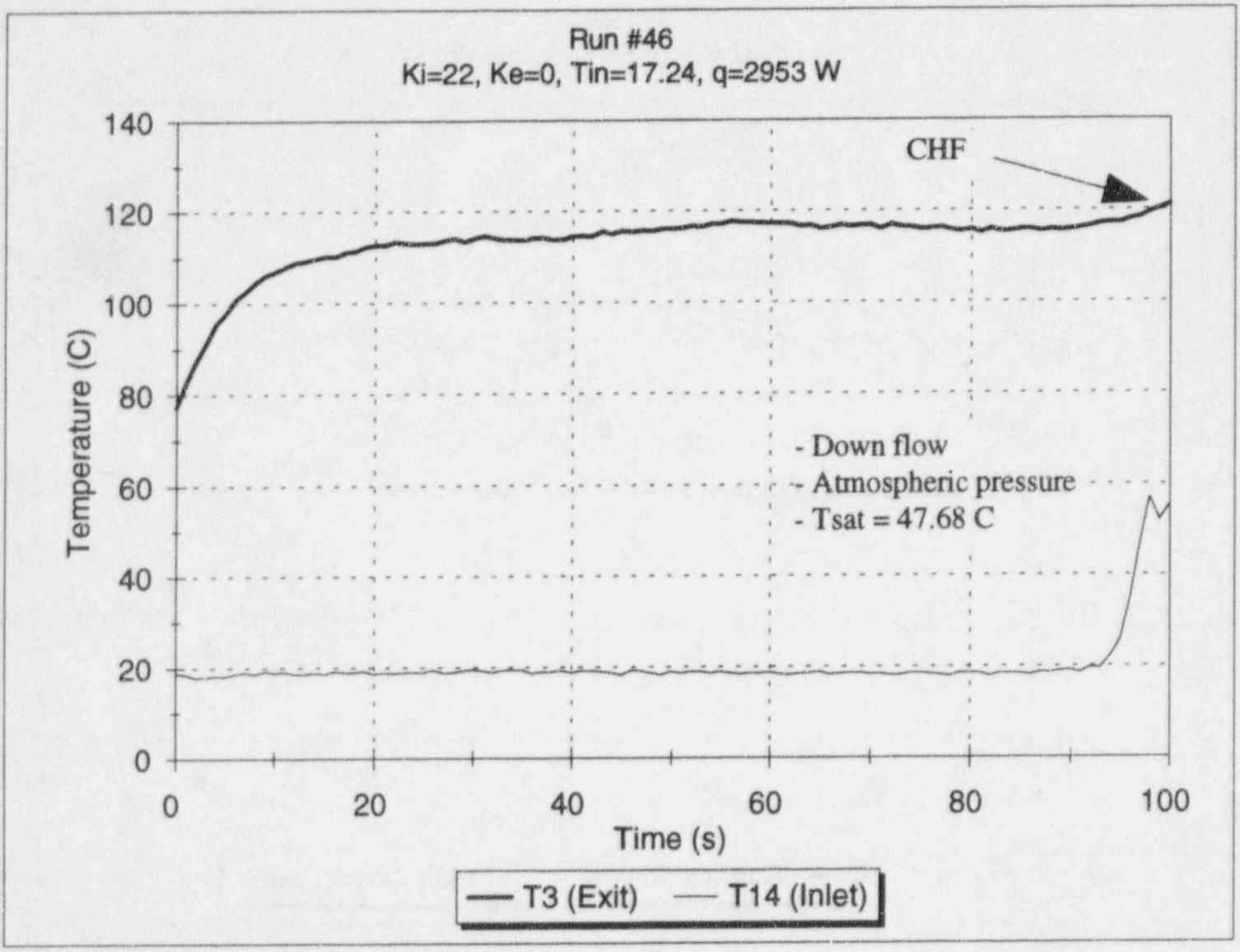

Figure 4.b Heater surface temperature at test section inlet and exit for Run # 46

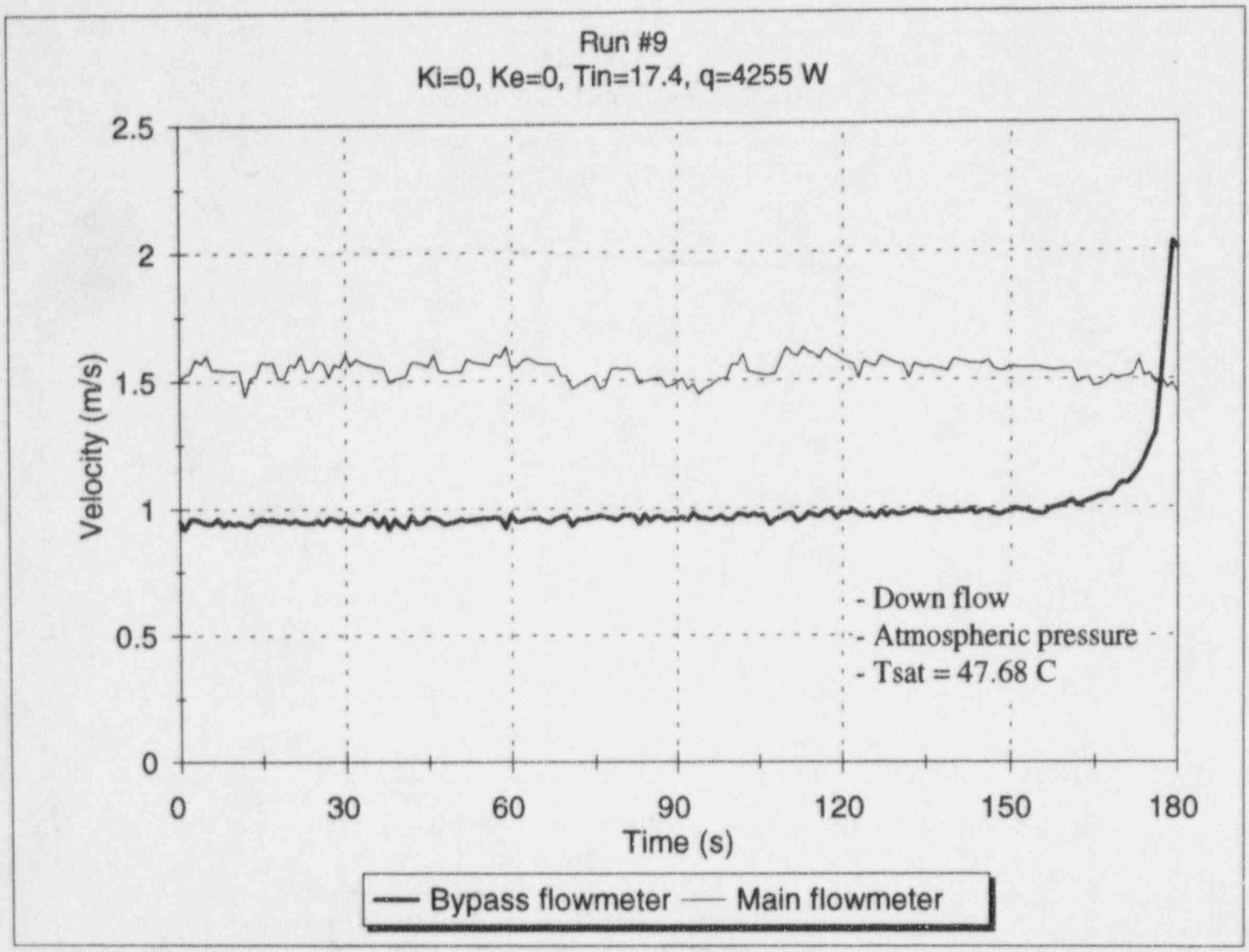

Figure 5.a Main and bypass velocities for Run # 9

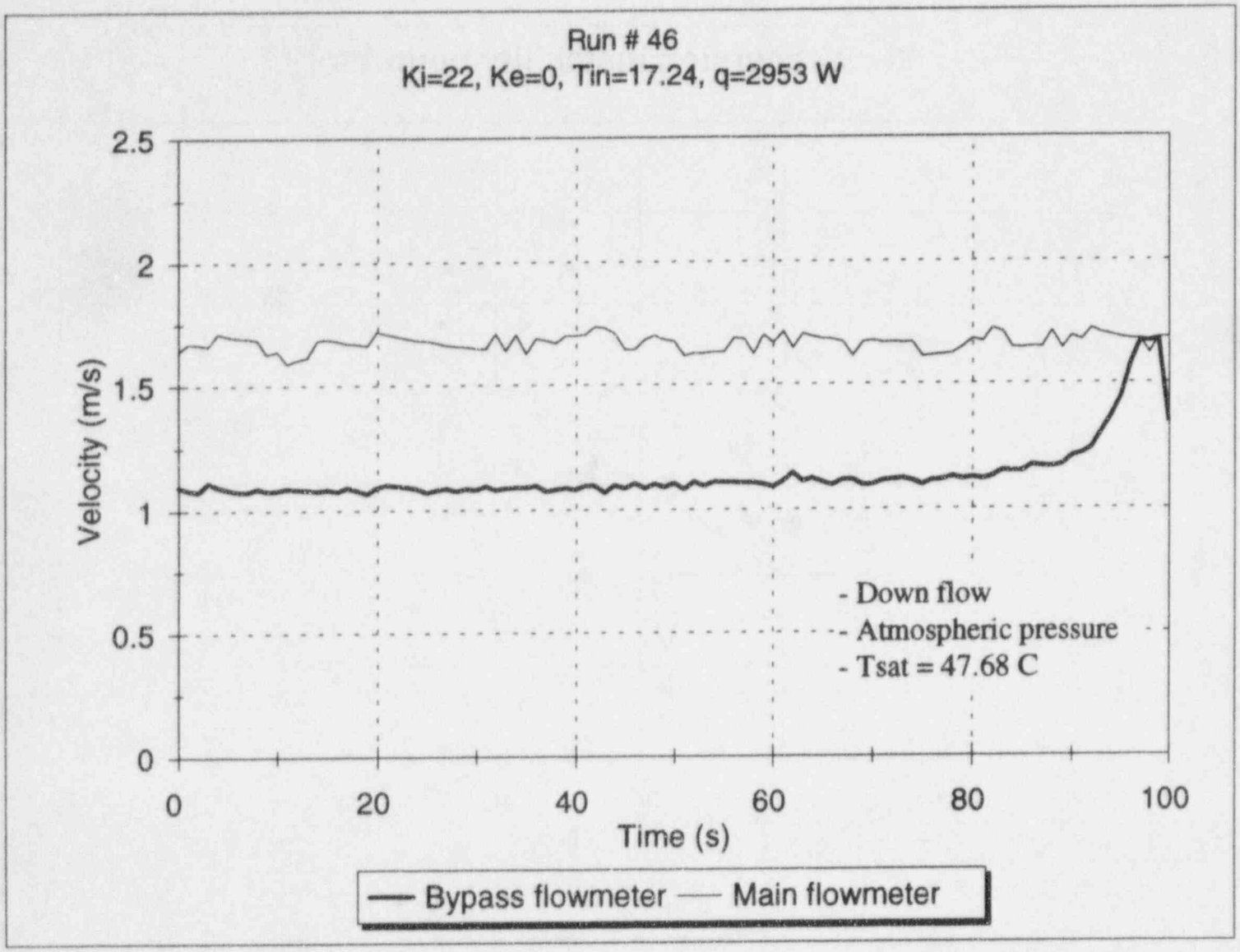

Figure 5.b Main and bypass flow velocities for Run # 9

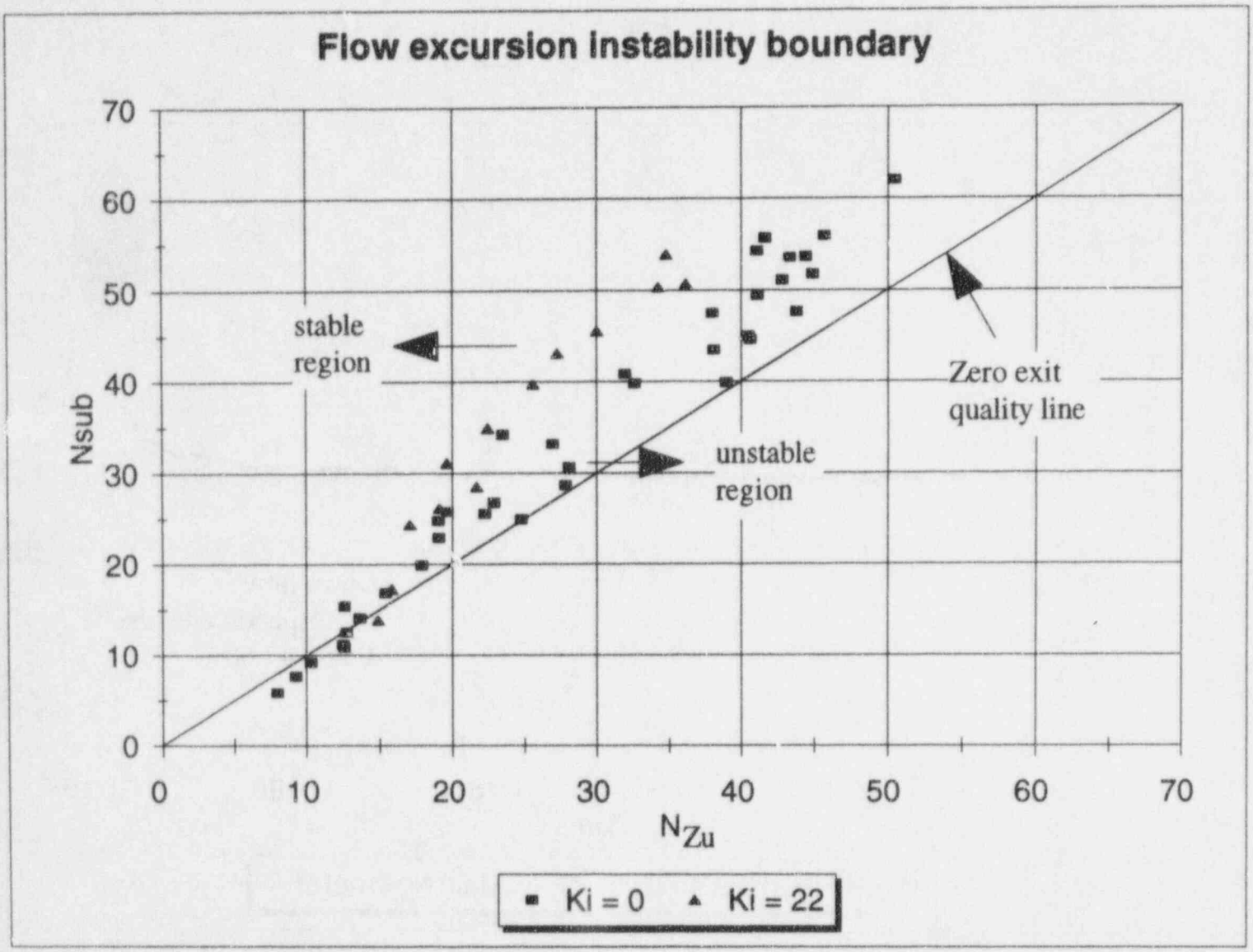

Figure 6 Flow excursion instability boundary

PROBLEMS IN EXPERIMENTAL AND MATHEMATICAL INVESTIGATIONS OF THE ACCIDENTAL THERMOHYDRAULIC PROCESSES IN RBMK NUCLEAR REACTORS.

B.I.Nigmatulin and L.K.Tikhonenko. Research & Engineering Centre (EREC) for Nuclear Plants Safety, Electrogorsk, Moscow region 142530, Russian Federation.

V.N.Blinkov. Aviation Institute, Kharkov 310070, Ukraine.

A.J.Kramerov. Russian Research Centre Kurchatov Institute (RRC KI), Moscow 123182, Russian Federation.

ABSTRACT.

In this paper the thermalhydraulic scheme and peculiarities of the boiling water graphite-moderated channel-type reactor RBMK are presented and discussed shortly. The essential for RBMK transient regimes, accidental situations and accompanying thermalhydraulic phenomena and processes are formulated. These data are presented in the form of cross reference matrix (version 1) for system computer codes verification. The paper includes qualitative analysis of the computer codes and integral facilities which have been used or can be used for RBMK transients and accidents investigations. The stability margins for RBMK-1000 and RBMK-1500 are shown.

RBMK FEATURES DESCRIPTION.

Safe operation of RBMK reactors in Russia, Ukraine and Lithuania is now a big concern of the world scientific community.

Water-graphite channel type RBMK nuclear reactors use uranium di-oxyde (UO_2) as a nuclear fuel, light water as a coolant and graphite as a moderator. The cylindrical core presents 1693 vertical fuel channels passing through the assembly of the square graphite columns. Each channel contains two fuel 18-rod bundles in series. The simplified thermalhydraulic scheme of power unit with RBMK-1000 reactor is shown in fig.1. The coolant circuit consists of two loops, each of them supplies coolant to half of the parallel heated channels due to Main Circulation Pumps 6 which rise the pressure from 7,0 to 8,4 MPa and delivers a total mass flow rate of 5200 Kg/s. The Pressure Header 11 distributes the coolant to twenty two Distributing Group

SCHEME OF POWER UNIT WITH RBMK-1000 REACTOR.

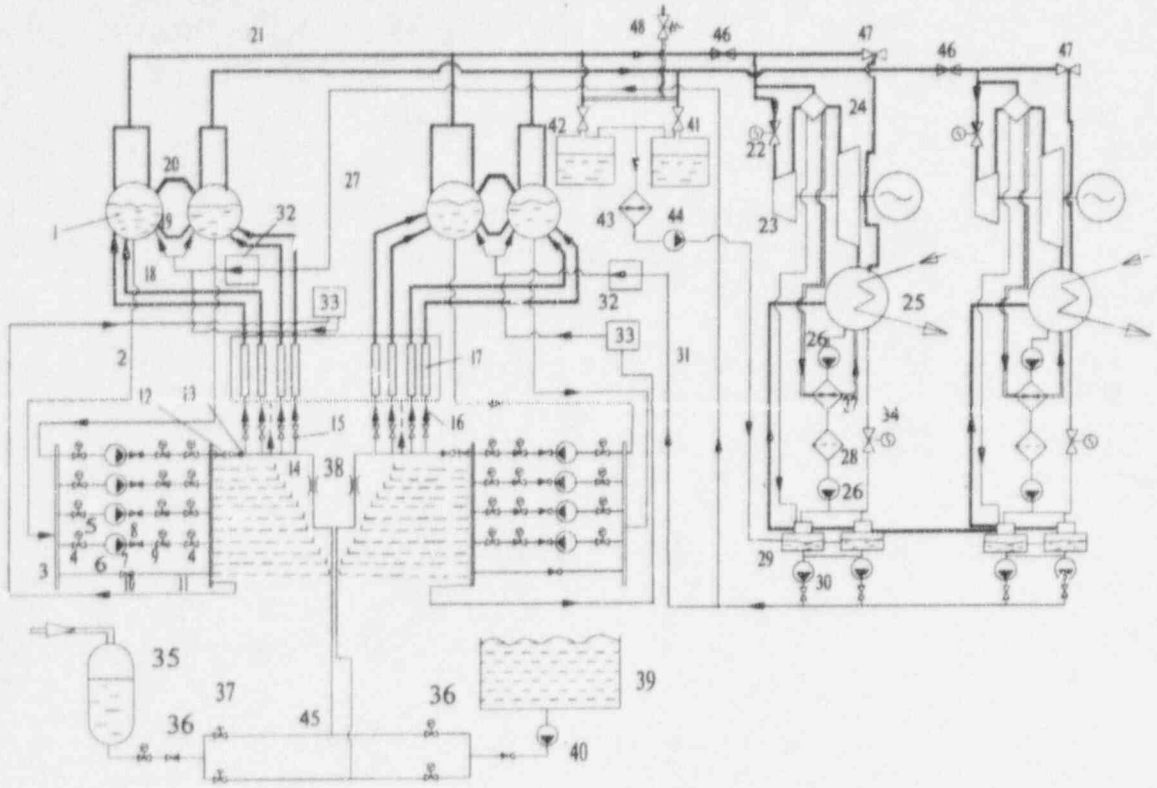

1-Drum-Separator (n=4); 2-Downward Pipe (ID=300 mm, n=48); 3-Suction Header (ID=900 mm, n=2); 4-Gate Valve (n=16); 5-Suction Line of Main Circulation Pump (ID=750 mm, n=8); 6-Main Circulation Pump (n=8); 7-Head Line of Main Circulation Pump (ID=750 mm, n=8); 8-Check Valve (n=8); 9-Throttle-Control Valve (n=8); 10-Bypass Line (ID=750 mm,n=2); 11-Pressure Header (ID=900 mm,n=2); 12-Flow-Rate Limiter (n=44); 13-Check Valve (n=44); 14-Distributing Group Header (ID=295 mm,n=44); 15-Multipurpose Valve (n=1693); 16-Low Water Communication (ID=50 mm,n=1693); 17-Fuel Channel (n=1693); 18-Vapour Water Communication (ID=70 mm,n=1693); 19-Water Equalizing Line (ID=300 mm, n=4); 20-Vapour Equalizing Line (ID=300 mm, n=4); 21-Turbine Steam Line (ID=600 mm,n=4); 22-Stop-Control Valve (n=4); 23-Turbine Set (n=2); 24-Separator-Superheater (n=4); 25-Turbine Condenser (n=2); 26-Condensate Pumps of the First and Second Rise (by five in parallel); 27-Low Pressure Heater (n=2); 28-Condensate Purification System; 29-Deaerator (n=4); 30-Feed Water Pump (n=5); 31-Feed Water Line (ID=372 mm,n=8); 32-Feed Water Flow Rate Control Unit (n=2); 33-Blowdown Water Purification and Cooling System; 34-Turbine Condenser Water Level Regulator; 35-Hydraulic Reservoir with Gas Pressurization (n=12),V_{Σ}=150 m^3); 36-Gate Valve (n=3); 37-Quick-Acting Valve (n=2); 38-Flow-Rate Limiter (n=2); 39-Water Storage Tank; 40-Pumps (n=8); 41-Dump Valve (n=4); 42-Bubbler (n=2); 43-Condenser (n=2); 44-Condensate Pump (n=2); 45-Emergency Cooling System Header (n=2); 46-Gate Valve (n=4); 47-Quick-acting Reducing Unit (n=4); 48-Main Safety Valve (n=8); 35...40,45 - Reactor Emergency Cooling System.

Fig. 1

Headers 14 and each of them distributes the coolant to about thirty eight fuel channels through Low Water Communications 16, each one is equipped at the inlet with Multipurpose Valve 15. The coolant in the fuel channels is partially vaporized (quality is up to 0,25) and arrives at two Drum Separators 1 through Vapour Water Communications 18. In each Drum Separator saturated water (7,0 MPa, 284 C) is mixed with the feed water (165°C) and flows back to the Suction Header 3 through twelve Downward Pipes 2. From the top of each Drum Separator the saturated steam flows through fourteen Turbine Steam Lines 21 to the Turbines 23.

Water-graphite channel type RBMK nuclear reactors possess the features of working process and design which may be essential and should be taken into account in conducting the experimental and mathematical modeling of transient regimes and accidental situations. The main features are the following:

1. Branching parallel channels configuration of circulation circuit. Such a geometry may cause development of oscillatory parallel-channel flow boiling instability.

2. Positive coolant void and temperature reactivity coefficients stimulate an instability in the neutron field and complicate control of the reactor.

3. High vapor quality at the heated channels exit (up to x = 0,25). This leads to heat power limitations due to critical heat flux danger.

4. High thermal capacitance of the heated zone structure due to graphite mass.

5. Limitations on acceptable temperatures of the fuel element zirconium wall (350°C), graphite (750°C) and (UO_2) fuel rods (2800°C).

6. Positive feed back $\delta Q \rightarrow \delta x \rightarrow \delta \Delta P_f \rightarrow \delta m \rightarrow \delta x \rightarrow \delta Q$ due to monotonic "pressure drop - flow rate" heated channel curve and positive feed back "boiling water void fraction - heat generation" $\alpha \rightarrow Q$ ($x \rightarrow Q$).

7. Limitations on separation process quality: liquid entrainment to Steam Lines limitations because of danger of vapor radioactivity increase by isotopes dissolved in the water; vapor entrainment to Downward Pipes limitations because of necessity to maintain positive suction head in the Main Circulation Pumps.

8. Considerable number of non-standard valves and automatic controllers requiring adequate mathematical description.

VERIFICATION MATRIX DESCRIPTION.

In spite of the fact that the construction of new RBMK NPP units is not projected at the present time, units are already built and in operation in Russia, Ukraine and Lithuania. Evidently, these will be in operation till the end of their service life. The main problem during this period is to improve the RBMK safety to a level comparable with that of WWER's and PWR's. This safety level is evaluated on the basis of system thermalhydraulic codes calculations. There is no such code for the RBMK and the problem of its elaboration should be accepted as a important one. Elaboration and verification of RBMK code (or codes) should be carried out on the basis of a verification matrix, which defines the list of essential RBMK transient regimes, emergency situations, accompanying thermalhydraulic phenomena, available experimental fasilities and data.

The verification matrix proposed in this paper accounts for the peculiarities of the RBMK reactor and contains three cross reference blocks:

- phenomenon versus test type. This part of the matrix contains the lists of the 16 steady, transient and emergency regimes and 31 of the most important thermalhydraulic phenomena;

- test type versus test facility. This part of matrix presents information about existing and projected integral facilities for the experimental modeling of the transients and accidents which are outlined in the matrix;

- phenomenon versus test facility. This part of matrix identifies the test facilities which are appropriate for specific phenomenon experimental reproduction.

At present there are three RBMK type experimental stands in Russia: facility №.108 (EREC), facility KS (RRC KI), facility BM (Research and Development Institute for Power Engineering ENTEK). These stands represent models of the fuel channels parallel assembly (17, fig.1) made with vertical scale violation and approximate pressure loss profile reproduction. The volume-power scale of the stands are $S = \frac{Q_m}{Q_p} = \frac{V_m}{V_p} \approx \frac{1}{1700} \dots \frac{1}{7200}$. The stands are not exactly similar to RBMK reactor from the stand point of components, configuration and scheme. They are able to adequately reproduce a limited number of the regimes and phenomena essential for RBMK.

Unlike the above-mentioned facilities design work for the integral stands ISB (EREC) and PSB (EREC) [1] was based on criteria proved for PWR, BWR, WWER concept: full height scale, nominal thermodynamic parameters of the coolant, the same volume-power scale for all components. The ISB and PSB stands are similar to RBMK reactor from standpoint of components, configuration and scheme, they are designed for adequate modeling of

CROSS REFERENCE MATRIX FOR TRANSIENTS AND ACCIDENTS OF RBMK
(Version 1)

Phenomenon/test type

- ● occuring
- ◑ partially occuring
- ○ not occuring

Integral facility/test type

- ● performed, complete data
- ◑ performed, data are not complete
- ◕ not performed, but ***can*** be performed
- ○ not performed

Integral facility/phenomenon

- ● data avialable and sufficient for code verification
- ◑ data available but not sufficient
- ◕ data not available but ***can*** be obtained on corresponding facility
- ○ data not available and can not be obtained on corresponding facility

		Test Type																Integral facilites					
		Steady & quasisteady tests	On-line refuelling	Local power increase	Power "jump"	Pressure "jump"	Loop flowrate "jump"	Loss of feedwater	Loss of Fuel Channel flowrate	Pressure Header break	Distributing Group Header break	Low Water Communication break	Fuel Channel break	Vapor-Water Communication break	Downward Pipe break	Steam line break	Feedwater line break	ISB (EREC)	PSB (EREC)	108 (EREC)	KS (RRC KI)	BM (ENTEK)	NPP
Thermalhydraulic phenomenon	3D effects & thermohydraulic-nuclear feedback	◑	●	●	●	●	●	●	●	●	●	●	●	●	●	●	●	○	○	○	○	○	◕
	Special valves operation	○	○	○	○	○	○	○	○	●	●	○	○	○	●	◑	●	○	○	○	○	○	◕
	Power, water level, pressure controllers operation	○	●	●	●	●	●	●	●	◑	●	●	●	●	●	●	●	○	○	○	○	○	◕
	Oscillatory instability in parallel channels	●	◑	◑	◑	◑	◑	◑	◑	◑	◑	◑	◑	○	◑	○	○	◕	◕	●	○	◑	○
	Critical flow through break	○	○	○	○	○	○	○	●	●	●	●	●	●	●	●	●	◕	◕	◑	○	○	○
	Drum-separator (DS) level dynamics	○	○	◑	●	●	●	●	◑	●	●	●	●	●	●	●	●	◕	◕	○	○	○	◑
	Flashing & condensation in DS	○	○	○	●	●	●	●	○	●	●	●	○	○	○	●	●	◕	◕	○	○	○	◑
	Separation & water entrainment out of DS	●	○	○	●	●	●	●	○	●	●	●	○	○	○	●	○	◕	◕	○	○	○	◑
	Steam entrainment to Downward Pipe	●	○	○	●	●	●	●	○	●	●	●	○	○	●	●	●	◕	◕	○	○	○	◑
	Void fraction/slip	●	●	◑	●	●	●	●	○	●	●	●	●	●	●	●	●	◕	◕	○	○	○	○
	Counter current flow	○	○	○	○	○	○	◑	○	●	●	●	◑	◑	◑	○	○	◕	◕	◑	○	○	○
	Stratification in horizontal flow	○	○	○	○	○	○	◑	○	○	●	●	◑	◑	◑	○	●	◕	◕	○	○	○	○
	Phase accumulation & ejection	○	○	○	○	○	○	◑	○	○	●	●	◑	◑	◑	○	○	◕	◕	◑	○	○	○
	Separation in Tees	○	○	○	○	○	○	◑	○	○	●	●	◑	◑	◑	○	●	◕	◕	○	○	○	○
	Natural circulation	●	○	○	○	○	○	◑	○	○	●	●	◑	◑	◑	○	●	◕	◕	◑	◑	◑	○
	Circulation stagnation in Fuel Channels	○	○	○	○	○	○	◑	○	○	●	●	○	○	○	○	○	◕	◕	◑	◑	○	○
	Mixture level formation & moving in Fuel Channels	○	○	○	○	○	○	◑	●	●	●	●	○	○	○	○	○	◕	◕	◑	◑	○	○
	Core subcritical heat transfer	●	●	●	●	●	●	●	●	●	●	●	●	●	●	●	●	◕	◕	◑	◑	◑	●
	Critical heat flux	○	○	◑	◑	○	◑	◑	●	●	●	●	●	●	●	○	○	◕	◕	◑	●	◑	○
	Core supercritical heat transfer	○	○	○	○	○	○	○	●	●	●	●	●	●	●	○	○	◕	◕	◑	○	◑	○
	Quench front formation & propagation	○	○	○	○	○	○	○	○	●	●	●	○	○	○	○	○	◕	◕	◑	●	○	○
	Radiation heat transfer	○	○	○	○	○	○	◑	●	●	●	●	●	●	●	○	○	○	○	○	○	○	○
	Heat exchange between damaged Fuel Channel & graphite	○	○	○	○	○	○	◑	●	●	●	●	●	●	●	○	○	○	○	○	○	○	○
	Emergency Core Cooling System water distribution to Fuel Channels	○	○	○	○	○	○	○	○	●	●	●	○	○	●	●	◑	◕	◕	◑	◑	○	○
	Flow oscillations & water redistribution between parallel Fuel Channels	○	○	○	○	○	○	◑	○	●	●	●	◑	◑	◑	○	◑	◕	◕	◑	◑	◑	○
	Pressure growth in Reactor space	○	○	○	○	○	○	◑	◕	◕	●	●	●	●	●	○	○	○	○	○	○	○	◑
	Pressure growth in Circuit space	○	○	○	○	○	○	○	○	●	●	●	○	●	●	●	●	○	○	○	○	○	○
	Thermal inertia of solid structures	○	○	○	○	○	○	◑	●	●	●	●	●	●	●	●	●	◕	◕	○	○	○	○
	Zirconium-steam reaction	○	○	○	○	○	○	◑	●	●	●	●	●	●	●	○	○	○	○	○	○	○	○
	2-phase pump behaviour	○	○	○	○	○	○	◑	○	●	●	●	○	○	○	○	○	○	○	○	○	○	○
	Noncondensible gas effects	◑	○	○	○	○	○	○	●	●	●	●	●	●	●	○	○	◕	◕	○	○	○	○
Integral facility	NPP	◑	◑	◕	◕	◕	◕	◕	◑	○	○	○	◑	○	○	○	○						
	108 (EREC)	◑	◕	○	◑	◑	◕	◕	○	◑	◑	◑	○	◕	○	◕	○						
	ISB (EREC)	◕	○	○	◕	◕	◕	◕	◕	◕	◕	◕	○	◕	◕	◕	◕						
	PSB (EREC)	◕	○	○	◕	◕	◕	◕	◕	◕	◕	◕	○	◕	◕	◕	◕						
	KS (RRC KI)	◑	○	○	◕	◕	◑	○	○	○	○	○	○	○	○	○	○						
	BM (ENTEK)	◑	○	○	○	◑	◑	○	○	○	○	○	○	○	○	○	○						

most thermalhydraulic phenomena enumerated in the matrix, and they are able to reproduce thirteen of a sixteen transient and accident regimes. The most adequate to the reactor-prototype is the integral stand PSB-RBMK equipped with standard Low Water Communications and Vapour Water Communications, two full-scale Fuel Channel models and standard Graphite Blocks. We suppose that construction and operation of the PSB - RBMK stand will allow the resolution of most of the local and system problems in RBMK transient thermalhydraulics.

As for the widely known Western computer codes, most of them are accessible at present in Russia and Ukraine, some of them are adapted and are being used in various institutes and laboratories. The mathematical models of those computer codes have a determined structure: they all are based on some form of mass, momentum and energy conservation equations. The modular structure and basic modules of the codes are similar and include thermalhydraulics of the coolant, power generation in nuclear fuel rod, heat transfer between solid structures and the fluid, thermophysical properties of the coolant, control systems and numerical methods. The major components models and sets of constitutive correlations are also similar. All the khown Western codes (TRAC, RETRAN, RELAP, CATHARE, ATHLET etc.) have been developed for simulation of thermal hydraulic behaviour during accidents and transients in vessel type reactors PWR and BWR. Noticeable differences between the mentioned codes can be revealed in flow models (from O-D in ATHLET to 3-D in the TRAC core model), in the level of interphase nonequilibrium (from homogeneous equilibrium to two-fluid), in some features of components models and in numerical methods. In application of the Western codes to RBMK analysis the distinction in results can be expected the such degree as the mentioned differences in mathematical models are essential in specific RBMK thermalhydraulic regimes.

The preliminary opinion of the authors of this paper is that code ATHLET [2] to a certain degree is able to simulate specific thermalhydraulic phenomena in RBMK reactor. This opinion is based on the first results of comprehensive codes verification program directed to RBMK safety improvement, running independently in the various Russian and Ukrainian institutes and laboratories (these results are to be published by the end of 1995). At the same time it is obvious that for certification of ATHLET to RBMK NPP modification of the code is required.

In parallel with work on Western computer codes verification and adaptation it is necessary to collect the information and to learn the possibilities of the specialized (directed to specific phenomenon or group of phenomena) codes, developed basically in the countries of the former Soviet Union. The following part of the paper shows the example of application of one of such a computer program.

BOILING FLOW INSTABILITY IN RBMK FUEL CHANNELS.

Instability in parallel channels is an important and very specific for RBMK phenomenon. The authors developed and verified by means of comparisons with experiments simplified mathematical model and computer program for nonlinear simulation of oscillatory regimes in parallel heated channels. These results have already been published [3-5]. Here we will give only brief description of the model and of the results obtained:

- one-dimensional distributed parameters 1P2T1W hydrodynamic model of transient two-phase flow;

- implicit numerical method [D.R.Liles, 6];

- thermal submodel based on energy equation for the wall [R.Taleyarkhan, 7];

- single heated channel under $\Delta P = const$ boundary conditions typical for parallel channels;

- such a simple model elucidated the physical nature of oscillations (density waves) and demonstrated ability to predict adequately flow parameters oscillations and stability margins.

This specialized computer code has been applied to calculation of the sability boundaries of RBMK-1000 (Chernobyl, Kursk, Smolensk, St.Peterburgh) and RBMK-1500 (Ignalina) reactors. The major difference between those two power units is in thermal core power: 3200 MW for RBMK-1000 versus 4800 MW for RBMK-1500 (electiral power equals 1000 MW for RBMK-1000 versus 1500 MW for RBMK-1500). Another essential difference is that RBMK-1500 fuel channels are equipped with flow turbulence stimulators for heat transfer enhancement, which change channel longitudinal pressure drop profile. Fig.2 shows calculated stability boundaries for RBMK-1000 and RBMK-1500 fuel channels at open Mulipurpose Valves (15, fig.1). The oscillatory regimes calculations in the vicinity of the stability boundaries brought the following results (fig.2,3):

- thermalhydraulic stability margin for RBMK-1000 exceeds the one for RBMK-1500;

- in RBMK-1000 fuel channels boiling coolant oscillatory regimes in minimum flow rate phase, dryout and corresponding wall temperature growth may occur;

- in RBMK-1500 fuel channels flow rate oscillations do not lead to heat transfer rate lowering.

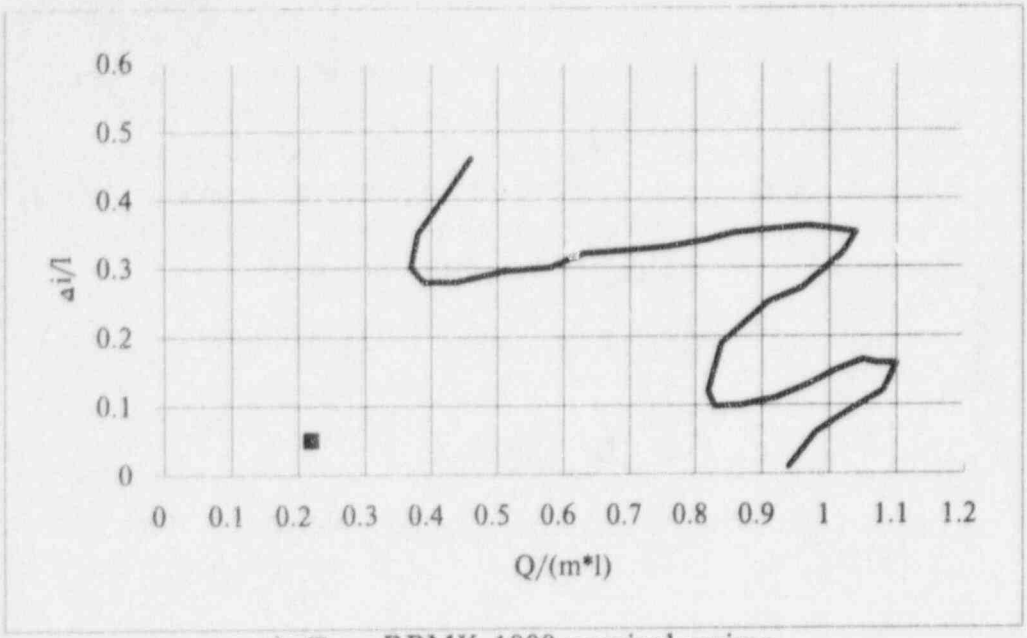

a) ■ - RBMK-1000 nominal regime

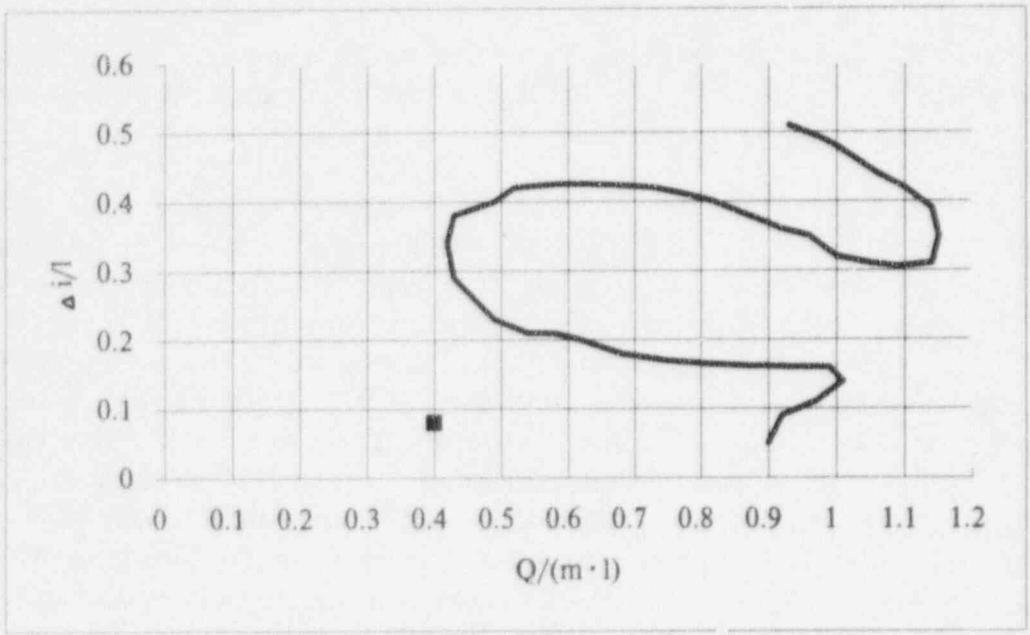

b) ■ - RBMK-1500 nominal regime

Fig. 2 Calculated stability margins for RBMK-1000 (a)
and RBMK-1500 (b) fuel channels.
Δi/l - dimensionless initial subcooling
Q/(m · l) - dimensionless heat load.

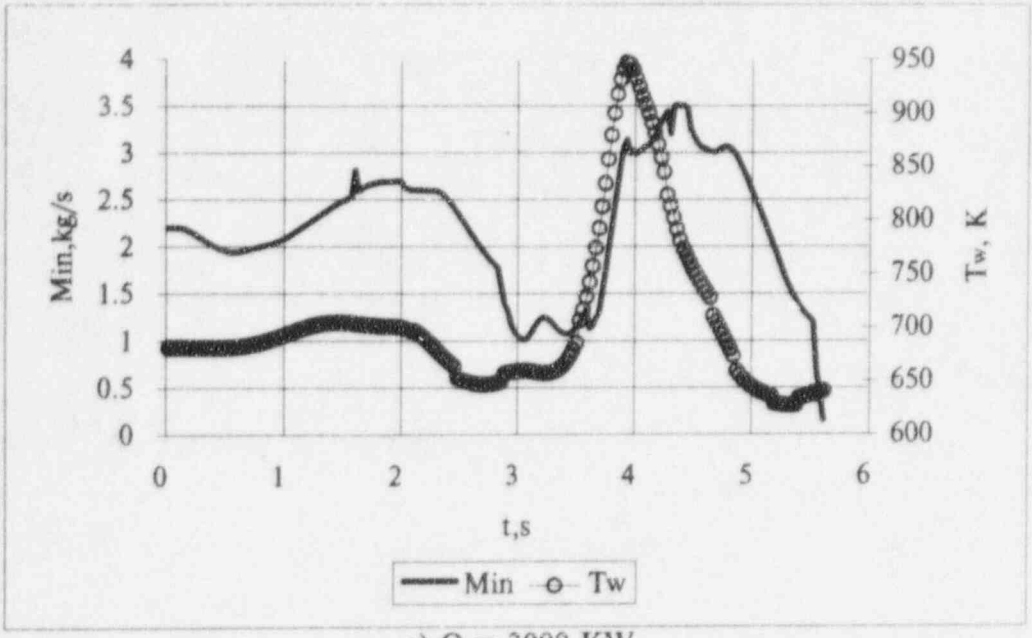

a) Q = 3000 KW

T_{in} = 503,15 K; P_{ex} = 6,9 MPa; P_{in} = 7,182 MPa; x_{ex} = 0,74 (steady).

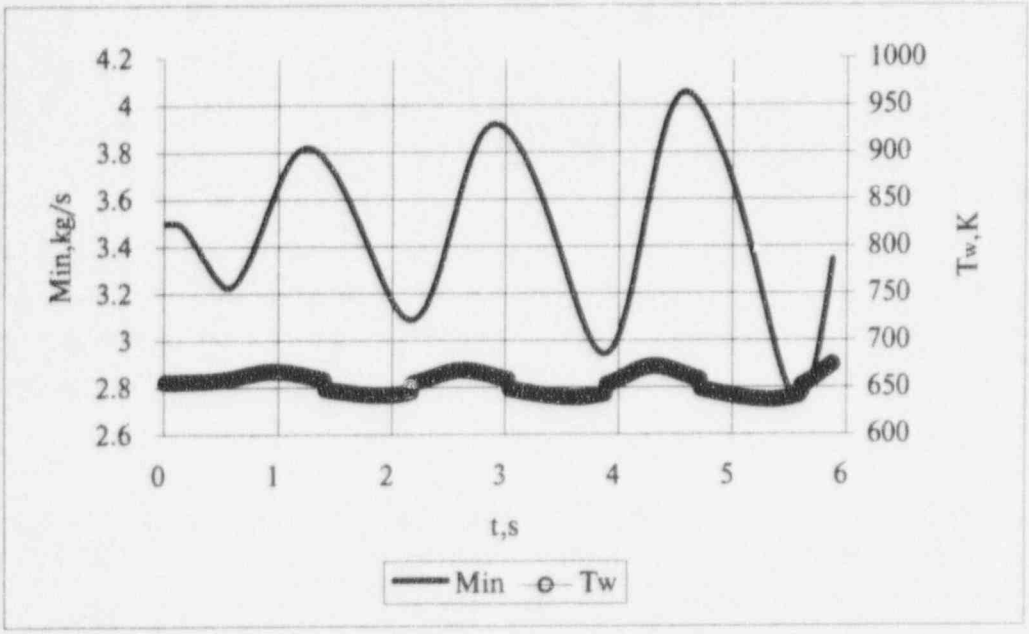

b) Q=4500 KW

T_{in} = 503,15 K; P_{ex} = 6,9 MPa; P_{in} = 7,678 MPa; x_{ex} = 0,7 (steady).

Fig.3. Flow rate and wall (at the fuel channel exit) temperature oscillations in the vicinity of stability boundary: a) RBMK-1000; b) RBMK-1500.

Consequently, operational parameters limitations for RBMK-1000 and RBMK-1500 are not identical from the viewpoint of boiling coolant stability providing and dryout avoiding.

CONCLUSIONS.

The paper first presents cross reference matrix (version 1) for system computer codes verification which takes into account the essential for RBMK boiling water graphite-moderated channel-type reactor thermalhydraulic peculiarities. Publishing of the matrix originates the comprehensive computer codes verification program directed to RBMK safety level improvement. The matrix proves the necessity of large scale integral stands ISB and PSB construction.

The paper demonstrates and comments stability margins for RBMK-1000 and RBMK-1500 power plants

NOMENCLATURE.

i - enthalpy, J/kg; l - latent heat of vaporization, J/kg; m - mass flow rate, kg/s; P - pressure, Pa; DP - friction pressure drop, Pa; Q - power of heat source, W; T - temperature, K; V - volume, m ; W - velocity, m/s; X - vapor quality; a - void fraction.

Subscripts.

in - inlet; ex - exit; w - wall; m - model; p - plant.

REFERENCES.

1. B.I.Nigmatulin. Modern methods of study of Nuclear Power Plants safety problem thermohydraulic aspects on large scale experimental stands. Teploenergetika № 8, 21-27 (1990).

2. DRUFAN-01/MOD2: Model description. GRS-A-846 (1983)

3. B.I.Nigmatulin, O.I.Melikhov, V.N.Blinkov, P.G.Gakal. The numerical analysis of boiling flow instability in parallel heated channels. Nuclear Engineering and Design № 139, 235-243 (1993).

4. B.I.Nigmatulin, V.N.Blinkov, O.I.Melikhov, P.G.Gakal. The numerical investigation of boiling flow instability in heated channels. Proceedings of an International Symposium on Instabilities in Multiphase Flows, Rouen, France, 89-100 (1992).

5. B.I.Nigmatulin, O.I.Melikhov, V.N.Blinkov, P.G.Gakal, N.A.Brus. The experimental and numerical analyses of boiling flow instability in parallel heated channels. Proceedings of an International Conference on New

Trends in Nuclear System Thermohydraulics, Pisa, Italy, 779-791, (1994).

6. D. R. Liles, Wh. M. Reed. A semi-implicit method for two-phase fluid dynamics. Journal of Computational Physics 26, 390-407 (1978).

7. R. Taleyarkhan, M. Podowski, R. T. Lahey. The effect of heater wall dynamics on density-wave oscillations in boiling channel. Heat transfer 1982. Proceedings of an 7th International Conference, Munich, Germany, Vol. 4, 249-254 (1982).

An Investigation of the Stability of A Boiling Water Reactor Under Natural Circulation Conditions Using TRAC-BF1

Lider, S., Robinson, G.E., and Baratta, A.J.
The Pennsylvania State University
Department of Nuclear Engineering
University Park, PA 16802

Refling, J.G.
Pennsylvania Power and Light Company
Two North Ninth St.
Allentown, PA 18101

Abstract

The stability of a BWR was investigated over a limited range of make up flow rates and operating pressures using the TRAC-BF1 computer code. Point kinetics with six delayed neutron groups was used to determine the reactor power response along with a constant power profile throughout the transient.

The main objective of this study is to determine whether the reactor conditions are stable under natural circulation after an MSIV closure ATWS. The actual ATWS scenario, therefore, was not followed. Two slightly different TRAC-BF1 models of the Susquehanna Steam Electric Station (SSES) which were developed and benchmarked against a MSIV Closure with Scram test case were utilized. A methodology to drive the reactor to its final operating condition was developed. In this methodology, a TRAC-BF1 run with the steady state option is made to obtain a thermal-hydraulic steady state. In steady state calculations of the TRAC-BF1 code, the neutronics feedback is bypassed, while the thermal-hydraulics and neutronics coupling is allowed in the transient calculations. Because of the non-zero convergence criteria used in the steady state runs, the reactor starts to depart from the thermal-hydraulic steady state after the transient mode is engaged. During the transient, some fluctuations are observed in the behavior of various parameters. Depending on the natural circulation conditions, especially the operating pressure, the observed fluctuations either die out or go into an unstable mode.

The results of the study showed that the higher operating pressures are likely to be more stable and there is a void reactivity related instability at the lower operating pressures. However, the effects of the axial power profile and the reactivity feedback coefficients suggest that a higher dimensional kinetics feedback is required to more accurately determine the transition region for different system parameters, such as operating pressure, between the stable and unstable final states.

INTRODUCTION

An Anticipated Transient Without Scram (ATWS), while of low probability, has received considerable attention because of its potentially serious consequences. One of the most serious ATWS events for the Boiling Water Reactor (BWR) is the postulated complete failure to scram following a transient event that has caused closure of all main steam isolation valves (MSIVs). The following is a brief description of the reactor behavior following a MSIV closure.

The transient begins with the closure of all MSIVs after which the reactor vessel is progressively isolated. Because the reactor is at power, the reactor vessel pressure rapidly increases. The pressure increase causes the collapse of some of the voids in the core, inserting positive reactivity which in turn increases the reactor power. The increase in the reactor power produces more steam which in turn causes further increase in the reactor pressure. When the reactor vessel pressure reaches the level of the safety relief valve set points, the SRVs open to reduce the rate of the pressure increase and the recirculation pumps are automatically tripped. With the tripping of the recirculation pumps, the core flow is reduced to between 20 and 30 percent of its former value as flow changes from forced circulation to natural circulation. With reduced flow, the temperature of the moderator in the core subcooled region is increased, producing voids, and introducing a significant amount of negative reactivity. The rapid increase of the reactor power is terminated, and the power, then, rapidly decreases to about 30 percent of the rated power.

The response of the reactor to the MSIV closure initiated ATWS has been studied previously; however, the previous studies have been focused on reactivity changes in the core and the typical thermal-hydraulic post-transient

events.[3,5,6] The majority of these studies have used RETRAN or RAMONA-3B codes to analyze the transient behavior of the reactor. In one study, a typical BWR/4 MSIV closure ATWS has been simulated using RAMONA-3B and TRAC-BD1 codes.[4] Another study used the TRAC-BD1 code, but the purpose of that study was to evaluate the TRAC code, not the transient.[7] Although these studies emphasize on the ATWS event, the stability of the reactor following an ATWS event has not previously been studied.

In this study, the stability of a BWR under natural circulation conditions over a range of make up flow rates and operating pressures, including three high, one intermediate, and three low operating pressures were investigated. For the lowest pressure of 1.72 MPa (250 psia), the effects of the axial power profile and the reactivity feedback coefficients on the reactor stability were also investigated. The TRAC-BF1 code with point reactor kinetics is chosen since it has been shown to be capable of simulating BWR under natural circulation conditions[8] and use of point reactor kinetics has been proven adequate to predict the general behavior of the transient, including density wave instabilities.[4,8]

TRAC-BF1 is the latest code release stemming from the TRAC-BWR code development program of the Idaho National Engineering Laboratory (INEL).[1,2] The advantage of TRAC-BF1 is that it uses a full two-fluid, nonequilibrium, nonhomogeneous thermal-hydraulic model of two-phase flow in all parts of the BWR system, including a three-dimensional treatment of the reactor vessel. In the next section, the TRAC-BF1 stability model used in this study is described, and in the method of analysis section, a brief explanation of the methodology is given. Finally, a discussion of some of the results while showing the examples of stable and unstable reactor behaviors is presented. For the readers convenience, the reactor conditions investigated are all summarized in Table 1.

MODEL DESCRIPTION

The TRAC-BF1 model of the Susquehanna Steam Electric Station (SSES) depicted in Fig. 1 consists of one two-dimensional and 18 one-dimensional components along with 31 junctions. The VESSEL, the only multi-dimensional TRAC-BF1 component, consists of thirteen axial levels, four radial rings, and one azimuthal region reducing the three-dimensional VESSEL model to two-dimensions. The first three radial rings cover the reactor interior components while the fourth is used to model the downcomer region.

Other than the two-dimensional VESSEL component, several one-dimensional components were used in the model, such as:

- PIPE components 31, 32, and 33 model the control rod guide tubes.
- CHAN components model the reactor core, including CHAN60 representing 4 hot fuel bundles, CHAN61 and CHAN62 representing 668 average fuel bundles, and CHAN63 representing 92 peripheral bundles.
- SEPD components 71 and 72 model the separator/dryer assemblies using TRAC-BF1's simple separator model.
- PUMP 12 and JETP 14 components model the recirculation lines.
- VALVE components 52 and 58 model the MSIVs and SRVs, respectively.
- FILL 44 component provides the feedwater inlet boundary condition, which is connected to the VESSEL component via PIPE 54 component.
- BREAK components 46 and 47 provide the pressure boundary conditions for the steam line. BREAK 46 is connected to the MSIVs while BREAK 47 is connected to the SRVs.

Along with these TRAC-BF1 components, we utilized the following features in constructing the model:

a) The transient was assumed to start at 0.0 seconds.

b) The point kinetics model with six delayed neutron groups along with the various reactivity feedback coefficients (i.e. void, moderator, Doppler) was used to determine the reactor power response.

c) The MSIV area which was adjusted to give the flow area which was necessary to meet the specified natural circulation conditions was used to simulate the open SRVs.

d) The pressure at the BREAK 47 component which sets the steam outlet boundary condition was set to atmospheric pressure to reflect the physical condition and the choked flow calculation option was turned on in the VALVE component.

e) It is assumed that no boron injection occurred.

f) A new method of analysis was developed and was used rather than following the actual ATWS scenario.

g) A steady state, full power, bottom peaked power profile was used in most of the cases.

h) An estimated power level based on a simple energy balance on the system was used in the steady state runs.

i) The recirculation pump speed was set to 0.0 rad/sec.

j) A constant feed water inlet flow was used throughout the transient.

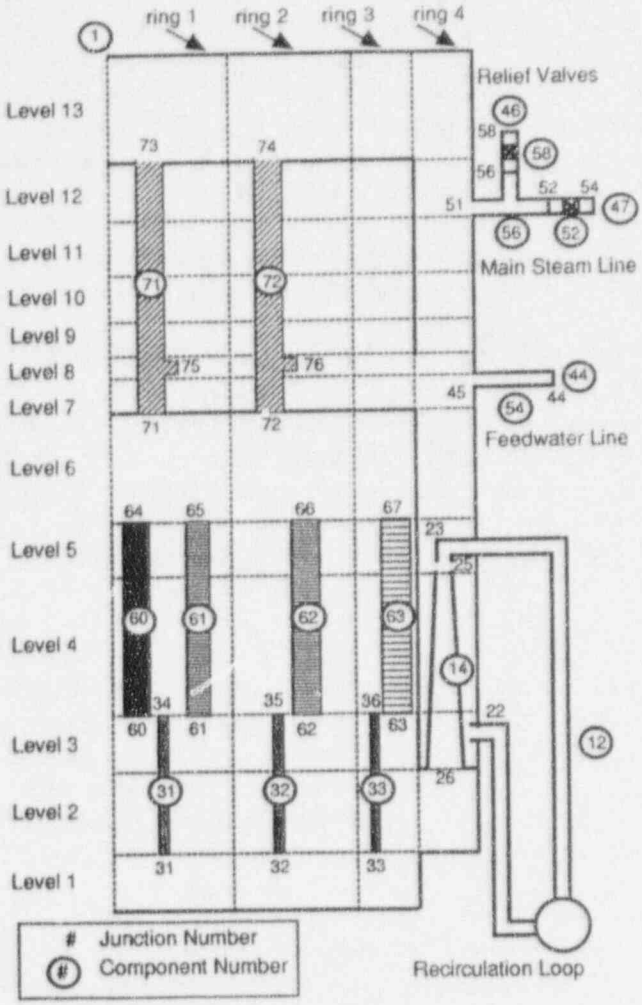

Figure 1. TRAC-BF1 model of SSES

Case #	Pressure (MPa)	Make up Flow (kg/s)	Feedwater Inlet Temp. (°C)	Reactor Power (MW_{th})
1	7.24	385.56	197.0	737.92
2	1.72	321.30	197.0	629.00
3	5.86	311.22	37.8	601.10
4	4.48	119.70	197.0	315.54
5	7.24	95.76	37.8	249.40
6	3.10	165.06	37.8	436.30
7	1.72	137.34	37.8	362.08

Table 1. Key parameters for investigated cases

METHOD OF ANALYSIS

Most of the ATWS analyses require approximately 1500-2000 seconds to simulate the transient.[3-6] Since the main objective is to determine whether the reactor is stable under the specified natural circulation conditions after an MSIV closure initiated ATWS, it is not necessary to follow the actual ATWS scenario. Therefore, a methodology was developed to shorten the TRAC-BF1 CPU time requirements. First, the thermal-hydraulic steady state conditions of the reactor are determined from a TRAC-BF1 steady state calculation for each specified condition given in Table 1, including system pressure, make-up flow rate, and the reactor power level which is calculated from a simple energy balance on the system. Then, after obtaining steady state conditions, a transient calculation with the neutronics feedback is performed. The non-zero convergence criteria creates an initial perturbation when the transient is started. The purpose behind this methodology is to speed up the generation of final operating states by initially decoupling the neutronics from the thermal-hydraulics. In general, converging the thermal-hydraulics does not take a long time.

The methodology has an underlying assumption that under the specified natural circulation conditions the reactor has only one final state regardless of the sequence of events followed during the transient. Therefore, it should be verified that the final state of the reactor is independent of path chosen to get there. Case 1 is taken to be the test case for this methodology. Using the specified state parameters, a parallel path and a sequential path were created. In the Parallel Approach, all actions necessary to bring the reactor from normal operating conditions to the specified natural circulation conditions are taken simultaneously, while in the Sequential Approach, the reactor is brought to the final state by performing one action at a time. The results indicate that the final state of the reactor is stable and is independent of the sequence of events followed to generate this state.

Table 2 shows the final stable state parameters for the Parallel and Sequential Approaches. As seen from the table, the results of both approaches agree with each other. The slight differences are due to the lower make up flow rate used in the Sequential Approach.

Once the methodology was shown valid, steady state reactor parameters were determined for each of the specified conditions in Table 1 using the steady state calculation mode of TRAC-BF1. These steady state parameters are summarized in Table 3. Transient calculations were initialized at these conditions, and the computations are completed with neutronic-thermal-hydraulic feedback in place.

TRAC-BF1 assumes that the reactor is at steady state, when the changes in the state parameters are smaller than a user-defined convergence factor. During the transient calculations, the initial perturbation is provided by this non-zero steady state convergence criteria and the reactor model starts to depart from the steady state. A slight increase in the power causes increases in the pressure and the core average void fraction. The increase in the void fraction introduces negative reactivity and causes the power to decrease which in turn reduces the pressure. As the pressure falls the collapsed water level increases and drives more flow through the core. With the higher core flow the core average void fraction decreases which introduces positive reactivity and the reactor power starts to increase. Depending on the natural circulation condition, the oscillations observed in various parameters either die out or go into an unstable mode.

Parameters	Parallel Approach	Sequential Approach
Feedwater Flow Rate, kg/s (Mlb/hr)	385.56 (3.06)	378.00 (3.00)
Steam Flow Rate, kg/s (Mlb/hr)	385.56 (3.06)	376.74 (2.99)
Reactor Pressure, MPa (psia)	7.19 (1043.0)	7.15 (1037.1)
Collapsed Water Level, meters (in)	8.60(338.7)	8.27 (325.7)
Total Reactor Power, MW_{th}	745.40	727.20

Table 2. The final state parameters for the Parallel and Sequential Approach

RESULTS AND DISCUSSION

The final states obtained after the transient runs are presented in Table 4. Figures 2 and 4 depict the total reactor power for a stable and an unstable final state. The steam dome pressure response for an unstable final state is given in Fig. 3.

After observing an unstable final state for Case 2, additional sensitivity calculations were performed to identify the effect of some parameters on BWR stability. First, the original case was assigned as Case 2a. Then, the void reactivity coefficients were artificially lowered to half of their previous values (Case 2b). Later, the feedwater inlet temperature was lowered from 197°C to 37.8°C (Case 2c). Finally, the bottom peaked axial power profile in Case 2c was modified to a top peaked profile (Case 2d).

The response of the total reactor power is given in Fig. 2 for Case 2a. Initially (0-600 seconds), it behaves like an unstable second order oscillator. At approximately 1200 seconds, it has a relatively broad peak of nearly 1000 MW_{th}. As the pressure increases decreasing the collapsed water level and core flow, the reactor power falls to a level of approximately 350 MW_{th}. The power hits a level of nearly 5400 MW_{th} at approximately 1400 seconds. For the rest of the transient, the reactor undergoes a bounded oscillatory behavior with some relaxation instabilities such as chugging which appear as sharp spikes in the channel flows and is also reflected in the behavior of other parameters. The steam dome pressure, depicted in Fig. 3, follows the same behavior as the power does but with some time delay. During the transient, the steam dome pressure ranges from about 1.2 to about 2.4 MPa (180 to 350 psia).

The void reactivity is affected by the reactor pressure. As the operating pressure is reduced, the void reactivity feedback becomes the dominant feedback mechanism to control the total reactivity, which, in turn,controls the reactor power. Along with controlling the reactor power, the void reactivity feedback has an important effect on the stability. As already discussed, Case 2a is unstable. However, with the modified (decreased) void reactivity feedback coefficients, Case 2b becomes stable.

Figure 4 indicates that the final state of Case 2b is stable. At this final stable state, the steam dome pressure is 1% higher than the target pressure while the steam flow matches the feed water inlet flow. The estimated power value of 601.1 MW_{th} agrees with the power level of 606.5 MW_{th} at the final stable state.

Case #	Reactor Power (MW_{th})	Reactor Pressure (MPa)	Steam Flow Rate (kg/s)	Core Avg. Void Frac. (%)	Collapsed Water Level (m)[a]
1[b]	--	--	--	--	--
2a	629.00	1.69	322.56	57.17	10.71
2b	629.00	1.69	322.56	57.17	10.71
2c	847.05	1.69	322.56	62.10	10.94
2d	847.05	1.68	321.55	59.13	10.90
3	601.10	5.86	307.82	46.44	12.40
4	315.89	4.44	117.84	32.97	9.80
5	249.40	7.24	96.26	11.51	13.07
6	436.30	3.03	165.19	45.55	9.02
7	362.08	1.71	137.14	43.88	10.35

[a] TAF is 9.07 meters

[b] reactor is not steady stated before the transient run

Table 3. Key parameters for thermal-hydraulically steady states

Case #	Reactor Power (MW_{th})	Reactor Pressure (MPa)	Steam Flow (kg/s)	Collapsed Water Level (m)[a]
1[b]	745.40	7.19	385.56	8.60
2a[c]	--	--	--	--
2b	631.90	1.68	321.43	10.62
2c[c]	--	--	--	--
2d[c]	--	--	--	--
3	606.50	5.92	311.22	12.45
4	315.43	4.51	119.51	9.99
5	249.90	7.24	96.26	13.06
6	435.20	3.03	165.31	13.04
7[c]	--	--	--	--

[a] TAF is 9.07 meters

[b] Parallel Approach results are given

[c] final state is unstable

Table 4. Reactor parameters at the end of the transient

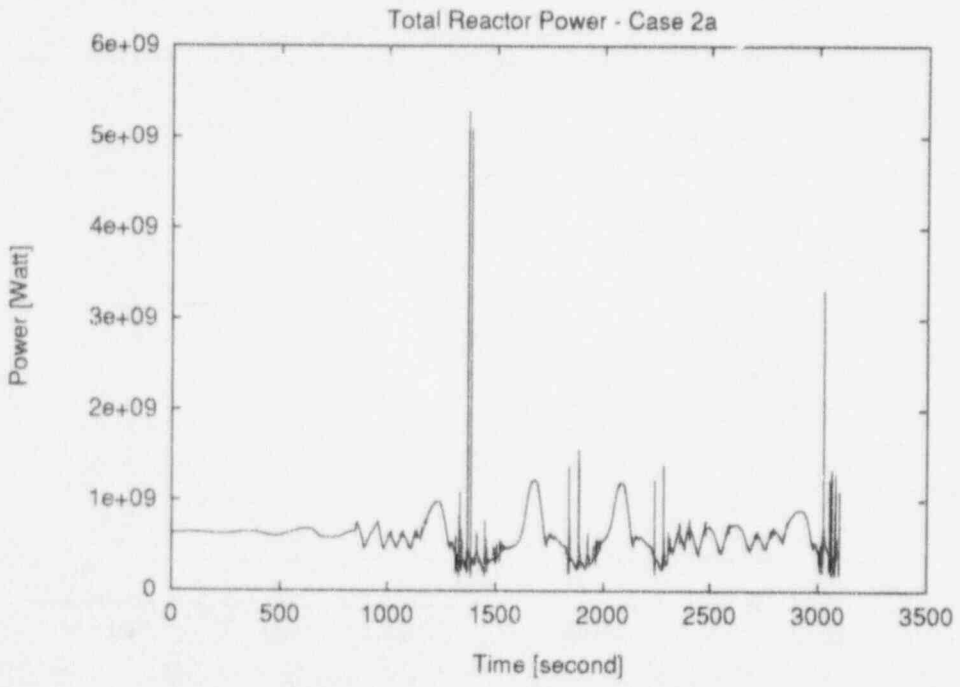

Figure 2. Total reactor power for an unstable case (Case 2a)

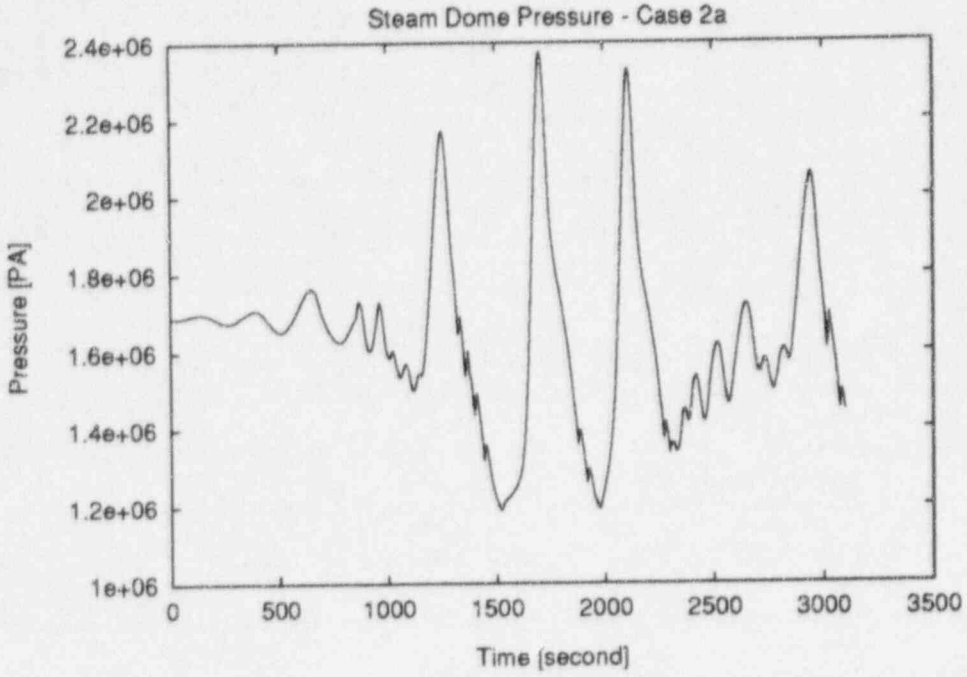

Figure 3. Steam dome pressure for an unstable case (Case 2a)

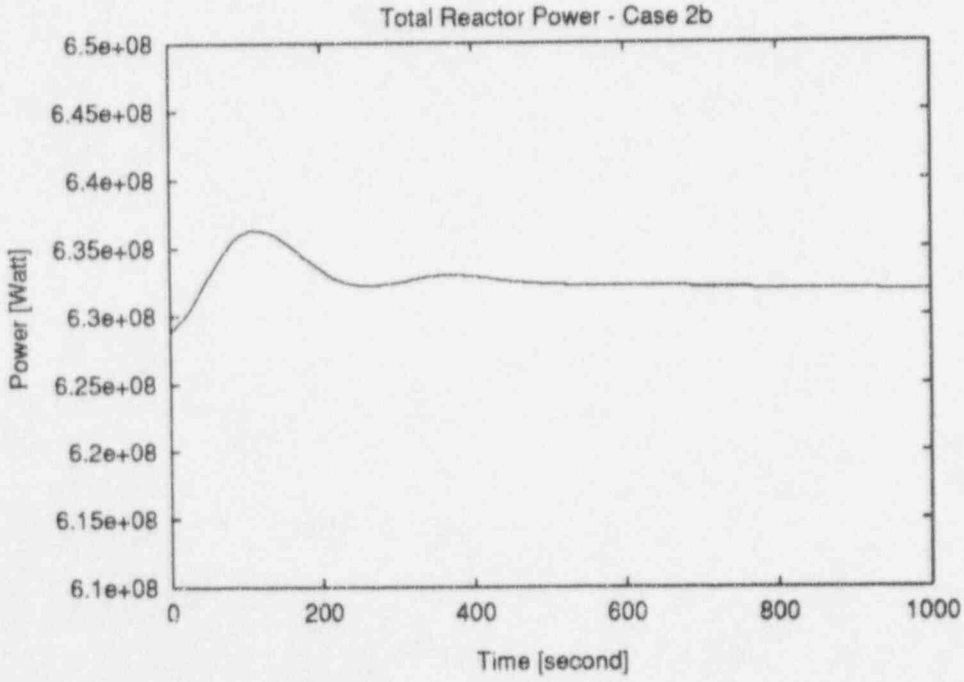

Figure 4. Total reactor power for a stable case (Case 2b)

Case 2c differs from Case 2a only in the feedwater inlet temperature. The results of these runs are found to be similar. The only difference is that the magnitude of oscillations observed in the behavior of different parameters is relatively smaller in Case 2c.

Case 2c uses a bottom peaked power profile reflecting the steady state operating conditions. However, in Case 2d, a top peaked power profile reflecting the thermal-hydraulically steady state natural circulation conditions is used. The results of Case 2d indicates a core failure pointing out the importance of the power profile. During the transient, fuel temperatures greater than the melting temperature are experienced along with the metal-water reaction at the outer surface of the fuel elements.

CONCLUSIONS

After obtaining results of all cases, it is concluded that the higher operating pressures are more stable when compared to the lower ones. In light of this conclusion, it is recommended that reactor operators keep an operating pressure of 4.48 MPa (650 psia) or above to avoid power oscillations which may endanger the fuel integrity.

TRAC-BF1 predicted an unstable final state for Case 2, and we decided to investigate further to identify the important parameter on the reactor stability. We investigated three additional cases. The results of Case 2b indicated that the precise determination of the void reactivity coefficients is very important for an accurate result. In Case 2d, we experienced temperatures higher than the melting point of the fuel pellets. In light of this result, we can conclude that the axial power profile can have an important effect on the reactor stability.

For the stable cases, we observed that the steam outlet flows match the feed water inlet flows which is a necessary condition for a stable system. Otherwise, the mass flow difference between inlet and outlet creates an unstable system. However, the steam dome pressures are within ±2.4% of the target values in these stable cases. These differences between the target and the final stable state pressures are mainly due to the precision of the MSIV area held open. On the other hand, the final power levels calculated in each case are consistent with the power level predicted by using a simple energy balance on the system.

ACKNOWLEDGMENT

The authors would like to thank Dr. Joseph L. Staudenmeier and Jason W. Hartzell, a fellow graduate student, for their contributions to this study.

The authors also thank the Pennsylvania Power and Light Company and The Pennsylvania State University Department of Nuclear Engineering for their financial support.

REFERENCES

1. D. Taylor et al., "TRAC-BF1/MOD1: An Advanced Best Estimate Computer Program for Boiling Water Reactor Thermal Hydraulic Analysis", NUREG/CR-3336, EG&G Idaho, Inc.

2. G. Singer et al., "TRAC-BD1/MOD1 Code Manual", EGG-2294, EG&G Idaho, Inc., (1984).

3. H.S. Cheng and D.J. Diamond, "Reactivity Transients During A Blowdown in a MSIV Closure ATWS", BNL-NUREG-41417 (1988).

4. C.J. Hsu, L. Neymotin and P. Saha, "Analysis of a Typical BWR/4 MSIV Closure ATWS Using RAMONA-3B and TRAC-BD1 Codes", BNL-NUREG-34942 (1984).

5. R.J. Dallman et al., "Severe Accident Sequence Analysis Program-Anticipated Transient Without Scram Simulations For Browns Ferry Nuclear Plant Unit 1", NUREG/CR-4165, EGG-2379, EG&G Idaho, Inc. (1987).

6. P. Saha et al., "RAMONA-3B Calculations For Browns Ferry ATWS Study", NUREG/CR-4739, BNL-NUREG-52021 (1987).

7. J.H. Jo and H. Connel, "Simulation of FIST Tests Using TRAC-BD1", Trans. Am. Nucl. Soc. 52, 477, (1986).

8. Borkowski, J.A., et al., "Time Domain Model Sensitivity in Boiling Water Reactor Stability Analysis using TRAC-BF1", Nucl. Tech., vol. 103, pp. 34-48, July 1993.

Analysis of the Void Wave Propagations: Wave Number Independent Characteristics

Chul-Hwa SONG,[1] Hee Cheon NO,[2] Moon Ki CHUNG[1]

[1] Korea Atomic Energy Research Institute
Thermal Hydraulics Department, Yusung P.O. Box 105, Taejon 305-600, Korea

[2] Korea Advanced Institute of Science and Technology
Department of Nuclear Engineering, 373-1 Gusung-dong, Yusung-ku, Taejon 305-701, Korea

Abstract

The propagation of the void waves is analytically investigated from the linear stability analysis of the two-fluid model. An analytical model on the wave dispersion is established from the generalized form of the void propagation equation. And the wave propagation parameters, which are independent of the wave number, are also derived based on the concept of "most unstable waves". This feature is expected to be very useful for analytically investigating the propagation characteristics of naturally generated void waves.

It is clarified that the hyperbolicity condition is a necessary, but not sufficient condition for stability. The analytical model of the void wave propagations, including the wave speed and the wave damping factor, is validated by comparing the predicted results with experimental data. The spatial gain factor is proposed to be used as an indicator to quantify the spatial wave damping. The predicted tendency shows qualitatively well the distinct features revealed in experiments, but they are very sensitive to the closure laws on the momentum interactions. Especially, the virtual mass coefficient very much affects the hyperbolicity condition and the wave damping.

1. INTRODUCTION

It has been expected that the flow instabilities occuring in the two-phase system might mathematically appear in the form of complex characteristics. Especially, the instability of void waves has been thought to be closely related to the hyperbolicity breaking condition of the two-fluid formulation which is applicable to bubble flow. For that reason, the void waves, that is, the propagations of void disturbances have been analytically investigated in several works [1~4].

Pauchon & Banerjee [1] investigated the charactersitics of void waves using a simplified two-fluid model. They found, through parametric study, that the wave characteristics are very sensitive to the closure parameters. Park et al. [2] and Lahey [3] extended the analysis of Pauchon & Banerjee [1] using the newly derived two-fluid model, and investigated the influence of different types of closure models on the characteristics of the two-phase flow system. Biesheuvel & Gorissen [4] performed a linear stability analysis by applying the kinetic theory to the dispersed bubbles and modeled some wave parameters. These works were mainly aimed at checking the integrity of the formulation and at assessing the closure laws through the analysis of the system characteristics and the wave celerities.

In these works, however, they did not establish the relationship between the wave stability condition and the hyperbolicity condition. And the wave propagation properties derived were, in general, dependent on the wave number. This feature might be one of the reasons for experimental investigators [e.g., 5~7] to examine the wave dispersion by

imposing known frequency of artificial disturbances to the flow. Therefore, it was very difficult in earlier works, except for the case of long wavelength limit, to validate the formulation and its closure laws in view of the predictability of the void wave propagations, which are dependent on the wave number, without relying on experimental data. And previous works did not give much attention to the wave damping in this regard since experimental information on the wave damping was not available. Since Matuszkiewicz et al. [5], some attempts [8,9] have been done to measure the wave damping.

The objectives of this study are to analytically investigate the wave damping and to clarify the relation between the hyperbolicity condition and the stability condition. An analytical model of the wave dispersion is established from the linear stability analysis of the two-fluid model. From the generalized form of the void propagation equation, the wave propagation properties are fully derived. They include the wave speed, the relaxation time and the wave damping factors. Based upon the concept of the "most unstable waves", the wave parameters, which are independent of the wave number, are also derived. This concept can eliminate the inevitability to impose artificial perturbations to the flow, which were previously required to compare analytical results with experimental data. The predicted results are compared with experimental data to examine whether the present model on the wave propagation properties, especially the wave damping factor, could predict experimentally observed tendency.

2. BASIC FORMULATION

Formulation of the two-fluid model

For a one-dimensional, incompressible flow without phase change, the governing equations can be formulated, from volume averaging of the instantaneous two-fluid model [10], as

$$\frac{\partial \alpha_k}{\partial t} + \frac{\partial}{\partial z}[\ \alpha_k \langle u_k \rangle] = 0 \tag{1}$$

$$\rho_k[\ \frac{\partial}{\partial t}(\alpha_k \langle u_k \rangle) + \frac{\partial}{\partial z}(\alpha_k \langle u_k \rangle^2)\ ] = -\alpha_k \frac{\partial \langle P_k \rangle}{\partial z} + \Delta P_{ki} \frac{\partial \alpha_k}{\partial z} + \frac{\partial}{\partial z}[\ \alpha_k(\tau_{zz,k} + \tau^T{}_{zz,k})] + M_{Gk} + M_{Ik} + M_{Wk}, \tag{2}$$

where

$$\langle f_k \rangle = \frac{1}{V_k} \int_{V_k} f_k \, dV,$$

and M_{Gk}, M_{Wk}, M_{Ik} and $\tau_{zz,k}$ denote the body force density, the wall friction force density, the interfacial force density, and the viscous stress, respectively.

The interfacial force density can be described for gas phase as $-M_{Ig} = M_g^D + M_g^{ND}$, where M_g^D and M_g^{ND} denote the drag force term and the non-drag force term, respectively. [10,11] By neglecting the reaction force due to bubble pulsation and the lift force, only the virtual mass force is left in the non-drag force term. The Reynolds stress for gas phase can be neglected and for liquid phase, it can be expressed as[1]

$$\tau^T_{zz,f} \equiv -\rho_f \langle u_f'^2 \rangle = -\rho_f [\ D_T \frac{\partial u_f}{\partial z} + k\alpha_g (u_g - u_f)^2\ ], \tag{3}$$

where D_T is called the axial diffusion coefficient [12]. k = 0.2, valid for dilute mixtures, is usually used. By neglecting the interfacial pressure difference for gas phase [2] and by considering the surface tension effect, the pressure difference between phases can be

expressed as

$$P_g - P_f \fallingdotseq -\eta\rho_f(1-\alpha_g)(u_g-u_f)^2 + \frac{4\sigma}{D_b}. \tag{4}$$

The coefficient, η is usually adopted to be 0.25. With neglecting the wall friction by gas phase, the wall friction by liquid phase can be expressed by a Moody-type model.

The interfacial drag force (F_D) is usually determined by:

$$M_g^D = \alpha_g F_D = 2f_i\alpha_g\frac{\rho_f}{D}(u_g-u_f)^2, \tag{5}$$

where f_i is the interfacial friction factor. The virtual mass force is expressed by [13]

$$F_{VM} = \rho_f C_{VM}\, a_{VM} - \frac{\partial \Delta P_{fi}}{\partial z}, \tag{6}$$

where the virtual mass coefficient, C_{VM}, is known to be 1/2 for dilute bubble mixtures. Bataille et al. [14] found that C_{VM} is an increasing function of bubble diameter, which can be best-fitted as:

$$C_{VM} = \begin{cases} 0.351*10^{0.0565D_b} & \text{for } D_b = 2.5-4\ mm, \\ 0.00194*10^{0.589D_b} & \text{for } D_b = 4-5.5\ mm. \end{cases} \tag{7a}$$

Zuber [15] proposed

$$C_{VM} = \frac{2\alpha_g+1}{2\alpha_f} \fallingdotseq \frac{1}{2} \text{ for small void fraction.} \tag{7b}$$

Assuming all reference parameters to be constant and measurable quantities, equations (1) and (2) can be expressed in dimensionless form as follows:

$$\frac{\partial \alpha_k}{\partial t^+} + \frac{\partial \alpha_k u_k^+}{\partial z^+} = 0 \qquad (k=f,g) \tag{8}$$

and

$$\frac{\partial}{\partial t^+}(\alpha_g u_g^+) + \frac{\partial}{\partial z^+}(\alpha_g u_g^{+2}) = -\frac{\alpha_g}{N_\rho}\frac{\partial P_g^+}{\partial z^+} - \frac{\alpha_g}{Fr_o^2} - \frac{N_D}{N_\rho}\alpha_g(u_g^{+2}-u_f^{+2}) - \eta\frac{\alpha_g}{N_\rho}\frac{\partial}{\partial z^+}[\alpha_f(u_g^{+2}-u_f^{+2})] - \frac{C_{VM}}{N_\rho}\alpha_g\left[\frac{D_g u_g^+}{Dt^+} - \frac{D_f u_f^+}{Dt^+}\right], \tag{9a}$$

$$\frac{\partial}{\partial t^+}(\alpha_f u_f^+) + \frac{\partial}{\partial z^+}(\alpha_f u_f^{+2}) = -\alpha_f\frac{\partial P_f^+}{\partial z^+} + \eta(\alpha_f-\alpha_g)(u_g^+-u_f^+)^2\frac{\partial \alpha_g}{\partial z^+} + \eta\alpha_f\alpha_g\frac{\partial(u_g^+-u_f^+)^2}{\partial z^+} - N_T\frac{\partial}{\partial z^+}(\alpha_f\frac{\partial u_f^+}{\partial z^+}) - k\frac{\partial}{\partial z^+}[\alpha_f\alpha_g(u_g^+-u_f^+)^2] - \frac{\alpha_f}{Fr_o^2} + N_D\alpha_g(u_g^+-u_f^+)^2 + C_{VM}\alpha_g\left[\frac{D_g u_g^+}{Dt^+} - \frac{D_f u_f^+}{Dt^+}\right] + N_\sigma\frac{\partial \alpha_g}{\partial z^+} - N_f u_f^{+2}, \tag{9b}$$

where the dimensionless numbers are defined as

$$N_\rho = \frac{\rho_g}{\rho_f}, \qquad Fr_o = \frac{u_{ro}}{\sqrt{gD}}, \qquad N_D = 2 f_i, \tag{10}$$
$$N_T = \frac{D_T}{u_{ro} D}, \qquad N_o = \frac{4C}{\rho_f u_{ro}^2 D_b}, \qquad N_f = 2 f_w.$$

Here, N_T is called the dispersion number which comes from eqn. (3).

Characteristics analysis

The system of the equations, (8) and (9), can be written in matrix form, with $N_T = 0$, as follows:

$$\mathbf{A}\frac{\partial \Phi}{\partial t^+} + \mathbf{B}\frac{\partial \Phi}{\partial z^+} = \mathbf{C}, \tag{11}$$

where the matrix Φ, $\mathbf{A}$, $\mathbf{B}$, $\mathbf{C}$ are defined in the appendix. The characteristics of the system can be found by setting the characteristic equation to be zero as follows:

$$\Delta \equiv | \mathbf{B} - \lambda^* \mathbf{A} | = a_1 \lambda^{*2} + a_2 \lambda^* + a_3 = 0, \tag{12}$$

where the dimensionless characteristics is defined as:

$$\lambda^* \equiv \frac{\lambda - u_f}{u_g - u_f}, \tag{13}$$

and

$$\begin{aligned} a_1 &\equiv \alpha_f A_1 + \alpha_g A_2, \\ a_2 &\equiv 2[\, -\alpha_f A_1 + \frac{B_2}{2}\,], \\ a_3 &\equiv \alpha_f A_1 - \alpha_f \alpha_g B_1 - \alpha_f B_2. \end{aligned} \tag{14}$$

Here, A_1, A_2, B_1, B_2 are defined in the appendix. Thus, the characteristics can be found as

$$\lambda_1^* = V^* \pm \sqrt{\frac{\nu^*}{\tau^*}}, \tag{15}$$

where

$$V^* \equiv -\frac{a_2}{2a_1}, \qquad \nu^* \equiv \frac{\alpha_f (a_2^2 - 4a_1 a_3)}{4}, \qquad \tau^* \equiv \alpha_f a_1^2. \tag{16}$$

The characteristic equation can have, in general, three types of solutions: two real solutions for hyperbolic domain, a single real solution for parabolic domain, and two complex conjugate solutions for elliptic domain. Physically, the hyperbolic, elliptic and parabolic domains represent regular flow, instability, and neutrally stable state between regular flow and unstable flow, respectively. The hyperbolicity condition is given by $\nu^* > 0$ to yield $a_2^2 > 4 a_1 a_3$. And the hyperbolicity breaking condition is obtained, by setting $\nu^* = 0$, to be

$$a_2^2 = 4 a_1 a_3. \tag{17}$$

It is noted that the consideration of algebraic terms only as momentum interaction terms and the assumption of the equal phasic pressure, as a limiting case, lead to the ill-posed problem.

Void propagation equation

Consider small fluctuations for void fraction and phasic velocity. Hereunder, the symbol "+" to denote a dimensionless quantity is omitted for simplicity. Then, from eqns. (8) and (9), the void propagation equation becomes, with neglecting nonlinear terms, as follows:

$$\frac{\partial \alpha}{\partial t} + C_{a_o}\frac{\partial \alpha}{\partial z} + \theta_o\Big[\Big(\frac{\partial}{\partial t} + C_{3_o}\frac{\partial}{\partial z}\Big)\Big(\frac{\partial}{\partial t} + C_{4_o}\frac{\partial}{\partial z}\Big)\alpha - \nu_o\Big(\frac{\partial}{\partial t} + U_o\frac{\partial}{\partial z}\Big)\frac{\partial^2 \alpha}{\partial z^2}\Big] = 0, \tag{18}$$

where

$$C_{a_o} \equiv \frac{K_2}{K_1}, \quad \theta_o \equiv \frac{K_3}{K_1}, \quad \nu_o \equiv -\frac{L_{1o}}{K_3}, \quad U_o \equiv j_o - \frac{L_{2o}}{L_{1o}}, \tag{19a}$$

and

$$C_{3_o},\ C_{4_o} \equiv V \pm \sqrt{\frac{\gamma}{\tau}}, \tag{19b}$$

with $V = \dfrac{K_4}{2K_3}, \quad \gamma = K_4^2 - 4K_3K_5, \quad \tau = 4K_3^2$.

Here, K_1, K_2, K_3, K_4, K_5 are defined in the appendix. Equation (18) introduces the diffusion term proportional to ν_o and the time lag (θ_o) in the response to any changes in the flow conditions, when compared to one derived from the drift-flux model [16].

The lower-order wave speed, C_{a_o}, can be expressed as

$$C_{a_o} = j_o + \frac{N_D(1-\frac{5}{2}\alpha_g)u_r^2 + N_f\alpha_g(\frac{1}{2}u_f^2 - \alpha_g u_f u_r)}{N_D u_r + N_f\alpha_g u_f}. \tag{20}$$

It is influenced only by the algebraic momentum source terms as in case of the kinematic wave speed defined in the drift-flux model [16]. With neglecting the wall friction, it can be simplified to

$$C_{a_o} - j_o = (1-\frac{5}{2}\alpha_g)u_r, \tag{21}$$

and it indicates $\alpha_g = 0.4$ for the condition of $C_{a_o} - j_o = 0$. It is noted that $\alpha_g = 0.3 \sim 0.4$ was observed at that condition, from the experiments [9], depending on the liquid flow rate.

C_{3o} and C_{4o} are called the higher-order wave speeds [17]. The interaction between the higher-order and lower-order waves occurs due to the presence of non-algebraic momentum source terms (e.g., the virtual mass force term). The relaxation time can be written as

$$\theta_o = \frac{N_p\alpha_f^2 + \alpha_f\alpha_g + C_{VM}}{2N_D + 2N_f\alpha_g u_f}. \tag{22}$$

The relaxation time can be interpreted as the time lag between any perturbations to the flow and its response. With eqn. (7a) in mind, it can be said that the relaxation time becomes larger as bubble size is increased, which is comparable with experimental observations [9] in terms of a flow time scale.

3. WAVE PROPAGATION PROPERTIES

Consider an evolution of spatially periodic, small disturbances to the quasi-fully developed basic flow. Small disturbances with wave number (κ) can be expressed in a normal mode by $\alpha \sim \exp[\, i(\kappa z - \omega t)]$. Then, from eqn. (18), the dispersion relation becomes

$$(C-\overline{C})^2 + iP(C-\overline{C}) - (Q+iR) = 0, \tag{23}$$

which is exactly the same as one proposed by Biesheuvel & Gorissen [4], where a phenomenological approach was used by applying the kinetic theory to the bubble flow. P, Q, R, $\overline{C}$ are defined in the appendix, and the phase velocity is expressed by

$$C \equiv \frac{\omega}{\kappa} = C_r + i\, C_i.$$

The solution of the dispersion relation can be written as

$$C = \overline{C} - i\frac{P}{2} \pm \sqrt{\frac{P^2}{4} - Q - iR}\,, \tag{24}$$

and it can be simplified, with $\nu_o = 0$, to

$$C \fallingdotseq \frac{1}{2}(C_{3_o}+C_{4_o}) - \frac{i}{2\kappa\theta_o} \pm \frac{i}{2\kappa\theta_o}[\, 1-(C_{4_o}-C_{3_o})^2\kappa^2\theta_o^2 + i\, 2\kappa\theta_o(C_{3_o}+C_{4_o}-2C_{a_o})]^{\frac{1}{2}}. \tag{25}$$

Here it is noted that $\nu_o = 0$ eliminates the diffusion term in eqn. (18)

The general solution of the dispersion relation can be written as

$$C_r = \overline{C} \pm [\, -\frac{P^2}{8} + \frac{Q}{2} + \frac{1}{2}\sqrt{(\frac{P^2}{4}-Q)^2+R^2}\,]^{\frac{1}{2}}, \tag{26a}$$

$$C_i = -\frac{P}{2} \pm [\, \frac{P^2}{8} - \frac{Q}{2} + \frac{1}{2}\sqrt{(\frac{P^2}{4}-Q)^2+R^2}\,]^{\frac{1}{2}}. \tag{26b}$$

And the stability condition, $\kappa C_i \leq 0$, gives two constraints: $P \geq 0$ and $P^2Q \geq R^2$. The first constraint is satisfied, for $\nu_o = 0$, by $\theta_o \geq 0$ which is valid only if the slip ratio between phases satisfies

$$S \equiv \frac{u_g}{u_f} > 1 - \alpha_g(\frac{N_f}{N_D}). \tag{27}$$

And the second constraint gives two conditions:

$$C_{3_o} \leq U_o \leq C_{4_o}, \tag{28a}$$

and

$$C_{3_o} - \kappa^2\nu_o\theta_o(U_o - C_{3_o}) \leq C_{a_o} \leq C_{4_o} + \kappa^2\nu_o\theta_o(C_{4_o} - U_o). \tag{28b}$$

For $\nu_o = 0$, the flow is stable for disturbances with any wavelength (λ) because eqn. (28b) becomes Whitham [17]'s stability condition, which is equivalent to eqn. (17). Since a limiting case of the stability condition is identical to the hyperbolicity condition, so the hyperbolicty condition is, in general, a necessary, but not sufficient, condition for stability.

In case of long wavelength limit ($\varkappa\theta_o \ll 1$), the wave speed (C_r) can be simplified to

$$C_r \fallingdotseq \begin{cases} C_{a_o} + \dfrac{\varkappa^2\theta_o^2(C_{4_o}-C_{3_o})^4}{16(2C_{a_o}-C_{3_o}-C_{4_o})} \\ C_{3_o}+C_{4_o}-C_{a_o} - \dfrac{\varkappa^2\theta_o^2(C_{4_o}-C_{3_o})^4}{16(2C_{a_o}-C_{3_o}-C_{4_o})} \end{cases} \tag{29}$$

and the temporal attenuation factor ($\varkappa C_i$) becomes for the first mode

$$(\varkappa C_i)_1 \fallingdotseq -\varkappa^2\theta_o(C_{a_o}-C_{3_o})(C_{4_o}-C_{a_o}) + \frac{1}{16}(C_{4_o}-C_{3_o})^4\varkappa^4\theta_o^3. \tag{30}$$

The temporal attenuation factor is always negative for the second mode so that this mode is strongly attenuated. It should be noted that the wave speed and the wave damping factor, defined by eqns. (29)~(30), are all dependent on the wave number even in the long wavelength limit.

The spatial damping of the void waves can be found by assuming that the wave number ($\varkappa$) is complex so that $\varkappa = \varkappa_R + i\varkappa_I$. Then a void fluctuation can be expressed by $\alpha \sim \delta\alpha \exp[-i(\varkappa z - \omega t)]$, where $\delta\alpha$ is the amplitude of void fluctuations. The imaginary wave number ($\varkappa_I$) can be expressed by

$$\varkappa_I = -\frac{1}{2\theta_o C_{3_o} C_{4_o}} [\, C_{a_o} \mp \Theta] \,, \tag{31}$$

where Θ is defined in the appendix. Here, we define

$$\beta \equiv \exp[\, \varkappa_I \Delta z] \tag{32}$$

as the "spatial gain factor". It indicates whether the waves grow or attenuate while flowing in the channel along the distance of Δz. This parameter is expected to be very useful for confirming the closure laws since it is a measurable quantity from experiments [9].

4. MOST UNSTABLE WAVES

The void waves propagate, in general, with a broad range of spectrum, but a major frequency component exists which is dominantly propagated. And it can be considered the so-called "most unstable waves" which will be more easily amplified than those with other frequency components.

The "most unstable waves" satisfy the following condition:

$$\frac{d}{d\varkappa}(\, \varkappa C_i \,) = 0, \tag{33}$$

and this gives the critical wave number ($\varkappa_c$) for most unstable waves, from eqn. (30), as follows:

$$\kappa_c^2 = \frac{8(C_{a_o}-C_{3_o})(C_{4_o}-C_{a_o})}{(C_{4_o}-C_{3_o})^4\theta_o^2} . \tag{34}$$

Then, the temporal attenuation factor and the wave propagation speed become

$$(\kappa C_i)_c = -\frac{4(C_{a_o}-C_{3_o})^2(C_{4_o}-C_{a_o})^2}{(C_{4_o}-C_{3_o})^4\theta_o} , \tag{35}$$

$$C_{r_c} = C_{a_o} + \frac{(C_{a_o}-C_{3_o})(C_{4_o}-C_{a_o})}{2(2C_{a_o}-C_{3_o}-C_{4_o})} , \tag{36}$$

respectively. It should be noted that both the propagation speed and the temporal attenuation factor are independent of the wave number. The wave propagation speed (C_{rc}) is, in general, larger than the lower-order wave speed, C_{a_o}, but it shows the value very close to C_{a_o}. Therefore, the measured wave speed should be the speed of the lower-order waves since, in actual flow circumstances, the waves with this most unstable frequency or wave number will be detected [9].

5. RESULTS AND DISCUSSION

Analytical model of the wave propagation properties, including generalized form of the wave parameters and those derived based on the concept of "most unstable waves", should be validated by comparing predicted results with experimental data. They include the data of Song et al. [9] where the naturally generated waves were investigated over a wide flow conditions, the data of Tournaire [6] in which frequency-dependent characteristics of void waves were well revealed, and those of Biesheuvel & Gorissen [4] where the naturally generated waves were observed in stagnant flow conditions.

Characteristics

The normalized characteristics, defined by eqn. (15), are shown in Fig. 1 for various values of the coefficients, C_{VM}, k and η. The hyperbolicity region is decreased as C_{VM} increases and k decreases, as previously observed [1~3]. But η does not affect the hyperbolicity as much. In Fig. 2, the hyperbolicity region is presented in terms of the critical void fraction, which satisfies the hyperbolicity-breaking condition. The hyperbolicity region is denoted by the region under the critical void curve in each case. As can be seen in Figs. 1(a) and 2, the hyperbolic region is strongly dependent on C_{VM} and it is decreased as C_{VM} increases.

For fixed value of the coefficients, C_{VM}, k and η, the critical void fraction is not affected much by the density number, N_p, over a wide range which corresponds to gas-liquid two-phase flow conditions. However, it decreases slowly as the density number is increased. This tendency is contrary to the experimental observations [18] such that the void fraction, at which the flow regime transition from dispersed particulate flow occurs, is much larger than in the gas-liquid flow case. This deviation between prediction and experiments may come from the fact that the momentum interactions between phases are not suitably taken into account in the physical modelling of the closure laws.

In Fig. 3, the critical void fraction is presented in terms of bubble sizes using Bataille et al [14]'s C_{VM} model expressed by eqn. (7a). The tendency observed from experiments [9] for D_b = 2.7, 3.8, 4.8 mm at j_f = 0.18 m/s, such that the bubble size has much influence on the development of bubble flow structures and its transition, can be

qualitatively well predicted with C_{VM} expressed in terms of the bubble size. In general, as the bubble size and C_{VM} are increased, the stable flow region is decreased.

Wave propagation speed

In Fig. 4, the wave propagation speed ($C_{r,}$), defined by eqn. (36) based upon the concept of "most unstable waves", is compared for the *standard* case of coefficients (C_{VM} = 0.5, k = 0.2, η = 0.25) with the data of Tournaire [6] at the imposed frequency of f = 0.6 Hz. Also, compared are the wave speed, $C_{a.w.}$, from the drift-flux model [16], and the wave speed, $C_{a.m.}$, from the empirical correlation of Mercadier [19].
The calculated values, in general, underpredict the wave speed. The results from the empirical correlation follow the experimental tendency better than the other two analytical models since the correlation came from the experimental condition, which is similar to Tournaire [6].

In Fig. 5, the predicted wave speed is compared with the experimental data [9] for D_b = 2.7, 3.8 and 4.8 mm at j_f = 0.18 m/s. The present model, denoted by $C_{r,}$, shows the same tendency as experimental data for three cases of bubble size. The calculated values, in general, overpredict the wave speed and the empirical correlation shows more unfavorable results than the other two models. For low liquid velocity conditions (j_f < 0.2 m/s), the predicted values by the present model are slightly larger than the measured value, but the deviation between the present model and experimental data [9] grows as void fraction is increased.

In Fig. 6, the present model, $C_{r,}$, is compared with the experimental data [4] for stagnant flow conditions. The analytical results from the present model and the drift-flux model slightly overpredict the tendency, but the empirical correlation shows very poor predictions at low void fraction.

When compared with the experimental data [4,5,9], the two analytical models can better predict the experimental observations than the empirical correlation, especially at the low void region where the closure laws adopted in the analytical model are valid for use.

Relaxation time

The relaxation time, θ_o, can be affected by the density number and C_{VM} as well as algebraic momentum source terms which include the interfacial drag force and wall friction. The relaxation time itself has some effects on the wave speed as well as the temporal and spatial damping factors. In Fig. 7, the relaxation time is calculated using the slip velocity from [9] at j_f = 0.12, 0.18, 0.275, 0.49 m/s with D_b = 2.7 mm. As the liquid flow increases, the relaxation time is decreased as observed by experiments [9] in terms of a flow time scale. And it is quite natural in view of its physical meaning.
In Fig. 7, also shown is the relaxation time calculated using the slip velocity from [4] for stagnant flow conditions under which the effect of liquid flow rate on the interactions between phases is eliminated. As void fraction increases, it is gradually increased, contrary to non-zero liquid flow conditions. By comparing this tendency with the above-mentioned decreasing tendency with void fraction, the predicted results reveal well the experimental observation [9] such that liquid flow rate greatly affects the wave propagation properties.

Wave damping factor

In Fig. 8, the temporal attenuation factor, xC_i, defined with eqn. (26b), is compared for several imposed frequencies of f = 0.6, 0.8, 1.0, 1.4, 2.0 Hz with the standard case of coefficients. The present damping model predicts an increasing attenuation with imposed frequency.

In Fig. 9(a), the spatial gain factor, defined by eqn. (32), is compared for several imposed frequencies of f = 0.6, 0.8, 1.0, 1.4, 2.0 Hz with the standard case of coefficients. As the frequency increases, the degree of spatial damping is increased, as observed in experiments [6, 7] where the imposed frequency very much affects the wave damping. In Fig. 9(b), the critical spatial gain factor, defined based on the "most unstable waves", is shown. It reveals quite well the tendency of wave damping even without using frequency information.

In Fig. 10, the critical spatial gain factor is shown for D_b = 2.7, 3.2 mm at j_f = 0.18 m/s. As the bubble size increases, the degree of spatial damping is shown to decrease, as observed by experiments [9]. The virtual mass coefficient affects very much the wave damping and the stability condition, as the bubble size does as observed in experiments [9]. If the bubble size effect on the flow phenomena is suitably included in the physical modelling of the momentum interaction terms, the analytical model could predict better the experimentally observed tendency. The spatial gain factor can predict qualitatively well the experimental observations on the wave damping, and it will be very useful for assessing the closure laws since it is a measurable quantity by experiments.

6. CONCLUSIONS

The analytical results on the system characteristics and the wave propagations are very sensitive to the closure laws on the momentum interactions, as previously observed. Especially, the virtual mass coefficient affects very much the hyperbolicity condition and the wave propagation properties.

The higher derivatives in the governing equation generally introduce a dependency of the wave propagation properties and the stability condition on the wave number. But the wave number dependency of the stability condition can be removed in the long wavelength limit. The consideration of algebraic terms only as momentum source terms and the assumption of the equal phasic pressure lead to the ill-posed problem.

The spatial gain factor is proposed to be used as an indicator to analytically quantify the degree of spatial damping, and it will be very useful for assessing the closure laws.

The relation between the hyperbolicity condition and the stability condition is analytically clarified. It is shown that the hyperbolicity condition is a necessary, but not sufficient condition for stability. Therefore, the analytical models should be, in general, hyperbolic in the parameter ranges where the void waves are stable.

From the concept of the "most unstable waves", the wave propagation properties could be evaluated independently of the wave number. This feature is expected to be very useful for analytically investigating the propagation characteristics for naturally generated void waves.

By comparing the analytical and experimental results on the spatial damping, it is possible to confirm the previous proposition such that the instability appearing from linear analysis corresponds to major transitions in the nature of the flow.

References

[1] C. Pauchon and S. Banerjee, "Interphase momentum interaction effects in the averaged multifield model: Part-II. kinematic waves and interfacial drag in bubbly flows", Int. J. Multiphase Flow 14 (1988)

[2] J.W. Park, D.A. Drew and R.T. Lahey, Jr., "Void wave dispersion in bubbly flows", Nuc. Eng. Des. 121, 1-10 (1990)

[3] R.T. Lahey, Jr., "Void wave propagation in two-phase flow", AIChE J. 37, 123-135 (1991)

[4] A. Biesheuvel and W.C. Gorissen, "Void fraction disturbances in a uniform bubbly fluid", Int. J. Multiphase Flow 16, 211-231 (1990)

[5] A. Matuszkiewicz, J.C. Flamand and J.A. Boure, "The bubbly-slug flow pattern transitions and instabilities of void fraction waves", Int. J. Multiphase Flow 13, 199-217 (1987)
[6] A. Tournaire, "Detection et etude des ondes de taux de vide en ecoulements diphasique a bulles jusqu'a la transition bulles-bouchons", Ph.D. thesis, Universite Scientifique et Medicale et Institute National Polytechnique de Grenoble (1987)
[7] J.M. Saiz-Jabardo and J.A. Bouré, "Experiments on void fraction waves", Int. J. Multiphase Flow 15, 483-493 (1989)
[8] J.W. Park, R.T. Lahey, Jr. and D.A. Drew, "The measurement of void waves in bubbly two-phase flows", Proc. NURETH-6, 1, 655-662 (1993)
[9] C.-H. Song, H.C. No and M.K. Chung, "Investigation of the bubble flow developments and its transition based on the instability of void fraction waves", Accepted for publication in Int. J. Multiphase Flow (1994)
[10] S. Banerjee and A.M.C. Chan, "Separated flow model, (I); analysis of the averaged and local instantaneous formulations", Int. J. Multiphase Flow 6, 1-24 (1980)
[11] D.A. Drew and R.T. Lahey, Jr., "Application of general consitutive principles to the derivation of multidimensional two-phase flow equations", Int. J. Multiphase Flow 5, 243-264 (1979)
[12] O. Levenspiel, Chemical Reaction Engineering, Wiley, New York (1968)
[13] C. Pauchon and P. Smereka, "Momentum interactions in dispersed flow: an averaging and a variational approach", Int. J. Multiphase Flow 18, 65-87 (1992)
[14] J. Bataille, M. Lance and J.L. Marie, "Some aspects of the modelling of bubbly flows", *In* Phase-Interface Phenomena in Multiphase Flow, Ed. by G.F. Hewitt et al., Hemisphere, pp. 179-194 (1991)
[15] N. Zuber, "On the dispersed two-phase flow in the laminar flow regime", Chem. Eng. & Sci. 19, 897-917 (1964)
[16] G.B. Wallis, One-Dimensional Two-Phase Flow, McGraw-Hill (1969)
[17] G.B. Whitham, Linear and Nonlinear Waves, John Wiley & Sons (1974)
[18] H.K. Kytomaa and C.E. Brennen, "Small amplitude kinematic wave propagation in two-components media", Int. J. Multiphase Flow 17, 13-26 (1991)
[19] Y. Mercadier, "Contribution à l'etude des propagations de perturbations de taux de vide dans les ecoulements diphasiques eau-air à bulles", Ph.D. thesis, Université Scientifique et Médicale et Institut National Polytechnique de Grenoble, Grenoble, France (1981)

NOMENCLATURE

a : Acceleration, m/sec^2
C : Wave propagation speed, m/sec
D : Flow channel diameter, m
D_b : Volume-equivalent bubble diameter, m or mm
f : Frequency, Hz, or Friction factor, *dimensionless*
g : Gravitational constant, m/sec^2
j : Mixture volumetric flux, m/s
j_f : Liquid superficial velocity, m/s
j_{gf} : Drift flux, m/s
k : Coefficient in the model for Reynolds stress, *dimensionless*
N : Dimensionless number, *dimensionless*
P : Pressure, *bar*
t : Time, *sec*
u : Phasic velocity, m/sec
V : Volume, m^3
z : Axial location, m

Greek Symbols

α	: Void fraction, *dimensionless* or *%*
β	: Spatial gain factor, *dimensionless*
η	: Coefficient in the model for interfacial pressure difference
i	: Imaginary number
κ	: Wave number, $1/m$
ρ	: Density, kg/m^3
τ	: Shear stress, N/m^2
ω	: Angular frequency, *radian*

Superscripts and Subscripts

$+$	: Dimensionless value	c	: Critical value
ex	: Experimental value	f	: Liquid phase
G	: Gravitational force term	g	: Gas phase
I	: Interfacial force term	i	: Interface between phases
k	: Index to denote a k-phase	o	: Value at reference condition
r	: Relative value	VM	: Virtual mass force term
W	: Wall force term		

Appendix : Expression for unknowns

$$\Phi = [\ \alpha_g,\ u_g^+,\ u_f^+\ ]^{-1},$$

$$\mathbf{A} = \begin{bmatrix} 1 & 0 & 0 \\ 1 & 0 & 0 \\ 0 & A_1 & -A_2 \end{bmatrix}, \quad \mathbf{B} = \begin{bmatrix} u_g^+ & \alpha_g & 0 \\ u_f^+ & 0 & -\alpha_f \\ B_1 u_r^{+2} & A_1 u_g^+ - B_2 u_r^+ & -A_2 u_f^+ + B_2 u_r^+ \end{bmatrix},$$

$$\mathbf{C} = [\ 0,\ 0,\ F_o\ ]^{-1},$$

$$A_1 = N_\rho + \frac{C_{VM}}{\alpha_f}, \qquad A_2 = 1 + \frac{C_{VM}}{\alpha_f},$$

$$B_1 = \eta + (2k-\eta)\frac{\alpha_g}{\alpha_f} + \frac{N_\sigma}{\alpha_f u_r^{+2}}, \qquad B_2 = 2\alpha_g(k-\eta),$$

$$A = \frac{\alpha_g}{\alpha_f}(1+\frac{C_{VM}}{\alpha_f}) - \frac{\alpha_f}{\alpha_g}(N_\rho + \frac{C_{VM}}{\alpha_f}),$$

$$B = -\frac{\alpha_f}{\alpha_g} u_g^+ (N_\rho + \frac{C_{VM}}{\alpha_f}) + \frac{\alpha_g}{\alpha_f} u_f^+ (1+\frac{C_{VM}}{\alpha_f}) + \eta + (2k-\eta)\frac{\alpha_g}{\alpha_f} + \frac{N_\sigma}{\alpha_f} + \frac{2(\alpha_f-\alpha_g)(k-\eta)}{\alpha_f \alpha_g},$$

$$D = (N_\rho + \frac{C_{VM}}{\alpha_f})/\alpha_g + (1+\frac{C_{VM}}{\alpha_f})/\alpha_f,$$

$$E = \frac{u_g^+}{\alpha_g}(N_\rho + \frac{C_{VM}}{\alpha_f}) + \frac{u_f^+}{\alpha_f}(1+\frac{C_{VM}}{\alpha_f}) - \frac{2(k-\eta)}{\alpha_f},$$

$$F = \frac{1-N_\rho}{Fr_o^2} - \frac{N_D}{\alpha_f} u_r^{+2} + \frac{N_f}{\alpha_f} u_f^{+2}.$$

$$L_{1o} = -\frac{N_T}{a_f}, \qquad L_{2o} = -N_T\frac{a_g}{a_f},$$

$$K_1 = \left(\frac{\partial F}{\partial \dot{j}_{wf}}\right)_o, \qquad K_2 = j_o\left(\frac{\partial F}{\partial j_{wf}}\right)_o - \left(\frac{\partial F}{\partial a}\right)_o,$$

$$K_3 = -D_o, \qquad K_4 = A_o - j_o D_o - E_o,$$

$$K_5 = B_o - j_o E_o.$$

$$\overline{C} = \frac{1}{2}(C_{3_o} + C_{4_o}), \quad P = \frac{1 + x^2\nu_o\theta_o}{x\theta_o},$$

$$Q = \frac{1}{4}(C_{4_o} - C_{3_o})^2, \quad R = \frac{1}{x\theta_o}[\,(C_{a_o} - \overline{C}) + x^2\nu_o\theta_o(U_o - \overline{C})\,],$$

$$\Theta = [\,-\frac{1}{2}\Delta + \frac{1}{2}(\Delta^2 + \Lambda^2)^{\frac{1}{2}}\,]^{\frac{1}{2}},$$

$$\Delta = \theta_o^2(C_{3_o} + C_{4_o})^2\omega^2 - C_{a_o}{}^2 - 4\theta_o^2 C_{3_o}C_{4_o}\omega^2.$$

$$\Lambda = -2\theta_o C_{a_o}(C_{3_o} + C_{4_o})\omega + 4\theta_o C_{3_o}C_{4_o}\omega$$

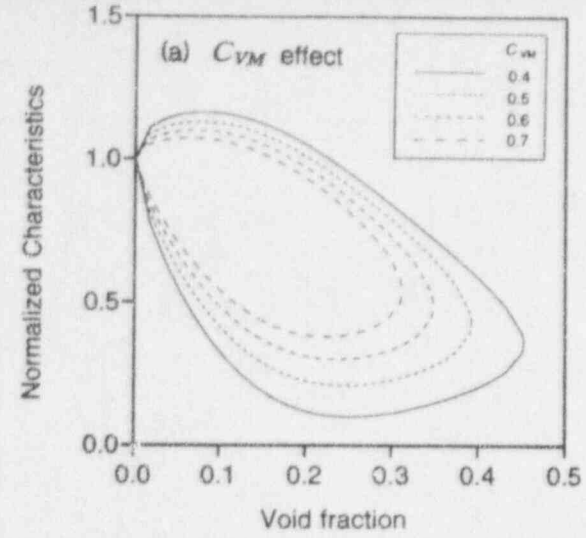

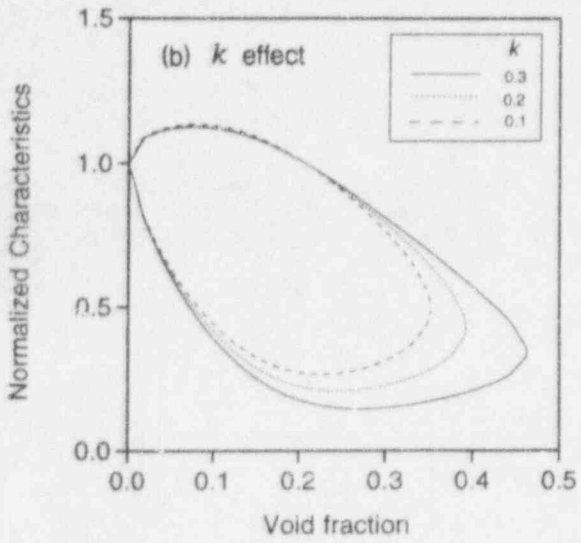

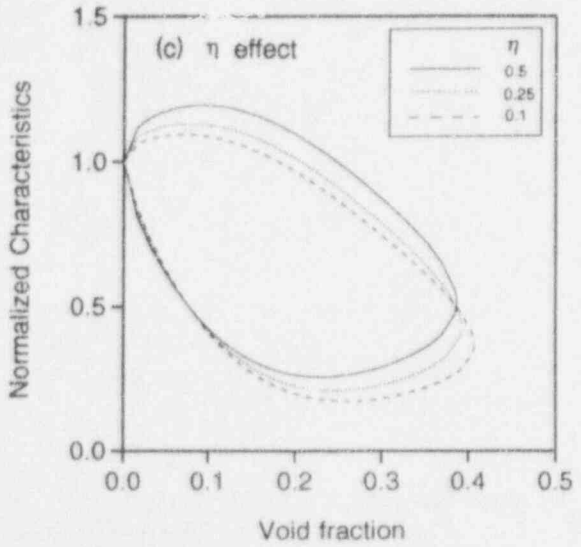

Fig. 1 Variation of the system characteristics

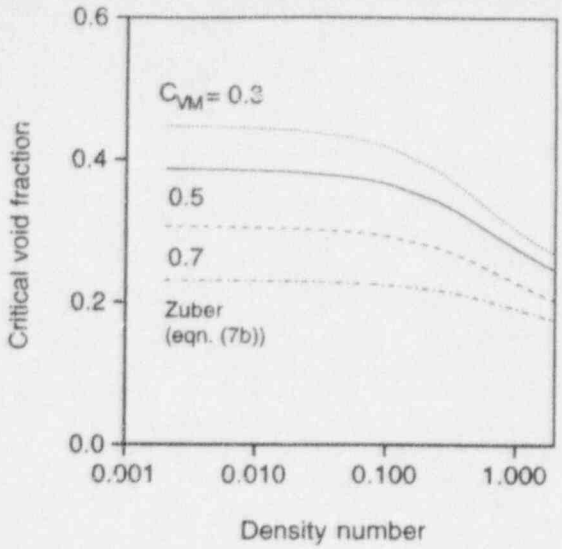

Fig. 2 C_{VM} effect on the critical void fraction

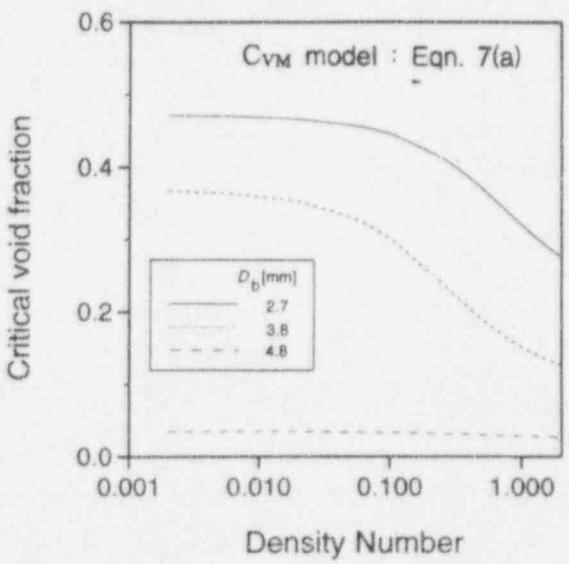

Fig. 3 Bubble size effect on the critical void fraction

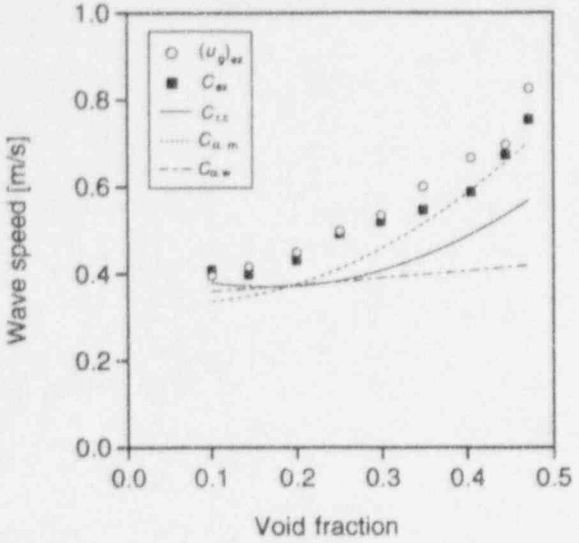

Fig. 4 Comparison of the predicted and measured wave speeds : data from Tournaire [6] for f = 0.6 Hz

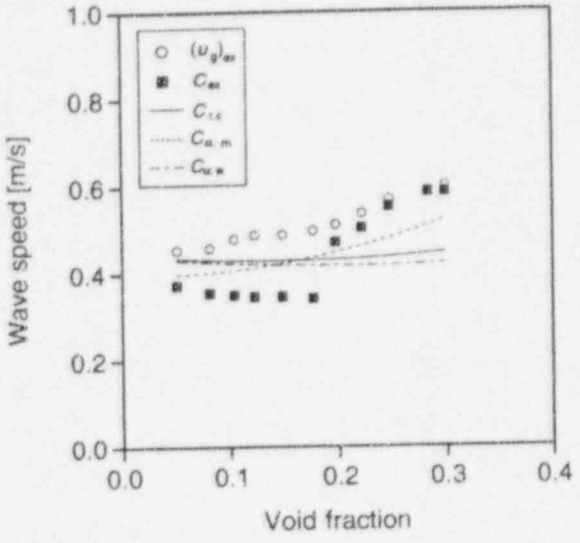

Fig. 5(b) Comparison of the predicted and measured wave speeds (II): data from Song et al. [9] for j_f = 0.18 m/s, D_b = 3.8 mm

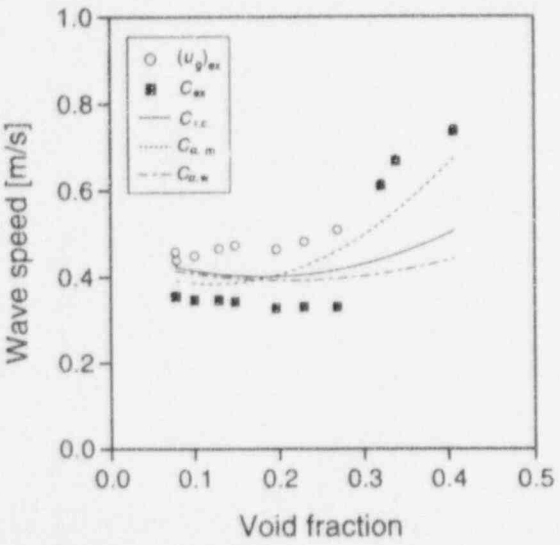

Fig. 5(a) Comparison of the predicted and measured wave speeds (I): data from Song et al. [9] for j_f = 0.18 m/s, D_b = 2.7 mm

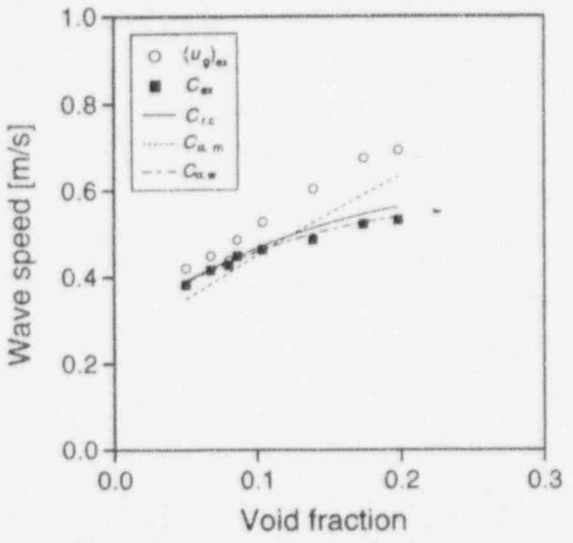

Fig. 5(c) Comparison of the predicted and measured wave speeds (III): data from Song et al. [9] for j_f = 0.18 m/s, D_b = 4.8 mm

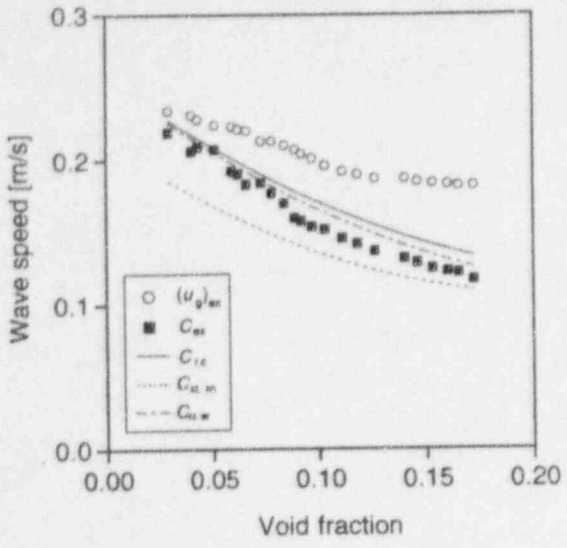

Fig. 6 Comparison of the predicted and measured wave speeds: data from Biesheuvel & Gorissen [4] for stagnant flow conditions

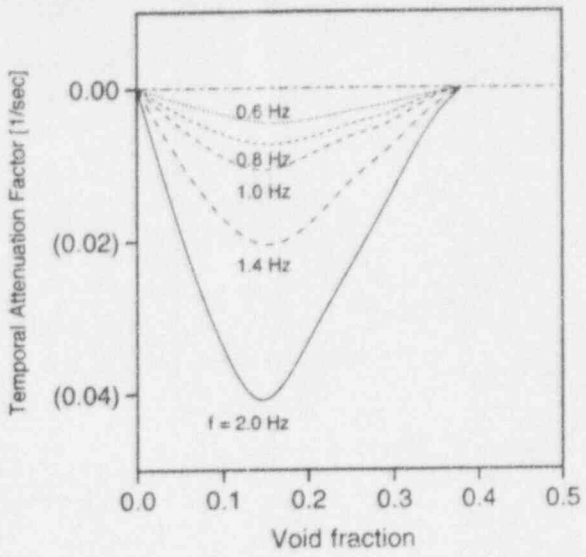

Fig. 8 Effect of the imposed frequency on the temporal attenuation factor: slip velocity from Tournaire [6]

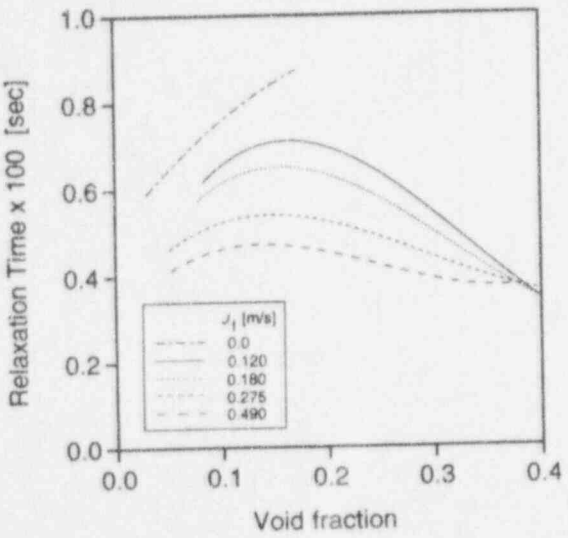

Fig. 7 Effect of the liquid flow rate on the relaxation time: slip velocity from Song et al. [9] and Biesheuvel & Gorissen [4]

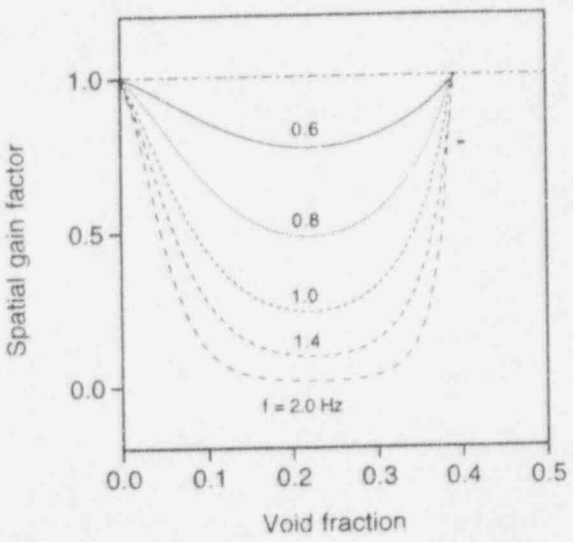

Fig. 9(a) Effect of the imposed frequency on the spatial gain factor: slip velocity from Tournaire [6]

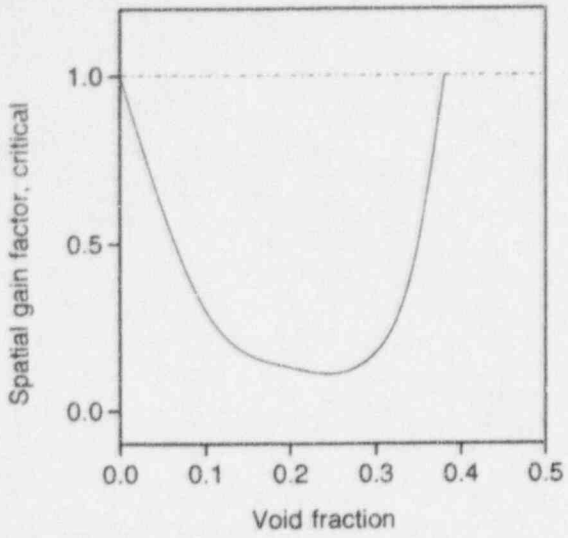

Fig. 9(b) Critical spatial gain factor : slip velocity from Tournaire [6]

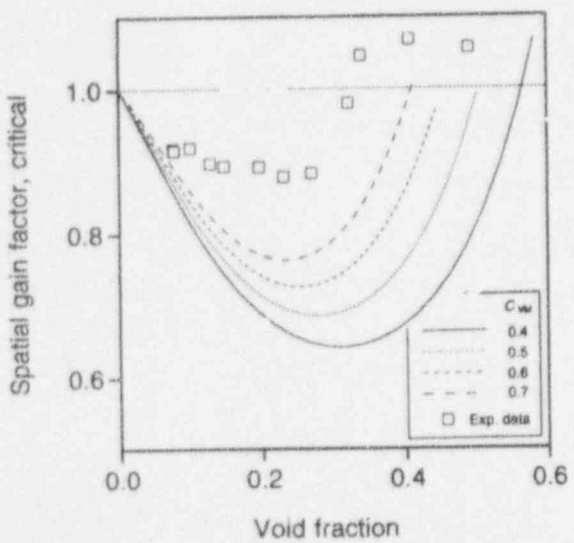

Fig. 10(a) Effect of the virtual mass coefficient on the critical spatial gain factor (I): slip velocity from Song et al. [9] for j_f = 0.18 m/s, D_b = 2.7 mm

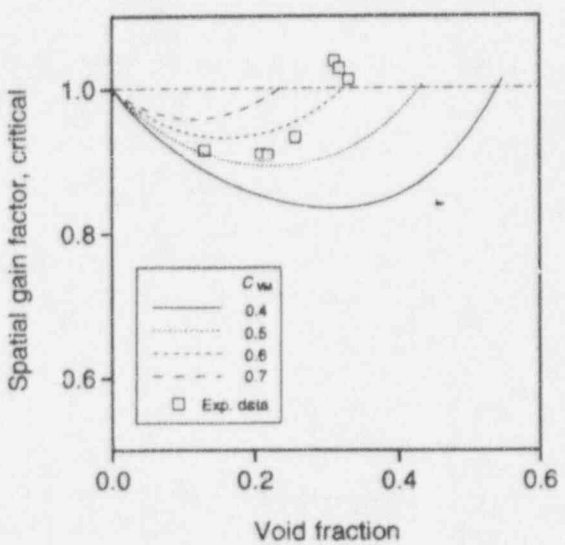

Fig. 10(b) Effect of the virtual mass coefficient on the critical spatial gain factor (II): slip velocity from Song et al. [9] for j_f = 0.18 m/s, D_b = 3.2 mm

Modeling and Numerical Simulation of Oscillatory Two-Phase Flows, with Application to Boiling Water Nuclear Reactors

Mauricio Pinheiro Rosa
Instituto de Estudos Avancados - CTA
Sao Paolo, Brazil

Michael Z. Podowski
Department of Nuclear Engineering and Engineering Physics
Rensselaer Polytechnic Institute
Troy, NY 12180-3590, USA

ABSTRACT

This paper is concerned with the analysis of dynamics and stability of boiling channels and systems. The specific objectives are two-fold. One of them is to present the results of a study aimed at analyzing the effects of various modeling concepts and numerical approaches on the transient response and stability of parallel boiling channels. The other objective is to investigate the effect of closed-loop feedback on stability of a boiling water reactor (BWR). Various modeling and computational issues for parallel boiling channels are discussed, such as: the impact of the numerical discretization scheme for the node containing the moving boiling boundary on the convergence and accuracy of computations, and the effects of subcooled boiling and other two-phase flow phenomena on the predictions of marginal stability conditions. Furthermore, the effects are analyzed of local loss coefficients around the recirculation loop of a boiling water reactor on stability of the reactor system. An apparent paradox is explained concerning the impact of changing single-phase losses on loop stability. The calculations have been performed using the DYNOBOSS computer code. The results of DYNOBOSS validation against other computer codes and experimental data are shown.

1. INTRODUCTION

The accuracy of computer simulations of the dynamics of two-phase systems and components depends on the combined effects of modeling assumptions and numerical methods used. Usually, the modeling framework is based on a set of postulated assumptions validated against selected experimental data. However, because of the complexity of the mechanisms governing two-phase flow and heat transfer, several different assumptions can be used to model a particular phenomenon. Examples include: kinematic nonequilibrium (phasic slip), thermodynamic equilibrium (subcooled boiling), wall effect (two-phase flow friction), and others. Although experimental evidence can be found for each model to confirm its validity, the issue of how different models compare to each other has not been fully investigated before; in particular, in regard to nonsteady-state and transient situations.

A similar conclusion can be drawn by studying the developments in the computational techniques for application in two-phase flows. The individual numerical methods are commonly related to specific (fixed) modeling assumptions and their accuracy is tested for particular geometries and situations. Needless to say, for some situations the results of simulations are not very sensitive to the modeling assumptions and numerical method used, whereas for some other conditions the calculations may substantially change as a result of using different assumptions or modified numerical schemes. The latter is of particular importance to complex systems, such as nuclear reactors, where the superposition of several physical phenomena of different nature, combined with possible nonlinear interactions between system components and uncertainties in plant data, make the goal of achieving accurate predictions of system dynamics a very challenging task.

The objectives of this paper are two-fold. One of them is to present the results of a study aimed at analyzing the effects of various modeling concepts and numerical approaches on dynamics and stability of parallel boiling channels. The other objective is to investigate the effect of closed-loop feedback on stability of a boiling water reactor (BWR).

2. FLOW-INDUCED OSCILLATIONS IN BOILING CHANNELS

Let us consider a system of parallel boiling channels connected between two large plena, one at the inlet and the other at the exit, as shown in Fig. 1(a). If the pressure drop between the plena remains constant even if the flow rates at the inlet to some channels oscillate, each oscillating channel can be analyzed separately using the (given) constant pressure drop as a boundary condition. A similar effect can be obtained by connecting a heated boiling channel in parallel with a single-phase adiabatic bypass channel (see Fig. 1(b)). If the bypass flow rate is much larger than that at the inlet to the boiling channel, the pressure drop between the plena will remain constant even if the channel inlet flow is subjected to oscillations. Assuming that subcooled liquid fluid enters the heated channel, the total length of the channel can be divided into two sections, a single-phase nonboiling section at the bottom and a two-phase boiling section in the upper part. Using a one-dimensional model of time-dependent flow and heat transfer phenomena along the channel, the moving boiling boundary can be evaluated as the location where the liquid enthalpy reaches the onset-of-boiling enthalpy, $h_l(z_B) = h_{l,B}$. This characteristic enthalpy is calculated differently, depending on the boiling model used in the analysis. For example, if subcooled boiling is neglected, $h_{l,B} = h_f$, whereas if subcooled boiling is accounted for, $h_{l,B}$ is typically defined as the location of the onset of significant void, $h_{l,B} = h_{l,d}$. In order to analyze the effects of subcooled boiling on the predicted dynamic response of a boiling channel, a drift-flux model has been used in the present analysis [1].

The actual form of a one-dimensional model of two-phase flow depends on the specific modeling assumptions made and the form of closure relations used [2]. Specifically, the number of first principle equations may vary from six for a full two-fluid model to three for a homogeneous equilibrium model (HEM). In any case, the continuity equations for both phases are usually used, either in their basic form:

for liquid phase

$$\frac{\partial\left[\rho_l(1-\langle\alpha\rangle)\right]}{\partial t}+\frac{\partial(G_l)}{\partial z}=-\Gamma \tag{1}$$

for vapor phase

$$\frac{\partial\left[\rho_v\langle\alpha\rangle\right]}{\partial t}+\frac{\partial(G_v)}{\partial z}=\Gamma \tag{2}$$

or by transforming them into the following equations:

void propagation equation

$$\frac{\partial\langle\alpha\rangle}{\partial t}+\langle u_g\rangle\frac{\partial\langle\alpha\rangle}{\partial z}=\upsilon_g\left[\Gamma-\frac{d\rho_g}{dp}\left(\langle\alpha\rangle\frac{\partial p}{\partial t}+\langle j_g\rangle\frac{\partial p}{\partial z}\right)\right]-\langle\alpha\rangle\frac{\partial\langle u_g\rangle}{\partial z} \tag{3}$$

volumetric flow continuity equation

$$\frac{\partial\langle j\rangle}{\partial z}=\upsilon_{fg}\Gamma-\left(\upsilon_g\langle\alpha\rangle\frac{d\rho_g}{dp}+\upsilon_f(1-\langle\alpha\rangle)\frac{d\rho_f}{dp}\right)\frac{\partial p}{\partial t}-\left(\upsilon_g\langle j_g\rangle\frac{d\rho_g}{dp}+\upsilon_f\langle j_f\rangle\frac{d\rho_f}{dp}\right)\frac{\partial p}{\partial z} \tag{4}$$

It has been assumed in Eq.(4) that $\rho_l=\rho_f$. In Eqs.(1)-(4), Γ is the volumetric phase change rate. In the case when thermodynamic equilibrium between the liquid and vapor phases is assumed (e.g. in saturated boiling, when it can be assumed that $T_l=T_v=T_{sat}$), Γ can be evaluated analytically as a function of the wall heat flux, variable system pressure and local void fraction [2]. Since a one-dimensional framework does not allow for a rigorous mathematical treatment of local lateral phenomena, a phenomenological closure laws is normally used to express the wall heat flux partitioning between nonboiling and boiling components [4]. In the analysis of boiling channel dynamics, the major thermodynamic nonequilibrium effect between the phases is concerned with subcooled boiling. The mathematical formulation used to account for this phenomenon depends on the modeling assumptions. Two commonly used options are: (a) a profile-fit model [3] in which the flow quality, $x=G_g/G$, is related to the equilibrium quality, x_e, using an algebraic relationship of the form, $x/x_e=1-\Psi(x_{e,d}/x_e)$, where $x_{e,d}$ is the equilibrium quality at the significant void detachment point, and, (b) a mechanistic model [4] using a first principle energy conservation equation, typically for either the mixture

$$\frac{\partial\langle\overline{\rho h}\rangle}{\partial t}+\frac{\partial(G\langle h\rangle)}{\partial z}=\frac{q'}{A_{xs}}+\frac{\partial p}{\partial t} \tag{5}$$

or for the liquid phase

$$\left[\rho_l(1-\langle\alpha\rangle)\right]\frac{\partial h_l}{\partial t}+\rho_l\langle j_l\rangle\frac{\partial h_l}{\partial z}+\Gamma(h_g-h_l)=\frac{q'}{A_{xs}}+\left(1-\rho_g\langle\alpha\rangle\frac{dh_g}{dp}\right)\frac{\partial p}{\partial t}-Gx\frac{dh_g}{dp}\frac{\partial p}{\partial z} \tag{6}$$

where $\langle\overline{\rho h}\rangle = \rho_l h_l(1-\langle\alpha\rangle) + \rho_g h_g\langle\alpha\rangle$, $G\langle h\rangle = G_l h_l + G_g h_g$, and an empirical correlation [4] is used to partition the wall heat rate into the nonboling heat convection and the boiling heat flux.

In the case of drift-flux model, the phasic slip is expressed using an algebraic closure law, so that the mixture momentum equation is sufficient to close the model. This equation can be written as

$$\frac{\partial G}{\partial t} + \frac{\partial}{\partial z}\left(\frac{G^2}{\langle\rho'\rangle}\right) + f\frac{\phi_{lo}^2}{D_H} + \sum_k K_k \phi_k \delta(z - z_k) + \langle\rho\rangle g = -\frac{\partial p}{\partial z} \qquad (7(6))$$

where $G = \rho_l u_l(1-\langle\alpha\rangle) + \rho_g u_g\langle\alpha\rangle$, $\langle\rho'\rangle = [\rho_l u_l^2(1-\langle\alpha\rangle) + \rho_g u_g^2\langle\alpha\rangle]/G$, $\langle\rho\rangle = \rho_l(1-\langle\alpha\rangle) + \rho_g\langle\alpha\rangle$, and δ is the Dirac's delta used here to account for local pressure losses (such as channel inlet and exit, or due to spacers and orifices) and the remaining notation is conventional.

Three options are accounted for in the model regarding subcooled boiling: a profile-fit model of subcooled boiling, a mechanistic model, and a bulk boiling model in which subcooled boiling is ignored. The channel has been divided into a specified number of nodes of equal length, as shown in Fig. 2. The numerical methodology used to solve the combined mass, energy and momentum equations [5] allows for varying the degree of implicitness, both spatial and temporal, in order to optimize the efficiency of the method (i.e., good accuracy combined with fast convergence). One of the most important modeling/numerical issues turns out to be the approach used to evaluate the boiling boundary. As can be seen in Fig. 3, for all three models mentioned above, the onset of boiling results in a sudden increase in the cross-section-averaged void fraction (i.e. $d\langle\alpha\rangle/dz = 0$ at $z = z_B-$ and $d\langle\alpha\rangle/dz > 0$ at $z = z_B+$), although to a different degree for each model. This is due to the ignoring the presence of small amount of vapor neat the channel wall upstream from the significant void detachment point, z_B. During transients, this discontinuity travels along the channel according to the changing local liquid enthalpy. For any fixed spatial discretization of the channel, such as that shown in Fig. 2, the boiling boundary may move from one node to another along the channel, and it is important that a smooth transition across nodal boundaries be preserved by the model (for details, see Ref 5).

A typical result of calculations for an oscillatory transient using a bulk boiling model is shown in Fig. 4. As can be seen there, the position of the boiling boundary oscillates between three nodes. As a result of this, the nodal volumetric flux (superficial velocity) of the mixture at the interfaces between these nodes undergoes asymmetrical oscillations, where the effect of intermittently occurring phase change is superimposed on the single-phase flow oscillations.

Based on the extensive numerical analysis [5] it has been shown that the modeling of the node containing the moving interface may have a significant effect on the accuracy and convergence of the overall boiling channel model. As an illustration, Fig. 5 shows the results of calculations for two models with the only difference between them being a different treatment of the transition node. In the "basic' case, the nodal parameters in this node were evaluated by length-weighted averaging over the instantaneous lengths of the nonboiling and boiling sections of the

node. In the 'improved' case, the transition node was sub-divided into the single-phase and two-phase segments, and the time-derivative of the boiling boundary was explicitly accounted for [5]. Whereas if a fine nodalization scheme is used both methods converge to the same result, it is clear that the improved method is much more efficient. Based on this and other tests, it can be concluded that applying a more rigorous approach to the transition (single) node may reduce by a factor of two (or even more) the total number of nodes needed to obtain accurate results.

The model discussed above has been numerically implemented as a FORTRAN code, *DYNOBOSS* [6] (*DYNAMICS OF NONLINEAR BOILING SYSTEMS*). Since the main purpose of this model has been to provide an accurate tool for the analysis of oscillatory transients and instabilities in boiling systems in general and boiling water nuclear reactors (BWR) in particular, the model testing included both the numerical methodology and the modeling concepts. Regarding the latter issue, the parallel channel model in *DYNOBOSS* has been compared against other models and experimental data. In particular, the results of a comparison against two frequency-domain models/computer codes, *NUFREQ-NP* [7] and *LINSTAB* [8], are shown in Fig. 6. Both results present marginal stability lines for a uniformly heated channel using the N_{PCH}-N_{SUB} map, where N_{PCH} and N_{SUB} are, respectively, the phase-change number and the subcooling number, defined as

$$N_{SUB} = \frac{(h_f - h_{IN})\,\vartheta_{fg}}{\vartheta_f h_{fg}} \quad , \qquad N_{PCH} = \frac{q' L_H \vartheta_{fg}}{u_{IN,o} A_{xs} h_{fg}}$$

In both *NUFREQ-NP* and *LINSTAB* the marginal stability line is obtained by analytically solving the linearized governing equations and using them to obtain system transfer function(s). Since predicting the marginal stability conditions is a very demanding test for any time-domain direct-interaction code using a full nonlinear model of two-phase flow (for example, see Ref. 9], the agreement shown in Fig. 6 clearly demonstrates the consistency and accuracy of the present method.

The testing of physical models in *DYNOBOSS* included a comparison of the results obtained using different modeling assumptions against each other and against experimental data. Fig. 7 shows the effect of subcooled boiling on the response of a boiling channel near the marginal stability line for various operating conditions. As can be seen, ignoring subcooled boiling has a destabilizing effect on the predictions. On the other hand, a comparison between the profile-fit and mechanistic models of subcooled boiling indicates that they yield similar results for low subcooling numbers but larger differences develop when N_{SUB} increases. It is interesting to notice that the mechanistic model always shows more stable oscillations than the other two models.

The impact of different models of subcooled boiling and phasic slip on the predicted onset of instability conditions in parallel channel systems is illustrated in Fig. 8, including a comparison against the experimental data of Saha [10]. As can be seen, whereas subcooled boiling has a small effect for high N_{SUB}, this phenomenon becomes very important for low subcoolings and its inclusion significantly improves the predictive capabilities of the present model. The effect of phasic slip is accounted for in *DYNOBOSS* by using the EPRI correlations [11] for the drift flux

parameters, C_o and V_{gj}. Again, it is shown in Fig. 8 that using local space- and time-dependent parameters improves agreement between the calculations and the data, as compared to using constant average drift-flux parameters corresponding to the steady-state system operating conditions.

3. LOOP FEEDBACK EFECTS ON BWR STABILITY

In most industrial applications, including boiling water nuclear reactors, parallel boiling channels are incorporated into closed loop systems. The dynamic behavior of boiling systems depends on their geometry, hydraulic characteristics (local pressure losses) and operating conditions. In particular, such systems may experience self-sustained oscillations caused by flow-induced density-wave instabilities. Several instability modes have been identified to date, including parallel channel instabilities, channel-to-channel instabilities and loop instabilities [2]. The former two modes are concerned with oscillations occurring in, or between, multiple channels with common inlet and exits. It is known that in either case an increase in the channel inlet (single-phase) pressure loss coefficient stabilizes the channels, whereas an increase in the exit (two-phase) loss coefficient destabilizes them. These effects are reflected in shifting the marginal stability line towards lower-heat-flux/higher-flow-rate regions, as well as in increasing the amplitude of oscillations of an already unstable channel (or channels) [2].

The stabilizing/destabilizing effects of, respectively, single-phase and two-phase local loss coefficients are commonly extended to the entire boiling loops. Rigorously speaking, however, the above conclusions apply only to the situations in which the external portion of the loop remains stable and, thus, there is no feedback between the conditions downstream of the channels and the parameters of the fluid entering the channels. Since the identification of appropriate and effective measures to stabilize boiling systems is an issue of considerable practical importance, an analysis into this effect has been performed for a boiling water reactor (BWR) loop using the *DYNOBOSS* code. A schematic of the BWR loop used for this purpose is shown in Fig. 9. The overall model consists of several interrelated models, including: boiling channels in the reactor core, transient heat conduction in reactor fuel elements, core neutronics (including the void and Doppler reactivity feedback effects), upper plenum, riser and steam separator, multi-sectional downcomer, recirculation pumps and lower plenum. The system components external to the reactor vessel are not modelled, so that the steam line pressure and feedwater parameters are used as input. Since the time constants for the in-vessel flow and heat transfer phenomena are small compared to those in the ex-vessel portion of the system, ignoring the feedback effect of the latter does not affect loop stability.

For the purpose of this analysis the reactor was assumed to operate in a natural circulation mode, producing approximately 50% rated power and 28% rated flow. At these operating conditions the reactor was marginally stable. In the first series of tests, the effect was investigated of increasing two-phase pressure loss on reactor stability. Several cases were studied, including an increase in the two-phase local pressure loss multiplier, higher loss coefficients of the fuel element spacers and at the core exit, and a lower steam separator loss coefficient. The results are shown in Fig. 10. They clearly indicate that the same trend occur in all cases. Hence, it can be concluded that any increase in the two-phase pressure losses destabilizes the BWR loop.

The second series of tests was focused on the effect of pressure loss coefficients in the single -phase portion of the BWR recirculation loop. Since liquid water is nearly incompressible (especially, since its temperature in different sections of the loop varies only slightly), the trend is independent of the location of the changed local loss coefficient. In the present case, the effect of the downcomer loss coefficient, denote here as $K_{l\phi}$, on system response was investigated. Two series of runs were performed. In one of them the downcomer loss coefficient was first decreased and then increased by 20%. The results are shown in Fig. 11(a). Surprisingly, the observed trend was opposite to what was expected, i.e. an increase in the loss coefficient destabilized the system whereas a lower loss coefficient yielded stable results. In order to check the effect of the magnitude of the change on the results, similar calculations were performed for $K_{l\phi}$ decreased and increased by a factor of two. As shown in Fig. 11(b), this time the reactor became stable for a higher $K_{l\phi}$ and unstable when this coefficient was reduced, both as expected. A possible explanation of the 'anomaly' shown in Fig. 11(a) was related to certain loop feedback effects. In order to identify the specific reasons, tests were conducted in which the actual calculated water enthalpy (temperature) at the inlet to the core was disregarded, and a constant steady-state value was used instead. A comparison between the results of these tests and the corresponding results obtained before for the 20% reduction/increase in the downcomer loss coefficient is shown in Fig. 12. As can be seen, in both cases the results with and without the inlet enthalpy feedback remain the same for about 30 s. Later, the case with feedback develops a trend opposite to that without feedback. The time at which the results start bifurcating corresponds to the residence time of the coolant flowing around the loop. Hence, it is clear that as long as the coolant enthalpy feedback is negligible, the effect of single-phase pressure loss coefficient on loop dynamics is the same as for parallel boiling channels. The effect of thermal feedback in the closed loop reactor system depends on the phase of core inlet enthalpy oscillations relative to the inlet flow oscillations. If an increase in the single-phase loss coefficient shifts these two variables from the in-phase mode in the marginally-stable case toward the mode in which the enthalpy oscillations lag behind the flow oscillations (by about 45° if $K_{l\phi} = 1.2$), the system becomes unstable. On the other hand, if the enthalpy oscillations precede those in core inlet flow rate (again, by about 45° if $K_{l\phi} = 0.8$), the BWR loop stabilizes. It is interesting to notice that this thermal feedback, although significant for small changes around the marginal stability line, is quickly overcome by the effect of increasing (or decreasing) flow resistance for large changes in $K_{l\phi}$ (see Fig. 11(b)).

4. CONCLUSIONS

The results have been presented of the analysis of dynamics and stability of boiling channels and systems. Various modeling and computational issues for parallel boiling channels have been discussed. In particular, the impact has been shown of the numerical discretization scheme for the node containing the moving boiling boundary on the convergence and accuracy of computations. Also, the effects of subcooled boiling and other two-phase flow phenomena on the predictions of marginal stability conditions have been investigated using the DYNOBOSS computer code. The results of DYNOBOSS validation against other computer codes and experimental data have been shown.

Furthermore, the effects have been analyzed of local loss coefficients around the recirculation loop of a boiling water reactor on stability of the reactor system. An apparent paradox has been

explained related to the unexpected impact of changing single-phase losses on loop stability.

REFERENCES

1. Zuber, N. and Findley, J.A., "Average Volumetric Concentration in Two-Phase Flow Systems", J. Heat Transfer, 1965.
2. Podowski, M. Z., "Instabilities in Two-Phase Systems", in *Boiling Heat Transfer - Modern Developments and Advances, R.T. Lahey, Jr.-ed.*, Elsevier Publishing Corporation, 1994.
3. Levy, S., "Forced Convection Subcooled Boiling - Prediction of Vapor Volumetric Fraction", GEAP-5157, General Electric Company, 1966.
4. Lahey, R.T., Jr. and Moody, F., "The Thermal-Hydraulics of a Boiling Water Reactor", ANS, 1977.
5. Pinheiro Rosa, M. and Podowski, M.Z., "Modeling And Computational Issues in the Analysis of Nonlinear Effects in Boiling Channel Instabilities", Proceedings of the 2nd Conference on Multiphase Flow, Kyoto, Japan, 1995 (in print).
6. Pinheiro Rosa, "Nonlinear Dynamics and Stability Analysis of Two-Phase Flow Systems, with Application to Boiling Water Nuclear Reactors", Ph.D. Thesis, Rensselaer Polytechnic Institute, Troy, NY, 1994.
7. Peng, S. J., Podowski, M. Z., Lahey, Jr., R. T. and Becker M., "NUFREQ-NP: A Computer Code for the Stability Analysis of Boiling Water Nuclear Reactors", *Nucl. Sci. & Eng.*, 88, 3, 1984.
8. Podowski, M. Z., and Zhou, J., "Hydrodynamic Stability Analysis of an Industrial Two-Phase Thermosyphon Heat Rejection System", ANS Transactions, Vol. 66, 1993.
9. Rohatgi, U.S., Mallen, A.N., Cheng, H.S. and Wulff, W., "Validation of the Engineering Plant Analyzer Methodology with Peach Bottom 2 Stability Tests", *Nucl. Eng. Des.*, 151, 1994.
10. Saha P., "Thermally Induced Two-Phase Flow Instabilities, Including the Effect of Thermal Non-equilibrium Between Phases", Ph.D Thesis, Georgia Institute of Technology, 1974.
11. Chexal B. and Lellouche, G., "A Full Range Drift-Flux Correlation for Vertical Flows", ANS Proceedings of the 1985 National Heat Transfer Conference, Denver, 1985.

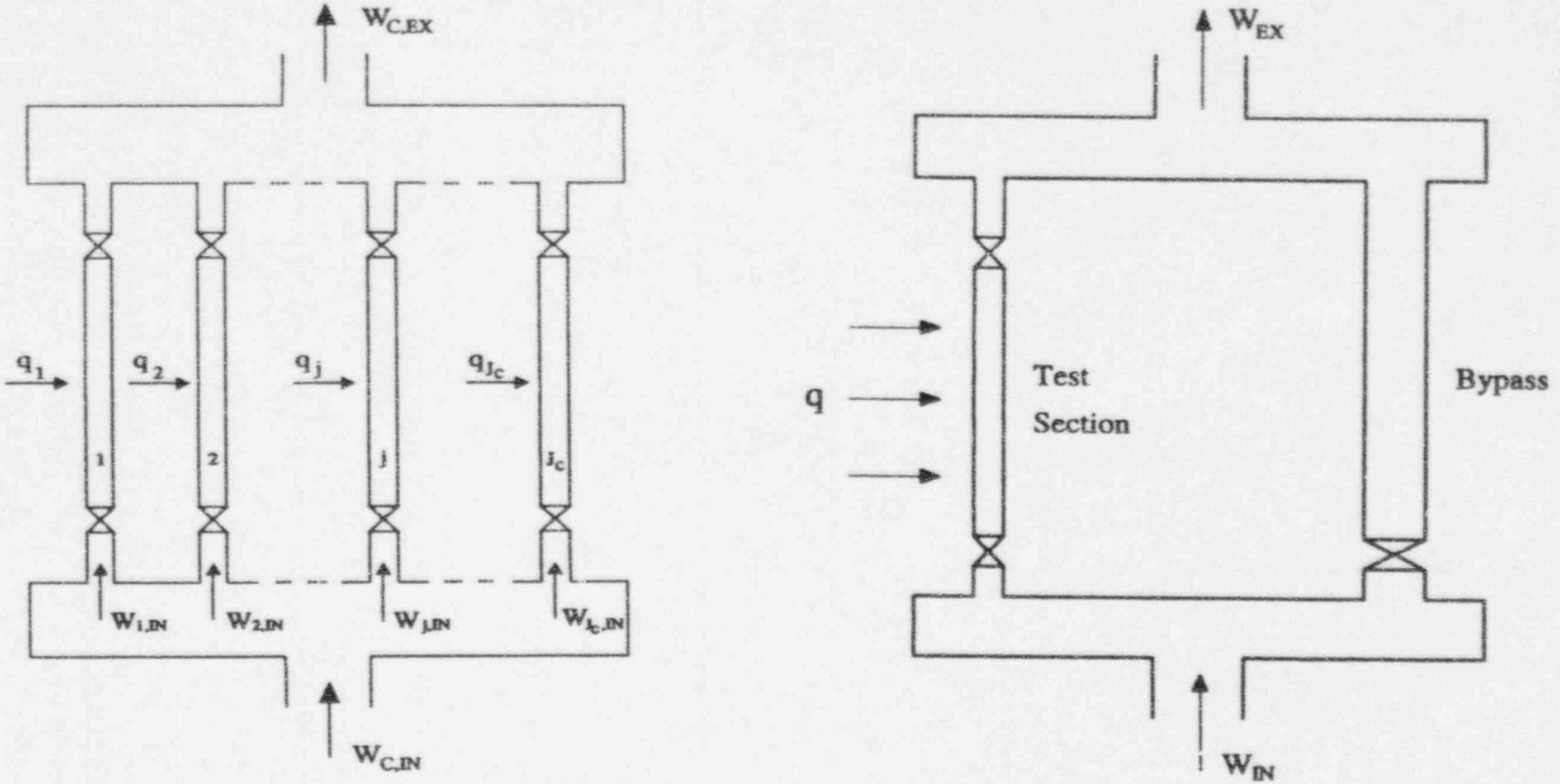

(a) Multiple parallel boiling channels

(b) A boiling channel in parallel with single-phase bypass

Figure 1. Parallel-channel configurations for the analysis of two-phase flow oscillations.

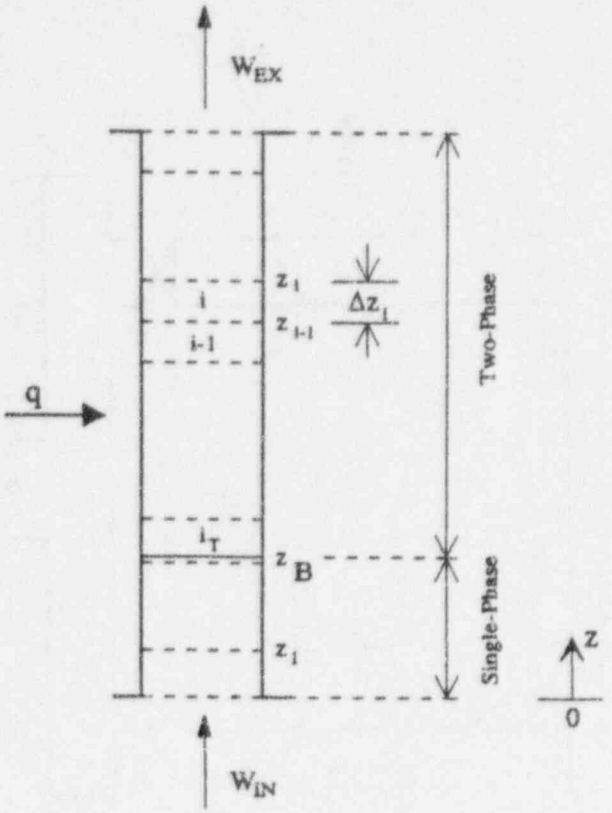

Figure 2. A schematic of boiling channel nodalization.

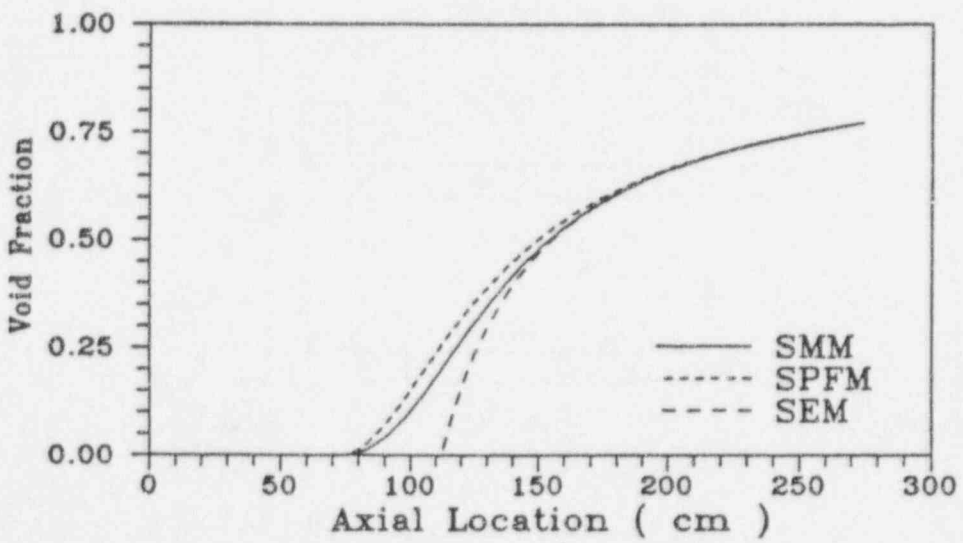

Figure 3. A steady-state axial void distribution in a boiling channel using different models of subcooled boiling:
(a) thermodynamic equilibrium model with phasic slip (SEM),
(b) profile-fit model of subcooled boiling with phasic slip (SPFM),
(c) mechanistic model of subcooled boiling with phasic slip (SMM).

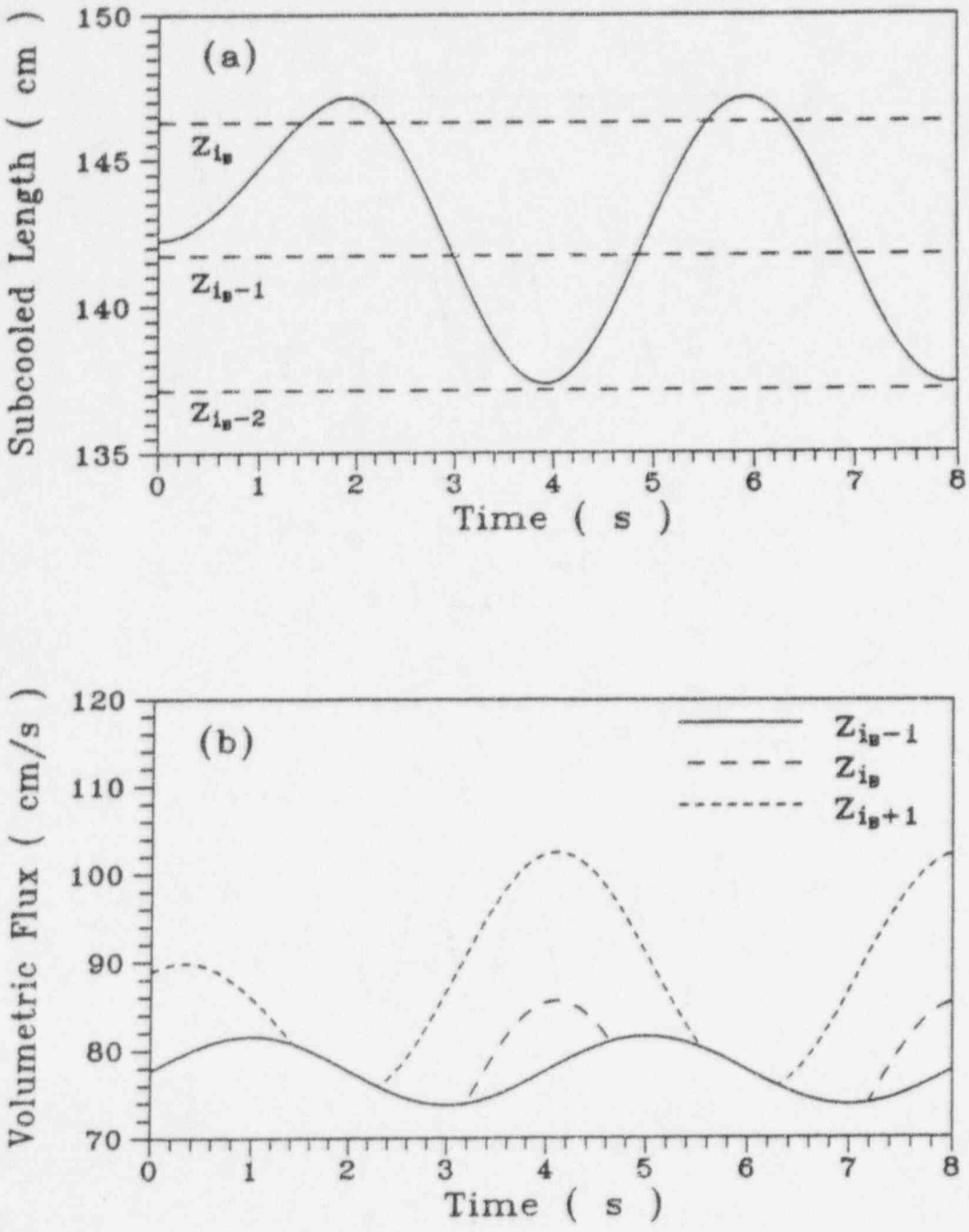

Figure 4. The response of a boiling channel to oscillations in inlet flow rate; (a) the time-dependent boiling boundary crossing nodal boundaries, (b) the superficial velocity of two-phase mixture at the nodal boundaries shown in Fig. 4(a).

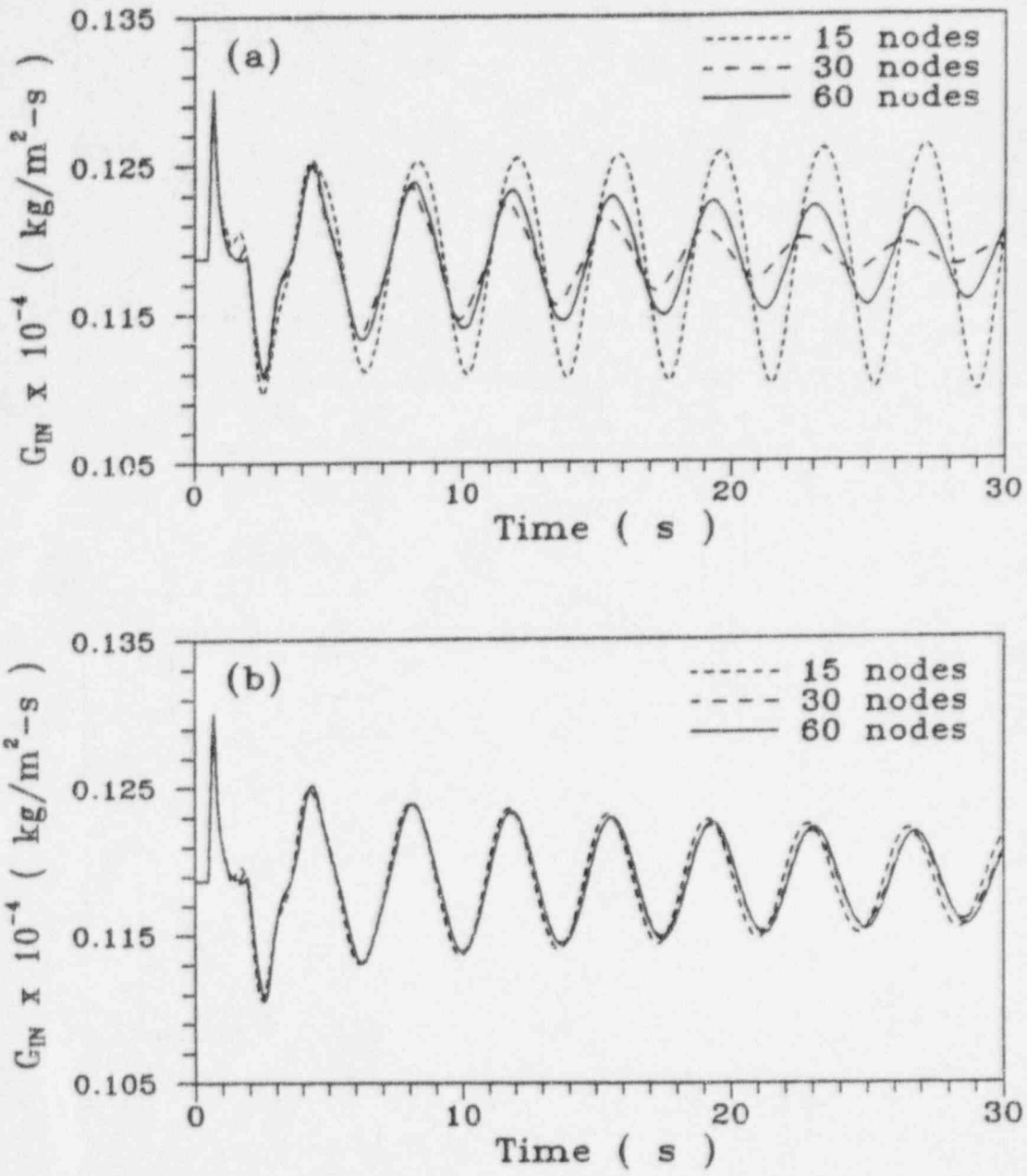

Figure 5. The effect of axial nodalization on the response of a boiling channel using two integration methods for the transition node:
(a) the basic method,
(b) the improved method.

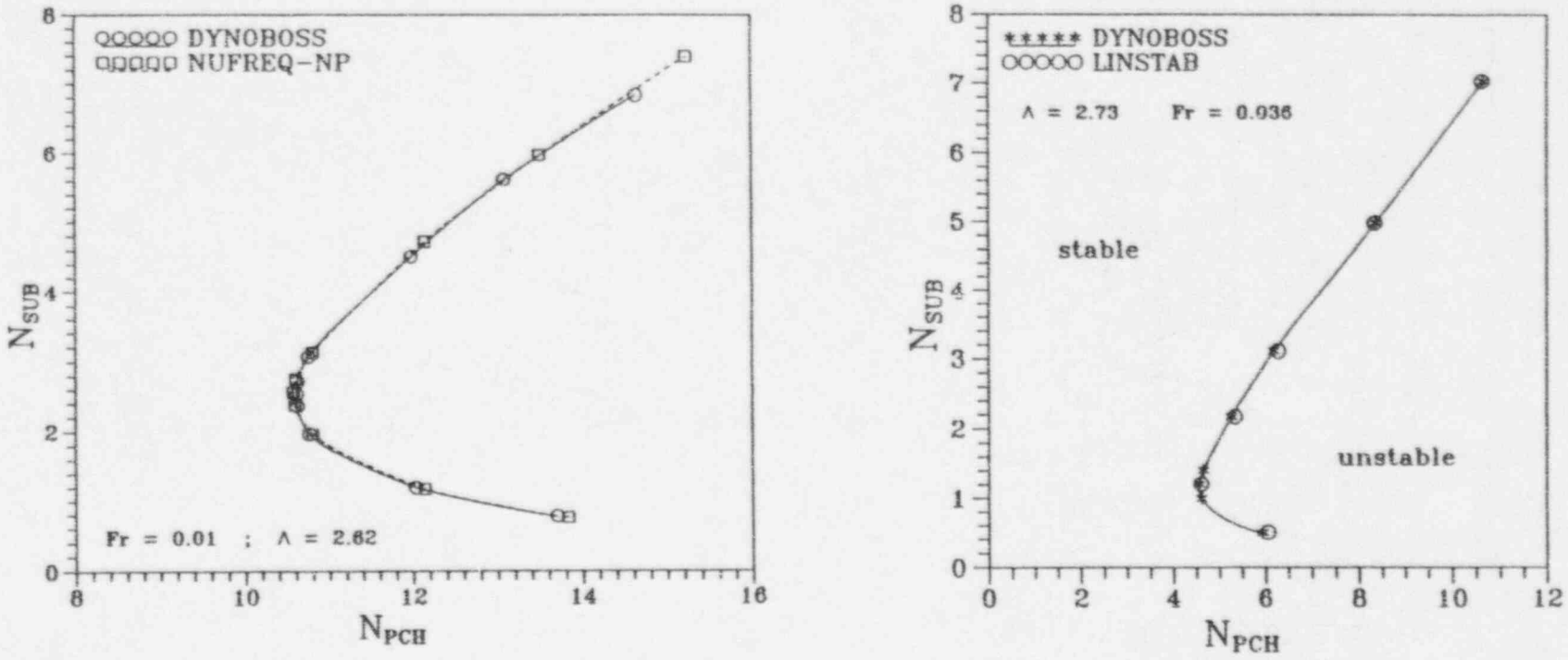

Figure 6. The calculated boiling channel marginal stability line in the N_{PCH}-N_{SUB} map. A comparison between *DYNOBOSS* and two frequency-domain codes, *NUFREQ-NP* [6] and *LINSTAB* [7].

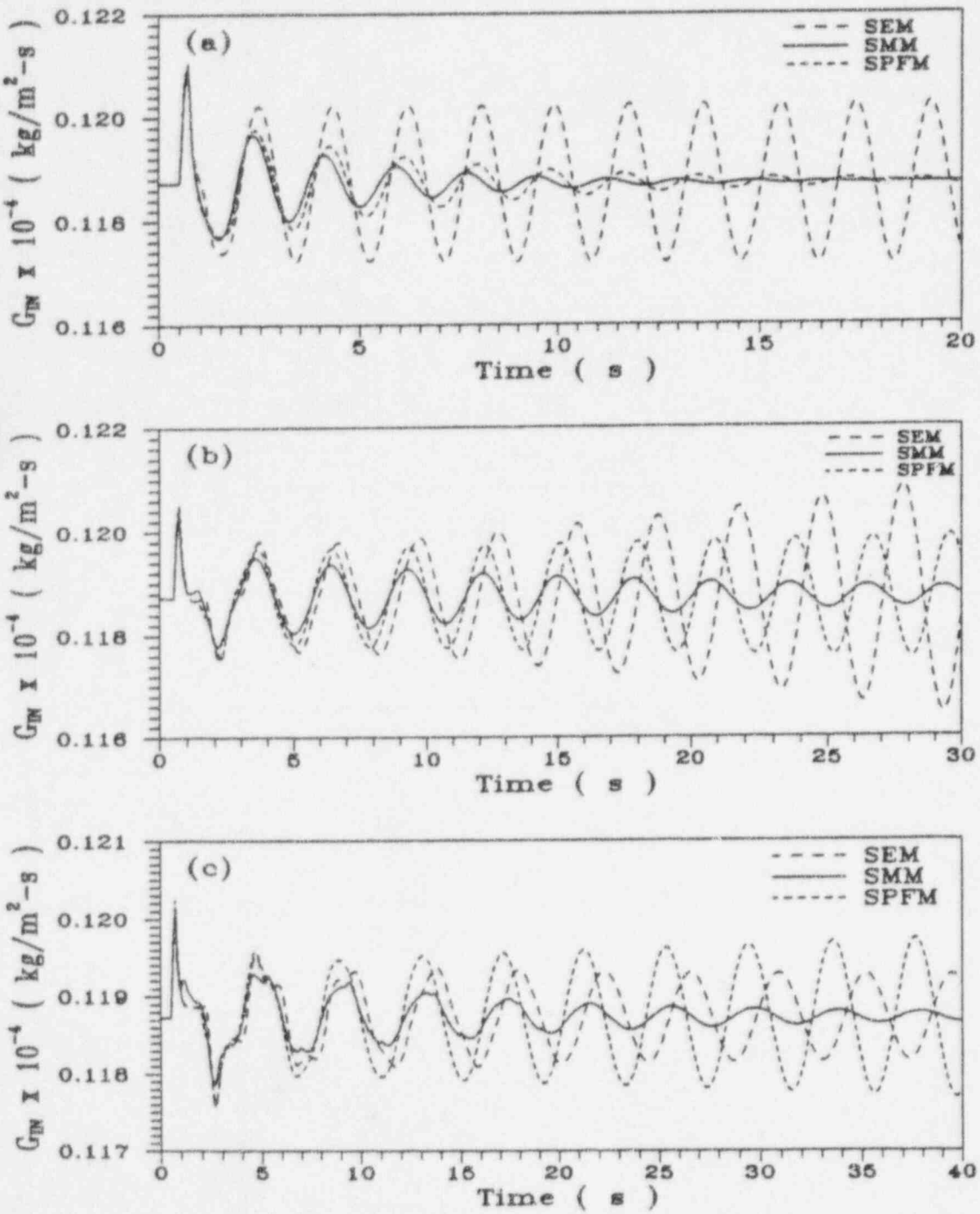

Figure 7. The response of a boiling channel to a perturbation in wall heat flux for three different modes of two-phase flow, SEM, SPFM and SMM: (a) $N_{SUB} = 1.0$, $N_{PCH} = 5.4$; (b) $N_{SUB} = 3.1$, $N_{PCH} = 7.6$; (c) $N_{SUB} = 7.0$, $N_{PCH} = 11.8$.

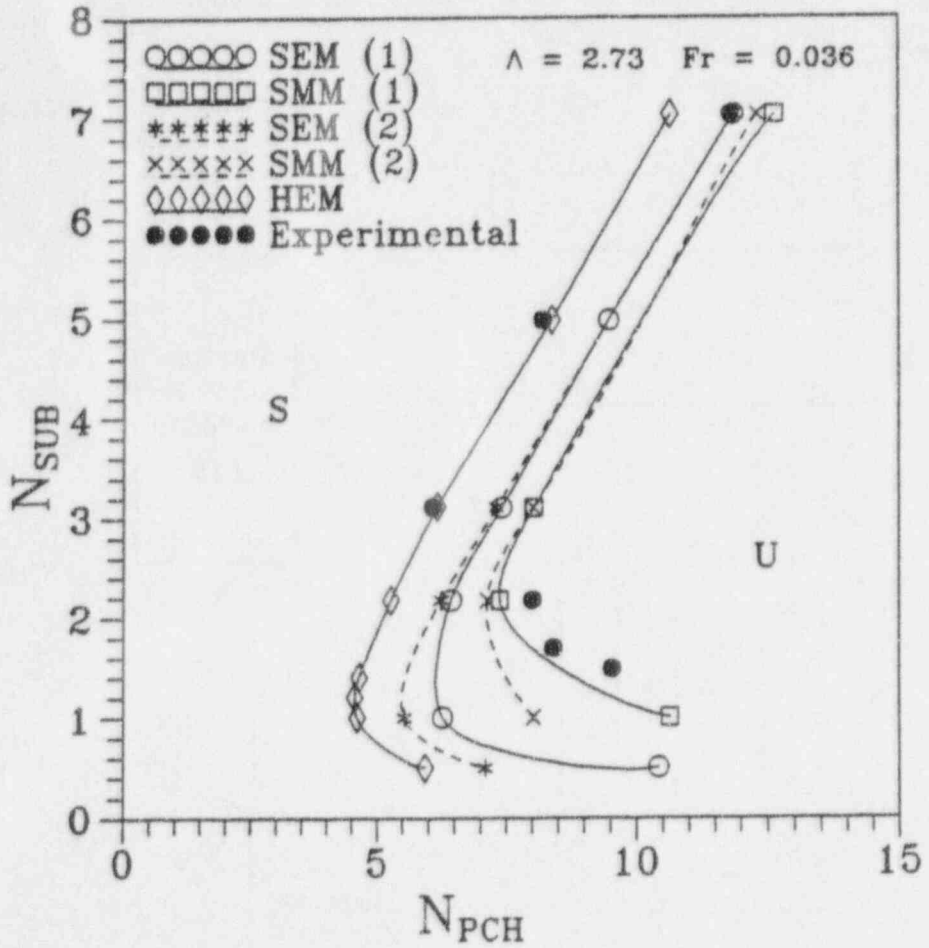

Figure 8. The effects of modeling assumptions for phasic slip and subcooled boiling on the calculated marginal stability boundary for a boiling channel; (1) space- and time-dependent drift-flux parameters, (2) average steady-state drift-flux parameters.

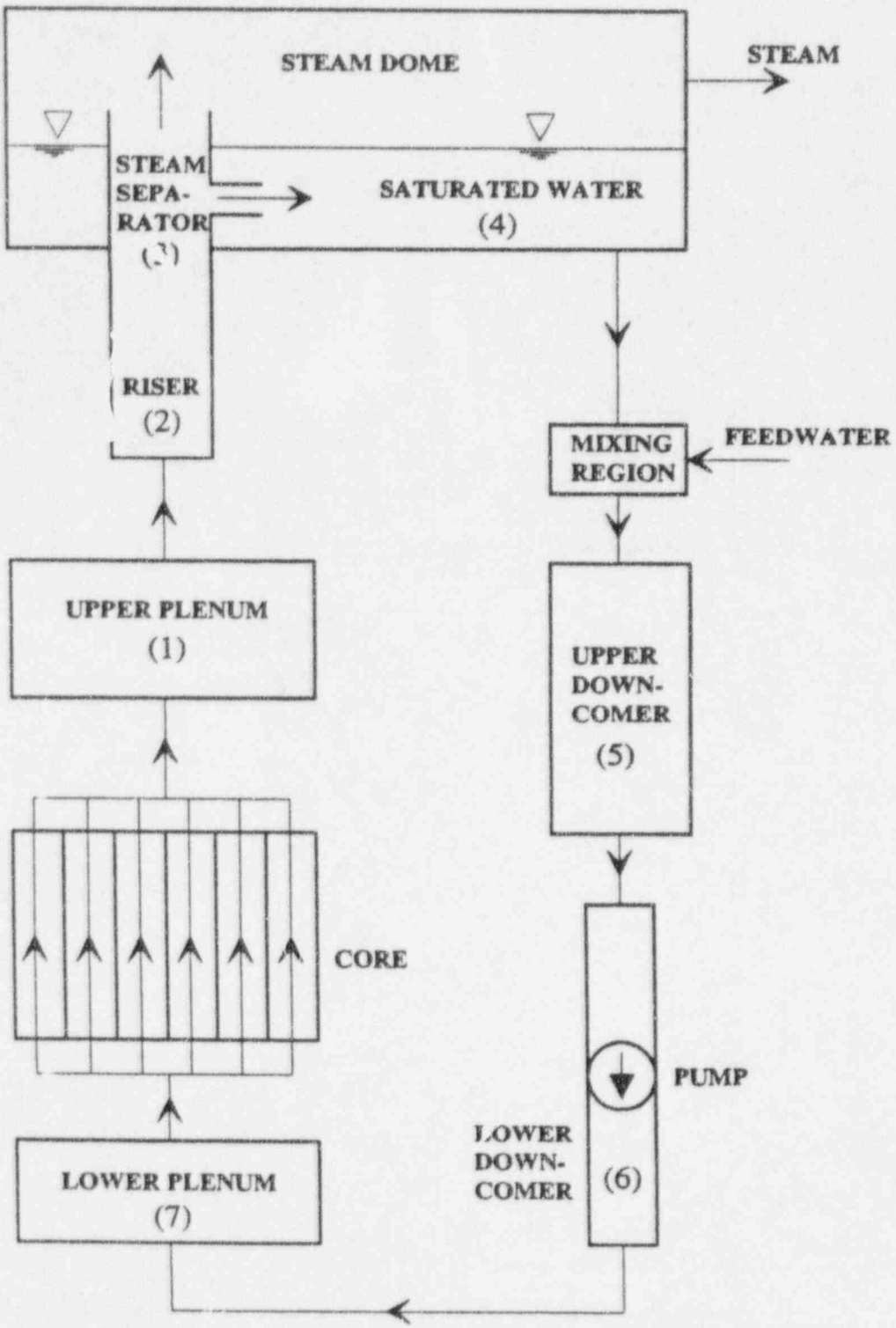

Figure 9. A schematic of the boiling water reactor (BWR) recirculation loop.

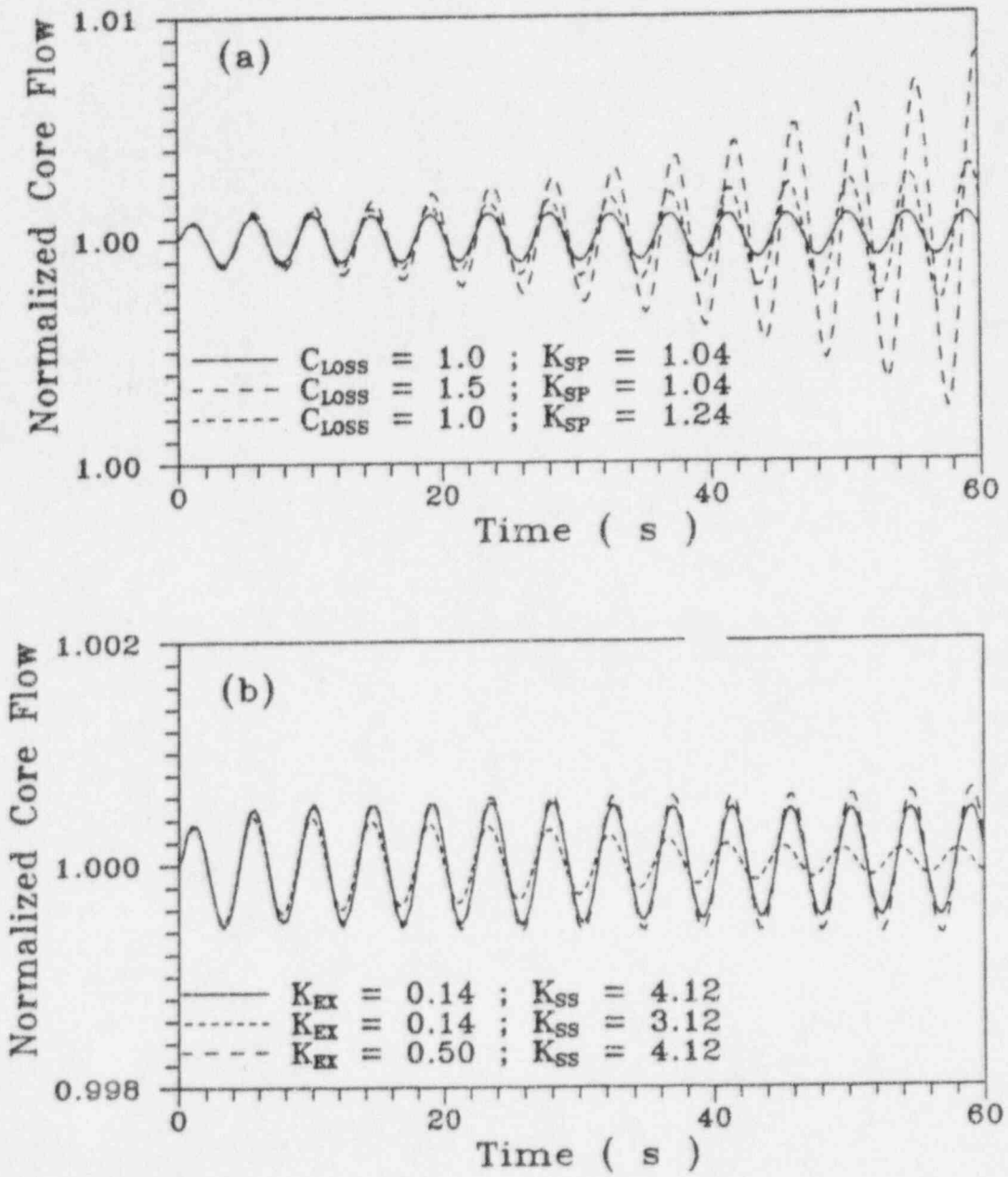

Figure 10. The effect of local pressure losses in the two-phase section of BWR loop on the response of a marginally-stable system: (a) local two-phase pressure loss multiplier and spacer loss coefficients, (b) core exit and steam separator local loss coefficients.

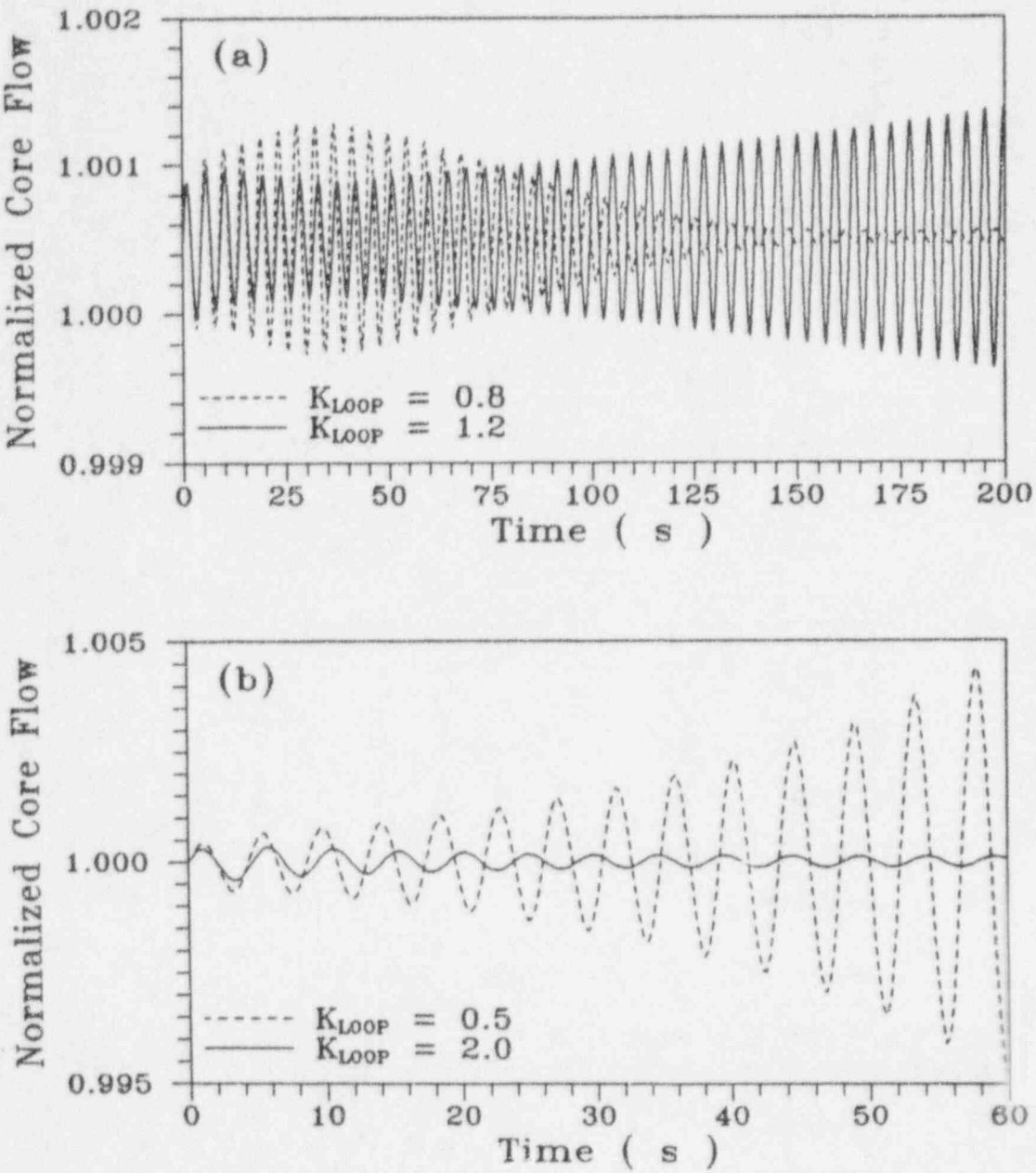

Figure 11. The effect of change in the single-phase loss coefficient on the stability of BWR loop; (a) $\Delta K_{1\phi} = \pm$ 20%, (b) $\Delta K_{1\phi}$ = - 50% and + 100%.

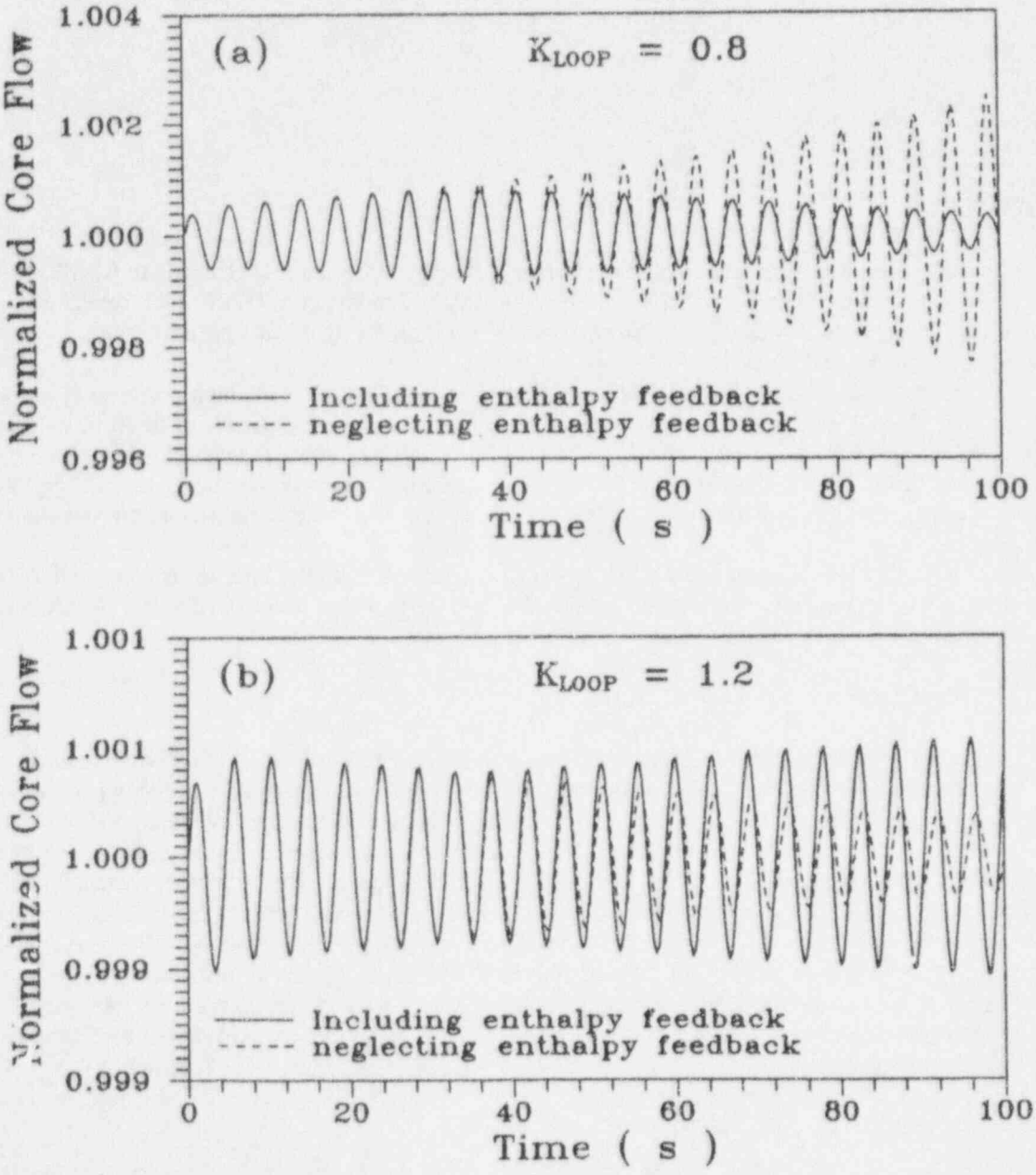

Figure 12. The effect of core inlet enthalpy feedback on BWR system stability, for a ± 20% change in the local loss coefficient in the single-phase section of the loop.

THERMAL-HYDRAULIC INSTABILITIES IN PRESSURE TUBE GRAPHITE - MODERATED BOILING WATER REACTORS

G. Tsiklauri, B. Schmitt
Battelle Pacific Northwest Laboratory, USA

ABSTRACT

Thermally induced two-phase instabilities in non-uniformly heated boiling channels in RBMK-1000 reactor have been analyzed using RELAP5/MOD3 code. The RELAP5 model of a RBMK-1000 reactor was developed to investigate low flow in a distribution group header (DGH) supplying 44 fuel pressure tubes. The model was evaluated against experimental data.

The results of the calculations indicate that the period of oscillation for the high power tube varied from 3.1s to 2.6s, over the power range of 2.0 MW to 3.0 MW, respectively. The amplitude of the flow oscillation for the high powered tube varied from +100% to -150% of the tube average flow. Reverse flow did not occur in the lower power tubes. The amplitude of oscillation in the subcooled region at the inlet to the fuel region is higher than in the saturated region at the outlet. In the upper fuel region and outlet connectors the flow oscillations are dissipated.

The threshold of flow instability for the high powered tubes of a RBMK reactor is compared to Japanese data and appears to be in good agreement. This work was sponsored by the United States Department of Energy under Contract DE-AC06-76RLO 1830.

INTRODUCTION

On March 24, 1991, the Unit 3 reactor at Leningrad Nuclear Power Plant, a 1000 MW pressure tube graphite moderated reactor, was automatically shutdown because of a pressure tube rupture in the upper part of the reactor core cavity [1,2]. The rupture occurred due to a failure of the inlet flow control valve to one of the core pressure tubes. It was estimated from a post-accident review, that this failure resulted in flow reduction of the inlet flow to less than 10% of the initial tube flow. The flow reduction initiated a fuel temperature excursion and also elevated the pressure tube wall temperature due to radiative heat transfer between the fuel rods and tube wall. Approximately 40-45 seconds after the inlet valve failure, the pressure tube ruptured. The reactor shutdown was initiated 3.7 seconds after the pressure tube rupture due to the high core cavity pressure.

Similar events are also possible for a partial break of the distribution group header, when quasi-stagnation or flow fluctuation at near zero pressure drop ΔP occurs. At this condition, the post-dryout heat transfer under low flow is not sufficient to prevent a pressure tube wall temperature excursion. The purpose of this paper is to validate RELAP5/MOD3 [3] for two-phase flow dynamic instability problems in RBMK reactors. The work includes two related accident analysis:

- Blockage of coolant at the pressure tube inlet.
- Blockage of DGH or partial break of DGH.

The general characteristics of the RBMK type reactor are as follows:

- Thermal core power 3200 MW.
- 1661 fuel tubes, 7 m active core, average linear heat flux 153 W/cm.
- Operating pressure 7 MPa.

- 37,600 tonne/hr total loop flow, an average of 6.288 kg/s per tube.
- 40 DGH with 42 pressure tubes in each.

The reactor has four steam drum separators, two hydraulic loops common at the steam header and 8 main circulation pumps (PCP), (6 operating, and 2 reserved).

RELAP5 Models for RBMK

Two RELAP5 models were developed that represent a 1/4 core and 1/2 core of an RBMK reactor. With these two models, minor modifications were made specific to the transient being simulated. For both models, the nodalization is setup to perform a detailed calculation of an affected core region (for a single or multiple tube rupture or blockage). The balance of the core is lumped into a single tube to allow the RELAP5 model to predict needed fluid conditions in the steam drum and inlet distribution headers. It was felt that a simple single tube model, with boundary conditions for these regions, would not allow sufficient degrees of freedom in the calculation to provide accurate results. The nodalization schemes for both models are shown in Figures 1 and 2. RBMK design data were provided by [1,2,4].

The 1/4 core model assumes a 1/4 core symmetry for the RBMK, contains two parallel fuel regions for the reactor core, and uses boundary conditions for the main coolant pump (Figure 1). A 1/4 core model is the minimum size needed to include a steam drum model, and is readily adaptable for assuming conservative core power distributions (i.e. assuming high/low power regions). The two fuel region model allows for one or more 'affected' tubes (fuel channels) to be modeled separate from the intact core for events such as tube rupture or blockage. The 1/2 core model contains four parallel fuel regions for the core, and a pump model to provide a complete loop simulation. The 1/2 core representation allows a more accurate calculation of the core average conditions as the RBMK core is split in-two hydraulically.

For both models, the affected tube is modeled hydraulically using 9 inlet connector volumes, 16 axial fuel volumes (14 active fuel regions), 6 upper tube volumes, and 5 outlet connector volumes. This nodalization allows for detailed pressure and temperature monitoring, and ease of defining the tube rupture location for different events without significant changes to the base model. The intact core is modeled using 5 inlet connector volumes, 7 axial fuel volumes (5 active fuel regions), 5 upper tube volumes, and 5 outlet connector volumes (these outlet connectors are set up to allow for future model expansions as needed). In the three channel model, a third channel is modeled hydraulically with the same detail as the affected core. Overall, the two channel model (1/4 core) represents 416 fuel channels, typically a single 'affected' channel and 415 lumped channels. The four channel model (1/2 core) represents 830 fuel channels, typically one or more 'affected' channels, two sets of parallel channels for the balance of the 44 tubes on one DGH, and the remaining 786 lumped channels.

The steam drum separator is modeled using 14 volumes. This is shown in Figures 1 and 2. This modelling detail allows for a more accurate inventory calculation, and in particular, a more accurate prediction of the fluid conditions for reverse flow into the affected tube(s). There are additional volumes for the inlet sparger volume (for feedwater return), an outlet downcomer for coolant return to the main coolant pumps (MCPs), and steam piping volumes leading to the turbines. The turbines and feedwater return pumps are not modeled explicitly. They are approximated using time dependent volumes to supply the necessary boundary conditions, with the fluid conditions taken from plant operating data. The steam drum is sized to represent a single drum for the 1/4 core model, and two steam drums for the 1/2 core model.

The heat structures modeled include the fuel pins and carrier rod, pressure tube and surrounding graphite, and the inlet and outlet connector piping walls. No heat structures are modeled at this time for the steam separator. The affected tube for both models contains two fuel pin heat structures that represent an equivalent of 6 and 12 fuel pins lumped together to represent the 18 fuel pins per rod bundle. This allows radial power peaking to be modeled for the 6 inner and 12 outer fuel rings of the fuel bundle. The unaffected tubes are modeled with a single heat structure representing an equivalent of 18 fuel pins lumped together.

For the affected core, the RELAP5/MOD3 radiative heat transfer model is used. Radiative heat transfer between the inner fuel ring, outer fuel ring, carrier rod, and tube wall is modeled. Appropriate view factors were calculated for each heat structure component. Preliminary calculations for the tube blockage event were made to

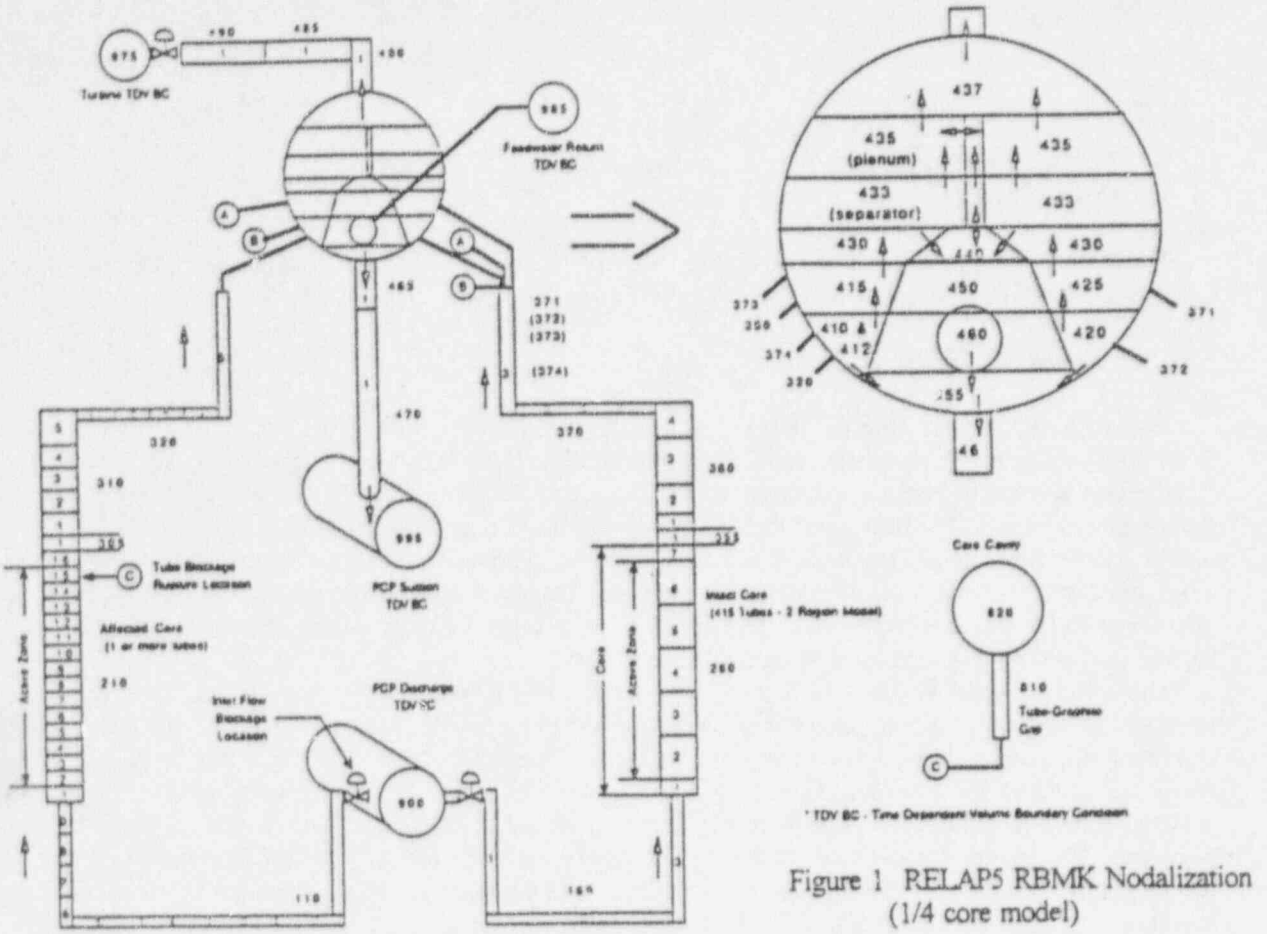

Figure 1 RELAP5 RBMK Nodalization
(1/4 core model)

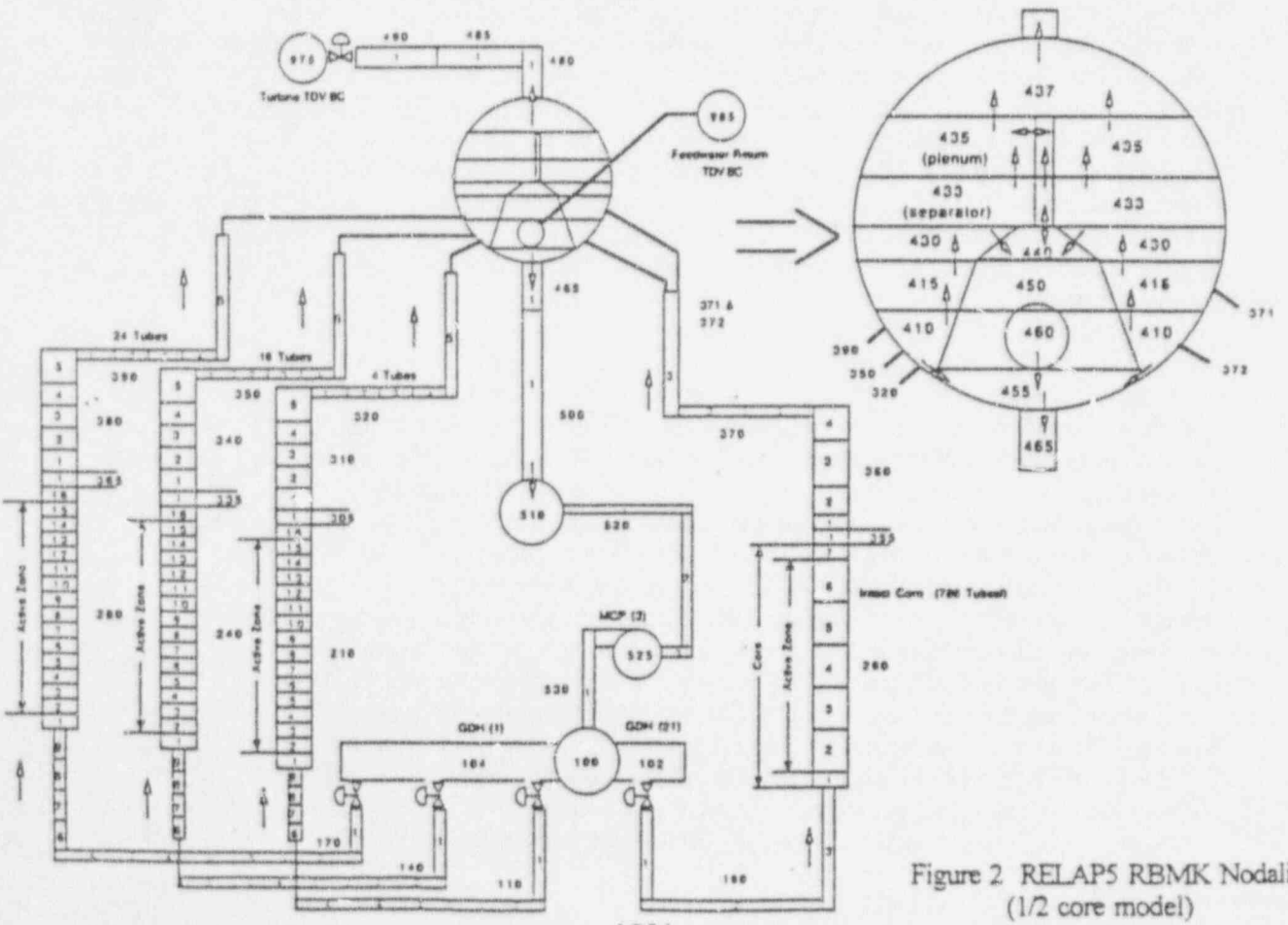

Figure 2 RELAP5 RBMK Nodalization
(1/2 core model)

investigate the surface emissivity for the fuel cladding and tube wall. Emissivity values of 0.5, 0.6 and 0.7 were evaluated. This range was considered to be typical for Zr (the cladding and tube wall material). An average value of 0.6 was chosen for the calculations presented here, as the preliminary results did not show a strong dependence over this range of emissivity.

The 1/2 core model was developed to investigate low flow induced oscillation (Figure 2). The model contains 4 core regions, three within the affected DGH representing 44 tubes, and one for the balance of the core. The three affected tube regions were defined as 4 high power tubes (ranging from 2.2 MW to 3.0 MW per tube), 18 medium power tubes (set at 2.2 MW per tube), and 22 low power tubes (set at 1.6 MW per tube). This distribution was based on previous work done at PNL for post-Chernobyl neutronics analysis [5].

The low flow condition for the affected DGH was simulated by defining a time dependent boundary condition at the inlet to the DGH to provide the desired flow conditions. Total power for the 4 tube core region was set at a predetermined power for each case analyzed (2.2 MW, 2.4 MW, 2.6 MW, and 3.0 MW). The model was run to achieve a steady state solution for full power/full flow, and then flow reduced to the affected DGH slowly until the point of flow instability was seen. The point of flow instability was defined as an oscillation amplitude of +/-30%. Flow to the DGH was then held constant at the point of instability to observe the "stabilization" of the flow instability.

CODE VERIFICATION

The first stage of verification includes calculation for steady-state parameters in the RBMK and some transient calculation against known experimental data. Limited results for code verification were presented at [6]. Results from the investigation of a tube blockage are presented.

The seconds stage of verification is for low flow instability. The RBMK calculations are compared against Japanese experimental data [7] for Type II threshold of flow instability. A sensitivity study of the RELAP5 model is included with the comparison.

RESULTS AND ANALYSIS

Tube Blockage

A series of tube blockage cases were evaluated with the 1/4 core model. Briefly, the Leningrad tube rupture was initiated by a failure of the inlet flow control valve to one of the core pressure tubes. It was estimated from a post-accident review, that this failure resulted in a flow reduction of the inlet flow to less than 10% of the initial tube flow. The flow reduction initiated a fuel temperature excursion and also elevated the pressure tube wall temperature due to radiative and convective heat transfer between the fuel and the pressure tube wall. Approximately 40-45 seconds after the inlet valve failure, the pressure tube ruptured in the upper core. A reactor shutdown was initiated 3.7 seconds after the pressure tube rupture due to the high core cavity pressure.

To evaluate this event, a parametric study was performed over the potential range of inlet flow blockage. Each calculation assumed an instantaneous reduction in the inlet valve flow area to simulate the valve failure of the Leningrad event. A total of five calculations were made, varying the inlet flow blockage to obtain a range of flow reduction between 2%-10% of the initial tube flow. Initial tube flow was 6.3 kg/s. Fuel cladding and pressure tube wall temperatures were evaluated every 0.5m with the 1/4 core model. It was assumed that pressure tube failure (rupture) would occur at an average tube wall temperature of 923K (650°C). This is the temperature at which tube softening is estimated to occur that then results in tube rupture [2]. With 0.5m volume nodalizations for the 7m active fuel region, the tube failure location was calculated to be either at the 6.25m or 6.75m core elevation, depending upon the individual case. A plot of the time to pressure tube failure was made for the five calculations, and is shown in Figure 3a. A minimum time to tube rupture of approximately 42 seconds was calculated (compared to the estimated time of 40-45 seconds).

An evaluation was also made of the general transient response, with reactor shutdown, for one of the calculations. Figures 3b through 3d show the results from an approximate 6% flow blockage calculation. Initial tube flow for this calculation was reduced from 6.3 kg/s to 0.38 kg/s. In each of these figures, a null transient is run to ensure steady state conditions have been reached prior to initiation of the blockage (e.g., the blockage

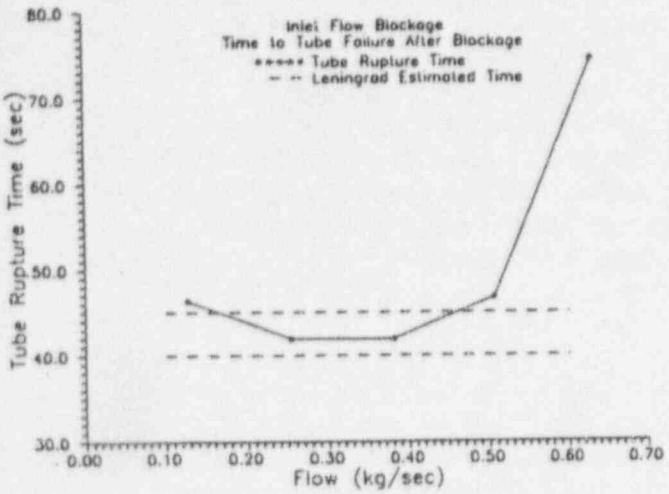

Figure 3a Time to Failure

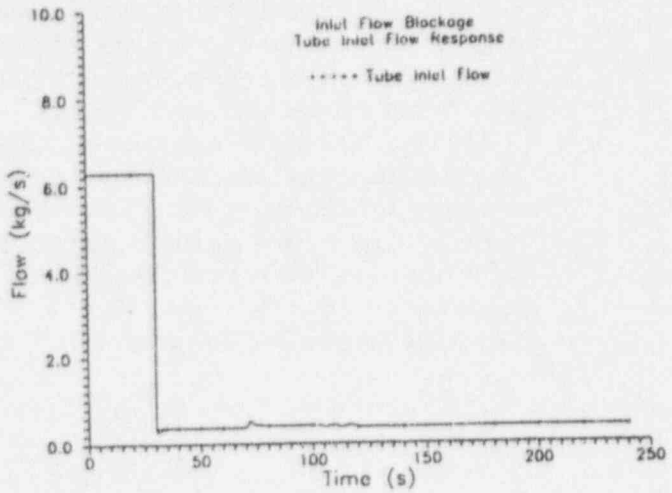

Figure 3b Inlet Flow

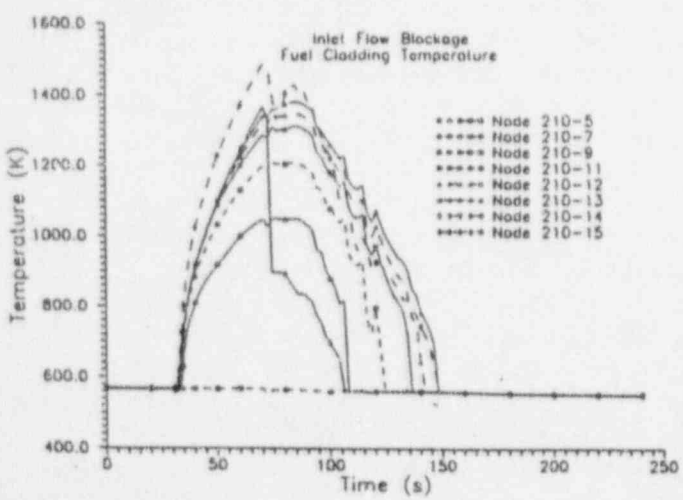

Figure 3c Cladding Temperature

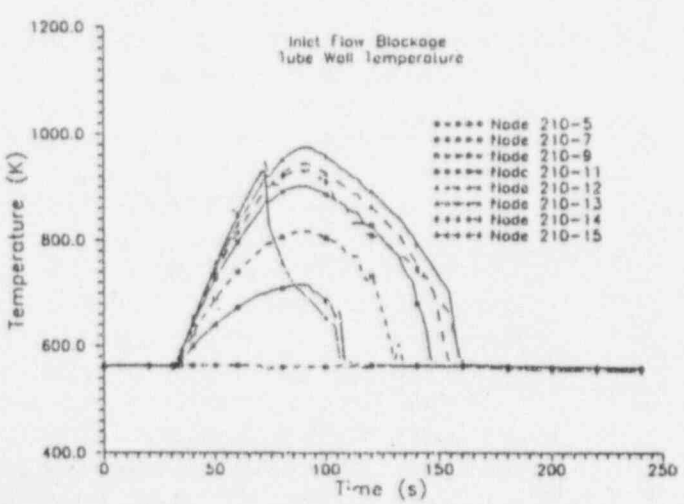

Figure 3d Tube Wall Temperature

occurs at 30 seconds). Figure 3b is the pressure tube inlet flow response. Figure 3c is the fuel cladding temperature response, and Figure 3d the pressure tube inner wall temperature response, for selected nodes. Refer to Figure 1 for the nodalization numbers. For this calculation, the tube was estimated to rupture 42 seconds after initiation of the blockage. A reactor shutdown was initiated 3.7 seconds after the rupture, resulting in the eventual quenching of the fuel cladding and pressure tube wall. Peak cladding temperature was calculated to be 1490K (1217°C) for this case, occurring between a core elevation of 6.0m and 6.5m (core node sizes were 0.5m in length). The general responses for this transient appear to be physically consistent.

Blockage of DGH

Low flow, high power instabilities were investigated using the 1/2 core model shown in Figure 2. The instability is initiated by reducing flow to the affected DGH, using a time dependent junction (simulating a partial blockage), while maintaining constant power. A nodalization and time step size sensitivity study was also performed. The results of the sensitivity study are presented first.

Sensitivity Study

Three areas of modeling sensitivity were investigated. These were core nodalization, outlet (steam) pipe nodalization, and time step size. The core nodalization study investigated three cases for fuel region nodalization; 7, 14 and 28 axial fuel nodes. The steam pipe nodalization study investigated three cases for steam outlet pipe nodalization; 2, 5 and 10 steam pipe nodes. The time step study was performed for three different time steps sizes; 2ms, 10ms and 12.5ms, for two different core nodalizations, 7 and 14 fuel region nodes. For the two nodalization studies, the time step size used was 12.5ms. This time step size was the calculated RELAP5 material Courant limit for the model (this time step limit was calculated by the RELAP5 code, [3]).

The nodalization study was performed by initializing the model with a 60 second null (steady state) transient, then reducing flow to the affected DGH from 276.5kg/s to 50kg/sec between 60 and 560 seconds. The 50kg/s flow is then maintained constant from 560 to 660 seconds to observe the flow instability. The time step study was performed by initializing the model with a 60 second null transient, then reducing flow to the affected DGH from 276.5kg/s to 60kg/sec between 60 and 120 seconds. The 60kg/s flow is then maintained constant from 120 to 180 seconds to observe the flow instability (a flow of 60kg/s was chosen as this was closer to the point of instability for the DGH than 50kg/s).

The core region nodalization study was performed for three noding schemes; 7, 14 and 28 fuel region nodes. The results are shown in Figures 4a and 4b. The 14 and 28 fuel node results behave very similarly. They exhibit initiation of flow instability at very nearly the same flow, and although they differ slightly during the first 10 seconds of instability (Figure 4a, from 450 to 460 seconds), once the instability has reached a stable period they maintain similar frequencies of oscillation (although off-set slightly). The 7 node results, however, show a significantly lower point of instability initiation (Figure 4a) and frequency of flow oscillation (Figure 4b). The 7 and 14 node results do show similar amplitudes of oscillation, with the 28 node results showing a larger amplitude.

The steam pipe nodalization study was performed for three noding schemes; 2, 5 and 10 steam pipe nodes. The results are shown in Figure 5. The results for the 5 and 10 steam pipe nodes behave very similarly. They exhibit similar initiation of flow instability and period of oscillation, differing in amplitude of oscillation only slightly during the first 10 seconds of instability (Figure 5, from 450 to 460 seconds). Once the instability has reached a stable period, they maintain similar flow oscillation amplitude and frequency. The 7 node results, however, show a significantly lower point of instability initiation, and frequency of flow oscillation. All three cases show similar amplitudes of oscillation.

The time step sensitivity study was performed using the 7 and 14 node fuel region models (with 5 steam pipe nodes), and three different time step sizes for each; 12.5ms, 10ms, and 2ms. Figures 6a and 6b compare the time step study for the 7 and 14 node fuel regions, respectively. The 7 node model shows minor deviations between the 12.5ms and 10ms, with more significant deviations in the period of oscillation for 2ms. The 14 node model shows excellent similarity for all three time step sizes.

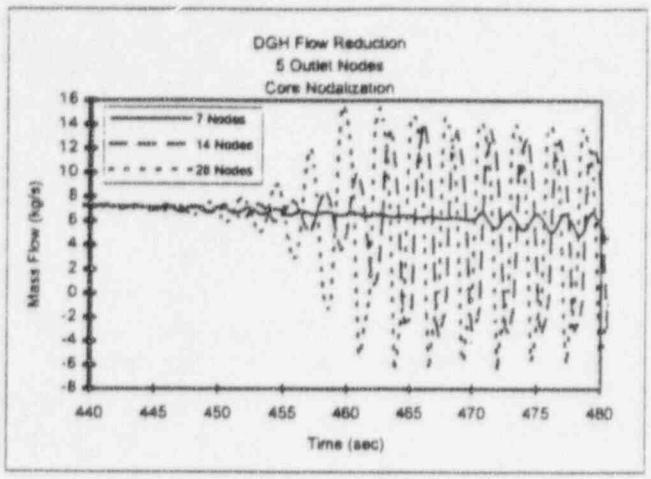

Figure 4a Core Nodalization

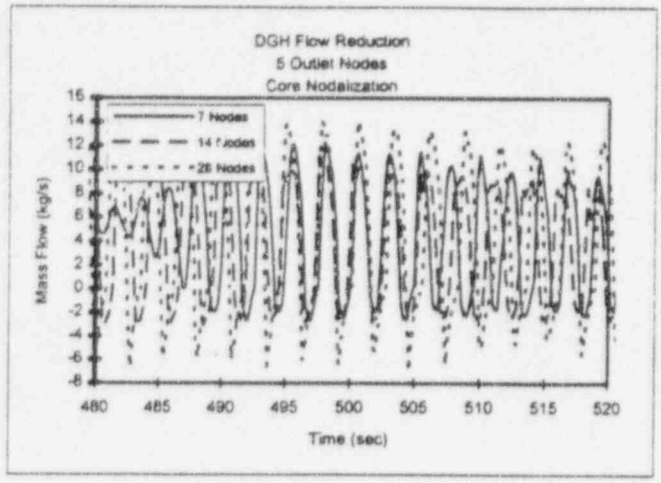

Figure 4b Core Nodalization

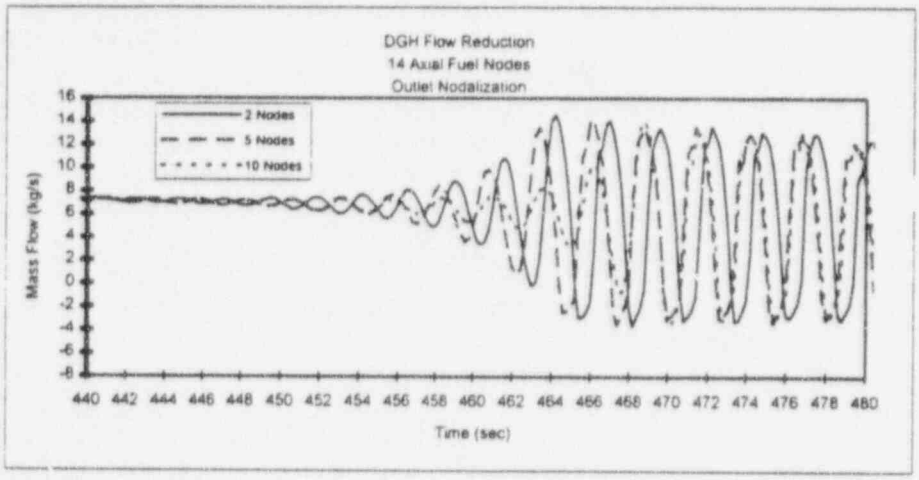

Figure 5 Outlet Nodalization

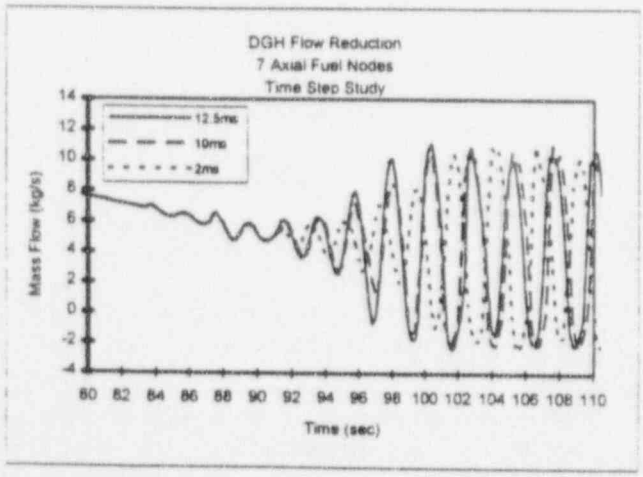

Figure 6a Time Step - 7 Fuel Nodes

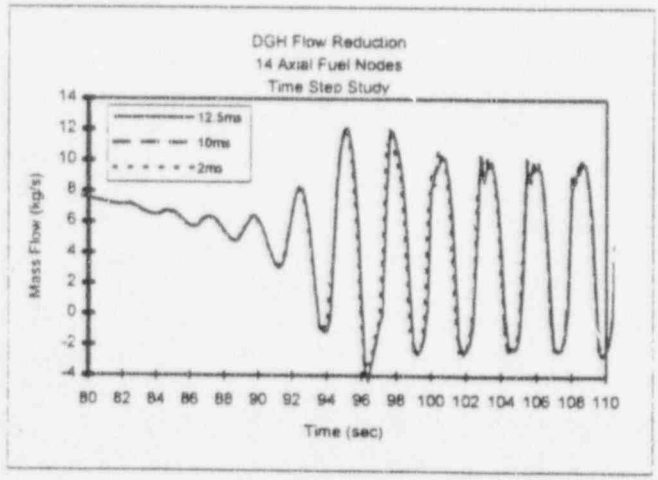

Figure 6b Time Step - 14 Fuel Nodes

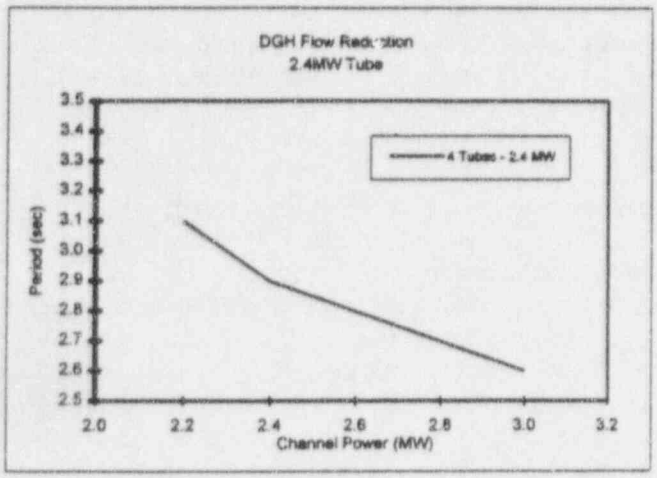

Figure 7a Period of Oscillation

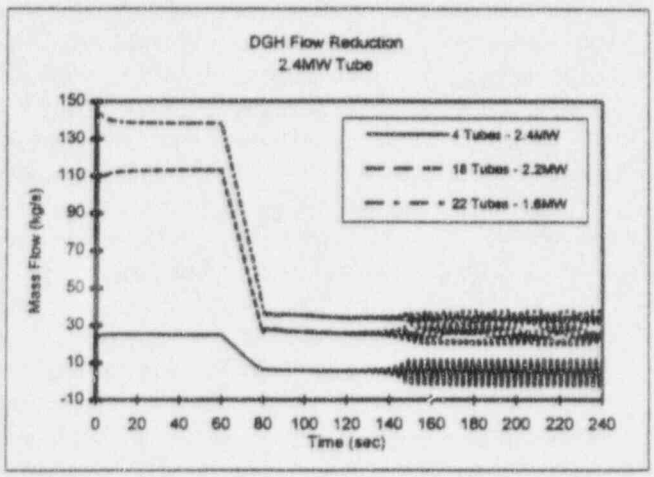

Figure 7b Tube Inlet Flow

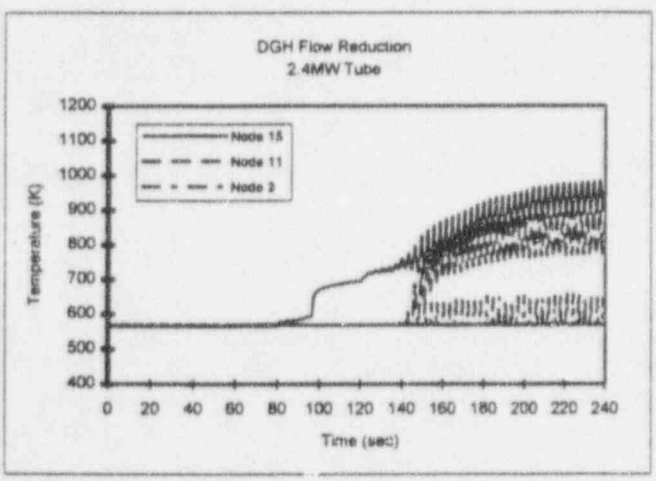

Figure 7c Cladding Temperature

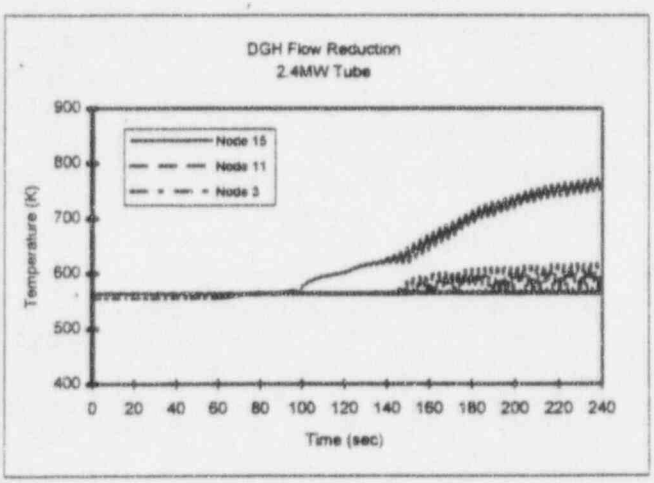

Figure 7d Tube Wall Temperature

Blockage Calculation

The base nodalization for the DGH partial blockage was for a 14 node fuel region, a 5 node steam pipe region, and a 12.5ms time step size. The instability study was performed by initializing the model with a 60 second null transient, then reducing flow to the affected DGH from 276.5kg/s to just above the point of flow instability in 20 seconds. This point was determined with preliminary calculations for each case evaluated. The DGH flow was then slowly reduced over 40 seconds to point of instability, and then maintained constant. Four different high tube powers were evaluated; 2.2MW, 2.4MW, 2.6MW, and 3.0MW.

The results of the calculations indicate that the period of oscillation for the high power tube varied from 3.1s to 2.6s, over the power range of 2.2MW to 3.0MW. This is shown in Figure 7a. The amplitude of the flow oscillation for the high powered tube varied from +10 kg/s to -2 kg/s (roughly +100% to -150% of the tube average flow based on the "steady state" flow just prior to initiation of the flow instability). This is shown in Figure 7b. Figures 7b, 7c and 7d present the results for one of the cases evaluated, a tube power of 2.4MW. The lower power core regions of the affected DGH experienced the same period of oscillation, but with lower amplitude. They also did not experience reverse flow. In addition, the lowest powered core region experienced flow oscillations of smaller amplitude than the medium powered core region. The amplitude of oscillation was referenced to the inlet flow of the fuel region, Figure 7b. In the upper fuel regions and outlet connector, the amplitude of the flow oscillation was dissipated in the upper regions of the core.

The fuel cladding and tube wall temperatures were monitored for three core elevations; the lower core, mid-core, and upper core (Figures 7c and 7d). The magnitude amplitude of the cladding temperature oscillation varied from +/-40 to +/-70K over the range of tube powers from 2.2 MW to 3.0MW, respectively. In the lower core region (node 3), temperature oscillations show alternation of wet and post-dry-out zones. In the upper core regions, where post-dryout has already occurred, temperature oscillations are due to flow and heat transfer coefficient changes. The amplitude of the tube wall temperature oscillation varied from +/-10 to +/-20K over the same range of power. Although the calculations were run long enough to produce a "stable" flow oscillation, the cladding and tube wall temperatures oscillations had not yet reached an "equilibrium" condition. For the highest power analyzed, 3.0MW, the tube wall temperature had nearly reached an "equilibrium," averaging approximately 805K, with an oscillation amplitude of +/-20K. The critical temperature for the RBMK pressure tube for tube rupture has been determined to be approximately 923K (650°C). Additional calculations are needed to evaluate the potential for tube rupture. Cladding temperature is far below the critical temperature for oxidation (1473K).

The results of the calculation clearly indicate that dryout in the upper regions of the core will occur prior to oscillation of the cladding temperature. Cladding temperature rises slowly in the upper core after initiation of the flow instability, then temperature rises sharply at the dryout point (Figure 7c) and reaches a new "equilibrium" temperature (the critical heat flux of the second mode) that continues to slowly rise. The cladding temperature oscillation is induced by the continued flow oscillation and moving of the boundary between the dry region and liquid.

The threshold of flow instability was calculated for each of the different powers for the high powered tube. These were compared to the data presented in Figure 8, Mochizuki [7]. The calculated threshold for the RBMK-1000 model appears to be in good agreement with this data. The data presented in Figure 8 suggest that for a DGH with high powered tubes, Type II instability is reached if flow is reduced below 1 to 2 kg/s, over the power range of 2.2 to 3.0 MW, respectively. These calculations were made for a limited power-flow range, and it is necessary to continue the analysis for flows less than 1 kg/s and powers less than 2.2 MW.

CONCLUSIONS

Results of a single tube blockage show good agreement with the available data for the Leningrad tube rupture event. The model was able to reasonably predict the time of tube wall failure for the expected flow blockage. Comparison of the threshold of Type II flow instability shows reasonable agreement over the range of RBMK tube power investigated, and can potentially be used for safety analyses of the DGH blockage events. Modeling sensitivity studies indicate the instability analysis results were not sensitive to the nodalization scheme and time step sizes used. This was for a 14 node fuel region, 5 node outlet (steam) pipe region, and a time step size of

12.5ms. For this nodalization, there was little sensitivity to time step between 2ms and 12.5ms. The results do indicate that fewer than these number of nodes in these two regions can significantly effect the results.

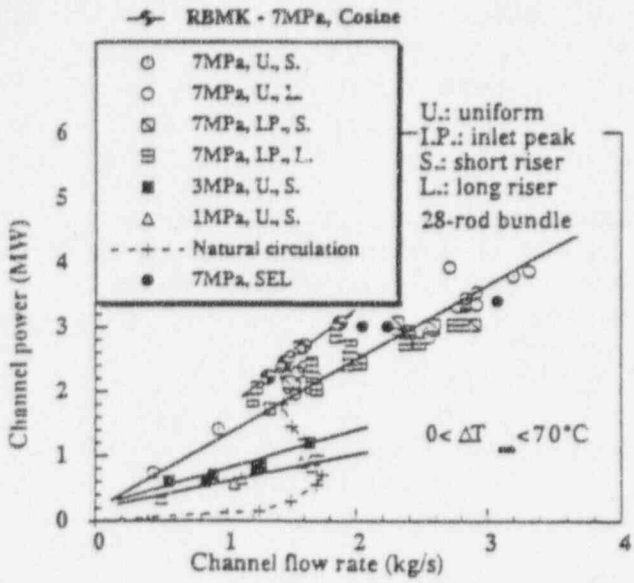

Figure 8 Type II Instability Threshold

REFERENCES

1. Cherkashov, Yuri M., "RBMK NPP Safety" Workshop of Safety of Soviet-Design Nuclear Power Plants, Chicago Illinois (November 20-21, 1992).

2. Gabaraev, B., Yu. Nikitin, O. Novoselsky, "An Assessment of the RBMK Core Cavity Overpressure Protection Piping System for Simultaneous Rupture of Several Pressure Tubes", RDIPE-PNL Workshop on N-Reactor Lessons, Richland, WA (July 20-22, 1993).

3. SCDAP/RELAP5/MOD3, Ver. 7o, Code Manuals I-III, EG&G Idaho Inc., NUREG/CR-5273 (September 1990).

4. Russian Academy of Sciences, Institute of Nuclear Safety, "Development of SCDAP/RELAP5 Model for the RBMK Graphite Reactor," Moscow (1993).

5. G.H. Meriwether and J.P. McNeese, "Flux Stability and Power Control in the Soviet RBMK-1000 Reactors," PNL Report, PNL-8781 (August 1993).

6. Tsiklauri, G., B. Schmitt, "RELAP5/MOD3 Code Assessment for Pressure Tube Graphite-Moderated Boiling Water Reactors," Proceedings of International Conference on "New Trends in Nuclear System Thermohydraulics", V1, pg. 573 (1994).

7. Mochizuki, H., "Flow Instabilities in Boiling Channels of Pressure Tube Type Reactor," Proceedings of Sixth International Topical Meeting on Nuclear Thermal Hydraulics, Vol. 1, pg. 269 (October 1993).

DYNAMICS OF SHOCK WAVE PROPAGATION AND INTERPHASE PROCESS IN LIQUID-VAPOUR MEDIUM

B.G.Pokusaev* and N.A.Pribaturin

Institute of Thermophysics,
Siberian Branch of Russian Academy of Sciences,
630090, Novosibirsk, Russia

*Moscow State Academy of Chemical Mechanical Engineering
107884, Moscow, Russia

ABSTRACT

This paper considers the experimental results and physical effects on the pressure wave dynamics of a vapour-liquid two-phase medium of bubble and slug structure. The role of destruction and collapse of bubbles and slugs, phase transition (condensation and evaporation) on pressure wave dynamics is also studied. The general mechanisms of the wave formation, behaviour and instability of a vapour-liquid structure under pressure waves, basic peculiarities of the interface heat transfer are obtained. In the experiments it has been shown that for the bubble medium the shock wave can be transformed into the powerful pressure pulse with an amplitude greater then the amplitude of the initial pressure wave. For the slug medium a characteristic structure of the amplificated wave is "comb"- like wave. It has been shown that the wave amplification caused by generation of secondary waves in a medium caused by destruction and collapse of bubbles and slugs. The obtained results can be useful at transient and emergency operational regimes of nuclear reactors, fuel tank, pipelines with two-phase flows and for development of safety models for chemical industry.

INTRODUCTION

Possibility of amplification or damping of pressure perturbations propagating in a vapour-liquid bubble flow is principal for the analysis of nonstationary processes in two-phase media. As is shown in works [1,2] for the case of rather weak waves ($\Delta p_0 / p_0 = 0.2$) the effect of thermal dissipation is so strong that a sharp pressure step is not forming. As the intensity of initial shock wave increases, the oscillatory shock waves can form in a vapour-liquid mixture as well as in bubble medium without phase transition [2]. Regularities of propagation of the weak ($\Delta p_0 / p_0 < 0.5$) shock waves in a vapour-liquid bubble medium being analysed in [1], based on assumption of the insignificant change of void fraction behind the wave front. It is not valid for the case of rather strong waves where partial or complete condensation is possible behind the pressure pulse front. This leads to a sharp change of acoustical properties of the medium in a wave and hence it should affect on the regularities of wave propagation.

EXPERIMENTAL APPARATUS AND METHOD.

The experiments on the dynamics of shock wave propagation in the vapour-liquid medium of different structures was made by use the shock tube method. The diameters of the using shock tube was 8, 25, 32, 52 mm and a length of test section was 1.5 - 2.5 m. The typical design of one of our shock tubes used in the experiments is shown in Fig.1. Its consists from the test section filled by vapour - liquid medium, a high pressure chamber, a diaphragm - change unit and thermostat. The vapour - liquid medium was generated by injecting vapour into the liquid through the bottom of tube. For the creation of bubble structure used the continuous vapour flow through capillaries, the slugs was generated by periodic supply of vapour into rest liquid by means open-close of the electromagnetic valve. The initial thermodynamic state of the medium was on the saturation line. The experiments were carried out in vapour-water and vapour-freon medium. The temperatures of the vapour, liquid was controlled by a thermocouple located immediately under the capillaries and inside the test section. The test section has an optical windows which served for the control of two-phase medium, determination of the size of bubbles and slugs, measurement of void fraction and high speed filming the behaviour of bubbles and slugs in pressure wave. The size of bubbles and slugs was determined by photography in the middle part of test section, the most probable size and mean square deviation were calculated by statistical method. The mean void fraction was determined by changing the level of liquid after the creation of two-phase medium. For this purpose used the shadow optical system using the He-Ne laser as a source of light. This techniques was used for the registration of the change of void fraction in pressure wave. The initial shock wave was generated by rupture of a diaphragm or a quick open of the electromagnetic valve which separate the test section from a high pressure chamber. For the measurement of the profile of pressure wave was used the piezoelectric sensors which were located along the length of the test section and measured the pressure inside the tube. The operating frequencies of these sensors with amplifiers was 0.1 Hz to 20 kHz. Calibration of the pressure sensors was carried out on the shock tube with thermal condition corresponded the thermal condition of using vapour-liquid medium. For the registration of signals from sensors used both the oscilloscopes and computer which was connected by interface with amplifiers. The main error in measurements of pressure wave was connected with the error of calibration and was not more then 10%, the error of the void fraction measurement by optical system not exceeds the 5%.

VAPOUR-LIQUID BUBBLE STRUCTURE.

Pressure wave of small amplitude. In the figures below the experimental results on dynamics of shock waves and vapour bubbles are shown. As is seen from Fig.2 weak pressure perturbations ($\Delta p_0 / p_0 < 0.5$) are much damped while propagation and their profile becomes monotonous. Here and on the further plots of $p=p(t)$ the different curves shown the pressure wave profile on the different distances from the level of vapour-liquid mixture (position $x=0$), the vertical length scale between different pressure profiles corresponds the length scale between different pressure sensors in the shock tube, the value of Δp on the vertical axis shows the scale of pressure perturbation. A front of condensation $\varphi = \varphi(t)$ looks like (Fig.2b) and can be easy calculate by using the well known dependence for the thermal regime of a

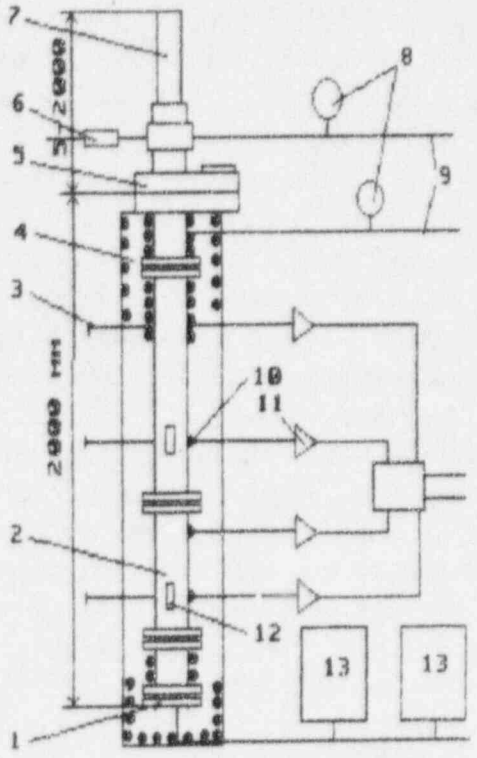

FIG.1 Scheme of shock tube for vapour-liquid medium. 1- vapour generator, 2- test section, 3- thermocouples, 4- thermostat (electrical for bubble regime, liquid for slug regime), 5- membrane unit, 6- valve, 7- high pressure chamber, 8- manometer, 9- gas supply, 10- pressure sensor, 11- amplifier, 12- windows, 13- liquid tank.

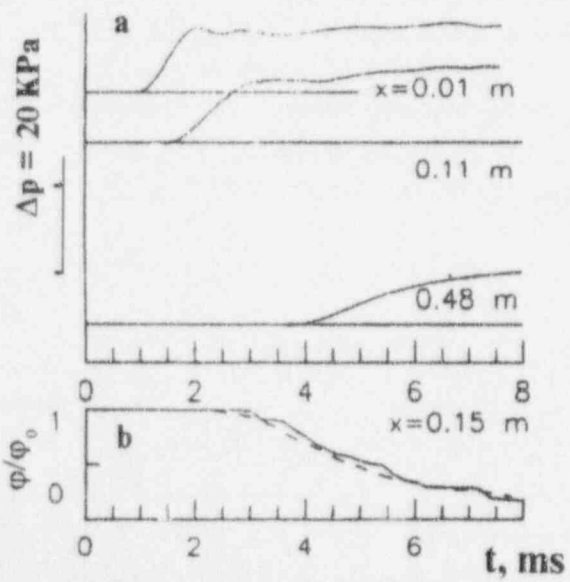

FIG.2 Propagation of weak shock wave in vapour-water medium. T_0 =391 °K, φ_0=1%, R=1.5mm, Δp_0 =15 KPa. ------ calculation on (1).

vapour bubble behaviour in pressure wave [2]: $dR / dt = q_l / h_{g,l}\rho_g$. Here q_l is the heat flux on the vapour-liquid boundary which can be written as [2]

$$q_l = -\frac{\lambda_l}{\sqrt{\pi a_l}} \int_0^t \frac{\partial T}{\partial \tau} \frac{d\tau}{\sqrt{t-\tau}}$$

Taking into consideration that $\varphi = (4/3)\pi R^3 N / V$, where N - number of bubbles in the unit of volume, one can obtain

$$\frac{\varphi}{\varphi_0} = 1 - \frac{3}{R_0} \int_0^t \frac{q_l}{\rho_g h_{gl}} dt \qquad (1)$$

For the calculation of $q_l(t)$ needs to use the transformation of the experimental profile of pressure wave to the change of temperature on the interface T(t) by using the Clapeyron - Clausius equation. As is seen from Fig.2b a calculated change of void fraction (dash line) agrees well with the experimental result.

In the works [1,2] it is shown that for this case the evolution of pressure wave is satisfactory described by one relaxation equation [2]:

$$\frac{\partial \tilde{p}}{\partial \tau} + \frac{\partial \tilde{p}}{\partial \zeta} + M\tilde{p}\frac{\partial \tilde{p}}{\partial \zeta} + \frac{M}{\sigma^2}\frac{\partial^3 \tilde{p}}{\partial \zeta^3} = -WM^{1/2} \int_0^\tau \frac{\partial \tilde{p} / \partial \tau'}{\sqrt{\tau - \tau'}} d\tau' \qquad (2)$$

where $\tau = c_0 t / l_0$, $\zeta = x / l_0$, $\tilde{p} = \Delta p / \Delta p_0$; $l_0, \Delta p_0$ - is the length and amplitude of initial pressure perturbation, $c_0 = \left[\gamma p_0 / \rho_l \varphi_0 (1 - \varphi_0)\right]^{1/2}$ is a sound velocity in the undisturbed two-phase mixture. Similarity criteria $M = (\gamma + 1)\Delta p_0 / 2\gamma p_0$, $\sigma^2 = 6M\varphi_0(1-\varphi_0)l_0^2 / R_0^2$ and $W = (3/2)(\kappa_l l_0 / \pi c_0 R_0^2 M)^{1/2} c_s^2 \rho_l C_{p,l} T_0 / \rho_g h_{lg}^2$, $W_* = W\sigma^{-1/2}$ define the contribution into distortion of the wave profile of disperse, nonlinear effects and interphase heat transfer. The wave profiles depends on the intensity of the initial pressure step. If the intensity of the initial wave is weak ($\Delta p_0 / p_0 < 0.3$) the wave profile in the medium is always monotonous, at $\Delta p_0 / p_0 > 0.3$ begin to form an oscillating profile of pressure wave. The shock wave existence is, however, limited to certain distances. For case $\Delta p_0 / p_0 = 0.5$, for example, the oscillations degenerate at 0.5 m from the entrance and at the large distances the influence of the nonlinearity is quite small. The wave profile on these distances is formed mainly by the interphase heat transfer.

The length of shock profile existence z^* can be estimate as a distance from the entrance of wave in medium where the influence of the nonlinear effect on the wave profile more then the thermal dissipation. The value z^* essentially depends by the thermal resistance of liquid and can be vary from 0.01 m to 100 m (thus for boiling water and $\Delta p_0 / p_0 = 0.3$, $z^* = 12$ mm at p =0.1 MPa and $z^* = 14$ m at p =8.5 MPa). The analysis of experiments on waterhammer with a flow of boiling freon-113 [3] is also incorporated in the frame of the above model. All results on the small amplitude pressure wave profiles can be shown as a map of wave regime which can build in coordinate M and W_*M (see Fig.3).

Amplification of pressure wave. Stronger waves acquire an oscillatory structure on early stages of their evolution. The condensation front here is also nonmonotonous. The bubbles make mainly 1.5 cycles of oscillations before they absolutely disappear. An increase of the initial shock wave amplitude up to

$\Delta p_0 / p_0 > 1.5$ results in qualitative change in the evolution of pressure waves. Experiments have shown that shock waves of such intensity may transform into short shock pulses of 300 - 500 μs duration; their amplitude significantly exceeds the amplitude of the incident wave (Fig.3). Vapour bubbles are collapsing in such pulse and can appear again behind the pressure pulse. A distance of the order of its length the pulse propagates without a significant change of its form. The condensation front becomes step - like form in a shock pulse (see curve $\varphi = \varphi(t)$) and coincides in time with the leading front of the pulse. Such step decrease of the condensation front is result of the collapse of all vapour bubbles. After the collapse the secondary spherical shock waves are radiated to the liquid. They look like circumferences and arcs in the photograph of the bubbles collapse - Fig.4a. This photograph was obtained by high-speed filming with the use of a laser stroboscope designed at the Institute of Theoretical and Applied Mechanics [4] together with the shadow optical system and high speed camera. The stroboscope generates the packet of the light impulses with different total duration and the interval between neighbouring impulses 30 μs. The duration of each impulse was 10 ns, thus the exposure time of each of the frames is 10 ns. On the fig.4b plots the curves R=R(t) for bubbles with different sizes (bubbles A,B,C), here the radius of bubble determines as $R = 0.5(D_{min}D^2_{max})^{1/3}$. As can see the large bubble - B collapse monotonously and generate in the liquid the powerful secondary shock wave. The time of the full collapse of a large bubble corresponds to the collapse of more less bubbles (A,C) at their secondary pulsation. This indicate on the tendency of the simultaneous collapse of the different - sizes vapour bubbles in a strong shock wave. The solid line on the fig.4b corresponds the decision of Rayleigh equation for the bubble B with assumption a constant pressure inside the bubble, the dash lines corresponds the assumption of adiabatic compression of a vapour in the bubbles A,B,C. The calculation of void fraction in the wave based on the Raleigh equation within assumption of constant pressure inside a bubble during collapse is also shown in Fig.3b by dash line. One can see a good agreement of the experimental result with the calculation by the inertial model of a bubble collapse.

The possible mechanism of the pressure pulse generation can be presented as follows: the secondary waves have velocities exceeding of the main wave (due to a decrease of a void fraction) and overtake its front. In this case a solitary wave forms as a result of interference. Common relations for the stationary shock wave with complete condensation provide some important estimations for this pressure pulse. Continuity and momentum conservation determine the wave velocity U and liquid velocity behind the wave front V, which within the assumption of incompressible liquid take form:

$$U^2 = \frac{\Delta p_0}{\rho_l \varphi_0 (1 - \varphi_0)}; \qquad V^2 = U^2 \varphi_0 \tag{3}$$

A necessary condition of the shock wave stability is inequality $U > c_0$ or $\Delta p_0 / p_0 > \gamma$. The experimentally defined threshold of shock pulses formation is close to this value. The "cell" model [5] of the vapour bubbles collapse can be used for the calculation of the maximum possible of amplitude pressure pulse. According to this model

$$p_{max} = p_\infty \left[1 + \frac{\Delta p_0}{p_\infty} \frac{\rho_l c_l}{p_\infty} \frac{\varphi_0}{1 - \varphi_0} \right]^{1/2} \tag{4}$$

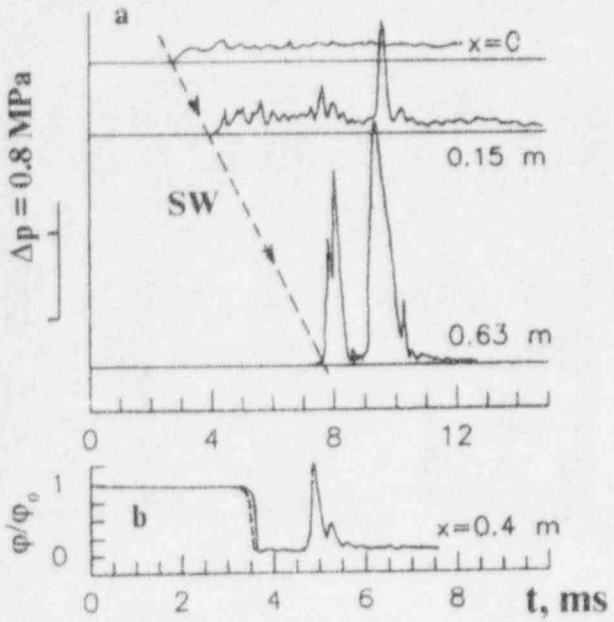

FIG.3 Generation of pressure pulse in vapour-water bubble mixture. p_0 =0.1MPa, φ_0=2%, R=2mm. ----- calculation, SW- line indicated the shock wave propagation.

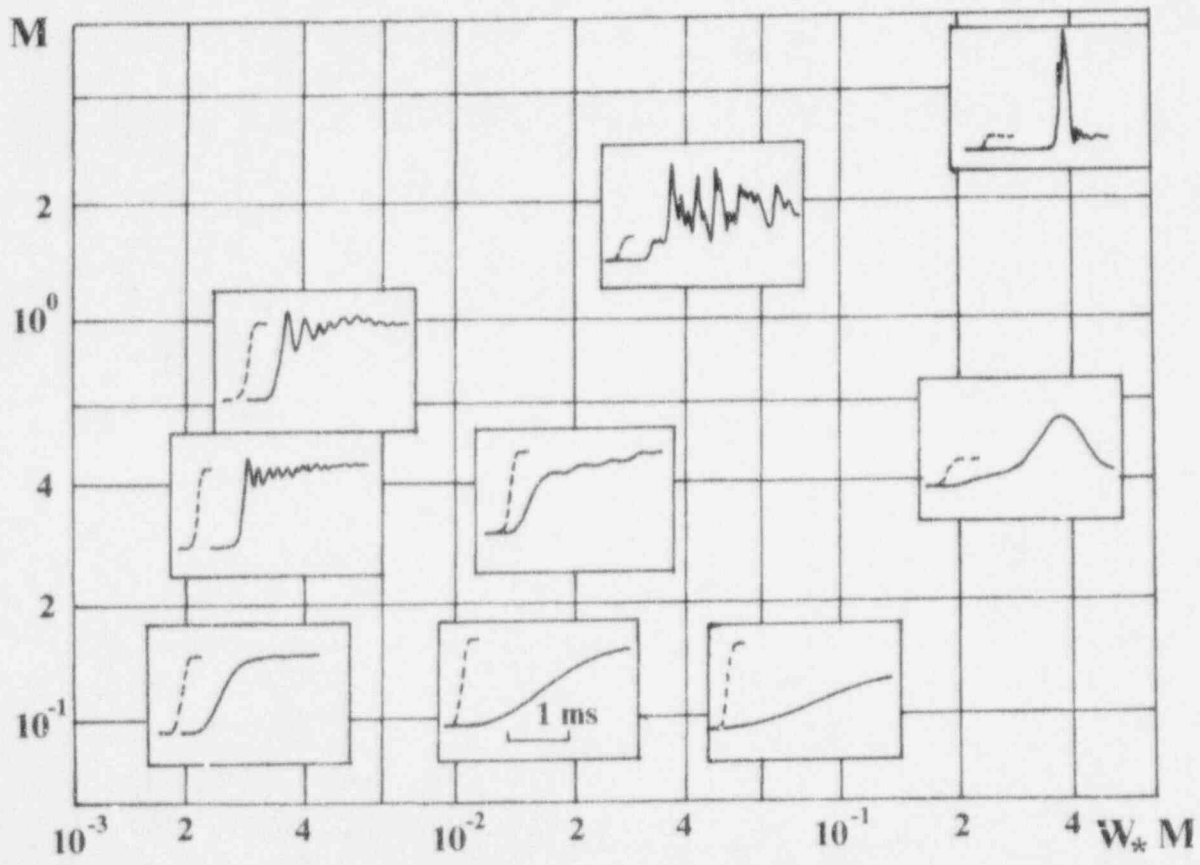

FIG.5 Map of pressure wave . gime in vapour-liquid medium

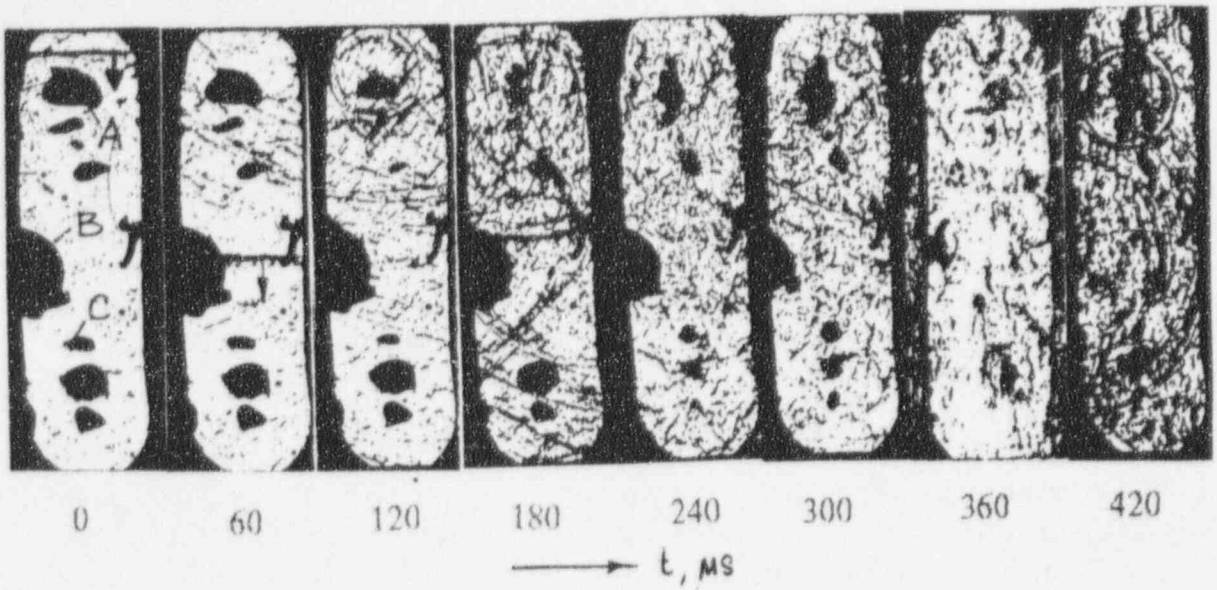

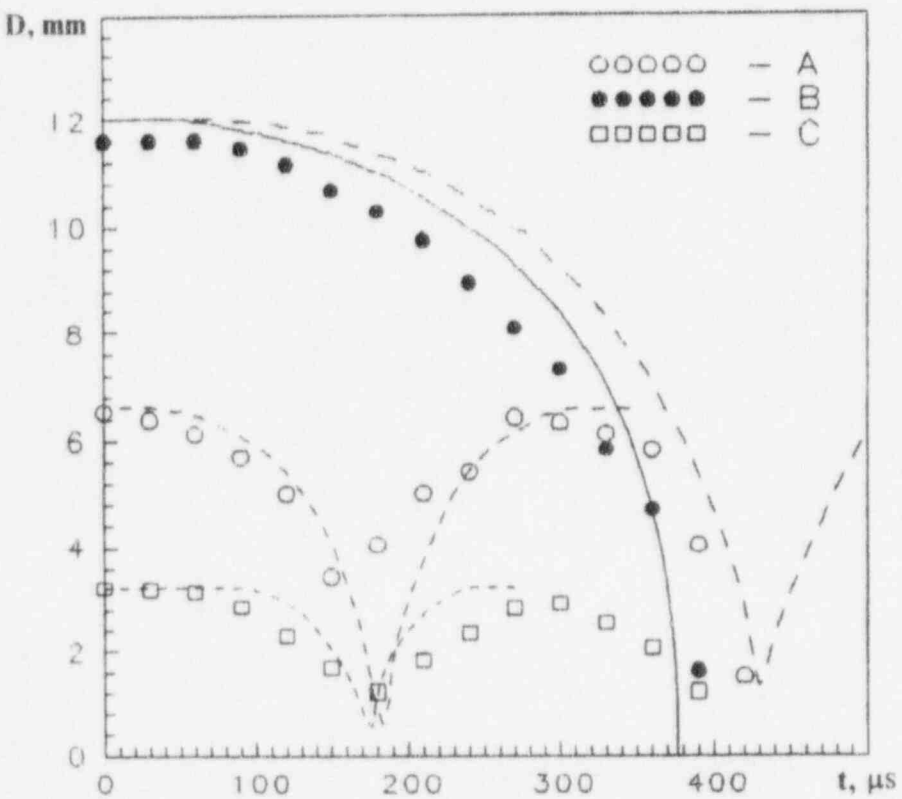

FIG.4 Behaviour of vapour bubbles in strong shock wave. Freon-113, p_0 =0.1MPa, Δp_0 =0.5MPa.

where $p_\infty = p_0 + \Delta p_0$. For $\Delta p_0 / \rho_l c_l^2 << \varphi_0 << 1$ $\Delta p_{max} \approx [\rho_l \Delta p_0 \varphi_0]^{1/2} c_l$. This value satisfactory describes the maximum possible amplitude of a pressure wave in our experiments. However, the use of "cell" model for the wave profile calculation leads to the results that are different from those obtained in the experiments. Perhaps, this is connected with a heat transfer law change on the last stage of a vapour bubble collapse. In this case the destruction of bubbles into smaller ones occurs and, as a consequence, the great intensification of heat transfer between vapour and liquid becomes a very important factor. Meanwhile, if using the formal procedure at the calculation of criteria W_*, that can obtain the values of M and W_*M equal 2-5 and 0.05-1 accordingly. Fig. 5 has shown that these values correspond to right upper zone of map. In opposite, the range of application of equation (2) for the prediction of pressure wave is the left down zone. Using this map can make up a prognosis of the dynamics of shock wave in different vapour-liquid medium. Thus, in medium with high values W* (water under lower static pressure, liquid metal) both damping and amplification of initial pressure wave are possible. This will be determine the amplitude of initial pressure perturbation or criteria M only. In contrast, for water at high static pressure (low value of W*) the generation of powerful pressure pulse can be a problem.

SLUG STRUCTURE

Collapse of single vapour slug. Let us consider the behaviour of a single vapour slug in a pressure wave with an amplitude $\Delta p_0 / p_0 > 1$. A change of pressure in the channel and a slug volume are given in Fig.6, whereas, Fig.7 shows the photographs of the slug behaviour in different time. Analysing the slug behaviour one can see a generation on the slug head the powerful cumulative jet. It breaks down the slug, and then an intensive growth of small disturbances on the interface takes place. Further, the slug destruction occurs and it turns into a cloud of small vapour bubbles. A complex pressure profile emerging in the channel is resulted by nonlinear pulsation of the formed cloud of bubbles. The maximum amplitude of these pulsation exceeds the maximum pressure of the first pulsation. If the intensity of the initial pressure disturbance begin to increase the "shock" regime of condensation appears (Fig.8). In this case the complete slug condensation happens in the front of the pressure wave. With this, a powerful pressure pulse is generated in the channel, its amplitude exceeds the amplitude of the initial loading by the order. The pressure pulse amplitude may be determined by using the simple relationships for waterhammer $\Delta p = \rho_l v_l c_l$, where v_l - is the velocity of liquid plug and the equation of liquid movement as a basis for calculations. Then

$$\frac{\Delta p_{max}}{p_0} = \left[2 \frac{\Delta p_0}{p_0} \frac{\rho_l c_l^2}{p_0} \frac{l_{g,0}}{l_l} \right]^{1/2} \qquad (5)$$

Here $l_{g,0}$, l_l - the length of vapour slug and liquid plug. Using the simultaneous measurements of pressure and volume of the slug and taking into consideration the correlation $dp / p + dV / V = (\gamma - 1) dQ / pV$ one can restore a heat release $Q(t) = \int_0^t q_l(t) F(t) dt$ during the slug condensation and, hence, the heat flux $q_l(t)$ on the interphase boundary. Using the assumption that the behaviour of the vapour is

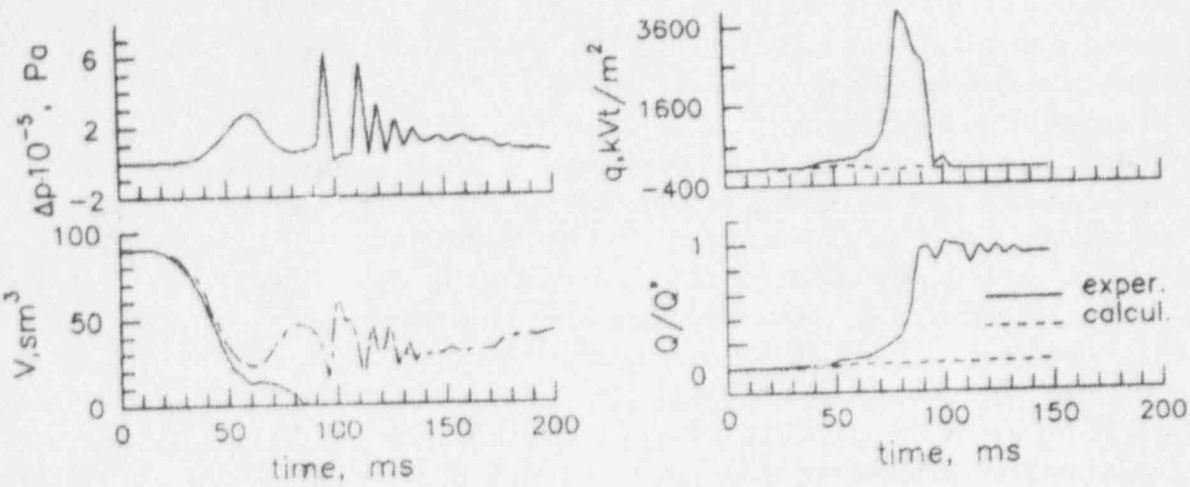

FIG.6 Change of pressure, volume, heat flux at shock loading of vapour slug. Freon-11, p_0 =0.1MPa, D=32mm, Δp_0 =0.15KPa

FIG.7 Behaviour of vapour slug at shock loading. Δp_0 =0.15KPa, D=32mm, freon-11, t=0,40,70,100 msec

adiabatic, vapour-liquid interface is in thermodynamic equilibrium and taking the vapour heat capacity on the saturation line one can obtain

$$\frac{\partial p}{\partial t} + \frac{\gamma p}{V}\frac{\partial V}{\partial t} = \frac{\gamma p}{\rho_g h_{gl}}\frac{F}{V} q_1(t) \qquad (6)$$

Fig.6 shows the measured values of p(t), V(t) and restored value $q_1(t)$ by using the equation (6). As is seen, at the end of the slug collapse the heat flux increases much. Let us compare the value of $q_1(t)$ restored from the experiment with the calculated value of heat flux obtained from the equation of heat conductivity for the liquid with the initially condition $T = T_0$ and boundary condition $T = T_s(t)$. For the definition of T(t) is used the experimental profile of p(t) and the Clapeyron - Clausius equation. The calculated value of V(t) can obtain from the equation (6) with using the pressure profile p(t), calculated value q(t) and the assumption that the surface form of slug keeps during the condensation. The calculated value of a slug volume, heat flux on the interphase boundary and heat release are shown by the dash line on Fig.6. As is seen the experimental values significantly exceed the calculated ones, which tells about considerable intensification of exchange processes. The analysis of all the data showed that the adequate agreement of the experimental data with calculations is observed only for weak ($\Delta p_0 / p_0 < 0.5$) pressure perturbations and only at the stage of the first compression of the slug. In the case of an increase in the initial pressure perturbation intensity can observe a more significant discordance of the experimental and calculated values V(t), q(t), Q(t). This factor should be taken into consideration in the theoretical models by introducing a coefficient of efficient turbulent heat conductivity.

Pressure wave of small amplitude. Alongside with general regularities of the experiments on the pressure wave propagation in a slug and bubble regimes of two-phase medium have also revealed the essential differences in the evolution of shock wave in slug chain compared to a bubble flow. The pressure wave structure here also differs much from that reported for a gas-liquid slug flow by [6]. Relatively weak waves $\Delta p_0 / p_0 < 1$ as well as in the case of a bubble medium acquire the oscillatory structure in the front at early formation stages (Fig.9), further oscillations attenuate and the front flattens. Such behaviour of the pressure wave is correspond to the map of wave regime - Fig.5, where the value of W* can be determined according of the size of slug [7]. An increase in the amplitude of an incident wave up to 1.2 results to the qualitative changes, the random high-amplitude pulses appear behind the front of a shock wave.

Strong amplitude pressure wave. The further increase in the amplitude of the initial pressure wave results in a rapid formation of a regular "comb"- like form of shock wave (Fig.10), each pulse of which corresponds to the collapse of the single slug in a slug chain and moves in the inverse direction (upwards) with the sound velocity in a pure liquid. In this case the first pulse corresponds to the front of complete condensation wave moving downwards. Its velocity agrees well with the expression for a stationary wave with complete condensation - U and is shown by solid line in Fig.11 and the CW-line on the Fig.10. A low-frequency rapidly attenuating precursor propagating with higher velocity (line SW) can be singled out in front of elastic wave. Its velocity is close to the value for a shock wave in a gas-liquid mixture $u = c_0\left[\Delta p_0 / p_0 + 1\right]^{1/2}$ [8], - dash line in the Fig.11. The threshold of the "comb"-like pressure wave generation ($\Delta p_0 / p_0 = 1.1\text{-}1.2$) is approximately equal

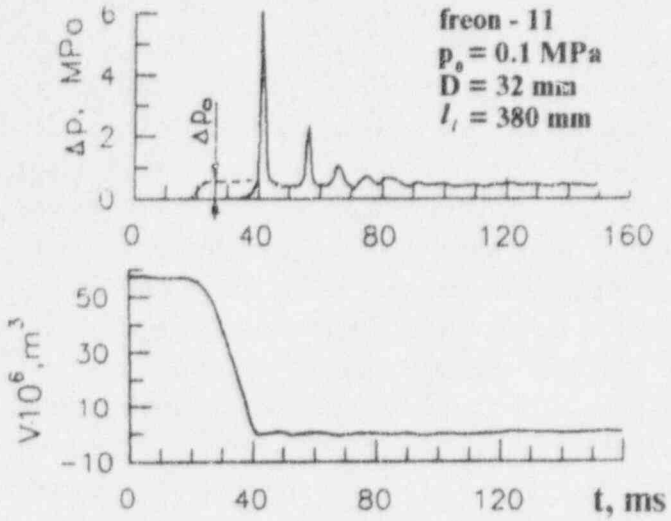

FIG.8 Collapse of vapour slug in strong pressure wave and generation of pressure pulse. ----- initial pressure wave.

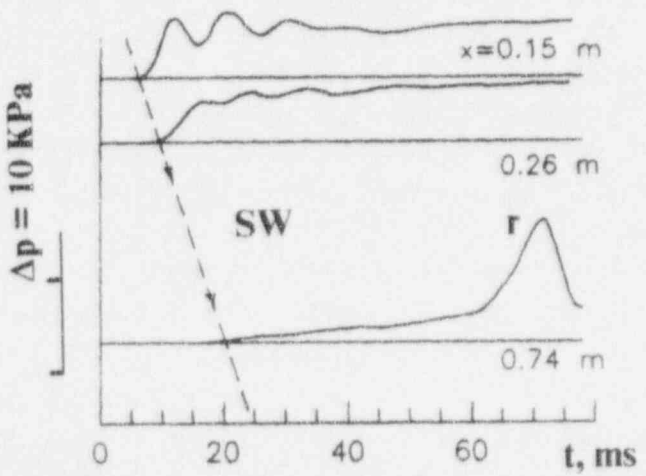

FIG.9 Propagation of weak shock wave in vapour-liquid slug medium. Freon-11, p_0 =0.1MPa, φ_0=20%, l_l=8mm, $l_{g,0}$ =30-35mm. r - reflected from shock tube bottom wave.

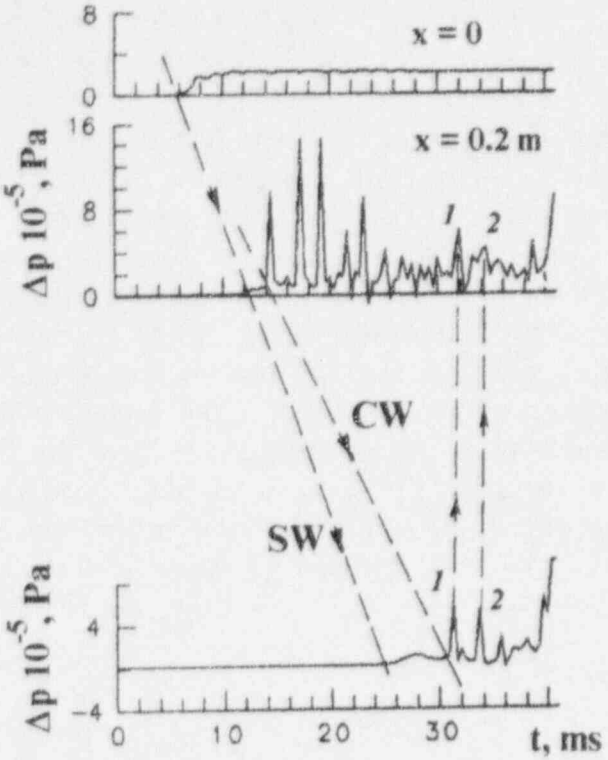

FIG.10 Strong shock wave evolution. Vapour-freon-11 medium, p_0=0.1MPa, φ_0=23%, D=8mm, x=0, 0.2, 0.65 m

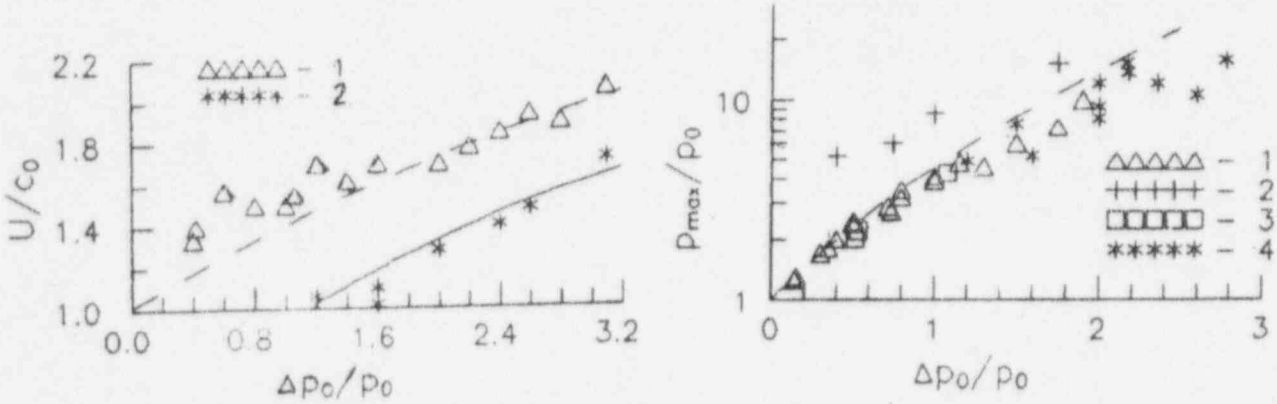

FIG.11 Wave velocity vs initial shock amplitude. 1-precursor, 2-first pulse of "comb" wave

FIG.12 Maximum pressure vs initial shock wave amplitude. Freon-11, p_0 = 0.1MPa, D=8mm,.Single slug: l_l =25-50mm, 1- $l_{g,0}$ =500mm, 2- $l_{g,0}$ =50-120mm. Slug chain: 3,4- φ_0 = 20-30%

to specific heats ratio γ, i.e. corresponds to a supersonic regime $U > c_0$ of the propagation of stationary wave with complete condensation, as it was in the case of a solitary shock pulse in a bubble medium. Thus, the splitting of the pressure wave propagating in vapour - liquid slug medium can occurs.

As can see from the experiments, the amplitude of the pressure wave in the medium is greater then the amplitude of initial wave. For the estimation of this amplitude the experiments with the collapse of a single vapour slug in pressure wave can be use. Fig.12 plots the amplitude of the pressure for the case of the single slug collapse, the maximum amplitude of the "comb" - like pressure wave formed in slug chain and the calculated value. As can see the maximum amplitude of shock wave corresponds with good accuracy the pressure which obtained during the collapse of single slug. Thus, in the limited case of initially strong pressure wave the correlation (5) can be use for the estimation of highest amplitude of shock wave which can appear in pipeline with slug structure of vapour-liquid flow.

This work was supported by the Russian foundation of fundamental investigation grant N 94-02-03971.

Table of nomenclature

- p - pressure
- Δp - perturbation of pressure
- V - volume
- T - temperature
- ρ - density
- φ - void fraction
- q - heat flux
- $h_{g,l}$ - latent heat of evaporation
- γ - adiabatic exponent
- R - bubble radius
- c - velocity of sound
- λ - thermal conductivity
- a - thermal diffusivity

subscripts

- 0 - initial unperturbed state
- l - liquid phase
- g - vapour phase

REFERENCES

[1] Nakoryakov V.E., Pokusaev B.G., Pribaturin N.A., Shreiber I.R., The wave dynamics of vapour-liquid medium, Int. J. of Multiphase Flow 14,6,655-677,(1988).

[2] Nakoryakov V.E., Pokusaev B.G., Shreiber I.R. Wave dynamics of gas- and vapor-liquid media. - New York a.o. Begell House Publishers, (1992).

[3] Akagawa,K., Fujii,T.,"Development of research on water hammer phenomena in two-phase flow", ASME-JSME Thermal Engineering Joint Conf.,Honolulu, 333-349,(1987).

[4] Bobko V.M., Karnauchov A.A., Kosarev V.F., Papurin A.N. Method of the particles photoregistration in high speed two-phase flow, J. Applied Mech. Tech. Physics, 5,115-119,(1982).

[5] Nigmatulin R.I., Dynamics of multiphase media", Moskow, Nauka, (1987).

[6] Nakoryakov V.E., Pokusaev B.G., Lezhnin S.I. Pribaturin N.A., Shock waves structure and their propogation in two-phase slug flow, Proc. 16th ISSW, Aachen, Germany , p.305-309,(1987).

[7] Pokusaev B.G.,Lezhnin S.I.,Pribaturin N.A., Waves in Gas-Liquid Medium of Slug Structure, Russian Journal Engineering Thermophysics, 1,4,259-290,(1991).

[8] Parkin B.R., Gilmore F.R., Brode H.L., Shock waves in bubbly water. Memorandum RM-2795-PR, (1961).

Evaluation of a Main Steam Line Break With Induced, Multiple Tube Ruptures: A Comparison of NUREG 1477 (Draft) and Transient Methodologies Palo Verde Nuclear Generating Station

May 30, 1995

Kathleen R. Parrish, P.E.
Arizona Public Service Company

Abstract

This paper presents the approach taken to analyze the radiological consequences of a postulated main steam line break event, with one or more induced tube ruptures, for the Palo Verde Nuclear Generating Station (PVNGS). The analysis was required to support the restart of PVNGS Unit 2, following the steam generator tube rupture event on March 14, 1993, and to justify continued operation of Units 1 and 3. During the post-event evaluation, the NRC expressed concern that Unit 2 could have been operating with potentially degraded tubes and that similar conditions could exist in Units 1 and 3. The NRC therefore directed that a safety assessment be performed to evaluate a "worst case" scenario, in which a non-isolable main steam line break occurs which induces one or more tube failures in the faulted steam generator. This assessment was to use the generic approach described in NUREG 1477 (Draft, June 1, 1993), "Voltage-Based Interim Plugging Criteria for Steam Generator Tubes - Task Group Report."

An analysis based on the NUREG approach was performed, but produced unacceptable results for off-site and control room thyroid doses. The NUREG methodology, however, does not account for plant thermal-hydraulic transient effects, system performance, or operator actions which could be credited to mitigate dose consequences. To deal with these issues, a more detailed analysis methodology was developed using a modified version of the Combustion Engineering Plant Analysis Code (CEPAC), that incorporates plant transient effects, iodine partitioning as a function of liquid level in the faulted generator, and operator actions consistent with the emergency procedures. This analysis examines the dose consequences for a main steam line break transient with induced tube failures (MSLBSGTR) for a spectrum of tube breaks equivalent to 1 to 4 double ended guillotine U-tube breaks. By incorporating transient plant system responses and operator actions, the analysis demonstrates that the off-site and control room dose consequences (thyroid) for a MSLBSGTR can be reduced to acceptable limits.

The transient based analysis, in combination with other corrective and recovery actions, provided sufficient justification for continued operation of PVNGS Units 1 and 3, and for the subsequent restart of Unit 2.

I. Introduction

This paper presents the approach taken to analyze the radiological consequences of a postulated main steam line break event with one or more induced tube ruptures (MSLBSGTR) for the Palo Verde Nuclear Generating Station (PVNGS). The analysis was required to support the restart of PVNGS Unit 2, following the steam generator tube rupture event on March 14, 1993, and to justify continued operation of Units 1 and 3. During the post-event evaluation, the NRC expressed concern that Unit 2 could be operated with potentially degraded tubes, despite the tube inspections, tube plugging, and other mitigating actions taken to ensure tube integrity, and that similar conditions could exist in Units 1 and 3. The NRC directed that a safety assessment be performed to evaluate a "worst case" scenario, in which a non-isolable main steam line break occurs which induces one or more tube ruptures in the faulted steam generator (MSLBSGTR), using the generic approach described in Section 4 of NUREG 1477 (Draft, June 1, 1993), "Voltage-Based Interim Plugging Criteria for Steam Generator Tubes - Task Group Report." The NRC further required that the NUREG 1477 approach be modified to explicitly account for several PVNGS plant specific features: lack of pressurizer power operated relief valves, low shut-off head safety injection pumps, plant-specific emergency operating procedures (EOPs), and the probability of one or more tube failures. The radiological consequences of such an event were not to exceed the applicable acceptance criteria. The NUREG 1477 methodology assumed a limiting dose of 30 REM thyroid for the 2 and 8 hour thyroid dose limits. In addition, the safety assessment had to demonstrate that the refueling water tank, the primary source of safety injection water, contained sufficient inventory to mitigate the event.

A plant specific analysis of thyroid dose consequences was performed based on the NUREG approach, but produced unacceptable results (see figures 1 through 4). The NUREG methodology does not, however, account for plant transient effects, system performance, or emergency procedures which could be credited to mitigate dose consequences for a MSLBSGTR. A more detailed analysis methodology was therefore developed, using a modified version of the Combustion Engineering Plant Analysis Code (CEPAC), that incorporated plant thermal-hydraulic transient effects, iodine partitioning as a function of liquid level in the faulted generator, plant specific system performance, and operator actions consistent with the PVNGS emergency procedures. This analysis examined the dose consequences for a MSLBSGTR, ranging from 1 to 4 double ended guillotine U-tube breaks and utilizing conservative assumptions for plant system response and operator actions. The analysis demonstrated that the offsite dose consequences (thyroid) for a MSLBSGTR, using Standard Review Plan (SRP) assumptions, could be maintained within 10 CFR Part 100 limits (300 REM), and that the control room dose consequences (thyroid) could be limited to 30 REM, by administratively limiting primary and peak iodine equilibrium activities to 0.6 μCi/gm and 12.0μCi/gm, respectively. In addition, a plant specific analysis of whole body dose consequences was performed, with acceptable results. These analyses, in combination with other corrective and recovery actions, provided sufficient justification for continued operation of PVNGS Units 1 and 3, and the eventual restart of Unit 2.

II. Principle Results - NUREG 1477 (Draft) Methodology

The requested safety assessment was initially performed based on the NUREG 1477 approach. This methodology, however, utilizes extremely conservative, simplifying assumptions that do not account for transient effects in determining offsite doses. In addition, the methodology specifies that the acceptance criteria for offsite dose consequences be limited to a small fraction of 10CFR Part 100 limits (10%, or 30 REM) for selected cases. The initial evaluation, as shown on figures 1 through 4, resulted in offsite dose consequences far in excess of 10CFR Part 100 limits. These results were consistent with those originally set forth in NUREG 1477, but were unacceptable as a basis for continued operation of PVNGS Units 1 and 3 or restart of Unit 2.

NUREG 1477 (Draft) presents a sensitivity study of the 2 and 8 hour dose consequences[1] of a postulated main steam line break with induced primary to secondary leakage ranging from 0.1 gpm to 1000 gpm. Dose consequences calculated in the draft NUREG, based on both Standard Review Plan (SRP) and realistic assumptions for 2 and 8 hour intervals, include:

1) EAB 2-Hour Thyroid Dose - Pre-existing Iodine Spike (PIS)
2) LPZ 8-Hour Thyroid Dose - PIS
3) EAB 2-Hour Whole Body Dose
4) LPZ 8-Hour Whole Body Dose
5) EAB 2-Hour Thyroid Dose - Event Generated Iodine Spike (GIS)
6) LPZ 8-Hour Thyroid Dose - Event GIS
7) Control Room Operator - Thyroid Dose

In addition, doses were calculated using SRP assumptions with realistic activities instead of the Technical Specification limits. The draft NUREG summarizes the initial conditions, assumptions, and methodology used to calculate doses, and presents the corresponding dose consequences for postulated constant leak rates from 0.1 gpm to 1000 gpm, but does not present explicit methodology (e.g. dose equivalent $Iodine_{131}$ concentrations assumed for the 2 and 8 hour GIS cases are not given). Hence, the dose consequence methodology for the PVNGS specific cases vary somewhat from that used for the draft NUREG.

---

1. The 2 hour doses are calculated at the exclusion area boundary (EAB), and the 8 hour doses are calculated at the perimeter of the Low Population Zone (LPZ).

II.1. Thyroid Dose Calculations for Postulated Accidents Using SRP Assumptions

Dose calculations similar to those presented in NUREG 1477 (Draft) were performed using PVNGS specific assumptions, as summarized in Table 1.

Table 1
Parameters Used For PVNGS Offsite Doses - SRP Assumptions

Parameter	Value	Units
χ/Q for 2 hour, EAB	.00031	sec/m^3
χ/Q for 8 hour, LPZ	.000051	sec/m^3
χ/Q for Control Room Doses 0 - 8 hours	.00197	sec/m^3
Breathing Rate	3.47×10^{-4}	m^3/sec
Dose Conversion Factor	1.48×10^6	REM/Ci (ICRP 2)
Pre-Accident Iodine Spike (PIS), T. S. limit	60	µCi/gm
Event Generated Iodine Spike (GIS), T. S. limit (initial primary activity, spiking factor)	1.0, 500	µCi/gm, spiking factor
Coolant Gross Activity, per T. S.	$100/\bar{E}$	µCi/gm

The MSLB event was reanalyzed for the current PVNGS cycles to establish initial conditions that ensure no fuel failure will occur during a MSLBSGTR event. Hence, the only source terms contributing to off-site doses are those due to the initial primary and secondary activities noted above.

The dose calculations were performed for a postulated MSLB, outside containment and upstream of the main steam isolation valves, with one or more induced tube ruptures. These calculations address induced tube leak rates ranging from 0.1 to 1000 gpm. These leak rates are assumed to be constant over the intervals of interest (2 and 8 hours). Primary to secondary leakage due to one or more induced tube breaks is assumed to occur at the start of the transient.

Doses for the PIS cases are calculated assuming a constant reactor coolant system (RCS) activity without accounting for the mitigating effects of diluting primary coolant activity due to safety injection. Doses for the 2 and 8 hour GIS cases are calculated based on the average RCS activities which would occur over the intervals of interest if activity additions due to spiking are applied to a fixed liquid volume (i.e., no mitigation due to safety injection). This data was extracted from the SGTR analyses presented in the PVNGS Updated FSAR. The average activities are assumed to be bounding for 1 or more tube failures. Dose consequences based on the NUREG methodology can be summarized by the following equation,

$$Dose_i = dcf \times br \sim Activity_i \times Leakrate \times T \times \chi/Q \qquad \text{Eq. 1}$$

where:
Dose = Thyroid dose over interval *t* (REM)
dcf = dose conversion factor (REM/Ci)
br = breathing rate (m^3/sec)
Activity = Activity of leak rate over interval *t* (Ci/gal)
(for GIS cases, an average is used)
Leakrate = Average leakrate (gal/min)
T = Interval of interest (min)
χ/Q = atmospheric dispersion factor (sec/m^3)

The results of the PVNGS dose calculations for the GIS and PIS cases based on SRP assumptions are shown in figures 1 through 4 (designated "S" on figures).

II.2. Whole Body Dose Calculations Using SRP Assumptions

The Whole Body Dose (WBD) calculations were performed in accordance with the methodology described in PVNGS Updated FSAR Section 15B, "Dose Models Used to Evaluate the Environmental Consequences of Accidents," and CE-NSPD-151-P, "CE Safety Analysis Methods for Calvert Cliffs Units 1 and 2 (June 1981)," as summarized below.

The total whole body source term available in the reactor coolant primary system was calculated for a postulated 60 µCi/gm dose equivalent $Iodine_{131}$, and 100/$\bar{E}$ µCi/gm for gross coolant activity. Based on the assumption that no DNBR induced fuel failure occurs for the postulated MSLB with induced tube failure event, this represents the total available whole body dose source term. The whole body dose is then calculated as:

$$WBD_a = K_\gamma \times \left(\bar{E}_\gamma + \left(\frac{K_\beta}{K_\gamma} \right) \bar{E}_\beta \right) \times R_a \times \chi/Q \qquad \text{Eq. 2}$$

Where:
WBD_a = Whole Bode Dose, REM, for the isotopes of concern,
K_γ = .23 REM x m^3 x dis/Mev x sec x Ci),
K_β = .25 REM x m^3 x dis/Mev x sec x Ci),
$\bar{E}_\gamma$ = average γ energy (Mev/dis) for isotopes of concerns,
$\bar{E}_\beta$ = average β energy (Mev/dis) for isotopes of concern,
χ/Q = atmospheric dispersion coefficient, sec/m^3, and
R_a = source term, Curies

A PVNGS gross activity limit of 100/$\bar{E}$ corresponds to approximately 83 µCi/gm for non-iodine WBD contributors. The RCS contains approximately 2.612 x 10^8 gm of water. The corresponding WBD source terms are then 15,670 Ci ($DEQI_{131}$) and 21,500 Ci (Xe, Kr isotopes). Using Equation 2, the corresponding whole body doses for the intervals of interest are:

WBD(2hr) < 3.0 REM

WBD(8hr) < 1.0 REM

These values are well within the 10CFR100 specified acceptance criteria of 25 REM. Hence, no further WBD calculations are deemed necessary.

II.3. Thyroid Dose Calculations for Postulated Accidents Using Realistic Assumptions

Realistic dose calculations were performed using PVNGS specific assumptions, as summarized in Table 2.

Table 2
Parameters Used For PVNGS Offsite Doses - Realistic Assumptions

Parameter	Value	Units
X/Q for 2 hour, EAB	.000043	sec/m^3
X/Q for 8 hour, LPZ	.0000049	sec/m^3
Breathing Rate	3.47×10^{-4}	m^3/sec
Dose Conversion Factor	1.07×10^6	REM/Ci (ICRP 30)
Pre-Accident Iodine Spike (PIS), realistic value, per NUREG 1477	12	µCi/gm
Event Generated Iodine Spike (GIS), administrative limit (initial primary activity, spiking factor)	0.6, 500	µCi/gm, spiking factor

The results of the dose calculations for the GIS and PIS cases based on realistic assumptions are shown in Figures 1 through 4. (designated "R" on figures).

II.4. Reductions in Calculated Offsite Dose by Applying Administrative Limits to Technical Specification Activities

In addition to the preceding calculations, dose calculations were also performed using the SRP assumptions, with primary activities reduced to realistic values (0.6 and 12 µCi/gm for the GIS and PIS cases, respectively). The results of these dose calculations are also shown in figures 1 through 4 (designated "I" on figures).

II.5. Control Room Doses

Control room dose calculations similar to those presented in the draft NUREG Section 4.1.5 were performed using PVNGS specific assumptions, as summarized in Table 1. The results are presented in figure 5.

II.6. Results Based on NUREG 1477 Methodology

As can be see from figures 1 through 5, a safety assessment of the radiological consequences based solely on the NUREG 1477 Draft methodology produces results far in excess of the allowable acceptance criteria.

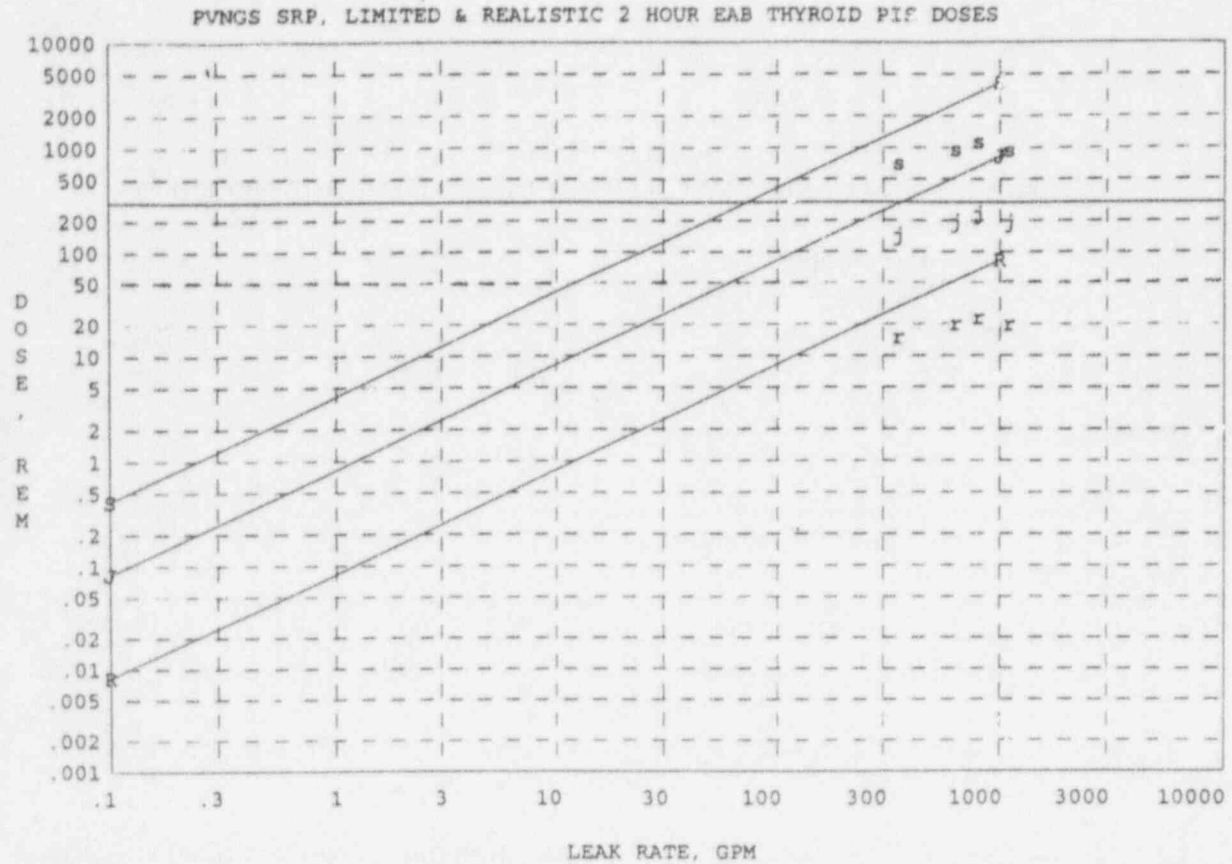

LEGEND (figures 1 through 5):

Based on	NUREG 1477 Results	CEPAC Results
SRP Assumptions	S	s
SRP Assumptions With Reduced Activity	J	j
Realistic Assumptions	R	r

Figure 1 - Two Hour EAB Thyroid PIS Doses

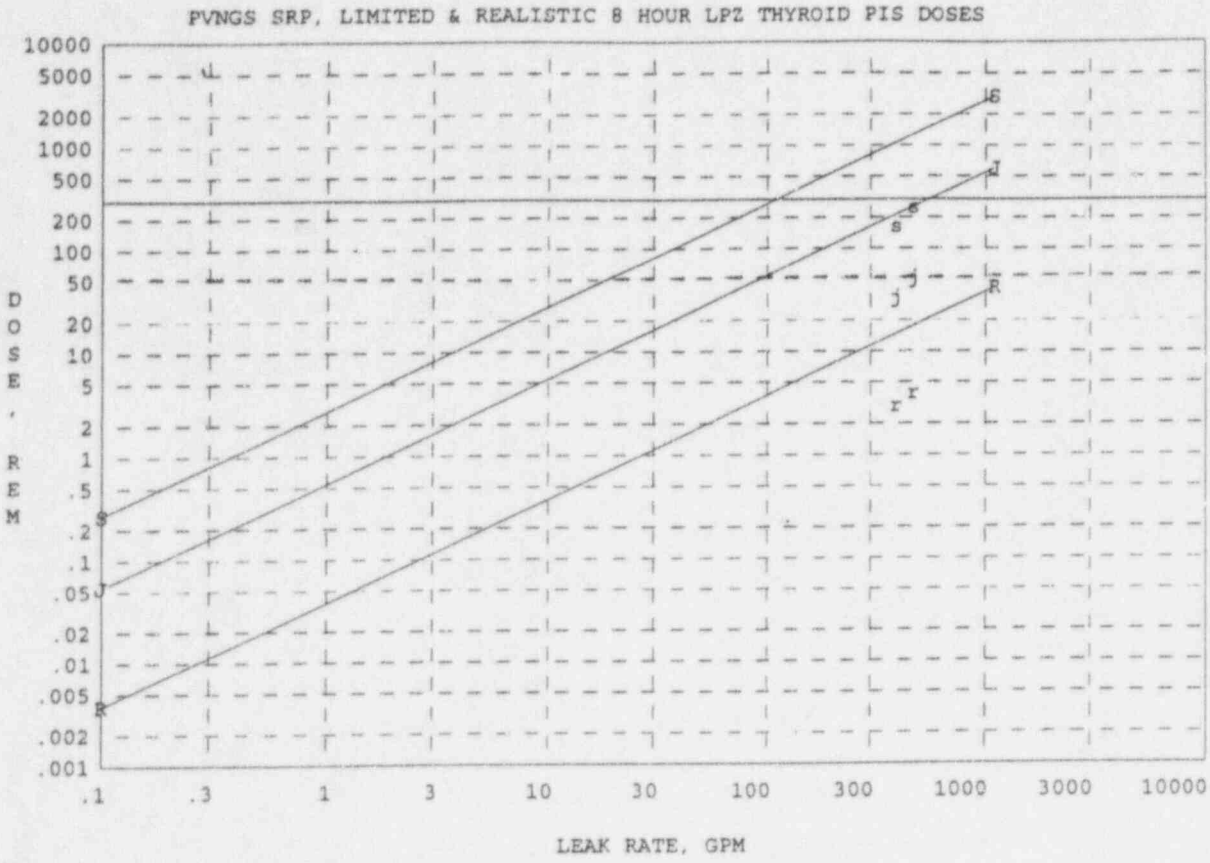

Figure 2 - Eight Hour LPZ Thyroid PIS Doses

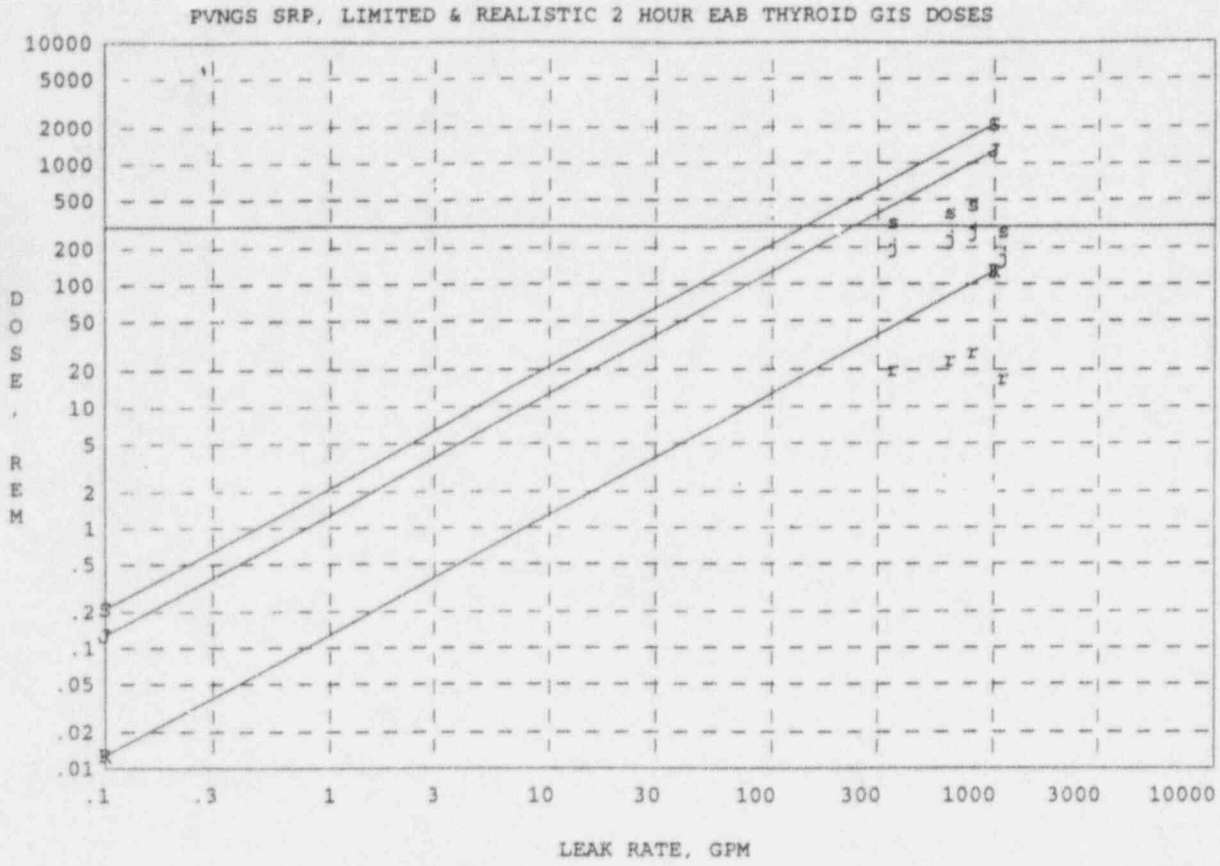

Figure 3 - Two Hour EAB Thyroid GIS Doses

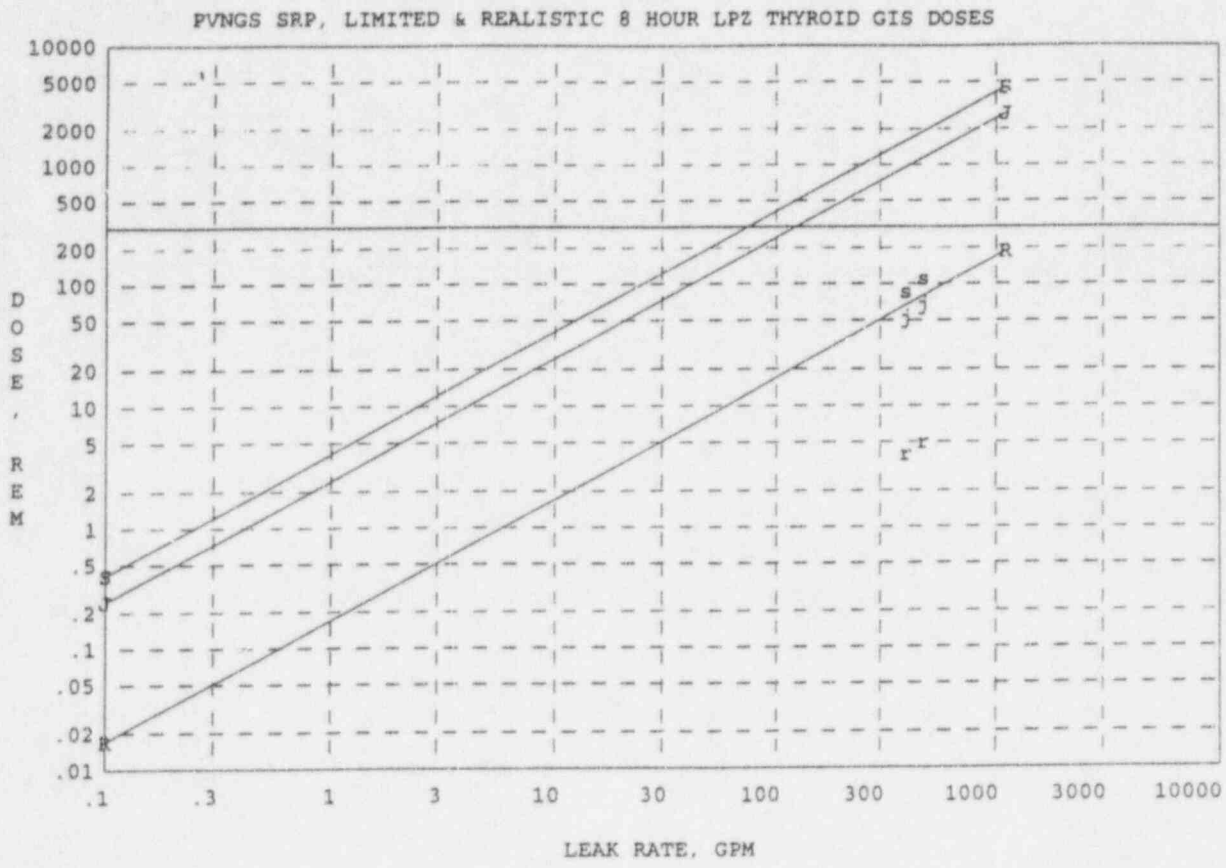

Figure 4 - Eight Hour LPZ Thyroid GIS Doses

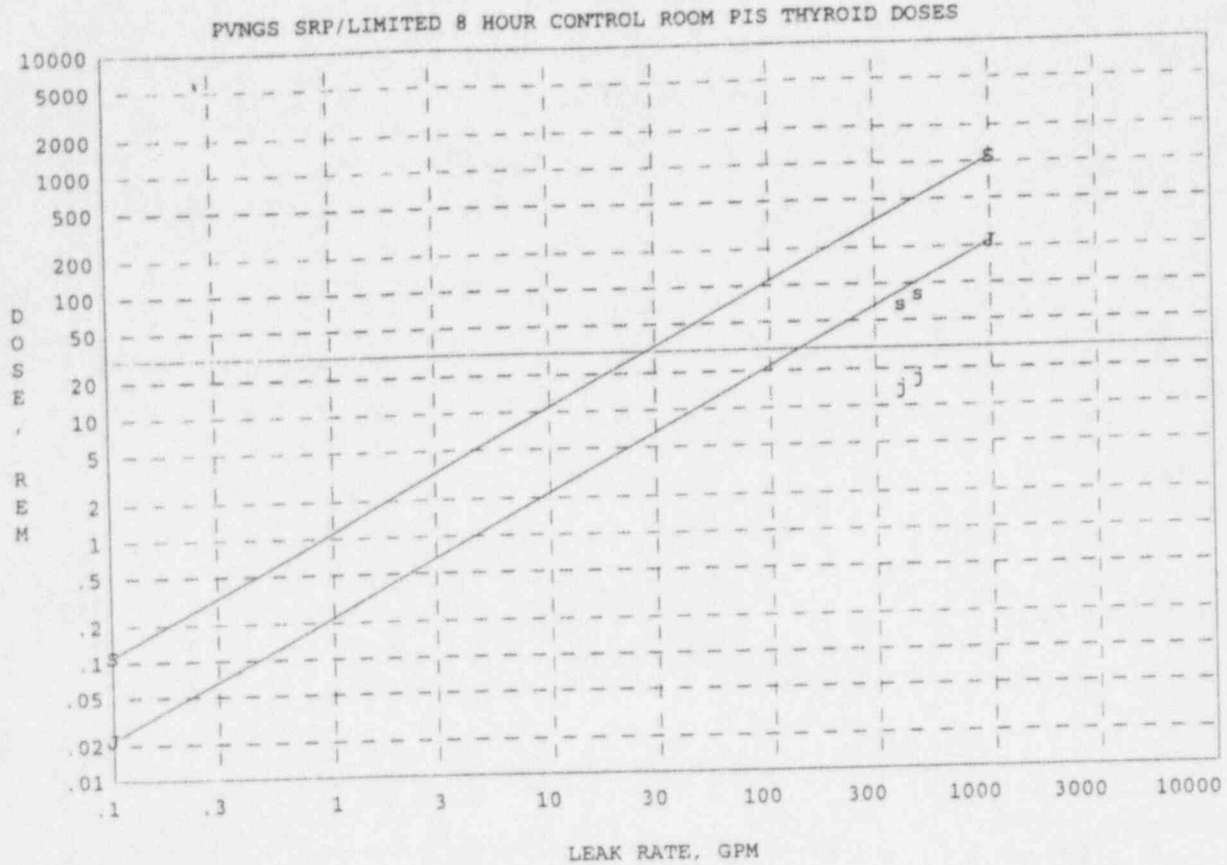

Figure 5 - Eight Hour Control Room Thyroid PIS Doses

III. Principle Results - CEPAC Methodology

To support continued operation of Units 1 and 3, as well as the restart of Unit 2, a more detailed safety assessment based on thermal-hydraulic transient effects was required. This assessment was performed in three parts:

First, a probabilistic risk assessment was developed to establish appropriate acceptance criteria for dose consequences as a function of the probability of occurrence. The assessment concluded that the probability of a MSLBSGTR event was sufficiently low to justify using offsite thyroid dose acceptance criteria up to 10 CFR Part 100 limits (300 REM) for both event generated (GIS) and pre-existing (PIS) iodine spike cases. The NRC concurred with this assessment, provided the corresponding dose consequences based on ***realistic*** assumptions for GIS cases were also less than 30 REM.

Second, the ABB-CE licensing codes were utilized to establish more stringent controls for the plant digital protection system that would ensure that a MSLBSGTR event with up to 3 simultaneous double-ended guillotine tube ruptures will not result in fuel failure.

Finally, CEPAC was modified as described below and used to simulate a main steam line break event with induced, multiple tube ruptures in order to calculate offsite and control room doses, and integrated leakage, across a spectrum of tube ruptures ranging from 1 to 4 double-ended guillotine breaks. Additional offsite doses were then derived from the values calculated by CEPAC, using both standard review plan assumptions and realistic assumptions.

III.1. CEPAC Code Modifications

For this analysis, the CEPAC source code was modified to incorporate the water quality definitions and sub-routines from the EPRI RETRAN-02 MOD 4 code,[5] to allow CEPAC to cover a greater range of thermal hydraulic conditions. In addition, the CEPAC dose calculation subroutine was modified to redefine the secondary side partition factor (DF) for bulk boiling as a function of ***steam generator liquid level***, such that the DF equals:

- 1.0 (i.e., all of the iodine in the boiled off inventory becomes) for intervals in which the SG level is less than 4.0 feet above the tube sheet),
- 0.10 when the SG liquid level is greater than 4.0 feet, but less than the height of the tube bundle (10% of the iodine in the boiled off inventory becomes airborne), and
- 0.01(iodine partitioning per SRP) when the SG liquid level equals or exceeds the height of the tube bundle (1.0% of the iodine in the boiled off inventory becomes airborne).

In addition, major edits and graphs were redefined, as needed, to capture the parameters of interest.

III.2. CEPAC Database

In addition to the source code changes, the CEPAC Palo Verde specific database was modified to reflect SRP assumptions as noted in Table 1. A sequence of events was then established to conservatively reflect plant system performance and operator actions due to a postulated

MSLBSGTR. Plant response was then examined for four different scenarios: a non-isolable MSLB with one through four double-ended guillotine tube breaks in the faulted SG. As a practical consideration, and based on data from the actual SGTR event in Unit 2, a DEG tube break is assumed to be equivalent to two induced axial breaks of the type postulated to occur due to a pressure transient across the tube bundle.

III.3. Initial Conditions and Assumptions

The initial conditions and parameters assumed in the analysis of the system response to a MSLB with induced, multiple tube failures are summarized in Table 3. The values of these inputs were conservatively selected to maximize the initial and integrated leakrate and the fraction of the leakrate that flashes once it enters the faulted generator, and hence the radiological release to atmosphere, during the course of the transient. The maximum allowed Technical Specification core inlet temperature, including instrument uncertainties, is used in the analysis. This results in a correspondingly high initial steam generator pressure and increases the steam releases through the main steam safety valves (MSSVs) and the atmospheric dump valves (ADVs) during the initial phases of the transient. An initial core flow of approximately 95% of design flow is used, corresponding to the minimum flow required by the Technical Specifications. This results in higher enthalpy fluid entering the steam generator, a resultant increase in flashing fraction, and higher activity releases through the main steam safety valves (MSSVs) and atmospheric dump valves (ADVs). A maximum initial pressurizer pressure was selected to increase the initial tube leak rate.

The assumed safety injection actuation signal (SIAS) setpoint results in the earliest possible delivery of high pressure safety injection (HPSI) flow. Furthermore, no delay time is applied to the signal. In addition, two HPSI pumps are assumed to be available, maximizing the flow delivered to the RCS following a SIAS. These assumptions result in higher post trip RCS pressures, and maximize the primary to secondary leakage.

Table 3
Initial Conditions and Parameters

Parameter, Units	Value
Initial Core Power Level,% Rated	100
Core Inlet Coolant Temperature, ^{o}F	570
Initial Flow,% Rated Flow	95
RCS Pressure, psia	2339
Steam Generator Pressure, psia	1108
Initial Pressurizer Liquid Volume, ft^3 (nominal)	890
Steam Generator Level, ft above tube sheet (~80%WR)	37.1

The following assumptions were made to maximize offsite dose:

- No loss of offsite power. RCS pump heat increases heat load on the faulted SG and delays level recovery, resulting in higher offsite doses. Pumps are not secured unless required by emergency procedures.
- Instrument uncertainties are bounded by assumed subcooling margin requirements during the controlled cooldown.
- All tube breaks are assumed to occur in the faulted SG.

The following operator actions were assumed for these transients, consistent with the PVNGS Emergency Operating Procedures.

- 5 minutes after SIAS - Operators trip 2 of 4 reactor coolant pumps (standard post trip action). This action was not credited for the 3 DEG tube break case. Effects on dose consequences are conservative.
- 30 minutes - Operators throttle HPSI due to high pressurizer level and subcooling margin (delayed to maximize dose consequences). Assumed for all cases.
- 40 minutes - Operators begin cooling plant with intact generator, as required.
- 60 minutes - Operators determine combined event is in progress due to loss of level in pressurizer and high subcooling margin and begin feeding the faulted generator. Not credited for the 4 tube case. No credit is taken for radiation monitoring or chemistry sampling.
- Operators are assumed to initiate shutdown cooling 2 hours after entry conditions are reached.
- Events terminate at 8 hours.

III.4. Sequence of Events and Systems Operation

Of the four scenarios analyzed, the MSLB with 3 DEG tube ruptures resulted in the highest offsite dose consequences, and is used as the representative case. Table 4 presents the sequence of events assumed to occur during a MSLB event which induces 3 DEG tube ruptures a few seconds after reactor trip. Off-site power is assumed to remain available throughout the event. This is conservative in terms of dose consequence, since it maximizes heat removal via the faulted generator throughout the event due to pump heat. To further maximize heat removal by the faulted generator, main feedwater to the intact generator is assumed to fail on reactor trip. Three DI ruptures represent approximately 5 times the initial leakage (approx. 250 gpm) that occurred during the PVNGS Unit 2 event. Figures 6 through 19 present the dynamic behavior of important NSSS parameters for this case.

At 0.0 seconds, a MSLB occurs on SG#2. The reactor trip and MSIS occur approximately 3 seconds later due to low SG pressure. The main steam isolation valves (MSIVs) close, isolating 3 of the 4 main steam lines. At 10 seconds, 3 double ended guillotine tube ruptures are assumed to occur in SG#2. At ~20 seconds, a SIAS occurs. At ~28 seconds an AFAS occurs on the faulted generator, but auxiliary feedwater flow is locked out due to low pressure in the faulted generator. The faulted generator essentially boils dry at ~200 seconds, but the RCS continues to cool down

Table 4
Sequence of Events for a Main Steam Line Break With 3 Induced Double Ended Guillotine Tube Breaks

Time (sec)	Event
0.0	Main steam line break occurs
3	Reactor trip on low SG pressure
3	MSIS occurs
10	3 U-tubes fail (double ended guillotine breaks)
20	SIAS, HPSI injection
27	Pressurizer empties
28	Aux. Feedwater Actuation Signal (AFAS) on SG#2 (locked out)
1810	Operator initiates auxiliary feedwater (one pump) to intact steam generator
1920	Operator throttles HPSI ~50% to reduce pressure - all throttle criteria met
2410	Operator begins a controlled cooldown plant with the intact SG and opens pressurizer vent path. Steaming rate, venting and feed rate to the intact SG are periodically adjusted to maintain desired conditions.
3600	Operator confirms primary to secondary leak is in progress and begins feeding ruptured steam generator (only 1 aux. feedwater pump credited)
3863	Level recovered in faulted steam generator to 4.0 feet above tube sheet
4162	Shutdown cooling entry conditions reached
5167	Level recovered in faulted steam generator to above U-tubes, ft.
28,800	Transient ends

due to boil off of the leakage. At ~1425 seconds, primary pressure rebounds to a maximum of 1164 psia, at which time HPSI flow essentially matches the leak rate and RCS makeup due to liquid contraction effects. Subcooling continues to increase due to the ongoing cooldown. At ~30 minutes, operators begin steaming and feeding the intact generator at a nominal rate of 650 gpm (only one auxiliary feedwater pump is assumed to be available). At 32 minutes, operators are assumed to throttle safety injection flow due to high pressurizer level and subcooling margin. At ~42 minutes the operators open the pressurizer vent to aid depressurization (both auxiliary and main spray are assumed to be unavailable) and increase steaming from the intact generator to establish and maintain a controlled cooldown per the Technical Specification cooldown limits. At 60 minutes, the operators are assumed to have determined that primary to secondary leakage is occurring in the faulted SG. At ~64 minutes, a steam/water interface is assumed to exist in the faulted SG, and a DF of 0.10 for bulk boiling is assumed. At approximately 86 minutes, the liquid level in the faulted SG is at or above the top of the tube bundle, and a DF of 0.01 for bulk boiling is assumed. The RCS temperature and pressure are now within the shutdown cooling system entry conditions (350 ^{o}F, 400 psia). Nevertheless, for purposes of conservatively determining offsite dose, all cooling is assumed to continue via the steam generators for 8 hours. This analysis assumes

that the shutdown cooling (SDC) system will be placed in service within 2 hours of reaching entry conditions, and that the RCS will be at cold shutdown conditions 4 hours after the SDC is placed in service. Hence, the actual event would be over within 8 hours.

III.5. Results of Transients Analyzed

Transients were performed for a MSLBSGTR with 1 through 4 DEG tube breaks for a two hour interval to determine the sensitivity of offsite dose to the number of tube breaks. The results of the sensitivity study (i.e., 1, 2, 3 and 4 DEG tube breaks) are summarized in Table 5. The corresponding average leak rates are also shown.

Table 5
Comparison of 2 Hour Off-Site Dose Consequences and Average Leak Rates from Transient Results for a Main Steam Line Break With Induced 1, 2, 3 and 4 DEG Tube Breaks

Dose Consequences, REM	1 Tube	2 Tubes	3 Tubes	4 Tubes
2 Hour EAB, SRP Assumptions, GIS	324	391	454	273
2 Hour EAB, Realistic Assumptions[a], GIS	20	24	28	17
2 Hour EAB, SRP Assumptions with realistic initial activities[a], GIS	**200**	**235**	**273**	**164**
2 Hour EAB, SRP Assumptions, PIS	707	960	1145	949
2 Hour EAB, Realistic Assumptions[a], PIS	15	20	23	20
2 Hour EAB, SRP Assumptions with realistic initial activities[a], PIS	**142**	**192**	**229**	**190**
Average 2 Hour Leak Rates, GPM	352	635	804	1105

a. 0.6 and 12 μCi/gm for GIS and PIS initial activities. Realistic dcf and X/Q values.

Based on these results, the MSLBSGTR events with 2 and 3 DEG tube breaks were analyzed for 8 hour intervals. The summary of offsite dose consequences for these cases is presented in Table 6. Of these two cases, the MSLBSGTR event with 3 DEG tube breaks was found to be more limiting.

A closer examination of the transient results reveal that there are several competing effects affecting the offsite dose consequences. Increasing the number of DEG tube breaks, and hence the leakrate, increases the offsite dose consequences until the leak itself begins to reestablish a steam/liquid interface within the faulted generator, and to significantly contribute to raising the liquid level above the top of the U-tube bundle. This effect is best shown in figure 18, which depicts the change in partition factor as a function of SG level. For the 3 tube case, step changes in partitioning occur at 64 and 86 minutes. In the 4 tube case, these step changes occur sooner, at 40 and 70 minutes. In addition, once the primary system has cooled sufficiently to allow the faulted SG to refill, the flashing fraction becomes very small (see figure 17). Hence, the partitioning effects tend to dominate the offsite dose consequences because the subsequent additions to offsite doses are strongly driven by bulk boiling, rather than the flashed fraction of the leakrate.

Table 6
Summary of Off-Site Dose Consequences for CEPAC Transients of a Main Steam Line Break With Induced Leakage for 2 and 3 DEG Tube Breaks

Dose Consequences	GIS Cases, REM		PIS Cases, REM	
Applicable Limits, 10CFR100	300		300	
Number of DEG Tube Breaks	2	3	2	3
2 Hour EAB, SRP Assumptions	391	454	960	1145
2 Hour EAB, Realistic Assumptions[a]	24	28	20	23
2 Hour EAB, SRP Assumptions with realistic initial activities (0.6 and 12 μCi/gm)	235	273	192	229
8 Hour LPZ, SRP Assumptions	86	111	165	200
8 Hour LPZ, Realistic Assumptions[a]	4	5	3	3
8 Hour LPZ, SRP Assumptions with realistic initial activities (0.6 and 12 μCi/gm)	52	67	33	40

a.0.6 and 12 μCi/gm for GIS and PIS initial activities. Realistic dcf and X/Q values.

III.6. Derivation of Offsite Doses From CEPAC Calculations

The CEPAC calculated 2 hour EAB GIS dose based on SRP Assumptions ($REM_{GISs2hr}$) is 454 REM. Corresponding realistic doses, and doses based on SRP assumptions with realistic activities, may be derived from these values by applying appropriate ratios of primary activity, dose conversion factors, and atmospheric dispersion factors, as shown below. To calculate the 2 Hour EAB GIS Dose, Realistic Assumptions ($REM_{GISs2hr}$):

$$REM_{GISr2hr} = REM_{GISs2hr} \times \left(\frac{ACT_r}{ACT_{srp}}\right) \times \left(\frac{DCF_r}{DCF_{srp}}\right)_{2hr} \times \left(\frac{X/Q_r}{X/Q_{srp}}\right)_{2hr} \quad \text{Eq. 3}$$

Such that:

$$REM_{GISr2hr} = 454 \times \left(\frac{0.6}{1.0}\right) \times \left(\frac{1.07\times10^{6}}{1.48\times10^{6}}\right) \times \left(\frac{0.000043}{0.00031}\right)_{2hr} = 27.32 \approx 28REM \quad \text{Eq. 4}$$

Similar ratios were applied to the CEPAC calculated doses to derive the offsite doses shown in Table 6.

The control room 8 hour GIS doses based on transient results were derived as follows:

$$REM_{CRGISs8hr} = REM_{GISs8hr} \times \left(\frac{1}{pf}\right) \times \left(\frac{X/Q_{cr}}{X/Q_{srp}}\right)_{8hr} \quad \text{Eq. 5}$$

where: pf = the protection factor for the control room essential air handing system. This value is 95 for PVNGS.

X/Q_{cr}= atmospheric dispersion factor for control room.

Then:

$$REM_{CRGISs8hr} = 111 \times \left(\frac{1}{95}\right) \times \left(\frac{0.00197}{0.000051}\right)_{8hr} = 45.13 \approx 46REM \quad \text{Eq. 6}$$

To calculate the Control Room 8 hour GIS dose for SRP assumptions with realistic activities:

$$REM_{CRGISj8hr} = REM_{CRGISs8hr} \times \left(\frac{ACT_r}{ACT_{srp}}\right) \quad \text{Eq. 7}$$

such that:

$$REM_{CRGISj8hr} = 46 \times \left(\frac{0.6}{1.0}\right) = 27.6 \approx 28REM \quad \text{Eq. 8}$$

Similarly, Control Room 8 hour PIS doses based on transient results are as follows:

$$REM_{CRPISs8hr} = REM_{PISs8hr} \times \left(\frac{1}{pf}\right) \times \left(\frac{X/Q_{cr}}{X/Q_{srp}}\right)_{8hr} \quad \text{Eq. 9}$$

Then:

$$REM_{CRPISs8hr} = 200 \times \left(\frac{1}{95}\right) \times \left(\frac{0.00197}{0.000051}\right)_{8hr} = 81.32 \approx 82REM \quad \text{Eq. 10}$$

To calculate the Control Room 8 hour PIS dose for SRP Assumptions with Realistic Activities:

$$REM_{CRPISj8hr} = REM_{CRPISs8hr} \times \left(\frac{ACT_r}{ACT_{srp}} \right) \quad \text{Eq. 11}$$

such that:

$$REM_{CRPISj8hr} = 82 \times \left(\frac{12}{60} \right) = 16.4 \approx 17REM \quad \text{Eq. 12}$$

III.7. Integrated RCS Leak

The average leak rate for a MSLBSGTR with 3 DEG tube breaks represent a maximum integrated leak of less than 230,000 gallons for an eight hour interval. An additional 28,500 gallons are needed to account for liquid contraction effects in the RCS, for a total RWST inventory makeup requirement of less than 260,000 gallons. The RWST at PVNGS has a minimum required capacity of 600,000 gallons, hence, inventory make-up is not a concern.

IV. Conclusions

The off-site and control room thyroid dose consequences obtained via transient analyses are depicted on figures 1 through 5 (see "s," "j" and "r" designators). A comparison of the off-site doses, determined using both the NUREG 1477 and CEPAC methodologies, makes it clear that accounting for transient effects significantly reduces dose consequences, when compared to those obtainable using the NUREG 1477 methodology. Nevertheless, a combination of both transient methodologies and administrative limits on dose equivalent iodine may be needed to ensure acceptable results.

With appropriate modeling, transient analysis codes can be utilized to conservatively assess the dose consequences of MSLBSGTR events, demonstrate acceptable results, and identify ways of further reducing dose consequences by incorporating additional guidance into the emergency operating procedures.

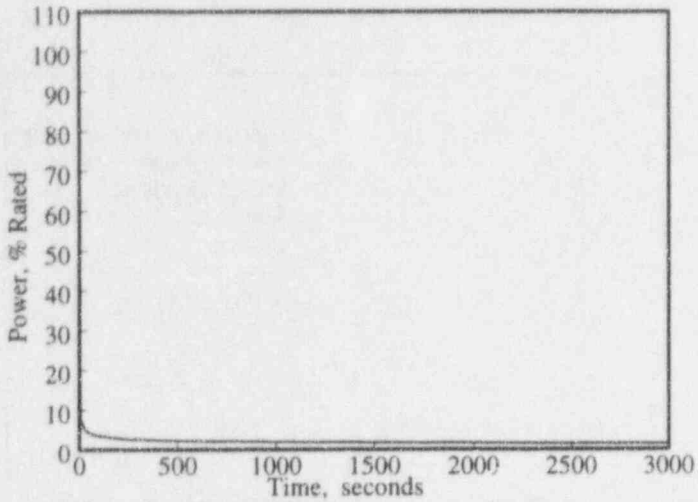

Figure 6, Core Power Vs. Time

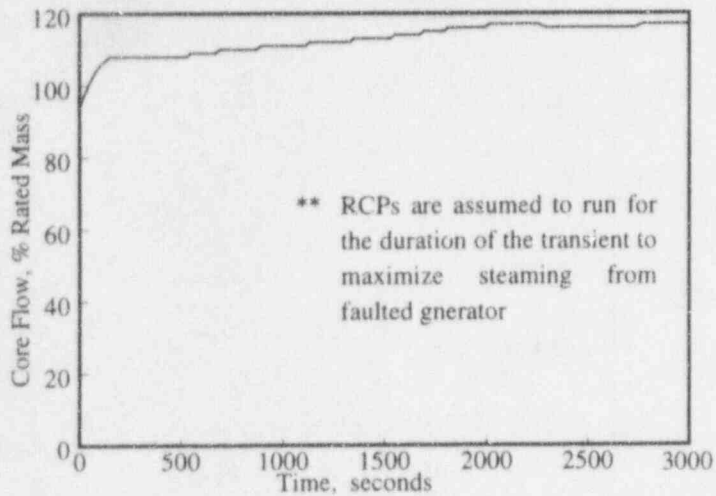

Figure 7, Core Flow Vs. Time

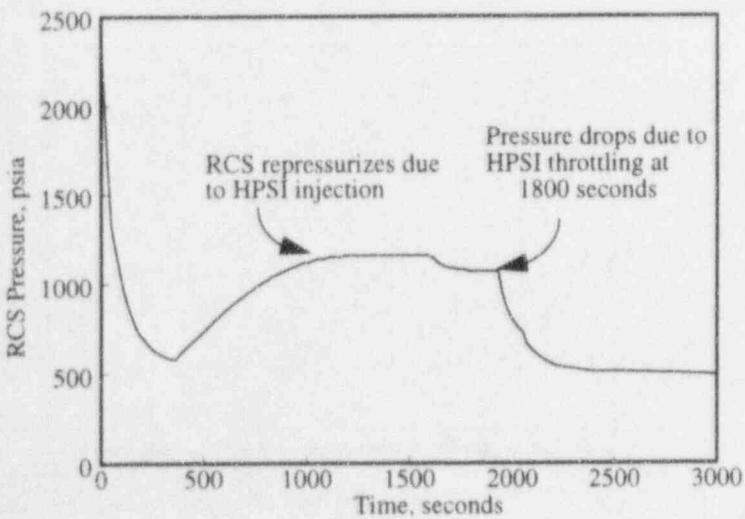

Figure 8, Core Flow Vs. Time

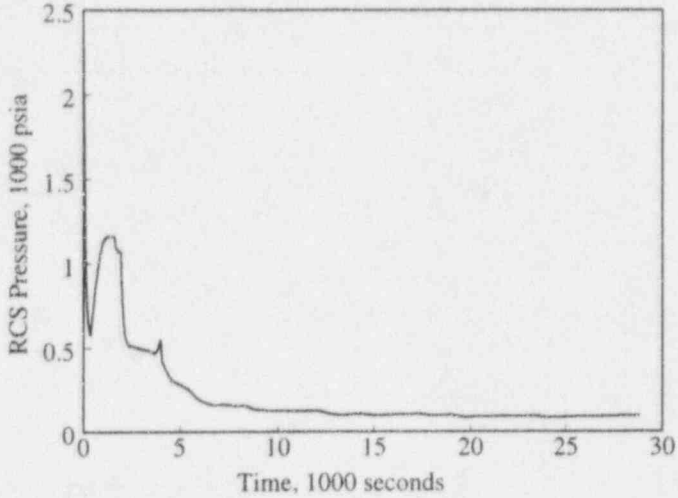

Figure 9, RCS Pressure Vs. Time

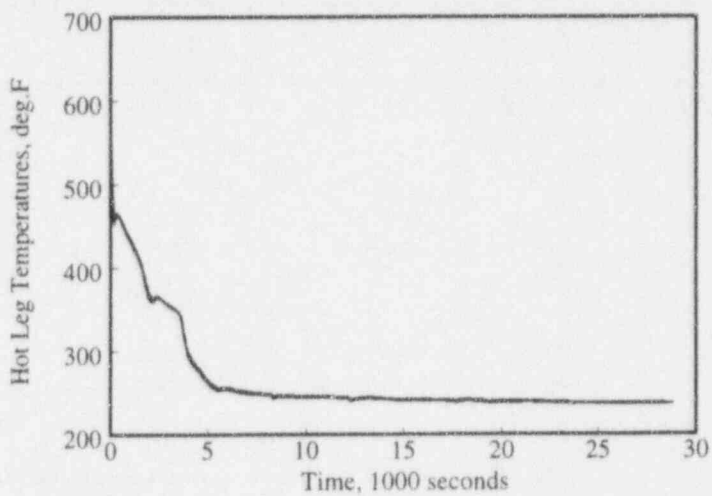

Figure 10, RCS Hot Leg Temp. (Loops 1&2) Vs. Time

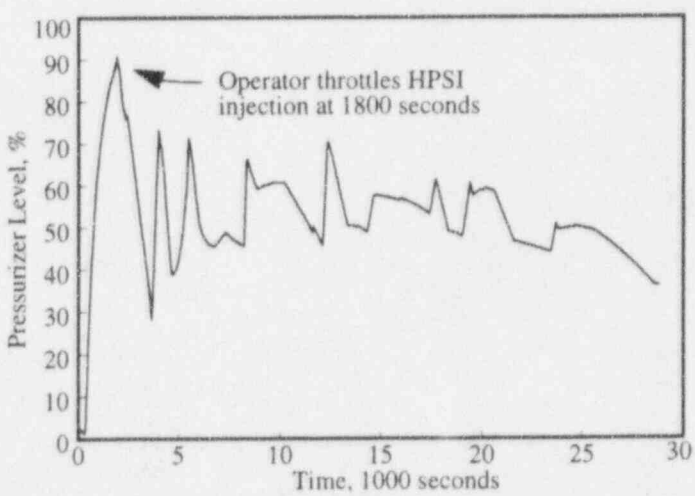

Figure 11, Pressurizer Level Vs. Time

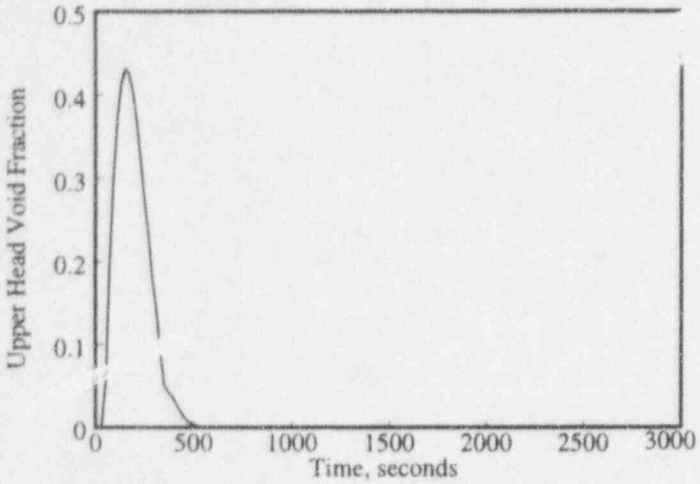

Figure 12, Upper Head Void Fraction Vs. Time

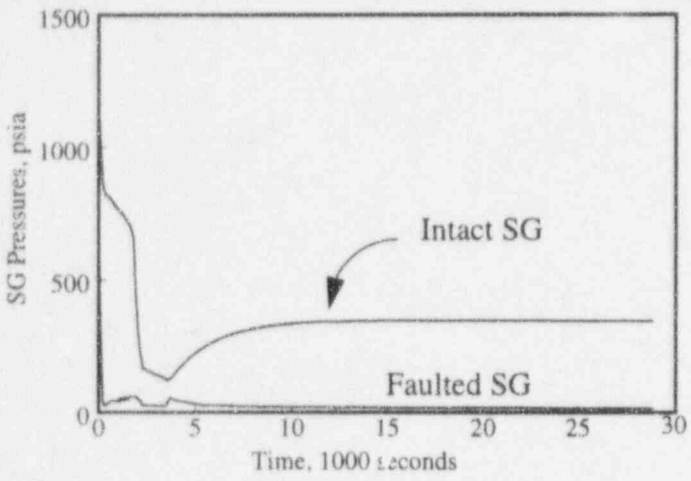

Figure 13, Steam Generator Pressures Vs. Time

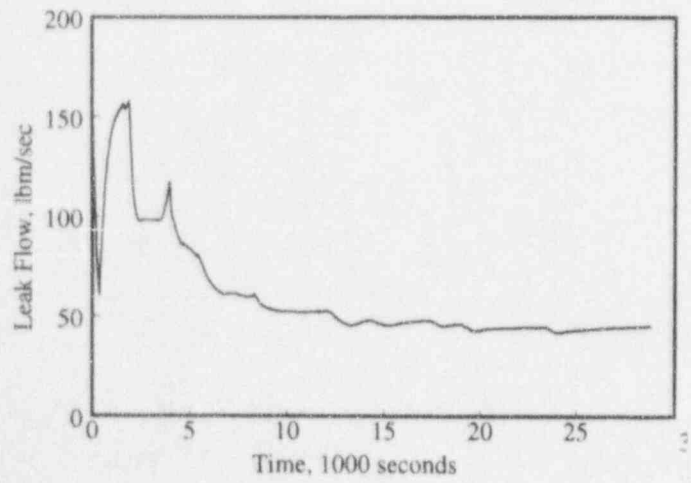

Figure 14, Tube Leak Rate (3 Tubes) Vs. Time

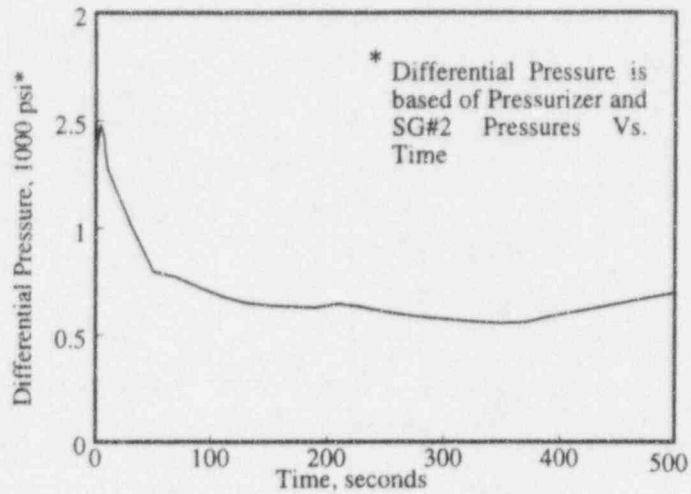

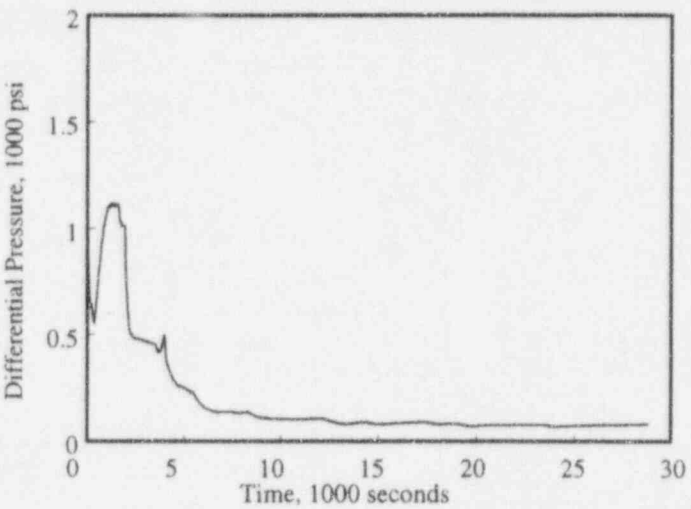

Figures 15 and 16, Differential Pressure Across U-Tubes Vs. Time

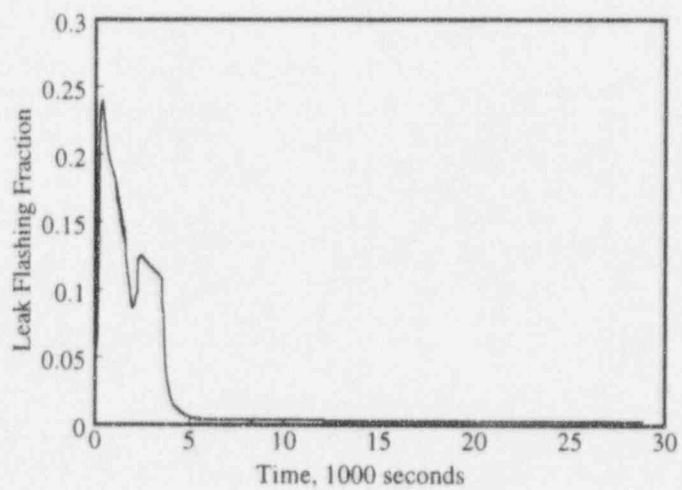

Figure 17, Leak Flashing Fraction Vs. Time

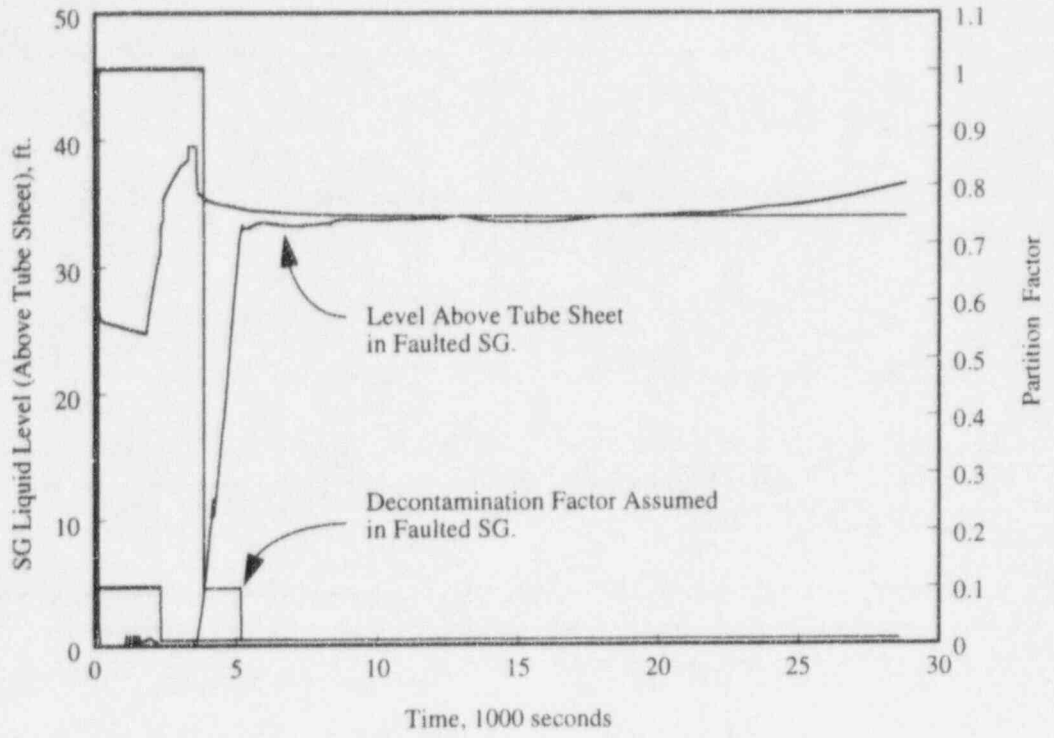

Figure 18, SG Levels Above Tube Sheet and Partition Factors

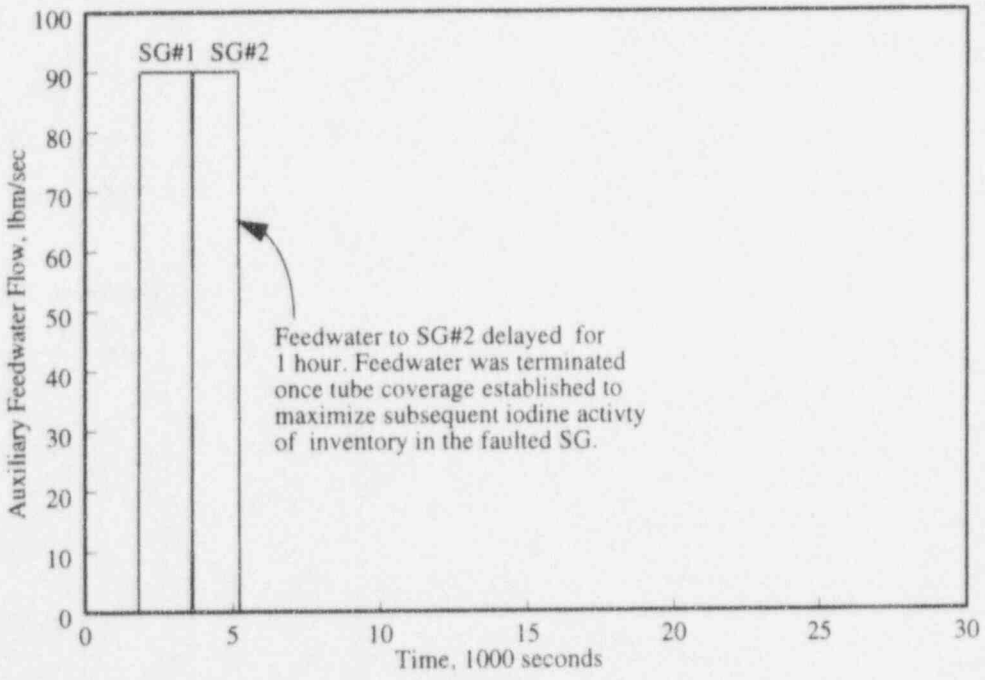

Figure 19, Auxiliary Feedwater Flows Vs. Time

V. References

1. PVNGS LER 93-001-00

2. NUREG 1477, "Voltage Based Interim Plugging Criteria for Steam Generator Tubes - Task Group Report," DRAFT, June 1, 1993.

3. CEPAC User's Manual, CE-CES-61, Rev. 0-P, April 1986.

4. CEPAC Technical Manual, CE-CES-61, Rev. 0-P, April 1986.

5. Electric Power Research Institute, RETRAN - A Program for Transient Thermal-Hydraulic Analysis of Computer Fluid Flow - Volume 1, Theory and Numerics (Rev. 2). EPRI-NP-CCMA, 1984.

6. K. Garbett, O. J. Mendler, G. C. Gardner, R. Darnsey, and M. Y. Young, "Coincident Steam Generator Tube Rupture and Stuck-Open Safety Relief Valve Carryover Tests: MB-2 Steam Generator Transient Response Program, NUREG/CR-4752 (EPRI-NP-4787), March, 1987.

7. J. M. Betancourt, et al, "Mitigation of Multiple Tube Ruptures in Both Steam Generators," Third International Topical Meeting Reactor Thermal Hydraulics, Newport, Rhode Island, October 1985.

Application of UPTF Data for Modeling Liquid Draindown in the Downcomer Region of a PWR Using RELAP5/MOD2-B&W

G. Wissinger and J. Klingenfus
B&W Nuclear Technologies, Lynchburg, VA 24506

ABSTRACT

B&W Nuclear Technologies (BWNT) currently uses an evaluation model that analyzes large break loss-of-coolant accidents in pressurized water reactors using several computer codes. These codes separately calculate the system performance during the blowdown, refill, and reflooding phases of the transient. Multiple codes are used, in part, because a single code has been unable to effectively model the transition from blowdown to reflood, particularly in the downcomer region where high steam velocities do not allow the injected emergency core cooling (ECC) liquid to penetrate and begin to refill the vessel lower plenum until after the end of blowdown. BWNT is developing a method using the RELAP5/MOD2-B&W computer code that can correctly predict the liquid draindown behavior in the downcomer during the late blowdown and refill phases. Benchmarks of this method have been performed against Upper Plenum Test Facility (UPTF) data for ECC liquid penetration and draining in the downcomer for models with and without reactor vessel vent valves using both cold leg and downcomer ECC injection. The use of this new method in plant applications should result in the calculation of a shorter refill period, leading to lower peak clad temperature predictions and increased core peaking. This paper identifies changes made to the RELAP5/MOD2-B&W code to improve its predictive capabilities with respect to the data obtained in the UPTF tests.

1.0 INTRODUCTION AND BACKGROUND

Large break loss-of-coolant accidents (LBLOCAs) have been treated analytically in three separate phases: blowdown, refill, and reflood. The blowdown phase is characterized by the rapid depressurization of the reactor coolant system to a condition nearly in pressure equilibrium with its immediate surroundings. Emergency core cooling (ECC) liquid flow is initiated once the reactor coolant system (RCS) pressure drops below the accumulator or core flood tank (CFT) pressure. The refill phase begins when the ECC liquid reaches the lower plenum. Once the ECC water level in the lower plenum reaches the bottom of the core, the reflood phase begins. The core is then cooled by steam and liquid droplets entrained by the steam generated below the rising quench front. The core is eventually covered by a two-phase mixture, and long-term cooling is established.

A key issue with regard to core cooling during an LBLOCA occurring in the cold leg is the extent to which ECC liquid can be delivered to, and accumulated in, the lower plenum during the later stages of blowdown. The "2D/3D Program"[1,2]

was undertaken to study the thermal-hydraulic phenomenon occurring during the end-of-blowdown, refill, and reflood phases of an LBLOCA. Transient simulations and quasi-steady tests were performed at the Upper Plenum Test Facility (UPTF) to investigate ECC bypass and lower plenum delivery on a full-scale facility with prototypical conditions.

UPTF is a full-scale model of a four-loop, 1300-MWe pressurized water reactor (PWR) including the reactor vessel, downcomer, lower plenum, core simulation, upper plenum, and four loops with pump and steam generator simulators. The thermal-hydraulic feedback of the containment is simulated using a containment simulator. ECC liquid can be injected either into the cold legs or directly into the downcomer. The steam produced in the core region and the water entrained by this steam flow are simulated by steam and water injection through the core simulator. Figure 1 shows the UPTF primary system and test vessel.

The following discussion summarizes the results of the UPTF tests[1,2]. Near the end of blowdown (EOB), the predominant steam flow direction is up the downcomer and out the broken cold-leg nozzle. This high upflow steam velocity entrains some or all of the ECC liquid injected into the cold legs and/or downcomer directly out the broken cold leg. Loss of this ECC liquid delays lower plenum refill and is referred to as "ECC bypass." After the majority of the residual vessel liquid is flashed and boiled, the downcomer upflow decreases, and the ECC liquid bypass decreases, allowing some liquid to accumulate in the downcomer and finally drain into the lower plenum. At the completion of blowdown, the lower plenum liquid level is near the bottom of the core barrel.

Moreover, the delivery rate of ECC liquid to the lower plenum during blowdown was shown to be highly dependent on the ECC injection location. Specifically, ECC liquid injected from locations opposite the broken cold leg has a greater tendency to be delivered to the lower plenum with complete delivery occurring prior to the end of blowdown. ECC liquid injected from locations adjacent to the break is largely bypassed to the break until the reflood period when the downcomer steam upflow velocities are reduced.

The results of the UPTF tests can be used to identify potential changes to BWNT's current evaluation model to aid in predicting the liquid draindown behavior in the downcomer during the late blowdown and early refill phases. While these changes are made to help develop an Appendix K-type evaluation model (i.e. NRC-imposed conservatisms specified in 10CFR50.46 applied), the results can also be used in statistical best-estimate-type methods.

2.0 APPLICABLE TESTS AND BOUNDARY CONDITIONS

The UPTF Test Program consisted of 30 tests comprising a total of 80 test runs. Two basic types of tests were performed within this program: (1) separate effects tests emphasizing "transparent" boundary conditions to quantify controlling phenomena in the primary system during LOCA and (2) integral tests that focused on system-wide behavior during a simulated transient to identify controlling phenomena in the primary system during a LOCA. Four separate effects test runs were selected for benchmark purposes with the base RELAP5/MOD2 code and the BWNT flow regime adjustments included in RELAP5/MOD2-B&W. These four runs include two cold-leg injection runs (Test

6, runs 131 and 133) and two downcomer injection runs with RVVVs (Test 22, runs 280 and 281). These four test runs provide different flow patterns that test the model changes under different thermal-hydraulic conditions representative of the two plant types that may ultimately use the new code flow regime adjustments. The boundary conditions for each of the tests modeled are presented in Tables 1 and 2. The results are summarized and discussed in References 1 and 2.

3.0 MODEL DESCRIPTIONS

The RELAP5/MOD2 nodalization of the UPTF test facility for cold-leg injection is shown in Figure 2. The downcomer injection noding arrangement is shown in Figure 3. The noding detail is derived from techniques applied to the NRC-approved evaluation models used by BWNT for plants that consider downcomer or cold-leg injection, or more importantly, plants with and without RVVVs, respectively. Plant transient benchmarks, facility benchmarks, and noding sensitivity studies performed to support the EM noding arrangements have demonstrated appropriate and converged thermal-hydraulic behavior. Additional axial detail is included in the upper downcomer region of plants with RVVVs to better resolve the mixture levels and fluid interactions in the vicinity of the cold leg nozzle belt. For these test runs, the single region downcomer models used in the EM noding were split into two azimuthal regions with cross flow paths connected at each elevation that is not totally blocked by a hot leg penetration. The uppermost downcomer volume for the non-RVVV test was not divided, because no significant azimuthal variations are expected in the thermal-hydraulic conditions above the cold leg nozzle elevations.

For the cold-leg injection test runs (Test 6, runs 131 and 133), Control Volumes 300 through 309 represent the downcomer region. Control Volumes 165 and 170 represent a single intact cold leg attached to one-quarter of the downcomer. Control Volumes 185 and 190 represent two intact cold legs. The two intact cold legs and the broken leg are attached to the remaining three-quarters of the downcomer. This configuration is suggested by the results of the UPTF test runs for the cold-leg injection plants. The ECC liquid injected in the single cold leg opposite the break will penetrate the lower plenum almost entirely with minimal steam upflow to impede its progress. The ECC liquid injected in the two cold legs adjacent to the broken leg will be partially bypassed by the steam upflow. This two-channel downcomer split allows a reasonable simulation of these results. The ECC boundary conditions are specified in Control Volumes 100, 102, and 104 and Junctions 101, 103, and 105. This noding will be used in cold-leg injection plants.

For the downcomer injection test runs (Test 22, runs 280 and 281), Control Volumes 290 through 309 represent the downcomer region. Control Volumes 165 and 170 represent two intact cold legs attached to half of the downcomer. Control Volumes 185 and 190 represent one intact cold leg. The one intact cold leg and the broken leg are attached to the remaining half of the downcomer. This configuration is suggested by the results of the UPTF test runs for the downcomer injection plants. The ECC liquid injected opposite the break will penetrate the lower plenum with minimal steam upflow to impede its progress. The ECC liquid injection adjacent to the broken leg will be largely bypassed by the high steam upflow. This two-channel downcomer split allows a reasonable simulation of these results. The ECC boundary conditions are

specified in Control Volumes 100 and 102 and Junctions 101 and 103. This noding will be used in the downcomer injection plants.

For both models, the steam generator simulators are not modeled. Instead, the steam flow from the steam generator simulators is added to the steam flow injected into the core region. The core boundary conditions are specified in Control Volume 400 and Junction 401. Since the reactor coolant (RC) pumps were blocked off for the tests that will be considered, only the portions of the cold legs between the RV and the pumps are modeled. Control Volumes 285 and 280 represent the broken cold leg up to the break. Control Volumes 165, 170, 185, and 190 represent the intact loops up to the pumps. Control Volume 505 represents the containment simulator with appropriate boundary conditions, and the break is modeled by Junction 504.

4.0 RELAP5/MOD2-B&W CODE CHANGES

RELAP5/MOD2-B&W[1], an improved version of the INEL code RELAP5/MOD2 used by BWNT, in its unmodified configuration is unable to adequately predict the end of ECC bypass and take advantage of the draindown effects demonstrated in the UPTF results. The coded vertical flow regime map used in the downcomer does not adequately represent the inverted annular and inverted slug flow particular to the ECCS bypass phenomena. Additionally, the one-dimensional downcomer models cannot resolve the multidimensional ECC bypass effects observed in the UPTF tests. Thus, the ECC liquid bypassed to the break is exaggerated to the extent that no ECC liquid is delivered to the lower plenum before blowdown is complete.

During the end-of-blowdown and refill phases, there are small azimuthal regions in the downcomer that contain plumes of ECC liquid surrounded by large regions of high steam upflow. The large volume sizes used in the current model mean that the plumes of ECC liquid are considered with the high steam upflow regions. RELAP5/MOD2 determines the flow regime to be annular-mist or inverted annular-mist, depending upon the wall temperatures, but it over predicts the interphasic surface area, because the control volumes are large and RELAP5 homogenizes the liquid as droplets within each control volume. Calculations of the interphasic area of the dispersed droplets based on a critical droplet Weber number in the range of 1.5 to 5 is more than three orders of magnitude larger than the interphasic area calculated for a pure annular plume of liquid. Use of the high interphasic area results in a gross over prediction of the net interphasic drag, leading to excessive carry-out of the ECC liquid during the end of blowdown.

If the downcomer were modeled with more detail, say eight to sixteen azimuthal channels, the void fractions in the ECC injection zones would be such that an inverted slug-type flow would be predicted and the interphasic area would then be appropriately calculated by the base RELAP5/MOD2 drag model. The zones without ECC injection would provide steam venting paths that are unabated by the dispersed liquid droplets imposed by a one- or two-channel model. This detailed modeling approach could possibly negate the need for code changes; however, this noding imposed on a full-plant LOCA model would either exceed the control volume capacity of the code or make the analysis so computer intensive that it would not be economically feasible. Since the interphasic drag is proportional to the interphasic area, a reduction of the interphasic drag term for the annular- and inverted annular-mist flow regimes in the

downcomer and lower plenum by three orders of magnitude will be used to counteract the over prediction of the interphasic area by RELAP5 and allow the use of the simplified noding.

The interphase heat transfer coefficients (HTCs) used in the downcomer and lower plenum also require some adjustments to account for the over prediction of the interphasic surface area and to match the pressure response observed in the tests. The interphase heat transfer coefficients in the annular mist and inverted annular mist flow regimes in the downcomer were reduced by 25 percent. The slug and inverted slug flow regime heat transfer coefficients were reduced by 50 percent.

Interphase heat transfer adjustments were also made in the lower plenum for the bubbly, slug, and annular mist flow regimes. As the pool level builds in this region, the interphasic area is simply the lower plenum area. RELAP5, however, homogenizes, or disperses, either the droplets in the steam or bubbles into the liquid within large control volumes used in the lower plenum. The heat transfer coefficients in the bubbly and slug flow regimes were multiplied by 0.005 and 0.05, respectively, to counteract the over prediction of the interphasic area. The annular mist regime interphase heat transfer was reduced by 50 percent to minimize the effect of large interphase heat transfer discontinuities as flow regimes are traversed.

The code interphase heat transfer changes were initially derived from thermal-hydraulic bases, but actually firmed up during the benchmarking process. Early benchmarks calculated reasonable ECC liquid draindown with the drag reduction only, but, the vessel pressure predictions were poor. The pressure predictions were improved by adjusting the interphase heat transfer coefficients in the downcomer and lower plenum. Additional work is still needed on this model to improve the overall predictions. Fortunately, the heat transfer adjustments have little impact on the calculated liquid draindown, and therefore, are of a lower priority.

5.0 RELAP5/MOD2-B&W PREDICTION OF UPTF TEST RESULTS

The measured[4] and predicted lower plenum collapsed liquid levels and downcomer pressures for Test 6 are shown in Figures 4 and 5 for Run 131 and Figures 6 and 7 for Run 133. The base RELAP5/MOD2 code with this model arrangement did not predict characteristic ECC liquid draindown for either case. The over prediction of the interphasic surface area led to high drag and condensation that resulted in nearly total ECC liquid carryout from the downcomer.

With the BWNT reductions to the interphasic drag and heat transfer terms, the code calculated ECC liquid penetration into the lower plenum. The lower plenum fill rate matched the data well, as shown in Figures 4 for Run 131. The pressure comparison was not as good. Some of the deviation in the rate of pressure change is attributed to the small system volume used in the RELAP5/MOD2-B&W model. The RELAP5/MOD2 model included only the reactor vessel and cold legs. Since the entire facility was not modeled, sudden changes in pressure were more rapid due to the smaller system volume. The remainder of the pressure misprediction is attributed to interphase condensation deficiencies in the coarse RELAP5/MOD2 system model. Throughout the benchmarking process, large deviations from the test system pressure had little influence on the calculated liquid draindown behavior. Some additional

work may be needed to improve the code interphase condensation model, but the overall effect on the improved liquid draindown shown in these benchmarks is minimal.

The comparison of lower plenum refill rate was not as favorable for Test 6, Run 133. Figure 6 shows that the refill rate was slightly slower than indicated. The pressure comparison, shown in Figure 7, was much better for this test between 30 and 70 seconds. The prediction was less favorable after 70 seconds.

The measured[5] and predicted lower plenum collapsed liquid levels and downcomer pressures for Test 22 are presented in Figures 8 and 9 for Run 280. Traces are included for both the base RELAP5/MOD2 code and modified version of RELAP5/MOD2-B&W. The base code results are shown to 50 seconds because the model failed to execute due to water property failures associated with the high interphasic condensation on the highly subcooled ECC liquid flow. The modified code results showed reasonable agreement with the UPTF data. The refill rate beyond 60 seconds was slightly higher than the data indicated. The pressure prediction for this case was quite good. The interphasic heat transfer models are apparently more appropriate for the thermal-hydraulic conditions encountered in the downcomer with RVVVs and downcomer ECC injection.

Test 22, Run 281 comparison of the measured[5] and predicted lower plenum collapsed liquid levels and downcomer pressures are shown in Figures 10 and 11. In this case with less ECC liquid subcooling, the base RELAP5/MOD2 code executed, but did not calculate significant ECC liquid draindown. The modified code prediction produced an excellent comparison with the draindown data. The comparison of the pressures was again much better than observed in the cold-leg injection tests.

6.0 Conclusions

It has been demonstrated that RELAP5/MOD2-B&W can predict characteristic ECC liquid draindown effects observed in the UPTF test facility with modifications made to account for the over prediction of the interphasic area in the downcomer and lower plenum regions of the reactor vessel. The coarse, two-channel downcomer models were successfully benchmarked against the test data reported for Test 6, Runs 131 and 133 for cold leg ECC liquid injection and Test 22, Runs 280 and 281 for downcomer ECC liquid injection with RVVVs. Additional improvements may still be needed in the interphasic drag model for the cold-leg injection applications. Nonetheless, these results provide a solid foundation from which an evaluation model using only the RELAP5/MOD2-B&W code can be developed.

Acknowledgment

The authors wish to thank Dr. Gene S. Rhee of the Office of Nuclear Regulatory Research for helping obtain the release of the data presented in this paper.

References

1. P. S. Damerall and J. W. Simons, "Reactor Safety Issues Resolved by the 2D/3D Program," NUREG/IA-0217, July, 1993.

2. P. S. Damerall and J. W. Simons, "2D/3D Program Work Summary Report," NUREG/IA-0216, July, 1993.

3. RELAP5/MOD2-B&W: An Advanced Computer Program for Light Water Reactor LOCA and Non-LOCA Transient Analysis, BAW-10164, Babcock & Wilcox, Lynchburg, VA.

4. 2D/3D Program Upper Plenum Test Facility Experimental Data Report, "Test No. 6 Downcomer Countercurrent Flow Test," prepared by Siemens/KWU, U9 316/88/18, December 1988.

5. 2D/3D Program Upper Plenum Test Facility Experimental Data Report, "Test No. 22 Downcomer Injection Test with Vent Valves," prepared by Siemens/KWU, E314/91/007, March 1991.

Table 1: CL Injection Tests Boundary Conditions

Test/ Run	Evaluation Time Period [s]	ECC Injection [kg/s]	Steam Injection, $M_{core} + M_{SG}$ [kg/s]	ECC Temperature	
				T_{ECC} [°C]	ΔT_{sub} [K]
6/131	33 - 113	~450 / ICL	~310 + ~90 [1]	~115	~15
6/133	30 - 120	~450 / ICL	~110 + ~90	~115	~15

NOTES: 1) The steam injection maintains this constant value until approximately 75 seconds when it is linearly ramped to 200 kg/s in the core and 45 kg/s in the steam generator.

Table 2: DC Injection Tests Boundary Conditions

Test/ Run	Evaluation Time Period [s]	ECC Injection [kg/s]		Steam Injection, $M_{core} + M_{SG}$ [kg/s]	ECC Temperature	
		Injection Nozzle 0°	Injection Nozzle 180°		T_{ECC} [°C]	ΔT_{sub} [K]
22/280	55 - 72	911	906	295 + 0	32	112
22/281	58 - 73	882	881	198 + 0	121	37

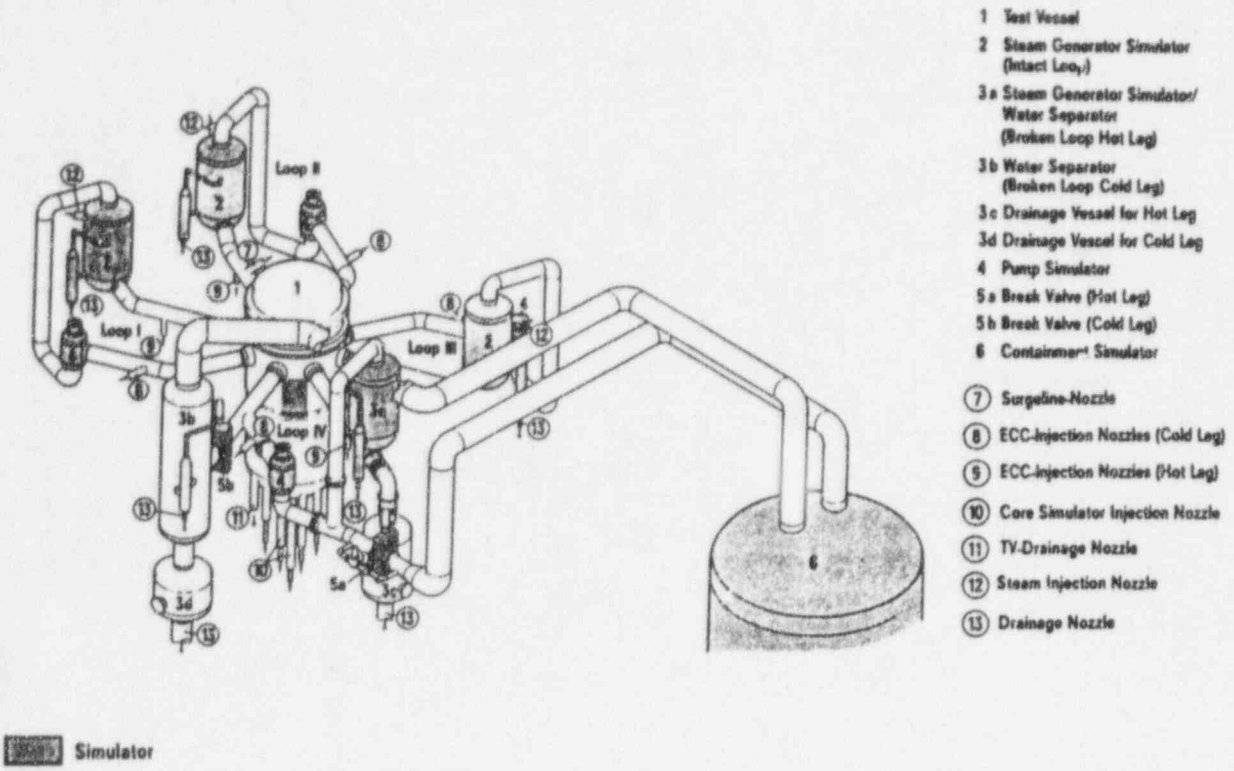

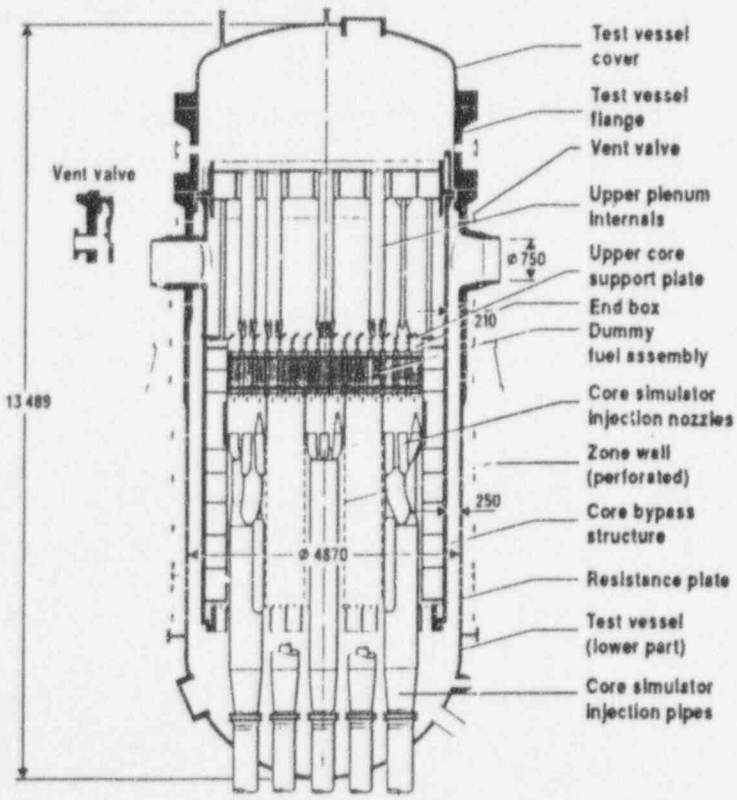

Note: All dimensions in mm

Figure 1: UPTF Primary System and Test Vessel

Figure 2: Cold Leg Injection Noding

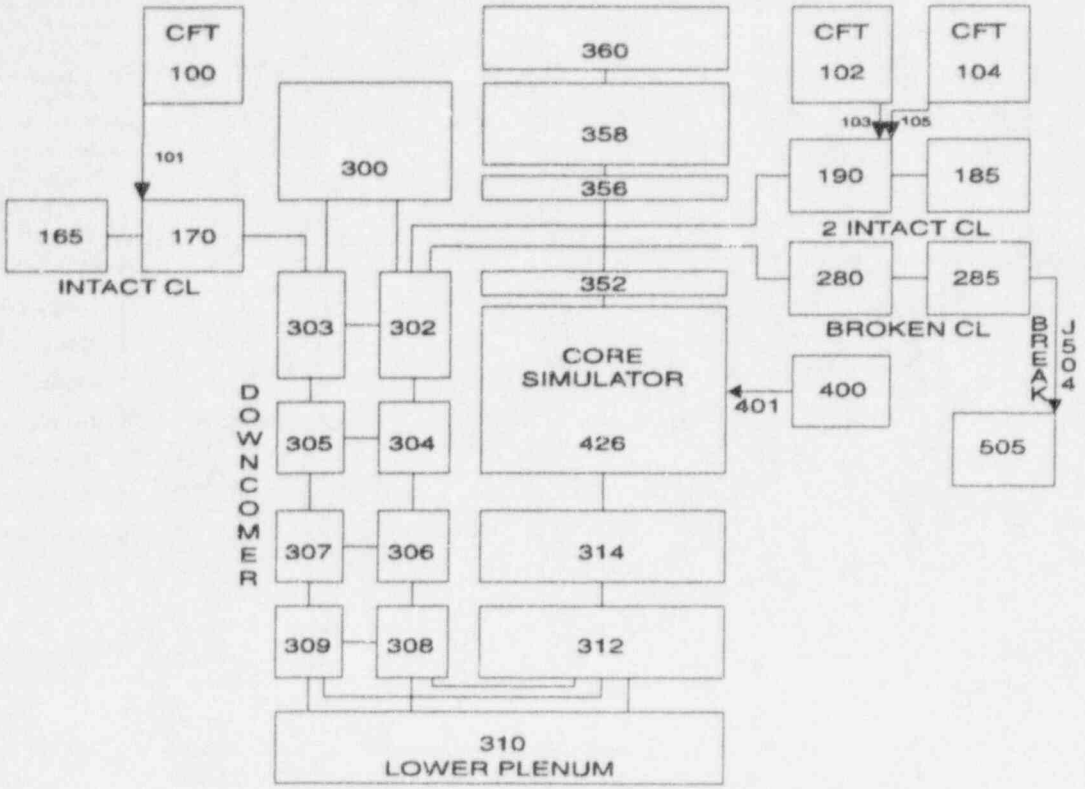

Figure 3: Downcomer Injection Noding

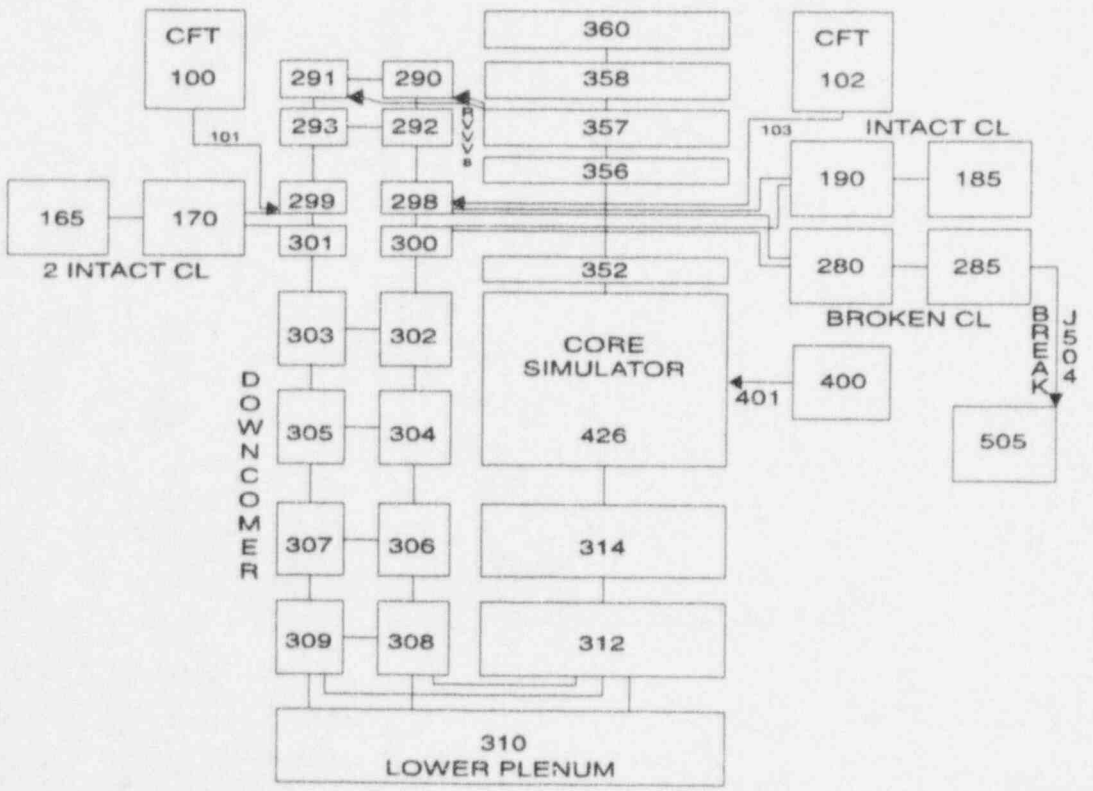

Figure 4: Test 6, Run 131 - RV Lower Plenum Liquid Level

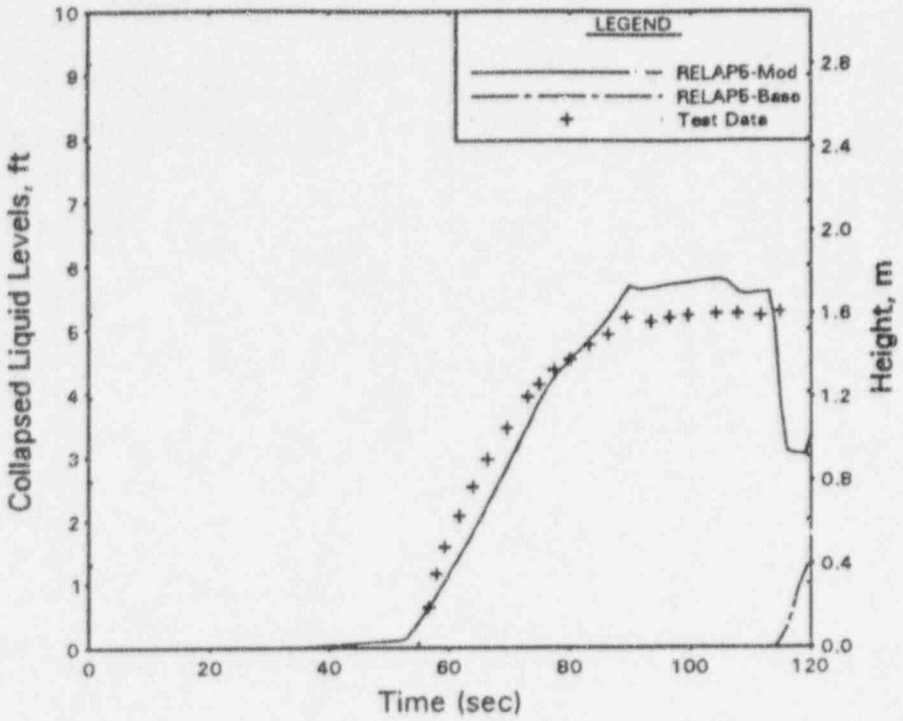

Figure 5: Test 6, Run 131 - Downcomer Pressure

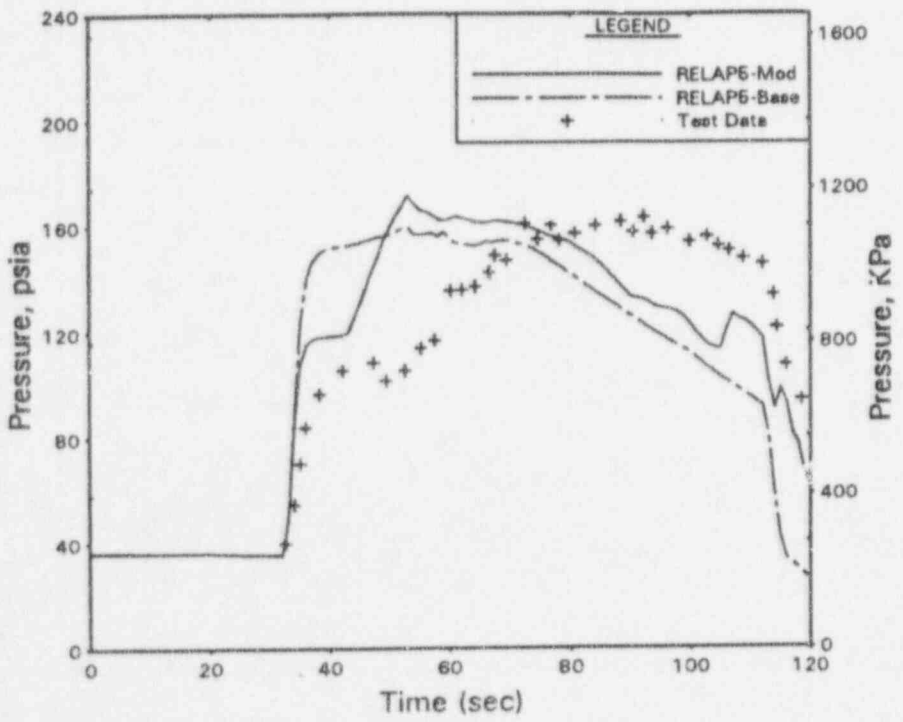

Figure 6: Test 6, Run 133 - RV Lower Plenum Liquid Level

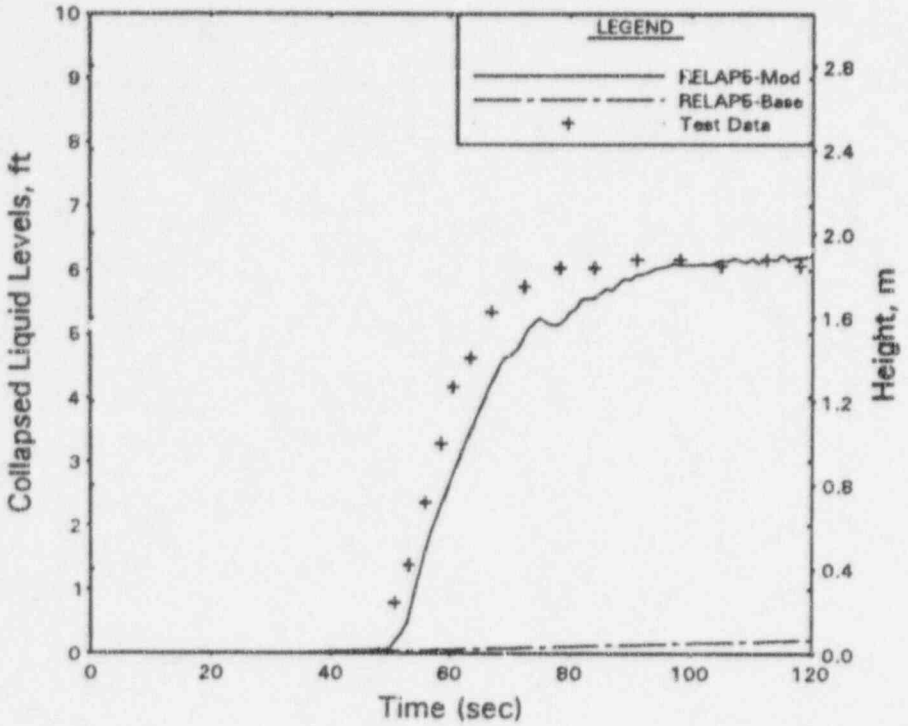

Figure 7: Test 6, Run 133 - Downcomer Pressure

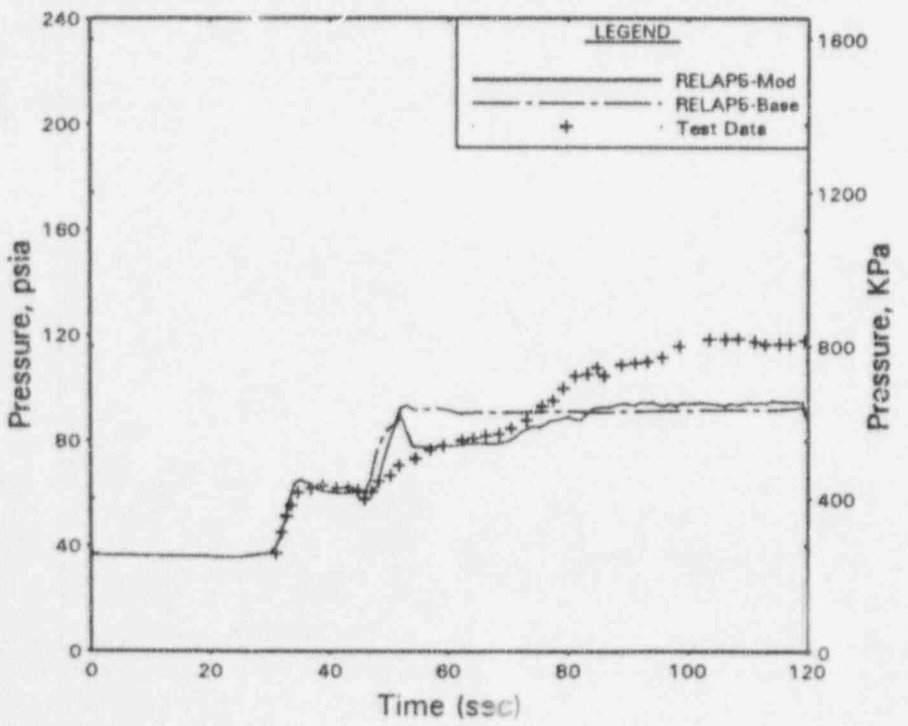

Figure 8: Test 22, Run 280 - RV Lower Plenum Liquid Level

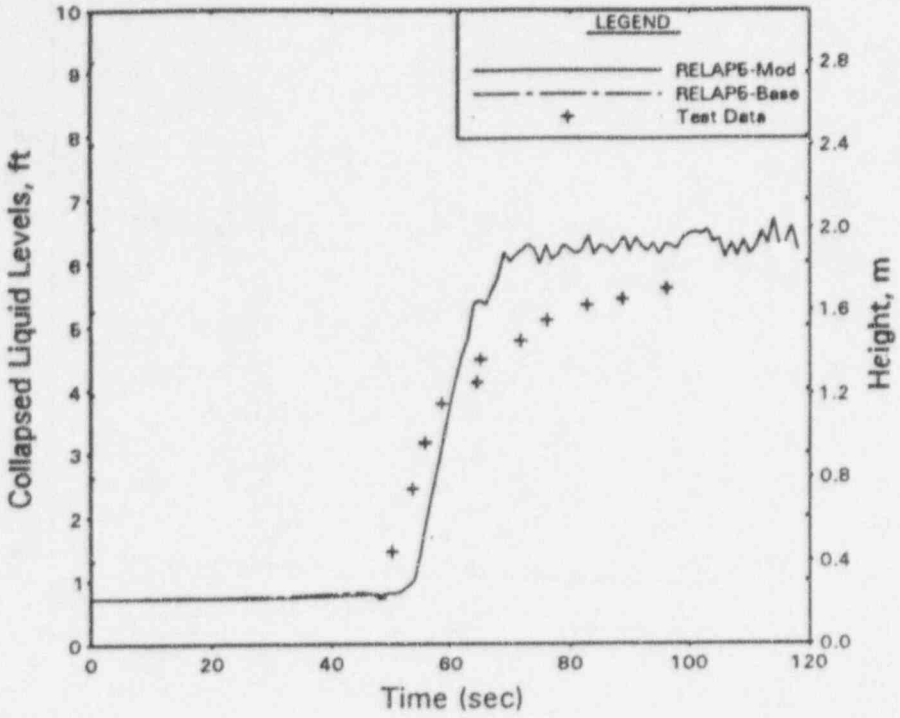

Figure 9: Test 22, Run 280 - Downcomer Pressure

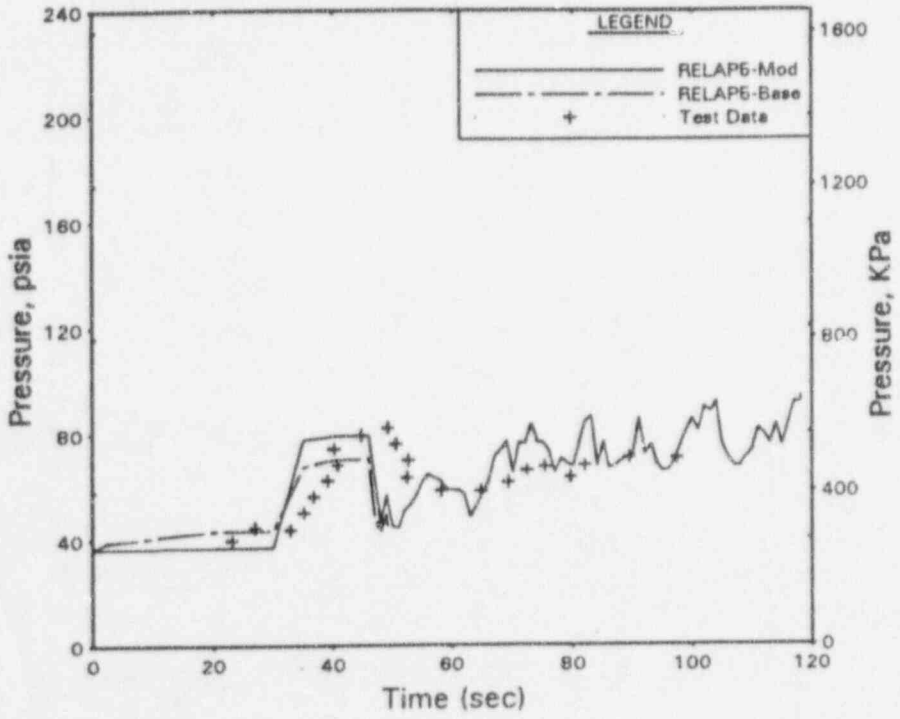

Figure 10: Test 22, Run 281 - RV Lower Plenum Liquid Level

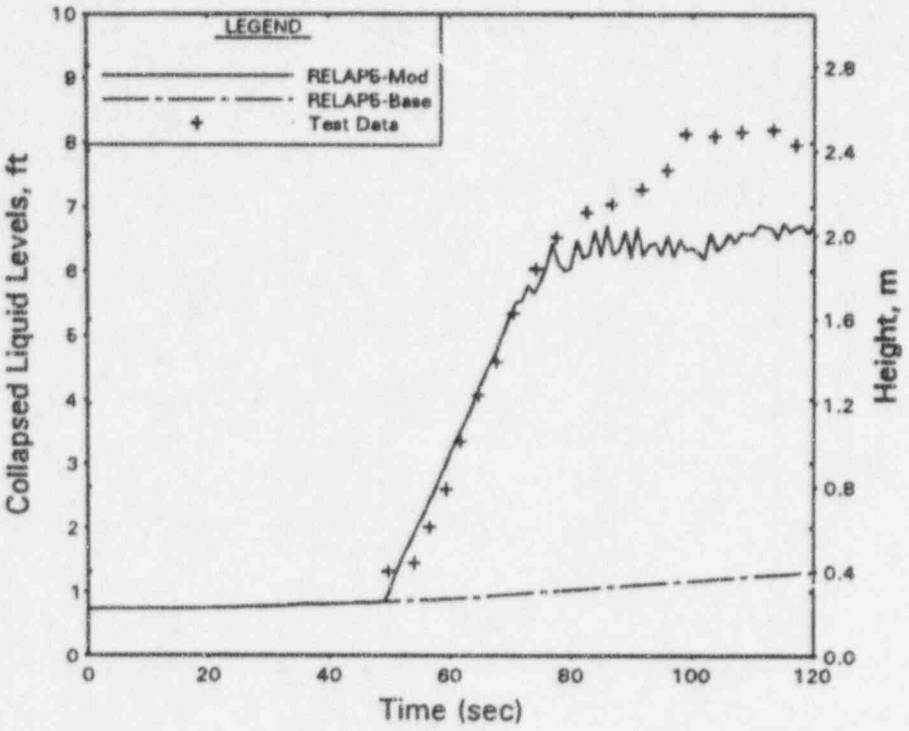

Figure 11: Test 22, Run 281 - Downcomer Pressure

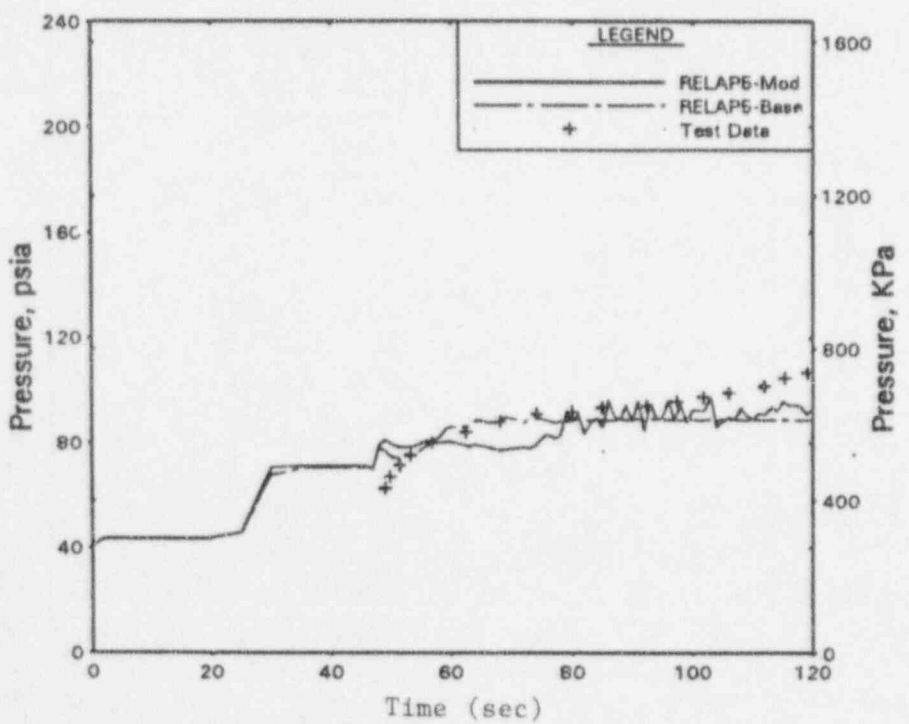

PLANT DATA COMPARISONS FOR COMANCHE PEAK 1/2 MAIN FEEDWATER PUMP TRIP TRANSIENT

Walter J. Boatwright, Whee G. Choe, David W. Hiltbrand, Curtis V. De Vore
TU Electric
Dallas, Texas

James F. Harrison
Virtual Technical Services
Richmond, Virginia

ABSTRACT

A RETRAN-02 MOD5 model of Comanche Peak Steam Electric Station was developed by TU Electric for the purpose of performing core reload safety analyses. In order to qualify this model, comparisons against plant transient data from a partial loss of main feedwater flow were performed. These comparisons demonstrated that good representations of the plant response could be obtained with RETRAN-02 and the user-developed models of the primary-to-secondary heat transfer and plant control systems.

INTRODUCTION AND BACKGROUND

TU Electric has developed the in-house capability to perform analyses required to support the reload safety analysis for its two-unit Comanche Peak Steam Electric Station (CPSES). The RETRAN-02 MOD5 computer code, described by McFadden, et al., (1992) is used for the non-LOCA transient and accident analyses. As part of the total effort required to develop the reload safety analyses methodologies, it is necessary to develop a qualified model of CPSES. Appropriate conservative assumptions may then be applied to the qualified model in order to perform the conservative reload safety analyses.

Through Generic Letter 83-11, the Nuclear Regulatory Commission (NRC) required that utilities performing their own reload safety analyses demonstrate their proficiency in using the code by submitting code verification performed by the utility. This submittal also allows the NRC to assess the technical competence of the utilities with respect to their ability to set up an input deck, execute a code, and properly interpret the results. Code verification acceptable to the NRC includes comparisons performed by the user of the code to experimental data, plant operational data, or other benchmarked analyses.

TU Electric's non-LOCA reload safety analysis methodologies were submitted to the NRC through several topical reports. The events addressed in these reports included transient initiated by increases and decreases in heat removal by the secondary side, loss of Reactor Coolant System flow transients, reactivity anomalies (e.g., uncontrolled rod withdrawal) and the steam generator tube

rupture accident. The appropriate assumptions required to assure that conservative analyses are performed are described in these topical reports. In addition, the results of comparisons of demonstration analyses, performed using TU Electric's methodologies, were compared against approved engineering calculations performed by the original fuel vendor and presented in the CPSES Final Safety Analysis Report. The comparisons demonstrated the conservatism of the TU Electric analysis methodologies relative to those analyses performed by the vendor.

Additional information was provided to the NRC which qualified the CPSES-specific, RETRAN-02 model as being adequately representative of CPSES. This additional information included benchmark comparisons with data collected from five plant transients. These plant transients were selected for the comparison based on the relatively high quality and quantity of available data and the minimum amount of involvement by the reactor operators. The five transients selected for the benchmark comparisons consisted of 50% and 100% load rejections, a partial and complete loss of main feedwater flow event, and a partial loss of forced Reactor Coolant System flow transient. Through these comparisons, it was possible to qualify the CPSES RETRAN-02 model, particularly the protection and control system modeling, reactivity feedback modeling, noding selection, and primary-to-secondary heat transfer characteristics. The comparison of the 50% load rejection event has been described by Boatwright, et al. The results of another of the benchmarks against plant data are summarized in this paper.

Based on the comparisons against actual plant data, TU Electric obtained the NRC's concurrence that the RETRAN-02 model adequately represented CPSES. Based on the information contained in the topical reports, the NRC approved TU Electric's methodologies for performing reload safety analyses of CPSES.

EVENT DESCRIPTION

CPSES consists of two 4-loop Westinghouse pressurized water reactors. The steam generators are of the vertical U-tube type with integral preheaters. During the second cycle of operation, CPSES Unit 1 was operating at 100% rated thermal power (RTP) when a transient in the Heater Drain System was experienced which eventually led to the trip of one of the two main feedwater pumps (MFPs). Over a 170 second period, the Heater Drain System response became increasingly unstable, causing the feedwater flow rate to gradually decrease until the "B" main feedwater pump tripped on low suction pressure. The MFP trip was followed by an automatic turbine power reduction to approximately 60% RTP. The automatic Rod Control System acted to reduce the reactor power to prevent exceeding any overpower limits. The reactor operators restarted the tripped MFP and stabilized the plant at 60% RTP.

The Steam Generator Water Level Control, Pressurizer Pressure Control, and Pressurizer Level Control Systems were in the automatic mode. The Steam Dump Control System was in the T-avg control mode. The Rod Control and the Main Feedwater Pump Speed Control Systems were in manual. The Rod Control System was placed in automatic as soon as the control room indications of the feedwater pump trip were received. Although there were several complicating factors during the recovery process, the tripped feedwater pump was restarted and the plant was stabilized at 60% power with both main feedwater pumps running.

The plant data for this analysis were derived from plant startup reports, test procedures, and the Test Data Acquisition System/Plant Data Acquisition System (TDAS/PDAS) computers. The TDAS/PDAS computers were used to monitor and record preselected plant operational parameters, using existing plant instrumentation, at 1 second intervals. The uncertainties associated with the plant instrumentation is typically on the order of 1% to 2% of the instrument span; although, the uncertainty associated with some non-safety-related instruments may be as much as 5% of the instrument span. In addition, the uncertainty associated with the flow indication increases significantly as the flow decreases from the nominal, "100%" value.

In general, the parameters required to perform a thorough benchmark calculation were available. The exceptions consisted primarily of the steam flow rates to the auxiliary steam loads. Nominal design values were used for these parameters. Subsequent sensitivity studies were performed to determine the sensitivity of the calculated results to these parameters. Other test data, such as sensor response times, were also gathered in order to simulate the difference between "actual" and "indicated" values.

ANALYTICAL METHODS AND MODELS

RETRAN-02 is a computer code developed through the Electric Power Research Institute and is used by TU Electric for the one-dimensional, transient, thermal-hydraulic analyses of water/steam systems. RETRAN-02 has a three equation thermal-hydraulic formulation with a slip model. RETRAN-02 is a very flexible code; thus, it is the analyst's responsibility to ensure that each RETRAN-02 model is adequate for a particular application.

For the CPSES model, each reactor coolant loop is explicitly modeled; however, the loop-independence is not retained in the reactor vessel and core. The Reactor Protection and Control System and the various reactivity feedback effects are modeled with 235 discrete trip functions and 1003 input and control blocks to simulate the response of the analog instrumentation. Even with this complexity, it remains necessary to provide some plant parameters, such as the main feedwater flow and temperature and the auxiliary steam loads, as forcing functions.

The secondary-side steam generator model consisted of three nodes. As shown in Figure 1, separate control volumes represented the integral preheater and the steam dome. The actual preheater region consists of five crossflow paths across the cold-leg side of the tube bundle. The fluid entering the preheater box is subcooled and is heated to at or near saturation prior to mixing with the recirculating fluid. This region is modeled as a single node with the input values of the flow area and flow length representative of the actual geometry. The remainder of the steam generator secondary side volume was contained in a third node. With the use of this large node, typical steam

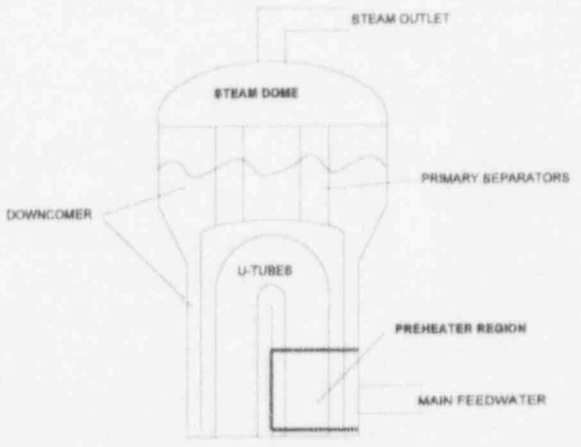

FIGURE 1. SIMPLIFIED SCHEMATIC OF THE CPSES-1 STEAM GENERATOR DESIGN AND NODING SCHEME

generator design features such as the recirculation path and the primary separators were not explicitly modeled. The standard bubble rise model available in RETRAN-02 was used to represent the primary separators, and the recirculation path was not explicitly modeled. A different modeling approach should be considered for the prediction of the steam generator water level. Because TU Electric's safety analysis methods use a conservative calculation of the steam generator water mass instead of the water level, a more detailed model, which includes an explicit representation of the recirculation flow path, has not been developed for use in the system model.

A best-estimate representation of the performance characteristics of the various protection and control systems was employed. Best-estimate point kinetics reactivity and decay heat parameters were also selected.

Although the event was generally symmetric, the model was initialized to simulate the small loop-to-loop variations in plant parameters by adjusting steam generator heat removal fractions to be consistent with plant data. Loop variations in transient response were modeled by using loop-specific data for steam and feedwater flow, corrected for instrument response and piping purge delay times.

Forcing function inputs were used for the turbine and steam dump loads (steam flow rate), and the main feedwater flow rate and temperature. Because the instrumentation response time is slow and the time response characteristics are not well-established, there is a relatively large uncertainty associated with the feedwater temperature indication. A forcing function is also used to represent the auxiliary steam loads. The steam requirements for these loads are not directly measurable; hence, the time-dependent magnitude of the steam load can only be estimated. The long-term system response is relatively sensitive to this parameter.

COMPARISON OF CALCULATED RESULTS TO DATA

Selected calculation results of the analysis are shown in Figures 2 through 7. Results calculated with RETRAN-02 are compared to plant data in Figures 3 through 7.

Although comparisons of numerous parameters were made, the overall adequacy of the integrated models of the reactivity feedback effects and the automatic control system models can be assessed through a comparison of the core power response. The automatic positioning of the control rods is a function of the indicated values of core power, coolant temperature, and turbine load. The coolant temperature is highly dependent on the core power, the steam generator conditions, and the primary-to-secondary heat transfer characteristics. The steam generator conditions are very sensitive to the operation of the steam dump system. Thus, the adequacy of virtually all of the control systems can be assessed through a comparison of the core power.

The following comparisons were judged to be acceptable if the differences between the actual and calculated values were within approximately 2% of the instrument span. The results were also deemed acceptable if the cause of the deviation was attributable to the uncertainty associated with an input forcing function. For example, the actual values of the auxiliary steam loads could deviate from the nominal design values by as much as 10%.

Loop 1 was the most unique of the four loops due to the anomalies that are evident in the main feedwater control valve behavior in the 500 to 600 second period, as shown in Figure 2. The response of Loops 2, 3 and 4 were essentially the same.

The core power response, as indicated by the N-16 Power Monitoring System (proportional to the fast neutron flux), is shown in Figure 3. The core power may be monitored through both the excore neutron flux and the N-16 Power Monitoring System; however, due to uncertainties in the effect of changes in downcomer temperature and rod insertion on NIS response, the N-16 power indication is typically more accurate. The close agreement between the calculated and measured responses is a demonstration of the adequacy of the integrated model in general and, in particular, of the control system models. The "plateaus," which are caused by control rod overshoot and deadbands in the automatic rod control system logic, are all predicted with the RETRAN-02 model. Figure 4 shows the actual control bank position in the core.

The comparison is considered to be very good. The slight differences in the rod position are attributed to the cumulative effects of uncertainties in the prediction of the reactivity balance during this transient. In addition, because a point kinetics model is used, such effects as the transient variations in the axial power shape are not captured.

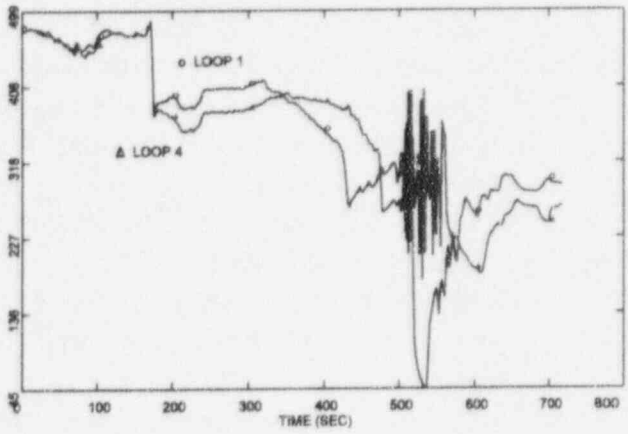

FIGURE 2. MAIN FEEDWATER FLOW RATES FOR LOOPS 1 AND 4, KG/SEC

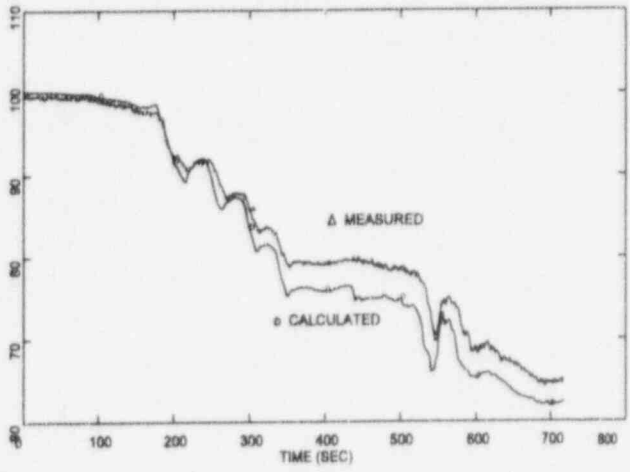

FIGURE 3. N-16 POWER INDICATION, LOOP 4, NORMALIZED (TYPICAL)

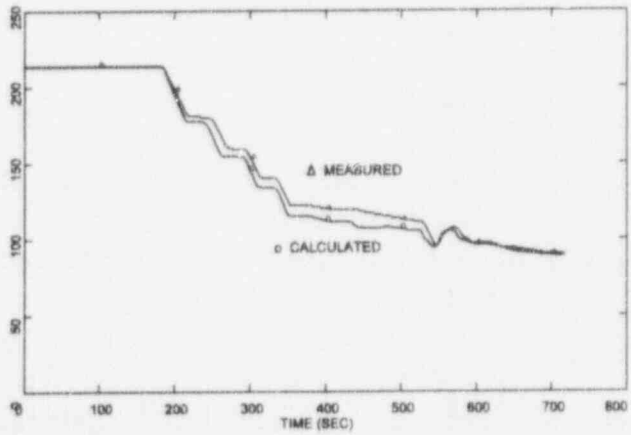

FIGURE 4. ROD CONTROL BANK "D" POSITION - STEPS WITHDRAWN

Once the accuracy of the core response has been evaluated, the adequacy of the primary-to-secondary heat transfer calculation can be assessed. Figure 5 is a plot of the total steam flow from the Loop 1 steam generator. The deviations late in the transient are attributed to the estimates of the auxiliary steam loads, which have either relatively imprecise or no flow instrumentation. Because the predicted response was judged to be sufficiently close to the measured data during the early parts of the transient, no effort was made to refine these estimates of the auxiliary steam loads. Given the forcing functions of feedwater flow and temperature and the reasonable comparison with the total steam flow from the steam generator, the adequacy of the steam generator model can be assessed through a comparison of the cold leg temperatures (steam generator outlet temperatures), as shown in Figures 6 and 7.

The cold leg temperature prediction follows the data well for the initial heatup, turbine runback, and steam dump flow periods. During the 500 to 600 second period, the Loop 1 feedwater flow rate decreases significantly and then recovers. This decrease is the basis for the spike in the Loop 1 cold leg temperature during this time period. Note that consistent with the observed feedwater flow rates presented in Figure 2, no such spike is observed in Loop 4. In summary, the integrated primary-to-secondary heat transfer was shown to be adequately modeled.

From the results of subsequent sensitivity studies, it was observed that the comparisons between the calculated and measured cold leg temperatures could be slightly improved through the use of additional noding in the preheater region. The design condition of the fluid entering the preheater is approximately 65°C subcooled and is heated to near saturation at the preheater outlet. Additional noding in the preheater allows the crossflow paths to be more

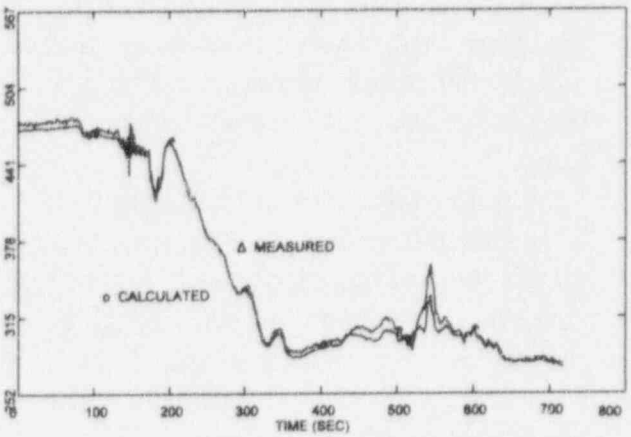

FIGURE 5. LOOP 1 STEAM GENERATOR OUTLET FLOW RATES, KG/SEC

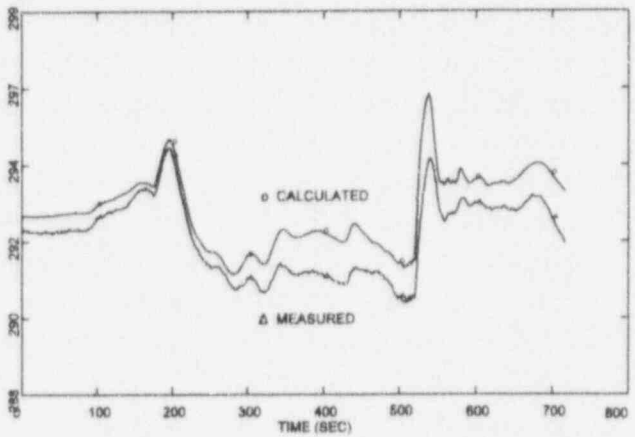

FIGURE 6. COLD LEG TEMPERATURE INDICATION - LOOP 1, °C

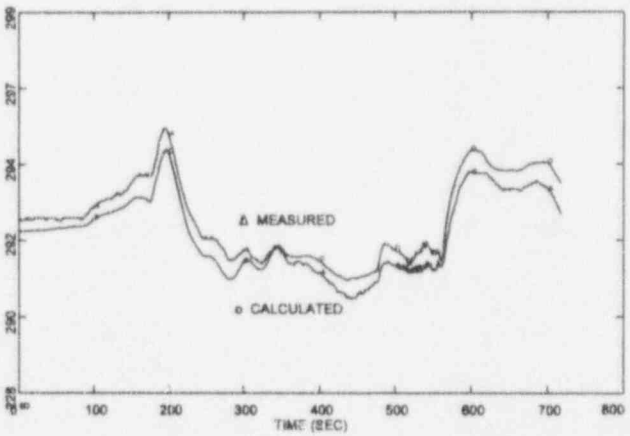

FIGURE 7. COLD LEG TEMPERATURE INDICATION, LOOP 4, °C

accurately simulated, thereby allowing for a more representative calculation of the cold leg temperature. The better agreement between the calculated and measured cold leg temperatures occurs in the early stages of the transient; when the feedwater fluid conditions are still near their initial values, there is no significant benefit to the use of additional detail. From these sensitivity studies, it was also observed that the agreement between the cold leg temperatures was not significantly improved when the number of nodes in the preheater was increased from two to five. It was also noted that the improved agreement in the measured and calculated cold leg temperatures resulted in only slight changes in the response of the core power or control rod position due to the small, negative value the moderator temperature coefficient present at the time of this test. In summary, based on these studies and the intended use of the model for reload licensing analyses, it was concluded that the use of a single preheater node provides an adequate representation of the steam generator response.

CONCLUSIONS

The results of this analysis demonstrate that the RETRAN-02, with this model of CPSES-1, can be used to provide good predictions of:

- The primary-to-secondary heat transfer rate;
- The core power response, including the reactivity feedback effects due to changes in moderator and fuel temperatures and control rod position; and,
- The rod control model, which correctly simulates actual plant response in which the control rods are inserted and withdrawn in response to temperature and power error signals.

REFERENCES

J. H. McFadden, et al., "RETRAN-02 - A Program for Transient Thermal-Hydraulic Analysis of Complex Fluid Flow Systems," Electric Power Research Institute, N-1850-CCM-A, Revision 5 (1992).

W. J. Boatwright, et al., 1994, "Plant Data Comparisons for Comanche Peak 50% Load Rejection Transient," *Trans. American Nuclear Society Summer Annual Meeting*, p. 452.

ACKNOWLEDGMENTS

The authors wish to acknowledge the contribution of S. M. Maier to the completion of this analysis and the contribution of D. W. Throckmorton to the initial development of the analytical activities.

RBMK-LOCA-Analyses with the ATHLET-Code

A. Petry	Gesellschaft für Anlagen- und Reaktorsicherheit (GRS) mbH Kurfürstendamm 200, 10719 Berlin, Germany
A. Domoradov, A. Finjakin	Research and Development Institute of Power Engineering, Moscow, Russia
A. Moskalev	Russian Scientific Centre Kurchatov Institute, Moscow, Russia

ABSTRACT

The scientific technical cooperation between Germany and Russia includes the area of adaptation of several German codes for the Russian-designed RBMK-reactor. One point of this cooperation is the adaptation of the Thermal-Hydraulic code ATHLET (**A**nalyses of the **T**hermal-**H**ydraulics of **LE**aks and **T**ransients), for RBMK-specific safety problems.

This paper contains a short description of a RBMK-1000 reactor circuit. Furthermore, the main features of the thermal-hydraulic code ATHLET are presented. The main assumptions for the ATHLET-RBMK model are discussed. As an example for the application, the results of test calculations concerning a guillotine type rupture of a distribution group header are presented and discussed, and the general analysis conditions are described.

A comparison with corresponding RELAP-calculations is given.

This paper gives an overview on some problems posed and experiences by application of Western best-estimate codes for RBMK-calculations.

Introduction

In the last years, several actions have been engaged by RBMK specialists in order to increase the safety of this reactor type. Some of these actions have been performed in the frame of international cooperation between RBMK specialists and specialists of other countries, who dispose of wide experience in the field of reactor safety.

In this context, a German-Russian scientific-technical cooperation on the adaptation and application of German containment-, thermal-hydraulic-, and 3D-neutron-kinetics-codes for RBMK-reactors and the additional verification of the codes on the basis of experiments modelling separate effects in various parts of the reactor circuit has been existing for already some years [3]. The works on the adaptation and application of the thermal-hydraulic code ATHLET have not yet been finished. However, as a result of the joint works effected up to now, we dispose of a detailed model, representing the main components of the RBMK-circuit and simulating nominal operating conditions.

To test the integral dynamic behaviour of the model, we began to provide calculations concerning typical transients and loss of coolant accidents of this reactor type. Calculations of some reactor transients were performed, which included for example, natural circulation regimes and obtained a good correspondence with measured values [4]. Test calculations on channel rupture, partial ruptures of DGH, rupture of pressure header, etc., were performed and showed, as

a matter of principle, the applicability of the integral thermo-hydraulic code ATHLET for analyses of RBMK-specific problems [5], [6], [7] .

One of the design basis accidents of the RBMK-reactor is a guillotine type rupture of a distribution group header (DGH) (d=293 mm). Calculations applying the ATHLET-code to test the prekent status of the model were performed.

Simultaneously, we have been carrying out post-test calculations for RBMK-experiments on the basis of experimental results, that were obtained at the Russian test facilities KS and KSB [3].

RBMK-1000 Circuit Description

RBMK (fig. 1) is the Russian acronym for "Channelized Large Power Reactor". It is a light water cooled, graphite moderated boiling channel-type reactor, and uranium dioxide is used as nuclear fuel. The main parameters of the RBMK-1000 reactor are shown in table 1 [1].

Table 1: Main Parameters

Thermal Power	3200 MW
Electrical Power	1000 MW
Coolant Temperature (core inlet)	270 °C
Coolant Temperature (core outlet)	284 °C
Coolant Flow Rate through Reactor	37500 t/h
Steam Pressure	6.9 MPa
Number of Channels	1661
Channel Outside Diameter	88 mm
Thickness of Channel Wall	4 mm
Maximum Power per Channel	3 MW
Fuel Elements per Channel	2
Fuel Rods per Fuel Element	18

Fig. 1: General view of the reactor

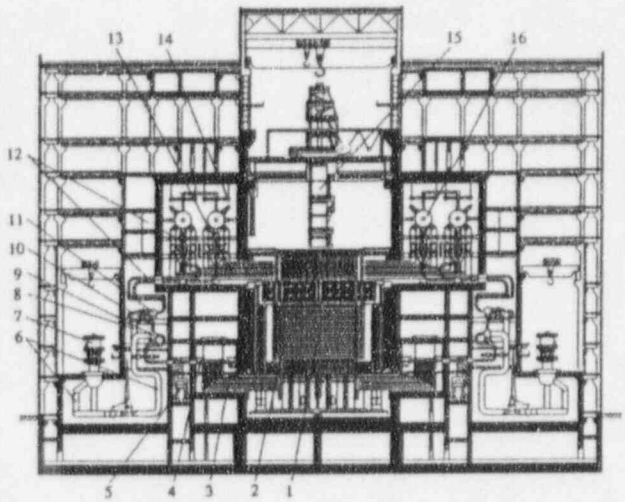

1 - graphite stack, 2 - fuel channel feeder pipes, 3 - water pipes, 4 - distribution header, 5 - emergency core cooling pipes, 6 - pressure pipes, 7 - main circulation pump, 8 -suction pipes, 9 - pressure header, 10 - bypass pipes, 11 - suction header, 12 - downcomers, 13 - steam and water pipes, 14 - steam pipes, 15 - refueling machine, 16 - separator drum

The circuit is divided into two nearly independent loops, cooling the same cylindrical nuclear core. Each loop has two separator drums, which separate the steam from the steam-water-mixture. The saturated water is mixed with the feedwater and flows through 24 downcomer pipes to the suction header. From the top of each drum separator, the saturated steam flows through the steam lines to the turbines (2 x 500 MW).

From the suction header, the water flows through four pipes to the four main circulation pumps (MCP). During normal reactor operation, only three pumps are operating in each loop. The fourth pump is at stand-by. From the MCP the water flows through pressure pipes to the pressure header and further on to 22 DGH. Through the water communication lines, each DGH is connected to about 38 fuel channels. In the fuel channel, the water is partially vaporized (up to

14.5 % in weight) and the steam-water-mixture flows to the steam-water pipes to the separator drums. The flow in each pipe, and therefore in each channel, is controlled by isolation- and control valves.

The RBMK-reactor has a large-sized core (height 7 m, diameter 11.8 m) with an assembly of square graphite blocks stacked into columns and provided with an axial opening. Most of the openings contain fuel channels.

Computer Code ATHLET

The ATHLET (Analysis of the Thermal-Hydraulics of Leaks and Transients) [8] is presently developed at GRS.

The objective of this development is to obtain a thermal-hydraulic code with a wide field of application, covering anticipated and abnormal transients, small, intermediate and large break accidents through all relevant phases (blowdown, refill and reflood) in PWR (Pressure Water Reactor) and BWR (Boiling Water Reactor) systems.

ATHLET has a strictly modular structure. The four main modules in accordance with the most important processes are

- thermofluid dynamics (TFO),
- heat conduction and heat transfer (HECU),
- neutron kinetics (NEUKIN),
- general control simulation module (GCSM).

On the basis of a general interface (GUSER) it is possible to couple additional "independent" modules to the main programme. The configuration is defined by the user's input data. The coolant system is simulated by a network of thermofluid "objects" (TFO).

The thermal-fluid-dynamic network is within the entire code structure an important part. Its essential structure element, the object, represents a unit standing above the single elements (control volume, junctions). Thus, it is the carrier of the physical models as well as basic element for the flexible structure of components and of optional pipe networks including multi-channel simulation with and without cross connections.

The ATHLET input and output is also based upon the object structure. By separation of geometry and model data from the nodalisation data, a high degree in transparency and flexibility concerning the adaptation of the dataset on each postulated problem can be realized. Beside the automatic checking of the input data with respect to completeness and consistency carried out by ATHLET, further auxiliaries are put at the user's disposal, which show in graphics the geometry and the object linkage as well as the objects' nodalisation and can thus be used for further verification and documentation of an input dataset.

For the calculation of the relative velocity between the phases a full range drift-flux model which is based on counter-current flow conditions is provided. With this drift-flux model the simulation of co-current as well as counter-current flow is possible. The model includes all flow patterns from homogenous to separated flow occurring in vertical and horizontal two-phase flow and the limitation of water penetration through a vertical flow duct against vapour upflow in different geometrical configurations.

In single-phase as well as in two-phase flow the irreversible pressure loss in a flow channel is considered. In this calculation, the irreversible frictional losses were calculated as function of Reynolds number and wall roughness. The increase of the losses in two-phase flow was considered by the two-phase multiplier of Martinelli-Nelson. The form losses were input values for forward and reverse flow.

Two control volume types are available. Within the ordinary control volume a homogenous mass and energy distribution is assumed. Within the "non-homogeneous" control volume, a mixture level is modelled. Above the mixture level, steam with water droplets, below the mixture level liquid with vapour bubbles may exist. The combination of ordinary and non-homogeneous control volumes provides the option to simulate the motion of a mixture level through a vertical component.

The heat transfer packages cover a wide range of single-phase and two-phase flow conditions. The package is organized in four levels: condensation, nucleate boiling, transition boiling, and film boiling. It includes the whole range of mass flows (stagnation, natural convection, forced convection) and the entire enthalpy range (subcooled water, liquid-steam mixture, superheated steam). In addition, the heat transfer model was adapted to the drift-flux model (velocity differences between steam and liquid). For the heat production in nuclear fuel elements, there is the point-kinetics and a 1D-kinetics model available.

The GCSM-model (General Control Simulation Model) is a block-oriented continuous system simulation language for the description of Balance of Plant-systems in a thermal-hydraulic computer code and can be used for the simulation of any usual control system, any trip logic system and the interactions between them and thermal-hydraulics.

The ATHLET assessment is based on a well balanced set of separate effect tests in full or at least in large-scale test facilities that permit the quantification of uncertainties in the simulation of the physical phenomena expected to occur in the full-scale geometry of a PWR or BWR. Assessment also includes validation against LOCA and transient experiments, performed in integral test facilities. Comparisons to real plant transients are also included.

ATHLET Input Deck for RBMK

As a result of the common works completed up to the present, a basic ATHLET input deck for RBMK-1000 is available. Fig. 2 shows the main components which are described modelling the circuit.

Fig. 2: Principal scheme of the circuit (one half)

For those calculations concerning the DGH rupture, the input deck was modified for this special problem. The ATHLET input graphic of the part from the feedwater-mixer to the top of reactor (one half, one channel) of the current model (fig. 3) gives a simplified overview.

The whole reactor system is represented by 162 thermofluid objects, which are subdivided into 607 control nodes with 647 junctions.

The reactor and the main circuit are divided into two halves (interconnected by a detailed

Fig. 3: ATHLET -Input Graphic of a part of the circuit model

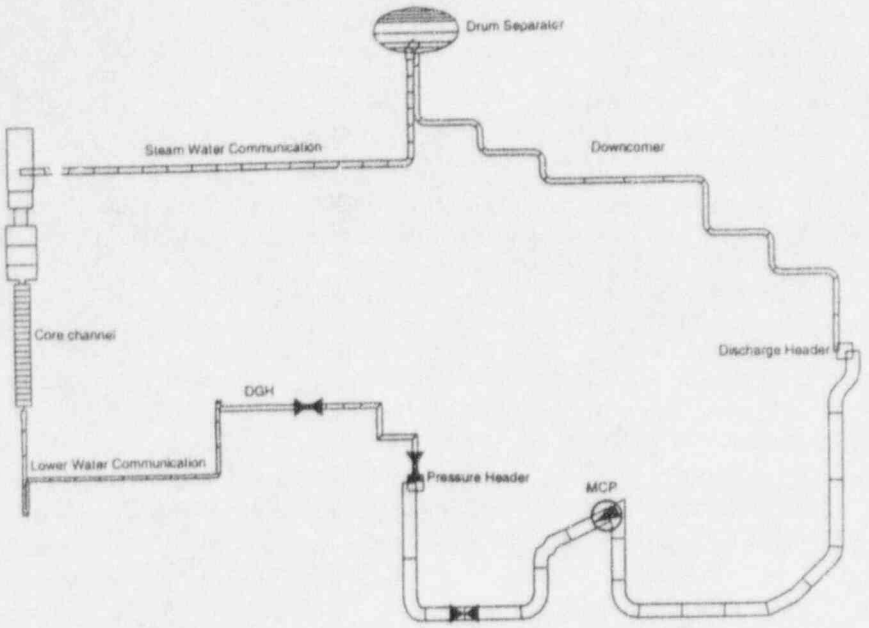

model of the steam system). A two loop scheme has to be used because the vapour generated in the intact half gets into the damaged half and reduces the depressurization rate.

The intact loop (half) is simulated by means of a simplified model, that means all components and flow paths are lumped into a single train of components and a single flow path. This part of the model contains a "single channel" with an average channel power (1.89 MW). The two drum separators per reactor half are combined by one separator model.

The damaged loop contains two DGHs. The first one is the intact DGH and represents 21 DGHs. The second one is the single damaged DGH. The intact DGH is connected with on average power channel (1.85 MW). It represents 789 channels.

The damaged DGH is connected with an average power channel which represents 41 channels and with a maximum power single channel (3 MW).

Unlike the previous calculations, where the inlet rate of the reactor emergency cooling system was only given as boundary condition (the so-called needed flow rate of the emergency cooling system of the project documents [2] was used), here the single components of the emergency cooling system (pressure accumulator, pumps, pipelines) were simulated thermo-hydraulically in detail. There the special ATHLET-models for accumulators (which consider the existence of nitrogen) and pumps were used.

This permits the model to consider the incident-specific real flow rate of the ECCS (Emergency Core Cooling System). Furthermore, this model makes it also possible to analyze incident sequences with failures of single components of the ECCS.

The flow restrictors in the pipes of the ECCS and in the inlets of the DGH, as well as the check valves in the DGHs were simulated in the necessary scope.

For the appliance of ATHLET on the RBMK, a special radiation model was developed which allows to take into consideration the possible radiation heat exchange between the rods of the inner row, the rods of the outer row, the central guide tube and the channel tube [11]. This model was taken over in the general ATHLET-basic version.

General Analysis Conditions

Prior to performing the ATHLET analysis (ATHLET MOD 1.1A), we calculated a 500 sec null-transient to reach balanced steady state conditions with nominal plant parameters. After this time period, the following scenario and the following conditions have been assumed:

At 0 sec, a guillotine rupture of a DGH occurred. As an additional assumption, the loss of power (in the RBMK reactor design documentation, the rupture of DGH has been considered with this assumption) was made.

After 0.1 sec the fast-acting scram system is activated by signal of pressure increasing in the water communication compartments. Simultaneously during the period of 0.4 sec, the fast-acting turbine valves are closed and the turbine generators are switched off. The main coolant pumps and feedwater pumps tripped and caused by loss of power, a switch-on of steam discharge valves to the condenser is prohibited. The vapour flow for the station own needs is considered. This steam flow is modelled as a function of the steam pressure in the separator.

As pressure increases in the circuit, the main safety valves open. The ECCS accumulators are activated by coincidence of pressure increasing signal in the water communication compartments and the signal of decreasing of the pressure difference between drum separator and pressure header below 0.5 MPa or the signal of separator level decreasing to the level - 1000 mm (signal of emergency cooling).

0.5 sec after existence of the signals mentioned, the fast-acting accumulator valves are opening. The Emergency Core Cooling Pumps of the damaged half (ECCP-DH) and of the intact half (ECCP-IH) are fed by diesel generators.

20 sec after the signal of emergency cooling, the valves of the ECCP-DH, and after 30 sec the valves of the ECCP-IH. are opening. 27 sec after the signal, the valves of the intermediate throttle installations of the accumulator system are closing.

Analysis results

With the failure of the internal power supply, a raise of the pressure in the circuit occurs, which results in the actuation of the main safety valves. The valves of the first group open after 10 sec, of the second group - after 11 sec, and of the third group - after 13 sec. After the safety valves open, the pressure in the circuit decreases.

The leakage rate from the pressure header (fig. 4) is determined by the flow restrictor in the distribution group header. At the beginning of the accident the temperature of the water at the outlet of the pressure header reaches appr. 270 °C, e. g. there is large subcooling at the entrance of the flow restrictor. Under those conditions the critical mass flow through the flow restrictor is approximately 1150 kg/sec. In the further process the pressure decreases, the subcooling gets lower and after appr. 40 sec the coolant in the pressure header boils up. Under these conditions a strong decrease of the flow rate from the pressure header follows till 540 kg/sec, and the next decrease progresses by the pressure drop in the circuit.

The flow rate from the channels and of the emergency cooling system (fig. 4) is determined by the critical flows in the flow restrictors of the ECCS and in the gate and control valves. It stabilizes by appr. 200 kg/sec.

The mass flow through the channels (fig. 5) of the damaged DGH drops at the beginning almost at the value 0. This is due to the fact that the water in the lower water communications is replaced by the water-steam-mixture possessing essentially lower density. Under those conditions, the temperature in the fuel element cladding and in the channel tube rises. The duration of this process is limited by two conditions:

- water inventory in the system of the lower water communication;
- critical mass flow through the gate and control valves.

Fig. 4

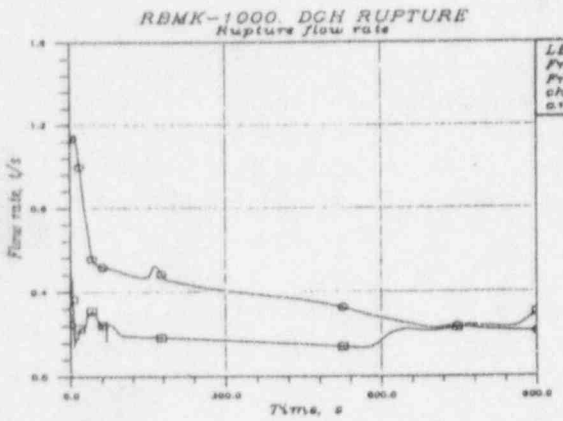

Fig. 5

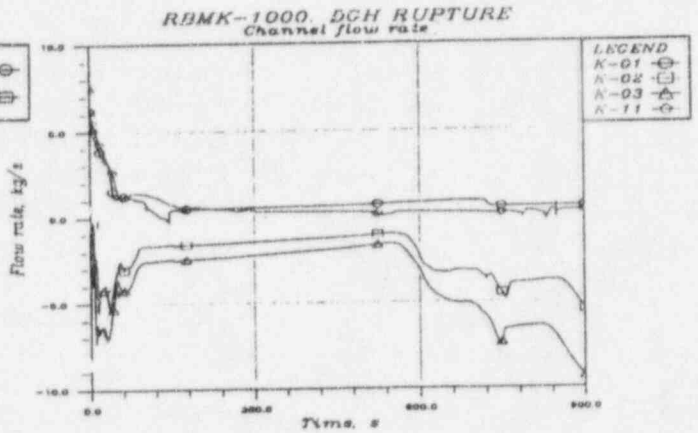

The temperature of the FE-claddings reaches the maximum at 670 °C after 7 sec. The maximum channel tube temperature is reached in 5 sec, at 405 °C (fig. 6). Afterwards, the negative coolant mass flow rises and that leads to the decrease of the temperature.

In the channels of the other DGH there is no notable rise in temperature of the fuel element (FE)-claddings and the channel tube.

The emergency cooling system begins to supply water after 27 sec by acquiring the according pressure difference (fig. 7). The accumulator system reaches maximum feed rate (1130 kg/sec) by 35 sec. Finally, the closure of the intermediate throttle valves leads to the lower feed rate by

Fig. 6

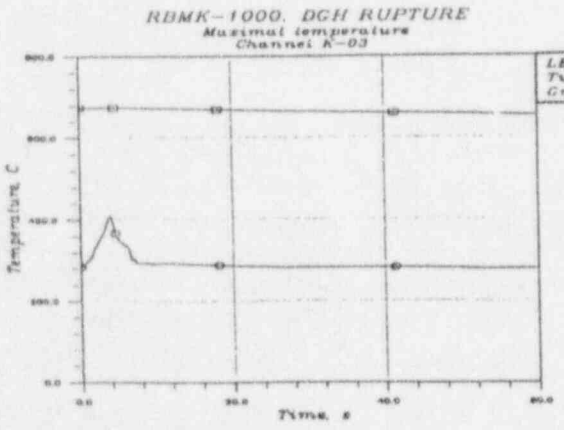

Fig. 7

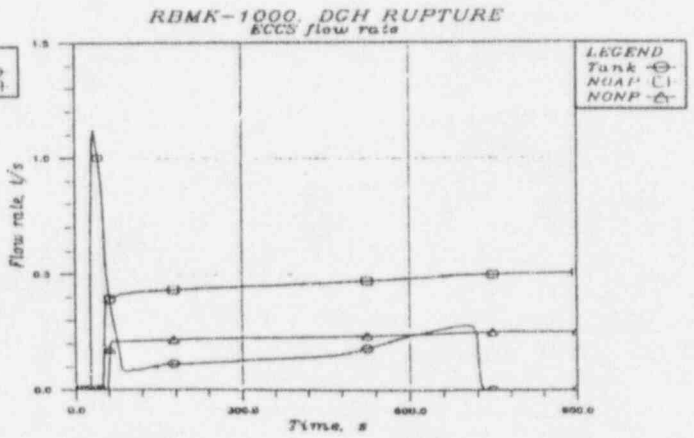

90 kg/sec and the further dropping of the circuit pressure results in the increase by 290 kg/sec. By t=713 sec the level in the accumulators drops at 0,4 m and the responsible valves close.

The feed rate from the ECCS to the damaged DGH header reaches its maximum by 125 kg/sec by t=78 sec and decreases continuously.

After 440 sec the level in the separator of the non-damaged half has risen, such that, water entrainment begins into the steam pipes and further into the accidental half. This process lasts appr. till t=750 sec, then only steam streams from the non-damaged into the accidental part.

At the break of the distribution group header with loss of power supply and normal function of the emergency cooling, the level in the separator of the damaged part drops under the measured level, but the separator is not drained completely and the level stabilizes. After 440 sec the level in the separator begins to rise because the water from the emergency cooling system reaches the separator and the mass flow through the downcomer is lower than from the emergency cooling system. By t=540 sec the level is again within the measuring range and stabilizes by t=720 sec by -460 mm. The surplus water from the emergency coolant system begins to stream into the channels of the damaged distribution group header. It results in the beginning of the channel cooling by t=720 sec. It leads to the increase of the mass flows in the channels of the damaged DGH and the leak mass flow from the channels and from the ECCS.

During the break of the distribution group header with the failure of the internal power supply the maximal cladding temperature reaches appr. 700 °C and the maximal channel tube temperature appr. 450 °C.

The possibility for the refill of the accidental separator and the cooling of the channels of the damaged distribution group header were shown in the case of normal functioning of the reactor emergency cooling system.

Comparison with RELAP-5 calculations [10]

The accident scenario is identical with that in the ATHLET-calculation. Nevertheless a slightly different nodalisation was used. For example, the core was simulated by 7 control volumes in RELAP5 /MOD 3 [9] and by 20 control volumes in ATHLET.

Both codes show a general coincidence in the simulation of the processes in the circuit (fig 8 and 9). The difference in the maximal claddings temperatures is not more than 25 K, and for the channel tube temperatures - not more than 10 K.

Fig. 8

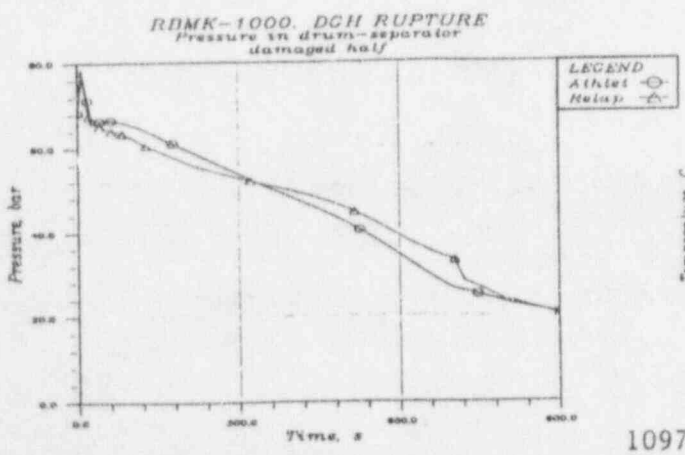

Fig. 9

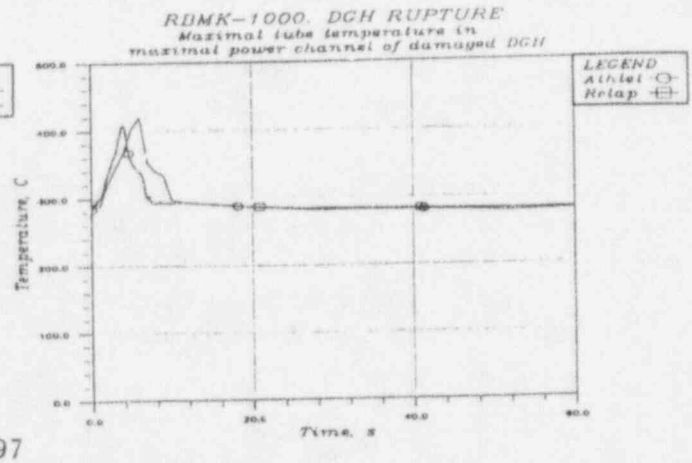

Some differences in the pressure behaviour in the separator can be explained by lower leak mass flow and lower boiling rate in the RELAP calculations.

The calculations by both codes showed a general possibility of separator refill and the channel cooling in the accidental part by water from the ECCS.

Conclusions

The specific constructional characteristics of the RBMK (e. g. the large-volume reactor core with graphit, the great number of pipelines and instruments instead of reactor pressure vessel, the large-volume separator) requires a verification of the assumptions and models applied in the Western codes, which were developed for other reactor types.

In same cases, a specific adaptation and additional verification might be necessary.

By now, a several-year experience in the application of the ATHLET-code for RBMK exists. For some RBMK-specific phenomena (stop-flow regimes, small LOCA's, stability experiments) verification calculations have already been carried out.

Also NPP-transients (e. g. natural circulation regimes) were taken as a basis for the validation of the dynamical behaviour of the ATHLET-model.

Presently, test calculations on design-basis-accidents, like e. g. the described rupture of the DGH, are carried out. The results show that the ATHLET-code is in principle applicable for the simulation of this incident class.

References

[1] N.A. Dolleshal and I.J. Emelianov, "Kanalnij jadernij energeticheskij reaktor", Atomisdat, Moscow (1980).

[2] "Technicheskoe obosnovanie besopasnosti reaktornoi ustanovki RBMK II bloka 3 SAES", Project Documentation (in Russian), (1989).

[3] S. Langenbuch, A. Petry, H. Wolff, "Weiterentwicklung von Methoden und grundlegende Arbeiten für sicherheitsgerichtete Analysen von RBMK-Reaktoren", GRS Report, GRS-A-2082, (1993).

[4] A. Domoradov, A. Moskalev, A. Finjakin, "Rashotnoe isledovanye reshima iestestvennoy zirkulazy" (in Russian), RDIPE Report, 4.206 OT, (1995).

[5] A. Domoradov, A. Moskalev, A. Finjakin, "Analys rasryva RGK po programe ATHLET" (in Russian), RDIPE Report, 4.202 OT, (1995).

[6] A. Domoradov, A. Moskalev, A. Finjakin, "Analys rasryva TK po programe ATHLET" (in Russian), RDIPE Report, 4.205 OT, (1995).

[7] A. Domoradov, A. Moskalev, A. Finjakin, "Analys rasryva paroprovoda po programe ATHLET" (in Russian), RDIPE Report, 4.204 OT, (1995).

[8] M.J. Burwell, G. Lerchl, J. Miro, V. Teschendorff, K. Wolfert, "The Thermalhydraulic Code ATHLET for Analyses of PWR and BWR Systems", Proc. 4th International Topical Meeting on Nuclear Reactor Thermal Hydraulics, NURETH-4, (1989).

[9] Ransom V.H., et al., RELAP5/MOD3 Code Manuals, EG&G Idaho, (1990).

[10] J. Nikitin et al., "Numerical Simulation of RBMK Design Accidents", RDIPE Report , 27.133 OT, (1994).

[11] A. Moskalev, A. Petry, "Development of a Radiation Transfer Model and its Coupling with the ATHLET-Code, GRS Technical Notice, TN-PEA-94-2, (1994)

Nomenclature

DGH	- Distribution group header
ECCS	- Emergency core cooling system
FE	- Fuel element
MCP	- Main coolant pump
PH	- Pressure Header
NOAP	- ECCS-pumps into the damaged half
NONP	- ECCS-pumps into the intact half
ECCP-DH	- Emergency Core Cooling Pumps of the damaged half
ECCP-IH	- Emergency Core Cooling Pumps of the intact half

Acknowledgement

This work was partly sponsored by the German Ministry for Education, Science, Research and Technology (BMBF).

SMALL-BREAK LOSS-OF-COOLANT ACCIDENTS IN THE UPDATED PIUS 600 ADVANCED REACTOR DESIGN*

B. E. Boyack, J. L. Steiner, S. C. Harmony, H. J. Stumpf, and J. F. Lime
Technology and Safety Assessment Division
Los Alamos National Laboratory

ABSTRACT

The PIUS advanced reactor is a 640-MWe pressurized water reactor developed by Asea Brown Boveri (ABB). A unique feature of the PIUS concept is the absence of mechanical control and shutdown rods. Reactivity is normally controlled by coolant boron concentration and the temperature of the moderator coolant. ABB submitted the PIUS design to the US Nuclear Regulatory Commission (NRC) for preapplication review, and Los Alamos supported the NRC's review effort. Baseline analyses of small-break initiators at two locations were performed with the system neutronic and thermal-hydraulic analysis code TRAC-PF1/MOD2. In addition, sensitivity studies were performed to explore the robustness of the PIUS concept to severe off-normal conditions having a very low probability of occurrence.

INTRODUCTION

The PIUS advanced reactor is a four-loop, Asea Brown Boveri (ABB) designed pressurized water reactor with a nominal core rating of 2000 MWt and 640 MWe [1]. A schematic of the basic PIUS reactor arrangement is shown in Fig. 1. The schematic is generally representative of the design except that the downcomer and riser are integrated rather than separated as shown in the schematic. Reactivity is normally controlled by coolant boron concentration and temperature; there are no mechanical control or shutdown rods. The core is submerged in a large pool of highly borated water and is in continuous communication with the pool water through pipe openings called density locks. The density locks provide a continuously open flow path between the primary system and the reactor pool. The reactor coolant pumps (RCP) are operated so that there is a hydraulic balance in the density locks between the primary system and the pool, keeping the pool water and primary coolant separate during normal operation. Hot primary-system water is stably stratified over cold pool water in the density locks.

PIUS has two scram systems. The first, an active-scram system, consists of four valved lines, one for each primary coolant loop, that connect the upper portion of the reactor pool to the suction side of the RCPs. Although the active-scram piping and valves are safety-class equipment, operation of the nonsafety-class RCPs is required for effective delivery of highly borated pool water to the primary system. In addition, the effectiveness of the active-

*This work was funded by the US Nuclear Regulatory Commission's Office of Nuclear Regulatory Research.

scram system is limited for loss-of-coolant accidents (LOCAs), which lower the pool level below the scram-line inlets. The second scram system is a fully safety-class passive-scram system that automatically actuates when motive power to the RCPs is lost or the active-scram system otherwise proves ineffective. Actuation of the passive-scram system occurs when the balance between the primary system and the pool is disrupted. Highly borated water from the pool enters the primary system via natural circulation, and this process both shuts the reactor down and cools the core. The heated coolant returns to the pool, which can be cooled by either an active, nonsafety-class system or a fully passive, safety-class system that circulates pool water to heat exchangers.

As part of the preapplication and eventual design certification process, advanced reactor applicants are required to submit neutronic and thermal-hydraulic safety analyses covering a sufficient range of normal operation, transient conditions, and specified accident sequences. ABB submitted a Preliminary Safety Information Document (PSID) [2] to the US Nuclear Regulatory Commission (NRC) for preapplication safety review in 1990. Early in 1992, ABB submitted a Supplemental Information Package to the NRC to reflect recent design modifications [3]. An important feature of the PIUS Supplement design was the addition of the previously described active-scram system as the first-line shutdown system for most transient and accident conditions. As this system cannot meet all scram requirements, the passive-scram system of the original PSID design was retained. Because PIUS does not have the usual rod-based shutdown systems, the response of PIUS following both planned reactor trips and a variety of accident initiators must be carefully examined and understood.

The PIUS safety analyses submitted by ABB are based on results from the RIGEL code [4], a one-dimensional (1D) thermal-hydraulic system analysis code developed at ABB Atom. Review and confirmation of the ABB safety analyses for the PIUS design constituted an important activity in the NRC's preapplication review. Los Alamos supported the NRC's preapplication review of the PIUS reactor. This paper summarizes the results of analyses performed to understand the response of the PIUS Supplement design to "small" piping breaks at the following locations (Fig. 1):

1. the pressure relief system piping at the top of pressure vessel, and
2. a single scram-line pipe near its junction with the suction side of the RCP.

Sensitivity studies were performed to explore the robustness of the PIUS concept to severe off-normal combination conditions having a very low probability of occurrence. These studies included failure of the active-scram system, reduced boron concentration in the reactor pool, and partial blockage of the lower density lock in combination with a break in the pressure relief system piping. Analyses of the response of the PIUS reactor to additional accident initiators including a large-break (LB)LOCA, main steam line break (MSLB), loss of offsite power, and reactor scrams are presented in Refs. 5–8, respectively.

TRAC ADEQUACY FOR THE PIUS APPLICATION

The TRAC-PF1/MOD2 code (TRAC) [9], version 5.3.05, was used for each small-break (SB)LOCA calculation. The TRAC code series was developed at Los Alamos to provide advanced, best-estimate predictions for postulated accidents in pressurized water reactors. The code incorporates four-component (liquid water, water vapor,

liquid solute, and noncondensible gas), two-fluid (liquid and gas), and nonequilibrium modeling of thermal-hydraulic behavior. TRAC features flow-regime-dependent constitutive equations, component modularity, multidimensional fluid dynamics, generalized heat structure modeling, and a complete control systems modeling capability. The code also features a three-dimensional (3D), stability-enhancing, two-step method, which removes the Courant time-step limit within the vessel solution. Many of these features have proved useful in modeling the PIUS reactor.

Code adequacy must be addressed when first applying a computer code to a new reactor type, e.g., PIUS. If TRAC analyses were supporting a design certification activity, a formal and structured code-adequacy demonstration would be needed. One such approach would be to (1) identify representative PIUS transient and accidents sequences; (2) identify the key systems, components, processes, and phenomena associated with the sequences; (3) conduct a bottom-up review of the individual TRAC models and correlations; (4) conduct a top-down review of the total or integrated code performance relative to the needs assessed in steps 1 and 2; and (5) correct significant identified deficiencies. The bottom-up review determines the technical adequacy of each model by considering its pedigree, applicability, and fidelity to separate-effects or component data. The top-down review determines the technical adequacy of the integrated code by considering code applicability and fidelity to integral test facility data.

Because the NRC was engaged in a preapplication review rather than a certification review, the NRC and Los Alamos concluded that a less extensive demonstration of code adequacy would suffice. Steps 1 and 2 were performed and documented [10]. A bottom-up review specific to the PIUS reactor was not conducted. However, the bottom-up review of TRAC conducted for another reactor type [11] provided some confidence that many of the basic TRAC models and correlations are adequate, although some necessary code modifications were also identified. A complete top-down review was not conducted. However, the ability of TRAC to model key PIUS systems, components, processes, and phenomena was demonstrated in an assessment activity [12] using integral data from the ATLE facility [4].

ATLE is a 1/308 volume scale integral test facility that simulates the PIUS reactor. Key safety features and components are simulated in ATLE, including the upper and lower density locks, the reactor pool, pressurizer, core, riser, downcomer, reactor coolant pumps, and steam generators. Key processes are simulated in ATLE including natural circulation through the upper and lower density locks, boron transport into the core (simulated with sodium sulfate), and control of the density lock interface. Core kinetics are indirectly simulated through a point kinetics computer model that calculates and controls the core power based upon the core solute concentration, coolant temperature, and heater rod temperature. There are differences in magnitude between the TRAC-calculated and measured values of key parameters. For example, for a test in which the ATLE RCPs were tripped, the TRAC-calculated peak lower density lock flow is about 25% less than measured. The TRAC-calculated natural circulation flow rate at the end of the test is about 12% less than measured. However, the key processes and phenomena of the ATLE test are simulated by TRAC, and the agreement between the calculated and measured parameters is judged by the authors to be reasonable.

The ability of TRAC to model key PIUS systems, components, processes, and phenomena was further demonstrated by benchmarking TRAC to the RIGEL code. The results of one such benchmark comparisons will be

discussed in the next section of this paper. The results of other TRAC-RIGEL benchmark activities are discussed in Refs. 5 and 8.

TRAC includes the capability for multidimensional modeling of the PIUS reactor thermal-hydraulic behavior. A multidimensional thermal-hydraulic model has been prepared and used to calculate the baseline pump-trip scram and MSLB transients [13] for the original PSID design and LBLOCA [5] for the PSID Supplement design. The 1D model is believed to adequately represent many PIUS transients and accidents, with the following important reservation. The most important physical processes in PIUS are related to reactor shutdown because the PIUS reactor does not contain control and shutdown rods. Coupled core neutronic and thermal-hydraulic effects are possible, including multidimensional interactions arising from nonuniform introduction of boron across the core. ATLE does not simulate multidimensional effects. The RIGEL thermal-hydraulic model is 1D and a point kinetics model is used. Although both 1D and multidimensional TRAC thermal-hydraulic models have been used for PIUS analyses, core neutronics are simulated with a point kinetics model in each case. At the present time, it is not known whether coupled multidimensional core neutronic and thermal-hydraulic effects are important.

TRAC MODEL OF THE PIUS REACTOR

A description of the TRAC fully 1D model of the PSID Supplement design is provided in Ref. 5. The TRAC-calculated and PSID Supplement steady-state values are tabulated below for comparison.

	TRAC	PSID Supplement
Core mass flow (kg/s)	12822	12880
Core bypass flow (kg/s)	200.2	200
Loop flow (kg/s)	3266	-
Cold-leg temperature (K)	531	527.1
Hot-leg temperature (K)	560.7	557.3
Pressurizer pressure (MPa)	9.5	9.5
Steam exit pressure (MPa)	4.0	4.0
Steam exit temperature (K)	540.3	543
Steam flow superheat (°C)	15.3	20
Steam and feedwater mass flow (kg/s)	243	243

Additional initial and boundary conditions for the calculated transients are generally as follows, except where otherwise noted. The reactor is operating at beginning of cycle with a primary loop boron concentration of 375 parts per million (ppm) and 100% power. The boron concentration in the reactor pool is initially 2200 ppm. When the active-scram system is activated, the scram valves open over a period of 2 s following event initiation, remain open for 180 s, and close over a period of 20 s. The feedwater pumps supplying coolant to the steam-generator secondaries are tripped at the time of reactor trip and the feedwater flow rate decreases linearly to zero in 20 s. The steam drum pressure on the steam-generator secondary side is kept constant at 3.88 MPa. If conditions arise in which the thermal interface in the lower density locks is displaced from its normal position, the movement is

detected by temperature sensors in the lower density lock and the RCPs change speed to restore the interface to its normal position, e.g., speeding up to lower an elevated thermal interface. However, the RCPs have an overspeed limit of 115%. If this limit is reached, the control of the density lock thermal interface can no longer be maintained, the lower density lock activates, and flow from the reactor pool enters the primary.

PRESSURE RELIEF LINE SBLOCA

The initiating event for the baseline transient is a break in the pressure relief system piping at the flange just outside the steel pressure vessel and upstream of the safety relief valves (Fig. 1). Steam flows through the break at a peak rate of 105 kg/s and then decreases in concert with the primary pressure until a two-phase flow through the break begins at 230 s. At that time the flow rate temporarily increases to 110 kg/s and then resumes its decrease, reaching 50 kg/s at 1200 s. A scram is initiated at 18 s when the primary system depressurizes to 8.5 MPa. Injection of highly borated water into the primary system through the scram lines causes a rapid decrease in the core power to decay levels (Fig. 2). During the interval the scram valves are open, inventory is displaced from the primary system into the reactor pool, primarily through the upper density lock (Fig. 3). While the scram valves are open, the RCP inlets are full of liquid. However, closure of the scram valves at 230 s induces a marked change in primary system behavior. Immediately following termination of the scram line flow, voiding occurs in the pump inlets, the RCPs increase to their overspeed limit of 115% of nominal (Fig. 4), and subsequently the RCP discharges become oscillatory (Fig. 5). The oscillatory behavior of the RCP discharges propagates throughout the primary system. For example, the density lock flows are highly oscillatory (Fig. 3). However, a net circulation pattern is established with pool water entering the primary system through the lower density lock and exiting the primary system through the upper density lock (Fig. 6). The net inflow through the lower density lock produces a continuing, albeit oscillatory, increase in the primary boron concentration (Fig. 7). Coolant temperatures decrease, for the most part, throughout the transient. However, the core inlet temperature increases following closure of the scram lines and the core outlet periodically saturates as the core flow oscillates in concert with the RCP discharges for an interval before subcooling is recovered.

A RIGEL calculation of the first 300 s of a SBLOCA in the pressure relief system piping has been reported [3]. The TRAC and RIGEL results are generally in qualitative agreement until 230 s when the scram valves close. There are moderate differences in the parameter values, but the same trends are predicted by the two codes. There are important phenomenological differences between the two calculations after 230 s. However, these differences are believed to arise from the timing at which events occur and, when considered in the perspective of extended transient times (e.g., 1200 s), are not significant. The TRAC-calculated results show the RCP controller demands an increase in speed at 210 s, about 10 s after the scram valves begin to close. The RCP overspeed limit is reached by 260 s. The flow oscillations predicted by TRAC arise approximately 40 s after the RCPs have reached their overspeed limit and are caused by voiding in the RCP inlets subsequent to closure of the scram valves. The RIGEL-calculated results show that the RCP controller demands an increase in speed at 255 s and the 115% overspeed limit is reached shortly before 300 s. The authors believe that oscillatory RCP flows would be calculated by RIGEL for times

greater than 300 s. A RIGEL calculation was reported for a break in the same location for the original PSID design [2]. During that transient, the RCP outlet flows were oscillatory after voiding arose in the inlets of the operating RCPs and after the RCP overspeed limit was reached.

Sensitivity studies were performed to explore the robustness of the PIUS concept. The first sensitivity study examined the response of the PIUS reactor to the baseline SBLOCA concurrent with a failure of the active-scram system. Similar end states were reached for the two calculations by 1200 s when the transient calculations were terminated. The course of the sensitivity study transient differed, however, in several respects. Because it lacked the rapid injection of boron from the active-scram system, core power decreased more slowly than in the baseline. Consequently, the buoyancy of the coolant in the rising section above the core increased as core coolant temperatures increased and voiding occurred in the core. The RCPs rapidly increased speed to the 115% overspeed limit in an attempt to control the position of the lower density lock thermal interface. The interface was maintained for 60 s, and during this interval the lower density lock was inactive and no boron entered the core. Thus, the initial decline in core power was the result of the negative reactivity insertions from increasing moderator temperatures and voiding in contrast to the baseline where the only source of negative reactivity insertion was from boron entering the core. The lower density lock activated shortly after the pump overspeed limit was reached and highly borated water entered the primary system from the reactor pool to maintain a shutdown core and to cool the core. Oscillatory primary-system behavior was calculated.

The second sensitivity study examined the response of the PIUS reactor to the baseline SBLOCA initiator concurrent with a reactor pool boron concentration of 1800 ppm, the level at which a reactor scram is initiated on lower pool boron concentration [3]. The lowered pool boron concentration was of no consequence; the only impact was to slightly lengthen the time to reduce primary-system temperatures to a same level as occurred in the baseline. Oscillatory behavior occurred in this sensitivity calculation.

The third study examined the response of the PIUS reactor to the baseline SBLOCA initiator concurrent with a 75% blockage of the lower density lock. The baseline and 75% blockage results are similar in all major trends and average quantities. There is, however, an important phenomenological difference between the two calculations. The baseline calculation displays a strong oscillatory character when the RCP inlets void following termination of the scram line flows. The blockage case is markedly different. Oscillations during the few intervals of existence are much smaller and decay with time. The density lock flows for this case (Fig. 8) are illustrative of the system behavior and may be compared with the density lock flows for the baseline case presented in Fig. 3. Partial blockage of the lower density lock appears to "stiffen" the coupled primary-pool system with the result that pump-induced oscillations do not grow to detectable levels and, when they do become detectable, are damped.

SCRAM LINE SBLOCA

A small-break initiator in a second location was analyzed—a break in a single scram line at a location near the RCP inlet. The scram-line diameter is slightly less than twice that of the pressure relief line, and coolant is lost from both the pool and pump ends of the break. Coolant is lost through only one end of the pressure relief line break. Thus, the scram-line SBLOCA is a more severe accident as measured by the amount of coolant lost from the system. The larger primary inventory loss adversely affects operation of the active-scram system as discussed below. The pool-side and pump-side break flows are shown in Fig. 9. Both break flows rapidly decrease from the maximum levels reached immediately following break initiation. The decreasing break flows are the result of a rapidly falling primary-system pressure and voiding at the break inlets. Early in the transient, the primary source of negative reactivity is from boron injected by the active-scram system following system activation on a low primary pressure signal. The active-scram system is only effective for the first 40 s of the transient because flows through the intact scram lines rapidly decrease when the pool liquid level approaches the elevation of the scram-nozzle connections. The negative reactivity inserted during the period of active-scram system operation rapidly reduces the core power to 1250 MWt (Fig. 10). The RCPs maintain control of the lower density lock interface until about 55 s. Between 40 and 55 s, a power-to-flow mismatch exists with power near the 1250-MWt plateau and core flow decreasing. The coolant (moderator) temperature increases to saturation (Fig. 11), and partial voiding of the core occurs. Both the increasing moderator temperature and voiding insert negative reactivity to further decrease the power to 380 MWt by 55 s. At this time, the RCPs reach their overspeed limit of 115%, the lower density lock activates, highly borated pool water enters the core, and the core power decreases to shutdown levels. For much of the transient, the flows through the upper and lower density locks are highly agitated. However, the integrated density lock flows clearly show a net natural circulation from the pool into the primary through the lower density lock and that a return flow to the pool via the upper density lock is established (Fig. 12). Thus, by 1200 s, the loss of coolant through the ends of the scram-line break is negligible, the core power is at shutdown levels, the loops are voided, and a natural-circulation flow between the primary and pool through the density locks is fully established.

SUMMARY OBSERVATIONS

1. Reactor shutdown to decay heat levels is predicted for each of the SBLOCA initiators. The active-scram system effectively reduces core power to decay levels for reactor scram when it is available. The passive-scram system effectively reduces core power to decay levels for transients in which the scram system is either unavailable or inoperable (e.g., the scram-line SBLOCA event after the pool water level declines below the scram-line inlet nozzles).
2. The PIUS core, as presently conceived, has inherent, compensating neutronic shutdown mechanisms. Neither operator or active-system actions are needed to accomplish reactor shutdown, even for the various event initiators combined with very low-probability occurrences.

3. Confidence in the baseline simulations is enhanced by the assessment activity performed using ATLE data. The ATLE processes and phenomena were correctly predicted by TRAC. However, there are quantitative discrepancies between key TRAC-calculated parameter values and the ATLE data and the reasons for these differences should be understood if PIUS is submitted to the NRC for design certification.

5. Our confidence in the predicted outcomes of the baseline simulations is enhanced by the code-to-code benchmark comparisons that have been conducted for the SBLOCA, active-system scram, and the LBLOCA. RIGEL and TRAC are two independently developed codes, yet the RIGEL- and TRAC-calculated results display many areas of similarity and agreement. There are also differences in the details of the transients and accidents calculated by the two codes. It is desirable that the reasons for these differences be explored if PIUS is submitted to the NRC for design certification.

6. Although the sensitivity calculations performed for each event type explore sequences well beyond the base of code assessment and code-to-code benchmark evaluations, the analyses reported herein indicate that PIUS will successfully accommodate such low-probability sequences. No phenomenological "cliffs" were encountered in any of the sensitivity studies.

7. At the present time, it is not known whether coupled multidimensional core neutronic and thermal-hydraulic effects are important. Additional shutdown phenomena need to be investigated, such as the effects of the boron injection front on the core axial power shape.

REFERENCES

[1] T. J. Pederson, "PIUS-A New Generation of Power Plants," *Second ASME/JSME International Conference on Nuclear Engineering*, San Francisco, California, March 21-24, 1993.

[2] "PIUS Preliminary Safety Information Document," ABB Atom, December (1989).

[3] C. E. Brinkman, "PIUS PSID Supplemental Material," ABB Combustion Engineering Power document LD-93-020, Enclosure 1 (1993).

[4] D. Babala, U. Bredolt, and J. Kemppainen, "A Study of the Dynamics of the SECURE Reactors: Comparison of Experiments and Computations," Nuclear Engineering and Design 122: 387-399 (1990).

[5] J. L. Steiner, S. C. Harmony, H. J. Stumpf, J. F. Lime, and B. E. Boyack, "Large Break Loss-of-Coolant Accidents in the Updated PIUS 600 Advanced Reactor Design," Los Alamos National Laboratory document LA-UR-93-4460 (1993).

[6] S. C. Harmony, J. L. Steiner, H. J. Stumpf, J. F. Lime, and B. E. Boyack, "One-Dimensional TRAC Calculations of Main Steam Line Break Events for the Updated PIUS 600 Advanced Reactor Design," Los Alamos National Laboratory document LA-UR-93-4358 (1993).

[7] B. E. Boyack, J. L. Steiner, S. C. Harmony, H. J. Stumpf, and J. F. Lime, "Loss of Offsite Power Events in the Updated PIUS 600 Advanced Reactor Design," Los Alamos National Laboratory document LA-UR-93-4206 (1993).

[8] B. E. Boyack, J. L. Steiner, S. C. Harmony, H. J. Stumpf, and J. F. Lime, "Reactor Scram Events for the Updated PIUS 600 Advanced Reactor Design," Los Alamos National Laboratory document LA-UR-93-4456 (1993).

[9] N. M. Schnurr, R. G. Steinke, V. Martinez, and J. W. Spore, "TRAC-PF1/MOD2-Volume I. Theory Manual," Los Alamos National Laboratory report LA-12031-M (NUREG/CR-5673) (1992).

[10] B. E. Boyack, "Assessment of the PIUS Physics and Thermal-Hydraulic Experimental Data Bases," Los Alamos National Laboratory document LA-UR-93-3564 (1993).

[11] B. E. Boyack and J. S. Elson, "Assessment of TRAC-PF1/MOD3 Code Adequacy for NP-HWR Thermal-Hydraulic Analyses," Los Alamos National Laboratory document LA-NPR-TN-010 (1992).

[12] H. J. Stumpf, "TRAC Calculations of a Pump-Trip Scram and Partial Loss of Heat Sink for the ATLE Test Facility," Los Alamos National Laboratory document LA-UR-93-4133 (1993).

[13] J. F. Line, J. S. Elson, J. L. Steiner, H. J. Stumpf, and B. E. Boyack, "TRAC Calculations of a Pump-Trip Scram and a Main Steam Line Break Accident for the PIUS 600 Advanced Reactor Design," Los Alamos National Laboratory document LA-UR-93-516 (1993).

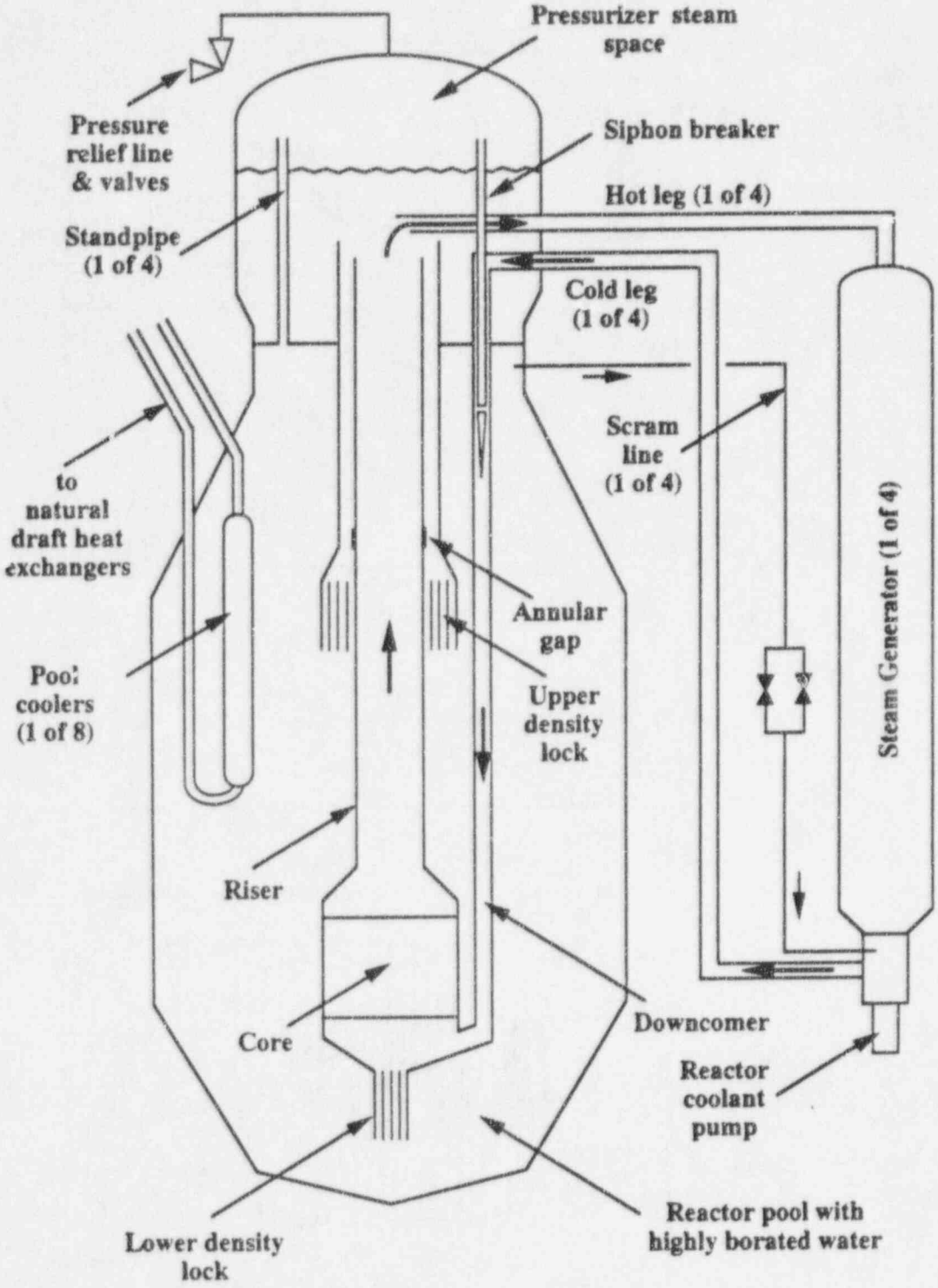

Fig. 1.
Schematic of the Pius Reactor.

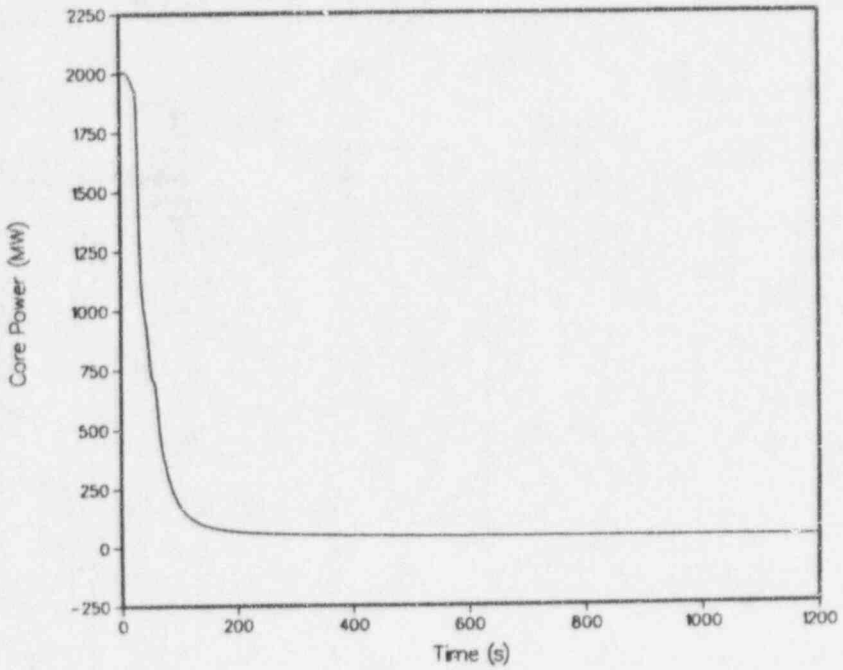

Fig. 2.
Reactor power for pressure relief line SBLOCA baseline case.

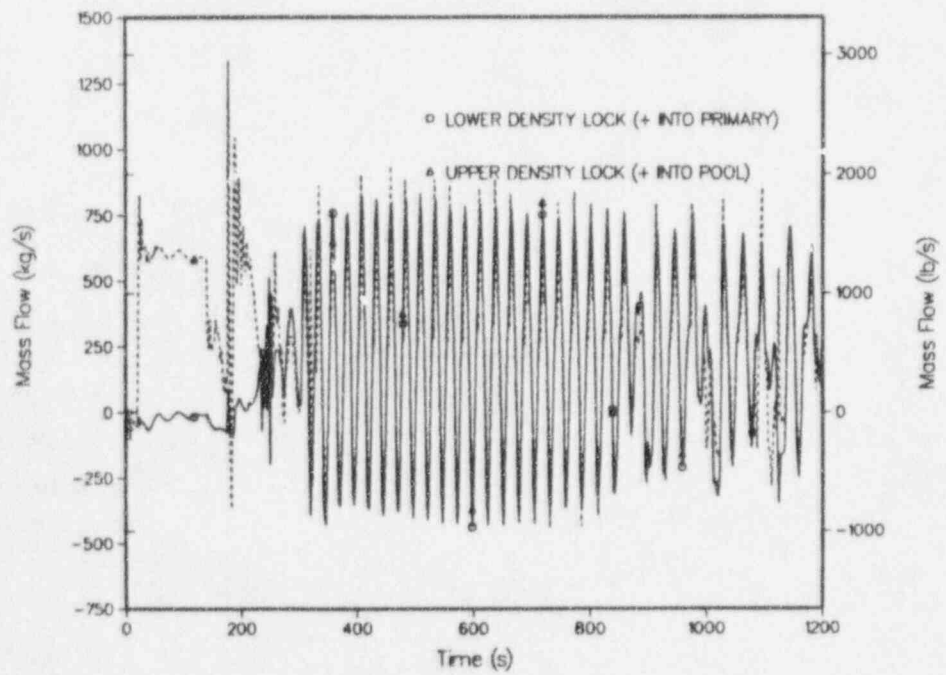

Fig. 3.
Instantaneous density lock flows for pressure relief line SBLOCA baseline case.

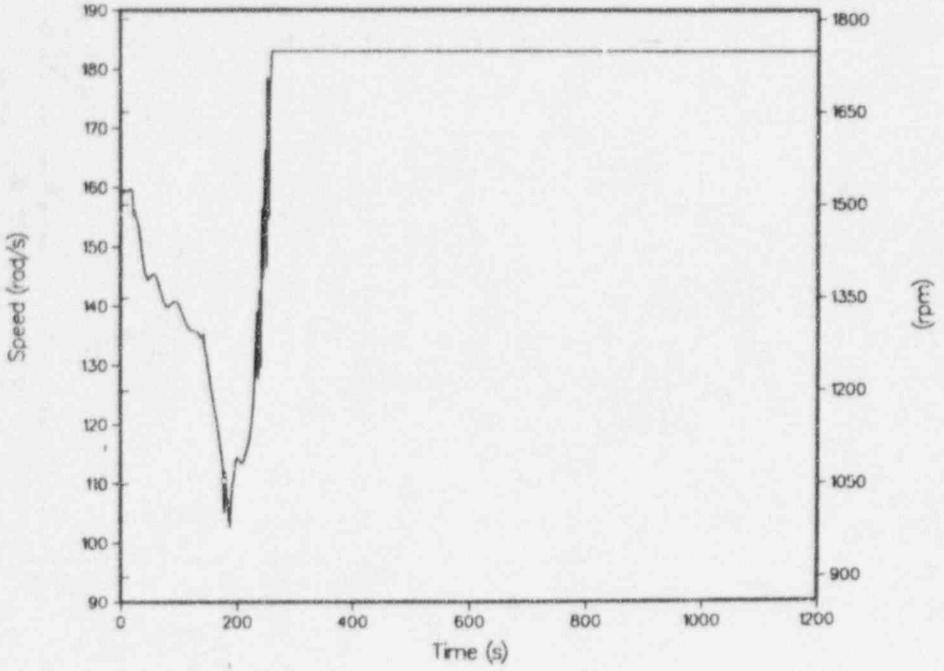

Fig. 4.
RCP speeds for the pressure relief line SBLOCA baseline case.

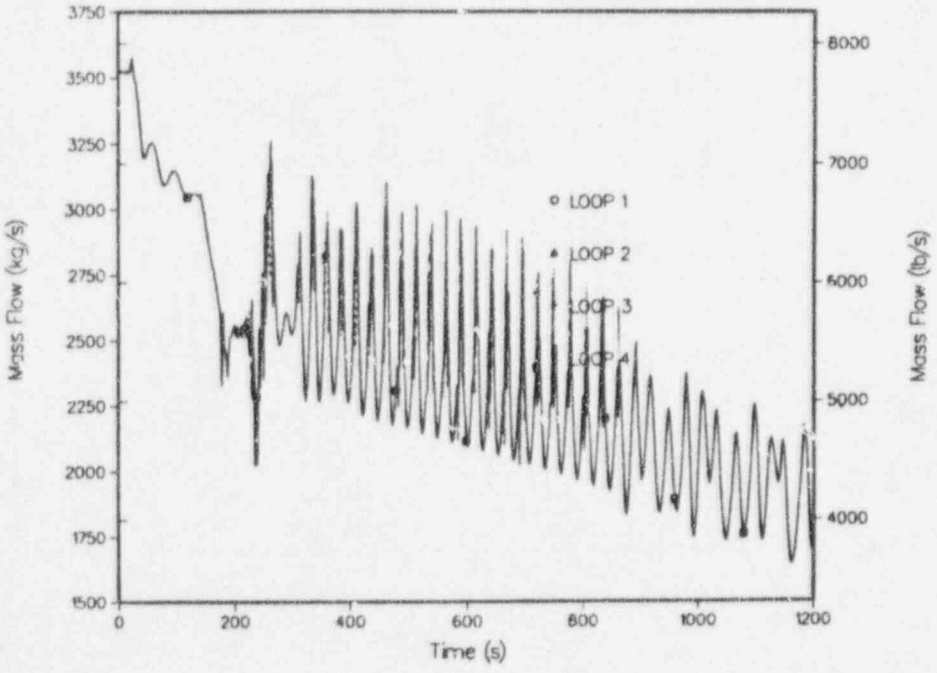

Fig. 5.
RCP outlet flows for pressure relief line SBLOCA baseline case.

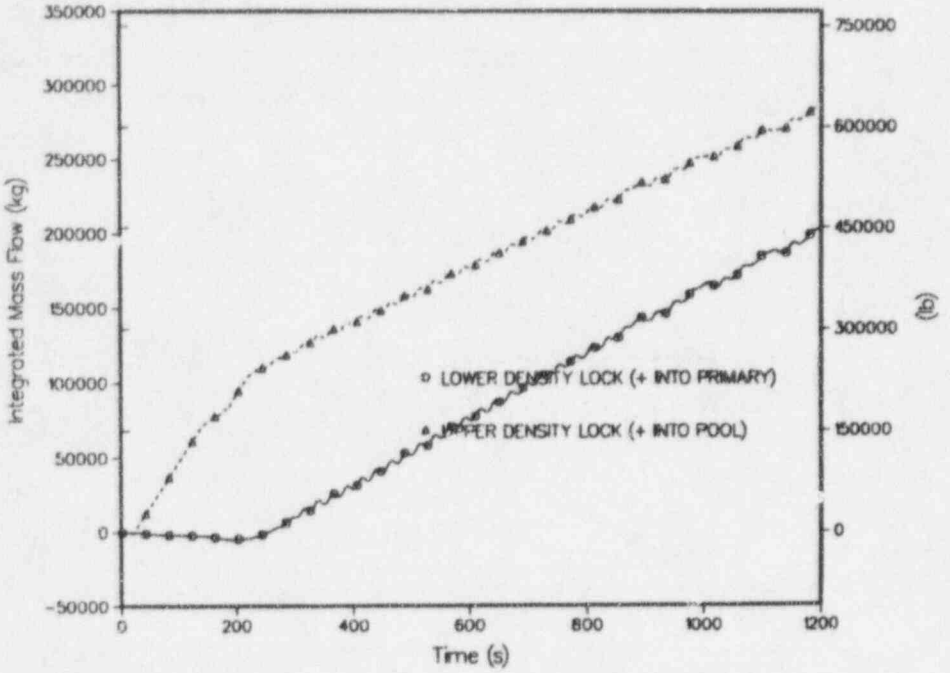

Fig. 6.
Integrated density lock flows for pressure relief line SBLOCA baseline case.

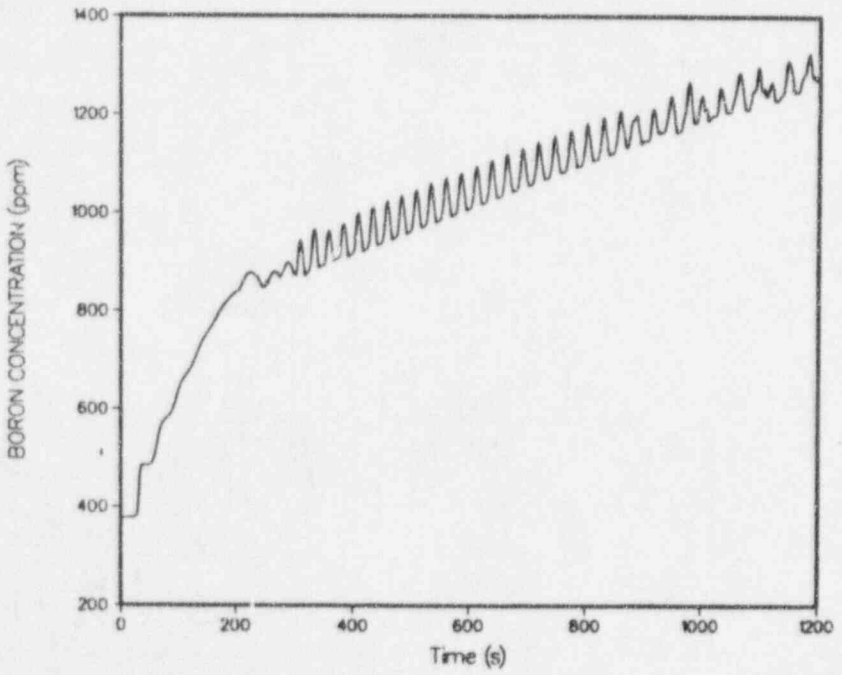

Fig. 7.
Primary boron concentration for pressure relief line SBLOCA baseline case.

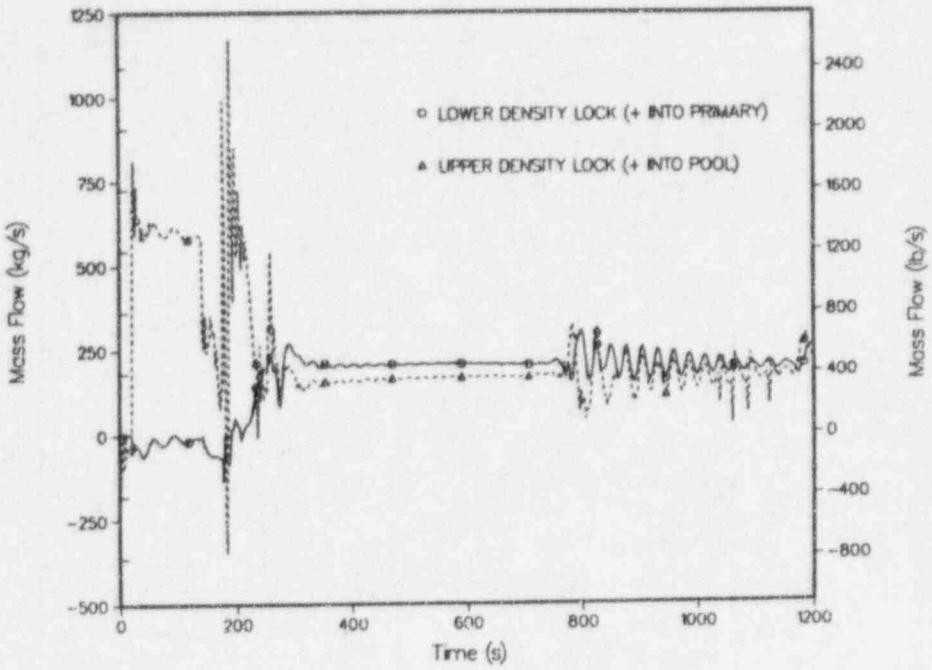

Fig. 8.
Instantaneous density lock flows for pressure relief line SBLOCA with 75% blockage of the lower density lock.

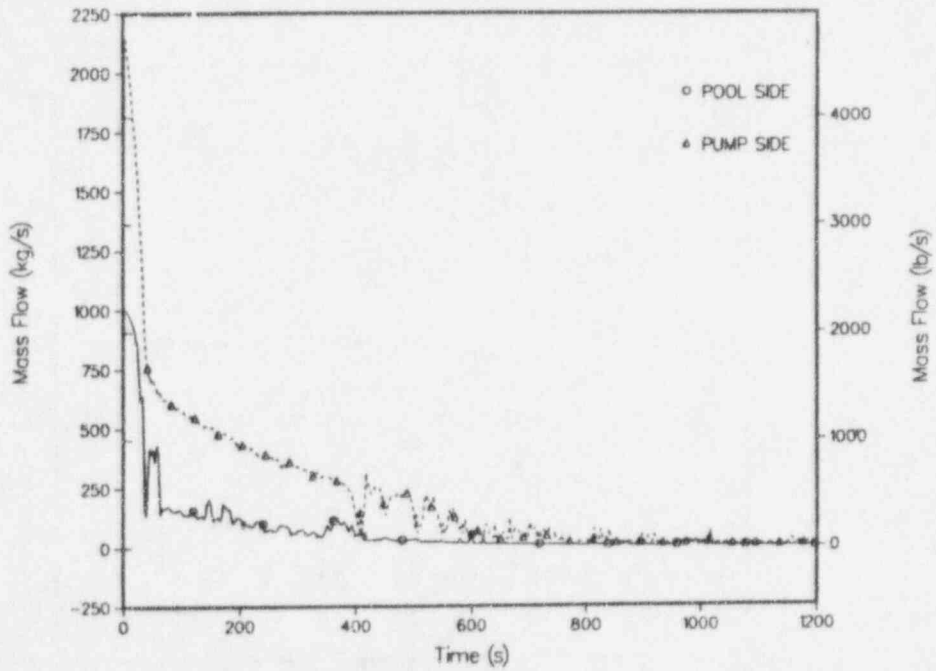

Fig. 9.
Break flows for the scram-line SBLOCA case.

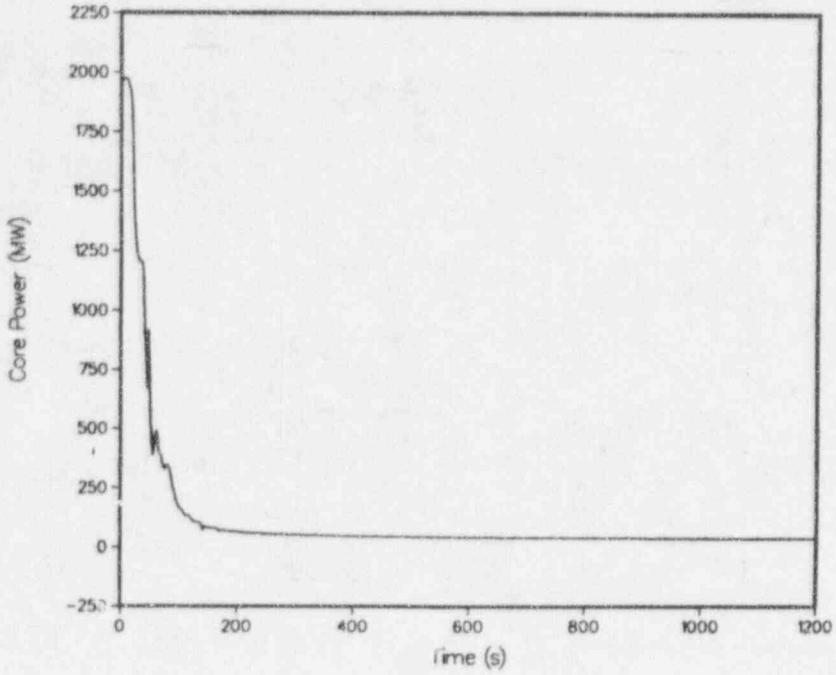

Fig. 10.
Core power for the scram-line SBLOCA case.

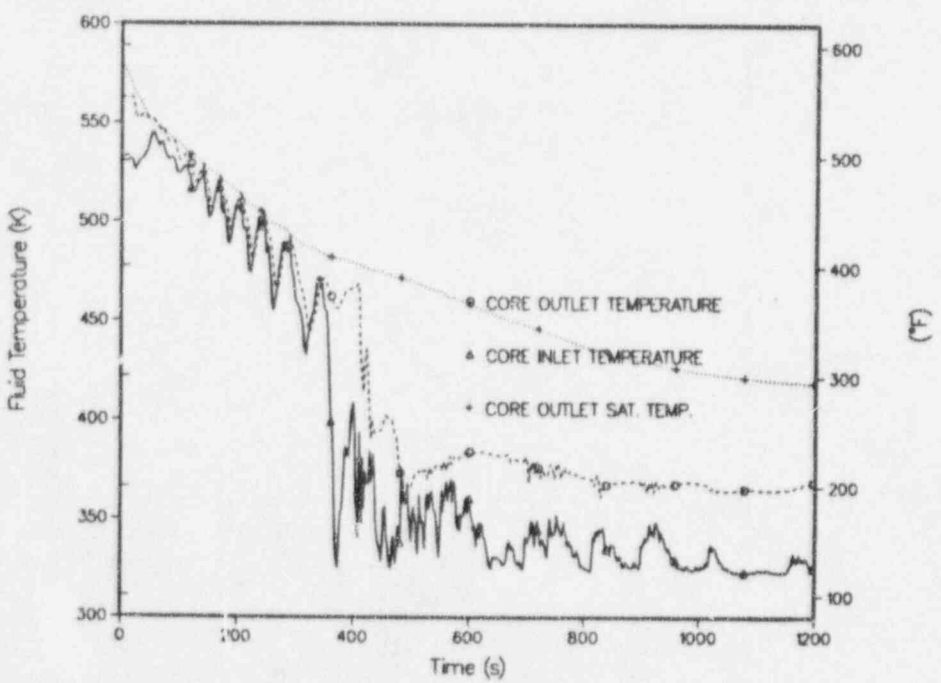

Fig. 11.
Core coolant temperatures for the scram-line SBLOCA case.

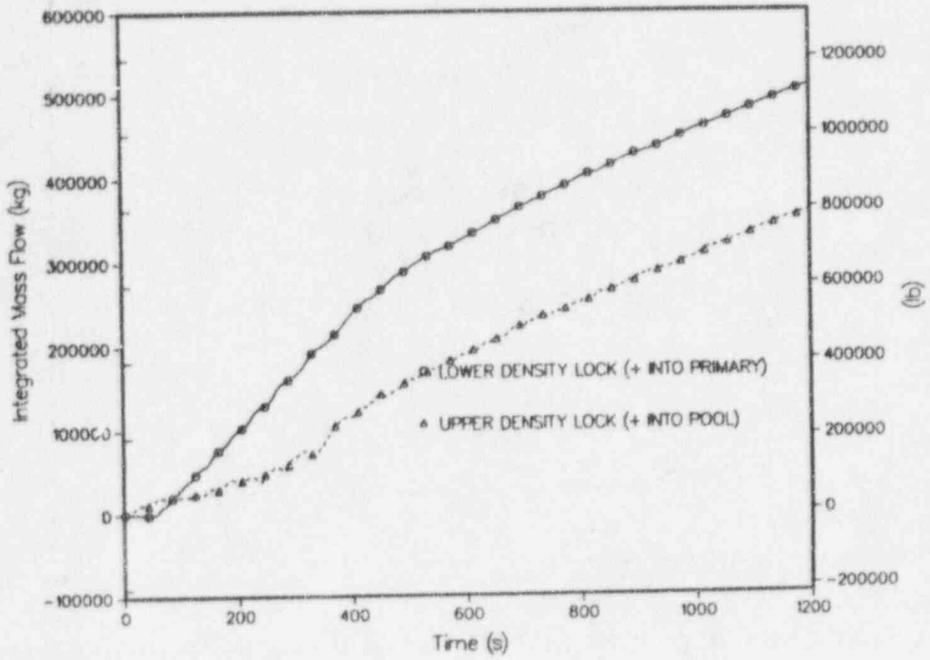

Fig. 12.
Integrated density lock flows for the scram-line SBLOCA case.

SIMULATION OF A BEYOND DESIGN-BASIS-ACCIDENT WITH RELAP5/MOD3.1

József Bánáti

Lappeenranta University of Technology
Department of Energy Technology
P.O. Box 20
FIN-53851 Lappeenranta
Finland

ABSTRACT

This paper summarizes the results of analyses, parametric and sensitivity studies, performed using the RELAP5/MOD3.1 computer code for the 4th IAEA Standard Problem Exercise (SPE–4). The test, conducted on the PMK–2 facility in Budapest, involved simulation of a Small Break Loss Of Coolant Accident (SBLOCA) with a 7.4 % break in the cold leg of a VVER-440 type pressurized water reactor. According to the scenario, the unavailability of the high pressure injection system led to a beyond design basis accident. For prevention of core damage, secondary side bleed-and-feed accident management measures were applied. A brief description of the PMK-2 integral type test facility is presented, together with the profile and some key phenomenological aspects of this particular experiment. Emphasis is placed on the ability of the code to predict the main trends observed in the test and thus, an assessment is given for the code capabilities to represent the system transient.

INTRODUCTION

An essential component of nuclear safety activities is the analysis of potential accidents in nuclear power plants. Various facilities are operated worldwide to establish a better understanding of the transient thermo-hydraulic behaviour of pressurized water reactor (PWR) systems. Data obtained from experiments gives the opportunity for validation of sophisticated computer codes that are used in simulations. In order to facilitate the development and improvement of thermal hydraulic simulation codes and identify the margins of applicability, international efforts are being conducted to verify those computer codes. The assessment process is also important in determining the extent to which these programs can be used as tools to analyze nuclear reactor safety. Comparison of the results from various codes must be performed with the realization that the modelling technique chosen significantly influences the calculation with code, and that the results are always user-dependent. Coordination of the experimental and analytical work can help to minimize the user effect and increase the experience with different versions of the codes applied to the same

experiment. With these objectives in mind, the IAEA organized four Standard Problem Exercises on the PMK in the period between 1985 and 1994, with wide interest from the member states. Lappeenranta University took part in the SPE series for the first time and the present project has been sponsored by the Finnish Academy.

The main purpose of the work described herein is to investigate whether RELAP5 is capable of simulating the primary and secondary system responses for a beyond design basis accident scenario in a special VVER geometry, involving an intensive core dry-out, and loop seal clearing phenomena in the hot and cold legs. Furthermore, the present analysis attempts, to some extent, to evaluate the effectiveness of the reactor safety system, applied in the accident management procedure.

DESCRIPTION OF THE PMK-2 FACILITY

The PMK-2 (Fig. 1.) is a one-loop, full-pressure, integral type model of the four VVER-440 type pressurized water reactors used in the Paks Nuclear Power Plant (NPP) in Hungary. The aspect ratio is 1:2070 for the volumes and the power, while the component heights and relative elevations are kept the same as in the reference plant, in order to preserve the driving head for natural circulation. VVER-440s have some unique features, which are different from most western-type plant concepts, such as horizontal steam generators, loop seals in both hot and cold legs and relatively high pressure in the safety injection tanks. Due to these dissimilarities, different system responses can be expected for most of the usual transients.

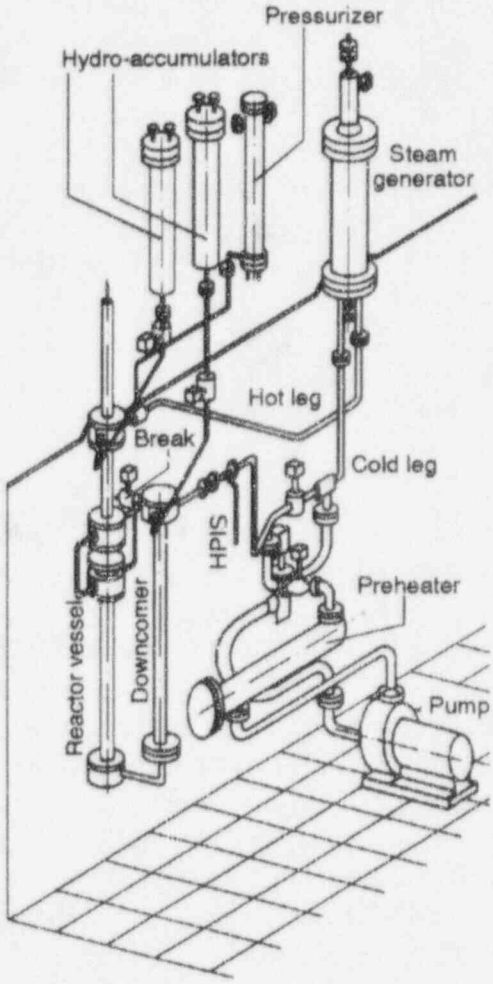

FIG. 1. AXONOMETRIC VIEW OF THE PMK-2

The primary and secondary sides of the PMK-2 correspond to six loops in the NPP. The facility includes a pressurizer, hot and cold legs, a circulating pump and a steam generator (Fig. 2). A flow diagram is presented in Fig. 3. The reactor vessel is simulated with a U-tube construction, consisting of an external downcomer and the core section. The core itself comprises 19 full length, electrically heated fuel rod simulators with a heated length of 2.5 m. The fuel rod pitch (12.2 mm) and diameter (9.1 mm) are identical to those of the reference reactor. The rods are arranged in a hexagonal bundle, representing the typical shape of a VVER bundle. The nominal core power output is 664 kW, with uniform axial and radial distributions. Electrical power to the core simulator is controlled continuously during a test according to a prescribed decay heat curve. The safety system includes the following components: two hydro-accumulators (safety injection tanks, SITs), high and low

pressure injection systems (HPIS and LPIS). The SIT-1 is connected to the top of the downcomer, while the SIT-2 injects water to the upper plenum. The LPIS is attached to the downcomer head. In the case of the SPE-4 experiment, the HPIS was excluded from the system and the break was located at the top of the downcomer. The steam generator model is a vertically distributed section of the horizontal VVER-440 SG, having 82 tubes bent in serpentine shape. The length of each tube is the same as the average tube in the reference apparatus. The PV23 valve acts as a steam relief valve, which opens at certain secondary pressures or by operator intervention. Steam output from the SG can be controlled by the PV22 valve. The circulating pump is situated in a by-pass line of the cold leg and its role is to establish nominal conditions. During steady-state, valve MV11 is closed and coolant is circulated through the bypass line. In the SPE experiments, only the pump coast-down process was simulated. In fact this means that at pump trip the flow rate is gradually reduced by closing the valve PV11 in a prescribed manner. When the flow rate drops below 5 % of the nominal value, the PV11 is fully closed and MV11 is opened simultaneously.

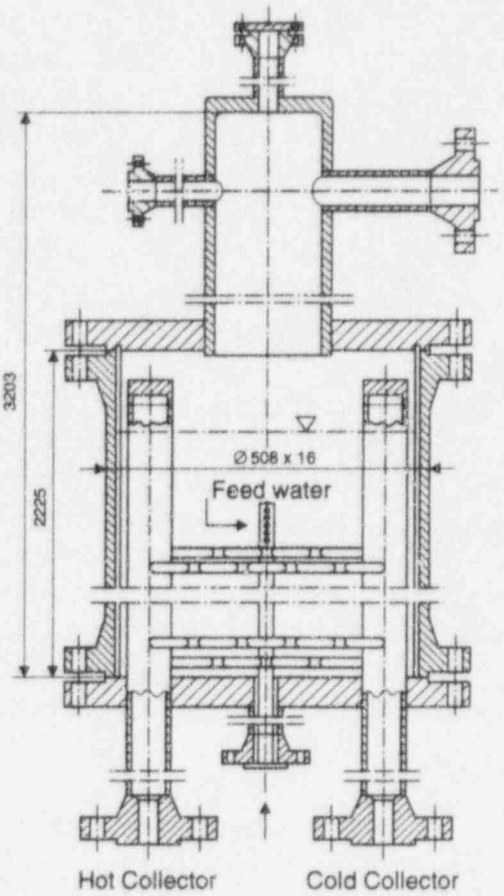

FIG. 2. STEAM GENERATOR MODEL

PROFILE OF THE SPE-4 EXPERIMENT

The transient was initiated from full rated power by opening the break valve MV31. At the same time the steam generator was isolated by closing the steam line valve PV22 and the control valve (PV21) in the feed water line. The system started to depressurize and soon reached the saturated condition. The reactor scram was activated in a few seconds, when the pressure in the primary side dropped below 11.15 MPa. The core power was reduced according to a prescribed curve, simulating the decay heat. The pump trip simulation was initiated at 9.21 MPa of the primary pressure and the duration of pump coast-down was 150 s. At the end of pump coast-down, secondary side bleed was started by opening the relief valve PV23 on the SG steam line. Hydro-accumulator injection started when the system pressure reached the actual setpoints (6.05 and 6.04 MPa) respectively. During this period, the primary pressure fell slightly below the secondary pressure. Water levels of 0.245 and 1.035 m, respectively in the SITs caused the isolation of these components. The hot leg was cleared for a very short period at 165 s, and final clearance took place at 350 s. Further depressurization was governed by the break flow and the cooldown of the facility due to heat losses to the environment. A gradual decrease of the liquid level eventually led to partial uncovery of the heated section of the core, characterized by a sharp increase in the heater rod surface temperatures. A signal indicating a secondary pressure of 0.93 MPa triggered the injection of emergency feed water into the steam generator, with a flow rate of 0.042 kg/s. Low pressure injection was initiated when the primary pressure dropped below 1.04 MPa. The experiment was terminated at 1800 s transient time.

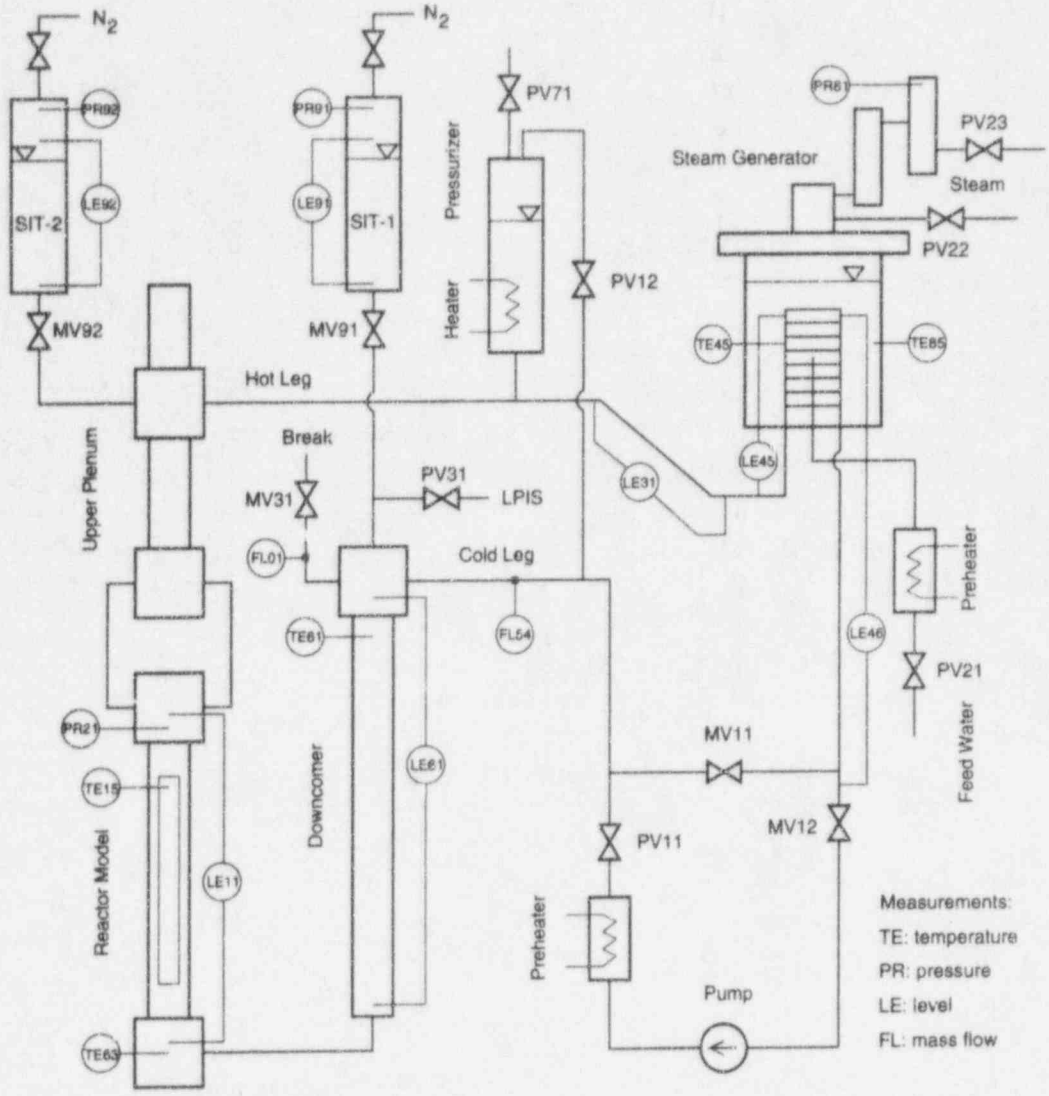

FIG. 3. FLOW DIAGRAM OF THE PMK-2 WITH SOME SELECTED MEASUREMENTS

RELAP5 MODEL DEVELOPMENT

Nodalization

An existing RELAP5/MOD2 model, developed for the earlier SPEs formed the basis of the present model, which has been modified for the upgraded facility according to the new input requirements of the MOD3.1 version of the code. The model, used in the base case calculation and detailed here, consists of 111 volumes, 127 junctions and 77 heat structures with a total of 342 mesh points. The nodalization scheme is illustrated in Fig.4. The core is modeled with two parallel channels: one heated and one unheated, each of those are horizontally interconnected. Crossflow junctions are used to join the components to the reactor vessel, as suggested in the code user guidelines. The break is modelled with a trip-valve junction at the downcomer head. The break assembly is connected to a time-dependent volume, which simulates the containment. The time-variation of back-pressure is given as a boundary condition. The tube section of the steam generator is modelled with three

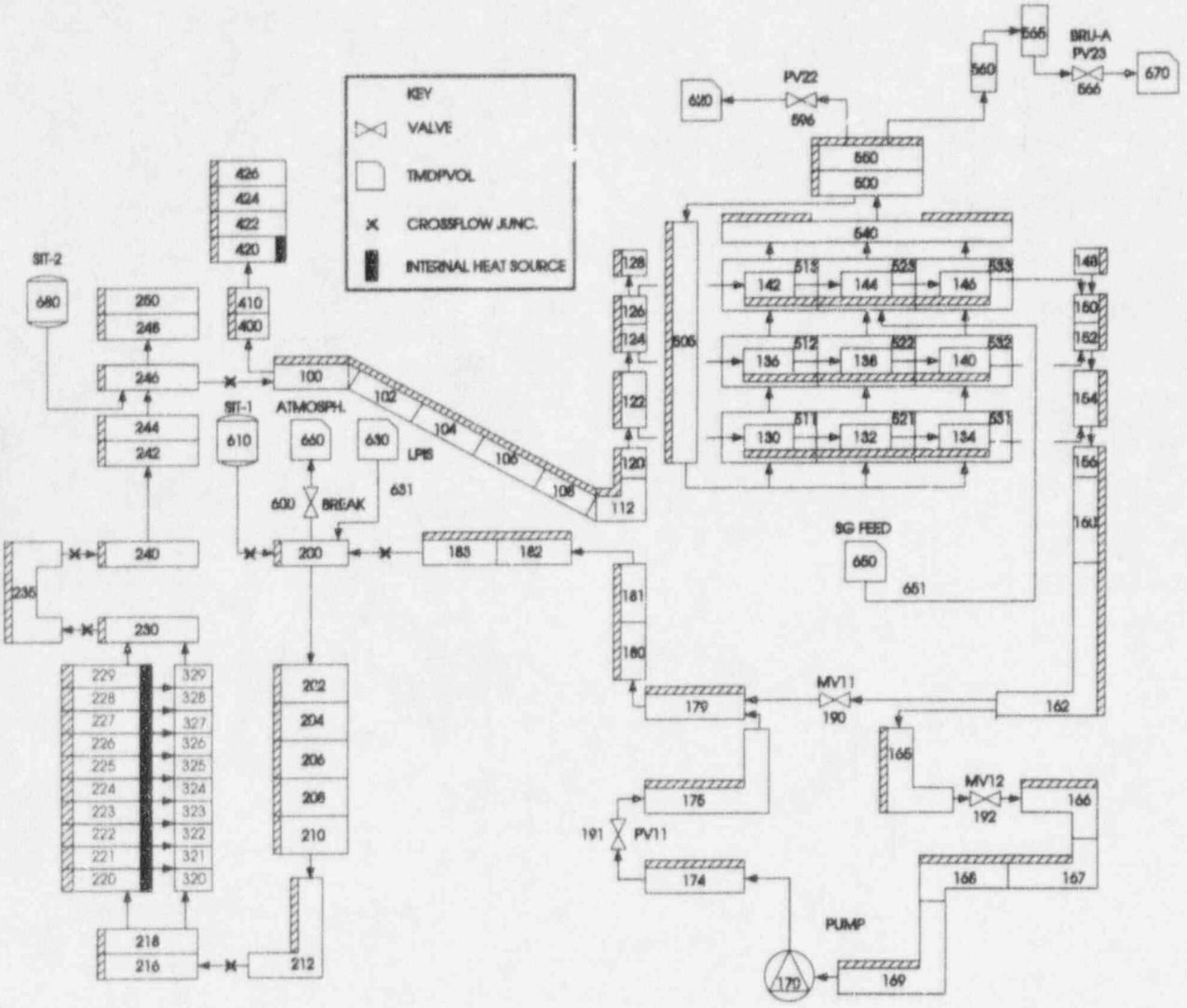

FIG. 4. RELAP5 NODALIZATION SCHEME OF THE FACILITY

horizontal channels, each divided into three volumes. The uppermost channel represents 30 tubes and its elevation is the same as the highest tube in the facility to allow steam flow when the liquid level drops below that level. The lowest channel, representing 22 tubes, is on the elevation of the lowest tube in order to allow water flow to the tubes as long as the water level exceeds the height of that level. The steam generator model consists of a separator component on the secondary side. Void fraction limitation values of 0.35 and 0.55 are used for vapour outlet and liquid fall-back junctions respectively. This configuration allows relatively high internal circulation.

TABLE I. MEASURED AND CALCULATED STEADY-STATE CONDITIONS

Parameter	ID	unit	accuracy +/-	measured	RELAP5
primary circuit					
pressure in upper plenum	PR21	MPa	0.05	12.33	12.20 *
loop flow	FL54	kg/s	0.02	4.91	4.91 *
core inlet temperature	TE63	K	1.0	540.1	545.9
core power	PW01	kW	3.0	665.1	665.1 *
SIT-1 pressure	PR91	MPa	0.05	6.05	6.05 *
SIT-2 pressure	PR92	MPa	0.05	6.04	6.04 *
SIT-1 level	LE91	m	0.02	1.465	1.465 *
SIT-2 level	LE92	m	0.02	1.855	1.855 *
pump Δp	DP16	kPa	1.0	1490	1487
steam generator Δp	DP41	kPa	1.0	43.4	41.0
heat losses to the environment	-	kW	-	23.4	22.6
secondary circuit					
SG pressure	PR81	MPa	0.02	4.56	4.56 *
SG level	LE81	m	0.05	2.88	2.515
feedwater flow	FL81	kg/s	0.02	0.35	0.35 *

* Set or controlled parameter

Steady-state

The strategy to achieve an appropriate data set for steady-state conditions requires several successive steps: the primary pressure and the initial level in the pressurizer and the steam generator were controlled by a time-dependent volume, which enabled in or outflow to or from the respective components. Primary loop flow was maintained by regulating the speed of the circulating pump. Heat exchange between the facility and the surroundings was simulated using constant heat transfer coefficients. These values were tuned to approximate the distribution of heat losses given in the test Specification Report [1]. On the secondary side, the feed water was injected at a constant mass flow rate and the code calculated the appropriate level in the steam generator. During the steady-state runs, the pressure loss coefficients were adjusted to the measured differential pressures. After a number of approaches, an initial opening ratio of 0.115 was found to be appropriate for the valve PV11 in the pump by-pass line, and gave sufficient pressure distribution in the loop. An initial search run, using the "steady-state" option of RELAP5, took 135.7 s to reach steady-state. With that condition the flows were negligible from the auxiliary control components and the levels were stable. Measured and predicted steady-state results are listed in Table I, and show fair agreement.

RESULTS AND DISCUSSION

The transient during an SBLOCA in the cold leg can be illustrated by examining the behaviour of the most important parameters over time. RELAP5/MOD3.1 predictions represent here the results of the best estimate technique used in the calculations. Recommended options were adopted from the code users manual. Experimental and calculated data are compared in plots, starting at Fig. 5. Based on the major occurrences, the whole experiment can be split into 4 periods as follows:

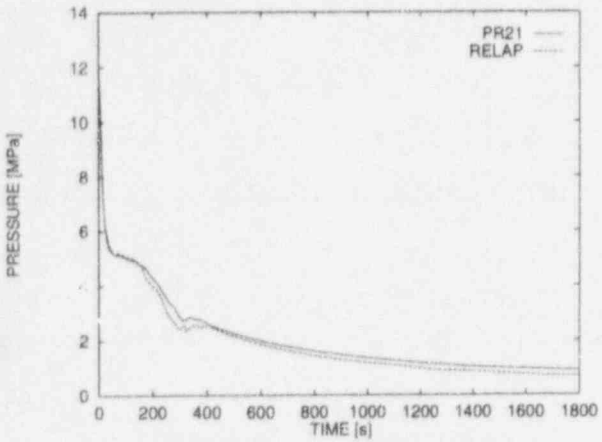

FIG. 5. PRIMARY SYSTEM PRESSURE

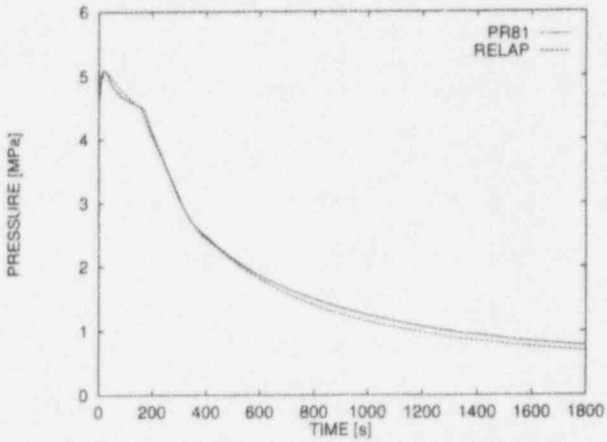

FIG. 6. PRESSURE IN THE SECONDARY SIDE

Phase 1 of the transient (between 0 and 160 s) can be characterized by a high mass and energy release through the break. A parametric study of the discharge coefficient gave the best reproduction of the break mass flow rate using values of 1.0, 1.2 and 0.85 in the subcooled, two-phase and superheated regions, respectively. As a result of the rapid depressurization in the primary system, the reactor was scrammed at 6 s and the break flow turned to two-phase in 45 s. The general profile of the primary pressure is well predicted by the code (Fig. 5). During this phase, a temporary increase can be observed in the secondary pressure, up to 5.1 MPa, when it fell back, reaching 4.5 MPa at the end of the pump coast-down (PCD) (Fig. 6). Since an important parameter, the flow rate of the steam ejected through the steam line was not measured, so the two-phase discharge coefficient of 0.8 was used for the relief valve BRU-A, in order to achieve the best matching for the secondary side pressure.

Phase 2 of the transient started at the end of PCD with initiation of the bleed, as an operator intervention. Depressurization of the SG persisted rapidly. The collapsed level in the core decreased continuously to a minimum level of ca.1.6 m. The general trend is well simulated but the minimum level is about 1.1 m higher in the calculation (Fig. 7.). This particular period showed high sensitivity to the PCD. The collapsed level in the hot leg loop-seal was temporarily cleared at 162 s. The timing of this event is perfectly predicted by the code, as can be seen in Fig.8. Subsequently the steam in the hot leg was partially condensed by the subcooled ECC water and the loop-seal was soon refilled. According to the measurements by local void probes and gamma densitometers (reported in [2]), there was clear evidence of a countercurrent flow limitation (CCFL) during the accumulator discharge, preventing the ECC water flowing down towards the core. Therefore, the CCFL option flag was set on in the RELAP model for the components of the core, the upper plenum and the downcomer. However, a separate run was performed without the CCFL option and the differences were negligible. After fast refilling, the pressure decrease was intensified and the SIT injection was

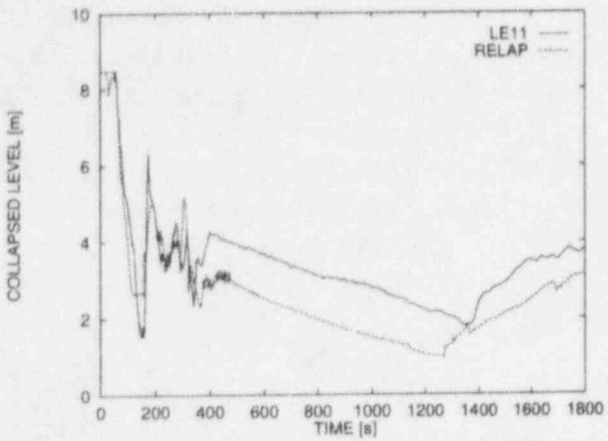

FIG. 7. COLLAPSED LEVEL IN THE CORE

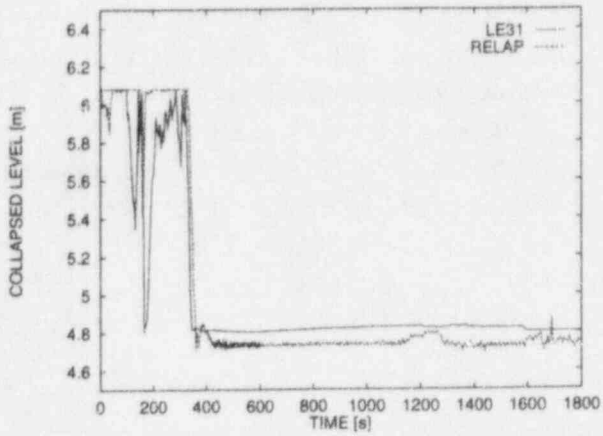

FIG. 8. COLLAPSED LEVEL IN HOT LEG LOOP-SEAL

also accelerated. The code predicted the level and pressure in both of the safety injection tanks very accurately, indicating that the calculated hydro-accumulator discharge process is in good overall agreement with the measured data. The collapsed level both in the cold collector side and downcomer side of the cold leg started to drop sharply and cleared at approx. 250 s and the discrepancy is not significant for this parameter (Fig.10). It is interesting to note that the primary pressure became lower than the secondary, for a short period between 250 and 350 s.

Phase 3, probably the most complicated period, started when the hydro-accumulators reached the minimum level and were valved off from the system. With the termination of the injection, the system pressure slightly increased and loop flow was temporarily discontinued. The cause of this flow interruption was attributed to the hot leg loop-seal, which is a unique feature of the VVER geometry. The loop-seal clearing phenomenon, based on the measured collapsed levels, is explained in detail in Fig. 9. When coolant entered the hot leg, the shape of the loop-seal prevented flow of the lower density mixture directly up into the steam generator. As the 2-phase mixture level reached the hot leg elevation, the average density in the inclined section decreased such that the manometric

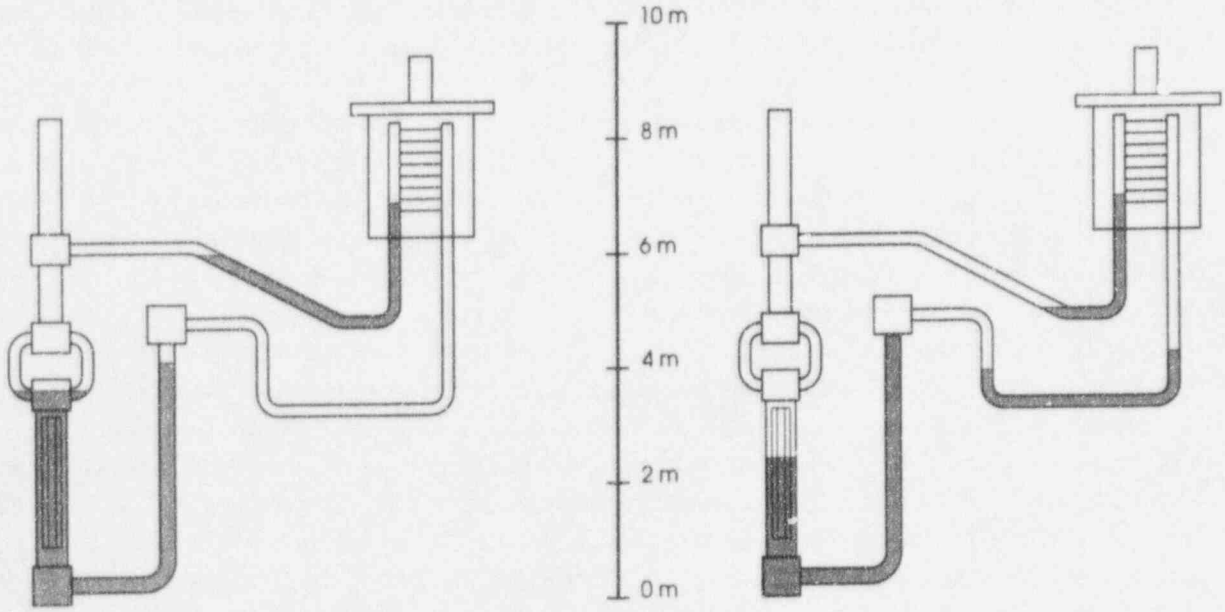

FIG. 9. COOLANT INVENTORY DISTRIBUTION DURING HOT LEG LOOP-SEAL CLEARING

pressure difference across the loop-seal retarded the buoyancy driven flow. Coolant distribution at the beginning of the process is depicted on the left side of Fig. 9. The hot leg level dropped rapidly towards the bottom of the loop-seal and pushed a certain amount of coolant to the cold leg, while the core collapsed level also fell and reached a minimum just before the loop-seal cleared, (right hand side of Fig. 9). RELAP5 has calculated the phenomenon basically well. Minor discrepancies can be found in the timing of the loop-seal clearing (approx. 20 s delay) and the core collapsed level: it reached a temporary minimum at 385 s but did not regain the elevation of about 4 m, as was measured in the experiment at 400 s. At the same time, the cold collector level (Fig.10) and the level in the downcomer (Fig.11) could be well reproduced.

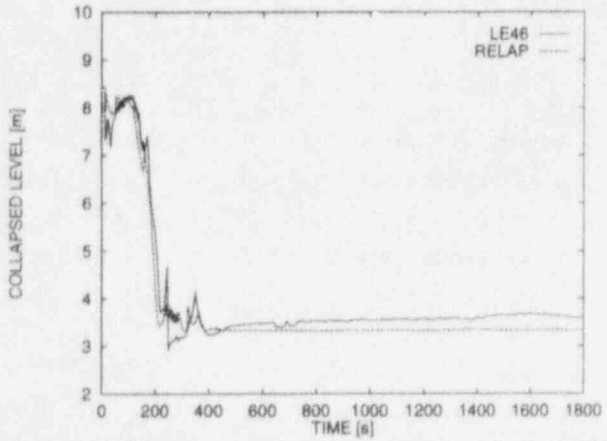

FIG. 10. COOLANT LEVEL IN THE COLD COLLECTOR

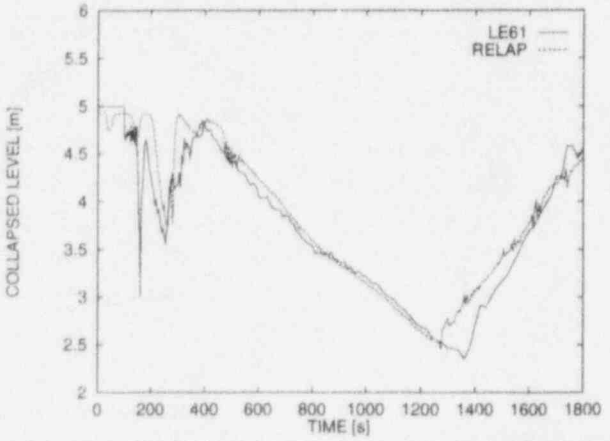

FIG. 11. COLLAPSED LEVEL IN THE DOWNCOMER

The thermal-hydraulic processes of the transient were slowed down in *Phase 4*. The break became uncovered, which caused a continual depletion of the primary system inventory. At approx. 660 s the core collapsed level decreased below the top of the heated length and a further decrease in the level down to an elevation of ~2.4 m led to a dryout at ~1100 s simulation time. Due to the poor heat transfer in the upper core region, the rod surface temperatures (Fig. 11) rose rapidly and this section of the core was completely voided. Subsequently, the primary pressure reached 1.04 MPa, the setpoint value of the low pressure injection system. The LPIS injection rewetted the heater rods and prevented their temperatures from increasing. During the dryout period, emergency feedwater was injected to the SG secondary side, providing more heat removal to the system. It can be seen in Fig. 12. that the code predicted slightly faster rise for the rod surface temperature, however the overall behaviour of the dryout was well simulated. It has to be emphasized that the gradients of the primary and secondary pressure curves were very low at this stage of the transient and so the timing of the LPIS and the SG feed were sensitive to these parameters. For example, a minor change in the primary pressure could cause a few hundred seconds delay or prematurity in the initiation of the LPIS injection. Fig. 11 shows that the code calculated the downcomer level with a reasonable accuracy. In the case of the core collapsed level, however, an underestimation is observed. The discrepancy is about 0.9 m, which is almost constant after the hot leg loop-seal clearing, when the level was not regained as much as observed in the experiment. The integrated break mass flows are essentially equal after 500 s. Thus the total inventory calculated and measured are equal. However, the core collapsed liquid level differs. This suggests that the inventory distribution is not the same. Fig. 13 indicates that the missing inventory is accumulated in the bottom of the steam generator hot

collector, since the collapsed level is overpredicted with approximately 1 m just after loop seal clearing. This phenomenon is perhaps the greatest discrepancy between the code predictions and the experimental data, and may be attributed to a problem in the countercurrent flow limitation model and it has a strong effect on the correct simulation of the dryout.

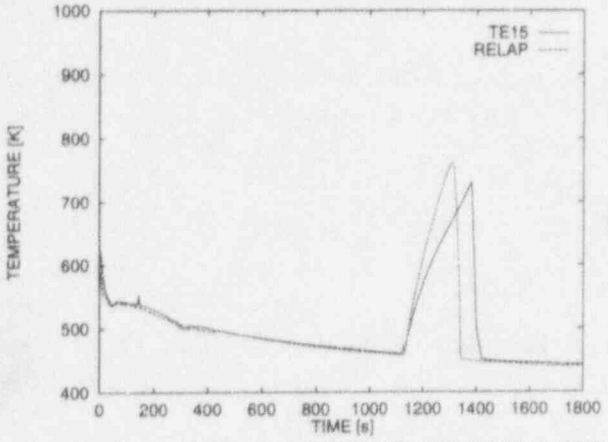

FIG. 12. ROD SURFACE TEMPERATURE AT THE TOP OF THE CORE

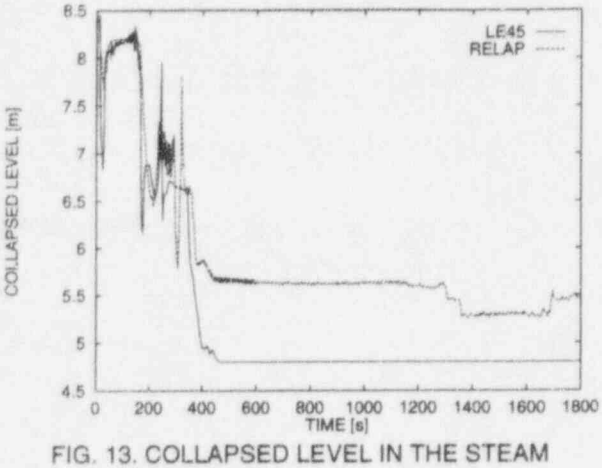

FIG. 13. COLLAPSED LEVEL IN THE STEAM GENERATOR HOT COLLECTOR

Run statistics

The simulation of 1800 s transient consumed 3679 s CPU-time on an HP 9000/710 Workstation, with an average timestep of 0.117 s. The CPU-time/transient-time ratio = 2.04

CONCLUSIONS

This paper has given a summary of the simulation of a beyond design basis accident with RELAP5/MOD3.1 computer code. The IAEA SPE-4 has been an excellent test for code assessment, since complex thermo-hydraulic phenomena were observed, such as nonequilibrium effects at cold accumulator injection, loop-seal clearing, mixture level formation and stratification, countercurrent flow limitation, dry-out and quenching in the core. The top of the downcomer appeared to be the most critical region for the one-dimensional RELAP to simulate these sophisticated 3-D effects. Special attention is therefore needed in modelling this limited area, where the break assembly, the accumulator and LPIS injection point are located. Finding the reasons for the underprediction of the core collapsed level, thus improving the CCFL simulation needs a further analysis.

It can be concluded that the code is capable of predicting the main parameters, even the most crucial rod surface temperatureat dryout and essentially the whole system transient. The calculated results are in good overall agreement with the measured data. However, a more detailed knowledge of the initial and boundary conditions of the transient (e.g. the distribution of heat and pressure losses, the surroundings of the "bleed-valve", etc.) would have resulted a more appropriate initial data set for the calculation.

The results of the present analysis show that the "bleed-and-feed" procedure can be used as an effective accident management measure, however, findings of the experiment and the calculations are not directly applicable to the reference plant.

REFERENCES

[1] L. SZABADOS et al., "Specification for the fourth IAEA Standard Problem Exercise", KFKI Atomic Energy Research Institute, Budapest, Hungary (1993).

[2] "Simulation of a Beyond Design Basis Accident with Bleed and Feed Preventive Measures", IAEA-TECDOC (draft), Vienna, (1994).

[3] J. BÁNÁTI, "Pre-Test Analysis of the 4th IAEA Standard Problem Exercise (Secondary Side 'Bleed and Feed') with RELAP5/MOD3.1", Research Report, Lappeenranta University of Technology , (1994). ISBN 951-763-830-2

[4] K.E. CARLSON et al., "RELAP/MOD3 Code Manual", NUREG/CR-5535, EGG-2596 (Draft), (1990).

[5] "Simulation of a Loss-of-Coolant Accident: Results of a Standard Problem Exercise on the Simulation of a Loss-of-Coolant Accident Organized by the International Atomic Energy Agency", IAEA-TECDOC-425, International Atomic Energy Agency (1987).

[6] "Simulation of a Loss-of-Coolant Accident with Hydroaccumulator Injection: Results of the Second Standard Problem Exercise on the Simulation on the Loss of- Coolant Accidents Organized by the International Atomic Energy Agency", IAEA-TECDOC-477, International Atomic Energy Agency (1988).

[7] "Simulation of a Loss-of-Coolant Accident with Rupture in the Steam Generator Hot Collector: Results of the Third Standard Problem Exercise on the Simulation on the Loss of Coolant Accidents Organized by the International Atomic Energy Agency", IAEA-TECDOC-586, International Atomic Energy Agency (1991).

[8] B. MAVKO, I. PARZER and S. PETELIN, "A Modeling Study of the PMK-NVH Integral Test Facility", Nucl. Technology, **105**, 231 (1994).

[9] P. CEBULL and Y.A. HASSAN, "Simulation of the IAEA's Fourth Standard Problem Exercise Small-Break Loss-ofCoolant Accident Using RELAP5/MOD3.1", Nucl. Technology, **109**, 327 (1995).

[10] J. BÁNÁTI, "Assessment of RELAP5/MOD3.1 Code for the IAEA SPE-4 Experiment", to be presented at the "International Symposium on Validation of System Transient Analysis Codes", ASME & JSME Fluids Engineering Conference, Aug. 13-18, 1995, Hilton Head, South Carolina, USA

RAPID DEPRESSURIZATION EVENT ANALYSIS IN BWR/6 USING RELAP5 AND CONTAIN

A. K. Müftüoğlu, M. A. Feltus

The Pennsylvania State University
Nuclear Engineering Department
University Park, PA 16802

Abstract

Noncondensable gases may become dissolved in Boiling Water Reactor (BWR) water level instrumentation during normal operations. Any dissolved noncondensable gases inside these water columns may come out of solution during rapid depressurization events, and displace water from the reference leg piping resulting in a false high level. These water level errors may cause a delay or failure in actuation, or premature shutdown of the Emergency Core Cooling System. (ECCS). If a rapid depressurization causes an erroneously high water level, preventing automatic ECCS actuation, it becomes important to determine if there would be other adequate indications for operator response and other signals for automatic actuation such as high drywell pressure. It is also important to determine the effect of the level signal on ECCS operation after it is being actuated.

The objective of this study is to determine the detailed coupled containment/NSSS response during this rapid depressurization events in BWR/6. The selected scenarios involve: (a) inadvertent opening of all ADS valves, (b) design basis (DB) large break loss of coolant accident (LOCA), and (c) main steam line break (MSLB). The transient behaviors are evaluated in terms of: (a) vessel pressure and collapsed water level response, (b) specific transient boundary conditions (e.g., scram, MSIV closure timing, feedwater flow, and break blowdown rates), (c) ECCS initiation timing, (d) impact of operator actions, (e) whether indications besides low-low water level were available. The results of the analysis had shown that there would be signals to actuate ECCS other than low reactor level, such as high drywell pressure, low vessel pressure, high suppression pool temperature, and that the plant operators would have significant indications to actuate ECCS.

INTRODUCTION

The solubility of noncondensables in liquid changes by a number of factors. The most important two factors are changes in pressure or temperature. With increasing pressure or temperature the solubility of gas in the liquid increases, resulting in a higher amount of noncondensable gas dissolved in the liquid. There would occur a release of gas from the liquid if the pressure keeping it in dissolved form decreases. The noncondensable gases present in the system would be dissolved in the coolant of an operating plant. If the pressure of the system drops, these gases would come out of solution. For operating conditions of a BWR, most of the noncondensables dissolved in the coolant would be released of the solution when the pressure is low as 3.1 MPa (~450 psig) [1].

The source of noncondensables in the reactor coolant is primarily radiolytic decomposition of water. The H_2 and O_2 molecules travel with the steam, and some fraction will enter the condensing chambers. Noncondensables may enter the reference leg volume by diffusion, or, with the condensate itself in the case of a slight leak in the

reference leg. In this later case, the condensate is nearly saturated with noncondensables. As the water in the reference leg is lost through the break, the condensate is drawn into the reference leg to replace the lost inventory.

During a rapid depressurization event involving loss of reactor coolant, the actual water level will drop. Any dissolved noncondensable gases inside the water level instrumentation water columns may come out of solution, and displace water from the reference leg piping resulting in a false high level. One of the potential effects of water level inaccuracies could be a delay or failure in ECCS actuation since one of the signals which triggers the low pressure and the high pressure cooling systems is reactor vessel water level. There are two items of particular concern. The first is the indicated level begins to show an increasing trend while the calculated level is still decreasing. The second concern is that during level recovery the indicated level may reach Level 8 early, which would close the HPCS injection valve even if there is a high drywell pressure signal present. This will terminate HPCS injection prior to restoring level above top of active fuel, which may in turn lead to an increase in peak clad temperatures. The overall effect of level inaccuracies during a severe accident could be improper actuation and/or operation of the ECCS.

The objective of this study is to determine the detailed coupled containment/NSSS response during this rapid depressurization events in BWR/6. The selected scenarios involve:

(a) inadvertent opening of all ADS valves;

(b) design basis (DB) large break loss of coolant accident (LOCA);

(c) main steam line break (MSLB).

The transient behaviors are evaluated in terms of: (a) vessel pressure and collapsed water level response, (b) specific transient boundary conditions (e.g., scram, MSIV closure timing, feedwater flow, and break blowdown rates), (c) ECCS initiation timing, (d) impact of operator actions, (e) whether indications besides low-low water level were available.

It is important to emphasize that the water level instrumentation was not modeled at these analyses. Furthermore, there is no credit taken for the availability of an accurate water level. The collapsed liquid level information represented as a part of the results is conservative since it would be lower than the actual two-phase water level during the depressurization transients. Collapsed liquid level is calculated by multiplying the cell length by the liquid fraction $(1-\alpha)$.

METHODOLOGY

The analyses were performed using a specially linked parallel version of SCDAP/RELAP5 [3] and CONTAIN [4] codes, developed at the Penn State University [5]. The integration of SCDAP/RELAP5, which is a best-estimate severe accident analysis code, with CONTAIN, that models the containment, allows for coupled containment/NSSS response, with greater accuracy and modelling flexibility, when compared to accident analysis using these two codes independently. The Parallel Virtual Machine (PVM) software [6] drives the RELAP5 and CONTAIN codes concurrently, using parallel/multiple-processing. The application of parallel processing is approached in a top-down manner, using the existing algorithms present in RELAP5 and CONTAIN. Message passing-based data transfer facilitates coupling between the in-vessel and ex-vessel portions of the calculations, which were performed on IBM RISC/6000 workstations.

Depressurization in the primary system occurs with a break. This break or leak may result in direct discharge into the drywell compartment of the containment as in loss of coolant accident or main steam line break cases, or yield to a discharge into the pressure suppression pool in the wetwell section of the containment as in the case of inadvertent opening of all automatic depressurization valves. The amount and the thermodynamic state of the coolant ejected from the break is calculated by RELAP5, the program which handles the in-vessel portion of the analyses. Since this blowdown will be the main source of pressure and temperature changes within the containment, this data must be transferred to CONTAIN, environment where the ex-vessel calculations are performed. On the other hand, the atmospheric conditions in the containment will be reflected back to the primary system response by updating the boundary conditions. The interaction between the coupled codes also needs to be regulated.

The most important data transferred form RELAP5 to CONTAIN is the amount of mass and the enthalpy of the liquid at the discharge. The CONTAIN computer code requires blowdown into the atmosphere of a cell or into the suppression pool to be input as a source table constructed with mass flow rate values along with

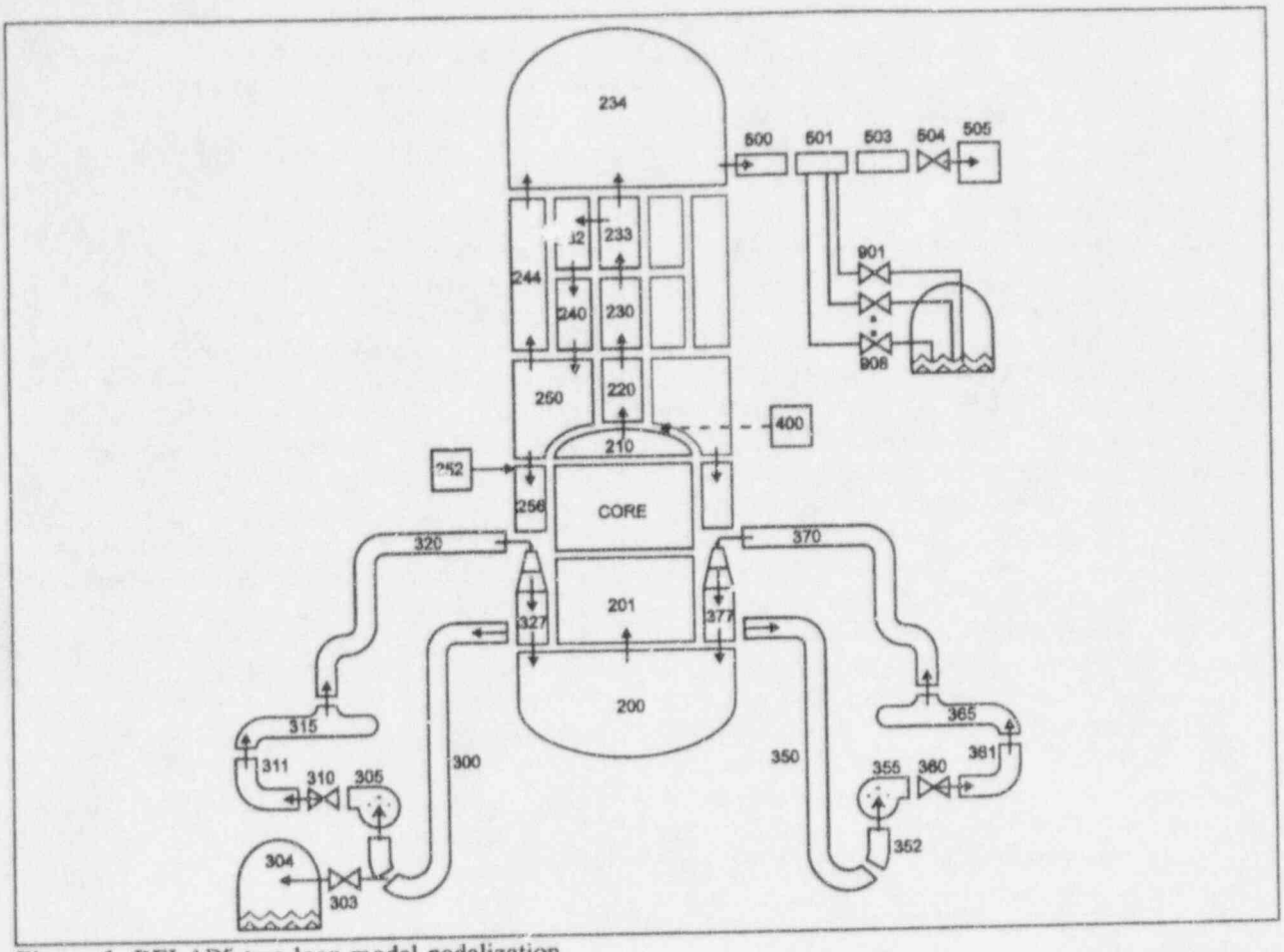

Figure 1 RELAP5 two-loop model nodalization.

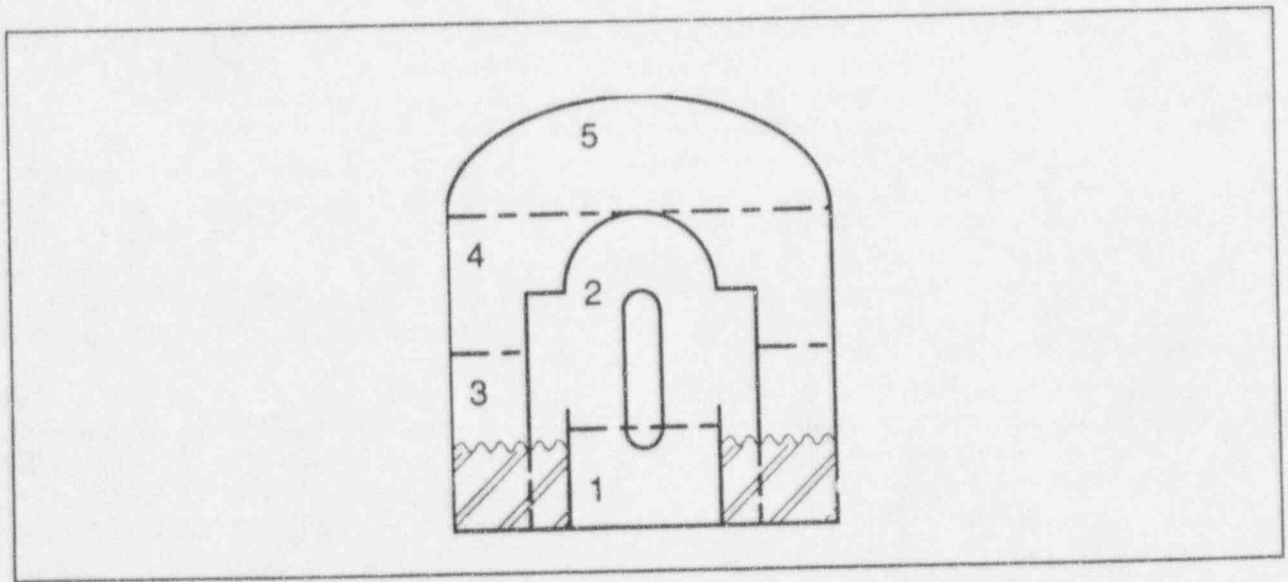

Figure 2 CONTAIN Nodalization.

temperatures or the enthalpies for corresponding transient time points. In this specific version of coupled RELAP and CONTAIN, mass flow rates and the enthalpies of the liquid leaving the system through a time dependent volume (the pressure boundary condition in RELAP) are passed to CONTAIN.

Another type of data, of secondary importance, passed from RELAP to CONTAIN, is the heat transfer from selected heat structures. This can contribute to the heating of a cell, or pressurization. The importance of this data is much more relevant when an analysis depends on the condensation of the blowdown steam in a certain containment compartment, most likely drywell, where other components exist as heat sources.

The influence of CONTAIN calculations on the RELAP calculations is the updating of the containment boundary conditions. This boundary conditions, formed by time dependent volumes and/or junctions in RELAP, involves pressure at the exit of the break, driving pressures for LPCI, suppression pool and containment temperatures and pressures. Without coupling, RELAP5 would be run stand-alone, then the results would be fed into the CONTAIN input deck as a time dependent mass flow rates and enthalpies source table, and then CONTAIN calculations would be performed. Following the containment calculations, boundary conditions would be updated in RELAP, and the iteration would be repeated. This method of serial coupling is not only more difficult, but also less accurate when compared to a truly parallel run.

The model used as input to RELAP5 is based on a BWR/6 [5,7]. For the inadvertent opening of all ADS valves case, and for the main steam line break case, an one-loop model is used. For the LOCA case, a two-loop model was developed. In the one-loop model, recirculation lines are lumped together. In the two-loop model, recirculation lines where modelled separately. Single loop model used for the ADS opening and MSLB cases, having 60 components, comprised of 58 volumes and 63 junctions. The two-loop model, shown in Figure 1, has 82 components, 77 volumes and 85 junctions.

The CONTAIN model, shown in Figure 2, is composed of five control volumes, corresponding to drywell, wetwell, pedestal, upper and middle containment cells. The RPV pedestal is connected to the drywell with a regular flow path. The drywell and wetwell are connected to each other via suppression pool vents. The wetwell is connected to the middle containment, and the middle containment compartment is connected to the upper containment control volume with open flow paths. Various heat structures are also included in the model in every cell.

TRANSIENT ANALYSES

Inadvertent Opening of All ADS Valves:

The inadvertent opening of all 7 ADS valves would be highly unlikely [7]. In order to have such a rapid depressurization event, several ADS valves must open inadvertently. The ADS uses 7 of 16 safety/relief valves to reduce reactor pressure following small breaks in the case of HPCS failure, so that the vessel pressure can be reduced to within the low pressure systems (LPCS and LPCI) design limits [7,8].

The opening of a single ADS valve is a credible event, and is an FSAR design basis event, which does not lead to a rapid depressurization. When a single ADS valve opens, the reactor system pressure is decreased slightly, and the feedwater control system keeps the vessel level within operating norms, so that no scram signal is initiated.

In the postulated inadvertent opening of all 7 Automatic Depressurization System (ADS) valves event, the ECCS signal on high drywell pressure would not immediately be activated because the ADS valves discharge directly into the suppression pool. A best-estimate analysis of an inadvertent opening of all ADS valves is performed by thermal-hydraulic coupling between the pool, drywell, reactor building and RPV.

During the 7 ADS opening event, LPCI flow would provide adequate ECCS inventory if LPCI were initiated promptly. LPCI is actuated on either low-low water level signal or a high drywell pressure signal. Since the ADS valves would discharge into the suppression pool, the drywell pressure would not be immediately changed. Noncondensable gases, dissolved in the water level instrumentation piping, would come out of solution and expand during the rapid depressurization. If noncondensable gases cause the vessel level instrumentation to read inaccurately high, then LPCI/LPCS actuation might be delayed.

Reactor scram signals based on low or low-low water level were not actuated under the assumption that the water level instrumentation would read falsely high with the noncondensables coming out of solution during the rapid depressurization. No credit was taken for the operator's recognizing that the water level instrumentation was

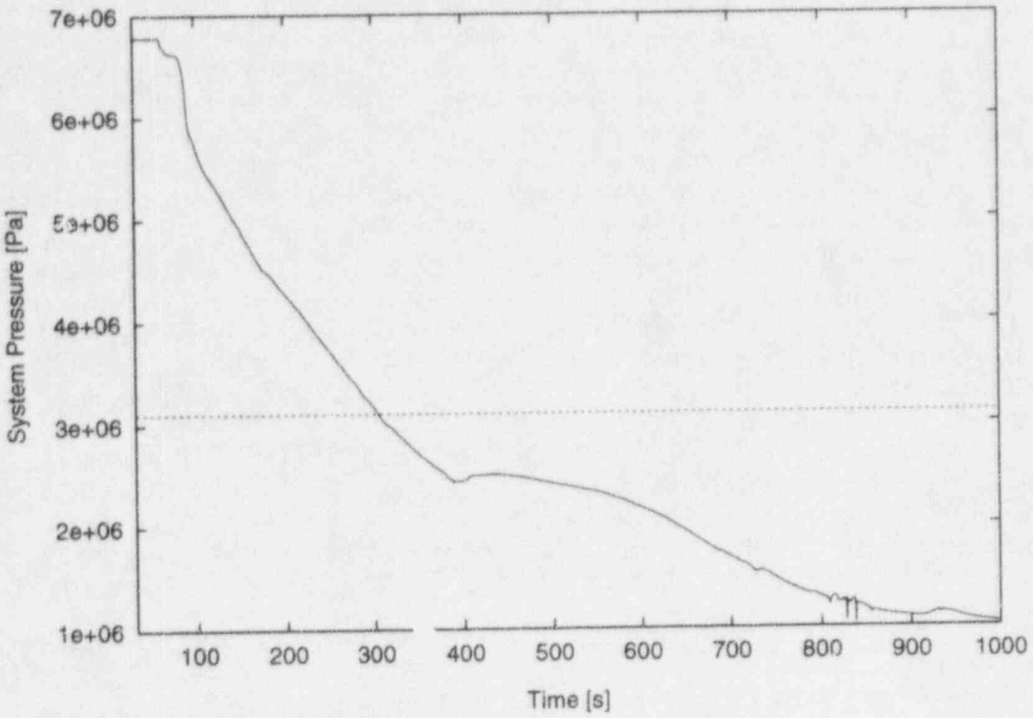

Figure 3 ADS Opening, system pressure.

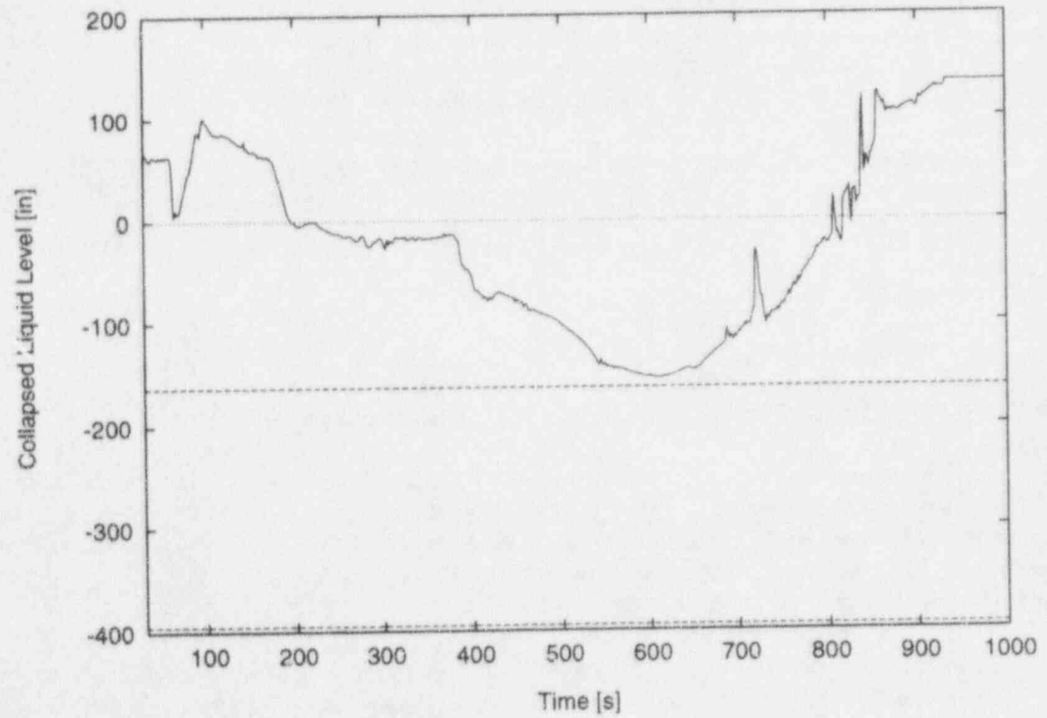

Figure 4 ADS Opening, collapsed liquid level.

inaccurate.

It was assumed, however, that the operator would respond according to normal operating procedures, and immediate actions required by plant Emergency Operating Procedures [8]. The operator is assumed to take those immediate actions as required by the reactor scram procedure [8]. For instance, a manual scram will be initiated when vessel pressure drops suddenly. The operator will trip the turbine, secure one motor-driven feedwater pump, and verify that the recirculation pumps remain running (n.b., this is true for the non-ATWS transients) [8]. It is also assumed that when 7 ADS valves inadvertently open, the operator will follow the procedures promptly. Current RPV control, flooding, and scram procedures [8] can handle this 7 ADS valve opening transient, and instruct the operator to shut MSIVs, and provide condensate and low pressure ECCS injection. Eventually, core makeup via feedwater/condensate flow would be assured because the operator would draw inventory from the condensate storage tank once the condenser hotwell is depleted.

Figures 3 and 4 show RPV pressure and collapsed liquid level, respectively for the best-estimate results for opening of all ADS valves transient. The best-estimate case assumes that: (a) the scram occurs at 60 seconds; (b) MSIV or TCV closure starts at 70 seconds and ends 90 seconds; (c) feedwater flow is reduced from full to 35% flow at 80 seconds, and the condenser inventory is depleted at 378 seconds; (d) LPCI is initiated at 2.24 MPa (325 psig) into the downcomer approximately at 600 seconds; and (e) no condensate is transferred from the storage tank. Figure 4 shows that the minimum collapsed liquid level occurs at ~600 seconds, but still remains above the TAF; however, the actual RPV two-phase mixture level would be higher than TAF. Some observations can be made as a result of the cases analyzed [9]. Note, however, that this study had a restricted scope, and as such, may not fully encompass all the possible parameters and issues associated with rapid ADS depressurization events. Several limited conclusions are drawn:

1. The reactor must be scrammed in order to have a significant reduction in system pressure down to 3.1 MPa (450 psig). If no scram occurs, the vessel pressure and level remain sufficiently high so that the noncondensable gases inside the level instrumentation are not released.

2. Condensate/feedwater flow rates and inventory depletion change not only vessel level history, but also pressure and LPCI timing response. For this BWR/6 model [7], when feedwater flow is maintained at least 35 % of nominal operating flow, the collapsed liquid level will remain above top of active fuel (TAF).

3. The operator will have sufficient information based on the containment response in terms of drywell, wetwell, and pool temperatures and pressures to determine that: (a) the ADS valves had inadvertently opened, (b) the water level instrumentation may be reading falsely high after the depressurization, and (c) LPCI should be initiated. Moreover, high drywell pressure setpoints should be reached in time to actuate LPCI cooling before the actual water level dropped to TAF.

It is necessary to emphasize that the case represented does not take any credit for the HPCS cooling, because it is assumed to be initially failed, or for some unknown reason never initiated. Therefore, the effect of a potential level indication error on HPCS, such as an early trip triggered by Level 8 signal, is eliminated.

Design Basis Large Break LOCA:

In the postulated design basis large-break loss of coolant accident, the ECCS signal on high drywell pressure would be immediately activated because the break discharges directly into the drywell. A best-estimate analysis of a DBA LBLOCA is performed by using thermal-hydraulic coupling between the pool, drywell, reactor building and RPV.

During the DBA LBLOCA event, LPCI and HPCS flow would provide adequate ECCS inventory if LPCI and HPCS were initiated promptly. LPCI is actuated on either a low-low water level (Level 1) signal or a high drywell pressure signal. HPCS is activated on low water level (Level 2) or high drywell pressure. If noncondensable gases become dissolved in the water level instrumentation piping, these gases would come out of solution and expand during the depressurization. If noncondensable gases cause the vessel level instrumentation to read inaccurately high, then LPCI actuation may be delayed. The activation of ECCS signals during this DBA LBLOCA is very quick, so that operator action is not usually credited in the FSAR analyses; however, operator response issues should be considered in this analysis to determine if the operator would have sufficient information to detect that the water level reading is erroneously high after the LOCA.

This DBA LBLOCA event assumes that a complete guillotine break occurs in the recirculation pump suction

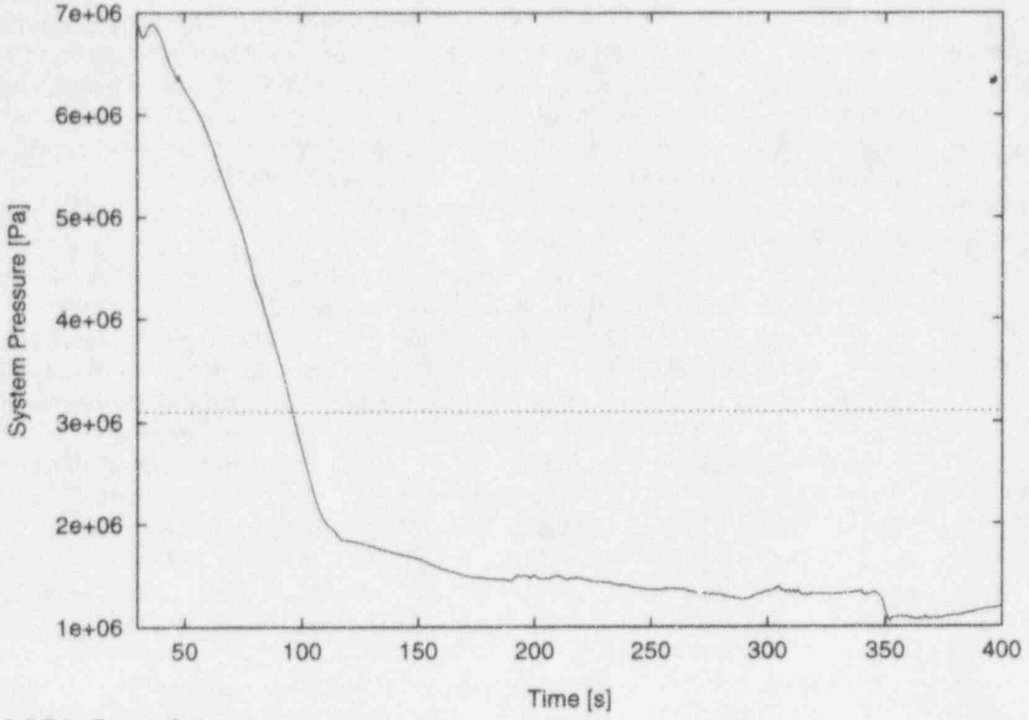

Figure 5 LOCA, Steam dome pressure.

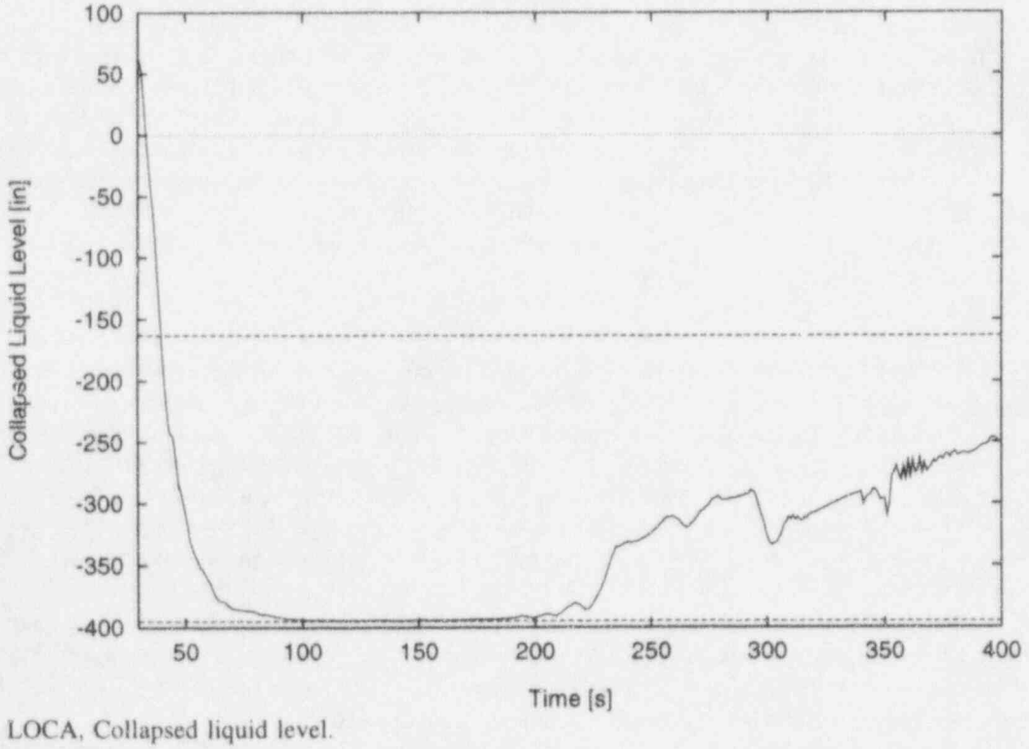

Figure 6 LOCA, Collapsed liquid level.

line. For this analysis, a 2.2 sqft break was used, and a total loss of offsite power was assumed, as per the DBA LBLOCA analysis given for the reference BWR 6, namely, River Bend [7]. In the analysis made for the DBA LBLOCA transient, the water level drops quickly below Top of Active Fuel (TAF), and below Bottom of Active Fuel (BAF), as predicted by the vendor's FSAR analysis [7]. The reactor automatically scrams almost immediately after the LBLOCA event starts. The recirculation pumps trips and the MSIV closure occurs very quickly. The loss of offsite power causes the feedwater pumps to trip. It should be noted that those BWR 6 plants with turbine driven feedwater pumps would also have a zero feedwater flow once the MSIVs are closed. The reference plant has only motor-driven feedwater pumps [7] so that the feedwater flow is lost after the loss of offsite power. The LPCI and HPCS systems are enabled at approximately 40 seconds when the diesel generators are energized, and would provide emergency cooling to the RPV.

For this DBA LBLOCA event, a double-ended guillotine break is assumed to occur in the recirculation pump suction line simultaneously with loss of offside power, as per the River Bend FSAR [7]. The reactor is assumed to scram at 0.5 seconds after the LOCA event occurs. The recirculation pumps are tripped at 2.0 seconds. The time between the isolation signal and the full closure of the main steam isolation valves is 4.0 seconds. The timing of the start of the MSIV closure was studied in the test matrix. The final best-estimate case has the MSIVs starting to close at 6 seconds and fully closed at 10 seconds, as given in FSAR Table 6.3-1 [7]. Feedwater flow is assumed to drop to zero within 10 seconds. HPCS and LPCI are enabled at approximately 40.0 seconds, when the diesel generators are ready at full power.

Figures 5 and 6 show RPV Pressure and Collapsed Water Level for this case. The following conclusions are drawn from the results [9]:

1. The reactor will scram automatically on a high drywell pressure signal. Containment isolation will occur quickly since the drywell pressure limit is reached quickly. No special operator actions are required for this DBA LBLOCA event.

2. The DBA LBLOCA yields a significant reduction in system pressure down to 3.1 MPa (450 psig) and even further.

3. The containment response in terms of pressure for the wetwell and drywell is fairly rapid and a large pressure increase occurs. The suppression pool temperature rises ~25 °C within a minute. The drywell temperature rises more sharply since the break discharges directly into it.

4. Since the recirculation line has broken below TAF, the RPV is essentially being drained quickly. The noncondensables would come out of solution and affect the water level later than the sudden level drop; hence, the early level readings will be adequate to indicate the rapid inventory loss, and activate ECCS.

During the reflood of the core, the coolant inventory of the vessel is replenished from ex-vessel sources. This coolant inventory was not under pressure comparable to system pressure prior to the accident, and has much lower temperature. Therefore, even the most conservative assumptions for the amount of the noncondensable gases dissolved in the reactor coolant are not applicable to ECCS inventory. This yields to the conclusion of no inaccuracy on the level will take place during the reflood, then no early trip of HPCS is expected.

Main Steam Line Break Accident:

For this MSLB event it is assumed that a complete guillotine break occurs in a single main steam line upstream of the MSIV, inside the drywell. This event was chosen because it would provide sufficient reactor pressure vessel (RPV) depressurization, coupled with containment (i.e., drywell, suppression pool, and reactor building) effects. It should be noted that this MSLB scenario is different from the MSLB case used in standard FSAR [7] documents. The FSAR MSLB Design Basis Accident (DBA) assumes that the break occurs downstream of the MSIVs, and outside the containment structures. With the FSAR MSLB DBA, the MSIVs would close quickly, and the RPV would not depressurize to the extent required by this analysis, namely, below 3.1 MPa (450 psig); therefore, a MSLB upstream of the MSIV was chosen.

In the postulated MSLB Accident, the ECCS signal on high drywell pressure would be immediately activated because the break discharges directly into the drywell. A best-estimate analysis of a MSLB event is performed by thermal-hydraulic coupling between the pool, drywell, reactor building and RPV because the mass flow rate through the steam line break depends on the containment backpressure.

During the MSLB event, LPCI and HPCS flow would provide adequate ECCS inventory if LPCI and HPCS

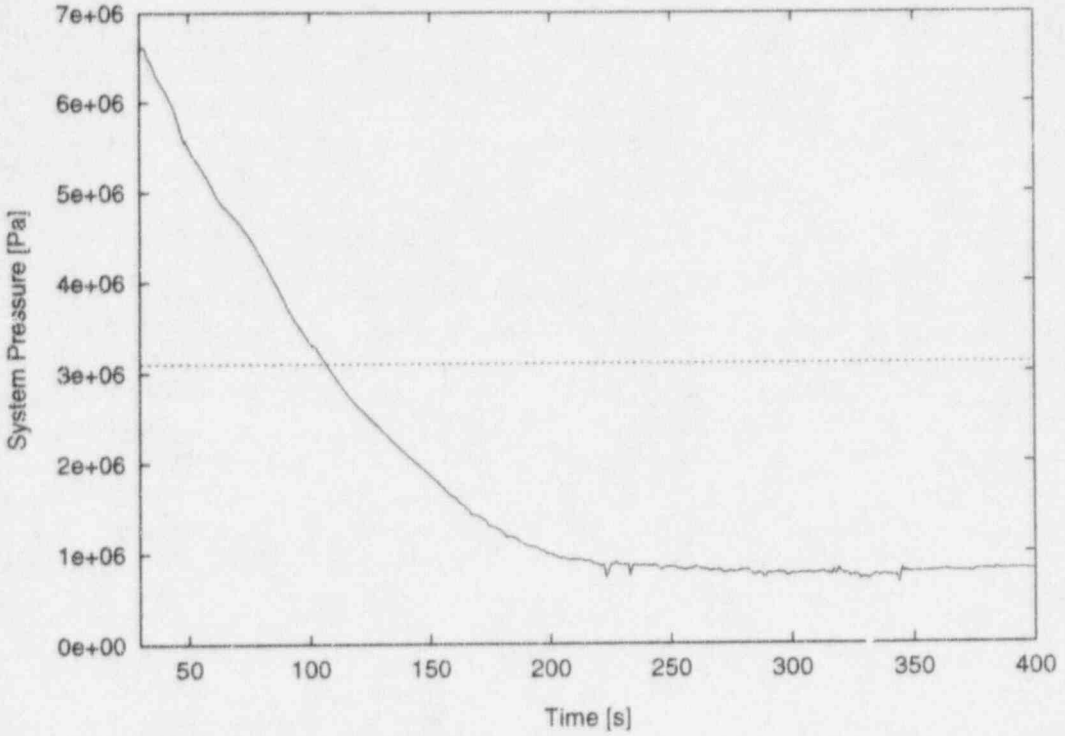

Figure 7 MSLB (Case III.9), Steam dome pressure.

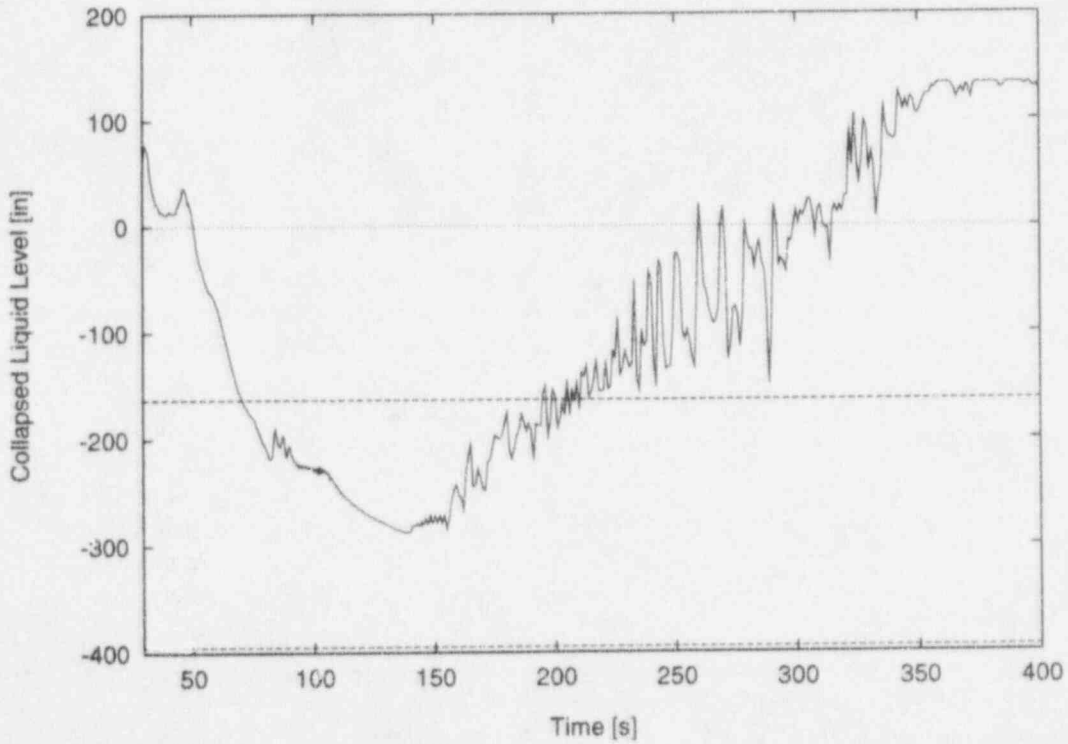

Figure 8 MSLB (Case III.9), Collapsed liquid level.

were initiated promptly. LPCI is actuated on either a low-low water level signal or a high drywell pressure signal. HPCS is activated on low water level or high drywell pressure. If noncondensable gases become dissolved in the water level instrumentation piping in high concentrations, these gases would come out of solution and expand during the depressurization. If noncondensable gases cause the vessel level instrumentation to read inaccurately high, then LPCI actuation may be delayed. The activation of ECCS signals during this MSLB accident is rapid, so that operator action will not be credited in these analyses; however, operator response issues should be considered in this analysis to determine if the operator would have sufficient information to detect that the water level reading is erroneously high.

This MSLB event assumes that a complete guillotine break occurs in a single main steam line upstream of the MSIV, inside the drywell. For this analysis, the break size considered is 2.536 sqft. The best-estimate coupled RELAP/CONTAIN results for the RPV pressures and collapsed liquid level is shown in the Figure 7 and 8. A 30-second RELAP5 null transient was used to assure that a true steady-state was obtained. At 30 seconds, the 2.536 sqft MSLB commences. The best-estimate case assumes that: (a) the scram occurs at 31.0 seconds, (b) MSIV or TCV closure starts at 30.5 seconds and ends at 34.5 seconds, (c) the feedwater flow is reduced from full to 35% flow from 40 to 60 seconds, (d) LPCI is initiated at 2.24 MPa (325 psig) into the downcomer approximately at 105 seconds, and (e) no condensate is transferred from the storage tank. During this MSLB, the collapsed liquid level drops quickly below Top of Active Fuel (TAF). The reactor automatically scrams almost immediately after the MSLB event starts. It should be noted that those BWR/6 plants with turbine driven feedwater pumps would also have a zero feedwater flow once the MSIVs are closed, but flow would be available from a single motor driven feedwater pump. The reference plant has only motor-driven feedwater pumps [7] so feedwater flow is available after the MSIVs close.

The following conclusions can be drawn from the results [9]:

1. The reactor will scram automatically on high drywell pressure signal. Containment isolation will occur quickly since the drywell pressure limit is reached quickly. No special operator actions are required for this MSLB event.

2. The MSLB yields a significant reduction in system pressure down to 3.1 MPa (450 psig) and even further.

3. The containment response in terms of pressure for the wetwell and drywell is fairly rapid and a large pressure increase occurs. The suppression pool temperature rises 15 °C within a minute. The drywell temperature rises more sharply since the break discharges directly into it.

4. Since the MSLB in effect drains the RPV quickly to liquid levels at TAF, prior to pressures reaching 3.1 MPa (450 psig). The noncondensables would come out of solution and affect the water level later than the sudden level drop; hence, the early level readings will be adequate to indicate the rapid inventory loss, and activate ECCS.

5. The operator should have sufficient information based on the containment response in terms of drywell, wetwell, and pool temperatures and pressures to determine that: (a) a MSLB has occurred, (b) the water level instrumentation may be reading falsely high after the depressurization, and (c) LPCI should be initiated. Moreover, high drywell pressure setpoints should be reached in time to actuate LPCI cooling before the actual water level dropped to TAF. Note that plant-specific Technical Specification limits are set lower than the limits used in FSAR analyses. Plant-specific setpoints and operating procedures would need to be considered to verify this conclusion for each BWR unit.

It is necessary to note that the best-estimate case, assumes that HPCS is initially failed or for some unknown reason never activated. Therefore, no credit for the HPCS cooling is taken.

CONCLUSIONS

The rapid depressurization events described demonstrate that there is sufficient RPV depressurization (i.e., less than 3.1 MPa) to potentially allow noncondensable gases to come out of solution and yield inaccurate level indications. Even if an erroneously high level is caused by noncondensables in the water level instrumentation, there are other system parameters and automatic actuation signals (e.g., low RPV pressure, high pool temperature, high drywell pressure), that provide additional information for the operator to verify that ECCS LPCI flow has been initiated, and to determine that the two-phase mixture level indicated by the reference leg piping is incorrect.

In the ADS opening case, 35% of nominal feedwater flow was sufficient to provide adequate core cooling

in terms of collapsed liquid level remaining above TAF. The opening of 7 ADS valves is roughly equivalent to BWR turbine bypass flow rate capability for most BWR/6 plants [7,8,10]. If a minimum of 35% of nominal feedwater flow can be maintained continuously without any depletion of condensate inventory after the 7 ADS valves open, then two-phase liquid level in the vessel will remain well above the TAF since the collapsed liquid level stays above TAF; however, this requires that the operator begin making up the condensate tank inventory from other sources very early in the transient. After the LOCA or MSLB, there is a sufficient system depressurization (i.e., less than 3.1 MPa) to potentially allow noncondensable gases to come out of solution and yield inaccurate level indications; however, the rapid inventory loss would cause a sudden level drop prior to reaching low pressures, so that initially accurate level indications will be available.

This research effort provides some insight into operator response and training needs involved with resolving current BWR water-level instrumentation issues. However, even if an erroneously high level is caused by noncondensables dissolved in the water level instrumentation, there are other system parameters (e.g., low RPV pressure, high pool temperature, high drywell pressure), that provide automatic signals and additional information for the operator to activate or verify that ECCS LPCI flow has been initiated, and to determine that the two-phase mixture level indicated by the reference leg piping is erroneous.

ACKNOWLEDGEMENTS

This research was performed under the auspices of the U.S. Nuclear Regulatory Commission under contract RS-NRR-93-027. The authors would like to thank Joseph Miller of the River Bend Station and the Clinton Nuclear Power Plant operating staff for their kind assistance for sharing plant-specific design and operational information for this study. Also Drs. Robinson and Baratta of The Pennsylvania State University deserve thanks for their technical contributions.

REFERENCES

1. Richard Zuercher, "Impact of Rapid Depressurization on BWR Level Devices Must Be Reported," Inside N.R.C., vol. 14, no. 17, August 24, 1992.

2. Richard Zuercher, "WNP-2 Report of 1-Hour, 30-Inch Error in Level Monitor is First," Nucleonics Week, vol. 34, no. 11, March 18, 1993.

3. V. H. Ransom, et al., RELAP5/MOD3 Code Manual Volume 1-5: (Draft), NUREG/CR-5535, EGG-2596, June 1990.

4. K.K. Murata, et al., User's Manual for CONTAIN 1.1, A Computer Code for Severe Nuclear Reactor Accident Containment Analysis, NUREG/CR-5026, SAND 87-2309, Rev. 4, September 1989.

5. Kevin Smith, "Multiprocessor Based Simulation of Degraded Core and Containment Responses," Ph.D. Thesis, The Pennsylvania State University (December 1992).

6. A. Beguelin, et al., "A User's Guide to PVM, Parallel Virtual Machine," ORNL/TM-11826, August 1991.

7. Gulf States Utilities, Updated Final Safety Analysis Report of the River Bend Station, Chapters 6, 7, and 15, August 1991.

8. Private communications with Clinton Nuclear Power Plant operating staff (June 1993).

9. A. K. Muftuoglu, "Coupled RELAP5/CONTAIN Analysis for Generic BWR/6 Rapid Depressurization Events", *M.S. Thesis, The Pennsylvania State University*, December 1994.

A THERMAL-HYDRAULIC CODE FOR TRANSIENT ANALYSIS IN A CHANNEL WITH A ROD BUNDLE

I.D.Khodjaev
Research & Engineering Centre of Nuclear Plants Safety,
Bezymyannaya 6, Electrogorsk, Moscow region, 142530 Russia
Fax: +7-096-43-3-05-15

ABSTRACT

The paper contains the model of transient vapor-liquid flow in a channel with a rod bundle of core of a nuclear power plant. The computer code has been developed to predict dryout and post-dryout heat transfer in rod bundles of nuclear reactor core under loss-of-coolant accidents. Economizer, bubble, dispersed-annular and dispersed regimes are taken into account. The computer code provides a three-field representation of two-phase flow in the dispersed-annular regime. Continuous vapor, continuous liquid film and entrained liquid drops are three fields. For the description of dispersed flow regime two-temperatures and single-velocity model is used. Relative droplet motion is taken into account for the droplet-to-vapor heat transfer. The conservation equations for each of regimes are solved using an effective numerical technique. This technique makes it possible to determine distribution of the parameters of flows along the perimeter of fuel elements. Comparison of the calculated results with the experimental data shows that the computer code adequately describes complex processes in a channel with a rod bundle during accident.

INTRODUCTION

An analysis of hydrodynamics and heat transfer crisis in channels with bundles of fuel rods is usually based on the homogeneous flows. This single-velocity approach makes it impossible to describe some essential features of dispersed annular flows because these features are significantly affected by the velocity difference between liquid film and the vapor-droplet core flow (this difference depends on the interphase friction force and on the film-core mass exchange). There are only a few studies which take into account the velocity difference between the liquid film and that of the core flow (Whalley [1], Thwigood, Kelly and Guildotti [2]; Nigmatulin et.al. [3]; Sakai and Sigawara [4]).

Usually subcooled fluid is transpoted to the inlet of the channel with a bundle of heated rods. Therefore, the initial section of the channel is characterized by the flow of subcooled liquid followed by bubbly flow which changes into a dispersed-annular flow. The subcooled liquid flow and the bubbly flow were described using single-velocity approximation (Nigmatulin et.al. [3]). In calculations, it was assumed that the bubbly flow in each cell was transformed into a dispersed-annular flow when the vapor volume concentration reached a critical value $\alpha_1^k \sim 0.6\text{-}0.8$. Moreover, the

velocity difference between liquid film and the vapor droplet core was taken into account in the dispersed-annular flow. We also assumed that the heat transfer crisis begins when the film thickness in one of the cells becomes less than $\delta^k = 60$ micron (Mikielewicz and Jerzy [5]). The following section of the channel is characterized by the vapor-droplet flow (dispersed regime). Based on this model, four basic flow regimes mentioned above were considered.

MATHEMATICAL MODEL OF THE DISPERSED-ANNULAR FLOW REGIME

We will consider a nonstationary dispersed-annular flow in a vertical channel with rods. Because the flow parameters are not uniform over the channel cross section, we subdivide the cross section into N cells (Fig.1). A liquid film flows over the rod surface in each cell, whereas a gaseous phase with droplets of the liquid moves in the interspace between the surface of the liquid film and the cell boundary. In peripheral cells the liquid film also moves over the unheated jacket surface. We assume that the mixture is at thermodynamic equilibrium and that the velocity of the vapor is equal to that of droplets. In this case, the basic equations of dispersed-annular flow regime are constructed with 8 equations, i.e., 3 - continuity, 3 - energy, and 2 - momentum. For example, the continuity equations for the three mixture components

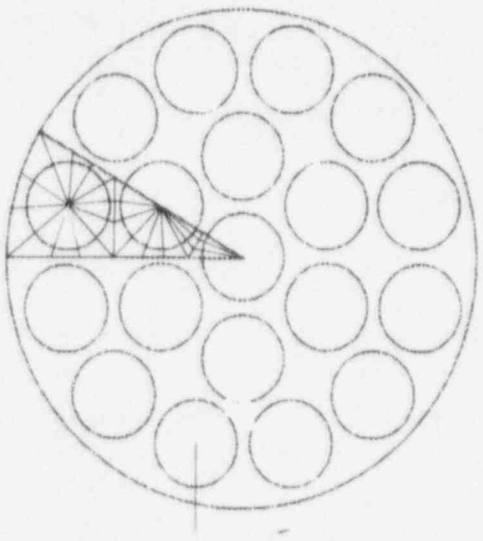

Fig. 1 Cross section of rod bundle

in each cell can be written as:

$$\frac{\partial\left(\rho_l^o \alpha_l^k\right)}{\partial t} + \frac{\partial\left(\rho_l^o \alpha_l^k v_l^k\right)}{\partial z} = \frac{1}{S^k} \sum_{l=1}^{N} J^{l,k} \left(\frac{\alpha_l^{*l} + \alpha_l^{*k}}{2} \right) \rho_l^o +$$

$$+\frac{1}{S^k}\sum_{l=1}^{N} K_t^{l,k}\rho_1^o\left(\alpha_1^{*l}-\alpha_1^{*k}\right)+j_{21}^k+j_{31}^k, \qquad (1)$$

$$\frac{\partial\left(\rho_2^o\alpha_2^k\right)}{\partial t}+\frac{\partial\left(\rho_2^o\alpha_2^k v_1^k\right)}{\partial z}=\frac{1}{S^k}\sum_{l=1}^{N} J^{l,k}\left(\frac{\alpha_2^{*l}+\alpha_2^{*k}}{2}\right)\rho_2^o+$$

$$+\frac{1}{S^k}\sum_{l=1}^{N} K_t^{l,k}\rho_2^o\left(\alpha_2^{*l}-\alpha_2^{*k}\right)+j_{32}^k-j_{23}^k-j_{21}^k$$

$$\frac{\partial\left(\rho_2^o\alpha_3^k\right)}{\partial t}+\frac{\partial\left(\rho_2^o\alpha_3^k v_3^k\right)}{\partial z}=j_{23}^k-j_{31}^k-j_{32}^k,$$

where $\alpha_2^{*k}=\alpha_1^k/\left(\alpha_1^k+\alpha_2^k\right)$ and $\alpha_1^{*k}=\alpha_1^k/\left(\alpha_1^k+\alpha_2^k\right)$ are the volumetric concentrations of droplets and vapor in the vapor-droplet flow core, respectively.

The left-hand side of the first equation in set (1) accounts for the uniform convective vapor flow between adjacent cells, and the second term on the right-hand side of the equations takes into account the turbulent mixing between these cells. Sirnilar terms appear in the second equation. In the third equation, the interchange of liquid between adjacent cells along the rod perimeter is neglected.

The inherent time of the process delelopment t_*=0.1-1 second. The distributions of volumetric concentrations of the mixture species are transferred along the channel length $L\approx 1$ m with velocities v_1~10 m/s and v_3, $(v_1 > v_3)$. The disturbances of both velocity and pressure introduced into flow propagate with the speed of sound $C > C_e$, where C_e is an equilibrium speed of sound in vapor-drop core of the flow. If $v_1 << C_e$, $t_* >> L / v_j$, the distributions of both velocity and pressure are of a quasi-stationary nature

$$\frac{\partial v_j}{\partial t}\sim\frac{v_j}{t_*}<<v_j\frac{\partial v_j}{\partial z}, \qquad \frac{\partial p}{\partial t}\sim\frac{\Delta p}{t_*}<<v_j\frac{\partial p}{\partial z}$$

Supposition of a quasi-stationary distribution of velocities and pressure of the mixture speciese means that the time-dependent variation of these parameters is determined by nonstationarity of boundary conditions for both flow rates and concentrations of the mixture species. With a smoother variation or pressure, flow rates, and heat fluxes with an inherent time of 0.1s and more, the outlined assumption holds qood (Nigmatulin et.al. [3]).

Equations (1) include unknown convective flow rates $J^{l,k}$ of the vapor-droplet mixture between adjacent cells. These flows are determined in such a way that the

pressure over the channel cross section is constant, and the sum of convective rates of the vapor-droplet mixture through any closed contour is equal to zero (Nigmatulin eta al [3]).

The film and droplet evaporation rates J_{31}^k, J_{21}^k are determined by the equations of heat fluxes to the surface of the film and droplets.

In order to estimate the rate of interphase interactions inside the cells (the entrainment intensity j_{32}^k, drop deposition intensity j_{23}^k, the turbulent transfer of the vapor-droplet mixture between adjacent cells $K_t^{l,k}$, and the interphase friction force in momentum equetions) the relationships in Nigmatulin et al. [3] were used.

The described model was successfully applied in [3] but the authors used a very coarse calculated grid; for each fuel rod, there was only one cell.

MATHEMATICAL MODEL OF THE DISPERSED FLOW REGIME

A liquid film may vaporize, and dispersed-annular regime transforms into a purely dispersed regime - flow of a mixture of vapor and drops. The heat exchange in this regime is characterized by significantly lower heat transfer coefficients than in the pre-crisis area, which may result in significant overheating of the heating surfaces compared to saturation temperatures.

Equations for a dispersed flow are derived from a similar system written for a dispersed-annular flow, if the liquid-film equations are dropped, and the appropriated terms are omitted in equations for vapor and drops. In addition must be taken into consideration: the relative velocity of vapor and drops is small, i.e., it is much smaller than the velocity of vapor (drops) $\left(\left|v_1^k - v_2^k\right| << v_1^k\right)$; therefore, slip is taken into account only when determining the heat flux from vapor to the drop surface, where even a slight slip may be significant (Nigmatulin R.I. [6]). Slip is determined without any account of drops inertia which is small compared to friction force. The vapor-drop flow may be thermodynamically nonequilibrium $\left(T_1^k \neq T_2\right)$ to a significant extent-vapor is overheated relative to the saturation temperature, and liquid in drops is on the saturation line $\left(T_2 = T_s(p)\right)$ and also $\rho_1^k \neq \rho_1^l$.

The following govering equations and corelations are used in the dispersed flow regime.

1. The continuity equations for the vapor and droplet components.
2. Momentum equations for the vapor-droplet mixture and for the droplets phase.
3. The internal energy equations for the vapor and droplets.
4. The equation of droplet size.
5. The equation of heat balance on interfacial surface.
6. The thermal conduction equations for the wall temperature.
7. Shear stress between wall and vapor.

8. Vapor-droplet interfacial drag.

9. Convective heat transfer between wall and vapor and between wall and droplets.

10. Vapor-droplet interfacial heat transfer.

It is assumed that the velocity and pressure distributions can be considered as quasi-stationary.

The above model of vapor-droplet flow with constitutive laws was successfully applied for vapor-droplet mixture in tube (Kroshilin and Khodjaev [7]). Here under conditions of a vapor-drop flow in the heated channel was shown that droplets taking heat when colliding with a heated surface make an essential contribution to heat removal from heated surface to the flow.

BOUNDARY AND INITIAL CONDITIONS

In order to solve the system of equations both boundary and initial conditions must be predetermined. The initial conditions define the liquid temperature distribution over a segment of flow of subcooled liquid, the volumetric concentration of vapor over the segment of bubbly regime of flow, and also, the volumes of liquid film and drops over the segment of a dispersed-annular regime of flow and the volumes of vapor over the segment of a dispersed regime of flow. These initial distributions are determined from a solution of a related stationary problem.

The boundary conditions required for both stationary and nonstationary problems define the velocity v_0^k, temperature T_0^k of a subcooled, and pressure p_0 at the channel inlet. The liquid velocity at the inlet to the segment with a bubbly regime of flow ($z = z_b$) equals its velocity at the channel inlet. The volumetric concentration of vapor at the inlet to the segment of bubbly regime of boiling is said to equal zero. Boundary conditions at the inlet to the segment with a dispersed-annular regime of flow follow from the conservation flow rate of vapor and liquid using parameters at a fixed exit of the bubbly regime of flow. The boundary conditions for the equations of dispersed regime of flow are prescribed in the section, which is taken as the beginning of a post-crisis area due to film drying-out .

RESULTS

Using described above dispersed - annular model, an analysis was made of experiments on the distribution of liquid film thickness along the rod perimeter under adiabatic conditions [8]. In [8] presented are results of liquid flowrate experimental study in the films along wetted perimeter of rods and channel body with a bundle of seven rods in conditions of hydrodinamic equlibrium of water-air dispersed-annular flow under pressure 0.3 MPa as well as in the vicinity of two type spacer grids. The study was conducted in a vertical channel with a bundle of seven rods - central rod of 15 mm inside diameter, and peripheral rods of 13.5 mm inside diameter installed with a pich of 16 mm. Channel diameter was 48 mm. The mixture samplings were carried out through completely or partially perforated walls of the body or of the rod. Water was fed to the working area by spraying to the flow core through 250 holes of 1 mm diameter, uniformly installed along channel flow area.

By this way of liquid feeding the flow hydrodynamic equilibrium was formed at least, at the distance of 0.85 mm from the chanel inlet. The main measurements were made at distanse of 1.5 m from the channel inlet. In Ref [8] give more detailed description of the construction of the working area , water air test facility and measure technique.

Test were conducted under pressure p=0.3 MPa , in change ranges of G=55÷ 2000 kg/(m^2 s) and vapor quality x=0.03 - 0.8. Water temperature was 20±2° C, air temperature was 20±3° C.

Figure 2 demonstrates satisfactory agreement between the experimental data and the calculated results. Figure 2 also shows that the relative liquid film flowrate along the rod perimeter has three local minim which correspond to narrow gates.

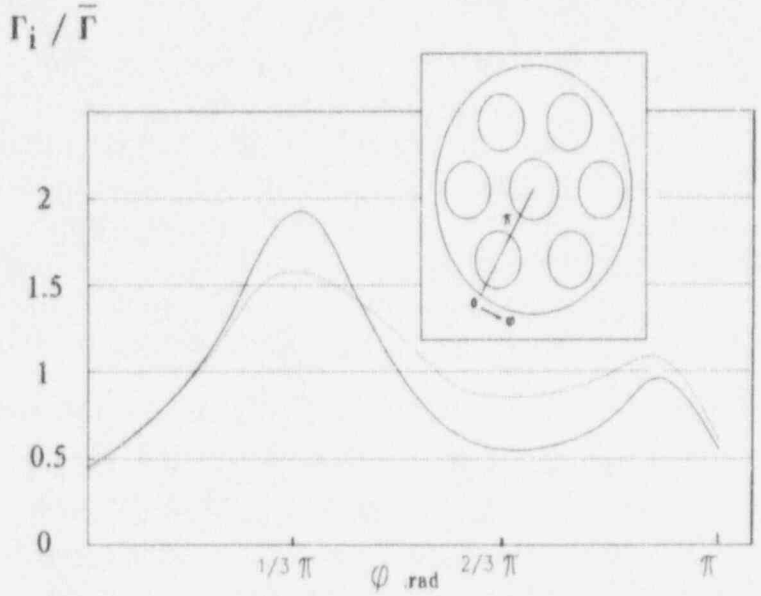

Fig. 2. Experimental (dotted lines) and predicted (solid lines) distributions of $\Gamma_i / \bar{\Gamma}$ (the ratio of the relative liquid film flowrate Γ_i ($\Gamma_i = m_{fi}/P_{wi}$) to the average relative liquid film flowrate $\bar{\Gamma}$) along the perimeter of anouter rod under the following stationary conditions: p=0.3 bar, the mass flow rate of the liquid G=500 kg/(m^2 s), quality x=0.5

Using the above dispersed-annular model, also, all experimental data on critical heat fluxes and pressure drops obtained in a full-scale model of the channel with a fuel rod bundle for an RBMK-1000 reactor for different profiles of heat release along the assembly length were analyzed (Osmachkin [9]). The predicted mean-square error for the critical heat flux Q is 9 %, whereas the error in using the correlations recommended in (Osmachkin [9]) is 28 %. Numerical calculations using the proposed method make it possible to locate the initiation of the heat transfer crisis along the rod perimeter. Notice that, according to the data for most of our experiments, the heat transfer crisis begins in the fuel element region close to the unheated jacked, which is in accordance with experimental data (Osmachkin [9],

Stolyarov et al. [10]) obtained at a full-scale model of the channel with a fuel rod bundle for an RBMK-1000 reactor. This result did not obtain by other investigators since available techniques and computer cods make it impossible to locate the initiation of the heat transfer crisis along the rod perimeter as these numerical procedures used a very coarse mesh of cells.

Unfortunately we have no complete experimental data of cladding temperature behavior of the channel with a fuel rod bundle for Boiling Water Reactor. In work by Stolyarov et al. [10]) the results of an experimental post dryout heat transfer with reference to fuel assemblies of boiling water cooled reactors are presented. The data were obtained at electrical heated 18-rod bundle (central rod is unheated, fig. 3) models with different types of grid spacers within the range of following parameters p=7.5 MPa, G=600-2000 kg/(m^2 s), q=0.2-1.1 MW/m^2 , and x=0.2-0.9. The cross section of this rod bundle represent RBMK-1000 reactor nature cross section with length 1100 mm. For the measuring cladding temperaure are using chrome's thermocouples. Starting conditions of the experiment are realizing at the constant of pessure at outlet and at the given flowrate and enthalpy at the inlet of the channnel. In test electrical power is gave to the bundle and increase slowly. In this work the cladding temperature in local section, where the beginning of a post-crisis was measured. Figure 4 demonstrates experimental and predicted distributions of cladding temperature along the perimeter of an outer rod at the outlet of assembly under the following stationary conditions: P=7.5 MPa, G=1500 kg/(m2 s), q=1.1 MW/m2, x=0.3. Figure 4 .shows that the heat transfer crisis begins in the fuel element region near the unheated jacket, where the cladding temperature is increased.

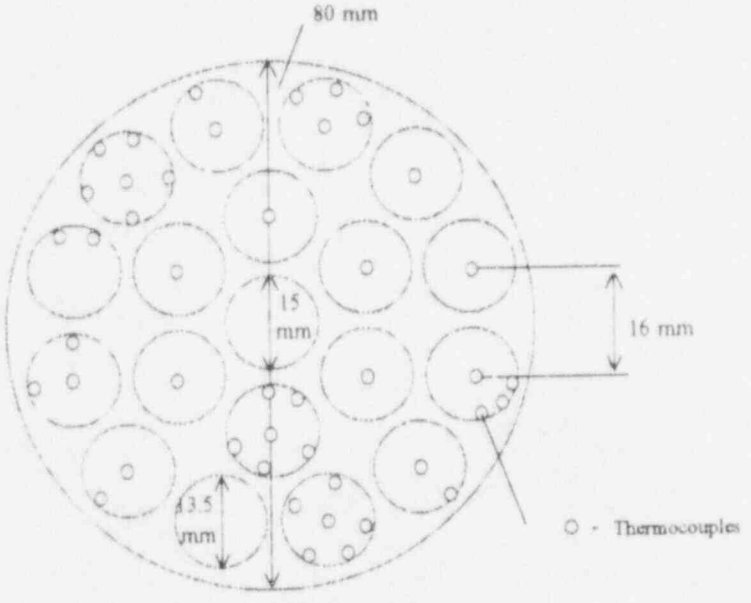

Fig. 3 Cross section of rod bundle of RBMK-1000 reactor;

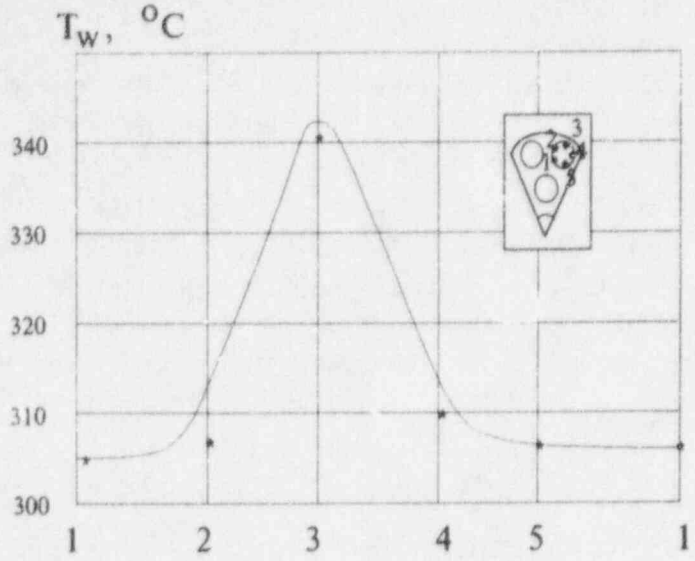

Fig. 4 Experimental (*) and predicted (solid lines) distributions of cladding temperature along the perimeter of rods at the section of a standart assembly, where begins the heat transfer crisis

The peculiarities of the vapor-liquid flow in a channel with a fuel rod bundle for an RBMK-1000 under stationary and nonstationary accident conditions, when simultaneously available all above discussed regimes of flow were studied using the numerical simulation.

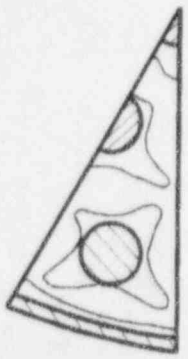

δ= 500 mkm

Fig. 5

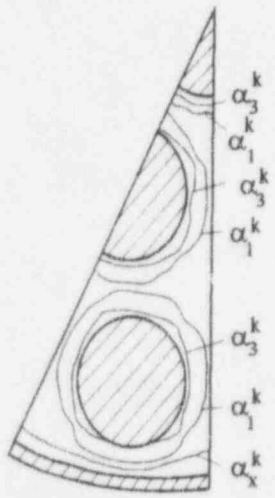

α=1

Fig. 6

Distribution of the film thickness (Fig. 4) and vapor, film concentrations (Fig. 5) along the perimeter of rods and outer jacket at the section of a standart assembly, where begins the heattransfer crisis.

Figures 5, 6 and 7 shows distribution of film thickness δ^k, the volume concentration of vapor α_1^k and film α_3^k, velocity of vapor v_1^k and film v_3^k along the perimeter of rods and the outer jacket at the section,were the heat transfer crisis begins under following stationary conditions, p=67 bar, inlet under heating ΔT=293 K, the mass flow rate of the liquid G=1500 kg/(m2 s), external heat released Q=3.5 MW (Dollezhal [11]). Figure 5 shows that in the region near the unheated jacket heat transfer crisis begins due to film drying out. The local minim of the film thickness correspond to the local minimum of the gap width (In RBMK-1000 reactor the minimum distanse between outer rod and the unheated outer wall is 2 mm). It is shown that minim volume concentrations α_1^k and α_3^k and minimum velocities v_1^k and v_3^k correspond to narrow gaps. The local maximum of the liquid film and vapor velocities correspond to those of the gap width. It is interesting that in cells, which correspond to narrow gaps of region near the unheated jacket, where heat transfer crisis begins there are more amount of drops than in other cells. This phenomenon is due to an additional removal of droplets from the outer jacket. Figure 8 demonstrates distributions α_1^k, α_3^k, v_1^k and v_3^k along the length of a rod at the location of the heat transfer crisis under the above conditions (Fig. 7). All regimes of flow are presented here. Bends in the curve showing variations of vapor volume concentration and velocity correspond to the transition from bubble flow to a dispersed-annular flow and from a

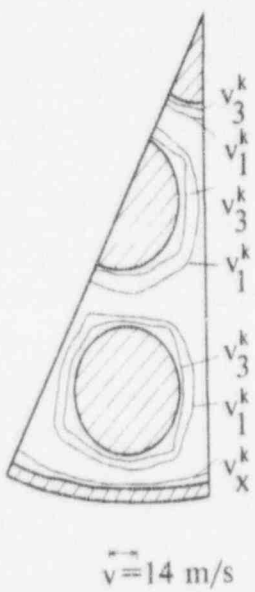

Fig. 7 Distribution of the vapor and film velocities along along the perimeter of rods and the outer jacked at the section of a standart assembly, where begins the heat transfer crisis

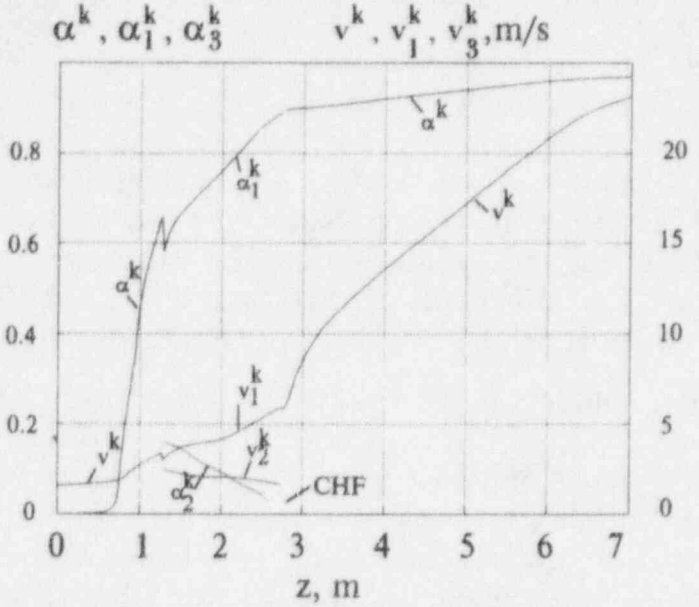

Fig. 8 Distribution of flow parameters along the length of a rod at the location of the heat transfer crisis.

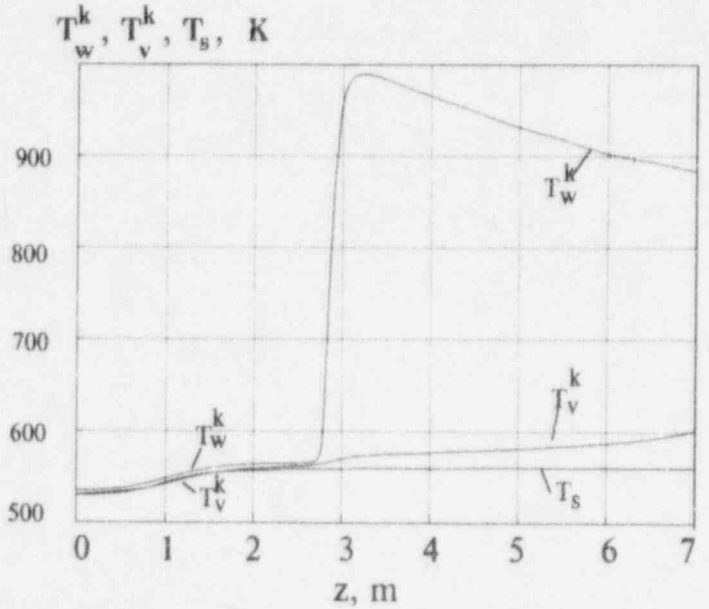

Fig. 9 Distribution of claddinng temperature T_w^k and flow temperature T_v^k along the length of a rod at the location of the heat transfer crisis

dispersed-annular flow to dispersed flow, and are in accordance with the hypothesis of an instantaneous transition from the bubble flow regime to a dispersed annular flow and from a dispersed-annular flow regime to a dispersed flow regime. Figure 9 shows distributions of cladding temperature T_w^k and vapor-droplet mixture temperature T_v^k along the length of a rod at the location of the heat transfer crisis under above conditions (Fig. 8).

According to Figures 8 and 9 a conclusion may be made that distributions of flow parameters along the length of rod bundle are analogously to distributions of flow parameters along the length of a round tube. Figure 10 shows a distribution of vapor-droplet mixture velocity along the perimeter of rods and outer jacket at the outlet of a standard assembly under the above conditions(Fig. 9). Figure 10 shows that the largest velocity achieved in the maximum gap width, and smallest velocity in the minimum gap width. The calculations also shows that at the outlet of a rod bundle under above conditions (Fig. 5 - Fig. 10) are 90 % vaporand 10 % droplets. Figure 11 shows distributions of cladding temperature T_w^k and dispersed flow temperature T_v^k along the perimeter of rods at the outlet of a rod bundle.

The calculations showed that in the nonstationary case, the heat transfer crisis occurred not on a rod of the outer row (as it does under stationary conditions), but on a rod of the second row in a region where the gap width was small. This is because of a decrease in the mixture flow rate over time, resulting in a sharp reduction in the intensity of dynamic entrainment. In this case, the crisis occurs primarily in regions where the intensity of evaporation is higher, i.e., in regions with a smaller gap width. Figures 12 and 13 shows distribution of flow parameters α_1^k, α_2^k, v_1^k, v_2^k (Fig.12) and δ^k, T_w^k, T_v^k (Fig.13) over timenear a rod of the second row (at the small gap width, where begins crisis) at the outlet of a standard assembly under the following nonstationary conditions: p=70 bar, ΔT=293 K , G=2800 kg/(m2 s) and Q=2 MW (the heat flux along the channel is constant); $t > 0$, the liquid flow rate at the channel inlet is reduced to zero over a period of

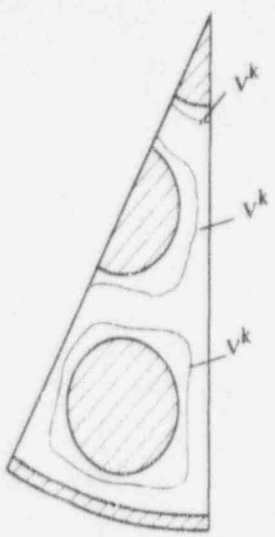

Fig. 10

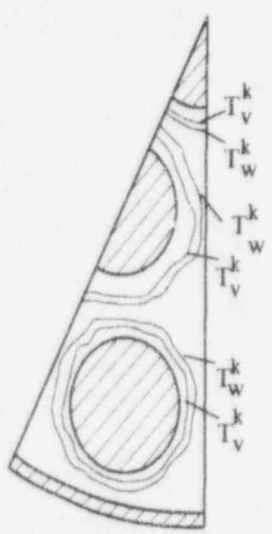

Fig. 11

Distribution of vapor-droplet mixture velocity (Fig. 10) and cladding temperature T_w^k, flow temperature T_v^k (Fig. 11) along the perimeter of rods at the outlet of a rod bundle

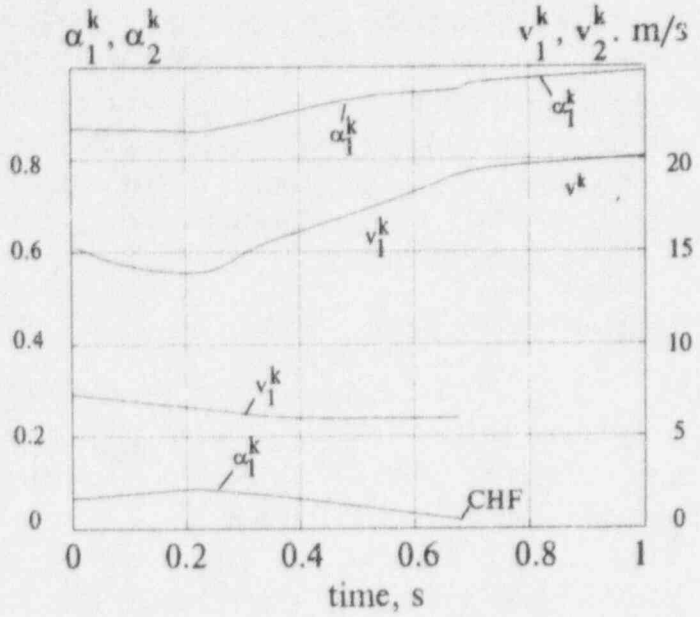

Fig. 12 Distribution of flow parameters over time at the location of the heat transfer crisis (at the axial directions at the outlet of a rod bundle).

0.1 s. Rise in liquid film thickness at early period of time (Fig.13) is because of a decrease in the droplet extrainment rate resulting from the reduction of the liquid flow rate at the channel inlet.This mechanism was previously described in (Nigmatulin et [12]) for the flow in a circular tube.

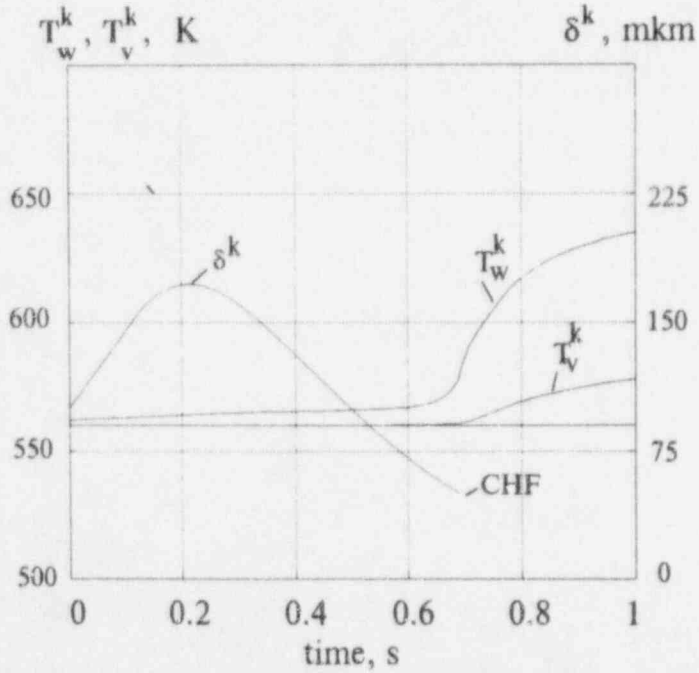

Fig. 13 Distribution of flow parameters over time at the location of the heat transfer crisis (at the axial directions at the outlet of a rod bundle).

CONCLUSIONS

Model of transient vapor-liquid flow in a channel with a rod bundle taking into account distributions of flow parameters along rod perimeters has been developed.

A comparison between the experimental data and the calculated results for vapor-liquid flows in a channel with rod bundles of different geometries shows that the proposed model is quite realistic for evaluating hydrodynamic parameters of such flows.

NOMENCLATURE

m	the flowrate, kg/s
p	the pressure in the mixture, Pa
P	the wetted perimeter, m
q	the heat flux, MW/m^2
S	area, m^2
t	the time, cek
v	the velocity, m/s
z	the coordinate along the channel axis, m
α	the volume concentration
Δp	the pressure gradient, Pa
δ	the film thickness, mkm
ρ	the density, kg/m^3

Subscripts

f	film
i	cell
j	number of phase (j=1, 2, 3)
s	saturation
v	vapor
w	wall
x	unheated jacket
1	vapor
2	droplet
3	liquid film

Superscripts

k, l	cells
o	microscopic

REFERENCES

[1] P.B.Whalley., "The calculation of dry out in rod bundle," Int.J.Multiphase flow ,.3, 25-31 (1977).

[2] M.J.Thurgood, J.M.Kelly and T.E.Guildotti, "COBRA/TRAC-A Thermal-Hydraulics Code for Transient Analysis of Nuclear Reactor Vessels and Primary Coolnt Systems " Richland, Washington, (1983).
[3] B.I.Nigmatulin, and A.E.Kroshilin, "Hydrodynamics of gaseous-liquid dispersed-annular flows in a rod bundle," J.Prikl. Mekh. Tekh. Fiz., 4 , 33-44 (1981).
[4] T.Sakai, S.Sugowarw, "Application of Tree-Fluid Code FIDAS to Dryout Prediction for Rod Bundles," Proc. Int.Conf. on Multiphase Flows "91-TSUKUBA, 1, 57-60 (1991)
[5] J. Mikielewicz and K.Jerzy, "Breakdown and evoporation ofthin shear driven liquid films," ICHMT, Summer seminar, Heat Transfer (1980).
[6] R.I.Nigmatulin, Dynamics of Multiphase Media, Moscow (1987.)
[7] V.E.Kroshilin and Ya.DKhodzhaev, "Nonstationary flow of a vapour-droplet flows in a heated channel," J. of Engineering physics and Thermophysics, 61, 939-945 (1991).
[8] B.I.Nigmatulin and S.D.Krushenok, "Study of Hydrodynamic Characteristics of gaseous-Liquid Disperse-Annular Flow in the Channel Containing a Bundle of Fuel Rods,"Proc. 4th Int. Top. Meet. on Nucl. Reac. Ther.-Hydraul., 1, 534-539 (1989).
[9] V.S.Osmachkin, "Investigation of ThermoHydraulics Characteristic of models of fuel bundle,"Proc. COMECON Seminar on Thermal Physics, IAE, Moscow, 49-55 (1974).
[10] E.V.Stolyarov, A.I.Yemelyanov, S.Yu.Savvin, and T.Yugay, "Post-dryout heat transfer in rod bundles," Proc. Int. Symposium "Thermophysics-90", Obninsk,.2, 353-362 (1991).
[11] N.A.Dollezhal and I.Ya Emelyanov, Channel Nuclear Power Reactor, Moscow, (1970)
[12] B.I.Nigmatulin, L.A.Klebanov and A.E.Kroshilin, "Heat Transfer Crisis at the dispersed-annular flows under Nonstationary Conditions," J.High Temperature, .18, 1242-1251 (1980).

ANALYSIS OF AN AP600 INTERMEDIATE-SIZE LOSS-OF-COOLANT ACCIDENT*

B. E. Boyack and J. F. Lime
Los Alamos National Laboratory
Los Alamos, New Mexico 87545

ABSTRACT

A postulated double-ended guillotine break of an AP600 direct-vessel-injection line has been analyzed. This event is characterized as an intermediate-break loss-of-coolant accident. Most of the insights regarding the response of the AP600 safety systems to the postulated accident are derived from calculations performed with the TRAC-PF1/MOD2 code. However, complementary insights derived from a scaled experiment conducted in the ROSA facility, as well as insights based upon calculations by other codes, are also presented. Based upon the calculated and experimental results, the AP600 will not experience a core heat up and will reach a safe shutdown state using only safety-class equipment. Only the early part of the long-term cooling period initiated by In-containment Refueling Water Storage Tank injection was evaluated. Thus, the observation that the core is continuously cooled should be verified for the later phase of the long-term cooling period when sump injection and containment cooling processes are important.

INTRODUCTION

The AP600 is an advanced passive 600 MWe reactor design being developed by Westinghouse in conjunction with the US Department of Energy's Advanced Light Water Reactor Technology Program. The AP600 has been submitted to the United States Nuclear Regulatory Commission (NRC) for design certification. In accordance with the design certification requirements of 10CFR52.47, advanced reactor applicants are required to submit neutronic and thermal-hydraulic safety analyses over a sufficient range of normal operation, transient conditions, and specified accident sequences. Review and confirmation of these analyses constitute an important activity in the NRC's AP600 design certification effort. In support of its design certification activities, the NRC performs audit calculations using best-estimate thermal-hydraulic codes. The NRC uses the TRAC code for analyzing AP600 large-break loss-of-coolant accidents (LBLOCAs). In addition, TRAC is being used to evaluate the AP600's response to an intermediate-break LOCA (IBLOCA). In this paper, the response of the AP600 to an IBLOCA event, a double-ended guillotine break (DEGB) of a direct-vessel-injection (DVI) line, is analyzed. The TRAC DVI-line IBLOCA is a direct counterpart to the Westinghouse calculation of an AP600 DVI-line IBLOCA.[1]

*This work was funded by the US Nuclear Regulatory Commission's Office of Nuclear Regulatory Research.

The AP600 is a two-loop design with one hot leg, one steam generator, two reactor coolant pumps (RCP), and two cold legs in each loop (Fig. 1). A pressurizer is attached to one of the hot legs. The reactor coolant pumps, a canned-motor design, are integrated into the outlet plena of the steam generators. The loop seal is eliminated with this design. The core is designed for a low power density. The design incorporates passive safety systems (Fig. 2) that rely only on redundant/fail-safe valving, gravity, natural circulation, and compressed gas. Two Passive Safety Injection System (PSIS) trains connect directly to the reactor-vessel downcomer through DVI lines. Attached to each DVI line are an accumulator (ACC), a Core Makeup Tank (CMT), and lines to large, safety-class water pools residing in the In-containment Refueling Water Storage Tank (IRWST) and sump.

Depressurization of the primary system is an essential process that is required to ensure long-term cooling of the AP600. The accumulators inject coolant into the reactor coolant system (RCS) only after the primary pressure has decreased to 4.83 MPa (700 psia). Coolant injection from the IRWST and sump can occur only after the reactor coolant system pressure decreases enough that the gravitational head of each pool is sufficient to force coolant into the DVI line. An Automatic Depressurization System (ADS) ensures the needed RCS pressure reduction. The ADS has four redundant stages. The first three stages connect the top of the pressurizer and the IRWST. The fourth stage connects the top of each hot leg and the containment. A direct discharge path to the containment is needed to ensure that the RCS pressure will equilibrate with the containment pressure so that the head-driven IRWST and sump injection can proceed.

The AP600 containment plays an essential role in the long-term cooling of the primary. Steam entering the containment, through either a break in the RCS or ADS operation, condenses on the inside of the steel containment shell. The condensate drains downward and a large fraction is delivered via gutters to either the IRWST or the sump. Heat transfer on the outside of the containment steel shell is by evaporation of liquid sprayed near the top of the steel reactor containment dome, and by convection to an air stream induced by buoyancy-driven flow.

For non-LOCA accidents, long-term heat removal is provided as the Passive Residual Heat Removal System (PRHRS), which removes core heat through buoyancy-induced circulation. Isolation valves on the PRHRS lines open upon receipt of the safeguards (S) signal and a buoyancy-induced flow transports primary coolant through the PRHRS. The PRHRS is ineffective for LBLOCAs, has a limited interval of effectiveness for IBLOCAs, and has an extended period of effectiveness for SBLOCAs.

TRAC CODE DESCRIPTION

The TRAC-PF1/MOD2 code,[2] Version 5.4, was used for this calculation. The TRAC code series was developed at Los Alamos to provide advanced, best-estimate predictions for postulated accidents in pressurized-water reactors. The code incorporates four-component (liquid water, water vapor, liquid solute, and noncondensible gas), two-fluid (liquid and gas), and nonequilibrium modeling of thermal-hydraulic behavior. TRAC features flow-regime-dependent constitutive equations, component modularity, multidimensional fluid dynamics, generalized heat structure modeling, and a complete control systems modeling capability. The code also features a three-dimensional (3D), stability-enhancing, two-step method, which removes the Courant time-step limit within the vessel solution. Throughout

the years of its development, the TRAC code has been assessed using data from a variety of experimental facilities and applied to a number of pressurized light reactor systems.

Code adequacy must be addressed when first applying a computer code to a new reactor type, e.g., AP600. One such approach is to (1) identify representative AP600 transient and accidents sequences; (2) identify the key systems, components, processes, and phenomena associated with the sequences; (3) conduct a bottom-up review of the individual code models and correlations; (4) conduct a top-down review of the total or integrated code performance relative to the needs assessed in steps 1 and 2; and (5) correct significant identified deficiencies. The bottom-up review determines the technical adequacy of each model by considering its pedigree, applicability, and fidelity to separate-effects or component data. The top-down review determines the technical adequacy of the integrated code by considering code applicability and fidelity to integral test facility data. A review of the TRAC-PF1/MOD2 code, such as that just described, is planned to assess code adequacy for the AP600 LBLOCA application. For the IBLOCA application, using TRAC to support confirmatory analyses will depend, in part, upon the significance of multi-dimensional phenomena during the transient. At present, the role of TRAC is complementary to other NRC analysis tools. Thus, the determination of adequacy for the IBLOCA application will largely rest on the similarity of processes and phenomena occurring in the AP600 during LBLOCA and IBLOCA events.

TRAC MODEL DESCRIPTION

The TRAC model of the AP600 is a finely-noded, multidimensional model of 184 hydrodynamic components [three vessel components and 181 one-dimensional (1D) components] encompassing 1,136 3D and 990 1D computational fluid cells, and 55 heat-structure components. The plant model has undergone an independent quality-assurance check. The TRAC AP600 plant model reflects the AP600 design information available on November 15, 1994.

A DEGB of DVI-line A (DVI-A) at the nozzle connecting DVI-A to the reactor vessel is assumed (Fig. 2). The vessel-side break area is constricted by a nozzle. The DVI-line side of the break is the pipe cross-sectional area. The nozzle orifice area is 5.1% of the total ADS discharge area. The DVI break disables one-half of the PSIS capacity of the AP600. A constant containment pressure of 0.31 MPa (45 psia) is assumed.

IBLOCA ANALYSIS—TRAC RESULTS

The key processes occurring in an AP600 during a postulated DVI-line IBLOCA are primary coolant system depressurization, inventory depletion, inventory replacement via emergency core coolant (ECC) injection, maintenance of continuous core cooling, and long-term decay heat rejection to the atmosphere. With due consideration for these key processes, four periods have been selected to characterize the AP600 IBLOCA transient: (1) break-dominated depressurization, (2) depressurization via ADS discharge to the IRWST, (3) depressurization via ADS discharge to the containment, and (4) long-term cooling. The selected periods (Fig. 3) provide a rational partitioning of the IBLOCA sequence because system depressurization is required to bring the AP600 to a safe shutdown condition. The sequence of events is provided in Table I.

Period 1 - Break-Dominated Depressurization

The first period is an interval of *break-dominated depressurization* initiated by a DEGB in DVI-A. The RCS rapidly depressurizes (Fig. 3) as mass and energy are lost through the break. The vessel-side break flow rapidly diminishes (Fig. 4) because fluid near the break flashes, increasing the resistance to flow through the break. As coolant flashes to vapor in the hotter parts of the RCS, the rate of primary depressurization rapidly slows and then stalls. However, coolant discharge from the vessel-side of the DEGB proceeds, continuing the reduction in RCS inventory (Fig. 5) and contributing to voiding in the higher elevations of RCS. The postulated break disables one-half of the PSIS capability, specifically the A train. The inventories of ACC-A, CMT-A and the coolant delivered by one IRWST discharge line (Fig. 6) are lost through the break and are discharged into the containment. Coolant recirculation begins immediately after the CMT isolation valves are opened following receipt of the S signal 9.2 s after break initiation. During the recirculation mode, the CMTs remain full. The intact CMT (CMT-B) continues to recirculate throughout this period and thus does not drain. However, the recirculation period of CMT -A lasts only a few seconds, after which it begins to drain as coolant is lost through the break at a faster rate than can be replenished through PBL-A, which feeds CMT-A. The break-dominated depressurization period ends at 172.6 s when the first-stage ADS is activated following the reduction of the inventory of CMT-A to the inventory set point (67% of initial inventory) at which the ADS actuation signal is generated.

Period 2 - Depressurization Via ADS Discharge to the IRWST

The second period of this transient is characterized by *depressurization via ADS discharge to the IRWST*. The period begins when the first-stage ADS actuates at 172.6 s and concludes when the fourth-stage ADS actuates at 482.7 s. Each of the first three ADS stages consist of two trains, which discharge primary system mass (Fig. 7) and energy into the IRWST. Failures of one first-stage and one third-stage train are assumed as a counterpart to the Westinghouse analysis of the same postulated accident.[1] First-stage ADS actuation releases sufficient mass and energy to restart primary system depressurization, even with one train inoperable (Fig. 3). The rate of depressurization is moderate, but increases further when the second-stage ADS starts to open at 242.7 s, a preset 70 s interval following first-stage ADS actuation. The second-stage ADS discharge area is approximately 10 times greater than that of the single operative first-stage ADS and, therefore, an observable increase in the rate of depressurization follows second-stage ADS actuation. The RCS pressure soon decreases to 4.83 MPa (700 psia), initiating coolant injection from the intact ACC (Fig. 8). The accumulator flow rate increases as the primary pressure continues to decrease. The increasing accumulator flow gradually terminates draining of the intact CMT attached to the same DVI line. A reverse flow through the intact CMT is predicted. Draining of the intact CMT does not resume until the ACC empties at the end of the third transient period. One train of the third-stage ADS starts to open at 362.7 s, a preset 120 s interval following ADS stage-2 actuation. One train of the third-stage ADS has one-half the discharge area of the two ADS stage-2 trains.

Throughout this period, the balance of inventory losses through the ADS and vessel-side break and inventory gains via CMT draining and accumulator injection vary. At the start of the period, the vessel-side break flow dominates the RCS inventory loss, being nearly an

order of magnitude greater than the inventory gain via CMT draining. The first-stage ADS flow is a small contributor to inventory loss, approximately the same magnitude as the CMT draining flow. At the end of the period, the downcomer liquid level has drained below the level of the DVI nozzle, reducing the vessel-side break discharge to nearly zero. The second- and third-stage ADS flows are the dominant contributors to the continuing loss of RCS inventory. The maximum ADS mass flow through stages 1–3 is reached by 350 s as ADS stage 2 fully opens. The total ADS flow is rapidly decreasing at the end of the period. Throughout the period, the RCS coolant inventory decreases (Fig. 5). The intact accumulator flow, however, continues at an increasing flow rate (Fig. 8) , setting the stage for refilling the vessel early in the next period of the transient. The period of RCS depressurization via discharge through ADS stages 1–3 to the IRWST ends at 482.7 s, when fourth-stage ADS is activated following the reduction of the inventory of CMT-A to 20%, the volume fraction at which the fourth-stage actuation signal is generated.

Period 3 - Depressurization Via ADS Discharge to the Containment

The third period of this transient is characterized by *depressurization via ADS discharge to the containment.* Each of two fourth-stage ADS lines connect to the top of a separate hot leg and exhaust directly to the containment. The objective of the fourth-stage ADS is to complete the depressurization of the primary system by reducing the RCS pressure below a level at which the IRWST pool head is sufficient to induce injection. The period begins when the fourth-stage ADS is actuated at 482.7 s, and concludes when the IRWST injection begins at 631 s. About 80 s after fourth-stage ADS actuation, the RCS pressure approaches the containment pressure (Fig. 3), establishing the precondition for IRWST discharge into the intact DVI line once the ACC attached to the same line empties.

The fourth-stage ADS discharge area is approximately 62% of the total ADS system discharge area. At the time of fourth-stage ADS actuation, the hot-leg piping contains only a little liquid and, therefore, RCS depressurization continues with only a moderate additional loss of coolant inventory over a period of approximately three minutes (Fig. 9). After the discharge flow is established following opening of the ADS fourth stage, the rate of RCS inventory loss through fourth-stage ADS oscillates but generally decreases as the period progresses. Inventory discharges through ADS stages 1–3 continue to diminish throughout the period and are small at the end of the period. Eventually, the rate at which coolant is injected by the intact ACC exceeds the coolant loss through all stages of the ADS and the vessel-side break. This occurs at about 535 s and the core begins to refill (Fig. 5). The intact ACC empties at 623 s (Fig. 8). Draining of the intact CMT resumes shortly before the intact ACC empties. IRWST draining through the intact DVI line begins shortly after the intact ACC empties at 631 s, marking the end of the period.

Period 4 - Long-Term Cooling

The TRAC-PF1/MOD2 calculation does extend very far into the long-term cooling period. Thus, the descriptive information provided for the long-term cooling period is based upon other sources.[3-5] The long-term cooling period begins with IRWST actuation and continues indefinitely. IRWST injection begins at 631 s. Draining of the IRWST is expected to take several days, after which water from the sump is recirculated indefinitely. Water from the IRWST passes to the vessel downcomer through the DVI lines. The injected water is heated in the core, a portion evaporates establishing a two-phase liquid

level in the core, and the steam generated in the core is discharged to the containment through the fourth-stage ADS. The passive containment cooling system plays an important role during the long-term cooling period. Steam released into the containment through either the break or fourth-stage ADS condenses on the inner surface of the steel containment shell, and drains downward either to gutters that return the condensed liquid to the IRWST or the sump. Heat transfer on the outside of the steel containment shell is by evaporation of water and buoyancy induced circulation of air until the PCCS water supply is exhausted. Thereafter, the buoyancy induced air flow is sufficient to remove the decay heat released into the containment.

IBLOCA ANALYSIS—OTHER RESULTS

Scaled DVI-Line IBLOCA in the ROSA Facility

The NRC has contracted with the Japan Atomic Energy Research Institute (JAERI) to perform AP600 confirmatory testing in the JAERI's ROSA facility. ROSA is not a perfect representation of the AP600 reactor, and numerous geometric distortions exist that must be considered when projecting the ROSA response to the AP600.[3] For example, AP600 has two cold legs per loop. AP600 has two cold-leg pressure balance lines, each connecting one CMT to one cold leg of the same loop. ROSA, however, has only a single cold leg per loop. Both the NRC and JAERI have concluded that while ROSA is not an exact scale model of the AP600, it is sufficiently similar to reproduce the most important thermal-hydraulic phenomena associated with AP600.

In October 1994, an IBLOCA experiment, AP-DV-01, was conducted in the ROSA facility.[3] This experiment simulated a DEGB in one of the AP600 DVI lines. Thus, one-half of the PSIS injection capability was disabled. Although a TRAC-PF1/MOD2 assessment of the test results is not planned, the test has been reviewed with the objective of highlighting areas of similarity and dissimilarity between the ROSA AP-DV-01 data and the TRAC-calculated results for the same postulated accident in AP600. ROSA experiment AP-DV-01 conditions differ in some respects from the TRAC counterpart model of a Westinghouse DVI-line LOCA.[1] For example, the ROSA break location is located ~6.8 m from the reactor vessel nozzle, which is equivalent to about 8.3 m from the reactor vessel nozzle in AP600. The break location for the TRAC DVI-line IBLOCA was at the reactor vessel nozzle. The ADS is fully functional in the ROSA test. One stage of the first- and third-stage ADS are assumed to fail in the TRAC calculation. A single heat exchanger and fluid train simulates the AP600 PRHRS in ROSA. Both AP600 PRHRS trains are simulated in the TRAC model. Other than the differences noted, the TRAC calculation is a reasonable counterpart to ROSA experiment AP-DV-01. A comparative assessment of the areas of similarity and dissimilarity between the TRAC calculation and ROSA experiment AP-DV-01 is briefly summarized as follows.

The following *similarities* between the ROSA test results and TRAC calculated results were identified. The sequence of events occurring during the ROSA experiment and in the AP600 calculation are similar. The pressurizer empties early due to flashing associated with the initial RCS depressurization. The pressurizer collapsed liquid level recovers following opening of the first-stage ADS. RCS depressurization stalls prior to ADS actuation when the hottest portions of the RCS saturate. The broken-line ACC discharges for an interval, terminates before ADS stage-1 initiation, and resumes after the RCS pressure once again decreases below the accumulator injection pressure. The broken-loop

CMT drains fairly rapidly into the broken DVI line and thence out the break. The intact-loop CMT has an initial period of recirculation, followed by a brief period of draining that is terminated following accumulator injection. CMT injection does not resume until the ACC is empty. CMT and IRWST injection proceed simultaneously after the ACC empties. Cladding temperatures follow saturation pressure. There is no core cladding heatup.

The following significant *dissimilarities* between the ROSA test results and TRAC calculated results were identified. The ROSA data show a shorter-duration primary pressure plateau following RCS saturation. The single ROSA PRHRS transfers sufficient energy from the RCS to the IRWST that RCS pressure begins to decrease before ADS stage-1 operation. The TRAC-calculated RCS pressure plateau persists until ADS stage 1 is actuated. TRAC models both of the PRHRS trains. In the TRAC AP600 calculation, asymmetries in the layouts of the two PRHRS trains result in different flows through the two heat exchangers, possibly reducing the total calculated heat removal through the PRHRS. Cladding temperatures follow RCS depressurization in both the ROSA data and the TRAC calculation, but the cooldown rate differs because a faster depressurization transient occurred in ROSA than that calculated by TRAC for AP600. In summary, the TRAC-calculated DVI-line IBLOCA is in general agreement with respect to the important systems, components, processes and phenomena occurring in ROSA test AP-DV-01. The primary area of disagreement relates to the system pressure response arising from PRHRS modeling and related processes and phenomena.

IBLOCA Analyses by Westinghouse Using NOTRUMP

In 1994, Westinghouse reported an analysis of a DVI-line IBLOCA.[1] The analysis was based upon a calculation performed with the NOTRUMP code. No core uncovery and cladding heatup is predicted to occur. This result is consistent with the TRAC-calculated result. In addition, the NOTRUMP-calculated and TRAC-calculated event times for reactor trip, S signal, start of RCP coastdown, ADS stage-1 actuation, start of intact-loop accumulator flow, ADS stage-2 actuation, ADS stage-3 actuation, and ADS stage-4 actuation are similar. Differences between the NOTRUMP and TRAC calculations were also observed. These included a shorter duration RCS pressure plateau, slower upper head draining, recovery of the downcomer mixture level after ADS actuation, and lower ADS flow rates predicted by NOTRUMP for the transient. Some of the differences may be related to the Appendix K methodology incorporated in the NOTRUMP model. Others, such as the the RCS pressure behavior following RCS saturation, may be related to different modeling approaches for the PRHRS.

When code-to-code comparisons are made, three potential causal areas must be explored. First, the same understanding of facility design and operation must be held by each team developing a code input model. Second, the input model must adequately represent the actual design and its operation. Third, code features or inadequacies may play a role. The areas of agreement between the NOTRUMP and TRAC results seem to indicate that the major features of both the codes and input models similarly represent AP600.

IBLOCA Analyses by the INEL

In 1995, Idaho National Engineering Laboratory (INEL) staff analyzed an AP600 DVI-line IBLOCA based on a RELAP5 calculation.[7] The objective of the effort was to provide a pretest AP600 counterpart calculation for ROSA DVI-line IBLOCA test AP-DV-01. Both

baseline and sensitivity calculations were performed. A brief assessment of the similarities and dissimilarities of the RELAP5 pretest and TRAC calculations of the DVI-line IBLOCA follows.

There were some differences in the problem statements for the two calculations. These arise from differing objectives for the two AP600 DVI line LOCA. The objective of the TRAC calculation is to replicate the conditions of a Westinghouse analysis[1] as previously discussed. Thus, one train of the first-stage ADS is assumed to fail. One train of the third-stage ADS is also assumed to fail. All trains of the ADS are assumed to function in the ROSA counterpart calculation. Although the break location for each calculation is in the DVI line between the vessel and tee to the IRWST, the break location in the TRAC is closer to the vessel. In the INEL calculation, the containment is initially assumed to be at atmospheric pressure and is allowed to pressurize using a rudimentary containment model; in the TRAC calculation, a constant 45-psia containment pressure was assumed. In addition, there are modeling differences related to the codes themselves. The baseline RELAP5 calculation modeled the downcomer as a single axial stack of fluid volumes. A sensitivity study was performed in which eight cross-connected axial stacks were used to simulate the multidimensional character of the downcomer.

There are significant areas of similarity between the TRAC and RELAP calculations. In general, the order and timing of events are similar. For example, the calculated times of IRWST injection are within 15 s. ADS actuation is predicted to occur about 45 s earlier in TRAC. RELAP5 calculated an interval during which draining of the broken CMT stalled when subcooled liquid from the downcomer entered the CMT and condensed vapor in the CMT. Because the ADS actuation signal is generated on CMT liquid level, all ADS actuations calculated by RELAP5 were delayed relative to the TRAC-calculated times. There are significant areas of similarity regarding processes and phenomena. Similarities are observed in the behavior of the ACC and CMT attached to the broken DVI line. The behaviors of the intact ECC trains are similar. The inventory trends of the downcomer and core calculated by the two codes are similar, with the exception discussed in the following paragraph. Both codes predict that the core remains cooled throughout the accident.

Several significant phenomenological differences were calculated by the two codes. First, RELAP5 calculated a significantly larger early reduction of core coolant inventory than TRAC. The collapsed liquid level decreased to 15% of the steady-state value early in the transient but rapidly recovered shortly thereafter. During the same interval, the TRAC-calculated core liquid fraction decreased to 70%. A RELAP5 sensitivity calculation was performed with RELAP5 with the eight-stack model. The collapsed liquid level again decreased to the bottom of the active fuel, but the duration of the core liquid level depression was reduced. The break flows calculated by the two codes immediately following the break are close. However, throughout the remainder of the period of *break dominated depressurization* , the average TRAC-calculated break flow is about 65% of the RELAP5-calculated break flow. Thus, the difference in early core collapsed liquid level calculated by the two codes is consistent with the differences in the calculated break flows. The different break locations used in the two calculations may be significant, but a sensitivity study has not yet been performed. Additional comparative reviews of the two calculations, and possibly sensitivity calculations for the two break locations, would provide the basis for understanding the root causes for the calculated differences. Second, following ADS actuation, RELAP5 calculates both more liquid in the pressurizer and a longer period during which the pressurizer retains liquid. The ADS failure specification in

the TRAC calculation is a contributing factor, although it is not clear if this is the total explanation. Third, the pressurization plateau interval during the blowdown period is shorter in the RELAP5 calculation. Los Alamos attributes the longer period of the pressure plateau in the TRAC calculation to be associated with a reduced amount of heat rejection to the PRHRS. Sensitivity studies could provide insights into the adequacy of the TRAC two-train PRHRS model.

SUMMARY OBSERVATIONS

The summary observations that follow are based upon information from four sources. The TRAC-calculation-based insights are complemented by a scaled DVI-line IBLOCA experiment, test AP-DV-01, conducted in the ROSA facility.[3] They are further complement by counterpart analyses based upon DVI-line IBLOCA calculations performed with other codes. The TRAC calculation documented in this report is a direct counterpart of a calculation performed by Westinghouse using NOTRUMP.[1] The INEL has performed a direct AP600 counterpart calculation to ROSA test AP-DV-01 using RELAP5/MOD3.[6]

Although similar processes, phenomena, and outcomes have been either calculated or observed in each source, uncertainties remain. As with any scaled experimental facility, atypicalities exist. Work underway at the INEL should help to characterize these atypicalities. Activities to demonstrate code applicability for AP600 LOCA processes are either in progress or planned. However, the uncertainty associated with TRAC and RELAP5 calculations of IBLOCA processes and phenomena have not been quantified to date.

The key processes occurring in an AP600 during a IBLOCA are RCS depressurization, inventory depletion, inventory replacement via ECC injection, maintenance of continuous core cooling, and long-term decay heat rejection to the atmosphere.

RCS depressurization is successfully accomplished by the ADS. The primary outcomes of ADS depressurization are accumulator injection beginning at 4.83 MPa (700 psia), IRWST injection beginning when the RCS pressure equilibriates with the containment pressure, and the IRWST pool head is sufficient to inject coolant into the intact DVI line.

There are several sources of RCS inventory depletion. During the period of *Break Dominated Depressurization*, period 1, the vessel-side break is the only source of RCS inventory depletion. The vessel-side break is a significant contributor to inventory depletion for the first one-third of period 2, the period of *Depressurization Via ADS Discharge to the IRWST*. Discharges through the first three stages of the ADS are the dominant cause of RCS coolant loss during this period. This is particularly tr after the vessel-side break flow diminishes when the downcomer liquid level drops below the downcomer connection to the broken DVI line. Some RCS coolant resides in the pressurizer following ADS stage-1 actuation, further reducing the circulating RCS coolant inventory. Following actuation of the fourth-stage ADS at the start of period 3, *Depressurization Via ADS Discharge to the Containment*, the fourth-stage ADS flow is the largest cause of RCS inventory reduction. However, the peak fourth-stage ADS flow is significantly lower than the peak flows through either the vessel-side break or ADS stages 1–3.

There are several sources of inventory replacement via ECC injection. Of course, the entire inventory of one ECC system train is lost as a direct result of the postulated DVI-line break. Thus, only the inventory of the intact ECC train is available for cooling the core. Intact-train accumulator injection begins following ADS actuation. Continuous draining of the intact-train CMT begins once the intact-train accumulator drains. IRWST injection into the intact DVI line begins following fourth-stage ADS actuation. Loss of RCS coolant inventory terminates once the ECC flow from the intact-train accumulator exceeds the RCS discharges through the vessel-side break, ADS stages 1-3, and ADS stage 4. This occurs at about 535 s, during period 3, depressurization via ADS discharge to the containment.

The core is continuously cooled. ECC coolant injection from the single intact train is sufficient to prevent core dryout.

Neither the calculations nor the ROSA test simulated that portion of the long-term cooling period when sump injection is active. In addition, the containment cooling system, which functions as an integral part of the long-term cooling process, was neither simulated in ROSA nor modeled in the calculations. Thus, the conclusion that the core is continuously cooled does not apply to the period of sump injection. The absence of this conclusion regarding the latter phase of the long-term cooling period does not imply that continuous core cooling is suspect. It only means that the needed analytical and/or experimental confirmation of cooling is unavailable at the present time.

References

1. "AP600 Design Change Description Report," Westinghouse Electric Corporation Proprietary Class 2C report (February 15, 1994).

2. J. C. Lin, et. al., "TRAC-PF1/MOD2 Code Manual," Volumes 1–4, Los Aamos National Laboratory report NUREG/CR-5673, also LA-12031-M (1994).

3. R. Shaw, T. Yonomoto, and Y. Kukita, "Quick Look Report for ROSA/AP600 Experiment AP-DV-01," Draft Report, Thermohydraulic Safety Engineering Laboratory, Japan Atomic Energy Research Institute (December, 1994).

4. Fletcher, C. D., Wilson, G. E., Davis, C. B., and Boucher, T. J., "Interim Phenomena Identification and Ranking Tables for AP600 Small Break Loss-of-Coolant Accident, Main Steam Line Break, and Steam Generator Tube Rupture Scenarios," Idaho National Engineering Laboratory DRAFT report INEL-94/0061; Rev. 0 (November 1994).

5. Wilson, G. E., "Transmittal of AP600 T/H Consultants Meeting Minutes," Idaho National Engineering Laboratory letter J6008-GEW-09-95 to T. Lee (February 15, 1995).

6. J. E. Fisher, "AP600 Double-Ended DVI Line Break ROSA Counterpart RELAP5/MOD3 Calculation," Lockheed Idaho Technologies Company DRAFT report (February 1995).

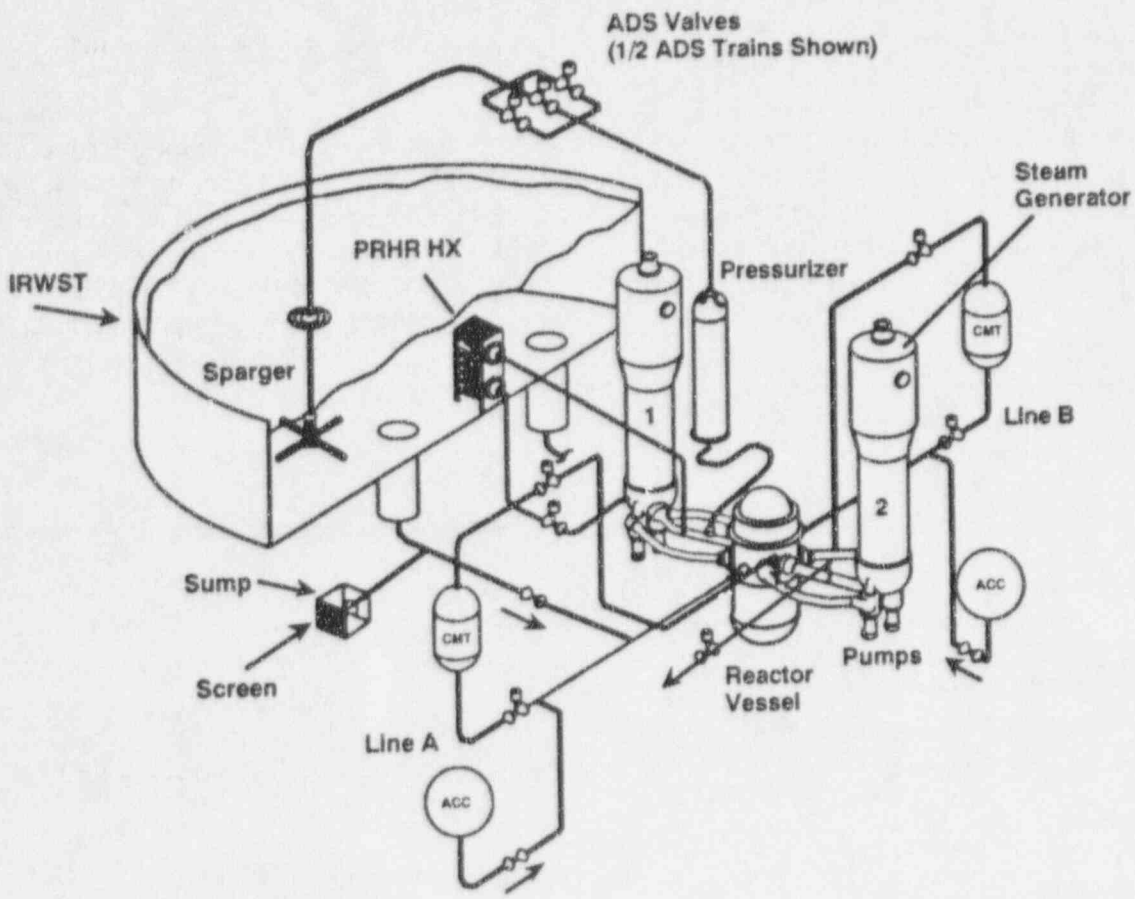

Fig. 1.
AP600 passive safety systems.

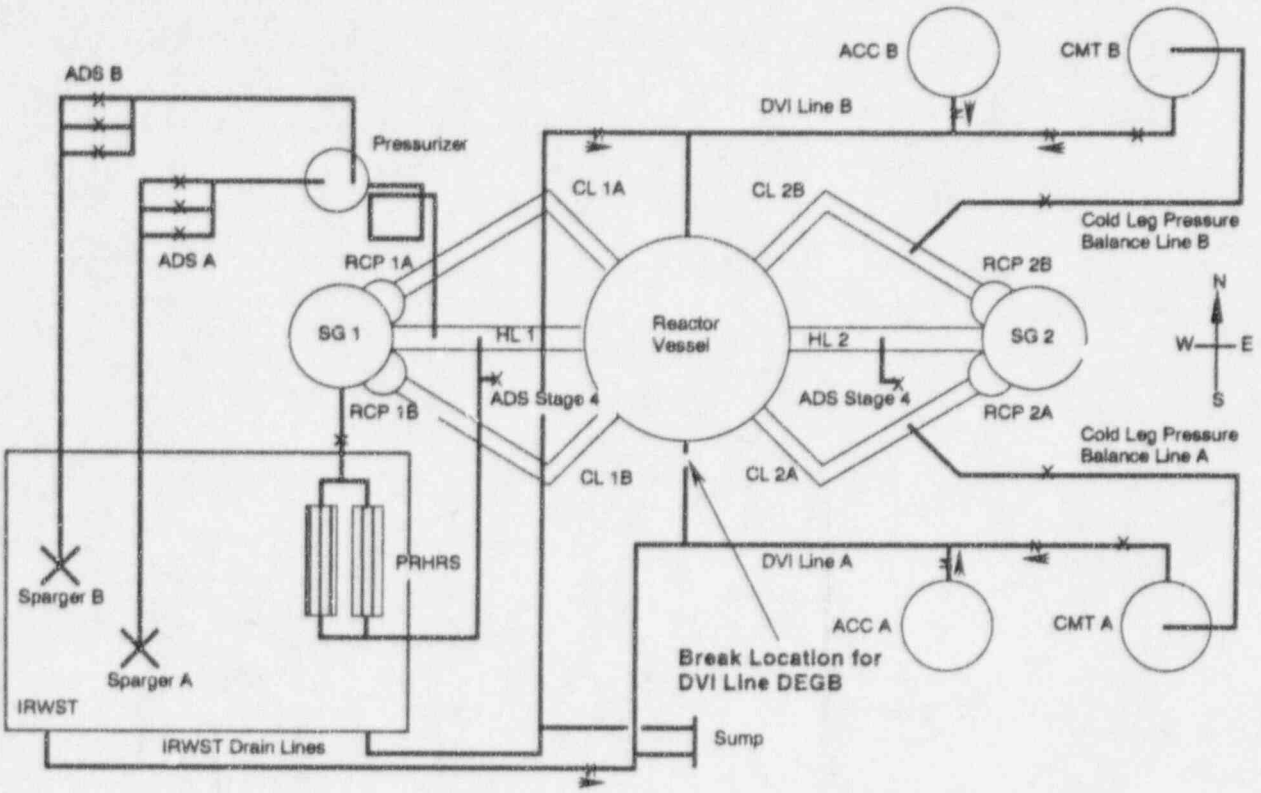

Fig. 2.
AP600 reactor coolant system and passive safety injection.

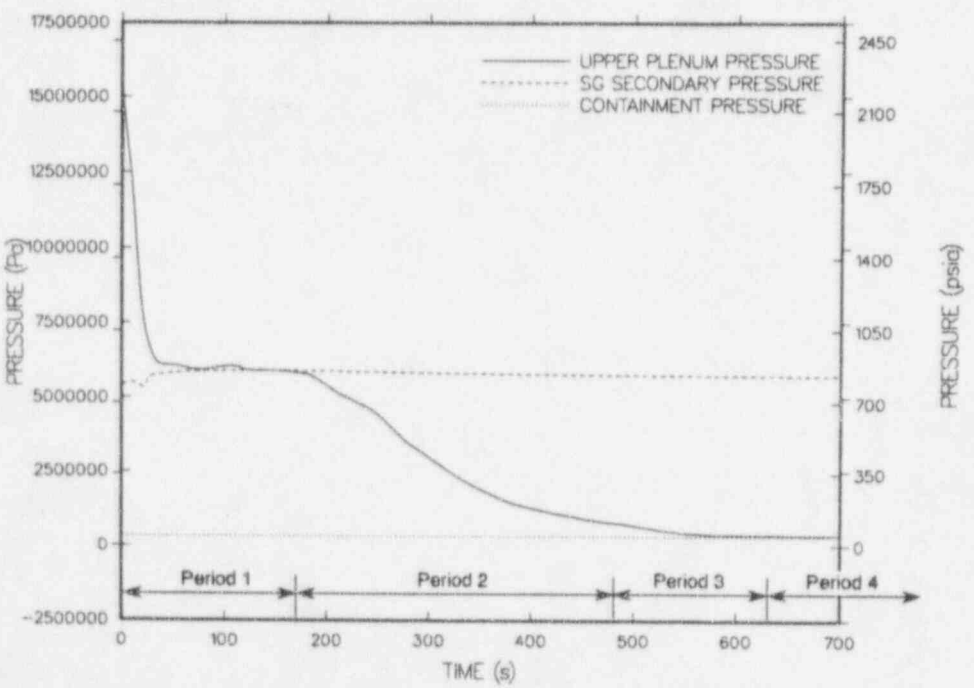

Fig. 3.
Primary and secondary pressures.

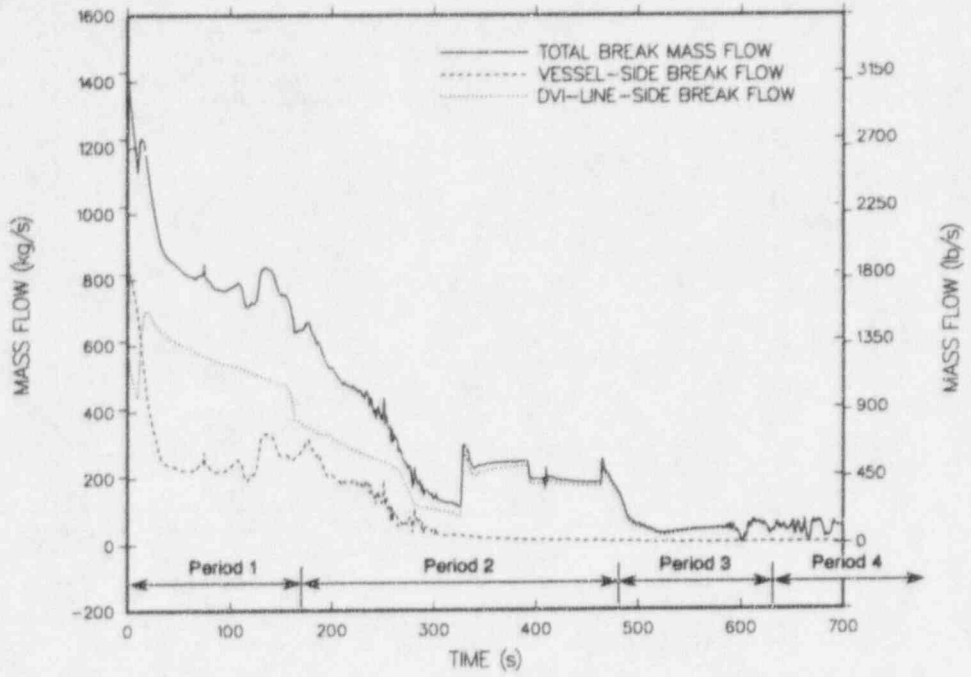

Fig. 4.
Break mass flows.

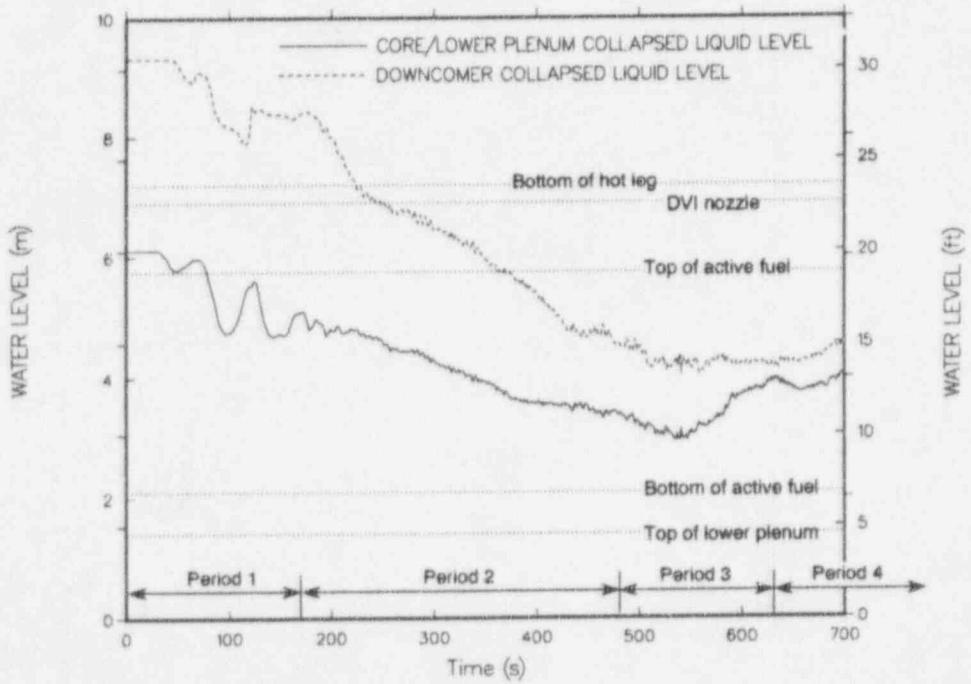

Fig. 5.
Downcomer and core collapsed liquid levels.

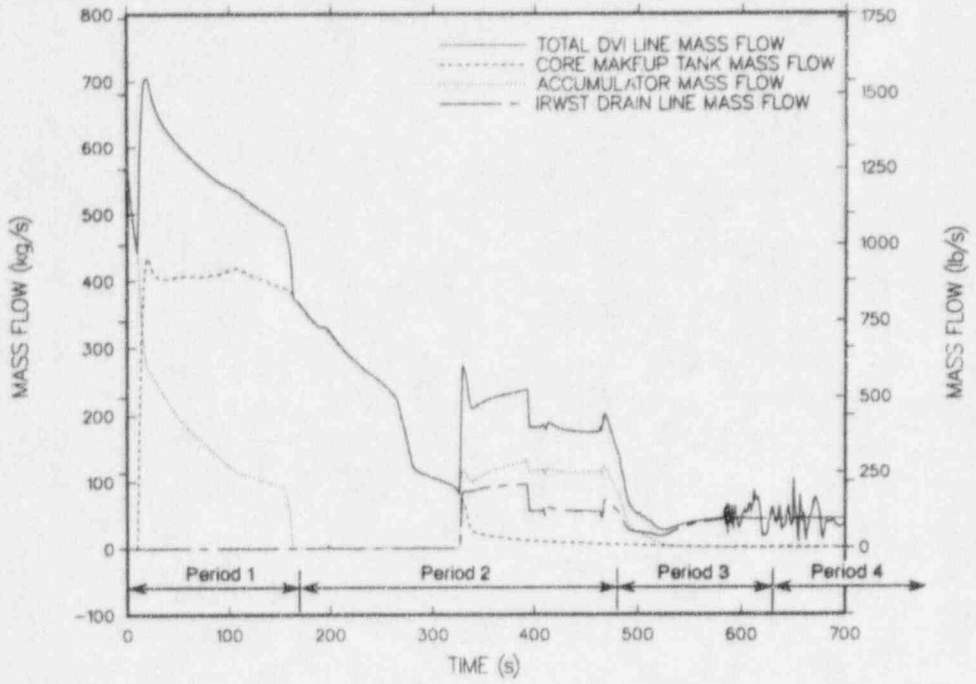

Fig.6.
Broken DVI line mass flow.

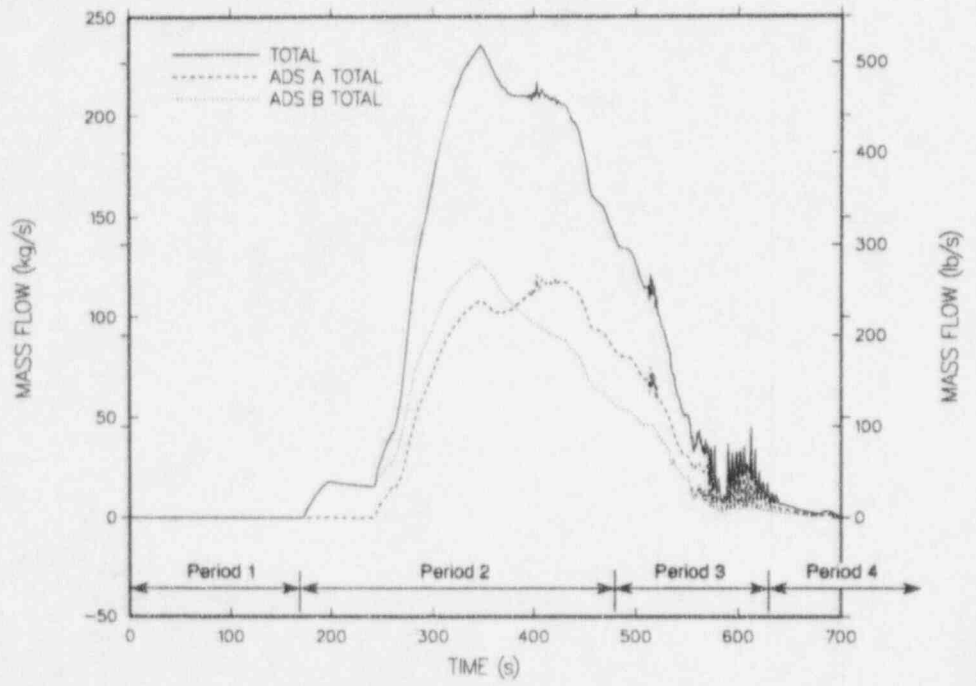

Fig. 7.
Total ADS stages 1-3 mass flow.

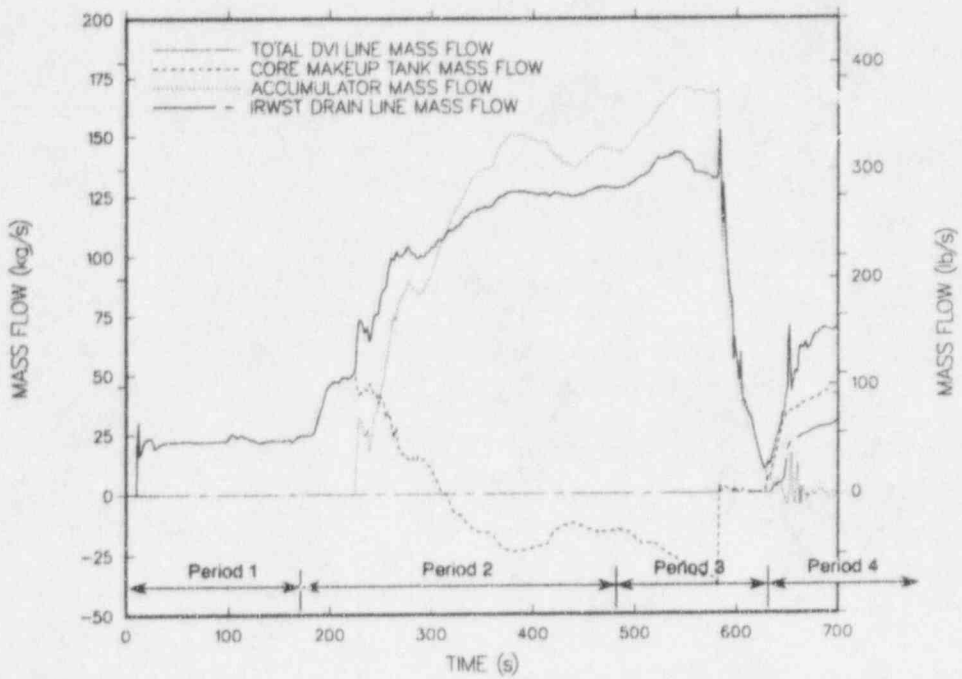

Fig. 8.
Intact DVI line mass flow.

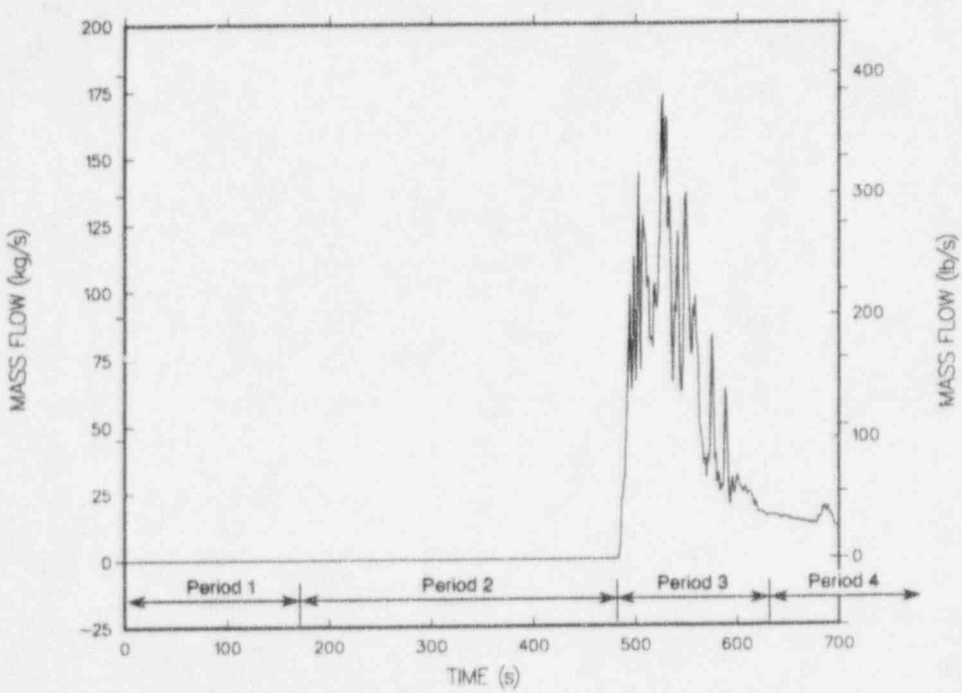

Fig. 9.
Total fourth-stage ADS mass flow.

TABLE I

IBLOCA SEQUENCE OF EVENTS

Time (s)	Event
0.0	Break occurs in DVI line A next to vessel.
8.3	Reactor trip on low pressurizer pressure.
9.2	"S" signal on low pressurizer pressure. Steam generator feedwater control valves starts to close.
10.4	PRHRS isolation valve starts to open. CMT isolation valves start to open.
18.9	Main steam line isolation valves start to close.
25.4	Reactor coolant pumps trip.
152.5	67% liquid volume fraction reached in CMT-A (broken DVI line).
172.6	ADS stage 1 control-valve trip signal. Stage 1 of ADS train B starts to open. Stage 1 of ADS train A assumed to be inoperative and does not open. Stage 1 valve opening time: 25 s.
242.7	ADS Stage 2 control-valve trip signal. Stage 2 valves of both ADS trains start to open. Stage 2 valve opening time: 105 s.
255.2	20% CMT level signal. This signal, plus a 120-s delay after Stage 3 valves open, allows actuation of ADS Stage 4 valves.
328	Flow through IRWST drain line-B (broken DVI line) begins.
337	CMT-A (broken DVI line) empties.
362.7	ADS Stage 3 control-valve trip signal. Stage 3 of ADS train A starts to open. Stage 3 of ADS train B assumed to be inoperative and does not open. Stage 3 valve opening time: 105 s.
482.7	ADS Stage 4a and 4c valves start to open. 85% valve area assumed. Valve opening time: 20 s.
512.7	ADS Stage 4b and 4d valves start to open. 85% valve area assumed. Valve opening time: 20 s.
516	Accumulator-A (broken DVI line) empties.
623	Accumulator-B (intact DVI line) empties.
631	Flow through IRWST drain line-A (intact DVI line) begins.

A CONCEPT OF
JAERI PASSIVE SAFETY LIGHT WATER REACTOR SYSTEM (JPSR)

Y.Murao, F. Araya, and T. Iwamura

Japan Atomic Energy Research Institute

Tokai-mura, Ibaraki-ken, 319-11, Japan

+81 (292) 82-6120

ABSTRACT

The Japan Atomic Energy Research Institute (JAERI) proposed a passive safety reactor system concept, JPSR, which was developed for reducing manpower in operation and maintenance and influence of human errors on reactor safety.

In the concept the system was extremely simplified. The inherent matching nature of core generation and heat removal rate within a small volume change of the primary coolant is introduced by eliminating chemical shim and adopting in-vessel control rod drive mechanism units, a low power density core and once-through steam generators.

In order to simplify the system, a large pressurizer, canned pumps, passive engineered-safety-features-system (residual heat removal system and coolant injection system) are adopted and the total system can be significantly simplified. The residual heat removal system is completely passively actuated in non-LOCAs and is also used for depressurization of the primary coolant system to actuate accumulators in small break LOCAs and reactor shutdown cooling system in normal operation. All of systems for nuclear steam supply system are built in the containment except for the air coolers as a the final heat sink of the passive residual heat removal system. Accordingly the reliability of the safety system and the normal operation system is improved, since most of residual heat removal system is always working and a heat sink for normal operation system is "safety class". In the passive coolant injection system, depressurization of the primary cooling system by residual heat removal system

initiates injection from accumulators designed for the MS-600 in medium pressure and initiates injection from the gravity driven coolant injection pool at low pressure. Analysis with RETRAN-02/MOD3 code demonstrated the capability of passive load-following, self-power-controllability, cooling and depressurization.

1. INTRODUCTION

Ordinary Pressurized Water Reactors (PWRs) consist of complex systems and there are tremendously large number of subsystems, components and parts to be maintained. Maintenance efforts are significantly large to detect defects and properly repair them, since correct performance of these systems is essential for reliable operation of plants and actuation of their safety systems. Therefore maintenance engineers are required highly technical efforts to obtain good performance of these systems.

Operators are also required to identify malfunction of these systems and properly operate the systems in order to avoid unallowable deviation. Accordingly human errors in operation and maintenance may give big influence on safety. Thus a large number of qualified engineers are required in the operation and maintenance work, however, it is expected to be difficult to employ all of required engineers in future, since well-trained engineers will not be able to be supplied enough to cope with the increase of nuclear plants. The increase of nuclear plants also requires the decrease in potential risk per unit not to increase the total potential risk in this world. One of solutions is simplification of reactor systems, which is very effective to improve the reliability on the systems, reduce required qualified manpower in operation and maintenance, improvement of safety and also reduce construction and operation cost.

Many attempt have been done to develop concepts of simplified PWRs with passive engineered-safety-features-system. The AP-600[1] and MS-600[2] PWR concepts have been proposed by featuring passive engineered-safety-features-systems which can eliminate the diesel generators, injection pumps and coolant supply systems for emergency. However, the reactor shutdown system is the same as that of ordinary PWRs,where the failure of the system

cannot be neglected.

In the PIUS[3] concept, stable operating condition is in a narrow band and a highly concentrated soluble boron is physically filled the core for reactor shutdown, if operating condition is shifted out of the narrow band. This reactor shutdown system is completely passive and reliable, however even small disturbance in operation can induce reactor shutdown, that is, the reactor system is safer but less practical as a power generating system. The SPWR[4] concept has been developed by extending the PIUS concept and is intermediate concept between the above-mentioned PWRs and the PIUS. Hydraulic-pressure-actuated valves trigger to inject soluble boron actively by logical signal or passively by decrease of pump discharge pressure. This is more stable than the PIUS, however, all of important events cannot be passively covered by the system. These reactor shutdown systems with soluble boron have some shortcomings; (1) replacement of the highly concentrated soluble boron in the core with diluted soluble boron yielded by evaporation and condensation processes in the system, (2) loss of soluble boron from the system by failure of boundary of the primary coolant containment system and (3) probability of flow channel blockage in the core due to crystallization of boric acid in boiling of the coolant.

Above-mentioned reactor concepts and ordinary PWRs use "chemical shim", that is, soluble boron for compensating the decrease of reactivity due to burnup of nuclear fuel. Accordingly their concentration is set to be high at the beginning of cycle and gradually decreased with increase of burnup, and finally becomes almost zero. Therefore it makes difficult to optimize water chemistry in the primary coolant so as to minimize yielding rate of the Corrosion Product (CP) and resultant radiation exposure by irradiated insoluble metal oxide particle (crud) deposited on the structure of the primary coolant system. Thus ordinary PWRs and previous advanced concepts have limitation in reduction of required qualified manpower in operation and maintenance by simplification of reactor system.

At the Japan Atomic Energy Research Institute (JAERI) a simplified PWR concept named JAERI Passive Safety Reactor (JPSR) System with full range self-power-controllability, that is, physical stability, has been developed by adopting a reactor with an

inherent matching nature of core power generation and heat removal rate and a passive engineered-safety-features-system, while in ordinary PWRs their self-power-controllability is limited in a narrow range near the operating point unless control rods and/or volume control system are actuated. This paper describes the concept and results of quantitative analysis on the performance with RETRAN-02/MOD3 code.

2. REACTOR SYSTEM

2.1 JPSR plant image

The JPSR consists of an in-containment-integrated Nuclear Steam Supply System (NSSS) and a steam and power conversion system. The NSSS consists of a reactor, a primary cooling system with once-through steam generators, a passive engineered-safety-features-system, auxiliary cooling systems and control systems. The reactor has an inherent matching nature of core heat generation and heat removal from the steam generators. The NSSS provides a nuclear reaction interruption capability against moderator density decrease in emergency and also an inherent load following capability in normal operation within a small volume change in the primary coolant system. Accordingly influence of failure in the control rod shutdown system can be minimized. In view from the steam and power conversion system, the NSSS is a physically-slave system to produce steam equivalent to the feed water mass flow rate as described later and no active control for the NSSS is necessary. In the development of the present concept, it was attempted to minimize necessary developing work is and also conserve capabilities of scale-up in the design. In this paper 600 MWe-class design is described. The gross electric and thermal outputs are designed to be fixed 630 Mwe and 1853 MWt, respectively. The image of the NSSS is shown in Fig.1.

2.2 Reactor

Araya and Murao[5] found in a preliminary analysis that the heat generation rate in the nuclear core can be balanced with heat removal rate at the steam generators within small volume change of primary coolant, if the moderator density reactivity coefficient is large enough and the fuel temperature reactivity coefficient (Doppler effect) is small enough. These

conditions are found to be established by eliminating the chemical shim (i.e. boron free operation) and decrease of linear heat rate of fuel rods. In a reactor with such a core, the nuclear reaction can be passively stopped by termination of heat removal at the steam generators. The soluble-boron-free-system has the following advantages; (1) the water chemistry ocan be optimized to reduce yield of the CP and formation of the crud and the CVCS more simplified by removing boron concentration and volume control subsystems, (2) maintenance work on the system becomes easier.

However the elimination of chemical shim requires a large number of Control Rod Drive Mechanism (CRDM) units. Installation of sufficient number of ordinary CRDM units is difficult, since there are technical restrictions in spacing of holes on the top head of the pressure vessel for penetrating connecting rods between CRDM units and control rods. Hence in-vessel CRDMs were adopted, which are being developed for a new marine reactor concept, MRX, at JAERI[6]. High temperature and pressure water-proof components such as a motor, a latch magnet, etc. have been developed. The in-vessel CRDMs are used for not only reactivity control but also active reactor shutdown and additionally for damping of xenon oscillation. The configuration of a fuel assembly is identical to that of a 17x17-type fuel assembly of typical PWRs. A low power density core was adopted to reduce the Doppler effect . This is also effective to reduce thermal load on the fuel in emergency. The average power density is set to be about 75% of that of current PWRs. Hence the core size is almost the same as the Takahama-3 PWR (870MWe PWR)[7] with three cooling loops and the AP-600.

The reactor pressure vessel is also shown in Fig.1 and radially same as that for the AP-600 design concept and axially longer than that for the ordinary three-loop PWRs and the AP-600 design (lower than the nozzle height in Fig. 1) in order to incorporate the in-vessel CRDMs. The diameter of the pressure vessel is only restriction to increase power, since there is no restriction in the passive safety system as described later. Elimination of the chemical shim and use of the in-vessel CRDMs remove probabilities of large reactivity insertion accident due to boron dilution or control rod ejection.

Table 1 shows the main parameters of the JPSR core. The nuclear characteristics in this table were evaluated[8] based on a three-dimensional core burn-up analysis with the SRAC code system[9]. Four-batch refueling strategy is adopted to obtain high burn-up more than 45GWd/t without increase of excess reactivity. The disadvantage of shortening a cycle length is mitigated by the low power density. All excess reactivities are compensated with control rod movements.

2.3 Primary cooling system

In order to have an inherent matching nature of core heat generation and heat removal rate in the reactor system, as shown in Fig.2, a once-through type Steam Generators (SGs) was adopted. In the once-through type SGs, the heat transfer is not governed by the temperature difference between coolant of both sides but SG feed water flow rate. This is very convenient to control heat removal rate by controlling feed water flow rate within a small temperature change of the primary coolant. Quasi-steady state relation between average coolant temperature and normalized power is shown in Fig.3. By assuming temperature rise in the core is 30 K, core inlet and outlet coolant temperatures are obtained as also shown in the figure. From the thermal characteristics of the B&W SG[10], the steam temperature can be estimated as shown in the figure. Usually the power generation turbine allow only temperature change of 8K in the normal operation. Since the B&W design (total heating tube length: 15.9 m) is not satisfied with this criteria, the superheated steam region (18 % of total length in the original design) was extended 3.4 m for satisfaction of the criteria. The structure is also shown in Fig.1.

Based on an analysis[11] with the RETRAN-02/MOD3 code[12], a large pressurizer of 46.7 m^3 was adopted so that the liquid expansion in the transient of 100 % down to 0 % power can be absorbed in regardless of pressure relief valves actuation and a volume control system of the primary coolant in operation becomes unnecessary. And only subsystems for primary coolant cleanup, chemical addition and hydrogen dissolving are necessary. Therefore the CVCS can be dramatically simplified.

Canned pumps are adopted as the main coolant pumps by considering its high reliability of their performance[13] and further simplification of the CVCS by eliminating a seal-water supply subsystem. Since the rotating inertia of canned pumps is lower than that of ordinary PWRs and flow coastdown is faster, the transient calculations have been performed to determine necessary inertia[14] with the RETRAN-02/MOD3 code. It was found from the sensitivity calculations with and without reactor scram that 8% of the pump inertia for the ordinary PWRs, 3110kg.m^2 [15] can prevent the occurrence of the Departure from Nucleate Boiling (DNB) for the JPSR even with regardless of reactor scram because of core power reduction due to the effect of the density reactivity coefficient. Analyses with subchannel code show that 6 % is enough to clear the DNB criteria. Further optimization of piping and pump specification is necessary.

2.4 Passive engineered-safety-features-system

2.4.1 Passive heat removal system

Probabilistic Safety Analysis (PSA)[16] showed that the original concept[11],[18] of the JPSR has a weak point on residual heat removal in loss of offsite power event, where the frequency of failure in startup system for the residual heat removal system gives big influence on frequency of the core damage. Then completely passive startup and actuation of the residual heat removal system was developed. The flow diagram of the passive-safety-features-system is shown in Fig.4.

Three units of residual heat exchanger are installed outside of the pressure vessel and each unit has a natural circulation loop connected to a gravity driven coolant injection pool cooled by air cooler units outside of the containment. One residual heat exchanger is connected to a nozzle of the pressurizer at the certain level and a hot leg which is not connected to the pressurizer. When heat removal rate becomes low and the water level of the pressurizer come to the nozzle level, flow circulation can be completely passively established in a pass from the upper plenum to itself through the pressurizer and the residual heat exchanger. Other two residual heat exchangers are connected to the line between the upper plenum and the downcomer through normally-closed active valves and, if necessary, passive

valves like check valves. The two heat exchangers are used for depressurization and heat removal during LOCAs and reactor shutdown cooling. The pool is cooled by natural circulation of water under atmospheric pressure and the heat is transferred to the outside-installed air coolers as a final heat sink.

The primary cooling system is placed in an inner containment. A large volume of gravity driven coolant injection pool is placed outside of the inner containment and inside of the outer containment. In LOCAs, steam and gas are discharged into the pool through the vent pipes. This pool is used for absorbing heat and iodine from the inner containment in LOCAs. Accordingly the containment spray system is unnecessary. And in severe core damage events, passive devices and active valves for injecting water to the reactor cavity. The fluid from safety valves and depressurizers connected to the pressurizer is fed into the pool by steam quencher to absorb the energy of the fluid.

It was specified that one unit of residual heat exchanger has a heat removal capacity of 6% of full power when the primary system is in the hot conditions and 0.3% in the cold conditions[19]. When four air cooler units are available and ambient air temperature is as high as 303K(30°C), the air cooling system can remove 1% of full power at the pool temperature of 348K(75°C). The heat removal capability of air cooler increases with the pool water temperature. The heat imbalance between heat from the residual heat exchanger and heat to the air coolers is stored in the pool in a certain time. Therefore the gravity driven coolant injection pool works as a heat reservoir.

It is evaluated from steady state calculation that the pool temperature increases to 324.4K(51.4°C) just after initiation of LOCA and then increases gradually to the maximum of 352K(69°C) at 15,000 seconds.

2.4.2 Passive coolant injection system

In emergency, the system pressure is depressurized down to the containment pressure for injecting coolant from the gravity driven coolant injection pool before the core becomes uncovered and overheated. In order to avoid core uncovery, the accumulator injection tanks and/or the high pressure water storage are installed. Preliminary analyses showed that the

effect of the high pressure water storage is small for the JPSR core cooling in large break LOCAs, since the JPSR has relatively large amount of water in the reactor pressure vessel. And also found that depressurization effect by cooling with the JPSR passive residual heat removal system in small break LOCAs is enough to actuate the accumulator system before the core uncovery. In order to avoid nitrogen injection from accumulator tank, the advanced accumulators for MS-600 concept were adopted. The accumulator has a vortex flow control device in the discharge nozzle. When the water level is high, the water enter the vortex chamber mainly radially and smoothly and the water can be discharged at high flow rate, however when the water level become low, the water enter the vortex chamber only tangentially and the discharged flow rate becomes lower because of vortex resistance. Therefore discharged flow rate is smoothly and passively changed from the flow rate of ordinary accumulator to the flow rate of the ordinary low pressure injection system. No nitrogen injection from the accumulators can eliminate the carry-over of the water accumulated in the pressure vessel during high-flow-rate-injection-period of accumulators. The pool is connected with the cold legs of the primary loops through check valves to inject water to the primary system by gravity force when the primary system pressure is depressurized to equalize the containment pressure. In certain conditions actively operated depressurization valves are opened by logical signal as a back-up. The volume of water in the pool is large enough to be used as a residual heat removal system after flooding the primary system up to the level of the pressure vessel nozzles for main coolant piping to ensure a natural circulation between the primary system and the pool. The pool is filled with borated water not so as to dilute the borated water injected into the primary system in emergency. The annulus air cleanup system and other air cleanup system in emergency also should be passive.

By realizing such a passive safety system, all of active components of "safety class" like emergency diesel generators for supplying power and pumps for supplying coolant to the emergency system can be unnecessary. Since almost all of the passive safety system is u[illegible] even in normal operation as described later, defects can be easily detected and operation and maintenance efforts to keep enough reliability can be dramatically reduced.

2.5 Auxiliary cooling system and control system

The gravity driven coolant injection pool is also used for heat sink of normal operating systems like a containment cooling system and a heat exchanger cooling system for the clean-up system. The passive residual heat removal system is also used for a reactor shutdown cooling system. Accordingly cooling system of the pool is always operating. Therefore high reliability of the safety systems and the normal operational systems can be expected. The cooling system needs forced convection systems to operate the system at a suitable operating temperature. The forced convection systems are not "safety class", since there is enough time for engineers working inside of the containment to evacuate outside even when the systems are failed. The total system can be simplified as shown in Fig.5.

The JPSR NSSS is necessary to control the primary system pressure, reactivity, neutron distribution in the core independently from the power demand. Since the JPSR NSSS is physically-slave system for the demand from the steam and power conversion system, the steam system is necessary to control the SG feed water mass flow rate. On the other hand the system becomes weaker against the overcooling ··· nts where the NSSS react as increase of power demand and the core power is increased. Installation of flow limiters at the exit of the SGs can reduce the impact from the events. For main steam line break, small water inventory in the once-through SG secondary side can mitigate the impact, since overcooling event is shortly over by spending heat removal material, i.e. water.

3. DYNAMIC RESPONSE OF JPSR IN TRANSIENTS

3.1 Inherent matching nature of the core power generation and the heat removal rate

Under the assumption of no actuation of the pressure regulation system the dynamic response of the NSSS in this concept is estimated with the RETRAN-02/MOD3 code[11]. In the B&W SG design, the water inventory is completely evaporated within about 30 seconds at 100% power in a loss of feed water event. By considering that the heat transfer in the SG is proportional to the water level which is decreased by evaporation, linear heat transfer decay was assumed in the loss of feed water event. Accordingly the transient can be assumed a

linear heat removal decay of 100% to 0% within 60 seconds. Because of an instability in calculation of the loss of full load event with the RETRAN code and interest in the load-following capability, the following transient was evaluated. The heat removal rate is changed from 100 % to 50 % of power in 30 seconds and changed to 100 % in 30 seconds after 50 % operation for 300 seconds with 100% of power instead of the above-mentioned transient. The transient of 100% power change can be extrapolate from the 50% transient, since no discontinuities was found in calculation. The other main parameters are listed in Table 1. There is no reliable once-through SG model for the RETRAN code, hence a calculation was performed by giving heat removal rate instead of giving steam flow rate at the exit of SGs. Reactivity coefficients on moderator density and fuel temperature are used with the values of those for the SPWR EOEC core data, since values for the JPSR are almost identical to the data as shown in Table 3. In the calculation the steam volume in the pressurizer and the interfacial heat transfer coefficient between two phases is assumed to be 29.6 m^3 and 5678.3 $W/(m^2K)$ (Recommended value in RETRAN manual), respectively. The reactor scram is not considered in the present calculation. Figure 6 shows the calculational results. The figure indicates that the core power generation rate quickly follows the change of the heat removal rate. Except for beginning of transient, reactivities on moderator density and fuel temperature are balancing with each other. And the overshoot of the pressure is 19.83 MPa and the maximum liquid expansion is 4.61 m^3 for 50% load reduction in 30 seconds for the steam volume of 29.6 m^3 in the pressurizer. The overshoot is lower than the criteria of maximum allowable pressure in accidental condition, 20.71 MPa.

Figure 7 shows the transients[14] of inlet flow in hot channel, core power and minimum DNBR (DNBR: a ratio of heat flux at a location to the DNB heat flux estimated at the location, minimum DNBR: DNBR value at a location where minimum value is detected for DNBR in a certain time). It is found that the core average coolant temperature is increased and the core power is decreased with decrease in the core inlet flow rate. This transient is caused by the inherent matching nature of core power generation and the heat removal rate.

3.2 Passive engineered-safety-features-system

In order to demonstrate the effectiveness of the JPSR passive engineered-safety-features-system was evaluated with the RETRAN-02 code for the events of loss of heat sink and a small break LOCA (1% split break at the cold leg). In the calculation of a loss of heat sink event, it is assumed that the main steam flow rate and feed water flow rate decay in 5 seconds, the residual heat exchanger connected to the pressurizer is only active and the reactor scram and pressure regulation are failed. It is also assumed that a valve between the pressurizer and the heat exchanger is turned open when the water level in the pressurizer come to the level of the nozzle, since there is no suitable overflow model for the pressurizer. As shown in Fig.8, the calculation revealed that the water level in the pressurizer increases with time after initiation of the event. In 70 seconds the heat removal rate exceeds the core power and the pressure is decreasing and approaching to about 12 MPa. Finally heat removal rate is balanced with core power. Therefore it is demonstrated that the core power is decreased and the residual heat can be completely passively removed by the passive residual heat removal system in regardless of reactor scram in loss of heat sink event. A big disturbance at about 200 seconds is caused by a temporally void formation in the core. In the small break LOCA, it is assumed that a residual heat exchanger between cold and hot legs in the intact loop becomes active by a signal of lower pressure than 12 MPa. And also assumed that the reactor scram is failed. Figure 9 show the pressure decrease with and without the effect of the residual heat exchanger. The figure shows the effectiveness of the heat exchanger for the depressurization for actuating the accumulator system which is designed to be actuated 4 MPa. The LOCA analysis was performed only for transient of depressurization down to the pressure for actuation of the accumulators and not yet for transients down to the pressure for actuation of the gravity driven coolant injection pool.

4. CONCLUSION

1) For reduction of qualified manpower in operation and maintenance, simplification of reactor systems and improvement of safety and the economy of future light water rectors,.

a concept of a simplified passive safety reactor system named JAERI Passive Safety Reactor (JPSR) system was developed. In the development of concept it was considered to minimize developing work and conserve scale-up capability in the design. The system consists of a Nuclear Steam Supply System (NSSS) and a steam and power conversion system. The NSSS has an inherent matching nature of core generation and heat removal rate and a physically-slave nature for demand from the steam and power conversion system.

2) The inherent matching nature is introduced by the core with high reactivity coefficient for moderator density and low reactivity coefficient for fuel temperature (Doppler effect) and once-through SGs. The NSSS is simple systems and has a passive engineered-safety-features-system. The inherent matching nature can be obtained by eliminating chemical shim and adopting in-vessel CRDM units and low power density core. Elimination of the chemical shim makes the systems simple and reduces radiation exposure due to optimization of water chemistry.

3) In order to simplify the system, a large pressurizer, canned pumps, passive residual heat removal systems and passive coolant injection system are adopted and the functions of volume and boron concentration control and seal water supply are removed from the CVCS. The emergency diesel generators and auxiliary cooling system of "safety class" are also eliminated. The passive residual heat removal system are commonly used for the auxiliary cooling system in normal operation and the reactor shutdown cooling system. All of systems are built in the containment except for the air coolers of the residual heat removal system.

4) The analysis of the system with the RETRAN-02/MOD3 code demonstrated that the core power is decreased with decrease in heat removal rate and core inlet flow rate. And also demonstrated that the residual heat can be completely passively removed by the passive residual heat removal system in regardless of reactor scram and pressure control in loss of heat sink event and the pressure can be reduced down to the accumulator actuation pressure by actuation of the passive heat removal system in small break LOCAs.

ACKNOWLEDGMENTS

The authors would like to express their appreciation to Dr. H. Yoshida for encouragement and hearty suggestions.

REFERENCES

(1) B. A. McIntyre, and R. K. Beck, Westinghouse Advanced Passive 600 plant, Nuclear Safety, Vol. 33, No. 1, 1992.

(2) T. Matsuoka, et al., Safety Features of the Simplified Mitsubishi Pressurized-Water Reactor, Nucl. Safety, Vol. 33, pp.196-208, (1992)

(3) C. Pind, and J. Fredell, Summary of Theoretical Analyses and Experimental Verification of The PIUS Density Lock Development Program, IAEA-TECDOC-677, pp.213-219, Dec. 1992.

(4) F. Araya, et al., Concept of Highly Passive Safe Reactor SPWR -2. Dynamic Analysis-, presented at International Specialists' Meeting on Potential of Small Nuclear Reactors for Future Clean and Safe Energy Source, TIT, Tokyo, Japan, Oct. 23-25, 1991.

(5) F. Araya and Y. Murao Possibility of a Pressurized Water Reactor Concept with Highly Inherent Heat Removal Following Capability, to be published as a Technical Report in the Journal of Nuclear Science and Technology in April, 1995.

(6) Y. Ishizaka, et al., Development of a Built-in Type Control Rod Drive Mechanism (CRDM) for Advanced Marine Reactor X (MRX), Proceedings of ANP'92, Vol. I, pp4.6, Tokyo, Japan, Oct. 25-29, 1992.

(7) World Nuclear Industry Handbook, Special Publications of Nuclear Engineering International, Reed Business Publishing Ltd, 1990.

(8) K. Okumura, and Y. Murao, Nuclear Design Study for JPSR, JAERI-Review 94-009, pp.107-109,1994.

(9) K. Tsuchihashi, et al., Revised SRAC Code System, JAERI-1302 (1983)

(10) Metropolitan Edison Co., Three Mile Island Nuclear Station-Unit 2, License Application, FSAR, DOCKET NO. 50-320-73, April 1974.

(11) Y. Murao, et al., A Concept of Passive Safety Light Water Reactor System Requiring

Reduced Maintenance Efforts, Ninth Proceedings of Nuclear Thermal Hydraulics, pp.210-219,1993 ANS Winter Meeting, San Francisco,(1993).

(12) C. E. Peterson, RETRAN-02 -A Program for Transient Thermal-Hydraulic Analysis of Complex Fluid Flow Systems, EPRI NP-1850-CCM, 1981.

(13) S. N. Tower, Nuclear Engineering and Design, Vol. 109, pp147-154 (1988).

(14) F. Araya, et al., Transient Thermal-Hydraulic Analyses for Design of JPSR, JAERI-Review 94-009,pp.110-112, 1994.

(15) License Application for Genkai 3 and 4, Attachment 10, 1982.

(16) T. Iwamura, and Y. Murao, Preliminary Design of Passive Residual Heat Removal and Containment Cooling System for JPSR, JAERI-Review 94-009, pp.113-115, 1994.

(17) T. Iwamura, et al., Study on Concept of JAERI Passive Safety Reactor (JPSR) (10) - Design Review with PSA Results-, presented at 1994 Fall Meeting of the Atomic Energy Society of Japan, F26, Sapporo, Japan, Sept. 28-30, 1994 (in Japanese).

(18) Y. Murao, et al., A Conceptual Design of JAERI Passive Safety Reactor (JPSR) and Its Thermal-Hydraulic Characteristics, Tenth Proceedings of Nuclear Thermal Hydraulics, pp.3-12,1994 ANS Winter Meeting, Washington,DC,(1994).

List of tables

Table 1 Major parameters for JPSR concept

Table 2 Comparison of reactivities for JPSR and SPWR

List of figures

Fig. 1 Plant image of JPSR

Fig. 2 Concept of primary cooling loop with inherent matching nature of core heat generation and heat removal rate

Fig. 3 Evaluated relation between reactor power and fluid temperatures

Fig. 4 Flow diagram of passive engineered-safety-features-system

Fig. 5 Outline of system organization of JPSR

Fig. 6 Dynamic responses to change of heat removal rate

Fig. 7 Transients in pump trip event

Fig. 8 Calculated transient on loss of heat sink event

Fig. 9 Calculated transient on small break LOCA

Table 1 Major parameters for JPSR concept

Parameters	Value
Thermal output (MWt)	1853
Number of loops	2
Primary system pressure (Mpa)	15.73
Core inlet coolant temperature (K)	558
Core exit coolant temperature (K)	598
Core average coolant temperature (K)	578
Fuel assembly type	17×17 type
Number of fuel assemblies	145
Number of fuel rods per assembly	264
Fuel assembly pitch (mm)	215
Fuel rod pitch (mm)	12.6
Cladding outer diameter (mm)	9.5
Pellet outer diameter (mm)	8.19
U-235 enrichment (w/o)	[4.0] ~ 5.0
Effective core height (mm)	3660
Equivalent core diameter (mm)	2920
Average liner heat rate (KW/m)	13.2
Number of refueling batch	4
Discharge burn-up (GWd/t)	[47] ~ 58
Fuel cycle length (EFPM)	[14] ~ 18
Moderator density reactivity coefficient BOC / EOC (% Δ k/k/g/cm^3)	36 / 34 (35.2)
Dopplor reactivity coefficient BOC / EOC (% Δ k/k/℃)	-2.5×10^{-3} / -2.7×10^{-3} (-3.4×10^{-3})

[ ] : case of 4.0w/o U-235

( ) : reference value of SPWR at EOC

Table 2 Preliminary results on excess reactivity and control rod worth in cold condition at BOC

Excess reactivity (% Δ k/k)	
Burnup	10.9
Xe effect	1.85
Power defect (HFP->CZP)	7.07
Total	19.82
Control rod worth (% Δ k/k)	
Ag-In-Cd	-23.58
B_4C powder (natural B)	-30.99
B_4C pellet (60% enriched B-10)	-42.07

Table 3 Comparison of reactivities for JPSR and SPWR

	JPSR (BOEC)	JPSR (EOEC)	SPWR (EOEC)
Moderator density reactivity coefficient (α_ρ : $\%\Delta k/k/g/cm^3$)	35.6	34.1	35.2
Doppler reactivity coefficient (α_T : $10^{-3}\%\Delta k/k/^\circ C$)	-2.51	-2.70	-3.40
$\lvert\alpha_\rho/\alpha_T\rvert$ ($\times 10^3\,^\circ C/g/cm^3$)	14.2	12.6	10.4

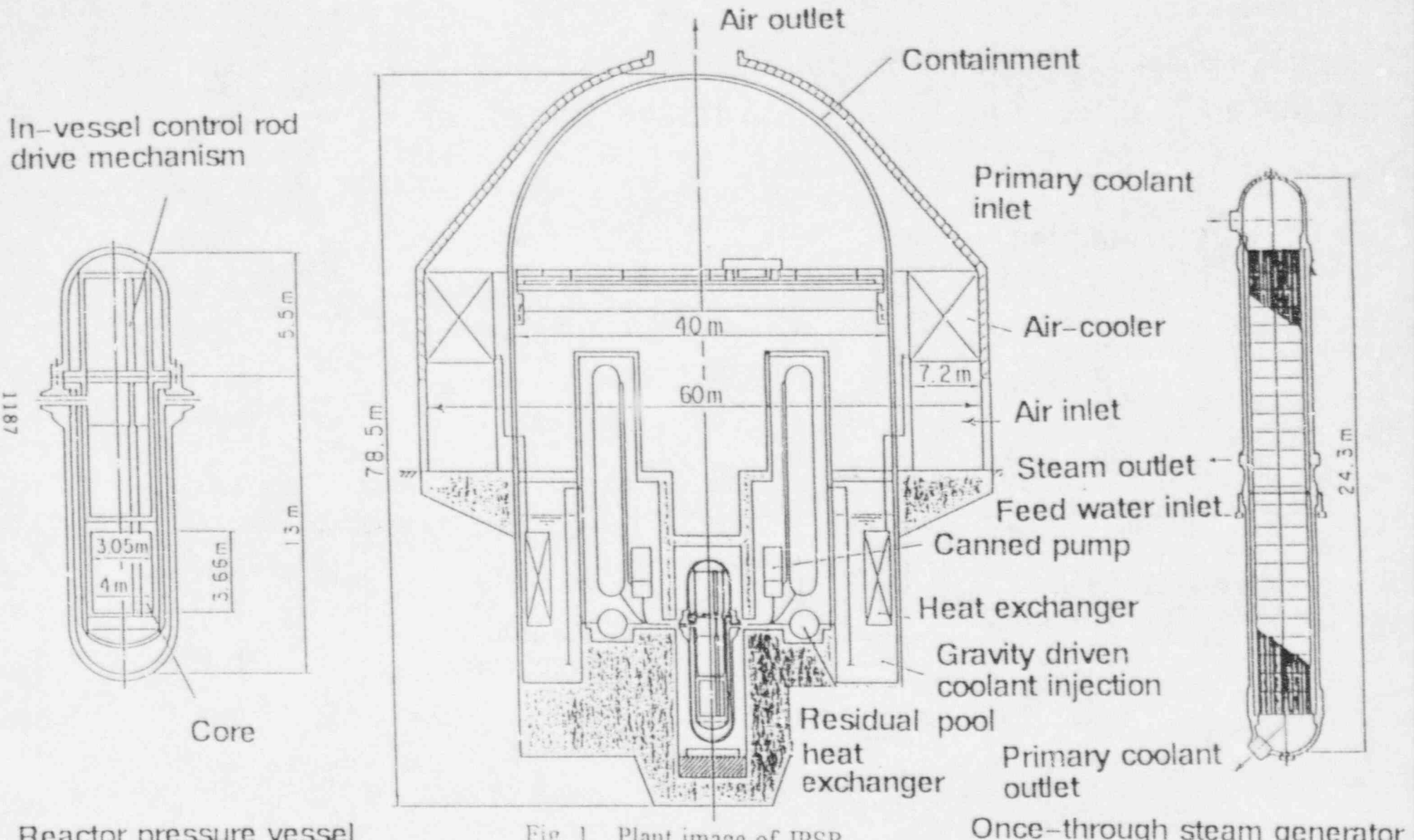

Fig. 1 Plant image of JPSR

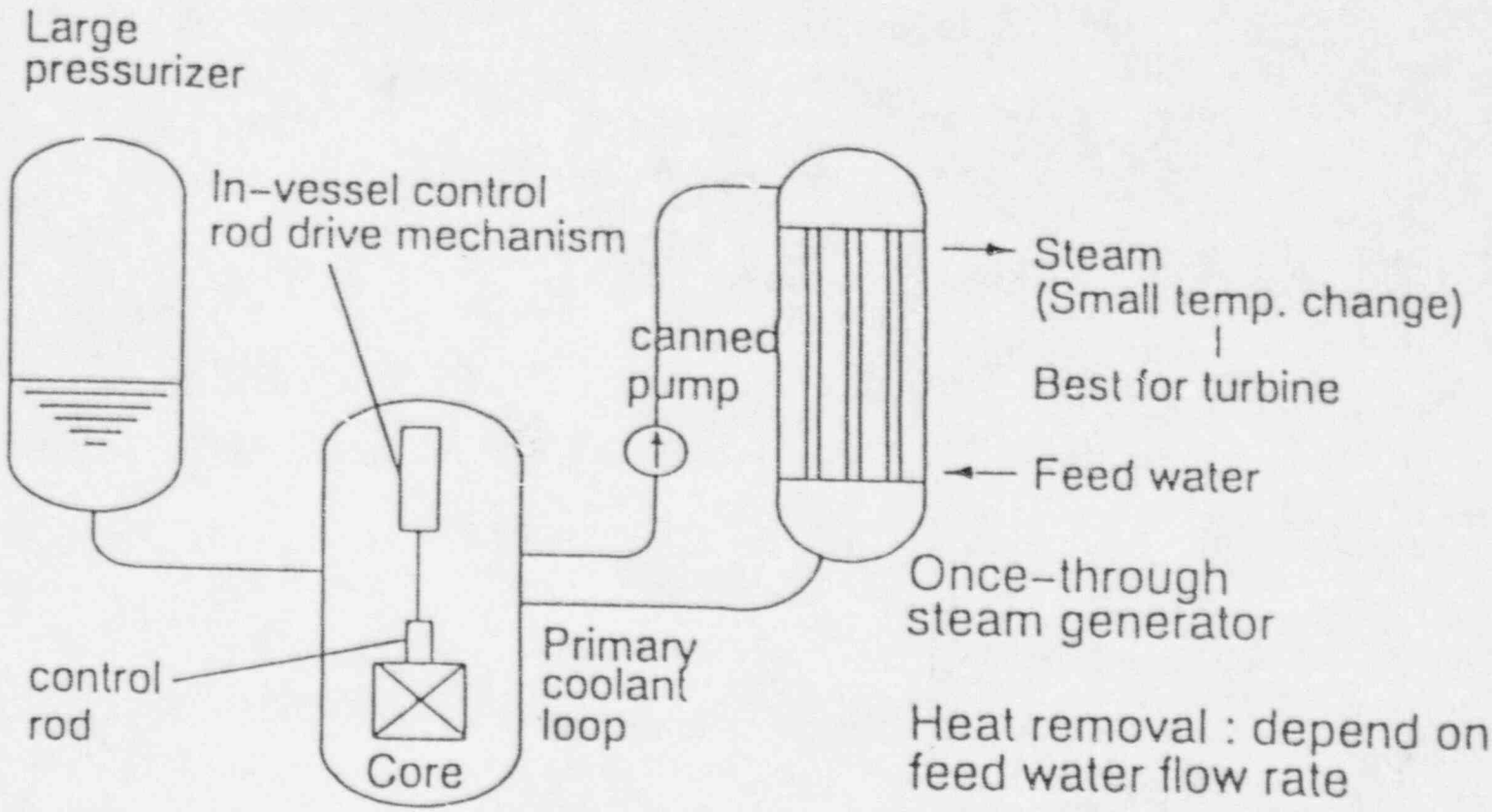

Fig. 2 Concept of primary cooling loop with inherent matching nature of core heat generation and heat removal rate

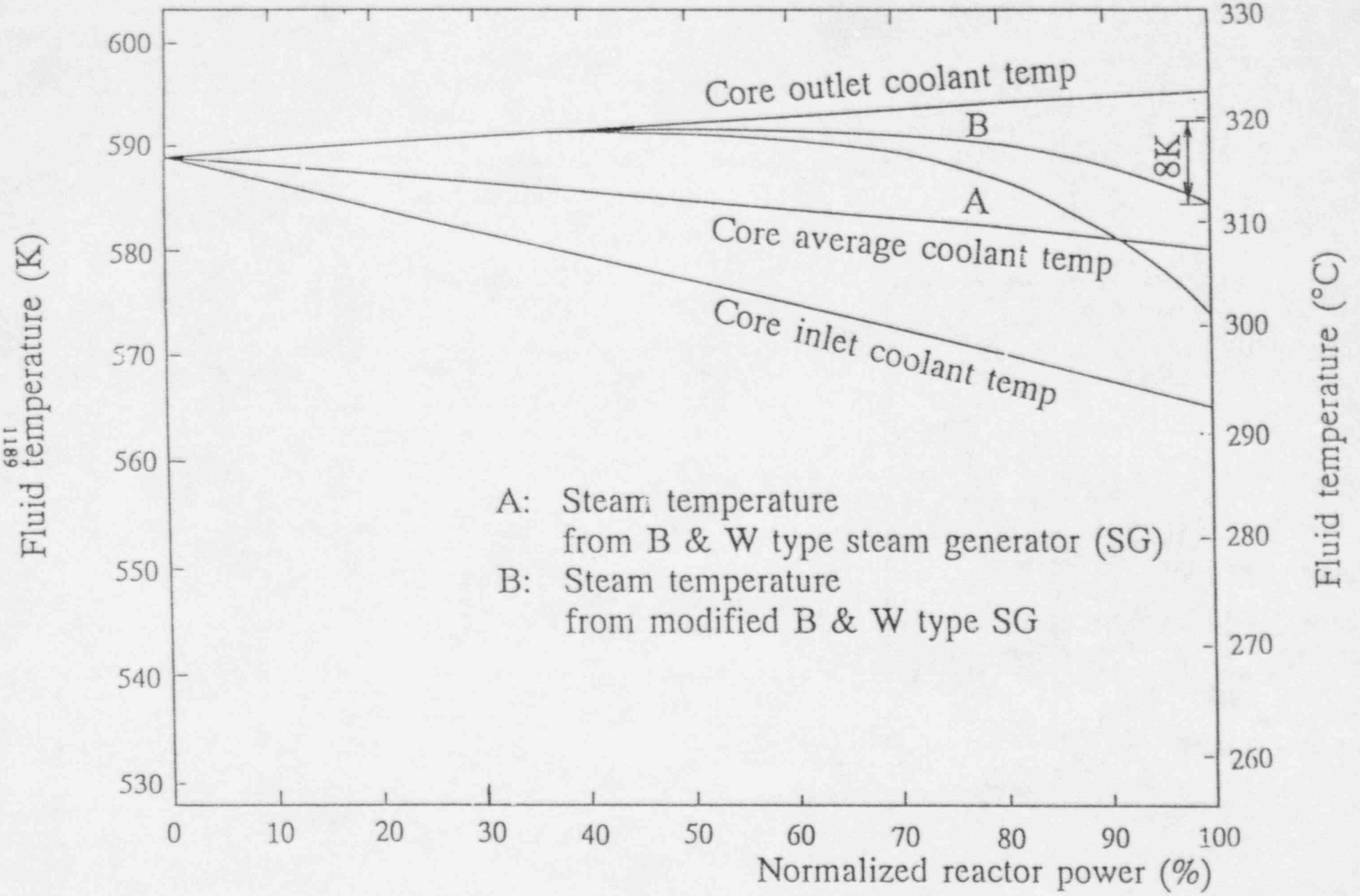

Fig. 3 Evaluated relation between reactor power and fluid temperatures

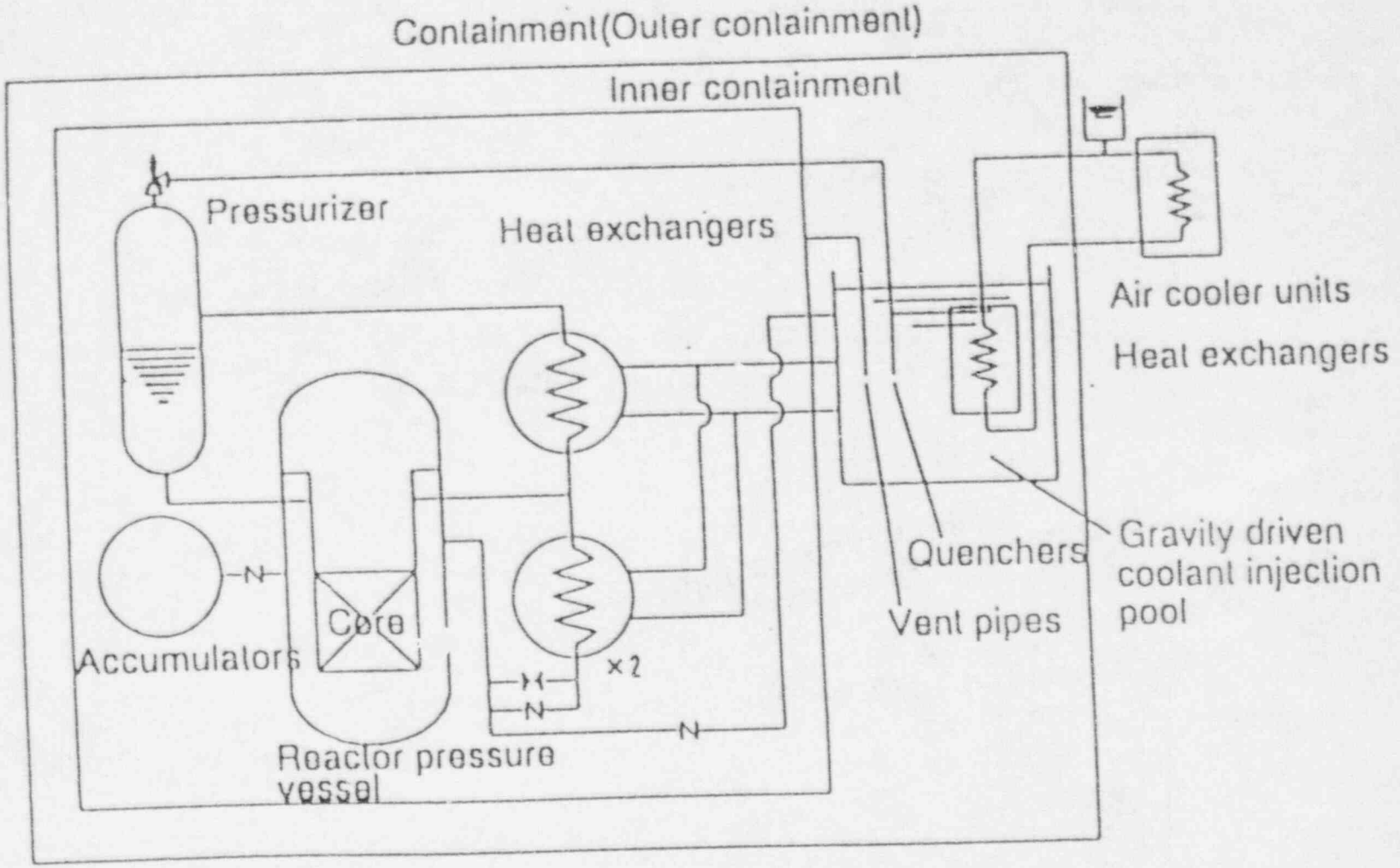

Fig. 4 Flow diagram of passive engineered-safety-features-system

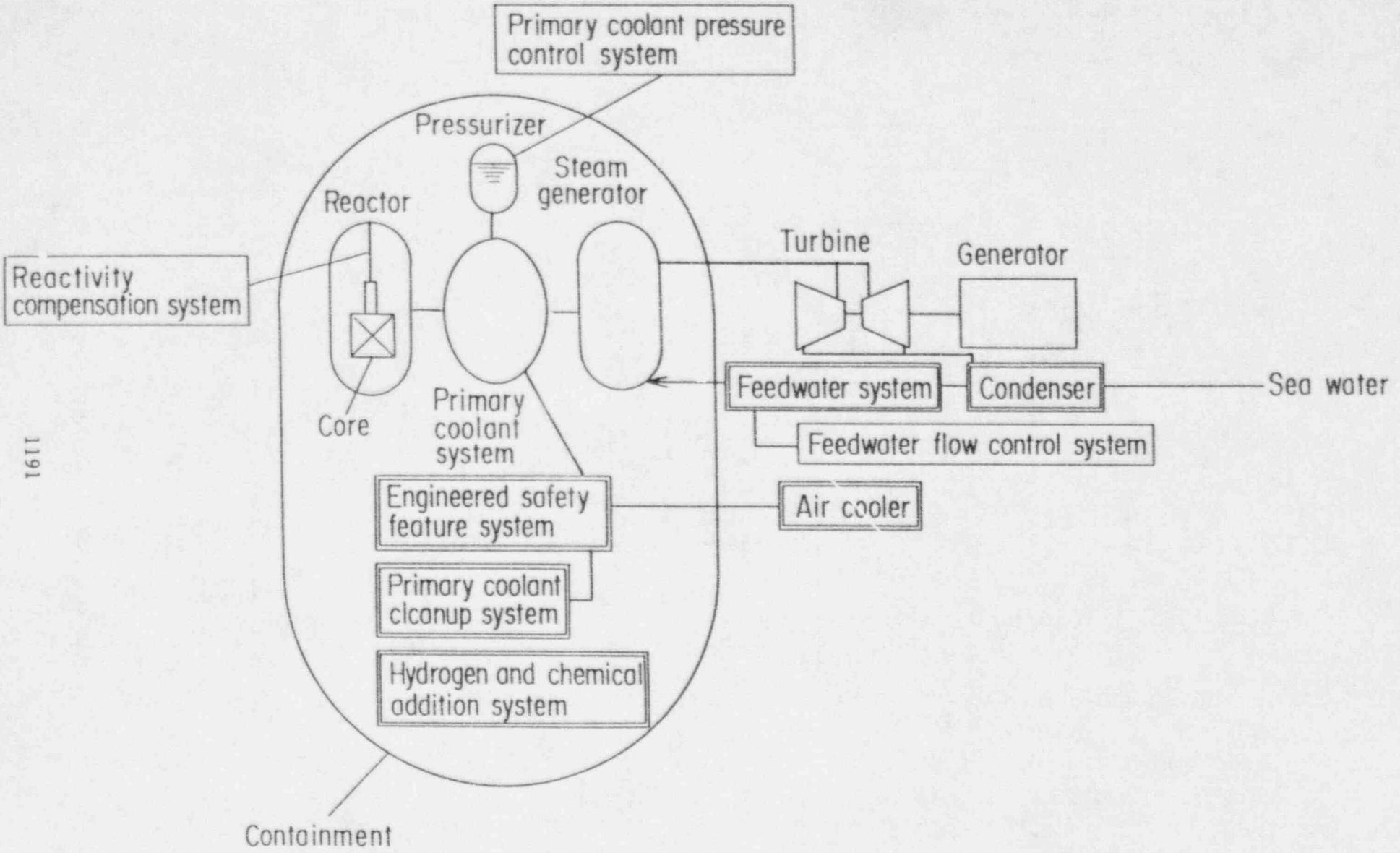

1191

Fig. 5 Outline of system organization of JPSR

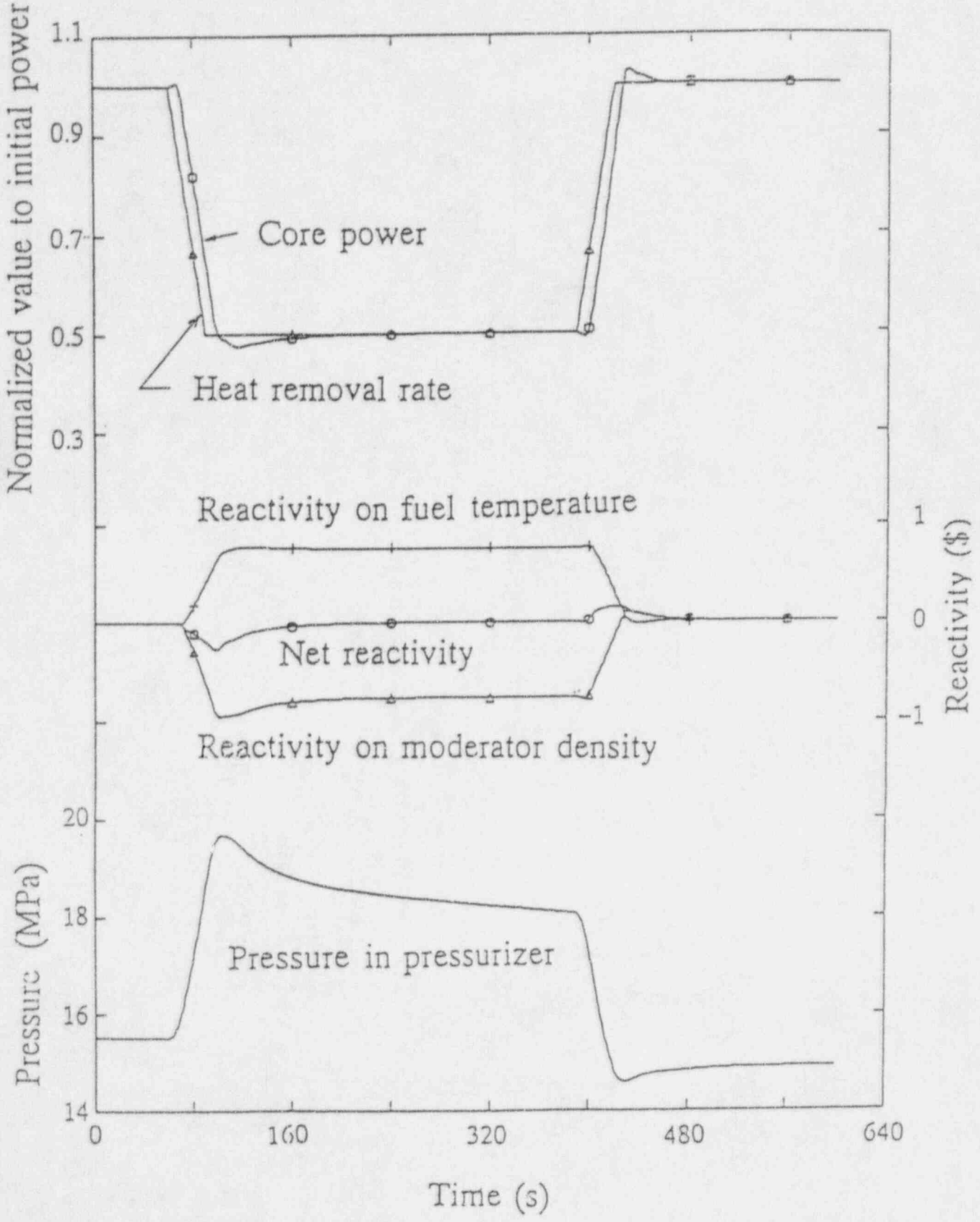

Fig. 6 Dynamic responses to change of heat removal rate

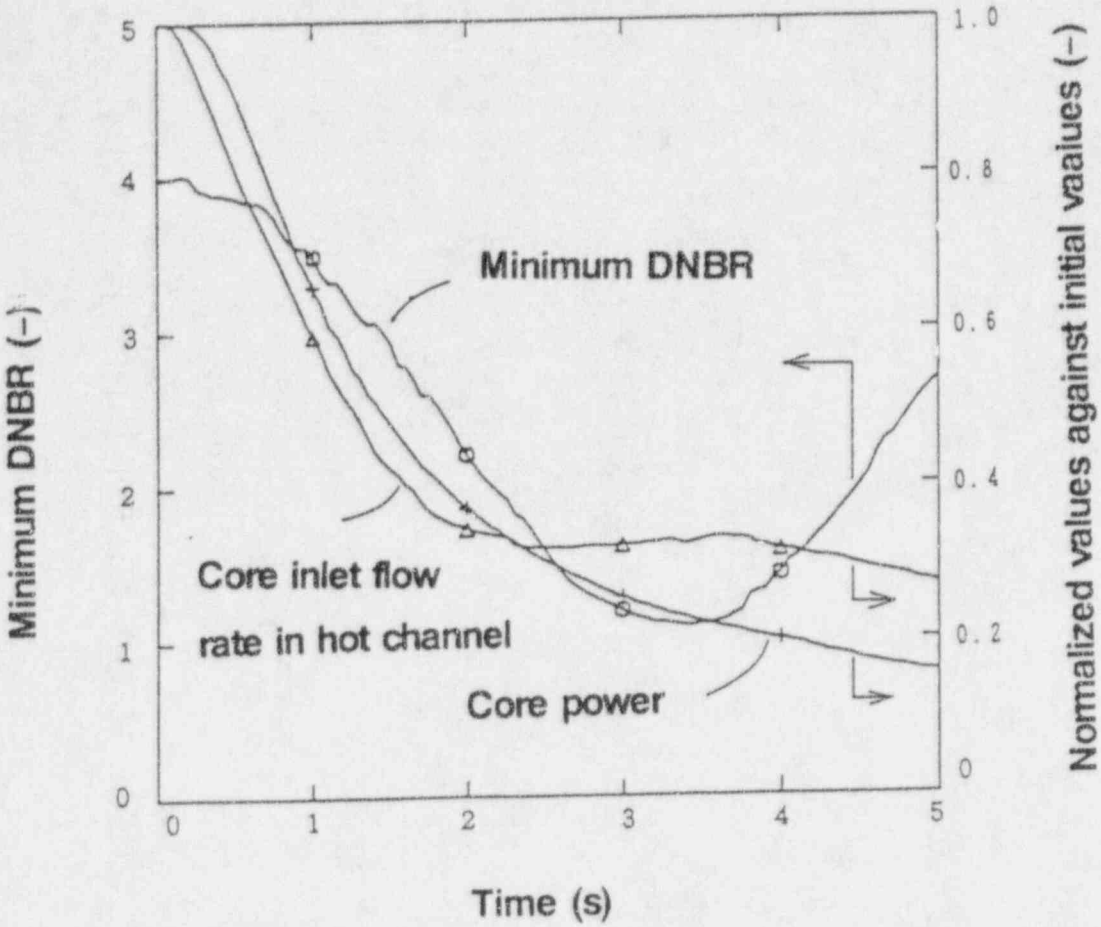

Fig. 7 Transients in pump trip event

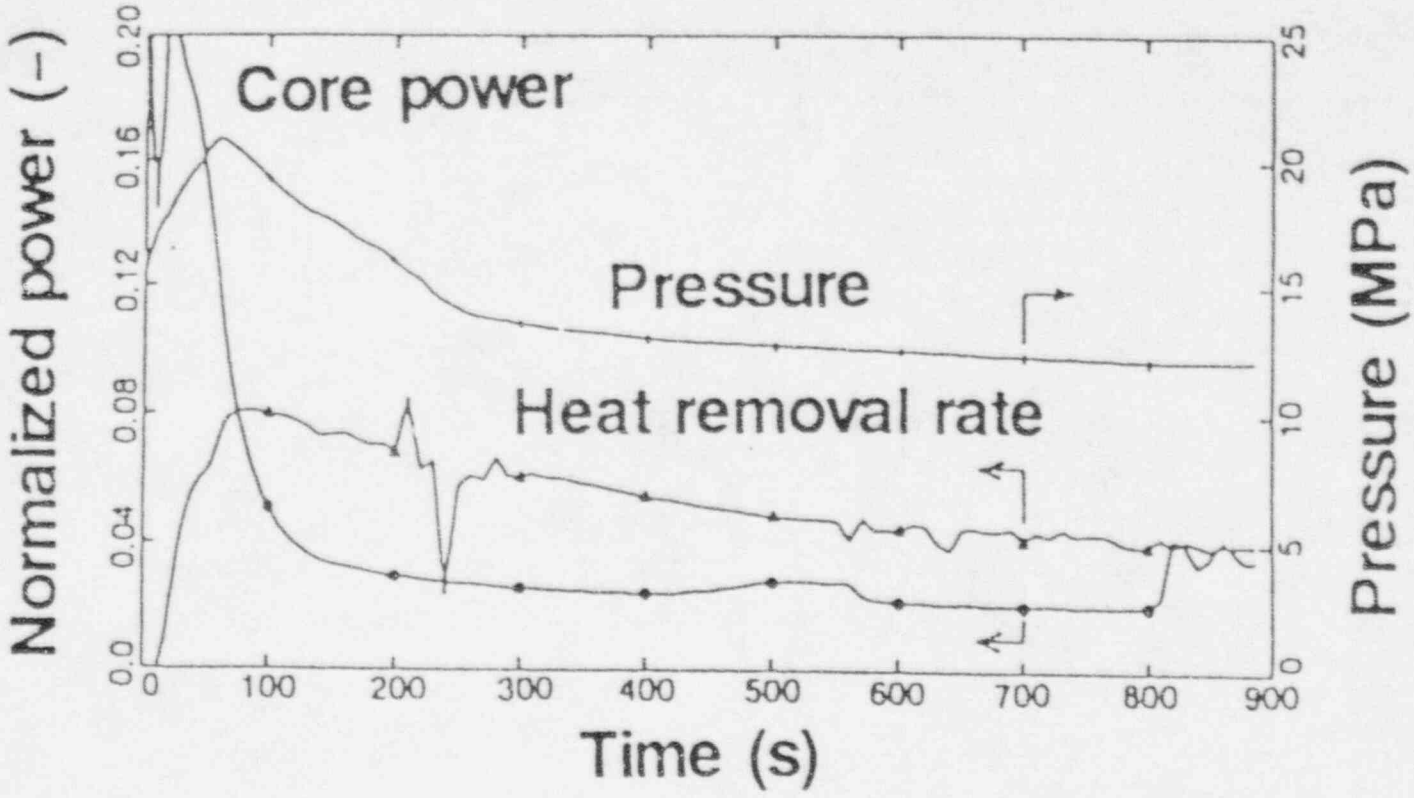

Fig. 8 Calculated transient on loss of ~~coolant~~ heat sink event

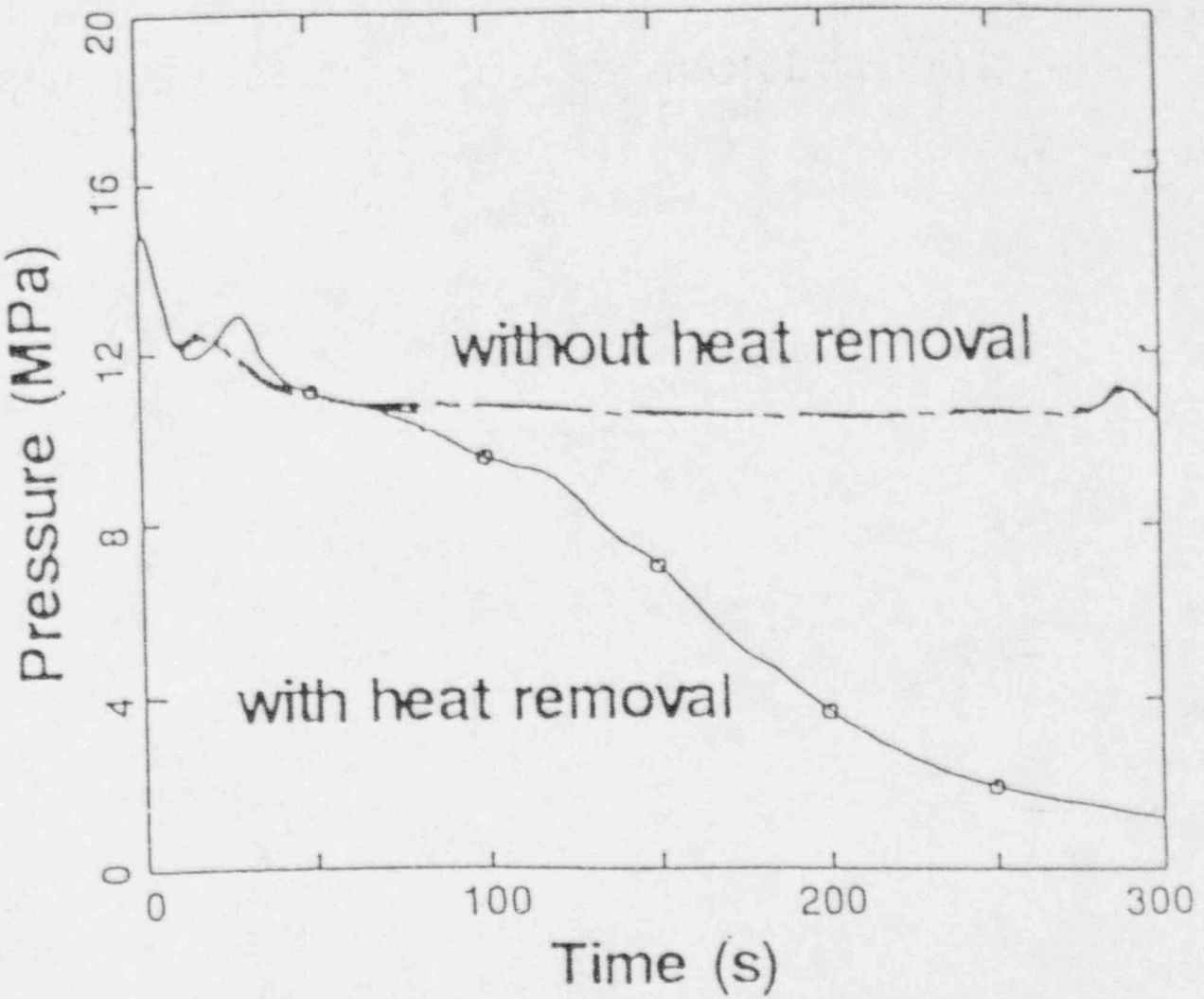

Fig. 9 Calculated transient on small break LOCA

Assessment of the Advantages of a Residual Heat Removal System Inside the Reactor Pressure Vessel

G.M GAUTIER
Commissariat à l'Energie Atomique
Direction des Réacteurs Nucléaires / Département d'Etudes des Réacteurs
Centre d'Etudes de Cadarache
13108 Saint-Paul-Lez-Durance
FRANCE

ABSTRACT

In the framework of research on diversified means for removing residual heat from pressurized water reactors, the CEA is studying a passive system called RRP (Refroidissement du Réacteur au Primaire, or primary circuit cooling system). This system consists of integrated heat-exchangers and a layout of the internal structures so as to obtain convection from the primary circuit inside the vessel, whatever the state of the loops. This system is operational for all primary circuit temperatures and pressures, as well as for a wide range of conditions: such as independent from the state of the loops, low volume of water in the primary circuit, compatibility with either a passive or an active operation mode, and compatibility with any other decay heat removal systems. This paper presents an evaluation of the performance of the RRP system in the event of a small primary circuit break in a totally passive operation mode without the intervention of any another system. The results of this evaluation show the potential interest of such a system: a clear increase of the time-delay for the implementation of a low pressure safety injection system and no need for the use of a high pressure safety injection system.

1. INTRODUCTION

For some years now, the Safety Authorities have recommended the implementation of passive systems to increase the safety of nuclear reactors, especially in the cases of regards residual heat removal [1]. Investigative studies performed at the CEA/DRN have focused on finding new systems for the removal of residual heat from pressurized water reactors. Among these new systems, the principle of a steam injector, a steam condensation system on the secondary side, as well as a system capable of removing the residual heat by means of exchangers integrated into the vessel have been examined. The latter comprises a heat sink placed as close as possible to the core, and its objective is to remove residual heat under any normal or accidental operating conditions. It has been called the RRP (Refroidissement du Réacteur au Primaire) or primary circuit cooling system. The evaluation presented herein only concerns the thermo-hydraulic performances of the RRP. The cost-effectiveness of this system will therefore not be examined.

2. MOTIVATIONS

In standard pressurized water reactors, the residual heat is first removed by the steam generators when the reactor is hot and under pressure (over ≈ 180°C and 3 MPa), then by another system for low temperature conditions. This second system is generally a loop connected to the primary circuit which has to be pre-conditioned before being put into operation. This residual heat removal principle has certain weak points: the cold source is

located far from the core, the operational field of the two systems covers a small overlap range, the active systems placed inside the containment are difficult to access in case of failure... . In view of these weak points, a diversified system, compatible with both passive and active operation modes, was researched.

3. DESCRIPTION OF THE RRP SYSTEM

The principle of the RRP system [2] consists of introducing a heat sink into the vessel as close as possible to the core, in order to create a removal route for the heat that is entirely independent of the state of the reactor loops. This heat sink is made up of several heat exchangers integrated into the vessel and placed above the core so that convection occurs inside the vessel between the core and these heat exchangers (Figure 1). The heat exchangers are contained in an annular space between two shells so as to channel the flow of primary circuit water along the tube bundle. This annular space comprises two series of openings, one in the upper part corresponding to the inlet of the primary coolant, the other in the lower part corresponding to the outlet of the primary coolant. This second series of openings allows the primary coolant to join the greater part of the primary circuit water from the loops. So that the flow along the integrated heat exchangers is always directed downwards, thus avoiding a core bypass during primary pump operation, a pump-type suction system is placed at the level of the outlet openings. This system creates a local underpressure such that the pressure at the outlet opening is slightly lower than the core outlet pressure. This is achieved by a venturi effect which is created by narrowing the flow area into the down-comer, inducing an increase of the coulant velocity. For a core pressure drop of 0.2 MPa, the velocity at the venturi passage is of 25 m/s.Thus, when the reactor is under normal operating conditions, that is to say with the primary pumps in operation, a small part of the primary flow by-passes the loops through the integrated heat exchangers. When the primary pumps are not in operation, for instance in the event of a loss of power, natural convection is started up inside the vessel between the core and the integrated heat exchangers. The upper openings are placed slightly under the lower level of the inlet and outlet nozzles of the primary loop, so as to allow natural convection in the vessel, even if the primary loops are completely dewatered. Thus, the RRP is a decay heat removal system, which is entirely independent from the state of the reactor loops, as long as there is a high enough water level in the vessel. In the case of an accident situation with a two-phase mixture in the vessel, the RRP remains operational, but is less efficient. This loss of efficiency contributes to a longer time-delay (cf paragraph 6).

The heat removed by the integrated heat exchangers is transferred to a final cold source by an intermediate solid circuit outside the vessel, designed to allow totally passive operation (according to the recommendations of the safety authorities). This is achieved by a circuit able to function in natural convection and comprising a water-air heat exchanger as a cold source. This heat exchanger has at its top a cooling tower to favour natural air convection (Cf. Figure 2). Active-passive compatibility is achieved by possible operation in forced or natural convection in the intermediate circuit and on the cooling tower.

The RRP system is composed of several independent trains. Each train comprises an integrated heat exchanger, an intermediate circuit, and a cooling tower. The RRP system is actuated by simply opening the air valves at the foot of the cooling towers. In order to make this procedure easier, the air valves are automatically opened in the event of a reactor scram.

4. MAIN CHARACTERISTICS OF THE RRP SYSTEM

When the primary circuit is intact, the aim of the RRP system is the removal of the residual heat in a totally passive manner, with no other intervention except for the opening of the air

valves. The only available cold source in addition to the RRP system is the thermal inertia that comes from the evaporation of the secondary water contained in the steam generators without make-up water. The envelope situation considered corresponds to a generalized loss of power, simultaneouly with a complete loss of feedwater supply, situation for which an unavailable RRP train and an unavailable steam generator thermal inertia are considered as aggravating factors. The power of the RRP system order totally passive operation is thus equal to the residual heat when the steam generators have just been emptied of their water by evaporation through the pressure relief valves. For this envelope situation, the residual power is removed in two ways : by the RRP and by the evaporation of the steam generator secondary water. In a standard PWR, the time needed to dry the steam generators with the residual power is of one hour. After one hour, the residual power is 1.3% of the nominal power. In the case of a PWR with an RRP, the time needed to dry the steam generators is of four hours. After that time, the residual power is slightly lower than 1% of the nominal power. The power of the two-train RRP must be equal to that of the residual power when the SGs are dry, in other words, 14 MW by train for an PWR of 900 MWe.

The objective above corresponds to operating conditions with unavailabilities. In normal operating conditions, that is to say with forced convection in the intermediate circuit and in the cooling towers, the heat removal capacity of the RRP system is significantly improved. This forced convection is required to bring the reactor to cold shut-down in a lapse of time compatible with usual reactor operation constraints.

For a 900 MWe PWR with three loops, like those used by Electricité de France [3], the RRP system would be composed of three independent trains. The main characteristics of the integrated heat exchangers are given in Table 1.

5. POTENTIAL ADVANTAGES OF THE RRP SYSTEM

The RRP system with its in-vessel heat exchangers -as close as possible to the heat source- aims to simplify residual heat removal to the utmost: the primary circuit is reduced to a simple hydraulic loop under natural convection, the intermediate circuit allows operation under natural convection and, upstream, it is once again natural convection that ensures release to the ultimate cold source by means of a cooling tower. This simplified design presents a certain number of advantages as regards safety:

- Single failure is taken into account thanks to several independent trains;
- Diversification of the residual heat removal routes: possibility of simultaneous operation of the RRP and the SGs;
- Extension of the operating range (under all pressures and temperatures);
- Compatibility with active or passive operating conditions;
- Permanent operation with forced convection in the intermediate circuit and closed air valves: elimination of the pre-conditioning phase and possibility of testing the RRP system with the reactor in operation;
- Limitation of the number of components:
  -Start-up by opening of the air valves located outside the containment
  -Pumps and fans, for active operation, also located outside the containment;
- Reduction of circuit sections carrying the primary coolant;
- Positioning the heat exchangers as close as possible to the core can only improve the efficiency of the system;
- Simplification of the procedures related to the removal of the residual heat resulting in a reduction of the probability of operator error;
- Limitless autonomy of the cold source;
- Small amount of primary circuit water required to ensure efficiency.

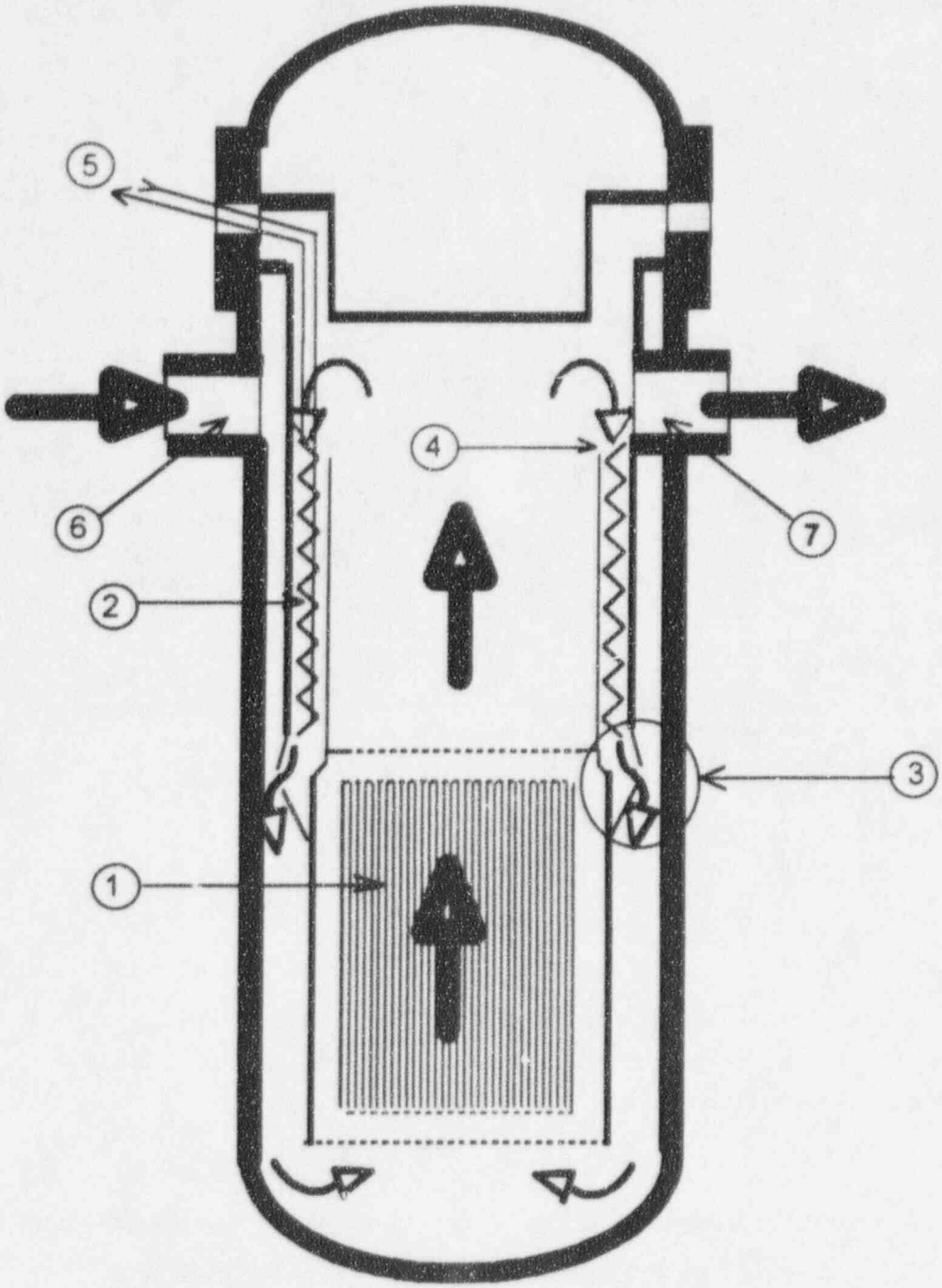

1	Core	5	Towards the air cooler
2	Integrated heat exchangers	6	Input nozzle
3	Suction system	7	Output nozzle
4	Upper opening		

Figure 1
Diagram of the Principle of Coolant Circulation in the Vessel.

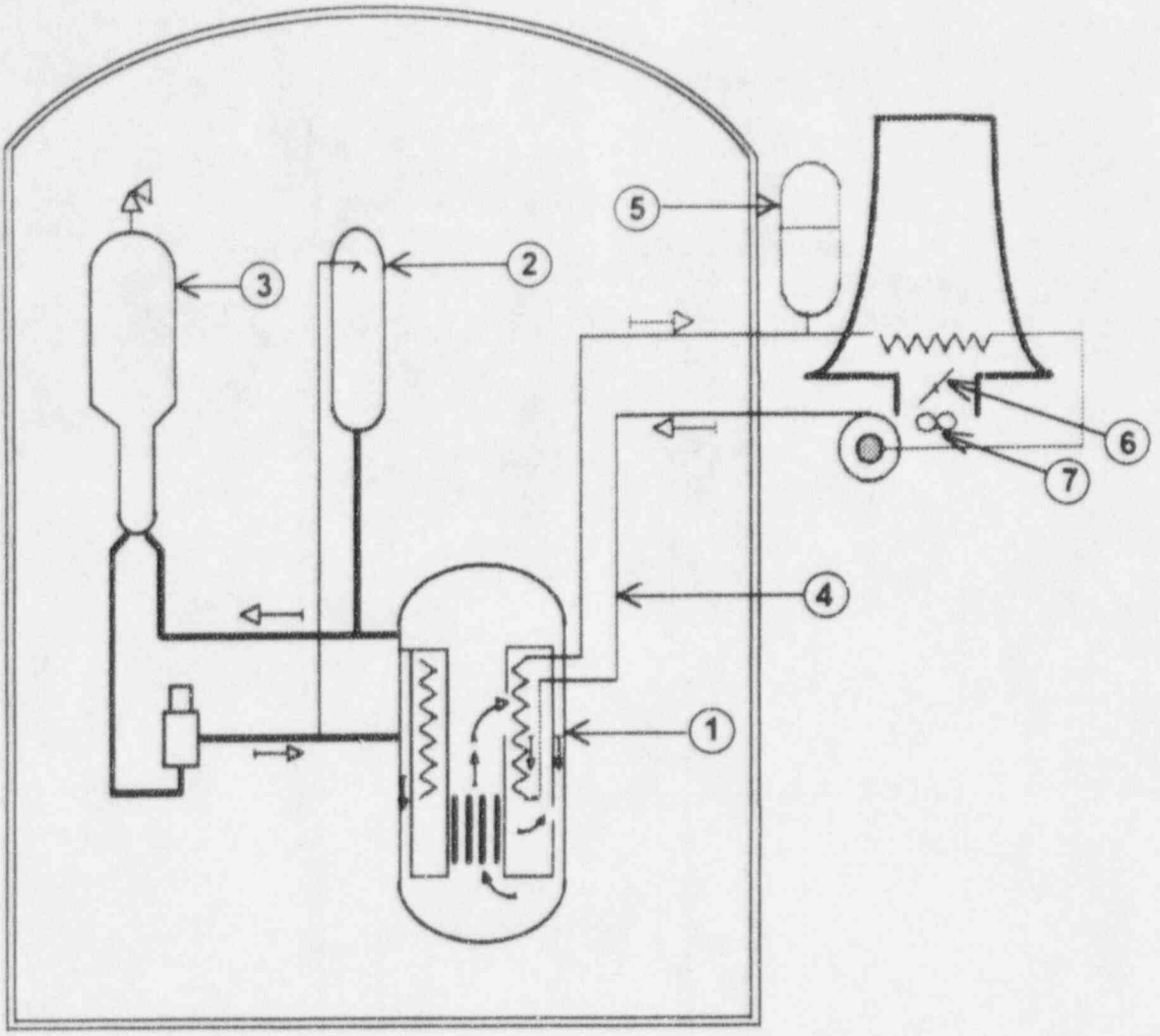

1	Reactor vessel with the integrated heat exchangers	4	Intermediate circuit
2	Pressurizer	5	Expansion tank
3	Steam generator	6	Air valve
		7	Air supply fan

Figure 2
Diagram of the Principle of the RRP System
with the Intermediate Circuit and Cooling Tower

Geometric Characteristics:

Number of integrated heat exchangers	3
External diameter of the tubes	19.05 mm
Thickness of the tubes	1.09 mm
Bundle spacing	28.5 mm
Type of array	triangular
Length of tubes	3 m
Number of tubes per heat exchanger	1050
Exchange surface area	190 m^2
mean elevation between core and heat integrated exchangers	3.5 m
elevation between the two heat exchangers of the inter. circuit	20m
height of the air cooling towers	35 m
Exchange surface area of the air cooler	5200 m2

Operating Characteristics (intact primary circuit):

Operating mode	passive	active
Number of RRP trains in service	2/3	3/3
Extracted heat	28	80 MW
Primary circuit inlet temperature	270.9	300.3 °C
Primary circuit outlet temperature	251.6	264.2 °C
RRP intermediate inlet temperature	231.6	231.8 °C
RRP intermediate outlet temperature	186.8	212.6 °C
Core primary circuit flow rate (natural convection)	292	428 kg/s
Intermediate circuit flow rate	69	300 kg/s

Characteristics of the Primary Vessel

Increase in diameter	≈ 0.6 m
Extension of the vessel body	≈ 3 m

TABLE 1: Main Characteristics of the RRP SYSTEM

At the present time,studies have mostly been on the thermo-hydraulic performances of the RRP in view of its decay heat removal. Several points must be examined in order to confirm the safety advantages of this system. These mainly are :

- The integrated exchangers must be designed so as to resist to different external events, such as earthquakes, and to the strain due to large LOCAs.
- The whole intermediate circuit must resist to the primary pressure.
- The integrated heat exchangers must be designed so as to be inspected and removed.
- The intermediate circuit can present a containment bypass risk, since it runs through the vessel and the containment, even though its design offers two barriers : the heat integrated exchanger and the air cooler. If the safety analysis were to show too high a bypass risk, safety isolating valves could be placed at the piping penetration of the containment, as is the case now for the secondary circuit.

6. ASSESSMENT OF RRP BEHAVIOUR IN ACCIDENTAL CONDITIONS

The RRP system has a great many potential advantages, especially that of being operational with only a small amount of primary circuit water, particularly in an accidental situation such as a break in the primary circuit. Such a situation always requires an injection of water in the primary circuit; the RRP system, however, should improve the management of these situations because of the presence of a heat sink located in the vessel. In order to evaluate this improvement, modelling of the RRP system was performed by means of the CATHARE computer code [4]. CATHARE (Code for Analysis of THermalhydraulics during an Accident of Reactor and Safety Evaluation) has been developed in order to perform best estimate calculations of pressurized water reactor accidents: PWR loss of coolant (large or small break, primary and secondary circuit). It has been developed in Grenoble by the French Atomic Energy Commission (CEA), Electricité de France (EdF) and Framatome.

The calculations were made on a French 900 MWe PWR model, including the integrated heat exchangers and the suction system (Cf. Figure 3). The introduction of the heat exchangers in the vessel induces has rather slight negative effects on the normal operating conditions. Indeed, with the same primary pump as that of the PWR of 900 MWe, the complete primary flow in the vessel decreases from 14490 kg/s to 14320 kg/s and the vessel pressure drop increases from 0.27 MPa to 0.31 MPa. When the primary pumps are in operation, the partial flow on the integrated heat exchangers and returning to the downcomer is of 260 kg/s. The core flow remains unchanged due to the return flow of the RRP, which adds itself to the slight drop in the vessel flow.

The thermo-hydraulic evaluation of the RRP has been done on an accident situation, taking into consideration no active intervention during the progress of the transient, that is to say no auxiliary feedwater supply of the steam generators, no safety injection (except the safety injection by the accumulators which are passive elements) and no other cold source. The anticipated situation only takes into account the RRP cold source and a complete black-out. Therefore, other aggravating factors will not be considered: all the RRP trains are operational. The intermediate circuit was modelled by a loop operating in natural convection.The CATHARE code is not able to calculate several series-connected circuits (primary circuit, intermediate circuit and air circuit of the air cooler), so, the power removed at the cold source is simulated by a limit condition, resulting from operating conditions modelling of the intermediate and air circuits. For a given geometry, these two circuits operating in natural convection, and for an inlet air temperature of 35°C, there is only one single operating point according to the power removed. Under these conditions, a parametric study at different powers enables us to deduce the following law of limit conditions:

$W = 51\,000.\ (\theta-35)^{1.27}$

where W is the total power removed in the three cooling towers (in watts),
θ is the temperature of the hot leg of the intermediate circuit (in °C).

At the present stage of the assessment, the study of the accidental transient conditions focused on the management of 5 and 10 cm primary circuit breaks in the cold leg. These transient conditions were selected because of the risk of core melting that could result from poor management. For small breaks, if there is no efficient intervention at high pressure, the primary circuit empties while remaining under high pressure, thus precluding any low pressure injection.

For each accidental transient, the assessment is made by comparing the results of two series of calculations, one considering no cold source (zero removal by the RRP), the other considering the RRP in operation.

6.1. A 5 cm-Break in the Cold Leg

RRP out of order (Figure 4)

In this accident, there is rapid depressurization to a plateau of 7.5 MPa (Figure 4a), which corresponds to the set pressure of the secondary side. This plateau is due to the two-phase equilibrium of the primary circuit, where the temperature is imposed by the secondary side temperature via the steam generators.

The residual heat is removed through two routes, one of these being the break itself, the other being the set of steam generators. The transient progresses in three stages.

1. Pressure Plateau - Flooded Break (2 200 s)

During this stage, the steam generators remove about 80 % of the residual heat and the remainder is removed at the break (Figure 4b). During this period, the flow at the break is essentially in liquid form. The vapour flow rate, and consequently, the enthalpic flow rate are low. The water mass of the primary circuit decreases by ≈ 55 kg/s (Figure 4c), until dewatering of the break.

2. Pressure Plateau - Break in vapour phase (2 200 to 3 500 s)

When the break is dewatered, the break flow rate decreases, and stabilizes around a value of slightly less than 20 kg/s. It is mainly formed of vapour which allows about 80 % of the residual heat to be removed at the break (Figure 4b). The steam generators remove the remainder while maintaining the primary circuit pressure at the same level as that of the first stage. This pressure does not allow a safety injection by the accumulators set at a pressure of 4 MPa (Figure 4f).

3. Core Temperature Rise

Around 3 500 s, the mass of primary circuit water lost is such that the core begins to uncover. The fuel rods are less and less cooled. The cladding temperature rises rapidly at a rate of close to 1°C/s (Figure 4e). At this time, the water mass in the primary circuit is 60 000 kg (Figure 4d) and continues to drop with a total flow rate at the break identical to that of the second stage. The primary circuit pressure is still the pressure imposed by the set pressure of the steam generators. It only begins to drop after 4 000 s, when the cladding temperature reaches high values.

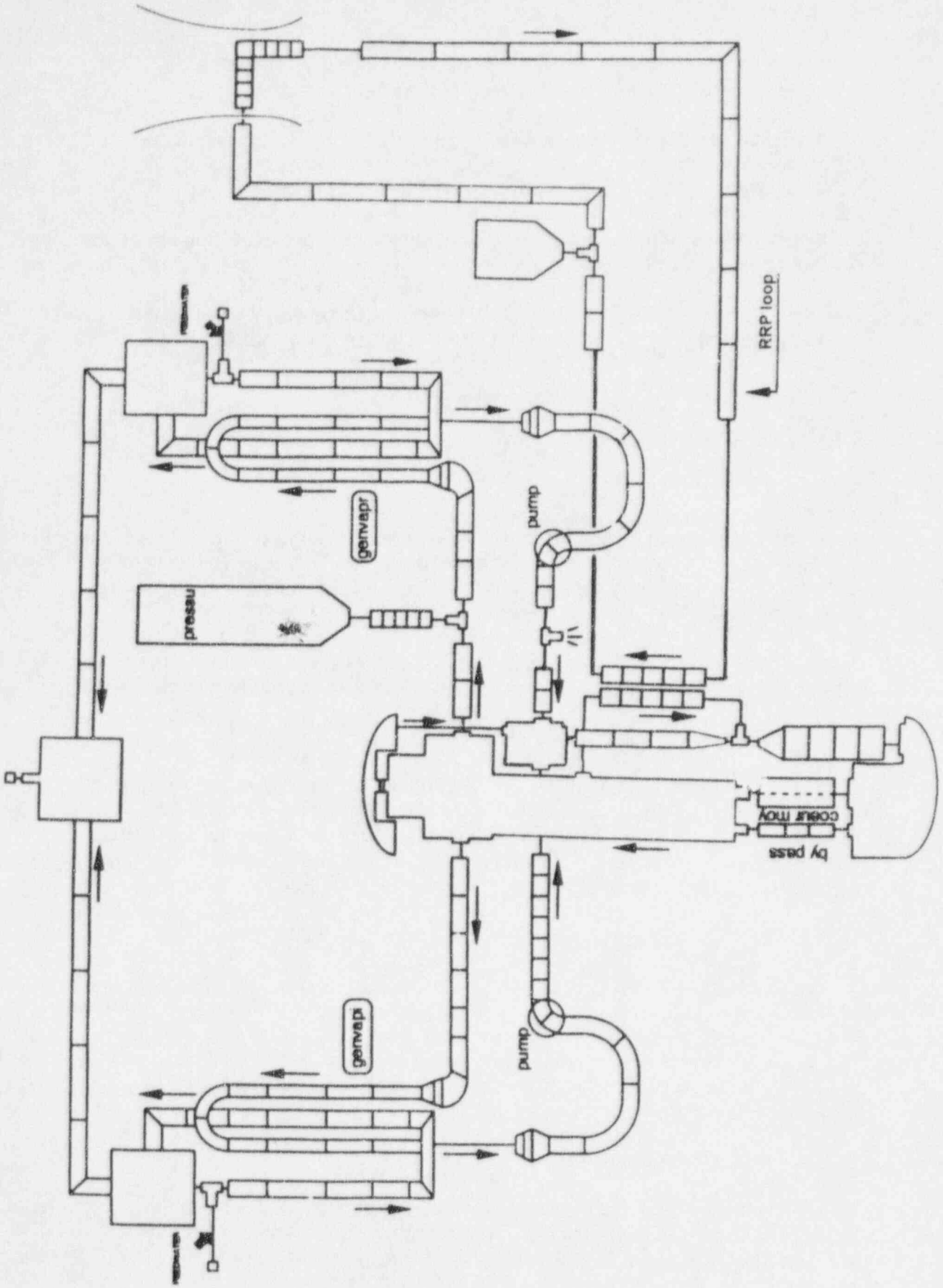

Figure 3
Diagram of the Primary Circuit and of the RRP for the CATHARE Modelling

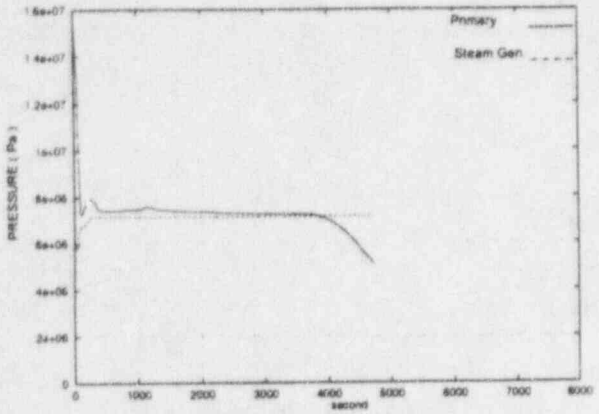

Fig. 4a: Pressure Evolution

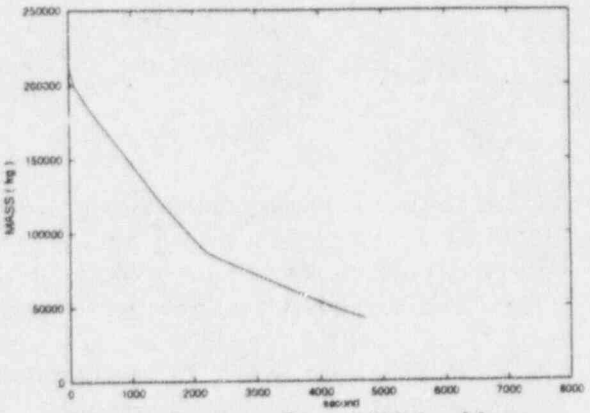

Fig. 4d: Primary Circuit Water Mass

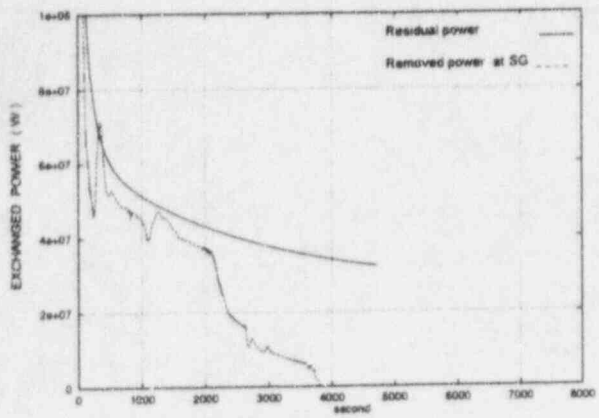

Fig. 4b: Heat exchanges

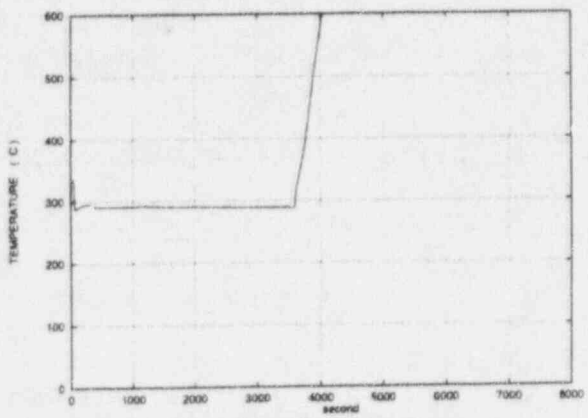

Fig. 4e: Cladding Temperature

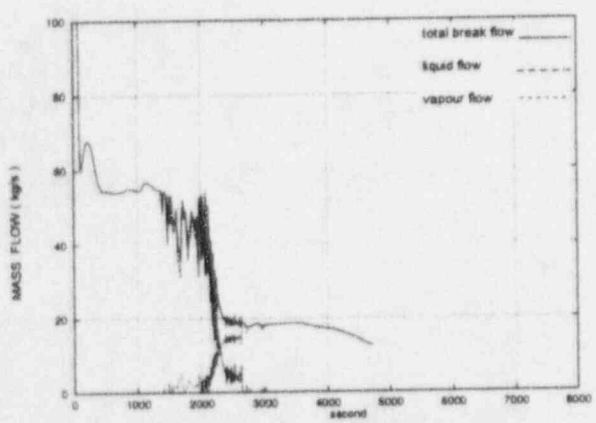

Fig. 4c: Break Flow Rates

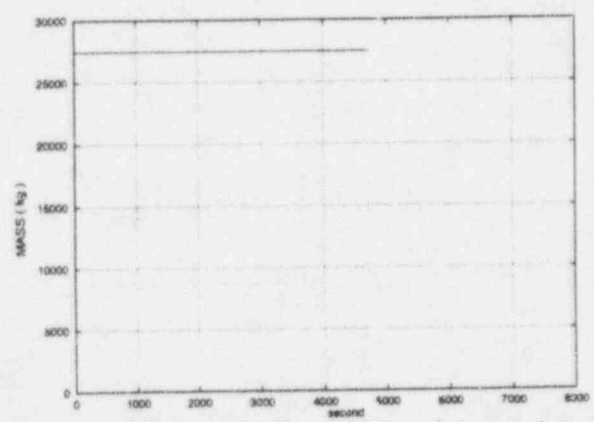

Fig. 4f: Mass of Water in the Accumulators

Figure 4
A 5 cm Break with no RRP Intervention

RRP system In Service (Figure 5)

The progress of this transient with the RRP system in operation can also be divided into three stages, although these are characterized by different phenomena

1. Pressure Plateau - Flooded Break (≈ 2 000 s)

As in the previous case, the beginning of the accident is characterized by a rapid drop of the primary circuit pressure to 7.5 MPa, a pressure imposed by the set pressure of the secondary relief valves (Figure 5a). At the beginning of this stage, a large part of the residual heat is removed by the steam generators, then by the RRP system which takes over at around 700 s (the time lapse for the power build-up of the RRP system), with a power of 40 MW (Figure 5b). As in the previous case, this stage is characterized by a flow at the break that is essentially liquid in form, with a flow rate of nearly 55 kg/s (Figure 5c). The vapour flow rate at the break being low, the residual heat removed at the break is also low. The end of this stage is characterized by dewatering of the break. At this time, the heat removed by the RRP system is practically equal to the residual heat, so that the steam generators no longer remove any heat. The secondary relief valves close. The primary circuit temperature and the primary circuit pressure are no longer linked to the secondary side and begin to drop. During this stage, natural convection inside the vessel between the core and RRP system heat exchangers has set in, to the advantage of the natural convection in the loops.

2. Depressurization - Break in vapour phase (from 2 000 to 3 500 s)

At the beginning of this period, the break is mainly supplied by the vapour with a flow rate of ≈ 17 kg/s (Figure 5c). The primary circuit pressure slowly decreases, as does the cladding temperature (Figure 5e) which follows the saturation temperature. The RRP system removes about 80 % of the residual heat, the remainder being extracted by evaporation of the primary circuit water at the break. At 3 500 s the mass of water in the vessel is 65 000 kg (Figure 5d), and the pressure reaches the threshold of the injection pressure of the accumulators, that is to say 4 MPa.

3. Safety Injection by the Accumulators

The injection flow rate is low in view of the fact that there is little pressure difference between the primary circuit and the accumulators (Figure 5f). It stabilizes at around 10kg/s for the three accumulators together. This flow rate compensates for the leakage of primary circuit water, which removes a small part of the residual heat through the break, so that the mass of primary circuit water remains constant. The primary circuit pressure continues to decrease slowly; it reaches about 1.8 MPa at 8 000 s after the beginning of the transient. Although the accumulators are not empty, the primary circuit pressure is low enough to allow the start-up of the low-pressure safety injection system.

6.2. A 10 cm Break in the Cold Leg

RRP Out of Service (Figure 6)

As in the 5 cm break, the transient progresses in three stages, but with more rapid kinetics.

1. Pressure Plateau - Flooded Break (≈ 600 s)

During this stage, the primary circuit pressure decreases very rapidly and stabilizes at about 7.5 MPa (Figure 6a), a value set by the set pressure of the steam generator valves.

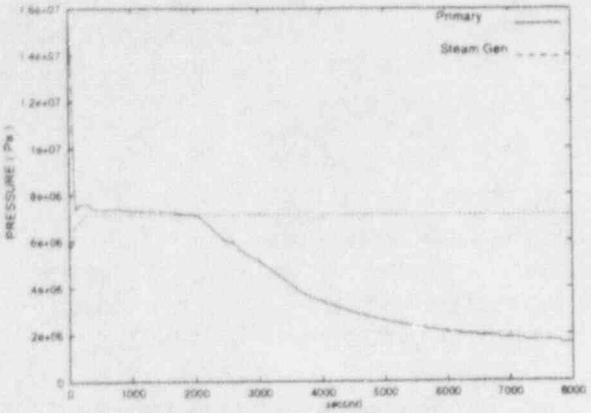

Fig. 5a: Pressure Evolution

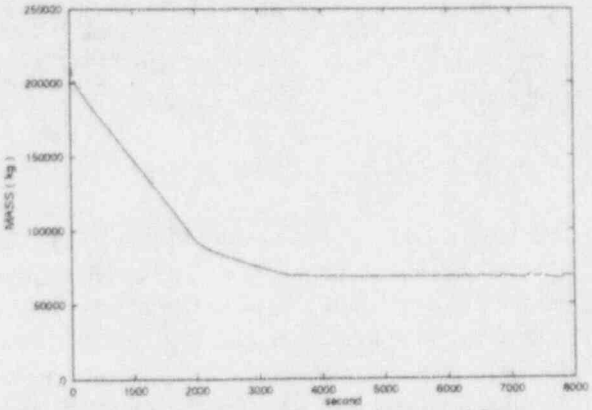

Fig. 5d: Primary Circuit Water Mass

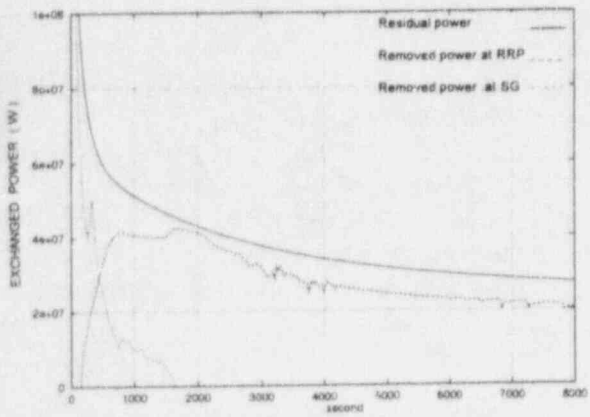

Fig. 5b: Heat exchanges

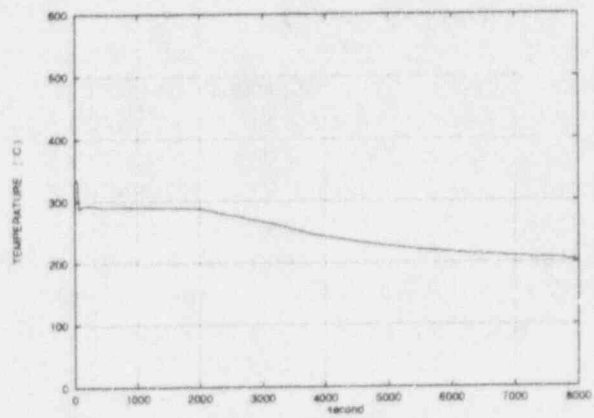

Fig. 5e: Cladding Temperature

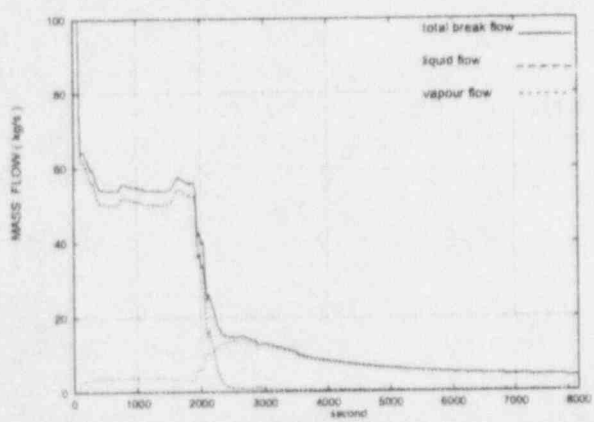

Fig. 5c: Break Flow Rates

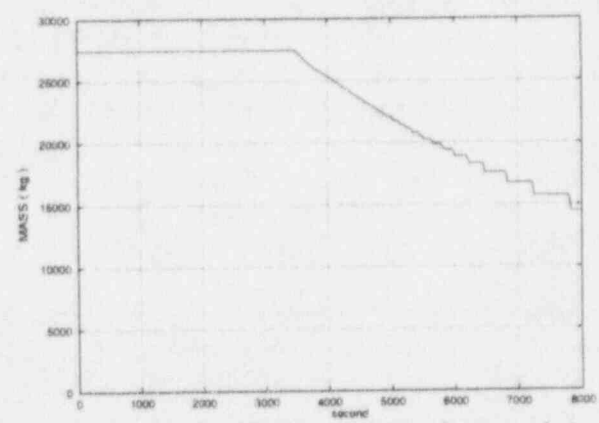

Fig. 5f: Mass of Water in the Accumulators

Figure 5
A 5 cm Break with RRP system Intervention

The flow rate at the break is high ≈ 220 kg/s (Figure 6c); it is mainly single-phase. After 600s, the mass of water remaining in the primary circuit is close to 80 000 kg (Figure 6d). During this period, the heat removed by the steam generators represents about 80 % of the residual heat.

2. Depressurization - Break in vapour phase (from ≈ 600 to ≈ 1 050 s)

After dewatering of the break, the flow rate is still high; this implies a decrease of the primary circuit pressure and thence, a slight drop in temperature of the coolant and the fuel cladding (Figure 6e). The steam generator no longer removes any heat, because some of the secondary water is slightly hotter than the primary circuit water (Figure 6b). All the residual heat is removed through the break. The total flow rate at the break is still high (≈ 50 kg/s) and contributes to decreasing the mass of water remaining in the vessel. After 1 000 s, the upper plenum is empty, the level of the water settled in the core is at mid-height. At the same moment, the primary circuit pressure reaches 4 MPa, the intervention threshold of the accumulators (Figure 6f).

3. Core Heating (after 1 050 s)

Although the accumulators are set in action, the mass of injected water is not enough to reflood the core; it only allows a constant amount of water of about 50 000 kg (Figure 6d) to be maintained in the vessel. The core flow rate is very low, of the order of a few tens of kg/s. The pressure drops, while the temperature of the fuel rises rapidly (Figure 6e). Because of the new temperature rise of the vapour associated with that of the cladding, a small part of the residual heat is removed by the steam generators. The greater part of the residual heat is removed through the break on the one hand, and by the rise in temperature of the fuel on the other hand.

RRP in Action (Figure 7)

1. Pressure Plateau - Flooded Break (≈ 550 s)

There is a rapid drop in pressure in the primary circuit (Figure 7a) which stabilizes at around the set pressure of the secondary circuit relief valves. The primary circuit temperature is close to 280°C (Figure 7e). During this period, the RRP system builds up power until it reaches slightly less than 40 MW (Figure 7b). The mass of primary circuit water decreases rapidly (≈ 220 kg/s). The RRP heat exchangers create a cold spot in the vessel, thus favouring natural convection inside the vessel to the detriment of the loops which are soon in vapour. As in the previous case, the end of this period is characterized by dewatering of the break with a stop to residual heat removal by the steam generators (Figure 7b).

2. Depressurization of the Primary Circuit - Break in vapour phase(from ≈550s to ≈1000s)

Because of the size of the break, there is a drop in the primary circuit pressure, as well as in the primary circuit temperature. As a result, there is a slight decrease in the natural convection of the RRP system, as well as in the extracted residual heat, which stabilizes at around 18 MW at 1 000 s. During this period, the flow rate at the break is ≈ 50 kg/s. At the end of this period, the mass of primary circuit water reaches 60 000 kg (Figure 7d); the accumulators have started to inject water, as the primary circuit pressure is slightly below their set pressure (Figure 7f).

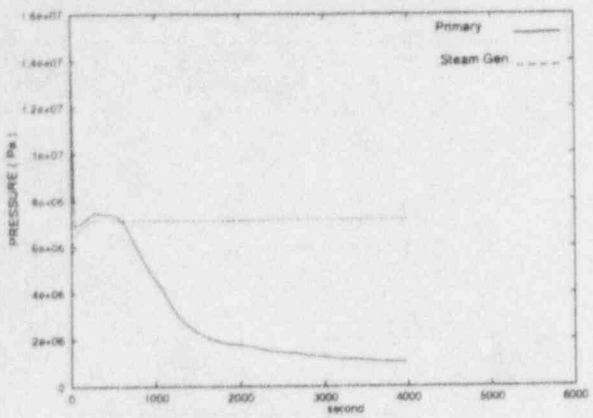

Fig. 6a: Pressure Evolution

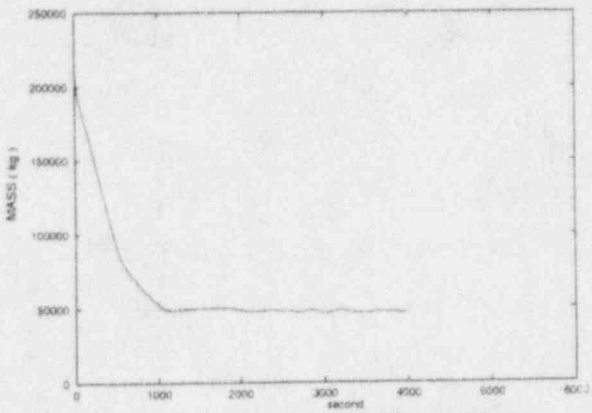

Fig. 6d: Primary Circuit Water Mass

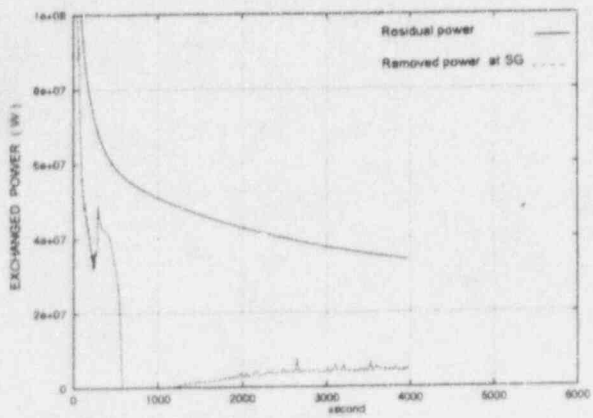

Fig. 6b: Heat exchanges

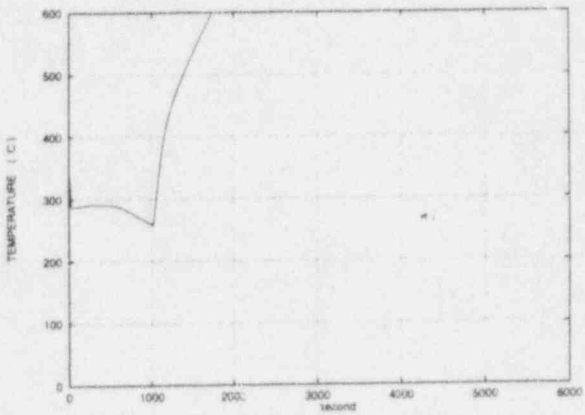

Fig. 6e: Cladding Temperature

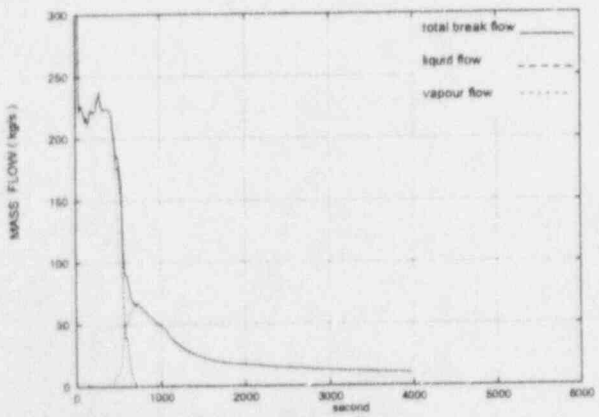

Fig. 6c: Break Flow Rates

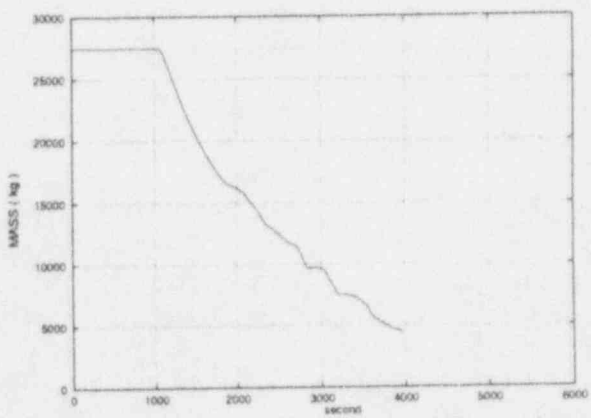

Fig. 6f: Mass of Water in the Accumulators

Figure 6
A 10 cm Break Without RRP Intervention

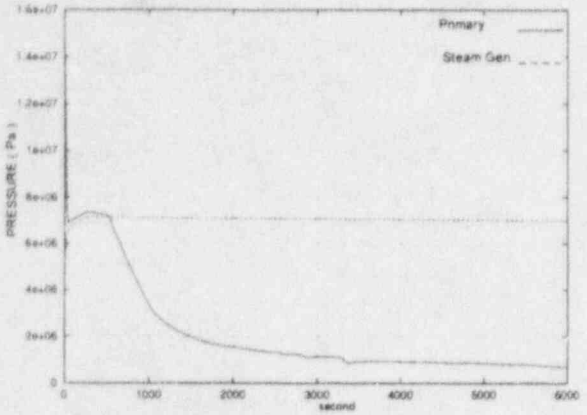

Fig. 7a: Pressure Evolution

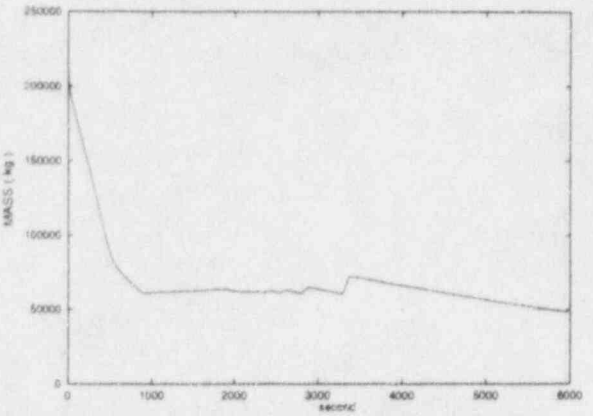

Fig. 7d: Primary Circuit Water Mass

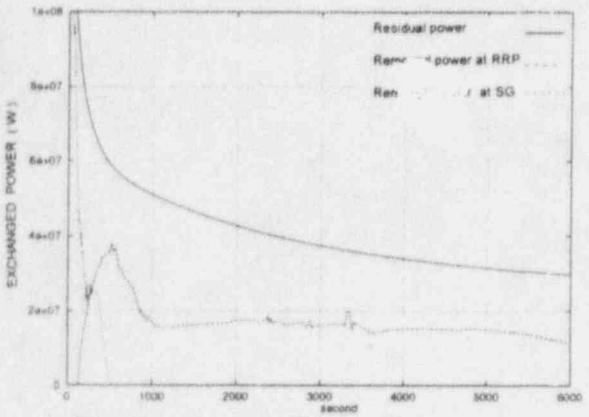

Fig. 7b: Heat exchanges

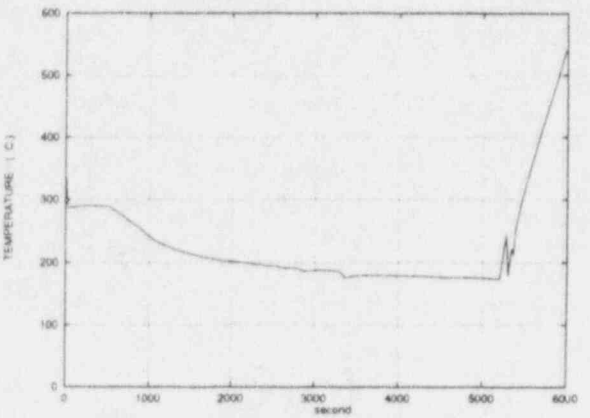

Fig. 7e: Cladding Temperature

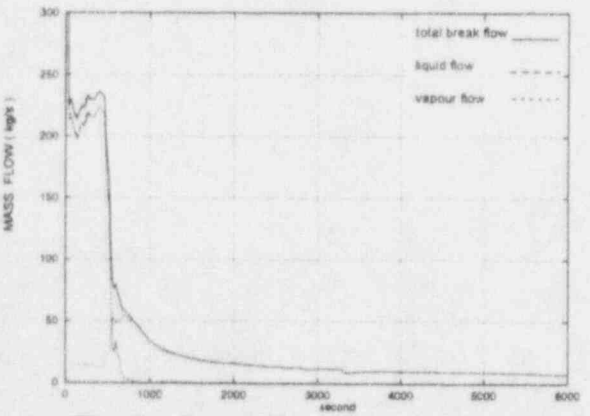

Fig. 7c: Break Flow Rates

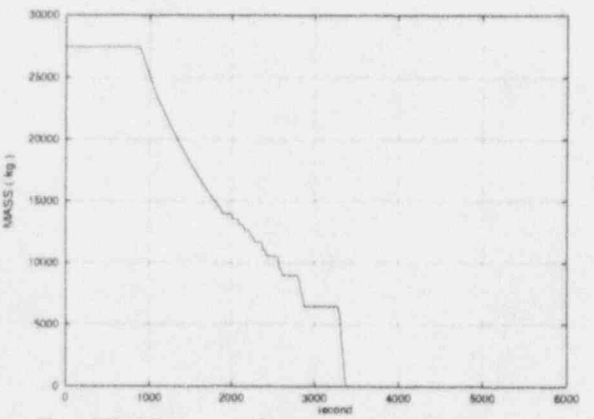

Fig. 7f: Mass of Water in the Accumulators

Figure 7
A 10 cm Break with RRP Intervention

3. Primary circuit Temperature Plateau (from 1 000 s to 5 200 s)

For 2 300 s, the safety injection ensured by the accumulators (Figure 7f) keeps the core flooded. From 3 000 s onwards, the primary circuit temperature follows the saturation temperature of the primary circuit pressure, that is to say about 180°C and 1 MPa. During this temperature plateau, the break and the RRP system participate equally in the removal of the residual heat (Figure 7b). From 5 000 s, the core begins to uncover. The cladding temperature rises at a rate of close to 0.5°C/s (Figure 7e). At this time, the primary pressure is close to 0.7 MPa, a pressure that is well below that of the commonly used low-pressure injection systems.

6.3. Comments

These transient conditions show the advantage of having an available heat sink as close as possible to the core. Once the primary pressure is lower than the set pressure of the secondary safety valves, the steam generators no longer participate in removing the heat from the core and it is then useless to cool them down. Any residual heat removal system has mainly to focus cooling the core rather than on cooling components of the primary circuit which no longer participate in the removal of the residual heat, such as the steam generators when their action stops. This is achieved by the RRP system through its heat sink placed as close as possible to the core. When the primary temperature drops to below that of the steam generators, the natural convection between the core and the steam generators disappears to the advantage of the natural convection between the core and the integrated heat exchangers. This heat sink allows the removal of part of the residual heat, hence a reduction of the removal at the break, and therefore less loss of primary water. The performance of this system, under completely passive operating conditions, thus means a significant gain for the management of small breaks when considering the time required to set low-pressure safety injection systems in action (5 000 s in the case of a 10 cm break instead of 1 000 s). High-pressure safety injection would no longer be necessary for these transient conditions.

These results were obtained with totally passive operating conditions of the RRP system, on the intermediate circuit and the cooling tower alike, in order to systematically take into account a generalized loss of power as the aggravating factor in the initial event. No pre-conditioning is necessary, as the intermediate circuit is always at the primary circuit temperature. Forced convection, obtained by intervention outside the containment, would enhance the performance of the RRP system: **a greater amount of residual heat removed**, and a reduction of the time required to reach full efficiency after start-up. The amount of residual heat extracted by the RRP system would be greater and would lead to a longer grace period before the intervention of the low-pressure injection systems.

7. CONCLUSIONS

The research on passive systems for the removal of residual heat has led to this role being fulfilled by in-vessel integrated heat exchangers with a special vessel layout so as to allow an internal convection compatible with normal reactor operating conditions. The RRP system can operate under any primary pressure or temperature whatever the passive or active operational mode. When the primary circuit is intact, the RRP system allows the passive removal of the residual heat with limitless autonomy.

The present assessment of the RRP system focused on the management of accidents such as a small break in the primary circuit and did not consider the intervention of any other system other than the RRP system. The transient calculations performed with the CATHARE computer code confirmed potential the interest of this system improving the management of these transients. For the management of breaks of a few centimetres in the

primary circuit that require the intervention of an injection system to make up for the loss of water, the RRP system allows a significant increase of the grace period before this intervention, and means that only a low-pressure injection system is needed.

The analysis of these transients allows us to hope for further, even more significant, improvement in their management by forced convection operation of the RRP system by means of active systems located outside the vessel. An analysis of the RRP system in the overall design should make it possible to estimate the far-reaching interest of the system due to its great number of potential advantages, relative to both safety and cost. Due to the important modifications of the vessel and of its internal equipment, the maximum power of a reactor with an RRP could be around 900 MWe. This system should be of great interest for small and medium reactors, for which an increase in safety using passive systems is desired.

REFERENCES

[1] 75 INSAG 5 - Safety of Nuclear Power - IAEA Vienna 1992.

[2] Core decay heat removal system in PWRs
G-M GAUTIER Patent N° 92 05220 - april 28, 1992

[3] EDF 900 MWe
Nuclear Power Plants
Electricité de France - 1991

[4] User's Manual of CATHARE 2 V1.3E
M.FARVACQUE CEA/DRN/DTP/STR/LML/EM/91-61

NRC REVIEW OF PASSIVE REACTOR DESIGN CERTIFICATION TESTING PROGRAMS: OVERVIEW, PROGRESS, AND REGULATORY PERSPECTIVE

Alan E. Levin
U. S. Nuclear Regulatory Commission

ABSTRACT

New reactor designs, employing passive safety systems, are currently under development by reactor vendors for certification under the U. S. Nuclear Regulatory Commission's (NRC's) design certification rule. The vendors have established testing programs to support the certification of the passive designs, to meet regulatory requirements for demonstration of passive safety system performance. The NRC has, therefore, developed a process for the review of the vendors' testing programs and for incorporation of the results of those reviews into the safety evaluations for the passive plants. This paper discusses progress in the test program reviews, and also addresses unique regulatory aspects of those reviews.

INTRODUCTION

Reactor vendors in the United States are currently developing new reactor designs for future deployment. Included in these designs are "passive" advanced light water reactors (ALWRs), such as General Electric's (GE's) Simplified Boiling Water Reactor (SBWR) and Westinghouse's AP600. The passive designs differ most significantly from current plants by virtue of their dependence upon inherent thermal-hydraulic processes, such as natural convection and gravity feed, to accomplish safety injection and emergency core cooling in the event of an accident. The Nuclear Regulatory Commission (NRC) has implemented a new process, certification of standardized reactor designs, for the licensing of the new designs. The design certification rule comprises Part 52, Title 10 of the Code of Federal Regulations (10 CFR 52), and requires that the reactor vendor meet certain requirements for a design to be certified. For the passive plants, these requirements include performance of comprehensive testing and analysis programs to demonstrate that the behavior of the passive safety systems over a range of postulated accidents is acceptable and can be predicted.

A previous paper (Levin, [1]) discussed the testing requirements contained in 10 CFR 52, described briefly the vendors' testing programs, and examined the NRC's regulatory perspective in its review of the vendors' programs. Since that paper was written, Westinghouse's AP600 testing program has been essentially completed, and review, evaluation, and analysis of the

data have begun. In addition, the NRC's evaluation of GE's SBWR test program has resulted in changes to that program, especially in the scope of testing. This paper provides an update of the NRC's design certification testing review, and discusses some of the insights gained through review of test results. In parallel, the NRC's confirmatory test programs are proceeding, with several tests having been performed in the AP600 high-pressure integral program at the Japan Atomic Energy Research Institute (JAERI); confirmatory tests in the AP600 "APEX" facility at Oregon State University (OSU) are also in progress; and construction and test program preparation for experiments in the SBWR "PUMA" loop at Purdue University are proceeding.

AP600 TEST PROGRAM

Westinghouse's AP600 test program has been described in previous publications (Andersen, [2]; Hochreiter, et al., [3]), and the design of the plant is described in [2] and (McDermott, [4]). The test program concentrates largely on thermal-hydraulics, and covers both the reactor (safety injection, passive core cooling, and related systems) and the containment (passive containment cooling system). Reactor-systems-related testing includes separate effects programs on the core makeup tanks (CMTs), automatic depressurization system (ADS), and passive residual heat removal (PRHR) system, and two integral programs: high-pressure, full-height integral testing in SPES-2 at SIET Laboratories (Piacenza, Italy) and low-pressure, long-term cooling tests in APEX, a reduced-height loop at OSU. Containment-systems-related testing has focused on the heat transfer performance of the passive containment cooling system (PCCS), using several facilities at Westinghouse's Science and Technology Center. In addition, studies of water coverage on the outside of unheated sectors of the containment shell have been performed at Westinghouse's Waltz Mill site, and wind tunnel testing to examine the effects of wind on the convective cooling of the shell was done at Canada's National Research Council and the University of Western Ontario.

Most of the major reactor-systems tests were performed during calendar year 1994, with the last tests (SPES-2 and ADS) completed in November. Much of the test data was provided to the NRC staff between July and December, primarily in the form of "quick-look" reports. Comprehensive final testing and analysis reports for these programs are due to be submitted to the NRC in 1995. Containment-related testing was completed in 1993, and test data have been submitted to the NRC. Westinghouse's analysis and modeling efforts in this area are continuing, as well.

As reported in [1], the NRC staff's previous review concentrated largely on facility designs, scaling, instrumentation, and test matrices. These aspects of the review are largely completed for the AP600, and the staff's conclusions have been incorporated into the AP600 draft safety evaluation report (DSER) [5]. The staff's efforts have now turned to review of the data from the test programs, to gain insight into the operation of the passive safety systems, and to understand the phenomena governing passive safety system performance and interactions. The NRC's review of the test programs is discussed below in more detail.

SBWR TEST PROGRAM

GE's SBWR test program has also been described previously (Rao, et al., [6]), and the plant design is discussed in (Upton, et al., [7]). This test program also concentrates on thermal-hydraulics, although selected tests also address valve performance and component structural performance. The SBWR design is in some respects similar to that of the AP600: gravity drain and/or natural circulation are the key processes controlling the response of many of the safety systems to accidents and transients. However, there are substantial differences between the two designs as well. The SBWR does not use any high pressure injection systems comparable to the AP600 CMTs. Proper operation of emergency core coolant injection systems requires that the plant depressurize to slightly more than containment pressure. The only high-pressure safety-related system in the SBWR is the isolation condenser, which actuates when normal methods of reactor system heat removal are not available, and is designed to operate up to full reactor pressure. In addition, the reactor and containment are closely coupled in the SBWR. The passive containment cooling system (PCCS) acts to remove decay heat, recycle water to the reactor, and maintain containment pressure within design limits, and must operate effectively to condense steam released to the drywell in the presence of the nitrogen used to inert the drywell. GE has characterized the design of the PCCS as the major innovation in the SBWR design. As a result, integral systems testing has focused to a substantial extent on long-term post accident behavior, simulating both the reactor and containment but with emphasis on containment performance. No high-pressure integral testing has been performed because of the necessity of achieving full depressurization to actuate ECC injection. In its initial evaluation of GE's SBWR test program [8], the NRC staff agreed that high-pressure integral testing was not required for SBWR design certification.

Major SBWR test programs include:

- the Gravity Driven Cooling System (GDCS) Integrated System Test (GIST), using a full-height, low-pressure facility, performed at GE in San Jose in 1988, focusing on performance of the GDCS;

- GIRAFFE, a long-term cooling test performed at Toshiba's Nuclear Engineering Laboratory in Kawasaki. Initial tests were performed in 1990, and the facility continues in operation up to the present time. The facility is full-height and has focused to date on containment performance beginning about one hour after an accident. Planned tests in 1995 will also examine earlier post-accident periods;

- PANDA, a second long-term cooling test, to be performed in 1995 at the Paul Scherrer Institute in Wuerenlingen, Switzerland. This facility is approximately 1/25 volume scale, and essentially full-height. The test program again focuses on containment performance at one-hour post-accident, although tests are planned simulating earlier post-accident periods;

- PANTHERS, a separate effects test facility at SIET Laboratories in Piacenza, Italy. Two major test programs are being run in this facility: full-scale heat exchanger performance tests using a PCCS heat exchanger, at pressures up to those expected in containment during accidents, and full-scale isolation condenser heat exchanger performance tests, at pressures up to reactor vessel design limits. PCCS tests have been completed, while IC testing is scheduled to begin about July 1995.

The staff has received reports from GE on the GIST and early GIRAFFE programs. Review activities have been directed primarily to evaluation of design, scaling, instrumentation, and test matrices for the upcoming (and, in the case of the PCCS heat exchanger, recently completed) tests in GIRAFFE, PANDA, and PANTHERS. Relatively little detailed evaluation of the GIST and GIRAFFE data has been performed by the NRC staff to date, as a result of circumstances that will be described further below. However, the staff has reviewed selected test results from both GIST and GIRAFFE. The results of those evaluations are described below.

NRC CONFIRMATORY TESTING

The NRC, through its Office of Nuclear Regulatory Research (RES), is sponsoring major confirmatory test programs related to the two passive designs. For the AP600, testing is in progress in the Rig of Safety Assessment (ROSA) Large Scale Test Facility (LSTF), at JAERI in Tokai-mura, modified for the AP600 design (Kukita, et al., [9]). The modified facility, designated ROSA-V, is an approximately 1/30-volume scale, full-height, full-pressure representation of the AP600 primary and secondary systems. The pre-existing ROSA/LSTF configuration meant that some compromises in the test loop design were made with respect to the representation of the AP600 layout. However, analysis of the facility has indicated that it is capable of reproducing thermal-hydraulic behavior similar to, and over the same parametric ranges as, the AP600. Testing in ROSA-V began early in 1994, with the initial phase of testing to be completed in June 1995. A follow-on series of tests is under consideration, beginning in early 1996. The test matrix includes simulated AP600 transients and accidents both within the design-basis envelope (e.g., small-break loss-of-coolant accidents) and beyond the design basis (multiple failures).

Initial results from the ROSA tests have shown behavior similar in many ways to that observed in Westinghouse's integral systems tests (Schultz, et al., [10]). However, the larger scale and capabilities of the modified LSTF have also had an effect on the behavior of the system over a range of simulated accidents. ROSA data are currently being evaluated along with Westinghouse's data from SPES-2 and APEX.

The NRC has also contracted with Oregon State University to perform confirmatory tests in the APEX loop; these tests began in early 1995. Most of these tests focus on beyond-design-basis scenarios, to help evaluate the robustness of the passive safety systems.

SBWR-related confirmatory tests will be conducted in a low-pressure, reduced-height test facility at Purdue University (Han, et al., [11]; Ishii, et al., [12]). The facility, called the Purdue University Multi-dimensional Integral Test Assembly (PUMA), is a 1/4-height, 1/400-volume representation of the SBWR, including both the primary system and the containment. Detailed design of the test loop is complete, and construction is in progress. A test matrix comprising approximately 25 tests, to be performed over approximately one year beginning in mid-1995, is being developed. Test conditions will include both design-basis and beyond design-basis conditions.

While the confirmatory tests are, by definition, not required for design certification, they are expected to assist the staff in better understanding the manner in which the passive plants respond to transients and accidents, and to generate additional data for validation of the NRC's computer codes. In addition, confirmatory test results from ROSA have raised issues that were not being addressed in the vendor's test programs, and which may have an impact on the plant's design-basis response. The staff has asked Westinghouse to address such issues in testing in its own facilities, and would expect to do the same should similar circumstances arise with respect to the SBWR. Planning of the confirmatory test programs has involved staff members from several disciplines, and has included loop design, instrumentation, and test matrix development. The confirmatory test programs are expected to make a valuable contribution to the staff's review of the passive plants.

NRC REVIEW OF VENDORS' TEST PROGRAMS

The staff began its reviews of the passive plant vendors' test programs in 1991, even before the applications for design certification had been submitted formally to the NRC. The initial reviews were reported in papers prepared by the staff for the Commissioners, or "SECY" papers. Westinghouse's program, with the exception of the issue of high-pressure integral systems testing, was evaluated in SECY-91-273 [13]. High-pressure integral testing was addressed separately in SECY-92-030 [14]. GE's test program was evaluated in SECY-92-339 [8].

As discussed previously, the staff's initial review focused on test facility design, scaling, instrumentation and planned testing, while the post-test review emphasizes assessment of the data, phenomenological insights, and application of the data to validation and verification of the vendors' licensing basis computer codes. In addition, as the test program reviews proceeded, the staff identified quality assurance as an additional concern. Both vendors, in their contracts with the Department of Energy, committed to meet the quality assurance requirements of the American Society of Mechanical Engineers' NQA-1 standard [15] for the ALWR programs. Subcontractors, including those outside the U.S., are also required to demonstrate adherence to NQA-1 or to show that their own QA programs (e.g., ISO-9000) are equivalent to NQA-1. The staff's initial assessments of selected test programs indicated that certain key aspects of NQA-1 had not been properly implemented. These assessments ultimately led to the decision to perform formal QA inspections for all vendor-related design certification testing. At this writing, QA inspections have either been performed or are scheduled for all AP600 and SBWR separate effects and integral systems test facilities.

As described in [1], the staff's review of Westinghouse's test program resulted in a recommendation that Westinghouse add a high-pressure, full-height integral system test to the AP600 test program. After protracted discussions between the staff and Westinghouse, and the staff's preparation of SECY-92-030, Westinghouse acceded to the staff's position and contracted with SIET to perform the SPES-2 test program. The staff performed detailed reviews of Westinghouse's test facilities and test matrices, and made numerous suggestions related to design, instrumentation, scaling, and the content of test matrices. During the test programs, staff representatives visited the test facilities to observe testing in progress and for the purpose of the QA inspections discussed above.

Data from the tests were initially submitted to the staff in quick-look reports. Final test reports, comprising (1) final compilations of data (Final Data Reports) and (2) detailed analysis of the data and explanation of phenomenological insights (Test Analysis Reports) have begun to be received by the staff, which is now performing a detailed review of the data. Key phenomena and system response characteristics have been identified for further evaluation, as well as for investigation in future confirmatory tests. Analysis of both the vendor's and the NRC's data using RELAP5 is proceeding. The results of the staff's initial test facility reviews, and limited evaluation of test data, were reported in the AP600 DSER, which was released in November 1994. A supplement to the DSER, which will focus on review of the test program reports and on code validation, is currently scheduled to be issued by the NRC in October 1995.

It is premature at this stage to draw detailed conclusions about the AP600's performance over the range of design basis accidents and transients. However, as reported in the DSER, the staff has not identified any insurmountable problems as yet in its review of the test programs. It must be emphasized, however, that a significant aspect--perhaps the most significant aspect--of the AP600 review that is dependent upon the test programs is evaluation of Westinghouse's reactor- and containment-systems analysis codes, and demonstration by Westinghouse of the codes' ability to predict plant behavior. The staff's review of the AP600 hinges directly on the analyses performed with those computer codes.

The staff's review of the SBWR testing program has moved along a substantially different track from that of the AP600. In GE's original discussions on the SBWR test programs, virtually all testing "required" for certification was identified by GE as having been completed. GE considered its remaining test program--initially only in PANDA and PANTHERS--to be almost completely "confirmatory," which meant that the testing was not really needed, but would be useful to show that the SBWR design and analyses based on the "required" testing demonstrated adequate safety performance. The staff took the position, in SECY-92-339, that the PANDA and PANTHERS testing was required for design certification. GE then proposed that the PCCS tests at PANTHERS be brought under the "umbrella" of required testing, but that the majority of the PANTHERS-IC and PANDA tests were still confirmatory. Further negotiations with GE on these issues made little progress for more than a year.

In the meantime, the staff began to review existing data from the GIST and GIRAFFE tests. The staff was aware that the GIST facility design was based on an early conceptual design of the SBWR, which differed in several ways from the design submitted for certification, and concerns had been raised about the adequacy of GIST data. In an attempt to gather information to facilitate RELAP modeling of GIST, NRC staff members visited GE in late 1992, and found significant problems in the GIST program documentation related to quality assurance, technical adequacy, and data reliability. Further staff review and discussions between the staff and GE had two immediate results: (1) GE "redefined" the purpose of the GIST program from being a full integral systems test to more of a separate-effects test of GDCS flow rate; and (2) the NRC staff recommended that additional testing be required to augment the information available from the GIST program. Another issue was raised regarding containment-related testing using lighter-than-steam non-condensible gas to represent the possible effects of hydrogen released into the containment during accidents. To address this, the staff recommended that tests be performed in the GIRAFFE facility.

In April 1994, GE committed to perform a complete reassessment of the SBWR testing program. The results of the reassessment, reported in the SBWR Test and Analysis Program Description (TAPD) [16], met the staff's requirements as far as inclusion of PANTHERS-IC and PANDA testing within the design certification program; GE also committed to perform additional tests in GIRAFFE with helium simulating hydrogen to address that issue. The major remaining open issue of additional reactor-systems-related testing to address GIST's inadequacies is also moving toward resolution: at the staff's suggestion, GE has designed four "systems interaction" tests at GIRAFFE to look at integral system behavior, including the effects of all passive safety systems, in the late blowdown (pressures less than about 1 MPa) and ECC injection phases of those design basis accidents expected to produce the minimum water level in the RPV. These tests would cover the period from about 10 minutes after accident inception to about 2 hours post-accident, thus overlapping the data from PANDA and other GIRAFFE tests. Final details of the "systems interaction" test series are still under review at this writing. As this last issue is resolved, GE is proceeding with its other test programs. The staff issued a draft evaluation of the TAPD in November 1994, and GE has committed to revise the TAPD in two phases during 1995, to address comments and questions raised by the NRC and by the ACRS. The staff will review those revisions, and expects to issue a final evaluation of the TAPD in late 1995 or early 1996.

The staff's review activities have been and will continue to be similar to those implemented for the AP600 testing review. Facility designs, scaling, instrumentation, and test matrices are reviewed prior to testing, and a detailed review of the data will be performed after the program is completed. Test observation is also planned at all facilities, and QA reviews either have been or will be performed of the SBWR test programs. Because much of the testing for the SBWR will not be completed until late in 1995, the staff's review of SBWR testing is not as far ahead as that of the AP600. In addition, GE has decided to focus its efforts on completing the test program, and has requested that the design certification review of other aspects of the SBWR be suspended. GE has informed the staff that it intends to assess the progress in resolving outstanding issues in the testing and analysis program early in CY 1996, and will decide on a schedule for restarting the rest of the design

certification review at that time. Accordingly, a schedule for completion of the design certification review, including issuance of a DSER, has yet to be established; however, the staff's review of the SBWR testing programs will proceed commensurate with GE's progress in performing the tests and providing the test data to the staff.

The ACRS has also been an active participant in the test reviews. The ACRS Thermal-Hydraulic Phenomena Subcommittee has conducted several meetings to review various aspects of the vendors' test programs, including visits to the vendors' test facilities. Subcommittee members and consultants, and ACRS staff members, also attend meetings between the NRC staff and the vendors.

REGULATORY PERSPECTIVE AND CONCLUSION

Regulatory review of the vendors' testing programs, on the scale required for design certification of the passive plants, has been a new activity for the NRC. The effort involves at least six technical review branches in the Office of Nuclear Reactor Regulation (NRR), with support from several additional branches in RES. As described previously, the test program review has also evolved to include QA as a part of the staff's activities.

The regulatory perspective on the test program review was described in detail in [1]. Perhaps the most important point is that, as far as the passive ALWRs are concerned, the NRC is certifying yet-to-be-built plant designs for a very long period, since the certification itself is valid for 15 years, can be renewed for another 15 years, and the plant may then operate for as long as another 60 years. Certification is based to a significant extent on the application of the results of the testing programs to validation of safety analysis computer codes and subsequent use of those codes to demonstrate that the plant design meets regulatory limits for design-basis accident and transient response. As the vendors' test programs have evolved--and especially for the AP600, as testing has progressed--the staff has discovered system behavior that was unexpected and which requires further evaluation by both the NRC and the vendor. An assessment is in progress of the phenomena involved to determine the extent to which behavior observed in the test facilities is expected in the reactor. It is anticipated, however, that the test results will ultimately have a significant impact on the development and assessment of both the vendors' and the NRC's computer models for the passive plants, and thus on the assessment of plant accident response. It is also expected that insights from the test programs will play a significant role in other aspects of the design certification process, such as determination of the inspections, tests, analyses, and acceptance criteria (ITAACs) required under 10 CFR 52 to ensure that a plant, as built, conforms to the design that the NRC has certified.

As noted previously, and as discussed in more detail in [1], the regulatory review of the vendors' test programs has not been without its challenges, both internal and external. Much of the safety system testing performed over the last 20 years on the current generation of plants was considered confirmatory. In contrast, the vendors' passive plant testing programs are part of the design certification process, and therefore must be reviewed by the NRC staff similar to all other information required for certification. This unique aspect of passive plant design certification

required the establishment of a systematic process for the test program reviews, both to ensure proper coordination within the NRC and to guide interactions with the reactor vendors (see [13]). Internal coordination of the reviews has been required to ensure that the concerns of all relevant technical review branches are addressed adequately. In addition, the assistance of RES has been required in conducting test program reviews, and RES also has specific requirements for test facility information and test data as it develops computer codes and plant and test facility models for NRC's independent assessment of test results and plant calculations. The external challenges have been described above, to some degree, as the staff has negotiated with both vendors about the need for additional testing, in both new and existing facilities. The staff has acknowledged that the test programs and the staff's review have come to require a substantial commitment of resources on the part of the plant vendors. However, the staff believes that the important role that the test programs have come to play in design certification justifies the effort required on the part of the NRC and the vendors.

The conclusion stated in [1] is still applicable: considering the unique aspects of the regulatory review of the passive plant test programs, and despite the problems and challenges that the review process has faced, the NRC staff believes that the process is generally working as it was envisioned, and that this review will ultimately provide substantial technical support to the staff's review of the passive plant designs and, in the end, their certification.

The test program review has to date produced in-depth assessments of the vendors' testing programs and is continuing with evaluation of data from the test facilities. Results of the review will serve as a significant part of the basis for assessing the vendors' safety analysis computer codes. The review process will continue throughout design certification, and will aid the NRC staff significantly in assessing the performance of passive safety systems in the advanced light water reactors.

REFERENCES

[1] A. E. Levin, "NRC review of passive reactor design certification testing programs: Overview and regulatory perspective," Proc. ARS '94, Int. Top. Mtg. on Advanced Reactors Safety, 2, 971-976 (1994).

[2] T. Andersen, "AP600: A new standard 600 MWe plant for a new order of business," Proc. 2nd ASME-JSME Nuclear Engineering Joint Conf., 2, 605-610.

[3] L. Hochreiter et al., "Integral testing of the AP600 passive emergency core cooling systems," Proc. ARS '94, Int. Top. Mtg. on Advanced Reactors Safety, 2, 991-1004 (1994).

[4] D. J. McDermott, "AP600 passive system design: An integrated approach," Proc. 2nd ASME-JSME Nuclear Engineering Joint Conf., 1, 729-734 (1993).

[5] "Draft safety evaluation report related to the certification of the AP600 design," USNRC Report, Draft NUREG-1512 (1994).

[6] A. Rao, et al., "Safety research for the SBWR," Proc. 20th Water Reactor Safety Information Mtg., NUREG/CP-0126, 1, 147-157 (1993).

[7] H. A. Upton, et al., "Simplified boiling water reactor passive safety features," Proc. 2nd ASME-JSME Nuclear Engineering Joint Conf., 1, 705-712 (1993).

[8] "Evaluation of the General Electric Company's (GE's) test program to support design certification for the simplified boiling water reactor (SBWR)," USNRC SECY-92-339, (1992).

[9] Y. Kukita, et al., "ROSA/AP600 testing: Facility modifications and initial test results," Proc. 22nd Water Reactor Safety Information Mtg., NUREG/CP-0140, 2, 203-216 (1995).

[10] R. Schultz, et al., "ROSA/AP600 characterization tests and analysis of 1-inch cold leg break test," Proc. 22nd Water Reactor Safety Information Mtg., NUREG/CP-0140, 2, 217-238 (1995).

[11] J. Han, et al., "NRC confirmatory testing program for SBWR," Proc. 21st Water Reactor Safety Information Mtg., NUREG/CP-0133, 1, 521-529 (1994).

[12] M. Ishii, et al., "Scaling of the Purdue University multi-dimensional integral test assembly (PUMA) design for SBWR," Proc. 22nd Water Reactor Safety Information Mtg., NUREG/CP-0140 (1995).

[13] "Review of vendors' test programs to support the design certification of passive light water reactors," USNRC SECY-91-273 (1991).

[14] "Integral system testing requirements for Westinghouse's AP600 plant," USNRC SECY-92-030 (1992).

[15] American Society of Mechanical Engineers, "Quality assurance program requirements for nuclear power plants," ANSI/ASME Standard NQA-1 (1983 and later versions).

[16] "SBWR test and analysis program description," General Electric Nuclear Energy Report, NEDC-32391 (1994).

Flooding of a Large, Passive, Pressure-Tube LWR

Pavel Hejzlar*, Neil E. Todreas and Michael J. Driscoll

Department of Nuclear Engineering, Massachusetts Institute of Technology, 77 Massachusetts Ave., Cambridge, MA 02139, USA

Abstract

A reactor concept has been developed which can survive loss of coolant accidents without scram and without replenishing primary coolant inventory, while maintaining safe temperature limits on the fuel and pressure tubes. The proposed concept is a pressure tube type reactor of similar design to CANDU reactors, but differing in three key aspects. First, a solid SiC-coated graphite fuel matrix is used in place of fuel pin bundles to enable the dissipation of decay heat from the fuel in the absence of primary coolant. Second, the heavy water coolant in the pressure tubes is replaced by light water, which also serves as the moderator. Finally, the calandria tank, surrounded by a graphite reflector, contains a low pressure gas instead of heavy water moderator, and this normally-voided calandria is connected to a light water heat sink. The cover gas displaces the light water from the calandria during normal operation, while during loss of coolant or loss of heat sink accidents it allows passive calandria flooding. Calandria flooding also provides redundant and diverse reactor shutdown.

This paper describes the thermal hydraulic characteristics of the passively initiated, gravity driven calandria flooding process. Flooding the calandria space with light water is a unique and very important feature of the proposed pressure-tube LWR (PTLWR) concept. The flooding of the top row of fuel channels must be accomplished fast enough so that in the total loss of coolant, none of the critical components of the fuel channel, i.e., the pressure tube, the calandria tube, the matrix and the fuel, exceed their design limits. The flooding process has been modeled and shown to be rapid enough to maintain all components within their design limits. Two other considerations are important. The thermal shock experienced by the calandria and pressure tubes has been evaluated and shown to be within acceptable bounds, while simultaneously cooling the graphite fuel matrix. This has been demonstrated for the bounding scenarios of sustained film boiling and rapid quenching to yield nucleate boiling on the calandria tube outer surface. Finally, although complete flooding renders the reactor deeply subcritical, various steam/water densities can be hypothesized to be present during the flooding process which could cause reactivity to increase from the initially voided calandria case. One such hypothesis which leads to the maximum possible density of the steam/water mixture in the still unflooded calandria space is entrainment from the free surface. It is shown that the steam/water mixture density yielding the maximum reactivity peak cannot be achieved by entrainment because it exceeds thermohydraulically attainable densities of steam/water by an order of magnitude.

---

* Presently at Czech Technical University, School of Mechanical Engineering, Dept. of Thermal and Nuclear Power Plants, Technicka 4, 16607 Prague 6, Czech Republic

1. INTRODUCTION AND REACTOR CONCEPT DESCRIPTION

A LWR reactor concept which can survive loss of coolant accidents without scram and without replenishing primary coolant inventory, while maintaining safe temperature limits on the fuel and pressure tube has been proposed[1],[2]. An important and unique feature of the concept is passive, gravity driven flooding of the calandria space with light water. This paper focuses on the issues associated with the thermohydraulics of the flooding process, to demonstrate the feasibility of the concept.

A schematic of this passive pressure tube LWR is shown in Figure 1. Note that Figure 1 is highly schematic to show the principle of operation rather than the actual arrangement. To build on proven technology to the largest extent possible, the proposed design is based on CANDU reactors. It consists of fuel channels, calandria vessel, shield tank and an entire primary system very similar to those of CANDU units. There are, however, several major features which differ from current CANDU designs. These include

- dry calandria, with no moderator, surrounded by a solid reflector and connected by a gas lock to a large water pool,
- passive means to flood the calandria,
- passively air-cooled large containment, and
- solid matrix-type fuel in the pressure tubes.

Under normal operation, the dry calandria space is filled with a gas under pressure slightly above atmospheric. The calandria bottom is equipped with passages with extended vertical walls submerged in a large water pool in the containment. During normal operation, the containment water level is kept below the calandria bottom in the space within the extended vertical walls by maintaining the calandria gas pressure in balance with the containment water column. Upon a pre-defined disturbance of primary system conditions the gas is released from the calandria, resulting in calandria flooding. Several means to initiate flooding of the calandria are possible. A passive fluid-operated fail-safe valve has been designed to accomplish this purpose[1]. Other means (or the combination of various means) of calandria flooding can be also used. For example, the electrically powered blower maintaining the gas pressure while operating could be designed to lose power and hence depressurize the gas space upon predefined disturbances in the primary system parameters.

After the calandria becomes flooded and the temperature of the flooding water in the calandria approaches saturation, steam escapes from the calandria upwards directly to containment atmosphere through the passages provided by the opened valves, condenses on containment walls, and the condensate returns to the water pool, completing the heat transport circuit. The containment steel shell is cooled by an annular air chimney created by the space between the steel shell and the protective prestressed concrete shell.

Figure 2 shows the fuel matrix arrangement in a fuel channel during a LOCA situation, i.e., without a coolant. Fuel elements consist of the SiC-coated graphite matrix with fuel compacts, arranged in two concentric rings, containing TRISO particles. The matrix elements are 50 cm long and slide in the channel on bearing pads. Cooling

during normal operation is accomplished by light water coolant flowing through 19 circular channels and one outer annular channel. Cooling during LOCA is accomplished via conduction, radiation and convection of the decay heat generated in the voided fuel elements to the flood water as shown in Figure 2 by the arrow.

The pressure tube is surrounded by a protective tube, also termed the calandria tube. This tube has the primary function of preventing excessive stress on the pressure tube during the flooding process. The gap between the calandria tube and pressure tube is specifically designed to have an effective thermal conductivity which allows sufficient heat transfer from the pressure tube to the calandria tube during accidents but prevents excessively rapid cooldown of the pressure tube wall, to alleviate thermal stress. As in current CANDU reactors, the gas in the gap serves for monitoring of leakage from pressure tubes.

The primary system is essentially the same as that of a published CE-CANDU design[3] except for the Emergency Core Cooling System (ECCS), which is not functionally required. Instead, flood water in the calandria provides the heat sink for the decay heat. Elimination of the traditional ECCS allows simplification, cost reduction associated with elimination of piping, valving and an ac safety grade power supply including diesel generators.

2. KEY ISSUES ASSOCIATED WITH THE FLOODING PROCESS

Gravity-driven calandria flooding is a unique and very important feature of the PTLWR concept, and has four important purposes:

- it ensures the removal of decay heat from the calandria tubes by boiling, evaporation and subsequent condensation on containment walls during an accident,
- it provides a large amount of water, which stores a considerable amount of decay energy, thus substantially reducing the heat rate transported through the containment walls early in the accident,
- it shuts down the reactor (if still operating) and renders it deeply subcritical by excessive neutron absorption (even in the boiling mode)[a], and
- it considerably reduces the decay heat load on the fuel matrix (by about 40%) by absorbing a large portion of gamma heating which would have been otherwise deposited in the fuel matrix.

In addition to these beneficial factors the calandria flooding process must be designed to achieve several important characteristics. These include:

- sufficiently short time to flood the top row of fuel channels,
- sufficient heat removal rate from the hot calandria tube,
- acceptable stresses in both the pressure tube and calandria tube, and
- creation of nc reactivity disturbances which would make the reactor critical.

---

[a] Note that the flooding water is non-borated, and still provides a negative reactivity of about 250 β, once all pressure tubes are fully covered.

The first important parameter of interest is the time at which the last (upper) row of fuel channels becomes fully flooded, i.e., immersed in a heat sink. The flooding of the top row of fuel channels must be accomplished fast enough so that for the total loss of coolant, none of the critical components of the fuel channel, i.e., the pressure tube, the calandria tube, the matrix and the fuel, exceed their design limits. An adiabatic heat up analysis of the PTLWR voided fuel channel[1] has shown that the pressure tube temperature is the first component to reach its reusability design limit of 500°C in about 150 seconds. Thus to prevent pressure tubes from exceeding this limit in LOCA accidents, the calandria flooding must be accomplished in less than 150 seconds. The speed of the flooding process will be studied in the next section.

The calandria tubes operate at relatively high temperatures of about 370°C which are further increased following LOCA until the tubes become submerged in the flood water. Since these high surface temperatures exceed the Leidenfrost point there is a concern that a sustained film boiling regime with inherently low heat transfer coefficient will develop and reduce the heat transfer rate between the tube surface and the flood water below acceptable limits. Fuel channel behavior in such a limiting scenario will be investigated in Section 4.

Conversely, rapid quenching to yield nucleate boiling on a calandria tube outer surface may result in unacceptable stresses in both the calandria tube and pressure tube due to thermal shock. These issues will be considered in Section 5.

Finally, although complete flooding renders the reactor deeply subcritical, various steam/water densities can be hypothesized to be present during the flooding process which could cause reactivity to increase from the initially voided calandria case. One such hypothesis which leads to the maximum possible density of the steam/water mixture in the still unflooded calandria space is entrainment from the free surface. Thermohydraulic limits on the entrainment from the free surface will be studied in Section 6 and it will be shown that steam/water mixture density yielding the maximum reactivity peak cannot be achieved by this phenomenon.

3. ANALYSIS OF THE FLOODING PROCESS

To evaluate the time needed to flood the top row of fuel channels, a simplified flooding model has been developed. It tracks the water level in the calandria as a function of time and permits evaluation of various flooding scenarios.

The following assumptions have been introduced for this preliminary stage of investigation:

- *Constant temperature of gas in the calandria during the entire transient.* The approach adopted omits the treatment of the energy equation in the gas space and includes only the mass conservation equation for the gas-vapor mixture. This simplification is satisfactory, since the temperature has a marginal effect on the rate of calandria flooding, i.e., only during the first second following the valve opening.
- *No density change due to voids in the water in the calandria is introduced into the buoyancy term of the momentum equation.* Although an exact treatment would require calculation of void distribution along the vertical coordinate, this is a conservative assumption since for a given pool height the reduced pool

density in the calandria (due to voids) will increase the driving force for water flow and speed up the flooding process.

- *Pressure drop across the tube bundle is treated as for one-phase flow.* Although the presence of bubbles in the water increases the pressure drop, which would conversely decrease the water flow rate, the results showed that the pressure drop across all rows of fuel channels is less than the inlet pressure losses by several orders of magnitude. Hence including a two-phase multiplier in the pressure loss term has no visible effect on the final results.
- *A prescribed fraction, (1-f_{steam}), of decay heat is assumed to contribute to the pool heatup while the rest of the decay heat, f_{steam}, is assumed to generate vapor which is assumed to be released instantly into the upper space.* A conservatively high value of f_{steam}=0.3 was used in the calculations. Because the pool remains strongly subcooled during the reflooding process, most of the vapor will condense inside the pool and the realistic steam fraction released from the pool into the upper calandria space was confirmed to be much less than 0.3[1].

A schematic of the flooding model is shown in Figure 3. There are four sections with different constant flow areas—Section #1 of height H, Section #2 representing the horizontal passage, Section #3 between the horizontal passage and the reflector, and Section #4 which represents the passage through the reflector. The calandria space has a variable flow area and is treated separately. Using the postulated assumptions the behavior of the medium in the calandria space can be described by a set of conservation equations as follows:

Mass conservation for the lower, flooded space

$$\frac{dM_f}{d\tau} = \dot{m} - \dot{m}_{vap} \tag{1}$$

with initial condition $M_f(\tau=0)=0$.

Mass conservation for the upper, gas space

$$\frac{dM_g}{d\tau} = -G_g A_g + \dot{m}_{vap} \tag{2}$$

with initial condition $M_g(\tau=0) = (V p_o M_{CO2})/(R T_{go})$.

The simplified energy conservation equation for the flooded space

$$\frac{d(M_f h)}{d\tau} = \dot{Q}_{flood} + G_f A_f h_{in} + p\frac{dV_f}{d\tau}, \tag{3}$$

where M_f and V_f are mass and water volumes in the calandria, respectively, and the $V_f dp$ term is taken as zero for incompressible water. Eq. 3 can be rewritten for subcooled liquid in terms of temperatures as

$$\frac{dT}{d\tau} = \frac{1}{M_f c_p}\left(\dot{Q}_{flood} + G_f A_f c_p (T_{in}-T)\right) \tag{4}$$

with initial condition $T(\tau=0) = T_0$.

Heat transferred from the fuel channels into liquid, $\dot{Q}_{flood}$, is computed as

$$\dot{Q}_{flood} = \frac{\dot{Q}_{wall}\,(1\text{-}f_{steam})}{N_{tubes}} \sum_{i=1}^{N_{rows}} N_i \tag{5}$$

where N_{rows} is the number of submerged rows, N_i is the number of tubes in the i-th submerged row and N_{tubes} is the total number of fuel channels. The fraction $1\text{-}f_{steam}$ is the prescribed fraction of decay heat which contributes to pool heat up. $\dot{Q}_{wall}$ is the heat rate transferred from the hot walls. It includes both the decay heat and the stored energy released from the fuel channels. The mass flow rate of the steam generated by this heat rate is thus

$$\dot{m}_{vap} = \frac{\dot{Q}_{wall}\, f_{steam}}{h_{fg}\, N_{tubes}} \sum_{i=1}^{N_{rows}} N_i \,. \tag{6}$$

The mass flow rate of flooding water is calculated from the momentum equation

$$\frac{1}{A}\frac{\partial \dot{m}}{\partial \tau} + \frac{1}{A}\frac{\partial \dot{m} v}{\partial s} = -\frac{\partial p}{\partial s} - \left(K + \frac{f}{D_e}\right)\frac{\rho\, v^2}{2} - \rho\, g \sin\beta \tag{7}$$

where v is velocity. Eq. 7 can be written after integration along the path coordinate, *s*, as

$$\frac{d\dot{m}}{d\tau} = \frac{\left[p_{at} - p - \frac{\dot{m}^2}{2}\left(\frac{1}{\rho_N A_N^2} - \frac{1}{\rho_1 A_1^2}\right) - \dot{m}\,|\dot{m}| \sum_{i=1}^{N}\left(K_i + f_i\frac{l_i}{D_{ei}}\right)\frac{1}{2\rho_i A_i^2} + g\sum_{i=1}^{N}\rho_i \Delta h_i\right]}{\sum_{i=1}^{N}\frac{l_i}{A_i}} \,. \tag{8}$$

with initial condition $\dot{m}(\tau=0) = 0$, where N is the number of sections (along the path counted from Section #1 at the location of the water level in the containment up to the current location of the tracked water level) with different constant flow areas, A_i; K_i is the total form loss in the i-th section and f_i is the friction factor in the i-th section.

The height of the water level of the heat sink in the containment, H, is calculated from the ordinary differential equation

$$\frac{dH}{d\tau} = -\frac{\dot{m}}{A_1\, \rho_f} \tag{9}$$

with initial condition $H(\tau=0) = H_0$. If the flooded water level, h, is below the calandria bottom it is calculated from the equation

$$\frac{dh}{d\tau} = +\frac{\dot{m}}{A_i\, \rho_f} \tag{10}$$

with initial condition $h(\tau=0) = h_0$. A_j is the flow area at the location of the current water level. Once the flooded water level reaches the calandria bottom, it is computed from geometrical relations. Gas mass flux from the calandria is calculated from a quasi-steady flow equation through the valve using isentropic expansion of an ideal gas:

$$G_g = 0.9\,\rho_g \sqrt{2\,\frac{\gamma}{\gamma-1}\,\frac{p}{\rho_g}\left(\varepsilon^{2/\gamma} - \varepsilon^{(\gamma+1)/\gamma}\right)}\,, \tag{11}$$

where $\varepsilon = p_{at}/p$ is the pressure ratio and $\gamma = c_p/c_v$ is the isentropic expansion coefficient. The coefficient 0.9 in Eq. 11 accounts for losses. If the pressure ratio is less than the critical ratio, the critical pressure ratio

$$\varepsilon = \left(\frac{2}{\gamma+1}\right)^{\gamma/(\gamma-1)} \tag{12}$$

is substituted into Eq. 11 to obtain critical flow.

Integration of the system of ordinary differential equations (1), (2), (4), (8), (9), and (10) was performed using a 4-th order Runge-Kutta method with automatic time step control.

The water level in the calandria as a function of time following the flooding initiation, calculated using the above model[1], is plotted in Figure 4. In the calculation, 30% of the generated steam, i.e., $f_{steam} = 0.3$, was assumed to be released instantly into the upper calandria space. Flooding of the top row of fuel channels is achieved in about 24 seconds, or if 2-out-of-4 valves fail to release the cover gas, in 33 seconds. This time scale compares very favorably with the fuel channel heat-up time scale, where the fuel matrix can withstand an adiabatic heat-up from decay heat for four hundred seconds without exceeding its allowed temperature limit. It is also five times less than the time at which the maximum local pressure tube temperature reaches the limit of 500°C, in an adiabatic heat-up scenario.

4. FUEL CHANNEL PERFORMANCE DURING LOCA

During LOCA, the fuel channel needs to dissipate decay heat by conduction, radiation and convection in steam/air mixtures to the heat sink without exceeding safe temperature limits. These limits are 1600°C for TRISO particle fuel to avoid increased fission product release, 1300°C for the SiC coating to avoid excessive oxidation, and 500°C for the pressure and calandria tubes to assure their reusability. The transient history of these limiting temperatures has been obtained by analysis of the heat transfer from the fuel matrix to the flooding water coupled to the neutron point kinetics equation[1]. This paper will focus on the heat transfer phenomena at the calandria tube-flood water interface.

During the flooding phase, two situations can be theoretically encountered—nucleate boiling and film boiling, depending on the heat flux and the initial temperature of the tube surface. Typical regions on a boiling curve are shown in Figure 5. The most important points on the curve are the minimum film boiling point, designated as E and the critical heat flux Point C. Point E, also known as the Leidenfrost temperature, can

be theoretically calculated from the minimum heat flux which will maintain film boiling, q''_{min}. If the flood water in the calandria is at the saturation condition, this heat flux is given in the form proposed by Zuber and Tribus[4]

$$q''_{min} = C\, h_{fg}\, \rho_g \sqrt[4]{\frac{\sigma(\rho_f-\rho_g)\, g}{(\rho_f+\rho_g)^2}} \tag{13}$$

where C is a non-dimensional constant between 0.09 and 0.18. Using the value of C=0.13 and properties of flooding water at atmospheric pressure, Eq. 13 yields the minimum film boiling heat flux of 27 kW/m^2.

The heat transfer coefficient for film boiling outside a horizontal cylinder is defined by the Bromley correlation [5]

$$h = 0.62 \sqrt[4]{\frac{\rho_g\,(\rho_f - \rho_g)\, g\, h_{fg}\, k_g^3}{\mu_g\, \Delta T_{sat}\, D}} \tag{14}$$

where D is the outer diameter of the cylinder, i.e. calandria tube.

If the temperature of the calandria tube at the outer surface is higher than $T_{sat}+\Delta T_{sat_{min}}$, heat transfer will be controlled by film boiling and the heat transfer coefficient is determined from Eq. 14. On the other hand, if the tube surface temperature is lower than $T_{sat}+\Delta T_{sat_{CHF}}$, the heat transfer is controlled by nucleate boiling. The Rohsenow correlation [6] for this regime

$$h = h_{fg}\, \mu_f \sqrt[2]{\frac{(\rho_f - \rho_g)\, g}{\sigma}} \left(\frac{c_{pf}}{C_s\, h_{fg}\, Pr_f}\right)^3 \Delta T_{sat}^2 \tag{15}$$

has been used to obtain the heat transfer coefficient. The factor C_s is a constant depending on the liquid-surface combination. A typical value of C_s for a water-metal combination is 0.013.

The CHF point is determined from the intersection of the nucleate boiling correlation, Eq. 15, and the CHF correlation outside a horizontal cylinder [7]

$$q''_{CHF} = 0.116\, h_{fg} \sqrt[2]{\rho_g} \sqrt[4]{\sigma(\rho_f - \rho_g)\, g}\ . \tag{16}$$

The value of $\Delta T_{sat_{CHF}}$ at Point C can be determined by substituting the critical heat flux from Eq. 16 into Eq. 15 as

$$\Delta T_{sat_{CHF}} = (h_{fg}\, \mu_f)^{-1/3} \left(\frac{(\rho_f - \rho_g)\, g}{\sigma}\right)^{-2/3} \left(\frac{c_{pf}}{C_s\, h_{fg}\, Pr_f}\right)^{-1} q''_{CHF}\ . \tag{17}$$

Since the heat transfer process is controlled by the surface temperature, the heat flux in the transition region will be increased towards the point of CHF once ΔT_{sat} drops below $\Delta T_{sat_{min}}$, as shown by arrows on Figure 5. In this region, the heat flux can be obtained directly from linear interpolation,

$$q'' = q''_{CHF} - \frac{q''_{CHF} - q''_{min}}{\Delta Tsat_{min} - \Delta Tsat_{CHF}} (\Delta Tsat - \Delta Tsat_{CHF}). \quad (18)$$

The major uncertainty lies in the exact determination of the temperature difference between the wall and saturation temperatures at the minimum heat flux, $\Delta Tsat_{min}$. The theoretical value of $\Delta Tsat_{min}$ can be obtained by substituting Eqs. 13 and 14 into relation $q''=h\ \Delta Tsat$ which yields $\Delta Tsat_{min} = 80°C$. However, this result does not correspond to experimental data. In practice, the minimum film temperature is affected by the surface conditions and liquid contaminants, resulting in much higher values for both the minimum heat flux and the minimum film boiling temperature. Whalley [7] states that the typical value for the minimum film boiling temperature for water at a pressure of 1 bar is 290°C. This corresponds to $\Delta Tsat_{min}$ of 190°C. Bergles and Thompson's[8] measurements yielded substantially higher minimum film boiling heat fluxes than the values obtained by Eq. 14. The minimum film boiling temperature for water at atmospheric pressure obtained in Bergles and Thompson's experiments was found to be about 400°C, which is even higher than the value stated by Whalley. Accordingly, it seems that there is no well defined minimum film boiling temperature.

If the flood water is subcooled, the Leidenfrost temperature is also a function of the degree of subcooling. The most realistic estimates of the Leidenfrost temperature as a function of subcooling were obtained by Bradfield[9] and Dhir and Purohit[10]. Their data were obtained by quenching spheres in water at atmospheric pressure. Dhir and Purohit correlated the data by

$$\Delta Tsat_{min} = 101 + 8\ \Delta T_{sub}\ (K). \quad (19)$$

Correlation (19) agrees very well with Bradfield's data. More recently, the effect of moderator subcooling on heat transfer conditions in CANDU fuel channels has been investigated by Gillespie[11]. These investigations conclude that for moderator subcoolings larger than 30°C, no film boiling should occur. Since the flooding water in the PTLWR has a temperature of 40°C, or a subcooling of 60°C, nucleate boiling is expected to occur on the outer surface of its calandria tubes.

Nevertheless, because of the uncertainties in the application of the correlations resulting from material and geometric differences, and because of the uncertainties in the actual value of the local subcooling, calculations were made for two bounding scenarios: the best-estimate case, which preserves the nucleate boiling regime, and for the hypothetical case with the sustained film boiling regime.

The scenario selected is a 100% break of the inlet header in both loops without scram. All heat transfer coefficients in all coolant channels were set to zero at the same time as the break occurs, thus neglecting the energy carried away by the coolant during blowdown. The initiation of the calandria flooding process was assumed to be delayed by about 10 seconds. Another conservatism was introduced in the analysis by setting the temperature of the flood water to saturation, i.e., the subcooling was neglected. The analysis results are presented for the hot channel at the location of maximum power density.

Operation in Nucleate Boiling Regime

A large value of the Leidenfrost temperature, that from Bergles' measurements was chosen, i.e., $\Delta Tsat_{min}$ = 300°C is chosen for this case to allow rapid achievement of nucleate boiling. Figure 6 shows the temperature traces of the inner fuel ring, matrix surface at the central coolant channel, the pressure tube, and the calandria tube for the channel at the top row, i.e., the last channel flooded. At the time flooding water reaches the uppermost row of fuel channels (35 seconds) the calandria tube surface temperature is slightly higher than the Leidenfrost point. Hence, the initial cooldown through the film boiling regime (after about 5 seconds) reduces the calandria wall temperature below the Leidenfrost point. Consequently, the calandria tube is rapidly quenched and its temperature drops close to the saturation temperature of flood water and is then maintained at this level until the end of the transient. The temperature of the pressure tube quickly follows that of the calandria tube, and the channel slowly cools down. All peak temperatures remain below their design limits.

Operation in Film Boiling Regime

To prolong the time period that the calandria tubes remain in film boiling, the Leidenfrost temperature was decreased below Bergles' values to 290°C (as cited by Whalley), and the flooding initiation was set at a later time so that the upper row is flooded at the 50th second. Figure 7 shows the time history of critical temperatures and Figure 8 plots the linear heat transfer rates in the gap between the matrix and the pressure tube, Q'gap, from the calandria tube to flood water, Q'out, and the linear heat generation rate in the fuel matrix, Q'gen (decay heat, fission power and released Wigner energy). Both the fuel and maximum matrix surface temperatures reach higher maximum values than for the nucleate boiling case, but the difference is small (only about 20°C). The peak is reached at a later time (280 seconds compared to 160 seconds in the nucleate boiling case). The limiting pressure tube temperature rises to about 500°C, until 50 s, when the flooding water reaches the last row. Since the calandria tube outer surface temperature is significantly above the Leidenfrost point, heat transfer to flooding water is by film boiling, and the pressure tube temperature remains at about 500°C. However, the heat flow from the matrix is controlled by the large heat transfer resistance of the gap between the matrix and the pressure tube (note that the gap linear heat rate has the lowest values). At the time of about 270 seconds, decay heat generation is smaller than the heat rate transferred from the system, causing a reverse in the matrix temperature trend.

An important conclusion from this hypothetical scenario is that even if the calandria tube does not quench below the Leidenfrost point, there is no problem in removing the heat load. In fact this scenario is preferable from the thermal stress point of view. Also note that there is no traditional CHF concern since the system can remove the heat under film boiling conditions. The only difference is higher pressure tube temperature, but one which does not exceed the 500°C limit[b] . The effect of film boiling on fuel matrix

[b] Real values of pressure tube temperatures are expected to be significantly less than this calculated estimate of 500°C due to very conservative assumptions such as setting the temperature of flood water to saturation, maintaining film boiling on the entire calandria tube surface and neglecting the energy carried away by the coolant during blowdown.

temperature is negligible, even though the pressure tube temperature is almost 400°C higher than in the nucleate boiling scenario. The reason for this is the prevailing radiative heat transfer mode (about 80%) across the matrix-pressure tube gap. The radiative heat transfer is proportional to the difference of upper temperature (i.e., at the matrix outer surface) to the fourth power and lower temperature (i.e., at the pressure tube inner surface) to the fourth power. Since the latter value is a much smaller number than the upper temperature to the fourth power, the increase in lower temperature, even if this decrease is relatively large, does not influence the heat rate significantly, compared to the effect of changes in the upper temperature. Consequently, the matrix is not significantly affected by even a large temperature change of the pressure tube.

5. STRESS IN THE QUENCHED CALANDRIA TUBES

Flooding of the calandria by cold water results in a rapid temperature decrease of the pressure tube wall and increased thermal stresses. In a loss of coolant accident, the stress in the pressure tube from primary pressure is small since the primary pressure is lost, hence the thermal stress from flooding does not lead to excessive stresses in the pressure tube. However, if the flooding process is initiated while the pressure tubes are under operating pressure or even higher (as may be the case in a loss of normal heat sink accident), the stress from primary pressure is increased by the thermal stress, which could lead to unacceptable stress levels. To mitigate stress excursions in such scenarios, the pressure tube is surrounded by a protective calandria tube which absorbs the first thermal shock wave and thus protects the pressure tube. Pressure tube stress analyses using Von Mises stress criterion, which combines both the thermal stress and the stress from primary pressure in all planes, confirmed the need for the protective calandria tube in such scenarios as well as it evaluated its effectiveness[1]. This section will focus on the calandria tube which does not need to bear a large pressure load, but is, during the quenching process, exposed to rapid temperature changes, inducing high thermal stresses.

A transient analysis of the thermal stress in the calandria tube during flooding was performed using the temperature distribution obtained from the computer code discussed in Section 4[1]. Several comments on the critical heat flux need to be pointed out. The CHF correlation for pool boiling applicable outside a horizontal cylinder[7], Eq. 16, is valid for saturated conditions. This equation was applied to the analysis of fuel channel temperatures in the previous section since it makes the temperature analysis conservative, i.e., leads to earlier occurrence of CHF and hence higher wall temperatures, since it does not take into account the subcooling of flooding water. For the thermal stress analysis, subcooling must be accounted for because it leads to enhanced critical heat flux, and hence faster cooling rates, i.e., delayed occurrence of CHF and hence lower wall temperatures. The effect of subcooling was incorporated in the thermal stress analysis using the relation proposed by Ivey and Morris [12]

$$q''_{CFH} = q''_{CFH,sat}\left[1 + 0.1\left(\frac{\rho_f}{\rho_f}\right)^{0.75}\frac{c_{pf}\,\Delta T_{sub}}{h_{fg}}\right] \qquad (20)$$

where $q''_{CFH,sat}$ is the critical heat flux obtained from Eq. 16 at saturated conditions and ΔT_{sub} is the subcooling. Bradfield's[9] data, which yield the highest minimum heat flux,

were utilized to obtain the minimum heat flux on the boiling curve. The heat flux in the transition region between the minimum heat flux and the critical heat flux is obtained by linear interpolation, Eq. 18.

Two scenarios have been analyzed. The first case involves inadvertent flooding of a calandria tube during normal operation. The second scenario involves a LOCA without scram sequence, in which the calandria tube heats up to temperatures above its normal operating point and then is flooded and quenched. The results for the first case are presented in Figures 9 and 10. Figure 9 plots the temperature development in the calandria tube wall. The wall has been divided into eight annuli of equal width, hence there are nine curves, each curve representing one cylindrical surface. When the cold water hits the hot tube surface, the difference between the wall and saturation temperatures, ΔT_{sat}, is large and sets the operating point in the transition region, between the minimum and critical heat flux. The heat flux in the transition regime is sufficiently high to cause cooldown of the outer surface. Figure 10 shows that the peak stress at the outer surface exceeds the allowed stress criterion of 1/3 ultimate tensile strength for Zr-2 by 30 MPa (the criterion depends on temperature and is shown for the outer surface temperature at the time when the maximum stress at this location is achieved) for a very short period of time (about 0.1s). Although the nominal stress limit is slightly exceeded at the tube outer surface, the excursion is still considerably below the material yield stress, and it also lies below another conventional criterion—2/3 of yield stress. Hence, this small and short duration excursion of stress at the outer surface above the 1/3 ultimate tensile strength criterion is acceptable.

The LOCA scenario results in a higher initial temperature of the calandria tube at the time the tube is flooded with cold water. The results are shown in Figure 11. To show the quenching process in more detail, only a short time span of 1 second, following the time when the top row of calandria tubes is flooded, is plotted. An interesting observation is that the thermal stress in this process is even less than in the previous case, even though the initial temperature of the calandria tube is higher. The reason for this behavior lies in the lower heat flux due to the higher ΔT_{sat} in the transition region in this LOCA case (note that in the temperature-controlled transition region, heat flux is inversely-proportional to ΔT_{sat}).

The analysis of thermal stress in the calandria tube from cold-water flooding suggests that calandria tubes should be able to withstand the quenching process undamaged. Thermal stress depends strongly on the boiling regime and on the value of critical heat flux and minimum heat flux. Experiments would be needed to determine the boiling curve for calandria tubes more exactly. Relatively high peak thermal stresses may require the use of Zr2.5%Nb instead of Zr-2 as a material for calandria tubes.

6. SECONDARY CRITICALITY ISSUES

Flooding of the calandria with light water introduces large reactivity changes into the system. Once the calandria is flooded, a large amount of light water, which has a relatively high neutron absorption cross section, renders the reactor deeply subcritical even if the flooding water is in bulk boiling. The concern is the reactivity behavior during the flooding process. When the flooding water enters the calandria, only a portion of the calandria is submerged, yielding therefore lower (from fully flooded)

water density per unit of total calandria space, and hence the hypothetical possibility of increasing the reactivity. Moreover, one can imagine a situation such that the steam or steam/water mixture (entrained from violently boiling flooding water in the lower portion of the calandria) fills the upper calandria space and causes an increase in reactivity. All these possibilities need to be examined to ensure that no large reactivity insertions are introduced during the calandria flooding process.

There are two major scenarios of calandria flooding. The first scenario includes intentional calandria flooding after loss of coolant (designated further as reflooding). The second scenario arises if the calandria is flooded inadvertently during normal operation (designated further as inadvertent flooding). Both scenarios behave differently because of the different amount of light water coolant inside the fuel channels. Another scenario, which is not associated with calandria flooding but has similar reactivity aspects, is the rupture of both pressure tubes and calandria tubes resulting in spraying of light water coolant into the calandria space. Important factors during these processes are the density of the steam/water mixture outside the fuel channel and the presence of control rods.

Various scenarios have been calculated[1] using the MCNP[13] model of the full core with control rods and variable water level in the calandria and variable steam/mixture density in the upper calandria space. The case yielding the largest reactivity rise was found to be an inadvertent flooding of the hot core at nominal conditions. Reactivity behavior for this case is plotted as a function of assumed steam/water density in the upper calandria space, ρ_m, in Figure 12. Individual points on the reactivity curve (from the left) characterizing the process can be described as follows:

- ρ_m=0 g/cm^3, k_{ef} =1.00 — operating point.
- ρ_m=0 g/cm^3, k_{ef} =0.99 — one row of fuel channels is flooded with boiling water, the upper calandria space is filled with CO_2. The reactivity drop is due to neutron absorption in the water pool at the bottom of the calandria.
- ρ_m=0.0006 g/cm^3, k_{ef} =0.98 — one row of fuel channels is flooded with boiling water, the upper calandria space is filled with saturated vapor corresponding to atmospheric pressure. The additional reactivity drop is due to absorptions in H_2O vapor in the upper calandria.
- ρ_m=0.01 g/cm^3, k_{ef} =0.997 — one row of fuel channels is flooded with boiling water, the upper calandria space is filled with steam/water mixture of density 0.01g/cm^3. The reactivity increase is caused by shading of the control rods (shading of control rods prevails over absorption in steam/water mixture).
- ρ_m=0.02 g/cm^3, k_{ef} =0.99 — one row of fuel channels is flooded with boiling water, the upper calandria space is filled with steam/water mixture of density 0.02g/cm^3. The reactivity decrease is due to the prevalence of absorption in the steam/water mixture over the shading effect of CRDs.

It can be observed from Figure 12 that secondary criticality could be achieved at the optimum mixture density of about 0.015 g/cm^3, assuming that this density is physically attainable. This raises an important question, i.e., "what is the maximum possible density of a steam/water mixture in the upper calandria space (still unflooded) during the flooding process?".

The most probable scenario is that the upper calandria space is filled with saturated steam with the density corresponding to the partial pressure of the vapor. The largest steam density in the saturated state will be achieved if no gas is assumed to be present in the calandria, i.e., the upper space contains only steam. Assuming atmospheric pressure in the calandria (note that calandria flooding is initiated several seconds after LOCA, before a significant pressure rise in the containment is experienced) this density is 0.0006 g/cm^3.

Higher density in the upper calandria space can be reached if the boiling process in the lower flooded portion is so vigorous that droplets of liquid are entrained high above the water level, and thereby increase the water content in the upper portion. The upper limit of the amount of liquid entrained into the unflooded calandria region can be estimated using the theory of entrainment from a free surface. This upper limit represents a conservative estimate yielding maximum water densities.

The assessment is based on the entrainment from a free surface study performed by Kataoka[14]. The notion of entrainment loses its validity when the superficial gas velocity is so great that there is no distinct water level. This occurs at the dimensionless entrainment number, $E_{fg} = 5.0$, defined as

$$E_{fg} = \frac{\rho_f j_{fe}}{\rho_g j_g} \tag{21}$$

where subscript fe refers to the entrained liquid phase. It can be also viewed as the criterion for the transition from churn-turbulent to annular or annular dispersed flow. The choice of 5 for the entrainment number is a conservative estimate for two reasons. First, it represents the upper limit for a churn-turbulent pool (the most violent pool). Secondly, a bubbly flow pool is more likely, since no gas is blown through the pool, only vapor bubbles from boiling contribute to the superficial gas velocity, j_g. Moreover, calculations have shown[1] that most of the vapor bubbles will condense in the considerably subcooled flood water before they can reach the surface. Another conservatism is introduced by taking the pool surface gas superficial velocity equal to 2m/s. This is the upper limit for pool entrainment data for which the correlation is valid. Using these data, the superficial velocity of entrained liquid can be evaluated to yield

$$j_{fe} = \frac{E_{fg} \rho_g j_g}{\rho_f} = \frac{5\ (0.598)\ 2}{1000} = 0.00598 \text{ m/s} \tag{22}$$

where water properties were taken for an atmospheric pressure of 0.1 MPa.

Eliminating total mass flow rate from the relations for superficial velocity of entrained liquid and superficial gas velocity defined as

$$j_{fe} = \frac{\dot{m}\ (1-x)}{A\ \rho_f}, \quad j_{fg} = \frac{\dot{m}\ x}{A\ \rho_g}, \text{ respectively,} \tag{23, 24}$$

yields the equation

$$j_{fe} = j_g \frac{\rho_g}{\rho_f} \frac{(1 - x)}{x}. \quad (25)$$

Using the values of $j_g = 2$ m/s, $j_{fe} = 6 \times 10^{-3}$ m/s and densities at 0.1 MPa, Eq. 25 can be solved yielding the flow quality, $x = 0.1667$.

This quality exists, however, only in close proximity to the pool surface. The quality will increase with the height above the pool free surface, i.e., liquid content decreases while vapor content increases. Although flow quality as a function of the height can be obtained from Kataoka's correlation, it is not done here. Instead it is conservatively assumed that the near-surface quality remains the same throughout the whole upper calandria space. Void fraction is then evaluated (assuming, conservatively, the slip ratio equal to 1.0) as

$$\alpha = \left[1 + \frac{\rho_g}{\rho_f} \frac{(1 - x)}{x}\right]^{-1} = 0.997 \quad (26)$$

and finally the maximum limit on attainable steam/water mixture density is

$$\rho_{m,max} = (1 - \alpha)\, \rho_f + \alpha\, \rho_g = 0.0035 \text{ g/cm}^3. \quad (27)$$

Another hypothetical scenario for creating a steam/water mixture with densities higher than steam at saturation is by spraying into the upper calandria space. This sequence would be possible if both the pressure tube and calandria tube rupture and the escaping coolant sprays into the calandria. The highest achievable densities for water sprinklers purposefully designed for that purpose are[15] ~0.1 vol% H_2O. This translates to a mixture density of 0.001*1g/cm^3 = 0.001 g/cm^3. Table 1 summarizes H_2O practical density limits in the unflooded portion of the calandria. All these conservatively high density estimates are less than the steam/water density of 0.015g/cm^3 at peak reactivity by an order of magnitude. Hence, the proposed PTLWR concept will not exhibit reactivity excursions in scenarios involving the ingress of steam water mixtures into the voided calandria space.

Table 1. Practical H_2O density limits in the upper calandria space

	Saturated steam	Entrainment limit	Spray limit	At maximum reactivity
H_2O density (g/cm^3)	0.0006	0.0035	0.001	0.015

7. SUMMARY AND CONCLUSION

An innovative design concept of a large, light water cooled and moderated reactor has been proposed. The reactor can survive loss of coolant accidents without scram and without replenishing primary coolant inventory, while maintaining safe temperature limits on the fuel and pressure tube. A unique feature of the reactor is passive, gravity-driven flooding of the normally voided calandria with non-borated light water which provides a heat sink and simultaneously shuts down the reactor. Several issues associated with the flooding process have been investigated. The flooding process has been modeled and shown to be rapid enough to maintain all components within their design limits. It has been shown that the fuel channel is capable of dissipating the decay heat even in case of sustained film boiling. The thermal shock experienced by the calandria tubes has been evaluated and shown to be within acceptable bounds for rapid quenching with nucleate boiling on the calandria tube outer surface. It is noted that in the detailed design stage, experiments on critical heat flux and minimum heat flux would have to be carried out to eliminate the uncertainties in these parameters, which have a significant impact on thermal stress in the calandria tubes. Finally, the effects of various steam/water densities in the upper unflooded calandria space have been explored and it has been demonstrated that steam/water mixture density yielding the maximum reactivity peak cannot be achieved by entrainment because the required value exceeds thermohydraulic limits on steam/water by an order of magnitude.

ACKNOWLEDGEMENT

This work was sponsored by the U.S. Department of Energy.

REFERENCES

[1] P. HEJZLAR, "Conceptual Design of a Large, Passive, Pressure-Tube Light Water Reactor," Sc.D. Thesis, Department of Nuclear Engineering, Massachusetts Institute of Technology (May 1994).

[2] P. HEJZLAR, N. E. TODREAS, and M. J. DRISCOLL, "Large, Passive, Pressure-Tube LWR with Voided Calandria," accepted for publication in *Nucl. Technol.*

[3] N. L. SHAPIRO, and J. F. JESICK, "Conceptual Design of a Large Heavy Water Reactor for U.S. Siting," CEND-379, Vol. III, Combustion Engineering (1979).

[4] N. Zuber, and M. Tribus, "Further Remarks on the Stability of Boiling Heat Transfer," Report 58-5, Univ. of California, Los Angeles (1958) (also cited in Whalley, 1987).

[5] L. A. Bromley, "Heat Transfer in Stable Film Boiling," *Chem. Eng. Prog.* 46, No. 5, 221 - 228 (1950).

[6] W. M. Rohsenow, "A Method of Correlating Heat Transfer Data for Surface Boiling Liquids," Trans. ASME, Vol. 74, 969 (1952).

[7] P. B. Whalley, Boiling Condensation and Gas-Liquid Flow, Clarendon Press, Oxford (1987).

[8] A. E. Bergles, and W. G. Thompson, "The Relationship of Quench Data to Steady-State Pool Boiling Data," *Int. J. Heat Mass Transfer* 13, 55-68 (1970).

[9] W. S. Bradfield, "On the Effect of Subcooling on Wall Superheat in Pool Boiling," *J. of Heat Transfer* 89, 269-270 (1967).

[10] V. K. Dhir, and G. P. Purohit, "Subcooled Film-Boiling Heat Transfer from Spheres," *Nuclear Eng. and Design* 47, 49-66 (1978).

[11] G.F. Gillespie and R. G. Mayer, "Moderator Boiling on the External Surface of a Calandria Tube in a CANDU Reactor During a Loss-of-Coolant Accident," Proc. of the International Meeting on Thermal Nuclear Reactor Safety, Chicago, August 29-Sept. 2, 1523-1533 (1982).

[12] H. J. Ivey, and D. J. Morris, "On the Relevance of the Vapor-Liquid Exchange Mechanism for Subcooled Boiling Heat Transfer at High Pressure, AEEW Report AEEW -R137 (1962) (cited in Whalley, 1987, p.143).

[13] J. F. BRIESMEISTER, Ed., "MCNP - A General Monte Carlo Code for Neutron, Photon and Electron Transport, Version 3A/3B/4," Los Alamos National Laboratory Report LA-7396-M, (1986) Revised in 1988 and 1991.

[14] I. Kataoka, M.Ishii, and K. Michima, "Generation and Size Distribution of Droplets in Gas-Liquid Annular Two-Phase Flow," Argonne National Laboratory Report ANL/RAS/LWR 81-3, (1981).

[15] G. H. McCaughey, and G. H. Bidinger, "Film Effects of Fire Sprinklers on Low-Enriched-Uranium Storage Systems," Trans. Am. Nucl. Soc., Vol. 56, 329 (1988).

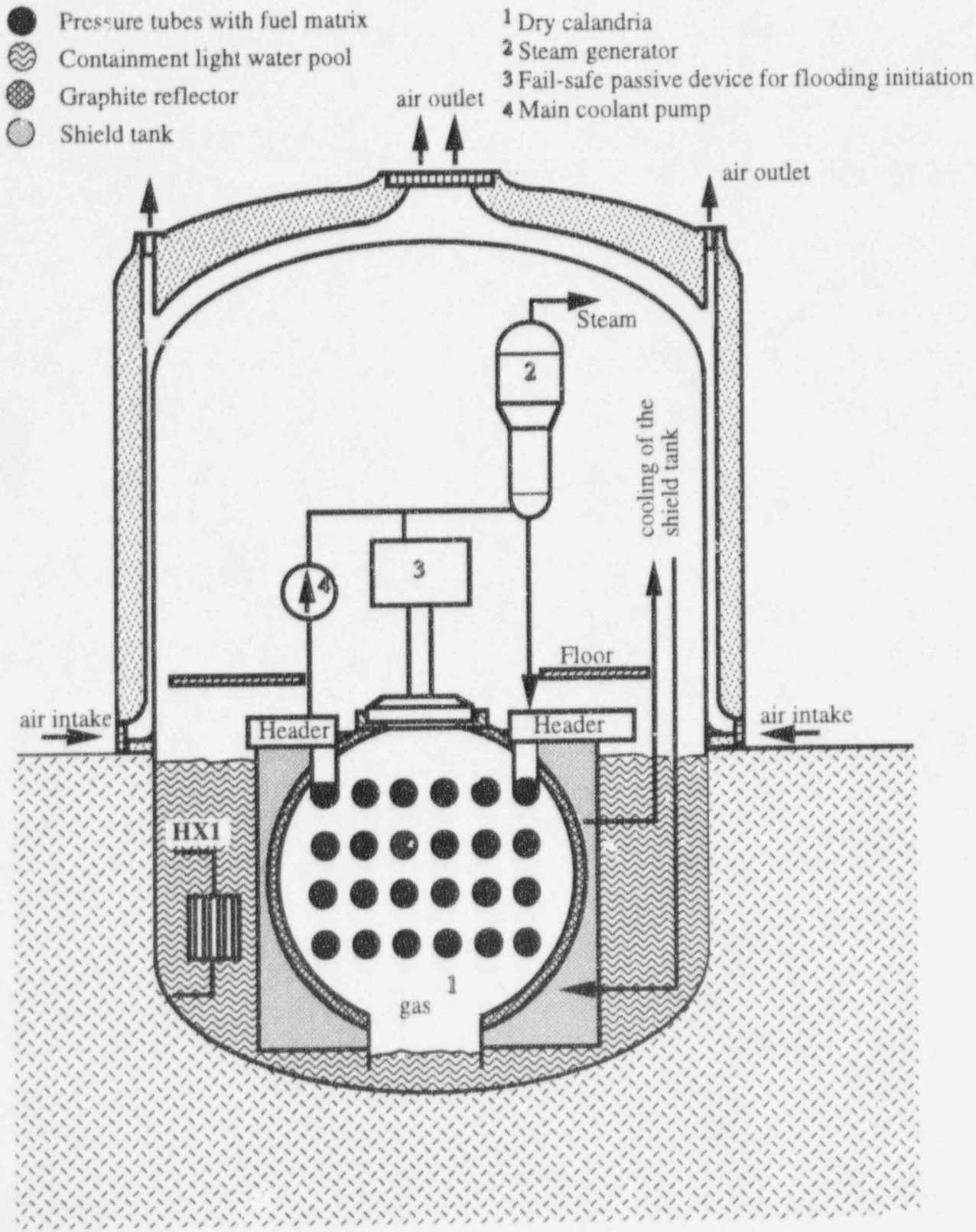

Not to scale

Figure 1. Schematic of the passive pressure tube LWR—overall concept.

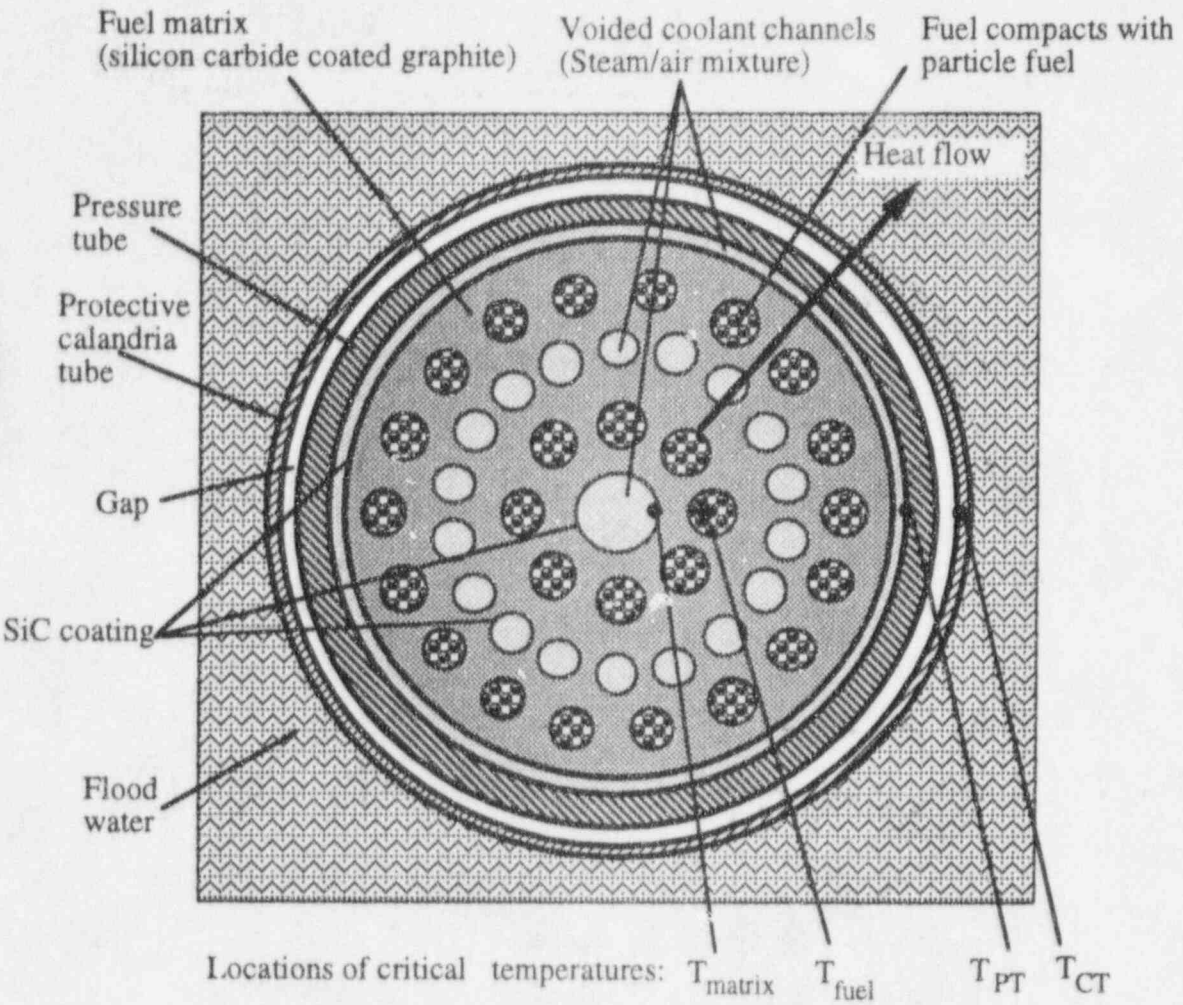

Figure 2. Flooded fuel channel.

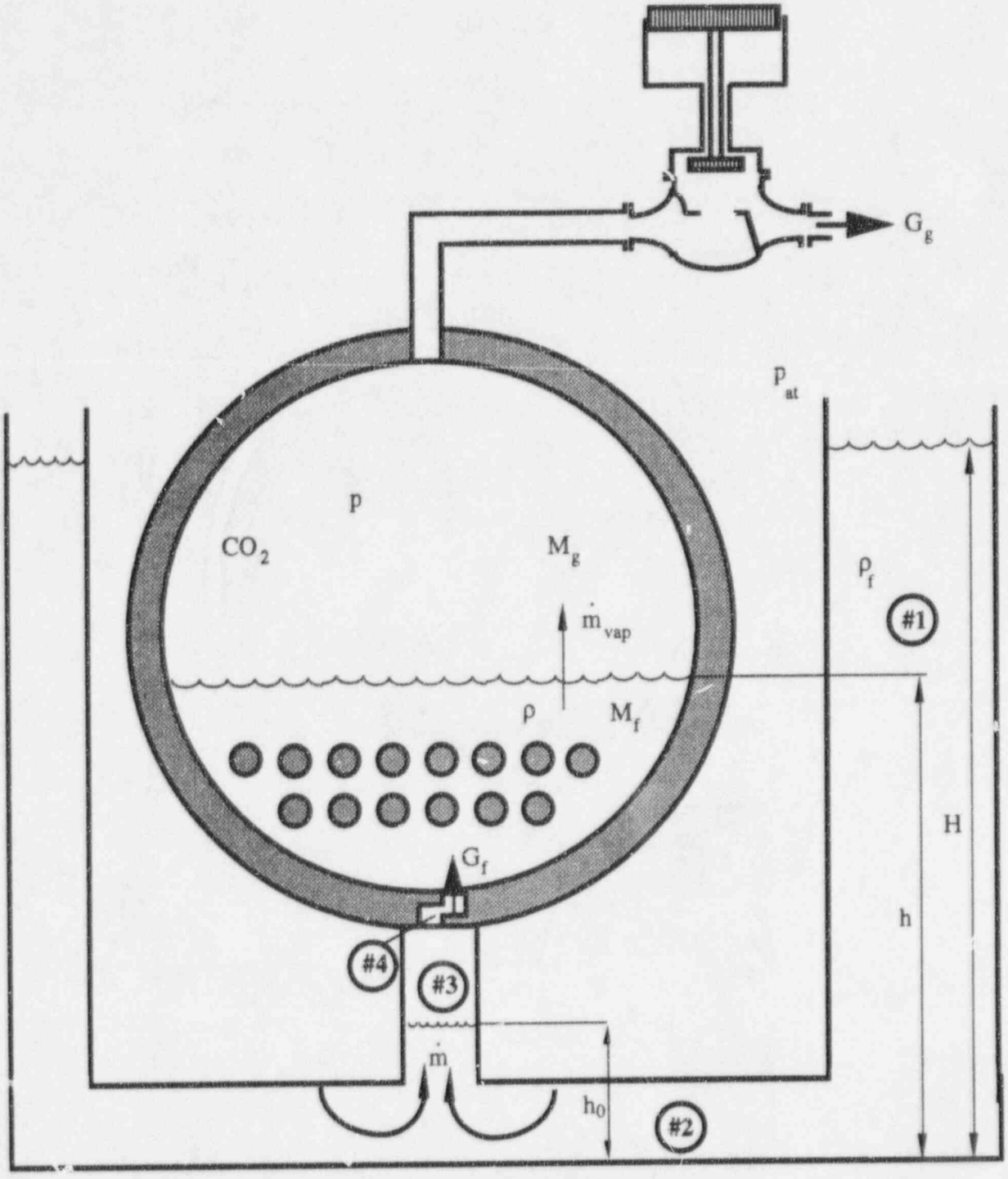

Figure 3. Computational schematic of calandria flooding showing nomenclature.

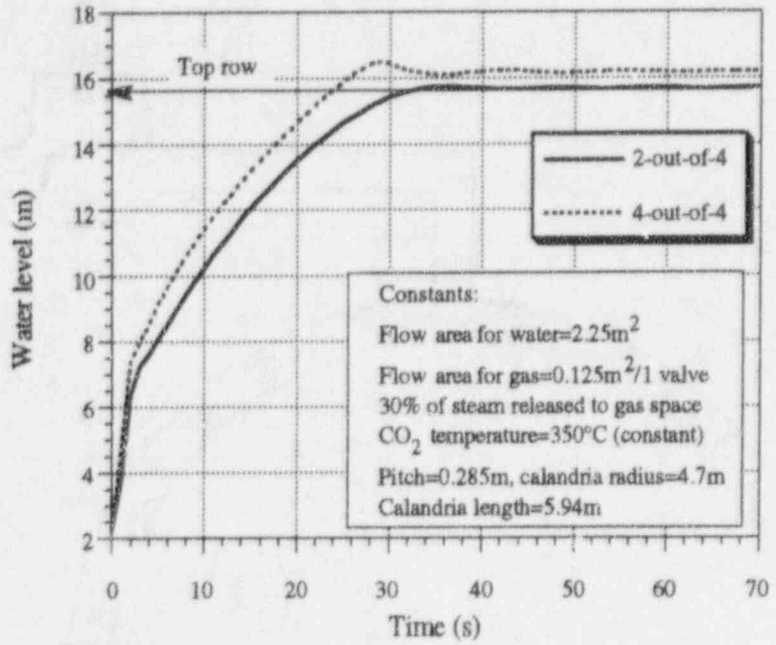

Figure 4. Calandria flooding curves for 4-out-of-4 and 2-out-of-4 valves opened.

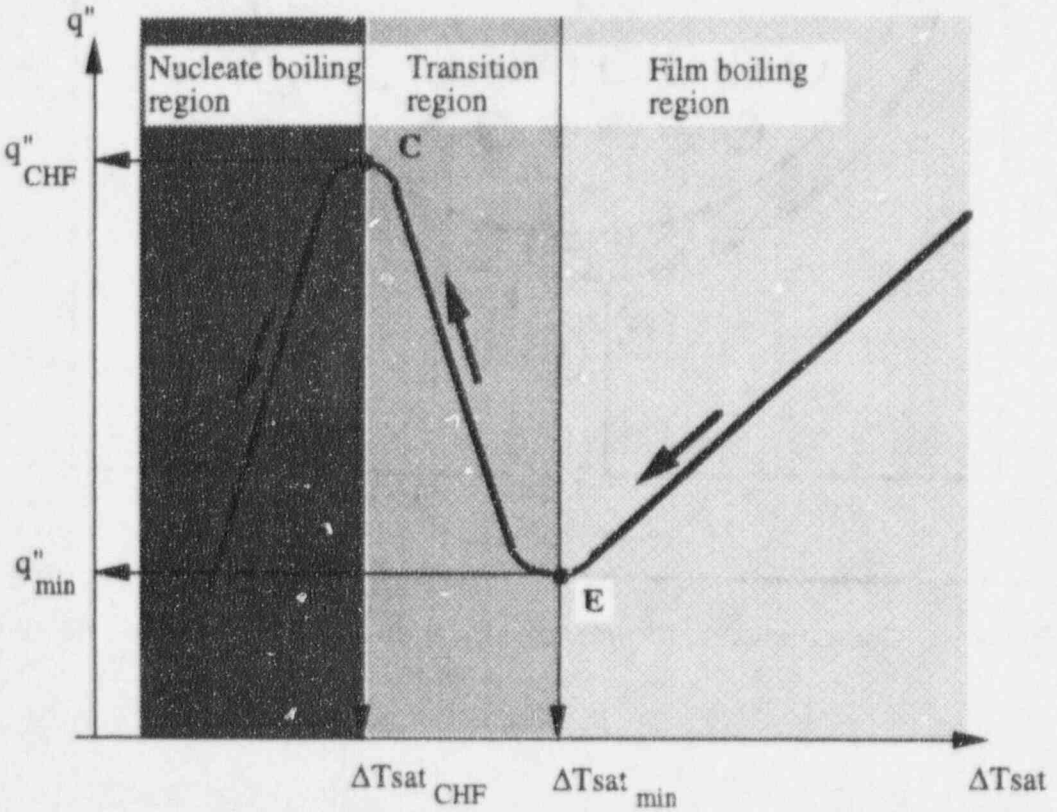

Figure 5. Calandria tube cooldown trajectory.

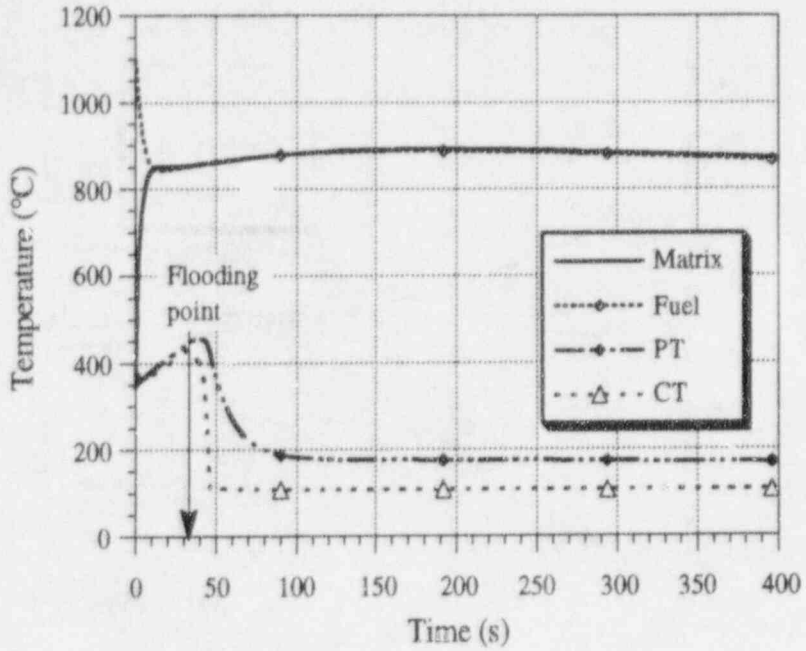

Figure 6. Temperature histories following LOCA without scram for assumption of early achievement of nucleate boiling.

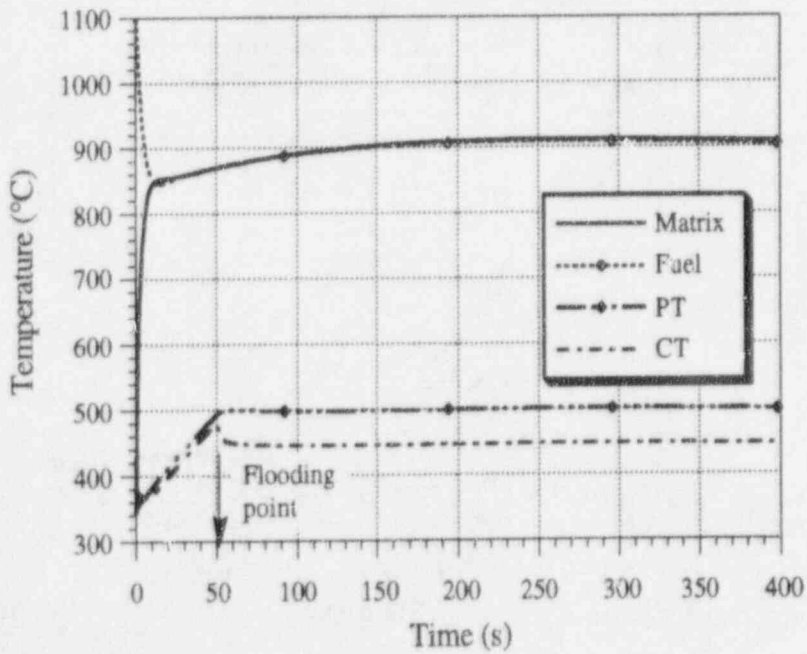

Figure 7. Temperature histories for sustained film boiling at calandria tube surface following LOCA without scram.

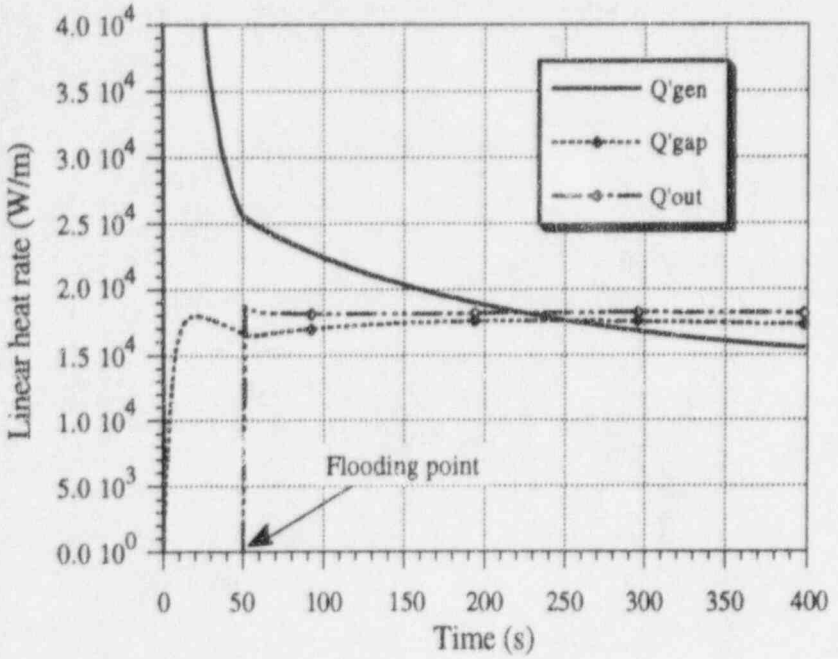

Figure 8. Linear heat rates for sustained film boiling at calandria tube surface following LOCA without scram.

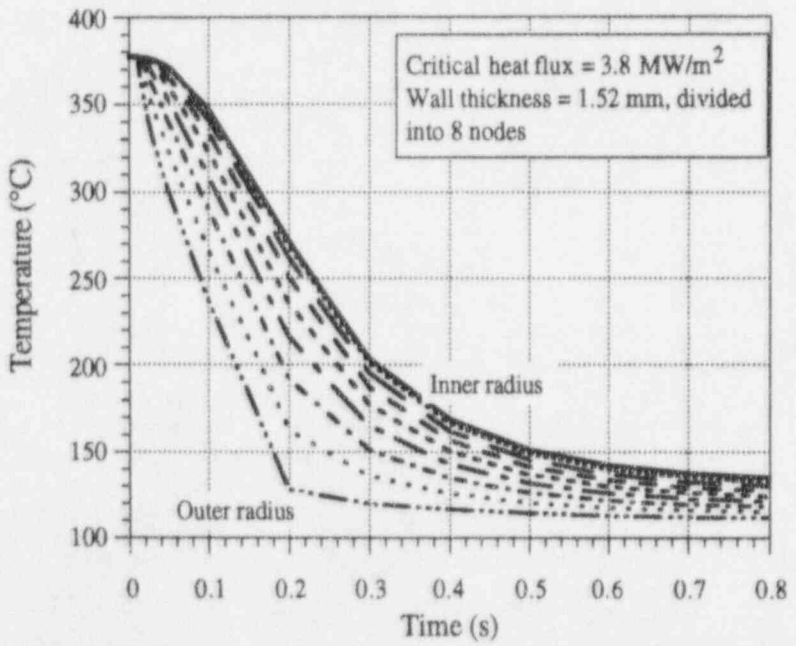

Figure 9. Calandria tube cooldown for inadvertent flooding process.

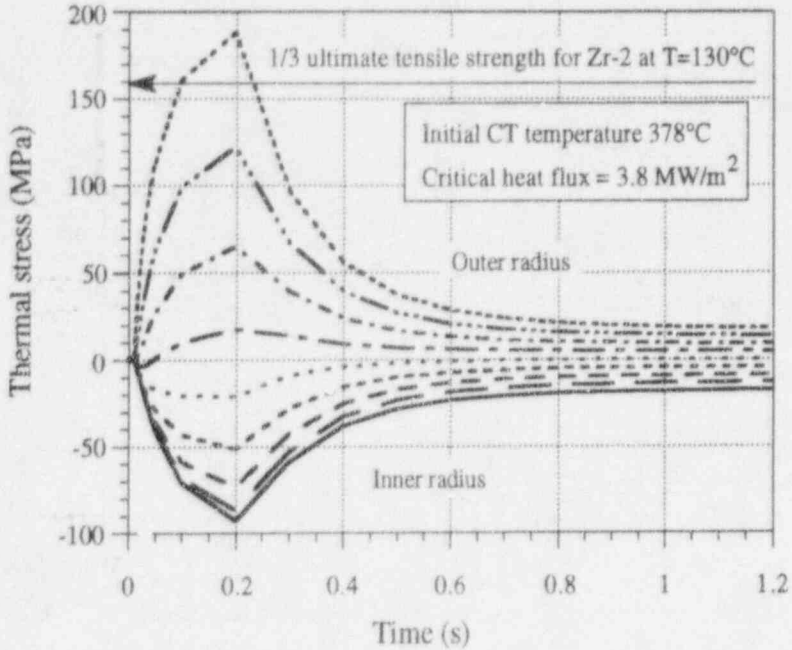

Figure 10. Time development of thermal stress in the calandria tube wall for inadvertent flooding process.

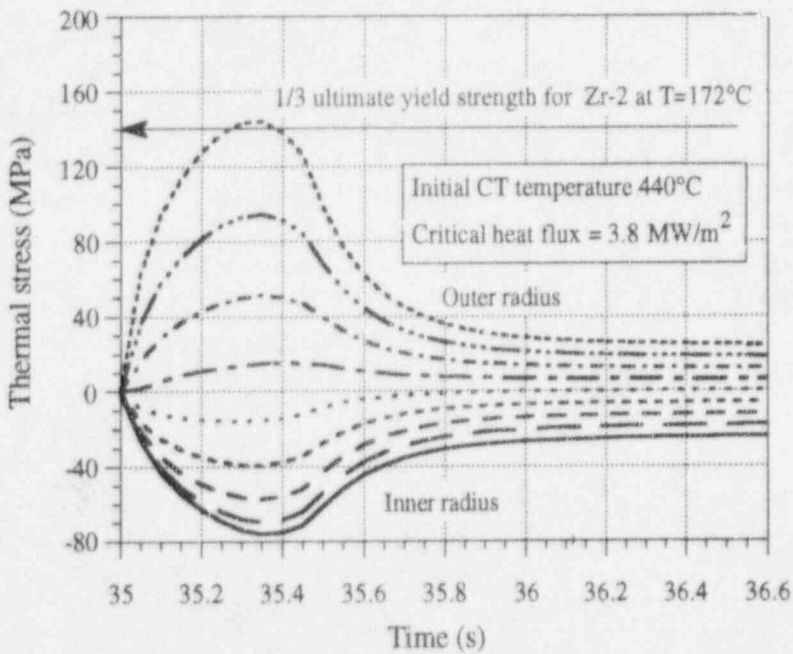

Figure 11. Time development of thermal stress in the calandria tube wall for LOCA without scram scenario.

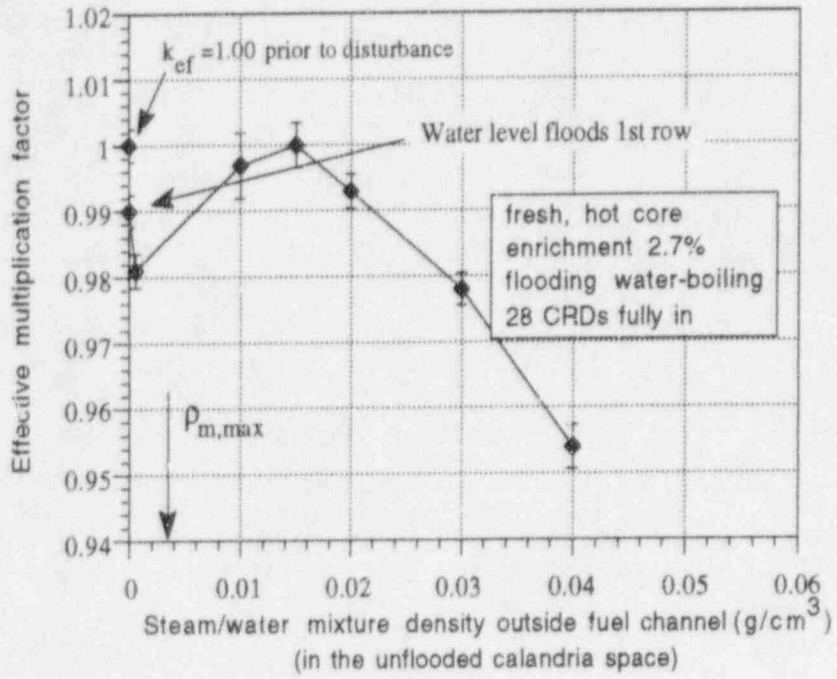

Figure 12. Reactivity behavior for calandria inadvertent flooding with hypothetical water entrainment for hot core.

SBWR PCCS VENT PHENOMENA AND SUPPRESSION POOL MIXING

P. Coddington

Thermal-Hydraulics Laboratory
Paul Scherrer Institute
CH-5232 Villigen PSI
Switzerland

M. Andreani

Nuclear Engineering Laboratory
Swiss Federal Institute of Technology
ETH-Zentrum, CH-8092 Zurich
Switzerland

Abstract

The most important phenomena influencing the effectiveness of the pressure suppression capability of the water pool within the Wetwell compartment of the SBWR Containment, during the period of Passive Containment Cooling System (PCCS) venting, have been critically reviewed. In addition, calculations have been carried-out to determine the condensation of the vented steam and the distribution of the energy deposited in the liquid pool. It has been found that a large contribution to the vapour suppression is due to condensation inside the vent pipe. The condensation rate of the steam inside the bubbles, produced at the vent exit, during their rise to the surface, may however be rather low, because of the large size of the bubbles. This can lead to vapour channelling to the Wetwell gas space. The above comments are likely to be ameliorated if the vent exit is a distributed source or sparger. Due to the large water flow rates within the "bubbly two-phase plume" generated by the gas injection, the water in the pool above the vent exit is likely to be heated nearly isothermally (perfect mixing). The effect of the suppression pool walls would be to enhance the recirculation and, consequently to promote mixing. The large size of the bubbles with respect to the vent submergence, the influence of the vent pipe diameter on the condensation therein and of the walls on pool mixing are the most severe difficulties in extrapolating the results from scaled experiments to prototypical conditions.

1 Introduction

Following a hypothetical Loss Of Coolant Accident in the General Electric (GE) Simplified Boiling Water Reactor (SBWR), the increase in the reactor containment pressure is determined in the long term by the pressure response of the Wetwell. In fact, some of the nitrogen in the Drywell of the containment flows with steam from the reactor pressure vessel (RPV), through the condensers of the Passive Containment Cooling System (PCCS), where the steam is condensed, into a vent pipe, which discharges the gas and the un-condensed steam into the suppression pool, about 0.75 to 1 metre below the pool surface.

The pressure increase in the Wetwell has thus two components: i) due to the flow of the nitrogen originally in the Drywell into the Wetwell, and ii) an increase in the steam partial pressure. The total mass of nitrogen in the SBWR containment is given, so that this bounds the increase of

the steam partial pressure, as this is controlled by any amount of steam escaping to the gas space (vapour channelling effect) in the Wetwell and by the rise in the water temperature at the surface of the pool due to the energy deposited by the condensed steam.

From the system behaviour perspective, there are two important considerations as the uncondensed steam mixed with nitrogen flows into the suppression pool: i) what fraction of the steam is condensed as the gas/vapour 'bubbles' rise to the surface of the suppression pool, and ii) how the energy, resulting from the steam condensation, and transferred to the surrounding water, mixes in the large volume of water in the suppression pool. It is the purpose of this paper to address these issues by examining the basic physical phenomena related to the flow of the steam-nitrogen mixture into the suppression pool.

Calculations will be presented for the typical conditions of the SBWR [1], with reference to the prototypical design and the geometries of three test facilities, characterized by three different volumetric scales R_V: PANDA [1] ($R_V = 1:25$), LINX[a] (separate effects facility, R_V not applicable), and GIRAFFE [3]($R_V = 1:400$).

2 Steam Condensation

Various steam condensation modes are possible along the path between the PCCS exit and the surface of the suppression pool. Four different regions (Fig. 1), each characterized by different heat and mass transfer characteristics, can be recognized:

- Condensation within the vent pipe
- Condensation during formation of the bubble
- Condensation during bubble uprise
- Condensation in the surface region (spout)

In this paper, calculations of the condensation rates in the first three regions are presented. As regards the condensation in the spout region, phenomenological considerations and an approximate calculation are presented in a separate work (Andreani and Tokuhiro [4]).

2.1 Condensation within the PCCS vent pipe

In order to determine the possible level of steam condensation within the vent pipe, the model of Meier [5] was used to evaluate the fraction of steam that condenses along the section of the vent pipe located below the surface of the suppression pool. This model features a numerical integration procedure for the one-dimensional mass, momentum and energy conservation equations describing annular flow inside a vertical tube surrounded by subcooled water. The liquid film was assumed to be laminar and the temperature of the gas-vapour mixture was considered uniform over the tube cross section and equal to the saturation temperature of the steam. The model has the flexibility

[a]The LINX program includes so far the following three experimental facilities:

1. LINX I - Small scale thermal plumes (Huggenberger et al. [2]).
2. LINX I.5 - Isothermal Air-water plume studies in a tank 0.8 x 1.0 m [29]
3. LINX II - An intermediate, high pressure (10bar), steam-air facility under construction. LINX II has a scale R_V of 1:190, based upon suppression pool surface area.

0.5 m/s: this is a typical liquid velocity for a two-phase air-water plume at 0.5 to 1.0 m above the vent [8,9].

The results of the calculations using the model of Meier [5] are presented in Figs. 2 to 5, for vent pipe diameters of 20 mm (typical of GIRAFFE), 40 mm (typical of LINX) 71.5 mm (PANDA) and 250 mm (SBWR). Each figure shows the mass flow of steam at the vent exit as a function of the inlet steam mass flow rate, for the three suppression pool temperatures of 40, 60 and 80°C. The length of the submerged part of the vent was taken to be 1.0 m. The maximum inlet steam mass flow rate, in each figure, corresponds to a vapour/gas velocity of 4.0 m/s; this is about twice the average velocity estimated for the SBWR [10]. The results presented show two major features: 1) there is significant condensation along the vent line even for high nitrogen mass fraction; and 2) the fraction of the inlet steam that is condensed increases as the vent diameter is decreased, since the vent pipe heat transfer area to flow area is proportional to 1/D (Huggenberger [11]). The results show, for example, that for the SBWR, with a pool temperature of 60°C and a vapour velocity of 2 m/s, about 31% of the steam is condensed, while for PANDA, LINX and GIRAFFE the percentage of steam condensed is about 53%, 63% and 76%, respectively. We see, therefore, that for the small scale facilities like GIRAFFE, that there will be significant scale distortions as a large fraction of the vent steam is condensed along the vent pipe. Additional vent pipe condensation calculations and further analysis of the results can be found in [12].

Because of the high fraction of steam condensed, the condensation along the vent pipe should be directly modeled in all analyses of the SBWR containment and PCCS system. This is particularly important for the small scale experiments.[b] A detailed analysis is also important because the highest heat fluxes to the pool will occur close to the surface and will therefore enhance any pool thermal stratification. However, stratification will be attenuated by the nitrogen content flowing from the vent into the pool and providing effective mixing of the volume of liquid located between the vent and the pool surface [10].

2.2 Condensation during bubble formation

The size of the steam bubbles originating by injection of pure vapour from small diameter tubes has been investigated in a few works [13][14][15]. These studies show that the volume of pure steam bubbles at detachment is smaller than for pure air bubbles under the same conditions: substantial condensation occurs during the formation stage and it becomes very large even for moderate subcoolings (10 to 20 K).

Studies on the size of bubbles resulting from the injection of mixtures of gas and vapour from large diameter vents have, however, not been reported in the literature. For these special conditions, the basic problem is to establish whether substantial condensation occurs before the bubble detaches, and to what extent mass transfer affects the stability of the bubble during its growth phase.

Qualitative results have been presented by Flanigan et al. [16]: for the same flow rate, two-component bubbles observed at the time of detachment from small orifices (up to 20.2 mm in diameter) were smaller than those resulting from injection of air alone.

The importance of condensation during the period prior to bubble detachment has been evaluated using the results of Mayinger and Chen [17,18]. These results provide a direct evaluation of the condensation rate around a pure steam bubble during its formation and are expressed in terms of a liquid-side heat transfer correlation. It is assumed that the liquid-side heat transfer correlation is relatively independent of the vapour-side heat transfer and so can be applied to bubble formation

[b] In view of these scaling considerations, our recommendation is that all future small scale experiments are performed with an insulated vent pipe.

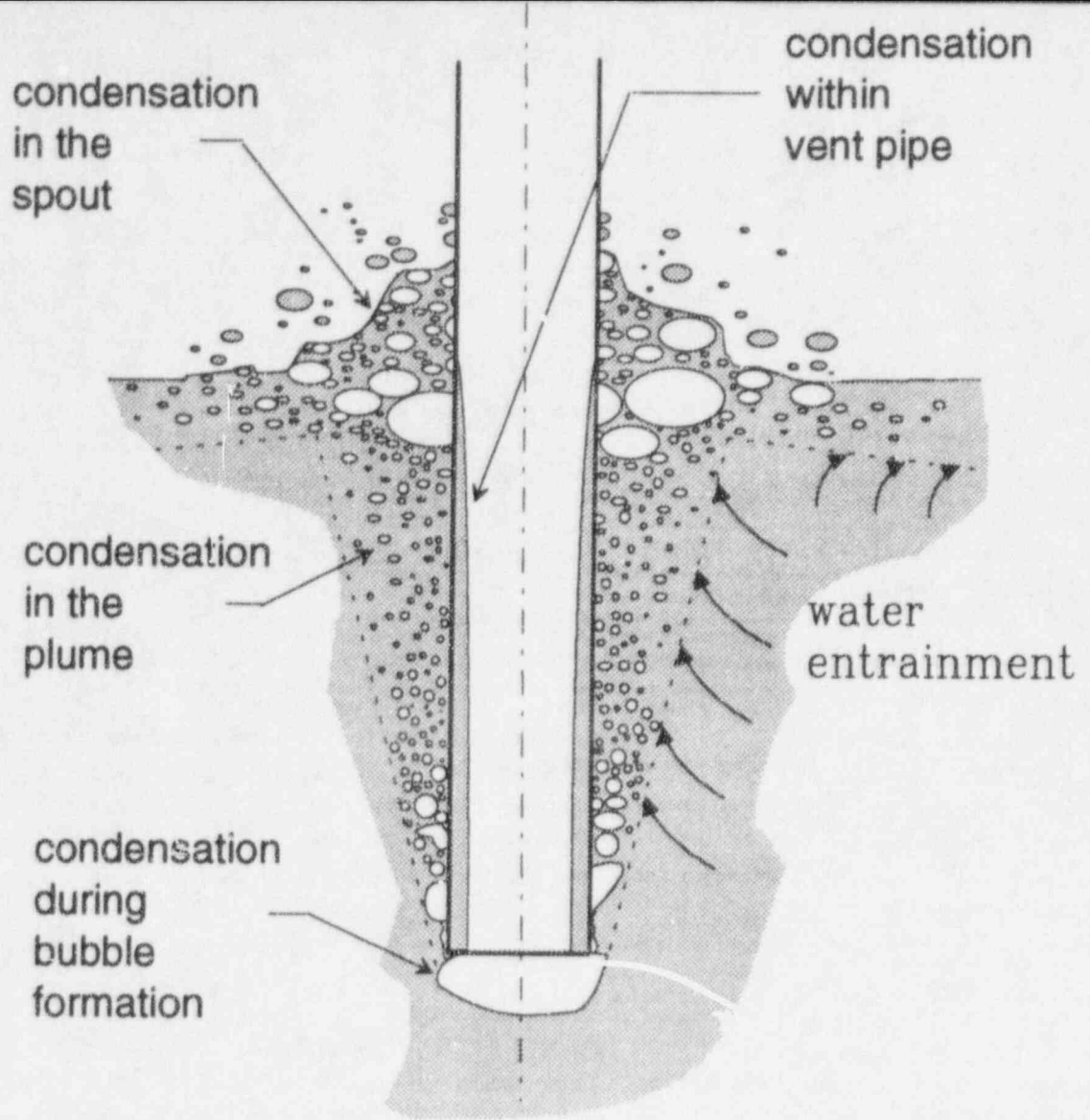

Figure 1: Schematic representation of the condensation processes and the two-phase plume resulting from the SBWR PCCS vent.

to use several different inside and outside heat transfer correlations, however for this analysis the correlations of Vierow and Schrock [6] and Chen [7] were used for the inside-tube and outside-tube heat transfer coefficients, respectively. It was further assumed that a typical bubble plume develops on the outside of the tube, and that gas blanketing does not reduce the heat transfer area on the outside wall. The latter situation can be expected for the largest gas injection rates, due to the large size of the initial bubbles (see §4.1).

The calculations were performed using the following inlet boundary conditions, which are typical of those for the SBWR during the Drywell venting period.

Steam partial pressure,	P_s	1.0 bar
Nitrogen partial pressure,	P_{N_2}	1.5 bar
Suppression pool temperature,	T_∞	40/60/80°C

The heat transfer on the pool side of the vent was evaluated assuming a liquid velocity of

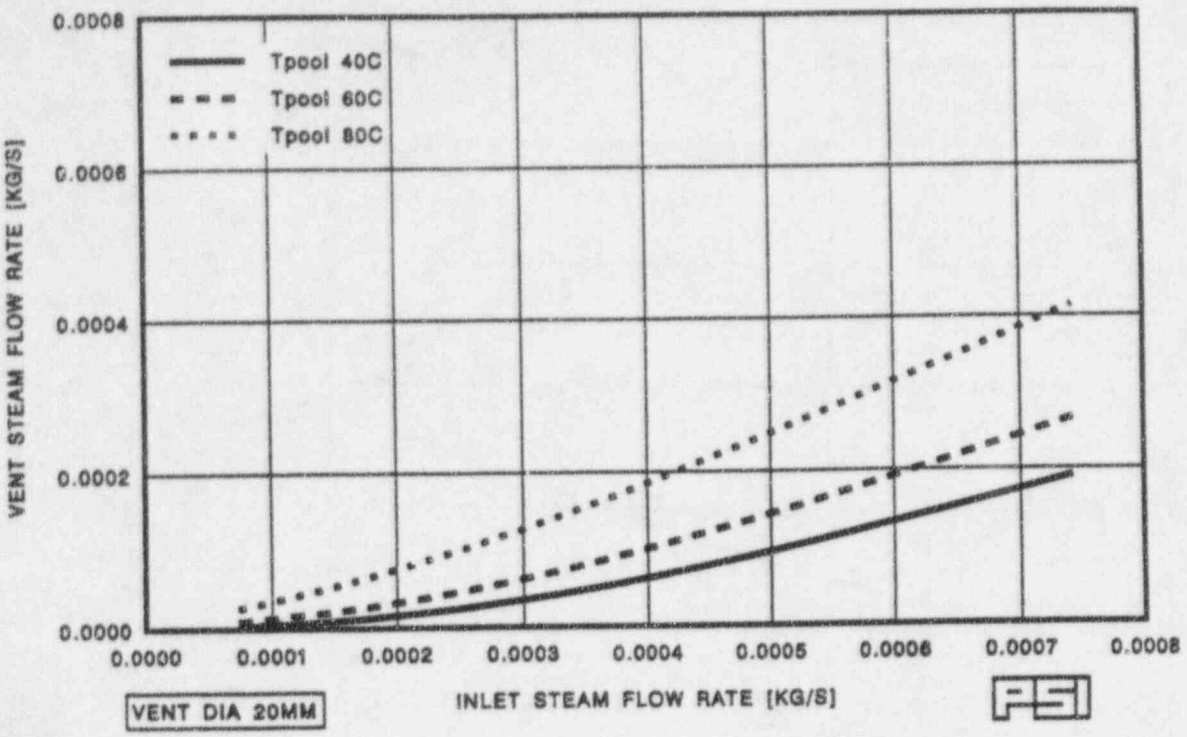

Figure 2: PCCS vent condensation: Vent steam flow rate for a vent diameter of 20 mm.

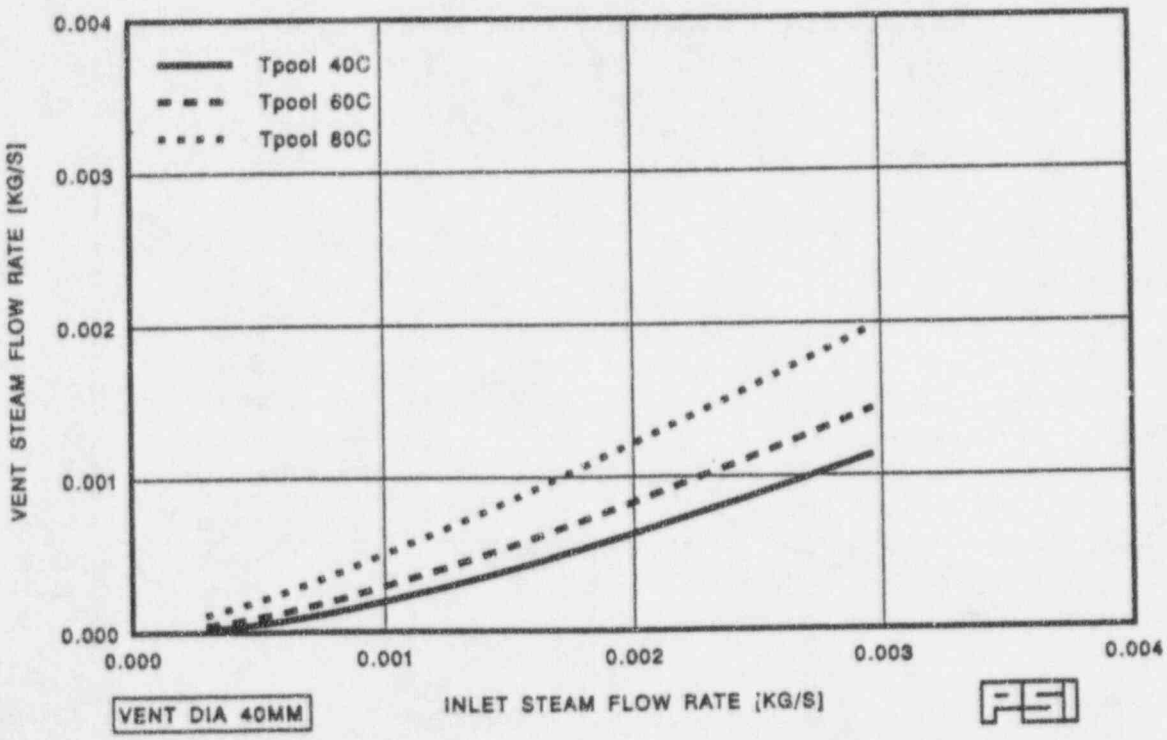

Figure 3: PCCS vent condensation: Vent steam flow rate for a vent diameter of of 40 mm.

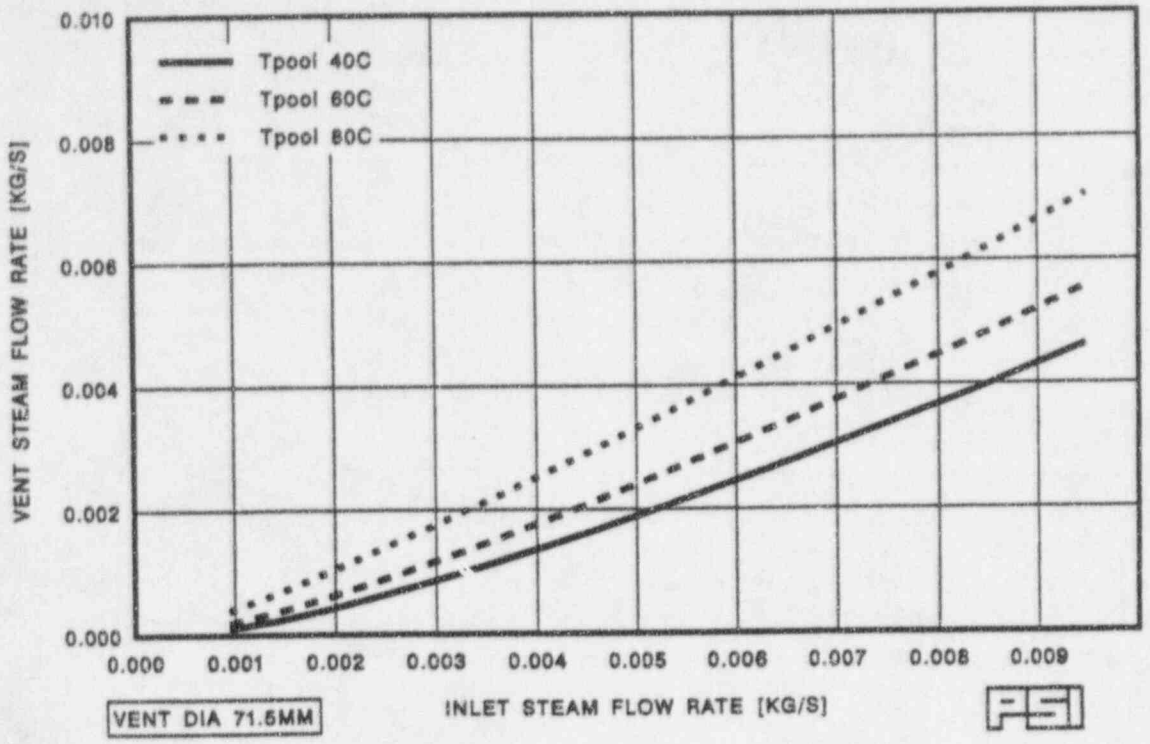

Figure 4: PCCS vent condensation: Vent steam flow rate for a vent diameter of of 71.5 mm.

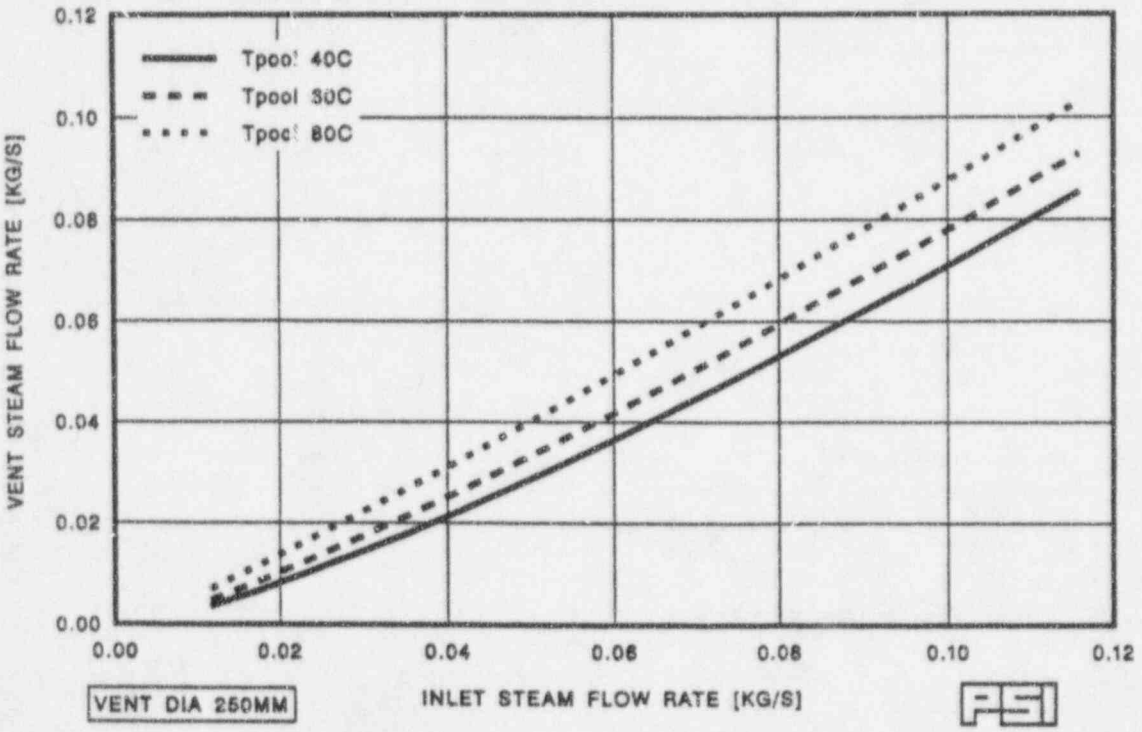

Figure 5: PCCS vent condensation: Vent steam flow rate for a vent diameter of of 250 mm.

at the end of the vent at least for bubbles up to a few cm in diameter. The above assumption, that the same external heat transfer coefficient can be used in the evaluation of condensation with and without non-condensable gases is usually made for rising bubbles [21,25] and is supported by the available experimental data. A model has been developed [19] to describe the growth and collapse of a bubble with a well defined surface, and containing saturated or superheated steam and air. This lumped-parameter model (based on mass and energy conservation equations) uses the liquid side heat transfer coefficients of Mayinger and Chen [18]. A vapour side heat transfer coefficient of $300\,\mathrm{W/m^2\,K}$ was taken from Moody [20], while the steam and air (non-condensable gas) are assumed to be uniformly distributed within the bubble. This is a reasonable assumption for bubbles of diameter greater than about 5 mm, as was shown in the analysis of Jacob and Mayor [21].

The results of the model are shown in Fig. 6 in the form of bubble diameter as a function of time, and in Fig. 7, which shows the fraction of the inlet steam that is condensed. Two calculations are shown, one for an almost pure air flow (air mole fraction 90%) and one for almost pure steam (steam mole fraction 90%). In both cases the total vapour volumetric flow rate Q_g was $3.66\,10^{-3}\,\mathrm{m^3/s}$ at a temperature of 400 K and pressure of 1 bar. The steam flow calculation shows three variants with different choices for the velocity used in the Reynolds number in the correlation of Mayinger and Chen [19]. These variants are shown because in the experiments of Mayinger and Chen the steam bubbles were formed in flowing rather than stagnant liquid, so that the velocity was well defined.

In order to evaluate the conditions at the time of detachment, the final bubble diameter must be determined. From a literature survey [22], it was found that for orifice diameters larger than a few mm, the correlations having the form proposed by Davidson and Schüler[23]:

$$V_b = C\,\frac{Q_g^{6/5}}{g^{3/5}} \tag{1}$$

represent well the bubble volume data in a wide range of gas flow rates and orifice diameters, including downwards-oriented discharges, for both the constant pressure and constant flow cases (at least for sufficiently large flow rates). The values of the constant C in Eq. (1) are, according to various authors, between 1.138 and 1.45.

Equation (1) was used to estimate the final bubble diameters and so from Fig. 7 the detachment times. Equation (1), for all the proposed values of C, gives a final bubble diameter of about 0.09 m, which for the air flow calculation corresponds to a growth time of about 0.1 s, while for the mainly-steam bubbles, the growth times range from 0.14 to greater than 0.2 s. This final value corresponds to the condensation of 25% to 55% of the vent steam flow (Fig. 7). Further calculations and analysis are given in [19].

The model and analysis presented above and in [19] show therefore, on the basis of the pure vapour data of Mayinger and Chen, that a significant fraction of the steam flow is likely to be condensed during the period of bubble formation, i.e., prior to detachment, for bubbles of a few cm in diameter. Although no data is available for the heat transfer during the formation of steam-air bubbles, the above is consistent with qualitative observations from more prototypical SBWR PCCS venting experiments that show significant condensation at the point of bubble generation (Peterson [24]).

For larger bubbles, such as those expected during the early phase of PCCS venting (see §4.1), no data are available, and the correlations used in the present model can only yield a qualitative estimation of the influence of the various parameters on the condensation rate.

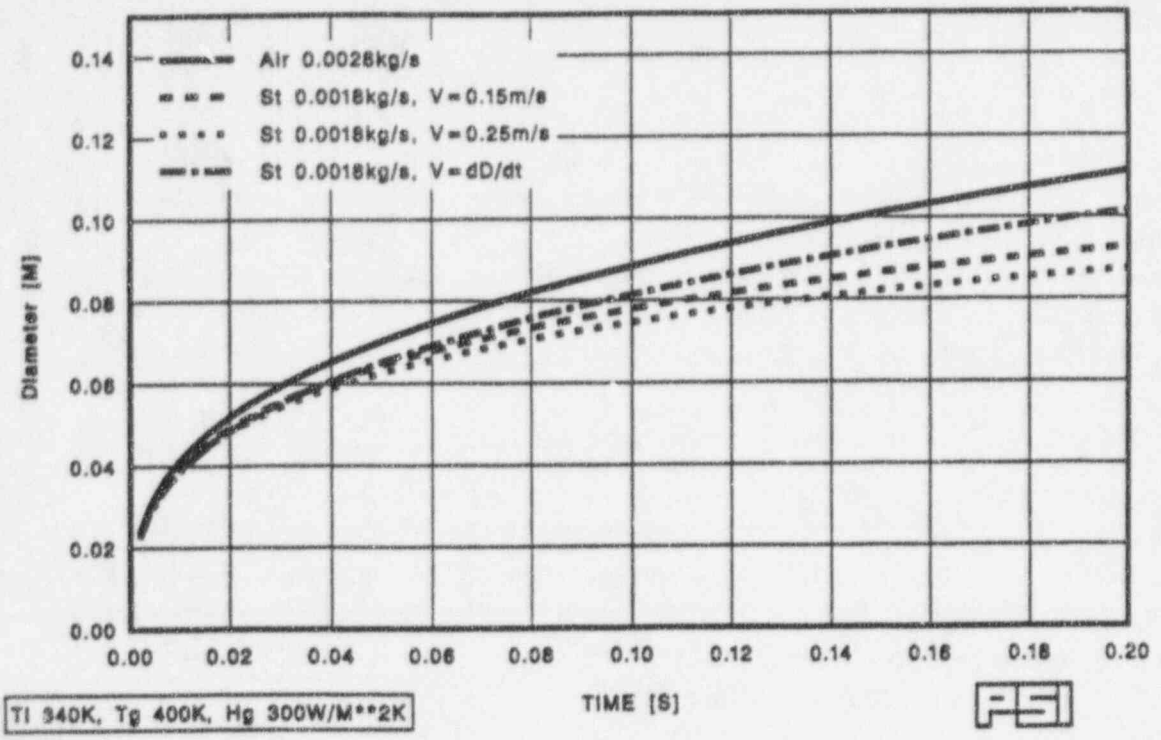

Figure 6: Bubble diameter during period of formation at the vent.

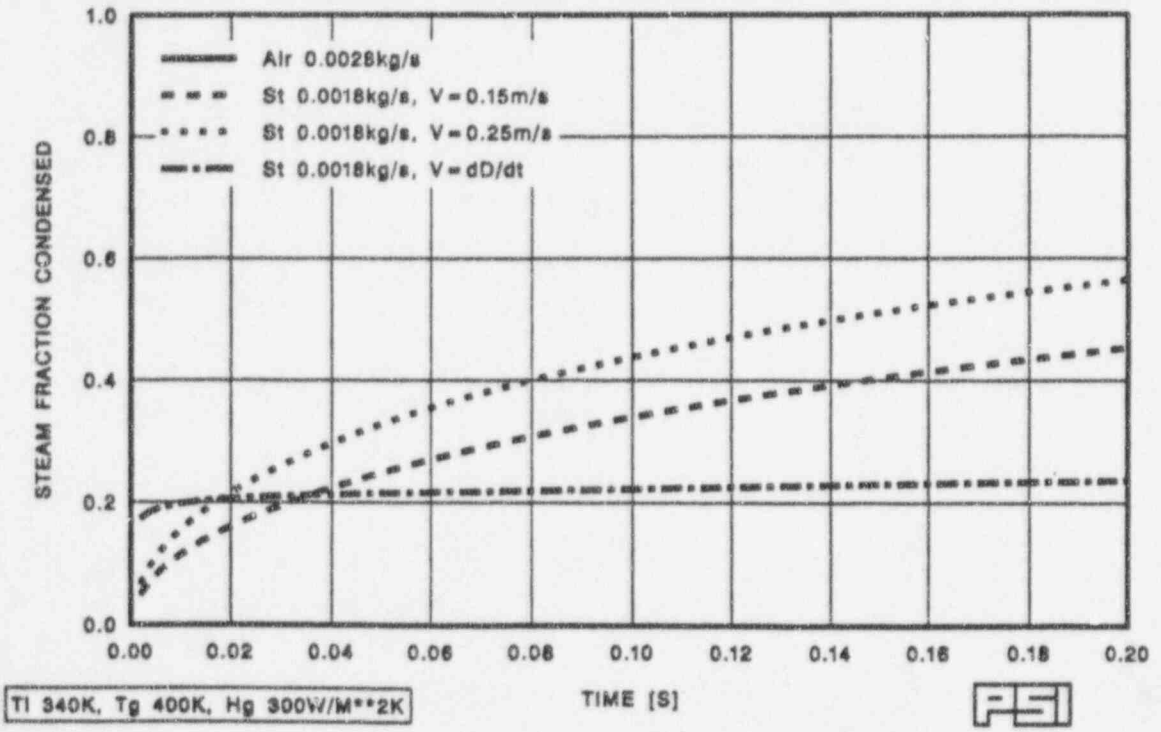

Figure 7: Fraction of steam condensed during bubble formation at the vent.

2.3 Condensation during bubble rise

Provided that the bubble formed at the vent exit breaks up within a short distance (see §4.2), a bubble swarm is produced and a well developed two-phase plume develops (as shown in Fig. 1). For the low vent submergence in the SBWR, the calculation of the bubble condensation rates aims at estimating whether the vapour channelling to the gas space in the Wetwell can be a real concern or not. To this aim, the comparison between the condensation time t_c of the bubble and its rise time t_r (between the detachment and its arrival at the pool surface) gives an estimate of the possibility that the bubble will break through the surface before being condensed.

The rise time can be calculated from the submergence L and the average absolute bubble velocity U_g (liquid velocity, U_l + bubble terminal velocity, U_∞):

$$t_r = \frac{L}{U_g} \tag{2}$$

For typical two-phase plumes, the average axial liquid velocity is between 0.5 and 1 m/s. The equilibrium mean bubble diameter for the bubble population at some distance from the injection point is 5 to 6 mm [22], the largest bubble in the population being typically two to three times larger. The terminal velocity for such large bubbles is:

$$U_\infty \sim 0.7\,(g\,2R_0)^{1/2} \tag{3}$$

which gives, for bubbles between a few mm and 20 mm in radius, terminal velocities between 0.25 and 0.6 m/s. Therefore, t_r is typically between 0.5 and 1 s.

For bubble condensation, it is stipulated that:

- Interaction effects can be neglected and the liquid pool is infinite.
- The bubble interface temperature is equal to the saturation temperature T_{SAT} at the partial pressure of the vapour in the bubble (the total pressure, if only steam is present).
- The condensation rate is heat transfer limited on the liquid side. Indeed, perfect internal mixing can be assumed for sufficiently large bubbles (Sideman and Moalem-Maron [25]).

Under these conditions, from the energy balance at the interface, the time-history of the radius R of a *pure steam bubble* is obtained [22] from

$$\beta = [1 - a\,Ja\,Pe^b\,Pr^c\,Fo]^d \tag{4}$$

with

$$\beta = R/R_o \qquad (R_o \text{ is the initial bubble radius})$$

$$Ja = \frac{\rho_f\,C_{pf}}{\rho_g\,h_{fg}}(T_{sat} - T_\infty) \qquad \text{(Jacob number)}$$

$$Pe = \frac{2R_o\,U_\infty}{\alpha_f} \qquad \text{(Peclet number)}$$

$$Fo = \frac{\alpha_f\,t}{R_o^2} \qquad \text{(Fourier number)}$$

where t is the time, α_f is the liquid thermal diffusivity, and the other symbols have their usual meaning; a, b, c and d are constants which depend on the correlation for the average liquid-side heat transfer coefficient [22]. Typically, for a variety of conditions covering bubble formation and detachment, as well as for non-spherical 'globules':

$$0.5 \leq a \leq 0.6; \quad 0.5 \leq b \leq 0.7; \quad 0.3 \leq c \leq 0.5; \quad 0.7 \leq d \leq 0.9 \tag{5}$$

From Eq. (4) it follows that the non dimensional time for the bubble collapse, i.e. $\beta = 0$, is

$$\tau = Ja\, Pe^b Pr^c\, Fo \sim 1/a \tag{6}$$

such that the collapse time varies like

$$t_c \sim \frac{R_o^2}{\alpha_f} \frac{1}{Ja\, Pe^b Pr^c} \tag{7}$$

In the above, Ja includes the subcooling dependence $\Delta T_{sub} = T_{SAT} - T_\infty$, while $Pe = Re\, Pr$ includes the bubble velocity dependence U_∞.

The influence of non-condensables on the condensation rate has been investigated by Sideman and Moalem-Maron [25] and Jacobs and Major [21], and for a uniform distribution of non-condensables, an approximate solution can be obtained [25] for the bubble collapse time τ

$$\tau = [\tau_o(\beta) + \tau_1 (\beta\, \beta_f)] \tag{8}$$

where β_f is the final bubble radius, which is asymptotically approached as the partial pressure of the vapour decreases to its saturation value at the liquid bulk temperature ($T_g \simeq T_\infty$), and the condensation process stops.

Approximate expressions for τ_1 and β_f have been used [25] for estimating the influence of the non-condensables on the condensation times. Calculations for various values of total pressure P, R_0 and steam molar fraction x_c have been carried-out [22], and here the most important results are reported:

(i) The condensation time is mostly affected by liquid subcooling and initial radius (Eq. 7). The (pure vapour) condensation times vary from typically 10 ms for small bubbles and high subcoolings to close to 1 second for large bubbles (R_0= 20 mm) and low subcooling.

(ii) For typical conditions of the SBWR, the presence of non-condensables increases the condensation time to $\beta - \beta_f < 0.01$ by up to a factor of 2 compared to the pure vapour bubble collapse under otherwise identical conditions.

(iii) The calculations show that the fluid parameters, i.e, Pe, Ja and the initial bubble size R_o have a much greater influence upon the condensation time than the presence of non-condensable gases.

(iv) In absolute terms, we see that only in the extreme cases, i.e. large bubbles and low subcoolings, does the condensation time approach and exceed the vapour rise time, and vapour channelling can occur.

3 Nature Of The Plume And Consequences For The Scaling

So far, the idealized picture of Fig. 1 has been used for representing the flow pattern above the vent. The real topology of the flow, however, can be dramatically different. Here, two geometries of the vent are considered: a) straight pipe and b) multinozzle vent, e.g., with 100 orifices.

3.1 Primary bubble size

Two regimes of PCCS venting can be defined for the SBWR, characterized by different ranges of volumetric flow rates per vent: 1)blowdown period (lasting few minutes) and 2) post-blowdown period (a few hours) [22]. Using Eq. (1) with $C = 1.138$ (the lowest value), the following SBWR vent bubble sizes can be evaluated for the two regimes. For the straight pipe:

1)	$Q_g \sim 1\,m^3/s$	$V_b \sim 0.289\,m^3$	D_b	=	0.82 m
2)	Q_g 0.05 to $0.1\,m^3/s$	V_b 0.0069 to $0.0182\,m^3$	D_b	=	0.24 to 0.33 m

The bubble sizes from each of the individual nozzles for the multinozzle vent are similarly:

1)	$Q_g \sim 0.01\,m^3/s$	V_b $0.00117\,m^3$	$D_b = 0.13$ m
2)	Q_g 0.0005 to $0.001\,m^3/s$	V_b $3.2\,10^{-5}$ to $7.3\,10^{-5}\,m^3$	$D_b = 0.04$ to 0.052 m

However, very large bubbles, i.e. greater then a few centimetres in diameter, are likely to break up into smaller bubbles due to inertia, viscous and surface tension forces. This is discussed next.

3.2 Bubble break up

According to most authors, the initial bubble breaks up within a distance between 3.5 to 10 times the bubble diameter. Wraith [26] observed that channelling of the gas to the pool surface may occur, unless the vent submergence is typically greater than three times the minimal bubble size. The minimal bubble size is the size assuming that the bubble travels about half a radius (R_0) above the vent before detachment. This criterion can be used to convert Eq. (1) with C=1.45 [26] into the following expression for the minimum vent depth L_m required to prevent channelling

$$L_m > 3\,(2.5\,R_0) > 7.5\,R_0 \tag{9}$$

$$L_m > 5.25\,\frac{Q_g^{2/5}}{g^{1/5}} = 3.33\,Q_g^{2/5} \tag{10}$$

with Q_g in m^3 and L_m in m.

Alternatively this can be inverted to give an upper bound to the flow rate (Q_g) for a given vent depth (L) above which channelling will occur

$$Q_g \leq 0.0158\,L^{5/2}\,g^{1/2} = 0.05\,L^{5/2} \tag{11}$$

with L in m.

For an SBWR vent depth of 0.75 m, this gives an upper bound to the flow rate of $0.024\,m^3/s$. Comparing this with the above, we see that it is much lower than the volumetric flow rates expected during blowdown and of the same order of magnitude as those expected thereafter. This means that if a 'straight-pipe' vent is used in the SBWR, there is a significant probability that direct channelling of nitrogen (and any un-condensed steam) will take place between the end of the vent and the suppression pool vapour space. This would then provide a direct path for un-condensed steam to flow into the suppression chamber vapour space. A certain probability for such an occurrence exists also for the multinozzle vent, but only during the blowdown period.

The bubble 'plume' above the vent is thus more likely to be similar to that depicted in Fig. 8. Under these conditions, a well developed plume does not exist, and the condensation process depends on the vent geometry.

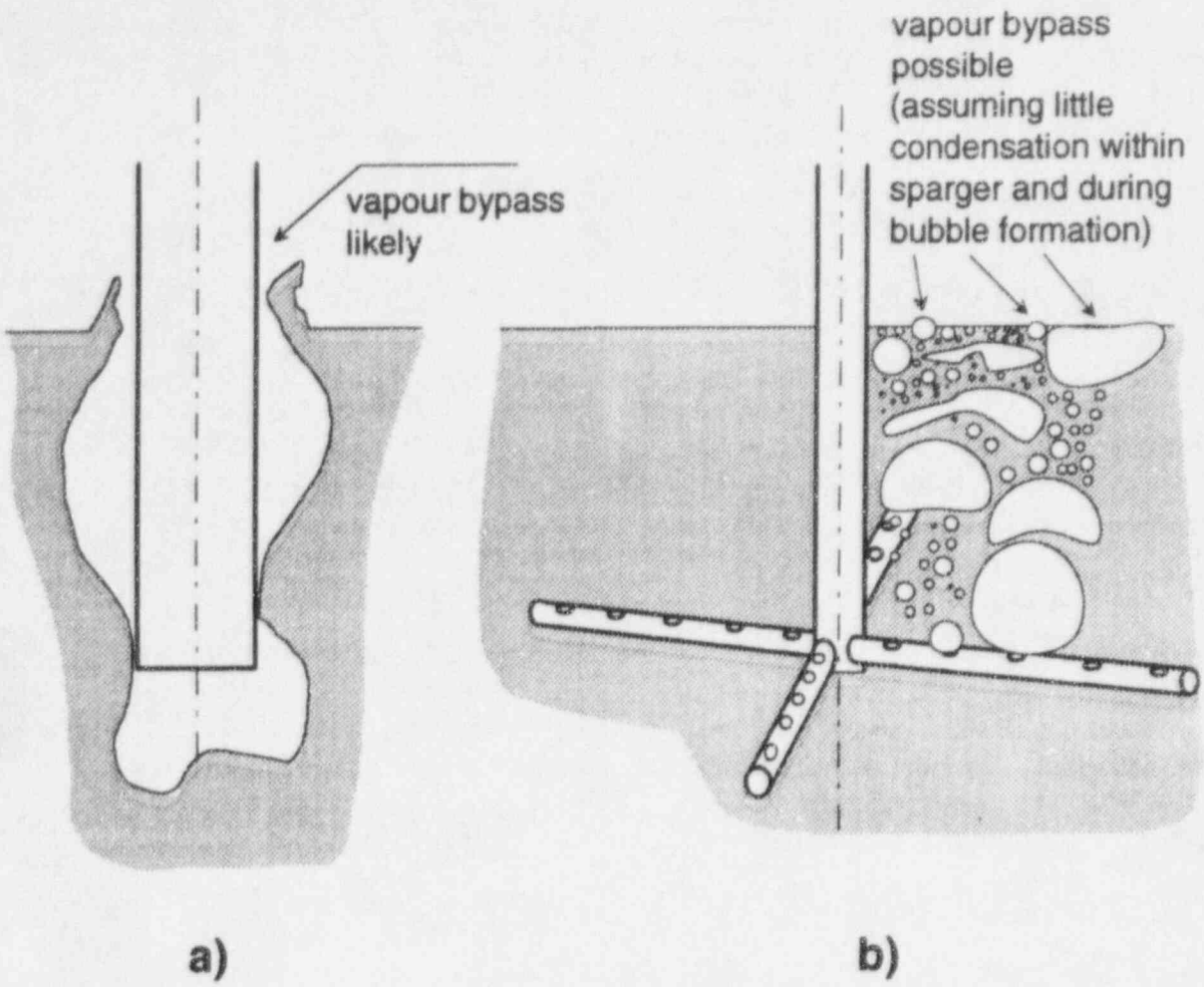

Figure 8: Sketch of the flow regimes expected for high gas flow rate discharges: a) straight pipe; b) multinozzle quencher.

3.3 Scaling

In the test facilities (subscript T), the submergence of the vent is the same as in the prototype (subscript P) because of the necessity to preserve the pressure heads, while the volumetric flow rates are scaled according to the volumetric ratio R_V (Yadigaroglu [27]). In order to gauge the representativeness of the data obtained from test facilities with respect to vapour channelling, the distortions due to scaling must be estimated. This issue is most conveniently addressed by comparing the ratio $R_t = t_c/t_r$ between the characteristic condensation time for a pure steam bubble and the time it takes for the bubble to arrive at the pool surface.[c] For the conditions considered. i.e, a single large bubble produced at the vent exit (Fig. 8a) no real plume develops, and so the contribution of the liquid velocity to the total rise velocity of the bubble can be neglected. With this assumption, and considering that the fluid in both the prototype and in the test facilities is the same, and the liquid subcooling is also the same, from Eqs. (1) to (5) and (7), one obtains:

[c]These considerations and the resulting scaling criteria do not include the extreme case of a single bubble of diameter equal or larger than the submergence.

$$R_t = \frac{t_c}{t_r} \sim Q_g^{1-3b/5} L^{-1} \tag{12}$$

Therefore, if a straight pipe is used in the SBWR, using Eq. (12) the ratio R_t in the test facilities is scaled according to:

$$\frac{(R_t)_T}{(R_t)_P} = \left[\frac{(Q_g)_T}{(Q_g)_P}\right]^{1-3b/5} \frac{L_P}{L_T} \tag{13}$$

As $L_P = L_T$ and $b = 0.5$ to 0.7, the ratio between condensation time and bubble rise time is a strong function of the volumetric flow rate. Consequently, the fraction of un-condensed steam escaping to the gas space of the Wetwell is also affected by a large distortion in the test facilities. Vapour channelling may not be detected in the test facilities, and may still occur in the prototype. It can be concluded, therefore, that the vapour channelling phenomenon *cannot be scaled* for a straight pipe geometry, when the submergence is scaled 1:1. (Experiments to clarify such issues will be performed within the LINX-II facility at various vent submergences).

However, if a multinozzle vent is used in the SBWR and the spacing of the orifices is such that no interaction between the adjacent plumes occurs, the global condensation process can be scaled, provided that the flow rates in the test facilities are equal to the flow rate from at least one individual nozzle.

4 Suppression Pool Mixing

Gas stirring of liquid basins (lakes, rivers, aeration tanks, ladle converters) is a rather widespread technique for promoting mixing between layers of fluid of different temperature or composition. Reviews of these studies for metallurgical, environmental, oil industry and several other applications have been performed by Coddington [22] and Andreani [28].

The work presented in this paper makes use of the data from several round (axi-symmetric) air-water two-phase plume experiments and their analysis, to develop a procedure (model) to determine the nature of the mixing that will occur when the steam energy is deposited in the suppression pool in the presence of the venting nitrogen.

In the analysis which follows, the bubbles are supposed to be much smaller than the vent submergence, so that a bubble plume can be assumed to exist (Fig. 1).

4.1 Infinite pool

In order to estimate the largest possible temperature rise of the water entrained into the plume by the condensing steam, and therefore the temperature difference between that of the pool surface and the entrained water, the following procedure (model) has been developed [10].

(i) All the steam flowing into the suppression pool is assumed to condense. The plume buoyancy is assumed to be dictated by the air (nitrogen) content alone. This (conservative) assumption will minimise the entrained liquid volumetric flow rate Q_l and so will maximise the temperature rise.

(ii) The assumption is made that the two-phase PCC venting contains sufficient non condensable gas (air or nitrogen) for it to behave similar to an air-water two phase plume.

(iii) The heat released into the plume by the condensation of the steam flow is assumed to be distributed uniformly within that fraction of the plume that lies within the voided part of the plume. Data from many two phase plume studies have shown that the width of the void profile is about 80% of the total plume width.

$$\text{i.e. } \lambda = (\text{void plume width/total plume width}) \sim 0.8$$

The volumetric flow of liquid within the voided plume width is taken to be $Q_l\,\lambda^2$. This is not strictly correct, but again will provide a minimum value for the liquid flow and so will maximise the temperature rise.

Under these assumptions, the temperature rise for a vent flow in which the steam mass flow rate is $\dot{M}_s$, and the air mass flow rate is $\dot{M}_a$ can be calculated from an energy balance applied to the resulting liquid volumetric flow rate:

$$\Delta T = T_{\text{plume}} - T_\infty = \frac{\dot{M}_s\, h_{fg}}{Q_l\,\lambda^2\,\rho_l\,C_{pl}} \tag{14}$$

where the only unknown is the liquid volumetric flow rate Q_l, which depends only on $\dot{M}_a$.

From the analysis of the available data for axi-symmetric air-water plumes produced in water tanks of large depths, it was concluded [10] that, for each distance above the vent source, a logarithmic fit could well approximate the experimentally observed dependence of Q_l on the air volumetric flow rate Q_a (Fig. 9). It is interesting to observe that at both distances represented in Fig. 9, the slope of the lines is the same. This provides some justification in extrapolating the data at 0.96 m to flow rates of up to 0.05 m^3(normal)/s.

For 0.96 m (distance, for which data is available closest to the submergence in the SBWR):

$$\log Q_l = 0.68 \log Q_a + 0.17 \quad (Q_l = 1.48\, Q_a^{0.68}) \tag{15}$$

The high entrainment rates predicted by Eq.(15) have been qualitatively confirmed in small scale experiments performed at Paul Scherrer Institute (Ruhstaller and Gort [29]). In these experiments, carried-out within the frame of the programme of scoping tests in support of the LINX experiments, the horizontal water flow rate on the surface of a 1 m deep water pool was measured (by integrating the velocity profiles) at different distances from the axis of the plume. Air (at several volumetric flow rates) was injected at the bottom of the pool through three different orifices: a porous plug and two tubes of 10 and 20 mm, respectively.

As an example, for $Q_a = 0.67 \cdot 10^{-3}$ m^3/s, the measured horizontal flow rate Q_l close to the turning point[d] (the precise position of which is, however, not known) of the plume was (for the various orifices used) between 0.02 and 0.028 m^3/s. Eq. (15) predicts, for the same conditions, a liquid flow rate of 0.01 m^3/s. The larger volumetric flow rates resulting from our experiments can be due to the effect of the wall and the entrainment in the horizontal spreading layer. Qualitatively, however, they confirm the large entrainments predicted by Eq. (15).

Using Eq. (14) in Eq. (13), the resultant temperature rise in the plume can be calculated. Various examples for flow rates typical of LINX and the SBWR, are given in Table I.

We see that under conditions of equal steam and air mass flow rates, the plume temperature rise ΔT at a distance of about 1 m above the vent, is typically 0.15 K or less for LINX flows, and about 0.3 K for the SBWR. These results show therefore, that because of the large buoyancy of a

[d] The radial distance from the centreline corresponding to the half-width of the plume at the pool surface

Steam Flow kg/s $\times 10^{-3}$	Air Flow kg/s $\times 10^{-3}$	Q_a m^3/s (normal)	Q_l m^3/s	ΔT K
LINX				
	0.3	0.00024	0.0052	1.86
	0.6	0.00056	0.0091	1.07
11.	1.4	0.0012	0.0154	0.628
	2.8	0.0024	0.0244	0.397
	5.6	0.00487	0.0396	0.244
	11.	0.00974	0.0634	0.153
2.8	2.8	0.0024	0.0244	0.10
5.6	5.6	0.00487	0.0396	0.122
11.	11.	0.00974	0.0634	0.153
22.	22.	0.0195	0.1016	0.19
SBWR				
120.	120.	0.105	0.32	0.326
440.*	120.	0.105	0.32	1.2

* This steam flow rate corresponds to un-condensed steam enthalpy of 1 MW.

Table 1: Plume temperature rise for various air and steam flow rates.

a well developed plume can be assumed.

For situations similar to that depicted in Fig. 8, no data are available yet, Eq. (14) does not hold, and a completely different analysis would be necessary. Only for guidance, one could consider the bubble 'starving' plume analysed by Hussain and Siegel [30] as a flow pattern similar to that in Fig. 8. For a low frequency bubble release, the entrainment (in the wake of the bubbles) can be taken as about 1.5 times the gas flow rate. Considering (Table I) that for all but the weakest gas injection rates, Q_l is never larger than $10\,Q_a$, also for conditions leading to few large bubbles (Fig. 8) the temperature rise of the entrained liquid should not exceed a few degrees.

4.2 Effect of the horizontal spreading

In the analysis above, the mixing process (how the hot layer interacts with the rest of the water in the pool) is implicitly assumed to be controlled by vertical stratification, with accumulation of buoyant fluid on top of the pool. The hot temperature front moves downwards as fast as necessary to satisfy continuity considerations. This approach implies that the hotter fluid spreads horizontally instantaneously as soon as it arrives at the surface, and does not possess any radial momentum.

With this approach, the presence of the walls of the pool can be neglected, and the mixing (vertical stratification) phenomena can be considered as being controlled uniquely by the strength

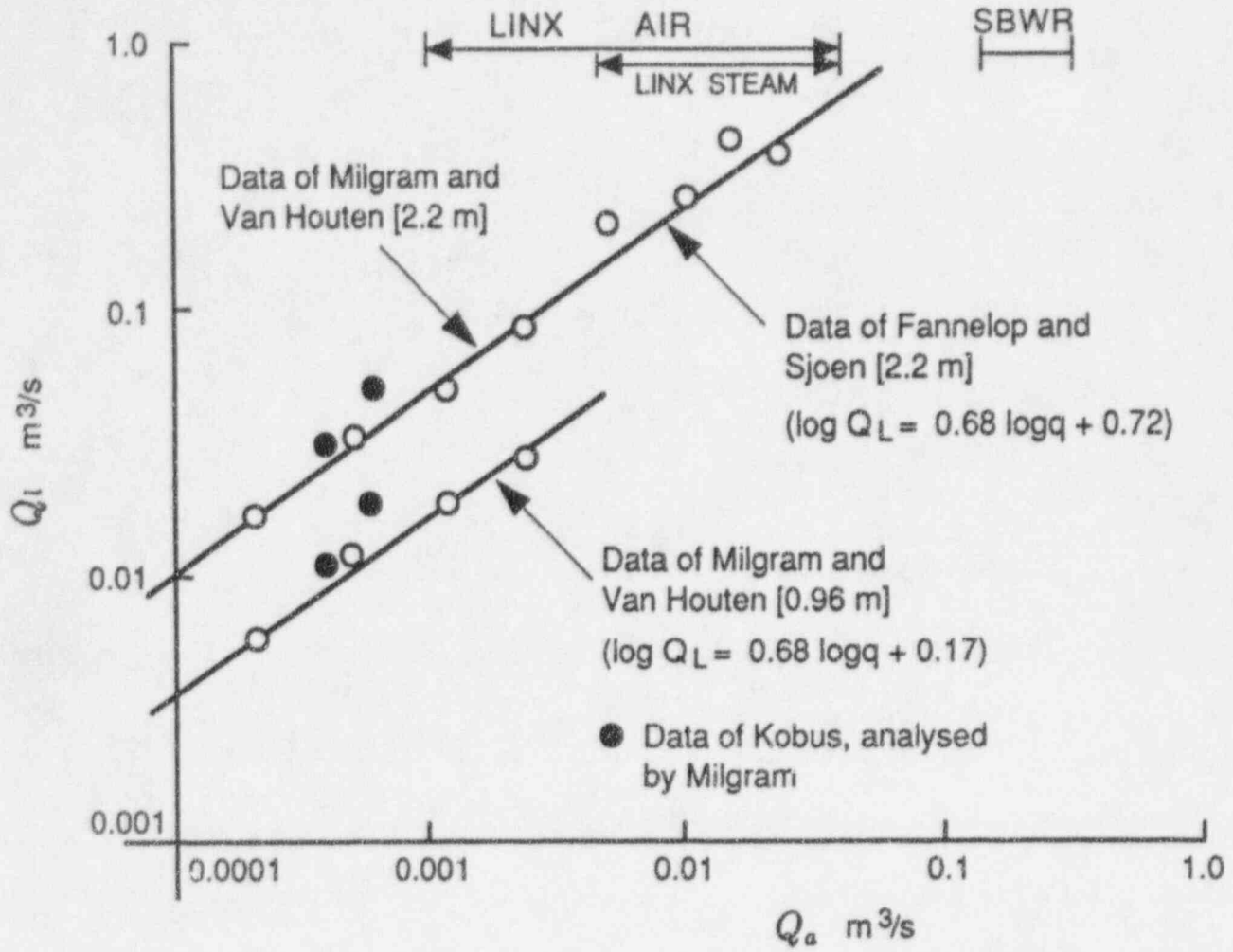

Figure 9: Liquid volumetric flow rate as a function of air (normal) flow rate for axi-symmetric air-water two-phase plumes (The distance above the vent source is given in brackets).

two-phase plume, the liquid entrainment is very large, and this leads to only a very small increase in the plume liquid temperature as a result of steam condensation.

The above model and assumptions provide therefore, a guide to the plume entrainment and resultant plume temperature rise for the LINX experiments and the SBWR. The actual plumes in LINX and the SBWR, however, will be influenced by a number of factors not relevant to the data analysed in [9]. For example, as discussed above, the LINX and SBWR plumes are unlikely to be fully developed and will therefore be influenced by the geometry of the injection (vent) device. This limiting approach can be justified, however, because even with the assumptions made, the plume temperature increase for most applications is significantly less than 1 K.

Because of the non-linear dependence of Q_l on Q_a (Eq. 14), the scaling of a concentrated point source is not possible. However, because of the small temperature rise in the plume for all conditions of interest, the distortions due to the scaling are likely to play a minor role, as long as

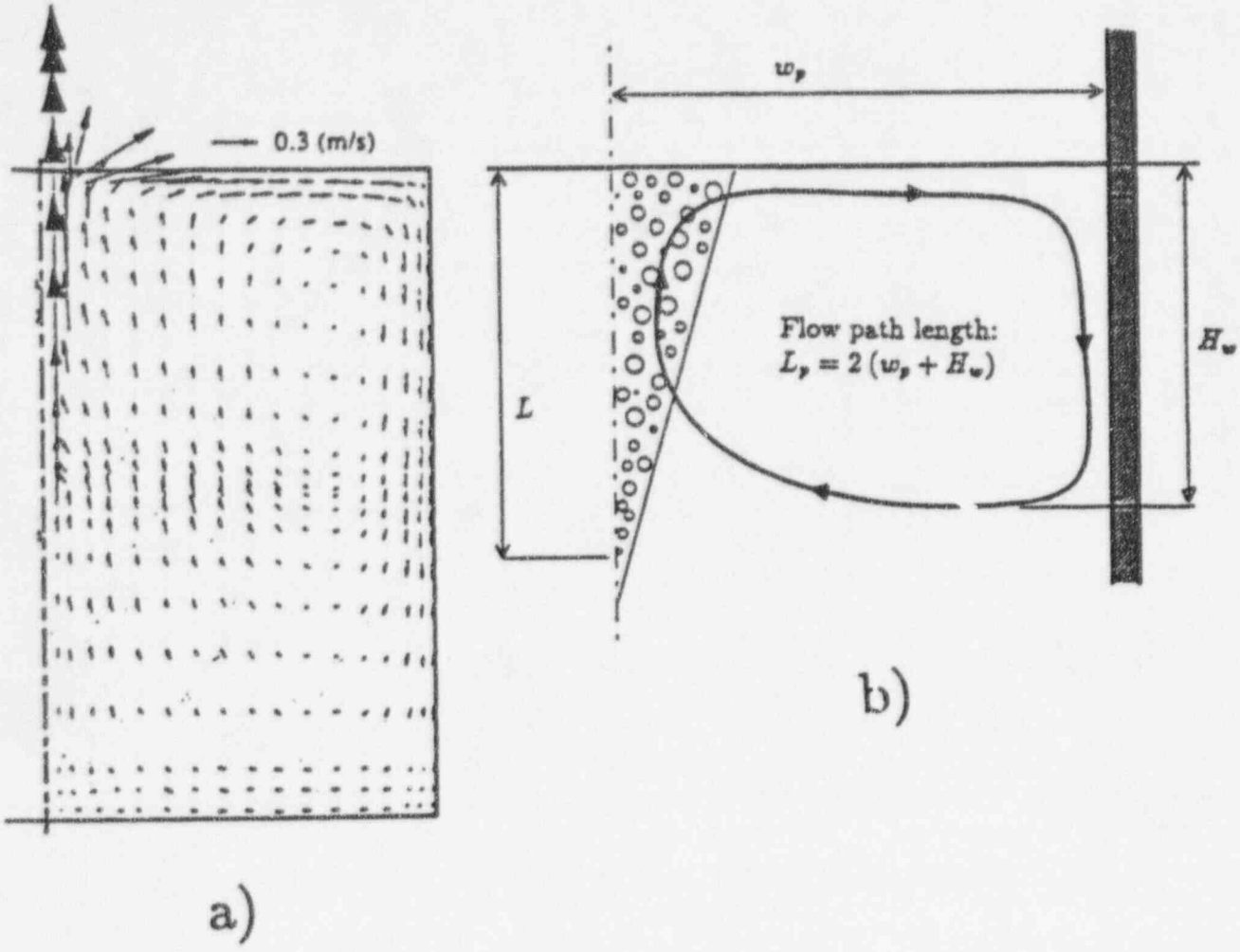

Figure 10: Flow pattern in a gas stirred liquid bath: a) numerical simulation by Ferng et al. [33]; b) schematic representation of the flow path of the fluid element.

of the buoyancy source and the volume of the active fluid (that above the injection point).

In reality, however, upon impact with the pool surface, the plume makes a 90° turn, and strong horizontal currents on the surface of the pool are generated.

For instance, Fannelop et al. [31] recently presented experimental results for a relatively weak linear source in a rectangular tank. Radial velocities were still appreciable at large distance from the source, several times larger than the submergence of the source.

Under these conditions, the global pool mixing is also influenced by the distance w_p of the wall from the axis of the two-phase plume and the penetration depth H_w of the return flow along the wall (Fig. 10). A visual evidence of the existence of such return flows has also been obtained from the small scale experiments described above [29]: small bubbles (but still well visible, consequently with diameter above 1 mm) were entrained to a large depth (20-30 cm) along the wall, giving evidence of vertical liquid velocities as large as their terminal velocities ($\simeq$ 10 cm/s).

Numerical simulations for bottom injection of air bubbles in small tanks showed [32] that the recirculation vortices can affect a considerable portion of the fluid and, for large injection rates, can even extend below the injection point [33][34].

The consequence of such a recirculation pattern is that all the fluid above the penetration depth H_w of the return flow will participate in absorbing the energy deposited by the condensing steam.

In the following, all the considerations will be based on the assumption of a 'well developed' plume. The main interest here is the evaluation of the decay of the velocity at the surface and the interaction of the surface flow with the wall. The measurement of the horizontal velocity is also important for determining the condensation/vaporization rates at the interface, as the mass exchange rate for a moving surface is expected to be much larger than for a stagnant pool. For instance, the condensation rate for a slowly moving liquid (a few cm/s) on the surface of a pool has been experimentally found to be a strong function of the Reynolds number of the flow on the surface (Celata et al. [35]).

Fannelop and Sjoen [36] developed an integral model for the analysis of both the vertical and horizontal portions of a round plume. They arrived at a relation between the maximum horizontal velocity V_s and the distance from the plume centre y:

$$V_s = V_{s,0}\left[1 + \beta\sqrt{2}\left(\frac{y^2}{b^2} - 4\right)\right]^{-1/2} \tag{16}$$

where b is the half width of the plume at the surface and β, the entrainment coefficient for the horizontal flow is of the same order of magnitude (10^{-1}) as the entrainment coefficient in the vertical section of the plume. From the assumption that the axial momentum of the plume is completely converted in radial momentum at the turning point, the initial velocity $V_{s,0}$ was calculated from the vertical centreline velocity. The comparison of the theory with the results of experiments in deep water basins showed acceptable agreement. This finding suggests that the conversion of axial momentum into radial momentum can be considered approximately correct.

The general conclusion from the review performed by Andreani [28] is that large horizontal currents are still present at large distance from the centreline of the plume, and that the intensity of the resulting convective flow can be conveniently correlated with the centreline axial velocity of the plume.

An attempt is done here to get a rough estimation of the influence of the wall on the mixing process. This will be used for establishing a tentative scaling law for the effect of geometry on the mixing phenomena in the prototypical suppression pool and the scaled model.

Using one of the several empirical expressions developed for the axial liquid centreline velocity U_{lc}, e.g. that presented by Xie and Oetmers [37]:

$$U_{lc} = 8.64\, Q_g^{0.25} \tag{17}$$

and assuming that the initial radial velocity is proportional to this value (Eq. 15), using Eq. (16), one obtains:

$$V_s \propto Q_g^{0.25}\, y^{-1} \tag{18}$$

The kinetic energy E_c of the horizontal jet is:

$$E_c \propto V_s^2 \propto Q_g^{0.5}\, y^{-2} \tag{19}$$

As the vertical penetration H_w of the horizontal jet along the closer wall is proportional to the kinetic energy, we have:

$$H_w \propto Q_g^{0.5}\, w_p^{-2} \tag{20}$$

The influence of the wall on the mixing phenomena will be properly reproduced in prototype and model if the same value of H_w is produced. This requires correct scaling for both Q_g and w_p:

$$\left[\frac{(Q_g)_P}{(Q_g)_T}\right]^{0.5} \left[\frac{(w_p)_P}{(w_p)_T}\right]^{-2} = \left[\frac{(H_w)_P}{(H_w)_T}\right] = 1 \tag{21}$$

Two geometrical configurations can be considered for such scaling in PANDA ($(w_p)_T$=2 m) in relation to SBWR ($(w_p)_P$=3.5 m), assuming that the centre of the vent exit is located at equal distance from all the walls:

Point source

$$\left[\frac{(Q_g)_P}{(Q_g)_T}\right]^{0.5} = \sqrt{25} = 5; \quad \left[\frac{(w_p)_P}{(w_p)_T}\right]^{-2} = \left[\frac{3.5}{2}\right]^{-2} = 0.326 \tag{22}$$

so that

$$\left[\frac{(H_w)_P}{(H_w)_T}\right] = 1.63 \tag{23}$$

This means that the liquid penetration at the nearest wall is smaller in the model than in the full-scale suppression pool and that the influence of the walls on the mixing phenomena will be smaller in the model than in the full-scale pool.

Linear source

If the model represents a slice of the linear source, the liquid flow per unit length can be considered the same for the two systems, so that the initial radial momentum will also be the same in the model and the prototype. In order to preserve the value of H_w, it will then be necessary to have the wall at the same distance from the plume centreline. The only possibility to avoid distortions is to distribute the gas flow from the quencher among a large number of orifices, so that the buoyancy source per unit length is small enough to produce in both the prototype and the model horizontal currents which are weak and cannot reach the wall.

5 Conclusions

The thermal-hydraulic phenomena which contribute to the reduction of a pressure build-up in the Wetwell of the SBWR have been identified and analysed.

An important mechanism which limits the pressurization of the suppression chamber is the condensation of the steam within the vent pipe, during bubble growth at the vent outlet and during bubble rise to the pool surface.

Large fractions of the vapour have been calculated to be condensed within the vent pipe and prior to detachment of the steam-gas bubble from the vent. This original finding reduces to some extent the concern about vapour bypass, i.e., the possibility that the gas mixture escapes to the gas space of the Wetwell, contributing to its pressurization. This could become a serious concern if the only phemomena considered were the condensation between the vent exit and the pool surface.

In fact, extrapolating correlations developed for low flow rates (as compared to the typical SBWR PCCS flows) of pure gas from orifices of diameters up to one third that of the PCCS vent, one finds that very large bubbles (up to 0.13 m in diameter even for a multinozzle geometry) can be expected at the vent outlet. Consequently, the time for the gas-steam mixture to reach the pool surface is likely to be much shorter than the characteristic collapse time for such bubbles. Under these conditions, direct channelling of the vapour from the vent pipe to the suppression chamber gas space is highly probable. The above comments are likely to be ameliorated if the vent exit is a distributed source or sparger. Since then the size of the bubbles will be reduced decreasing the potential for vapour "break through" and increasing the fraction of steam condensed during the formation of the bubbles.

Several aspects of the development of a two-phase steam and air plume resulting from the venting of nitrogen and steam below the surface of the SBWR suppression pool have been reviewed and used for the analysis of the mixing in the pool. Because of the large bubbles originating at the vent exit, however, a small-bubble plume is unlikely to exist. In fact, the break-up length for such large bubbles is comparable with the vent submergence. Thus even for the multinozzle quencher, a true bubbly flow regime is not likely to develop until some considerable distance downstream of the vent location.

In order to evaluate to what extent the localized deposition of the vapour energy will lead to thermal stratification, and, consequently to an increase of the partial pressure of vapour in the gas space, a simplified model for calculating the water temperature difference between the depth of the vent and the pool surface has been developed. The procedure (model) developed makes use of existing air - water round bubbly plume data and models, to predict the volumetric flow of liquid entrained within a two phase plume as a function of the air volumetric flow rate. It is then assumed, that a bubble plume develops above the vent exit. The heat transferred, by the condensation of the steam (assuming no vapour bypass), to the water entrained into the rising plume is assumed to be distributed uniformly just to the liquid flowing within the plume. The large buoyancy of a two phase plume leads to large plume velocities and therefore to high entrainment rates. Consequently, for gas-steam flow rates typical of the SBWR the water temperature rise is only about 0.3°C. For undeveloped plumes, where the water entrainment may be ten times lower, the resulting temperature rise would be still lower than a few degrees.

Therefore, the volume of water between the surface of the pool and the vent exit will heat-up in a more or less uniform manner (perfect mixing).

Mixing is further enhanced by the interaction of the horizontal spreading layer of hotter liquid with the walls of the pool. Indeed, convective currents create recirculation patterns which tend to oppose any stratification.

A few difficulties have been identified in studying the PCCS venting phenomena in volume-scaled test facilities: increased importance of the condensation within the vent pipe, distortions in the relation between condensation and rise times for the bubbles and diminished effect of the the walls. It is possible to avoid distortions of bubble condensation and wall effects, only if the actual geometry of the SBWR vent is a multinozzle manifold. Distortions in the condensation within the pipe, however, cannot be avoided, unless the pipe is partly insulated.

Acknowledgements

The authors wish to thank M. Meier for performing the calculations of the condensation rates within the vent pipe.

This work was partly funded by the Swiss National Energy Research Foundation (NEFF) under contract Nr. 514.

References

[1] H.A.Upton, F.E.Cooke and J.K.Sawabe, "Simplified Boiling Water Reactor Passive Safety Features," Proc. 2nd ASME-JSME Nuclear Engineering Joint Conf., 1, 705-712 (1993).

[2] M.Huggenberger, H.Nöthiger, B.L.Smith and T.V. Dury, "Single-Phase Mixing in Open Pools," Proc. 5th Int. Top. Meet. on Nuclear Reactor Thermal Hydraulics (NURETH-5), 2, 547-555 (1992).

[3] H.Nagasaka, K.Yamada, M.Katoh and S.Yokobori, "Heat Removal Tests of Isolation Condenser Applied to a Passive Containment Cooling System," Proc. 1st JSME-ASME Int. Conf. on Nucl. Eng., b-1, 257-263 (1991).

[4] M.Andreani and A.Tokuhiro, "Condensation in the Spout Region of a Gas-Vapour Plume rising in a Subcooled Water Pool," Proc. 2nd Int. Conf. on Multiphase Flow-ICMF '95-Kyoto', 2, PC2-17 (1995).

[5] M.Meier, "Computer Model of a Passive Containment Cooling Condenser Tube," Semester Project, Nuclear Engineering Laboratory, Swiss Federal Institute of Technology (1992).

[6] K.M.Vierow and V.E.Schrock, "Condensation in a Natural Circulation Loop with Noncondensable Gases, Part I - Heat Transfer," Proc. 1st Int. Conf. on Multiphase Flow 91 Tsukuba, 1, 183-190 (1991).

[7] J.G.Collier, Convective Boiling and Condensation, McGraw-Hill, New York, 2nd Ed. (1981).

[8] A.K.Chesters, M.van Doorn and L.H.J. Goossens, "A General Model for Unconfined Bubble Plumes from Extended Sources," Int. J. Multiphase Flow 6, 499-521 (1980).

[9] J.H.Milgram, "Mean Flow in Round Bubble Plumes," J. Fluid Mech. 133, 345-376 (1983).

[10] P.Coddington, "A Procedure for Calculating Two Phase Plume Entrainment and Temperature Rise as Applied to LINX and the SBWR," PSI internal report TM-42-94-01, Paul Scherrer Institute, Switzerland (1994).

[11] M.Huggenberger, "PANDA Experimental Facility Scaling of the System Lines," PSI internal report TM-42-94-14, ALPHA-412-A (DRAFT), Paul Scherrer Institute, Switzerland (1994).

[12] P.Coddington, "SBWR and Experimental Facility PCCS Vent pipe condensation," PSI Internal report to be published, Paul Scherrer Institute, Switzerland (1995).

[13] H.C.Simpson, G.C.Beggs and D.M.Isikan, "Collapse of Steam Bubbles in Sub-Cooled Water," Proc. 8th Int. Heat Transfer Conf., 4, 1919-1926 (1986).

[14] A.Jeje, B.Asante and B.Ross, "Steam Bubbling Regimes and Direct Contact Condensation Heat Transfer in highly Subcooled Water," Chem. Eng. Sci. 45, 639-650 (1990).

[15] S.C.Cho and W.K.Lee, "Steam Bubble Formation at a Submerged Orifice in Quiescent Water," Chem. Eng. Sci. 46, 789-795 (1991).

[16] L.J.Flanigan, D.D.Paul, R.P.Collier, R.A.Cudnik and R.N.Oehlberg, "Radionuclide Scrubbing in Water Pools: Bubble Hydrodynamics," Proc. 2nd Int. Topical Meet. on Nuclear Reactor Thermal Hydraulics (NURETH-2), 1, 137-144 (1983).

[17] F. Mayinger and Y.M. Chen, "Heat Transfer at the Phase Boundaries of Condensing Bubbles," 1983 European Two Phase Flow Group Meeting, Swiss Federal Institut for Reactor Research, Zurich, June 14 - 17, 1983.

[18] F.Mayinger and Y.M.Chen, "Heat Transfer at the Phase Interface of Condensing Bubbles," Proc. 8th Int. Heat Transfer Conf., 4, 1913-1918 (1986).

[19] P.Coddington, "Bubble Heat Transfer and Condensation," PSI Internal Report to be published, Paul Scherrer Institute, Switzerland (1995).

[20] F.J.Moody, "Dynamic and Thermal Behavior of Hot Gas Bubbles Discharged into Water," Nucl. Eng. and Des. 95, 47-54 (1986).

[21] H.R.Jacobs and B.H.Major, "The Effect of Noncondensible Gases on Bubble Condensation in an Immiscible Liquid," J. Heat Transfer 104, 487-492 (1982).

[22] P.Coddington, "A Review of the SBWR PCCS Venting Phenomena," PSI internal report TM-42-94-02, Paul Scherrer Institute, Switzerland (1994).

[23] J.F.Davidson and B.O.G.Schüler, "Bubble Formation at an Orifice in an Inviscid Liquid," Trans. Inst. Chem. Engrs. 38, 335-342 (1960).

[24] P.F.Peterson, private communication, 1993.

[25] S.Sideman and D.Moalem-Maron, "Direct Contact Condensation," Advances in Heat Transfer 15, 227-281 (1982).

[26] A.E. Wraith, "Gas Lancing in Metal Refining: an Air-Water Model Study," Advances in Extractive Metallurgy and Refining, 303-316, Ed. M.J. Jones, London (1972).

[27] G.Yadigaroglu, "Scaling of the SBWR related Tests," General Electric report, NEDC-32288 (1994).

[28] M.Andreani, "Study of the Horizontal Spreading of Rising Two-Phase Plumes and its Effects on Pool Mixing," PSI Internal Report TM-42-94-05, Paul Scherrer Institute, Switzerland (1994).

[29] P.Ruhstaller and R.Gort, "Analytical and Experimental Investigation of Two-Phase Plumes," Semester Project, Nuclear Engineering Laboratory, Swiss Federal Institute of Technology (1994).

[30] N.A.Hussain and R.Siegel, "Liquid Jet Pumped by rising Gas Bubbles," J. Fluids Eng. 98, 49-57 (1976).

[31] T.K.Fannleop, S.Hirschberg and J.Küffer, "Surface Currents and Recirculating Cells generated by Bubble Curtains and Jets," J. Fluid Mech. 229, 629-657 (1992).

[32] Y.Matsumoto and Y.Murai, "Flow Structure in Bubbly flow," Proc. Seminar on Two-Phase Flow Dynamics, Schrock V.E. and Sakaguchi T. eds., Univ. of California, Berkeley, CA (1992).

[33] Y.M.Ferng, C.C.Chieng and C.Pan, "Numerical Analysis of Two-Phase Flow in Gas-Stirred Reactors," Proc. Inst. Mech. Engrs. 204, 311-319 (1990).

[34] M.P.Schwarz and T.L.Koh, "Numerical Modelling of Bath Mixing by Swirled Gas Injection," Proc. 4th Int. Conf. on Injection Metallurgy, SCANINJECT IV, 6:1-6:17 (1986).

[35] G.P.Celata, M.Cumo, G.E.Farello, and G.Focardi, "Direct Contact Condensation of Steam on a Horizontal Surface of Water," Wärme und Stoffübertragung 21, 169-180 (1987).

[36] T.K.Fannelop and K.Sjoen "Hydrodynamics of Underwater Blowouts," AIAA 18th Aerospace Science Meeting, AIAA Paper 80-0219 (1980).

[37] Y.Xie and F.Oeters, "Experimental Studies on the Flow Velocity of Molten Metals in a Ladle Model at Centric Gas Blowing," Steel Research 63, 93-104 (1992).

SCALING FOR INTEGRAL SIMULATION OF THERMAL-HYDRAULIC PHENOMENA IN SBWR DURING LOCA

by

M. Ishii, S. T. Revankar, R Dowlati, I. Babelli, W. Wang, H. Pokharna, M. L. Bertodano, V. H. Ransom, R. Viskanta, and James T. Han*

School of Nuclear Engineering
Purdue University
West Lafayette, IN 47907

*U.S. Nuclear Regulatory Commission
Office of Nuclear Regulatory Research
Washington, DC 20555

A scaling study has been conducted for simulation of thermal-hydraulic phenomena in the Simplified Boiling Water Reactor (SBWR) during a loss of coolant accident. The scaling method consists of a three-level scaling approach. The integral system scaling (global scaling or top down approach) consists of two levels, the integral response function scaling which forms the first level, and the control volume and boundary flow scaling which forms the second level. The bottom up approach is carried out by local phenomena scaling which forms the third level scaling. Based on this scaling study the design of the model facility called Purdue University Multi-Dimensional Integral Test Assembly (PUMA) has been carried out. The PUMA facility has 1/4 height and 1/100 area ratio scaling, corresponding to the volume scaling of 1/400. The PUMA power scaling based on the integral scaling is 1/200. The present scaling method predicts that PUMA time scale will be one-half that of the SBWR. The system pressure for PUMA is full scale, therefore, a prototypic pressure is maintained. PUMA is designed to operate at and below 1.03 MPa (150 psi), which allows it to simulate the prototypic SBWR accident conditions below 1.03 MPa (150 psi). The facility includes models for all components of importance.

1. INTRODUCTION

The General Electric-Nuclear Energy Company (GE) has developed a new boiling water reactor called the Simplified Boiling Water Reactor (SBWR) [1]. The SBWR has a simplified coolant circulation system and a passive emergency cooling system. The engineered safety systems and safety-grade systems in the SBWR are: (1) the Automatic Depressurization System (ADS), (2) the Gravity-Driven Cooling System (GDCS), (3) the Passive Containment Cooling System (PCCS), (4) the Isolation Condenser Systems (ICS), and (5) the Pressure Suppression Pool (SP). The GDCS and PCCS are new designs unique to the SBWR and do not exist in operating BWRs. The ICS is similar to those in some operating BWRs. The PCCS is designed for low-pressure operation (less than 1.03 MPa or 150 psia), but the ICS is capable of high pressure operation as well (up to 7.58 MPa or 1100 psia). It is necessary to study the performance of the new safety system and its interactions in order to assess the response of the

SBWR under postulated accident conditions. Since it is not feasible to build and test a full power prototypical system, a scaled integral facility is the best alternative. This paper addresses the scaling method used in the design of a model facility called PUMA. The PUMA facility is funded under the US-NRC confirmatory testing program of the SBWR [2].

The integral test facility scaling method should provide a rational basis by which to scale-up the integral model test results to the prototype conditions. Therefore, it is necessary to have a rational scaling method that establishes the interrelationship between the important physical variables associated with mass, force and energy of the prototypical system and the model. In view of this, a well balanced and justifiable scaling approach has been developed for the design of the SBWR integral test facility. For this task a three level scaling approach is used. This three level scaling approach consists of, (1) integral scaling, (2) boundary flow scaling, and (3) local phenomena scaling. The integral scaling is derived from the integral response functions for major variables in single and two-phase flow. This scaling insures that both the steady state and dynamic conditions are simulated. It also determines the geometrical requirements and time scale. The integral scaling results in the simulation of all the major thermal-hydraulic parameters. The boundary flow scaling simulates the mass and energy inventory of each component and flow among these components.

The third level scaling is used to insure that key local phenomena can be reasonably scaled. Even under the global simulation of flow, mass and energy, various local phenomena which affect the constitutive relations should be addressed through this third level of scaling. Local phenomena scaling have been carried out in detail. After some distortions in local phenomena and geometry are identified, the impact of the distortions on the integral thermal-hydraulic response of the model facility are discussed.

2. GENERAL SCALING CONSIDERATIONS

The scaling criteria for a natural circulation loop under single-phase and two-phase flow conditions have been developed by Ishii, et al. [3-5]. The criteria includes the effects of fluid properties, so one can also apply them for reduced-pressure system scaling. For single-phase flow conditions, continuity, integral momentum and the energy equations in one-dimensional area averaged forms are used. First, relevant scales for the basic parameters are determined, then the similarity groups are obtained from the conservation equations and boundary conditions. The heat transfer between the fluid and structure can be included in the analysis by using the energy equation for the structure. From these considerations, the geometrical similarity groups, friction number, Richardson number, characteristic time constant ratio, Biot number and heat source number are obtained. It should be noted that the simulation of a long, large pipe section by a small scale model may encounter some difficulties if the prototype system does not have a reasonably large loss coefficient in addition to the wall frictional loss.

For a two-phase natural circulation system, similarity groups have been developed from a perturbation analysis based on the one-dimensional drift flux model. The set of mass, momentum and energy equations are integrated along the loop, and the transfer functions between the inlet perturbation and various variables are obtained. The scaling parameters developed from the

integral transfer functions represent the whole-system similarity conditions, and are applicable to transient thermal-hydraulic phenomena.

The scaling approach that has been used for the design of many existing US-NRC thermal-hydraulic research facilities is summarized in [6]. The so-called "full-pressure full-height method" was used for most of these facilities. The scaling approach recommended by the NRC, based on the experience accumulated from extensive LOCA studies in scaled integral test facilities, is summarized in a comprehensive paper by Boucher, et al. [7]. The present scaling method is an extension of the previously developed scaling approach by Ishii, et al. [3-5] and consists of three levels of scaling detail. First, integral scaling methods are applied to the system circulation paths. Second, component boundary flow scaling considerations are applied in order to preserve integral mass and energy inventory. Third, scaling criteria are developed that preserve the similarity of local phenomena such as choking, condensation and bubble rise time. These levels of scaling detail are described in the following sections.

3. GLOBAL SCALING (Top Down Approach)

3.1 Integral System Scaling (1st Level)

It is imperative to have the single-phase flow similarity requirements as a ready reference, as they are needed to simulate the single-phase to two-phase flow transition. The system consists of a thermal energy source, energy sink and connecting piping system between components. For a natural circulation loop under single-phase flow conditions the similarity parameters are obtained from the integral effects of the localbalance equations (continuity, momentum and energy) along the entire loop. Detailed methodology on the scaling analysis is provided in [8].

The fluid continuity, integral momentum, and energy equations in one-dimensional, area-averaged forms are used along with the appropriate boundary conditions and the solid energy equation. From the dimensionless forms of these equations, important groups characterizing geometric, kinematic, dynamic and energetic similarity parameters are derived.

If similarity is to be achieved between processes observed in the prototype and in a model, it is necessary to satisfythe following requirements:

$$A_{iR} = \left(a_i / a_o\right)_R = 1 \tag{1}$$

$$L_{iR} = \left(l_i / l_o\right)_R = 1 \tag{2}$$

$$\left(\sum_i F_i / A_i^2\right)_R = \left[\sum_i \left(f_i \frac{l_i}{d_i} + K_i\right) / \left(a_i / a_o\right)^2\right]_R = 1 \tag{3}$$

$$R_R = \left(\beta\ \Delta T_o l_o / u_o^2\right)_R = 1 \tag{4}$$

$$St_{iR} = \left(h l_o / \rho_f c_{pf} u_o d_i\right)_R = 1 \tag{5}$$

$$T_{iR}^{*} = \left[\left(l_o / u_o\right) / \left(\delta^2 / \alpha_s\right)_i\right]_R = 1 \tag{6}$$

$$B_{iR} = \left(h\delta / k_s\right)_{iR} = 1 \tag{7}$$

$$Q_{siR} = \left(q_s''' l_o / \rho_s c_{ps} u_o \Delta T_o\right)_{iR} \tag{8}$$

where subscript *i* designates a particular component and R denotes the ratio of the value of a model to that of the prototype.

$$\psi_R \equiv \frac{\psi_m}{\psi_p} = \frac{\psi\ for\ model}{\psi\ for\ prototype} \tag{9}$$

The reference velocity, u_o, and temperature difference, ΔT_o are obtained from the steady-state solution. If the heated section is taken as the representative section, these characteristic parameters are expressed as follows:

$$u_o = \left[\frac{4\ \beta\ g\left(\frac{q_o''' l_o}{\rho_f c_{pf}}\right)\left(\frac{a_{so}}{a_o}\right) l_h}{\sum_i \left(F_i / A_i^2\right)}\right]^{1/3} \tag{10}$$

and

$$\Delta T_o = \left(\frac{q_o''' l_o}{\rho_f c_{pf} u_o}\right)\left(\frac{a_{so}}{a_o}\right) \tag{11}$$

where the subscripts *o* and *so* refer to the core flow area and heated surface area, respectively.

The frictional similarity requirement, Eq. (3), can be satisfied independently of the remaining scaling requirements [3-5]. Hence, from the remaining scaling requirements, it can be shown that the following conditions should be satisfied for a complete simulation:.

$$(u_o)_R = \left(\frac{\beta\, q'''_o\, l_o^2}{\rho_s\, c_{ps}} \right)_R^{1/3} \tag{12}$$

$$(\Delta T_o)_R = \left(\frac{q'''_o\, l_o}{\rho_s\, c_{ps}\, u_o} \right)_R \tag{13}$$

$$(\delta_i)_R = (\delta)_R = \left(\frac{\alpha_s\, l_o}{u_o} \right)_R^{1/2} \tag{14}$$

$$(d_i)_R = (d)_R = \left(\frac{\rho_s\, c_{ps}}{\rho_f\, c_{pf}} \right)_R \left(\frac{\alpha_s\, l_o}{u_o} \right)_R^{1/2} \tag{15}$$

$$(h_i)_R = (h)_R = (k_s)_R \left(\frac{u_o}{l_o\, \alpha_s} \right)_R^{1/2} \tag{16}$$

where the parameters without the component subscript, i, denote universal values that must be satisfied in all components. In addition to the above, the geometric similarity requirements dictate that

$$\left(\frac{l_i}{l_o} \right)_R = 1 \quad and \quad \left(\frac{a_i}{a_o} \right)_R = 1 \tag{17}$$

must also be met.

With these conditions, Eqs. (3, 12-16), the effects of each term in the conservation equations are preserved in the model and prototype without any distortions..

It is important to note that the above set of requirements does not place constraints on the power density ratio, q'''_{oR}. However, they do put a restriction on the time scale as follows:.

$$\tau_R \equiv \left(\frac{l_o}{u_o} \right)_R \left[\left(\beta\, q'''_o l_o^2 \right)_R / \left(\rho_s\, c_{ps} \right)_R \right]^{1/3} \tag{18}$$

The small perturbation technique and integral response function have been used by Ishii and Kataoka [3] to develop similarity criteria for two-phase flow systems. The important dimensionless groups that characterize the kinematic, dynamic and energetic fields are given as follows:

$$\textit{Phase Change No.} \quad N_{pch} \equiv \left(\frac{4q_o''\delta\, l_o}{du_o\, \rho_f\, h_{fg}}\right)\left(\frac{\Delta\rho}{\rho_g}\right) = N_{Zu} \tag{19}$$

This phase change number has recently been renamed as the Zuber number, N_{Zu}, in recognition of Zuber's significant contribution to the field.

$$\textit{Subcooling No.} \quad N_{sub} \equiv \left(\frac{h_{sub}}{h_{fg}}\right)\left(\frac{\Delta\rho}{\rho_g}\right) \tag{20}$$

$$\textit{Froude No.} \quad N_{Fr} \equiv \left(\frac{u_o^2}{g l_o\, \alpha_o}\right)\left(\frac{\rho_f}{\Delta\rho}\right) \tag{21}$$

$$\textit{Drift - Flux No.} \quad N_{dl} \equiv \left(\frac{V_{gl}}{u_o}\right)_l \textit{(or Void - Quality Relation)} \tag{22}$$

$$\text{Time Ratio No.} \qquad T_l^* \equiv \left(\frac{l_o / u_o}{\delta^2 / \alpha_s}\right)_l \tag{23}$$

$$\text{Thermal Intertia No.} \qquad N_{thl} \equiv \left(\frac{\rho_s\, c_{ps}\, \delta}{\rho_f\, c_{pf}\, d}\right)_l \tag{24}$$

$$\text{Friction No.} \qquad N_{fl} \equiv \left(\frac{fl}{d}\right)_l \left[\frac{1 + x\left(\Delta\rho / \rho_g\right)}{\left(1 + x\Delta\mu / \mu_g\right)^{0.25}}\right]\left(\frac{a_o}{a_l}\right)^2 \tag{25}$$

$$\text{Orifice No.} \qquad N_{ol} \equiv K_l \left[1 + x^{3/2}\left(\Delta\rho / \rho_g\right)\right]\left(\frac{a_o}{a_l}\right)^2 \tag{26}$$

where V_{gj}, h_{fg}, h_{sub}, and x are the drift velocity of the vapor phase, heat of evaporation, subcooling and quality, respectively In addition to the above-defined physical similarity groups, several geometric similarity groups such as (l_i / l_o) and (a_i / a_o) are obtained.

The Froude, friction and orifice numbers, together with the time ratio and thermal inertia groups, have their standard significance. Subcooling, Zuber and drift-flux numbers are associated with the two-phase flow systems. Their physical significance is discussed in detail elsewhere [3-5].

Eqs. (19) through (26) represent relationships between the dimensionless groups and the generalized variables of a two-phase flow system. The dimensionless groups must be equal in the prototype and model if the similarity requirements are to be satisfied. Hence, the following conditions result:

$$\left(N_{Zu}\right)_R = 1, \left(N_{sub}\right)_R = 1, \left(N_{Fr}\right)_R = 1, \left(N_{dl}\right)_R = 1$$

$$\left(T_i^*\right)_R = 1, \left(N_{thi}\right)_R = 1 \left(N_{fi}\right)_R = 1, \text{and } \left(N_o\right)_R = 1 \tag{27}$$

It can be shown from the steady-state energy balance over the heated section that N_{zu} and N_{sub} are related by

$$N_{Zu} - N_{sub} = x_e \left(\frac{\Delta\rho}{\rho_g}\right) \tag{28}$$

where x_e is the quality at the exit of the heated section. Therefore, the similarity of the Zuber and subcooling numbers yields

$$\left(xe\right)_R \left(\frac{\Delta\rho}{\rho_g}\right)_R = 1 \tag{29}$$

This indicates that the vapor quality should be scaled by the density ratio. When combined with Eqs. (25) and (26), Eq. (28) shows that the friction similarity in terms of N_{fi} Noi can be approximated by dropping the terms related to the two-phase friction multiplier. Similarity of the drift-flux number requires void fraction similarity, $\left(\alpha_e\right)_R \approx 1$

Excluding the friction, orifice and drift-flux number similarities from the set of similarity requirements (Eq. (27)) and solving the remaining equations, one obtains the following similarity requirements:

$$\left(u_o\right)_R = \left(l_o\right)_R^{1/2} \tag{30}$$

$$\left(h_{sub}\right)_R = \left(\frac{h_{fg}\rho_g}{\Delta\rho}\right)_R \tag{31}$$

$$(q_o'')_R = \left(\frac{\rho_f \rho_g h_{fg}}{\Delta \rho} \right)_R \left(\frac{d}{\delta} \right)_R \tag{32}$$

$$\delta_R = (l_o)_R^{1/4} (\alpha_s)_R^{1/2} \tag{33}$$

$$d_R = \left(\frac{\rho_s c_{ps}}{\rho_f c_{pf}} \right)_R (l_o)_R^{1/4} (\alpha_s)_R^{1/2} \tag{34}$$

The velocity scale shows that, in contrast to the case of single-phase flow scaling, the time scale for a two-phase flow system is not an independent parameter. From Eq. (30), the time scale in two-phase flow is uniquely established as,

$$\tau_R = \frac{t_m}{t_p} = \left(\frac{l_o}{u_o} \right)_R \tag{35}$$

This implies that if the axial length is reduced in the model, then the time scale is shifted in the two-phase flow natural circulation loops. In such a case, the time events are accelerated (or shortened) in the scaled-down model by a factor of $(l_{oR})^{1/2}$ over the prototype.

3.2 Mass and Energy Inventory and Boundary Flow Scaling (2nd Level)

The scaled mass and energy inventory histories must be preserved for integral similarity to be achieved. The integral system response scaling methods assure this similarity when friction-dominated loop flow is considered. However, when vessel or system discharges occur that are dominated by nonfrictional momentum effects, such as at a point of choked flow or any nozzle flow in which the pressure drop-flow relation is dominated by kinetic loss or by cavitation effects, then additional constraints apply. At such discharge points the fluid velocity depends on the local pressure ratio across the device, which is preserved in a full-pressure scaled system such as the PUMA facility. In nonfrictional momentum-dominated flows, the fluid velocity is the same in the model as in the prototype. Therefore, the flow area at such discharge points must be scaled to preserve mass and energy inventory rather than loop kinematics. An overall criterion for similar behavior between the prototype and the model is that the depressurization histories be the samilar when compared in the respective (scaled) time frames.

This integral condition will be satisfied if the differential pressure change is the same at corresponding times, i.e.,

$$\frac{dp_m}{dt_m} = \frac{dp_p}{dt_p} \tag{36}$$

The scaling criteria for similarity of the friction-dominated natural circulation flows yields the result that the time scale of the model, or laboratory time, is related to the prototype time. Depressurization rates of the model and the prototype are related in laboratory time by

$$\frac{dp_m}{dt_m} = (1/\tau_R) \tag{37}$$

This condition will be satisfied if the corresponding component vessel inventories are similar, i.e.,

$$\left(\frac{M_m}{V_m}\right)_{t_m} = \left(\frac{M_p}{V_p}\right)_{t_p} \tag{38}$$

where M_p and M_m are the prototype and model vessel inventory masses, and Vp and Vm are the respective prototype and model vessel volumes. This relation must hold for each component as well as for the overall system if complete similarity is to be ensured

Mass Inventory and Mass Flow Scaling

For integral experiments, accurate simulation of the mass and energy inventory is essential. This requires a separate scaling criteria for the system boundary flows such as the break flow and various ECCS injection flows. The scaling criteria, stated in Eq. (38), are obtained from the overall control volume balance equations.

Denoting the total volume by V and the mean density by $< \rho >$,the coolant mass inventory balance equation can be written in a dimensionless form that applies to both the model and the prototype system as

$$\frac{d}{dt^*} < \rho^* > = \Sigma m_{in}^* - \Sigma m_{out}^* \tag{39}$$

where

$$t^* \equiv t/(l_o/u_o) \tag{40}$$

$$m_{in}^* \equiv \frac{m_{in}\,\tau_o}{\rho\, V} \approx \frac{\rho_{in}}{\rho}\left(\frac{a_{in}}{a_o}\right)\left(\frac{u_{in}}{u_o}\right) \tag{41}$$

and $\tau_o = (l_o/u_o)$ for either the prototype or the model. The definition for m_{out}^* can be given similarly. For equal model and prototype pressure simulation, $\left(\rho_{out}^*\right)_R = (\rho_{out}/\rho)_R$ is simply unity. Hence, the simulation of the boundary flow requires

$$\left(\frac{a_{out}}{a_o}\frac{u_{out}}{u_o}\right)_R = 1 \tag{42}$$

This is a similarity condition for the flow area and velocity combined. Therefore, it is not necessary at discharge points to satisfy the independent conditions for area and flow given by Eqs. (17) and (30), which must be satisfied by the other components of the loop. The form of the discharge scaling criterion given by Eq. (42) is very convenient from the standpoint of practical implementation. For example, the break flow velocity, u_{out}, can not be independently controlled if choking occurs. In the case of choking, Mach number similarity is maintained. Thus, for an equal-pressure system the break flow is prototypic in the sense that $(u_{out})_R = 1$, whereas the basic scaling $(u_o)_R = (l_o)_R^{1/2}$ and the criterion given in Eq. (42) predict that the break flow area should be scaled according to

$$\left(\frac{a_{in}}{a_o}\right)_R = \left(l_{oR}\right)^{1/2} \tag{43}$$

which would result in a reduction of the break flow area beyond the geometrical scale used for the loop flows.

Energy Inventory and Energy Flow Scaling

From the control volume balance, the energy inventory is given in dimensionless form by

$$\frac{dE^*}{dt^*} = q^* - w^* + \Sigma m_{in}^* h_{in}^* - \Sigma m_{out}^* h_{out}^* \tag{44}$$

where

$$m_{in}^* h_{in}^* = m_{in} h_{in} \frac{\tau_o}{\rho v h_o} \approx \left(\frac{\rho_{in}}{\rho}\right)\left(\frac{a_{in}}{a_o}\right) \tag{45}$$

In view of Eq. (45), for a full pressure simulation, i.e. $(h_o)_R = 1$, it is necessary to have

$$\left(h_{in}\right)_R = 1 \tag{46}$$

This physically implies that the inflow or outflow should have a prototypic enthalpy. The above dimensionless energy equation also shows that the initial energy inventory should be scaled by the volume ratio.

3.3 Pressure Scaling

The work scope and program objectives of PUMA are focused on the low-pressure region of operation following the initial depressurization of the vessel beginning from approximately 1MPa

(150 psi). In considering the pressure scaling of the integral test facility, following two effects should be evaluated separately:

1. System pressure level, which affects all the thermal-hydraulic properties of the liquid, vapor and phase changes.

2. Individual component or inter-component pressure distributions.

Considering the pressure scaling in these two separate effects is somewhat analogous to the well-known Boussinesq assumption. The prototypic pressure is taken as the system pressure scaling base. Hence, the system pressure and all other fluid properties are considered to be prototypic, which greatly simplifies the scaling procedures. Thus, the global pressure scaling is given by $p_R = 1$.

Under prototypic system pressure scaling, the thermodynamic and transport properties at every component are also considered prototypic. However, the pressure distribution in each component may not be prototypic. It should be noted that the pressure distribution within a component or between components can be the controlling factor in determining the flow by forced convection or natural circulation. This aspect of the pressure effect in a reduced-height system should be considered separately. At the initial blowdown phase of a LOCA or other transient, the major intercomponent flow occurs due to the initial pressure difference between the reactor pressure vessel and the containment. For this initial phase, the pressure difference between these two components should be prototypic at the same elevation, i.e. $\left(\Delta p_{ij}\right)_R = 1 \ at \ Z_R = l_R$, where the notation i and j stand for the reactor vessel and containment, respectively.

However, in the case of natural circulation-dominated flow, such as the reactor vessel internal circulation, GDCS injection or PCCS venting, the hydrostatic head is the essential driving force. For this case, the differential pressure is scaled by the reduced height scaling. Hence,

$$\left(\Delta P\right)_R = l_R \quad \left(at \ \Delta Z_R = l_R\right) \tag{47}$$

For PUMA, the initial differential pressure scaling is set by the initialization process with isolated components. At the later stages of accident simulation, most of the significant liquid flows between components are driven by the hydrostatic head. These flows are accurately simulated by using proper height scaling of all major elements and components based on $\Delta Z_R = l_R$, which implies the complete axial geometrical similarity. This condition, together with the void distribution simulation based on the integral scaling, insures that the differential pressure is scaled by the reduced height scaling.

3.4 Height Scaling

Under the prototypic pressure simulation, the system geometry can be determined from the integral system scaling and the boundary flow scaling discussed above. The dynamic scaling requirements for a two-phase flow system are given by Eqs. (19-27). In general it is difficult to match all these similarity criteria for a scaled down system, so a careful evaluation of each of these requirements should be made.

In considering the dynamics of the system, two conditions should be considered separately. The first is on the quasi-steady flow simulation and the second is the dynamic response of the system, including the inertia effect. It is clear that the Froude number and friction number scale the dynamic response. When the inertia forces are not important, only the balance between the frictional resistance and gravitational force should be considered. This can be achieved by taking the product of these two numbers. Thus, natural circulation number is defined as

$$N_{nc} = N_f N_{fr} = \left[\frac{friction}{inertia}\right]\left[\frac{inertia}{gravity\ head}\right] \tag{48}$$

This equation can be extended to include the minor loss coefficient as

$$N_{nc} = (N_f + N_o)\, N_{Fr} \tag{49}$$

Using kinematic and energy similarities, a less restrictive requirement, $(N_f + N_o)_R = 1$, is obtained for an approximate dynamic similarity between the inertia term and flow resistance. The advantage of this requirement relative to the two independent requirements of $(N_f)_R = 1$ and $(N_o)_R = 1$ is significant. Under a homogeneous flow assumption, the above less restricitive requirement can be approximated by

$$(N_f + N_o)_R \approx \left(\frac{fl}{d}\right)_R^2 = 1 \tag{50}$$

By using the geometrical similarity criteria,

$$\left(\frac{fl}{d} + K\right)_R = 1 \tag{51}$$

These two scaling criteria Eqs.(50-51) apply to gravity driven flow. A careful analysis of Eq. (51) clearly indicates the great advantage of using the reduced-height system for a given volume scale in satisfying the dynamic similarity criteria. By reducing the flow area, the hydraulic diameter is reduced by $d_R = \sqrt{a_R}$, except at bundle sections such as the core. For most small integral test facilities, it is necessary to have $l_R > d_R$ in order to maintain a reasonably large axial height so that the naturally existing two-phase level fluctuations do not adversely affect various transient phenomena. In general, the ratio of the first friction term itself is always larger than unity. However, by reducing the height of a facility, this ratio can be made closer to unity by increasing d_R for a fixed value of v_R. The second significant point is that the minor loss coefficient

is an easy parameter to adjust through small design modifications in such a way that $K_R < 1$ to compensate for increased friction. Hence by properly modifying the K value, Eq. (51) can be achieved.

4. Local Phenomena Scaling (3rd Level, Bottom Up Approach)

Although the global scaling criteria satisfy the system response similarity, the local phenomena may not be satisfied. Hence, it is important to study the local phenomena scaling in detail. The following is a list of local phenomena to be considered in the SBWR: (1) reactor vessel flow dynamics and instability scaling, (2) choked flow case, (3) unchoked flow case, (4) relative velocity and flow regime, (5) critical heat flux scaling (CHF), (6) flashing in the chimney, (7) condensation in suppression pool, (8) vent phenomena in suppression pool, (9) mixing in stratified fluid volumes, (10) natural circulation, (11) heat source and sink, (12) PCCS venting into suppression pool, (13) condensation in PCCS condensers, (14) stratification in the drywell, and (15) stratification in the suppression pool are considered. The scaling of these phenomena are considered in detail in [8].

5. Scale of the PUMA Facility

To determine the overall size of the proposed facility, it is necessary to consider four essential factors; (1) the need to scale relations to the existing facility, (2) the need to compensate for the shortcomings of existing facilities or complement the overall data base, (3) the need for a stand-alone justifiable rationale for the choice of a_R and l_R, *and* (4) the overall impact on the total cost.

For the PUMA facility, the above factors have been examined in detail. Based on these considerations, a 1/4 height and 1/400 volume scale have been chosen as the most desirable design. The existing or under-construction integral facilities for the SBWR are all full height. The GE-GIST facility [9] is a low pressure, full-height facility, thus $l_R = 1$ and $a_R = 1/508$. The GIRAFFE facility [10] in Japan has $l_R = 1$ and $a_R = 1/400$. The planned PANDA facility [11] has $l_R = 1$ and $a_R = 1/25$. The aspect ratio, l_R / d_R, for these facilities are 22.5, 20 and 5, respectively. In view of the overall cost and the volume scale of these facilities, a new facility at the volume scale of about 1/400 appears to be optimum. This will match the mass and inventory of the GIST and GIRAFFE facilities.

Since the existing facilities are all full-height, the impact of the actual total height on various phenomena can be evaluated sufficiently. However, the existing facilities fall into the category of thin and tall systems, which have some major shortcomings. In Table 1, the dimensions of various components of the SBWR are compared between prototype, full-height, 1/4-height and 1/8-height scaled models for a 1/400 volume scaled facility. As shown in Table 1, the 1/8-height scaled model is close to a linearly scaled model, with very large diameter. For 1/8 height scale, the required core power is also large. The 1/4 height and $a_R = 1/100$ scaled facility has moderate power requirement and with aspect scaling ratio factor of only 1/2.5, which is very close to the prototype system.

The present quarter-height system with the volume scale of 1/400 has the advantage of well-matched gravity to frictional forces. Furthermore, due to relatively large cross-sectional areas, the important phenomena of two or three dimensional voiding patterns and flow regimes in the core and chimney can be better simulated. This is considered to be particularly important for assessing the effects of various instabilities such as manometer oscillation, density wave instability, geysering and flashing-induced cyclic phenomena on the natural circulation cooling and stability of the GDCS. The scientific design of the PUMA facility is complete and the construction of the facility is underway. The schematic of the PUMA facility is shown in Figure 1. The facility includes models for all the major components of SBWR safety and non-safety systems that are important to the transient response to a postulated LOCA and other transients. Thus it includes the reactor pressure vessel, drywell, suppression pool, GDCS, ICS, PCCS, and auxiliary system like feed water line, CRD line and RWCU/SDC.

The present scaled model cannot represent all detailed geometrical features of the SBWR. The model design was based on a number of considerations. First, the requirements of global scaling were met, then important local phenomena were identified and scaled. In some cases, both global and local scaling cannot by satisfied simultaneously. In such cases, the requirement on global scaling was kept intact and certain compromises on local scaling were made. In addition to scaling considerations, hardware components were evaluated for ease of construction, operation and cost. Certain geometrical features for some components were thus distorted in PUMA. Details on these distortions and their impact on the loop thermal-hydraulics have been discussed in [8].

6. CONCLUSIONS

This paper discusses the scaling approach for the integral simulation of thermal-hydraulic phenomena in the new SBWR design. The PUMA model facility is based on the application of a three-level scaling method. In the global scaling: i)the integral loop scaling ensures steady-state and dynamic characteristics are well simulated, and ii)the mass and energy boundary flow scaling ensures flow and inventory similarity. The resultant design is a 1/4 height, 1/400 volume scaled test facility, where all major safety and non-safety thermal-hydraulic components of the SBWR are simulated. The power is scaled by 1/200 and the test facility operates at the prototypic pressure. One of the unique feature of this facility is that it has aspect ratio of 2.5 which is smaller than any existing full-height scaled test facilities. Some issues relating the scaling of the local phenomena and their impact on the system thermal-hydraulics are also discussed.

Acknowledgements

The authors wish to acknowledge the comments and support provided by the following individuals during the design of the PUMA facility; NRC: T. L. King, F. Eltawila, L. M. Shotkin, and D. E. Besset, BNL: U. S. Rohatgi, G. Slovik, Y. Parlatan and J. Jo, INEL: J. L. Anderson and K. G. Condie, and GE Nuclear Energy personnel.

References

1. GE Nuclear Energy, "SBWR Standard Safety Analysis Report 25A5113 Rev. A, August (1992).

2. Han, J.T., Bessett, D.E. and Shotkin, L.M., "NRC Confirmatory Testing Program for SBWR," Proceedings of the Twenty-First Water Reactor Safety Information Meeting, Bethesda, Maryland, October 25-27 (1993).

3. Ishii, M., Kataoka, I., "Similarity Analysis and Scaling Criteria for LWRs under Single Phase and Two-Phase Natural Circulation", NUREG/CR-3267, ANL-83-32 (1983).

4. Kocamustafaogullari, G., Ishii, M., "Scaling Criteria for Two-Phase Flow Natural and Forced Convection Loop and their Application to Conceptual 2x4 Simulation Loop Design", ANL-83-61, NUREG/CR-3420 (1983).

5. Kocamustafaogullari, G., Ishii, M., "Reduced Pressure and Fluid to Fluid Scaling Laws for Two-Phase Flow Loop", NUREG/CR-4584, ANL-86-19 (1986).

6. Condie, K.G., Larson, T.K., Davis, C.B., McCreery, G.E., "Evaluation of Integral Continuing Experimental Capability (CEC) Concepts for Light Water Reactor Research-PWR Scaling Concepts", NUREG/CR-4824, EG&G 2494 (1987).

7. Boucher, T.J., DiMarzo, M., Shotkin, L.M., "Scaling Issues for a Thermal-Hydraulic Integral Test Facility", NPC Paper.

8. Ishii, M., Revankar, S. T., Dowlati, R., Bertodano, M. L., Babelli, I., Wang, W., Pokharna, H., Ransom, V. H. and Viskanta, R., "Scientific Design of Purdue University Multi-Dimensional Integral Test Assembly (PUMA) for GE SBWR", Purdue University Report PU-NE 94/12, Draft NUREG/CR report (December 1994).

9. Billig, P.F., "Simplified Boiling Water Reactor (SBWR) Program Gravity-Driven Cooling System (GDCS) Integral Systems Test-Final Report," GEFR-00850, October (1989).

10. Tsunoyama, S., Yokobori, S., Arai, K., "Development of Passive Containment Cooling System," Proc. International Topical Meeting on Advanced Reactor Safety, Hyatt Regency, Pittsburgh, April 17-21 (1994).

11. Yadigaroglu, G., "Scaling of the SBWR Related Test," Report NEDC -32258, November (1993).

Nomenclature

A	Flow area scale
a	Cross-sectional area [m^2]
B_i	Biot number
c_p	Specific heat [J/kg-C]
d	Diameter [m]
E	Energy [J]
F	Total pressure loss coefficient
f	Friction factor, friction
g	Gravitational acceleration [m/s^2]
h	Enthalpy [J/kg]
h	Heat transfer coefficient [W/m^2 K]
h_{fg}	Latent heat of vaporization [J/kg]
h_{sub}	Subcooling enthalpy [J/kg]
K	Minor loss coefficient
k	Thermal conductivity [W/m-K]
l	Length [m]
M	Mass [kg]
m	Mass flow rate [kg/s]
N_d	Drift flux number
N_{Fr}	Froude number
N_f	Friction number
N_{nc}	Natural circulation number
N_o	Orifice number
N_{pch}	Phase change or Zuber number
N_{sub}	Subcooling number
N_{th}	Thermal inertia ratio
N_{Zu}	Zuber number
p	Pressure [Pa]
q'''	Volumetric heat flux [W/m^3]
Q_s	Heat source number
R	Richardson number
Ra	Rayleigh number (Gr Pr)
St	Modified Stanton number
t	Time [s]
T	Temperature [^oC]
T^*	Time ratio number
u	Velocity [m/s]
V	Volume [m^3]
V_{gi}	Drift velocity [m/s]
w	Work [J]
x	Quality
Z	Distance [m]

Greek Symbols

β	Volumetric thermal expansion coefficient [K^{-1}]
δ	Conduction depth [m]
Δ	Difference
α	Thermal diffusivity [m^2 /s]
α	Void fraction
ρ	Density [kg/m^3]
τ	Time Constant [s]
Σ	Summation
Ψ	Parameter

Subscripts

e	Exit
f	Fluid
g	Gas
i	ith component
in	Inlet
m	Model
o	Reference point/component
out	Outlet
p	Prototype
R	Ratio
s	Surface, solid

Superscripts

*	Dimensionless quantity

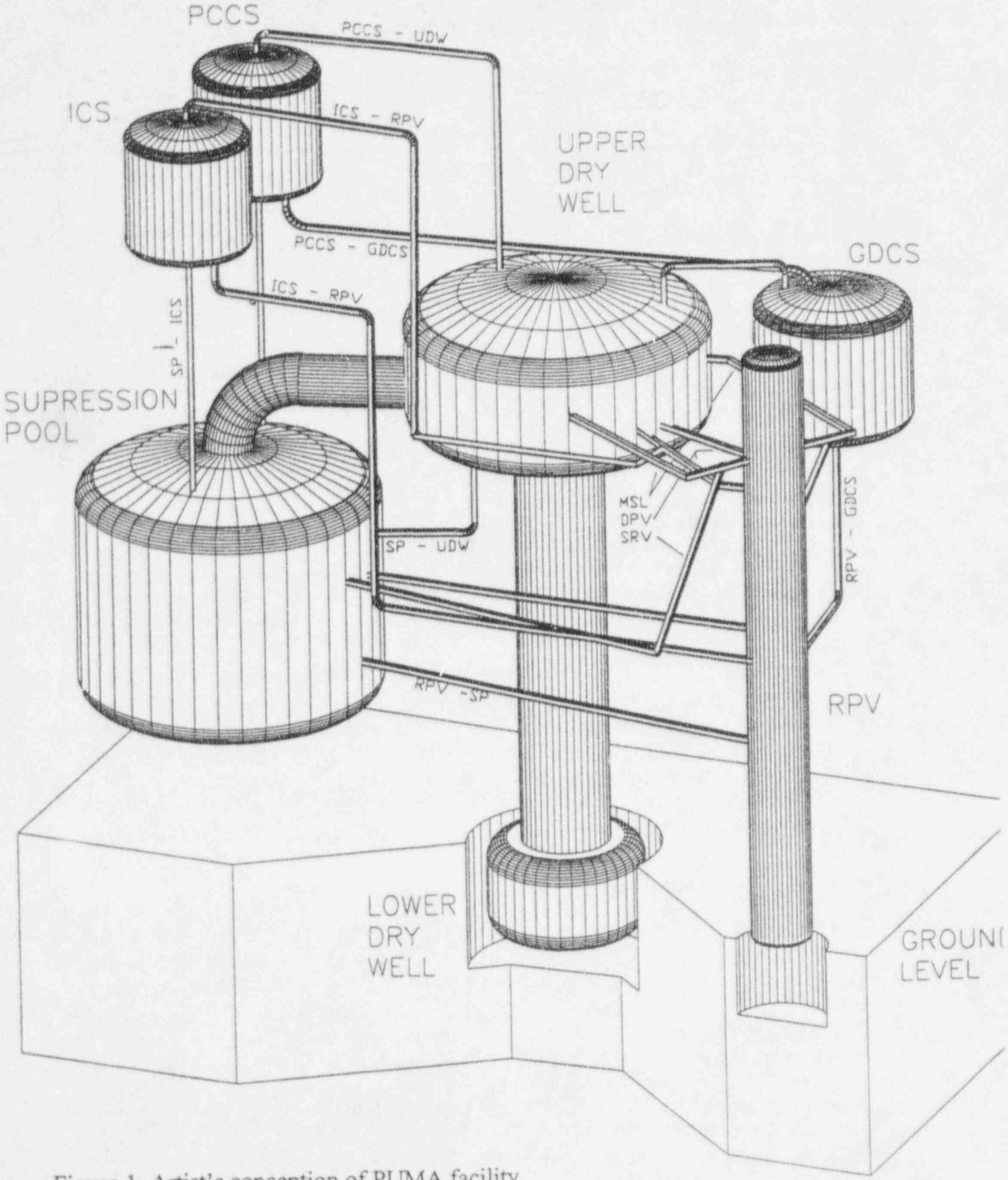

Figure 1. Artist's conception of PUMA facility.

TABLE 1. COMPARISONS FOR MAJOR COMPONENTS AND DIMENSIONS OF DIFFERENT HEIGHT SCALING*

COMPONENT	PROTOTYPE	1/1 HEIGHT	1/4 HEIGHT (PUMA)	1/8 HEIGHT (LINEAR)
REACTOR PRESSURE VESSEL				
Total height (mm)	24600	24600	6150	3075
I.D. (mm)	6000	300	600	848.7
Total volume (m^3)	669	1.67	1.67	1.67
CORE				
Rod material	Zr clad	S.S alloy	S.S alloy	S.S alloy
Active length (mm)	2743	2743	685	342.9
Total power	45 mW	112.5W	225 kW	318.2 kW
Core shroud I.D (mm)	5150	257.5	515	728.4
CHIMNEY SECTION				
Total height (mm)	9000	9000	2250	1125
Partition height	6500	6500	1625	812.5
# of divided areas	25	9	9	9
I.D. of shroud (mm)	4955	247.75	495.5	700.8
CONTAINMENT				
Wall material	Concrete/steel	S.S	S.S	S.S
Upper head volume(m^3)	3770	9.4	9.4	9.4
Upper head height (mm)	6100	6100	1525	762.5
Upper head dia.(mm)	28050	1402.5	2800	3967.5
Lower head volume (m^3)	1696.5	4.24	4.24	4.24
Lower head height (mm)	27200	27200	6800	3400
Lower head dia. (mm)	8911	445.55	891.1	1260.4
SUPPRESSION POOL				
Initial water volume (m^3)	3255	8.13	8.13	8.13
Initial gas space (m^3)	3819	9.55	9.55	9.55
Height (mm)	11950	11950	2987	1493
Diameter (mm)	27450	1372.5	2800	3882.6
GDCS POOL (1 OF 3)				
Diameter (mm)	Not circular	450	900	1273
Height (mm)	6100	6100	1525	762.5
Volume (m^3)	348	0.87	0.87	0.87

*Note: The volume scaling ratio is kept as 1/400 for all different height scaling.

A PRACTICAL VIEW OF THE INSIGHTS FROM SCALING THERMAL-HYDRAULIC TESTS

Alan E. Levin and G. Donald McPherson
U.S. Nuclear Regulatory Commission

ABSTRACT

The authors review the broad concept of scaling of thermal-hydraulic test facilities designed to acquire data for application to modeling the behavior of nuclear power plants, especially as applied to the design certification of passive advanced light water reactors. Distortions and uncertainties in the scaling process are described, and the possible impact of these effects on the test data are discussed. A practical approach to the use of data from the facilities is proposed, with emphasis on the insights to be gained from the test results rather than direct application of test results to behavior of a large plant.

INTRODUCTION

The U.S. Nuclear Regulatory Commission (NRC) is currently reviewing the test programs developed by reactor vendors to support certification of two "passive" nuclear power plant designs: Westinghouse's AP600 and General Electric's (GE's) simplified boiling water reactor (SBWR). In addition, the NRC is conducting confirmatory integral systems testing related to both passive plant designs. One of the most important issues in the review and development of these programs is that of scaling of the thermal-hydraulic experiments related to the passive plant designs. Separate-effects (SE) and integral systems (IS) tests are included in the test programs, and the review of the scaling approach used for the tests has considered both broad, overall scaling and extremely detailed issues on the subsystem and phenomenological levels. However, one element that often seems to be overlooked in the scaling review is some reflection upon the insights to be gained using the scaled experiments when it comes to application of the experimental data to analyses of the behavior of the actual passive plants over a range of accidents and transients. The purpose of this paper is to describe a somewhat more pragmatic approach to the issue of scaling, and to try to relate what will be seen in the experiments to actual plant behavior.

This paper derives from the authors' experiences related to review of scaling analyses provided by the passive plant vendors for their test facilities, as well as from participating in the development of facility designs for the NRC's confirmatory test programs, both past and present. Statements and conclusions herein represent the authors' technical judgments

and opinions based on these experiences. Some of these opinions may differ from those held by other experts in the field. However, reliance on experimental data from scaled facilities has become a vital aspect of the design and analysis of nuclear power plants, and is, in fact, essentially mandated by the NRC's design certification rule in Title 10, Part 52 of the Code of Federal Regulations (10 CFR 52), which, for the first time, makes testing supporting code development and validation an integral part of the licensing process. We believe, therefore, that the issues of how facilities are scaled and how the data are used are important topics to be considered by the technical community, and hope that this paper provokes further discussion.

DEVELOPMENT OF SCALING PARAMETERS FOR THERMAL-HYDRAULIC EXPERIMENTS

When the decision is made to build a scaled experimental facility to study the behavior of a full-size plant or component, one of the first questions that must be answered relates to the size of the test apparatus. Obviously, the most desirable approach is to test the full-size component, system, or plant. While this is feasible for some SE component or systems tests (depending on the size of the component or system), it is not practical to build a full-size plant for the purpose of performing IS tests. Once the size--or at least the budget constraining the size--is chosen, the technical question of scaling must then be considered.

The conventional approach to scaling is to write the conservation equations for mass, momentum, and energy for the facility, and to make them dimensionless by the use of reference quantities. The resulting equations have dimensionless coefficients multiplying each of the terms of the equations, which themselves are dimensionless. If the coefficients, which consist of fluid properties, system geometric parameters, and other fluid or system characteristics (velocity, temperature, power, etc.) can be matched between the facility and the full-size plant, it is generally assumed that the test loop's behavior will be the same as that of the plant. This approach is satisfactory, as far as it goes, but the above discussion does not represent the entire story with regard to scaling.

First, the conservation equations themselves represent an assumption as far as system behavior is concerned. If one is dealing with single-phase flow, the three conventional conservation equations are generally used (this represents the momentum equation, a vector equation that actually represents three scalar equations, as a single equation). However, unless one is dealing strictly with the behavior of single-phase laminar flow, even these equations represent an approximation, since the turbulent flow equations represent a time-averaged form of those for laminar flow, and the shear stress terms in the momentum equation incorporate both molecular and "eddy" contributions. When the issue of two-phase flow is considered, however, the picture becomes far more complex. There are several different models for two-phase flow, employing anywhere from three (homogeneous equilibrium mixture model) to six (full non-equilibrium two-fluid model) equations. Each of these models comprises a different approximation for the behavior of two-phase flow, and it is impossible to say *a priori* which is "most correct." For some types of systems, e.g., those operating at relatively low void fractions, the homogeneous equilibrium model may give perfectly acceptable results, while for others, more complex models are required. When these equations are put into

dimensionless form, the coefficients of the dimensionless derivative terms represent scaling parameters, but insofar as they are derived from a particular model of the system, these parameters reflect the assumptions inherent in the choice of one model over another.

Second, the conservation equations as cast in their original forms are almost useless for the analysis of practical systems. Again relating back to the equations for single-phase turbulent flow, the "eddy" terms, reflecting turbulent transport, in the momentum and energy equations cannot be calculated from a first-principles approach, because we do not understand the behavior of turbulence well enough to do so. Models representing either fully or partially empirical approaches to the calculation of--for instance--momentum and heat transport must therefore be used in these equations, and terms in these empirical models, e.g., heat transfer coefficients, can then be part of the scaling parameters derived from the conservation equations. This point is even more critical in two-phase flow equations, since two-phase flow processes are understood even less well than those in single-phase flow, and models for transport of mass, momentum, and energy in two-phase tend to be far more limited--in terms of empirical database and range of application--than those used for single-phase flow. It is also noteworthy that such models are developed from data extending over a specific parametric range. Applying an empirical model or correlation for conditions substantially outside of its database can give very poor results both in an absolute sense and when applied to development of scaling relationships.

The third aspect influencing scaling also relates to assumptions made by the designer. Theoretically, one must go through the scaling process for each component--pipe, vessel, valve, etc.--of the experimental apparatus, since geometry, fluid properties, and other relevant parameters can vary from location to location in a large test loop (and possibly from place to place in a single large component, depending on design--for instance, the core, upper plenum, and lower plenum of a reactor vessel). These parameters may also vary substantially over the course of a planned test program (a matrix of tests to study a wide range of simulated transients and accidents), and sometimes over a single test. The result, were this to be done--especially for a large integral test loop operating in two-phase flow in at least some components--would be an enormous list of dimensionless parameters. Each parameter would have a range associated with it reflecting the variation expected throughout the test program. Matching each one of those parameters to get "perfect" scaling would be virtually impossible (unless, as previously mentioned, a full-size plant model could be constructed). The designer must therefore make choices about which processes in the test loop are most important to try to preserve. This assumes some level of understanding on the designer's part about the expected behavior of the prototype plant over the range of conditions to be simulated in the test facility, but it represents a further judgment on the part of the scaling analyst as to how to proceed with facility design, and does not preclude the elimination of one or more important scaling parameters. This type of analysis can be aided by reference to the dimensionless conservation equations, by means of an order of magnitude analysis. If the range of parameters over which a facility or plant will be operated--or what may be present in an accident or transient--is known, these parameters can be substituted into the governing dimensionless equations, yielding numerical coefficients. One needs also to estimate the magnitude of the differential terms in the equations. If the numerical coefficients

multiplied by the differential terms are consistently very small compared to other terms in the equations, this is a sign that the process represented is likely of minor importance and can be dropped without major distortions in system behavior. Order or magnitude analyses are useful, but also represent, to some extent, assumptions as to the characteristic behavior of the system, and must therefore be done carefully so as not to eliminate key parameters.

If done with care, the result of the process described above should be a manageable list of scaling parameters that can be used in a practical sense to assist in the design of the facility, but which inevitably includes many approximations as described above.

DESIGN OF SCALED FACILITIES

The design of scaled test facilities generally proceeds concurrent with the development of scaling parameters for that facility. There are--theoretically--an infinite number of ways to design a scaled facility, but as a practical matter, the choice of a design often comes down to one fundamental issue: whether to build a full-height or reduced-height facility.

Full-height facilities have several attractive properties. First, the scaling analysis is often simplified, since variations in the scale apply only to the cross-sectional area of the components. Second, when full-height scaling is used in concert with 1:1 power-to-volume scaling, the timing of events in the scaled facility, compared to the full-size plant, can be made 1:1. This simplifies analysis of the data from the test loop. There are, however, some fundamental disadvantages to this approach. Budgetary or space constraints often limit the volumetric (area) scale--defined as facility volume divided by plant volume--of this type of facility to a relatively small number. The largest ex-reactor integral PWR test facility in the world is the ROSA/LSTF (Koizumi, et al., [1]; Annunziato, et al., [2]) in Japan, which was designed originally as 1/48 scale of a 4-loop Westinghouse PWR. Other such facilities are considerably smaller: BETHSY [2], in France, is 1/100 scale of a 3-loop Framatome PWR, and SPES-1 [2] in Italy was designed at slightly smaller than 1/400 of a Westinghouse 3-loop design. Using BETHSY as an example, the 1/100 scale means a reduction factor of 10 in component diameters. Thus, the simulated reactor vessel is of the order of 2 ft. in diameter, and the pressurizer becomes about a 6-in.-diameter pipe. Obviously, multi-dimensional thermal-hydraulic behavior is sacrificed in this type of scaling approach.

In addition, other distortions are often noted with full-height scaling, especially with regard to heat sources and sinks, since the surface-area-to-volume ratio in a full-height test loop is much larger than in the prototype plant. Another problem is the proper scaling of pressure drops through the system. Though the rationale for choosing full-height scaling is often related to natural convection behavior and the desirability of maintaining prototypic elevation differences between thermal centers, the distortions in heat sources and sinks, coupled with the difficulty of scaling pressure drops in components with very small diameters can distort the natural convection behavior of the loop. Yet another concern is the possible introduction of non-prototypic influence of fluid properties to the system, especially in two-phase flow. Large reductions in component diameters can make surface tension

a prominent factor in two-phase flow behavior in the test loop, while it would not be in the prototype. Similarly, if pipe diameters are reduced sufficiently to cause transitions in flow regimes, or to be near the diameter of a single bubble, non-prototypic effects may become important. To deal with some of these potential problems, pipe diameters are often increased to permit better scaling of pressure drops, two-phase flow regime transitions, and so forth.

An alternative to full-height scaling is use of a reduced-height facility. It is possible, in this approach, to keep from drastically reducing the diameter of system components, thereby avoiding some of the problems with full-height scaling. It may still, however, be difficult to deal with multi-dimensional phenomena in a reduced-height facility, since the cost of building large-diameter components can be quite large. A major drawback to a reduced-height scaling approach relates to the timing of events in the scaled facility compared to the prototype. Satisfying key scaling requirements in a reduced-height loop generally leads to the distortion of timing of thermal-hydraulic processes in the facility. Use of facility data to predict plant response must account for this fact, and any resultant distortions that may occur. There is one advantage of the timing distortion: simulation of transients over long periods--which may be important for the passive light water reactors--can be run in shorter times than would be required for the event in the prototype.

Irrespective of the scaling approach chosen, it is important to be aware of the distortions and non-prototypic aspects of the test facility, compared to the plant. While the scaling parameters themselves can assist in the application of test data to analysis of plant behavior, blindly applying the test results can lead to very poor insights into plant behavior, and may result in "non-conservative" analyses.

Essentially all scaled test facilities will, by their nature, embody some measure of distortion. Some of the reasons for those distortions, and their possible consequences, have been discussed previously. Aside from the distortions that occur because of scaling considerations, other types of non-typical behavior (with respect to expected plant response) may arise for other reasons. In the case of both the vendors' and the NRC's passive plant test programs, for example, existing facilities were modified extensively to make them resemble more closely the relevant plant design (see, for example, Boucher, et al., [3]; Bianconi, et al., [4]). One role that scaling analyses and scoping calculations can play in these cases is to permit facility designers to assess the impact of configuration differences on the behavior of the facility compared to that of the plant. This can help to highlight those areas in which test facility response might be expected to be different from that in the plant, and can assist designers in determining if certain configuration differences are acceptable. Where budgets are limited--as they usually are--a sort of semi-quantitative "cost-benefit" analysis can be made, in which the most cost-effective modifications, in terms of making facility response more characteristic of plant response, are undertaken first. Configuration differences that appear to be of second-order importance can then be addressed analytically (if it is physically and financially feasible to do so). The term "semi-quantitative" is used because, while the costs can be quantified, the "benefits" are more a matter of engineering judgment.

It should be noted that scoping calculations may be undertaken with code models that have not been validated for the application to the plant or the test facility. This could lead to a fundamental mistake, in which unvalidated codes are used to design a facility that will in turn be used to assess the codes. To avoid this, it is important, at this stage in the development of a facility design, that the codes be used in a limited fashion, simply as one means of assessing aspects of the design. Calculational results should not be used to establish test facility design; rather, this should be done by application of the key scaling parameters derived through an independent scaling analysis. This is addressed further in the following sections.

USE OF COMPUTER CODES AS SCALING AND ANALYSIS TOOLS

One of the most controversial aspects of both the scaling process and the analysis of plant behavior compared to that of a test facility is the use of computer codes to "aid" these activities. In some cases, there seems to be a fundamental misunderstanding of the role of the computer codes in these processes, which may lead to misapplication of the codes and faulty analyses of both test results and prototype response.

The computer codes most often employed to assist in the scaling, design, and operation of test facilities are large-scale systems codes, such as RELAP (Ransom, et al., [5]) and TRAC [6]. These codes attempt to model virtually all primary system components of a plant, and much of the secondary system as well. Control variables can also be defined to "turn on" or "turn off" specific systems or functions, such as ECC injection or reactor coolant pumps, based on the condition of other parts of the plant, so as to simulate the reactor control and safety systems.

On the most basic level, the systems codes solve the conservation equations of mass, momentum, and energy in every component of the system to arrive at a simulation of system (plant or test loop) response to an accident or transient. However, there are many subtleties to the ways in which these codes do their calculations, some of which may not be appreciated by designers, analysts, other technical personnel, and even by code users, who may treat the code largely as a "black box" to which they provide input (plant model, initial conditions, boundary conditions) and from which they receive results (plant response).

Even at the basic level, the code does not represent a full, physically or mathematically accurate representation of the equations that describe facility behavior. First, as noted previously, the choice of a model represents some approximation in the equations themselves. In RELAP, for instance, the conservation equations represent the full, non-equilibrium, two-fluid model for two phase flow, commonly referred to as a "six-equation" formulation. Each phase has its own equations of mass, momentum, and energy, with interphase transport terms included in the equations to model the exchange of these quantities between liquid and vapor. Of particular note is the treatment of the momentum equation, where a one-dimensional approximation is employed. The loss of system response information by use of this approach is often minimal, but there may be cases in which multidimensional behavior

plays a significant role, especially in large open volumes of fluid or in components with small aspect ratios (i.e., length-to-diameter). In these cases, artificial constructs may be used to approximate multi-dimensional transport, but the mathematics of such approaches is often not rigorous, and can lead to non-physical results.

In addition to the changes in the basic equations, it must be recognized that computers do not solve the differential conservation equations themselves, but rather finite difference approximations of the differential equations. The distinction here is, perhaps, subtle, but it is also crucial. The components are divided into control volumes, and the equations are integrated over those volumes. The resulting difference equations look similar to the differential equations, but information has been lost in the process. Rather than permitting continuous variation of parameters through the system, the difference equations deal with averages over the control volumes. A single number therefore represents some average characteristic (velocity, temperature, density, pressure) of a finite volume of fluid (liquid or vapor or both) in the system. This approximation of the differential equations usually works reasonably well, but there is information missing (which can be demonstrated by looking at Taylor expansions of the terms in the equations), that can affect the code results in some cases. The way in which the variables are defined can also affect code behavior. One conventional way of assigning values allows some parameters, e.g., pressure, to be defined at the center of a calculational cell, while others, e.g., velocity, are defined at the cell boundary. This so-called "staggered" mesh aids in the stability of the code calculation, but can also distort some results. Another common problem is "numerical" diffusion; this results when the numerical scheme creates artificial transport of some quantity (e.g., energy) from one cell to another. This can impact calculations involving stratification, which may have artificially-induced gradients in temperature due to numerical diffusion, rather than relatively sharp interfaces. The definition of cell-based average quantities can also lead to non-physical behavior, especially in boiling and condensation, and most noticeably at low pressures. At near-atmospheric pressures, the specific volume of vapor becomes quite large; thus a small mass of vapor (quality) can result in large volumes (void fraction). If a cell filled with vapor suddenly condenses, it may fill with liquid, and its average density may increase substantially. Since there are terms in the conservation equations involving the temporal change in density, a large change in a cell's density over a very small time step can make this type of term dominate in the equation, leading to numerical instabilities or other non-physical results.

Aside from the issue of the numerical approximation to the differential equations and related calculational irregularities, the equations also contain empirical models to relate the transport terms in the equations to parameters that can be calculated or measured. As discussed previously, these models are necessary as a simplification of the basic physics controlling complex two-phase processes. Examples of these models are correlations for interphase energy and momentum transport, two-phase heat transfer from structures, and void fraction (as a function of quality). Most such correlations are developed from separate-effects experiments that have specific ranges of application (system pressure, temperature, geometry, flow rate, etc.). Where multiple correlations are needed to cover the range of parameters, the codes generally have logic included to switch between correlations. However, in some cases, the correlations are discontinuous at the extremes of their

ranges, necessitating an "ad-hoc" smoothing of the interface to prevent the discontinuities from destabilizing the code calculations. It is also important to realize that most of the experimental data used to derive the empirical correlations used in systems codes have been acquired in steady-state experiments, but are being applied to transient calculations. This is done despite the fact that there is often not good evidence that this procedure is proper; however, the difficulty in making accurate measurements during transients--especially in two-phase flow--dictates the use of this procedure as the best available method.

The point in raising these issues regarding the approximations, distortions, and assumptions inherent in large systems codes is to show that the codes do not necessarily represent a rigorous application of the equations used to scale experimental facilities, and using the code as a "scaling tool" without an appreciation of this fact can lead to erroneous conclusions. It is impossible for the code to assess the relative importance of some aspect of system design (e.g., multi-dimensional thermal-hydraulic behavior) if that aspect of system behavior is not modeled in the code. Furthermore, as mentioned previously, application of the code without verification that the models in the code are appropriate for the range of parameters in both the test loop and in the prototype plant can lead to undependable results. One of the primary reasons for performing the tests is to demonstrate that the code is capable of producing results similar to the experiment; if the facility scaling is done properly, it should then be demonstrable that the range of significant dimensionless parameters covered in the experiment is similar to that expected in the plant, which would lead to the conclusion that the test results can be "scaled up" using the code to allow calculation of the plant response to a similar range of events. However, the plant designer or analyst must take great care in this "scaling up" in recognition of the limitations of the codes and the experiments. Sensitivity analyses are required to demonstrate the "robustness" of the code calculations to changes in parameters within the range of variation (with uncertainties) that would be expected in the plant. In addition, where questions arise about behavior that is not represented in the systems codes (e.g., multi-dimensional behavior), additional separate effects experiments and/or analyses using specialized codes with these types of models (e.g., computational fluid dynamics codes) may be needed to assess the influence of these processes.

A system designer or analyst can also bring valuable insight to the scaling process, based on experience with experimentation and scaling, and also on detailed knowledge of the design of the prototype plant. While it is difficult to do "back-of-the-envelope" calculations of plant response involving so many complex interacting systems, it may be possible to make realistic judgments as to behavior that is of primary importance to system response and to determine some "second order" effects that may be eliminated without having a significant impact on application of test results to plant analysis. This insight can then be used to assist in the development of test procedures, to highlight an area in which the analytical codes' capabilities need to be assessed, and to assist in the application of data from the scaled experiment to calculation of the prototype plant's response.

APPLICATION OF DATA FROM SCALED EXPERIMENTS TO PLANT ANALYSES

The ultimate goal of using scaled facilities to perform tests related to plant behavior is use of the data to validate computer models for plant analyses. While separate-effects tests on full-size components or systems can provide insights into their actual behavior in the plant, the same assertion cannot necessarily be made with regard to tests in scaled facilities. The direct application of test results to plant behavior, i.e., treating the test facility as a "simulator" for the plant, can lead an analyst or designer to draw incorrect or misleading inferences about plant response during accidents and transients.

Perhaps one of the most valuable aspects of a carefully-performed scaling analysis is to allow facility designers and analysts to focus on a set of key parameters. One procedure that has proven helpful in this regard is the use of Phenomena Identification and Ranking Tables (PIRT) (see [7]). The PIRT process is, to some degree, an exercise in engineering judgment: experts are asked to identify thermal-hydraulic phenomena, and to estimate their importance in assessing system behavior. The process can be done in two directions: on a global, system-based level (top-down), or on a fundamental phenomenological level (bottom-up). The PIRT process can assist in identifying those areas in which a code's modeling capability may be weak, and can also help to identify phenomena that should be captured within the scope of a testing program. However, the PIRT process must be applied with caution to the design of experiments, especially integral systems tests. If PIRT is employed as a static process to help develop a test program, there appears to be an implicit assumption that the answers are known before the program is developed and performed. To have real value, the PIRT must be viewed as "living" process, so that phenomena that were not identified--or that may have been identified but ranked "low"--but are found during testing to play an important role in system response, can be included and assessed.

Although allowances must be made for the fact that not all of the answers are known before a test program is conducted, scaling, including careful use of the PIRT procedure, should be able to help pinpoint many of the controlling parameters that influence system response to a given event. The applications of these types of insights include:

- Facility design, so that distortions affecting key parameters are minimized to the extent possible and instrumentation is chosen and located, and data acquisition equipment configured, to maximize the value of the test data;

- Test matrix development, to allow a limited test program (due to budget, time constraints, or both) to address key parameters in the most effective manner;

- Code development and assessment, to focus analysts' attention on the need for high-fidelity models that affect or are affected by the key parameters.

- Comparison of data generated from facilities of different scale under conditions that are nominally comparable. In this instance, properly performed scaling can also help to establish appropriate initial and boundary conditions, to make the tests as close to be "counterparts" as is practical.

The authors view these types of insights from scaling as perhaps the most valuable from an overall systems perspective. While scaling on a local phenomenological basis is valuable in assessing behavior related to a specific set of thermal-hydraulic conditions, it is sometimes possible to lose the focus on understanding system response that is often the most important aspect of testing--especially integral systems testing--in scaled facilities. Integral systems testing is most often designed to exercise computer code models and correlations developed from separate-effects tests on a system-wide basis, not to focus on small-scale phenomena. It may therefore be difficult to use integral systems tests to investigate local phenomena over a closely specified range. A well-designed testing program should contain a mix of separate-effects and integral systems tests that can provide both the phenomenological and system-wide databases needed for code assessment. This is the intent of the regulations governing testing requirements for passive plants in 10 CFR 52, and forms the basis for the NRC's review of the vendors' testing programs. In addition, while the NRC's confirmatory test programs are not required from a regulatory point of view, they are intended to improve the NRC staff's understanding of passive plant behavior, and have been designed using a systematic approach to scaling, as well.

CONCLUDING REMARKS

The authors have presented a review of the process of scaling facilities for the acquisition of well-characterized test data. The data are then used to validate computer codes used to predict the response of nuclear power plants to a range of postulated accidents and transients. The view presented here is designed to be realistic: we recognize that it is impossible to design a "perfectly" scaled experimental facility, both because of inherent physical limitations and the fact that our understanding of key physical processes may not be capable of characterization from "first principles." It is necessary to keep in mind the distortions that are bound to occur in both the physical facility itself and in our modeling of it, to evaluate those distortions, to minimize the influence on system behavior that may result, and to estimate the uncertainties that these considerations impose on the test data. Nevertheless, we do believe that it is possible to design scaled experimental loops that provide an adequate representation of local and system-wide phenomena expected in a full-size facility, and that testing in such loops forms an essential part of the process of evaluating the behavior of innovative nuclear reactor concepts.

REFERENCES

[1] Y. Koizumi et al., "ROSA-IV large scale test facility for PWR SBLOCA integral simulation test," Proc. Specialist Mtg. on Small Break LOCA Analysis in PWRs, 1, 555-569 (1985).

[2] A. Annunziato, et al., "Small break LOCA counterpart test in the LSTF, BETHSY, LOBI, and SPES test facilities," Proc. 5th Int. Top. Mtg. on Reactor Thermal Hydraulics, VI, 1570-1576 (1992).

[3] T. J. Boucher, et al., "Scaling and design of LSTF modifications for AP600 testing," EG&G Idaho, Inc. Report, NUREG/CR-6066 (1994).

[4] G. Bianconi, et al., "Small break calculation for the AP-600 plant and the SPES-2 experimental facility," Proc. 5th Int. Top. Mtg. on Reactor Thermal Hydraulics, I, 60-66 (1992).

[5] V. H. Ransom, et al., "RELAP5/MOD3 code manual," EG&G Idaho, Inc. Report, NUREG/CR-4312 (1985)

[6] Safety Code Assessment Group, "TRAC-PF1/MOD1, an advanced best-estimate computer program for pressurized water reactor thermal hydraulic analysis," Los Alamos National Laboratory Report, NUREG/CR-3858 (1981).

[7] Technical Program Group, "An integrated structure and scaling methodology for severe accident technical issue resolution," EG&G Idaho, Inc. Report, NUREG/CR-5809 (1991).

ANALYSIS OF OVERFLOW-INDUCED SLOSHING IN AN ELASTIC-WALL VESSEL USING PHYSICAL COMPONENT BFC METHOD

Daogang LU*, Akihiko TAKIZAWA** and Shunsuke KONDO*

* Department of Quantum Engineering and Systems Science
Faculty of Engineering, University of Tokyo, Tokyo 113, Japan

** Nuclear Power R&D Center, Tokyo Electric Power Company, Yokohama, 230, Japan

ABSTRACT

Newly developed "physical component boundary fitted coordinate (PCBFC) method" is applied to the fluid-structure interaction problems. The applicability was verified through several benchmark problems. Then, 2D experiment on overflow-induced fluid-structure interaction instability was simulated. The computation showed occurrence scope of instability essentially the same as that obtained by experiment. By computations with modified initial and boundary conditions, several basic factors for the occurrence of this instability were obtained.

1. INTRODUCTION

In LMFBR, a thin-wall weir is installed inside main reactor vessel to form a circulation loop of cold sodium for the protection of the main vessel from the hot coolant sodium. Under such conditions, there is a possibility of overflow-induced vibration of the weir coupled with sloshing of the coolant once observed in French Demonstration LMFBR "Super Phenix (SPx)."[1] Therefore it is very important for the safety assessment of LMFBR to study the mechanism and conditions for the occurrence of this sloshing-vibration instability.

Although the instability observed in SPx is a 3D phenomenon, essentially the same instability was observed experimentally in a 2D rectangular tank having a spring-supported rotatable weir by Fukuie and Hara.[2] Their experimental apparatus is illustrated in Figure 1. They observed occurrence scope of the instability, and found that there are two threshold values for the instability; i.e., that of the flow rate and that of the fall height, and that occurrence scope reduces when the spring becomes stronger.

To the authors' knowledge, computer simulation of this fluid-elastic instability has not been reported yet. Models were constructed to explain this instability (see Kaneko,[3] Suzuki & Hara, [4] and Eguchi[5]). However applicability of these models are only limited since these models were based on unrealistic simplifications like either potential flow assumption or spring-mass model.

In the present paper, we simulate this instability using the PCBFC method,[6],[7] and try to explain the mechanism of the instability by making most of the merits of computation. We will explain the computational method in Section 2 and analyze several benchmark problems in Section 3. The simulation results will be shown in Section 4. Then, using "computer discovery procedure,"[7] we will discuss several basic aspects of the mechanism of the instability in Section 5. The concluding remarks will be given in the final section.

2. METHOD

The PCBFC method is a BFC method having "physical component (PC)" as variables. The PC is effective for assuring the numerical stability and accuracy of free surface and other flow boundaries. The analysis space of PC is "physical curvilinear space (PCS)." The PCS is a space congruent to the physical space having oblique coordinates that run along the analysis grids. "Differential geometry of PC (DGPC)" was formulated by applying the theorems of differential

geometry and manifold theory to the PCS. The governing equations for incompressible fluid are described using the DGPC as follows;

$$\nabla_{(i)}u^{(i)} = 0, \quad (equation\ of\ continuity) \tag{1}$$

$$\begin{aligned}\frac{\partial u^{(i)}}{\partial t} &= -u^{(j)}\nabla_{(j)}u^{(i)} - \frac{1}{\rho}g^{(ik)}\nabla_{(k)}p \\ &+\nu\nabla_{(j)}g^{(jk)}\nabla_{(k)}u^{(i)} + f_l g^{(ij)}\nabla_{(j)}x^l, \quad (Navier-Stokes\ equation)\end{aligned} \tag{2}$$

where p, ρ, ν and f_l are the pressure, density, viscosity, and the constant of external forces (gravity) respectively, and $\nabla_{(j)}u^{(i)}$ is covariant derivative of the PCS.

Free boundary (free surface) is controlled by the pressure condition and the kinematic condition. Wall boundary (rotatable wall) is controlled by the fluid pressure and force of the spring as follows;

$$I\ddot{\theta} + k(\theta + \theta_0)L^2 = \int_0^{\eta} pydy, \tag{3}$$

where I, k, L, η and θ are the moment of inertia of the wall, constant of spring, distance from the hinge to the spring, water level and angle of the wall respectively, and the integral term expressed the total torque imposed on the wall by the fluid pressure. Virtual acceleration caused by grid movement is assessed as follows;

$$u^{(i)}(a) = u^{(i)}(b) + L_V u^{(i)} \cdot \Delta t, \tag{4}$$

where (a) and (b) denote "after" and "before" the grid movement, respectively. $L_V u^{(i)}$ is the Lie derivative of $u^{(i)}$ in the direction of V and is expanded as follows;

$$L_V u^{(i)} = V^{(j)}\nabla_{(j)}u^{(i)} - \Gamma^{(i)}_{(tj)}u^{(j)}, \tag{5}$$

where t and $\Gamma^{(i)}_{(tj)}$ are time and time connection coefficient, respectively. The first and second terms in the right-hand side of above equation are the corrections for mesh displacement and mesh rotation (deformation), respectively. The second term vanishes for the Lie derivative of pressure.

In this study, we newly extend the above mentioned PCBFC method to have the ability of tracking moving wall boundary. Because we choose the downstream tank as the analysis domain, we further incorporate the overflow module used in the existing analytical models[3],[4] into the PCBFC method. The overflow rate is estimated by the following empirical formula;[8]

$$q(t) = \frac{2}{3}Cd\sqrt{2g}\ h^{\frac{3}{2}}(t), \tag{6}$$

where Cd and $h(t)$ denote experimental coefficient and thickness of overflow at the top of the weir respectively, and $Cd = 0.611$ is recommended. $h(t)$ in the above equation is solved by discretizing the following flow rate conservation equation of the upstream tank;

$$W\ \dot{h}(t) + q(t) - \frac{1}{2}H^2\dot{\theta}(t) = V \cdot W, \tag{7}$$

where H, W and V denote height, width of inlet and inlet velocity of the upstream tank, respectively. Overflow is assumed to be a free drop with no friction of the wall considered. So, the injection velocity of overflow into the liquid in the downstream tank is estimated as follows;

$$Vinj = \sqrt{2g\Delta H}, \tag{8}$$

where ΔH is a fall height. Also based on the assumption of free drop, time delay during overflow is estimated as follows;

$$\tau = \sqrt{2\Delta H/g}. \tag{9}$$

Then we can determine the width of overflow at the free surface of the downstream tank as follows;

$$B(t) = q(t)/Vinj. \tag{10}$$

Fujita et al.[9] have measured the delay time by experiment. The delay time measured is no more than 20% longer than that obtained by free drop assumption.

3. BENCHMARK PROBLEMS

Applicability of the PCBFC method for the free surface flow has been demonstrated.[6],[7] In the present work, several benchmark problems were solved for validation of the present extension to the moving wall problems. Since there are no corresponding experiments, our numerical results are compared with the analytical results or results obtained by other numerical methods.

Firstly, solitary wave propagation problem[10] was analyzed. Profile of the wave (see Figure 2) as well as its run-up height at the wall showed good agreement with those in Reference [10]. It only took 10.4 seconds of C.P.U time to perform this 600-step (30 second) simulation using HITAC-M880 mainframe computer.

Secondly, sloshing in elastic-wall tank without forced circulation[11] was analyzed. A tank with a spring-supported rotatable right wall was filled with free-surface liquid, and the sloshing was started by setting the rotatable wall out of the equilibrium position and then relaxing it. Oscillation of the wall produced a sloshing of free surface as shown in Figure 3 (a). Flow pattern and free surface shape are very similar to those obtained by FE method.[11] Beats phenomenon was observed as shown in Figure 3 (b). Beats period is in good agreement with the theoretical prediction, which is shown in the end of this section.

Then we further analyzed flow-induced sloshing in an elastic-wall tank. We chose the geometry shown in Figure 4 (a). Flow-induced sloshing is observed in this tank when the right wall is rigid.[12],[7] by making the right wall rotatable and supported by a spring, we numerically produced flow-induced sloshing coupled with oscillation of the right wall without any numerical instability. The computed flow pattern is shown in Figure 4 (a), and the time histories of sloshing and wall oscillation in Figure 4 (b). From the computational results, we discovered several new characteristics of sloshing related to the elasticity of the vessel wall: (1) resonant sloshing occurs even when the wall is flexible; (2) period of the sloshing becomes larger than that in rigid tank, and changes with stiffness of spring and moment of inertia of the right wall; (3) growth rate of the sloshing changes with with stiffness of spring and moment of inertia of the right wall; and (4) oscillation of the wall grows with sloshing in the same frequency and phase.

In parallel with the numerical analysis, we have made theoretical analysis of the sloshing characteristics in elastic-wall tank using potential flow assumption. We discovered by this analysis the existence of two natural frequencies ($\omega_\pm$) of the sloshing in an elastic-wall tank, and derived formulae for the growth rate of sloshing (GR_η) and that of wall (GR_θ) oscillation as follows; [13]

$$\omega_\pm^2 = \frac{[(1+E/I)\omega_n^2 + \omega_b^2] \pm \sqrt{[(1+E/I)\omega_n^2 + \omega_b^2]^2 - 4(1+E/I-F/I)\,\omega_n^2\omega_b^2}}{2(1+E/I-F/I)}, \tag{11}$$

$$GR_\eta = GR_{rigid} \cdot \frac{\omega_-^2}{\omega_n^2}\,\left[\frac{G}{F}(1-\frac{\omega_-^2}{\omega_n^2}) + \frac{\omega_-^2}{\omega_n^2}\right]\frac{\omega_+^2-\omega_n^2}{\omega_+^2-\omega_-^2}, \tag{12}$$

$$GR_\theta = GR_\eta \cdot E_k, \tag{13}$$

where E, F and G are coefficients determined by the size of tank, and ω_n, ω_b, GR_{rigid} and E_k are natural frequency of sloshing in rigid tank, natural frequency of the wall, growth rate of sloshing in rigid tank and factor of spring which is inversely proportional to the stiffness of the spring. The new characteristics in the third benchmark problem are mostly predicted by these formulae, and the beats frequency in the second benchmark problem is successfully predicted by the following formula;

$$T = \frac{4\pi}{\omega_+ - \omega_-}. \tag{14}$$

4. SIMULATION OF OVERFLOW-INDUCED SLOSHING

We numerically simulated overflow-induced fluid-elastic instability. Computed flow interior, free surface, and weir position of the down stream tank are shown in Figure 5 (a). Time history of the angle of the weir is shown in Figure 5 (b). Numerical stability of free surface is never violated even though the overflow hits the free surface. It is observed from the computation that the weir moves to the left end when left side of the free surface moves to the highest, and vice versa.

For comparison with the experiment, we also illustrate the occurrence scope of the instability by computation in Figure 6. The occurrence of instability is judged by the history of the angle of the weir. From the computation it is observed that the instability disappears when the flow rate of circulation loop or the fall height exceeds their threshold values, and the occurrence scope reduces when the strength of spring is increased. These trends are in agreement with those observed in the experiment.

5. FACTORS FOR THE OCCURRENCE OF INSTABILITY

There are four parameters in this instability: circulation flow rate ($q_0 = V \cdot W$), fall height of overflow (ΔH), stiffness of the spring (k), and moment of inertia of the weir (I). ΔH has influence on both the delay time (τ) which the overflow spends to drop from the top of the weir to the free surface of the downstream tank, and the injection velocity (V_{inj}). Both q_0 and V_{inj} have influence on the average flow velocity at the free surface (U). Therefore we carried out analysis focusing on the four basic parameters: τ, U, k and I. In order to single out the effect of each parameter, we performed several cases of computations with simplified initial and boundary conditions of the original problem.

5.1. Oscillation of Overflow Rate

First, to investigate the importance of oscillation of the overflow rate, we model the overflow rate by the following formula;

$$q(t) = V_{inj} \cdot B(t) = V_{inj} \cdot B_0(1 + \beta \sin \omega t), \tag{15}$$

where $q(t)$, V_{inj}, B_0, ω and β are overflow rate, inlet velocity, average inlet width in downstream tank, natural frequency of the system, and a coefficient related to the amplitude of vibration of weir, respectively. We chose the Reference-1 case in Figure 6 and made series of computations by changing β from 0 to 0.3. As a result, sloshing was observed when the weir is either fixed or rotatable, and as shown in Figure 7 growth rate of sloshing increases almost linearly with the increase of β. The small intercept at x-axis may correspond to the damping effect by the viscosity of fluid. Therefore we concluded that oscillation of the overflow rate is a crucial element to the occurrence of fluid-elastic instability.

5.2. Effect of τ

Second, to investigate the importance of τ, we performed a series of computations by fixing $\Delta H = 3cm$ and artificially changing τ. Figure 8 shows the computed result on the change of growth rate of sloshing in terms of τ (unit in period T). We can see from this figure that τ has strong effect on the occurrence of instability: the instability appears only in the narrow band of τ around $0.1T$.

5.3. Effect of U

Third, to investigate the effect of inlet flow rate , we performed a series of computations by also fixing $\Delta H = 3cm$ and changing flow rate from $3cm/sec$ to $23cm/sec$. As illustrated in Figure 9, the average velocity (U) near the free surface increases with the increase of inlet flow rate, and the growth rate of sloshing shows decrease and becomes negative after a peak. It has been shown that large U results in large "sloshing Froude number (Frs)" and Frs exceeding the threshold is known to have the effect called "flow-caused damping."[7] Frs of the case having inlet flow velocity larger than $15cm/sec$ exceed the threshold value $Frs_c \approx 0.30 \sim 0.35$ in Figure 9. We can conclude that instability is suppressed by the flow-caused damping after the peak. The peak in Figure 9 is created because the motive forces of instability is proportional to the oscillation amplitude of overflow rate as shown in Figure 7.

Finally, to further investigate the effect of U to the occurrence of instability, we performed a series of computations by artificially keeping the delay time to be that of the Reference-1 case ($0.07sec$), and changing the injection velocity according to the fall height appeared in Figure 6. Figure 10 shows the effect of injection velocity on the instability. We can see also in this figure that U has the critical effect to suppress the sloshing by the "flow-caused damping" effect.

The fall height corresponding to its delay time is also marked at the top of Figure 8. It can be seen from this figure that for the range of fall height appeared in Figure 6, the corresponding τ is well inside the positive band around the first peak of growth rate in Figure 8. So through Comparison of Figure 8 with Figure 10, we can conclude that in the present geometry the flow-caused damping has larger influence than the effect of τ discussed in the previous subsection.

5.4. Effect of k and I

Large k means the spring is stiff and results in small β in Equation (15). Small β results in small growth rate of sloshing as shown in Figure 7. Therefore we concluded that smaller β causes the reduction of occurrence scope as shown in Figure 6 (b), and the instability can never be excited when β is very small, for being suppressed by the viscosity of fluid. Effect of I is now under study.

6. CONCLUSIONS

A newly developed PCBFC method was successfully extended to the analysis of free-surface flows in a vessel with multiple moving boundaries. Accuracy, numerical stability, and high computational speed of the present method were validated by the analysis of several benchmark problems.

Using this method, a complex instability phenomenon of overflow-induced sloshing coupled with the oscillation of vessel wall was simulated successfully. The successful simulation in spite of the existence of direct injection of flow at the oscillatory end of free surface demonstrated the excellence of the PCBFC method.

Several computations with modified initial and boundary conditions indicated that the oscillation of overflow rate is the principal cause of the instability. Explanations to the threshold value of flow rate as well as fall height for the occurrence of instability were given as follows; effect of "flow-induced damping" works to suppress the instability if the flow rate is too large or the fall height is too high: delay time of overflow also has some effect to the occurrence of instability.

REFERENCES

[1] S. Aita, Y. Tigeot, C. Bertaut, and J. P. Serpantie, "Fluidelastic Instability of a Flexible Weir: Experimental Observations", *ASME PVP 104*, 41-50 (1986).

[2] M. Fukuie, and F. Hara, "Experimental Study of Self-excited Vibrations of a Flexible Weir due to Flow Discharge," *Trans. JSME 55-517*, 2282-2289 (1989) (in Japanese).

[3] S. Kaneko, H. Nagakura and R. Nakano, "Analytical Model for Self-excited Vibration of an Overflow Flexible Plate Weir," *ASME PVP 258*, 151-162 (1993).

[4] F. Hara and T. Suzuki, "Dynamic Instability Analysis of Self-excited Vibration of a Flexible Weir due to Fluid Discharge," *ASME PVP 244*, 45-58 (1992).

[5] Y. Eguchi and N. Tanaka, "Fluid-elastic Vibrations of Flexible Overflow Weir," *JSME International Journal III-33*, 323-329 (1991).

[6] A. Takizawa, S. Koshizuka, and S. Kondo, "Generalization of Physical Component Boundary Fitted Coordinate (PCBFC) Method for the Analysis of Free Surface Flow," *Int'l Jour. Num. Methods Flu. 15*, 1213-1237 (1992).

[7] A. Takizawa, and S. Kondo, "Development of Physical Component Boundary Fitted Coordinate (PCBFC) Method for the Analysis of Free Surface Flow," *Proc. Int'l Conf. on Nonlinear Mathematical Problems*, 1-16, Iwaki, Japan (1993).

[8] F. M. Henderson, Open Channel Flow, pp. 175, Macmillan Pub. Co., New York (1966).

[9] K. Fujita, T. Ito, T. Kodama, S. Adachi, K. Sekine, H. Ozaki, Y. Eguchi and K. Yamamoto, "Study on flow-induced vibration of a flexible weir due to fluid discharge: effect of weir stiffness," *ASME PVP 258* 143-150 (1993).

[10] T. Nakayama, "Boundary Element Analysis of Nonlinear Water Wave Problems," *Int'l Jour. Num. Methods Eng. 19*, 953-969 (1983).

[11] Y. Eguchi, N. Tanaka, and T. Koga, "Simulation of Thermal and Dynamic Fluid-structure Interaction in a Fast Breeder Reactor," *Proc. 1st Int'l Conf. on Supercomputing in Nuclear Applications*, 86-91, Mito, Japan (1990).

[12] K. Okamoto, H. Madarame, and T. Hagiwara, "Self-induced Oscillation of Free Surface in a Tank with Circulating Flow," *Proc. 5th Int'l Conf. on Flow Induced Vibration*, 1991-1996 IMechE (1991).

[13] D. Lu, A. Takizawa, and S. Kondo, "Sloshing Characteristics of Free-surface Liquid in Elastic-wall Vessels", *Jour. Fluids and Structures* , to be submitted.

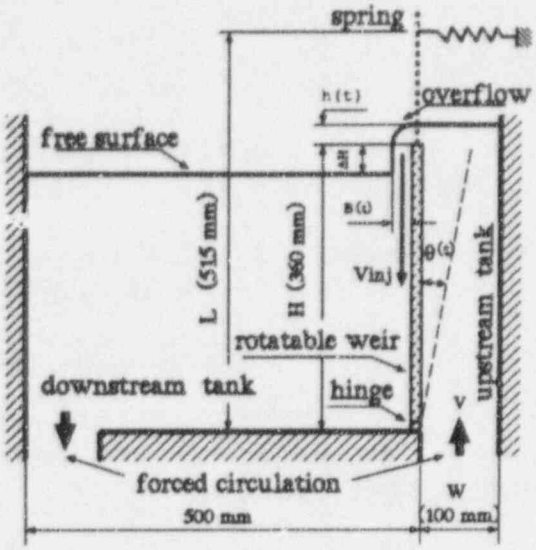

Figure 1: Experimental apparatus of Fukuie and Hara

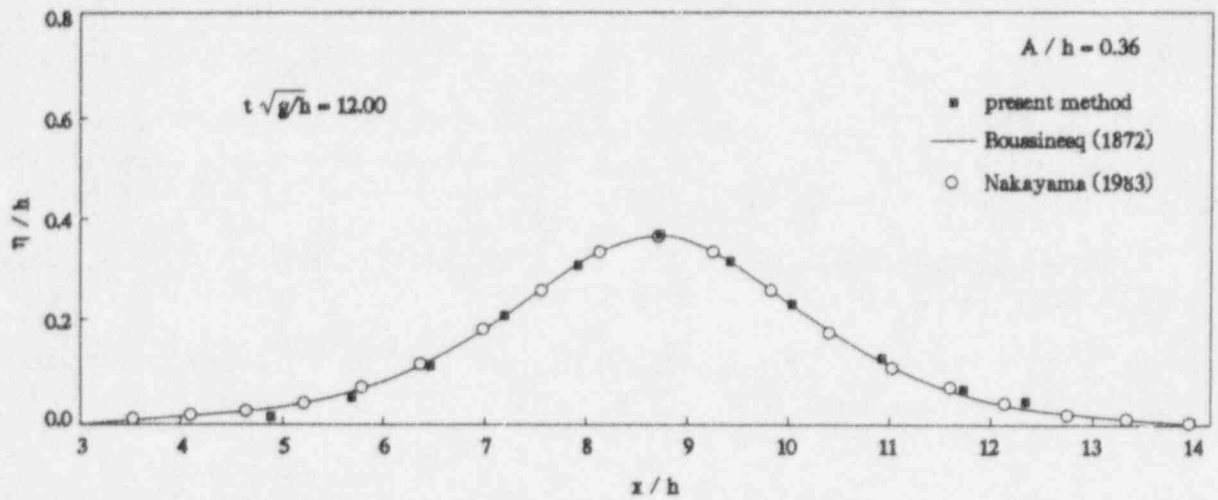

Figure 2: Profile of solitary wave

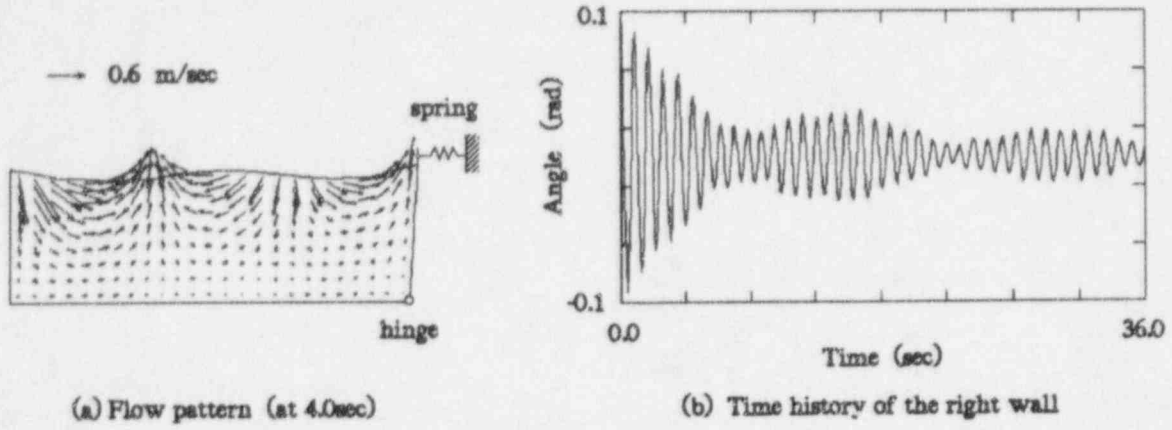

(a) Flow pattern (at 4.0sec)

(b) Time history of the right wall

Figure 3: Fluid-wall interaction in elastic-wall tank

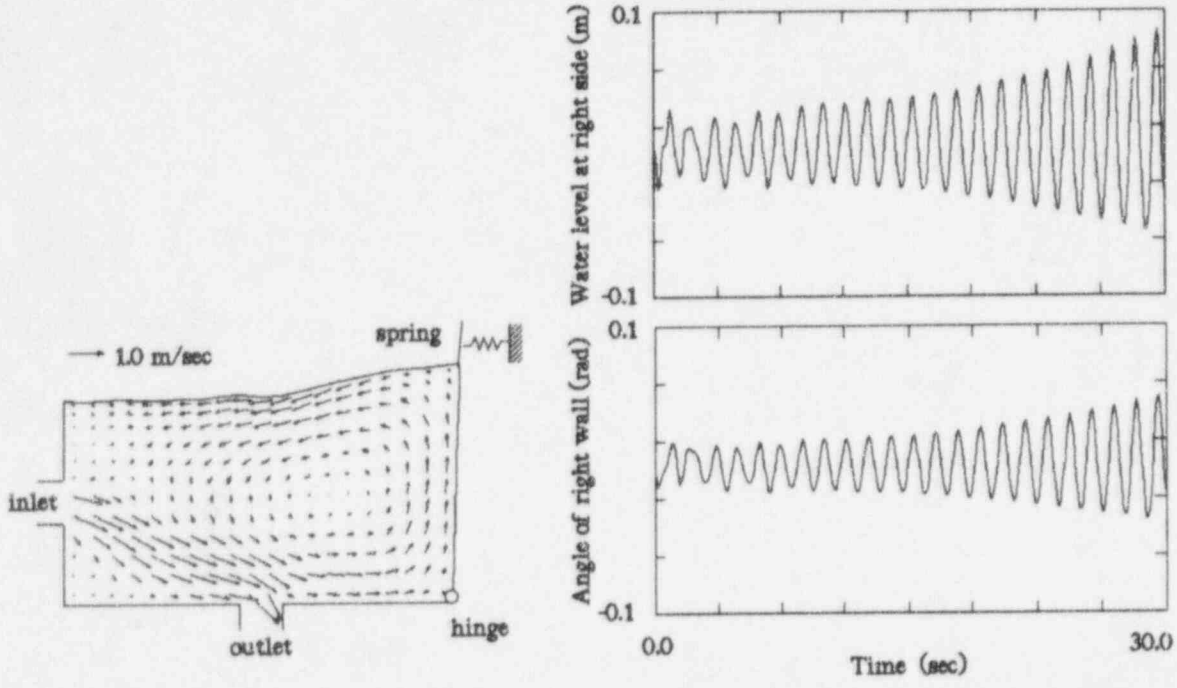

(a) Flow pattern (at 22 sec)

(b) Histories of water level and wall angle

Figure 4: Flow-induced sloshing in elastic-wall tank

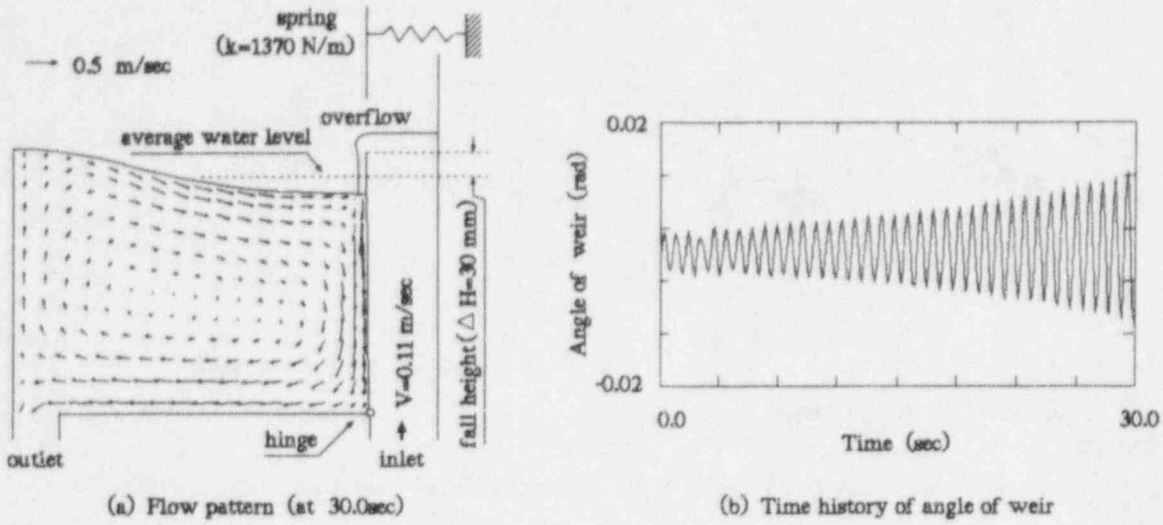

(a) Flow pattern (at 30.0sec)

(b) Time history of angle of weir

Figure 5: Simulation results of overflow-induced instability (Reference-1 case in Figure 6)

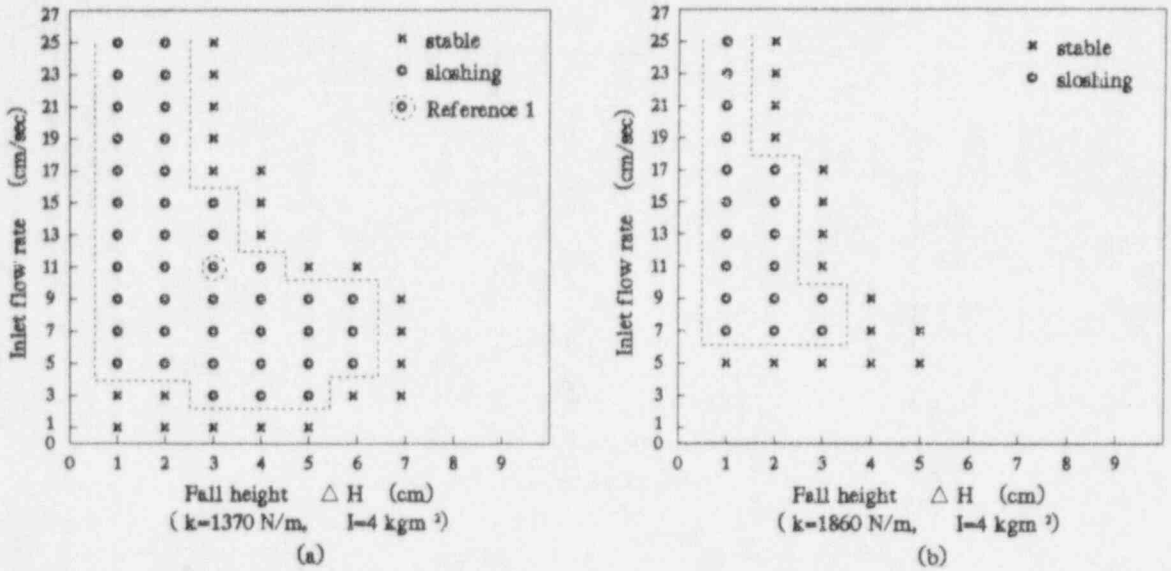

Figure 6: Occurrence scope of instability

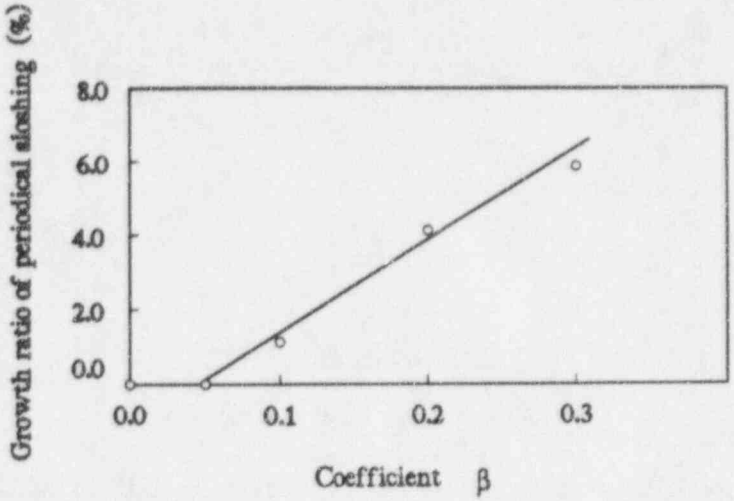

Figure 7: Effect of coefficient β on instability (the weir is rotatable)

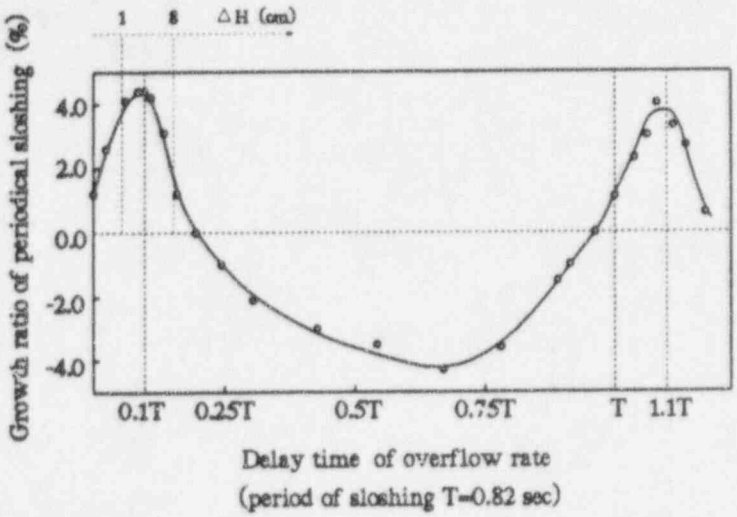

Figure 8: Effect of delay time on instability

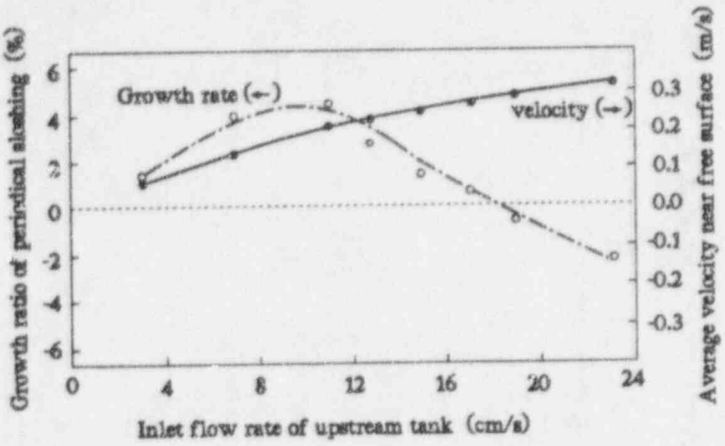

Figure 9: Effect of inlet flow rate on instability (fall height is $3cm$)

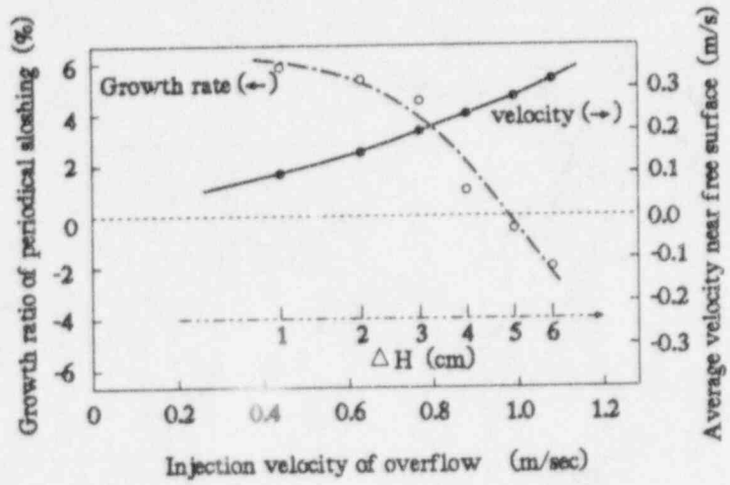

Figure 10: Effect of injection velocity on instability
(delay time and inlet flow rate are fixed $0.07sec$ and $11cm/sec$, respectively)

Study on Mixed Convective Flow Penetration into Subassembly from Reactor Hot Plenum in FBRs

J. Kobayashi, H. Ohshima, H. Kamide and Y. Ieda

Power Reactor and Nuclear Fuel Development Corporation
O-arai Engineering Center
4002 Narita, O-arai, Ibaraki 311-13 JAPAN
TEL : +81-29-267-4141 / FAX : +81-29-266-3867

ABSTRACT

Fundamental experiments using water were carried out in order to reveal the phenomenon of mixed convective flow penetration into subassemblies from a reactor's upper plenum of fast breeder reactors. This phenomenon appears under a certain natural circulation conditions during the operation of the direct reactor auxiliary cooling system for decay heat removal and might influence the natural circulation head which determines the core flow rate and therefore affects the core coolability. In the experiment, a simplified model which simulates an upper plenum and a subassembly was used and the ultrasonic velocity profile monitor as well as thermocouples were applied for the simultaneous measurement of velocity and temperature distributions in the subassembly. From the measured data, empirical equations related to the penetration flow onset condition and the penetration depth were obtained using relevant parameters which were derived from dimensional analysis.

1. INTRODUCTION

The Direct Reactor Auxiliary Cooling System (DRACS) is one of the primary decay heat removal systems of the Fast Breeder Reactor (FBR). From the viewpoint of passive safety, it is desirable that the decay heat be removed solely by natural circulation when even the pony motor (a motor operating at say 10% capacity of a primary motor) of the primary system cannot be operated. During the operation of DRACS, relatively cold temperature fluid, exiting from the heat exchangers directly immersed in the hot plenum (DHX), tends to flow down forwards the fuel subassemblies under certain natural circulation conditions. In fact, such a phenomenon has been observed in several water experiments simulating loop-type[1] and pool-type reactor[2]. This phenomenon, mixed convective flow penetration, is likely to influence not only structural materials through possible thermal shock, but also the natural circulation head which determines core flow rate and therefore , the core coolability. Therefore, it is important to understand the phenomenon of the mixed convective flow penetration and to establish an evaluation methods for it.

Related experiments of a fundamental nature using water were also carried out at MIT[3,4]. Barakat et.al's system has annular channel heated by a centrally-positioned rod. Jerng et. al's system simulated a lower plenum, rod bundle section, neutron shield section and upper plenum, and they reported Gr/Re^2 was a relevant parameter for both onset and depth of

penetration. In this study, water experiments were carried out in order to confirm that their results were applicable to another system, especially in the upper neutron shield section of reactor core v ere the temperature field is uniform due to low flow rate under natural circulation conditi n and high conductivity of sodium. Fundamental understanding of flow conditions in the upper plenum is also of great interest. The observation results of the penetration flow phenomenon and empirical equations describing the penetration flow onset condition and the penetration depth which were derived from measured data are presented.

2. EXPERIMENTAL INSTALLATION

Figure 1 schematically shows the experimental installation. This experimental installation consists of the test loop, test section and measuring instruments.

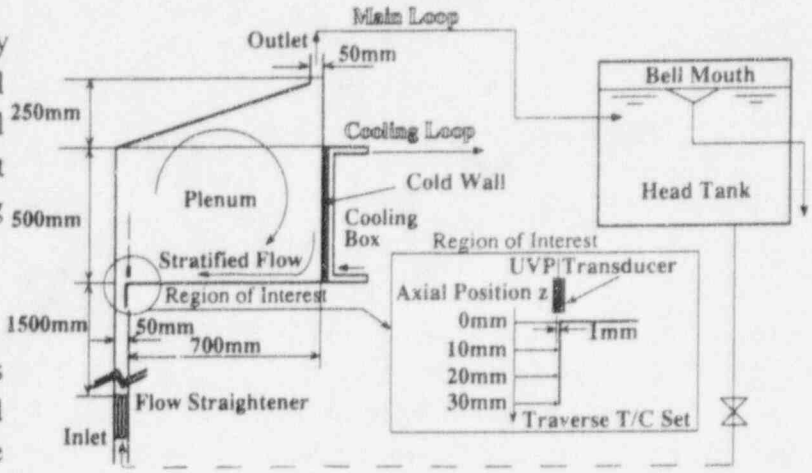

Fig. 1 Test Section

2.1 Test Section

The test section is composed of a plenum, a cold wall and a vertical inlet square channel, simulating the hot plenum, the heat exchanger of DRACS and the lower power subassembly, respectively. The plenum is a thin rectangular tank with a depth (y-axis) of 150 mm. The body was made of transparent acrylic resin for flow visualization and the possibility of using measurement of LDA (Laser Doppler Anemometry). Hot fluid is supplied to the plenum from the inlet channel and flows through the plenum toward the outlet. The test section walls were maintained adiabatic. The lower part of the inlet channel has a flow straightener. The length of the inlet channel excluding the part of the flow straightener is 1500 mm. The velocity distribution was set to be uniform at the outlet of the flow straightener. The cold wall is made of a copper plate 5 mm in

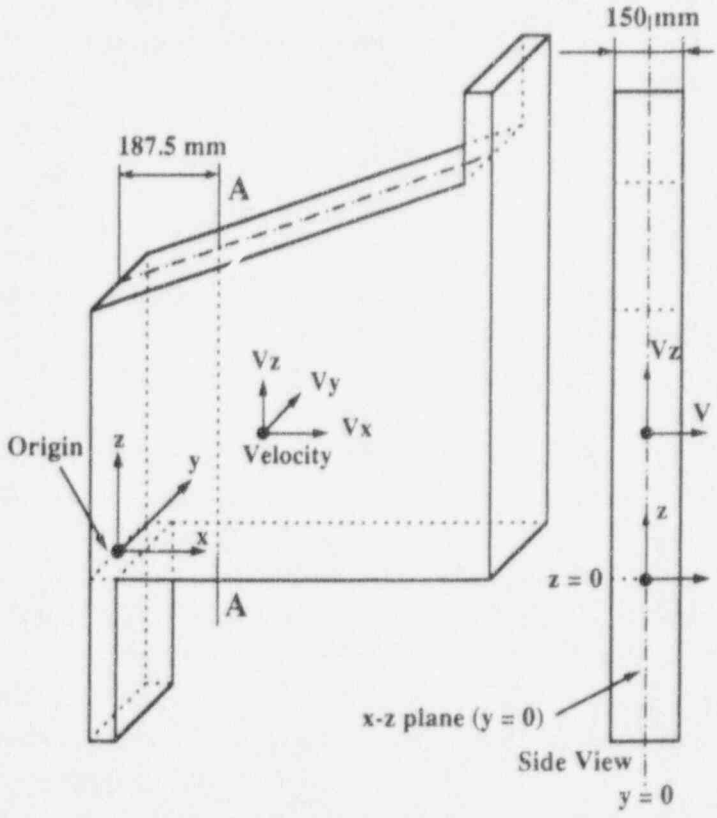

Fig. 2 Test section and coordinate System

thickness and the temperature distribution on the cold wall was kept uniform by the cooling loop during the experiment. Definition of coordinate system for measurement is shown in Fig. 2.

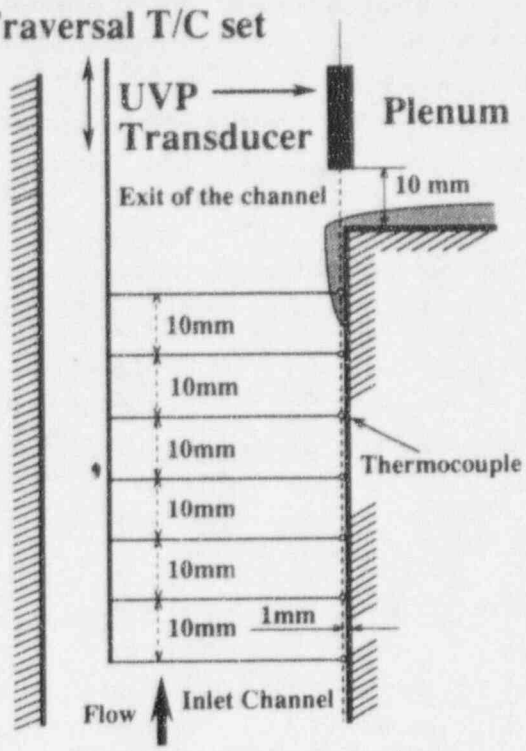

Fig. 3 Instrumentation

2.2 Test Loop

The experimental apparatus has two water loops: 1) the main loop which supplies water into the test section at constant temperature and flow rate through the inlet channel and in order to avoid fluctuation in the flow rate of the pump, a head tank was placed over the test section with a bell-mouth in order to keep a constant head. This kept the inlet flow rate deviation of the test section to a minimum. 2) The cooling loop which is connected to the cooling box in order to keep cold wall constant temperature. The temperature deviation of the inlet flow of both the test section and the cooling box was within 0.2 °C.

2.3 Instrumentation

Velocity measurement in the plenum using LDA and temperature measurement using a traversing T/C along A-A line (see Fig. 2) were conducted. Figure 3 shows the measurement points along the vertical inlet channel. Velocity and temperature fields in the vertical channel were measured with two instruments. One is the Ultrasonic Velocity Profile monitor (UVP)[5] which was used for an axial profile measurement of the vertical velocity components. The UVP utilizes a pulsed echographic technique of ultrasound and can measure a velocity profile along a ultrasound beam line in a vector form quasi instantaneously. Temperature was measured using a T-type (copper-constantan) thermocouples (T/C) of 1 mm diameter. There are seven measuring points corresponding to elevations equally-spaced at 10 mm intervals. This 7 T/C set have 300mm traverse range.

3. TEST CASES

The test cases are designated herein as Experiments I, II and III.

3.1 Experiment I

In Experiment I, velocity measurements in the whole plenum were made using LDA in order to obtain 2 dimensional velocity field. Both temperature and velocity (by LDA) measurements were also carried out along with A-A line as illustrated in Fig. 2.

3.2 Experiment II

In Experiment II, the simultaneous measurements of axial velocity and temperature moment profiles were carried out by UVP and T/C set in a vertical channel. The purpose of this experiment was to obtain a correlation of penetration flow movement with temperature distribution. Four cases, their conditions as shown in Table 1, were conducted. In all cases,

fluid temperatures at the inlet of both the vertical inlet channel and the cooling box were kept at the same levels. The mean velocity in the channel inlet was varied as the test parameter. The data acquisition time for velocity measurement was 137 seconds and it was fixed. During the time 1024 profiles were obtained. The data acquisition time for temperature measurement was matched with velocity measurement, and 1024 profiles were obtained too.

Table 1 Test Cases of Experiment I (*A is a run name of each test case.)

Teperature at channel inlet (^oC)	Temperature of feed water of cooling box (^oC)	Velocity at channel inlet (cm/sec)			
		2.5	2.75	3.0	4.0
50.0	12.5	A	B	C	D

Table 2 Test Cases of Experiment II

Temperature at channel inlet (^oC)	Temperature of feed water of cooling box (^oC)	Velocity at channel inlet (cm/sec)						
		2.5	2.75	3.0	4.0	5.0	6.0	7.0
50.0	12.5	A	B	C	D	E	F	G
45.0	12.5				H	I	J	
40.0	12.5			K	L	M	N	
35.0	12.5			O	P	Q	R	
30.0	12.5			S	T	U		
25.0	12.5			V	W			
20.0	12.5			X				
50.0	16.0					Y	Z	
50.0	20.0					AA	BB	
50.0	25.0					CC	DD	

3.3 Experiment III

In Experiment III, temperature measurements were carried out by a traversing T/C probe set inside the channel inlet. Table 2 shows test cases of the experiment III. The purpose of this experiment was to obtain an empirical equations relating the onset condition of penetration flow and penetration depth. Thirty test cases were carried out. In order to obtain enough accuracy on statistics, the data acquisition time was 10,000 seconds (about 3 hours). And the sampling interval was 0.5 seconds.

4. EXPERIMENTAL RESULT

4.1 Result of Experiment I

Figure 4 shows the vector velocity field in the plenum as measured by LDA. The corresponding conditions of this case were: 1) velocity at channel inlet of 4.0 cm/sec, 2) temperature at channel inlet 50 °C, and 3) temperature of feed water of cooling box 12.5 °C).

From this result, a large clockwise recirculating flow was observed in the plenum. A representative temperature and horizontal velocity component distribution along line A-A measurement are shown in Fig. 5 and Fig. 6 respectively. The fluid cooled by the cold wall flows from the cold wall towards the exit of the inlet channel forming a stratified layer along the bottom horizontal section, of the hot plenum. This cold fluid flow then interacts and mixes with the hot fluid flowing upward through the inlet channel in the vicinity of the exit of the inlet channel. Cold fluid penetration into the inlet channel was then observed under certain conditions. The LDA-measured velocity distribution inside the inlet channel is shown in Fig. 7. It appears evident that in the inlet channel, fully developed turbulence flow was established. (Re number of the velocity at channel inlet of 4.0 cm/sec is about 4900, 5.0 cm/sec is about 6100, 6 cm/sec is about 7300, 10 cm/sec is about 12200, respectively.)

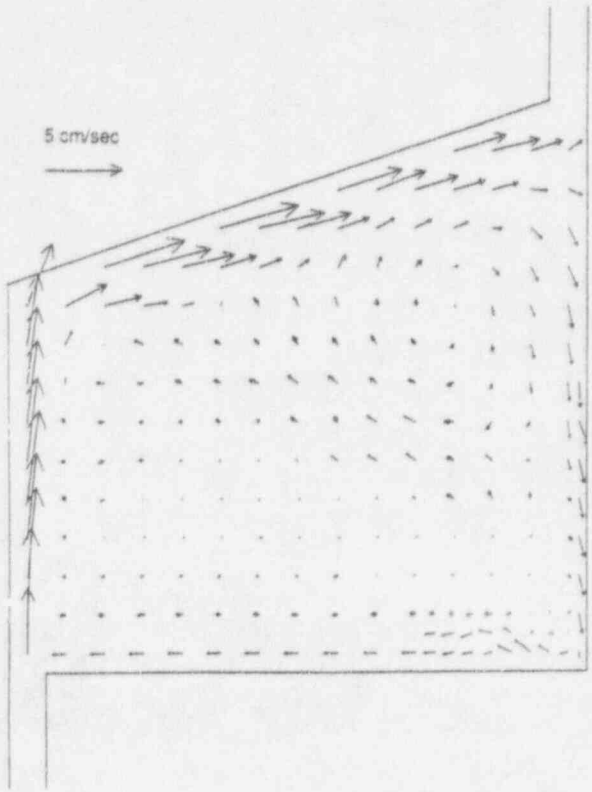

Fig. 4 Velocity Field of the Plenum

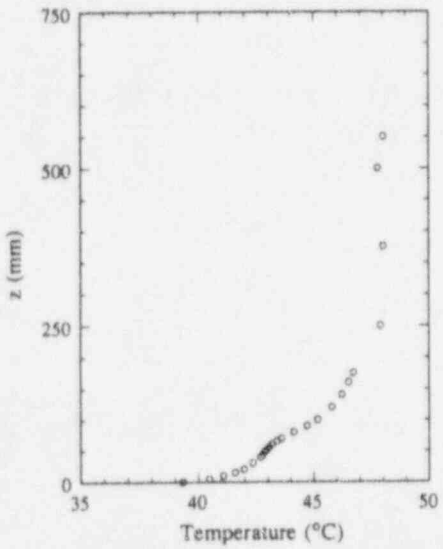

Fig. 5 Temperature Distribution along A-A Line of Case-D

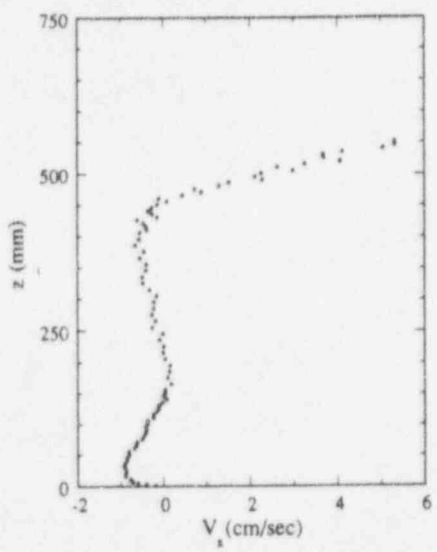

Fig. 6 Horizontal Velocity Component Distribution along A-A Line of Case-D

4.2 Result of Experiment II

On the typical case that penetration flow was observed, transient profiles of velocity were compared with those of temperature in the vertical inlet channel as shown in Fig. 8. The vertical axis is the axial position from just above the top of the inlet channel and

the horizontal axis is the time-scale. The velocity profiles are indicated in gray scale. As the velocity at the top of the penetration flow is very small, the white band shows the boundary between the main upward flow and the penetration flow. With regard to the temperature profiles, the thermocouples detect a temperature decrease when penetration occurs as one moves along

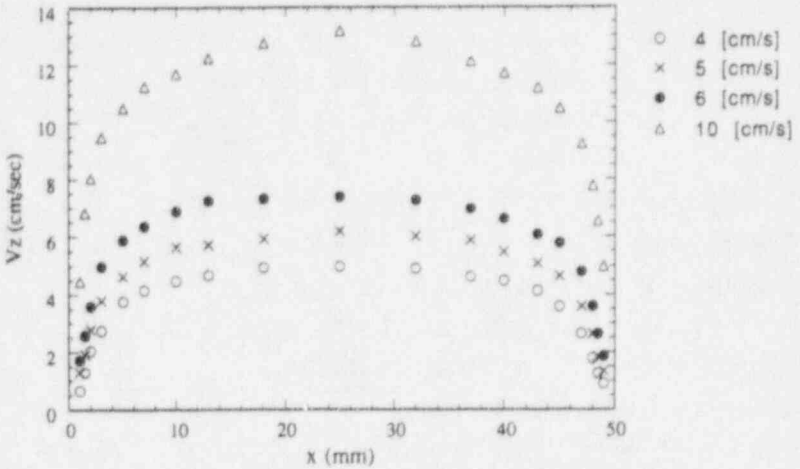

Fig. 7 Profile of Velocity Component Vz in x-direction at z=-200mm in the Inlet Channel

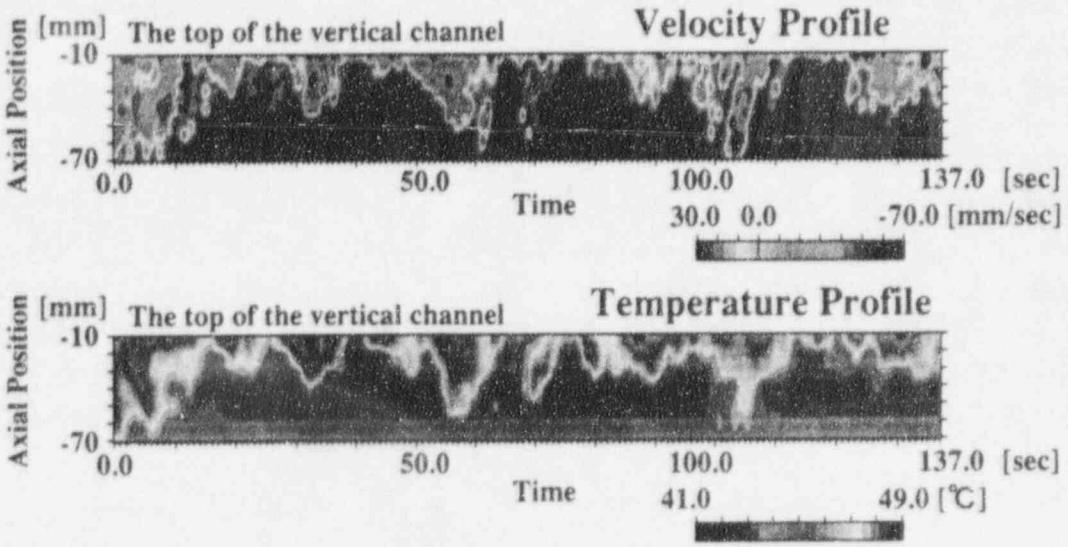

Fig. 8 Transient Velocity and Temperature profiles of penetration flow

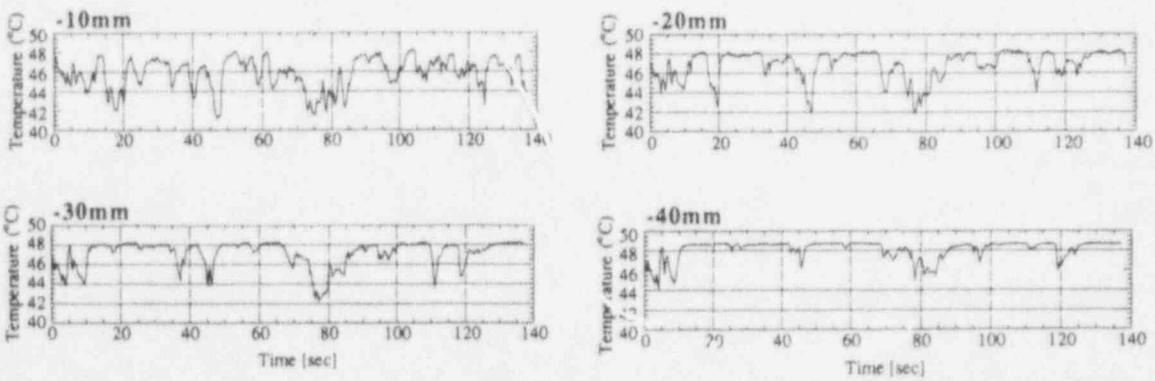

Fig. 9 Transient Signature of Fluid Temperatures in Inlet Channel

(downward) the axial measurement position (see Fig. 3).

4.3 Result of Experiment III

Penetration flow was detected by the temperature measurement in the inlet channel using a traversing thermocouple inserted at the top of the channel to a depth of 300 mm down the channel. Temporal temperature data of typical case that penetration flow was observed were plotted in Fig. 9. As the depth from the top of the channel increased, the penetration frequency clearly decreased more.

5. DISCUSSION

From the results of Experiment I., we found that the trend of temperature profiles were expectedly similar to the velocity profiles. We therefore defined the penetration depth and the onset condition of penetration flow only by analyzing temperature data. To discuss the penetration depth and the onset condition of penetration flow quantitatively, we defined the maximum penetration depth and the penetration flow onset as follows:

[1] Definition of Maximum Penetration Depth

Penetration frequency is determined by using the observed trend of fluid temperature data, that is, by counting the number of temperature decrease for 10,000 seconds (2.78 hr). The maximum penetration depth is defined as the depth at which the penetration count rate falls below 10 counts per 10000 seconds. Figure 10 shows the maximum penetration depth according to this definition.

[2] Definition of Penetration Flow Onset

The penetration flow onset is defined by using the definition of penetration depth. More than 10 mm of maximum penetration depth is regarded as the occurrence of the penetration flow.

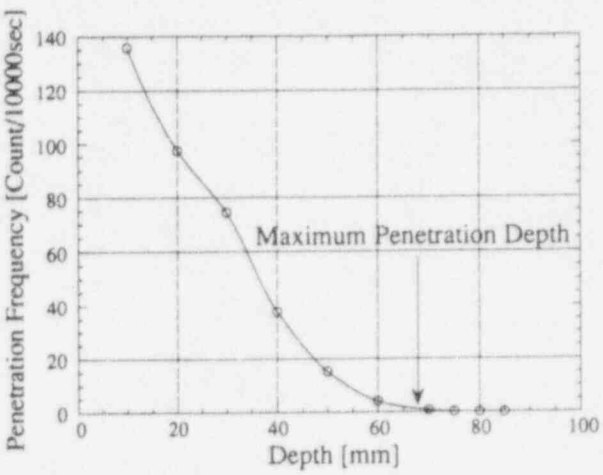

Fig. 10 Definition of Maximum Penetration Depth

5.1 Onset Condition of Mixed Convective Flow Penetration

When we consider the onset condition, we realize that it depends on the local liquid temperature difference between the channel and the plenum and on the flow velocity at the inlet of the plenum, i.e., the balance of the upward inertial force of the main flow and the buoyancy force of cold flow coming from the cold wall. According to the definition of the occurrence of penetration

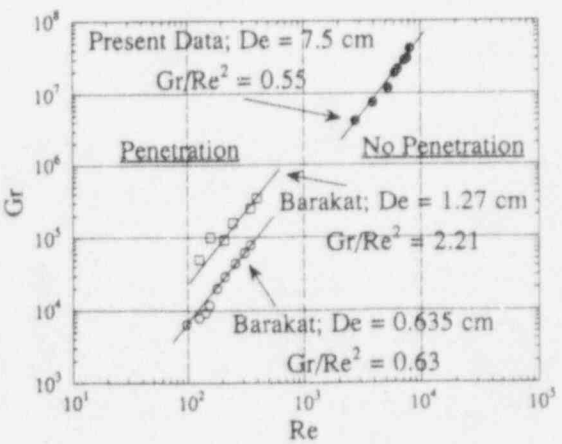

Fig. 11 Onset Condition of the Penetration Flow

flow, we plotted the result of all cases in Fig. 11. Using the temperature data which was obtained from Experiment I, we estimated physical quantities of fluid (density, specific heat, viscosity, ...) and calculated the Gr and Re numbers. The temperature at a depth of 1000mm from the edge of the inlet channel was taken as representative of the temperature of main flow, and the temperature at the bottom of the plenum along line A-A was used as representative temperature of penetration flow. The vertical and horizontal axes are Gr and Re-numbers, respectively. From this result, the onset condition was derived as follows:

$$Gr/Re^2 = Ri = \text{const.} \qquad (1)$$

The value of Gr/Re^2 was 0.55 in this experiment. Figure 11 shows the experimental result of Barakat and Todreas[4] (Their system has annular channel heated by a centrally-positioned rod, however present system is different from theirs, similar result was obtained.).

5.2 Depth of Penetration

Jerng and Todreas reported that Gr/Re^2 was a relevant parameter for both onset and depth of penetration[3]. However present data were difficult to plot on Gr/Re^2 as shown in Fig. 12. For the dispersion area ($Ri < 2.0$), the maximum depth of penetration fitting to Gr/Re^2 is shown as equation (2) and shown in Fig. 13.

$$z/De = 0.281(Ri)^{1.547}+0.161 \qquad (2)$$

The coefficient of correlation between the present data and equation (2) is 0.762.

On the other hand, as illustrated in Fig. 14, the penetration depth is described by

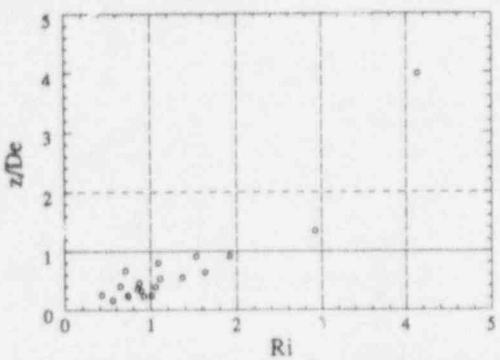

Fig. 12 Maximum Penetration Depth related to Ri number

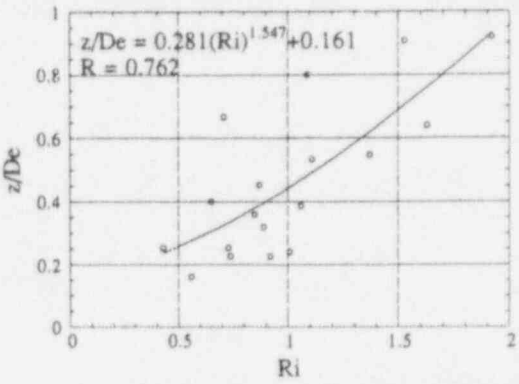

Fig. 13 Fitting Curve to Ri number

buoyancy, inertia, conduction and entrainment effects. By dimensional analysis, we first present the relevant physical properties, velocity, penetration depth, and buoyancy as,

$$(z)^{\pi_1}(v)^{\pi_2}(\lambda)^{\pi_3}(\mu)^{\pi_4}(\rho)^{\pi_5}(C_P)^{\pi_6}(\rho g\beta\Delta T)^{\pi_7} \qquad (3)$$

We then matched formula (3) to the inlet channel's hydraulic diameter, De. Details are given in the Appendix and the resulting equation is,

$$z/De = (Gr/Re^3)^a(Re)^b(Pr)^c \qquad (4)$$

Equation (4) suggests a relevant parameter for the depth of penetration as Gr/Re^3.

Thus Figure 15 shows the result when the depth of penetration is plotted versus Gr/Re^3. The corresponding regression curve of this result is shown as equation (5).

$$z/De = (5.70E+5)(Gr/Re^3)^{1.816}+0.262 \qquad (5)$$

The coefficient of correlation between the present data and equation (5) is 0.910.

Then the parameter m1, m2, m3 in equation (6) obtained by the method of least squares is shown as equation (6) and Fig. 16.

$$z/De = (m1)(Gr)(Re)^{m2}+m3 \qquad (6)$$

$$z/De = (1.663E+3)(Gr)(Re)^{-2.999} \qquad (7)$$

The coefficient of correlation between the present data and equation (7) is 0.956.

From the result of equation (5) and (7), relevant parameter for depth of penetration is $GrRe^m$, where $m < -2.0$. The reason that the result differ from Jemg et. al are as follows:

1. Difference in velocity distribution inside the inlet channel. The velocity distribution inside the inlet channel greatly affects the depth of penetration.
2. While our temperature distribution in the inlet channel is uniform, in their system's it is not flat. This affects the local buoyancy force.
3. In the process of penetration, the buoyancy-driven penetrating flow subsides due to mixing with the main flow. The result of the shearing force resulted in observed entrainment of the penetrating flow by the main flow.
4. The range of Re number is different from theirs.

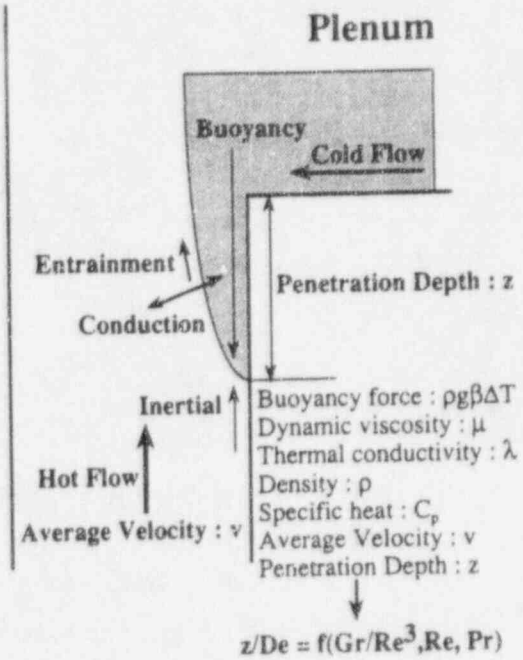

Fig. 14 Physical Mechanism of Penetration Flow

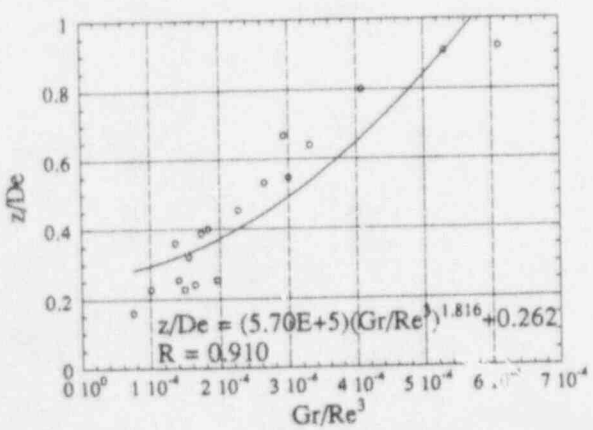

Fig. 15 Fitting Curve to Gr/Re^3

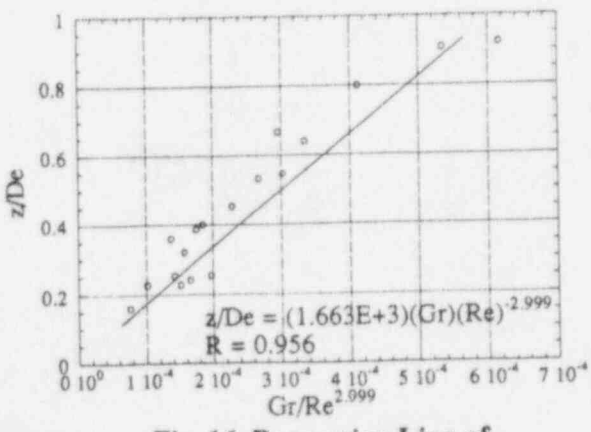

Fig. 16 Regression Line of Maximum Penetration Depth

6. CONCLUSION

Water experiments were performed to obtain a fundamental understanding of the penetration flow in a vertical square channel. Correlations of the penetration flow onset condition and the penetration depth have been obtained.

The onset condition of the penetration flow could be correlated with the Richardson number, which represents a ratio of the buoyancy force to the inertial force in the vertical channel, as follows:

$$Gr/Re^2 = Ri = 0.55.$$

It is considered that the penetration depth is determined based on buoyancy, inertia, conduction and entrainment effects. The depth of penetration cannot described by Ri number. And we obtained that the depth of penetration could be described by $GrRe^m$, where $m < -2.0$.

The study of the mixed convective penetration phenomenon using sodium is being carried out at PNC. We will apply the results of this water experiment to the sodium experiment.

NOMENCLATURE

z	: The depth of penetration	[m]	
De	: Hydraulic diameter of inlet channel	[m]	
v	: Axial mean velocity of channel	[m/s]	
λ	: Thermal conductivity	[W/mK]	
μ	: Coefficient of viscosity	[Pa s]	
ρ	: Density	[kg/m^3]	
C_P	: Specific heat at constant pressure	[J/kgK]	
$\rho g\beta DT$	: Buoyancy force	[kg/m^{2}s^2]	
(g	: Acceleration of gravity	[m/s^2])	
(β	: Volume coefficient of expansion	[1/K])	
(T	: Temperature	[K])	
Re	: Reynolds number	=	$\rho vDe/\mu$
Gr	: Grashof number	=	$De^3g\beta\Delta T\rho^2/\mu^2$
Pr	: Prandtl number	=	$C_P\mu/\lambda$

Appendix

$(z)^{\pi_1}(v)^{\pi_2}(\lambda)^{\pi_3}(\mu)^{\pi_4}(\rho)^{\pi_5}(C_P)^{\pi_6}(\rho g\beta\Delta T)^{\pi_7}$ same as (3)

then, formula (3) was matched to nondimension along with the physical parameters.

$[L]^{\pi_1}[L/t]^{\pi_2}[H/Lt\Theta]^{\pi_3}[M/tL]^{\pi_4}[M/L^3]^{\pi_5}[H/M\Theta]^{\pi_6}[M/t^2L^2]^{\pi_7}$

where,

L is length, M is mass, t is time, H is Heat and Θ is temperature.

and then,

L: $0 = \pi 1 + \pi 2 - \pi 3 - \pi 4 - 3\pi 5 - 2\pi 7$

M: $0 = \pi 4 + \pi 5 - \pi 6 + \pi 7$

t: $0 = -\pi 2 - \pi 3 - \pi 4 - 2\pi 7$

H/Θ: $0 = \pi 3 + \pi 6$

Next, $\pi 2$, $\pi 4$, $\pi 5$ and $\pi 6$ were expressed by $\pi 1(z)$, $\pi 3(\lambda)$ and $\pi 7(\rho g\beta\Delta T)$.

$\pi 2 = \pi 1 - 3\pi 7$

$\pi 4 = -\pi 1 - \pi 3 + \pi 7$

$\pi 5 = \pi 1 - 2\pi 7$

$\pi 6 = -\pi 3$

Therefore,

$(zv\mu^{-1}\rho)^{\pi_1}(\lambda\mu^{-1}C_P^{-1})^{\pi_3}\{v^{-3}\mu\rho^{-2}(\rho g\beta\Delta T)\}^{\pi_7}$,

We introduce artificially the fraction (De/De) to define the Re-number and the aspect ratio (z/De).

$\{(z/De)(Re)\}^{\pi_1} \alpha (Pr)^{\pi_3}(Gr/Re^3)^{\pi_7}$

Hence,

$z/De = (Gr/Re^3)^a(Re)^b(Pr)^c$ same as (4)

REFERENCES

[1] K. Satoh and H. Miyakoshi, "Study of Decay Heat Removal by Natural Circulation", Proceedings of NURETH-4, vol. 1, pp.378-383

[2] Y. Ieda, et al., "Thermohydraulic Study on Natural Circulation Decay Heat Removal for a Pool-Type LMFBR", Proceedings of FR'91, vol. 2, pp.16.9-1(1991)

[3] D. W. Jerng and N. E. Todreas, "Mixed Convective Flow Penetration in Vertical Channels", Proceedings of NURETH-5, pp.1720-1728(1992)

[4] A. I. Barakat, N. E. Todreas, "Mixed Convection Buoyancy-Induced Backflow in a Vertical Single-Rod Channel Connected to an Upper Plenum", Proceedings of NURETH-4, pp.746-752(1989)

[5] Y. Takeda, "Development of Ultrasound Velocity Profile Monitor(UVP) and its Experience", Proceedings of NURETH-4, pp.418-423(1989)

LARGE EDDY SIMULATION OF MIXING BETWEEN HOT AND COLD SODIUM FLOWS - COMPARISON WITH EXPERIMENTS

J.P. SIMONEAU
FRAMATOME
LYON

H. NOE
EDF
LYON

B. MENANT
CEA
GRENOBLE

ABSTRACT

The large eddy simulation is becoming a potential powerful tool for the calculation of turbulent flows. In nuclear liquid metal cooled fast reactors, the knowledge of the turbulence characteristics is of great interest for the prediction and the analysis of thermal stripping phenomena.
The objective of this paper is to give a contribution in the evaluation of the large eddy simulation technique is an individual case. The problem chosen is the case of the mixing between hot and cold sodium flows. The computations are compared with available sodium tests. This study shows acceptable qualitative results but the simple model used is not able to predict the turbulence characteristics.
More complex models including larger domains around the fluctuating zone and fluctuating boundary conditions could be necessary. Validation works are continuing.

1 - INTRODUCTION

In liquid metal fast reactors, the use of sodium as coolant ensures high heat transfer coefficients. In some parts of these reactors, temperature gradients are occurring due to thermal-hydraulic phenomena such as thermal stratification or mixing between tow flows. When they are combined with turbulent flows, these gradients induce temperature fluctuations, and hence the high heat transfer coefficients may cause damaging effects on the neighbouring structures (thermal stripping).

In classical approaches, such temperature fluctuations cannot be assessed via numerical computations : the standard, well known, k-ε model only predicts mean fields and an isotopic kinetic turbulent energy. The regions of temperature gradients are known but not the temperature fluctuations. The turbulence characteristics needed to predict the mechanical behaviour of the structures are mainly the amplitude and the range of frequency of the temperature fluctuations. These values can be obtained from sodium or more frequently water tests (Simoneau & Smith, 1993) or even from in situ measurements. But most of the time, no tests are available because of their high cost and the difficulty to perform it, and conservative assessments are used (maximum temperature difference in the domain, large range of frequencies).
In order to obtain more realistic loadings and calculated damages, a reduction of the conservative ranges of the amplitude and of the frequencies would be useful.
For a few years, the increasing of power of new computers enables to start a new numerical approach : the large eddy simulation (LES) of turbulent flows.

The present paper presents a first evaluation of the large eddy simulation technique implemented in the TRIO-VF code on a particular case. The chosen configuration is the mixing between two sodium flows at different temperature in a tee junction for which sodium tests are available.

In a first part, the experiments are described, then the numerical results are discussed and compared with experimental ones. Finally, future trends are expressed.

2 - THE SODIUM TESTS

2.1 - The experimental set-up

A tee merging hot and cold sodium flows is set in the sodium loop called CASTOR, located in the CEA laboratories at Cadarache (France). The temperature difference between the two feeding pipes is obtained by shunting a part of the sodium entering the purification device. The outlet of this device is connected to the cold inlet of the tee, while the shunted sodium feeds the hot inlet (see figure 1). 6 thermocouples are located downstream the merging along the meridional line, in front of the hot inlet, 11 other ones are set on a mobile rake and provide a mesh of measures in the symmetry plane of the tee (see figure 2). The sensors are chromel-alumel ones and use a differential system.

2.2 - Test procedure

The mean temperature of the loop is about 250 °C. The prescribed temperature difference is obtained by heating the whole sodium loop to the hot prescribed temperature and by adjusting the purification device to get the cold one. The flowrates are also adjusted. The loop is firstly operating during a stabilization period.
Each of the 17 thermocouples fluctuating signal is recorded during 5 minutes. Moreover, the mean temperature (obtained by a low filtering) and the root mean square value of the fluctuations (obtained from high filtering) are also saved.

The time constant of the thermocouples is between 10 and 20 ms which allows to catch frequencies higher than 10 Hz.

2.3 - Test retained for computation

9 tests have been carried out. The range of Reynolds number (based on flow in instrumental part) spreads out from $0.5\ 10^5$ to $3\ 10^5$, while the ratio cold flowrate/hot flowrate lies within 0.7 to 4.3.
The test leading to the greater fluctuations has been chosen for the numerical comparison, it is characterized by :

Re	$1.05\ 10^5$
Qc/Qm	1,1
ΔT	30 °C

3 - THE LARGE EDDY SIMULATION

3.1 - The numerical model

The large eddy simulation is based on an early method developed in 1963 by Smagorinsky. But its implementation is only accessible now to computers (Chollet and Lesieur, 1982). This kind of simulation has been quickly developed recently by several research groups, and many variants of the original Smagorinsky model are now presented (Voke et al. 1994).

The present simulations use the finite volume code TRIO (Grand et al, 1988). It solves the transient three dimensional Navier-Stokes equations (Boussinesq approximation) using the LES technique. The time marching is explicit (first order) while the space discretization is of third order (modified QUICK). The basis of the LES methods is a separation of each flow variable into two components : a large scale one which is solved explicitly and a subgrid scale one which is modelled separately. This separation is obtained using a spatial filter (box filter) and leads to a subgrid scale Reynolds stress modelled via an eddy viscosity (structure function model, see Silveira Neto et al, 1993).

3.2 - The geometrical model

The spatial domain includes the main pipe, whose length is from a distance of 1 diameter before the tee junction until 4 diameters after this junction (see figure 2). Each spatial mesh is about $(3\ mm)^3$ and the whole domain is discretized in $25 \times 94 \times 25 = 58\ 750$ meshes, with a quasi regular grid.
Walls of the pipes are represented by steps (in the y-z plane), but this has only a small influence on the parietal flow and no significant influence on the mixing region considered.
The boundary conditions (summarized on figure 2) are prescribed velocities at hot and cold inlets and zero pressure gradient at the outlet. The standard wall function is used for the solid walls.

3.3 - The simulation

The simulation is first carried on coarse grid ($\simeq 7000$ meshes), in order to obtain a converged mean flow field. Hence, a grid refinement occurs (up to the mesh mentioned above in § 2.2). The LES model is used for the coarse grid but a steady flow is obtained.
On the contrary, a time varying flow field is observed as soon as the simulation begins with the finer grid. No external user-defined perturbations are needed at the inlet boundary conditions : the physical configuration is unstable enough to launch eddies. After a short period, the fluctuations are established and the numerical results are recorded for analysis.

The time step is about $2\ 10^{-3}$ s. The Digital DEC 3000 computer calculates about 0.15 seconds of physical time per 1 hour of CPU time.

A main run (reference calculation) covering a period of about 40 seconds is performed LES-1 case).
Other calculations including some modifications of the boundary conditions have also been performed on shorter times.

4 - RESULTS AND COMPARISON

4.1 - The flow and temperature fields

In the reference calculation (noted LES-1), the boundary conditions are fixed steady velocities and temperature on the two inlets and with a flat velocity profile. The results are time averaged and compared with experimental profiles on figure 3. They show a noticeable difference at the merging of the two flows : the hot jet is not as mixed as it was measured. It is not perturbated during its entrance in the cold pipe.
On the computed flow fields, we can observe only disturbances of two kinds (see instant flow field on figure 4 and instant temperature field on figure 5) :

* wake eddies behind the hot jets (fig.4),
* shear eddies between hot and cold flows. (fig. 5).

These observations are in good qualitative agreement with other experiments detailed in Fric and Roskho, 1994 (the smoke streamlines presented show those two phenomena). The hot jet also oscillates in the symmetry plane of the tee along the z-axis but the base of the hot jet is stable. It seems that in the test, the hot jet is disturbed as soon as it enters in the cold pipe.

In order to explain the differences between the measures and the numerical results, a steady calculation has been carried out using a k-ε model and using the exact geometry : the upstream conditions are set at several diameters before the tee junction for the two flows, furthermore the radius knuckle of the hot pipe is modelled.
A first calculation on this new mesh performed with no turbulence at the inlet does not give a much better result than the LES one. But a second calculation on this new mesh, with a turbulence intensity of 25 % at each inlet, gives good agreement with the measured mean temperature profiles (figure 3).

Hence, the following conclusions can be given :

* the hot and the cold flows are turbulent in the test loop before the tee junction,
* the domain calculated by the LES technique must be enlarged rather far from the section of interest, which may lead to a high number of meshes.

4.2 - **The frequency analysis of the temperature**

As explained in the § 1, the range of frequencies is of great interest for mechanical analysis of the thermal stripping risk. A frequency analysis of the LES calculation is obtained thanks to 8 "numerical sensors" located in the symmetry plane of the tee.
A duration of about 40 seconds is recorded and then analyzed using a Fast Fourier Transform. Figure 6 presents the spectrum obtained (reported on log-log axes) for a sensor located in the mixing region.

The frequency analysis show :

* a typical curve shape with a maximum for medium frequencies, and minima for lower and higher frequencies,
* a decreasing slope for high frequencies as $f^{-5/3}$ to f^{-2},
* a singular peak at about 2 to 3 Hz.

The spectra obtained from the tests (see figure 7) shows :

* the same curve shape,
* a decreasing for high frequencies as f^{-2},
* several peaks around 1 Hz and a continuous maximum of the spectra around this value,
* the decreasing of the spectra is observed for frequencies lower than 0.1 Hz.

Two phenomena may explain the observed differences :

* the computation duration is only of 40 seconds, which is not enough to catch the flow variation of about 0.1 Hz,
* the period obtained numerically are due to the oscillation of the wake of the hot jet, which is only a part of it. If a greater mass of sodium is fluctuating, so lower frequencies may be expected.

A further LES computation has been performed with the following modifications (noted LES-2 case) :

* Hot inlet : a velocity profile for the normal velocity is prescribed (simplified profile derived from the profile calculated with the model using exact geometry).
* Hot and cold inlets : perturbations of 25 % (noise) of the normal velocity are imposed, with a frequency of 10 Hz. This value is much higher than the range of interest (which is around 1 Hz).

The instant fields issued from this new computation show that now, the whole jet is fluctuating, from its very entrance into the cold pipe. The numerical run has not been carried on a sufficiently long time (only $\simeq$ 10 seconds) but the spectra analysis of the numerical results show the same peak between 2 and 3 Hz. The peak at 10 Hz is also obviously seen. No new frequency under 2 Hz is found to appear (figure 8).

We can conclude in a similar way as in the previous chapter § 4.1 that an extended domain with fluctuating boundary conditions, seems to be necessary to conclude the validation on this test.
However, some perturbations may occur in the CASTOR sodium loop so that the main fluctuation frequency could be due to other phenomena than the tee junction (bends, pump, purification device...).
Informations about the fluctuations of the velocity before the flow merging are needed to assess those phenomena. And for a further validation, a more instrumented (velocity fluctuation...) test is needed.

4.3 - The amplitude of the fluctuations

The root mean square (RMS) of the instant temperature are available for both the tests and the LES simulation.
The figure 9 presents those values at the wall in front of the hot inlet and shows that the LES simulation underestimates the amplitude of the fluctuations just behind the merging of the two flows. In the numerical model, the mixing and hence the fluctuations occur later in the streamwise direction than in the experiment. Figure 10 shows that, after 4 diameters from merging, the amplitude of the fluctuations decreases because the hot and cold sodium are now better mixed. This may be a consequence of the lack of fluctuation of the whole hot jet.
The peak to peak amplitude rises about 80% of the whole amplitude (temperature difference between hot and cold flows). The extreme values are obtained with low frequencies while high frequency fluctuations occur with lower amplitudes.

5 - FUTURE WORKS

This paper present an attempt of validation work of the LES technique.

More validation work is needed and it could be developed in the following axes :

* use of a test able to give reliable boundary conditions,
* computation of an extended domain in order to avoid the influence of the boundary conditions,
* computation on finer meshes, to check an eventual mesh size influence,
* longer time of computation for a reliable low frequency analysis.

6 - CONCLUSION

In this study, a large eddy simulation technique has been used to assess the turbulent characteristics of the flow field in a tee junction between a hot and cold sodium flows. The predictions have been compared with experimental results.

This study is a first contribution in the ongoing validation process of the LES technique in industrial nuclear applications and specially in the context of thermal stripping problems occurring in liquid metal fast reactor. The latest powerful computers make the LES technique as a potential valuable tool.

The present results show that a simple modelling of the tee junction is not sufficient to get a good agreement with the numerical results in terms of frequencies and amplitudes of the fluctuation, and an extended computational domain or realistic and complex boundary conditions would be at least necessary.

The validation work will continue with those trends, it is mandatory before using this technique as an industrial tool.

REFERENCES

* **Chollet J.P., Lesieur M.**
Parametrization of small scales of three dimensional isotopic turbulence utilizing spectral closures, **J. atms. Sci**, 38, 1982, pp. 2747-2757.

* **Fric T.F., Roskho A.**
Vortical structure in the wake of a transverse jet, **J. fluid mechanics**, vol 279, nov 1994, pp.1-47.

* **Grand D., Villand H., Coular N.**
Computation of flow with distributed resistance and heat sources. **Proceedings of the third international symposium on refined flow modelling and turbulence measurements**, Nippon Toshi Center Tokyo, 1988, pp. 427-434

* **Silveira Neto A., Grand D., Metais O.,Lesieur M.**
A numerical investigation of the coherent vortices in turbulence behind a backward facing step. **J. Fluid Mechanics**, vol. 256, nov. 1993, pp. 1-26

* **Simoneau J.P., Smith M.**
Fluctuations in the bottom stratified area of a liquid metal reactor hot pool. **Proceedings of NURETH 6**, October 5-8, 1993, pp. 548-553

* **Voke P., Kleiser L., Chollet J.P.**
Direct and large eddy simulation I, selected papers from the first ERCOFTAC workshop on direct and large eddy simulation, Kluwer, Dordrecht, 1994, pp. 434

NOMENCLATURE

D : Cold pipe diameter
Re : Reynolds number = ρ V.D / μ
Q_c : cold flowrate (m^3/s)
Q_H : hot flow rate (m^3/s)
ΔT : temperature difference between hot and cold flows
I : turbulence intensity at inlets.

Figure 1 Apparatus set up

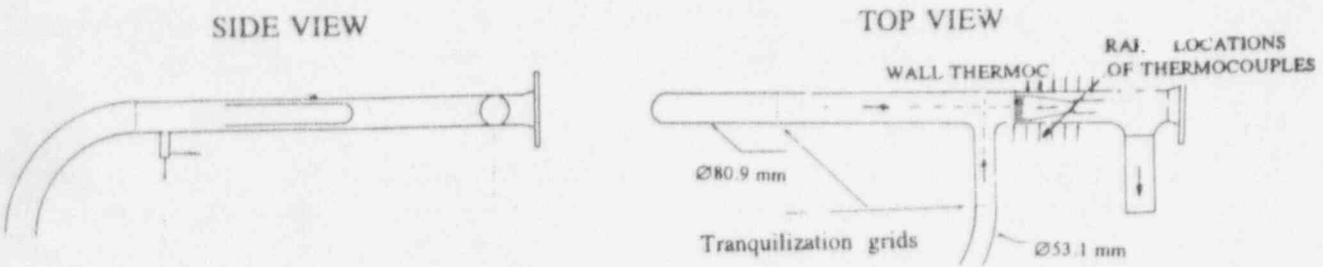

Figure 2 Spatial domain and boundary conditions - TRIO LES calculation

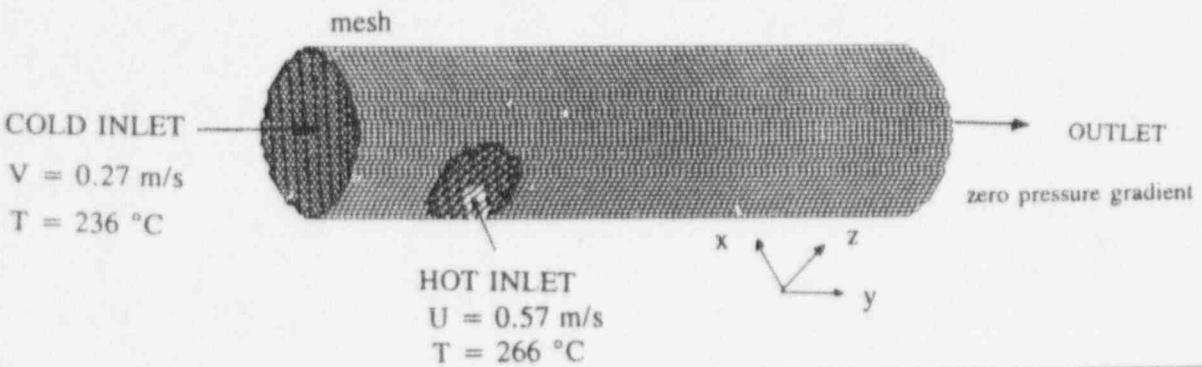

Figure 3 Time averaged temperature profiles :

measured, computed via LES and k-eps (I=25%)

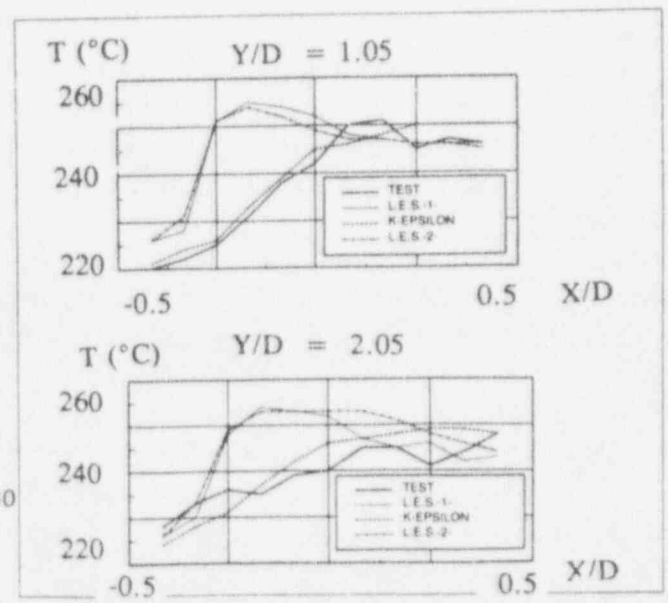

Figure 4 Instant temperature fields (LES)

plane x = constant

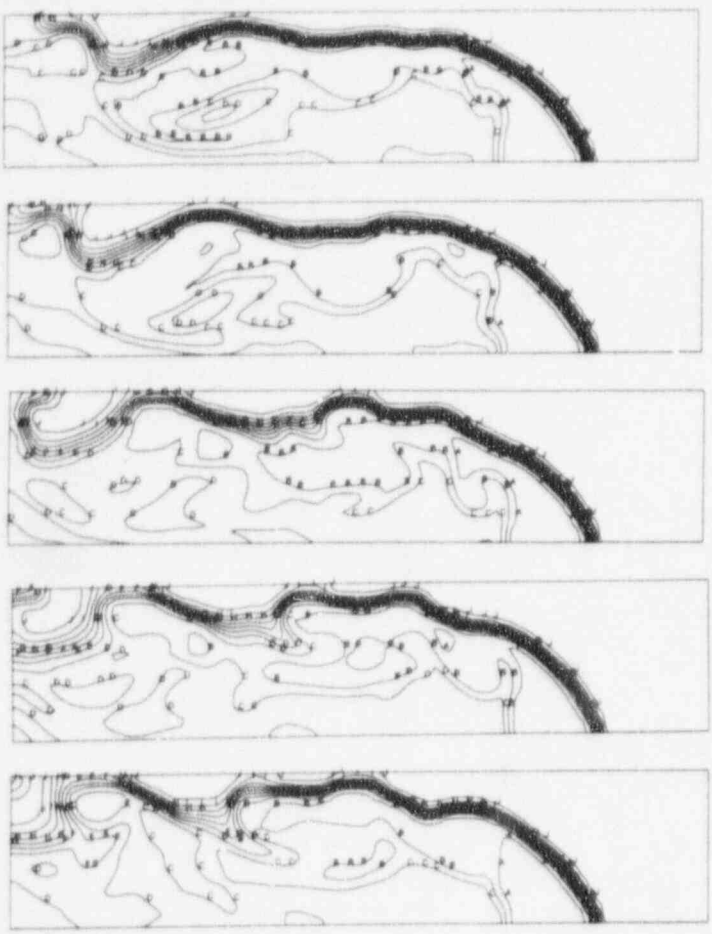

Figure 5 Instant temperature fields (LES)

plane z = constant

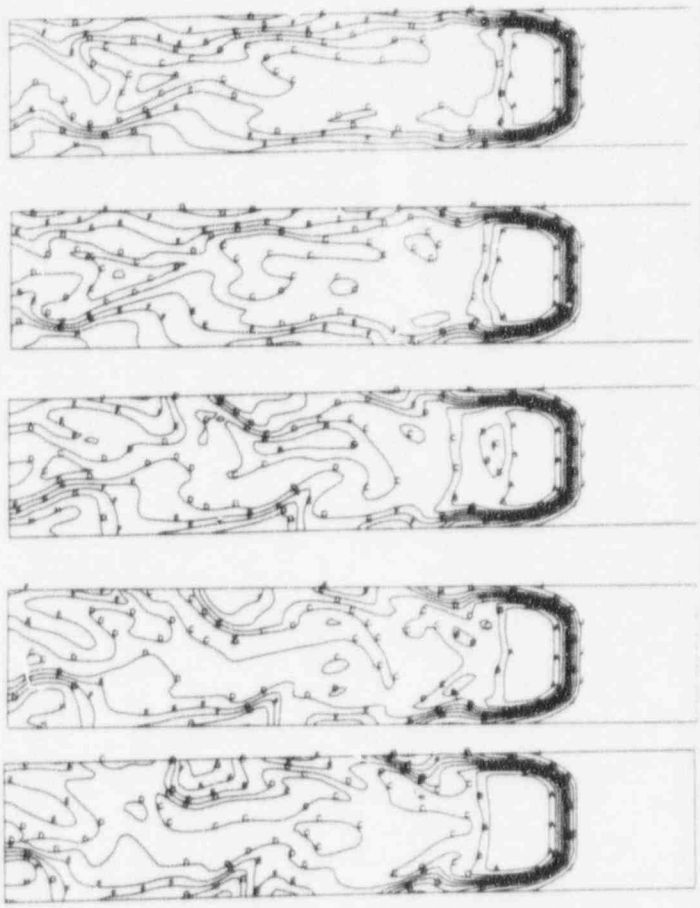

TEMPERATURE
ADIM.
LOCAL MX= 265.7
LOCAL MN= 235.7

A	264.2
B	261.2
C	258.2
D	255.2
E	252.2
F	249.2
G	246.2
H	243.2
I	240.2
J	237.2

Figure 6 Spectra of calculated values (TRIO LES)

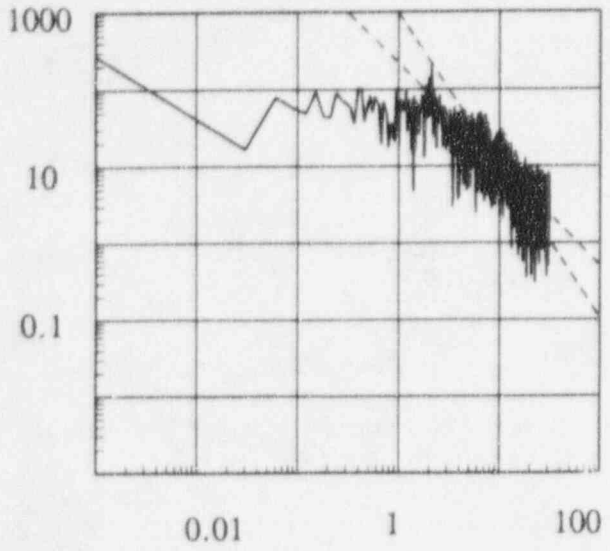

Figure 7 Spectra of measured values

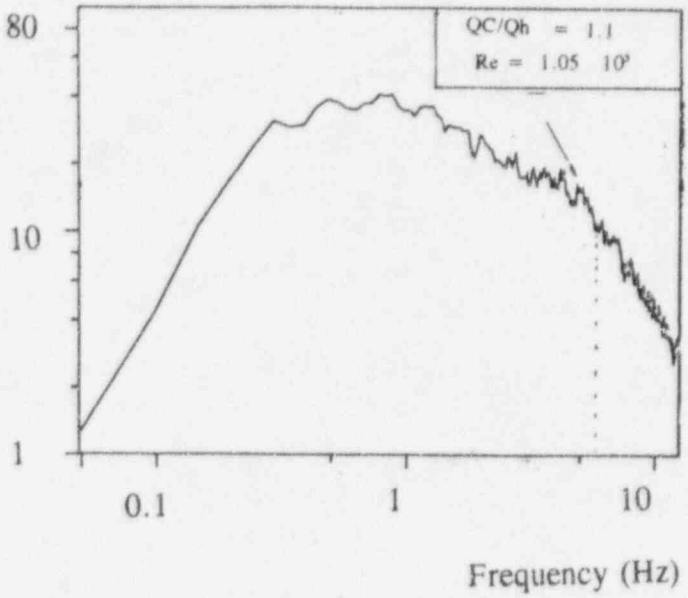

Figure 8 Spectra of calculated values TRIO LES-2,

(2nd calculation)

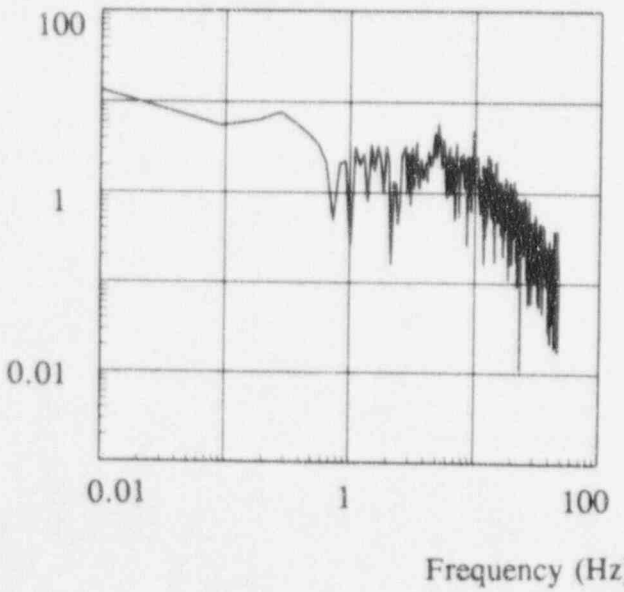

Figure 9 Amplitude of fluctuations

(measured and computed via LES)

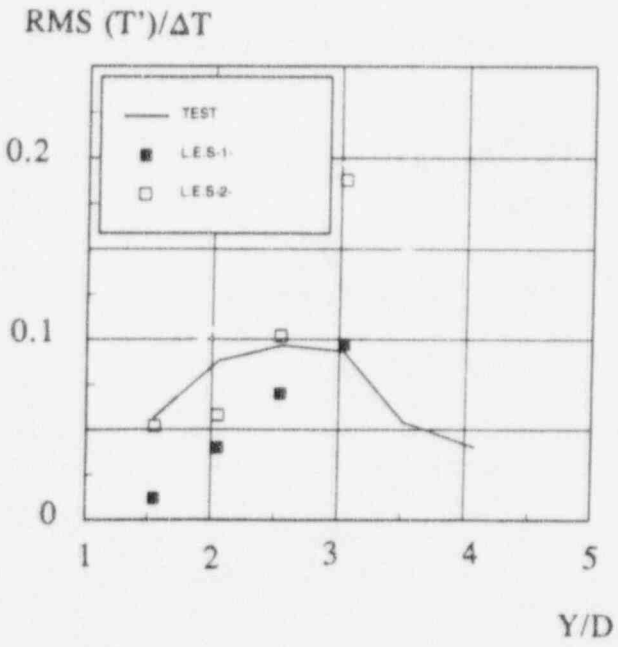

NATURAL CONVECTION HEAT TRANSFER ON TWO HORIZONTAL CYLINDERS IN LIQUID SODIUM

K. Hata, M. Shiotsu, Y. Takeuchi, K. Hama and A. Sakurai

Institute of Atomic Energy, Kyoto University
Uji, Kyoto 611, Japan

Abstract

Natural convection heat transfer on two horizontal 7.6 mm diameter test cylinders assembled with the ratio of the distance between each cylinder axis to the cylinder diameter, S/D, of 2 in liquid sodium was studied experimentally and theoretically. The heat transfer coefficients on the cylinder surface due to the same heat inputs ranging from 1.0×10^7 to 1.0×10^9 W/m^3 were obtained experimentally for various setting angles, γ, between vertical direction and the plane including both of these cylinder axis over the range of zero to 90 °. Theoretical equations for laminar natural convection heat transfer from the two horizontal cylinders were numerically solved for the same conditions as the experimental ones considering the temperature dependence of thermophysical properties concerned. The average Nusselt numbers, Nu, on the cylinders obtained experimentally were compared with the corresponding theoretical values on the Nu versus modified Rayleigh number, R_f, graph. The experimental values of Nu for the upper cylinder are about 20 % lower than those for the lower cylinder at $\gamma = 0°$ for the range of R_f tested here. The value of Nu for the upper cylinder becomes higher and approaches that for the lower cylinder with the increase in γ over range of 0 to 90°. The values of Nu for the lower cylinder at each γ are almost in agreement with those for a single cylinder. The theoretical values of Nu on two cylinders except those for $R_f < 4$ at $\gamma = 0°$ are in agreement with the experimental data at each γ with the deviations less than 15 %. Correlations for Nu on the upper and lower cylinders were obtained as functions of S/D and γ based on the theoretical solutions for the S/D ranged over 1.5 to 4.0.

1. INTRODUCTION

Study on the correlation for natural convection heat transfer from a horizontal rod bundle in liquid sodium is important as a database for the design of a heat exchanger in a fast breeder reactor in relation to decay heat removal at a loss of flow accident. Nevertheless, there is no reliable correlation even for two horizontal cylinders with various setting angle for gravitational direction and for the distance between the cylinders.

There have been many correlations on natural convection heat transfer from a horizontal cylinder in non-metallic and metallic liquids, and gases, presented theoretically and experimentally. The theoretical correlations such as the correlation by McAdams [1] for non-metallic liquids, and gases, and Kutateladze's correlation [2] for metallic liquids were based on boundary layer approximation; they were found to become inapplicable in the region of low Rayleigh numbers where thickness of thermal boundary layer is no longer negligible in comparison with the cylinder diameter in general. Several correlations [3, 4] were presented based on the experimental data corresponding to a wide range of Rayleigh numbers. Quite recently some of the authors [5] presented the generalized correlation based on the rigorous numerical solutions for a wide range of R_f: the correlation is briefly explained later.

There have been a few works on interactions between two or more horizontal cylinders in natural convection of air: Marsters [6] carried out a study of five horizontal cylinders in

a vertical array. They have found that for closely spaced arrays, individual tube Nusselt numbers are smaller than those for a single cylinder, and for wide spacings individual tube Nusselt numbers are higher than those for a single cylinder. Lieberman and Gebhard [7] have conducted the experiments for heated wires with the wire spacing ranging from 37.5 diameters to 225 diameters arranged in a plane array which could be oriented so that its plane made angles of 0°, 30°, 60° and 90° with the vertical.

The purpose of this paper is to study experimentally and theoretically on the correlation to predict the heat transfer from two same horizontal cylinders assembled with the ratio of the distance between each cylinder axis to the cylinder diameter, S/D of 2. The works dealt with are: (1) to obtain the experimental data of each natural convection heat transfer from two horizontal cylinders systematically for a wide range of heat input at the setting angles of the cylinders between the vertical direction and the plane including both of the cylinder axis over the range of zero to 90 °, (2) to obtain the numerical solutions of the average and local Nusselt numbers on two horizontal cylinders from a theoretical laminar natural convection equations for the same conditions as the experimental ones, (3) to compare experimental results with corresponding theoretical values to confirm the reliability of both results, and (4) to present a correlation to describe the effects of γ and S/D on natural convection heat transfer on each horizontal cylinder surface based on the theoretical solution.

2. EXPERIMENTAL APPARATUS

Experimental apparatus consists of a test vessel containing a test heater, a vapor condenser, an inert gas supply, a vacuum system, a sodium purification system and instrumentation. Explanations on major parts of the apparatus are as follows.

2.1 Test Vessel

The test vessel is shown schematically in Fig. 1. It is a cylindrical vessel of 30 cm in inner diameter and 70 cm in height containing liquid sodium of about 30 liter. Measuring device of the vertical temperature distribution in the liquid consisting of several K type thermocouples

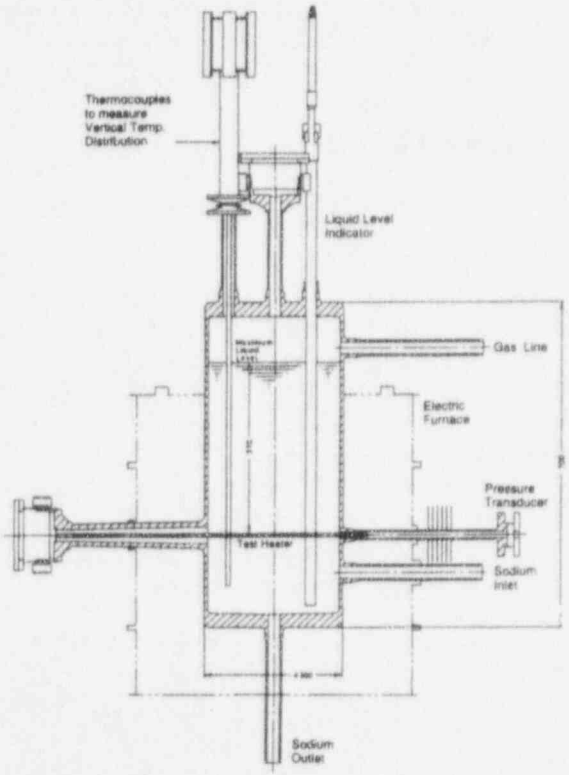

Fig.1 Schematic diagram of test vessel.

and one standard PR(13 %) thermocouple is mounted vertically by using a flange on the top of the vessel. Two test cylinders are mounted horizontally at the height of about 170 mm from the inner bottom of the vessel. Lower part of the vessel up to the height of 500 mm is in an electric furnace whose power is PID controlled to keep the liquid in the vessel at a desired temperature.

2.2 Test cylinders and heating system

The two test cylinders were assembled with the ratio, S/D, of 2 on a flange as shown in Fig. 2. Both test cylinders have the diameter of 7.6 mm and heated length of 50 mm. Each test cylinder is a nickel sheathed once-through current type with a spiral tantalum heating element one end of which is connected to an electrode with a potential tap, the other end being grounded to liquid sodium. Boron nitride is used as the electrical insulation material. Eight 0.5 mm diameter K type thermocouples are embedded in the grooves on each test cylinder surface, brazed and surface finished. The flange for these two horizontal cylinders can be rotated every 30°. The angle between the vertical direction and the plane including both of the cylinders axis plane is called in this work the setting angle γ: $\gamma = 0°$ means the location where the upper cylinder is just above the lower one, and $\gamma = 90°$ means that one is just beside the other. The thermocouple locations are shown in Fig. 3(a) to (d), for $\gamma = 0$, 30, 60, and 90°, respectively.

The heating current to each test cylinder is supplied by a power amplifier which can supply a direct current of up to 300 amperes at a power level of 10 kW. The input signal of the power amplifier is controlled by a digital computer so that the heat generation rate in the test cylinder agrees with a desired value. In this work, heat inputs to the two test cylinders are equally given.

2.3 Instrumentations

Signal voltages expressing the heating current and the terminal voltage of the test heater, heater surface temperatures and bulk liquid temperatures are sent to each insulated amplifier, and the amplified signals are led to a digital computer through AD converters. The heat flux,

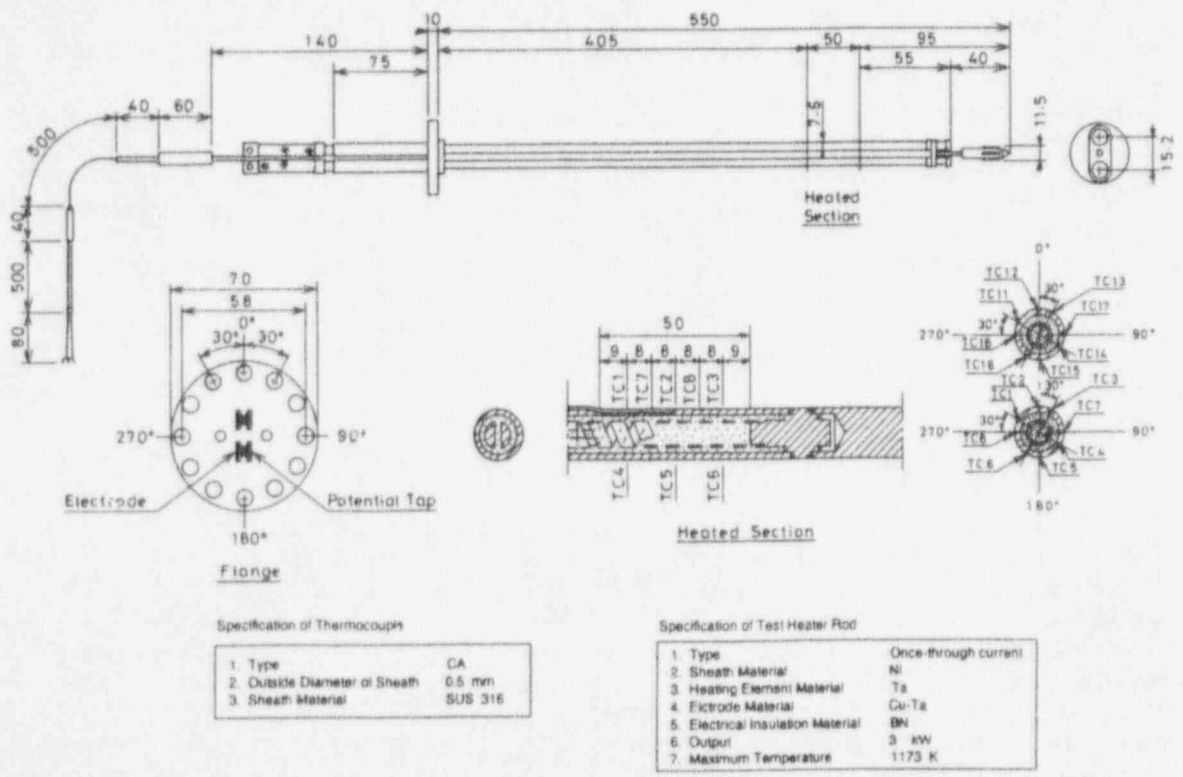

Specification of Thermocouple

1.	Type	CA
2.	Outside Diameter of Sheath	0.5 mm
3.	Sheath Material	SUS 316

Specification of Test Heater Rod

1.	Type	Once-through current
2.	Sheath Material	Ni
3.	Heating Element Material	Ta
4.	Electrode Material	Cu-Ta
5.	Electrical Insulation Material	BN
6.	Output	3 kW
7.	Maximum Temperature	1173 K

Fig.2 Schematic diagram of two horizontal cylinders assembled with S/D value of 2.

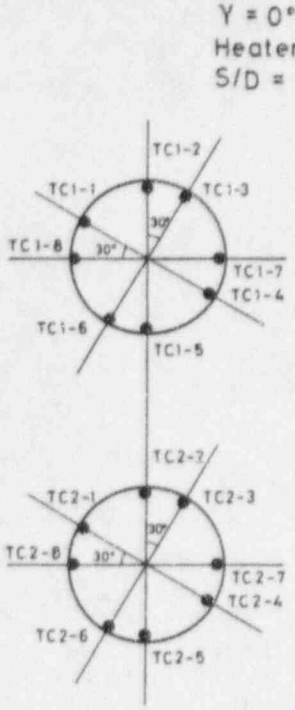

Fig.3(a) Thermocouple locations for $\gamma = 0°$.

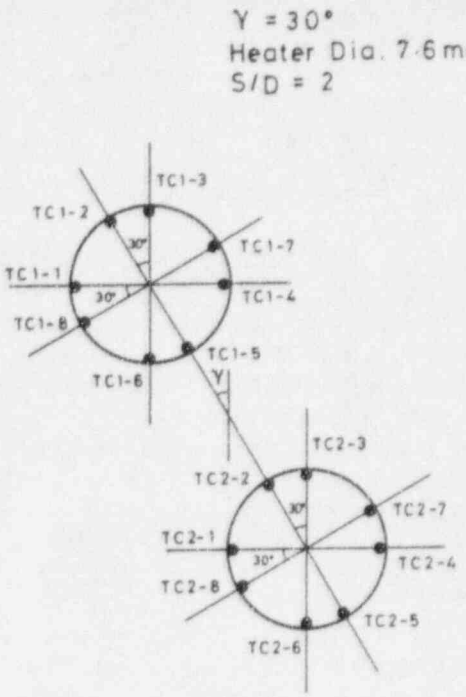

Fig.3(b) Thermocouple locations for $\gamma = 30°$.

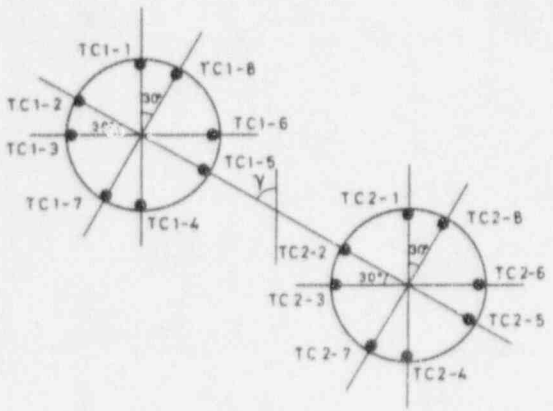

Fig.3(c) Thermocouple locations for $\gamma = 60°$.

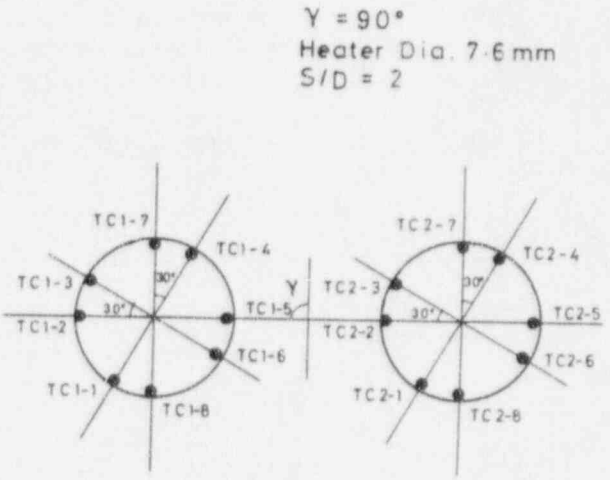

Fig.3(d) Thermocouple locations for $\gamma = 90°$.

q_i is calculated from the measured values of the heating current and the terminal voltage. The measured output voltage for each thermocouple is converted to temperature by using the voltage-temperature relation preliminary calibrated for each thermocouple. The heater wall temperature, T_w, was calculated from the measured temperature at 0.25 mm inner positions from the surface by solving the thermal conduction equation in the heater sheath supposing a uniform surface heat flux, q. Measurement error was estimated to be $\pm$ 1 % in the heat flux and $\pm$ 2 K in the heater wall temperature. The edge effect on natural convection heat transfer from both cylinders was estimated based on the numerical solution for 3-dimensional model to be about 5 % and 2 % for the upper and lower cylinders respectively at the outermost thermocouple locations of 9 mm from both ends of heated section, and negligibly small

at other thermocouple locations.

3. EXPERIMENTAL METHOD AND PROCEDURE

Experiments were performed as follows. After charging up liquid sodium to the test loop from the storage tank, sodium was purified to an oxide content of less than 5 ppm by circulating it through a cold trap at the temperature of 390 K for about 8 hours. Then, the circulation pump was shut off and liquid level in the test vessel was adjusted to about 300 mm above the horizontal test cylinders. Liquid temperature was raised and kept constant at 673 K by using the electric furnace. Pressure of Argon cover gas was kept constant at around atmospheric. After the system has reached a steady state with negligible vertical temperature distribution in the liquid, electric current to the test cylinders was gradually raised to a desired heat flux level. After reaching the steady state, measurements were made for 76 s with the time intervals of 0.1 s.

4. EXPERIMENTAL RESULTS AND DISCUSSION

4.1 The Correlation for Nu Previously Obtained for a Horizontal Cylinder

The generalized correlation of natural convection heat transfer from a horizontal cylinder based on rigorous numerical solutions for natural convection without the boundary layer approximation previously obtained by some of the authors [5] is firstly explained. The theoretical values of Nu for a wide range of Rayleigh numbers for Pr ranging from 0.005 to 10 were well expressed by a single curve on the Nu versus modified Rayleigh number $R_f[= Gr^* Pr^2/(4 + 9Pr^{1/2} + 10Pr)]$ graph. The following correlation for Nu was obtained to express the theoretical values as a function of R_f by least square fitting within ± 4 % error.

$$Nu = 10^z \tag{1}$$

where

$$\begin{aligned} z &= 0.193385 + 0.145037 \log R_f + 0.664323 \times 10^{-2} (\log R_f)^2 \\ &\quad -0.232432 \times 10^{-3} (\log R_f)^3 - 0.238613 \times 10^{-4} (\log R_f)^4 \end{aligned} \tag{2}$$

The correlation based on the theoretical values expressed the authors' experimental data on single horizontal cylinders of 7.6 and 10.7 mm in diameter in liquid sodium for a wide range of R_f within $\pm$ 10 % deviation and many conventional experimental data obtained by other workers on various diameter cylinders in various liquids and gases with Pr from 0.005 to 6.7, for R_f from about 10^{-8} to 10^6 within $\pm$ 20 % deviation.

The correlation was also compared [8] with existing correlations. The values by Churchil et al.'s correlation [3] are lower than those by Eq.(1) for $R_f > 10^{-4}$ with the maximum deviation of 20 %. The values by the correlation becomes far higher than that by Eq.(1) with decreasing R_f from 10^{-4}. It was confirmed that Churchil et al.'s correlation could not express generally the natural convection heat transfer from ingle horizontal cylinders with various diameters in various liquids and gases. The values predicted by Raithby and Hollands' correlation [4] are in good agreement with those by Eq.(1) in most of the R_f range. However, in the range $10^{-6.5} < R_f < 10^{-1.5}$, the values by their correlation are about 10 % higher than those predicted by Eq.(1) and in good agreement with the conventional experimental data in the range. It seems that the correlations based on experimental data have a possibility of containing the same order of errors as the experimental errors.

In this work, average heat transfer coefficients on two cylinders measured for a wide range of heat input and corresponding theoretical value are plotted to compare with each other on a Nu versus R_f graph.

Table 1 Experimental Conditions.

System Pressure	$85 \sim 94$ kPa
Upper Cylinder Diameter D	7.6 mm
Upper Cylinder Length	50 mm
Lower Cylinder Diameter D	7.6 mm
Lower Cylinder Length	50 mm
S/D (S=Distance between Cylinder Axis)	2
γ (Setting Angle)	0°, 30°, 60°, 90°
Liquid Temperature	673 K
Liquid Head	300 mm
Heat Flux q	$2 \times 10^4 \sim 2 \times 10^6$ W/m^2 $q_{UpperCylinder} = q_{LowerCylinder}$
$R_f(= Gr^* Pr^2/(4 + 9Pr^{1/2} + 10Pr))$	$0.1 \sim 14$

Table 2 Parameters for Calculation.

System Pressure	101.3 kPa			
Upper Cylinder Diameter D	7.6 mm			
Lower Cylinder Diameter D	7.6 mm			
S/D (S=Distance between Cylinder Axis)	1.5, 2, 3, 4, 5			
γ (Setting Angle)	0°, 10°, 30°, 60°, 90°			
Liquid Temperature	673 K			
Heat Flux q	1×10^4, 7×10^5,	2×10^4, 1×10^6,	7×10^4, 2×10^6 W/m^2	2×10^5,
Gr^*	1.20×10^4, 9.33×10^5,	2.41×10^4, 1.38×10^6,	8.54×10^4, 3.06×10^6	2.49×10^5,
$Ra^*(= Gr^* Pr)$	5.98×10, 4.50×10^3,	1.20×10^2, 6.59×10^3,	4.24×10^2, 1.42×10^4	1.23×10^3,
$R_f(= Gr^* Pr^2/(4 + 9Pr^{1/2} + 10Pr))$	0.0637, 4.60,	0.128, 6.65,	0.448, 13.8	1.29,

4.2 Experimental results for upper and lower cylinders at each setting angle

Natural convection heat transfer coefficients on two horizontal 7.6 mm-diameter cylinders at the same heat input were measured. Experimental conditions are tabulated in Table 1.

The experimental results for the two cylinders are compared with the rigorous solutions for the theoretical model of laminar natural convection heat transfer from two horizontal cylinders with a uniform heat flux obtained for the same conditions as the experimental ones considering the temperature dependence of thermophysical properties by using a commercial CFD cord PHOENICS [9]. Outline of the theoretical equations and calculation method are shown in APPENDIX 1. Table 2 shows the parameters used for the calculation.

In case of the setting angle $\gamma = 0°$: Experimental results of average heat transfer coeffi-

cients in case of $\gamma = 0°$ (upper cylinder is just above the lower one) are plotted on Nu vs. R_f graph in Fig. 4. Open circles show the results for the lower cylinder and open triangles show those for the upper cylinder. As can be seen in the figure, the value of Nu for the upper cylinder at each R_f is about 20 % lower than that for the lower cylinder. The Nu values for single cylinders predicted by Eq.(1) are shown in the figure as a solid curve for comparison. The experimental results of Nu for the lower cylinder are almost in agreement with the curve for whole range of R_f tested here. Numerical solutions of Nu for the lower and upper cylinders are also shown in the figure as solid circles and solid triangles, respectively. The numerical solution for the lower cylinder is from about 8 % to 17 % lower than the experimental one. The solution for the upper cylinder is about 15 % lower than the experimental one for $R_f \geq 4$; the difference becomes larger with the decrease in R_f from 4.

Figure 5 shows the peripheral distribution of local Nusselt numbers, Nu_θ, on the upper and lower cylinders for the data shown in Fig. 4 at $R_f = 6.9$ ($q = 1.0 \times 10^6$ W/m^2) in comparison with the numerical solutions of Nu_θ for a single cylinder. The Nu_θ is the value at the angle θ from the bottom ($\theta = 0°$ at the bottom). The data for the lower and upper cylinders are shown as solid circles and solid triangles, respectively with the fluctuation range. Considering the symmetry of the phenomena in case of $\gamma = 0°$, measured values on the left hand side are plotted at a corresponding angle on the positive θ region. As can be seen in the figure, Nu_θ data for the lower cylinder almost agree with the values for a single cylinder. On the contrary, Nu_θ data for the lower part of the upper cylinder($\theta \leq 90°$) are affected by the thermal boundary layer of the lower cylinder: they become lower than those for the lower cylinder and single cylinder with the decrease in θ from around 90°. The Nu_θ at $\theta = 0°$ is about 63 % of that for the lower cylinder. Numerical solutions of the Nu_θ for the lower and upper cylinders at $R_f = 6.9$ are also shown as open circles and open triangles, respectively, in the figure. The theoretical Nu_θ for the lower cylinder are almost in agreement with the corresponding experimental data and with the curve for the single cylinder. However, those for the upper cylinder are about 15 % lower than the corresponding experimental data for all the θ range. That causes the theoretical Nu values about 15 % lower than the corresponding

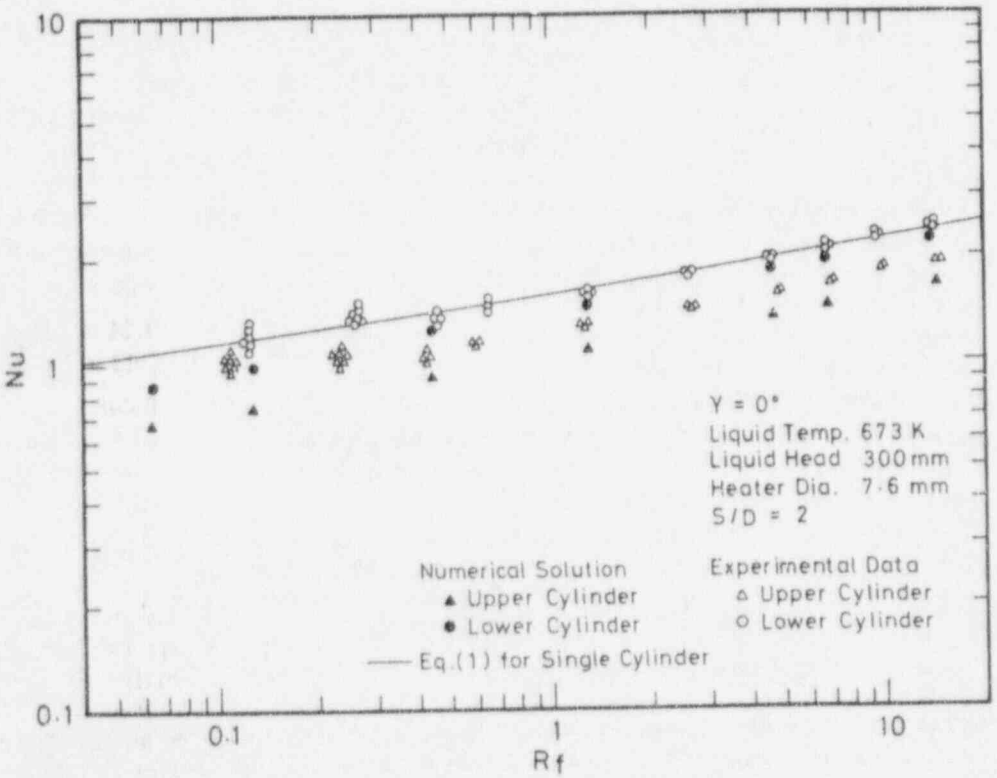

Fig.4 Experimental data of Nu for lower and upper cylinders at $\gamma = 0°$ compared with the theoretical solutions.

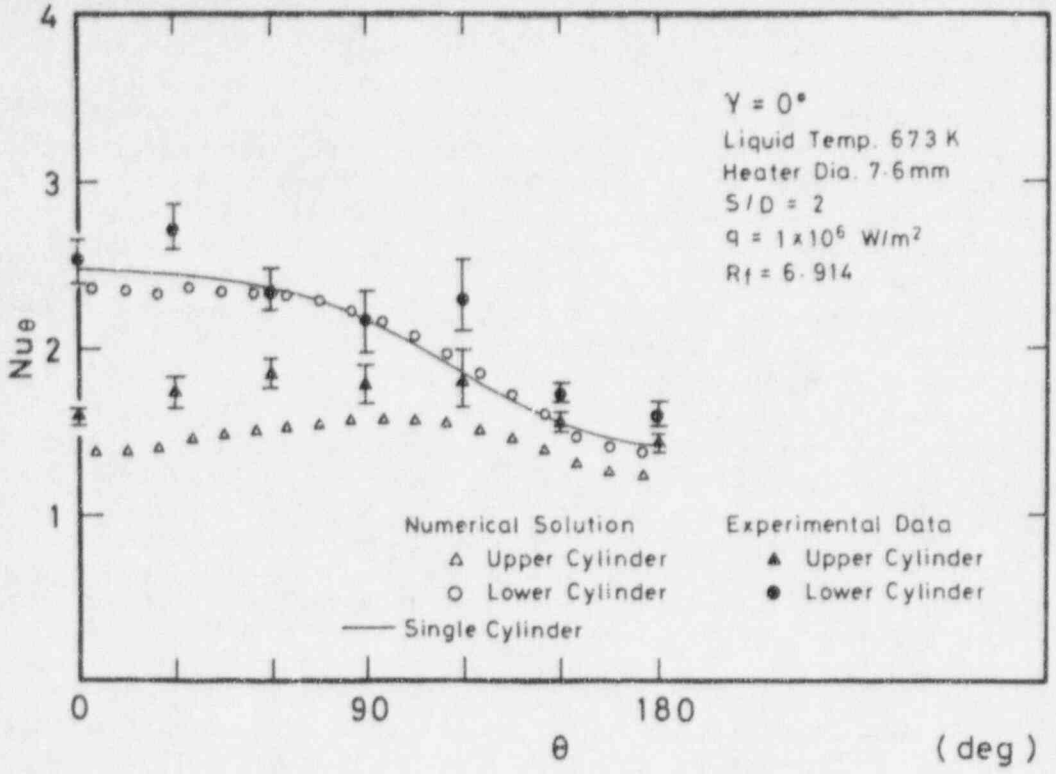

Fig.5 Comparison of Nu_θ data for $\gamma = 0°$ with the theoretical solutions.

experimental data as mentioned above. This may be due to some error in the setting angle γ because of the thermal deformation in the test cylinders.

In case of the setting angle $\gamma = 30°$: Average heat transfer coefficients in case of $\gamma = 30°$ are shown in Fig. 6. The Nu values for the upper cylinder are about 20 % lower than those for the lower cylinder for the R_f lower than 1.3. They approach the latter values with the R_f becoming higher than 1.3, and finally arrive at the value about 14 % lower than the latter values at $R_f = 14$.

Numerical solutions of the Nu for the lower and upper cylinders are also shown in the figure for comparison. The solutions for the lower and upper cylinders are about 10 % lower than the average of the corresponding experimental data.

Figure 7 shows the typical distribution of Nu_θ on the upper and lower cylinders for the data shown in Fig. 6 at $R_f = 6.7$. As can be seen in the figure, Nu_θ data for the lower cylinder almost agree with the values for a single cylinder, although the data are somewhat scattered. On the contrary, Nu_θ data for the upper cylinder in the positive θ region (right hand side of the cylinder facing the lower cylinder) are lower than those for the lower cylinder and single cylinder being affected by the thermal boundary layer of the lower cylinder. Numerical solutions of Nu_θ for the lower and upper cylinders at $R_f = 6.7$ are shown as open circles and open triangles, respectively, in the figure. As shown in the figure, the solutions for the lower and upper cylinders are almost in agreement with the corresponding experimental data.

In case of the setting angle $\gamma = 60°$: The data of Nu in case of $\gamma = 60°$ are shown in Fig. 8. The Nu values for the upper cylinder are about 14 % lower than those for the lower cylinder. The theoretical solutions of Nu for the lower and upper cylinders are also shown in the figure for comparison. The solutions for the lower cylinder almost agree with the corresponding experimental data, and those for the upper cylinder are about 6 % higher than the average of corresponding experimental data.

Figure 9 shows the distribution of Nu_θ on the upper and lower cylinders for the data shown in Fig. 8 at $R_f = 6.7$. As seen from the figure, Nu_θ data for the lower cylinder agree with the value for a single cylinder at θ around 0°, and they become higher and lower

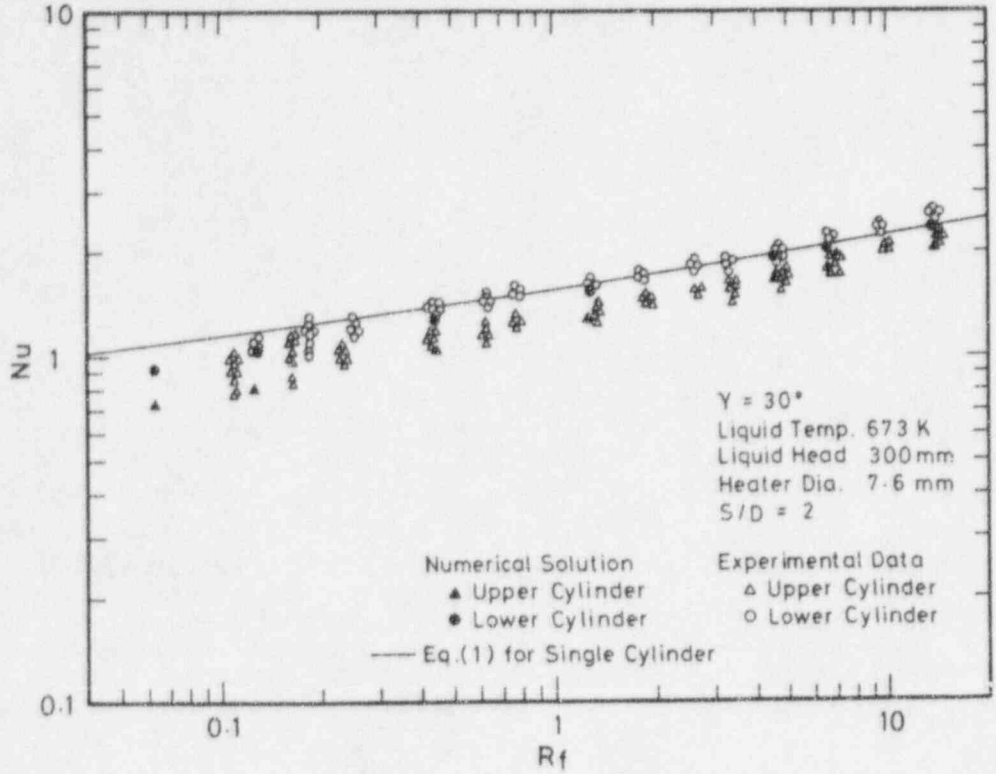

Fig.6 Experimental data of Nu for lower and upper cylinders at $\gamma = 30°$ compared with the theoretical solutions.

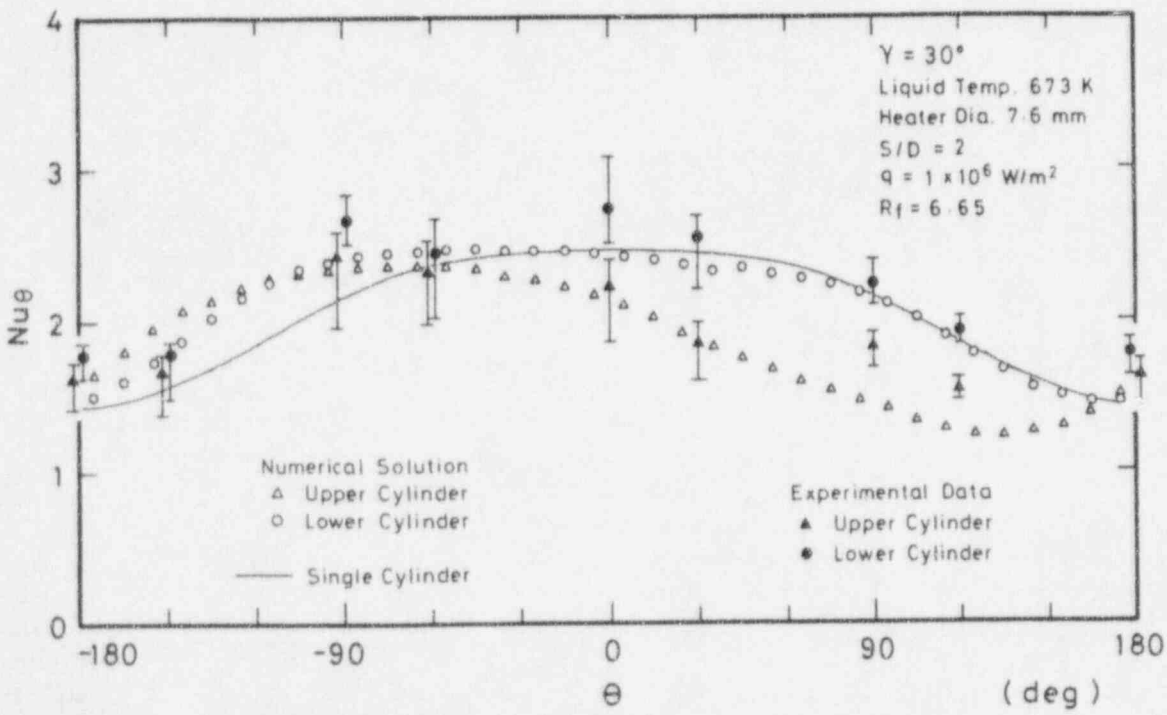

Fig.7 Comparison of Nu_θ data for $\gamma = 30°$ with the theoretical solutions.

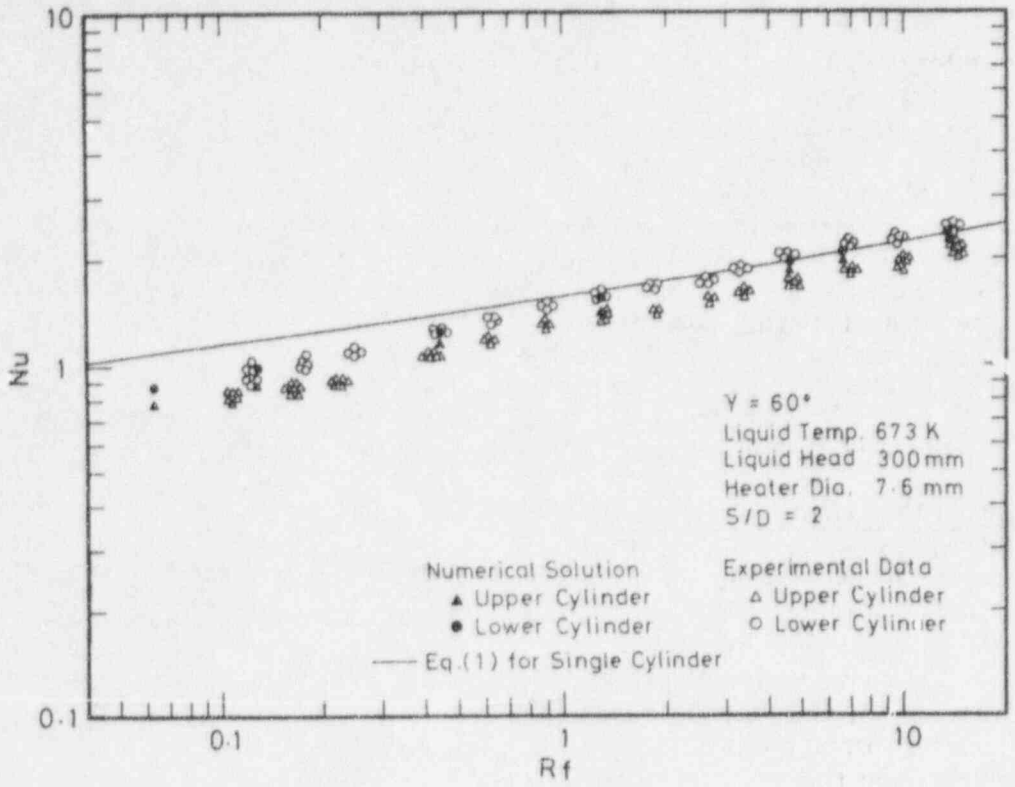

Fig.8 Experimental data of Nu for lower and upper cylinders at $\gamma = 60°$ compared with the theoretical solutions.

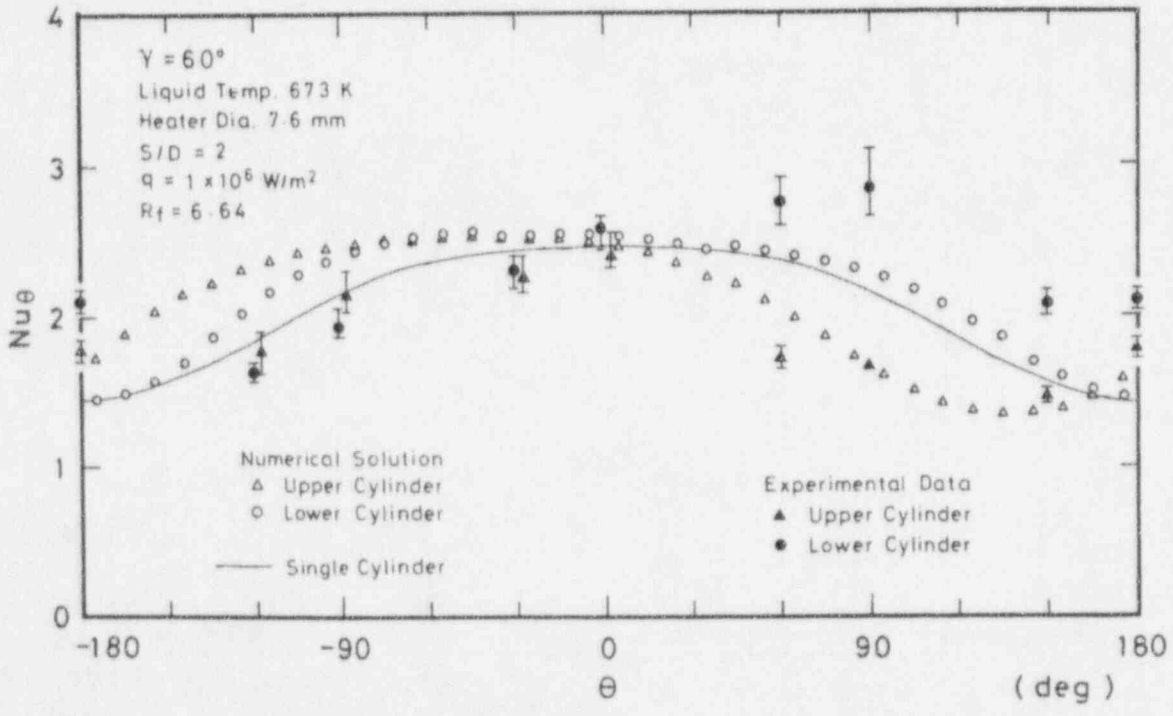

Fig.9 Comparison of Nu_θ data for $\gamma = 60°$ with the theoretical solutions.

than the corresponding values for a single cylinder with increasing and decreasing θ from the value, respectively. Namely, the heat transfer in the left side of the lower cylinder facing the upper cylinder is disturbed and that in the opposite side is enhanced by the upper cylinder. On the other hand, Nu_θ in the positive θ region of the upper cylinder (right side of the cylinder facing the lower cylinder) are lower than those for the lower cylinder, although the data in the negative θ region are almost in agreement with those for a single cylinder. The theoretical solutions of Nu_θ for the lower and upper cylinders at $R_f = 6.7$ are shown in Fig. 9. In comparison with the experimental data, the solutions of Nu_θ for the lower cylinder agree with the experimental data at $\theta = 0°$ but they are higher and lower than the experimental data in the negative and positive range of θ, respectively. These differences compensate with each other and the theoretical Nu values for the lower cylinders are almost in agreement with the experimental data as mentioned above. The solutions of Nu_θ for the upper cylinder almost agree with the experimental data in the positive θ range but they are 11 % at $\theta = -30°$, 15 % at $\theta = -90°$ and 32 % at $\theta = -120°$ higher than the experimental data in the negative θ range. These differences causes the Nu higher than the experimental data.

In case of the setting angle $\gamma = 90°$: The data of Nu in case of $\gamma = 90°$ (one cylinder is just beside the other) are shown in Fig. 10. As the peripheral distribution of local surface temperatures on one cylinder is almost symmetrical to that on the other cylinder, Nu are obtained based on the measured local surface temperatures on both cylinders. The Nu value at $R_f = 0.1$ is about 26 % lower than the curve for a single cylinder; it increases and gradually approaches the curve with the increase in R_f and almost agrees with the curve for $R_f \geq 5$. It should be noted that, in the cases of $\gamma = 60°$ and $90°$, Nu for both cylinders become lower than the corresponding values for a single cylinder in the lower R_f range due to the mutual effect. On the contrary, in the cases of $\gamma = 0°$ and $30°$, Nu for the lower cylinder almost agree with those for a single cylinder, and only the heat transfer from upper cylinder is disturbed by the mutual effect. The theoretical solutions of Nu are also shown in Fig. 10 for comparison. They are in agreement with the corresponding experimental data within the scattering range.

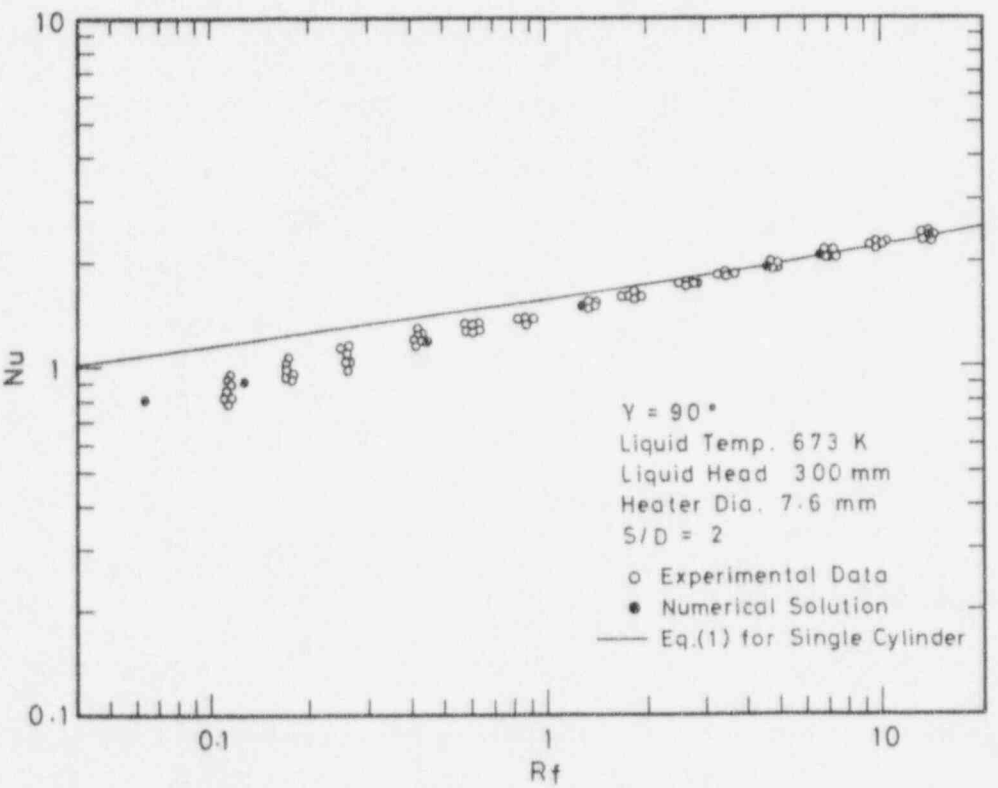

Fig.10 Experimental data of Nu for lower and upper cylinders at $\gamma = 90°$ compared with the theoretical solutions.

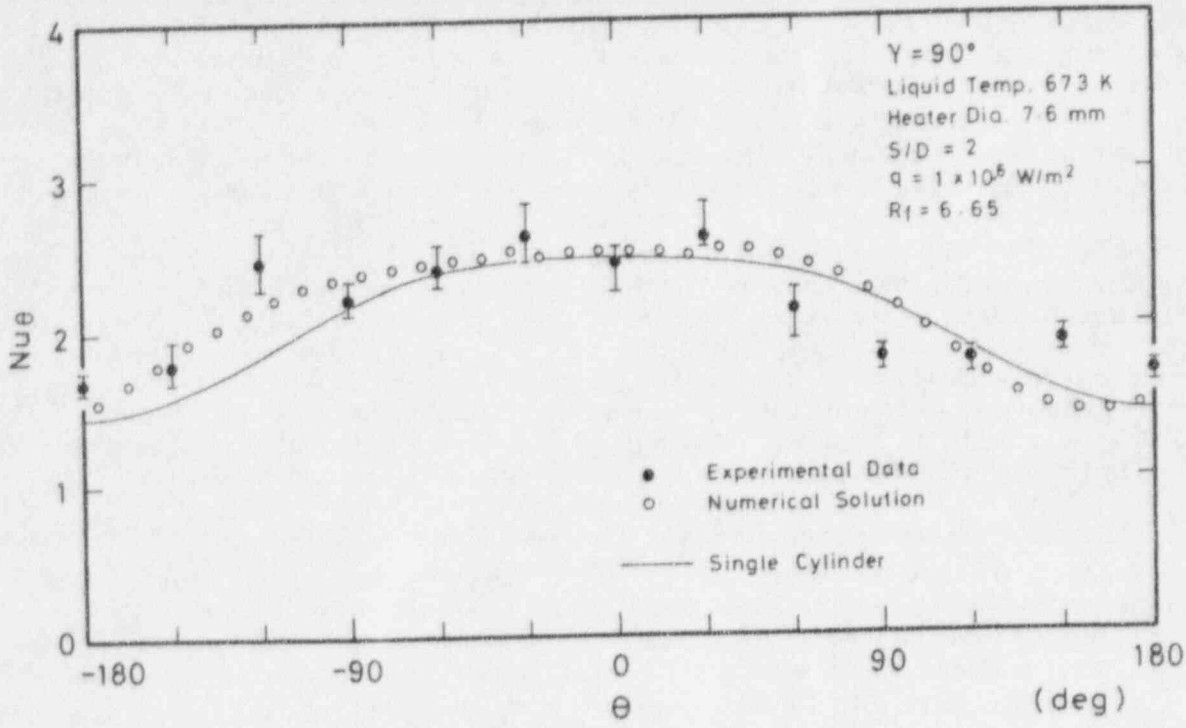

Fig.11 Comparison of Nu_θ data for $\gamma = 90°$ with the theoretical solutions.

Figure 11 shows the typical distribution of Nu_θ on the left side cylinder (which is the upper cylinder for $\gamma < 90°$) for the data shown in Fig. 10 at $R_f = 6.7$. As the peripheral distribution of heat transfer coefficients on one cylinder is almost symmetrical to that for the other cylinder, Nu_θ data on the right side cylinder are also plotted in the figure at the corresponding θ. Though the Nu_θ data in the negative and positive θ range are slightly higher and lower than the values for a single cylinder, respectively, they are almost in agreement with those for a single cylinder. The theoretical solutions of Nu_θ at $R_f = 6.7$ are shown in Fig. 11. The solution almost describes the angular distribution of the Nu_θ.

4.3 Correlation of natural convection heat transfer on two horizontal cylinders

The numerical solutions agreed with the Nu data except those for $R_f < 4$ at $\gamma = 0°$ within 15 % difference. The effect of S/D on natural convection heat transfer from each of the two horizontal cylinders was estimated based on the numerical solutions of the above mentioned theoretical model. The calculations were made for the S/D of 1.5, 2.0, 3.0 and 4.0 at the γ of 0°, 30°, 60° and 90° for R_f ranging from 0.064 to 13.8. The ratios of the calculated Nu values to those for a single cylinder given by Eq.(1) at the same condition, Nu/Nu_{sc}, are shown versus γ with S/D as a parameter in Figs. 12(a), 12(b) and 12(c) for the R_f values of 0.448, 4.6 and 13.8, respectively. The open symbols show the values for the lower cylinder and the solid symbols show those for the upper cylinder. As can be seen in these figures, the values of Nu/Nu_{sc} for the upper cylinder are lower for the lower values of S/D, γ and R_f. The values of Nu/Nu_{sc} for the lower cylinder show nearly the same trend of dependence on S/D, γ and R_f, although they are far higher than the corresponding values for the upper cylinder.

The calculated values of Nu/Nu_{sc} for the upper and lower cylinders are approximately expressed by the following correlations.
For the upper cylinder:

$$Nu/Nu_{sc} = 1 - 0.60\exp[-A\ R_f^m\ (S/D)] \tag{3}$$

where $A = 0.29 + 6.8 \times 10^{-3}\gamma$, $m = 0.12 + 1.67 \times 10^{-3}\gamma$

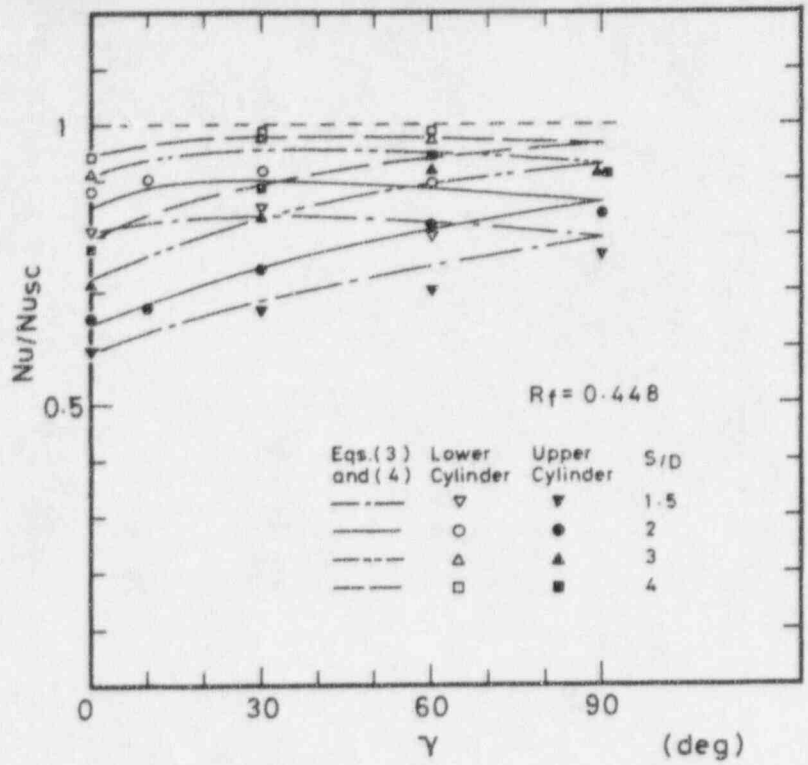

Fig.12(a) Nu/Nu_{sc} versus γ for upper and lower cylinders with S/D as a parameter at $R_f = 0.448$.

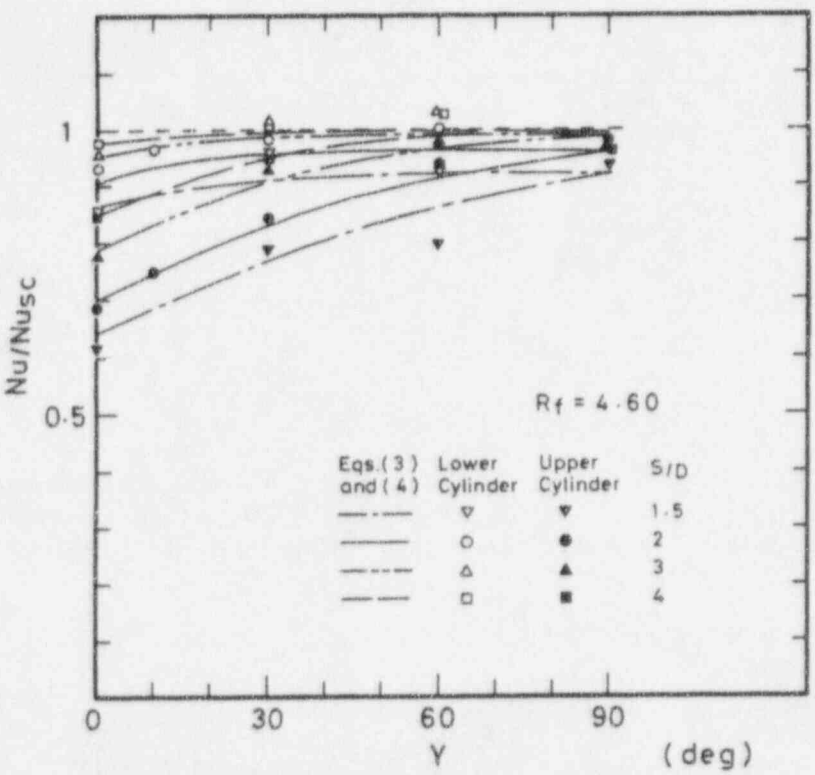

Fig.12(b) Nu/Nu_{sc} versus γ for upper and lower cylinders with S/D as a parameter at $R_f = 4.6$.

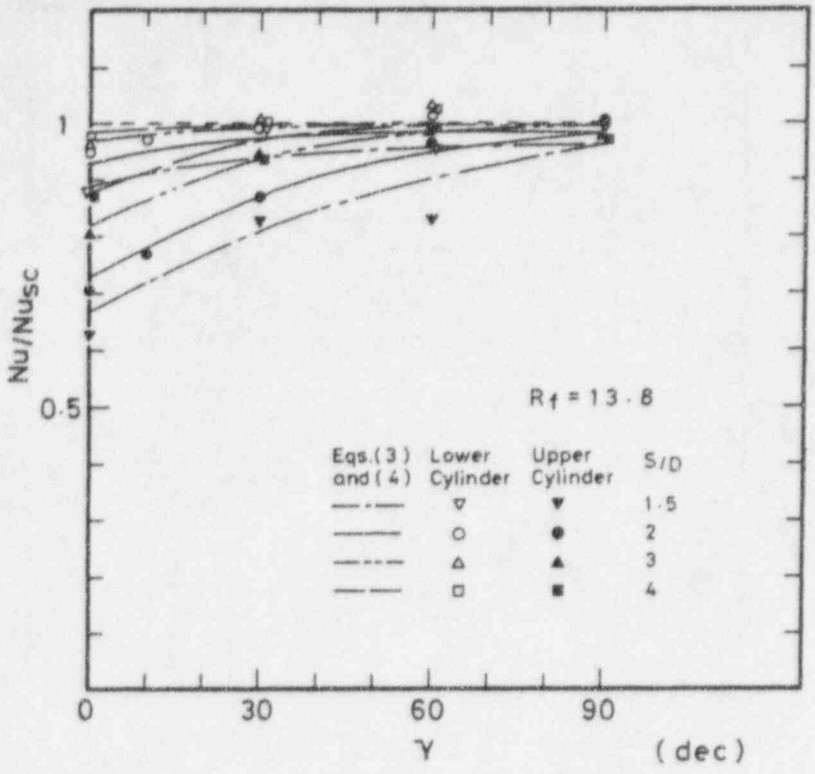

Fig.12(c) Nu/Nu_{sc} versus γ for upper and lower cylinders with S/D as a parameter at $R_f = 13.8$.

For the lower cylinder:

$$Nu/Nu_{sc} = 1 - C\exp[-K\ R_f^n\ (S/D)] \tag{4}$$

where

$$C = 0.4 + 2.2 \times 10^{-3}\gamma,$$

$$K = 0.56 + 0.34(S/D)\sin\gamma \qquad 0 \le \gamma \le \arcsin(D/S)$$

$$= 0.9 \qquad \gamma > \arcsin(D/S)$$

$$n = 0.16 + 1.2 \times 10^{-3}\gamma$$

The curves of Nu/Nu_{sc} derived from these correlations are shown in Figs. 12(a) to (c) for comparison. They are in agreement with the numerical solutions for the upper and lower cylinders within -5 and +9 % error. The correlations for two cylinders including the effect of S/D and γ for liquid sodium were obtained. The detailed study on extended correlations for multicylinders based on these correlations will appear elsewhere in the near future.

5. SUMMARY AND CONCLUSIONS

Experimental data of natural convection heat transfer on two horizontal cylinders for the same heat inputs were obtained systematically for a wide range of modified Rayleigh number R_f at the setting angles of the cylinders, γ, over the range of 0° to 90°.

The data of average Nusselt number, Nu, for the upper cylinder are about 20 % lower than those for the lower cylinder at $\gamma = 0°$. The values of Nu for the upper cylinder become higher and approach those for the lower cylinder with the increase in γ to 90° where they

agree with each other. The data of local Nusselt number, Nu_θ, were also analyzed to see the mutual interaction in more detail.

The Nu and Nu_θ values on two horizontal cylinders were obtained from a theoretical laminar natural convection equations for the same conditions as the experimental ones.

The experimental data of Nu for each cylinder except those for $R_f < 4$ at $\gamma = 0°$ were in agreement with the corresponding theoretical ones within ± 15 % difference, although differences larger than this value were sometimes obtained in Nu_θ.

Theoretical solutions of Nu for two cylinders with the S/D values ranging from 1.5 to 4 were obtained for the various angles of γ.

Correlations for Nu for the cylinders were obtained as functions of S/D and γ based on the theoretical numerical solutions. These correlations are useful to understand the natural convection on multicylinders in the liquid.

NOMENCLATURE

A = non-dimensional quantity in Eq.(3)
C = non-dimensional quantity in Eq.(4)
D = cylinder diameter, m
Gr^* = $g\beta q D^4/\lambda\nu^2$, Grashof number for constant heat flux
g = acceleration of gravity, m/s^2
K = non-dimensional quantity in Eq.(4)
m = exponent in Eq.(3)
Nu = average Nusselt number
Nu_{sc} = average Nusselt number for single cylinder
Nu_θ = local Nusselt number at the position specified by the angle at the circumference
n = exponent in Eq.(4)
Pr = Prandtl number
q = heat flux, W/m^2
Ra^* = $Gr^* Pr$, Rayleigh number for constant heat flux
R_f = $Gr^* Pr^2/(4 + 9Pr^{1/2} + 10Pr)$, modified Rayleigh number
S = distance between the center axis of two parallel horizontal cylinders, m
β = volumetric expansion coefficient, K^{-1}
γ = setting angle of the two horizontal cylinders, deg
θ = peripheral angle from the bottom of the cylinder, deg
λ = thermal conductivity, W/(m K)
ν = kinematic viscosity, m^2/s

REFERENCES

[1] W.H. McAdams, Heat Transmission, 3rd ed., McGraw Hill, New York, p.176 (1954).
[2] S.S. Kutateladze et al., Zhidkometallitsheskye Teplonositeli, Atomizdat, Moscow (1958).

[3] S.W. Churchil and H.H.S. Chu, "Correlating Equations for Laminar and Turbulent Free Convection from a Horizontal Cylinder," Int. J. Heat Mass Transfer, 18, 1049-1053 (1975).
[4] G.D. Raithby and K.G.T. Hollands, Natural Convection, Handbook of Heat Transfer Fundamentals, W.M. Rohsenow et al., ed. MacGraw Hill, New York, pp.6-1 - 6-94 (1985).
[5] Y. Takeuchi, K. Hata, M. Shiotsu and A. Sakurai, "A General Correlation for Natural Convection Heat Transfer from Horizontal Cylinders in Liquids and Gases," General Papers in Heat Transfer, ASME Publication HTD-Vol.204, 183-189 (1992).
[6] G.F. Marsters, "Arrays of Heated Horizontal Cylinders in Natural Convection," Int. J. Heat Mass Transfer, 15, 921-933 (1972).
[7] J. Lieberman and B. Gebhard, "Interactions in Natural Convection from an Array of Heated Elements, Experimental," Int. J. Heat Mass Transfer, 12, 1385-1396 (1969).
[8] Y. Takeuchi, K. Hata, M. Shiotsu, and A. Sakurai, "A General Correlation for Natural Convection Heat Transfer from Horizontal Cylinders in Liquids and Gases," (in Japanese), Proc. of 71st JSME Fall Annual Meeting, Vol.D, 4-6 (1993).
[9] D.B. Spalding, The PHOENICS Beginner's Guide, Pub. by CHAM, UK (1991).
[10] S.V. Patankar, Numerical Heat Transfer and Fluid Flow, Hemisphere, New York (1980).

APPENDIX 1

THEORETICAL SOLUTION OF LAMINAR NATURAL CONVECTION EQUATIONS

A.1 Fundamental Equations

The unsteady laminar two dimensional basic equations in boundary fitted coordinates as shown in Figs. 13(a),(b) for $\gamma = 0°$, and 14(a),(b) for $\gamma = 30°$ are described as follows.

(Continuity Equation)

$$\frac{\partial \rho}{\partial t} + \frac{\partial}{\partial x}(\rho u) + \frac{\partial}{\partial z}(\rho w) = 0 \tag{5}$$

(Momentum Equation)

$$\frac{\partial}{\partial t}(\rho u) + \frac{\partial}{\partial x}(\rho u u) + \frac{\partial}{\partial z}(\rho w u) = -\frac{\partial P}{\partial x} + \frac{\partial}{\partial x}\tau_{xx} + \frac{\partial}{\partial z}\tau_{xz} \tag{6}$$

$$\frac{\partial}{\partial t}(\rho w) + \frac{\partial}{\partial x}(\rho u w) + \frac{\partial}{\partial z}(\rho w w) = -\frac{\partial P}{\partial z} + \frac{\partial}{\partial x}\tau_{xz} + \frac{\partial}{\partial z}\tau_{zz} - \rho g \tag{7}$$

(Energy Equation)

$$\frac{\partial}{\partial t}(\rho c_p T) + \frac{\partial}{\partial x}(\rho c_p u T) + \frac{\partial}{\partial z}(\rho c_p w T) = \frac{\partial}{\partial x}\{\frac{\lambda}{c_p}\frac{\partial}{\partial x}(c_p T)\} + \frac{\partial}{\partial z}\{\frac{\lambda}{c_p}\frac{\partial}{\partial z}(c_p T)\} \tag{8}$$

where

$$\tau_{xx} = 2\rho\nu\frac{\partial u}{\partial x}, \quad \tau_{zz} = 2\rho\nu\frac{\partial w}{\partial z}, \quad \tau_{xz} = \tau_{zx} = \rho\nu(\frac{\partial u}{\partial z} + \frac{\partial w}{\partial x}) \tag{9}$$

u, w are the x, z components of a velocity vector, respectively.
The control volume discretization equations were derived from these equations by using the hybrid scheme [10]. The thermophysical properties for each control volume are given as those at each volume temperature. The equations are numerically analyzed together with the following boundary conditions.

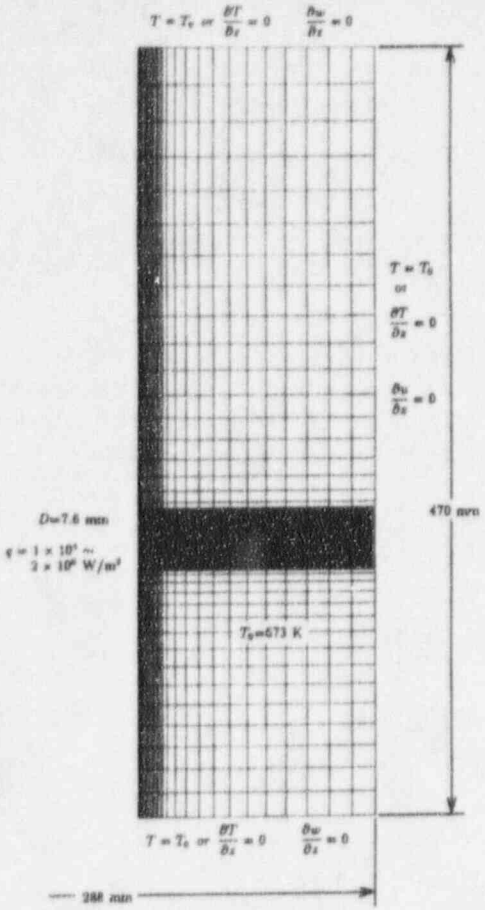

Fig.13(a) Boundary fitted coordinates for $\gamma = 0°$.

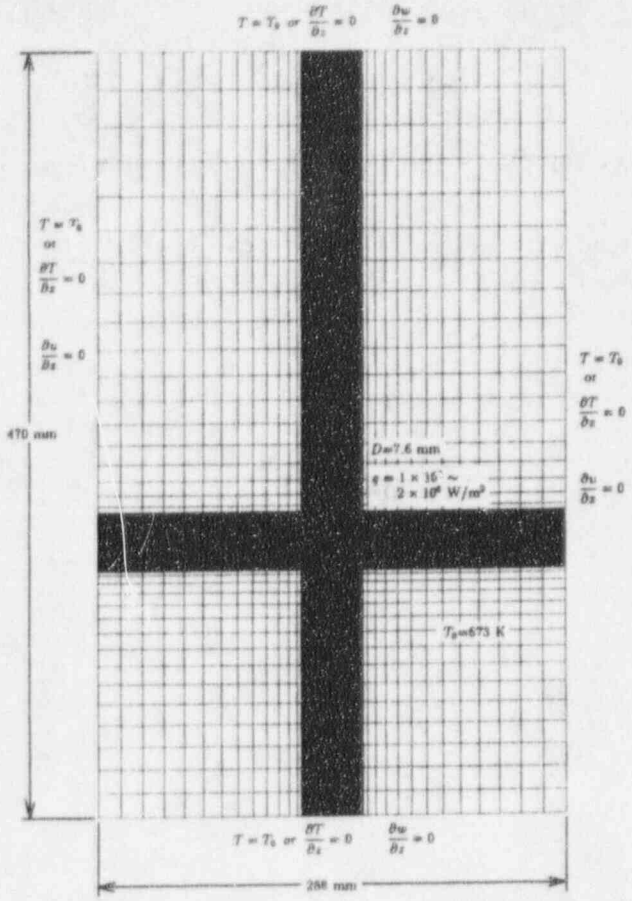

Fig.14(a) Boundary fitted coordinates for $\gamma = 30°$.

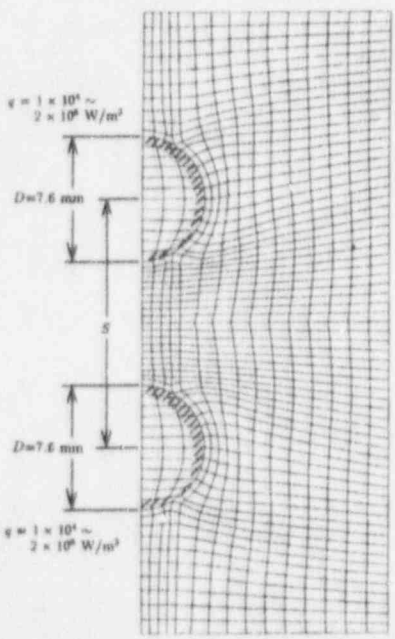

Fig.13(b) Details of Boundary fitted coordinates for $\gamma = 0°$.

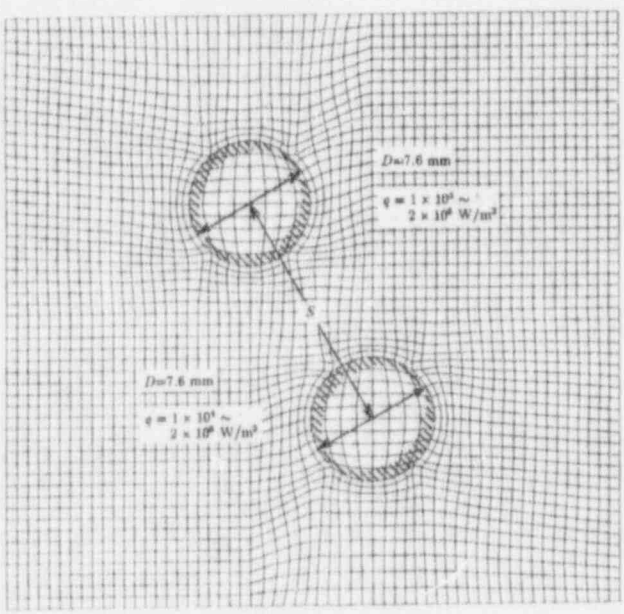

Fig.14(b) Details of Boundary fitted coordinates for $\gamma = 30°$.

On the surfaces of cylinders: constant heat flux, and non-slip condition.

At the left and right outer boundary: $T = T_0$, $\frac{\partial u}{\partial x} = 0$ (for in-flow)
$\frac{\partial T}{\partial x} = 0$, $\frac{\partial u}{\partial x} = 0$ (for out-flow)
At the lower and upper boundary: $T = T_0$, $\frac{\partial w}{\partial z} = 0$ (for in-flow)
$\frac{\partial T}{\partial z} = 0$, $\frac{\partial w}{\partial z} = 0$ (for out-flow)

where T_0 is a bulk liquid temperature. The procedure for the calculation of the flow field is the SIMPLE algorithm which stands for Semi-Implicit Method for Pressure-Linked Equations.

Stepwise increase in surface heat flux was considered as an initial condition, and numerical calculation was continued until the steady-state was obtained. Table 2 shows the parameters used for the calculation. Average heat transfer coefficient on the cylinder surface was obtained by averaging the calculated local temperatures at every 10° in θ. All the calculations were made by using the PHOENICS code [9].

EVALUATION OF WRAPPER TUBE TEMPERATURES OF FAST NEUTRON REACTORS USING THE TRANSCOEUR-2 CODE

B. VALENTIN
CEA/DRN/DEC/SECA/LHC CEN Cadarache bat. 219
13108 St Paul Lez Durance Cedex, France

G. CHAIGNE
FRAMATOME/NOVATOME 12 rue Juliette Récamier
69000 Lyon, France

P. BRUN
CEA/DRN/DEC/SECA/LHC CEN Cadarache bat. 219
13108 St Paul Lez Durance Cedex, France

Abstract This paper deals with the thermal loading estimation of wrapper tubes using the TRANSCOEUR-2 code. This estimation requires a knowledge of two temperature fields: the first involves the peripheral sub-channel temperatures of each sub-assembly calculated by the design code CADET, and the second, outside the sub-assemblies, is the inter-wrapper flow temperature field calculated by the thermal-hydraulic code TRIO-VF with boundary conditions taken from CADET. Theoretical models of the three codes are presented as well as the first TRANSCOEUR-2 wrapper tube temperature calculation performed on the European Fast Reactor (EFR) Core Design 6/91 (CD 6/91) under nominal power conditions. The results show a temperature variation of 115°C between the bottom of the lower blanket and the top of the upper blanket fuel sub-assemblies in the center of the core and 95°C at the core periphery.The wrapper tube temperatures are higher in the center than in the external core.

1. INTRODUCTION

For safety reasons, the mechanical behavior of sub-assemblies must be known in order to attain two main objectives : verification of the stress level on each wrapper tube when the reactor is in operation, and the wrapper strain involving the impossibility of unloading the sub-assemblies after the reactor trip. These objectives require a knowledge of the irradiation conditions of the sub-assembly (neutronic studies) and the thermal loading estimation of wrapper tubes (thermal-hydraulic studies).

These thermal-hydraulic studies may be done through calculations. They require evaluation of two temperature fields : the first one inside each sub-assembly is calculated by the CADET code, the second outside the sub-assemblies is the inter-wrapper flow temperature computed by TRIO-VF with boundary conditions taken from CADET.

A new code, entitled TRANSCOEUR-2 has been developed to produce the data of the two preceding thermal-hydraulic codes, to manage their interfaces, to process the two temperature fields and to calculate wrapper tube temperatures with them. After the presentation of each code modeling (CADET, TRIO-VF, TRANSCOEUR-2), this paper concludes with the first application of the TRANSCOEUR-2 code on the European Fast Reactor (EFR) Core Design 6/91 (CD 6/91) under nominal power.

2. GENERAL THERMAL-HYDRAULIC PRESENTATION

2.1 Simplified hydraulic description of the core

The sodium flow goes into the core from the diagrid. The major part is distributed among all the sub-assemblies according to their particular pressure drop. The flow runs from the bottom to the top. At the core outlet , one part of the flowrate is submitted to an over-pressure profile due to the Above Core Structure (ACS), inducing an upper inter-wrapper flow going down into the core center and ascending at the periphery (fig. 1). Another contribution of the inter-wrapper flowrate comes from a leak located at the sphere-cone bearing level at the bottom of the hexagonal wrapper tubes (fig. 1).

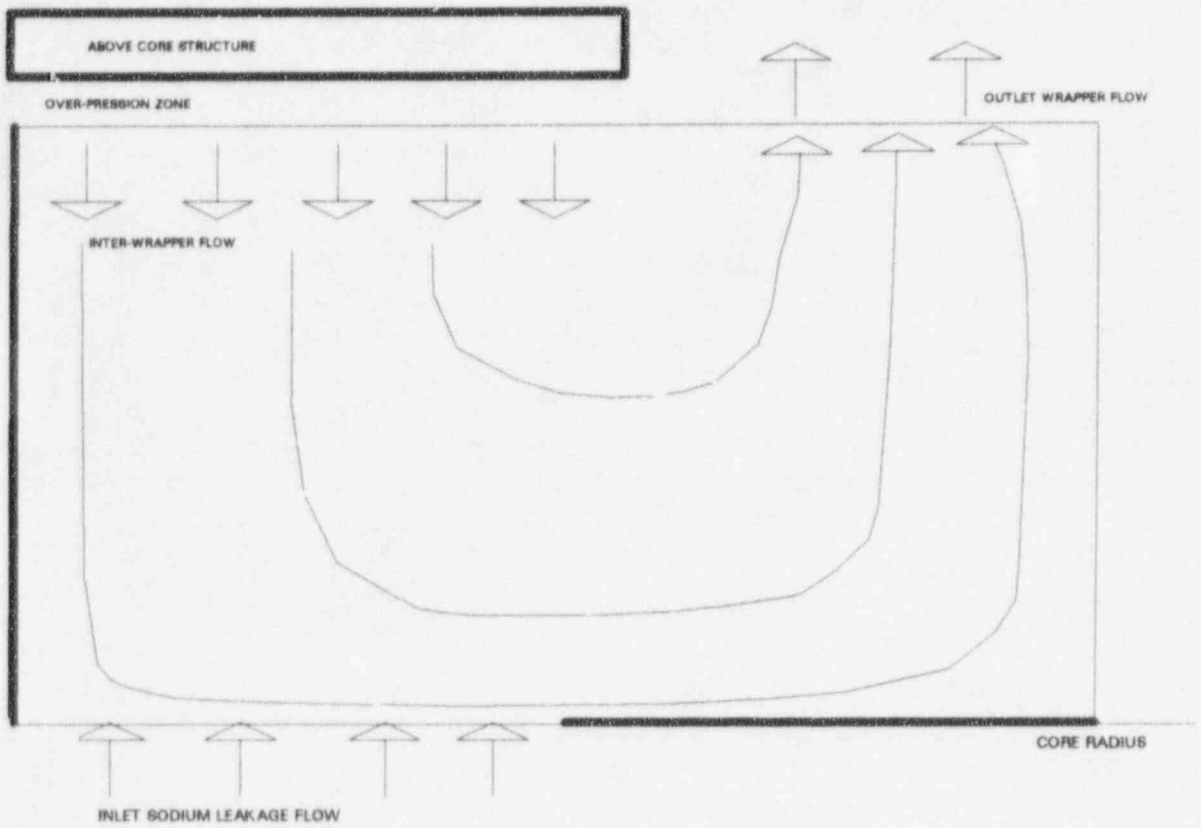

fig. 1. Simplified hydraulic description

2.2 The method of the wrapper tube temperature calculation.

The inlet coolant in the sub-assembly heats up along the pin bundle. This heating is calculated by the design code, CADET while the finite volume code, TRIO-VF estimates the thermal-hydraulic behavior of the inter-wrapper flow with boundary conditions coming from CADET. The calculation is iterative. When the convergence is reached, the six side temperatures of each hexagonal wrapper tube are known from the bottom to the top of the core.

TRANSCOEUR-2, federating these calculations, requires (fig. 2) knowledge of geometric data for each sub-assembly, neutronic characteristics (axial profile and maximum linear power) and the core flow distribution.

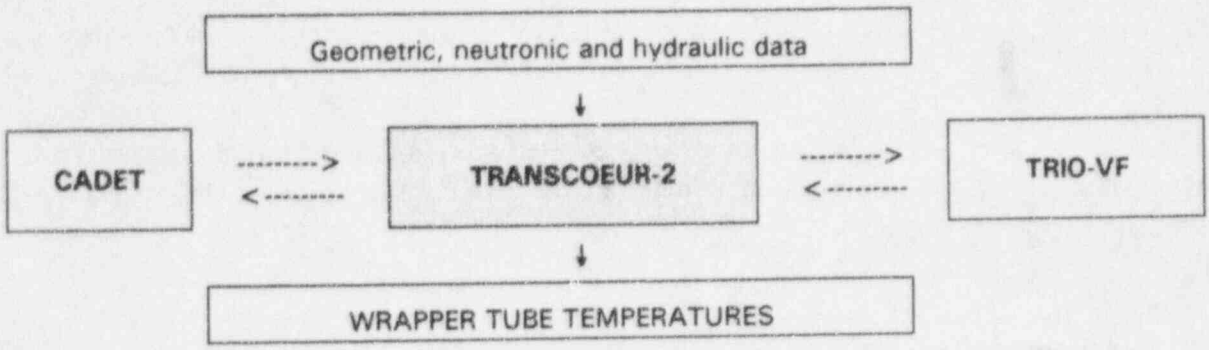

Fig. 2. Diagram of wrapper tube temperatures calculations.

3. CODE DESCRIPTION

3.1 The CADET sub-assembly code.

The design code, CADET, calculates the thermal-hydraulics of parallel sub-channels (the pitch is triangular) coupled with each other inside a bundle cooled by sodium. The pins are arranged in a hexagonal ring. The coolant temperature is given by an energy balance for each sub-channel at level Z.

$$q_j\,(Z)\,.\,Cp\,.\,[\theta_j\,(Z+\Delta Z) - \theta_j\,(Z)] = W_j - \sum_a B_j^a\,[\,\bar{\theta}_j - \bar{\theta}_a\,] - B_j^r\,[\bar{\theta}_j - \bar{\theta}_r]$$

$$B_j^a = B'^a_j + B''^a_j + B'''^a_j$$

Thermal coupling between sub-channels is accomplished using a (B_j^a) coefficient taking into account heat transfer which is due to the :

- radial conduction through the coolant : $B'^a_j = (\lambda / l_j^a)\, d_j^a\, \Delta Z$
- sodium deflected by helical spacer wire : $B''^a_j = q_j^a\, Cp\, \Delta Z$
- turbulent diffusion : $B'''^a_j = 2.2*10^{-6}\,(d_j^a / l_j^a)\, Re^{0.84}\, \Delta Z\, Cp$

The first heat transfer mechanism is calculated by FOURIER's law, whereas the second (q_j^a the linear deflected flow) and the third are evaluated by experimental correlations as a function of sub-assembly geometry, fluid physical properties and flowrate. The deflected sodium flow q_j^a is calculated with:

$q_j^a = C_1 * (q_a + q_j)/((S_a + S_j) * h)$ $C_1 = 1.0 * 10^{-6}$ for triangular to triangular sub-channel

$q_j^a = C_2 * (q_a + q_j)/((S_a + S_j) * h)$ $C_2 = 9.2 * 10^{-7}$ for triangular to rectangular sub-channel

$q_j^a = C_3 * \Sigma q_j/(h * \Sigma s_j)$ $C_3 = 2.6 * 10^{-5}$ for peripheral sub-channels

The sub-channel flowrate is calculated with the continuity and momentum equations and with an assumption of iso-pressure hydraulic conditions for each calculated level. These equations are:

$$Q = \sum_j q_j$$

$$\Delta P_j + (\rho_j - \rho).g.\Delta Z = \Delta P - \rho.g.\Delta Z$$

ΔP is the pressure drop law written :

$$\Delta P = F(\mathrm{Re}) \frac{\Delta Z}{\delta_j} \rho \frac{U_j^2}{2}$$

with $F(\mathrm{Re}) = a\,\mathrm{Re}^b$ and a,b coming from a turbulent flow pressure drop model [1]. The sub-channel flowrate (forced convection), axially constant, depends on the hydraulic diameter (δ_j).

An algorithm numbers the sub-channels to reduce the matrix bandwidth. The linear system is triangulated, stocked by the sky line method and solved by a direct method.

3.2. The TRIO-VF thermal-hydraulic code.

TRIO-VF [2] is a finite volume calculation code which can describe complex flow in steady state or transient conditions. The fluid is newtonien, incompressible and confirms the BOUSSINESQ approximation.The flows are laminar or turbulent with DIRICHLET (imposed velocity or temperature) or NEUMANN (imposed flux) boundary conditions [2]. The conservation equations are the statistic average of the NAVIER-STOKES general conservation equations.

The continuity, momentum and energy equations are integrated with the GAUSS theorem on control volumes to obtain macroscopic balance equations. The time discretisation is semi-implicit. The solution of the linear system may be obtained by a direct method or iterative method (conjugate gradient).

3.3 The TRANSCOEUR-2 code.

The objective of TRANSCOEUR-2 is the evaluation of sub-assembly wrapper tube thermal loading which is necessary in order to determine their strains in the core and the handling forces. Calculation of these temperatures requires :

- core neutronic data,
- a flow through each sub-assembly,
- thermal coupling existing between the internal and external sub-assembly sodium flow along the wrapper tubes (fig. 3) : calculation of the wrapper tube temperatures is iterative.

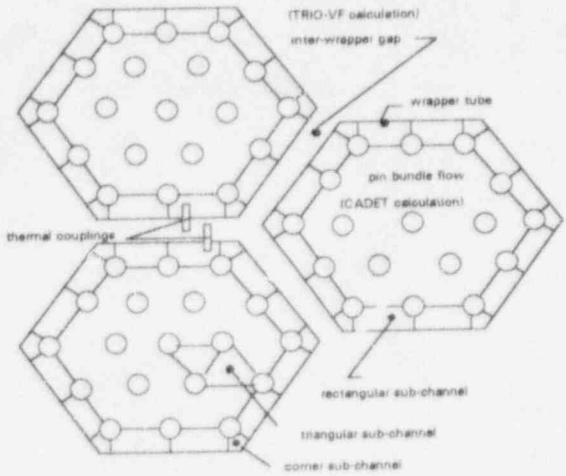

Fig. 3. Simplified diagram of flows and couplings.

TRANSCOEUR-2 processes the thermal coupling, generates the data for the two computer codes (TRIO-VF and CADET), manages their interfaces and calculates the wrapper tube temperatures.

a) hypothesis for sub-assembly calculation

CADET estimates the thermal-hydraulic behavior of each sub-channel inside a sub-assembly cooled by sodium forced convection. The wire wrap effects are taken into account (& 3.1). The boundary conditions are given by a global heat transfer coefficient (conduction through the wall and boundary layer on each wrapper tube side) with the inter-wrapper temperature calculated by TRIO-VF in the previous iteration. Due to the power, flowrate and geometric symmetries, only one third of the core fuel sub-assemblies is calculated, the CADET data file relative to each sub-assembly is created by TRANSCOEUR-2

The CADET calculation gives in particular the sodium temperature field in the peripheral sub-channels. TRANSCOEUR-2 processes these temperatures for the TRIO-VF inter-wrapper flow data file.

b) hypothesis for inter-wrapper flow modelisation

The inter-wrapper flow is described by an axisymmetric geometry (for TRIO-VF data file - fig 4) The mesh boundary name "north side" is defined. The "north side" allows thermal coupling with peripheral sub-channel temperatures inside the volume mesh.

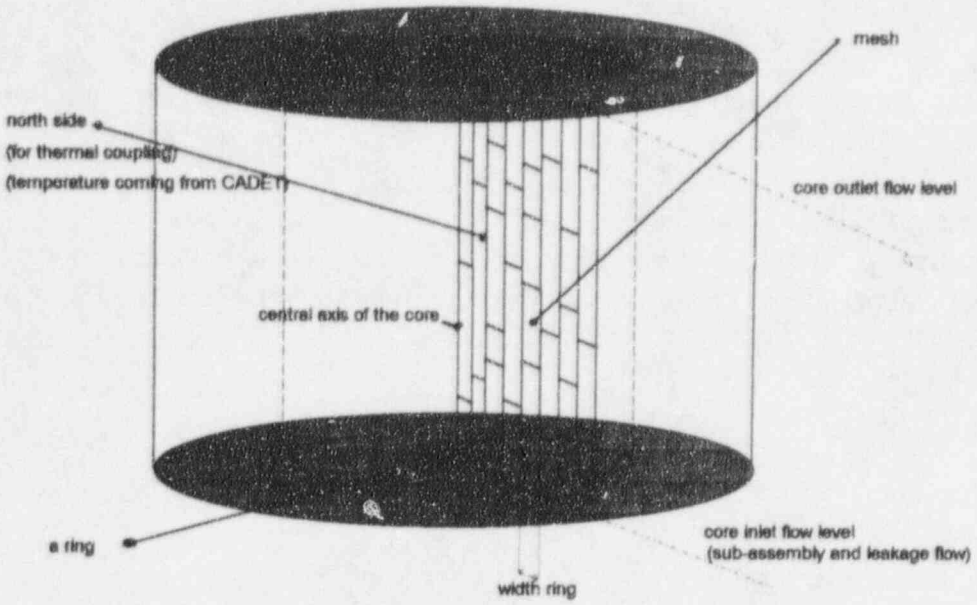

Fig. 4. core mesh principle.

The inter-wrapper flow model uses the porous media approach. The obstacles that the sodium encounters (the sub-assemblies) are taken into account by pressure drop coefficients [3] and porosity defined by the following :

- axial porosity is equal to the ratio of the sum of the hexagonal areas on the considered ring divided by the area of this ring,
- radial porosity, attributed to each ring is equal to the inter-wrapper gap divided by the center to center hexagonal sub-assemblies.

The model uses the TRIO-VF laminar equations (no turbulence model).
The sub-assemblies are grouped according to "families" (fuels, breeders, neutronic protection, internal storage) integrated in radial zones. Only the fuel sub-assembly zone is coupled with the internal temperature field estimated by CADET (thermal boundary conditions). The other sub-assemblies are adiabatic (if they have inner flow or if this is not the case, they are power sources in the core) and their wrapper tube temperatures are not calculated. The inter-wrapper leakage flow at the bottom of the sub-assemblies and the over-pressure due to the Above Core Structure (ACS) are the hydraulic boundary conditions.

c) the TRANSCOEUR-2 iterative scheme

TRANSCOEUR-2 calculates the wrapper tube temperatures when the thermal convergence between TRIO-VF and CADET is reached (the first TRIO-VF calculation is performed from an adiabatic reference sub-assembly CADET calculation). The TRANSCOEUR-2 iterative loop is given in fig. 5.

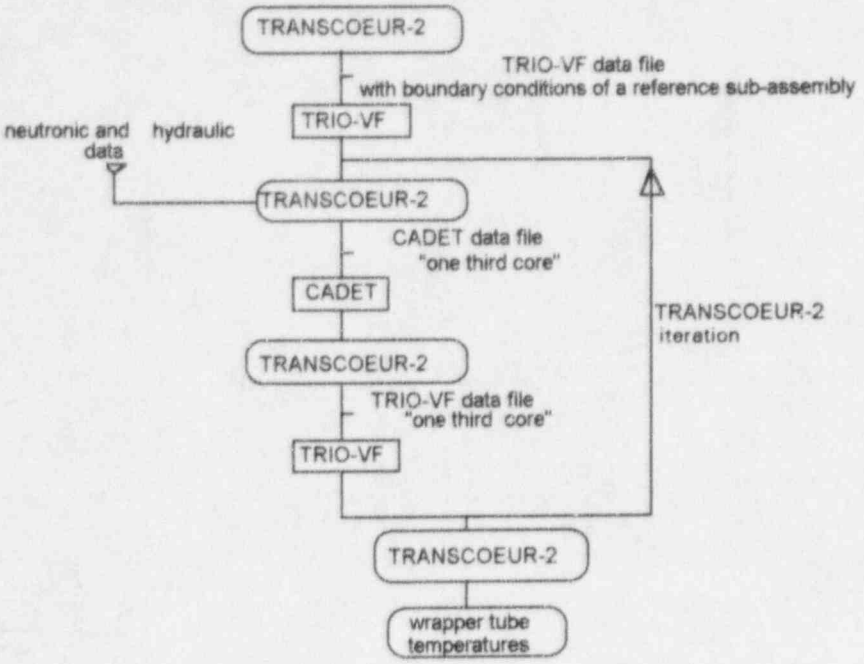

fig. 5. TRANSCOEUR-2 iterative loop

4. APPLICATION OF TRANSCOEUR-2 ON EFR

4.1 EFR core and sub-assembly data.

The study is carried out with data relative to the power operation of the EFR CD6/91 reactor. The thermal power is 3600 MW, the inlet sodium temperature in the diagrid is 395°C, the mean core outlet temperature is 545°C, the core pressure drop is 5×10^5 Pa, the total core flowrate (with bottom leakage flow of 200 kg/s) is 18700 kg/s. The core is meshed by 22 radial meshes (core radius = 3.97 m) and 29 axial meshes (core height = 4.32 m).

There are 444 fuel sub-assemblies in the core, each of which has 331 pins (diameter=8.2×10^{-3}m) disposed on a triangular pitch (9.44×10^{-3} m). Tube thickness is 4.4×10^{-3} m and the inter sub-assembly gap is 5.0×10^{-3} m. Due to symmetry conditions (see §3.3), 132 fuel sub-assemblies are calculated by CADET. The height CADET computation ranges between the bottom of the lower axial blanket (core level =1.54 m) and the top of the upper axial blanket (core level =2.95 m).

4.2 EFR wrapper tube temperatures.

a) inter-wrapper flow thermal-hydraulic fields

The velocity field (fig. 6) shows the weak influence of the leakage flow. The inter-wrapper flowrate (5% of the core flow) due to the over-pressure profile (see fig. 1) takes up pratically all the core volume and exits by the upper right part of the core.

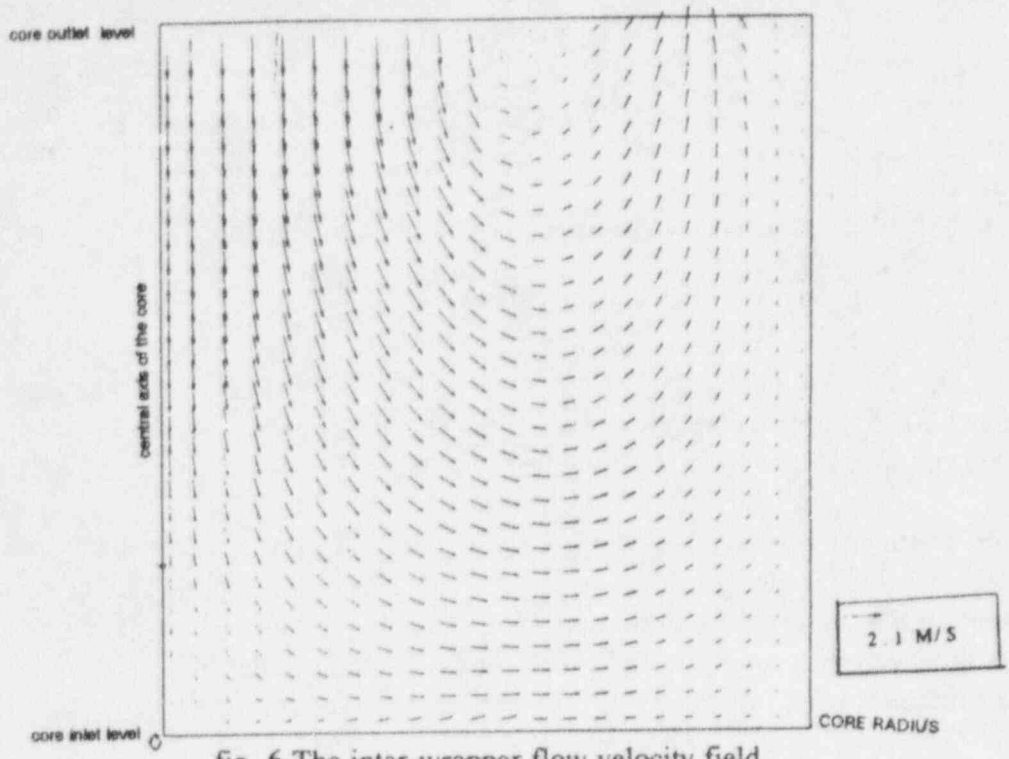

fig. 6 The inter-wrapper flow velocity field

The temperature field (fig. 7) allows visualization of the radial thermal influence zones of the EFR core: the hotter part is the fissile zone ($528°C < T < 563°C$) including a part of the breeder zone (non-coupling with the inter-wrapper flow). A second zone includes breeder and steel sub-assemblies where the radial thermal gradient is very high ($\sim 135°C/m$). The third zone (neutronic protection) has non negligible radial thermal gradient ($\sim 55°C/m$). The other regions (internal storage ...) are cold. Comparison of this temperature field with one having thermal coupling shows that the influence of the descending flowrate (on the wrapper tube temperatures) is sensitive up to the middle of the lower expansion volume.

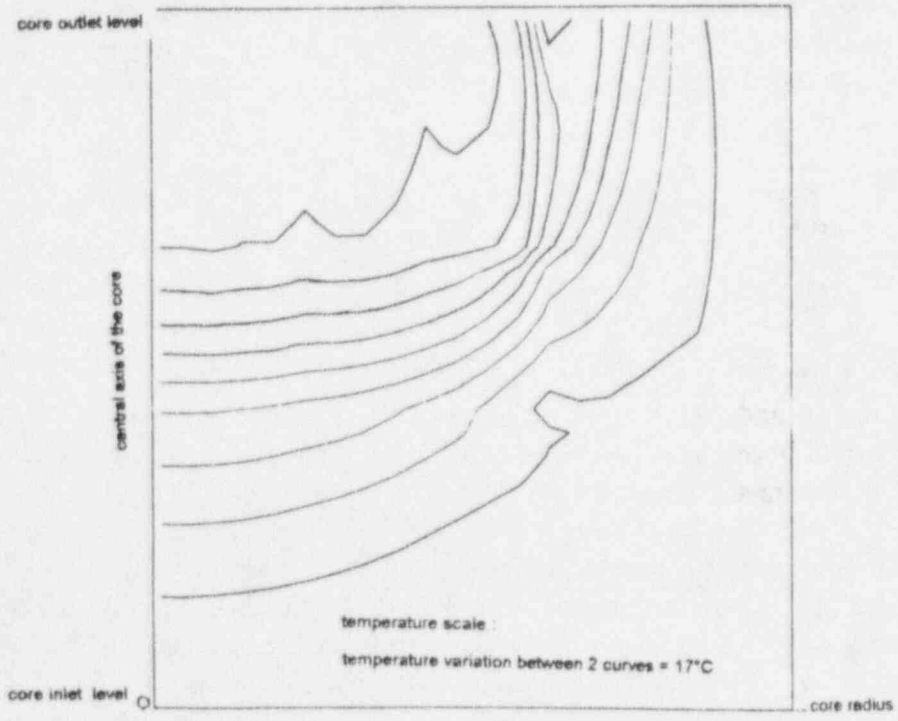

fig. 7 The inter-wrapper flow temperature field

b) wrapper tube temperatures.
Two iterations in TRANSCOEUR-2 (see fig. 5) were necessary for the convergence. The thermal coupling due to the inter-wrapper flow represents 1.3% of nominal power and substantially modifies the inter-wrapper thermal-hydraulic flow pattern (variation of the axial and radial velocities up to 25%, modification of the thermal gradient) and the inter-wrapper flow inlet temperature due to the ACS (see fig. 1).

Three representive sub-assemblies are analysed: The first (named 31/30) in core 1 is located on the second ring mesh (it is the first sub-assembly coupled with the inter-wrapper flow). The second (named 31/21) is in core 2 (eighth ring mesh) and the third (named 41/18) is in core 3 (eleventh ring mesh, last coupled sub-assembly).

Wrapper tube heating depends on its position in the core. The temperature difference between the bottom of the lower axial blanket to the top of the upper axial blanket is 115°C for sub-assembly 31/30 (located in the center of the core) and 95°C for sub-assembly 41/18 at core periphery. The axial temperature variation along the wrapper tubes is related to their locations. The wrapper tube median fiber (located at half thickness of the wrapper tube) temperature is plotted in fig. 8.

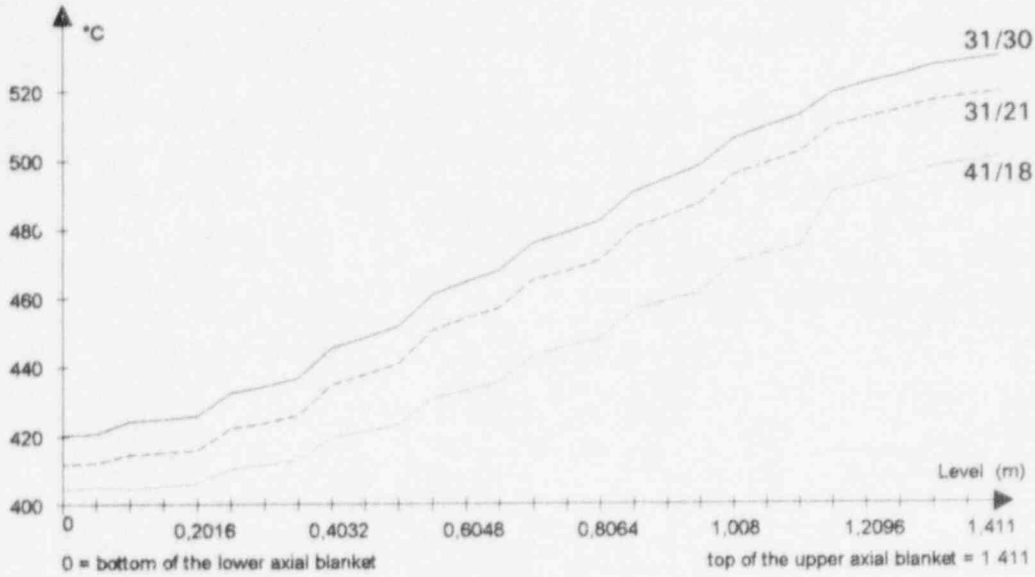

fig. 7 Median fiber temperature

The temperature profile and the thermal gradient (also dependent on the radial position) are a function of the thermal-hydraulic conditions in the inter-wrapper flow and in the six bordering sub-assemblies. Calculations show a variation of temperature ΔT_{max} between the six wrapper tube sides, greater for sub-assembly 41/18 ($\Delta T_{max} \cong 8°C$) than for sub-assembly 31/21 ($\Delta T_{max} \cong 2.5°C$) and sub-assembly 31/30 ($\Delta T_{max} \cong 1.5°C$). Sub-assembly 41/18 is surrounded with fuel and breeder sub-assemblies whereas 31/30 and 31/21 have a border more homogeneous.
ΔT_{max} is the temperature difference between the hotter side and the coldest side of the median fiber wrapper tube at the top of the upper axial blanket.

5. CONCLUSION

The application of TRANSCOEUR-2 to EFR CD 6/91 demonstrates the importance of the inter-wrapper flow on temperatures and thermal gradients of the wrapper tubes. TRANSCOEUR-2 shows that the temperatures are high for the central sub-assemblies of the core and the thermal gradients are great in the core periphery. These results will be used for the study of mechanical behavior of EFR. Parametric studies on (pressure drop, heat transfer coefficients, over-pressure profile, leakage flow of the sphere cone bearing ...) are now being developed with the aim of participating in the TRANSCOEUR-2 validation. Further work is planned to extend the field of application on all the hexagonal wrapper tubes of the core. Complete TRANSCOEUR-2 thermal-hydraulic validation will be carried out HIPPO experiments [4] (non-isothermal water experiments on inter-wrapper flow on a 1/8 scale reactor model). The next step will be to federate the thermal-hydraulic core design calculations of the core flow distribution, of the maximum clad temperature (with or without uncertainties) in TRANSCOEUR-2.

REFERENCES

[1] E. H. NOVENDSTERN, "turbulent flow pressure drop model for fuel rod assemblies utilizing a helical wire-wrap spacer system," Nuclear engineering and design 22, 19-27 (1974)

[2] B. Menant, M. Villand and D. Grand, "detailed numerical studies of the thermohydraulic in the hot plenum of liquid metal fast breeder reactor," Proc. 6th NURETH", Grenoble (1994).

[3] I. E. Idel'cik, Pressure drop memento, Editions EYROLLES, PARIS, (1986).

[4] C. BETTS, MW ASHTON, G. SPENCE, C. ESSIG, J.C. ASTEGIANO, J.M. CHEREL, A. MORSE, "EFR primary system thermohydraulic status on R/D design studies", Proc Int. Conf. on fast reactors and its fuel cycles, Kyoto (1991)

NOTATION

$\theta_j(Z)$	sub-channel j température at the level Z (°C)
W_j	dissipated power in sub-channel j (w)
B_i	thermal coupling coefficient (w/°C)
Cp	sodium heat capacity (J/kg.°C)
h	helical space wire pitch (m)
q_j	sub-channel j flowrate (kg/s)
q_j	deflected sodium flow from j to adjacent sub-channel a (kg/ms)
S_i , S_a	section flow of sub-channel j or sub-channel a
$\bar{\theta}_x$	mean température at the level Z (°C)

SIMULATION OF DECAY HEAT REMOVAL BY NATURAL CONVECTION IN A POOL TYPE FAST REACTOR MODEL - RAMONA - WITH COUPLED 1D/2D THERMAL HYDRAULIC CODE SYSTEM

N. Kasinathan, A. Rajakumar, G. Vaidyanathan and S.C. Chetal

Nuclear Systems Division
Indira Gandhi Centre for Atomic Research
Kalpakkam 603 102 INDIA

ABSTRACT

Post shutdown decay heat removal is an important safety requirement in any nuclear system. In order to improve the reliability of this function, Liquid metal (sodium) cooled fast breeder reactors (LMFBR) are equipped with redundant hot pool dipped immersion coolers connected to natural draught air cooled heat exchangers through intermediate sodium circuits. During decay heat removal, flow through the core, immersion cooler primary side and in the intermediate sodium circuits are also through natural convection. In order to establish the viability and validate computer codes used in making predictions, a 1:20 scale experimental model called RAMONA with water as coolant has been built and experimental simulation of decay heat removal situation has been performed at KfK Karlsruhe. Results of two such experiments have been compiled and published as benchmarks. This paper brings out the results of the numerical simulation of one of the benchmark case through a 1D/2D coupled code system, DHDYN-1D/THYC-2D and the salient features of the comparisons. Brief description of the formulations of the codes are also included.

1. INTRODUCTION

Post shutdown decay heat removal (DHR) should be assured with very high reliability in any nuclear reactor system. In liquid metal (sodium) cooled fast breeder reactors (LMFBR) this is achieved by the provisions of redundant safety grade DHR systems (SGDHRS) directly removing heat from the hot pool through Immersion Coolers (IC) which are in turn connected to natural draught Air-cooled Heat Exchanger (AHX) via intermediate sodium circuits. Prototype Fast Breeder Reactor (PFBR) is a 500 MWe commercial sized fast reactor being designed in India. This is a pool type reactor and four redundant SGDHR circuits as discussed above have been provided. Preliminary sizing calculations and one dimensional lumped parameter transient analysis (using DHDYN-1D Code) of long duration total power supply failure situations have been analysed and the results are reported elsewhere [1].

In support of the European Fast Reactor (EFR) program, which envisages to use the SGDHRS option, a 1:20 scale experimental model using water as simulant fluid called RAMONA (Reactor Model for Natural Convection Studies) has been built in Germany. The purpose of this facility is to investigate the detailed invessel

thermohydraulics and the results are used to verify one and multi-dimensional thermohydraulics codes [2]. Two benchmark experiments involving simulation of simultaneous primary pumps and reactor trip from an initial steady state corresponding to 40 % power and flow conditions have been performed. The detailed description of the tests and the results have been documented and supplied to validate several code systems being used to theoretically evaluate the SGDHRS [3,4]. Several code systems, like LEDHER [2], coupled DYANA-1D/ATTICA-2D [5], finite element based ASTEC [6], the 3D finite difference codes COMMIX-2(V) [7] and FLUTAN [8] etc. have been utilised to predict the RAMONA experiments and have been reported to be reasonably validated.

In order to analyse and evaluate thermal loadings on the structures of PFBR, in-house developed codes DHDYN-1D and THYC- 2D [9] are being used. In order to validate these codes, the RAMONA benchmark experiment case-1 [3] was analysed through a combination of these two codes. Earlier the DHDYN-1D code, which is a lumped parameter transient analysis code, alone was used to simulate the benchmark experiments and the results were given in an earlier paper [10]. This gave a reasonably good prediction of the evolution of the core flow. But the magnitude of the axial thermal stratification in the hot pool predicted was three times greater than that observed in the experiments. This was attributed to the use of the simplified hot and cold pool thermal models. Hence it was felt that better and more realistic predictions of pool temperature can be obtained by interfacing the 2D thermohydraulic code THYC-2D modelling the hot and cold pools, with the DHDYN-1D code modelling the other portions of the circuit like core, Intermediate Heat Exchanger (IHX), DHX and primary circuit hydraulics. This paper presents the brief descriptions of the modelling principles utilised in the DHDYN-1D and THYC-2D codes, methodology of interfacing these two codes, input from the experiments and the results of the analysis. Along with the comparison with the actual experimental results, the performance of the codes vis-a-vis some of the other code systems stated above is also brought out.

2. DHDYN-1D CODE

This is a one dimensional (1D) lumped parameter system analysis code modelling the thermal portions of the core, IHX and DHX, the hydraulics in the core - IHX primary side - primary pump - inlet plenum and the hydraulics in the DHX primary side. In the core thermal model the active heated length of each radial region (comprising some convenient number of subassemblies for actual reactor applications or a annular heated channel associated with half of the adjacent heater rings in the RAMONA model) is divided into some convenient number of axial nodes. Energy balance over each of the resulting discrete volumes give the set of equations describing the core. In order to realise faster computations, axial heat conduction in the heater ring (fuel pin for actual reactor) and inter channel heat transfer effects are neglected. Then the following governing equations result for each discrete volume of the heater ring coolant channel.

$$C_c \frac{dT_o}{dt} = Q_c c_p (T_i - T_o) + (UA)_{hr-c}(T_{hr} - \bar{T})$$

$$\bar{T} = \frac{T_i + T_o}{2}$$

$$C_{hr} \frac{dT_{hr}}{dt} = (UA)_{hr-c}(\bar{T} - T_{hr}) + \dot{q}_{hr}$$

For IHX and IC thermal models, the heat transfer length is divided into some convenient number of volumes on the primary and secondary sides. Application of energy balance over each set of volumes of primary and secondary side results in the governing equations. For defining the primary to secondary side heat transfer, average temperature of each volume obtained as a weighted mean of the respective volumes inlet and outlet temperatures are used. The weighting factors are obtained from the assumption that a log-mean temperature difference (LMTD) approach can be taken for each set of volumes. The use of such weighting factors helps to retain the linear nature of the governing equations, which in turn simplifies the finite differencing of the governing equations. The derivation of the expression for these weighting factors is given elsewhere [11]. Further simplifying assumption like (i) distribution of tubes and shells material thermal capacities equally between the primary and secondary fluids (so that no explicit equations for the material temperatures are needed) and (ii) negligible axial heat conduction are also made. The following governing equations are obtained for each set of the discrete volumes.

$$C_{pr} \frac{dT_{pr_o}}{dt} = Q_{pr} c_p (T_{pr_i} - T_{pr_o}) + (UA)_{hx}(\bar{T}_{se} - \bar{T}_{pr})$$

$$C_{se} \frac{dT_{se_o}}{dt} = Q_{se} c_p (T_{se_i} - T_{se_o}) + (UA)_{hx}(\bar{T}_{pr} - \bar{T}_{se})$$

$$\bar{T}_{pr} = F T_{pr_i} + (1 - F) T_{pr_o}$$

$$\bar{T}_{se} = F T_{se_o} + (1 - F) T_{se_i}$$

$$F = \frac{1}{y} - \left(\frac{1}{e^y - 1}\right)$$

$$y = (UA)_{hx}\left\{\frac{1}{(Qc_p)_{pr}} - \frac{1}{(Qc_p)_{se}}\right\}$$

The hydraulic model which estimates the transient evolutions of the core - IHX and DHX primary side flows are obtained from the

integral momentum balance equation over the required segment of flow and it is of the form

$$I\frac{dQ}{dt} = P_i - P_o + \Delta P_{pd} - \{g\Sigma(\rho\delta Z) + \Delta P_f\}$$

$$\Delta P_f = KQ\langle Q\rangle$$

$\Sigma(\rho\delta Z)$ is obtained as the path integration of the fluid density e along the nominal flow direction. ΔP_{pd}, the pump developed head is obtained from the homologous characteristics of the pump as a function of the pump speed and flow, wherever present. Transient evolutions of free levels (in the hot pool and cold pool/pump stand pipe) is obtained through the equation of the form:

$$\rho S\frac{dZ}{dt} = Q_i - Q_o$$

3. THYC-2D CODE

THYC-2D is a two dimensional thermal hydraulic computer code to analyse the steady state and transient incompressible fluid flow with heat transport in specified regions in any system. It solves the Navier-Stokes equations using the finite volume method [12]. The generalised Navier-Stokes equation is given by

$$\frac{\partial}{\partial t}(\beta_V \rho \Phi) + \nabla\bullet(\beta_S \rho \bar{u} \Phi) = \nabla\bullet(\beta_S \Gamma_\Phi \nabla\Phi) + \beta_V S_\Phi$$

where, Δ is the divergence operator, Γ_Φ is the diffusion coefficient, $\bar{u}$ is the velocity field, S_Φ is the source term, β_V is the volumetric porosity, β_S is the surface permeability and Φ takes the following values each of which gives rise to a particular conservation equation as follows:

$\Phi = 1$ gives the continuity equation

$\Phi = \bar{u}$ gives the x direction momentum equation

$\Phi = \bar{v}$ gives the y (or r in cylindrical coordinate system) direction momentum equation and

$\Phi = h = c_p T$ gives the energy balance equation

Turbulence has been modelled using the constant turbulent viscosity and conductivity model as given below:

$$\Gamma_u, \Gamma_v = \mu_{eff} = \mu_{lam} + \mu_{tur}$$

where μ_{tur} is the turbulent viscosity, which in turn is obtained as

$$\mu_{tur} = 0.00028 \rho u_{max} l$$

with l being a charecteristic dimension for the geometry under consideration. In this analysis l is chosen to be the distance between the upper core structure (UCS)and the main vessel. u_{max} is the velocity of fluid in the region between the UCS and core.

$$\Gamma_h = k_{eff} = k + \frac{c_p \mu_{tur}}{\mathrm{Pr}_{tur}}$$

The turbulent Prandtl number, Pr_{tur} is taken as 0.8

The flow is considered incompressible with the Boussinessq approximation used to evaluate buoyancy forces. An upwind scheme is used for all advection terms, which takes into account of the velocity directions through control surfaces. The flow equations are solved using the SIMPLE algorithm [12]. The internal structures inside the regions of analysis is represented through porous medium formulation and with permeable surfaces wherever necessary.

Specific to the RAMONA analysis, a grid matrix of 35x46 is selected. The layout of the grid is done such that temperatures evaluated in the calculation domain coincides with the measurement locations as described in the benchmark [3]. The redan structure separating the hot and cold pools is specified with appropriate material properties to allow heat conduction across it.

4. RAMONA BENCHMARK CASE-1 EXPERIMENT

The schematic of the RAMONA facility is shown in Figure 1. The experiment performed was simultaneous tripping of all the primary and secondary pumps along with core power reductions from 30 kW to 1 kW (simulating reactor scram). The immersion coolers (or the DHX) start the DHR operations at 240 s after scram. Figure 2 shows the power, primary and secondary flows evolutions and Figure 3 shows the operating conditions of the DHX secondary side total flow rate and inlet temperature evolution. These data are used as input conditions to the DHDYN-1D/THYC-2D code system to be described in the following paragraphs.

5. DHDYN-1D/THYC-2D CODE SYSTEM INTERFACE

This interface is achieved by supplying the boundary conditions required for each of the code from the results of the other code's solutions as shown in Figure 4. The core channels outlet temperatures, IC primary side outlet temperature, IHX primary side outlet temperature, core channel - IHX flow rate and IC primary side flow rate are obtained through DHDYN-1D portion. The temperature field calculated by the THYC-2D portions gives the IHX and IC inlet temperatures and the core channel inlet temperatures. The buoyancy forces required for the hydraulic calculations are obtained using the densities evaluated at different locations of the hot and cold pool by the THYC-2D code and the densities

evaluated inside the core channels and heat exchangers by the DHDYN-1D code. The pump inlet in the cold pool and the IHX and IC inlets are represented as mass sink in the appropriate locations in the THYC-2D representation of the hot and cold pools. The mixed mean temperature at the pump inlet location form the inlet condition for the inlet plenum. The core channel inlet temperature is available from the temperature field of the inlet plenum.

For the initial steady state calculations, the final temperature field has been obtained by repeated iterations through THYC-2D and DHDYN-1D codes. For the transient calculations the procedure shown in Figure 4 is followed, where iterative calculations is done only in the THYC-2D portion of the code.

6. RESULTS AND DISCUSSIONS

The 2D flow field and temperature contours obtained during the initial steady state (ISS) (t = 0 s) and for times 140 s, 500 s, 4000 s, 9000 s and 14400 s are shown in Figures 5 and 6. The times 140 s and 500 s corresponds to short time after primary pump stop and complete establishment of natural convection (NC) flow in the IC primary side respectively.

The ISS is characterised with uniform temperatures throughout the hot and cold pool because of forced convection. The flow field shows a strongly recirculating region midway between the IHX and above core structure (ACS) and a relatively stagnant cavity between the core and redan. Around the time when the pumps stop, a strong recirculation is present in the cavity. After the establishment of NC flow in the IC, it can be seen that the upper redan surface is washed by cold flow from IC, mixing of the core flow and IC flow occurs midway between the core and ACS and close to core centreline, and flow enters the ACS through the openings in the lower cylindrical portion. The gradual stratification especially in the hot pool, is seen clearly in the temperature contours.

The core flow rate evolutions as obtained in the experiment, and through the codes DHDYN-1D/THYC-2D, DYANA/ATTICA [5] and ASTEC [6] are shown in Figure 7. The experimentally measured core flow goes down to zero immediately after the pump stop, recover to 29 g/s at 300 s, goes down again to 6 g/s at 30 min and gradually recovers to 30.5 g/s at 4 h. Present simulation shows a lowest value of 10 g/s immediately after pump stop, recover to 23 g/s at about 275 s, goes down again to 19 g/s at 18 min and recovers to 35 g/s at the end of 4 h. Estimations made by the ASTEC and DYANA/ATTICA codes for the duration upto 500 s show similar comparison like that obtained in the present simulation.

The velocity profile measurements made in the region between the upper edge of the core and outer-lower edge of the ACS and its comparison with the calculations is shown in Figure 8 for ISS (30 kW) and final steady state (1 kW) in natural convection. From this it can be seen that THYC-2D predictions of the velocity profiles matches well with the experiments, indicating the 2D nature of the flow field in that location.Comparison under natural convection condition is found to be better than that under forced flow conditions.This could be due to the fact that the turbulence in the hot plenum is not well represented by the constant turbulent

viscosity model under forced flow conditions. From reference [7] it appears that in the COMMIX-2(V) analysis only around 600 grids has been selected in the r-z direction compared to 1610 grids in the present calculations. This probably could explain the higher deviation of COMMIX-2(V) velocity predictions from the experiments as seen in figure 8.

The evolution of the mean core inlet and outlet temperatures in the experiment and the predictions are shown in Figure 9. The mean core outlet measured during the ISS is 41.5 deg C whereas in the estimations it is 44 deg C. This was so in the predictions made by FLUTAN code also [8]. This could be explained from the fact that the measured temperatures are in the centre of the core channels, whereas the calculated temperature is an average of the individual channel mean temperatures. During the transient evolution the minimum core oultet temperature reached is 39 deg C (at 100 s) in the experiment whereas it is 41 deg C (at 130 s) in the prediction. The core inlet temperature reaches a peak of 39 deg C (at 1 h 7 min) in the experiment and it is 41 deg C (at 54 min) in the predictions. At the end of 4 h, the inlet temperature reaches 37 deg C in the experiment whereas it cools down to 35 deg C in the calculations. The core oultet reaches a peak of 45.5 deg C at about 37 min whereas in the calculations it reaches 50.3 deg C at 30 min. In general, the DHDYN-1D/THYC-2D predicts a faster rate of change of tempeature than that observed in the experiment both while being heated and cooled.This is due to the higher value of the predicted core flow. The faster rate of increase of the core outlet temperature has also been observed in the COMMIX-2(V) predictions [7]. This is perhaps due to the neglect of axial conduction in the thermal model of the heater rings.

Several thermocouple trees are provided in the RAMONA facility to measure the temperature field in the hot and cold plenum [3]. Temperature measurements by a thermocouple tree located midway between the ACS and the pump standpipe, covering the top to the bottom of the hot pool including the cavity and designated as HT2-1 and measurements by another thermocouple tree, located between the IC and the main vessel, covering the length of the IC and designated as HT8-2 along with the code predictions at the same locations are shown in Figure 10. From the measurements in HT2-1 it can be seen that the DHDYN-1D/THYC-2D code predicts higher magnitude of thermal stratification in the upper part of the hot pool (335 mm to 580 mm elevation) and larger mixing in the lower part of the hot pool (130 mm to 335 mm elevation) during the first one hour of the transient. In the actual experiment this stratification pattern is more uniform. Further it is seen that the cooling of the top layer of the hot pool starts much earlier in the actual experiments. The rate of cooling is larger in the calculation than that observed. Similar variations can also be seen to be present in the predictions made by COMMIX-2(V) code [7] in which results were reported for a duration of 1 h. From the measurements in HT8-2 also it can be seen that the present calculation predicts higher magnitude of thermal stratification in the upper part of the hot pool. The predictions of the temperature measured in the axial locations of 335 mm and 310 mm, which are closest to the IC primary outlet, show a large deviation. COMMIX-2(V) being a 3D code, its predictions are much better as seen in the Figure 10. This shows that for proper prediction of thermal

stratification in the lower part of the pool 3D modelling is essential

Hot pool axial direction temperature profile at various times in the course of the transient for another thermocouple tree HT2-3 and the code predictions are shown in Figure 11. From this also it can be seen that the magnitude of thermal stratification in the upper part of the hot pool is predicted to be larger than that observed in the experiment. During the ISS the THYC-2D predicts uniform temperatures throughout the hot pool and it is mainly due to the constant turbulent viscosity and conductivity model used in the cavity region also. The variation of the lower part of the hot pool is seen to be better predicted by the THYC-2D. At the end of 15000 s (4 h 10 min) the lower part of the hot pool is 33.5 deg C whereas it is predicted as 32.5 deg C. Strong thermal stratification is found to occur in the zone between 260 mm to 340 mm whereas this is predicted to occur between 300 mm to 390 mm.

7. SUMMARY AND CONCLUSIONS

The DHDYN-1D/THYC-2D code system was used to simulate the RAMONA benchmark experiment and the predicted results were compared with the reported measurements.

The core flow rate evolution during the transient was well predicted except for the second minimum around half an hour from the start of the transient. Such was the case even in other predictions using even 3D codes for the hot and cold pool simulation. Similar results were obtained in the earlier one dimensional analysis.

The predicted values of the velocity distribution in the region between the upper edge of the core and lower edge of the ACS, during the initial steady state and final steady state conditions compared very well with the measurements.

As regards the various pool temperature predictions, the trend was well predicted in most of the regions. Major deviation results only in the region closest to the IC outlet in the hot pool, because of the large 3D effects. As regards the magnitude of thermal stratification in the hot pool, predictions show it around 2.5 deg.C whereas it is around 3.5 deg.C in the actual measurements.

In conclusion, utilisation of the combined DHDYN-1D/THYC-2D code system for this problem gave more satisfactory results than using only the DHDYN-1D code. Hence it is recommended to utilise such combined code systems for further design work. Further work on DHDYN/THYC-3D to bring in 3D effects is being taken up.

ACKKOWLEDGEMENT

We thank Dr. D. Weinberg and Dr.H. Hoffmann of KfK, Karlsruhe, for supplying the details and results of the RAMONA Benchmark Experiments.

REFERENCES

[1] N. Kasinathan et al, "An Overview of DHR Studies for Indian FBR Program", Proc. IAEA-IWGFR Spec. Meet on Evaluations of DHR by Natural Convection, Oarai Engg Centre, PNC, Japan, Feb 1993.

[2] H. Hoffmann et al, "Thermohydraulic Model Experiments and Calculations on the Transition from Forced to Natural Circulation for Pool Type Reactors", Proc. VI ANS Winter Meet. Washington, p.143, 1990.

[3] D. Weinberg et al, "Thermohydraulic Investigations on the Transition from Forced Nominal to Natural Circulation DHR Operation Conditions in RAMONA - Description of a Benchmark Problem", EFR Project: AGT4/SG11, July 1990.

[4] D. Weinberg et al, "RAMONA Benchmark Experimental Results of Case 1 and Case 2", EFR Project: AGT4/SG 11, June, 1991.

[5] C. Essig et al, "Consistent Thermal Hydraulic Approach of EFR Decay Heat Removal by Natural Convection", Proc. NURETH-5, p.135, 1992.

[6] S.E. Georgeosura and J.A. Keeton, "A Three Dimensional Simulation of a Pool Type Fast Reactor Model using the ASTEC Code", Proc. NURETH-5, p.180, 1992.

[7] D. Weinberg et al, "Comparison of Transient 3D Calculations with RAMONA Model Experiments", Proc. NURETH-5, p.571, 1992.

[8] D. Weinberg et al, "The Status of Studies Using RAMONA and NEPTUN Models on Decay Heat Removal by Natural Convection for the EFR", Proc. IAEA-IWGFR Spec. Meet. on Evaluations of DHR by Natural Convection Oarai Engg. Centre, Japan, 1993.

[9] K. Velusamy et al, "Thermal Hydraulic Analysis in the Design of PFBR Inner Vessel", Proc. Fourth Int. Conf. on Liquid Metal Engg. Tech., Avignon, France, Oct. 1989, pp.408.1.

[10] N. Kasinathan et al, "Analysis of Decay Heat Removal by Natural Convectoin in PFBR", Proc. IAEA-IWGFR Spec. Meet on Evaluation of Decay Heat Removal by Natural Convection, Oarai Engg. Centre, Japna, 1993.

[11] S.L. Additon and W.L. Frisch, "Transient Heat Exchanger Simulation Employing Analytic Nodal Average Temperature in the Finite Difference Equation", Trans. ANS Vol.15, p.259, 1972.

[12] S.V. Patankar, Numerical Heat Transfer and Fluid Flow, McGraw Hill, New York, 1980.

NOMENCLATURE

C	Thermal Capacity, J/deg C
c_p	Specific heat, J/kg/deg C
F	Weighting factor for average temperature calculations in each discrete volume of the heat exchanger thermal model
g	Acceleratoin due to gravity, m/s^2
I	Fluid inertia, m^{-1}
K	Friction pressure drop coeffcient
k	Thermal conductivity, W/m/deg C
P	Pressure, N/m^2
Q	Flow rate, kg/s
q	Heater ring power, W
S	Cross-sectional area, m^2
T	Temperature, deg C
t	time, s
(UA)	Overal heat transmittance rate, W/deg C
Z	elevation, m
μ	Viscosity, kg/m/s
ρ	density, kg/m^3

Subscripts

c	coolant
f	friction
hr	heater ring
hx	heat exchanger
i	inlet
o	outlet
pd	pump developed
pr	primary fluid
se	secondary fluid
lam	laminar
eff	effective

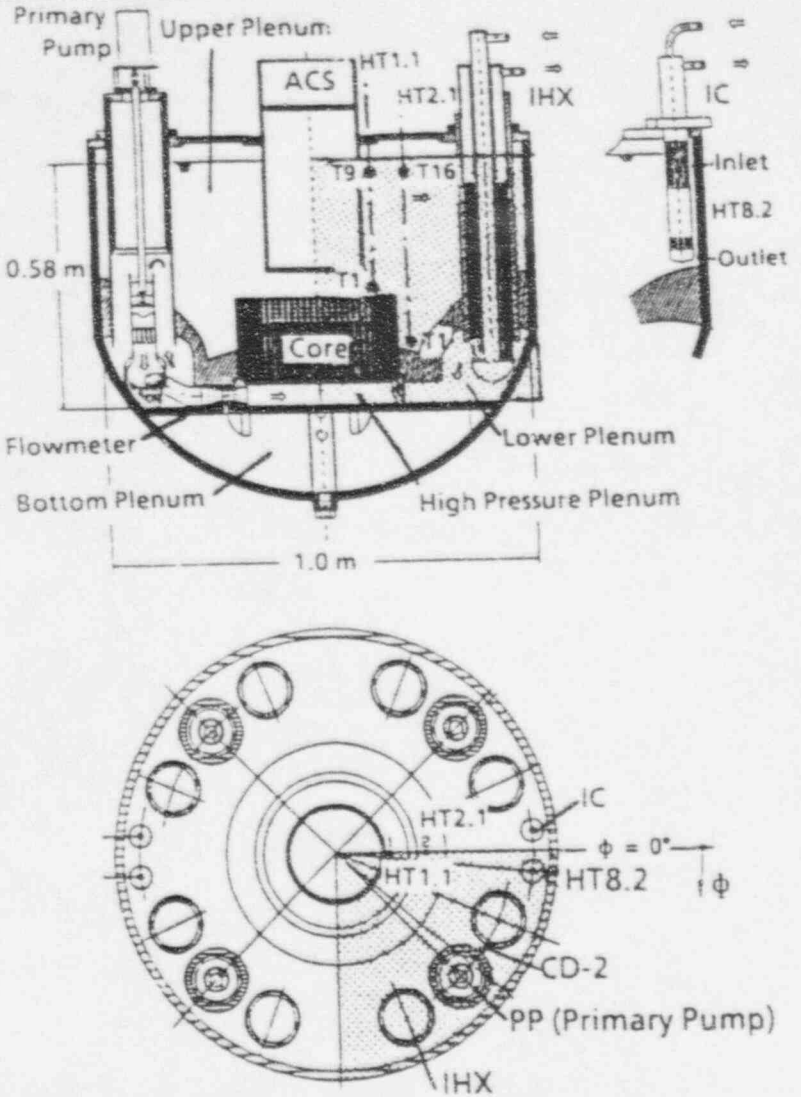

FIG 1. RAMONA SCHEMATIC AND LAYOUT OF THERMOCOUPLE TREES

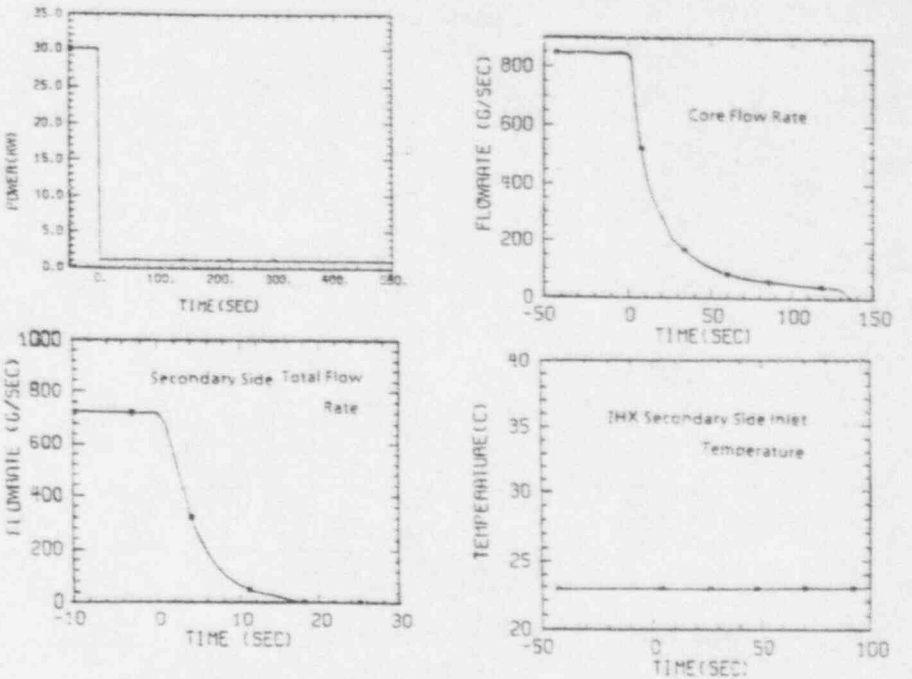

FIG 2. CORE POWER, PRIMARY AND SECONDARY FLOWS AND SECONDARY INLET TEMPERATURE INPUTS.

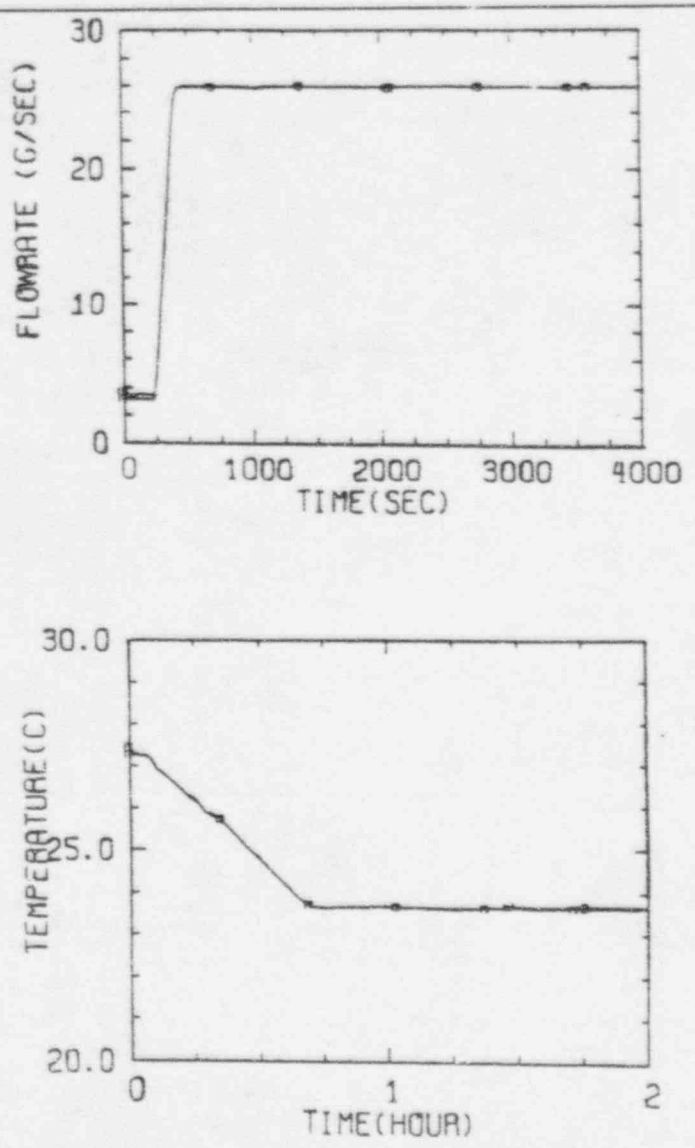

FIG 3. IMMERSION COOLER OPERATING CONDITIONS

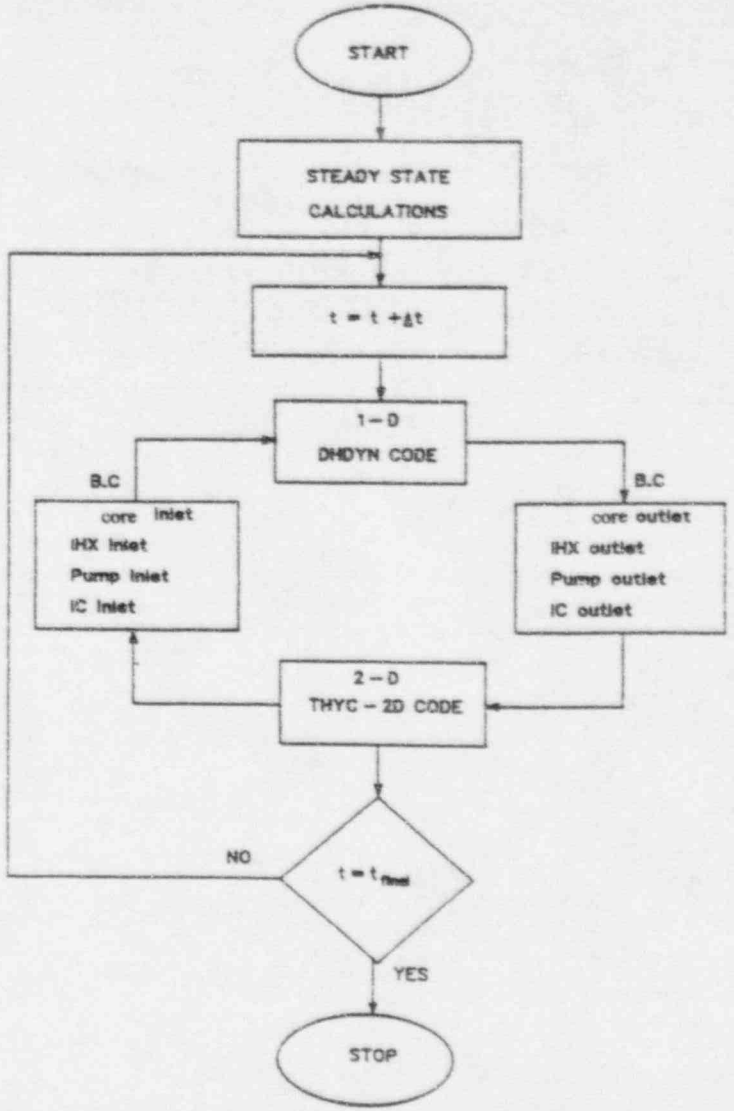

FIG 4. INTERFACING OF DHDYN-1D AND THYC-2D CODES

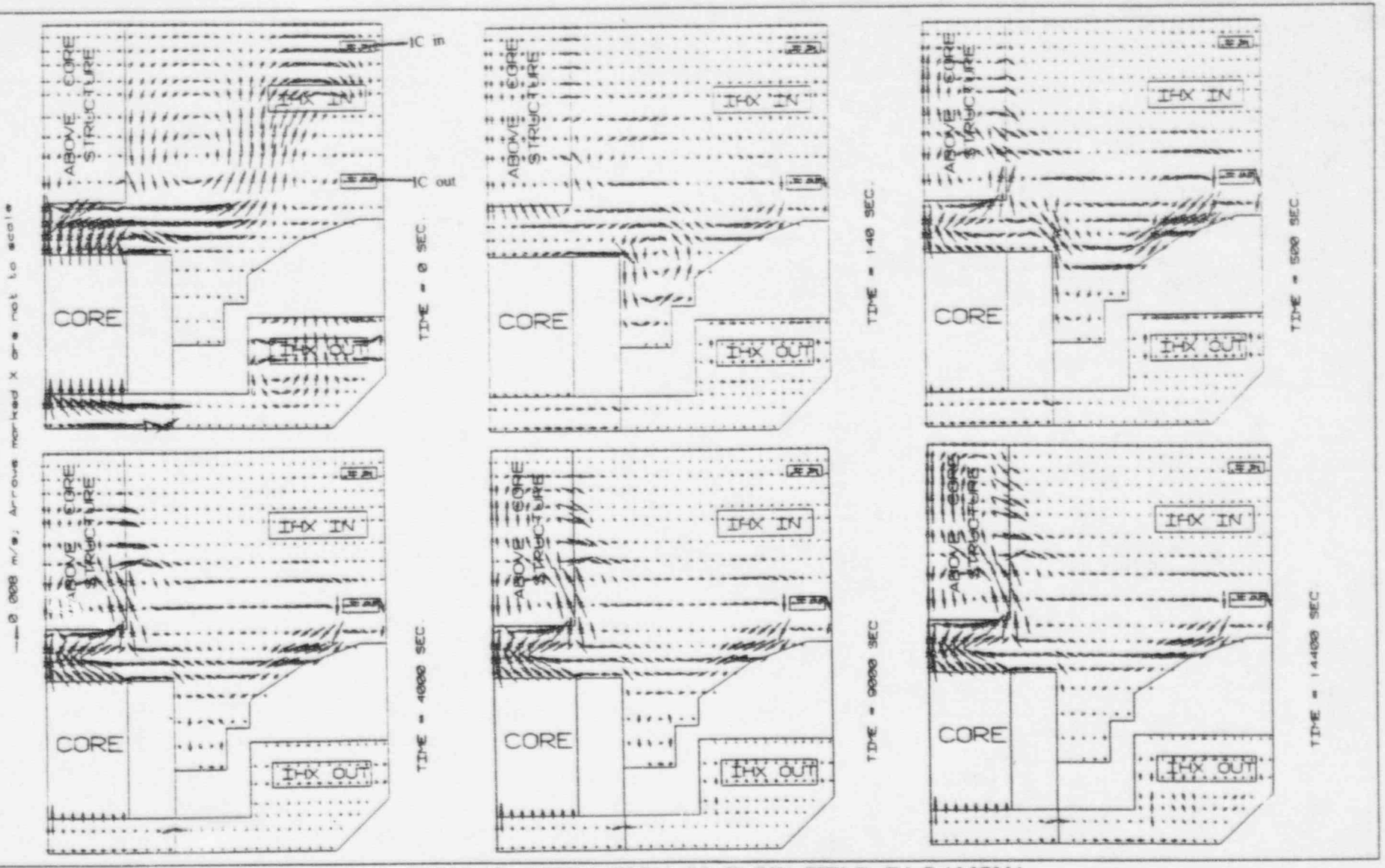

FIG 5. THYC-2D ESTIMATION OF FLOW FIELD IN RAMONA

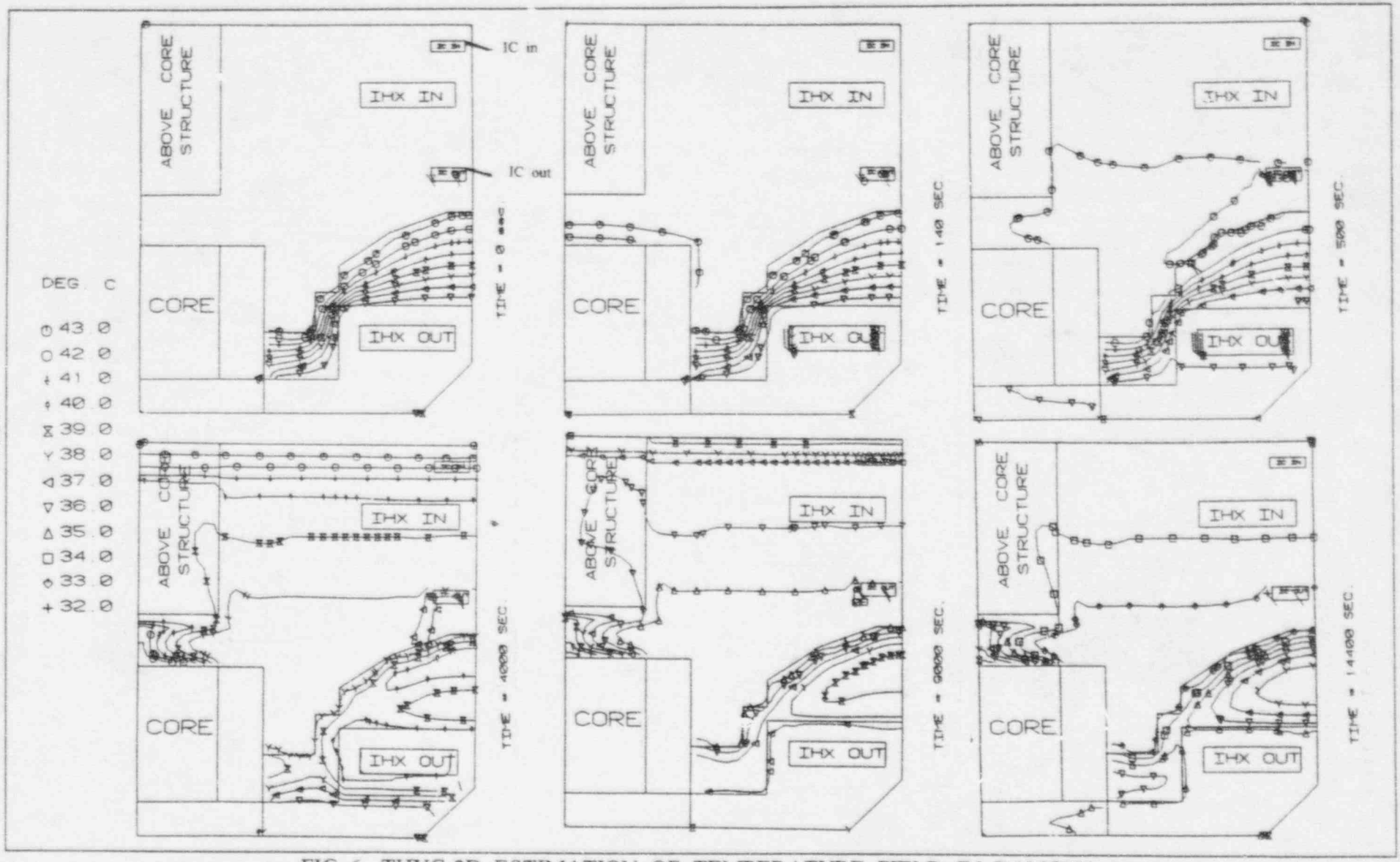

FIG 6 THYC-2D ESTIMATION OF TEMPERATURE FIELD IN RAMONA

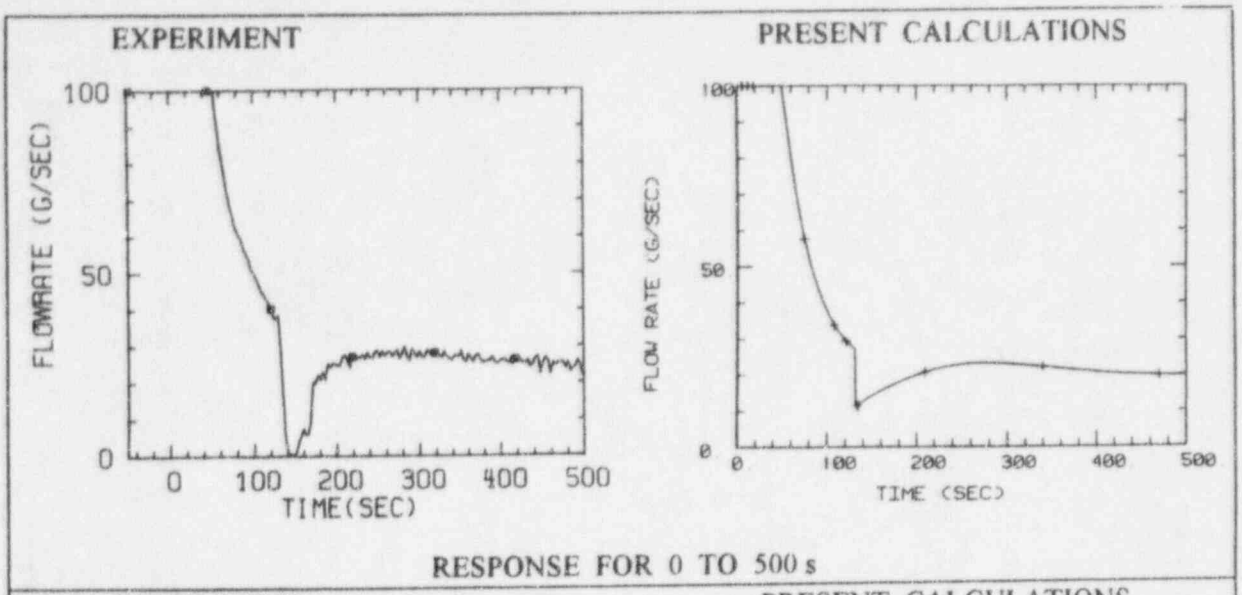

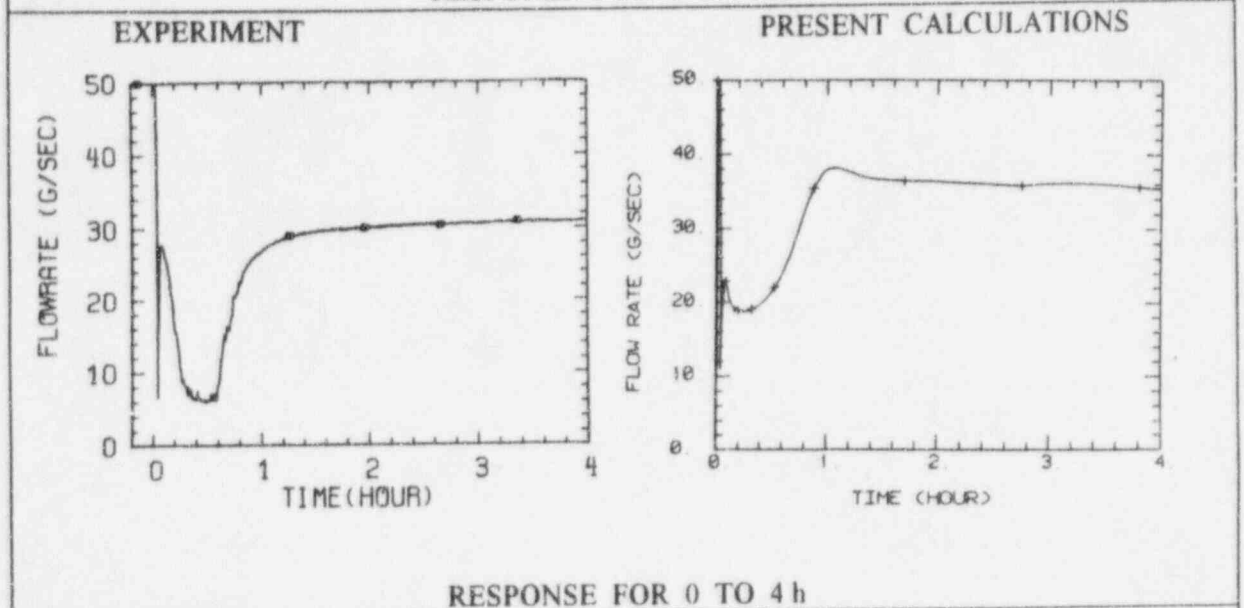

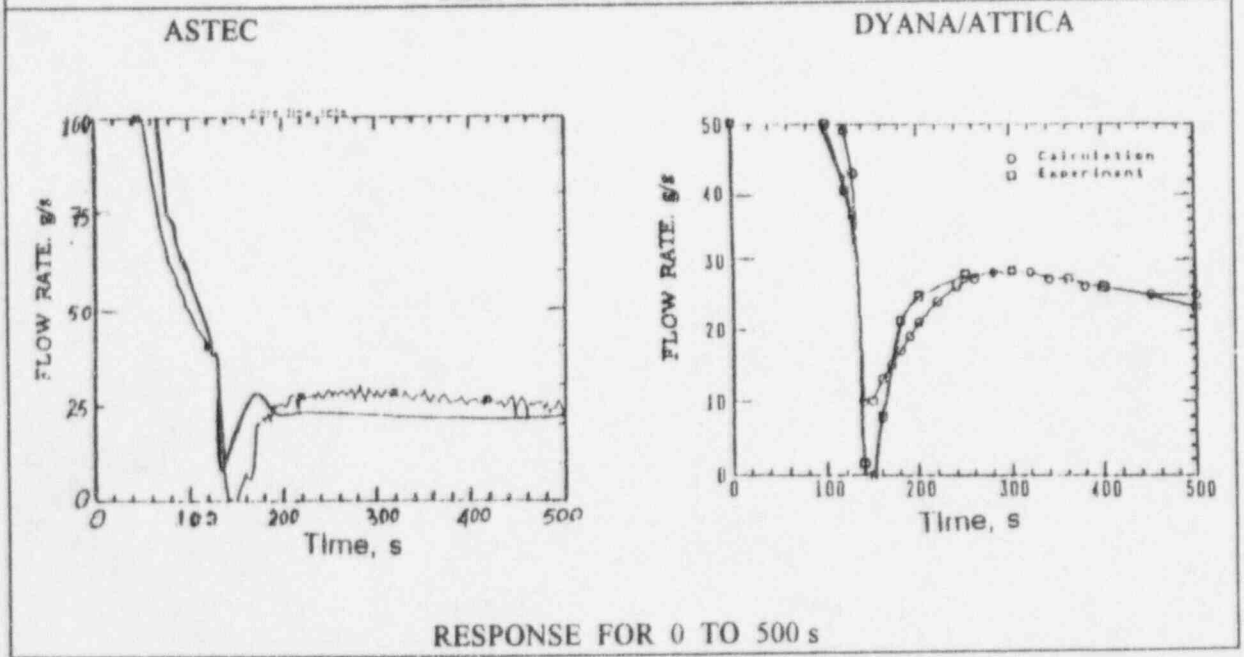

FIG. 7. CORE FLOW RATE COMPARISON

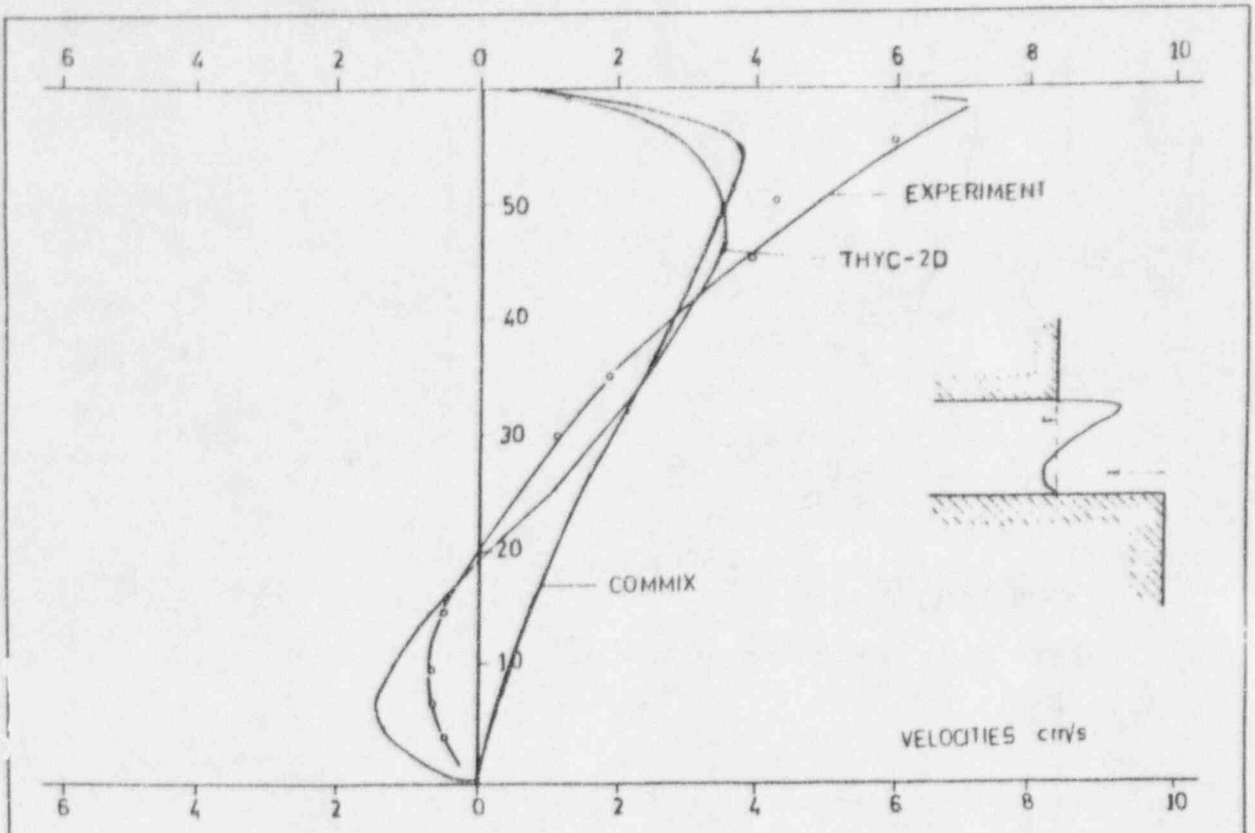

INITIAL STEADY STATE VERTICAL VELOCITY DISTRIBUTION
Radius = 117 mm, Angle = 0 and Power = 30 kW

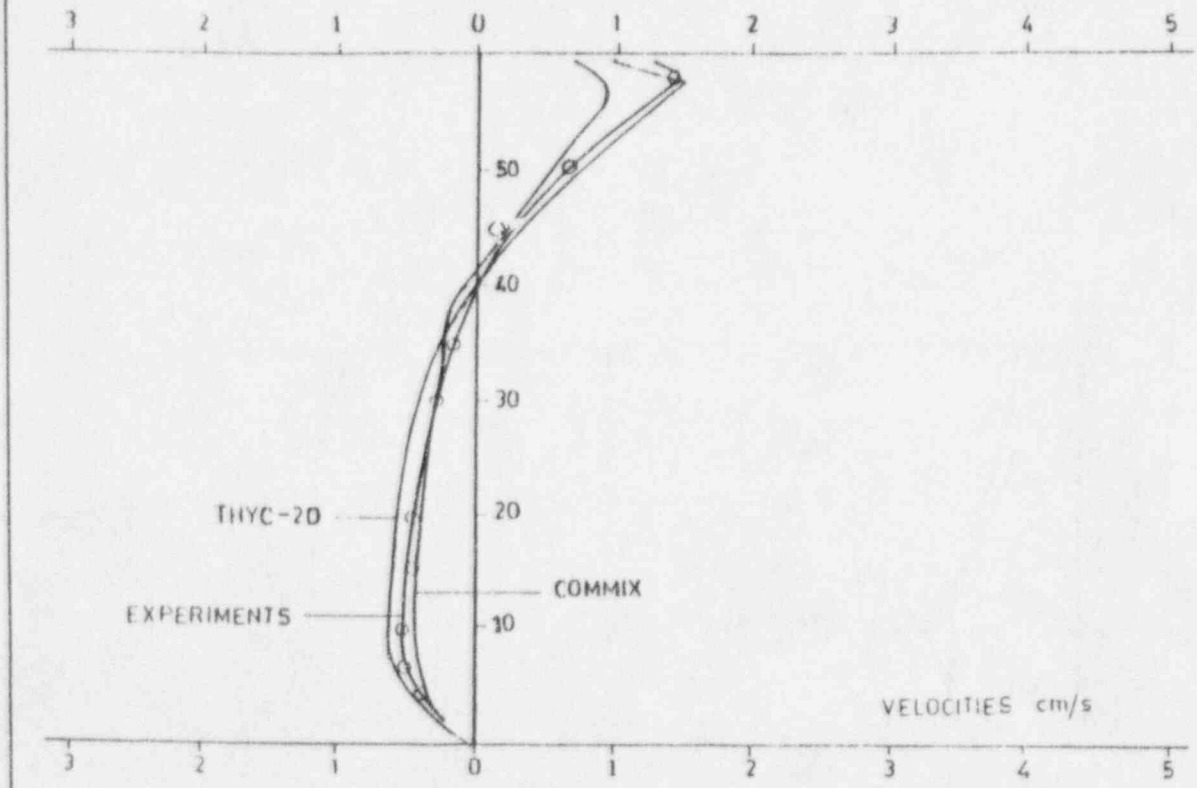

FINAL STEADY STATE VERTICAL VELOCITY DISTRIBUTIONS
Radius = 117 mm, Angle = 60 and Power = 1 kW

FIG. 8 VELOCITY PROFILE MEASUREMENTS AND PREDICTIONS

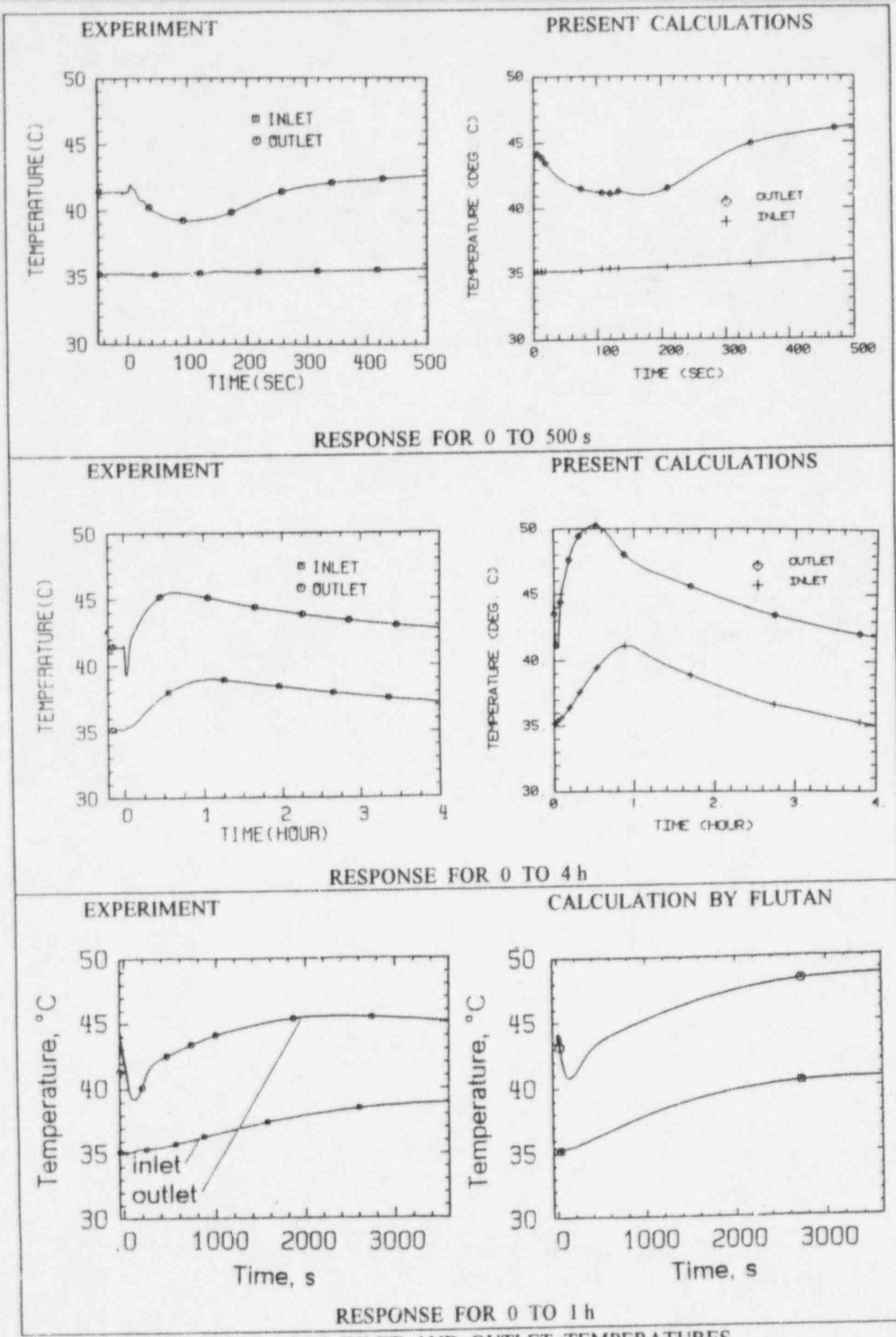

FIG. 9 CORE INLET AND OUTLET TEMPERATURES

EXPERIMENT

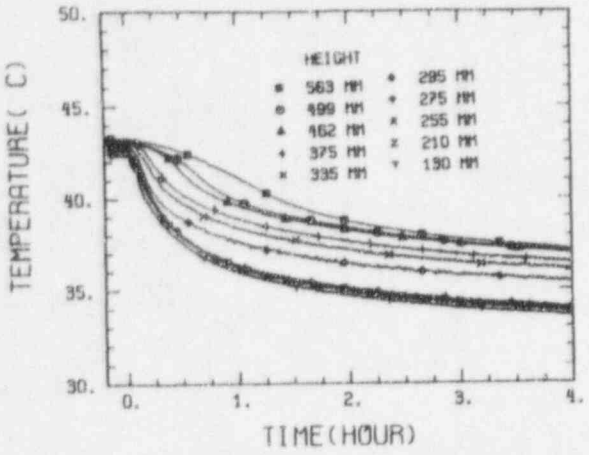

PRESENT CALCULATIONS

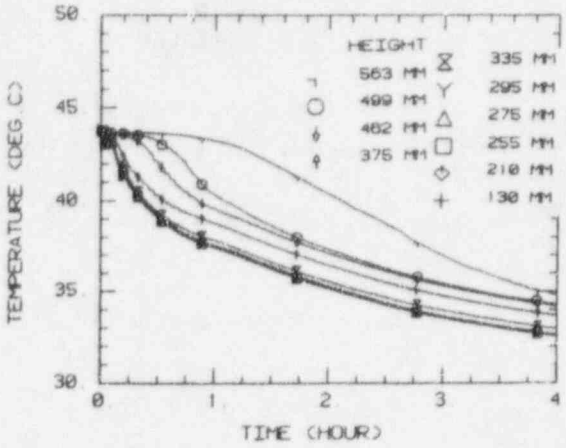

TEMPERATURE COURSES OF HOT PLENUM HT2-1 TREE

EXPERIMENT

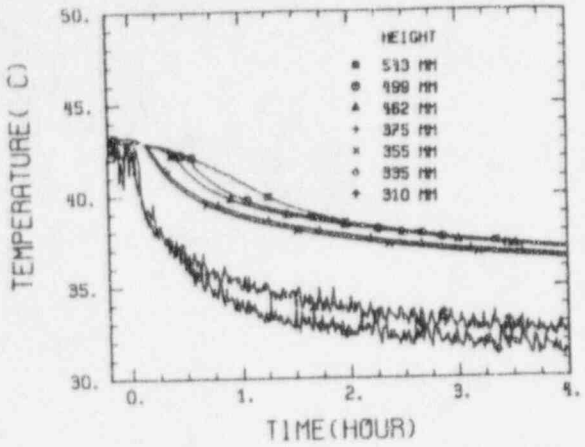

PRESENT CALCULATIONS

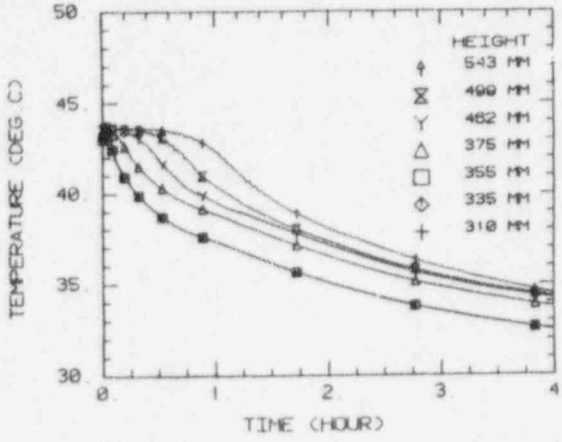

TEMPERATURE COURSES OF HOT PLENUM HT8-2 TREE

COMMIX 2(V) PREDICTIONS

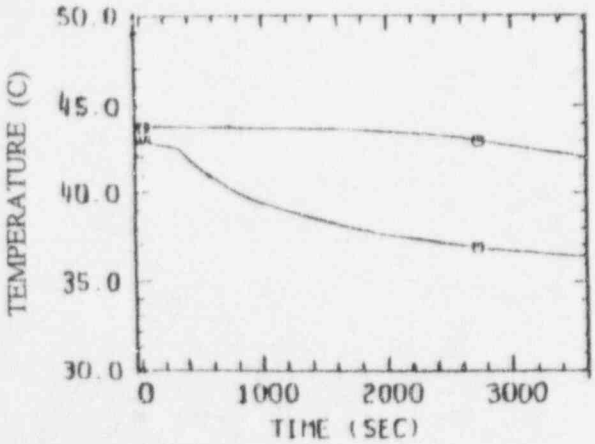

HIGHEST AND LOWEST TEMPERATURES OF VERTICAL TRAVERSE HT2-1

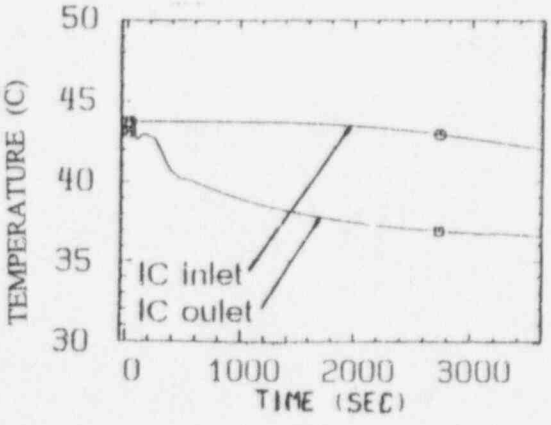

TEMPERATURES NEAR THE INLET AND OUTLET OF THE IMMERSION COOLERS

FIG. 10. HOT POOL TEMPERATURES

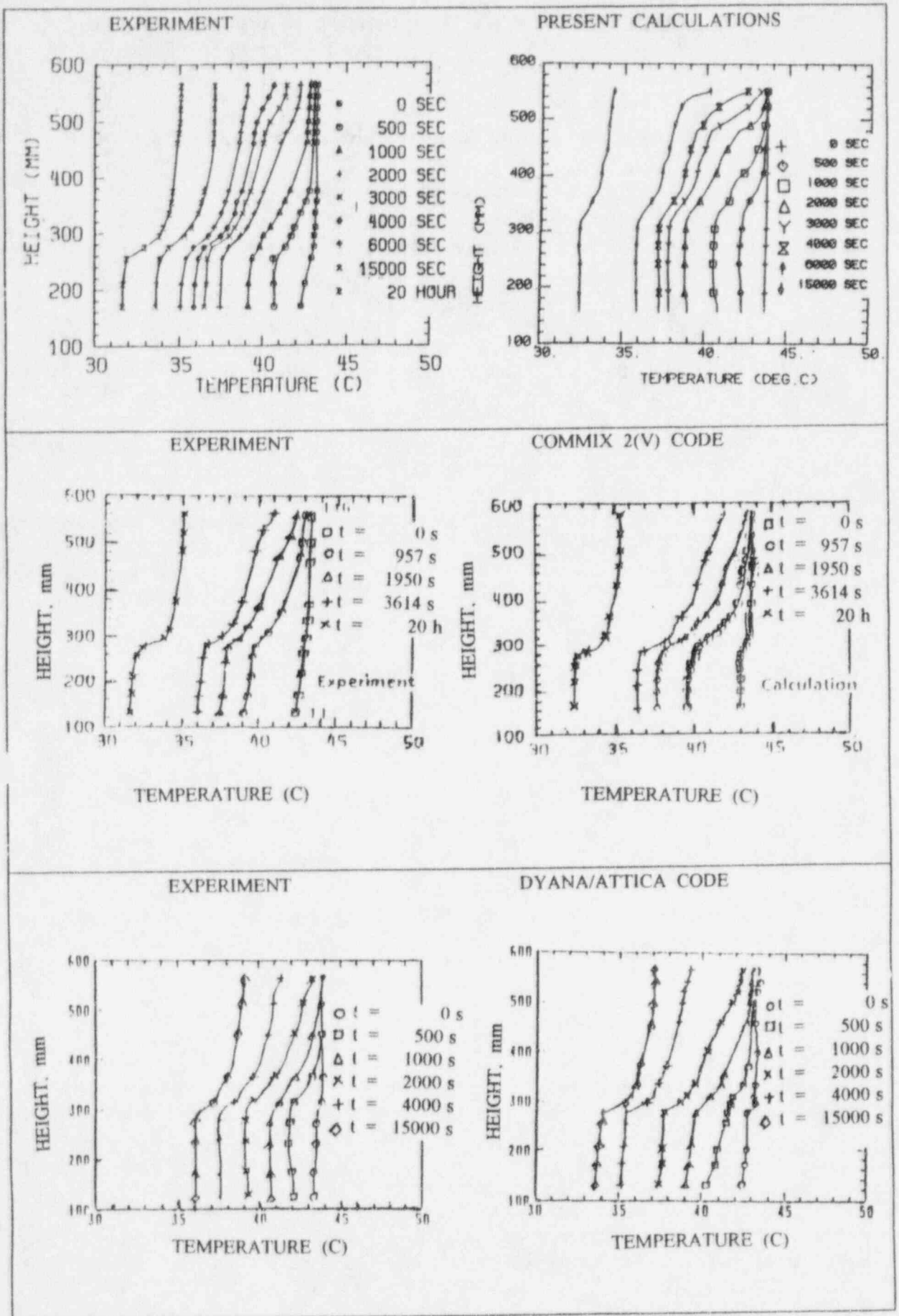

FIG. 11. VERTICAL TEMPERATURE TRAVERSE HT2-3

CONJUGATE HEAT TRANSFER ANALYSIS OF MULTIPLE ENCLOSURES IN PROTOTYPE FAST BREEDER REACTOR

K.Velusamy, V.Balasubramanian, G.Vaidyanathan and S.C.Chetal

Nuclear Systems Division
Indira Gandhi Centre for Atomic Research
Kalpakkam - 603102 , INDIA

ABSTRACT

Prototype Fast Breeder Reactor (PFBR) is a 500 MWe sodium cooled reactor under design. The main vessel of the reactor serves as the primary boundary. It is surrounded by a safety vessel which in turn is surrounded by biological shield. The gaps between them are filled with nitrogen. Knowledge of temperature distribution prevailing under various operating conditions is essential for the assessment of structural integrity. Due to the presence of cover gas over sodium free level within the main vessel, there are sharp gradients in temperatures. Also cover gas height reduces during station blackout conditions due to sodium level rise in main vessel caused by temperature rise. This paper describes the model used to analyse the natural convection in nitrogen, conduction in structures and radiation interaction among them. Results obtained from parametric studies for PFBR are also presented.

1.0 INTRODUCTION

PFBR is a pool type sodium cooled fast reactor under design. The reactor assembly is schematically shown in Fig 1. Primary sodium at 380 deg C is pumped into the core and it comes out into the hot pool at a mixed mean temperature of 530 deg C. From the hot pool, sodium enters the shell side of the intermediate heat exchanger (IHX), where it transfers heat to secondary sodium flowing inside the tubes. The secondary sodium in turn transfers heat to water in once through steam generators (SG), to produce steam for running a turbine generator. The primary sodium exits from the IHX at 380 deg C to the cold pool, before being pumped back. The hot and cold pools are separated by the inner vessel. The main vessel (MV) serves as the primary boundary. In the extremely unlikely event of MV failure, sodium is contained by the safety vessel (SV), which is concentric to the MV. The biological shield (BS) is lined with carbon steel liner on the inner surface facing the SV and is cooled by air. The MV is supported by a conical shell on the reactor vault concrete. The junction between the MV and roof slab is a region of large temperature gradient. The gradient is the highest during station blackout, when the sodium temperature in the pool can go as high as 600 deg C. The increased heat flux to the roof slab will raise the temperature of the conical support shell. The temperature

gradients lead to thermal loading of the above structures and are required to assess the structural integrity.

The MV, the SV and the liner form two vertical cylindrical annuli. The annuli are filled with nitrogen. With high temperature of sodium during station blackout (~600 deg C), radiative heat exchange among the structures is quite considerable. The radial temperature drop across the thickness of MV and SV is quite small compared to that in the axial direction and hence the heat transfer in the structures is one dimensional. Within the argon cover gas and nitrogen, natural convection takes place. A schematic of the enclosures is shown in Fig 2. To analyse the interaction of radiation, convection and conduction amongst the structures forming multiple enclosures, a detailed model has been developed and translated into a computer code "SHELL". This code has been linked to a 2-Dimensional thermal hydraulic code THYC-2D[1]. THYC-2D estimates flow and temperature distributions in nitrogen taking the surface temperature of structures estimated by SHELL. It uses Boussinesq approximation to assume the fluid as incompressible and to account for the buoyancy force in the height-wise momentum equation. The code SHELL estimates the radiosity values for various enclosures as well as temperature distribution in the structures taking into account the fluid temperature calculated by THYC-2D. The two codes are used iteratively.

This paper presents an outline of the mathematical model and the results of a 2-Dimensional analysis of flow and temperature in nitrogen and structures during station blackout condition.

2.0 MATHEMATICAL MODEL

2.1 Energy Equation for Structures

The annuli have a small width compared to the diameter and hence the curvature effects are neglected and the analysis is carried out in Cartesian co-ordinates. The surfaces of the structures are gray and diffuse. The energy balance over an elemental length Δx around a point P in a structure, shown in Fig 3, is

$$\left[Kt\frac{dT}{dx}\right]_e - \left[Kt\frac{dT}{dx}\right]_w + h_1(T_{f1} - T_P)\Delta x + h_2(T_{f2} - T_P)\Delta x + \varepsilon_1 H_1 \Delta x + \varepsilon_2 H_2 \Delta x = \varepsilon_1 \sigma T_P^4 \Delta x + \varepsilon_2 \sigma T_P^4 \Delta x \quad (1)$$

where H is the radiant heat flux or irradiation falling on the surface. The subscripts 1 and 2 refer to the two faces of the element which are exposed to different ambient conditions. Also the emissivities of the faces ε_1 and ε_2 could be different. The above equation can be put in finite difference form as

$$a_P T_P = a_E T_E + a_W T_W + (h_1 T_{f1} + h_2 T_{f2})\Delta x - [\varepsilon_1(\sigma T_P^4 - H_1) + \varepsilon_2(\sigma T_P^4 - H_2)]\Delta x \quad (2)$$

where,

$$a_E = \frac{Kt}{\Delta x_e} \quad , \quad a_W = \frac{Kt}{\Delta x_w} \quad \& \quad a_P = a_E + a_W + (h_1 + h_2)\Delta x$$

The radiant heat flux H is related to the radiosity B through the relation[2],

$$B = \varepsilon\sigma T^4 + \gamma H \quad (3)$$

where, γ is the reflectivity. Out of the radiant heat flux H which is falling on the surface, γH is reflected back by the surface and αH is absorbed. Since the surfaces are opaque and gray

$$\gamma H = (1 - \varepsilon)H \quad (4)$$

From eqns.(3) and (4), eqn.(2) reduces to

$$a_P T_P = a_E T_E + a_W T_W + (h_1 T_{f1} + h_2 T_{f2})\Delta x - [\frac{\varepsilon_1}{1-\varepsilon_1}(\sigma T_P^4 - B_1) + \frac{\varepsilon_2}{1-\varepsilon_2}(\sigma T_P^4 - B_2)]\Delta x \quad (5)$$

The RHS of the above equation contains non-linear source term. This has to be linearised to promote convergence as explained by Patankar[3]. Discretisation equations similar to eqn.(5) are derived for all the nodes.

2.2 Evaluation of Radiosities

The radiosity depends on the temperature of the individual surface element, the shape factors of the elemental surface area with respect to all the other elements and the emissivities of the surfaces. Let there be N elemental surface areas which constitute an enclosure. The radiosity of the 'i'th elemental surface at a temperature T_i with emissivity ε_i is,

$$B_i = \varepsilon_i \sigma T_i^4 + (1 - \varepsilon_i)H_i \quad (6)$$

The radiant energy falling on the 'i'th surface is the algebraic sum of individual radiosities, multiplied by appropriate shape factors. Therefore we have,

$$A_i H_i = \sum_{j=1}^{N} B_j A_j F_{j-i} \quad (7)$$

where, F_{j-i} is the shape factor from element 'j' to element 'i'. By reciprocal relation,

$$A_i F_{i-j} = A_j F_{j-i} \tag{8}$$

Substituting eqns.(7) and (8) in eqn.(6),

$$B_i = \varepsilon_i \sigma T_i^4 + (1-\varepsilon_i) \sum_{j=1}^{N} B_j F_{i-j} \tag{9}$$

This can be rearranged as

$$\sum_{j=1}^{N} B_j \left[\frac{\delta_{ij} - (1-\varepsilon_i) F_{i-j}}{\varepsilon_i} \right] = \sigma T_i^4 \tag{10a}$$

where, Kronecker delta δ_{ij} is 1 if i=j and is zero otherwise. Equation (10a) can be written in matrix form as,

$$[A]\{B\} = \{\sigma T^4\} \tag{10b}$$

Equation set similar to (10b) are derived for each enclosure viz. MV-SV annulus, SV-liner annulus and sodium free level-roof slab enclosure. In eqn.(10b), the coefficient matrix $[A]$ is only a function of surface emissivity and shape factors. Hence once $[A]$ is calculated, its inverse $[A]^{-1}$ can be calculated and kept stored once for all. Then for any set of surface temperature $\{T\}$ the radiosity can be simply calculated as

$$\{B\} = [A]^{-1}\{\sigma T^4\} \tag{10c}$$

2.3 Evaluation of Shape Factors

From first principles, the shape factor from surface 'i', arbitrarily oriented to surface 'j' (see, Fig 4) is given by

$$F_{i-j} = \frac{1}{A_i} \int_{A_j} \int_{A_i} \frac{Cos\beta_i \; Cos\beta_j \; dA_i \, dA_j}{\pi r^2} \tag{11}$$

Application of Stoke's theorem to convert the surface integrals into contour integrals, as detailed by Sparrow and Cess [2], leads to

$$F_{i-j} = \frac{1}{2\pi A_i} \oint_{C_j} \oint_{C_i} \left[\ln(r) dx_i dx_j + \ln(r) dy_i dy_j + \ln(r) dz_i dz_j \right] \tag{12}$$

where, x, y and z are respectively horizontal, vertical and depth-wise directions. Analytical expressions for shape factors are available only for elements sharing a common edge and elements facing each other[2]. For other cases they have to be numerically evaluated. In the present 2-D analysis, the depth-wise direction is, theoretically, of infinite length. However, for the numerical evaluation of the shape factors, it

is taken sufficiently long, but finite, compared to the lateral dimensions. As a cross-check, the total sum of the shape factors $(\sum_j F_{i-j})$ from any element 'i', to all the surrounding elements 'j' was evaluated and found to be very close to unity. Typically about 200 steps in the z-direction was needed when the elements concerned do not share a common edge and about 1000 steps was needed when they share a common edge.

2.4 Governing Equations for Fluid Flow

The conservation equations of mass, momentum and energy for a laminar, viscous, incompressible and Newtonian flow (of nitrogen)in 2-Dimensional Cartesian co-ordinates are:

Mass:

$$\frac{\partial}{\partial x}(\rho u) + \frac{\partial}{\partial y}(\rho v) = 0 \tag{13}$$

Momentum:

$$\frac{\partial}{\partial x}(\rho u^2) + \frac{\partial}{\partial y}(\rho uv) = -\frac{\partial P}{\partial x} + \frac{\partial}{\partial x}(\mu\frac{\partial u}{\partial x}) + \frac{\partial}{\partial y}(\mu\frac{\partial u}{\partial y}) \tag{14}$$

$$\frac{\partial}{\partial x}(\rho uv) + \frac{\partial}{\partial y}(\rho v^2) = -\frac{\partial P}{\partial y} + \frac{\partial}{\partial x}(\mu\frac{\partial v}{\partial x}) + \frac{\partial}{\partial y}(\mu\frac{\partial v}{\partial y}) + \rho g\beta(T_f - T_{fr}) \tag{15}$$

Energy:

$$\frac{\partial}{\partial x}(\rho C_p u T_f) + \frac{\partial}{\partial y}(\rho C_p v T_f) = \frac{\partial}{\partial x}(K\frac{\partial T_f}{\partial x}) + \frac{\partial}{\partial y}(K\frac{\partial T_f}{\partial y}) \tag{16}$$

In eqns.(13)-(16), Boussinesq approximation is invoked to treat the fluid as incompressible and to account for the buoyancy force in the height-wise momentum eqn.(15). The density ρ is evaluated at the reference temperature T_{fr}. In eqns.(14) and (15), the non- gravitational pressure P = p + ρgy, where p is the thermodynamic pressure.

3.0 COMPUTER CODES

3.1 SHELL

The formulations given in sec. 2.1-2.3 have been converted into a computer program SHELL. The program consists of two parts.

The first part calculates the emissivity-shape factor matrix $[A]$ for each enclosure and its inverse $[A]^{-1}$. The enclosing surfaces are broken into a predetermined number of

elemental surfaces. For example, the annulus between MV and SV is broken into 76 elemental surfaces, with 26 each on MV and SV and 12 each on Baffle-2 and annulus bottom. This part need to be executed only once as the coefficients of $[A]$ are constants.

The second part determines the temperature distribution in the shells/structures forming the enclosures. It first calculates tentative radiosity values $\{B\}$,for various enclosures, using the appropriate $[A]^{-1}$ and the assumed initial temperature distribution in the structures. Once the tentative values of $\{B\}$ are known, the discretisation equation set (5), for each structure (such as MV, SV, liner etc., see Fig 2) is formed. These equation sets are solved by Thomas algorithm [3]. Since eqn.(5), is non-linear, iteration is necessary. This inner iteration is repeated till the absolute sum of the residues in the discretisation equations is less than 10^{-3} for each structure. With these fresh temperatures of the structures, fresh radiosity values are evaluated. For these fresh radiosity values, again the structural temperatures are calculated . This outer iteration is continued till the normalised change in the structural temperature is less than 10^{-5} .

3.2 THYC-2D

THYC-2D solves eqns.(13)-(16), to find out the flow and temperature distributions in nitrogen, by the control volume based discretisation method [3]. It uses a staggered grid arrangement, wherein the velocity components are stored at the faces of the control volumes while the pressure and temperature are stored at the centre of the control volumes. To resolve the Pressure-Velocity coupling , it employs the SIMPLE algorithm [3]. It uses the Upwind scheme for combining the convective and diffusive fluxes, during the process of deriving the discretisation equations. The discretisation equations are solved by Thomas algorithm, employing 2-directional sweep [3]. Convergence is declared once the normalised absolute sum of the residues in the discretisation equations reduces below 10^{-5}

3.3 Boundary Conditions and Coupling of THYC-2D and SHELL

For the calculation of temperature distribution in the structures, SHELL uses the fluid temperatures, T_f, estimated by THYC-2D. For the specification of boundary condition on the liner, which is surrounded by the biological shield concrete and the shield cooling air coil, a 1-Dimensional radiation-conduction model (which considers the heat transfer in the concrete as purely radial) is used. similar 1-D models are adopted for the specification of boundary conditions in the radial gap between roof slab and MV and in the axial gap

between baffle-2 and roof slab bottom. The temperature distribution in the sodium pool during DHR condition is taken from 1-Dimensional study [4], involving modelling of reactor core, hot and cold pools, decay heat removal system etc.

In THYC-2D, no slip boundary condition is used for the velocity components on the solid surfaces. For the calculation of temperature distribution in nitrogen space, the structural temperatures calculated by SHELL are used as boundary conditions. The program SHELL is incorporated as a subroutine in THYC-2D and is called during each iteration of THYC-2D.

It may be highlighted here that the convective motion of argon cover gas has been accounted by specifying appropriate heat transfer coefficient and bulk argon gas temperature.

4.0 COMPUTATIONAL DETAILS

A 28*28 non-uniform grid pattern was used in THYC-2D for the estimation of nitrogen flow and temperature distributions. Steady state solution was obtained by time marching method. For the calculation of radiosity values, each enclosure is divided into 76 elemental surfaces, compatible with the grid employed in THYC- 2D. The emissivity of sodium and that of structures exposed to sodium are taken as 0.05 and 0.2 respectively based on the experimental results of Furukawa et al.[5]. Emissivity of surfaces exposed to nitrogen is taken as 0.6 [6]. The heat transfer coefficient of argon was taken as 10 W/m^2K In fact, no significant change in the temperature was observed when it was reduced to 5 W/m^2 K.

5.0 RESULTS AND DISCUSSION

5.1 Detailed Model

The stream lines and isotherms of nitrogen, within the annuli are shown in Figs 5 and 6. The axial temperature distribution in the MV, SV and the innermost liner are shown in Fig 7. During DHR condition, the sodium pool is stratified. This is reflected in the isotherms of nitrogen in the annuli. Above the sodium free level (11 m), MV is exposed to cover gas at a temperature of 475 deg C. Above baffle-1, it sees roof slab at a temperature of 120 deg C. This leads to a reduction of MV temperature from sodium free level to MV-roof slab junction. This situation of cold temperature above hot temperature establishes natural convection in nitrogen. The left leg (adjacent to MV) of the natural convection loop is deeper than the right leg (adjacent to SV). This is because, above the sodium level, SV temperature is higher than that of MV. This is due to the fact that MV is cooled by argon cover gas and roof shell while such phenomena are absent in the case of SV. The SV primarily looses the heat, it acquires by

radiation from hot regions of MV, by re- radiating to the cold regions of MV. The axial temperature gradient in the MV, as a function of height, is shown in Fig 8. It can be seen that the gradient is high at sodium free level and at MV-roof slab junction (12.8 m). The numerical value at the sodium free level is 1019 deg C/m while at MV-roof junction it is 1800 deg C/m. The heat flux to roof slab through baffle-2 is estimated as 3070 W/m^2 .

5.2 Simple Model

To reduce the temperature gradient, different geometric arrangements as shown in Fig 9, were studied. The THYC-2D/SHELL combine was found to take large computer time, especially for the convergence of the nitrogen flow field. In order to assess the importance of natural convection, the program SHELL was used to find the heat flux and temperature distribution by

(i) completely neglecting natural convection of nitrogen and

(ii)accounting natural convection in a simplified way using a bulk heat transfer coefficient and nitrogen temperature, referred to as 'simple model'.

The MV temperature distribution above sodium level, obtained from detailed as well as simplified models are shown in Fig 10, for the reference case, i.e. case-1. It can be seen that the temperature gradients predicted by the various models are quite close. Such a comparison was carried out for case-2 also and similar conclusions were arrived at.

The temperature distribution in MV, above sodium free level, predicted by the 'simple model', is shown in Figs 11 and 12, for different cases. The salient results are presented in Table-1. The major findings of the study for different geometric arrangements are as follows:

- Removal of baffle-1 increases the temperature gradient of MV at sodium free level by 250 deg C/m.
- Removal of baffle-2 reduces the temperature gradient at MV-roof slab junction by about 270 deg C/m. But it increases the heat flux to roof slab through baffle-2 by 2300 W/m^2 .
- Removal of insulation between MV and roof slab shell increases heat exchange between MV and roof slab, the roof shell being maintained at 120 deg C. Because of this, the temperature of MV in the top region reduces. This leads to a reduction in the temperature gradient at MV-roof slab junction by ~250 deg C/m and the heat flux through baffle-2 by ~350 W/m^2 .

As already mentioned, in MV, temperature is the maximum at sodium free level and hence the temperature gradient around this region should be as low as possible. It is also preferred to have low temperature gradient near MV-roof slab junction. Moreover, the heat flux to roof slab through baffle-2 should

be as low as possible. Based on these considerations, the geometry of case-2 is the optimum one.

6.0 SUMMARY

This paper has highlighted the details of the methodology adopted to analyse conjugate heat transfer in multiple enclosures with application to the Prototype Fast Breeder Reactor. The iterative use of two codes SHELL and THYC-2D has been explained. The computer time has been optimised by adopting a simplified model, grossly accounting natural convection of nitrogen, without affecting the results and hence the conclusions. Effects of different geometry, with and without insulation, on the temperature gradients in the main vessel and heat flux to roof slab have been brought out. It has been found that case-2 provides a good compromise between temperature gradient in main vessel and heat flux to roof slab through baffle-2.

REFERENCES

[1]K. Velusamy et al., "Thermal Hydraulic Analysis in the Design of PFBR Inner Vessel," Proc. 4th Int. Conf. on Liquid Metal Engg. and Tech., Avignon, France, 408 (1988).

[2]E.M. Sparrow and R.D. Cess, Radiation Heat Transfer, McGraw-Hill, New York (1978).

[3]S.V. Patankar, Numerical Heat Transfer and Fluid Flow, McGraw-Hill, New York (1980).

[4]N. Kasinathan et al., "Analysis of Decay Heat Removal by Natural Convection in PFBR", Proc. IAEA/IWGFR Specialist Meet on Evaluation of DHR by Natural Convection in Fast Reactors, O-oari, Japan (1993).

[5]O. Furukawa et al., "Experimental Study of Heat Transfer through Cover Gas in LMFBR", Proc. 3rd Int. Conf. on Liquid Metal engg. and Tech., London, England (1984).

[6]J.P. Holman, Heat Transfer, McGraw-Hill, London (1981).

NOMENCLATURE

A_i, A_j	- area of surfaces i and j (m^2)
dA_i, dA_j	- elemental parts of surfaces i and j (m^2)
B	- radiosity (W/m^2)
C_i, C_j	- contour of surfaces i and j (m)
C_p	- specific heat (J/Kg-K)
h	- heat transfer coefficient (W/m^2K)
H	- radiant heat flux (W/m^2)
K	- thermal conductivity (W/m-K)
r	- distance between the elemental surfaces i & j
t	- thickness of the shell (m)
T	- temperature of the shell (K)
T_f	- temperature of the fluid (K)
T_{fr}	- reference temperature of the fluid (K)
u, v	- velocity components in x & y directions (m/s)
x, y, z	- horizontal, vertical & depth-wise co-ordinates
α	- absorptivity of the surface
β	- coefficient of volumetric expansion (K^{-1})
β_i	- angle between the surface normal of dA_i and the line connecting dA_i and dA_j
β_j	- angle between the surface normal of dA_j and the line connecting dA_j and dA_i
ε	- emissivity of the surface
μ	- viscosity of nitrogen ($N-s/m^2$)
ρ	- density of nitrogen (Kg/m^3)
σ	- Stefan-Boltzmann constant (W/m^2K^4)
γ	- reflectivity of the surface

Table-1: Results of Parametric study by simple model

Case	Temp. grad. at MV-roof junction (deg.C/m)	Temp. grad. at sodium free level (deg.C/m)	Heat flux to roof slab through Baffle-2 (W/m^2)
Case-1	1800	1019	3070
Case-2	1488	1045	2716
Case-3	1218	1061	5000
Case-4	1140	1308	4755
Case-5	727	1406	3046
Case-6	800	1349	3720
Case-7	325	1293	5240
Case-8	420	1045	5700
Case-9	633	1273	2755

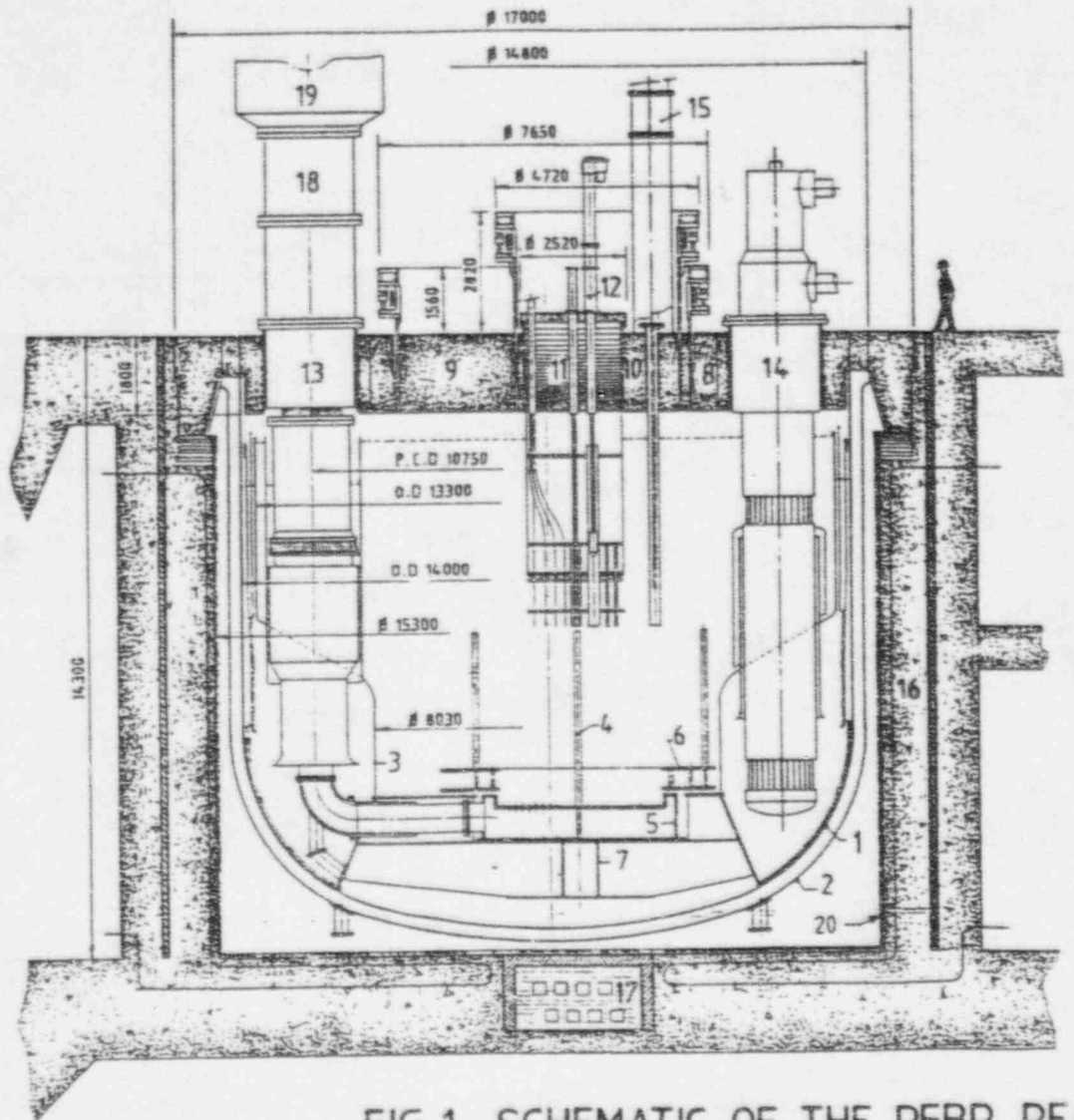

1. MAIN VESSEL
2. SAFETY VESSEL
3. INNER VESSEL
4. CORE SUB-ASSEMBLIES
5. GRID PLATE
6. AUXILIARY GRID PLATE
7. CORE SUPPORT STRUCTURE
8. ROOF SLAB
9. LARGE ROTATABLE PLUG
10. SMALL ROTATABLE PLUG
11. CONTROL PLUG
12. CONTROL ROD DRIVE MECHANISM
13. SODIUM PUMP
14. I.H.X
15. I.V.T.M
16. REACTOR VAULT (BIOLOGICAL SHIELD)
17. NEUTRON DETECTORS
18. FLYWHEEL FOR SODIUM PUMP
19. DRIVE MOTOR FOR SODIUM PUMP
20. LINER & INSULATION

FIG.1 SCHEMATIC OF THE PFBR REACTOR ASSEMBLY

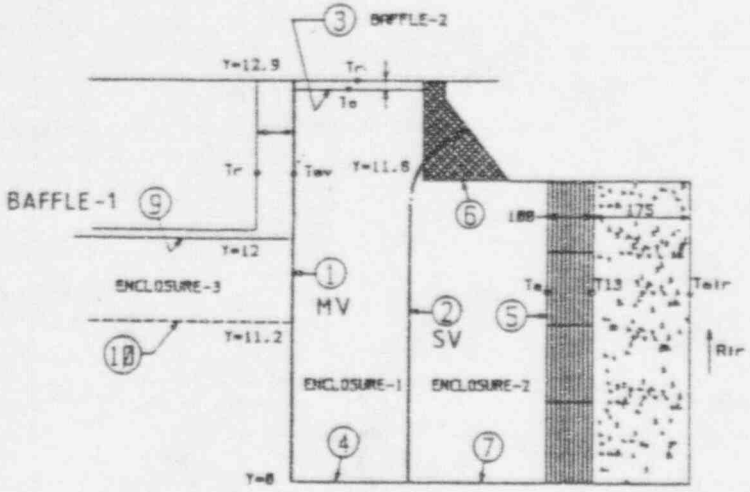

FIG. 2 SCHEMATIC OF THE MODEL

(ENCLOSURES AND SHELL NUMBERS AS USED IN "SHELL")

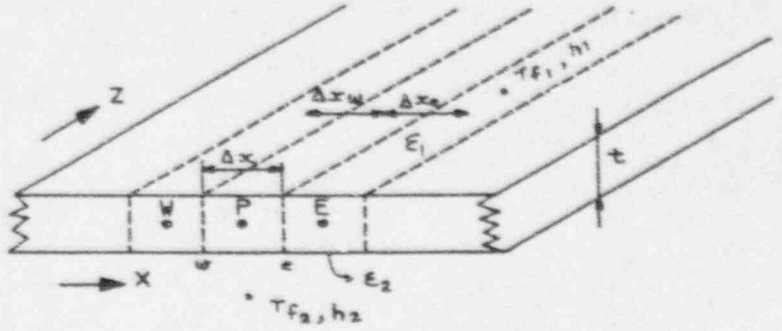

FIG.3 CONTROL VOLUME AND SCHEMATIC OF A SHELL

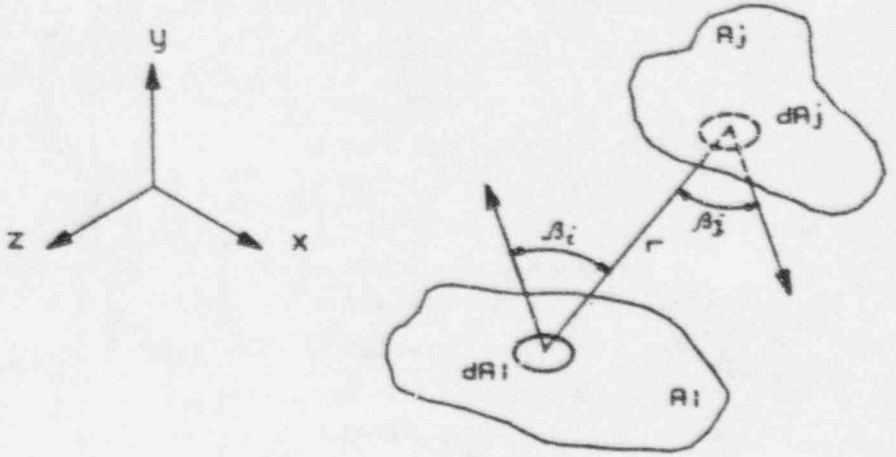

FIG.4 ARBITRARILY ORIENTED SURFACES

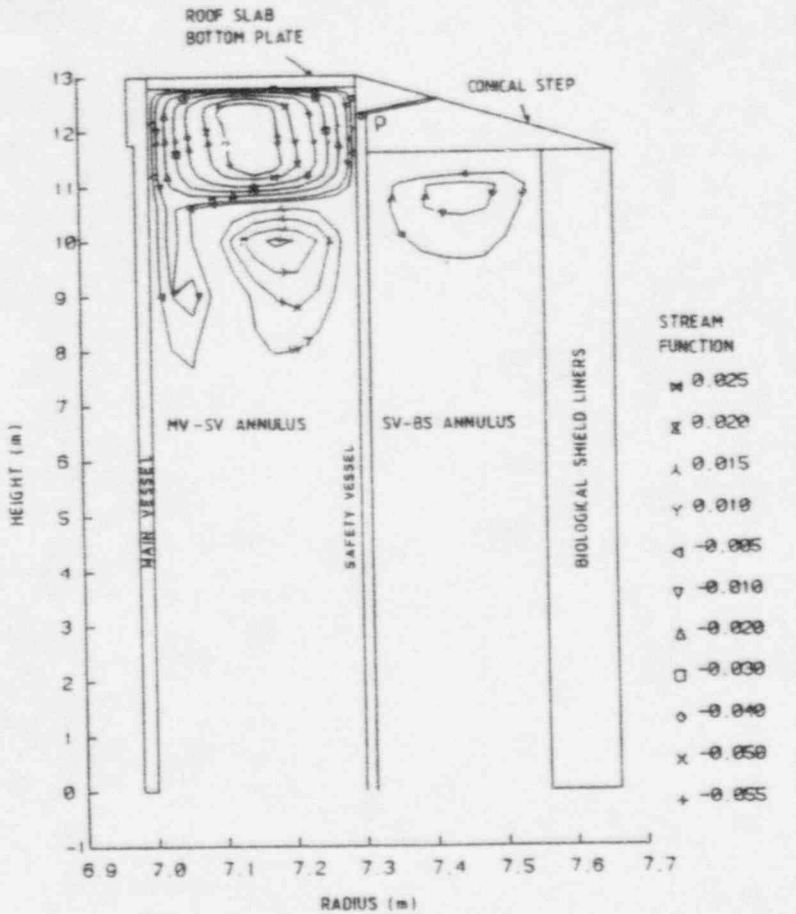

STREAM LINES IN MV-SV-LINER ANNULI

FIG.5

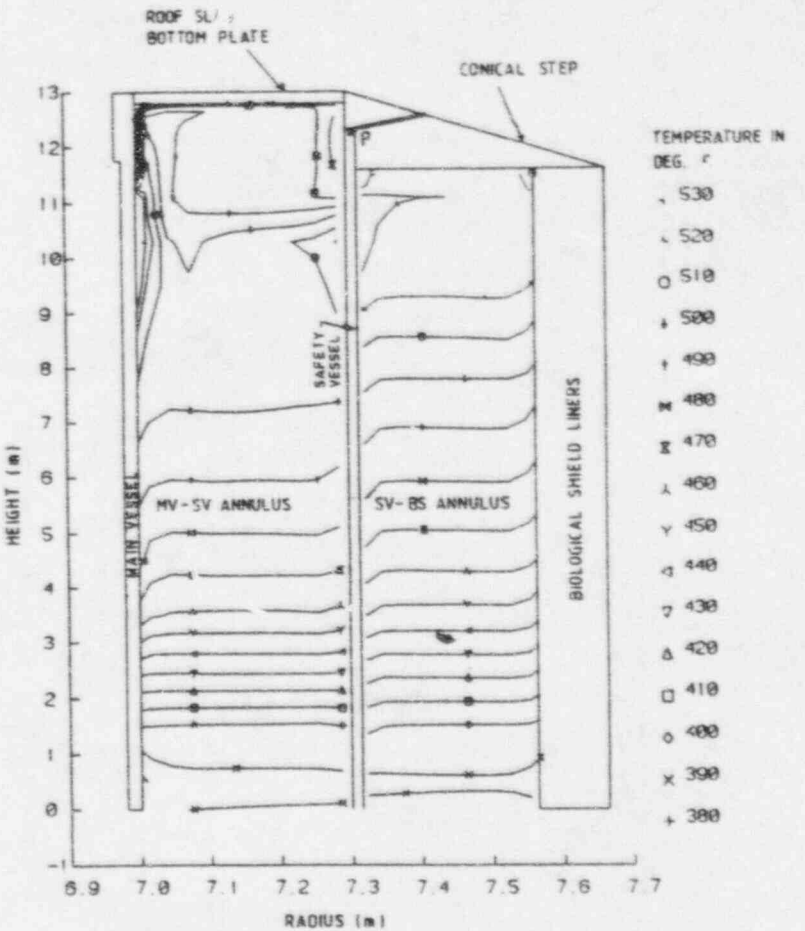

ISOTHERMS IN MV-SV-LINER ANNULI

FIG. 6

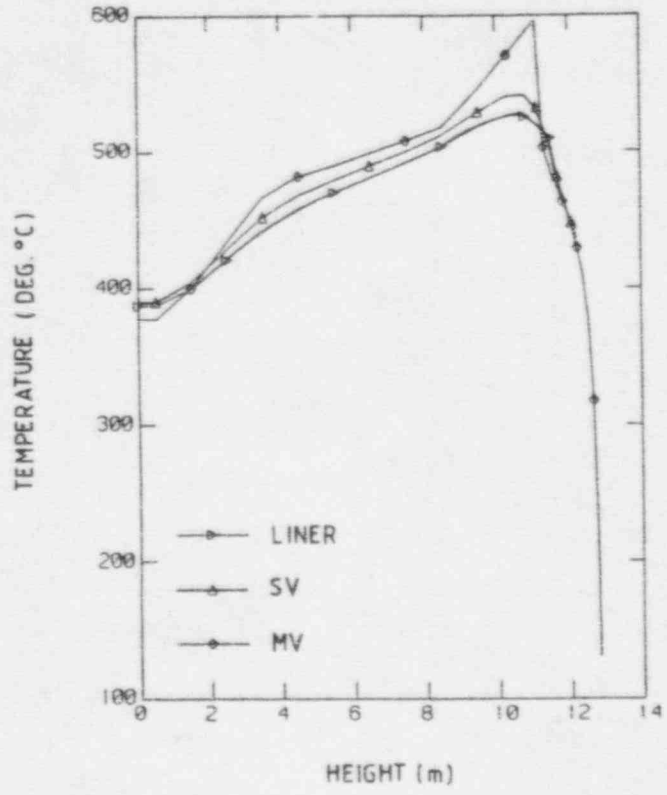

AXIAL TEMPERATURE DISTRIBUTION IN THE VESSELS

FIG. 7

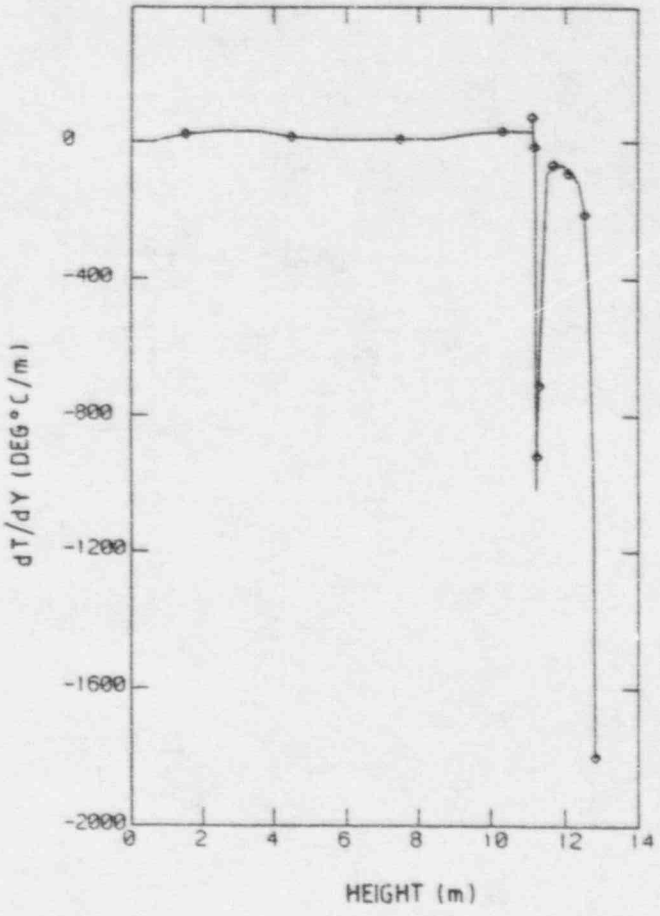

AXIAL TEMPERATURE GRADIENT ON M.V

FIG. 8

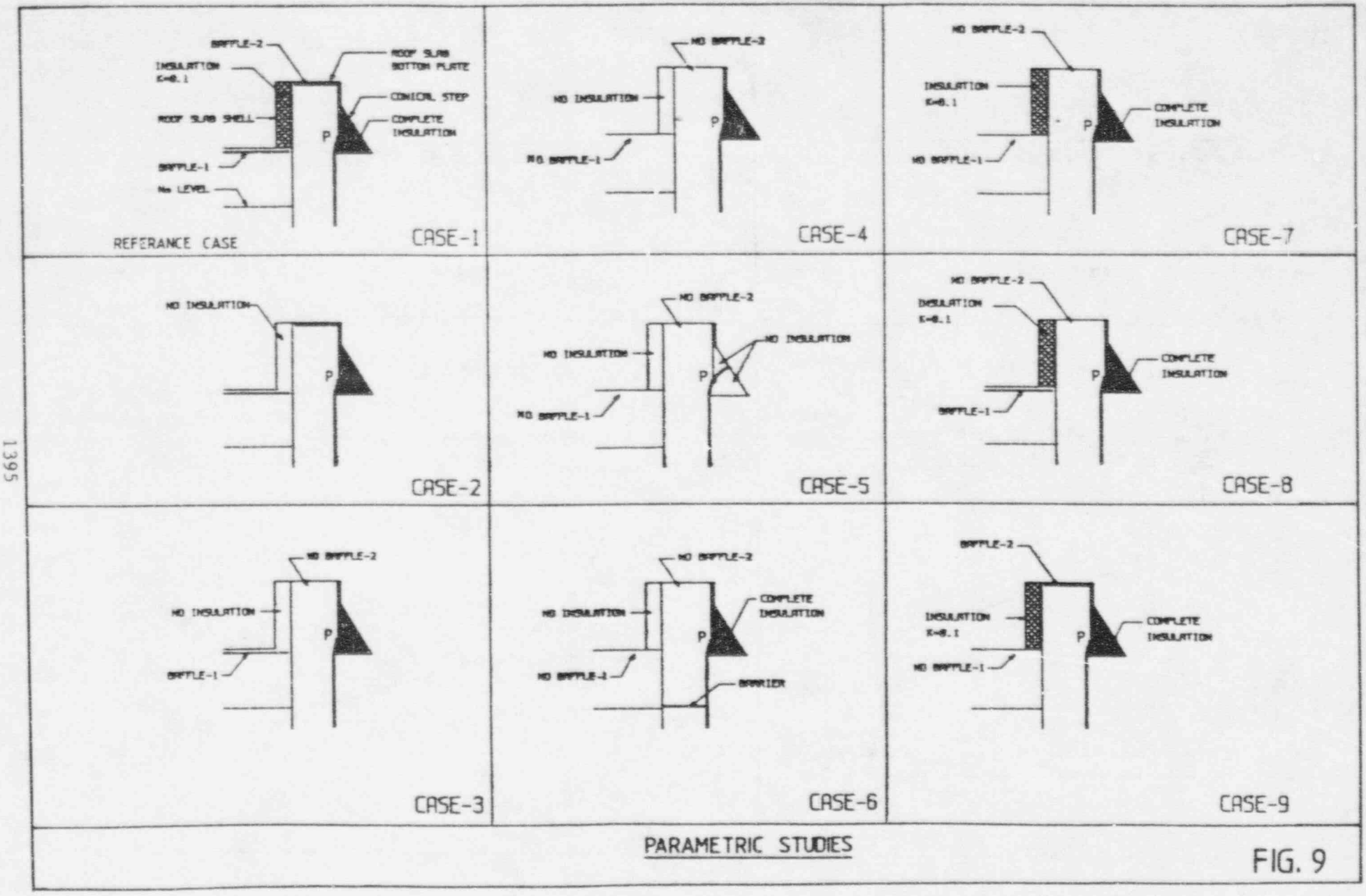
BAFFLE-2
ROOF SLAB BOTTOM PLATE
INSULATION K=0.1
CONICAL STEP
ROOF SLAB SHELL
COMPLETE INSULATION
P
BAFFLE-1
No LEVEL
REFERANCE CASE
CASE-1
NO BAFFLE-2
NO INSULATION
NO BAFFLE-1
CASE-4
INSULATION K=0.1
CASE-7
NO INSULATION
CASE-2
CASE-5
CASE-8
CASE-3
CASE-6
BARRIER
CASE-9
PARAMETRIC STUDIES
FIG. 9

1395

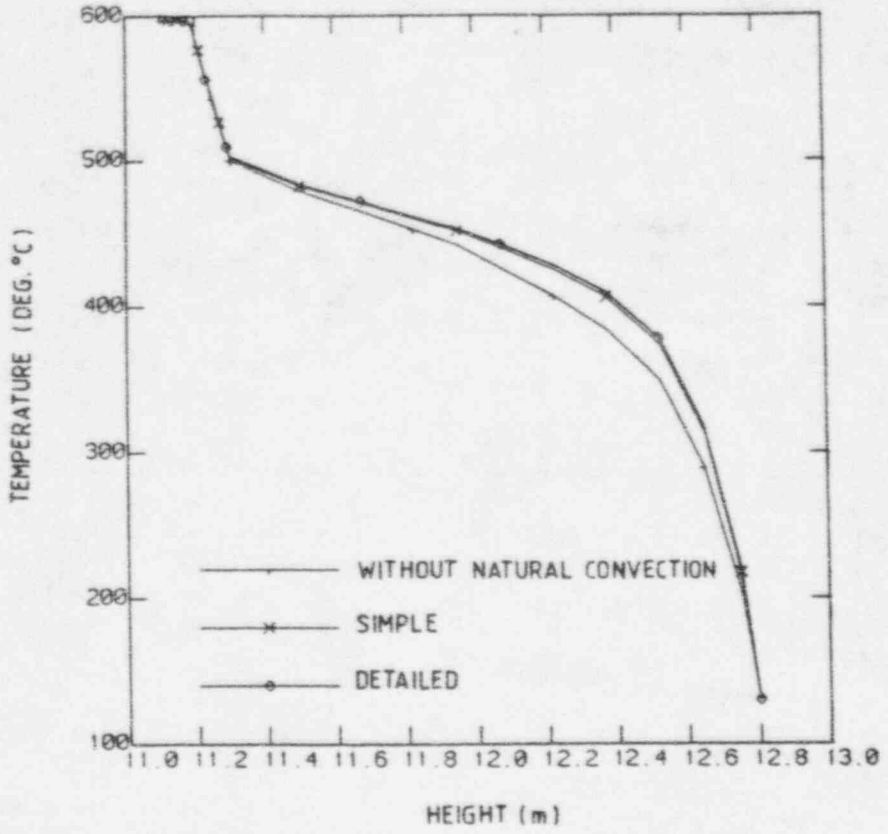

AXIAL TEMPERATURE DISTRIBUTION IN MAIN VESSEL

FIG. 10

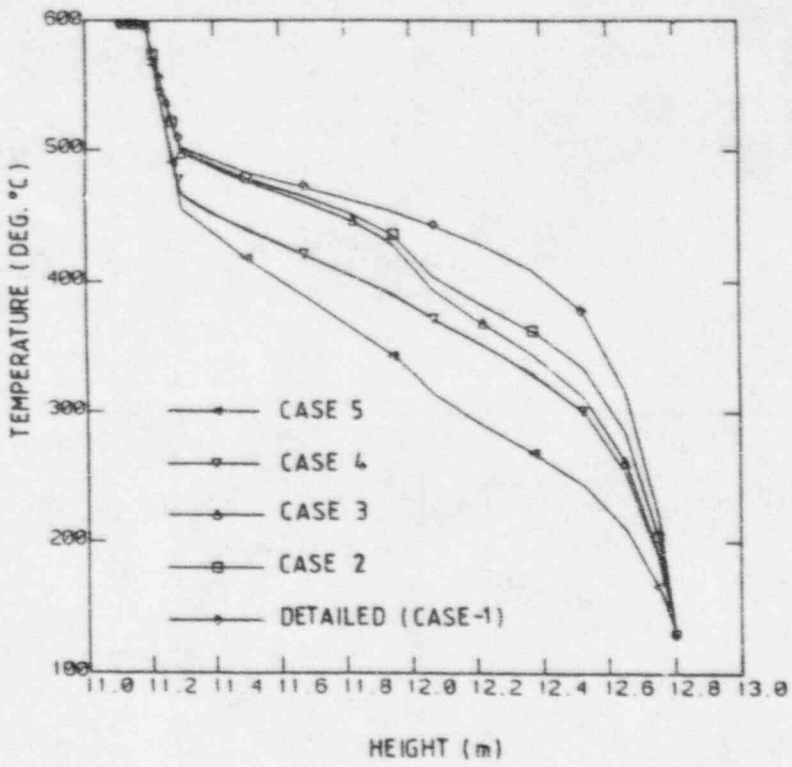

AXIAL TEMPERATURE DISTRIBUTION IN MAIN VESSEL

FIG. 11

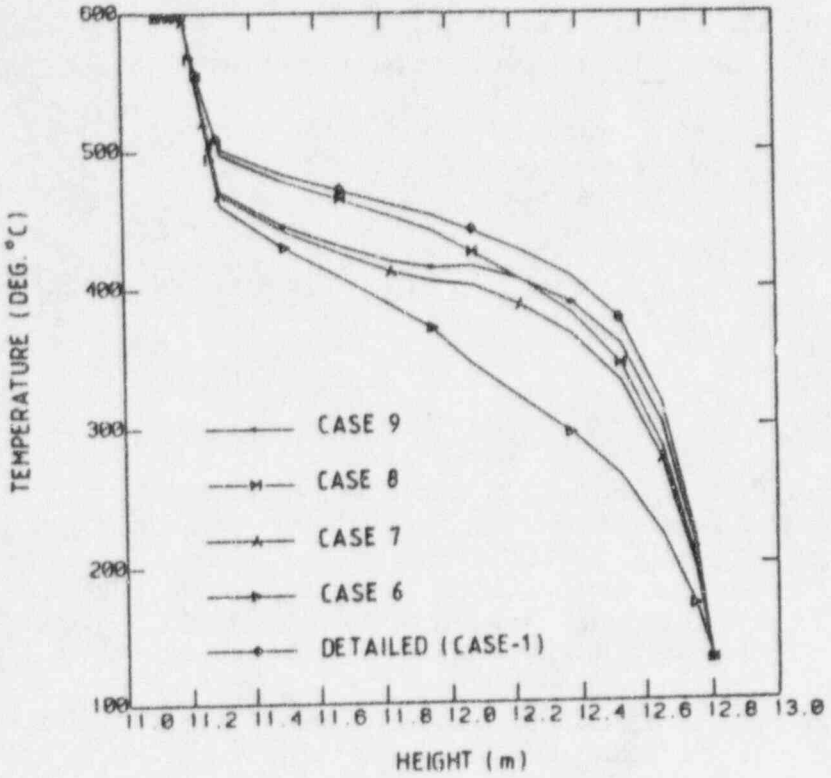

AXIAL TEMPERATURE DISTRIBUTION IN MAIN VESSEL

FIG. 12

Computational Modeling for Hexcan Failure under Core Disruptive Accidental Conditions

T. Sawada, H. Ninokata and A. Shimizu
Research Laboratory for Nuclear Reactors
Tokyo Institute of Technology
2-12-1 O-okayama, Meguro-Ku,
Tokyo 152, Japan
Tel: (+81) 3-5734-3062 Fax: (+81) 3-5734-2959

ABSTRACT

This paper describes the development of computational modeling for hexcan wall failures under core disruptive accident conditions of fast breeder reactors. A series of out-of-pile experiments named SIMBATH has been analyzed by using the SIMMER-II code. The SIMBATH experiments were performed at KfK in Germany. The experiments used a thermite mixture to simulate fuel. The test geometry of SIMBATH ranged from single pin to 37-pin bundles. In this study, phenomena of hexcan wall failure found in a SIMBATH test were analyzed by SIMMER-II. Although the original model of SIMMER-II did not calculate any hexcan failure, several simple modifications made it possible to reproduce the hexcan wall melt-through observed in the experiment. In this paper the modifications and their significance are discussed for further modeling improvements.

1. INTRODUCTION

The formation of an escape path for the molten fuel and steel through the inter-subassembly gaps can terminate a transition phase under core disruptive accident (CDA) in fast breeder reactors (FBRs) leading to neutronically benign configuration [1]. Therefore, it is a crucial issue to calculate properly the time, position and size of a hexcan failure in the evaluation of the consequence of CDA. Maschek et al. [2] and Niwa [1] assessed that no power burst could be expected any more in a CDA sequence if more than 30% of the fuel inventory was discharged from the core.

Royl et al. studied the fuel removal through subassembly gaps during the disruption phase of loss-of-flow accidents [3] Stansfield discussed the phenomenology and modeling of hexcan failure under thermal attack of molten core materials in SCARABEE tests [4]. Peppler and Will analyzed the hexcan failures observed in SIMBATH series tests and classified them into three types of failure mode [5]. Recently a hexcan failure modeling in the SURFASS code was reported by Tosello et al [6].

For the examination of hexcan failure mechanism, a typical 7-pin bundle test of the SIMBATH experiments, i.e., VTH83, was calculated by SIMMER-II. We selected this test, because it was well examined through previous studies [7, 8]. The SIMBATH represents out-of-pile simulation experiments in fuel mock-ups using a thermite mixture, that were performed at KfK in Germany. The VTH83 test simulated an unprotected loss-of-flow-driven transient overpower (ULOF-d-TOP) condition. SIMMER-II is a powerful tool to calculate a CDA sequence from initiating to transition phase. In spite of the significance of hexcan failure as an escape path for molten core materials, the validation and model improvement based on experiments have not been carried out for the related model in SIMMER-II. In this study the modeling capability and desirable further improvement are discussed through the calculation of a SIMBATH test by SIMMER-II.

2. REVIEW OF EXPERIMENT

Figure 1 shows the schematic arrangement of the SIMBATH VTH83. The main part of the test section consisted of simulated active core, or thermite region, and upper/lower simulated breeding zones. An aluminum-iron oxide thermite mixture was filled in each pin. The test section had typical reactor dimensions. That is, pin diameter was 7.6 mm with 8.8 mm pitch and the hydraulic diameter was 3.04 mm. The 7-pin bundle was mounted in a hexagonal wrapper tube and sustained by spacer grids. The exothermic chemical reaction of thermite typically set free the heat of 3680 J per centimeter pin length. This resulted in an average temperature of the melt of 3500 K. After the onset of thermite ignition, the first pin failure occurred at 64 m sec. The whole thermite pins disintegrated in 350 ms. Tight flow blockages formed at 150 ms and 210 ms in the upper and lower simulated breeding zones, respectively, to bottle up the thermite region. At 366 ms marked pressure oscillations were observed. Those were assumed due to local thermal interactions between molten thermite and residual liquid sodium. A molten pool formed around the bottom of the thermite region, which thermally attacked the hexcan wall. Finally at 391 ms, the hexcan wall failed at -55 mm in the lower simulated breeding zone.

Figure 2 shows the X-ray photograph of the test section after the test [9]. It is shown that the hexcan wall has extensively eroded and partially melted through. Based on the experimental measurements and observation, the motion of melt in the pool prior to hexcan failure was assumed to be very slow and a separation of alumina and steel should have taken place. The alumina concentrated in the upper portion of the melt. It was also deduced from the metallurgical analyses of the post-test failed hexcan. Under these conditions a protective crust of alumina could not be formed on the hexcan wall surface so that an intensive heat transfer from the melt to the surrounding wall took place. It resulted in melting of hexcan wall over an axial length of about 20 mm.

3. COMPUTATIONAL TOOL

SIMMER-II [10] is a two-dimensional thermohydraulics code coupled with neutronics. It uses Eulerian mesh noding on an r-z cylindrical or x-z Cartesian coordinate system. Two fluid fields are defined, that is, liquid field for six liquid components and vapor field for five vapor components. The two-phase flow regime is the dispersed bubbly or droplet flow. The molten components can freeze on structures or solidify as mobile particles. The molten fuel freezes only on the concave surface of hexcan wall. It cannot freeze on cladding. The molten steel can freeze both on the hexcan wall and cladding. The hexcan wall can fail in two modes: either by thermal breakup, i.e., melt-through, or by exceeding the temperature-dependent yield stress.

For the study described here, minor modifications were introduced into the code. According to the original model of SIMMER-II, molten fuel can freeze onto the hexcan wall to form a crust. The crust can merely re-melt due to an intensive heat flux and does not peel off. The analyses of SIMBATH experiments have reported the possible exfoliation of a crust [11]. Moreover, under a molten pool where the molten thermite was well separated from steel, it was found that no protective crust could be established. Therefore, the model for the crust was modified such that the crust can consecutively breakup. The regions and period for the crust breakup are specified by input.

4. COMPUTED RESULTS

4.1 Computational Procedure

Figure 3 shows the region modeled by SIMMER-II. The vertical section including the thermite zone was modeled into 2×93 r-z mesh noding. In the first ring, the innermost pin and associated liquid sodium were modeled. The second ring was for the other 6 pins with liquid sodium, the hexcan wall and the bypass flow area. In the figure, the initial material distributions were shown in terms of volume fractions. A thermite mixture is made of aluminum and iron oxide. It reacts exothermically as follows.

$$2Al + Fe_2O_3 \rightarrow Al_2O_3 + 2Fe + 4.11\ kJ/g \qquad (1)$$

In the modeling for this study, the molten thermite mixture consisting of alumina and iron was treated as single material component: *liquid fuel* in terms of SIMMER-II. Likewise the molten thermite froze as being mixed so that it did not freeze selectively. For the calculations following assumptions were made:

- The initial temperature of molten thermite mixture was 3500K,
- The initial temperature of in-pin gas was 2500K,
- The freezing temperature of thermite mixture was 2200K,
- The minimum intact hexcan wall macroscopic, i.e., smeared, density was 100 kg/m^3.

The input data for the calculations were set up at the 100 ms from the onset of thermite ignition. At this time about 10% of the whole thermite pins had disintegrated and a void region had developed in the coolant channel. There was a reason to start the calculation halfway into the transient. That is, SIMMER-II does not model the gas ejection from failed pins to a single-phase coolant flow channel. The gas ejection is key as the driving force to the materials relocation. Hence, a two-phase region must have developed in the flow at the beginning of the calculations. The gas ejected from pins dominated the development of the void region and following molten materials relocation.

4.2 Computed Results

(a) Base case

Here we discuss the computed results of base-case calculation, in which minor modifications concerning thermite crust breakup were not applied [7, 8]. Figure 4 shows the calculated materials distribution at 0.391 s when the hexcan melted through in the experiment. In the base case, a hexcan melt-through was not calculated. The whole thermite zone was bottled up by flow blockages that formed both in the upper and lower simulated breeding zones. Although at this time the molten thermite and steel mostly drained at about the bottom of the thermite zone, the thermal erosion of the hexcan proceeded most severely around +300 mm.

(b) Crust breakup case

Figure 5 shows the calculated materials distribution at 0.391 s when the modification of crust breakup is applied to the thermite region. In this calculation, the crust formed on the hexcan wall was broken up consecutively and practically no crust was established on the hexcan wall of the thermite zone. Due to the lack of protective layer of crust, the erosion of the hexcan wall proceeded more than the base case. However, the hexcan did not melt through.

According to the liquid-structure heat transfer model of SIMMER-II, the heat-transfer rate per unit volume from liquid-field component m to structure-field component k, q_{mk}, is calculated as

$$q_{mk} = \frac{h_m h_k A_k}{h_m + h_k} \frac{\alpha_m}{1-\alpha_S}(T_m - T_k) \qquad (2)$$

where h_m and h_k are heat-transfer coefficients for structure component m and liquid component k, respectively; A_k is the surface area per unit volume for structure component k; α_m is the volume fraction of liquid-field component m, α_S is the total structure-field volume fraction; T_m is the temperature of liquid component m, and T_k is the temperature of structure component k. The factor of $\alpha_m/(1-\alpha_S)$ is applied, because the two-phase flow regime in SIMMER-II is the dispersed droplet flow. By the experimental observations from the X-ray films at the early stage of the pin disintegration, it was shown that the dispersed droplet flow was dominant. Later, however, when the molten thermite and steel became rich in the test section, most part of molten materials spread on the hexcan surface which formed annular flow with droplets. A typical diagram of such a flow condition is shown in Figure 7 [12]. Under this condition, the multiplication by the factor, $\alpha_m/(1-\alpha_S)$, underestimates the heat-transfer rate.

In the calculations by SIMMER-II, the volume fraction of liquid thermite and steel in the pin-disintegrated zone was about 0.1 in the later stage into pin disintegration, with a peak value of 0.3. The total volume fraction of structure was 0.6 in the pin-disintegrated zone. Based on these values, we performed three calculations with various multiplication values for the heat-transfer rate. In the case 0, case 1 and case 2, the multiplication values were 2.0, 3.5, and 5.0, respectively. In the calculation case 0, the hexcan wall did not fail. Figure 6 shows the calculated materials distribution of the case 1 at 0.350 s. The hexcan wall melted away at +325 mm. A deep thermal erosion occurred around the position of the melt-through. Figure 8 shows the history of hexcan wall temperature at selected nodes. In the case 2 calculation, the hexcan failed at 0.290 s.

In the SIMBATH 7-pin bundle experiments, five tests under UTOP and ULOF-d-TOP conditions were analyzed for hexcan failure [5]. In four tests out of the five, the hexcan failed. It was found that the locations and times of hexcan failure were +240 mm (0.283 s), +170 mm (0.165 s), +380 mm (0.318 s), and -55 mm (0.391 s). In the first three tests, the hexcan failure occurred during the disintegration of thermite pins. Only in the last test, VTh83, the hexcan failed after the completion of the disintegration of whole thermite pins. With regard to the failure position, the calculated results of the VTh83 test showed rather the tendency of the other three 7-pin bundle tests. In the three tests, the ablation and melt-through of the hexcan occurred in the thermite zone. The crusts once built up on the hexcan surface were unstable under annular flow and locally detached, which intensified the heat insertion from the melt into the hexcan leading to the hexcan melting.

In the VTh83 test, the hexcan did not fail during the pin disintegration stage and, later, the molten thermite formed a subassembly-scale pool in the bottled-up configuration. It was judged from the experimental measurements that in the molten thermite pool, the separation of molten alumina from molten steel/iron had occurred. This promoted an intensive heat transfer from the melt to the hexcan wall and finally it caused the hexcan melt-through. This process could not be modeled by SIMMER, because the thermite mixture (molten thermite and steel/iron) was treated as a single mass component. There was also a possibility that the hexcan melt-through began from an azimuthally local point at about same height of the hexcan. Namely, the heat flux could locally attack the hexcan wall. Such a localized thermal attack cannot be modeled in SIMMER-II, because it is a two-dimensional code. However, by the detailed examinations of the experiments, any exact explanation was not found why only in the VTh83 test the hexcan thermally endured during the pin disintegration stage.

Anyway, we assume that detailed mechanisms of the stability of crusts on the hexcan surface and the thermohydraulics within the bottled-up pool can determine the course of hexcan failure more precisely. Based on the above discussions further model improvements and validation concerning hexcan failure should be took place for: (1) two-

phase flow regime, (2) formation and exfoliation of crusts, and (3) melt attack in three dimensional manner.

5. CONCLUSION

The hexcan wall failure of SIMBATH experiment was analyzed by SIMMER-II. It was found that some simple modifications to enhance the heat flux from melt to the hexcan wall were very effective to reproduce the hexcan melt-through observed in the experiment. Concerned with these modifications, further improvements and validation were pointed out for SIMMER-II.

Acknowledgments

We thank Dr. W. Peppler and Mr. H. Will of KfK very much for providing us with data from the SIMBATH experiments and for discussions about the calculated results. This study was part of a collaboration between Tokyo Institute of Technology and KfK and partly supported by PNC.

References

1. H. NIWA, "Future Research Needs on Material Interaction and Relocation in LMFR Safety," Proc. IAEA/IWGFR Tech. Committee Mtg. on Evaluation of Material Coolant Interaction and Material Movement and Relocation in Liquid Metal Fast Reactors, O-arai, Japan, 579-593 (1994).

2. W. MASCHEK, G. FIEG, and M. FLAD, "Experimental Investigations of Freezing Phenomena of Liquid-Particle Mixtures in the THEFIS Facility and Their Theoretical Interpretation," Proc. Int. Fast Reactor Mtg., Snowbird, UT, Vol. I, 519-529 (1990).

3. P. ROYL, B.D. GANAPOL, and Ch.R. BELL, "A study of fuel removal via inner blanket subassembly gaps during the disruption phase of hypothetical loss of flow accidents in heterogeneous LMFBR cores," Nucl. Techn. 71, 145-161 (1985).

4. R.G. STANSFIELD, "Thermal Attack and Wrapper Failure in the SCARABEE Tests BE+1, BE+2, BE+3 and BE+3bis," Proc. 13th LMBWG Mtg., Winfrith, UK (1988).

5. W. PEPPLER and H. WILL, "Analysis of hexcan failures occurring during the simulation of severe accident in liquid metal cooled reactors," Nucl. Engrg. Des. 110, 73-93 (1988).

6. A. TOSELLO, P. ANZIEU, and P.Y. CAMARO, "Hexcan Failure Modelling for Subassembly Meltdown in the SURFASS Code," Proc. Internat. Topl. Mtg. Sodium Cooled Fast Reactor Safety, Obninsk, Russia, 2-221 - 2-227 (1994).

7. T. SAWADA, "Recalculation of Material Movement and Relocation Experiments with the SIMMER-II Code," Proc. 14th LMBWG Mtg., Brasimone, Italy (1991).

8. T. SAWADA, H. NINOKATA, and A. SHIMIZU, "Calculation of a materials relocation experiment simulating a core disruptive accident condition in fast breeder reactors," Nucl. Engrg. Dec., *to be published.*

9. W. PEPPLER and H. WILL, "Analysis of Hexcan Failure Occurring during the Simulation of Severe Fast Breeder Accidents SIMBATH Out-of-pile Experiments," KfK-Primärbericht $01.02.07_p13A$ (1987) *unpublished.*

10. W.R. BOHL and L.N. LUCK, "SIMMER-II: A Computer Program for LMFBR Disrupted Core Analysis," LA-11415-MS (1990).

11. P. MENZENHAUER, W. PEPPLER, and H. WILL, "Vergleich der Materialbewegungen und Ausfriervorgänge in zwei Bündelexperimenten unter simulierten ULOF- und TOP-Störfällen, SIMBATH $V_{Th}83$ und $V_{Th}74$," KfK-Primärbericht $01.02.07_p09D$ (1985) *unpublished.*

12. W. PEPPLER and H. WILL, "SIMBATH, Dokumentation der Ergebnisse der Experimente $V_{Th}130$ und $V_{Th}154$," KfK-Primärbericht $01.02.07_p14B$ (1989) *unpublished.*

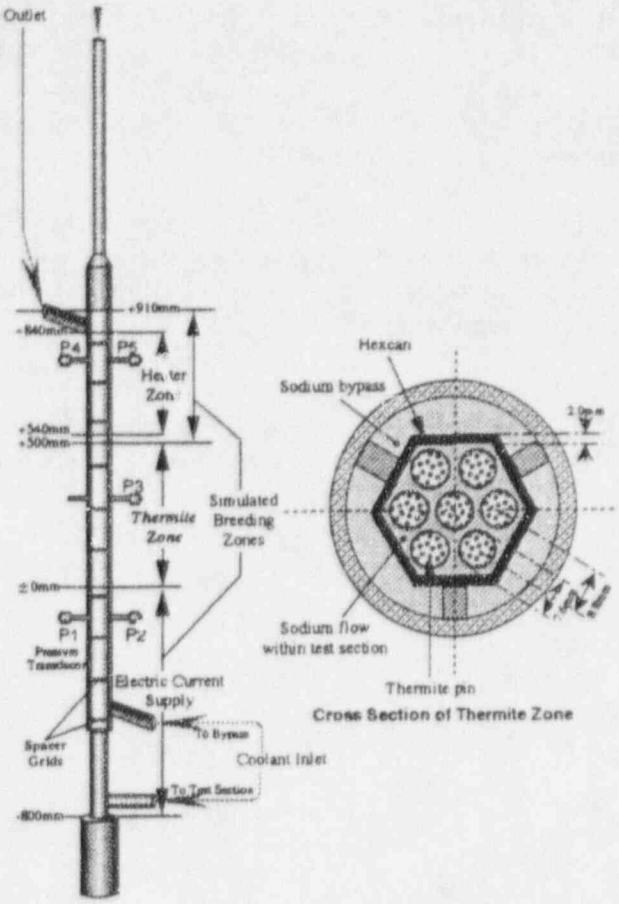

Figure 1 Test Section of SIMBATH VTh83

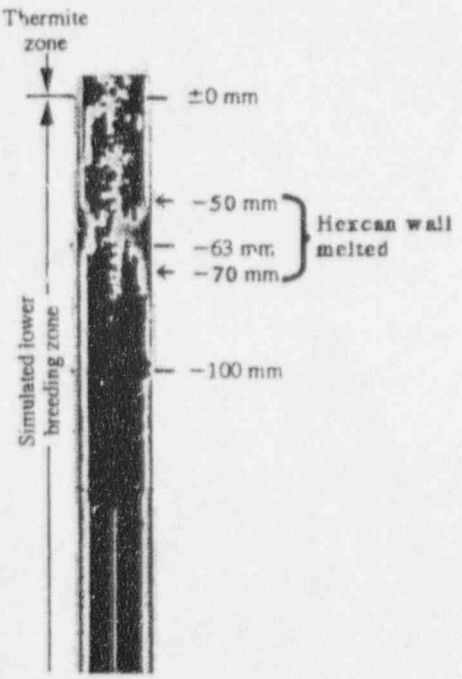

Figure 2 SIMBATH VTh83. Post-tset X-ray photograph of test section

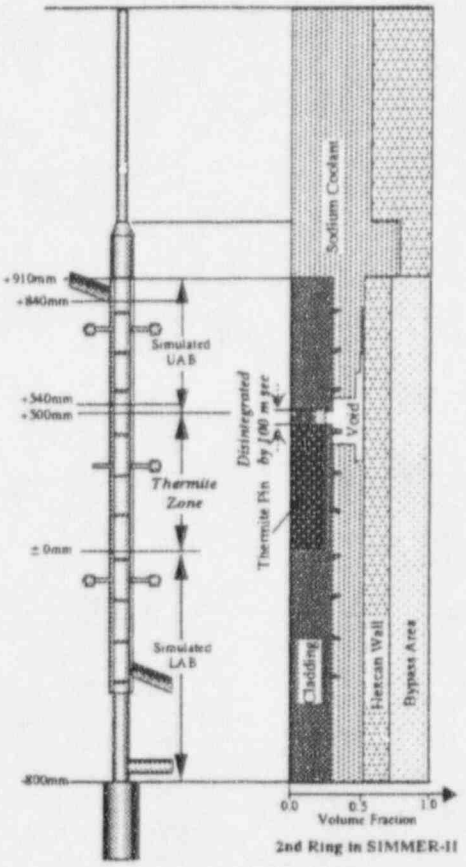

Figure 3 Test section modeled by SIMMER-II and initial materials distribution.

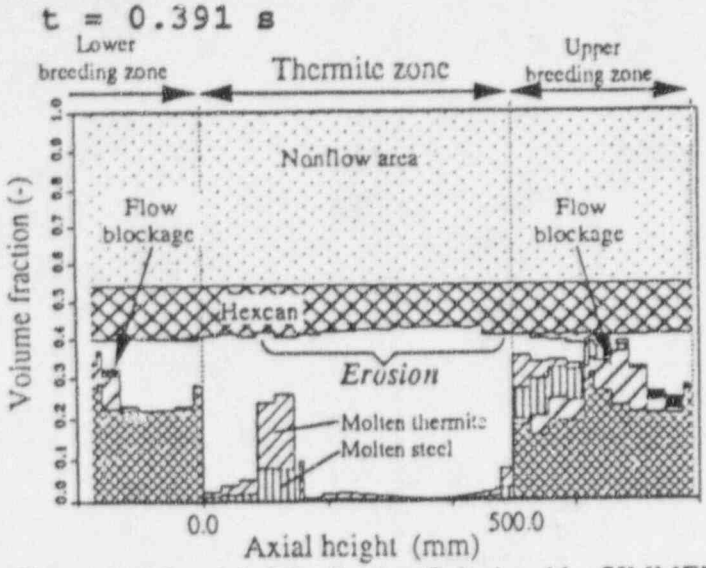

Figure 4 Materials Distribution Calculated by SIMMER-II Base Case w/o Modifications

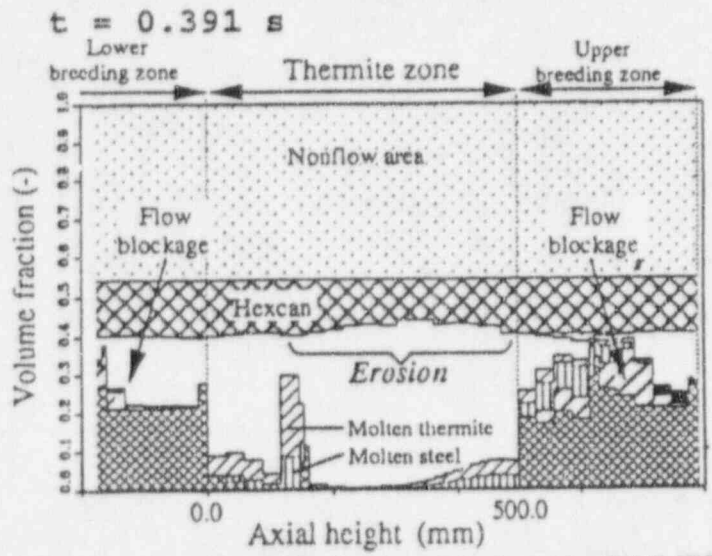

Figure 5 Materials Distribution Calculated by SIMMER-II Crust Breakup Case w/o Enhancement of Heat Flux

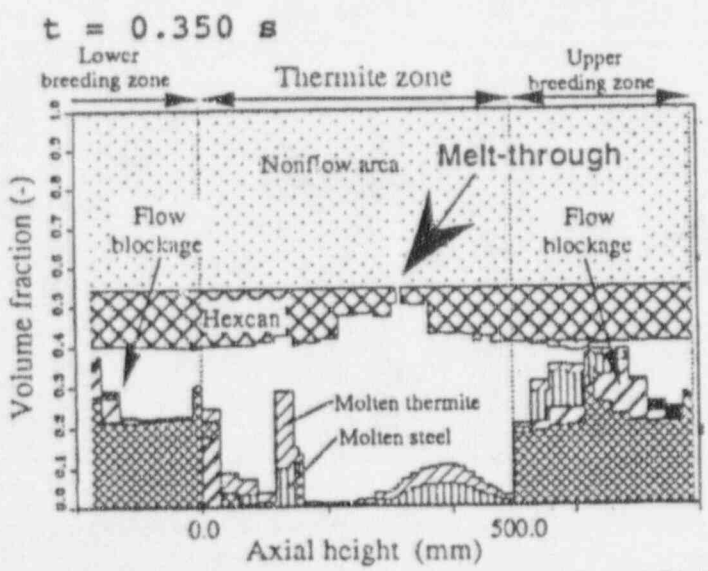

Figure 6 Materials Distribution Calculated by SIMMER-II Crust Breakup Case with Enhancement of Heat Flux (case 1)

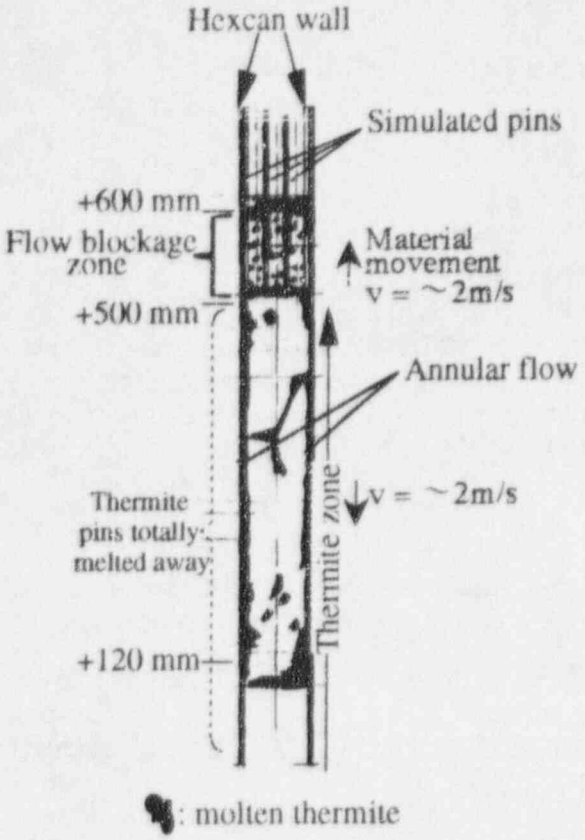

Figure 7 Typical annular/droplet flow observed in a SIMBATH test

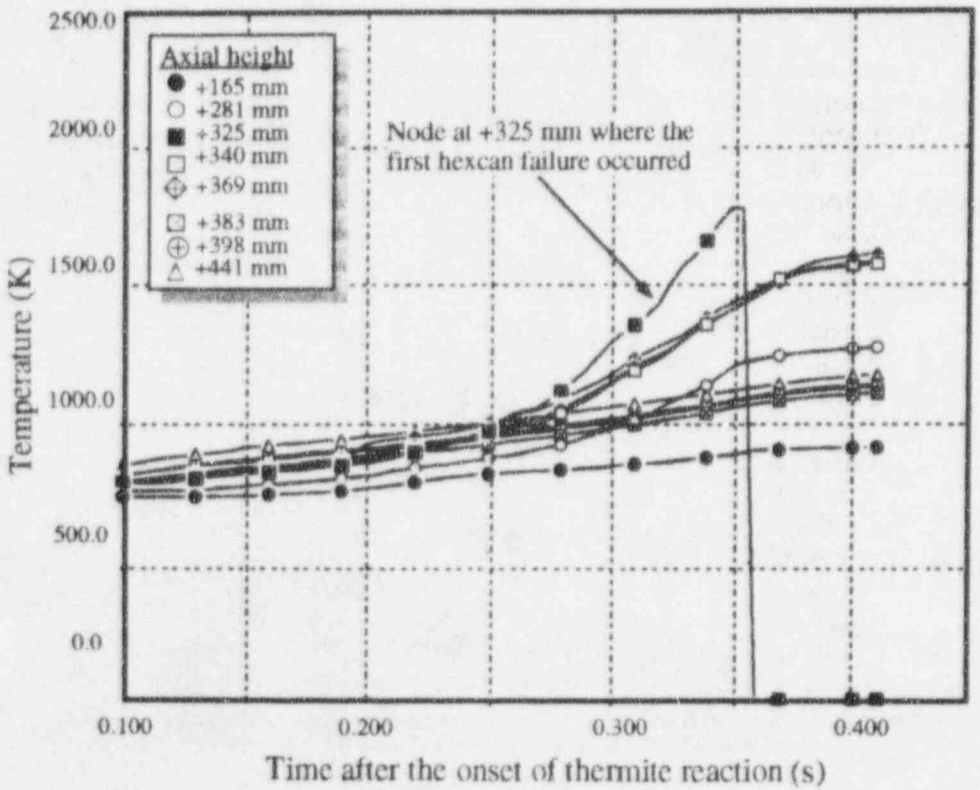

Figure 8 History of hexcan temperature calculated by SIMMER-II

INVESTIGATIONS ON SUMP COOLING AFTER CORE MELT DOWN

J.U. Knebel

Forschungszentrum Karlsruhe - Technik und Umwelt
Institut für Angewandte Thermo- und Fluiddynamik (IATF)
Postfach 3640 • D-76021 Karlsruhe • Federal Republic of Germany
Telephone +49 7247-82-3451 • Telefax +49 7247-82-4837
E-Mail j.knebel@iatf.kfk.de

ABSTRACT

This article presents the basic physical phenomena and scaling criteria of decay heat removal from a large coolant pool by single-phase and two-phase natural circulation flow. The physical significance of the dimensionless similarity groups derived is evaluated. The above results are applied to the SUCO program that is performed at the Forschungszentrum Karlsruhe. The SUCO program is a three-step series of scaled model experiments investigating the possibility of an optional sump cooling concept for the European Pressurized Water Reactor EPR. This concept is entirely based on passive safety features within the containment. The work is supported by the German utilities and the Siemens AG. The article gives first measurement results of the 1:20 linearly scaled plane two-dimensional SUCOS-2D test facility. The experimental results of the model geometry are transformed to prototypic conditions.

1. INTRODUCTION

In recent years new safety requirements for the next generation of nuclear power plants have been formulated. The complete accommodation of even severest reactor accidents within the containment for any period of time and the restriction of fission product releases to the environment (below *1 vol.%/d*) is the most progressive claim for future nuclear power plants. In addition more and more passive safety equipment is intended to be implemented. Supposing a core melt down accident and considering the problem of melt stabilization, these requirements can be achieved by an initially dry spreading of the core melt on the containment basemat in combination with a passive sump water flooding and passive cooling from above. This proposal is sketched in figure 1. Additional information is given by Weisshäupl and Bittermann [1], Knebel [2] and Kuczera et al. [3]. The reactor pit and the spreading compartment are connected by a sloping discharge channel that is closed by a sacrificial steel plate. After a certain time, the steel plate passively fails due to the accumulating core melt and refractory material. The core melt, then, eventually covers the bottom of the spreading compartment that is dry during normal operation. The bottom and lateral structures of the spreading compartment are equipped with a protection layer for thermal loads. The spreading compartment is connected with the In-Containment Refuelling Water Storage Tank by pipes for water flooding. These pipes are closed during normal operation and opened passively by the hot core melt. Limited flow rates are allowed in order to prevent energetic fuel-coolant interactions. In case of a LOCA, only a very shallow water layer can be formed in the spreading compartment as a consequence of condensing steam [1]. After the flooding of the core melt, the decay heat is transferred

from the core melt to the sump water by conduction, convection and evaporation. A natural sump water circulation transports the decay heat to water cooled heat exchangers. The heat exchangers are located in sub-compartments of the spreading compartment to protect them from thermal radiation during the period of dry core melt spreading. In addition, condensers are provided. Considering the decay heat decrease with time, the short-term behaviour of the system is characterized by two-phase natural circulation phenomena due to the high local heat fluxes along the core melt surface whereas the long-term behaviour shows single-phase natural circulation. A secondary system that is an intermediate natural circulation loop finally removes the decay heat to the environment. The core melt interacts with the sump (coolant pool) creating a stable stratification. The homogenization of the coolant pool temperature by flow mixing represents a crucial aspect for the reduction of thermal loads to system components. In addition, it is of interest under which boundary conditions it is possible to keep the coolant pool locally or entirely subcooled. The safety grade of the system is greatly increased in respect to accident transients if the coolant pool is large enough to provide an intermediate heat storage. The correct simulation of the single-phase and two-phase natural circulation and of the pool mixing process is an important requirement for a down-scaling procedure. A licensable proof must be based on both extensive observations in scaled model experiments and validated three-dimensional calculations.

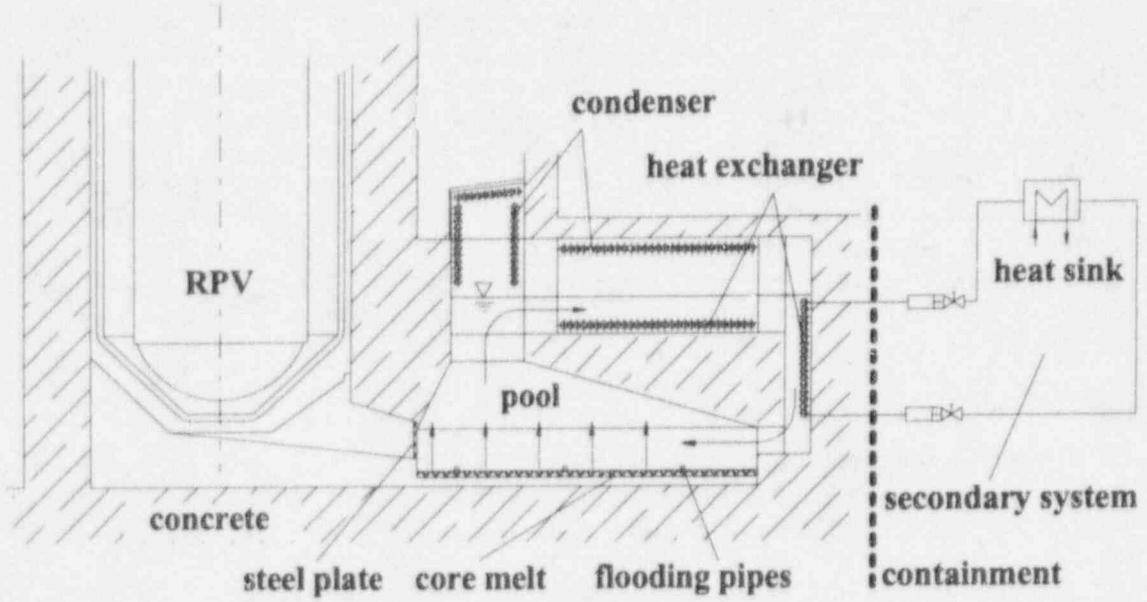

Figure 1: Optional sump cooling concept of the European Pressurized Water Reactor EPR.

2. SCALING CRITERIA

Before designing scaled model experiments simulating the optional sump cooling concept given in figure 1, one has to develop scaling criteria that account for the concept-relevant physical phenomena. These are the limits of core melt coolability, first, under short-term two-phase natural circulation and, second, under long-term single-phase natural circulation. In addition, one is interested in the heat transfer mechanisms along the core melt, heat exchangers and condensers, the temperature/velocity field and the flow pattern in the coolant pool, the influence of geometrical parameter variations, e.g. cross-sectional flow areas, heat exchanger design and arrangement, sump water height.

Following the considerations of Ishii and Kataoka [4], the scaling criteria for a natural circulation system can be obtained from the integral effects of the local one-dimensional balance equations along the natural circulation loop.

2.1 Single-phase similarity groups

A non-dimensionalization of the balance equations gives for single-phase flow the following set of similarity groups.

Richardson number $$Ri = \frac{g\,\beta\,\Delta T_0\,l_0}{u_0^2} \propto \frac{buoyancy\ force}{inertia\ force} \,. \tag{1}$$

Friction number $$F_i = \left(\xi_v + K\right)_i \propto \frac{friction\ force}{inertia\ force} \,. \tag{2}$$

Stanton number $$St_i = \frac{\alpha\,l_0}{\rho\,c_p\,u_0\,d_i} \propto \frac{wall\ convection\ heat\ transfer}{axial\ fluid\ convection\ heat\ transfer} \,. \tag{3}$$

Length ratio $$L_i = \frac{l_i}{l_0} \,. \tag{4}$$

Cross-sectional flow area ratio $$A_i = \frac{a_i}{a_0} \,. \tag{5}$$

Here, g is the acceleration of gravity and β is the coefficient of linear thermal expansion of the coolant. ξ_v and K are loss coefficients accounting for all frictional and orifice losses respectively in the i -th section of the loop. The loss coefficients will generally be a function of geometry and velocity. α is denoted the heat transfer coefficient. ρ and c_p are the density and the heat capacity of the coolant. d_i is the hydraulic diameter. The relevant distance along which the buoyant up- and downdraft act is denoted by l_0. a_0 is a characteristic cross-sectional flow area. The characteristic velocity scale u_0 and temperature change scale ΔT_0 can be deduced from the momentum and the energy balance for stationary conditions and a heating power per unit volume of $\dot{q}_0$ as follows.

$$u_0 = \left(\frac{2\,\beta\,g\,\dot{q}_0\,l_0^2}{\rho\,c_p \sum_i \left(F_i / A_i^2\right)} \right)^{1/3} \,. \tag{6}$$

$$\Delta T_0 = \frac{\dot{q}_0\,l_0}{\rho\,c_p\,u_0} \,. \tag{7}$$

The pool mixing that is characterized by the Richardson number, occurs predominantly by entrainment of cold fluid from the heat sink that appears as a horizontally spreading quasi-free jet, into the hot updrafting fluid above the heat source. The entrainment mainly depends on the vertical pool temperature stratification and on the horizontal cold fluid velocity. The Stanton number scales the decay heat removal by the heat exchangers. In addition, geometrical similarity groups giving length scales and cross-sectional flow area scales can be obtained. In order to preserve similarity of the single-phase natural circulation and of the overall mixing process the similarity group ratios *(R)* between the model (*M*) and the prototype (*P*)

$$\Pi_R = \Pi_M / \Pi_P \tag{8}$$

must be unity.

In addition, a characteristic time scale for charging or discharging heat into or out of the coolant pool that acts as an intermediate heat storage can be derived. It is the ratio of the total enthalpy of the coolant pool to the total power of the heat source.

$$\tau_c = \frac{\rho c_p (T_P - T_S)}{\dot{q}} \quad . \tag{9}$$

Here, $T_P - T_S$ is the temperature difference between primary and secondary side of the system, $\dot{q}$ is the heating power $\dot{Q}$ per unit volume V of the coolant pool. This time scale can be non-dimensionalized by the steady-state turn-around time between heat source and heat sink.

$$\tau_a = \frac{l_0}{u_0} \quad . \tag{10}$$

Thus, a dimensionless transient time scale is obtained

$$\Pi_t = \frac{\tau_c}{\tau_a} \tag{11}$$

that is a measure for the integral heat up or cool down behaviour of the system.

Besides the integral momentum and heat transfer, the local fluiddynamic state that may be laminar or turbulent and, moreover, vary across the coolant pool is a crucial aspect of a buoyancy induced mixing process. The magnitude of the Reynolds number and the Peclet number is commonly used as a criterion for the transition from laminar to turbulent momentum and heat transport, respectively. In geometrically similar small-scale models that use the same working fluid as the prototype, the power and thus the velocity are reduced. Therefore, the Reynolds number ratio may differ significantly from unity and the flow conditions may change from turbulent in the prototype to laminar in the model. In order to simulate the mixing process in the coolant pool correctly, it must be assured by an adequate scaling of both the geometry and the power that the turbulent flow condition of the prototype is at least qualitatively maintained in the model. This requirement practically limits the size of a scaled model experiment.

2.2 Two-phase similarity groups

For a two-phase natural circulation system Ishii and Kataoka [4] derive the following additional set of similarity groups from a perturbation analysis after the introduction of the drift-flux model into the balance equations.

Phase change number $$N_{PCh} = \frac{\Gamma_G / \rho_G}{u_m / l_0} = \frac{\textit{fluid residence time}}{\textit{reaction time}} \quad . \tag{12}$$

Subcooling number $$N_{Sub} = \frac{\Delta h_{sub}}{\Delta h_{LG}} \cdot \frac{\Delta \rho}{\rho_G} = \frac{\textit{subcooling}}{\textit{latent heat}} \quad . \tag{13}$$

Drift flux number $$N_d = \frac{\rho_L}{\rho_m} \frac{U_{Gj}}{u_m} = \frac{\textit{drift transport}}{\textit{convective transport}} \quad . \tag{14}$$

Froude number $$N_{Fr} = \frac{u_m^2}{g\, l_0\, \varepsilon} = \frac{\textit{inertia force}}{\textit{gravity force}} \quad . \tag{15}$$

Density ratio $$N_\rho = \frac{\rho_G}{\rho_L} = \frac{\textit{vapor density}}{\textit{fluid density}} \quad . \tag{16}$$

Friction number $$N_f = \frac{f_m\, l_0}{2\, d} = \frac{\textit{wall friction force}}{\textit{inertia force}} \quad . \tag{17}$$

Here, the subscripts G and L denote the gas and the liquid phase representatively. Γ_G is the volumetric gas exchange rate, Δh_{LG} is the latent heat, U_{Gj} is the vapour drift velocity and ε is the void fraction.

The phase change number N_{PCh} takes into account the change of phase due to the heat transfer to the sump water. The subcooling number N_{Sub} scales the subcooling of the sump water entering the heated section and, thus, the dimension of the purely liquid region along the core melt. These two numbers, N_{PCh} and N_{Sub}, are important for the scaling of both the dynamical and the steady-state conditions of a natural circulation system. The drift flux number N_d describes the relative motion between the liquid and the vapor phase and, thus, the kinematic similarity of the system. As the drift velocity U_{Gj} depends on the flow regime, the drift flux number is the similarity group that accounts for the flow patterns and the void fraction distribution. Again, in order to preserve similarity of the two-phase natural circulation the above set of similarity groups has to be the same in the model and in the prototype.

3. MODEL EXPERIMENTS ON THE SUMP COOLING CONCEPT

At the Forschungszentrum Karlsruhe the feasibility of the optional sump cooling concept is investigated and demonstrated by the SUCO program that consists of three consecutive scaled model experiments summarized in table 1. These experiments are aimed to investigate the short-term and the long-term behaviour of the natural circulation within the flooded spreading compartment only. The process of flooding itself and possible energetic fuel-coolant interactions are no objectives of these studies.

Taole 1: SUCO program at the Forschungszentrum Karlsruhe.

Parameters	EPR 1500 MW ^{D}WR Scale 1:1	SUCO Volume 1:20 Power 1:20 Heights 1:1	SUCOT Volume 1:356 Power 1:356 Heights 1:1	SUCOS-2D Lengths 1:20 Power 1:20^3/4 Heights 1:20
Working fluid	*water*	*water*	*water*	*water*
Spreading Area, m^2	*160*	*8*	*0.45*	*0.4/4*
Water Height, *m*	*5.5*	*5.5*	*5.5*	*0.275*
Decay Heat, *MW*	*25*	*1.25*	*0.07*	*0.003125/4*
Heat Flux, W/cm^2	*15.6*	*15.6*	*15.6*	*0.783*

The first scaled model experiment is the geometrically similar 1:20 linearly scaled plane two-dimensional SUCOS-2D test facility simulating a representative slab of the simplified geometry of figure 1. A sketch together with the main dimensions and components is given in figure 2. The width of the test facility - giving the representative slab- is *25 %* of the scaled width. The test facility consists of an insulated glass tank allowing various flow visualization measurement techniques. The working fluid is water. The core melt is simulated by a copper plate that can be heated from below with three identical heating rods mounted in grooves that divide the plate into three independent sections. The plate is insulated from below. The heat exchangers are modeled using flat plate heat exchangers that can be operated individually relative to volume flux and inlet temperature. In order to measure the temperature field within the pool and the sub-compartments the SUCOS-2D test facility is equipped with six traversable thermocouple fences with 55 thermocouples altogether. Figure 2 shows one schematic fence representatively. The thermocouples are of type K [5] with *0.5 mm* outer diameter. The measuring system consists of isolated measuring pods with an internal PT100 resistance thermometer as reference junction and a *16 bit* analog-to-digital converter.

The objectives of this small scale test facility are integral phenomenological thermo-hydraulic investigations for the long-term single-phase behaviour. This test facility allows

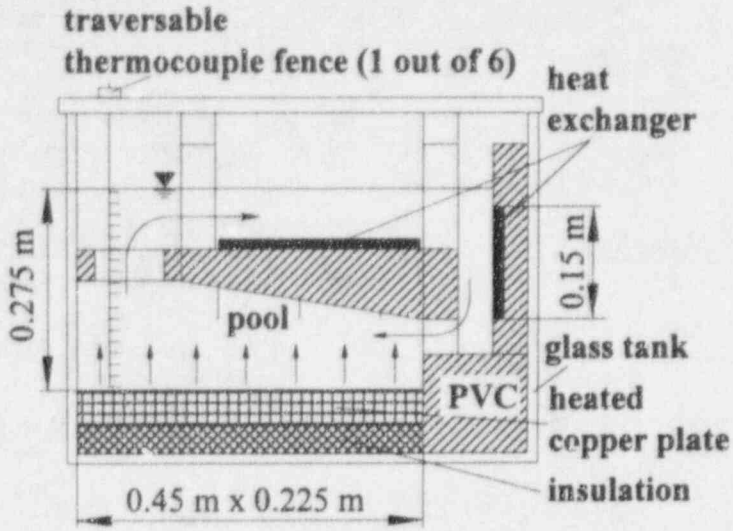

Figure 2: Sketch of the SUCOS-2D test facility at the Forschungszentrum Karlsruhe.

an easy variation of the geometry, e.g. cross-sectional flow areas. The dominating integral physical processes, such as pool mixing, are scaled correctly as the Richardson number ratio Ri_R and the transient time scale ratio Π_{tR} are equal to unity.

The second scaled model experiment is the real height SUCOT test facility with a volume and power scale of 1:356. The local heat flux ratio q''_{WR} is kept equal to unity. Providing a realistic surface structure of the heated plate this test facility allows the investigation of two-phase natural circulation phenomenology such as flow patterns, formation, rise and collapse of bubbles and flashing. Using the same working fluid as in the real reactor, this test facility preserves the phase change number N_{PCh} and the subcooling number N_{Sub} correctly. In addition, an identical void fraction distribution and thus same flow patterns as a function of geodetic height are produced with this model. The SUCOT test facility is in its building up phase and is going to give first experimental results by the end of 1995.

As final step, a SUCO test facility that is a plane two-dimensional slab of the real geometry with a volume and power scale of 1:20 is under consideration. This test facility could provide the coolability limits of a two-phase or single-phase natural circulation system together with the demonstration of its operational performance. All components except for the core melt are of real materials. The transferability of the experimental findings to the prototypical three-dimensional effects is done either by an additional small-scale three-dimensional test facility or by numerical calculations using the FLUTAN [6] code.

4. EXPERIMENTAL RESULTS

The SUCOS-2D test facility is equipped with traversable thermocouple fences. A calibration of the thermocouples gives deviations of less than $\pm 0.05\ K$ in reference to a PT100 resistance thermometer between $20\,°C$ and $80\,°C$. The energy losses from the test facility to the ambient are below $8\,\%$. Most of these losses are via the top surface where the thermocouple fences are introduced into the test facility.

Figure 3 gives a characteristic shadow graph of the SUCOS-2D sump geometry with both heat exchangers in operation and a chimney blockage of $67\,\%$. The section of the test facility that connects the sump with the upper sub-compartments is referred to as chimney. A chimney blockage of $67\,\%$ gives the geometrically similar scaling of the prototypical geometry.

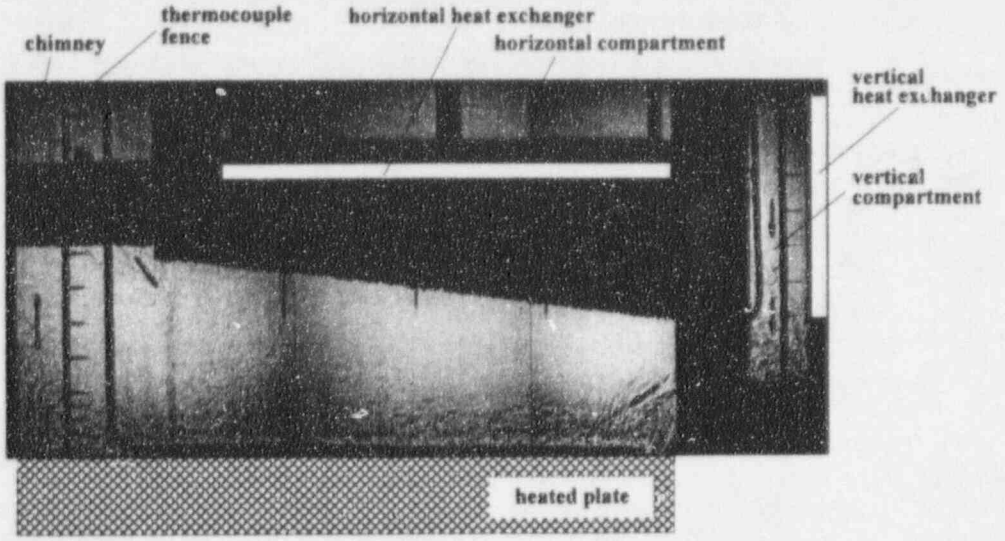

Figure 3: Characteristic shadow graph of the SUCOS-2D sump geometry.

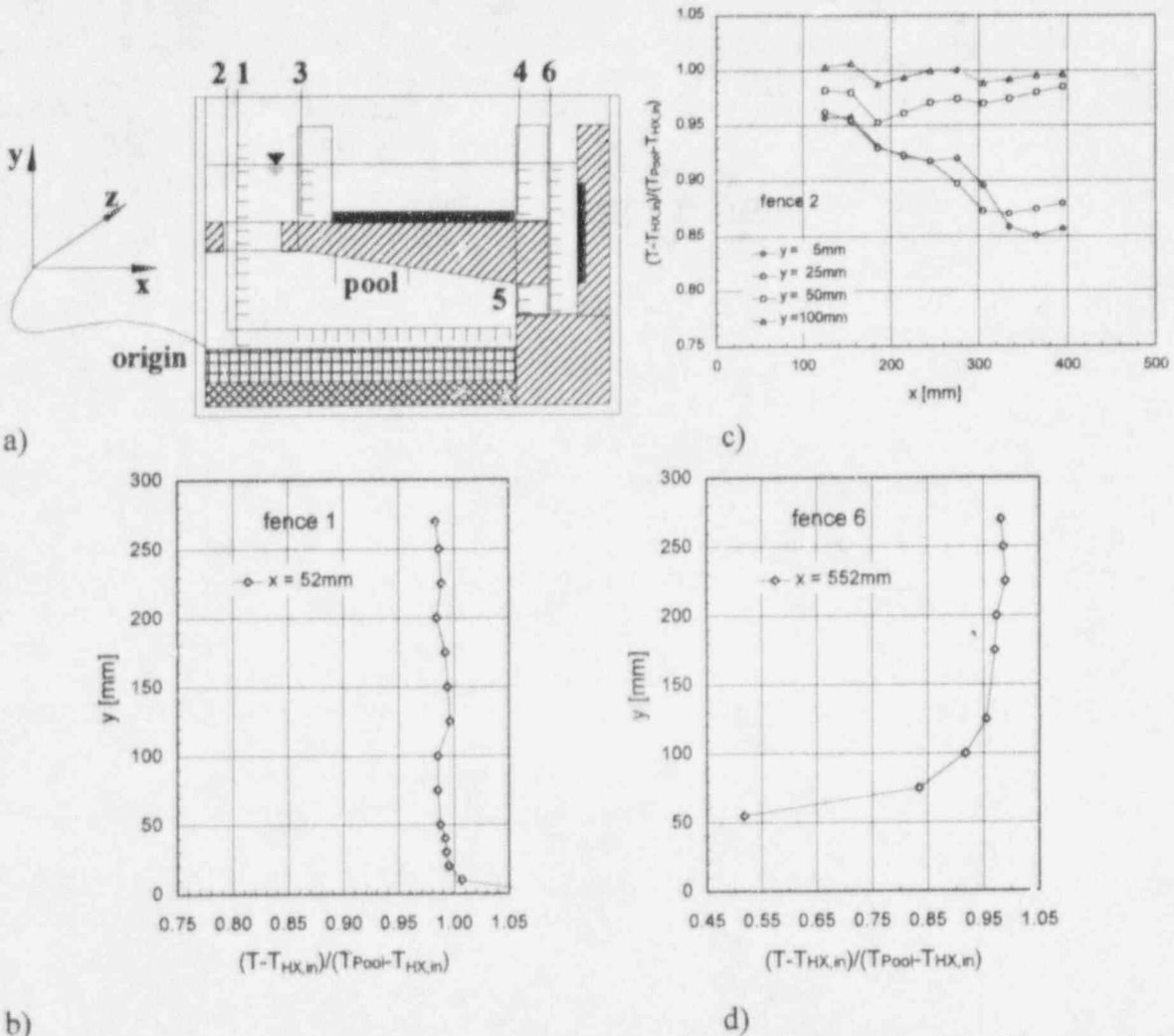

Figure 4: Coordinate system and thermocouple fences, schematic (a). Characteristic temperature profiles of thermocouple fences 1 (b), 2 (c) and 6 (d). Heating power *313 W*, chimney blockage of *67 %*, both heat exchangers in operation, coolant mass flux of *20 g / s*, inlet temperature *20 °C*.

Generally, a clockwise rotation is observed that is confirmed by numerical results given in [3]. One can clearly detect a downdraft and an intense mixing in the lower part of the sub-compartment parallel to the vertical heat exchanger and a distinct partial downdraft out of the chimney. The sub-compartment parallel to the vertical heat exchanger is referred to as vertical compartment in the following. The horizontal flow along the heating plate produced by the quasi-free jet results in a well-defined mixing zone and a more or less uniform and stagnant pool above. The flow paths are indicated qualitatively using arrows.

Figure 4a-d gives characteristic normalized temperature profiles $(T - T_{HX,in}) / (T_{Pool} - T_{HX,in})$ of thermocouple fences 1, 2 and 6. The pool temperature T_{Pool} is the mean value of three thermocouples introduced in the pool. The temperatures are taken relative to the heat exchanger inlet temperature $T_{HX,in}$. The positions of the thermocouple fences and of the three thermocouples to measure the pool temperature are indicated schematically in figure 4a. The origin of the cartesian coordinate system is in the front left corner of the pool. The thermocouple tips of fences 1 and 6 are positioned in the middle of the chimney ($x = 52\ mm$) and the vertical compartment ($x = 552\ mm$) respectively. Both heat exchangers are in operation, each having a coolant mass flux of $20\ g/s$ with an inlet temperature of $20\,°C$. The chimney blockage is $67\,\%$. The results show a very homogeneous vertical temperature distribution in the pool and the chimney. This is due to an intensive mixing process and a good homogenization of the coolant pool temperature (figure 4b). Besides close to the heated plate, lower temperatures are observed only within the mixing zone. Close to the heated plate at $y = 5\ mm$ and $y = 25\ mm$, fence 2 shows a linear temperature increase. Below the jet a zone of recirculation with higher temperatures is observed at $x \geq 350\ mm$. At the measuring positions $y = 50\ mm$ and $y = 100\ mm$ that is at the end and above the mixing zone, respectively, the normalized temperatures are $2\,\%$ below or equal to the normalized pool temperature (figure 4c). Fence 6 in figure 4d gives the mixing of cold and hot fluid in the lower part of the vertical compartment producing the cold jet.

Generally, the experiments give an increase in pool temperature with increasing heat exchanger inlet temperature. The introduction of a chimney blockage of $89\,\%$, and thus an increase in flow resistance, increases the pool temperature. The maximum mean temperature differences within the whole natural circulation system are below $10\ K$.

The key question with scaled model experiments is the transformation of the experimental results to prototypic conditions. One objective of the SUCO program is to find out under which boundary conditions it is possible to keep the coolant pool locally or entirely subcooled in the long-term behaviour. This is a crucial aspect for the reduction of thermal loads to system components. Thus, one is interested in a transformation formula that gives the prototype pool temperature as a function of the model pool temperature, the model heat exchanger inlet temperature and geometric parameters. The heat exchanger inlet temperature is looked upon as characteristic for the ultimate heat sink temperature.

The derivation of a transformation formula is divided into two steps. First, one has to describe the heat transfer mechanism at the heat exchanger in terms of a Nusselt-Reynolds correlation. As one has a natural circulation flow that is induced by a temperature difference between a heat source and a heat sink, a forced convection heat transfer correlation can be used as a first approximation.

$$Nu = \frac{\alpha\, d}{\lambda} = 0.0155 \left(\frac{u\, d}{\nu} \right)^{0.83} Pr^{0.5} . \tag{18}$$

Here, λ is the thermal conductivity, ν is the kinematic viscosity and Pr is the Prandtl number. The heat transfer coefficient α can be written as

$$\alpha = \frac{q''_W}{(T_{SC} - T_{HX,in})} \tag{19}$$

with $\left(T_{SC} - T_{HX,in}\right)$ being the characteristic difference between the vertical compartment fluid temperature and the heat exchanger inlet temperature. In order to avoid the vertical compartment temperature that is difficult to measure, and to find a simplified expression for the characteristic temperature difference in the model, figure 5 relates it to the heat exchanger inlet temperature and to geometric parameters. Depending on the heat exchangers in operation one finds linear relationships with identical slopes a and different ordinate offsets b.

$$\left(T_{SC} - T_{HX,in}\right)_M = a \cdot T_{HX,in\,M} + b \ . \tag{20}$$

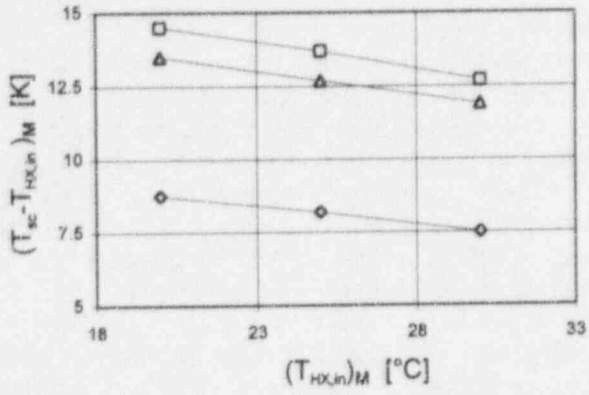

Figure 5: Characteristic difference between the vertical compartment fluid temperature and the heat exchanger inlet temperature $\left(T_{SC} - T_{HX,in}\right)_M$ versus the heat exchanger inlet temperature $T_{HX,in\,M}$. (◊) Vertical and horizontal, (Δ) horizontal and (□) vertical heat exchanger in operation.

By introducing eq. (19) into eq. (18), forming the ratio between model and prototype and including eq. (20), the characteristic temperature difference in the prototype can be written as

$$\left(T_{SC} - T_{HX,in}\right)_P = 6.35 \cdot \left(a \cdot T_{HX,in} + b\right)_M \ . \tag{21}$$

Here, according to table 1, the local heat flux ratio q''_{WR} can be derived as proportional to the length scale ratio l_R.

Second, the vertical compartment fluid temperature T_{SC} has to be related to the pool temperature T_{Pool}. Using eq. (7) together with eq. (6) this gives

$$\left(T_{Pool} - T_{SC}\right)_P = 2.7 \cdot \left(T_{Pool} - T_{SC}\right)_M \ . \tag{22}$$

Here, the volumetric heating power ratio $\dot{q}_R$ is equal to unity as is given in table 1. Taking the Friction number ratio in eq. (6) equal to unity is a conservative approximation for the range of Reynolds numbers investigated.

Finally, the combination of eqs. (21) and (22) results in an expression for the prototype pool temperature.

$$\left(T_{Pool} - T_{HX,in}\right)_P = \left(6.35 - 2.7\right)\left(a \cdot T_{HX,in} + b\right)_M + 2.7\left(T_{Pool} - T_{HX,in}\right)_M \ . \tag{23}$$

Taking the decay heat at a time of ten days into the accident, which is taken as the end of the short-term two-phase and beginning of the long-term single-phase behaviour, and a secondary side temperature of $20°C$, one gets prototype pool temperatures of $T_{Pool} = 80°C$ with both heat exchangers in operation, $T_{Pool} = 108°C$ with the horizontal heat exchanger in operation and $T_{Pool} = 116°C$ with the vertical heat exchanger in operation. This means

that the reactor sump can conditionally be kept subcooled at the beginning of the long-term behaviour.

In order to lower the pool temperature the heat transfer has to be improved. This can easily be done by introducing more heat transfer area. Future model experiments will be equipped with a second vertical heat exchanger along the left wall of the vertical compartment and an array of vertical heat exchangers sitting on top of the horizontal heat exchanger, their axes being parallel to the main flow direction. Thus, the stable stratification above the horizontal heat exchanger and its thermal isolation can be broken up.

5. CONCLUSIONS

At the Forschungszentrum Karlsruhe the SUCO program provides the means to demonstrate the basic physical phenomena of passive decay heat removal from a large coolant pool. Using three consecutive model experiments the two-phase short-term and the single-phase long-term behaviour can be scaled correctly. First measurements with the SUCOS-2D test facility give a qualitative view of the temperature field within the sump for the long-term single-phase natural circulation. A stable natural circulation is found for all operational conditions investigated. Optical investigations show a well-defined mixing zone above the heated plate and a more or less uniform and stagnant pool above. An increase in heat exchanger inlet temperature and an introduction of flow resistances result in higher pool temperatures. The coolant pool acts as an intermediate and homogeneous heat storage.

A transformation of the experimental results of the model to prototypic conditions results in a subcooled reactor sump in the long-term behaviour. The optional sump cooling design realizes a reliable, passive long-term decay heat removal system.

Future work is directed into detailed parameter variation studies, mainly regarding heating power as a function of time and location. In addition, more effective heat exchanger arrangements and more heat transfer area will be introduced in order to increase the subcooling of the reactor sump.

NOMENCLATURE

a	cross-sectional flow area, m^2
a	slope eq.(21), *dimensionless*
A	cross-sectional flow area ratio, *dimensionless*
b	ordinate offset eq.(21), $1/K$
c_p	heat capacity, $J / kg\ K$
d	hydraulic diameter, m
f_m	two-phase friction factor, *dimensionless*
F	Friction number, *dimensionless*
g	gravitational constant, m / s^2
h	enthalpy, J / kg
K	orifice loss coefficient, *dimensionless*
l	length, m
L	length ratio, *dimensionless*
N_d	drift flux number, *dimensionless*
N_f	friction number, *dimensionless*
N_{Fr}	Froude number, *dimensionless*
N_{PCh}	phase change number, *dimensionless*
N_{Sub}	subcooling number, *dimensionless*
N_ρ	density ratio, *dimensionless*
Nu	Nusselt number, *dimensionless*
Pr	Prandtl number, *dimensionless*
$\dot{q}$	volumetric heating power, W/m^3

q''_W wall heat flux, W/m^2
Q heating power, W
Ri Richardson number, *dimensionless*
St Stanton number, *dimensionless*
T temperature, K
u velocity, m/s
U_{Gj} vapor drift velocity, m/s
V volume, m^3

Greek letters

α heat transfer coefficient, W/m^2K
β expansion coefficient, $1/K$
Γ_G volumetric mass exchange rate, kg/m^3s
ε void fraction, *dimensionless*
λ thermal conductivity, W/mK
ν kinematic viscosity, m^2/s
$\xi_{2\varphi}$ frictional loss coefficient, *dimensionless*
Π_t transient time scale, *dimensionless*
ρ density, kg/m^3
τ time scale, s

Subscripts

G gas phase
HX,in heat exchanger inlet
i i-th section
L liquid phase
m mixture
M model
P primary side, prototype
R ratio
sub subcooling
S secondary side
SC sub-compartment
W wall
0 reference constant

REFERENCES

[1] H. A. Weisshäupl and D. Bittermann, "Large Spreading of Core Melt for Melt Retention/Stabilization", Proc. 5th Int. Seminar on Containment of Nuclear Reactors, August 23-24, Karlsruhe, FR Germany, pp. 347-355 (1993).

[2] J. U. Knebel, "Investigations on Sump Cooling After Core Melt Down", Proc. Int. Nuclear Congress ENC '94, October 2-6, Lyon, France, Vol. II, pp. 521-525 (1994).

[3] B. Kuczera, W. Eglin, and H. A. Weißhäupl, "Towards an Enhanced Quality in Pressurized Water Reactor Safety", Kerntechnik 59, pp. 151-155 (1994).

[4] M. Ishii, I. Kataoka, "Scaling Laws for Thermal-Hydraulic Systems Under Single Phase and Two-Phase Natural Circulation", Nucl. Engrg. Des. 81, pp. 411-425 (1984).

[5] R. L. Powell, W. J. Hall, C. H. Hyink, L. L. Sparks, G. W. Burns, M. G. Scroger, H. H. Plumb, "Thermocouple Reference Tables based on the IPTS-68", U.S. Department of Commerce, National Bureau of Standards (1974).

[6] H. Borgwaldt, W. Baumann, G. Willerding, "FLUTAN Input Specifications", KfK-Report 5010, Kernforschungszentrum Karlsruhe, FR Germany (1992).

CONTAINMENT ATMOSPHERE RESPONSE TO EXTERNAL SPRAYS

Joseph Green and Kazys Almenas
Nuclear & Materials Engineering Department
University of Maryland at College Park
College Park, MD 20742

ABSTRACT

The application of external sprays to a containment steel shell can be an effective energy removal method and has been proposed in the passive AP-600 design. Reduction of the steel shell temperature in contact with the containment atmosphere enhances both heat and mass transfer driving forces. Large scale experimental data in this area is scarce, therefore the measurements obtained from the E series tests conducted at the German HDR facility deserve special attention. These long term tests simulated various severe accident conditions, including external spraying of the hemispherical steel shell. This investigation focusses upon the integral response of the HDR containment atmosphere during spray periods and upon methods by which lumped parameter system codes, like CONTAIN, model the underlying condensation phenomena. Increases in spray water flowrates above a minimum value were ineffective at improving containment pressure reduction since the limiting resistance for energy transfer lies in the noncondensable-vapor boundary layer at the inner condensing surface. The spray created an unstable condition by cooling the upper layers of a heated atmosphere and thus inducing global natural circulation flows in the facility and subsequently, abrupt changes in lighter-than-air noncondensable (H_2/He) concentrations. Modeling results using the CONTAIN code are outlined and code limitations are delineated.

1. INTRODUCTION

The use of external sprays on the outside surface of the containment steel shell has been proposed as a means of energy removal in passive designs. This has renewed interest in the area of condensation heat transfer in general and in external spray induced condensation in particular. The field of condensation heat transfer in the presence of noncondensable gases has been extensively studied in the past. A recent review of the relevant literature is provided in the work by Green [1] Classical studies of the subject are presented in publications by Sparrow [2,3] Minkowycz [4], Mori [5] and Fujii [6]. Although insightful from a theoretical standpoint, such detailed boundary layer solutions are generally not useful for performing containment analysis. For this purpose a range of approaches which can be implemented into nodal system codes have been formulated. The most extensively used methods employ the analogy between heat and mass transfer as described by Herr [7], Vernier [8] and Bestion [9]. The analogy method is the basis for the structural heat transfer model implemented into the USNRC best estimate code CONTAIN (Murata [10]) as well as other codes such as COMPACT (Smith [11]), GOTHIC (Kennedy [12]) and MAAP4 (Paik [13]). More specific studies in this area include the analysis of condensation energy transfer processes for geometries and surfaces used in components of the advanced design reactor systems and containments. Of recent interest has been the experimental and analytical work reported by Dehbi [14], Siddique [15,16], and Vierow [17]. Huhtiniemi [18], and Stein [19] note enhanced heat transfer over that of a vertical plate for condensation on the underside of a cooled wall and attribute this to the effect of falling film droplets and enhanced natural circulation mixing of the gas-vapor boundary layer. Application of external sprays to containment cooling has been evaluated by Covelli [20] who provided one of the earliest analysis of the use of outer shell sprays as a pressure reduction method during the later stages of severe reactor accidents. He presents a mechanistic and simplified numerical model of external containment sprays in order to deduce imposed structural thermal stresses. These studies provide a groundwork for understanding the integral response of containment atmospheres to external spray.

In spite of extensive theoretical studies and a large data base dealing with various aspects of condensation, very few studies are available which simultaneously treat external sprays and condensation heat transfer in the presence of noncondensables. This is especially true for experimental data obtained in large scale experimental facilities which can be scaled with reasonable certitude up to prototypical size and conditions. In general, recent experimental data obtained from small and large scale test facilities (SST and LST) associated with the AP-600 design are maintained proprietary (Kennedy [12,21], Wright [22], Spencer[9], and Peters [24]). Some data is available from the small scale facility of Cha [25]. In this context some of the experimental results obtained as part of the HDR E11 test series deserve further analysis.

The HDR facility has provided large scale experimental containment results in a number of containment safety related areas. Of interest to this paper are two tests (E11.2 and E11.4) intended to model the impact produced on the containment by a small break transient of very long duration (up to 56 hrs) which leads to core damage. During the evolution of the transient a wide range of energy/mass source terms were simulated. This included primary system blowdown, long term decay energy input, release of a heated mixture of He and H_2 to simulate the $Zr-H_2O$-water oxidation reaction as well as heating of the sump water to simulate energy input due to core melt. These tests have been extensively documented in the past (Bader [26], Holzbauer [27], Wenzel [28], and Valencia [29,30]). Near the end of these two lengthy tests, spray water was applied to outside surface of the steel containment dome. The spray was applied at constant but step-wise increasing flow rates for a total time of ~4 hours. Since the HDR facility is extensively instrumented a large data base regarding the containment atmosphere and structure response during a spray event has been generated. The uniqueness of this database is due in part to the HDR facility instrumentation not typically available in other test facilities. This includes atmospheric composition measurements and atmospheric velocity meters oriented in several directions. This aspect of the E series tests has not remained completely unnoticed. Thus Tuomisto [31] made use of Covelli's work coupled with results from the HDR E11.2/E11.4 experiments for application to the Loviisa VVER-440 containments. They found that the natural circulation heat and mass transfer analogy methods considerably underestimate the experimental energy transfer to the HDR steel shell. In their case the estimate of an upper pressure envelope was desired therefore the models were accepted as adequate since they lead to conservatively overestimated containment pressure. The study showed that the calculated HDR containment pressure using a single volume representation is highly dependent upon the method used for determining the internal condensing/convective heat transfer coefficients whereas changes in spray mass flowrate (even by factors of 2x) did not produce significantly different results.

This study focuses on the data collected during the spray periods of the HDR E series tests and on the implications that these experimental results have for the modeling of containment response by means of nodal system codes.

2. HDR CONTAINMENT ATMOSPHERE RESPONSE TO EXTERNAL SPRAYS

Experimental geometry and conditions

The KFK HDR facility is a decommissioned light water reactor containment having a volume of 11,060 m^3 and height of 60 m. As shown in Figure [illegible] HDR is a highly compartmentalized facility, and while this complicates analytical efforts, this is the price paid for [illegible] with an actual containment. The gain is that the experimental results implicitly incorporate the effect of a realistic inventory of internal heat sinks and surfaces. Of importance to this study is the 3 cm thick steel shell which surrounds the facility and which is separated by a 60 cm width annular gap from the outer concrete superstructure. Over 700 instrument data channels are recorded for a typical test. This includes traditional thermocouples and pressure transducers along with measurements of gas concentrations, local atmospheric velocities and internal structural temperatures.

As noted, the E series tests extended for tens of hours during which the containment was subjected to a range of boundary conditions expected during a long term, severe accident. The boundary condition of special

interest to this study is the step wise incremented spraying of the external upper half of the hemispherical dome. This occurred late in the test sequence when internal containment conditions were approaching thermal equilibrium. For both the E11.2 and E11.4 experiments containment pressure was allowed to decrease to approximately 1.75 bar via natural cooldown prior to the onset of spraying. In both tests the extended injection of external steam as well as the introduction of the 85%/15% (by volume) helium/hydrogen mixture has ceased. As shown in Table 1, the roughly 4 hr spray period begins with an initial mass flowrate of 6 kg/sec which is raised in 2 kg/s increments as the test progresses.

Only the uppermost portion (upper 5 meters) of the dome region shell was sprayed during these tests. A schematic of the spray head placement and the location of temperature instrumentation is shown in Figure 2. The spray was delivered through an arrangement of 48 spray nozzles (32 at 45 meters, 12 at 49 meters and 4 at 50 meters) and the runoff was collected at the 45 meter elevation in a plastic gutter apparatus. The spray water temperature was nearly constant at 10°C.

In order to determine the heat transfer to the steel shell, several sets of four thermocouples were placed at the elevations shown in Figure 2. These measurements trace the time history of the heat transfer path from the inner containment atmosphere to the gas space in the annular gap. The balance of this section reviews measurement results which are impacted by the external spray.

Pressure and Temperature Response

The containment pressure response during shell spray periods for the two E-series tests are shown in Figure 3 along with associated CONTAIN code model predictions. The decrease in pressure just prior to the initiation of sprays is due to natural cooldown following the cessation of external steam introduction. The first qualitative observation which can be made is that the rate of pressure decrease is not visibly dependent upon the outer shell spray flowrate. This is a direct illustration of the circumstance that once the outer shell is completely wetted (this is achieved by the lowest spray rate of 6 kg/s), the principal resistance to energy transfer is transposed to the noncondensable atmospheric diffusion layer on the inside surface of the steel shell. An approximate quantitative assessment of the pressure response shows that a change in the pressure decrease does occur for both tests during the spray periods. Two periods can be distinguished: an initial one showing a larger pressure decrease rate, followed by a period during which the rate of pressure decrease is smaller. For example, during the E11.4 test for the first ~50 minutes after initiation of sprays, the rate of pressure drop is approximately ~4 Pa/s while for the 160 minutes until the end of spraying the rate decreases to ~1.2 Pa/s. The response of the E11.2 experiment shows a similar transition occurring after ~135 minutes of spray duration, with roughly similar

TABLE 1 - HDR OUTER SPRAY CHRONOLOGY

EVENT	TEST E11.2 (min.)	TEST E11.4 (min.)
End of Gas Introduction	772	2200
End of Steam Introduction	959[a]	2790[b]
Start @ 6 kg/s	975	2800
Increase to 8 kg/s	1095	2920
Increase to 10 kg/s	1155	2980
Increase to 12 kg/s	1185	3010
End of Spray	1200	3012

a Steam introduction at 0 m
b Sump Boiling

values of the linearized depressurization rate for the two periods. Neither of the transitions are correlated to changes in the spray flow rate and the significantly different time of their occurrence implies that the cause for the change are processes which occur on the inside of the shell. In this particular case it is the higher atmospheric stratification and the resulting internal atmospheric currents which determines the delayed transition to lower depressurization rates for test E11.2. As described elsewhere (Wolf [32,33], Valencia [30]) steam and gas introduction for the E11.2 test was performed high in the containment resulting in highly stratified conditions.

Atmospheric pressure is an integral parameter influenced by all processes occurring in the containment thus a better illustration of the energy transfer rates occurring locally is provided by the measured traces of the steel shell thermocouple quadruples shown in Figure 4. The figure shows that temperatures in the annular space and at both metal surfaces respond to changes in the spray mass flowrates. However as seen, after an initial period, the containment atmosphere temperature is in effect 'decoupled' from the changes occurring in the shell temperature. This is shown especially clearly for test E11.2 where a decrease in shell temperatures produced by a larger spray flow rate at ~1100 minutes is accompanied by a constant (and at some locations a slightly increased) nearby internal atmospheric temperature. The test data shows that the rate of decrease in containment temperature and pressure are not influenced by increased external spray flowrates. Other phenomena, in this case the initiation of containment wide atmospheric currents, are dominating the internal containment response.

The above observations are relevant since they illustrate that during a long duration accident (for these tests sprays are initiated ~16 and 46 hours after the break) the containment atmosphere response can not be considered independently, but must be analyzed together with the thermal history of all the internal structures. It is the structures, which by virtue of their considerably larger heat capacity will dominate atmospheric cool down and depressurization rates. The response of the containment atmosphere will therefore be strongly influenced by changes in internal circulation currents which influence energy transport to and from internal heat sinks, and will respond only in a secondary and delayed manner to changes in outside boundary conditions like external sprays.

Atmospheric Concentration Measurements

Relative steam and gas concentration traces from instruments located in the dome region are shown in Figures 5 (a,b) and 6 (a,b) for the E11.4 and E11.2 tests respectively. For both tests the initiation time of the external sprays can be clearly deduced from these measurements. As would be expected, the spray caused increase in the condensation rate leads to a drop in the volumetric steam concentration. Since the figures depict the relative molar concentrations, the decrease in vapor content is mirrored by a corresponding increase in both air and lighter noncondensables.

The vapor content figure can provide a partial explanation for the already noted variation of the depressurization rate. The figures show that for both tests the vapor removal rate changes once the relative vapor concentration reaches the 20 to 15 molar % level. The relative vapor concentration has a large influence on the condensation rate, but this is only a partial explanation, since the change in vapor content also alters the relative atmospheric densities and leads to an initiation of recirculation currents. The direction of these currents can be inferred from the concentration measurements obtained by instruments located above the two main vertical flow paths. For the E11.4 test, concentration measurements located in the elevator shaft register a sharp increases in steam concentration (Figure 5d) while a corresponding decrease for the spiral stair side (Figure 5c) is seen. Steam from the lower segment of the containment is carried up the elevator shaft side of the containment via the natural circulation flows. The dome atmosphere, which has become depleted in steam, then flows downward into the spiral staircase. Molar gas mixture and noncondensable levels show an anticipated opposite effect. Gas concentrations in the containment dome region are seen to rise during the initial 50 minutes of E11.4 spraying. Green [1] shows that once the global flowpath is set in motion at 2850 minutes, a sharp drop in the gas concentration is realized for the elevator shaft pathway with a corresponding rise for the downward flow in the spiral stair. Gas at higher elevations is then transported to lower levels by the sweep downward.

In the case of the E11.2 experiment, global circulation patterns up and down the containment are not evident. Rather there is indication of upward motion in both major flow passages. From the start of spraying until ~1120 minutes the steam concentrations on both sides of the HDR containment remain relatively constant. After that time steam fractions drop sharply (Figure 6 c,d). Evidence of the downward progression of mixing flows is seen by the time delay between the sharp change in measured concentrations as depicted in these two figures. Gas mixture concentrations show an anticipated opposite behavior, staying relatively constant at ~2.5% for the initial 2 hrs of spraying and then rapidly rising to over 12% by volume once flow patterns are developed. A somewhat cluttered illustration of the light gas concentration measurements during external spraying is given in Figure 7. The highly stratified atmosphere is slowly mixed, down to the 16 meter level, by the flow patterns developed as the result of the external sprays.

Velocity Measurements

A less successful, but nevertheless interesting indication of containment atmosphere motion is provided by a series of turbine-like velocity-meters located in the major flowpaths. An approximate indication of flow direction can be inferred via the use of two turbine-meters placed at 90° angles to one another. Atmospheric motion, especially in the dome region can acquire various directions, thus these instruments can not be expected to reflect the entire flow field. Another limitation is that the lower limit of detection for these instruments is 0.1 m/s. In spite of these drawbacks, the instruments do manage to provide direct evidence of the initiation and decay of strong internal circulating currents. Selected examples of atmospheric velocity measurements during the spray periods are presented in Figures 8 and 9.

As shown in Figure 8 (a), for the E11.4 test, the external spray generated immediately measurable (although intermittent) velocities in the uppermost dome region ranging from ~10 to 30 cm/s. At the same time the shaft velocities (Figures 8(c) and 8(d)), remain below the levels at which the turbine is initiated until ~50 minutes after the beginning of the spray period. At this time strong flows are registered moving up the elevator shaft side and down the spiral stair sides of the HDR containment. Figure 8 (c) & 8 (d) record velocities ranging from 1 to 2 m/s in the open shafts which once initiated increase in magnitude. The flow pattern encompasses nearly the entire containment, with velocities exceeding 1.5 m/s measured even at a 10 meter elevation.

As has been noted, during the E11.2 test steam was introduced at a higher elevation, leading to remarkably stable temperature and concentration stratification. It required a duration of the spray period in excess of ~2 hours until sufficient steam was condensed in the dome region to establish significant natural circulation flows. The initiation of these flows is illustrated in the velocity measurements shown in Figures 9 (a-d). As seen, all the turbine-meters are quiescent during the first ~2 hours of the spray period. At ~1100 minutes of test time, the turbines are able to register atmospheric velocities, first high in the dome region and shortly thereafter also in the shaft regions which connect to the lower sections of the containment. The velocities do not reach the levels noted for the E11.4 test nor do they penetrate as low in the containment. This is reasonable, since for the E11.2 test the steam is placed preferentially in the upper regions of the containment and consequently, after the dome steam is partially condensed, less is available to move upwards along the vertical shafts.

Internal energy transfer rates

The energy transport to and from the structural surfaces of the HDR containment has been analyzed in detail by Green [1]. It is shown that the process depends primarily on local atmospheric composition, the surface to atmosphere temperature difference and the local atmospheric velocity. Other parameters, such as pressure, surface condition, film thickness and film turbulence have only secondary influences. From the modeling standpoint, of the three noted primary parameters, the most problematic is certainly the local atmospheric velocity. Reference [1] proposes a modification to the CONTAIN code which leads to an improved utilization of the computed inter-compartmental velocity, but it should be expected that within the framework of lumped parameter codes the ability

to represent local velocity will remain limited. Inspection of the available measured energy transfer data provides insight into the influence of this parameter.

A brief quantitative analysis of the serial thermal resistances to heat transfer from the externally sprayed cooling water to the inside atmosphere of the containment is instructive. The outside liquid film formed by the flowing cold spray water can effectively be ignored in this case in comparison to the remaining resistances since the large flow and the cold temperature (10°C) yield high heat transfer coefficients. As a result, the convective heat transfer from the film surface to the flowing annulus gases is not analyzed further. (Unlike the AP-600 design these HDR tests did not include a significant flow of the annular gas counter-current to the falling film. Significant evaporation of the external liquid film is not evident.) A second resistance to heat transfer is provided by conduction through the steel shell. The thermal conductivity of the 3 cm thick shell is ~43 W/m°C which equates to a resistance of 7.0×10^{-4} m²°C/W. Conduction through an inner condensate film will vary depending upon the film thickness and temperature. Inclusion of a 0.5 mm thick film along with a typical layer of paint/rust produces a combined resistance of ~1×10^{-3} m²°C/W. The measured experimental heat transfer coefficients (to be shown) were predominantly under 500 W/m²°C during spray periods (in fact predominantly in the range 100-300 W/m²°C). This confirms that the inner convective/condensing boundary layer would yield a high-end resistance of 2×10^{-3} m²°C/W thus forming by far the major barrier to heat transfer.

As shown in Figure 2, at various locations of the steel shell, a "quadruple" set of thermocouples measure the local temperature from the outside gap to an atmospheric temperature near the interior shell surface. The time dependent temperatures can be used to infer local heat fluxes and heat transfer coefficients using inverse heat transfer calculations based on the methods of Beck [34]. Representative time traces of the inferred heat transfer coefficients for both tests at the 48 meter elevation of the dome shell are shown in Figure 10 (a), (b). As a rule, inverse computation methods yield quite 'noisy' results, this is emphasized in this case because of the high conductivity of the carbon steel. Nevertheless, in spite of the clearly evident fluctuations, a meaningful average value of the internal surface heat transfer coefficient (h) can be inferred. It is thus instructive to compare these values with other measured results and expected trends.

The measurements show that during the spray period, the experimental heat transfer coefficients first trend downward and subsequently, over significant time periods (on the order of 1/2 hour) exhibit constant or upward bulges. The initial trend approximately follows the change in the vapor concentration, the most important parameter determining h magnitude. However, as shown in Figure 5 (a) the vapor concentration continues to decrease for the entire spray duration, but the inferred h value is reasonably steady at ~225 W/m²°C over lengthy time spans. The remaining heat transfer measurements at this elevation follow this pattern with some locations showing substantial increases in the value of h when global flows begin at 2850 minutes. The only measured parameter which approximately tracks these changes is the local velocity. Thus comparing Figures 9 (a, b) and 10 (b), shows that the increase observed at ~1100 minutes for test E11.2, coincides with the onset of measurable atmospheric motion. This quantifies the importance of local atmospheric motion and also illustrates the limitations in h modeling in the framework of lumped parameter codes.

As noted, at the time the sprays are turned on in the E test series, the transient has progressed for a long time and various internal structures have reached or are approaching thermal equilibrium. The initiation of sprays disturbs this equilibrium by introducing a new energy sink, and when it does so, the containment structures are no longer being heated by the atmosphere but instead are acting as sources of energy. The pressure reduction is then governed by the natural cooldown of the entire containment. For example, note in Figure 3 that when the external sprays are stopped, the containment pressure for both tests exhibits a slight increase with time over extended periods. No additional energy sources are being provided at this time, so this is an illustration that energy is being removed from the structures as they cool and deposited into the atmosphere thereby causing the rise in pressure.

This process can be observed by examining the temperature and profiles for a representative concrete heat structure located at 23.5 meters in the spiral stair of the HDR containment. The concrete block has been

instrumented with thermocouples at 5 and 15 mm from the exposed surface and is one of those located directly in a major flowpath. Applicable temperature traces over the period of shell spray for both E11.2 and E11.4 are shown in Figure 12 (a,b). Once flow patterns are established for both tests it is seen that the atmospheric temperature just adjacent to the structure face is measurably lower than the temperatures internal to the block and the inferred (inverse heat transfer calculation) surface temperature. This implies not a condensing environment but rather an evaporating one.

3. MODELING OF EXTERNAL SPRAYS USING THE CONTAIN CODE

The CONTAIN code version 1.12(c110v) was utilized to model the E11 series of experiments using the nodalization schemes shown in Figure 12. As the figure shows, the upper dome is segmented so that the region encompassed by the external spray can be represented by separate nodes. The resulting CONTAIN code generated pressures are shown in Figure 3. Details regarding the models and the overall ability of CONTAIN to evaluate conditions for the E11.4 and E11.2 tests can be found in the reports by Green [1] and Tills [35] respectively.

In general, as the comparisons shows, the ability of the code to reproduce the time history of an integral parameter such as pressure is satisfactory. As should be expected, it produces a better match for the relatively homogeneous atmospheres prevailing during test E11.4, then for the highly stratified atmospheres which characterized the E11.2 test. For both tests, the code underestimated the amount of energy removed during the spray periods and therefore over predicted the containment pressure. However, considering the complexity of the HDR containment, the variety of boundary conditions present during the tests and comparing this to the simplicity of region-averaged parameters that a nodal approach imposes, the achieved agreement is quite remarkable.

It is certainly reassuring that the most important parameter determining containment integrity, the atmospheric pressure, can be evaluated with a high level of confidence. However, this does not imply that all energy transfer rates are modeled adequately. The long term pressure is strongly dependent on the balance between the energy source terms and the heat capacity of the internal heat sinks. When energy transport to heat structures becomes conduction limited, the importance of an accurate representation of the time dependent energy transport rates in the evaluation of containment pressure decreases. The limitations of nodal methods have been analyzed in numerous publications, a number of which are noted in the introduction. This section considers several phenomena which are unique to modeling of external sprays.

The most important phenomenon determining the accuracy of energy transport across a steel shell has already been noted. Namely, once sufficient external spray volume is available that the outer surface is wetted, the diffusive noncondensable rich boundary layer which forms on the inside of the shell surface becomes the major resistance to heat transfer. The total energy transport rate will then be sensitive to those model features which represent this resistance.

The CONTAIN surface heat transfer model is based upon the heat and mass transfer analogy. The total heat flux to a structure is evaluated as the sum of condensing, convective, radiative and aerosol contributions. In the analysis of the E.11 tests, energy transfer rates due to aerosols and radiation are small and are not considered. The algorithm implemented in CONTAIN first determines a convective Nusselt number using empirical correlations based upon an appropriate choice of a flow regime. A more detailed explanation of the heat transfer model in CONTAIN is provided in references [10,1].

Heat transfer from the steel shell to the external water film is one of the primary limitations of the CONTAIN code version used. For this work a constant energy removal rate from the modeled dome structure was imposed. Several values were tested (heat transfer coefficients to the annulus region ranging from 300 to 3000 $W/m^{2o}C$) with the result being that the predicted response was relatively insensitive to this value since the limiting resistance was located at the inner condensing surface. However, it is expected that variations in the external film

thickness and even patches of wet and dry areas would develop leading to non-uniform energy removal rates from the shell. This is especially relevant to the AP-600 where the film flows along the length of the exterior shell. Recent code enhancements (not available for this investigation) have been implemented in CONTAIN which allow for external film tracking and film evaporation. These enhancements are currently being tested.

Geometric Effects

One of the characteristics of the HDR external spray tests is that only the upper segment of the containment shell was wetted. Figure 2 shows that the segment in question encompasses the curved hemispherical portion of the upper dome region. This makes a comparison with theoretical models more difficult because the majority of studies analyzing condensation in the presence of noncondensable gases considered flat vertical or horizontal surfaces. The variable orientation of the hemispherical interior surface can impact the evaluation of the internal resistance to heat transfer in two ways:

1) The empirical correlations used in CONTAIN apply either to horizontal or vertical surfaces.

2) Indirect evidence suggests that not all of the condensate formed on the hemisphere runs off as a surface film. A portion of it "rains out" in the form of droplets. Falling droplets would increase the turbulence in the noncondensable enhanced boundary layer and alter heat transfer rates.

Although inconclusive, test data from the spray period does hint that droplets are falling from the dome surface rather than flowing along the inner surface. Inner shell thermocouple measurements at elevations just below the spray apparatus do not register the passing of a cooler liquid film as would be expected. The presence of falling droplets is also indicated by sudden step temperature decreases observed for exposed dome region thermocouples. This is attributable to drops which occasionally intercept the exposed thermocouple bead thus lowering its temperature.

Lighter-Than-Air Noncondensable Gases

As noted in the introduction, a He/H_2 mixture was released into the HDR containment atmosphere prior to initiation of external sprays. The subsequent transport and distribution of these gasses has been documented elsewhere [30, 32, 33]. In this study we consider only the effect they have on the thermal resistance of the noncondensable boundary layer.

Lighter-than-steam noncondensables, as expected, act in some respect quite differently when compared to heavier gases such as air. Thus the higher diffusivity of these lighter gases will reduce inhibition to condensation heat transfer. Once transported into the gas-vapor boundary layer the He and H_2 are more likely to diffuse back into the bulk mixture.

In another respect the lighter than steam gases can have an inhibiting effect. Thus for vertical surfaces their accumulation in a boundary layer will have an 'inverse' impact on density driven flows. That is, whereas an accumulation of heavier-than-steam gases, as well as density increases produced by lower boundary layer temperatures, will generate downward motion of the gaseous boundary layer, the accumulation of lighter than steam gases, will reduce these differences, and if they are present in sufficiently high concentration could reverse the direction of the buoyancy driven flows entirely. Under natural circulation conditions, correction for such density effects can be accommodated through the use of a modified Grashoff number as proposed by Vernier [8].

$$Gr^* = \frac{g L^3}{\nu^2} [\beta (T_\infty - T_i) + \gamma (X_i - X_\infty)]$$

Presently, condensing heat transfer models used by the CONTAIN code do not incorporate modifications to account for such boundary layer stagnation.

For the above listed reasons it can be anticipated that the CONTAIN code can model the energy transfer rates observed in the hemispherical surfaces only to a limited extent. As shown in Figure 13 (a-c) that is indeed the case. The figures present a comparison of the experimentally inferred heat transfer coefficients during the spray periods of E11.2 and E11.4 with equivalent values computed by the standard, as well as a 'modified' CONTAIN model. The modified model implemented the above definition of the Gr number. As a benchmarking point, the figures also include the extensively used Uchida [36] correlation which is dependent only on the local vapor to noncondensable mass fraction.

As shown, the experimental values are significantly greater than any of the CONTAIN models and higher as well as the single parameter Uchida correlation. This observed difference illustrates the impact of the following phenomena not accounted for in the calculations:

- Local atmospheric velocities.
- Increase in boundary layer turbulence due to falling condensate drops.

The models used have several additional limitations such as the noted issue of surface orientation, the enhancement of diffusivity by He and H_2, the alteration of the buoyancy by the same gases and a list of even more secondary effects. However on the basis of extensive comparisons of separate effect and integral heat transfer measurements with model results, it is concluded that the noted two are the dominant ones. On the basis of the available experimental information it is difficult to asses their individual contribution quantitatively.

4. CONCLUSIONS

The use of external containment sprays to reduce containment accident atmospheric pressures has been proposed for advanced reactor designs. In the presence of noncondensable gases it is the diffusive gaseous boundary layer on the inside surface of the containment steel shell that represents the major resistance to energy removal and therefore must be well understood. This investigation has focussed upon the integral response of the HDR containment atmosphere to external shell spraying during the E11.2 and E11.4 experiments and the methods employed by the best-estimate tool CONTAIN in modeling such condensation related phenomena.

The HDR test data shows that increased spray mass flowrates above the minimum rate which wetted the outer surface did not result in appreciably increased energy removal rates. This is a direct consequence of the resistance imposed by noncondensables gases at the inner condensing surface of the shell. The rate of energy transport across the shell is therefore strongly influenced by phenomena which influence this boundary layer.

One of the effects of the external sprays is that by cooling the upper containment atmosphere an unstable density inversion is generated. Eventually, global natural circulation flow patterns developed for both tests. These flows serve to break up and mix the gas-vapor boundary layer and thus enhance energy transfer rates over those of stagnant conditions.

The effect of the induced atmospheric motions upon measured heat transfer rates is clearly demonstrated during both tests. Steam concentrations in the dome region over these time periods decrease significantly yet the heat transfer values do not show the anticipated decrease expected from such a large change in composition. The inferred heat transfer parameters show that bulk atmospheric motion can counteract the effect of increased noncondensable gas concentrations. In the case of E11.2, the heat transfer coefficients show clear downward trends in heat transfer rates due to the effect of increased noncondensable gas concentrations resulting from the initial 130 minutes of shell spraying. No measured velocities were recorded during this time period. Shortly thereafter, the

unstable situation created by the spray, produces bulk motions which in turn cause the measured heat transfer coefficients to increase or hold constant during the remainder of the spray procedure.

The CONTAIN code was used to model the E11 experiments with reasonable results. The code does not capture all of the aspects associated with outer shell spraying such as droplet formation or the effects of lighter-than-air noncondensable gases. Modifications such as a revised Gr number correlation and analogy defect correction factors are still insufficient to reproduce HDR experimentally measured heat transfer coefficients. Further modifications which include the effect of bulk atmospheric motions, a wavy film interface and boundary layer mixing due to falling droplets would aid the codes ability to model external shell spraying.

This work was performed under contract #NRC-04-91-062.

5. REFERENCES

[1] Green, Joseph and K. Almenas, *The Impac. of Bulk Atmospheric Motion Upon Condensation Heat Transfer in the Presence of Noncondensable Gases*, PhD. Thesis - Un'versity of Maryland and MDNE-93-005 Report to the U.S.N.R.C., (June, 1994).

[2] Sparrow, E. M., and S. H. Lin, *Condensation Heat Transfer in the Presence of a Noncondensable Gas*, Transactions of the ASME - Journal of Heat Transfer, pp. 430-436, (August, 1964).

[3] Sparrow, E. M., W. J. Minkowycz, and M. Saddy, *Forced Convection Condensation in the Presence of Noncondensables and Interfacial Resistance*, International Journal of Heat Mass Transfer, Vol. 10, pp. 1829-1845, (1967).

[4] Minkowycz, W. J., and E. M. Sparrow, *Condensation Heat Transfer in the Presence of Noncondensables, Interfacial Resistance, Superheating, Variable Properties, and Diffusion*, International Journal of Heat Mass Transfer, Vol. 9, pp. 1125-1144, (1966).

[5] Mori, Y., and K. Hijikata, *Free Convective Condensation Heat Transfer with Noncondensable Gas on a Vertical Surface*, International Journal of Heat Mass Transfer, Vol. 16, pp. 2229-2240, (1973).

[6] Fujii, T., "Theory of Laminar Film Condensation", Springer-Verlag, New York, (1991).

[7] Herr, J. F., J. R. Kadambi and U. S. Rohatgi, *Condensation in Presence of Non-Condensible Gases*, Gas-Liquid Flows 1993, FED-Vol. 165, pp. 77-86, (1993).

[8] Vernier, P.J., and P.Solignac, Atest of Some Condensation Models in the Presense of Noncondensable Gas Against ECOTRA Experiment, Nuclear Technology, Vol. 77, pp.82-91, (april,1987)

[9] Bestion, D., and P. Coste, Study on Condensation Modeling in the CATHARE Code with and without Noncondensable Gases, International Conference on New Trends in Nuclear System Thermalhydraulics, Vol. 1, pp. 311-318, Pisa, Italy, (June, 1995).

[10] Murata, K. K., et. al., User's Manual for CONTAIN 1.1, A Computer Code for Severe Nuclear Reactor Accident Containment Analysis, NUREG/CR-5026, SAND87-2309, (November, 1989).

[11] Smith, P. N., and P. Ellicott, A UK Analysis of Light Gas Distribution Experiment E11.2 in the HDR Facility, Nuclear Engineering & Design, Vol. 140, pp. 61-68, (1993).

[12] Kennedy, Marcia D., Heat Transfer Predictions for Containment Analysis Codes: A Comparison of Westinghouse-GOTHIC's Mechanistic Correlations and the Tagami Correlation, 93-WA/HT-77, Proceedings of the ASME - Winter Annual Meeting (1993).

[13] Paik, C. Y., M. A. McCartney, R. E. Henry and J. H. Scobel, MAAP4 Models and Its Application to Westinghouse AP600 Plant, ASME/JSME Nuclear Engineering Conference, Vol. I, pp. 561-572, (1993).

[14] Dehbi, A. A., M. W. Golay and M. S. Kazimi, *The Effects of Noncondensable Gases on Steam Condensation Under Turbulent Natural Convection Conditions*, Program for Advanced Nuclear Power Studies, Report No. MIT-ANP-TR-004, Massachusetts Institute of Technology, (June, 1991).

[15] Siddique, M., M. W. Golay, and M. S. Kazimi, *The Effect of Hydrogen on Forced Convection Steam Condensation*, AICHE Symposium Series on Heat Transfer, Philadelphia, Vol. 85, No. 269, pp. 211-216, (1989).

[16] Siddique, M, M. W. Golay, and M. S. Kazimi, Local Heat Transfer Coefficients for Forced-Convection Condensation of Steam in a Vertical Tube in the Presence of a Noncondensable Gas, Nuclear Technology, Vol. 102, pp. 386-402, (1993).

[17] Vierow, K. M., V. E. Schrock and P. F Peterson, Condensation in a Natural Circulation Loop with Noncondensable Gas Present - Part I Heat Transfer, Japan-U.S. Seminar on Two-Phase Flow Dynamics, University of California, Berkeley, (July, 1992).

[18] Huhtiniemi, I, J. J. Barry, and M. L. Corradini, *Condensation in the Presence of a Noncondensible Gas: The Effect of Surface Orientation*, AICHE Symposium Series on Heat Transfer - Philadelphia, Vol. 85, No. 269, pp. 205-210, (1989).

[19] Stein, R. P., D. H. Cho and G. A. Lambert, Condensation on the Underside of a Horizontal Surface in a Closed Vessel, in Multiphase Flow and Heat Transfer, HTD-Vol. 47, 23rd National Heat Transfer Conference - Denver, V. K. Dhir and S. C. Chen editors, pp. 85-91, (August, 1985).

[20] Covelli, et. al., *Simulation of Containment Cooling with Outside Spray After a Core Meltdown*, Nuclear Engineering & Design, Vol. 69, pp. 127-137, (1982).

[21] Kennedy, M. D., J. Woodcock, R. F. Wright, and J. A. Gresham, Westinghouse-GOTHIC Comparisons with 1/10 Passive Containment Cooling Tests, International Conference on New Trends in Nuclear System Thermalhydraulics, Vol. 2, pp. 535-540, Pisa, Italy, (June, 1995).

[22] Wright, R. F., D. R. Spencer and F. Delose, Reactor Passive Containment Cooling System Small Scale Containment Cooling Tests, Proceedings of the ANS/ASME Nuclear Energy Conference, San Diego, CA, (August, 1992).

[23] Spencer, D. R., J. Woodcock, R. F. Wright, J. E. Schmidt, M. Parnes and D. E. Christenson, Reactor Passive Containment Cooling System Tests Scaling Evaluation and Analysis, ASME/JSME Nuclear Engineering Conference, Vol. 1, pp. 663-670, (1993).

[24] Peters, F. E., A. T. Pieczynski, and M. D. Carelli, Advanced PWR Passive Containment Cooling Experimental Program, International Conference on New Trends in Nuclear System Thermalhydraulics, Vol. 2, pp. 37-43, Pisa, Italy, (June, 1995).

[25] Cha, Jong Hee, and Hyung Gil Jun, Heat Transfer in the Passive Containment Cooling System, International Conference on New Trends in Nuclear System Thermalhydraulics, Vol. 2, pp. 29-36, Pisa, Italy, (June, 1995).

[26] Bader, *Erganzungsberict Versuchsprotokolle Versuchgruppe CON E11*, PHDR Nr. 10.017/90, (March, 1990).

[27] Holzbauer, H., L. Wolf and L. Valencia, *Erste Auswertund der Versuchsergebnisse zum Druckaufbau und sur Wasserstoffverteilung der Versuchsreihe E11*, 14 Statusbericht, HDR Report (Arbeitsbericht 05.48/90), December, 1990.

[28] Wenzel, H., et. al., *Versuchsprotokoll - Versuch E11.2*, and *Versuchsportokool -Versuch E11.4*, Nr. 10.010/89 and 10.013/89.

[29] Valencia, L., et. al., *Design Report - Hydrogen Distribution Experiments E11.1 -E11.5*, PHDR Working Report No. 10.004/89, (August, 1992).

[30] Valencia, Luis A., Hydrogen Distribution Tests Under Severe Accident Conditions at the Large-Scale HDR-Facility, Nuclear Engineering & Design, Vol. 140, pp. 51-60, (1993).

[31] Tuomisto, Harri and Yrjo Hytonen, *Application of HDR Experiments E11.2 and 4 to Demonstrate Effectiveness of External Spray Cooling for Loviisa Containments*, Statusberickt des Projektes HDR-Sicherheitsprogramm des Kernforschungszentrums Karlsruhe, December 1990, Arbeitsberict 05.48/90, pp. 101-128.

[32] Wolf, L., T. Cron, D. Schrammel, and H. Holzbauer, *Hydrogen Mixing Experiments in the HDR Containment under Severe Accident Conditions*, Proceedings of the Twenty-First Water Reactor Safety Information Meeting, NUREG/CP-0132, (1993).

[33] Wolf, L., H. Holzbauer, and T. Cron, Detailed Assessment of the HDR Hydrogen Mixing Experiments E11, International Conference on New Trends in Nuclear System Thermalhydraulics, Vol. 2, pp. 91-103, Pisa, Italy, (June, 1995).

[34] Beck, J., Users Manual for CONTA - Program for Calculating Surface Heat Fluxes from Transient Temperatures Inside Solids, SAND83-7134, (December, 1983).

[35] Tills, J. L., Analysis of the HDR Test E11.2, Draft Report to the USNRC, (1993).

[36] Uchida, H., A. Ogama, and Y.Togo, Evaluation of Post-Incident Cooling Sytems of Light Water Reactors, Third International Conference on Peaceful Uses of Atomic Energy, Geneva, pp.436, (1965).

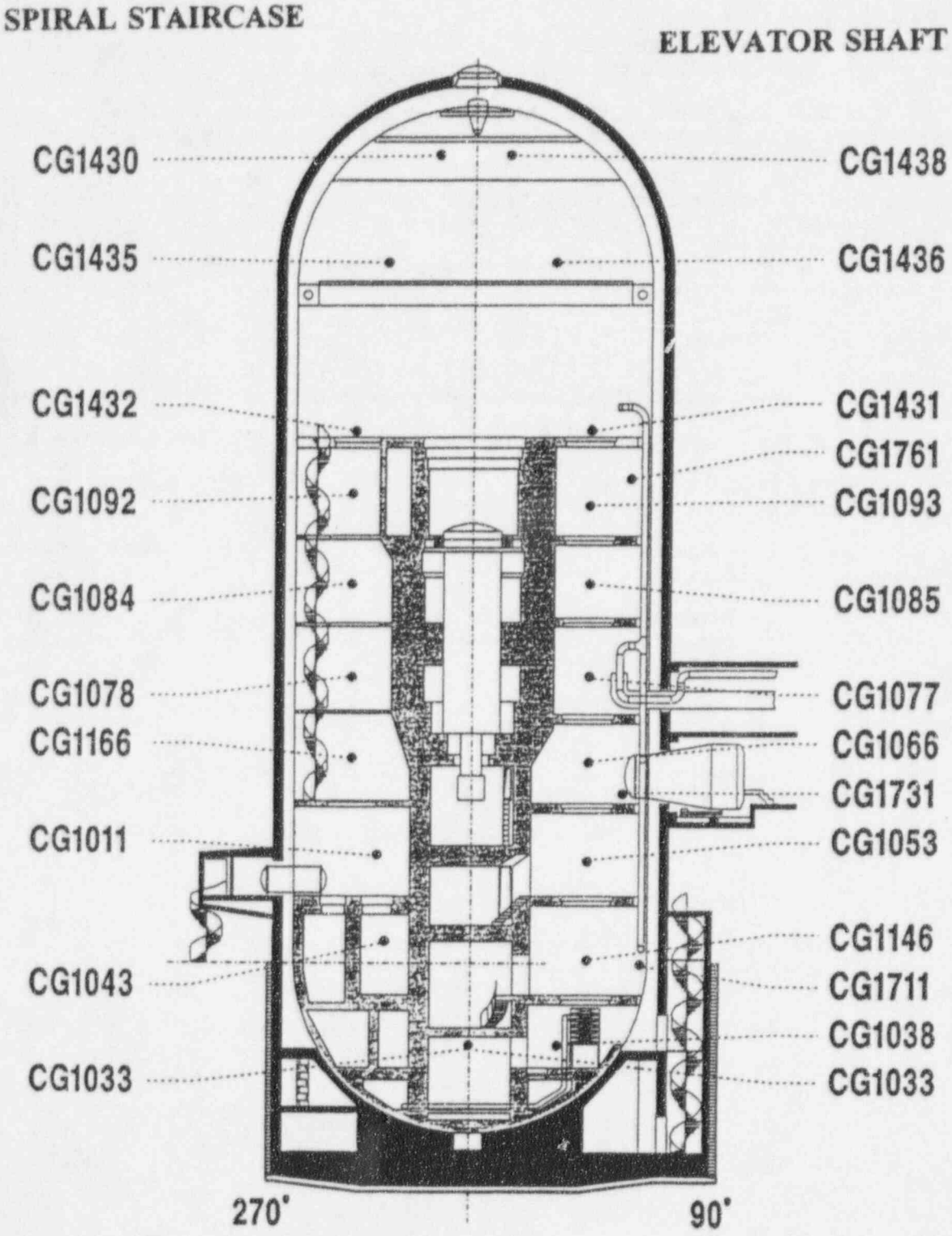

Figure 1 - HDR Containment and Measurement Locations

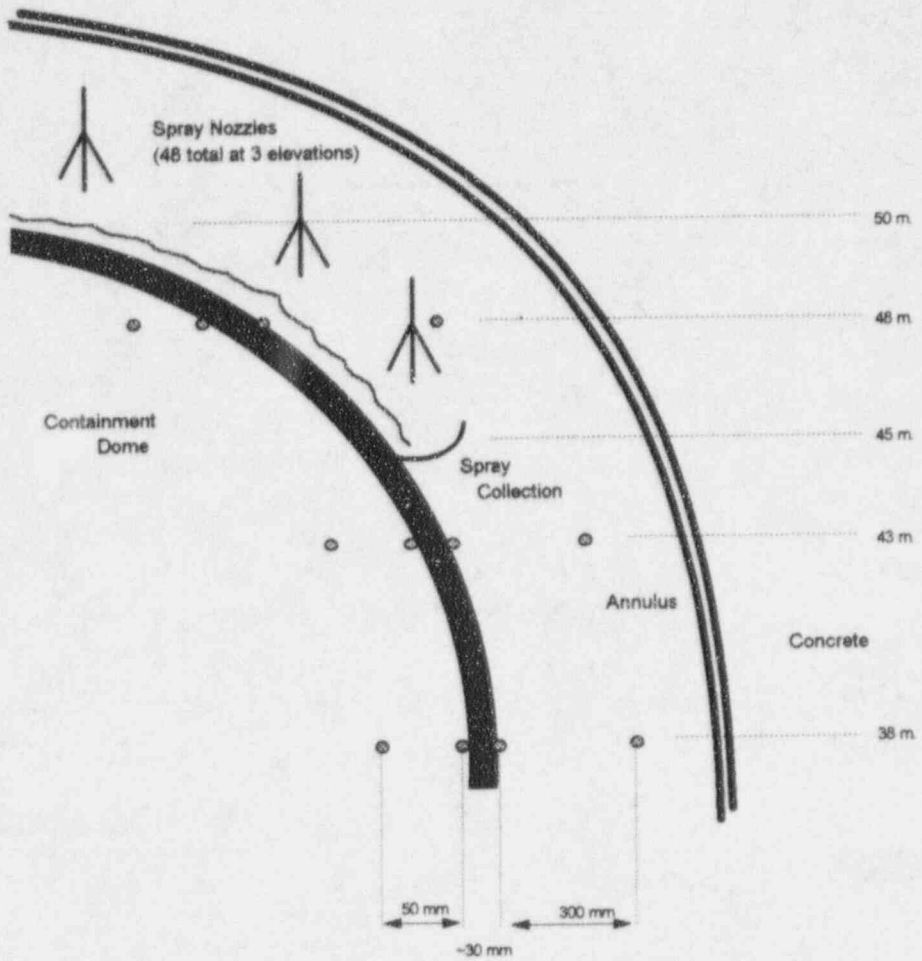

FIGURE 2 - HDR SPRAY ARRANGEMENT & HEAT TRANSFER MEASUREMENT LOCATIONS

Figure 3 (a) – Experimental & Predicted Pressures

E11.4

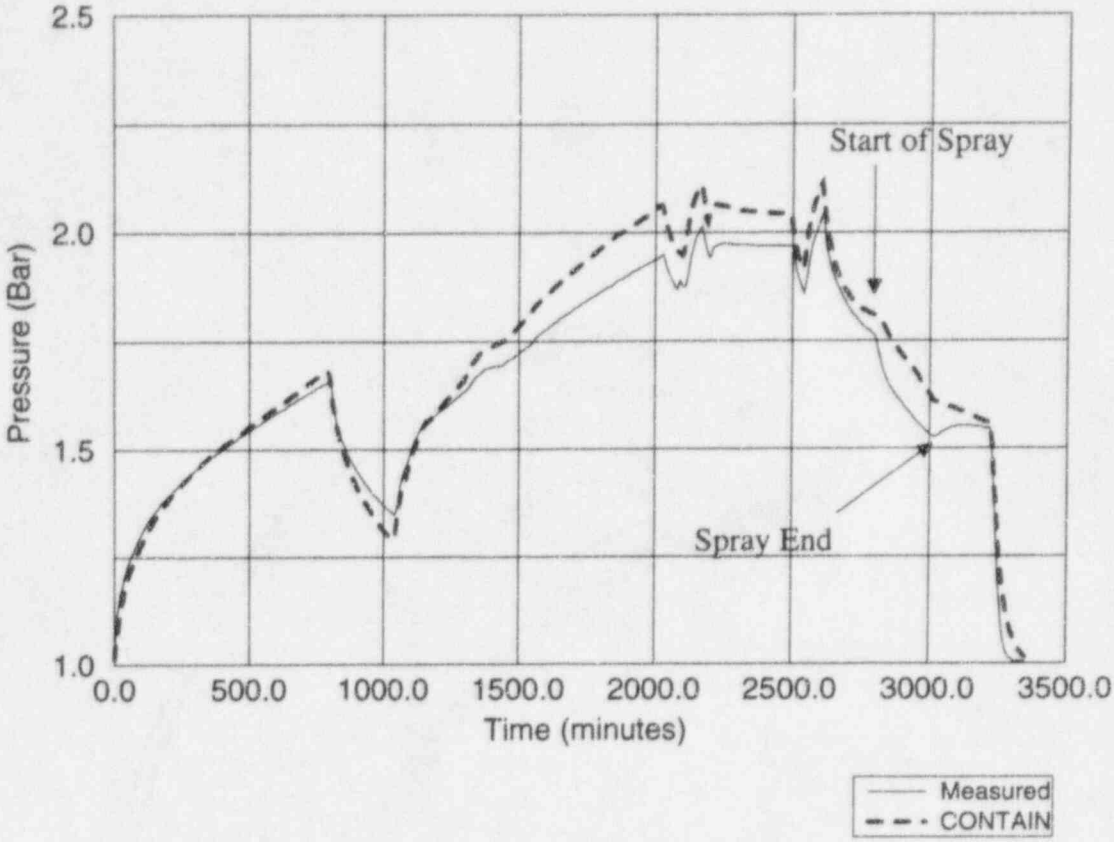

Figure 3 (b) – Experimental & Predicted Pressures

E11.2

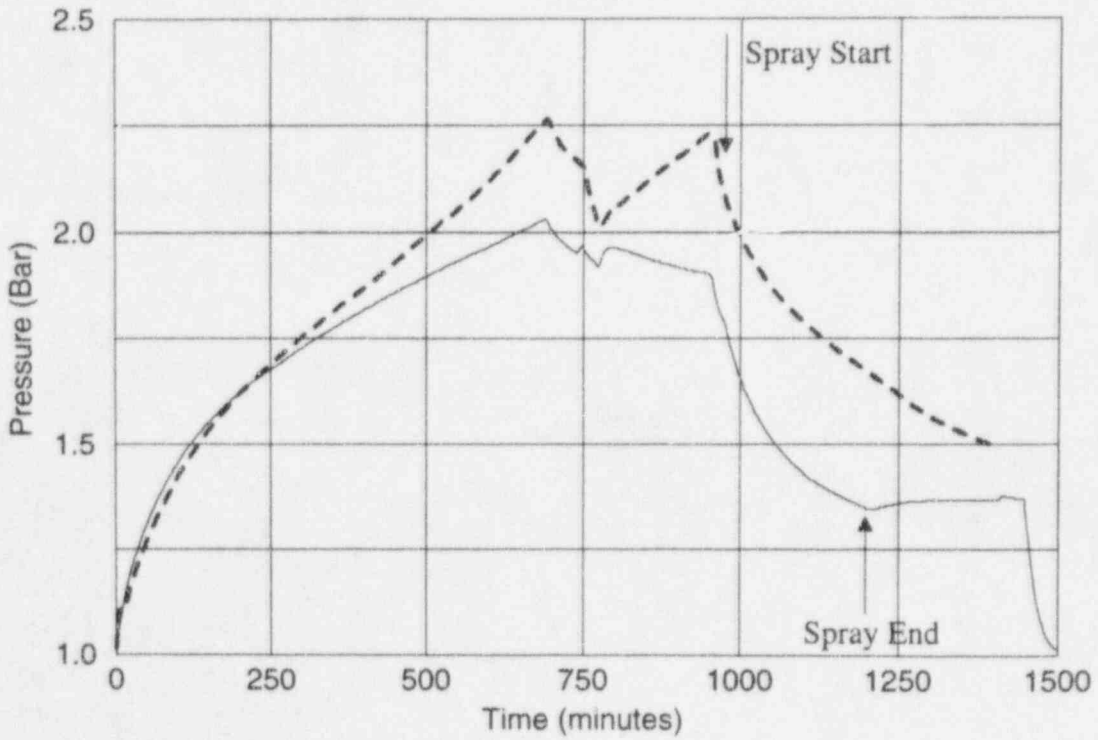

Figure 4 (a) – Shell Temperatures

E11.4 – Location 31 at 48 meters

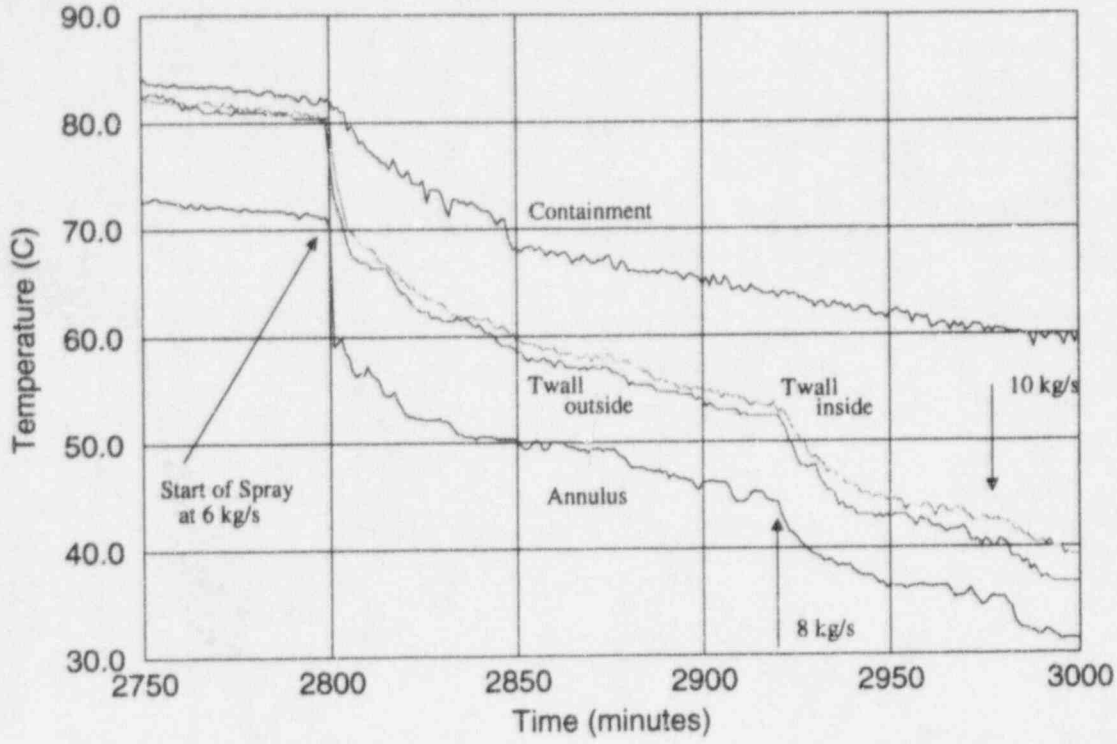

Figure 4 (b) – Shell Temperatures

E11.2 – Location 31 at 48 meters

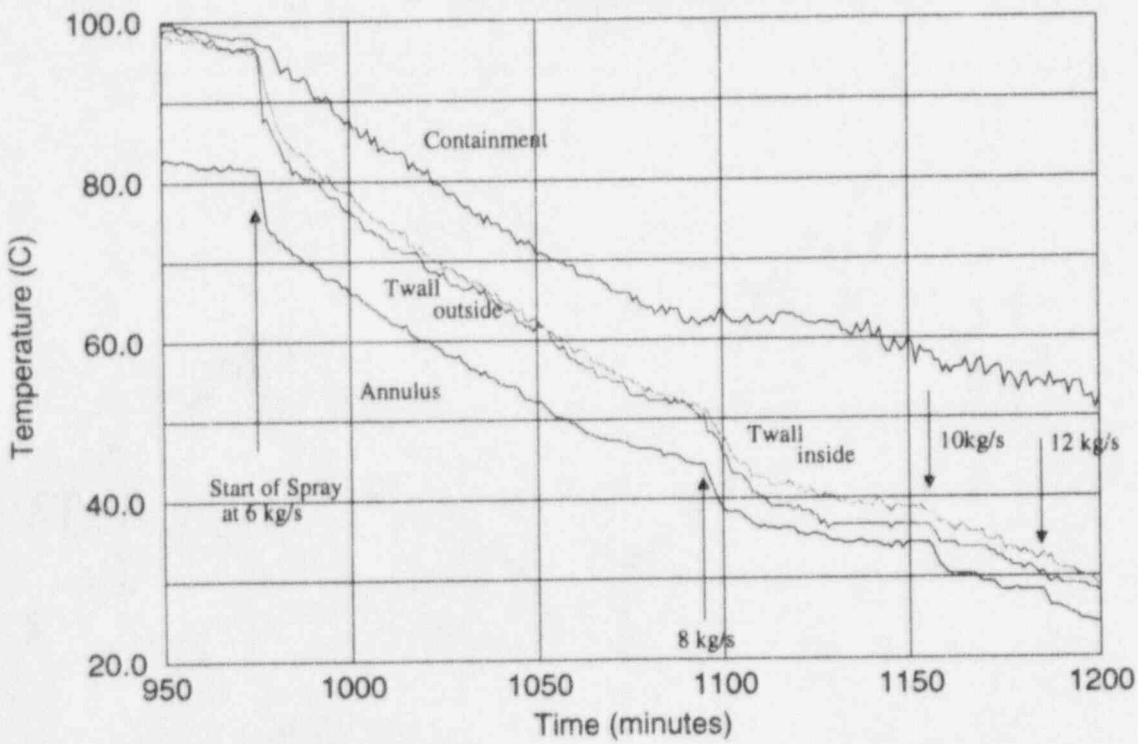

Figure 5 (a) – Steam Concentration

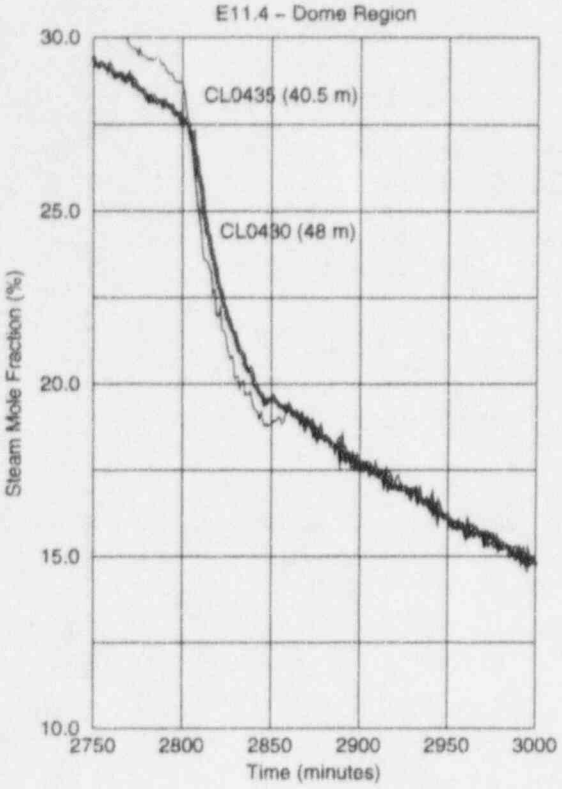

Figure 5 (b) – He + H2 Concentration

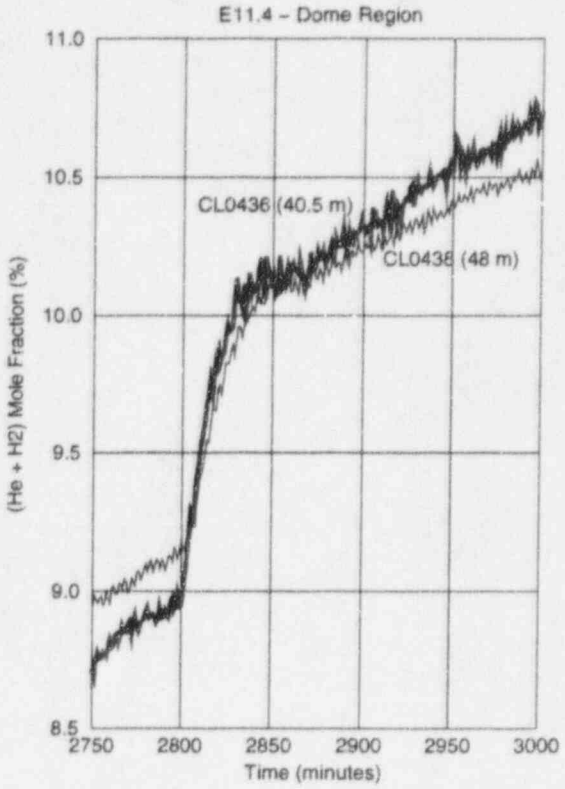

Figure 5 (c) – Steam Concentration

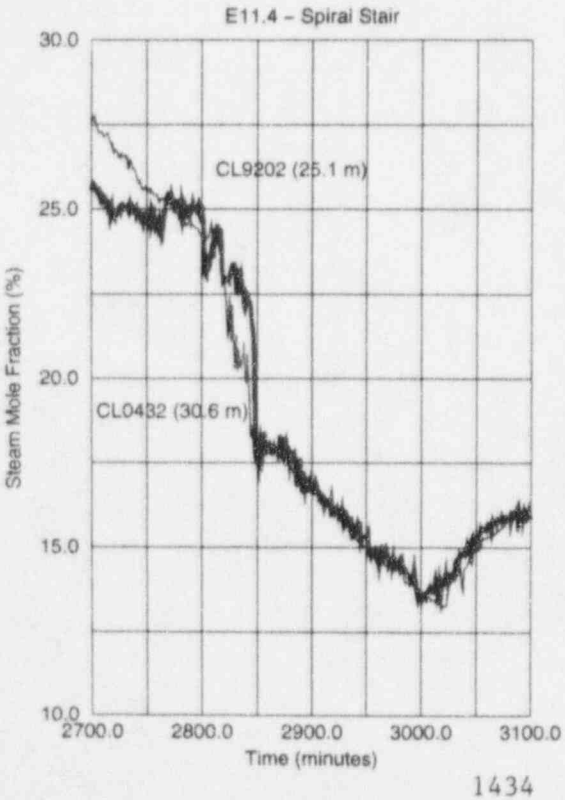

Figure 5 (d) – Steam Concentration

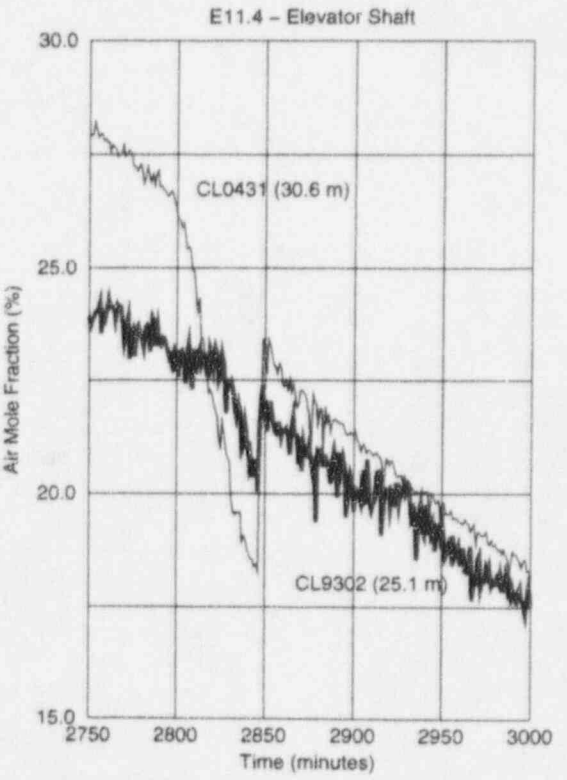

Figure 6 (a) – Steam Concentration

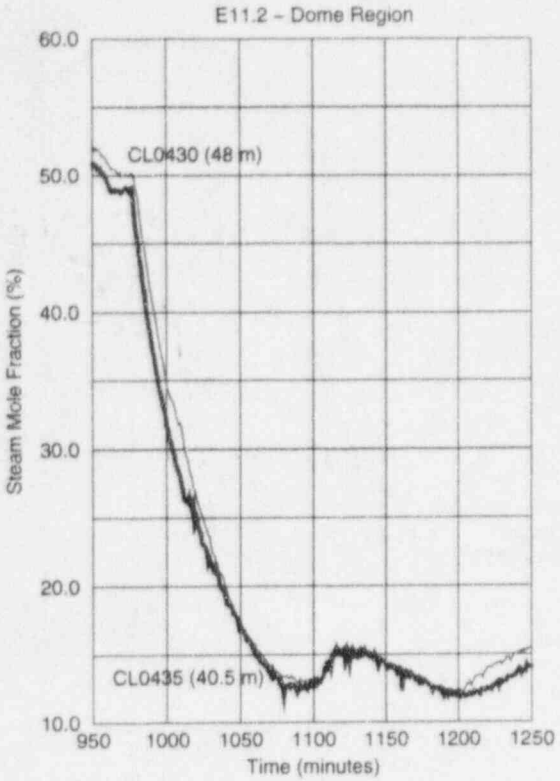

Figure 6 (b) – He + H2 Concentration

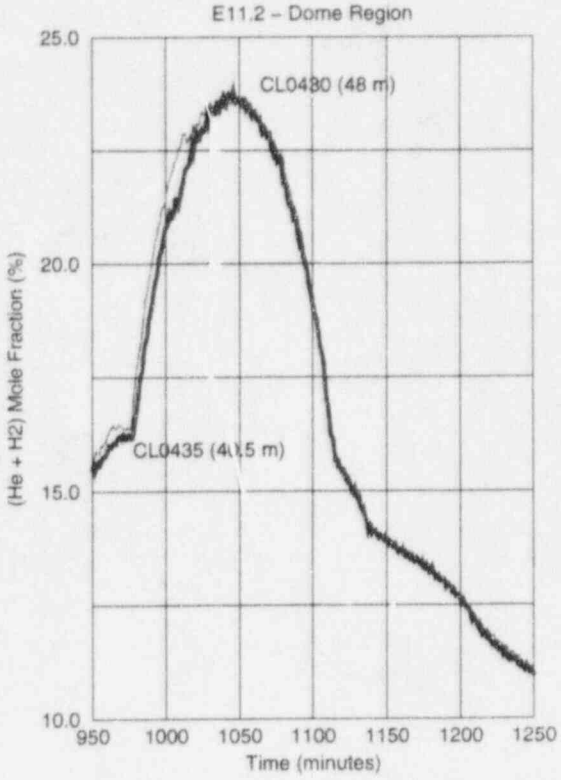

Figure 6 (c) – Steam Concentration

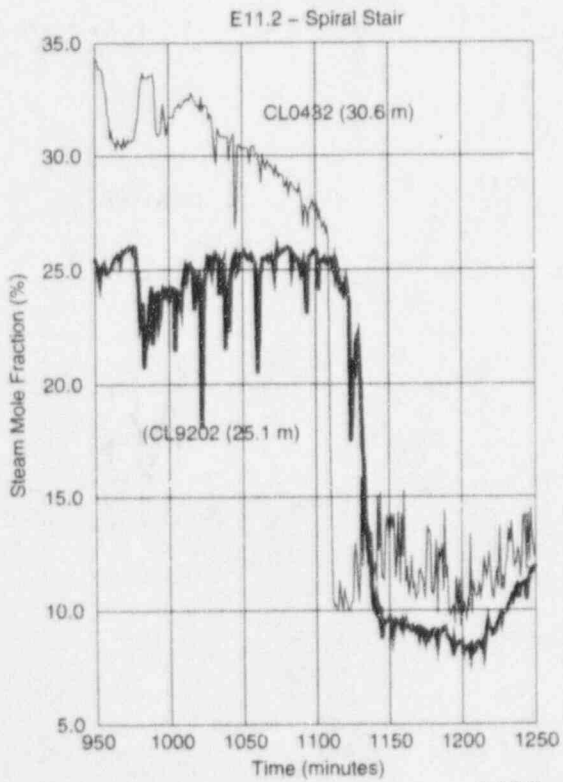

Figure 6 (d) – Steam Concentration

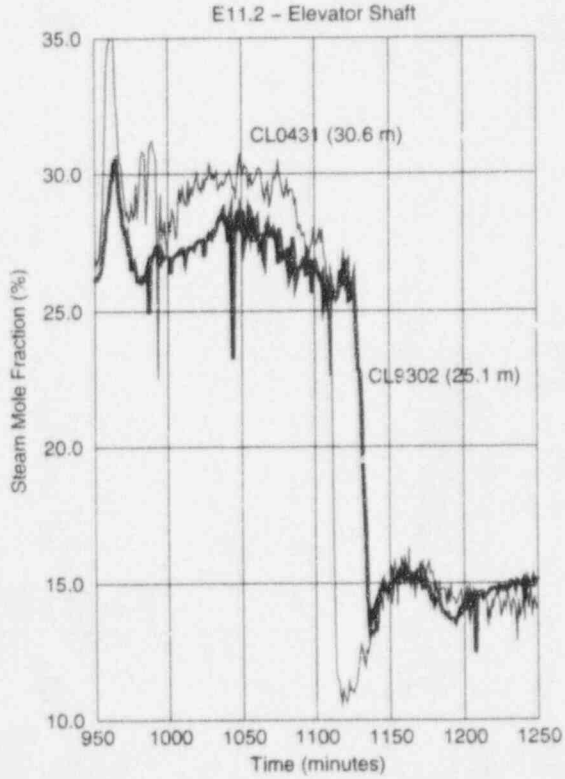

Figure 7 – Experimental Gas Concentrations

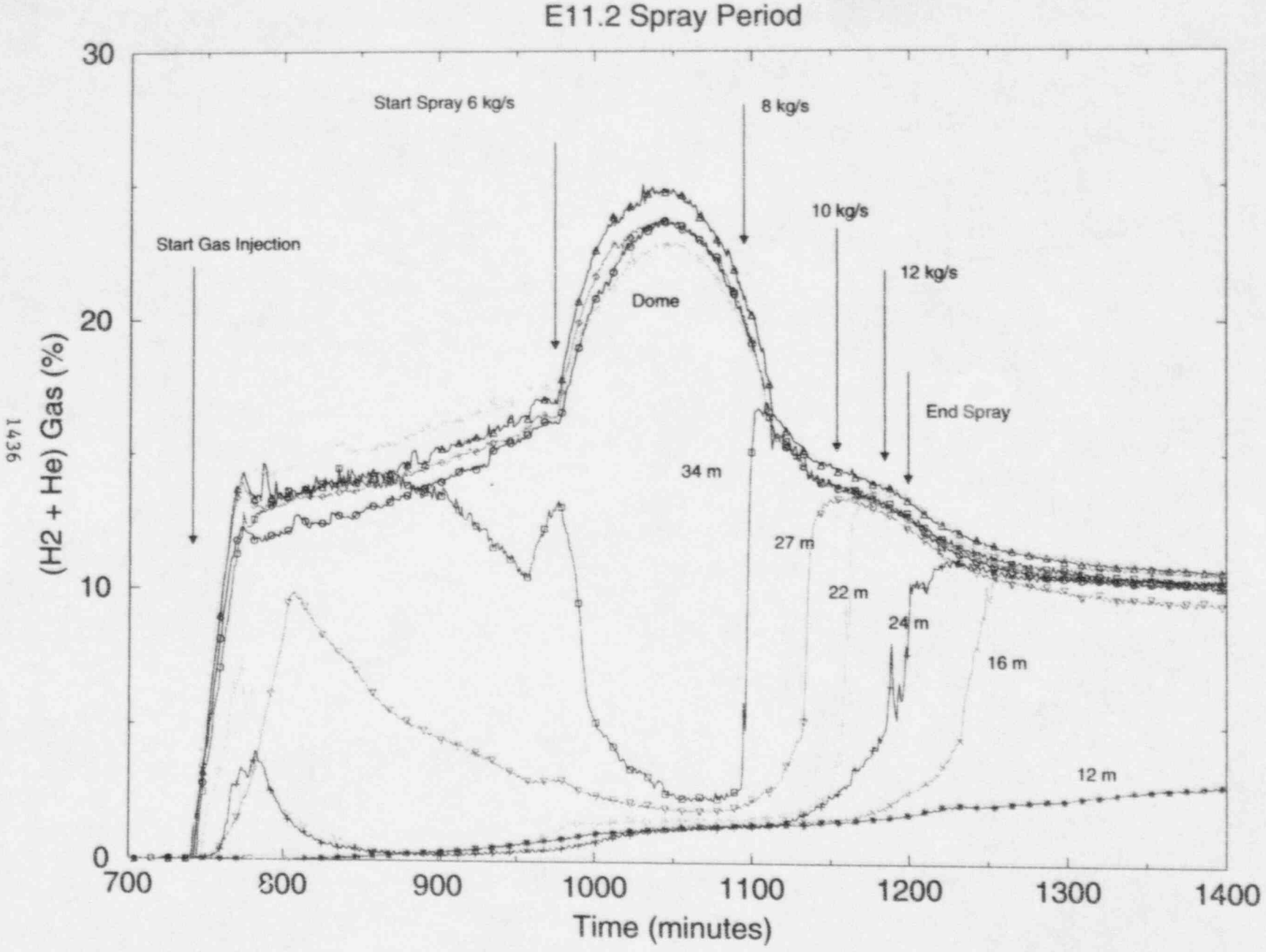

1436

Figure 8 (a) – Velocity in Dome

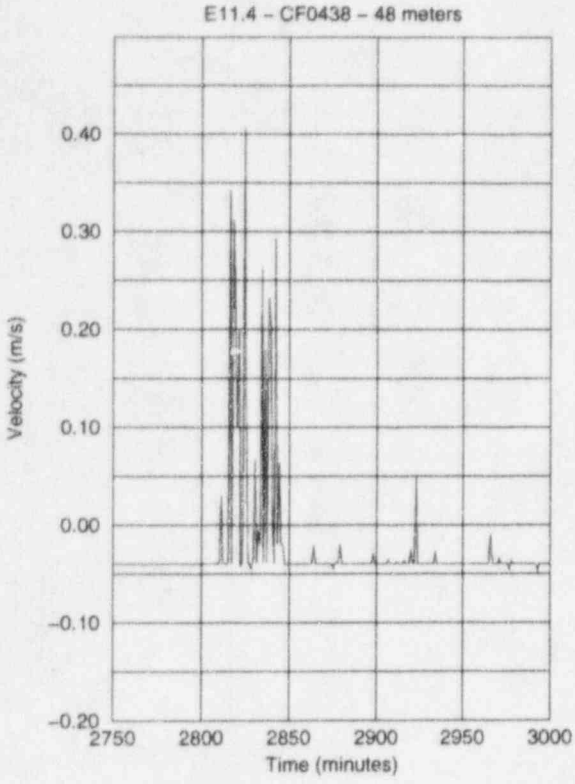

Figure 8 (b) – Velocity in Dome

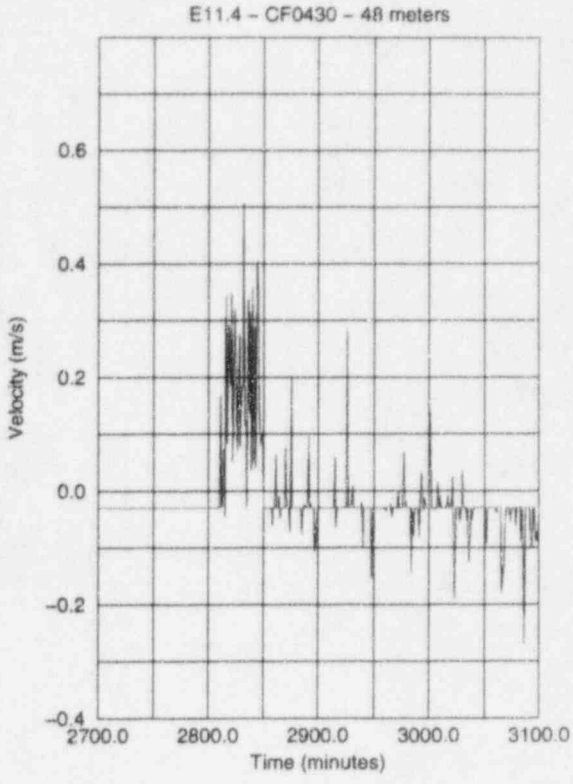

Figure 8 (c) – Spiral Stair Velocity

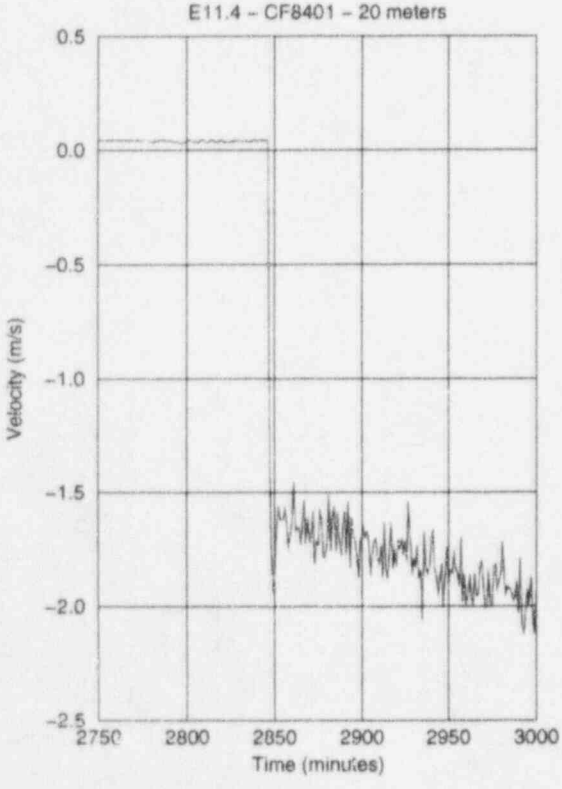

Figure 8 (d) – Elevator Shaft Velocity

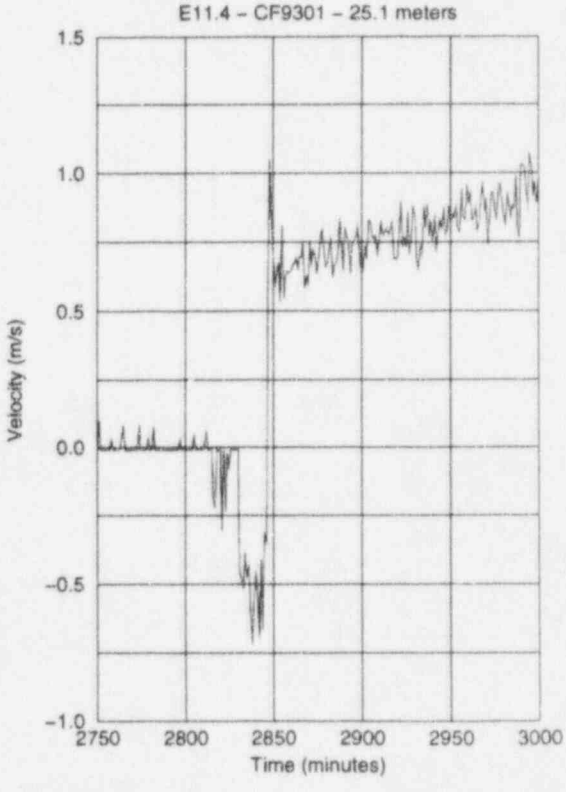

Figure 9 (a) – Velocity in Dome

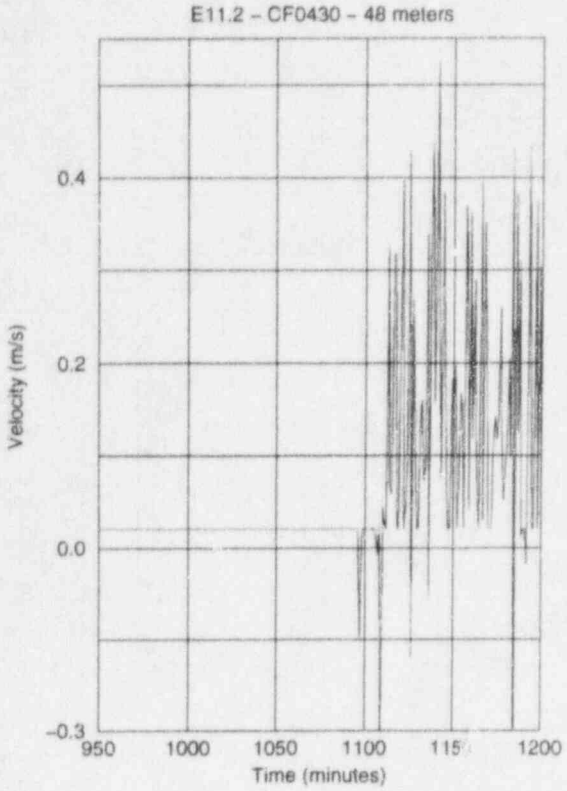

Figure 9 (b) – Velocity in Dome

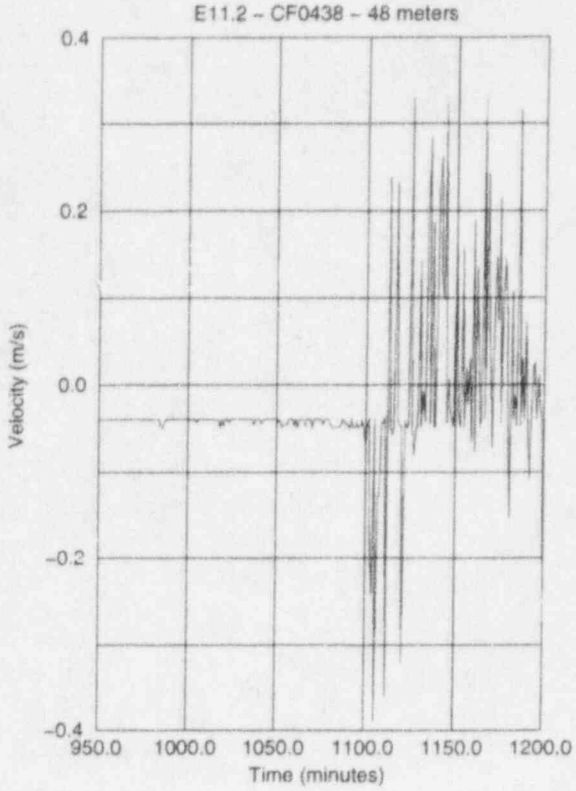

Figure 9 (c) – Elevator Shaft Velocity

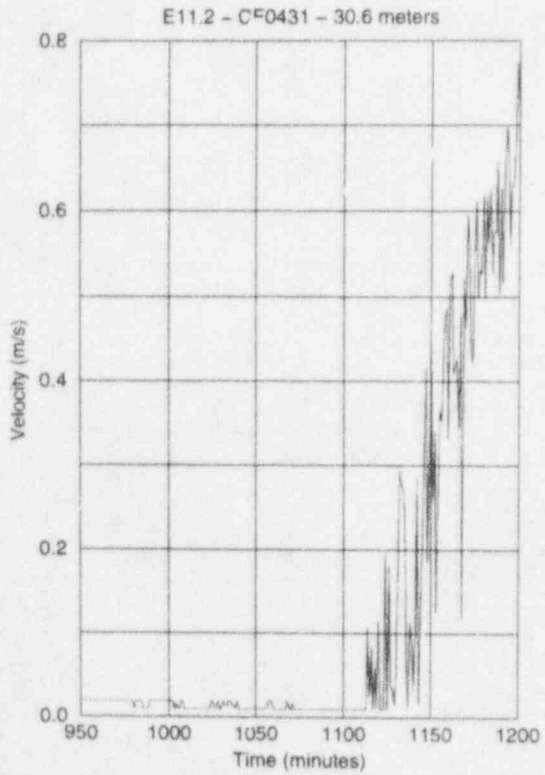

Figure 9 (d) – Spiral Stair Velocity

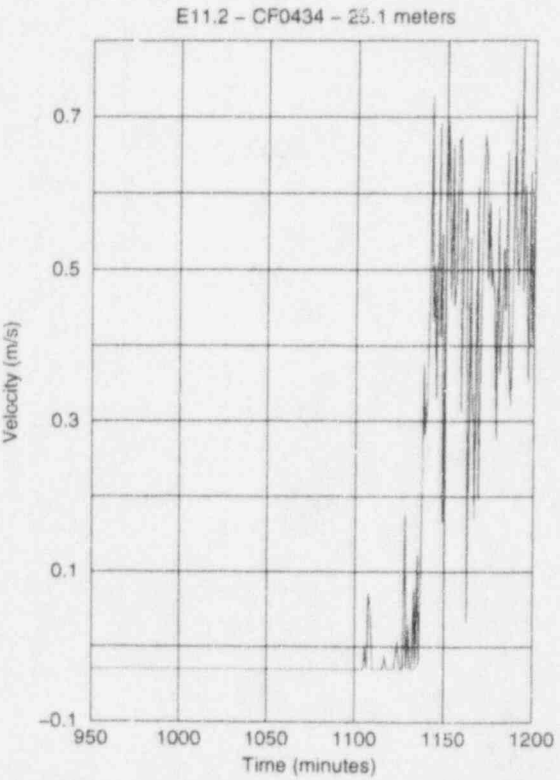

Figure 10 (a) – Location 33 @ 48 m.

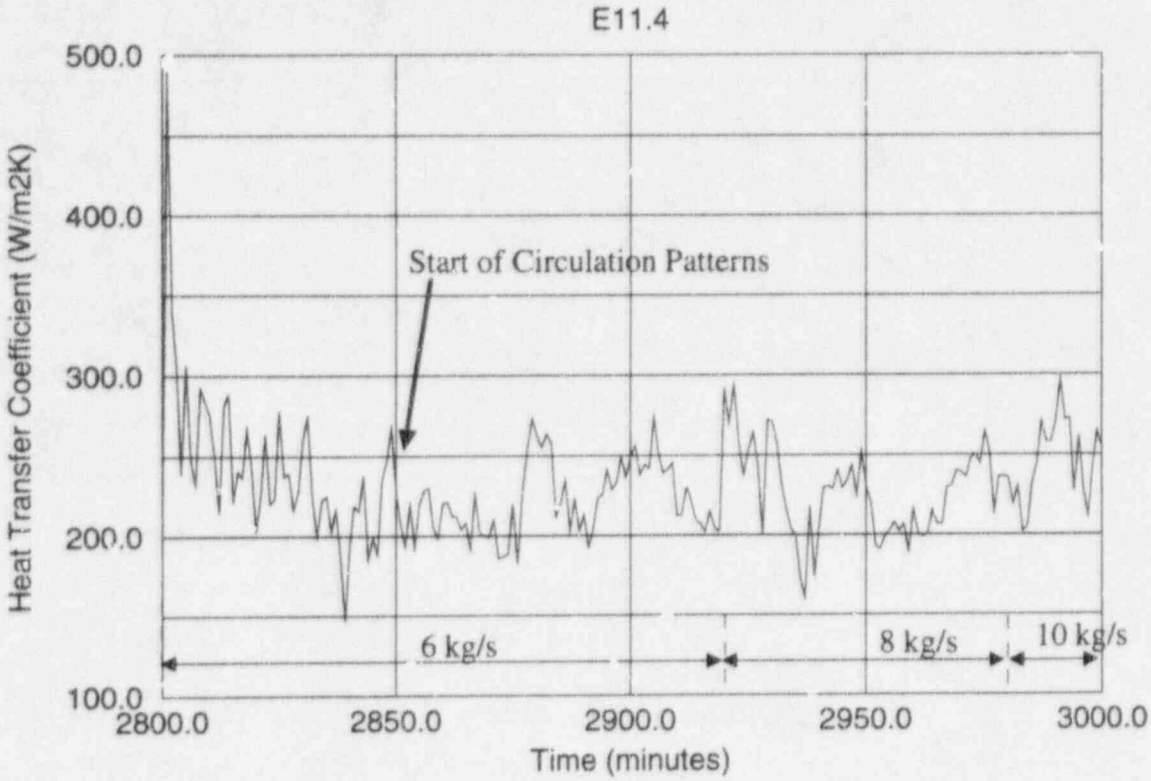

Figure 10 (b) – Location 31 @ 48 m.

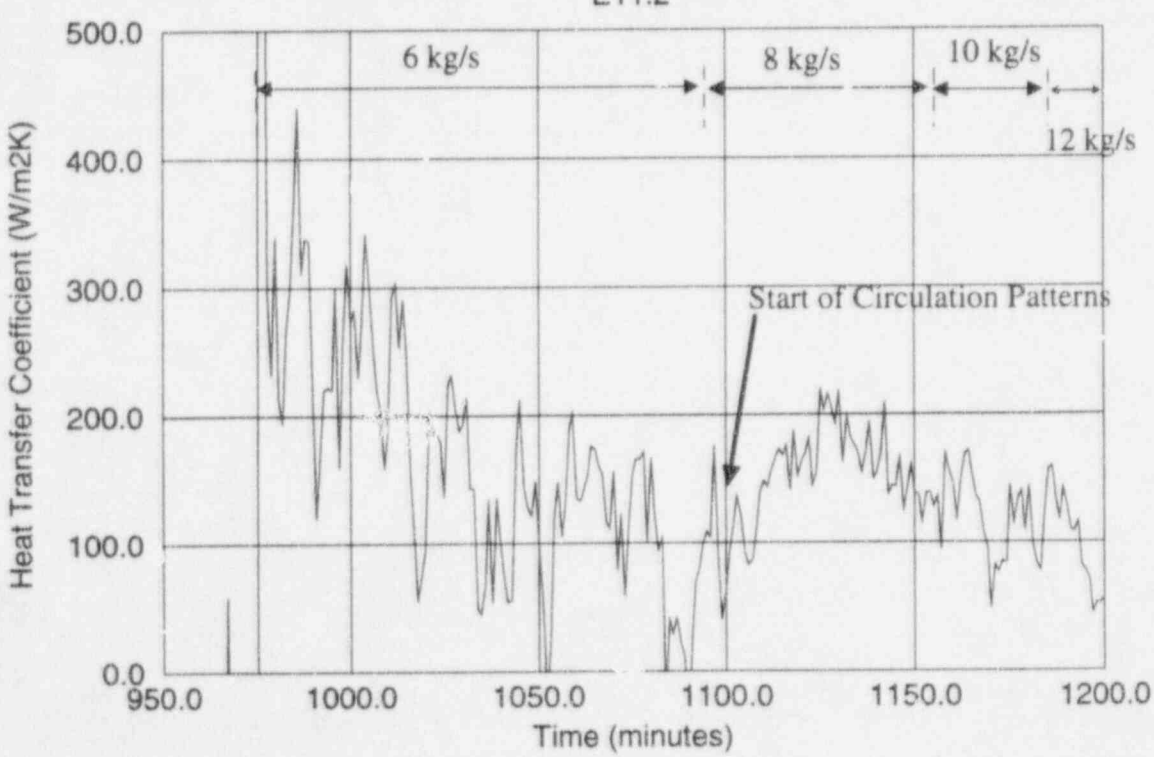

Figure 11 (a)– Concrete Block #84

E11.2 – Spray Period

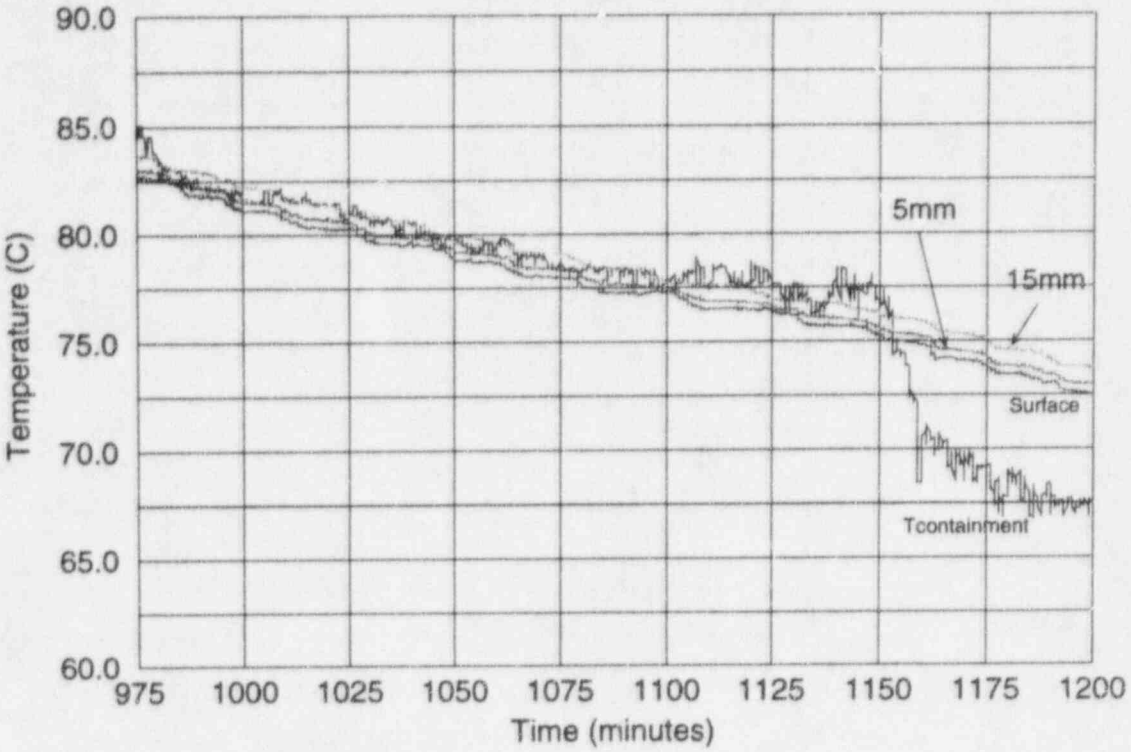

Figure 11 (b) – Concrete Block #84

E11.4 – Shell Spray Period

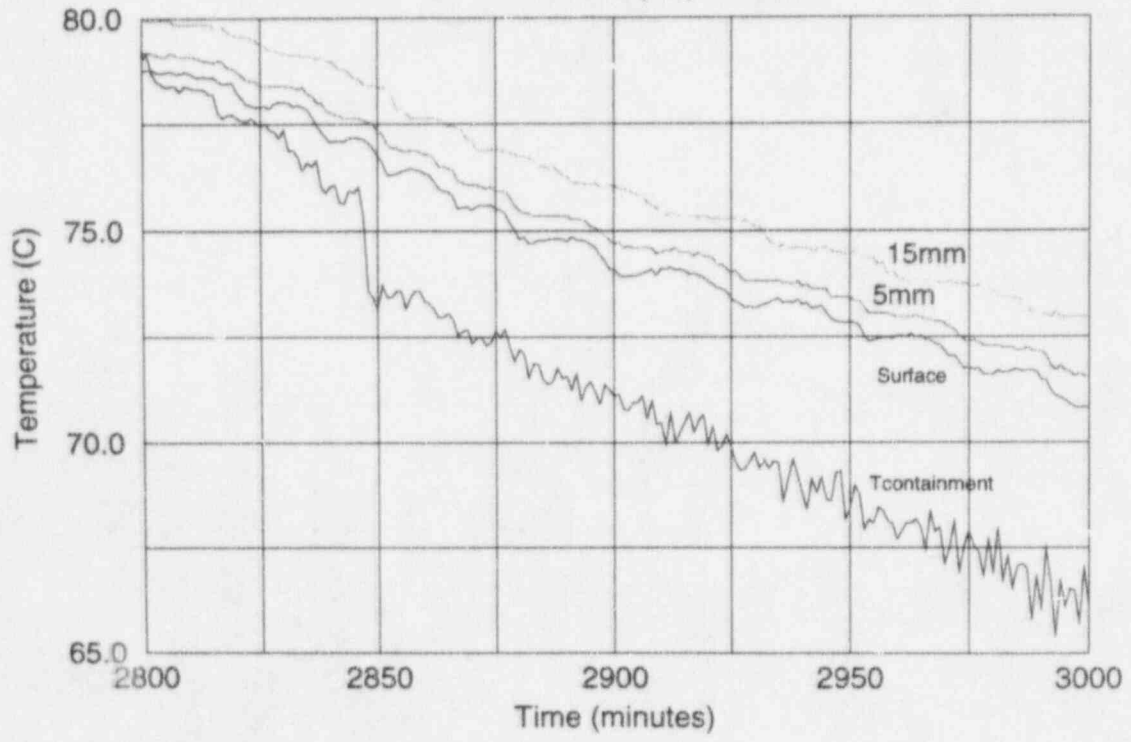

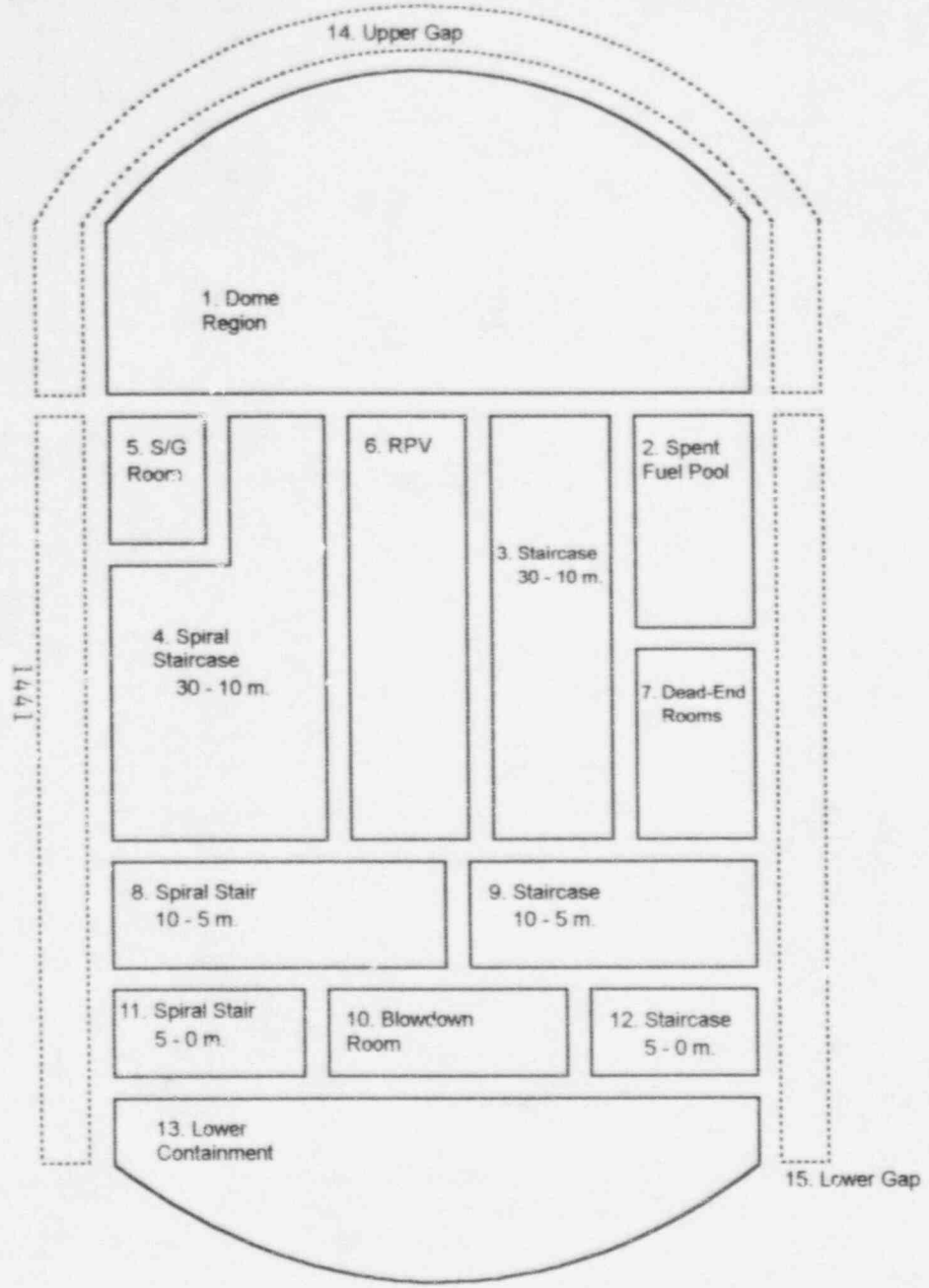

(a)

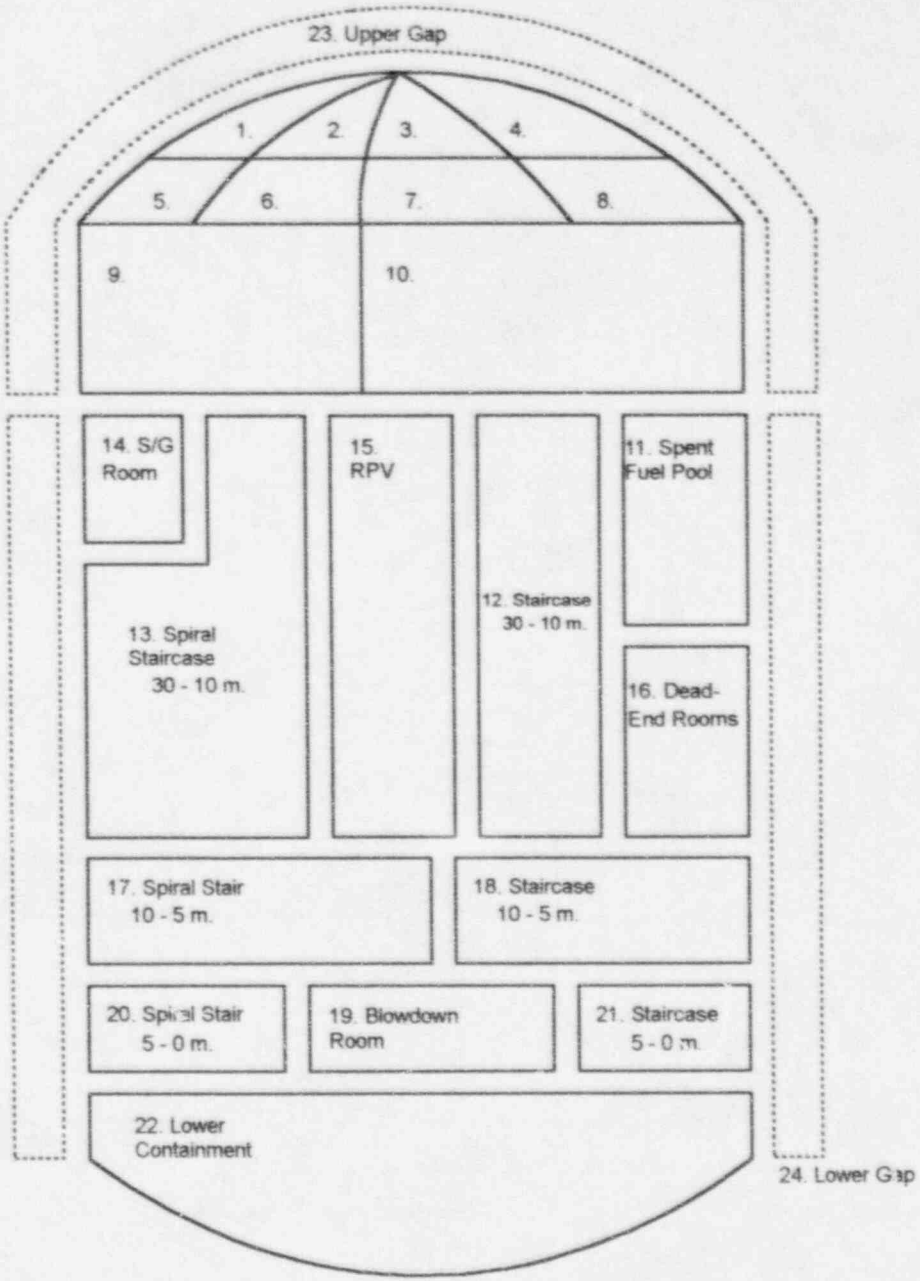

(b)

FIGURE 12 - CONTAIN NODALIZATIONS OF HDR

Figure 13 (a) – Shell Heat Transfer

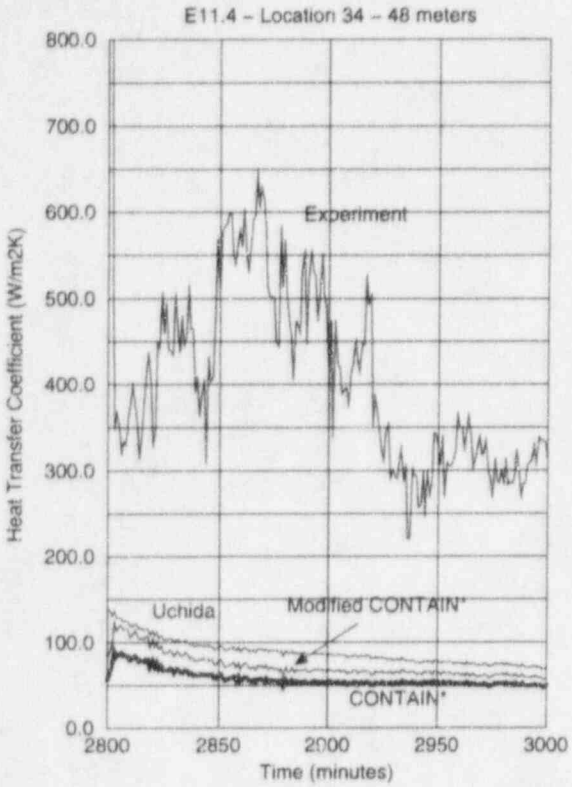

Figure 13 (b) – Shell Heat Transfer

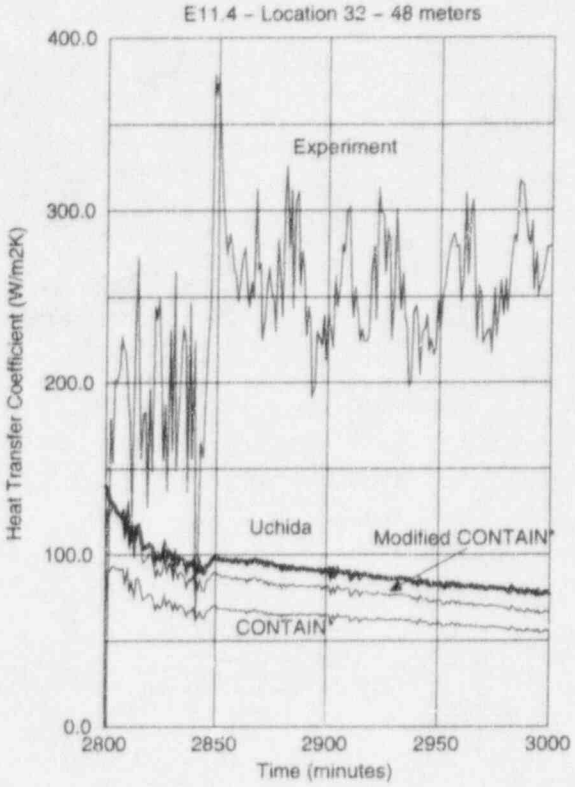

Figure 13 (c) – Shell Heat Transfer

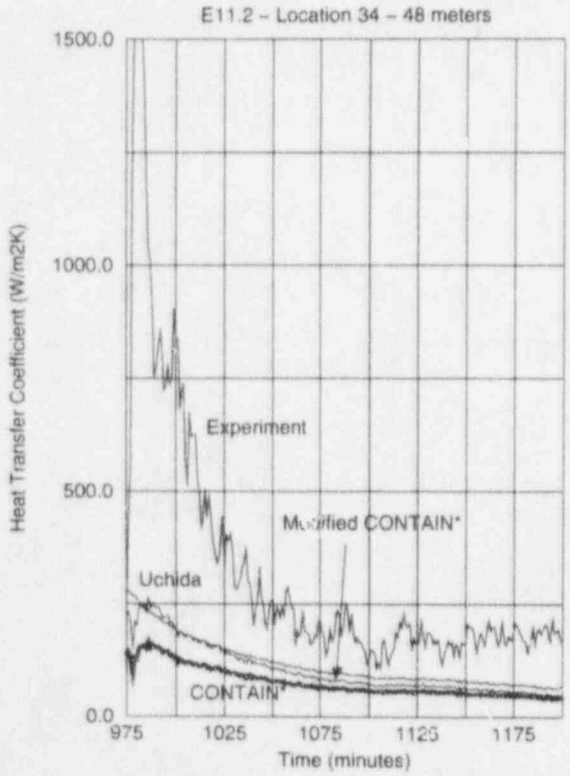

MODELING OF LOCAL STEAM CONDENSATION ON WALLS IN PRESENCE OF NON-CONDENSABLE GASES. APPLICATION TO A LOCA CALCULATION IN REACTOR CONTAINMENT USING THE MULTIDIMENSIONAL GEYSER/TONUS CODE

L.V. BENET, C. CAROLI, P. CORNET, N. COULON, J. MAGNAUD

Commissariat à l'Energie Atomique, DRN/DMT/SEMT, 91191 Gif sur Yvette cedex
FRANCE

ABSTRACT

This paper reports part of a study of possible severe pressurized water reactor (PWR) accidents. The need for containment modeling, and in particular for a hydrogen risk study, was reinforced in France after 1990, with the requirement that severe accidents must be taken into account in the design of future plants.

This new need of assessing the transient local hydrogen concentration led to the development, in the Mechanical Engineering and Technology Department of the French Atomic Energy Commission (CEA/DMT), of the multidimensional code GEYSER/TONUS for containment analysis.

A detailed example of the use of this code is presented. The mixture consisted of non-condensable gases (air or air plus hydrogen) and water vapor and liquid water. This is described by a compressible homogeneous two-phase flow model and wall condensation is based on the Chilton-Colburn formula and the analogy between heat and mass transfer.

Results are given for a transient two-dimensional axially-symmetric computation for the first hour of a simplified accident sequence. In this there was an initial injection of a large amount of water vapor followed by a smaller amount and by hydrogen injection.

1. INTRODUCTION

During a core-melt accident, oxidation of the fuel cladding produces a large amount of hydrogen, which may burn (more or less slowly) or detonate spontaneously when the hydrogen concentration reaches a given value (approximately 10% volume concentration, see Figure 4.f). Such an explosion could damage containment integrity.

Increasing interest in assessing the hydrogen risk led, during the '80s, to work in two directions. In one, multi-compartment codes were developed, based on a lumped parameter approach. In the other, general multidimensional codes were used for solving mass, energy and momentum equations using spatial discretization.

The first approach was sufficient due to the main characteristics of concrete containment (high thermal inertia and low thermal leakages) and because heat transfer is very efficient in steam condensation. Lumped parameter codes like CONTAIN, RALOC, JERICHO or MAAP [1]

give a realistic representation of the pressure evolution but underestimate the stratification and are sensitive to the sub-compartment splitting.

Multi-dimensional codes like GOTHIC/WGOTHIC [2] or GASFLOW/HMS [3] give a good representation of stratification in large volumes, but there are few versions which take into account mixed gas-liquid behavior. These codes also require very long computing times. Nevertheless, they are able to predict local hydrogen concentrations, thus providing indicators of deflagrations and detonations.
If lumped parameter codes are likely to be used for a long time by safety authorities for the overall analysis of accident scenarios, it will be increasingly necessary to associate these with detailed studies carried out with mechanistic codes so that the assumptions made in the lumped parameter codes can be justified. Thus, CEA/DMT has undertaken a program for the development of a representative containment code, GEYSER/TONUS, and for experiments using a specifically instrumented containment mock-up, MISTRA [4], for support and validation of the modeling.

The overall objective of our work is to contribute to overcoming the hydrogen risk in a possible reactor accident. Our immediate goal is to calculate local hydrogen concentrations during all the transient stages in a loss-of-coolant-accident (LOCA).
From a hydraulic viewpoint, a typical accident can be characterized by injection of a large quantity of water vapor, followed by hydrogen release in the containment. Such accident sequences may last several hours or even days.
For this, a coupled multi-dimensional-lumped parameter code is needed in order to analyze complete scenarios. GEYSER/TONUS, which is based on existing software programs, serves as an overall homogeneous modeling tool.

2. MAIN FEATURES OF THE CODE

We started from the existing TRIO-EF [5][6] and CASTEM 2000 [7] multi-dimensional codes developed by CEA/DMT. These are general programs dedicated, respectively, to thermal hydraulic and mechanical analysis. We developed multi-D and 0-D operators and algorithms to solve the coupled equations describing the mixture behavior. We use the GIBIANE object-oriented language to manage the data (objects) and the operators, which provides great flexibility in constructing various numerical algorithms.
GEYSER/TONUS is a set of independently executable procedures formed using the TRIO/CASTEM "tool box". The code construction and structure is detailed in a companion paper presented at this conference [8].

The numerical method is based on the approximate solution of mass, compressible Navier-Stokes and energy equations. Turbulence is modeled by a constant eddy viscosity but it could be computed (in the future) with a K-ε model, now available in TRIO. We use a mixed finite-volume/finite-element discretization. The finite element method (Galerkin weighted residual method) with linear elements is used for the spatial discretization of momentum equations [5]. For all other conservative equations, a finite volume integration is used. Time discretization is obtained by a first order scheme associated with an upwinding of the convective terms (MUSCL).

3. MODELING

We use a homogeneous two-phase flow model. The different species, air, water vapor, water droplets, hydrogen, have the same velocity and temperature. The gas mixture is considered to be a perfect, viscous, compressible gas and its physical properties (viscosity, diffusivity, heat capacity) depend on the mixture composition but not on its temperature.

Equations

We solve 5 conservation equations (total density ρ in kg/m3, total water density ρ_w in kg/m3, momentum ρV in kg/m2/s, specific internal energy ρe in J/m3, hydrogen density ρ_h in kg/m3) coupled with the equation of state ($P = (\gamma - 1)\rho e$). The mass of water includes both vapor and suspended droplets.

Equilibrium is assumed to be instantaneous. Bulk condensation occurs if the thermodynamic equilibrium leads to a partial water vapor pressure above the saturation pressure at the local temperature.

Equality between these two pressures determines the liquid mass quality. Thus, we assume that the water droplets remain in suspension in the mixture because the droplets are micrometric and at low concentrations.

Mass transfer :

Mass transfer to the walls by condensation is based on the Chilton-Colburn approach and the analogy between heat and mass transfer.

The mass condensation rate is given by:

$$j_s = \frac{\alpha}{D}\left(\rho_v - \rho_{ve}(T_w)\right) Sh$$

α is the vapor diffusion coefficient

D the containment diameter

ρ_v the vapor density

$\rho_{ve}(T_w)$ the saturated vapor density at the wall temperature

Sh is the Sherwood number and by analogy with the Nusselt number can be written [10]:

$$Sh = 3.656 + 0.021\, Sc^{0.6}\, Re^{0.8}$$

$Re = \frac{\rho V D}{\mu}$ is the Reynolds number

$Sc = \frac{\mu}{\rho D}$ is the Schmidt number

μ is the mixture dynamic viscosity

This mass flux is removed from the mixture at the wall.

At present, water condensing on the wall and its energy disappear from the calculation. In future computations, this mass could flow to the containment base and a fraction of its heat could be transferred to the concrete.

Heat transfer :

The heat flux at the computational boundary is divided into two parts. The first corresponds to convection heat transfer and the second to condensation.

Heat transfer by convection at the wall is modeled by a heat exchange coefficient and a given wall temperature that is time-dependent. This is now obtained by a semi-empirical correlation for the Nusselt number [9] :

$$Nu = 3.656 + 0.021\, Pr^{0.6}\, Re^{0.8}$$

with $Nu = \dfrac{H\,D}{\lambda}$

H is the heat transfer coefficient

λ the mean thermal conductivity of the mixture

$Pr = \dfrac{\mu\, Cp}{\lambda}$ is the Prandtl number

The condensation heat transfer is given by :

$$j_e = j_s\, \varepsilon_v$$

ε_v is the vapor internal specific energy (J/Kg)

In order to simplify these preliminary calculations we use constant transfer coefficients, in the future we could use wall functions.

4. CALCULATIONS

Geometry:

The mesh consisted of 304 quadrilateral elements representing half of a PWR dome with a height of 36 m and a radius of 22 m. The water vapor or hydrogen was injected from the reactor pool along the symmetry axis through a surface area of 83 m^2.

Initial conditions:

	total pressure	relative humidity	mixture temper.	wall temper.
t = 0 s	0.1 MPa	Pv/Psat = 0.9	40 °C	37 °C

Boundary conditions:

Two simplified accident sequences (first hour), belonging to the small break LOCA category, were carried out. These computations for the main containment volume were 2-D and axially-symmetric. There were no mass or heat transfers at the containment base except for the injections.

First sequence:

	vapor inj. rate	H_2 inj. rate	pressure inj.	temper. inj.	wall temper.
1st step t = 0 to 1 mn	556 kg/s	0 kg/s	total pressure of the mixture	$T_{sat}(P)$	37 °C
2nd step t = 1 to 60 mn	18 kg/s	0 kg/s	total pressure of the mixture	$T_{sat}(P)$	$T_w = 37 + 2\,t$ T(°C), t(mn)

For the second step, two computations were made in order to evaluate the importance of the wall temperature:
- *Computation 1.a:* the wall temperature increased linearly with time (2°C/min) to model the heating of the wall. This increase was estimated by using a previous 0-D JERICHO calculation.
- *Computation 1.b*: the wall temperature remained constant (37 °C). In this case the condensation rate is clearly overestimated because the condensation heat is partially transmitted to the wall.
We will essentially comment on *computation 1.a.*

Second sequence:

	vapor inj. rate	H_2 inj. rate	pressure inj.	temper. inj.	wall temper.
1st step t = 0 to 1 mn	556 kg/s	0 kg/s	total pressure of the mixture	$T_{sat}(P)$	37 °C
2nd step t = 1 to 10 mn	18 kg/s	0 kg/s	total pressure of the mixture	$T_{sat}(P)$	$T_w = 37 + 2\,t$ T(°C), t(mn)
3rd step t=10 to 60 mn	0 kg/s	0.15 kg/s	total pressure of the mixture	627 °C	$T_w = 37 + 2\,t$ T(°C), t(mn)

Convergence criteria:
We solved the set of all partial differential equations and the equation of state for the unknowns ρ, ρ_w, ρ_h, ρV, ρe and P by an implicit method.
Internal iterations (denoted i) were performed for all of the unknowns (including ρ_v, γ and $\rho_{ve}(T_w)$) at each time step. The convergence criterion was, for each unknown X:

$$\text{Max}\,|X_i - X_{i-1}| \,/\, \text{Max}\,|X_i| < 2\text{x}10^{-4}.$$

5. RESULTS

5.a First sequence (no hydrogen release)

General description of the transient:
The overall variation during the vapor injection transient is described by an initial rapid increase (first step) in mass (Figure 1.d) and pressure (Figure 1. b). The same rapid increase is seen in the mean temperature (Figure 1.a) and wall condensation rate (Figure 1.f).

The first step (556 kg/s vapor injection rate) ended at t = 1 mn:

end 1st step	vapor mass	air mass	total pressure	relative humidity	mean temperature	condensation rate (walls)
t =1 mn	32 tons	55 tons	0.26 MPa	0.9	139 °C	43 kg/s

Computation 1.a:
For the second step, the injection rate was reduced to 18 kg/s. Pressure and temperature variations are reversed because mass removal becomes greater than injection. The gaseous mixture loses vapor and is cooled while the wall temperature increases. Thus, the wall condensation rate decreases and mist appears (see Figures 1.e and 1.d).
At approximately 10 mn, there is a new slow inversion of the pressure evolution. The pressure and temperature again rise rapidly after the mist disappears (at t = 33 mn).

Our calculation ends at t = 1 h and the parameters are (Figures 3.d to 3.f):

end of 2nd step	vapor mass	air mass	total pressure	relative humidity	mean temperature	condensation rate (walls)
t = 1 hour	66 tons	55 tons	0.4 MPa	0.93	155 °C	0 kg/s

0-D analysis:
The vapor injection rate and wall temperature determine all the thermal-hydraulic behavior and the latter controls the extracted mass and heat fluxes. The pressure, which is uniform throughout the containment volume, is the main parameter controlling both condensation and system temperature. The variations with time are qualitatively the same as those obtained by lumped parameter codes (see Figures 1.a to 1.f).

In figure 1.f we can see a change in the slope, approximately after 10 mn. At this time the condensation rate was falling under the injection rate (18 kg/s). This also corresponds to a pressure minimum. Then the pressure rise slows down the decrease of the condensation rate.

The increase in energy due to the pressure rise in the first minute of the transient sequence is the major contribution to the average gas heating and is the reason for the rapid disappearance of the bulk condensation front that is formed at the beginning of the injection. At t = 1 mn, the relative humidity is 0.9 and the average temperature is 70°C higher than that obtained without compression with mixing alone. We can observe the same effect during the pressure decrease phase (1 < t < 10 mn). This pressure decrease creates a rapid cooling which induces bulk condensation. These effects can be seen in Figure 1.c, which compares the real temperature variation with the isentropic equivalent temperature variation for air or vapor alone.

By comparing figures 1.a and 1.e, it can be seen that the temperature remains almost constant between 10 and 33 mn, which also corresponds to the presence of mist during the same time. This may be explained by the fact that the mist increases the thermal inertia of the system and, in particular, reduces the overall heating rate during the second step.

The large effect of wall temperature is seen by comparing the two computations 1.a and 1.b. There is an appreciable pressure increase with the 2°C/mn increase in wall temperature. *Computation 1.b* with a constant wall temperature (37°C) and the same vapor injection rate shows a regular pressure decrease. This points out the importance of both the fraction of heat transferred to the wall and wall heating. We will focus on these effects in future work.

2-D analysis:
Only the pressure is uniform in the containment volume (<1% difference between top and bottom).

The different velocity fields, for both injection rates, show common features (see Figures 2.d or 2.f):
- a plume of vapor-rich gas quickly rises above the injection area along the symmetry axis,
- boundary layers extend along the roof and the upper part of the wall,
- a large toroidal dead area between the above two limits, where the velocities are very low.

During the first minute, the flow regime moves from forced to mixed convection. During the same time, the vapor injection velocity decreases from 10 to 5 m/s (because the density of injected vapor increases). The plume velocity is always about 10 m/s. The second step is pure free convection.

In all cases, we observe a more or less steep mass stratification in this dead area (see Figures 2.a to 2.c and 3.f).

The density variations producing these flows are created essentially by the different proportions of vapor in the gas mixture. At t = 1 mn, the mass fraction of vapor at the axis is 0.9, while it is 0.05 in most depleted vapor region. At this time, the stratification is the steepest with a highly enriched vapor pocket (75% vapor mass fraction) at the highest level and very little vapor at the bottom (Fig 2.a). The steepness of the stratification then decreases with time.

Temperature is not correlated with mass here (Fig 2.c and 3.a or 3.d and 3.f), as opposed to incompressible flows. For example, we do not observe any thermal stratification, except at the beginning (t = 30 s).

Detailed analysis from 1 to 60 mn:

- 1 to 10 mn: a new free convection regime is formed, consecutive to a dramatically reduced injection rate. We can see that in this phase both pressure and temperature are decreasing. The flow regime appears to be rather unstable (see Figure 2.e).

The new rising plume with less vapor, and which is therefore heavier, cannot penetrate the light mixture pocket in the upper section of the containment. This mixture slowly becomes heavier due to the combined effect of wall and bulk condensation. Bulk condensation appears first along the walls, which are colder. The plume rises to the top of the containment after 10 mn (Fig 2.f) when the vapor mass fraction in the upper cell is reduced to 40 %.

At t = 10 mn, a wide cell of superheated vapor remains in the intermediate dead area (see Fig. 3.c). Vapor stratification is weakened due to vapor loss. The total pressure is 0.21 MPa and the mean temperature 99°C.

- 10 to 33 mn: this corresponds to a free convection regime, with a fully developed plume and suspended droplets. This presence of mist characterizes this phase (see Fig. 1.e).

The injected vapor is warmer than the bulk and therefore it condenses when entering the containment. The mass of liquid in suspension reaches its maximum at t = 20 mn and fills the whole space (meaning that all the mixture is saturated). Evaporation of the mist slows down the rate of pressure and temperature increases. The rate of wall condensation continues to decrease, but less rapidly than during the first phase, because the higher section of the containment is once again supplied with vapor.

At t = 33 mn, the mass fraction of vapor has increased up to 43 %, there are no longer any droplets in the mixture and there is no more wall condensation because the wall temperature approaches the bulk temperature.

- 33 to 60 mn: this corresponds to the dry inflation of the containment. There is no more condensation and the pressure increases linearly following the injection. The temperature also increases rapidly.

The mass stratification decreases, whereas the mixture becomes richer in vapor. The bulk of the vapor is superheated and there is still a warm cell in the dead region (see Fig. 3.d).

5.b Second sequence (0.15 kg/s hydrogen injection)

The average values are shown in Figures 1.a, 1.b and 1.e and their spatial distribution in Figures 4.a to 4.e. The overall features, appart from hydrogen behavior, are the same as those previously described.

We can observe, at least for this simulation, the following behavior:
- hydrogen is rapidly spatially diluted by the mixture,
- hydrogen stratifies and the steepness of this stratification increases with time.
Secondary effects induced by stopping the vapor injection are:
- bulk condensation lasts longer and is greater. This is due to the fact that there is no longer any energy added by a pressure increase and thus no further heating.

Our aim in obtaining these multi-dimensional results was to locate the mixture composition in the Shapiro diagram. Three points of the mixture are in Figure 4.f, one in the stratification, another in the plume and the third close to the injection area. We recall that this computation is only for illustration, in particular the injection of pure hydrogen may be unrealistic.

6. CONCLUSIONS

As yet, we have only the first version of the GEYSER/TONUS code dedicated to evaluation of the hydrogen risk in a severe reactor accident. The multi-D features can also contribute to a better understanding of the physics involved.

In particular, this allows us to point out the main aspects of the flow structure (plume, boundary layers, stratification in the intermediate region). We can also observe the importance of heat and mass transfer at the wall as well as the energy imparted by the pressure increase.

The most important thing is to be able to predict hydrogen distribution, particularly for stratified flows or in presence of mitigation systems. These predictions can be used as starting points for combustion or detonation computations.

A set of basic validations will be carried out in the near future. It is also planned to use several CEA mock-ups such as MISTRA [4] and COPAIN [11] to assess the models.

REFERENCES

[1] The Assessment of Containment Codes by Experiments Simulating Severe Accidents Scenarios. H. Karwat. Publication of the European Communities, EUR 14159 EN, 1992.

[2] Westinghouse-GOTHIC Distributed Parameter Modelling of HDR Test E11.2. J.S. Narula, J. Woodcock. Proc. 3rd International Conference on Containment and Design, Toronto, Canada, October 19-21, 1994.

[3] Hydrogen Mixing Studies (HMS): Assessment Manual. K.L. Lam, T.L. Wilson, J.R. Travis. Report NUREG/CR-6060, June, 1993.

[4] MISTRA: an Experimental Program about the Thermodynamical Behaviour of Reactors Containments in Case of Severe Accidents. J.M. Humbert, A. Méjane. Technical Workshop, Containment Integrity and Energetic Threats, Saclay, France, October 13-14, 1994.

[5] The Finite Version of the TRIO Code. J.P. Magnaud, S. Goldstein. Proc 7th International Conference in Fluid Mechanics, Huntsville, USA, April 3-7, 1989.

[6] TRIO-EF : A General Thermal Hydraulics Computer Code Applied to the AVLIS Process. J.P. Magnaud, M. Claveau, N. Coulon, P. Yala, D. Guilbaud, A. Méjane. International Symposium on Laser Isotope Separation, Los Angeles, USA, January 19-20, 1993.

[7] A Modern Approach of Computer Codes for Structural Analysis. P. Verpeaux, A. Millard, T. Charras, A. Combescure. 10th Conference on Structural Mechanics in Reactor Technology, Anaheim, California, USA, August 14-18, 1989.

[8] GEYSER/TONUS : A Coupled Multi-D Lumped Parameter Code for Reactor Thermal Hydraulics analysis in Case of Severe Accidents. M. Petit, M. Durin, J. Gauvain. 7th Conference on Nuclear Reactor Thermal-Hydraulics, Saratoga Springs, USA, September 10-15, 1995.

[9] Convective Heat and Mass Transfer. W.M. Kays. McGraw-Hill Book Co. 1966.

[10] Transport Phenomena. R.B. Bird, W.E. Stewart, E.N. Ligtfoot. John Wiley. 1960.

[11] Steam Condensation Modelling. Micaelli & al. Technical Workshop Containment Integrity and Energetic Threats, Saclay, France, October 13-14, 1994.

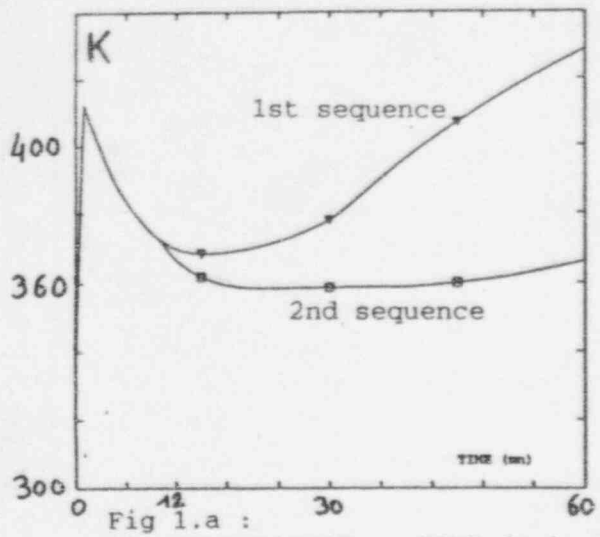

Fig 1.a :
MEAN TEMPERATURE vs TIME (mn)

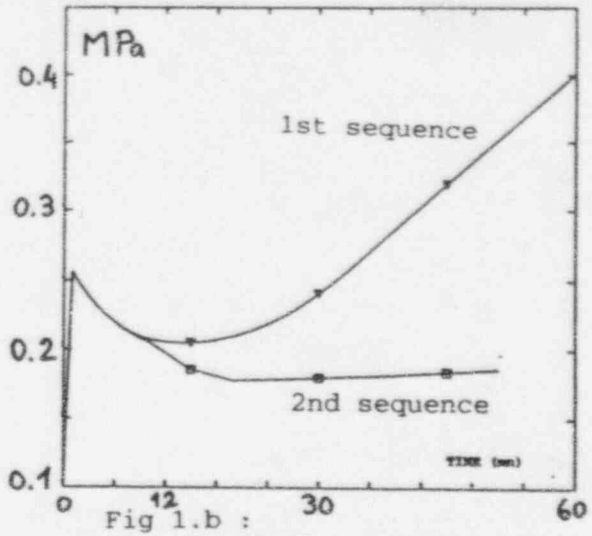

Fig 1.b :
TOTAL PRESSURE vs TIME (mn)

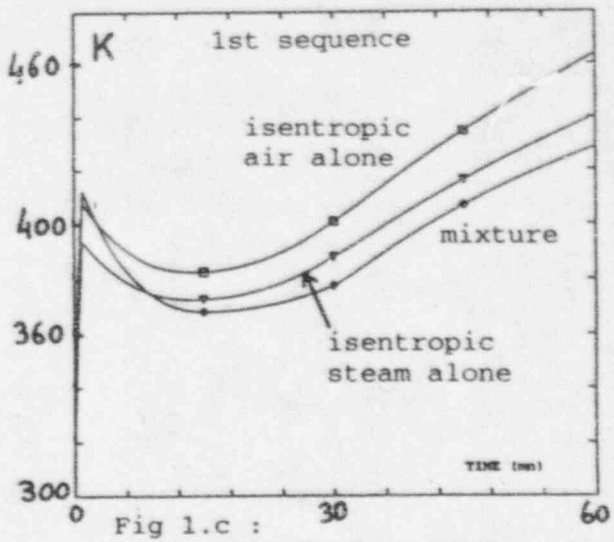

Fig 1.c :
MEAN TEMPERATURE vs TIME (mn)

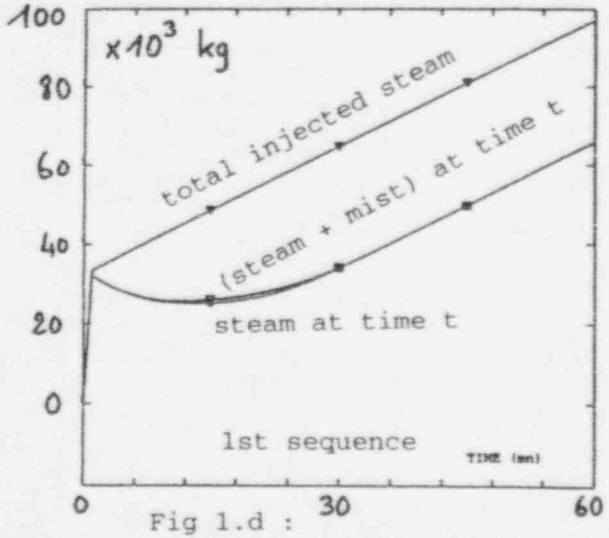

Fig 1.d :
WATER MASS vs TIME (mn)

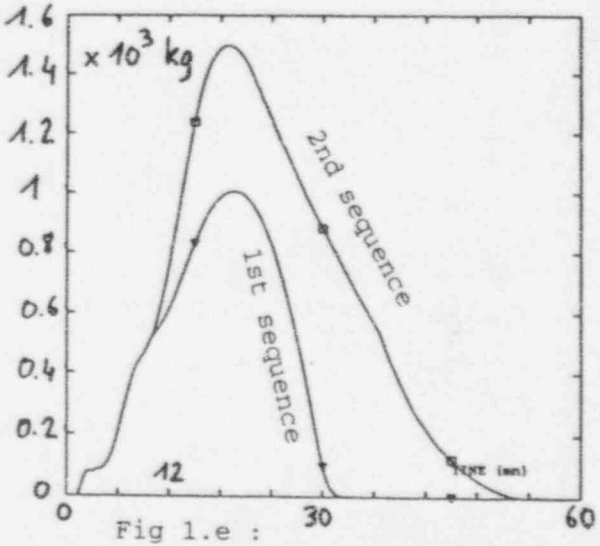

Fig 1.e :
DROPLETS MASS vs TIME (mn)

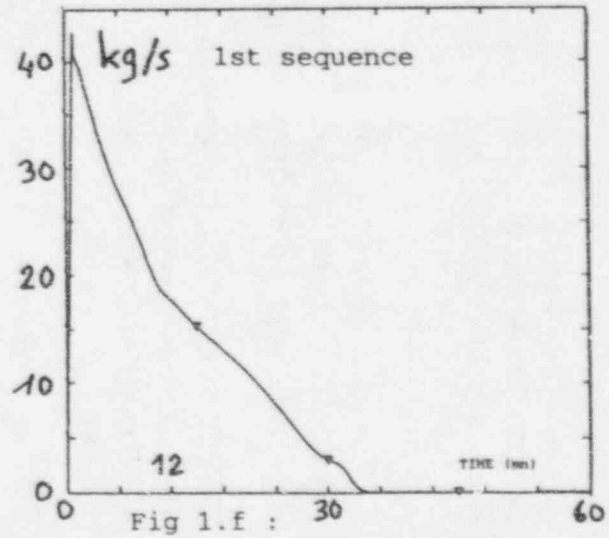

Fig 1.f :
TOTAL CONDENSATION FLUX
vs TIME (mn)

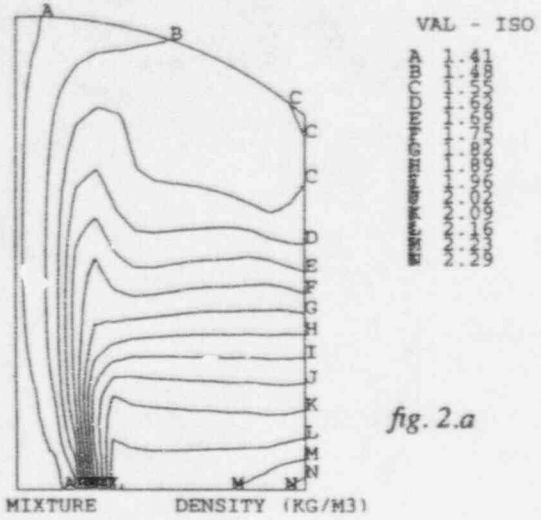

fig. 2.a

time : 1 mn

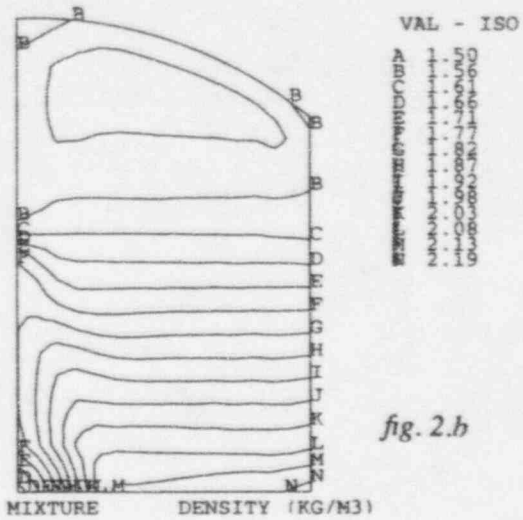

fig. 2.b

time : 2 mn

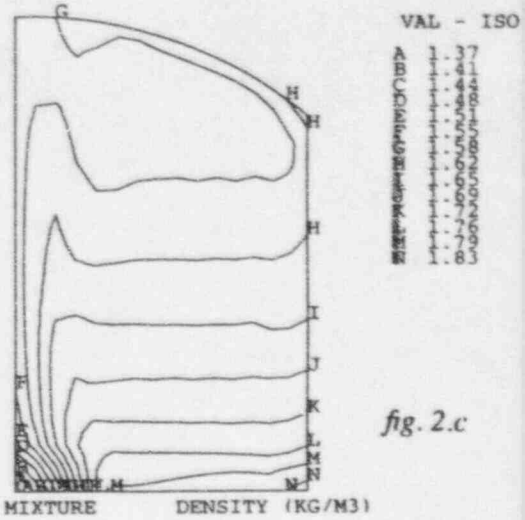

fig. 2.c

time : 10 mn

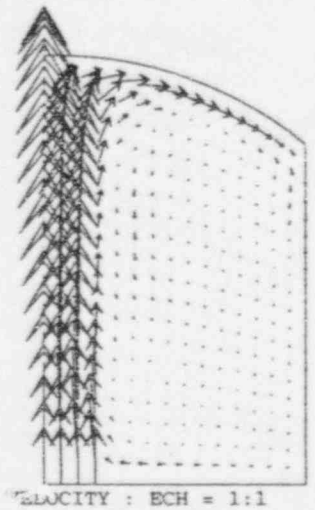

fig. 2.d

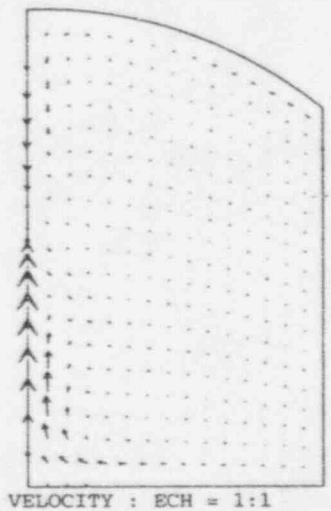

fig. 2.e

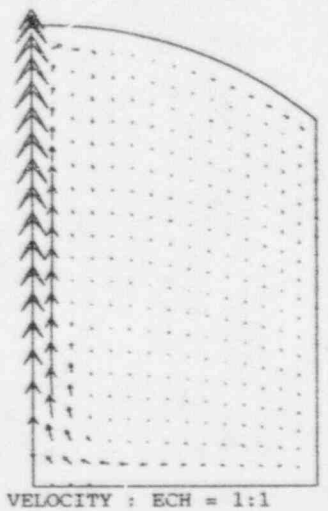

fig. 2.f

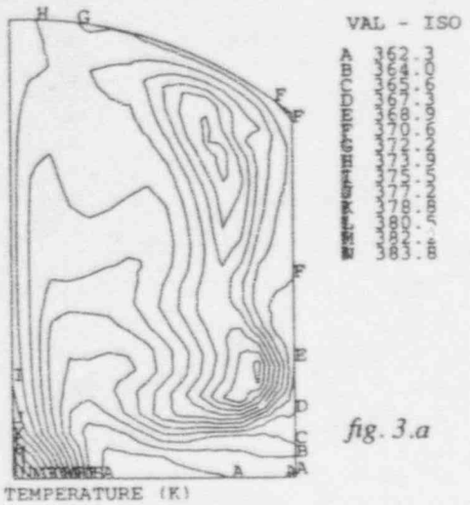

fig. 3.a

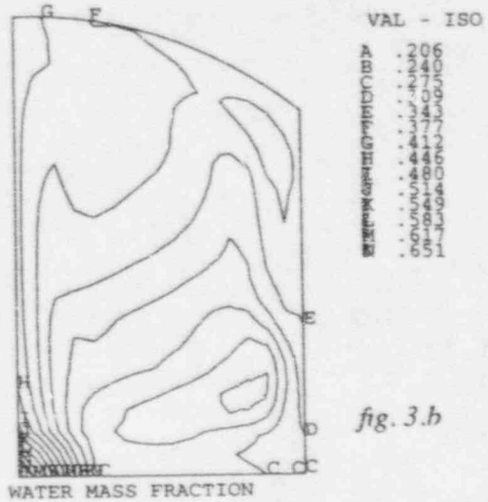

fig. 3.b

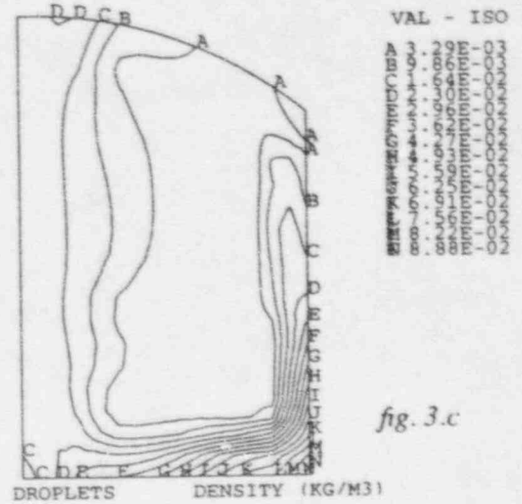

fig. 3.c

time : 10 mn

time : 60 mn **(1st sequence)**

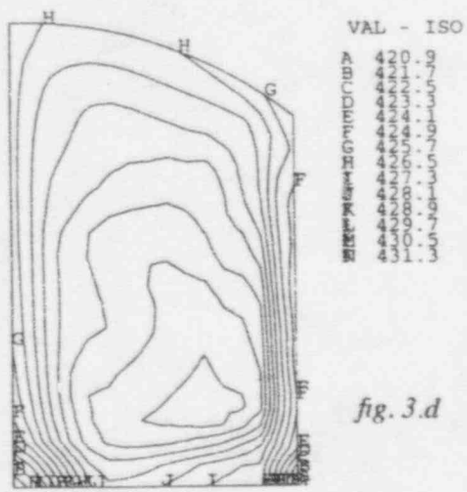

fig. 3.d

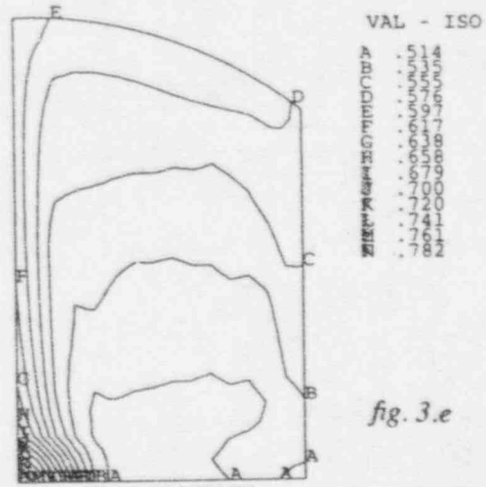

fig. 3.e

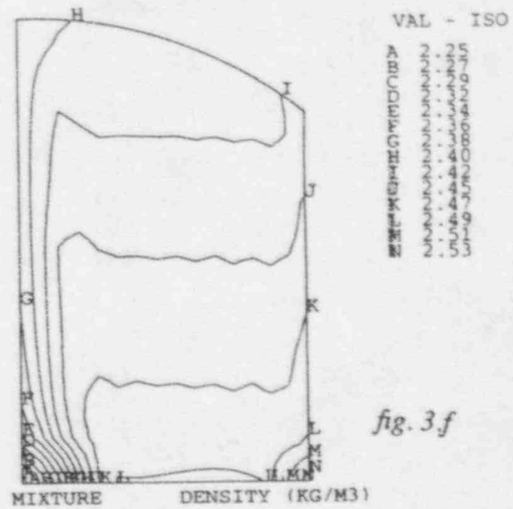

fig. 3.f

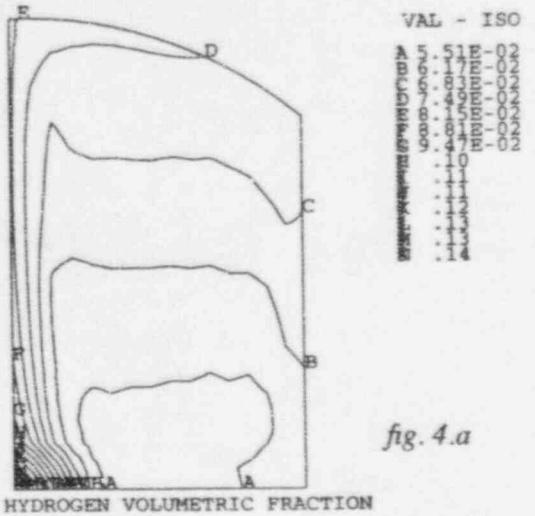

fig. 4.a

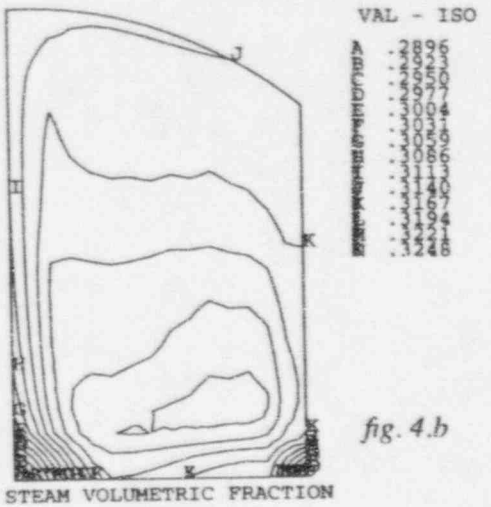

fig. 4.b

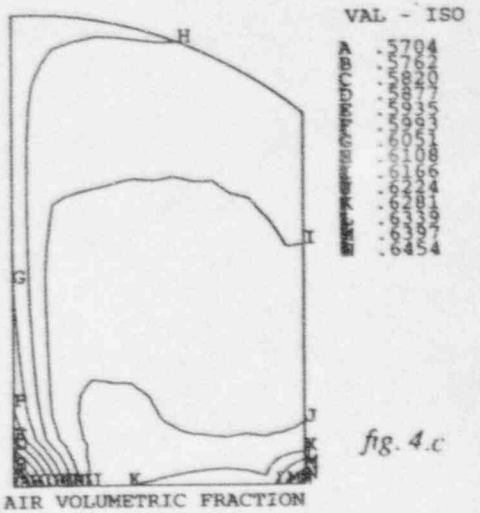

fig. 4.c

time : 60 mn **(2nd sequence)**

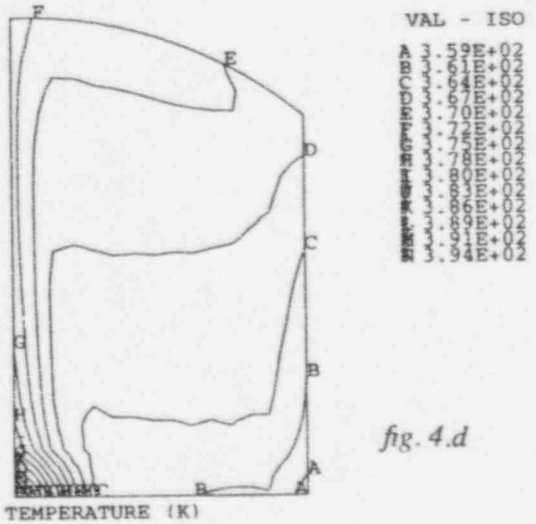

fig. 4.d

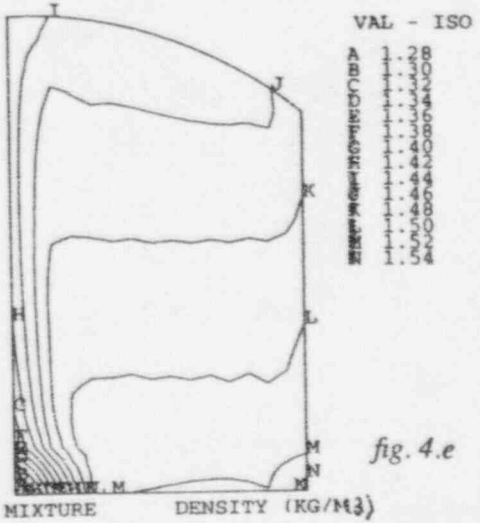

fig. 4.e

(a) injection area ;

(b) axial area ;

(c) stratified area ;

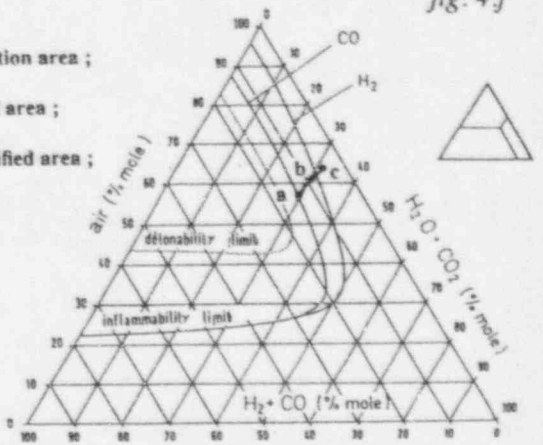

fig. 4.f

Shapiro diagram

THE MODELLING OF WALL CONDENSATION WITH NONCONDENSABLE GASES FOR THE CONTAINMENT CODES

C. Leduc, P. Coste, V. Barthel and H. Deslandes

* Commissariat à l'Energie Atomique
CENG STR/LML
17 Avenue des Martyrs
38054 GRENOBLE Cedex 09

ABSTRACT

This paper presents several approaches in the modelling of wall condensation in the presence of noncondensable gases for containment codes. The lumped-parameter modelling and the local modelling by 3-D codes are discussed. Containment analysis codes should be able to predict the spatial distributions of steam, air, and hydrogen as well as the efficiency of cooling by wall condensation in both natural convection and forced convection situations. 3-D calculations with a turbulent diffusion modelling are necessary since the diffusion controls the local condensation whereas the wall condensation may redistribute the air and hydrogen mass in the containment. A fine mesh modelling of film condensation in forced convection has been developed taking into account the influence of the suction velocity at the liquid-gas interface. It is associated with the 3-D model of the TRIO code for the gas mixture where a k-ε turbulence model is used. The predictions are compared to the Huhtiniemi's experimental data. The modelling of condensation in natural convection or mixed convection is more complex. As no universal velocity and temperature profile exist for such boundary layers, a very fine nodalization is necessary. More simple models integrate equations over the boundary layer thickness, using the heat and mass transfer analogy .The model predictions are compared with a MIT experiment. For the containment compartments a two node model is proposed using the lumped parameter approach. Heat and mass transfer coefficients are tested on separate effect tests and containment experiments. The CATHARE code has been adapted to perform such calculations and shows a reasonable agreement with data.

INTRODUCTION

This paper presents several approaches in the modelling of wall condensation in presence of noncondensable gases for containment codes. Different types of modelling concepts are tested on both separate effect tests and integral containment experiments. The lumped parameter modelling and the local modelling for 3-D codes are discussed with respect to the basic phenomena and to their simulation in containment analysis codes.

In the new generation of nuclear reactors, more attention is drawn on the efficiency of the containment cooling including passive residual heat removal systems. Advanced containment codes should be able to predict the spatial distribution of steam, air and hydrogen as well as the efficiency of cooling by wall condensation in both natural convection and forced convection situations. Then, 3-D calculations with a turbulent diffusion modelling are necessary since the diffusion controls the local condensation whereas the wall condensation may redistribute the air and hydrogen mass in the containment.

A fine mesh modelling of film condensation in forced convection is proposed, associated with the 3-D model of the TRIO code [1] for the gas mixture where a k-ε turbulence modelling is used. "Laws of wall" are used. They take into account the influence of the suction velocity at the liquid-gas interface, and the possibility of a wavy interface, affecting the viscous sublayer thickness. The model predictions are compared to the available experimental data like the Huhtiniemi's experiment [2,3].

The modelling of condensation in natural or mixed convection is more complex than the ideal forced convection case. A multi-dimensional calculation of mass diffusion through such boundary layers encounters physical and numerical modelling difficulties. A very fine nodalization may be required as there is no universal velocity profile similar to the logarithmic inertial sublayer in the forced convection case. Some existing models correlate the transfer coefficients through the boundary layer, but the origin of the boundary layer must be specified and the heat and mass transfer coefficients depend on the distance from this origin. These correlations use the analogy between heat and mass transfer, and a correction factor for high mass transfer rates. A selection of heat and mass transfer coefficients is proposed for both natural and forced convection. A hybrid Grashof number is used for natural convection condensation taking into account both temperature differences and mass concentration gradients effects on density differences. The modelling results are compared with a MIT experiment [4,5].

For the calculation of the containment compartments a two-node model is proposed using the more classical lumped-parameter approach. Different heat and mass transfer coefficients are tested on separate effect tests [4,5] and integral containment experiments [6,7]. The CATHARE code [8] has been adapted to perform such calculations. The adaptation consists in modifying the volume module to describe film condensation. Two models have been tested. One is close to the Uchida [9] correlation. The other uses the Nusselt theory for a laminar liquid film flowing down a vertical wall and a semi-empirical correction factor to take into account the noncondensible gas presence. Calculation results show a reasonable agreement with data.

All the proposed models are assessed with respect to two major concerns:

- the accuracy of the predictions
- the applicability to a containment code taking into account numerical limitations

From this discussion, the characteristics of a containment code are defined including both fine mesh 3-D modelling and lumped-parameter approach for the compartments. The final objective of our work is to develop a containment code using the 3-D module [10] and the Volume module [11] of the CATHARE code. The 3-D module -provided with the k-ε model of the TRIO code- could be used for large compartments and the Volume module (0-D module with lumped-parameter model) for small compartments of a containment. The use of CATHARE modules for the containment will allow a very easy coupling between the thermalhydraulic calculations of the reactor circuit, of the containment and of some inside containment safety systems.

CLASSIFICATION OF FILM CONDENSATION PROCESSES

There are two types of condensation on cold walls: filmwise and dropwise. Filmwise condensation occurs when the condensate wets the surface and a liquid film is formed. Dropwise condensation occurs on non-wetting surfaces, where the vapor condenses in drops which grow and roll over the surface. It is commonly accepted that filmwise condensation is more common than dropwise condensation in containment buildings as the dropwise condensation usually changes quickly to film during the initial period of condensation. then only the film condensation is considered. Depending on the conditions (film Reynolds number, wall inclination,..;) the film may be *laminar smooth, laminar wavy, or turbulent wavy*. One must also distinguish films developing on *vertical walls , inclined walls or horizontal walls* as condensation will occur mainly on side walls and on the roof of the containment. The wall inclination mainly affects the film dynamics and its wavy structure.

Forced convection condensation may exist along walls of a containment when gas movements are created by a steam break discharge jet, by spray actuation, or by any other momentum driven cause.

Large natural convection cells in the containment may be -among other things, such as break location- the result of heterogeneous condensation, or of temperature and noncondensable gas concentration gradients. Such convection cells may create wall boundary layers similar to the previous forced convection case. But smaller scale natural convection boundary layers may also be established along vertical walls. In this last case, called *the natural convection condensation*, the flow in the boundary layer results from local density gradients created by the condensation process itself and the gas velocity parallel to the wall outside the boundary layer (external velocity) is zero. The *mixed convection condensation* correspond to a boundary layer with a non zero external velocity and when the velocity profile in the boundary is significantly affected by local density gradients. To be fully rigorous, any boundary layer associated with condensation in the presence of noncondensable gases is in mixed convection or natural convection conditions as it includes temperature and gas concentration gradients.

CLASSIFICATION OF FILM CONDENSATION MODELLING APPROACHES

The film condensation in the presence of noncondensable gases involves many physical processes. The heat flux through the wall is controlled by several thermal resistances:

-1- thermal resistance of the wall which is a high resistance for a concrete wall
-2- thermal resistance of the liquid film which remains generally low
-3- thermal resistance associated with the gas to interface transfers

These three resistances are in series and are added. In the presence of noncondensable gas, the third resistance is in fact the combination of two resistances in parallel associated to the convective and condensation heat transfers. The convective heat flux is controlled by thermal exchanges within the gas boundary layer. The condensation term is generally much higher than the convective term. It is controlled by the mass diffusion of the vapour through the noncondensable gases which accumulate near the interface. In the situation of interest, the mass diffusion and the wall thermal resistance are the governing processes. However, a pure steam condensation may exist on containment structures during the blowdown phase of an accident, and the two first resistances control the transfers.

The following classification of modelling approaches is proposed:

-A- Local models with 3-D containment calculation
  -A1- Full 3-D boundary layer calculation
  -A2- 3-D boundary layer calculation using "law-of-wall" or "wall functions" (see for example Kim [12]) for the inner layer
  - A3- Models with transfer coefficients through the boundary layer
  -A4- Models with averaged transfer coefficients through the boundary layer
-B- Lumped-parameter approach

In type A models, a 3-D calculation of the gas mixture flow is performed in the containment space. It generally includes a turbulence model of the k-ε type. These models are able to predict the mass, momentum and energy diffusion effects on the velocity, temperature and noncondensable mass fraction space repartition.

When all boundary layers along the walls are calculated with sufficient accuracy -Type A1-, the model is able to predict all transfers in the boundary layer and the redistribution of gas components due to condensation with accumulation of noncondensable gases near the film interface. Such models require a turbulence model accounting for low Reynolds number effects and a very fine nodalization with several meshes in the viscous sublayer.

Type A2 models use laws of wall applicable in the logarithmic zone of the inner layer which are well established at least for forced convection boundary layers. This allows a coarser

mesh size near the wall without significant degradation in the prediction of the transfers and of the gas components repartitions.

Type A3 models do not calculate precisely the boundary layers and use transfer coefficients for momentum mass and energy. They use correlations for the friction coefficient, the Nusselt number and the Sherwood number. A much coarser meshing can be used as the first node near a wall can be outside of the boundary layer. The abcissa from the beginning of the boundary layer is a parameter of the correlations. In the complex geometry of a containment, it may be difficult to specify where are the beginning of all boundary layers particularly when convection movements are created by a steam jet or by other processes. However rather precise correlation are available for some ideal cases such as : natural convection or forced convection along a vertical flat plate. Then such models may be an acceptable alternative when CPU cost considerations do not allow a fine nodalization. It must be mentioned that these models cannot calculate correctly the internal circulation of the boundary layer with the associated noncondensable gas relocation effects.

The Type A4 is a further simplification of A3 where the transfer coefficients are averaged over the whole length of the boundary layer. Only the length scales such as vertical wall heigth or roof dimension have to be specified. A worse prediction of the space repartition of the wall heat transfer induces some loss of accuracy.

The Type B lumped-parameter approach does not calculate the space repartition of the velocity, temperature and noncondensable gas fraction within the containment. Only averaged scalar quantities (pressure, temperature, mass fractions) are predicted in one or a few control volumes. These model use also boundary layer transfer coefficients. However, the forced convection case cannot be treated as there is no gas velocity prediction. Moreover the numerical diffusion associated with the reduced number of control volumes does not allow a precise calculation of temperature and component mass fraction repartition. Due to these important shortcomings, a conservative approach is generally used in the choice of the heat transfer coefficients.

This classification is not exhaustive. One can also imagine for example to use an integral method for the boundary layer calculation, or a 1-D boundary layer modelling coupled to a 3-D containment calculation. Such methods were not considered in the present work. Only type A and B method could be implemented rather easily in the TRIO code. The current version of the TRIO code can calculate the dynamics, and heat and mass transfers for a mixture of several gases. Turbulent diffusion is predicted using a k-ε model associated with classical laws of wall.

IMPLEMENTATION OF FILM CALCULATION IN THE TRIO CODE

Mass and momentum equations are solved for the films along all walls. A heat transfer coefficient through the film is also written.
Mass balance equation:

$$\frac{\partial \delta.\rho_f}{\partial t} + \mathrm{div}(\delta.\rho_f.\vec{V}_f) = d\Gamma \qquad (1)$$

Momentum equation in the *laminar film* case:

$$\tau.dx = \mu_f \frac{\partial u_f}{\partial y} dx = (\delta - y).(\rho_f - \rho_g).g.\sin\theta.dx + \tau_i.dx$$

and after integration, the mean film velocity is:

$$V_{lam} = \frac{(\rho_f - \rho_g).g.\sin\theta}{3\mu_f}\delta^2 + \frac{\tau_i}{2\mu_f}\delta \qquad (2)$$

Solving equations 1 and 2 determines the film thickness δ and the mean film velocity as functions of τ_I and $d\Gamma$. The heat transfer is simply:

$$\Phi_{iw} = \frac{\lambda_f}{\delta}.(T_i - T_w) \tag{3}$$

For the *turbulent condensate film*, more complex expressions are used for the mean velocity and heat transfer coefficient. Following Kim [12], the universal velocity profile for a flow between parallel plates is used (Leduc [13]).

PROPOSED MODELLING OF THE TURBULENT FORCED CONVECTION CONDENSATION

The proposed modelling is of type A2 with a 3-D boundary layer calculation, a k-ε turbulence model and laws of wall. The same approach was tested by Kim [12] but it is here improved by taking into account the interface suction effects due to condensation.

Let us consider first the *smooth interface case.*
For a forced convection boundary layer without suction effect, the fluxes of momentum and heat to the wall are calculated by correlations which are derived from the universal velocity profile. The efficient diffusivities of momentum and heat near the wall are calculated from the well known logarithmic profiles for velocity and temperature. But these logarithmic profiles do not hold for forced convection boundary layers when a significant mass transfer occurs at the wall. As the mass transfer rate increase, the momentum, thermal and mass transfer boundary layers will be reduced in size because of the suction effects due to the condensation process. This reduction in the boundary layer will increase heat and mass transfer coefficients. With the classical hypothesis of the turbulent forced convection boundary layers, the total apparent shear stress τ, molecular plus turbulent, is constant near the wall and equal to the wall shear stress τ_w in the inner region of the boundary layer :

$$\tau(y) = \tau_w \tag{4}$$

In presence of a liquid film, the interfacial shear stress τ_i replaces τ_w.
When suction effect is considered, Kays [14] has shown that shear stress profile can be written as:

$$\frac{\tau}{\tau_i} = 1 + v_i^+(u^+ - u_i^+) \tag{5}$$

where u is the velocity parallel to the wall

$u*$ is the friction velocity : $u* = \sqrt{\frac{\tau_i}{\rho}}$

$u^+ = \frac{u}{u_*}$ is the dimensionless velocity parallel to the wall

$u_i^+ = \frac{u_i}{u_*}$ is the dimensionless velocity parallel to the condensate interface.

$v_i^+ = \frac{v_i}{u_*}$ is the dimensionless velocity perpendicular to the interface.

According to many authors, the expression of the mixing length in the inner layer

$$l = K y$$

with K being the Von Karman constant

and $y^+ = \frac{y \cdot u_*}{\nu}$ the dimensionless wall distance,

is still valid for forced convection with suction when the mass flux is not too high.
Then, in the same manner as eq.4 results in a logarithmic velocity profile , eq. 5 gives the more complex profile :

$$u^+ - u_i^+ = \frac{\left[\frac{v_i^+}{2.K}.\ln\left(\frac{y^+}{10,8}\right) + \exp\left(\frac{10,8.v_i^+}{2}\right)\right]^2 - 1}{v_i^+} \qquad (6)$$

This law applies in the range $30 < y^+ < 100$; this part of the boundary layer is called inertial sublayer. This equation 6 is used as a boundary condition for the momentum equations in the directions parallel to the wall.
Similar laws of wall for the thermal and mass transfer boundary layers can be deduced from the previous law. Heat and mass transfer eddy diffusivities can be obtained using the Reynolds-Colburn analogy for momentum, heat and mass transfer. This analogy states the equality of eddy diffusivities. The turbulent Prandtl and Schmidt numbers

$$Pr_t = \frac{\nu_t}{\lambda_t} \qquad \text{and} \qquad Sc_t = \frac{\nu_t}{D_t}$$

are equal to 1 in the Reynolds analogy. The constant value 0.9 resulting from several code validation calculations is taken in TRIO although some measurements have found non-uniform values of this term. However, it is a reasonable and convenient approximation for fluids for Pr and Sc > 0.5.

$$\text{So} \qquad \frac{\nu_t}{\nu} = K^2.y^{+2}.\frac{\partial u^+}{\partial y^+} = K.y^+.\left[\frac{v_i^+}{2.K}.\ln\left(\frac{y^+}{10,8}\right) + \exp\left(\frac{10,8.v_i^+}{2}\right)\right]$$

With these expressions, the temperature and air mass fraction dimensionless profiles are:

$$T^+ = \frac{1}{v_i^+}\left[\frac{v_i^+}{2.K}.\exp\left(-\frac{10,8.v_i^+}{2}\right).\ln\left(\frac{y^+}{10,8}\right)+1\right]^{2.Prt}.\exp\left(13,2.Pr.v_i^+\right) - \frac{1}{v_i^+} \qquad (7)$$

$$Xa^+ = \frac{1}{v_i^+}\left[\frac{v_i^+}{2.K}.\exp\left(-\frac{10,8.v_i^+}{2}\right).\ln\left(\frac{y^+}{10,8}\right)+1\right]^{2.Sct}.\exp\left(13,2.Sc.v_i^+\right) - \frac{1}{v_i^+} \qquad (8)$$

where $$T^+ = \frac{\rho.c.(T_i - T).u_*}{\Phi_{gi}} \qquad (9)$$

and $$Xa^+ = \frac{(Xa_i - Xa).u_*}{\frac{j_i}{\rho}} \qquad (10)$$

Φ_{gi} : convective heat flux

j_i : mass diffusion flux at the interface. $\quad j_i = d\Gamma X_{ai} = -\rho X_{ai} V_i$.

$d\Gamma$ i s the interfacial mass flux.

The resulting expressions of the convective heat flux Φ_{gi} (from eq.7 and 9) and mass transfer flux $d\Gamma$ (from eq 8 and 10) are used as boundary conditions for the energy and mass balance equations.The first point P of the meshing must be at a distance from the interface located in the inertial sublayer. Boundary conditions are also necessary for k and ε. Assuming that, in this inertial layer, the turbulence production is equal to the dissipation rate,

$$\varepsilon = -\frac{\tau}{\rho}\frac{\partial u}{\partial y} = \frac{u_*^4}{\nu K y^+}\left[1+v_i^+\left(u^+-u_i^+\right)\right]\left[\frac{v_i^+}{2K}\ln\left(\frac{y^+}{10.8}\right)+\exp\left(\frac{10.8v_i^+}{2}\right)\right] \qquad (11)$$

and:

$$k = \left[\frac{\nu_t\,\varepsilon}{C_\mu}\right]^{1/2} = \frac{u_*^2}{\sqrt{C_\mu}}\left[1+v_i^+\left(u^+-u_i^+\right)\right] \qquad (12)$$

The interface temperature is at saturation conditions:

$$T_i = Tsat(P_{vi}) \qquad (13)$$

P_{vi} is calculated assuming an ideal gas mixture:

$$X_{ai} = \frac{1-P_{vi}/P}{1-\frac{P_{vi}}{P}\left(1-M_v/M_a\right)} \qquad (15)$$

An energy balance at the interface gives:

$$\Phi_{iw} = \Phi_{gi} + H_{vl}\,d\Gamma \qquad (16)$$

The coupling between the film calculation (for example eq.1 and 2) with the 3-D calculation is made using eq. 6, 7, 8, 9, 10, 11, 12, 13, 14, 15.

The possibility of a *wavy interface* i s also taken into account. Indeed, if a wavy interface occurs between the vapor and the liquid film, this promotes the condensate rate, by affecting the viscous sublayer thickness y_S. Following Kays [14], this sublayer thickness is modeled as a function of the roughness Reynolds number

$$Re_k = \frac{u_*.k_s}{\nu_g}$$

where the effective roughness ks can be correlated (Kim [12]) by Wallis's simple correlation :

$ks = 4.\delta$

δ : mean condensate film thickness

for $Re_k < 5$, $y_S = 10.8$: interface behaves as perfectly smooth

for $Re_k > 70$, $y_S = 0.$: interface behaves as fully rough

For simplification, a linear evolution of y_S is assumed in the transition range $5<Re_k<70$.
In the case of a fully wavy interface, the near wall mixing length is modified to:

$$l = K\left(y+\delta y_o\right) \qquad \text{and } \delta y_o = \frac{\nu}{u_*}\;0.031\,Re_k$$

Taking into account the suction effects, the law of the wall is modified to:

$$u^+ - u_i^+ = \frac{\left[\frac{v_i^+}{2.K}.\ln\left(\frac{32.6\,y^+}{Re_k}\right)+1\right]^2 - 1}{v_i^+}$$

Φ_{gi} and $d\Gamma$ expressions (from eq. 7-9 and 8-10) are replaced by :

$$\phi_{gi} = \frac{c.d\Gamma.(T - T_i)}{1-\left(1+v_i^+.Re_k^{0,2}.Pr^{0,44}\right).\left[\frac{v_i^+}{2.K}.\ln\frac{32,6.y^+}{Re_k}+1\right]^{2.Prt}}$$

$$d\Gamma = \frac{\rho.(X_{ai} - X_a).u_*.v_i^+}{X_{ai}.\left\{\left(1+v_i^+.Re_k^{0,2}.Sc^{0,44}\right).\left[\frac{v_i^+}{2.K}.\ln\frac{32,6.y^+}{Re_k}+1\right]^{2.Sct} - 1\right\}}$$

Velocity profiles, heat and mass transfer laws, and boundary conditions for k and ε for the transition range were also obtained.

MODELLING OF THE TURBULENT NATURAL CONVECTION CONDENSATION

The use of wall functions

The natural convection condensation case is more difficult as there is no universal velocity profile as the logarithmic law or modified logarithmic law for the inertial layer. Probably because of experimental difficulties, the characteristics of turbulent natural convection boundary layers are not yet fully clarified and the modelling is still subject to controversy. Yet, some authors (Kim [12] , Nin [15] , Triboix [16]) use a temperature profile of forced convection type. But Nin and Triboix noticed that calculations using law of wall derived from this profile predicted heat transfers which were sensitive to the mesh size near the wall or interface. It means that there is some inconsistency between the law of wall and the calculated profile resulting from the turbulence model. Specific laws of wall taking correctly into account buoyancy effects on velocity and turbulence profiles would be necessary. Henkes et al ([17] , [18]) have studied a natural convection boundary layer, trying to develop such wall functions. They conclude that no fully satisfactory wall function is still available.

In the absence of adequate laws of wall, a full 3-D calculation of the boundary layer including the viscous sublayer may be an alternative (modelling of type A1). This requires a much finer nodalization near the wall (First node at about $y^+ = 0.1$ according to Herrero [19]). Attention must be paid to the turbulence model. The buoyancy forces have indeed a significant influence on the turbulence field in natural convection and mixed convection. A stable density stratification damps turbulent fluctuations whereas an instable stratification enhances turbulence production. Additive terms for the k and ε transport equations are required. Such terms which are functions of a "flux Richardson number" were proposed by Rodi [20] and are implemented in the TRIO code [1] . A low-Reynolds number k-ε model is also required. Jones and Renz [21] have studied the turbulent natural convection condensation using such a model [22] and recommend it. The implementation of a low-Reynolds number model in TRIO is in progress.

The use of transfer coefficients:

A more simple approach consists in the use of transfer functions which do not require a 3-D calculation of the boundary layer (type A3, A4). Heat and mass transfers at the interface are calculated using Nusselt and Sherwood number correlations.

$$Nu_x = \frac{\phi_{gi}.x}{\lambda.(T_\infty - T_i)} \qquad Sh_x = \frac{d\Gamma.Xa_i.x}{\rho.D.(Xa_i - Xa_\infty)}$$

x is the abcissa from the beginning of the boundary layer.

In natural convection, a Grashof number must be defined which must take into account density differences due to both temperature and noncondensable gas gradients (Vernier [23,24]). The following "hybrid" Grashof number is defined:

$$Gr_x = [\beta (T_\infty - T_i) + \gamma (Xa_i - Xa_\infty)].\frac{g\,x^3}{\nu^2}$$

with:

$$\beta = \frac{1}{\rho}\frac{\partial \rho}{\partial T} \quad , \quad \gamma = \frac{1}{\rho}\frac{\partial \rho}{\partial X_a}$$

Classical correlations [25] may be used:

Laminar flow:	$(10^4 < Gr\,Pr < 10^8)$	$Nu_x^o = 0.56 \quad (Gr\,Pr)^{0.25}$
Transition range :	$(10^8 < Gr\,Pr < 10^{10})$	$Nu_x^o = 0.13 \quad (Gr\,Pr)^{0.33}$
Turbulent flow:	$(10^{10} < Gr\,Pr\,)$	$Nu_x^o = 0.021 \quad (Gr\,Pr)^{0.4}$

and, using the Reynolds-Colburn analogy,

Laminar flow:	$(10^4 < Gr\,Sc < 10^8)$	$Sh_x^o = 0.56 \quad (Gr\,Sc)^{0.25}$
Transition range :	$(10^8 < Gr\,Sc < 10^{10})$	$Sh_x^o = 0.13 \quad (Gr\,Sc)^{0.33}$
Turbulent flow:	$(10^{10} < Gr\,Sc\,)$	$Sh_x^o = 0.021 \quad (Gr\,Sc)^{0.4}$

The correlation for the transtion range has the advantage to result in transfer coefficients independent on the abcissa x .Classical correction functions [26,23,24] for the suction effects have to be applied: $\Phi_{gi} = \theta \quad \Phi_{gi}{}^o$ and $d\Gamma = \theta \quad d\Gamma^o$

The superscript (^{o}) corresponds to values without any suction effect.

$$\theta = \frac{Ln(1+R)}{R} \qquad R = \frac{Xa_\infty - Xa_i}{Xa_i}$$

This model has been implemented in the 3-D code TRIO. A coarse meshing is allowed as the first point of the node has to be in the bulk, outside of the boundary layer.

CALCULATION RESULTS

Forced convection model

The proposed model for forced convection is compared with the experimental data of HUHTINIEMI [2,3] : an air-steam mixture flows into a rectangular channel with a condensing aluminium surface that has a painted surface finish. The mixture flow was concurrent in all the tests with condensate flow. Several test series were performed, with the orientation of the condensing surface varied from 0-90° (plate surface was facing downwards at 0°), with an air mass fraction from 0 to 0.87, and with an inlet velocity of 1 to 3 m/s. The experimental

uncertainty in heat transfer coefficient measurements was determined to be approximatively 10%. Heat transfer rates were observed to increase with flow velocity and vapor content.
The model predictions are compared to experimental data for:

vertical condensing plate	Vin = 1 m/s
vertical condensing plate	Vin = 3 m/s
horizontal condensing plate	Vin = 1 m/s

Figures 1, 2 and 3 compare the measured average heat transfer coefficients and predictions with two wall functions:

- without suction effects (using classical forced convection logarithmic laws)
- with suction effects as described above

All predictions underestimate the heat transfers. However, taking into account suction effects significantly improves the results. Predictions for Vin = 3 m/s deem acceptable considering the experimental uncertainty. But for the low velocity case (Vin = 1 m/s) the remaining underprediction suggests that pure forced convection wall functions are no longer valid in this case which is closer to the mixed convection. This is confirmed by Figures 4, 5 and 6 which present sensitivity tests to the mesh size near the wall. $y^+(1)$ corresponds to the position of the first calculated node. For Vin = 3, the predictions do not depend on $y^+(1)$ in the range where the velocity profile (eq. 6) is assumed to be valid. This proves the consistency of the turbulence model of the 3-D calculation with the law of wall. On the contrary, the mesh sensitivity obtained for Vin = 1 in both horizontal and vertical cases shows some inconsistency. Surprisingly, the experimental average heat transfer coefficients for these two cases are rather similar although density gradients are respectively perpendicular and parallel to the gravity force. It is known that for the horizontal case, the density stratification is unstable and creates additive mixing effects. For the vertical case, other processes having a similar effect should be identified.

Figure 7 presents the local heat transfer coefficient along the plate. A slight increase in the local heat transfer coefficient at the exit of the test section could be interpreted as an evidence of density gradient effects. Local heat transfer rates are highest at the beginning of the cooled plate and decrease due to developing concentration and temperature boundary layers. But the decrease is compensated by the development of a natural circulation pattern.The decreasing trend is underestimated and the increase is not predicted. Predicted heat transfer rates decrease with air mass fraction and lower velocity, as expected.

Natural convection model

The simple model with transfer coefficients (type A3) was used to calculate the MIT steam condensation experiment [4,5] in the presence of air. The experimental apparatus consists in a cylindrical steel vessel that is 5 m long and 0.45 m in diameter. Inside the vessel is placed a condensing cylinder made of a copper tube 3.5 m long and 0.38 m in diameter. The vessel is fully insulated so that condensation takes place only on the surface of the copper cylinder. An initial mass of air is present in the vessel. Steam is generated at the bottom of the vessel by heaters immersed in boiling water, at a rate that keeps the vessel pressure at a constant predetermined value. Bulk velocities are very low in these tests and a pure natural convection condensation occurs. Steady-state is reached when the steam flowrate equals the condensate flowrate and pressure is constant.
The conditions of the calculated test are:

Pressure	P = 3 bars
Steam flowrate	Q_v = 5.66 g/s
Mean air mass fraction	X_a = 0.34

Calculations are performed imposing the experimental steam flowrate. The predicted steady state pressure is 3.3 bars corresponding to an underestimation of the mass transfer coefficient. A more extensive validation is required but this first result suggest that such transfer correlations may be adequate for natural convection.

The lumped-parameter modelling (type B) was also tested on separate effect tests [4,5] and large scale tests [6,7] . The CATHARE Volume module is used. It is a 0-D module with a 2-fluid model. Mass balance equations are written for each component of the gas mixture and for the liquid phase. Energy balance equations are written for each phase. They are coupled with wall conduction calculations. Several such volumes may be coupled by junctions. At the junctions, momentum equations are written, but phase velocities are only calculated at junctions and not within the volume. Two heat transfer models have been implemented:

- The Uchida model [10]

- A modified Nusselt model

The Nusselt model was modified to take into account noncondensable mass diffusion effects. The interface temperature is calculated using a simplified mass diffusion modelling developed in the CATHARE code for film condensation inside tubes (Bestion [27], Coste [28]). The condensation flux expression with suction correction factor becomes:

$$\Phi_{cond} = H_{vl}\, d\Gamma = D\, \rho\, Sh\, H_{vl}\, \frac{1}{L} \ln\left(\frac{X_{ai}}{Xa_{\infty}}\right)$$

is simplified using a linearization:

$$\Phi_{cond} = F(X_a)\, \frac{\partial \Phi_{cond}}{\partial T_i} \left[Tsat(Pv_{\infty}) - Tsat(Pv_i)\right]$$

$F(X_a)$ is an empirical function of the noncondensable mass fraction used as a correction multiplier for the non linearity of the Φ_{cond} expression. It was adjusted on film condensation data in tubes [27].

The Sherwood number correlations for natural convection of the previous section are used. The transfer coefficients are integrated over the whole length of the wall L.

Comparison between data and calculations

The MIT experiment [4,5] is used for validation of the film condensation models. Several tests are calculated using a single volume for the vessel. The steam flowrate is imposed at the bottom of the vessel. Figure 10 presents the ratio of predicted to experimental vessel pressure for different mean air mass fractions. A maximum error of 7% (resp. 16%) is obtained with the modified Nusselt model (resp. Uchida model).

The Battelle Model Containment F2 experiment Phase 1 [6,7] is used for a validation on a more representative geometry. Figure 8 presents the geometry of the experiment with several compartments and the modelling with six volume modules of the CATHARE code. The initial state is at air ambient conditions. The pressure is increased stepwise by injecting steam at the bottom of Compartment R2 (Volume V2B). The three first steps with pressures of about 1.2, 1.55, 1.8 bar are simulated from zero to 65000 seconds. A sensitivity test with the upper compartment R9 (Volume V2A) is divided in three volumes. In the calculation, the injected steam flowrate is regulated in order to follow the experimental pressure. A comparison of experimental and calculated steam flowrates is presented in Figure 9. It is overestimated in the

calculations indicating an underestimated heat transfer and condensation rate. A better agreement is obtained when the upper space is modelled with three volumes. This illustrates the diffusive effects of a too coarse nodalization. In this test, the steam occupies only the uppermost region of the containment and condensation occurs mainly on upper walls. Large volumes spread the steam and increase the condensing wall area. The acceptable predictions with the three volumes for R9 probably result from many compensating errors:

CONCLUSIONS

A review of modelling approaches for the film condensation in containment codes was proposed. It ranges from 3-D modelling of the containment space with fine mesh calculation of all wall boundary layers, up to lumped-parameter models.

A fine mesh modelling of the forced convection boundary layers with a k-ε turbulence model and wall functions is developed and implemented in the TRIO code. The validation shows that taking into account suction effects in wall functions greatly improves the predictions.

In the absence of universal wall functions for natural convection boundary layers, a fine mesh modelling of this case requires a low-Reynolds number k-ε turbulence model and a calculation of the viscous sublayer. Further work is neccessary for assessing this method.

Such fine mesh modellings remain very CPU time consuming with present computers to be used in industrial containment codes. But they are necessary for reference codes which could be used for quantifying uncertainty of more simple codes or for some selected transients when safety issues require a high accuracy.

Simple modelling with transfer coefficients associated to a 3-D calculation or lumped parameter models may give acceptable results provided that appropriate correlation are used. One must keep in mind that the prediction of noncondensable gases accumulation and relocation processes cannot be precise when boundary layers are not precisely described.

A project of industrial containment code is in progress on the basis of the CATHARE code. The small compartments could be modelled with the lumped parameter model. The large upper dome will be modelled with the CATHARE 3-D module where heat and mass transfer correlations, and the k-ε turbulence model of TRIO are being implemented. Fine mesh modelling of wall regions would be also possible using the proposed models for natural and forced convection.

NOMENCLATURE

c	heat capacity
$d\Gamma$	interfacial mass flux
D	mass diffusivity
g	gravity acceleration
Gr	Grashof number
Hvl	latent heat
K	Von Karman constant
k	turbulent kinetic energy
L	wall length
M	molar mass

P	pressure
Pr	Prandtl number
Pv	partial pressure of steam
Q	mass flowrate
Re	Reynolds number
Sc	Schmidt number
Sh	Sherwood number
T	temperature
V	film velocity
v,u	gas velocity components
x	vertical abcissa
Xa	noncondensable mass fraction
y	distance from wall
ε	dissipation rate
δ	mean film thickness
ρ	density
τ	shear stress
θ	angle between axis perpendicular to the wall and vertical axis
μ	dynamic viscosity
ν	kinemetic viscosity
Φ	heat flux
λ	heat conductivity

subscripts

a	relative to noncondensable gas
cond	condensation
f	relative to the film
i	interface
g	relative to gas
s	relative to viscous sublayer
t	turbulent quantity
v	relative to vapour
w	relative to wall
∞	relative to bulk conditions

REFERENCES

[1] V. BARTHEL, M. VILLAND, TRIO.VF Note de présentation Version Complète Janvier 91, Note Technique CEA, STR/LML/91-09

[2] I.K. HUHTINIEMI, Ph.D., "Condensation in the presence of noncondensable gas: effects of surface orientation", University of Wisconsin - Madison, 1991

[3] I.K. HUHTINIEMI, M.L. CORRADINI, Condensation in the presence of noncondensable gases, Nuclear Engineering and Design, 141, (1993), pp 429-446.

[4] A. A. DEHBI, M. W. GOLAY, M. S. KAZIMI, The effect of noncondensable gases on steam condensation under turbulent Natural convection conditions,
Report N° MIT-ANP-TR-004

[5] A.A. DEHBI, M.W. GOLAY, and M.S. KAZIMI, " The effects of noncondensable gases on steam condensation under turbulent natural convection conditions",MIT-ANP-TR-004, Massachusetts Institute of Technology (June 1991)

[6] K. FISCHER, T. KANSLEITER, M.SCHALL, L. WOLF, CEC Thermal hydraulic Benchmark Exercice on FIPLOC Verification Experiment F2 in Batelle Model Containment Specification for Phase 1, Battelle Institut e. V, Frankfurt, FRG

[7] K. FISCHER, M.SCHALL, L. WOLF, CEC Thermal hydraulic Benchmark Exercice on FIPLOC Verification Experiment F2 in Batelle Model Containment Long Term Heatup Phase - Results for Phase 1 - Final Report, Battelle Institut e. V, Frankfurt, FRG

[8] D. BESTION, General Description of Cathare 2 V1.3, V1.3E, V1.3U
Rapport CEA, STR/LML/EM/94-265

[9] H. UCHIDA ; A, OYAMA ; Y, TOGO , Evaluation of post-accident cooling systems of LWR's, Proc, Int. Conf. Peaceful Uses of Atomic Energy, 13, pp.93-102, 1965.

[10] F. BARRE, I. DOR, C. SUN, The Multi-dimensional Module of Cathare 2 , companion paper, NURETH 7

[11] I. DOR, Cathare 2 V1.3, Description of the Volume Module. (Vol 2),
Rapport CEA, STR/LML/EM/94-248

[12] M.H. KIM, ML. CORRADINI, Modeling of condensation heat transfert in a reactor containment, Nucl. Engrg. Des. 118 (1990), pp 193-212

[13] C. LEDUC, Modelling of turbulent condensation heat transfer in the presence of a noncondensable gas, European Two Phase flow Group Meeting, Piacenza,6-8 June, 1994

[14] W. M. KAYS, M. E. CRAWFORD, Convective heat and mass transfer, Mac Graw-Hill, New York, 1980, 2nd edition

[15] J. NIN, J. VAN DER KOOI, Grid optimization of k-ε turbulence model simulation of natural convection in rooms, Roomvent'92, Third international Conference, Aalberg, Denmark, September 1992

[16] A. TRIBOIX, Y. GLENAT, Couplage conduction-convection-rayonnement par la méthode des volumes finis. première partie. Modélisation de la turbulence et description des échanges convectifs en paroi, Revue Générale de Thermique, n° 387, mars 94

[17] R.A.W.M. HENKES and C.J. HOOGENDOORN, Numerical determination of wall functions for the turbulent natural convection boundary layer along a heated vertical plate, Int. J. Heat and Mass Transfer, Vol 32, No.1, pp 157-1097,169,1989

[18] R.A.W.M. HENKES and C.J. HOOGENDOORN, Comparison of turbulence models for the natural convection boundary layer, Int. J. Heat and Mass Transfer, Vol 33, No.6, pp 1087-1097,1990

[19] J. HERRERO, The effect of grid size in near-wall k-ε calculations of mass transfer rates at high Schmidt numbers, Int. J. Heat and Mass Transfer, Vol. 37, N° 5, pp 882-884, 1994

[20] W. RODI, Influence of buoyancy and rotation on equations for the turbulent length scale, 2nd Symposium on turbulent shear Flows, Imperial Colledge, London, 1979

[21] W. P. JONES. and U. RENZ , 1974, Condensation from a turbulent stream onto a vertical surface, Int. J. Heat Mass Transfer, vol 17, PP1019-1028.

[22] W. P. JONES. and B. LAUNDER , 1973, The calculation of low Reynolds number phenomena with a two-equation model of turbulence, Int. J. Heat Mass Transfer, vol 16, PP1119-1130.

[23] P. VERNIER, M. DALBE , 1984, Analyse des études de base sur la condensation en présence d'incondensable le long d'une paroi plane, Commissariat à l'Energie Atomique, Rapport CEA-R-5284.

[24] P. SOLIGNAC, P. VERNIER, fevr. 1985, Test de quelques modèles de condensation en présence d'incondensable avec les expèriences ECOTRA, C.E.N.G., Note TT/SEF/85-1

[25] ROHSENOW, W.M. , Heat transfer and temperature distribution in laminar film condensation, Transaction of the ASME,
November 1956

[26] BIRD, R.B. ;STEWART, W.E. ,LIGHTFOOT, E.N., 1960, Transport phenomena, J. WILEY, NEW-YORK.

[27] D. BESTION, P. COSTE, and S. BARSOTTI, Study on condensation modelling in the CATHARE code with and without noncondensable gas, Int. Conference on New Trends in Nuclear System Thermalhydraulics, May 30-June 2nd, 1994, Pisa

[28] P. COSTE, and D. BESTION, A simple Modelling o mass diffusion effects on condensation with noncondensable gas for the Cathare code, to be presented at the Second International Conference on Multiphase Flow, Kyoto, Japan, April 3-7, 95

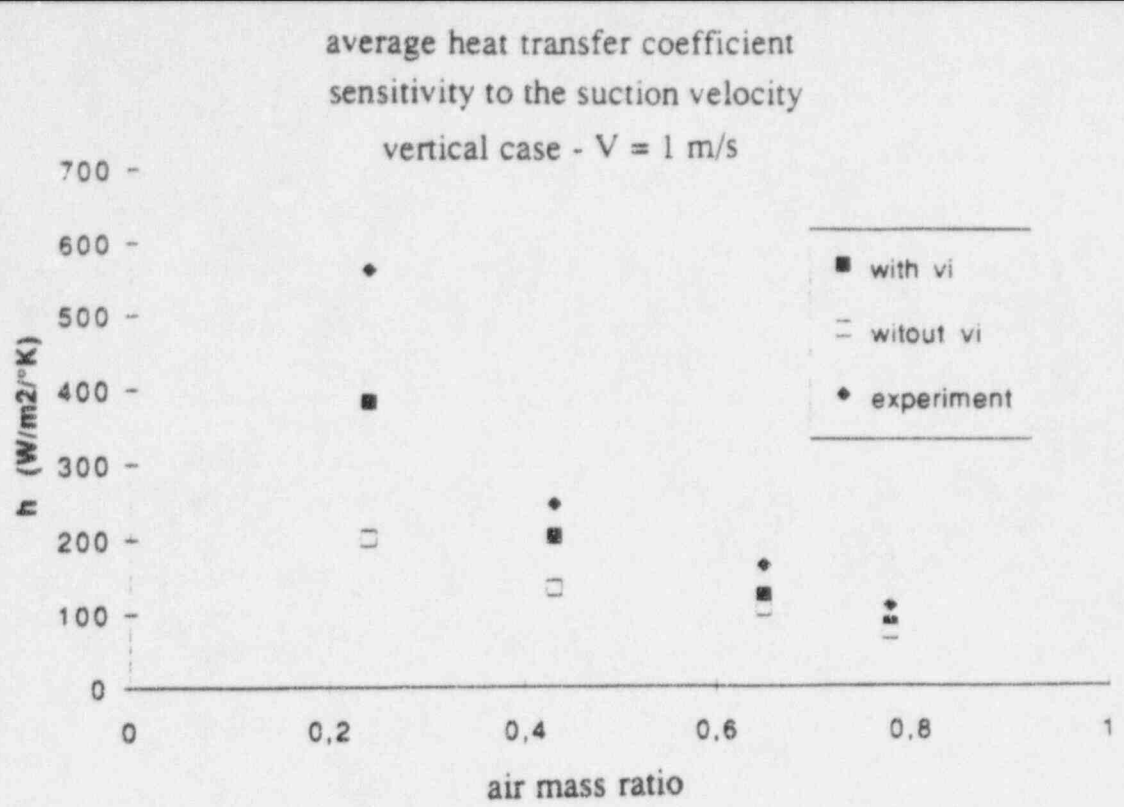

Fig.1 : HUTINIEMI's experiment - Calculation with and without suction effects

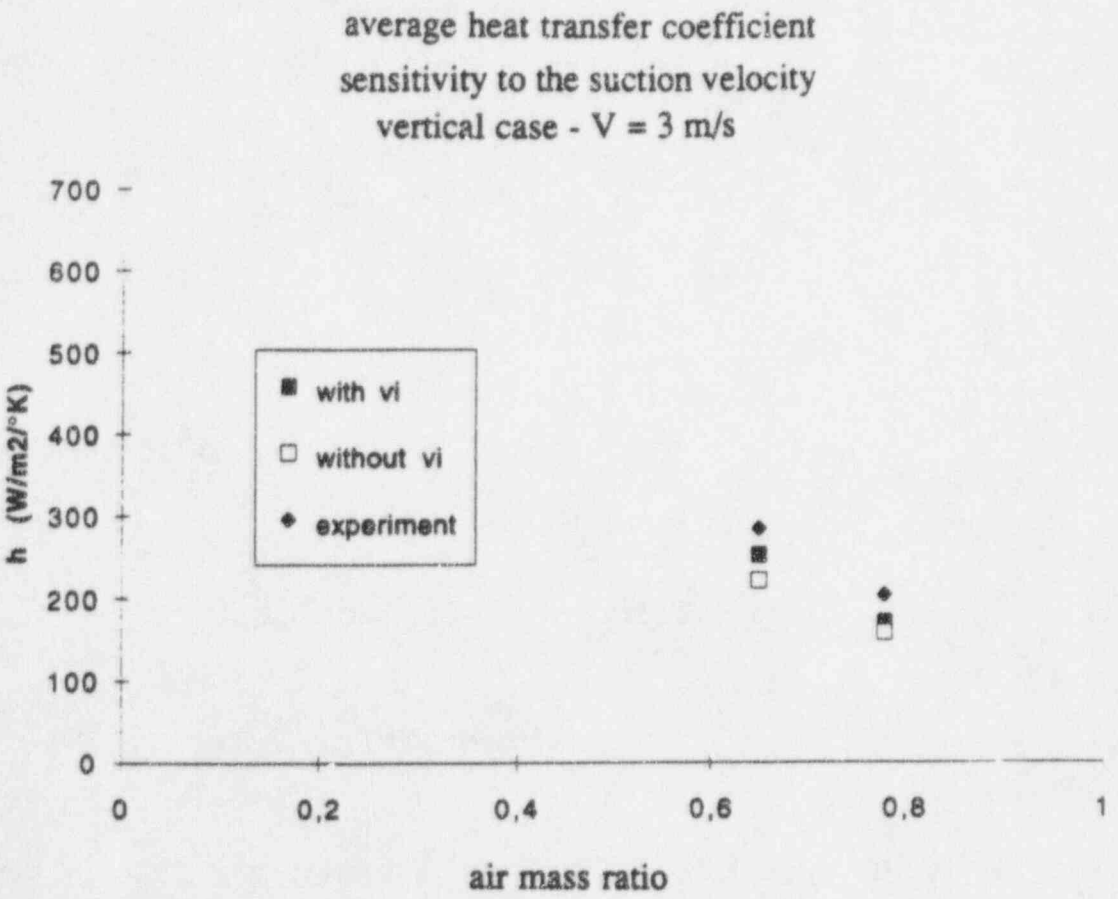

Fig.2 : HUTINIEMI's experiment - Calculation with and without suction effects

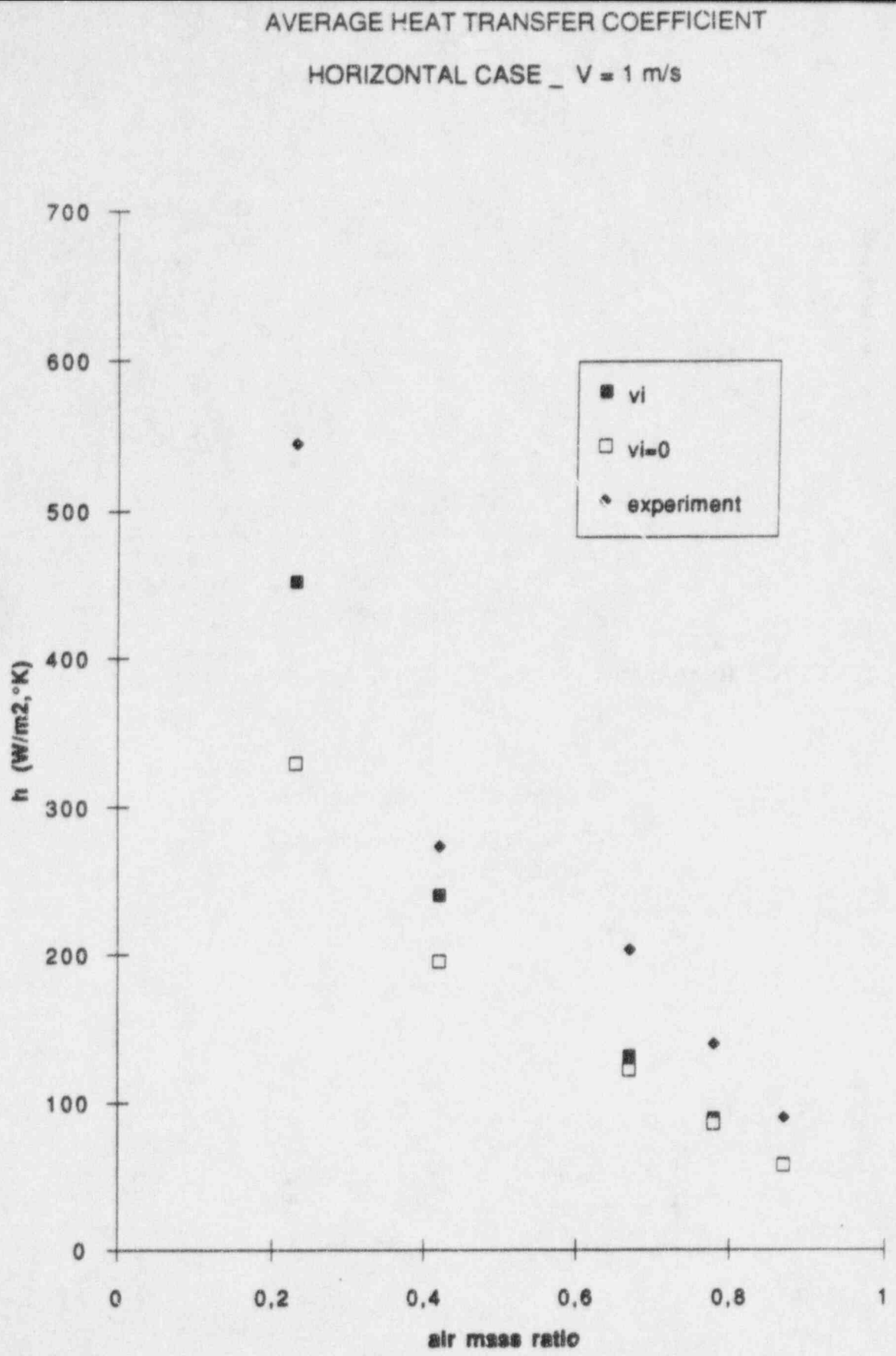

Fig.3 : HUTINIEMI's experiment - Calculation with and without suction effects

AVERAGE HEAT TRANSFER COEFFICIENT
VERSUS THE NONDIMENSIONAL DISTANCE
OF THE NEAREST NODE TO THE WALL

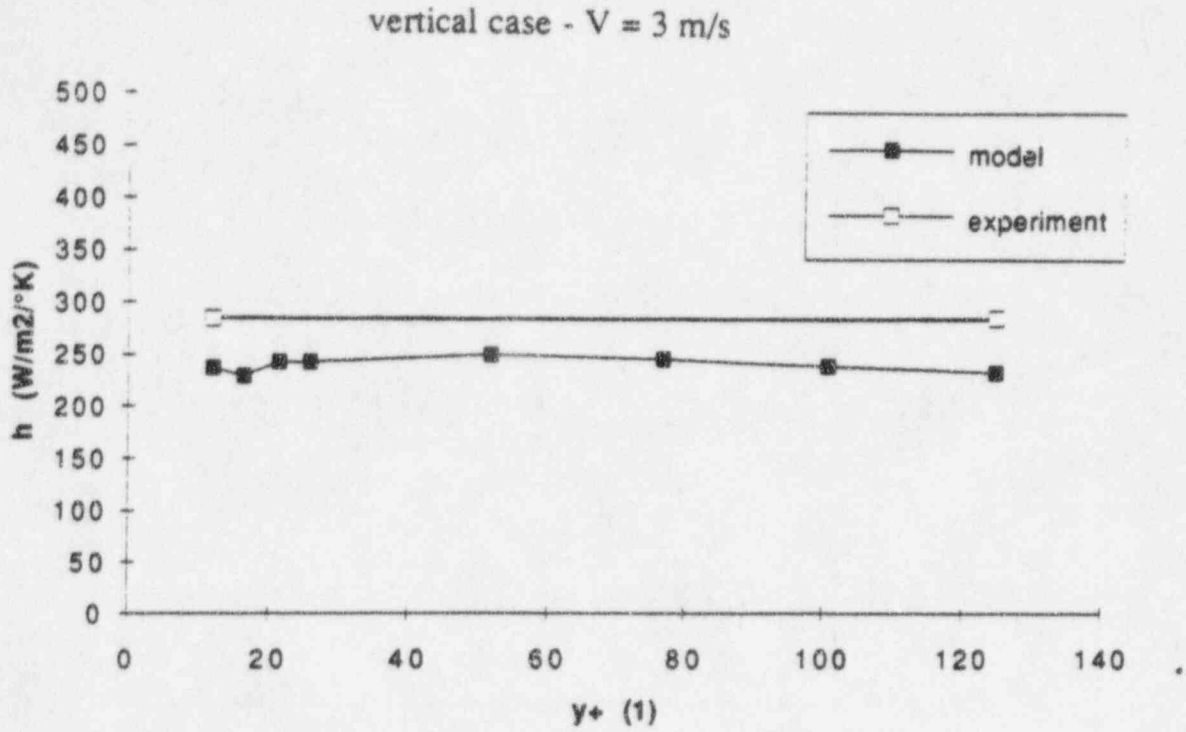

Fig.4 : HUTINIEMI's experiment - Sensitivity to the first mesh size

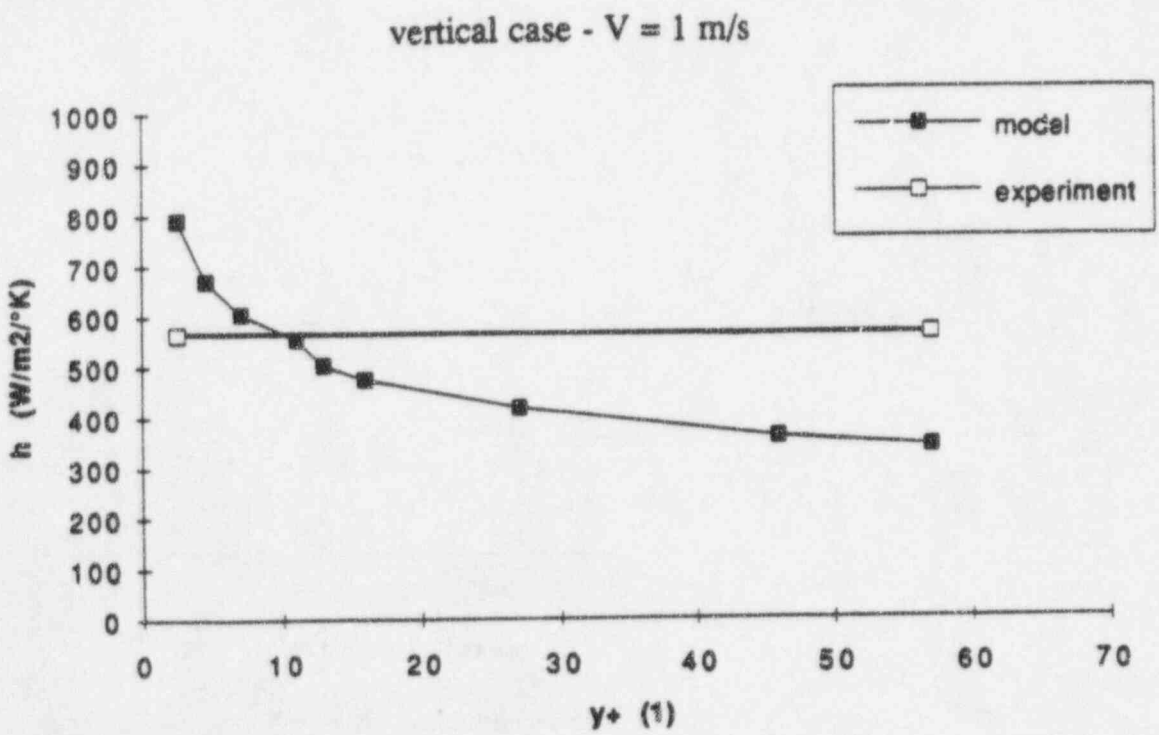

Fig.5 : HUTINIEMI's experiment - Sensitivity to the first mesh size

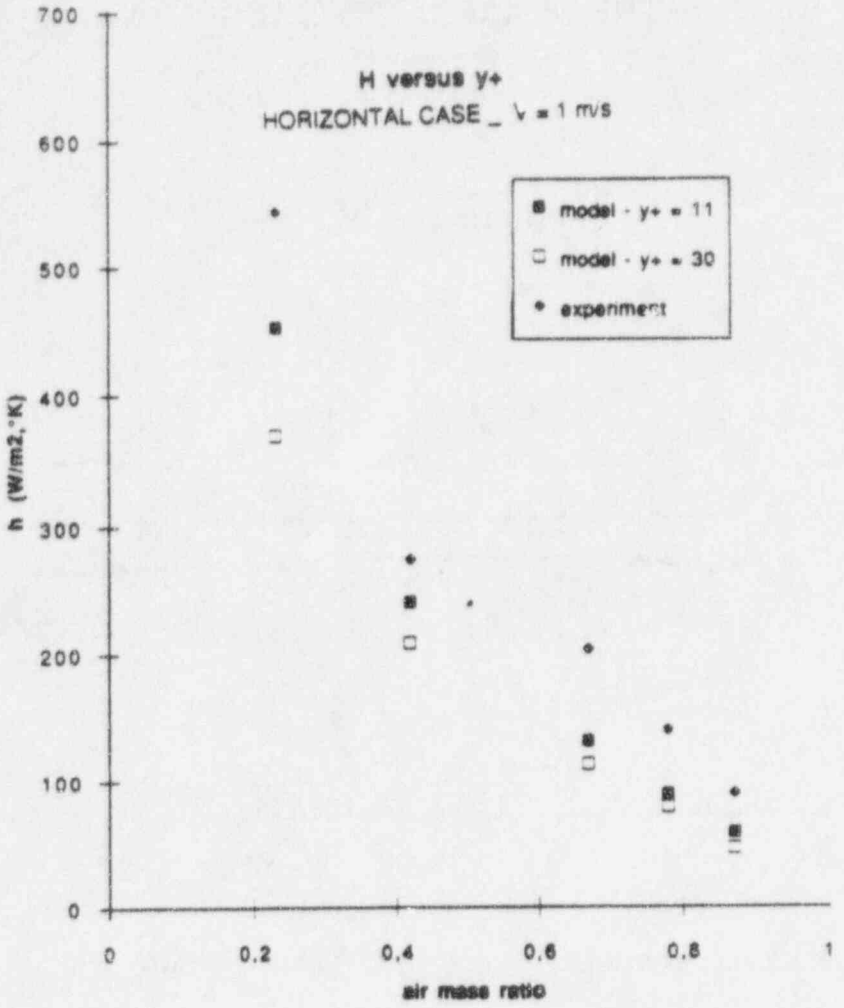

Fig.6 : HUTINIEMI's experiment - Sensitivity to the first mesh size

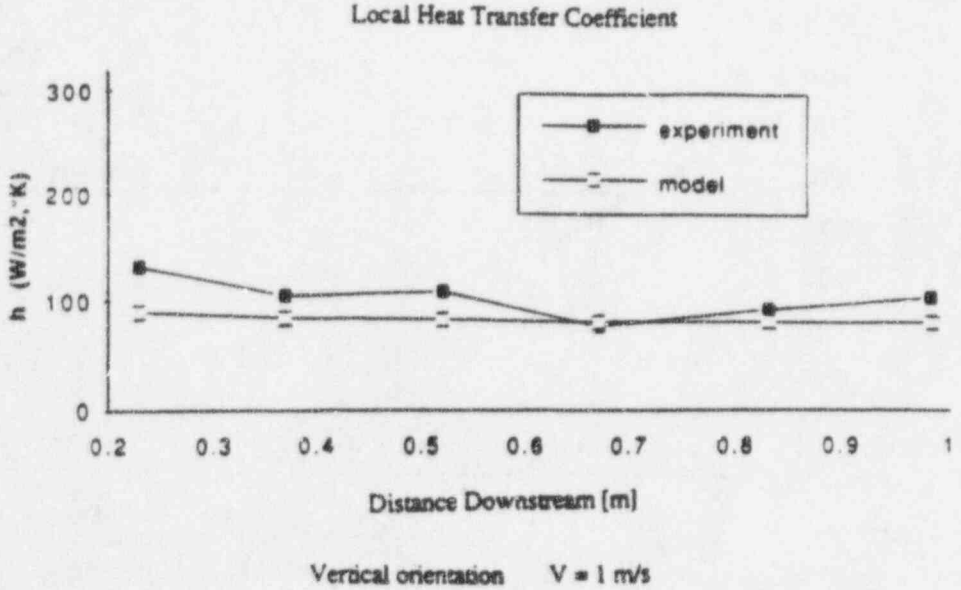

Fig.7 : HUTINIEMI's experiment - Axial profile of heat transfer coefficient

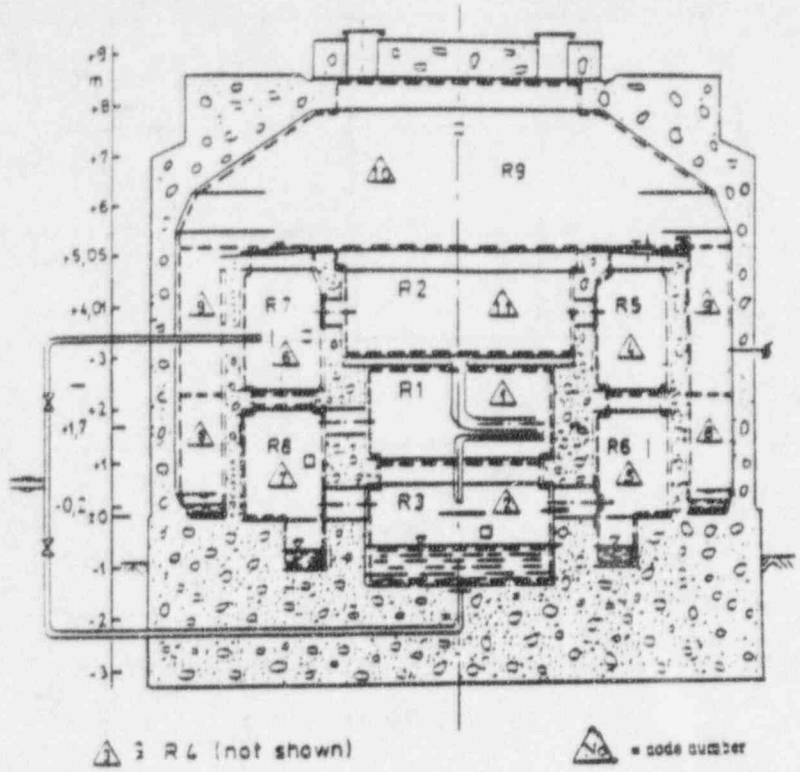

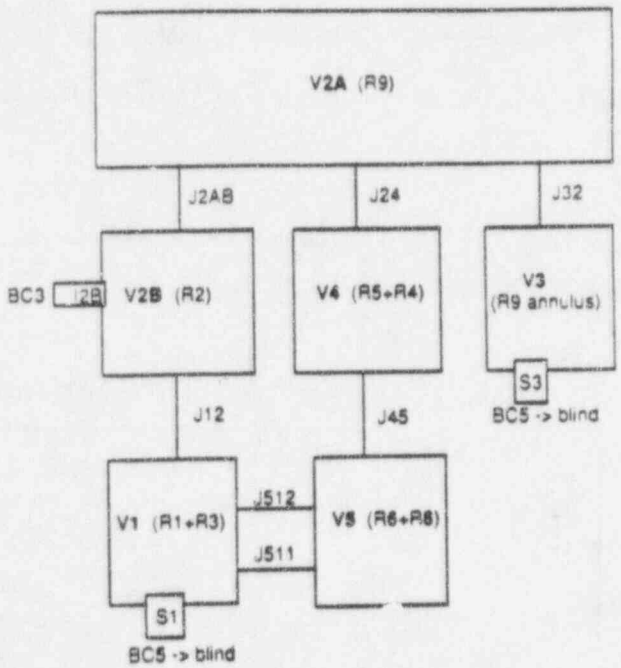

V1 to V5 : CATHARE volumes
J... : CATHARE junctions
I2B, S1, S3.: Boundary conditions
R1 to R9 : refers to the Battelle experiment description

Fig 8: BATTELLE Model Containment and modelling with the CATHARE code

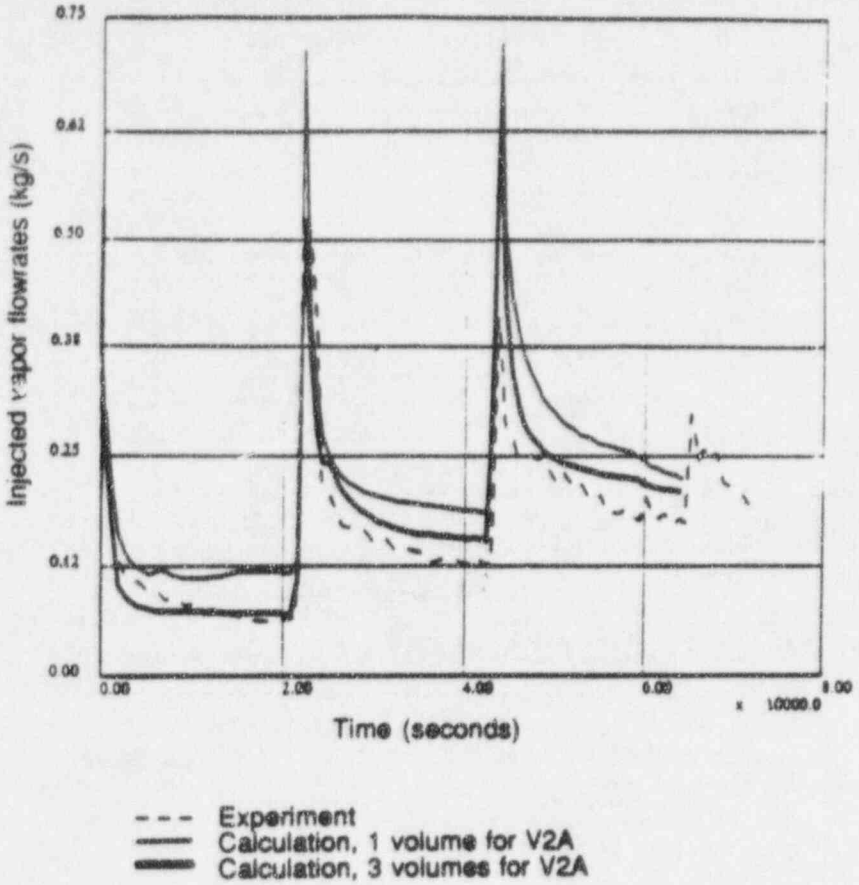

Fig.9 : BATTELLE Model Containment calculation with the CATHARE lumped parameter modelling

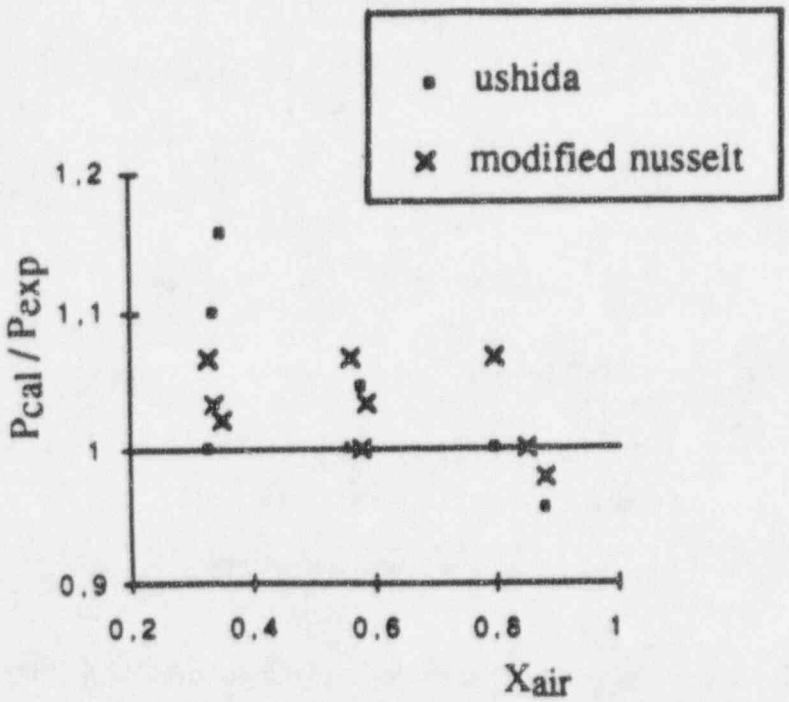

Fig.10 : MIT experiment [3] - Calculation with the CATHARE lumped parameter modelling

AN INTERPRETATION OF PASSIVE CONTAINMENT COOLING PHENOMENA

Bum-Jin Chung
Nuclear Inspection & Enforcement Division
Ministry of Science & Technology
Jungang-Dong, Gwacheon, Kyunggi-Do, KOREA

Chang-Sun Kang
Department of Nuclear Engineering
Seoul National University
Silim-Dong, Kwanak-Gu, Seoul, KOREA

ABSTRACT

A simplified interpretation model for the cooling capability of the Westinghouse type PCCS is proposed in this paper. The PCCS domain was phenomenologically divided into 3 regions; water entrance effect region, asymptotic region, and air entrance effect region. The phenomena in the asymptotic region is focused in this paper. Due to the very large height to thickness ratio of the water film, the length of the asymptotic region is estimated to be over 90 % of the whole domain. Using the analogy between heat and mass transfer phenomena in a turbulent situation, a new dependent variable combining temperature and vapor mass fraction was defined. The similarity between the PCCS phenomena, which contains the sensible and latent heat transfer, and the buoyant air flow on a vertical heated plate is derived. The modified buoyant coefficient and thermal conductivity were defined. Using these newly defined variable and coefficients, the modified correlation for the interfacial heat fluxes and the ratios of latent heat transfer to sensible heat transfer is established. To verify the accuracy of the correlation, the results of this study were compared with the results of other numerical analyses performed for the same configuration and they are well within the range of 15 % difference.

INTRODUCTION

The advanced reactor containment design concept requires a passive containment cooling capability which provides an ultimate heat sink in an accident situation. Various passive containment cooling system (PCCS) designs, which use natural forces, were proposed by many organizations and most of them incorporate natural convection cooling mechanisms. Among them Westinghouse type PCCS design[1] seems to have a strong cooling capability because it has an additional cooling mechanism - the evaporative cooling of the water film which runs down along the steel containment vessel by gravitation. But due to the introduction of this additional cooling mechanism, the estimation of the cooling capability by either numerical or experimental method is difficult in spite of the relatively simple geometric configuration.

The expected PCCS phenomena are combined heat and mass transfer at the air-water interface, counter current flow situation of falling water and buoyant mixed-air flow, and highly turbulent natural convection air flow since the Rayleigh number for the proposed system(at least 20 meters high) is greater than 10^{13}. Much experimental and numerical effort has been made to estimate the cooling capability of the design but the inherent complexity of the phenomena are not yet clearly identified.

In this study, based upon the system configurations and previous knowledge of the physics of the system, a simplified interpretation model on cooling capability was sought. Through suitable approximations, the similarity between the PCCS phenomena, which contain the sensible and latent heat transfer, and the buoyant air flow on a vertical heated plate is derived.

PROBLEM DESCRIPTION AND DERIVATION OF GOVERNING EQUATIONS

Figure 1 shows the AP-600 PCCS configurations[1]. Water film, running down along the steel containment vessel, is heated by the containment wall and cooled by buoyant air flow, which exhibits counter current situation.

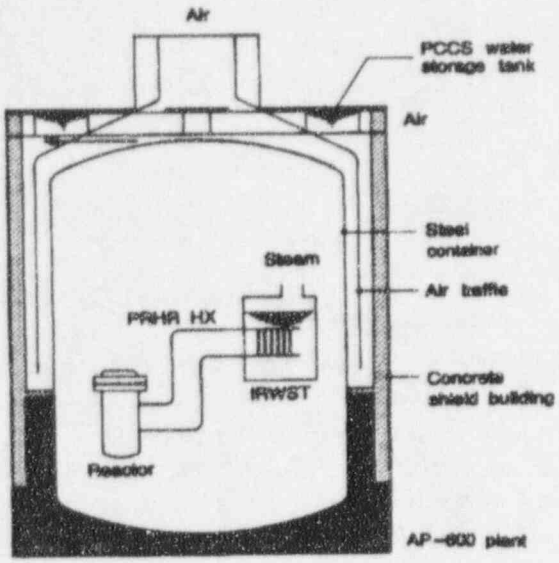

Figure 1. AP-600 passive containment cooling system.

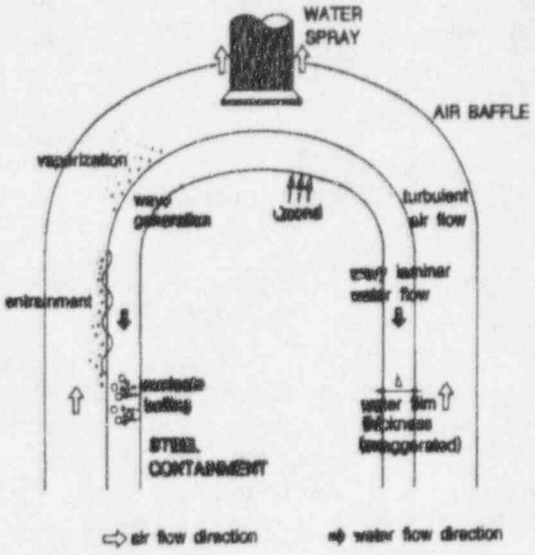

Figure 2. Schematization of PCCS Phenomena.

Since the water film is cooled not only by sensible heat transfer but also by latent heat transfer, combined heat and mass transfer phenomena are expected. Nucleate boiling, entrainment of water-vapor, and wave generation at the interface of water and air flow are also possible phenomena but are not expected in view of the operating condition. Figure 2 presents the schematization of the possible PCCS phenomena.

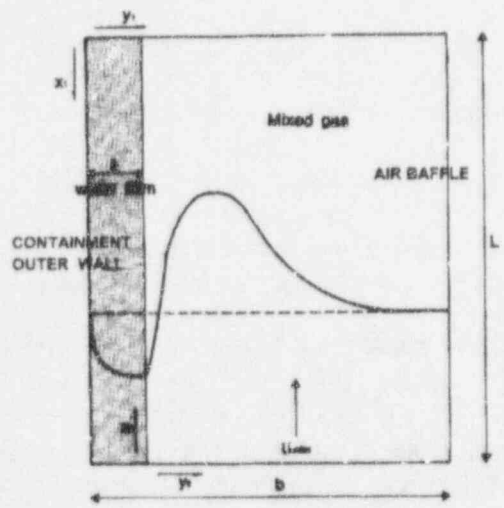

Figure 3. Simplified calculation domain.

Through the careful consideration of the system dimensions and operating conditions, some of the phenomena can be excluded in the analysis. Since the diameter of the containment is large, the effects of curvature are neglected and the calculation domain is safely approximated to 2-dimensional rectangular domain[2], which is presented in Figure 3.

Due to high Rayleigh number($>10^{13}$) in this system, the strong turbulent intensities are expected in the natural convection mixed air flow.

According to the conceptual design of the Westinghouse PCCS, the containment height should be larger than 20 m and water film thickness should be less than 1 mm. It means height to thickness ratio of water film is greater than 20,000. Water film flow characteristics depend on film Reynolds number which is function of both film thickness and viscosity. For the thin water film in this system, laminar water film flow assumption is

relevant. The data on Westinghouse PCCS were based upon the Westinghouse reports[1]. Thus whether the thin film can reach the bottom and how the non-wetting parts can be prevented on containment surface are not considered in this study. But the film thickness variation along the flow in containment heat flux condition is reported to be less than 15 % so that it is reasonable to make a constant film thickness assumption[3].

Nucleate boiling and entrainment of water vapor were not considered in the analysis due to the thin water film. The waves generated at the interface of water and air flow are reported to have some effects on the interface heat flux but they do not change the major scales. Therefore wave effects are not considered in the analysis. Table 1 summarizes the critical parameter values used in phenomena modeling[4,5,6].

Table 1. Critical parameter values for gravity film and buoyancy-induced gas flow.

Assumptions	Critical parameter values
Laminar liquid film	$Re_f \leq 1500$
No film break-up	$\delta \geq 0.01$ mm
No nucleate boiling	$q_w \leq 8$ kW/m^2
Laminar gas flow	$Ra_H \leq 10^9$
No entrainment	$\delta < 5$ mm

The 2-dimensional, steady state, laminar flow in the water film is described by the following equations:

Momentum

$$\frac{\partial}{\partial y_1}(\nu_1 \frac{\partial u_1}{\partial y_1}) + g = 0 \tag{1}$$

Energy

$$u_1 \frac{\partial T_1}{\partial x_1} = \frac{\partial}{\partial y_1}(\alpha_1 \frac{\partial T_1}{\partial y_1}) \tag{2}$$

Entrance Condition

$$x_1 = 0 \; ; \; u_1 = 0 \, , \; T_1 = T_\infty \tag{3}$$

Heated Wall Condition

$$y_1 = 0 \; ; \; u_1 = 0 \, , \; T_1 = T_w = constant. \tag{4}$$

The 2-dimensional, steady, turbulent, boundary layer flow in the mixed gas side is governed by the following conservation equations along with Boussinesq assumption, which assumes the flow is incompressible except for the buoyancy terms in the momentum equation:

Continuity

$$\frac{\partial u_2}{\partial x_2} + \frac{\partial v_2}{\partial y_2} = 0 \tag{5}$$

Momentum

$$u_2\frac{\partial u_2}{\partial x_2} + v_2\frac{\partial u_2}{\partial y_2} = \frac{\partial}{\partial y_2}(\nu_{2,e}\frac{\partial u_2}{\partial y_2}) + g[\beta(T_2 - T_\infty) + \beta^*(W_2 - W_\infty)] \tag{6}$$

Energy

$$u_2\frac{\partial T_2}{\partial x_2} + v_2\frac{\partial T_2}{\partial y_2} = \frac{\partial}{\partial y_2}(\alpha_{2,e}\frac{\partial T_2}{\partial y_2}) \tag{7}$$

Vapor Mass Concentration

$$u_2\frac{\partial W_2}{\partial x_2} + v_2\frac{\partial W_2}{\partial y_2} = \frac{\partial}{\partial y_2}(D_{2,e}\frac{\partial W_2}{\partial y_2}) \tag{8}$$

Entrance Condition

$$x_2 = 0\ ;\quad u_2 = 0\ ,\ v_2 = 0\ ,\ T_2 = T_\infty\ ,\ W_2 = W_\infty \tag{9}$$

Adiabatic Wall Condition

$$y_2 = b\ ;\quad u_2 = v_2 = 0\ ,\ \frac{\partial T_2}{\partial y_2} = 0\ ,\ \frac{\partial W_2}{\partial y_2} = 0 \tag{10}$$

The solutions from the liquid side and the gas side must satisfy the following interface conditions:

Continuity Conditions

$$\begin{aligned} &\textit{velocity} && u_1 = u_2 = u_I\ , \\ &\textit{temperature} && T_1 = T_2 = T_I\ , \\ &\textit{shear stress} && \tau_1 = \tau_2 = \tau_I \end{aligned} \tag{11}$$

Thermodynamic Equilibrium Conditions

$$\begin{aligned} q_I &= \left[-k_1\frac{\partial T_1}{\partial y_1}\right] = q_{sensible} + q_{latent} \\ &= \left[-k_{2,e}\frac{\partial T_2}{\partial y_2}\right] + m_I\, h_{fg}\ , \end{aligned} \tag{12}$$

$$m_I = \rho_s v_I\ , \tag{13}$$

$$v_I = -\frac{D_{2,e}}{1 - W_2}\frac{\partial W_2}{\partial y_2}\ ;\quad y_2 = 0\ . \tag{14}$$

PHENOMENA SIMPLIFICATION

New dependent variable

A new dependent variable combining temperature and mass concentration can be formulated in this specific problem. In a turbulent flow situation, the Reynolds analogy

between turbulent heat and momentum transfer can be readily extended to turbulent mass transfer. Thus Lewis number unity assumption is more valid[7]. The values of the thermal diffusivity and the mass diffusion coefficient in turbulent flows are the same and both the energy and vapor mass concentration equations are homogeneous. Thus one can conclude that if the boundary conditions of energy and mass concentration equation fall in the same class(e.g. Dirichlet or flux boundary condition), the distributions of the solution regardless of their absolute value should be the same. We will assume that the interface conditions for the energy and mass concentration equations have the same form but it will be verified later in this paper.

$$\begin{aligned} \theta_2 &\equiv \beta(T_2 - T_\infty) + \beta^*(W_2 - W_\infty) \\ &= \beta'(T_2 - T_\infty) \end{aligned} \tag{15}$$

Interface conditions

Interface conditions are the mathematical descriptions of physics at the air-water interface. In this problem, the physical quantities which appear in the interface conditions are u_I, τ_I, T_I, q_I, m_I, and W_I. Among the six quantities, only two are independent. If u_I is fixed, τ_I is automatically determined and vice versa. And if the interface temperature, T_I, is known, the quantities, q_I, m_I, and W_I are determined thermodynamically. For the gas-liquid flow interface problem, the effect of the interface shear stress is generally assumed to be negligible[4]. Thus in this problem, there remains only one independent quantity, T_I.

Duct flow

PCCS geometry is a natural convection flow duct. The bulk temperature of mixed air increases as it moves upward so that the buoyancy forces are different according to the elevations. But in duct flow situation, the mass flow rate at all elevations should be the same except for the negligibly small addition of water vapor. Thus with the buoyancy effect, the chimney effect, which is very similar to the forced convection phenomena, is expected. Thus duct height can be divided by the prevailing mechanisms; chimney effect dominant region and natural convection effect dominant region. As the chimney effect dominant height can be a scale, the minimum requirement for the experimental facility height can be formulated by comparing the forced and natural convection boundary layer expressions. The boundary layer expressions of natural convection and forced convection is formulated as:

$$(\delta_T)_{NC} \sim L_3 \, Ra_{L_3}^{-\frac{1}{4}} \, Pr^{-\frac{1}{4}} \quad , \tag{16}$$

$$(\delta_T)_{FC} \sim L_3 \, Re_{L_3}^{-\frac{1}{2}} \, \mathrm{Pr}^{-\frac{1}{2}} \quad . \tag{17}$$

They represent the thermal distances between the heat-exchanging entities. The type of convection mechanism is decided by the smaller of the two distances, since the wall will leak heat to the nearest heat sink. Thus the natural convection dominant criterion is

$$(\delta_T)_{NC} < (\delta_T)_{FC} \quad . \tag{18}$$

From this criterion a length scale is formulated:

$$L_3 \sim \frac{u_{inlet}^2}{g \, \Delta\theta} \tag{19}$$

where $\Delta\theta \equiv \beta\Delta T + \beta^* \Delta W$. Using the reference data, the length of the air entrance region is estimated to be 1 m order.

Table 2. Reference and input data[3].

α = 0.16 cm^2/s	L = 20 m
ν = 0.48 cm^2/s	Δ = 0.3 mm
$\beta \sim 1/T_c$ = 0.003	$\Delta T \sim$ 75 °C
$\beta^* \sim M_{air}/M_{vap} - 1$ = 0.6081	$\Delta W \sim$ 0.5353
g = 9.8 m/s^2	$u_{inlet} \sim$ 2 m/s
D ~ 3×10^{-5} m^2/s	T_∞ = 15 °C
	T_W: 60~90 °C

This means that the prevailing heat transfer mechanism in the air inlet and in the rest of the duct are different. Thus the test facility height should be high enough to prevent the entrance effects.

Asymptotic Region

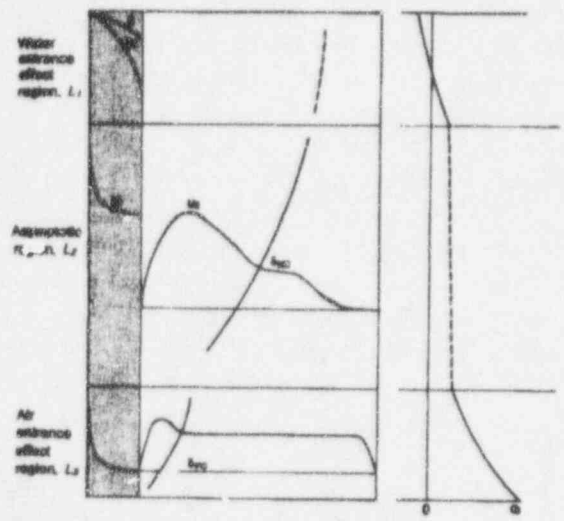

Figure 4. Phenomenological separation of the calculation domain.

In view of the large height to thickness ratio of the water film, the asymptotic region is expected. The film thickness is very thin compared to its height. It means that the velocity and temperature profiles of water film will be quickly fully developed. Also due to the duct flow situation of air flow, there must be two length scales in the water flow direction. This situation is presented in Figure 4. The length scale of the water entrance effect region can be calculated by the fully developing distance i.e. the distance that the evolving boundary layer of the water flow approaches the film thickness.

$$L_1 \sim \frac{u_{max}\,\Delta^2}{\alpha_1} \sim \frac{g\,\Delta^4}{2\,\alpha_1 \nu_1} \qquad (20)$$

This length scale is estimated to be less than 1 m. Hence from the two length scales, one can conclude that the length of the asymptotic region is estimated to be over 90 % of the whole domain.

Vapor Momentum

It is well known that the momentum contribution in the mixed air flow due to water vaporization can be neglected in view of the mass transfer analogy. Thus the blowing velocity at the interface was not considered in the analysis.

FLOW EVOLUTION CHARACTERISTICS

In the derivation of the similarity, interface temperature condition is a key parameter but it is also an unknown in this problem. Nevertheless one can expect that the interface temperatures are determined by the physical characteristics of each flow and also have a trend along the flow direction. Hence in this analysis, we assumed the interface temperature trend along the flow direction and then derived physically relevant interface temperature condition based upon each flow characteristics.

Water film flow evolution characteristics

The momentum equation for the water film is an ordinary differential equation and the boundary condition on heated wall is known and the interface condition can be assumed to be a free shear stress condition due to the previous reasoning on liquid-gas interface. Thus the solution is

$$u_1(y_1) = -\frac{g}{2\nu_1} y_1^2 + \frac{g\Delta}{\nu_1} y_1 \ . \tag{21}$$

Since the maximum-minimum principle is valid in the heat equation[8], the analytic solution of the heat equation using the maximum velocity is possible with the unknown interface condition. The assumed interface temperature condition can be written as;

$$T_I(x_2) \sim x_2^{\,n} \ . \tag{22}$$

Thus the analytic solution for the heat equation is

$$\begin{aligned} \overline{T_1} = \ & 1 - \overline{y_1} + P\,\overline{y_1}\,(L_2 - x_1)^n \\ & + P \sum_{j=1}^{\infty} \left(\int_0^{x_1} \exp(x\pi^2 j^2 (x_1 - \lambda)) \frac{2n}{j\pi} \cos j\pi\,(L_2 - x_1)^{n-1} d\lambda \right) \sin j\pi\,\overline{y_1} \ , \end{aligned} \tag{23}$$

where

$$\overline{T_1} \equiv \frac{T_1 - T_\alpha}{T_w - T_\infty} \ , \quad \overline{y_1} \equiv \frac{y_1}{\Delta} \ . \tag{24}$$

Buoyant air flow evolution characteristics

Using the new dependent variable, the governing equations for the buoyant air flow are transformed as follows;

$$\frac{\partial u_2}{\partial x_2} + \frac{\partial v_2}{\partial y_2} = 0 \ , \tag{25}$$

$$u_2 \frac{\partial u_2}{\partial x_2} + v_2 \frac{\partial u_2}{\partial y_2} = \nu_{2,e} \frac{\partial^2 u_2}{\partial y_2^2} + g\theta_2 \ , \tag{26}$$

$$u_2 \frac{\partial \theta_2}{\partial x_2} + v_2 \frac{\partial \theta_2}{\partial y_2} = p_{2,e} \frac{\partial^2 \theta_2}{\partial y_2^2} \ , \tag{27}$$

where $p_{2,e} = \alpha_{2,e} = D_{2,e}$.

The self-preservation analyses are possible. This means that if we change the coordinate systems from x_2-y_2 to x_2-y_2/δ, where δ is the boundary layer thickness, the solutions can be divided by the amplitude function which depends only on x_2 and the profile function which depends only on y_2/δ. Substituting the following equations to the transformed equations, the balance between each quantity reveals.

$$u_2(x_2, y_2) = A(x_2)\, f(\eta) \quad , \tag{28}$$

$$v_2(x_2, y_2) = B(x_2)\, h(\eta) \quad , \tag{29}$$

$$\theta_2(x_2, y_2) = T^*(x_2)\, k(\eta) \quad , \tag{30}$$

$$\text{where} \quad \eta = \frac{y_2}{\delta(x_2)} \quad . \tag{31}$$

The results are

$$\begin{aligned} &\delta \sim x_2{}^{m} \, , \\ &B \sim x_2{}^{-m} \, , \\ &A \sim x_2{}^{1-2m} \, , \\ &T^* \sim x_2{}^{1-4m} \, . \end{aligned} \tag{32}$$

Above results reveal the relationship between all the physical quantities and the assumed interface condition (22).

Interface Temperature Condition

As denoted in Figure 5, the analytic solution of the energy equation of the water film shows the interface heat flux behavior with respect to x_1 and n:

$$\begin{aligned} q_{I,1} &= \frac{1}{P} \frac{\partial \overline{T_1}}{\partial \overline{y_1}} \bigg|_{\overline{y_1}=1} \\ &= -\frac{1}{P} + (L_2 - x_1)^n + \sum_{j=1}^{\infty} \left(- \int_0^{x_1} \exp[-\pi^2 j^2 (x_1 - \lambda)] \cdot 2n (L_2 - x_1)^{n-1} d\lambda \right) \end{aligned} \tag{33}$$

Meanwhile from the self-preservation analysis of the buoyant air flow, the interface heat flux should be

$$\begin{aligned} q_{I,2} &\sim (L_2 - x_1)^{\frac{5}{4}n - \frac{1}{4}} \\ &= Q(L_2 - x_1)^{\frac{5}{4}n - \frac{1}{4}} \, , \end{aligned} \tag{34}$$

where P, Q are unknown constants, defined at the arbitrary x_1, where the water film temperature is nearly linear.

As in Figure 5, two interface heat flux behaviors are by chance very similar.

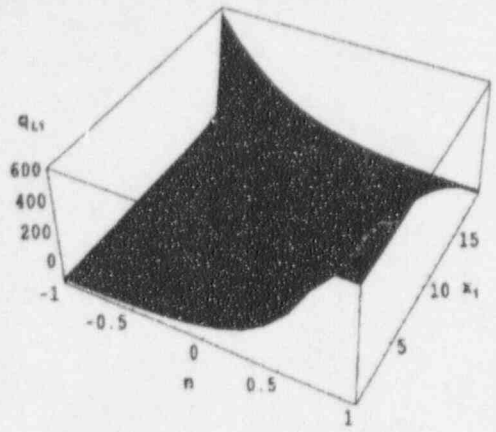

Figure 5(a) Behavior of interface heat flux w.r.t. x_1 and n from the analytic solution of water film

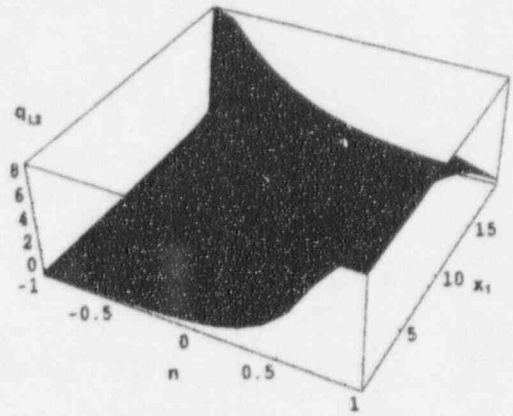

Figure 5(b) Behavior of interface heat flux w.r.t. x_1 and n from the self-preservation of buoyant air flow

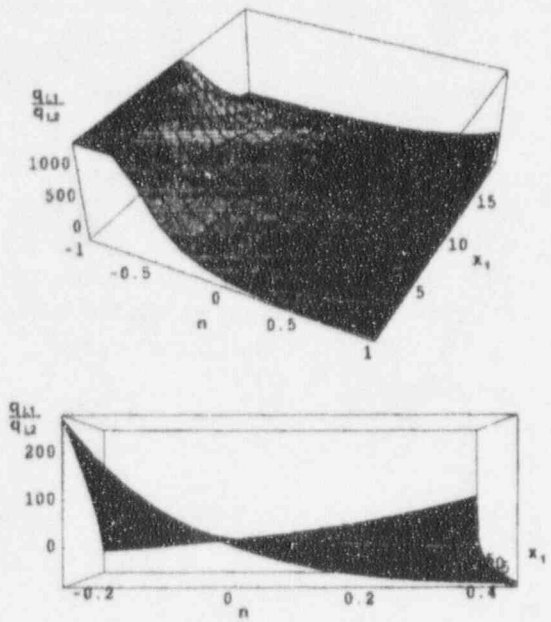

Figure 6. Behavior of interface heat flux ratio w.r.t. x_1 and n.

The above two equations should be simultaneously satisfied at the interface. Equating the two equations at the interface, the interface temperature condition can be estimated.

$$\frac{T_w - T_\infty}{T_w - T_I} - \frac{T_I - T_\infty}{T_w - T_I}\left\{(L_2 - x_1)^n + \sum_{j=1}^{\infty}(\ldots)\right\} \tag{35}$$

$$\theta = (L_2 - x_1)^{\frac{5}{4}n - \frac{1}{4}}$$

where (...) =

$$\int_0^{x_1} \exp(x\pi^2 j^2 (x_1 - \lambda)) 2j (L_2 - x_1)^{n-1} d\lambda$$

Figure 6 shows the interface heat flux ratio with respect to x_1 and n. Regardless of x_1, the interface heat flux ratio should be unity in order to simultaneously satisfy both water and air flow characteristics. From Figure 6, one can conclude n should be 0 i.e. Interface temperature should be constant. Since this condition is satisfied, the above assumption on the new dependent variable, θ, is proved to be reasonable.

SIMILARITY

Based on the above analyses, since the interface temperature is constant in the asymptotic region, the buoyant mixed air flow in the PCCS and the natural convection air flow are governed by the same class of equations and boundary conditions. In other words, the equation (25)~(27) have the same form as the governing equations and boundary conditions for a buoyant air flow system except for using β' and k' instead of β and k.

Therefore the two systems are similar. In the combined heat and mass transfer phenomena interface heat flux are expressed by

$$q_I = -k' \left(\frac{\partial T_2}{\partial y_2} \right)_I \tag{36}$$

where

$$k' \equiv -\left(k_{2,e} + \rho_s D_{2,e} h_{fg} \frac{1}{1 - W_{2,I}} \frac{W_{2,I} - W_{2,\infty}}{T_{2,I} - T_{2,\infty}} \right)$$

And buoyance force term expression is

$$g \theta_2 = g \beta (T_2 - T_\infty) \tag{37}$$

$$\text{where} \quad \beta' \equiv \beta + \beta^* \left(\frac{W_2 - W_\infty}{T_2 - T_\infty} \right)_I$$

If the parameters are properly absorbed in the transformation procedure, both systems are governed by one set of equations. It means that the solution for each system is identical in form. Thus one can conclude that if β′ and k′ are used in place of β and k in buoyant air flow solution and/or correlation, the interface heat flux for the mixed buoyant air should be estimated.

VERIFICATION

Using these newly defined variable and coefficients, the interfacial heat fluxes and the ratios of latent heat transfer to sensible heat transfer are computed using McAdams correlation, which is one of the adopted correlation in WH-GOTHIC[9]. It is well known that the heat trarsfer from the water film is governed by the gradient of the air flow temperature profile and the adiabatic wall mainly affects the tail part of the temperature profile. In this sense, it is a proper natural convection heat transfer correlation in this Ra number range.

Substituting the equivalent conductivity and equivalent buoyant coefficient to McAdams correlation,

$$Nu = 0.13 (Gr \cdot Pr)^{1/3} \tag{38}$$

or

$$h = k' \times 0.13 \left(\frac{g \beta' \Delta T}{\alpha \nu} \right)^{1/3} . \tag{39}$$

The interface heat flux expressions from water and air are:

$$q_1 = -k_1 \frac{T_w - T_I}{\Delta} ,$$

$$q_2 = h(T_I)(T_I - T_\infty) . \tag{40}$$

Equating the above equations, the interface temperature and heat flux are calculated. Also the ratio of latent and sensible heat transfer can be calculated by

$$\frac{q_{latent}}{q_{sible}} = \frac{\left(\frac{\rho_s D_{2,e} h_{fg}}{1 - W_{2,I}} \frac{W_{2,I} - W_{2,\infty}}{T_{2,I} - T_{2,\infty}} \right)}{k_{2,e}} \tag{41}$$

To verify the accuracy of the modified correlation, the results of this study are to be compared with other studies. But in view of the Rayleigh number expression, the containment height is the only parameter that affects Rayleigh number in third power. The Rayleigh number in this system is larger than 10^{13}. To achieve the similar turbulence intensity and to overcome the entrance effect of water film and air, the experimental facility height scale should be the same scale, order of 10 m. No other method, say increasing ΔT, will be sufficient in achieving similar Rayleigh number. Also the questions on whether the thin water film covers the whole containment outer vessel and how to prevent the non-wetting area, are not clearly solved yet.

Due to the present lack of relevant experimental data, the results of this study should be compared with the results of numerical analyses. The results of the numerical study in reference 3 and the data provided by the personal contact with author, Mr. Kang were used in comparison. The study in reference 3 adopted the same governing equations and boundary conditions and were performed for the same configuration. But in this verification only constant wall temperature condition and 0.06 kg/m·s film flow rate condition were considered. As denoted in Table 3, the results are well within the range of 15 % difference.

Table 3. Comparisons of the results from scale analysis and numerical method.

(a) Interface heat flux(W/m^2)

Tw(°C)	Scale analysis	Numerical method	Relative error(%)
70	3781	4442	-14.9
80	6902	6573	5.0
90	12730	11753	8.3

(b) Ratio of latent to sensible heat transfer

Tw(°C)	Scale analysis	Numerical method	Relative error(%)
60	6.8	7.2	5.4
70	9.3	9.7	4.2
80	12.9	12.6	2.2
90	18.5	18.1	2.2

CONCLUSION

The similarity between the PCCS phenomena, which contain the sensible and latent heat transfer, and the buoyant air flow on a vertical heated plate was derived. This means that if we know the solution(or correlation) for the buoyant air flow system, we can use the solution(or correlation) also for the PCCS system. In this sense, this interpretation model is very simple to use and to apply in similar situation such as water drop covers the whole vessel without running down.

In the course of the study, three length scales were derived - L_1, L_3, and 10 m - two length scales reflect the air and water entrance effect and one the turbulent intensity. Using the length scales, one can design an experimental facility in his/her purpose.

This study also has some restriction. If the containment wall temperature is so high that the water film dries our running down, and if the water film thickness is so large that the entrance effect becomes too large to provide asymptotic region the similarity might not be established. And also wave effects are not included in this study.

Mathematically the similarity for the constant wall heat flux condition can be shown. But physically, due to the drying-out possibility the result is less feasible. Surely in the containment situation, the constant temperature assumption is more likely than the constant wall heat flux assumption.

Based upon the comparison with another calculation, the results of this study are well within the range of 15 % difference, which is a reasonable for this analysis. For the most probable operating conditions, the errors are near 5 %. This interpretation model is therefore considered to reflect the PCCS phenomena reasonably well.

TABLE OF NOMENCLATURE

b	gap thickness
D	diffusion coefficient
F	nondimensionalized stream funtion
g	gravitational acceleration
h	heat transfer coefficient
h_{fg}	latent heat of evaporation
k	coductivity
L	containment height
L_1	length of film entrance region
L_2	length of the asymptotic region
L_3	length of water entrance region
M	molecular weight
m	mass transfer rate
P, Q	unknown coefficient
p	pressure
q	heat flux
T	temperature
$\overline{T}$	nondimensionalized temperature
u	x velocity component
v	y velocity component
x	longitudinal coordinate
y	transversal coordinate
W	mass fraction of vapor
Ra	Rayleigh number
Re	Reynolds number
Pr	Prandtl number
Nu	Nusselt number
α	thermal diffusivity
β	thermal expansion coefficient
β^*	concentration expansion coefficient
δ	boundary layer thickness
μ	viscosity
ν	kinematic viscosity
η	similarity variable
Δ	water film thickness
τ	shear stress
θ	modified temperature
ρ	density
A(x), B(x), $T^*(x)$	amplitude function for u, v, and θ
$f(\eta)$, $h(\eta)$, $k(\eta)$	profile function for u, v, θ

Subscript

ρ	density
1	water film
2	mixture air
a	air
f	film
I	interface
inlet	inlet
e	effective coefficient
v	vapor
w	wall
x	local value
∞	ambient
FC	forced convection
NC	natural convection

REFERENCES

1. H. J. Brushi, "AP-600 Overview," Westinghouse Nuclear Plant Program (1991)
2. Y. Jaluria, "Natural Convection Heat and Mass Transfer," Pergamon, Oxford (1980)
3. H. Kang, J. Song and U. Lee, "Numerical Analysis of Cooling Characteristics By Water Film in Passive Containment Cooling System," Int. Conf. on New Trends in Nuclear System Thermohydraulics, Pisa, Italy (1994)
4. R. B. Bird, W. E. Stewart and E. N. Lightfoot, "Transport Phenomena," John Wiley & Sons Inc. (1960)
5. H. Chiang and C. Kleinstreuer, "Analysis of Passive Cooling in a Vertical Finite Channel Using a Falling Liquid Film and Buoyancy-Induced Gas-Vapor Flow," Int. J. Heat Mass Transfer, Vol. 34, No. 9, 2339-2349 (1991)
6. A. Koestel, R. G. Gido and J. S. Gilbert, "Film Entrainment and Drop Deposition for Two-Phase Flow," NUREG/CR-1634
7. William M. Kays and Michaele E. Crawford, "Convective Heat and Mass Transfer 2nd edition," McGraw-Hill Book Company (1980)
8. P. Duchateau and D. W. Zachmann, "Theory and Problems of Partial Differential Equations," Schaum's Outline Series in Mathematics, McGraw-Hill Book Company (1986)
9. M. D. Kennedy, J. Woodcock, R. F. Wright, and J. A. Gresham, "Westinghouse-GOTHIC Comparisons with 1/10 Passive Containment cooling Tests," Int. Conf. on New Trends in Nuclear System Thermohydraulics, Pisa, Italy (1994)

Detailed Thermal-Hydraulic Computation into a Containment Building

A. CARUSO, I. FLOUR, O. SIMONIN

EDF/LNH
6, quai Watier BP 49
F-78401 Chatou Cedex 01 - France

C. CHERBONNEL

EDF/SEPTEN
12-14, avenue Dutriévoz
F- 69628 Villeurbanne - France

ABSTRACT

This paper deals with numerical predictions of the influence of water sprays upon stratifications into a containment building using a two-dimensional two-phase flow code. Basic equations and closure assumptions are briefly presented. A test case in a situation involving spray evaporation is first detailed to illustrate the validation step. Then results are presented for a compressible recirculating flow into a containment building with condensation phenomena.

INTRODUCTION

The subject of this work is the numerical prediction of compressible recirculating two-phase flow into a PWR containment building when a primary loss-of-coolant has occured. Such an accident can degenerate into a severe one with an exagerate production of steam and noncondensable gases such as CO, CO_2 and particulary H_2 as well as high temperatures and pressures. To limit them, heat exchangers, which are being studied, can be used. However, the flow which is generated can produce a thermal stratified zone at the top of the building (due for example to a bad efficiency of the exchangers) and damage the structures. To remove such stratified zones and homogenize the atmosphere, cold water is sprayed from the top of the building, therefore creating a two-phase recirculating flow. The aim is then to simulate the behaviour of such flows using numerical codes.

Basically, two approaches can be used to model turbulent two-phase flows loaded with small inclusions : Lagrangian and Eulerian. In the Lagrangian formulation a large number of particles trajectories are calculated using a previously computed fluid flow field, and several iterations can be necessary to get a solution which accounts for the mutual interaction of the two phases (see, for example, Sommerfeld /6/). In the Eulerian approach, or two-fluid model approach, separate governing equations are written (and solved) for the mean characteristics of both phases, coupled through the interphase transfer terms. In practice, even in the Eulerian formulation, the closure assumptions, which have been used and validated, are based on the Lagrangian analysis of the single particle behaviour. However for many industrial situations, the dispersed phase loading is quite large and the interaction phenomena between phases take prominent part. In this kind of flows, the Eulerian approach which leads to an implicit coupling between phases may become inevitable.

Consequently, a two-dimensional numerical code Mélodif /1,2/ and, more recently, a three-dimensional one ESTET-ASTRID (3D) /3/ have been developed and validated for several years at the "Laboratoire National d'Hydraulique" for the predictions of fluids-inclusions (bubbles, droplets or particles) turbulent recirculating flow. Thus, separate Eulerian conservation equations are formulated for both phases including interphase transfer terms (mass, momentum and enthalpy). Turbulence fields in the continuous phase are predicted by means of a q^2-ε eddy viscosity model with additionnal terms which account for the interaction between the two phases. Modelling of the dispersed phase turbulence is achieved by an extension of results obtained in the framework of the Tchen's theory for dispersion of discrete particles transported by homogeneous turbulent fluid flows. The object of this paper is to briefly describe the main features of the models (which are in great details described in /1,2,3/) and to present and discuss their application to problems of gas stratification in the containment building.

1. SET OF EQUATIONS

The governing equations for turbulent reactive two-phase flow have been derived directly from the local instant conservation in single-phase flow by density-weighted averaging with in addition local balances of mass, momentum and energy at the interface :

$$\frac{\partial}{\partial t}\alpha_k \rho_k + \frac{\partial}{\partial x_i}\alpha_k \rho_k U_{k,i} = \Gamma_k \qquad (1)$$

where, $U_{k,i}$ is respectively the mean velocity for the continuous (k=1) and dispersed (k=2) phases, α_k the volumetric fraction, ρ_k the mean density and Γ_k the rate of interfacial mass transfer between phases,

$$\alpha_k \rho_k \frac{\partial}{\partial t} U_{k,i} + \alpha_k \rho_k U_{k,j} \frac{\partial}{\partial x_j} U_{k,i} = -\alpha_k \frac{\partial}{\partial x_i} P_I + \alpha_k \rho_k g_i$$
$$- \frac{\partial}{\partial x_j}\alpha_k \rho_k < u''_{k,i} u''_{k,j} >_k + I_{k,i} - U_{k,i}\Gamma_k \qquad (2)$$

where P_I is the mean pressure of the gaseous phase, $I_{k,i}$ the part of the interfacial momentum transfer between phases after substraction of the mean gas pressure contribution, $u''_{k,i}$ the fluctuating part of the local instantaneous velocity, $< . >_k$ the averaging operator associated to phase k, with

$$U_{k,i} = < u_i >_k \qquad < u''_{k,i} >_k = 0 \qquad (3)$$

and

$$\alpha_k \rho_k C_{p,k} \frac{\partial}{\partial t} T_k + \alpha_k \rho_k C_{p,k} U_{k,j} \frac{\partial}{\partial x_j} T_k =$$
$$- \frac{\partial}{\partial x_j}\alpha_k \rho_k C_{p,k} < \theta''_k u''_{k,j} >_k + \Pi_k - H_k \Gamma_k \qquad (4)$$

where T_k is the mean temperature of phase k, $C_{p,k}$ the specific heat of phase k and θ''_k the corresponding fluctuations, Π_k the rate of interfacial energy transfer between phases.

Γ_k , $I_{k,i}$ and Π_k satisfy :

$$\sum_{k=1}^{2} \Gamma_k = 0 \qquad \sum_{k=1}^{2} I_{k,i} = 0 \qquad \sum_{k=1}^{2} \Pi_k = 0 \qquad (5)$$

2. MODELLING OF INTERFACIAL TRANSFER

2-1 Interfacial mass transfer

The rate of interfacial mass transfer between phases is formally derived from the local analysis of the quasi-steady-state evaporation of a lonely spherical droplet, by averaging on the dispersed phase, neglecting the turbulent fluctuations of the gas properties viewed by the droplets :

$$\Gamma_1 = -\Gamma_2 = \alpha_2 \rho_1 \frac{6}{\bar{d}^2} D_v Sh_v Log\left[\frac{1 - X_v}{1 - X_{v\,sat}}\right] \qquad (6)$$

where X_v is the mean mass fraction of vapour in the gaseous mixture, $X_{v\,sat}$ the value at saturation obtained from Clausius-Clapeyron expression in terms of the mean characteristics of the droplets, D_V the molecular diffusivity of the vapor in the surrounding gaseous mixture and Sh_V the Sherwood number, given in terms of the mean droplet Reynolds number Re and Schmidt number Sc :

$$Sh_v = 2. + 0.55\, Re^{1/2}\, Sc^{1/3} \qquad Re = \frac{\rho_1 < \left| \vec{v}_r \right| > \bar{d}}{\mu_1} \qquad Sc = \frac{\mu_1}{\rho_1 D_v} \tag{7}$$

2-2 Interfacial momentum transfer

The analysis of local balance of forces acting on an isolated droplet subject to evaporation process leads to the following average expression :

$$I_{k,i} = U_{\sigma,i}\, \Gamma_k + \Gamma'_{k,i} \tag{8}$$

The first term on the right hand side of the equality characterizes the momentum transported by the mass flux exchanged between phases, the corresponding velocity $U_{\sigma,i}$ is equalled to the mean dispersed velocity $U_{2,i}$. The second term represents the phase interaction force induced by the local perturbation of the fluid flow due to the droplets influence /2/. For large density ratio, it reduces to the drag force contribution written in terms of the particle relaxation time :

$$\Gamma'_{1,i} = -\Gamma'_{2,i} = \alpha_2\, \rho_2\, V_{r,i} / \tau^F_{12} \tag{9}$$

$$1 / \tau^F_{12} = \frac{\rho_1}{\rho_2}\, \frac{3}{4}\, \frac{C_D}{\bar{d}} < \left| \vec{v}_r \right| > \qquad C_D = \frac{24}{Re} \left[1 + 0.15\, Re^{0.687} \right] \tag{10}$$

$V_{r,i}$, the averaged value of the local relative velocity between each particle and the surrounding fluid, can be expressed in terms of the total difference between the mean velocities and a drifting velocity $V_{d,i}$ which accounts for the transport of droplets by large scale turbulent fluid motion.

According to theoretical results in homogeneous turbulent flows, $V_{d,i}$ is written using Boussinesq hypothesis with a dispersion coefficient given in terms of q_{12} , the covariance between the velocity fluctuations of each phase and an eddy-particle interaction time /1/ :

$$V_{d,i} = -D^t_{12} \left[\frac{1}{\alpha_2} \frac{\partial \alpha_2}{\partial x_i} - \frac{1}{\alpha_1} \frac{\partial \alpha_1}{\partial x_i} \right] \tag{11}$$

$$D^t_{12} = \frac{1}{3}\, q_{12}\, \tau^t_{12} \qquad q_{12} = < u''_{1,i}\, u''_{2,i} >_2 \tag{12}$$

2-3 Interfacial enthalpy transfer

The rate of interfacial enthalpy transfer can be obtained from the local analysis in the general form :

$$\Pi_k = H_\sigma\, \Gamma_k + \Pi'_k \tag{13}$$

The first term on the right hand side of the equality characterizes the enthalpy transported by the mass flux exchanged between phases and accounts for the heat of evaporation, the corresponding enthalpy H_σ is equalled to the vapour enthalpy at the temperature of the droplets. The second term represents the phase interaction term induced by the local perturbation of the fluid flow due to the droplets influence, and can be written in terms of the difference between the mean temperatures :

$$\Pi'_1 = -\Pi'_2 = \alpha_2 \rho_2 C_{p,2} \left[T_2 - T_1 \right] / \tau^T_{12} \tag{14}$$

$$1 / \tau^T_{12} = \frac{\lambda_1}{\rho_2 C_{p,2}} \frac{6}{\bar{d}^2} \, Nu \tag{15}$$

where Nu is the mean Nusselt number given by :

$$Nu = 2. + 0.55 \, Re^{1/2} \, Pr^{1/3} \qquad Pr = \frac{\mu_1}{\lambda_1} C_{p,1} \tag{16}$$

2-4 Additional equations

The closure of the equations set is completed by the computation of further equations :

- a state equation for the gaseous mixture and correlations for thermodynamic properties,
- a balance equation for the mass fraction of vapour in the gaseous phase X_v :

$$\alpha_1 \rho_1 \frac{\partial}{\partial t} X_v + \alpha_1 \rho_1 U_{1,i} \frac{\partial}{\partial x_i} X_v = \frac{\partial}{\partial x_i} \alpha_1 \rho_1 K^t_1 \frac{\partial}{\partial x_i} X_v + \left[1 - X_v \right] \Gamma_1 \tag{17}$$

- a balance equation for the number of droplets per unit of mass of the dispersed phase X_d :

$$\alpha_2 \rho_2 \frac{\partial}{\partial t} X_d + \alpha_2 \rho_2 U_{2,i} \frac{\partial}{\partial x_i} X_d = \frac{\partial}{\partial x_i} \alpha_2 \rho_2 K^t_2 \frac{\partial}{\partial x_j} X_d - X_d \Gamma_2 + \Gamma_d \tag{18}$$

where Γ_d , the rate of change in the number density due to breakup and agglomeration, is assumed to be negligible. N_d, the number of droplets per unit volume of the two-phase mixture can be written in terms of the variable X_d and leads to a local expression for the mean diameter :

$$N_d = \alpha_2 \rho_2 X_d \qquad \pi \bar{d}^3 / 6 = 1 / \left[\rho_2 X_d \right] \tag{19}$$

3 TURBULENCE MODEL

All the correlations are computed with the help of the eddy viscosity concept :

$$\rho_k < u''_{k,i} u''_{k,j} >_k = -\rho_k \nu^t_k \left[\frac{\partial U_{k,i}}{\partial x_j} + \frac{\partial U_{k,j}}{\partial x_i} \right] + \frac{2}{3} \delta_{ij} \left[\rho_k q^2_k + \rho_k \nu^t_k \frac{\partial U_{k,m}}{\partial x_m} \right] \tag{20}$$

$$\rho_k < u''_{k,i}\,\theta''_k >_k = -\rho_k K_k^t \frac{\partial T_k}{\partial x_i} \qquad (21)$$

ν_k^t and K_k^t are computed for each phase. q_k^2 is the turbulent kinetic energy of phase k :

$$q_k^2 = \frac{1}{2} < u''_{k,i}\,u''_{k,i} >_k \qquad (22)$$

3.1 Continuous phase turbulence

The continuous phase turbulence is computed by means of a q^2-ε eddy viscosity model /8, 9/ with additional terms which account for the interaction between the two phases for the turbulent kinetic energy and its dissipation rate, respectively /2, 7/ :

$$\Pi_{q_1} = \alpha_2 \rho_2 \frac{1}{\tau_{12}^F}\left[q_{12} - 2\,q_1^2 + V_{d,i}\,V_{r,i} \right] \qquad \Pi_{\varepsilon_1} = C_{\varepsilon,3} \frac{\varepsilon_1}{q_1^2} \Pi_{q_1} \qquad (23)$$

3.2 Dispersed phase turbulence

Turbulent predictions of the dispersed phase are achieved by an extension of results for the Tchen's theory of dispersion of discrete particles by homogeneous and steady turbulent fluid motion /2, 4/. They can be computed from the continuous phase ones :

$$q_2^2 = q_1^2 \left[\frac{\eta_r}{1+\eta_r} \right] \qquad q_{12} = 2\,q_1^2 \left[\frac{\eta_r}{1+\eta_r} \right] \qquad \eta_r = \frac{\tau_{12}^t}{\tau_{12}^F} \qquad (24)$$

The time scale of the fluid turbulence viewed by the particles, or eddy-particle interaction time, relates to the fluid Lagrangian correlation function computed along particle paths and is mainly affected by the mean particle relative motion :

$$\tau_{12}^t = \tau_1^t \left[1 + C_\beta\,\xi_r^2 \right]^{-\frac{1}{2}} \qquad (25)$$

the characteristic time of the eddy-particle interaction with the fluid Lagrangian turbulent time scale defined by :

$$\tau_1^t = \frac{3}{2} C_\mu \frac{q_1^2}{\varepsilon_1} \qquad \xi_r = \left| \overrightarrow{V_r} \right| \Big/ \sqrt{\frac{2}{3} q_1^2} \qquad (26)$$

Finally

$$\nu_2^t = \tau_{12}^t \frac{1}{3} q_{12} + \frac{1}{2} \tau_{12}^F \frac{2}{3} q_2^2 \qquad K_2^t = D_{12}^t + \tau_{12}^F \frac{2}{3} q_2^2 \qquad (27)$$

Extensive details of the models can be found in /2, 4/.

4. NUMERICAL METHOD

The numerical method is based on finite differences/volumes discretization and an incremental version of the original fractionnal step method /5/ :

- an advection step solved by the method of characteristics with high order of interpolation to minimize numerical diffusion
- a diffusion step which take into account all the contribution explicitely (pressure, source terms,...)

These two steps are solved separately on each phase :

- a pressure step, which take into account the mass conservation of the two-phase mixture by solving a quasi-elliptic equation for the time increment of mean pressure,
- a strong momentum coupling between phases is achieved by an implicit computation of the time increment of the interphase transfer term.

More details can be found in /1, 3/.

5. VALIDATION : Spray evaporation in turbulent air flow

In order to validate the numerical method, the models and the closure assumptions, computations have been carried out previously for many turbulent two-phase flow configurations and, in particular, the predictions have been compared with detailed experimental results for gas-solid flows (round and plane jets, swirling injection, vertical channel flow, pulverised coal combustion) and bubbly flows (vertical and horizontal pipe flows, sudden expansion) /1, 2, 3/. Another test case more representative of the following practical application is presented here.

The test case is based on experimental data from the LSTM of Erlangen /6/. It consists in a spray evaporation of isopropyl alcohol in a coflowing annular heated air. Figure 1 shows the test case description. The configuration is axisymmetric.

At each inlet, velocities, temperatures, turbulent quantities distributions for the two phases, mass flux and diameter distributions of droplets for the dispersed phase are imposed. At the walls, a wall function approach is used.

The inlet temperature of the droplets are 31°C, while air is injected at 80°C. The mesh is maded up 56x101 nodes.

Various results including velocity and temperature fields as well as radial profiles are presented in figures 2 to 6.

Predictions concerning velocity and mass fluxes are in good agreement with mesurements. The computed mean diameters are not so well predicted apart from the flow stream direction ; this is probably due to the very low value of the volumetric fraction in such zones which leads the results to be very sensitive to exceptional large droplet crossing. As a matter of fact, it is very difficult to account for this effect both in the modelling approach and in the mesurements.

6. APPLICATION: Spray into a containment building

Spraying water is a safety method to decrease temperature and pressure into a containment building and homogenize the atmosphere when an accident like a primary loss-of-coolant has occured. Due for example to a bad efficency of heat exchangers, stratifications may appear. Local accumulation of hydrogen may take place leading to explosion. Furthermore, high temperature gradients can generate severe stresses on structures.

Calculations have been performed to a schematic configuration shown in figure 7. It corresponds to the upper part of a real building. All the equipments such as steam generators, bridge,... are neglected and the geometry is supposed to be axisymmetric. The mesh contains 54x81 nodes.

An initial computation is performed, in order to simulate the influence of heat exchangers to the motion of the atmosphere when an accidental production of steam feeds this volume. The production corresponds to 20 Megawatts residual power at 110 °C and to 7.33 kg/s of steam. The flow consists of air and saturated steam (one phase flow, considered as a mixture of gaseous species). Heat exchangers are numerically simulated by sink mass and energy terms.

As seen in figures 8, the computation predicts a thermal stratification at the top of the building and a laminar zone with very low velocities.

This state is taken as the initial state for a second computation which then simulate the effects of a cold water spray upon this stratification. The spray inlets are shown in figure 7. Its

total rate is 280 kg/s. The mean diameter of water droplets is 100 microns and their temperature is 20°C. Walls are supposed adiabatic.

This computation neglected the enthalpy transported by the mass flux exchanged between phases (first term on the right hand side of equation 13). Future computations will take into account this term.

The total simulation represents 70 real seconds. Steam condenses upon the drops as they fall through gaseous mixture. Contrary to the previous validation test, condensation takes place instead of evaporation. Yet, the model remains the same.

Figure 9 displace a sequence showing the behaviour of the two-phase flow via the temperature and velocity fields of the continuous phase.

The stratification is quickly destroyed and the mixture becomes more and more homogenized. This is due at the beginning to the influence of the momentum transfer from the water spray and then by the gravitational effects generated by the temperature gradients. Even though condensation is not negligeable from a thermal point of view, it does not contribute very much to the destruction of the stratification and the homegenization of the atmosphere.

In order to analyse the flow and see the interaction between the droplets and the gas flow, a computation considering a constant diameter of the droplets (100 microns) has been performed. Figure 10 shows the η_r quantity field (see equation 24). η_r denotes the ration between the time scale of the fluid turbulent motion viewed by the particles (τ^t_{12}) and the characteristic time of particles entrainment by the fluid motion (τ^F_{12}). Except near the lower part inlet, η_r is globally much greater than unity. This means that particles dispersion is quasi controlled by transport due to gas turbulence, that is by $V_{d,i}$, the fluid particle turbulent drift velocity defined by equation 11. So, inertial effects are negligeable.

The ξ_r quantity field (see equation 26) is shown in figure 11. ξ_r directly influence the τ^t_{12} value in regard with τ^t_1, the time scale of the energetic turbulent eddies (equation 25). In the major part of the computational domain, ξ_r is much less than unity, which denotes that particles disperse as a passive scalar, except in the lower part where particles dispersion efficiency is reduced by the trajectories crossing effects due to the settling velocity.

Of course, size particles is not constant. The inlets droplets may have various diameters and may evoluate with condensation. However, another computation with 500 microns diameter for droplets (maximun size which can be obtained at the inlets) remains the same qualitative results.

Finally, the model proposed could be simplified, directly computing the mean dispersed phase velocity $V_{2,i}$ from the mean continuous phase velocity $V_{1,i}$, the mean relative velocity $V_{r,i}$ equal to the settling velocity and the mean fluid particle turbulent drift velocity $V_{G,i}$. Thus a transport-diffusion equation over α_2, the volumetric fraction of particles, is only required. Nevertheless, crossing trajectories effects have to be taken into account.

CONCLUSION

A separated two-phase flow model, developed for predicting fluid-inclusions turbulent recirculation flows, has been detailed. A validation case has been presented, and satisfactory agreement between experimental results and numerical calculations have been observed for mean quantities. The same model has been used to compute the influence of cold water sprays upon a stratified state into a containment building, when heat exchangers are not efficient enough. Such a situation is quickly eliminated and the atmosphere tends to be homogenized in terms of temperature.

Up to now, noncondensable gases such as CO, CO_2 and especially H_2 have not been taken into account in these computations ; the main reason is the inlet boundary condition which is actually not precisely known. Future computations will aim at applying global codes to the lower part of the building in order to obtain realistic inlet rates of such quantities. This would be used as inlet boundary condition to compute the noncondensable fields into the upper volume of the building.

NOMENCLATURE

$C_{p,k}$: specific heat
D_v : molecular diffusivity
H_k : mean k-phase enthalpy
$I_{k,i}$, $\tilde{I}_{k,i}$: Interfacial momentum transfer
k : refer to phase k (k=1 gas, k=2 droplets)
K_k^t : turbulent diffusivity
N_d : number of particles per unit of volume
Nu : Nusselt number
P_1 : gaseous pressure
q_1^2 : turbulent kinetic energy
q_{12} : covariance betwen the velocity fluctuations of the two phases
Pr : Prandtl number
Re : Reynolds number
Sc : Schmidt number
Sh_v : Sherwood number
t : time
T_k : mean k-phase temperature
u''_i : fluctuating part of the instantaneous velocity
$U_{k,i}$: mean k-phase velocity
$V_{d,i}$: fluid-particle turbulent drift velocity
$V_{r,i}$: mean relative particle-surrounding fluid velocity
x_i : coordinates
X_d : number of particles per unit of mass
X_v : mean vapour mass fraction
$X_{v\,sat}$: mean mass fraction at saturation
α_k : k-phase volumetric fraction
Γ_k : rate of interfacial mass transfer
Γ_d : rate of change in the number density
ε_1 : gaseous turbulent dissipation rate
Π_k : rate of interfacial enthalpy transfer
Π_k : interaction energy fluid-droplet
Π_{q1} : source term for turbulent energy
$\Pi_{\varepsilon 1}$: source term for dissipation rate
ρ_k : mean k-phase density
ν_k^t : k-phase turbulent viscosity
θ''_k : fluctuating part of the instantaneous temperature

REFERENCES

[1] O. Simonin and P.L. Viollet : "Prediction of an oxygen droplet pulverization in a compressible subsonic coflowing hydrogen flow", Proc. Int. Symp. on Numerical Methods for Multiphase flows, ASME FED, Vol 91, pp 73-82. 1990

[2] O. Simonin and P.L. Viollet : "Modeling of turbulent two-phase flow jets loaded with discrete particles", in Phase-Interface phenomena in Multiphase flows, G.F Hewitt, F. Mayinger and J.R. Riznic (Editors), Hemisphere Publishing Corp., pp 256-269, 1990

[3] D. Thai Van, J.P. Minier, O. Simonin, P. Freydier and J. Olive, "Multi dimensionnal two-fluid model computation of turbulent two-phase flow", Proc. Int. Symp. on Numerical Methods for Multiphase flows. ASME FED, Vol 185, pp 277-291, 1994

[4] E. Deutsch, O. Simonin : "Large eddy simulation applied to the motion of particles in stationary homogeneous fluid turbulence", in Turbulence Modification in Multiphase flows, ASME FED, Vol 110, pp 35-42, 1991

[5] A.J. Chorin, Numerical solutions of the Navier-Stokes equations, Math. Comp. 22, 745 (1968)

[6] M. Sommerfeld, G. Kohnen, H.H. Qiu : " Spray evaporation in turbulent flow : Numerical calculations and detailed experiments by Phase-Doppler anemometry", Revue de l'Institut Français du pétrole, EDITIONS TECHNIP, Vol 48, n°6, PP 677-695, 1993

[7] S.E. Elgobashi, T.W. Abou-Arab: "A two-equation turbulence model for two-phase flows", Phys. Fluids, Vol 26, n°4, 931-938 (1983)

[8] W. Rodi, "Turbulence models and their application in hydraulics", State-of-the-art paper, presented by the IARH-section on Fundamentals of Dividion II : Experimental and mathematical fluid Dynamics, Delft

[9] P.L. Viollet, "The modelling of turbulent recirculating flows for the purpose of reactor thermal-hydraulic analysis", Nuclear Eng. and Design, Vol 99, 365-377 (1985)

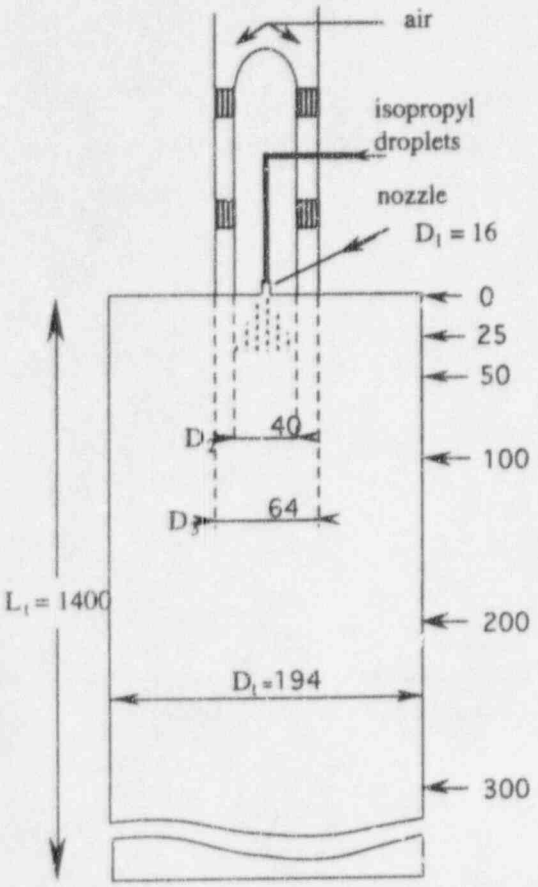

Figure 1 : Schematic configuration of spray evaporation test case (distances in mm)

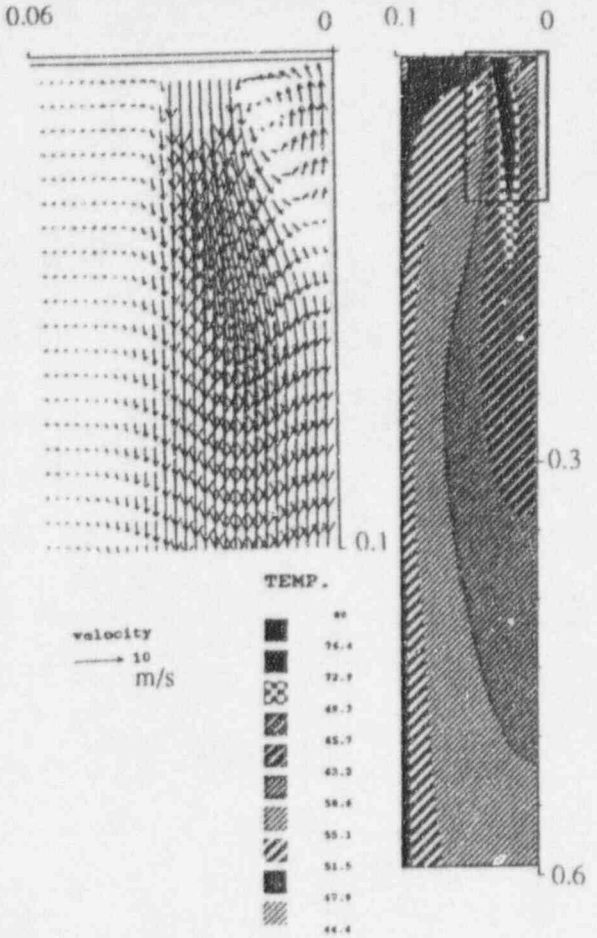

Figure 2 : velocity and temperature fields of the continuous phase near the nozzle

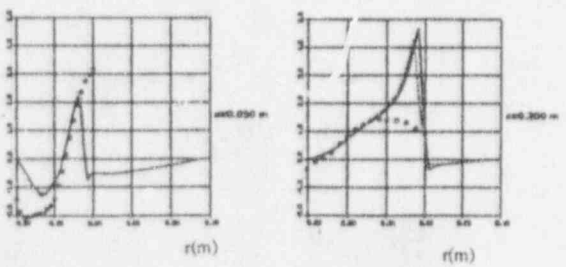

Figure 3 : radial profiles of the mean radial velocity of the dispersed phase at z=0.05 m (a) and z=0.2 m

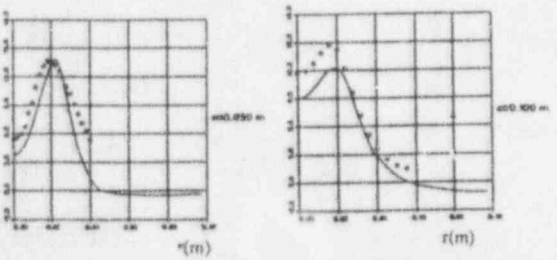

Figure 4 : radial profiles of the mean axial velocity of the dispersed phase at z=0.05 m (a) and z=0.21m

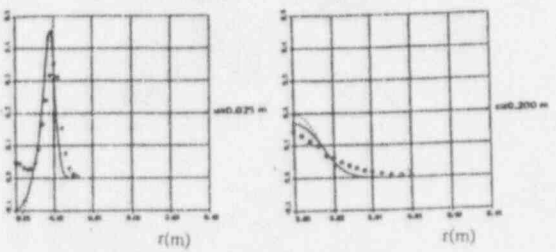

Figure 5 : radial profiles of the mean mass fluxes of the dispersed phase at z=0.025 m (a) and z=0.2 m

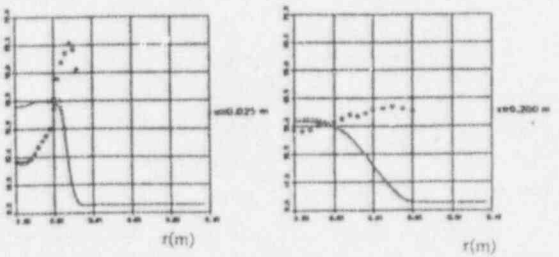

Figure 6 : radial profiles of mean diameter particles at z=0.025 m (a) and z=0.2 m

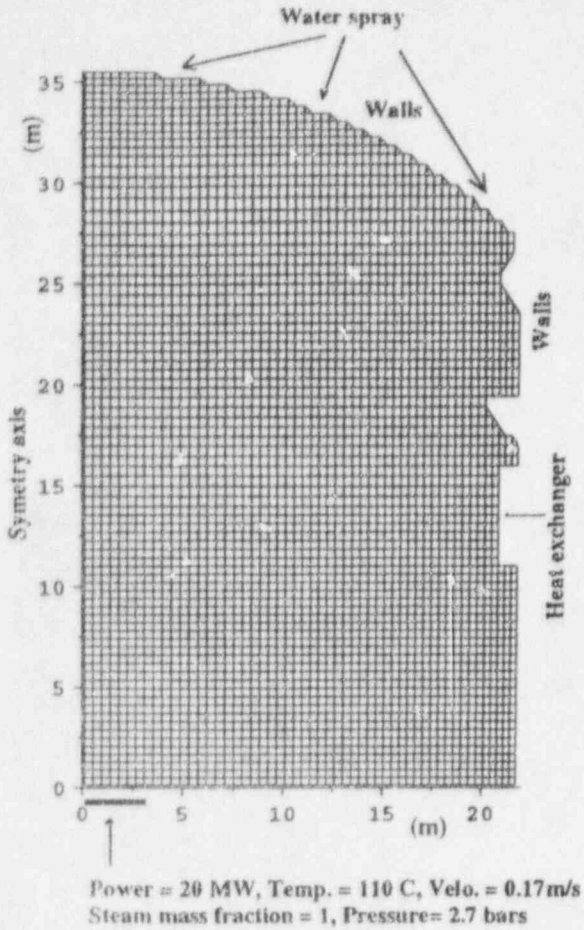

Figure 7 : Containment building configuration

Figure 8 : One-phase flow computation : temperature and velocity fields

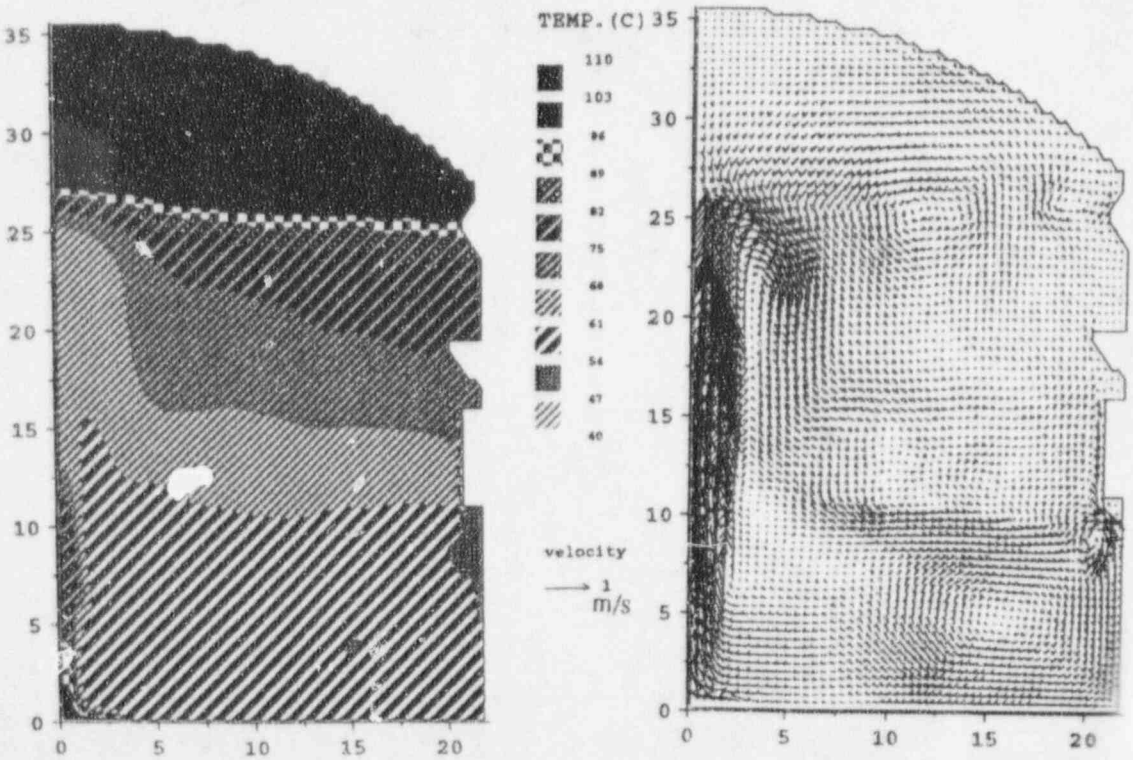

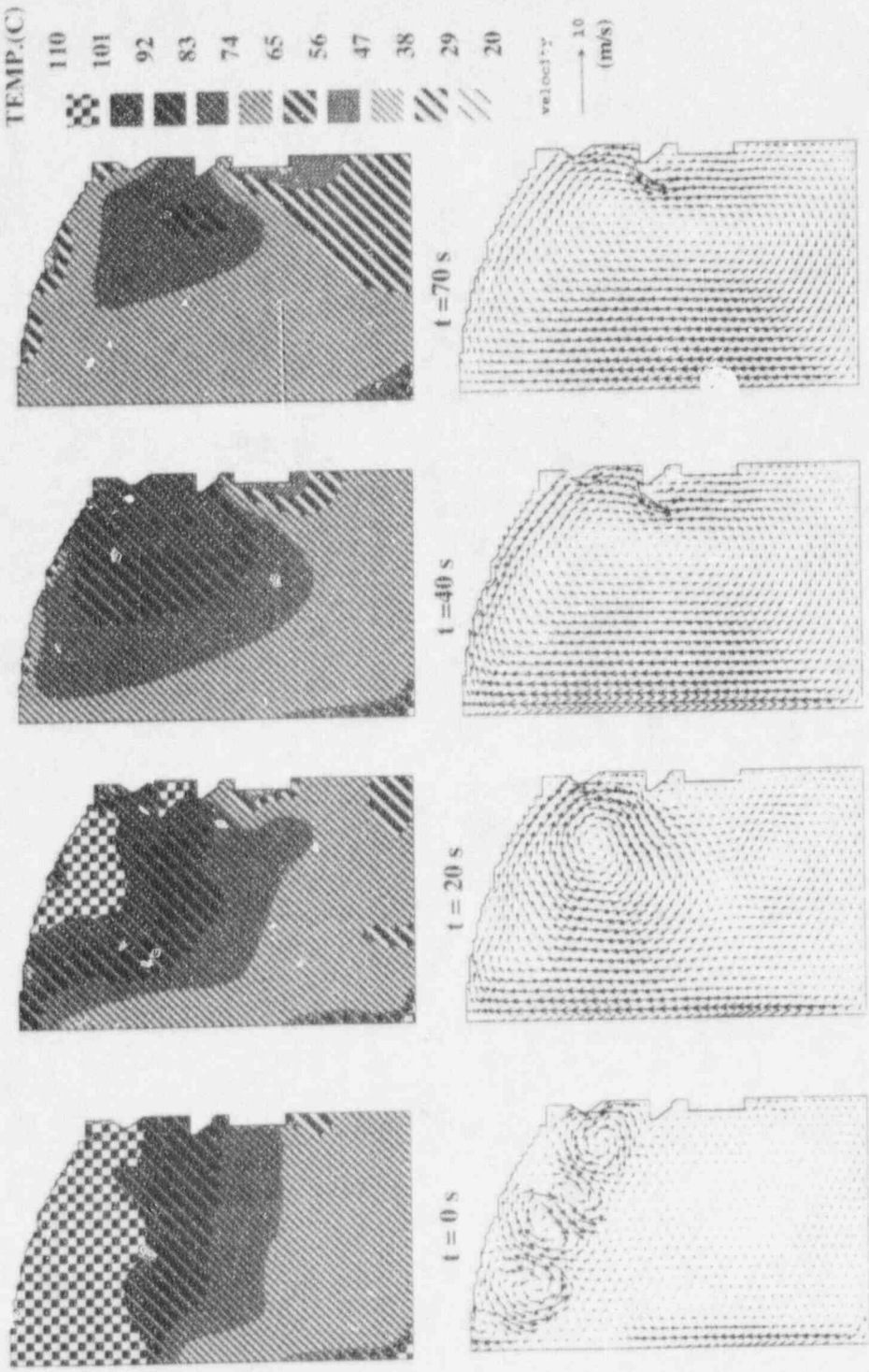

Figure 9 : Two-phase flow computation: temperature and velocity fields of the continuous phase at different times

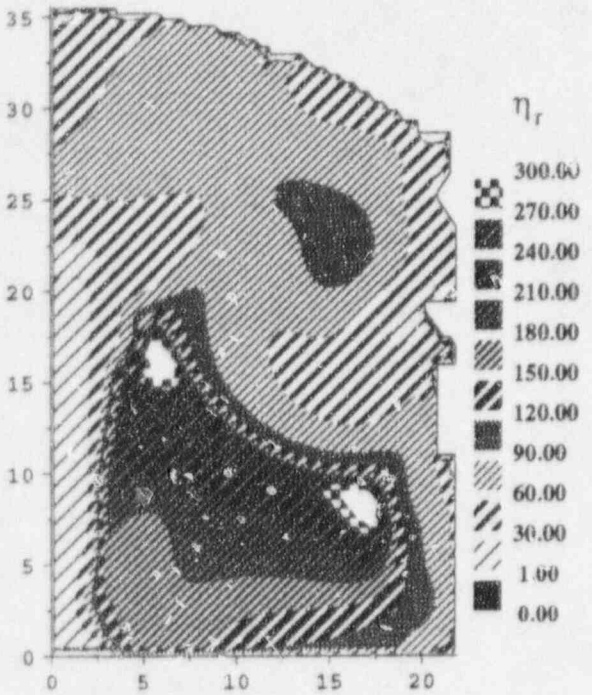

Figure 10 : Two-phase flow computation : $\eta_r = \tau_{12}^t / \tau_{12}^F$ field

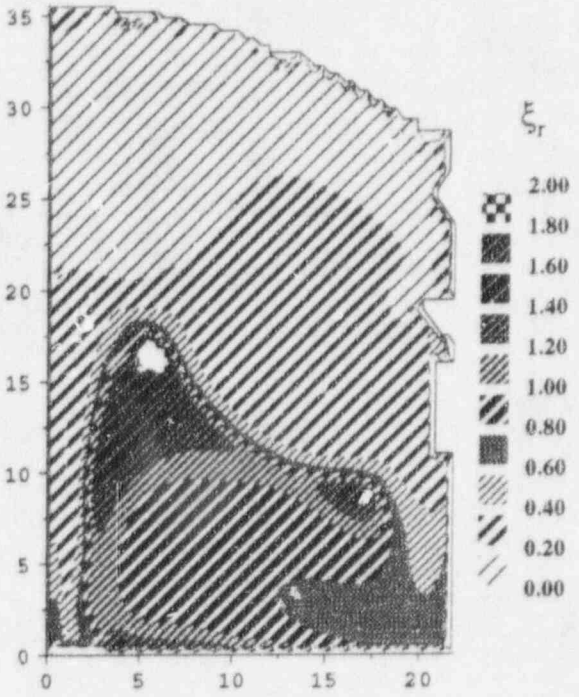

Figure 11 : Two-phase flow computation : ξ_r field

Free Convective Condensation in a Vertical Enclosure

R. J. Fox, P. F. Peterson
Department of Nuclear Engineering
University of California at Berkeley
Berkeley, CA 94720

M.L. Corradini and A.P. Pernsteiner
Nuclear Engineering and Engineering Physics Department
University of Wisconsin
Madison, WI 53706

ABSTRACT

Free convective condensation in a vertical enclosure was studied numerically and the results were compared with experiments. In both the numerical and experimental investigations, mist formation was observed to occur near the cooling wall, with significant droplet concentrations in the bulk. Large recirculation cells near the end of the condensing section were generated as the heavy noncondensing gas collecting near the cooling wall was accelerated downward. Near the top of the enclosure the recirculation cells became weaker and smaller than those below, ultimately disappearing near the top of the condenser. In the experiment the mist density was seen to be highest near the wall and at the bottom of the condensing section, whereas the numerical model predicted a much more uniform distribution.

The model used to describe the formation of mist was based on a Modified Critical Saturation Model (MCSM), which allows mist to be generated once the vapor pressure exceeds a critical value. Equilibrium, nonequilibrium, and MCSM calculations were performed, showing the experimental results to lie somewhere in between the equilibrium and nonequilibrium predictions of the numerical model. A single adjustable constant (indicating the degree to which equilibrium is achieved) is used in the model in order to match the experimental results.

INTRODUCTION

The objective of this work is to model and understand the fundamental phenomena that occur in a two component, two phase reflux condenser. The two components consist of vapor (condensable species) and a gas (noncondensable species). The vapor is further separated into two phases (vapor and liquid) and the liquid phase is treated as a dispersed mist or fog. The system schematic is shown in Fig. 1. The system under consideration consists of a sealed, vertical enclosure containing a fixed amount of noncondensable gas with pure vapor entering from below. Condensation takes place along an isothermal cooling wall, generating a thin liquid film that returns condensate back through the inlet boundary.

Because enclosure condensation with noncondensables can be characterized by strong natural convective forces and the boundary conditions are inherently nonlinear, convergent solutions have remained elusive. Models which make use of stagnant gas approximations and shut-off regions are not valid when the natural convective effects become important. This study is aimed at understanding the unstable, natural convection flows which may occur in such systems and their effect on heat transfer. Various simplifying assumptions are used to develop a model which retains most of the important phenomena while remaining tractable.

Flat plate boundary layer analyses of condensation in the presence of noncondensables have been conducted by many investigators. Some of the works include those by Minkowycz et al. [1], Sparrow et al. [2], Hijikata et al. [3,4], Legay-Desequelles et al. [5], and Jones et al. [6].

Minkowycz and Sparrow [1] considered the natural convective condensation occurring on a vertical flat plate in the presence of noncondensable gases. For steam-air mixtures at low pressures and temperatures and low air concentrations in the bulk, thermal-diffusion, diffusion thermo, and interfacial resistance were found to be second order effects. They found a significant reduction in the overall heat transfer rate compared to the pure vapor Nusselt solution, owing to the accumulation of noncondensable gas near the condensing surface and a corresponding reduction in the vapor pressure (and therefore the saturation temperature) near the interface. They found that superheating became more important when the noncon-

densable gas was present, owing to the decrease in latent heat transfer relative to the sensible heat transfer. In a later paper, Sparrow and Minkowycz [2] considered the heat and mass transfer taking place by forced convective condensation on a horizontal flat plate in the presence of noncondensables by treating separately the liquid film and gaseous boundary layers. In putting aside the examination of variable fluid property effects, their analysis of steam-air mixtures showed the reduction in the heat transfer rate was less sensitive to the presence of a noncondensable gas than the gravity induced flows studied earlier by Sparrow et al. [1].

In the works by Minkowycz and Sparrow [1,2], the vapor was assumed to undergo condensation only at the liquid-vapor interface and the potential for condensation in the bulk gas phase was ignored. In contrast to this assumption, Hijikata et al. [3,4] studied the effect of imposing an equilibrium condition on the condensing vapor (within the bulk gaseous phase) and found that the effect on transport can be important for $Le > 1$ and/or when large temperature differences exist between the bulk flow and the wall. The works by Jones et al. [5] and Legay-Desequelles et al. [6] are similar in nature to those of Hijikata et al. except turbulence in the vapor phase was also considered those works [5,6].

The conditions for supersaturation and subsequent fog formation have been studied in detail by Toor [7] and Brouwers [8,9]. Both works assumed that mist was allowed to form in such a way as to satisfy local equilibrium conditions. Brouwers [8,9] found that mist was more likely to form at low system pressures (owing to increased curvature of the saturation line) and when $Le>1$ (owing to the increased diffusional transport of energy over that of species).

The issue of nonequilibrium bulk phase condensation has been investigated by Rosner [10], Epstein and Rosner [11], Hayashi et al. [12] and Sekulic [13]. These investigators made use of the Critical Supersaturation Model (CSM) in order to study the impact on heat and mass transfer in boundary layer systems. In the CSM mist is allowed to form only when the vapor pressure exceeds some critical value. The work by Epstein and Rosner [11] predicted that mist droplets, once formed in sufficient quantities at some critical supersaturation, rapidly grow to a size for which surface tension effects become unimportant and the mist is then in thermal equilibrium with its surroundings. Sekulic [13] used the CSM to model the condensation inside a boundary layer where the vapor pressure exceeds the saturation pressure up to critical supersaturation but beyond which equilibrium is then assumed, giving rise to a discontinuous jump in the vapor pressure and concentration. Similarly, Hayashi et al. [12] applied the CSM to a turbulent convective field, modifying the supersaturation ratio, S, to account for turbulent fluctuations.

The phenomena related to condensation in enclosures can be quite different from those found in free convective condensation. Dunn and Reay [14] provide an overview of the fundamental and design considerations for closed, stable condensers along with a description of the variable conductance behavior that occurs when noncondensables are present. The simplified flat front model is described in Dunn and Reay [14]. The model assumes that the interface between the active condensing and shutoff regions is perfectly flat and the length of the active region can be calculated by knowing the noncondensable gas inventory and system pressure. Peterson et al. [15] developed analytic and numerical methods for use in the analysis of two-dimensional gas-loaded thermosyphons that do not assume a perfectly flat interface between the condensing and shutoff regions, resulting in a simplified integral formulation for the design of stably stratified condensers. However such stable analyses are not applicable when the natural convective forces become important.

For unstable systems, Peterson et al. [16] conducted experiments using steam-air mixtures in order to study the stability and bifurcation phenomena that occur in systems containing species with different molecular weights. They found that increasing Rayleigh numbers induced a series of bifurcations that ultimately led to large scale chaotic fluctuations. Aiding and retarding convective motion induced by density differences due to differences in molecular weight, were studied by Mori and Hijikata [17]. They found boundary layer separation to occur when the difference in molecular weights between the gas and vapor were large, resulting in significant heat transfer augmentation. Fox et al. [18], using the methods developed here, conducted a study on binary mixtures in a closed thermosyphon. With hexane-pentane mixtures, the more volatile and lighter species (pentane) was found to stratify in the upper portion of the condenser, shutting that region off to condensation. Using hexane-R11 mixtures, the downward flows of the more volatile and heavier species (R11) were found to induce varying degrees of instability (depending on the species loading and power level) that markedly affected the heat and mass transfer. Further work using steam-helium and steam-air mixtures in vertical flux thermosyphon with mixed and forced convective condensation is presented in [19].

Although many of the separate effects of condensation in the presence of noncondensable gases have been studied in detail before, knowledge is lacking in the combined effects that may occur in the natural convective condensation that occurs inside enclosures. The early works in condensation discussed above typically focused on the steady, boundary layer forms of the governing equations that are applicable to the study of flows over flat plates or the flow inside tubes.

Few attempts have been made to study the complex, time dependent flows that occur in condensers loaded with vapor/gas mixtures containing species with different molecular weights. Only the experimental works of Peterson et al. [16] have studied these effects in any detail. In addition the issue of condensation in the bulk gas phase has not been applied to the study of condensation in enclosures when the natural and forced convective effects are of comparable magnitude and when transient effects become important. The work presented here attempts to build on the knowledge gained by previous investigators of more simplified systems by combining most of the relevant physics into a comprehensive model in order to describe the condenser discussed below.

1. EXPERIMENT DESCRIPTION

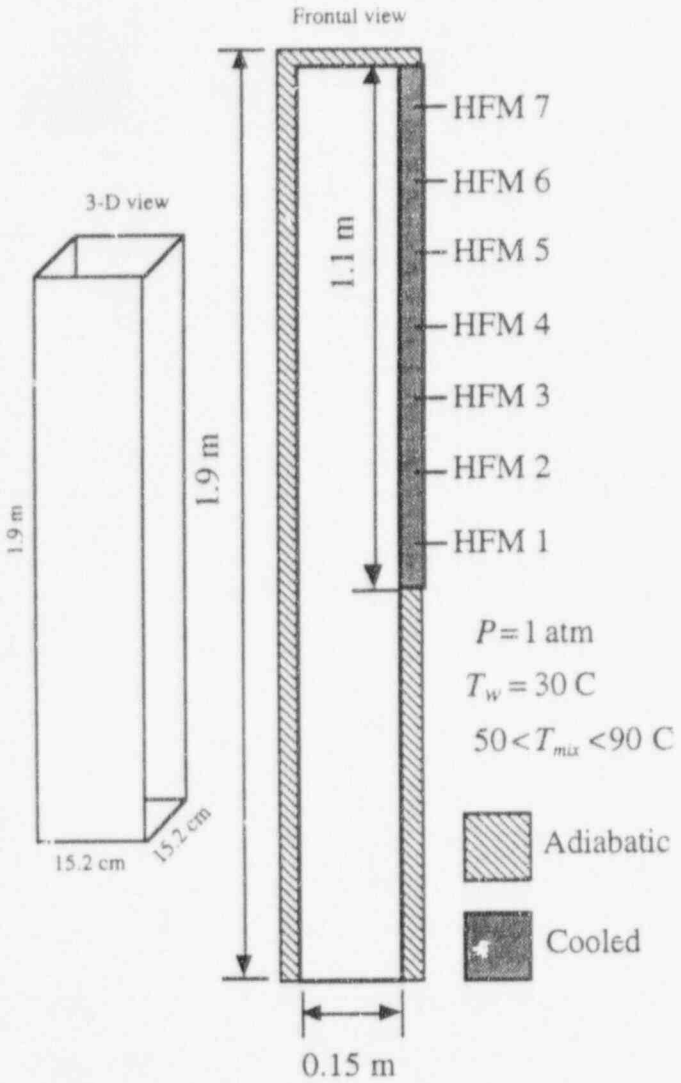

Figure 1 Experimental Apparatus and Model Schematic

The experiments consisted of a vertical condenser loaded with a steam/air mixture operating under total reflux. Steam entered the bottom of a rectangular condenser through a diffuser and underwent condensation on a single aluminum wall. Figure 1 presents a schematic of the experimental system. The dimensions of the condenser were 15 cm wide by 15 cm deep by 190.4 cm tall. The aluminum condensing plate was 106.6 cm high and cooled by seven identical cooling plates mounted on the backside of the condensing wall. Each of the seven plates contained an independent coolant conduit, machined in a spiral pattern to provide uniform cooling. Because the condensing plate was only the last 56% of the total condenser height the first 83.8 cm acted as an entrance length in order to damp fluctuations and non uniformities in the entrance flow. Condensate returned to the evaporator (not shown) through a drain line at the bottom of the condenser before returning again as steam.

The heat energy removed through the cooling plate was measured using two separate techniques: 1) Heat Flux Meters (HFM) and 2) Coolant Energy Balance (CEB). The heat flux meters consisted of an array of four thermocouples embedded in a Teflon strip. The Teflon strips were located in grooves which were machined into the test wall. A linear least squares fit was used to obtain the temperature gradient inside the wall. The coolant energy balance method was accomplished by measuring both the rise in the coolant temperature and the coolant mass flow rate between the inlet and outlet for each cooling plate.

The system was allowed to reach steady state after approximately 15 minutes, with a steam/air mixture at 1 atm. Small leaks in the system allowed air to enter or exit the condenser in order to maintain the system pressure at 1 atm. The average mixture temperature, T_{mix}, was varied between 50 and 90 °C. The cooling plates were held at a nearly constant 30 °C.

Because the system is truly three-dimensional, the use of a two-dimensional model is questionable. However, it was noted in the experiment visualization that the primary flows were substantially two-dimensional, owing to the shear layer generated near the wall which drives the flow in only one direction (down). This is similar to an infinitely deep (into the paper as viewed in Fig. 1) shear driven cavity, ignoring the presence of the front and back walls and their influence on the flow. Of course this is not precisely the case since there is always some three dimensional effects; this may help to understand some of discrepancies between the results of the experiments and the numerical model.

2. MODEL DESCRIPTION

2.1 Simplifying Assumptions

Various simplifying assumptions are used in the modeling of the system under consideration. Some of the assumptions result from physical considerations while others are necessary in order to make the problem more tractable. The primary assumptions used in the formulation are briefly described below.

- The vapor, gas, liquid mixture is assumed to be a continuum, with a dispersed phase of liquid mist droplets existing throughout the flow. The volume fraction of droplets is very low, $\alpha_l = V_l/V < 2.0\times10^{-4}$ (where V_l is the volume occupied by the liquid droplets and V is the mixture volume), and their influence on the flow and transport properties is ignored. Further, the density of the droplets is assumed to be sufficiently low that interaction between the droplets can be ignored. In addition the droplets are assumed to be small enough that their relaxation time is short enough to ignore any slip between the phases. These approximations are consistent with those used by previous investigators of systems with mist formation, Legay-Desesquelles et al. [5], Hijikata et al. [4], Toor [7] and Brouwers [8,9].

- The flow in the vapor, gas, liquid mixture is assumed to be laminar. No attempt is made to include a turbulence model for the higher convective velocities. This approximation may reduce the transport rate in the regions of high recirculation and incipient turbulence.

- For simplicity the density is specified to be spatially constant, except for the source term in the vertical momentum equation (buoyancy). This approximation results in a significant simplification of the governing equations and reduces the computational effort. It should be stressed that the main reason for imposing this idealization is for simplicity. However, some discussion of this idealization is given in [19].

- The initial conditions discussed in Sec. 2.5 are highly idealized. However, they serve as a starting point for the calculation until the quasi steady-state flows are achieved. Issacci et al. [20] have shown that the initial transient involves the formation of acoustic waves which may alter the pressure and velocity field during the initial transient. They found that such initial fluctuations based on sonic behavior can safely be ignored after a few seconds into the quasi-steady transient.

- For simplici[illegible]e transport properties are set constant. In reality such properties as c_p, μ, and k vary with composition and temperature. The variation of such properties is neglected in favor of concentrating on idealized forms of the governing equations.

- The system pressure is assumed low enough that deviations from ideal gas behavior can be safely ignored. This also allows the use of a constant latent heat of vaporization that is independent of pressure. Also, the volume fraction of liquid droplets is very small since the density of liquid is much higher than vapor at low pressures, allowing the gas/vapor/liquid mixture to be treated as a continuum that ignores the fi[illegible]ume of particles.

- T[illegible]sport is specified to occur by convection and ordinary diffusion alone. The energy flux due to species interdiffusion, as described by Bird et al. [21], is neglected (owing to the specification of a constant specific heat $c_p = c_{p,l} = c_{p,v} = c_{p,g}$). The Dufour or diffusion-thermo effect which is usually of minor importance is also neglected. Also mass diffusion as a result of the thermal diffusion or the Soret effect is neglected since the temperature gradients are not extreme. See Minkowycz et al. [1] and Bird et al. [21] for a discussion of these approximations. In general, the primary transport phenomena are governed by the coupling between the continuity, momentum, and species equations. It turns out that these equations are weakly coupled to energy, although temperature effects on the buoyancy term are present (to a lesser extent than composition) and temperature changes due to mist formation may be significant near the wall. Since mass transfer by species condensation and natural convection due to species gradients govern the dominant transport phenomena of interest here, the simplifying assumptions used for the energy equation are likely to be second order effects.

2.2 Governing Equations

From the assumptions given in Sec. 2.1, the general equation for all conserved quantities can be written as:

$$\frac{\partial}{\partial t}(\phi) + \nabla\cdot(\mathbf{u}\phi) = \nabla\cdot\Gamma + S \qquad (1)$$

Table 1 Terms of the Conservation Equation

Equation	ϕ	Γ	S
Continuity	$\overline{\rho}$	0	0
Momentum (x)	$\overline{\rho}u$	$\mu\nabla u$	$-\partial P_m/\partial x$
Momentum (y)	$\overline{\rho}v$	$\mu\nabla v$	$-\partial P_m/\partial y + F_B$
Energy	$\overline{\rho}H$	$k\nabla T + h_{fg}(\rho_v+\rho_g)D\nabla\left(\frac{\rho_v}{\rho_v+\rho_g}\right)$	0
Vapor	ρ_v	$(\rho_v+\rho_g)D\nabla\left(\frac{\rho_v}{\rho_v+\rho_g}\right)$	$-\dot{m}$
Mist	ρ_l	0	$\dot{m}$
Vapor+Mist	$\rho_v+\rho_l$	$(\rho_v+\rho_g)D\nabla\left(\frac{\rho_v}{\rho_v+\rho_g}\right)$	0

where ϕ is a scalar or vector field subject to convective transport $\mathbf{u}\phi$, diffusive transport Γ, and source term S. Table 1 lists the conserved quantities along with their transport terms.

These equations are not fundamental but rather forms derived using simplifying assumptions. The quantities u and v represent the mass average velocities defined as $\overline{\rho}u = \rho_g u_g + \rho_v u_v + \rho_l u_l$, where u_i is the velocity of species i. The quantities ρ_v, ρ_g, and ρ_l represent the mass per unit volume of mixture for the vapor, gas, and liquid respectively. This notation is consistent with the previous works of Toor [7] and Legay-Desesquelles et al. [5]. The mixture densities should not be confused with the single phase densities by themselves, i.e. $\rho_l \neq 1000$ kg / m^3, rather ρ_l is the density of the mist or fog per unit volume of mixture. The mass fraction of each component is defined as $\omega_i = \rho_i/\overline{\rho}$. The source term in the liquid phase equation and the sink term in the vapor phase equation, $\dot{m}$, represents the volumetric mist formation rate. The vapor and liquid equations are added together in order to remove this unknown quantity. The local density of liquid comes from the mist models discussed in Sec 2.3. which are used to partition the constituents into each phase based on the local conditions. The source term in the vertical momentum equation can be written as $S = -\partial P_m/\partial y + F_B$, with $F_B = (\rho - \overline{\rho})g$. The quantity F_B is the buoyancy force given by the difference between the local and average densities.

In addition to the transport equations presented above, an equation of state for the vapor (which governs the local density for use in the momentum equation) can be written assuming ideal behavior. The vapor pressure corresponds to the total pressure (Dalton's law) and the local vapor density (ideal gas law) in the following way (and similarly for the non-condensable gas):

$$P_v = Px_v = \frac{\rho_v RT}{M_v} = \rho RT\frac{\omega_v}{M_v} \tag{2a}$$

$$P_g = Px_g = \frac{\rho_g RT}{M_g} = \rho RT\frac{\omega_g}{M_g} \tag{2b}$$

where $x_v = \dfrac{\frac{\omega_v}{M_v}}{\frac{\omega_v}{M_v}+\frac{\omega_g}{M_g}}$, $x_g = \dfrac{\frac{\omega_g}{M_g}}{\frac{\omega_v}{M_v}+\frac{\omega_g}{M_g}}$,

and $\rho_i = \rho\omega_i$. The quantities M_v and M_g are the molecular weights of vapor and gas respectively, x_v and x_g the mole fraction of vapor and gas respectively and the products $\rho\omega_v$ and $\rho\omega_g$ the local vapor and gas densities respectively. In Eq. (2) the local vapor density is based on the equation of state. At a fixed vapor pressure (constant vapor density), Eq. (2) indicates that a decreasing vapor mass fraction results in an increasing mixture density ρ. In this case, when mist formation is present the local density increases through the formation of liquid droplets. The equation of state for the liquid is determined from the relation: $\omega_g + \omega_v + \omega_l = 1$ and Sec 2.3. discusses the details of how the vapor and liquid are partitioned into each phase.

Equation (2) makes use of the fact that the sum of the partial pressures of vapor and gas must be equal to the total pressure. From Eq. (2) the local mixture density for use in the source term of the momentum equation is then

$$\rho = \frac{P}{RT\left(\frac{\omega_v}{M_v}+\frac{\omega_g}{M_g}\right)} \tag{3}$$

The energy flux originates from two terms: Fourier conduction, and mass diffusion. We can write the diffusive energy flux as follows

$$\Gamma_H = \sum_i \Gamma_i H_i + k\nabla T \tag{4}$$

where H_i is the enthalpy of component i and Γ_i the diffusive mass flux of component i. The enthalpy of each species is fixed by the datum: $H_g = 0$ at $T = T_o$, and $H_l = 0$ (for saturated liquid water at $T = T_o$). The enthalpy difference between the vapor and liquid is given by the latent heat of vaporization: $H_v - H_l = h_{fg}(T_o)$ for saturated liquid at $T = T_o$. The enthalpies of each component are then written as:

$$H_g = c_{pg}(T - T_o) \tag{5a}$$

$$H_v = c_{pv}(T - T_o) + h_{fg}(T_o) \tag{5b}$$

$$H_l = c_{pl}(T - T_o) \tag{5c}$$

where T_o is a reference temperature, taken to be that at the start of the transient (the isothermal cooling wall temperature, $T_o = T_w$). It should be noted that the latent heat could of just as easily been applied to the liquid phase by defining the enthalpy datum: $H_v = 0$, with the liquid enthalpy written as $H_l = c_{pl}(T - T_o) - h_{fg}(T_o)$. The difference is arbitrary since there is just one datum for the substance water. In Eq. (5b), h_{fg} behaves like the "heat of reaction" in the chemical reaction systems presented by Kays and Crawford [22]. In fact, the formulation for both systems is similar although most chemical reaction systems do not involve the formation of a liquid phase. By expanding the summation for the diffusive fluxes of enthalpy and noting that the sum of the diffusive fluxes of mass is zero ($\sum \Gamma_i = 0$) we can write the following equation for the diffusive flux of energy (assuming equal specific heats):

$$\Gamma_H = h_{fg}\Gamma_v + k\nabla T \tag{6}$$

2.3 Mist Formation

The following section is devoted to the development of the mist formation conditions and result in a liquid/vapor equation of state. The total enthalpy is the sum of constituent enthalpies given in Eq. (5) weighted by the species mass fraction:

$$H = \sum \omega_i H_i = c_p(T - T_o) + h_{fg}\omega_v \tag{7}$$

where ω_i is the mass fraction of each species (i=v, g, and l for the vapor, gas and liquid respectively). In principle, the value for c_p should be given by a weighted sum of the individual c_{pi}'s, i.e. $\bar{c}_p = \sum \omega_i c_{pi}$. Instead, for computational ease, c_p is set equal to the value of a single constituent.

The treatment of mist formation has been considered previously by other investigators, including the boundary layer analyses of Hijikata et al. [23] and Brouwers [8,9]. Hijikata [23] postulated that the vapor/gas mixture jumps to local thermodynamic equilibrium once the conditions for mist formation are met. Hijikata's method is modified here somewhat by assuming that the vapor/gas mixture is in one of three states:

Model 1: Complete nonequilibrium ($\dot{m} = 0$).

Model 2: Complete local thermodynamic equilibrium.

Model 3: Partial equilibrium (partial supersaturation).

The conservation equations for the vapor and mist contain the condensation rate, $\dot{m}$, the rate at which vapor condenses into mist. This value is negative in the vapor source and positive in the mist source. By

combining the equations for vapor and mist we obtain a simplified equation for the total quantity of vapor and mist, ω_{vl}. This action eliminates the unknown condensation rate, $\dot{m}$. The lost information is replaced by forcing the mist and vapor to be in one of the three states given above. When equilibrium or the equilibrium fraction model (MCSM) are used, the following logic is used to partition the vapor and liquid (note that for convenience of notation, the mass fraction $\omega_i = \rho_i/\overline{\rho}$ is used):

superheated condition $(\omega_{vl} \le \omega_{vs})$:

$$\omega_v = \omega_{vl}; \quad \omega_l = 0; \quad \omega_g = 1 - \omega_v \tag{8a}$$

mist condition $(\omega_{vl} > \omega_{vs})$:

$$\omega_v = \omega_{vs}\left(\frac{1-\omega_{vl}}{1-\omega_{vs}}\right); \omega_l = \omega_{vl} - \omega_v; \omega_g = 1 - \omega_{vl} \tag{8b}$$

where

$$\omega_{vs}(T) = \frac{\rho_v}{\rho_v + \rho_g} = \frac{1}{1 + \frac{M_g}{M_v}\left(\frac{P}{P_{sat}(T)}\frac{1}{S} - 1\right)} \quad \text{and}$$

$$S = \frac{(P_v)_{SSL}}{P_{sat}(T)}$$

where $\omega_{vs}(T)$ is the maximum mass fraction of vapor which can be supported before mist formation occurs, $P_{sat}(T)$ the saturation pressure of pure vapor and $(P_v)_{SSL}$ is the vapor pressure at the supersaturation limit.

As discussed in Sec 1.2, previous investigators have made use of the CSM, assuming that once critical supersaturation is reached, the vapor pressure drops either discontinuously to the equilibrium value or a particle growth theory is invoked in order to model the transient nature of the droplet kinetics. Unfortunately, for a transient (on the macroscale), elliptic problem such as the one being modeled here, the CSM must be modified in order to avoid the discontinuities that give rise to numerical instabilities. The Eulerian based modeling pursued here precludes the use of any transient/kinetic droplet analyses. The Modified CSM used here (MCSM) consists of a correction factor applied to the expression for the critical supersaturation ratio S. This correction factor allows mist to form at some point below the critical supersaturation but remain supersaturated without a discontinuous jump to equilibrium. The model then strikes an approximate balance between full critical supersaturation and full equilibrium.

Theoretical expressions for S have been developed based on kinetic theory. Carey [24] gives an explicit expression for S in terms of the vapor temperature and surface tension.

$$S = \frac{(P_v)_{SSL}}{P_{sat}(T_v)} = C\exp\left\{\left[\frac{E^*\left(-\ln J^*\right)^{1/2}}{2\left(E^*\right)^{1/2} + \left(-\ln J^*\right)^{3/2}}\right]\right\} \tag{9}$$

where

$$J^* = \frac{J\rho_l}{N_A}\left(\frac{\pi M_v}{2\sigma N_A}\right)^{1/2}\left[\frac{RT}{P_{sat}(T)}\right], E^* = \frac{16\pi\sigma^3}{3k_B R^2 T^3 \rho_f^2}.$$

The quantity J is the nucleation rate, $J = 10^6$ nuclei/m^{3}s, N_A Avogadro's number, k_B the Boltzmann constant, σ the surface tension of the liquid droplets, and ρ_f the density of the liquid droplets. The value for the nucleation rate $J = 10^6$ nuclei/m^{3}s is taken from Carey's text [23]. This value was found to match well with experimental results for a number of different systems. The constant C modifies the theoretical prediction in such a way as to balance the model between the critical and equilibrium conditions. For C=1 the theoretical predictions given by Eq. (9) are approximately 2.3 times smaller than the critical saturation ratio seen in the experiments by Yellott [25]. A value of C=0.75 is used in the model to bring S to around 1/3 the experimental value. Thus the model supersaturation is only about 1/3 the experimental value but is short of full equilibrium. The constant C is used as an adjustable parameter that cannot be determined *a priori* but rather is used to match the experimental data. Different values of C can be used to adjust the supersaturation ratio S, in turn altering the point at which mist is allowed to form.

2.4 Global Mass Balance and System Pressure

In order to calculate the global rate of change of density, the mass flux is integrated over the boundary to obtain the rate of change of inventory. Density is assumed to vary temporally but not spatially, except for the buoyancy terms in the momentum equation. The integration yields the following global mass conservation equation:

$$\frac{d\overline{\rho}}{dt} = \frac{1}{WH}\left(\int_0^W \left(J_v + J_l\right)_{y=0} dx - \int_0^H \left(J_v + J_l\right)_{x=W} dy\right) \tag{10}$$

where W and H are the width and height of the condenser respectively shown in Fig. 1 and the total fluxes across each boundary come from the boundary

conditions. Equation (10) provides the necessary relation for the discrete temporal change of density.

The system pressure is obtained by assuming ideal gas behavior for the steam/air mixture and by noting that the average density is equal to that given by a summation of the discrete local densities over the entire condenser. The local density is integrated over the condenser to give

$$\frac{1}{A}\int_0^H\int_0^W \rho(x,y)dA = \frac{1}{A}\int_0^H\int_0^W \frac{P}{RT\left(\frac{\omega_g}{M_g}+\frac{\omega_v}{M_v}\right)}dA \quad (11)$$

where $A = HW$ and $dA = dxdy$. Normally, a similar integration of energy over the system domain would also be required in order to determine the state of the system. However, in Eq. (11) the temperature determined by the mist formation state given in Sec. 2.3 is assumed to be constant over the period Δt. This obviates the need for a similar integration of energy by assuming that the change in temperature is small over the discrete integration time. The left hand side of Eq. (11) is the average density and the pressure is constant so it can be removed from the integration. Solving for the system pressure yields

$$P = \frac{\bar{\rho}RHW}{\int_0^W\int_0^H \frac{dxdy}{T\left(\frac{\omega_g}{M_g}+\frac{\omega_v}{M_v}\right)}} \quad (12)$$

The pressure is used to determine the interface temperature at the condensing surface and P is self-adjusted so that the entering vapor mass and condensing mass flow become equal.

2.5 Boundary Conditions

The interface between the vapor and cooling wall is impermeable to noncondensable gas and the diffusive flux of vapor and gas are equal and opposite, i.e.

$$J_{g,i} = \left(u\rho_g - \Gamma_g\right)_i = \left(u\rho_g + \Gamma_v\right)_i = 0 \quad (13)$$

where $J_{g,i}$ is the total flux of gas at the interface, both convective and diffusive. At the interface vapor is condensed and carried away by a thin liquid film. The above equation can be solved for the velocity at the interface:

$$u_i = -\frac{1}{\rho_{g,i}}\Gamma_{v,i} \quad (14)$$

Using the above equation for the convective flux of gas, the summation of the total fluxes of each species at the interface results in the following mass balance:

$$\dot{m}_c = \sum J_k = \sum\left(u\rho_k - \Gamma_k\right)_i = u\left(\rho_v + \rho_l\right)_i - \Gamma_{v,i} \quad (15)$$

where the subscript i denotes the value at the interface, the subscript k denotes the species index (i.e. k=g, v, *or* l) and $\Gamma_{v,i}$ is the diffusive flux of vapor at the interface.

An energy balance at the interface results in the following

$$q_w = -k_w\left.\frac{\partial T}{\partial x}\right|_{w,i} = -k_v\left.\frac{\partial T}{\partial x}\right|_{v,i} + \left(u\rho_v - \Gamma_v\right)_i h_{fg} \quad (16)$$

where k_w and k_v are the wall and vapor thermal conductivities respectively. In principle the temperature drop in the liquid film must also be known in order to make use of Eq. (16). In practice, however, for the particular cases studied in this work, the primary resistance to heat and mass transfer is in the vapor phase and the temperature drop through the liquid film and wall are not discussed here further. One can assume that the interface temperature is nearly equal to the wall temperature without significant loss in accuracy, However, this approximation was not used in the complete model presented in [19]. Refer to [19] for a detailed discussion of the treatment of the liquid and wall side heat transfer. We can use the expression for the velocity at the interface given by Eq. (14) to rewrite Eq. (16) as

$$-k_w\left.\frac{\partial T}{\partial x}\right|_{w,i} = -k_v\left.\frac{\partial T}{\partial x}\right|_{v,i} - \left(\frac{\rho_v + \rho_g}{\rho_g}\right)_i \Gamma_{v,i} h_{fg} \quad (17)$$

where $\rho_{v,i} = \rho_{v,sat}\left(P, T_i\right)$. Again, because the primary temperature drop occurs in the vapor phase, $\rho_{v,i} = \rho_{v,sat}\left(P, T_i\right) \approx \rho_{v,sat}\left(P, T_w\right)$ and the heat flux through the liquid film and wall is easily accommodated by the relatively low heat flux coming from the vapor phase.

In order for the system to conserve the total amount of noncondensable gas the net flux of gas across each boundary must be zero, i.e. $J_g = 0$. The top and left side boundaries are adiabatic and solid. The right side boundary is both the condensing and adiabatic depending on the vertical location. The heat and mass flux at the condensing wall is given by the

interface condition. The heat flux and mass flux entering the system comes from the heat load or power Q'. Since $Ja = c_p(T_e - T_w)/h_{fg} << 1$, the sensible heat of vapor is ignored in the heat balance on the system. The following boundary conditions are imposed on the governing equations of the vapor, gas, liquid mixture. A homogeneous Neumann type boundary condition is specified for the motion pressure field. It has been proven that homogeneous Neumann boundary conditions for the pressure ensure a consistent scheme independent of the Reynolds number at all types of boundaries, including solid walls and inflow/outflow boundaries (Huser et al. [26] and Gresho [27]). Although, the vapor and liquid conservation equations are combined in order to eliminate the mist formation rate, boundary conditions for each phase are necessary for completeness. Because the mist is swept towards the liquid film, a zero gradient boundary condition is imposed on the liquid phase at the condensing surface.

@ $y=0$ (18a)

$$u = 0;\ v = v_{in};\ J_H = \frac{Q'}{W};\ J_v = \left(\frac{Q'}{h_{fg}W}\right);\ J_l = 0;\ \frac{\partial P_m}{\partial y} = 0$$

@ y=H (18b)

$$u = 0;\ v = 0;\ J_H = 0;\ J_v = 0;\ J_l = 0;\ \frac{\partial P_m}{\partial y} = 0$$

@ $x=0$ (18c)

$$u = 0;\ v = 0;\ J_H = 0;\ J_v = 0;\ J_l = 0;\ -\frac{\partial P_m}{\partial x} = 0$$

@ $x=W$ (18d)

$$u = \frac{\dot{m}_c}{\overline{\rho}};\ v = 0;\ J_H = q_w;\ J_v + J_l = \dot{m}_c;\ \frac{\partial \rho_l}{\partial x} = 0;\ \frac{\partial P_m}{\partial x} = 0$$

where the J_ϕs represent the total flux of each quantity (H, ω_v, and ω_l) normal to the boundary, W the width of the condenser, H the height of the condenser, and Q' the linear heat rate applied to the evaporator. The entering velocity, v_{in}, comes from an energy balance at the evaporator:

$$v_{in} = \frac{Q'}{\overline{\rho} h_{fg} W} \tag{19}$$

The initial conditions are set so that the velocity everywhere is zero, the temperature is at the cooling wall temperature, the density is that given by the pressure through the ideal gas law, and the pressure is at the saturation pressure for the cooling wall temperature. The initial conditions are then written as

@ $t=0$ (20)

$$u = 0;\ v = 0;\ H = \omega_{v,0} h_{fg};\ \rho_v = \rho_{v,0};$$

$$\overline{\rho} = \frac{P_{sat}(T_w) M_v}{R T_w \omega_{v,0}};\ \rho_l = 0$$

where $\rho_{v,0}$ is the initial vapor density and $\omega_{v,0}$ is the initial vapor mass fraction. Without any applied power the system would remain stationary, since the vapor/gas combination is at the saturation pressure given by the wall temperature and no condensation takes place. Only increases in pressure will induce condensation and subsequent bulk motion of fluid. The total number of moles of gas set by the initial condition does not change, $\overline{\rho}_g = \rho_{g,0}$, where $\rho_{v,0} + \rho_{g,0} = \overline{\rho}_0$.

2.6 Discretization

The incompressible flow model developed here imposes a finite non-zero divergence that is spatially constant, resulting in a correction to the continuity equation which can be handled in a straightforward manner in a predictor-corrector scheme once the temporal change in global density is calculated appropriately. This simplification results in a tremendous savings because the sonic velocities are not used to restrict the time step size.

The governing equations are discretized on a staggered mesh, with velocities defined on the cell boundaries and scalars at the center. The pressure-velocity coupling is satisfied using a variant of the Marker and Cell method (MAC) presented in Fletcher's [28] text. The temporal discretization of the momentum equation is accomplished in the following manner:

$$\frac{(\overline{\rho}\mathbf{u})^{n+1} - (\overline{\rho}\mathbf{u})^n}{\Delta t} = -\nabla^n \cdot \mathbf{J}_\mathbf{u} - \nabla \cdot P_m^{n+1} + S \tag{21}$$

where ∇^n is the discrete divergence operator and $\mathbf{J}_\mathbf{u}$ the total flux of momentum including both convective and viscous terms. We postulate the velocity and pressure fields to behave in the following way:

$$\mathbf{u}^{n+1} = \mathbf{u}^* + \mathbf{u}' \tag{22}$$

$$P_m^{n+1} = P_m^n + P_m' \tag{23}$$

where $\mathbf{u}^*$ is an approximation to the velocity field at time $n+1$ and $\mathbf{u}'$ is a correction that allows the mass continuity equation to be satisfied. Similarly, P_m' is the correction to the motion pressure field at P_m^n,

where P_m is the computational pressure, a second order approximation to the real motion pressure, Huser et al. [26]. Inserting Eq. (22) and Eq. (23) into Eq. (21) results in the following equation:

$$\frac{\overline{\rho}^{n+1}\mathbf{u}^* - (\overline{\rho}\mathbf{u})^n}{\Delta t} + \left\{\frac{\overline{\rho}^{n+1}\mathbf{u}'}{\Delta t}\right\} =$$

$$-\nabla^n \mathbf{J}_\mathbf{u} - \nabla P_m^n + \left\{-\nabla P_m'\right\} + S \qquad (24)$$

In Eq. (24) the quantities in braces represent the correction terms. The velocity correction, $\mathbf{u}'$, corresponds to the pressure correction P_m' and the terms in braces are set equal to each other:

$$\mathbf{u}' = -\frac{\Delta t}{\overline{\rho}^{n+1}} \nabla P_m'. \qquad (25)$$

The predictor step can then be written as

$$\frac{\overline{\rho}^{n+1}\mathbf{u}^* - (\overline{\rho}\mathbf{u})^n}{\Delta t} = -\nabla^n \mathbf{J}_\mathbf{u} - \nabla P_m^n + S. \qquad (26)$$

Continuity must be satisfied at the new time step. The discrete representation for continuity is expressed as

$$\frac{1}{\overline{\rho}^n}\frac{\overline{\rho}^{n+1} - \overline{\rho}^n}{\Delta t} + \nabla \mathbf{u}^{n+1} = 0. \qquad (27)$$

The first term of Eq. (27) represents the discrete, global change in density throughout the condenser. The term is necessary in order to obey global continuity. The transient density term acts as a mass source or sink for the continuity equation. Typically, the velocity components in incompressible flows are characterized as divergence free vector fields. However, the introduction of a source or sink term does not limit our ability to make use of the incompressible solution algorithms, so long as the source or sink is introduced in a consistent manner.

Using Eq. (26) for the initial guess of the new velocity field, and Eq. (25) for the velocity correction, Eq. (27) can be rewritten as

$$\frac{1}{\overline{\rho}^n}\frac{\overline{\rho}^{n+1} - \overline{\rho}^n}{\Delta t} + \nabla\left(\mathbf{u}^* + \mathbf{u}'\right) =$$

$$\frac{1}{\overline{\rho}^n}\frac{\overline{\rho}^{n+1} - \overline{\rho}^n}{\Delta t} + \nabla\left(\mathbf{u}^* - \frac{1}{\overline{\rho}^{n+1}}\nabla P_m'\right) = 0 \qquad (28)$$

Solving Eq. (28) for the pressure correction results in the following Poisson equation:

$$\nabla^2 P_m' = \frac{\overline{\rho}^{n+1}}{\Delta t}\left(\frac{1}{\overline{\rho}^n}\frac{\overline{\rho}^{n+1} - \overline{\rho}^n}{\Delta t} + \nabla \cdot \mathbf{u}^*\right). \qquad (29)$$

The boundary conditions for Eq. (29) come from the prescription of the normal velocity at the boundary. From Eq. (25) since the velocity is known on the boundary for the time step n, the velocity correction is identically zero, leading to a homogeneous Neumann condition for the pressure correction, Eq. (29). A multigrid method is used to solve the above Poisson equation that results in an order of magnitude increase in the convergence rate over the standard Successive Line Over Relaxation (SLOR) coupled with a Tri-Diagonal Matrix (TDMA) algorithm and is discussed in detail by Fox [19].

The nonlinear convective terms are solved for using the flux corrected transport (FCT) scheme developed by van Leer [29]. Such FCT schemes have proven useful in high speed shock capturing models but have been all but ignored for viscous incompressible flows. Recent studies [19,30] have shown that FCT schemes can be used with great success in the modeling of low speed flows where the steeper gradients in the scalar in vector fields are resolved nicely with minimal impact of numerical diffusion.

2.7 Modeling

The numerical model was modified in a attempt to simulate the experimental system. In the interest of reducing the computational effort associated with a large computational domain the entrance length was reduced from 83.8 cm to 50 cm in the model. This approximation appears to be valid considering the largest flow structures are no larger than the condenser width (15 cm) and entrance effects ought to be negligible beyond a few widths (3.2 widths). Only the right side of the condenser was made available for condensation, all other surfaces were specified to be impermeable and adiabatic. The solution procedure was modified to search for a constant pressure rather than to dissipate a specified heat load. With the amount of noncondensable gas fixed, the power was varied automatically until both the inlet and outlet mass fluxes resulted in a pressure of 1 atm. Different mixture temperatures were achieved by varying the noncondensable loading. Although the final point is reached through different means in the experiment (air leaking in and out with flow rate given) and the numerical model (steam flow rate adjusted with air concentration given), the system parameters are the same once a quasi steady state is reached.

A grid resolution of 64x128 was used in the numerical simulation, resulting in a maximum grid Reynolds number, $Re = v\Delta y/\nu < 500$ (such Re is within the range found suitable for the application of the FCT algorithm used here [19]). The resolution of more microscale detail would be computationally expensive and would reduce the size of the overall parameter space investigated in this work.

Unfortunately, the experiments were conducted long before the model was developed and the discrepancy between laminar and turbulent flow behavior is difficult to justify. The model is strictly laminar where as the experiments were found to be turbulent at times and in various places. No attempt was made to extend the model to include turbulent behavior. This fact may help to account for some of the discrepancies seen between the experiment and model results.

It should be stressed that the correction factor applied to the MCSM model is purely ad hoc. No attempt to justify or determine the value of C was done. It stands to reason that it ought to be less than unity and greater than zero. Determining the precise value would require an extremely detailed model describing the dynamic growth and translation of droplets in a strongly coupled flow field. The value C=0.75 was chosen simply to match the experimental results best. It is only one attempt to wed theory and experiment but the value itself, as well as how one determines it, is questionable at this time. More than likely, the value of C has a strong dependense on many of the experimental parameters and model assumptions and should not be taken as constant for different situations.

2.8 System Parameters

The thermophysical properties of air were used in the calculation in order to reduce the number of variables being solved for in the model. This approximation will likely yield adequate results, particularly near the condensing surface where the air concentrations are relatively high and the transport is most sensitive to the thermophysical properties. The wall temperature and the transport properties used were T_w=303.15 K, h_{fg}=2.256x10^6 J/kg , $\bar{c}_p$ =1.0x10^3 J/kg-K, k_v=0.03 W/m-K, μ=20.7x10^{-6} N-s/m^2, k_l=0.653 W/m-K, μ_l=467.3x10^{-6} N-s/m^2, ρ_l=1000 kg/m^3. The mass diffusion coefficient was again estimated using the method described by Bird et al. [21] using the wall temperature. Given the range in air concentrations and temperatures the use of constant properties is also questionable. However, because the sharpest gradients occur near the wall, it is appropriate to use the temperatures and compositions found there to estimate the overall transport properties. The bulk flow is not affected strongly by differences in the transport properties due to the relatively large Reynolds numbers found there (convection dominates over diffusion in the bulk).

3. EXPERIMENTAL RESULTS

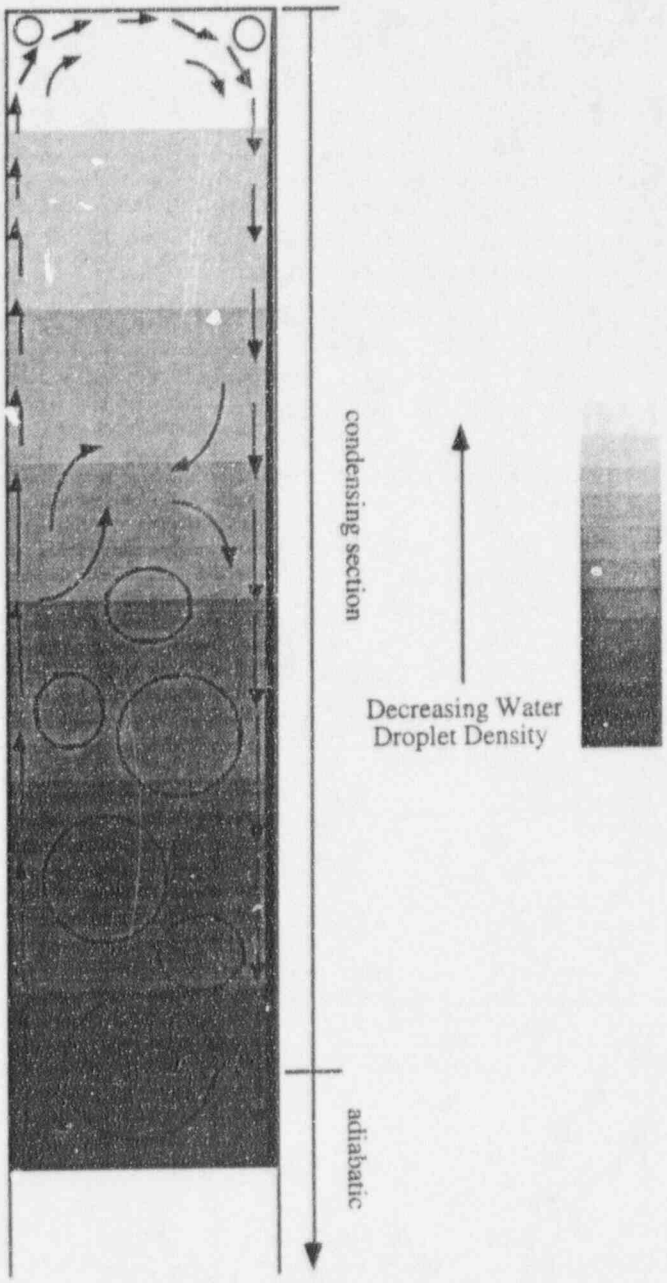

Figure 2 Observed Experimental Flow Patterns

A review of the experiment results show a strongly natural convective flow field. The $Fr = \bar{\rho} v_{in}^2/(g\Delta\rho W)$ (based on the calculation where $\Delta\rho$ is the density difference between the evaporator and wall) for even the strongest forced convective flow at high power is significantly less than unity (Fr<0.04), resulting in a flow in which natural con-

vection dominates. For these systems when $Fr<<1$ the resulting flows are found to be substantially natural convective in nature. Figure 2 is a plot of the observed flow patterns and mist density distribution inside the condenser. The condensation at the wall brought vapor and gas toward the surface, resulting in the accumulation of a heavy, noncondensable rich fluid. The visual observations indicated a primarily two-dimensional flow pattern. As the gas fell downward a set of recirculation cells were generated. The strength and size of the recirculation cells grew as the gas accelerated downward. Large recirculation cells spanning the width of the condenser were found in the lower regions of the condensing section (as ascertained by visual observation of the mist motion). The cells became weaker further up in the condenser and spanned only a fraction of the condenser width. Ultimately, the flow became relatively quiescent near the top of the condenser, with velocities reduced to a fraction of what they were lower in the condenser.

The mist concentration was found to be the highest near the bottom of the condensing section and near the wall. The sensible cooling near the wall was larger than the diffusive mass transfer, i.e. $Le = \alpha/D < 1$, and subcooled regions developed, owing to the increased rate of thermal diffusion over mass diffusion, resulting in the formation of subcooled regions. The subcooled regions generated near the wall fed into the lower portion of the condenser as the heavy, misty layer accelerated downward. The recirculation regions near the bottom of the condensing section mixed with the subcooled fluid near the wall.

4. MODEL RESULTS

Three sets of calculations were performed using the parameters listed above, one for each mist model (equilibrium, nonequilibrium, and MCSM). The velocity and scalar fields were found to fluctuate in time until a quasi steady flow was achieved, after which the fluctuations were reduced and the time average mass flow in was equal to the time average mass flow out by condensation. Figure 3 is a plot of the streamlines and mist density distribution for a typical run using the MCSM model. The lighter regions in Fig. 3 represent regions with a lower mist density. The flow did not vary significantly over long integration periods, however three seconds of the transient are shown in Fig. 3 in order to show where the recirculation cells were generated. The similarity between the numerical calculations and experiment is noteworthy. Strong recirculation cells near the end of the condensing section occupied the width of the condenser, with weaker, smaller cells higher up. The flow became mostly parallel to quiescent in the upper portion of the condenser, with the velocities a fraction of what they were down below. The mist formation and distribution is somewhat similar to that seen in the experiment except the distribution in the bulk is more uniform than that seen in the experiments. A heavy misty layer near the wall was generated which fed into the lower regions, creating a high mist concentration down below.

Although the instability in the condensing boundary layer caused some fluctuations in the local heat transfer coefficient, the magnitude of the fluctuations were not large and the variations are not plotted here for the sake of brevity.

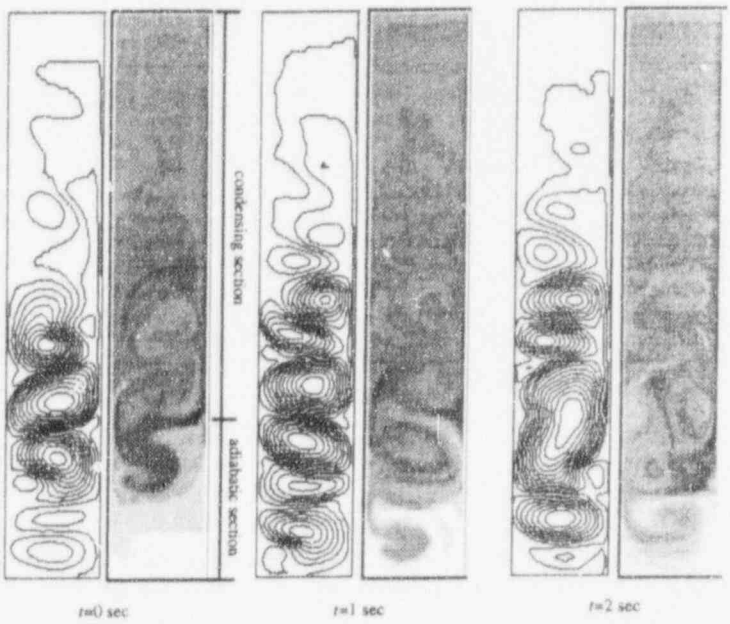

Figure 3 Streamlines and Mist Distribution $(T_{mix} = 78.2\ ^{\circ}C)$

Although the qualitative agreement was good between the theory and experiment a comparison of the local heat transfer rates shows some discrepancies. Figure 4 is a plot of the local heat transfer coefficient for two specific cases. The local heat transfer coefficient is defined as $h = q''/(T_{mix} - T_w)$, where q'' is the local heat flux and T_{mix} the mixture temperature (defined as the average temperature along the centerline of the condenser and typically within 1 K of the average temperature of the entire condenser). Both the experimental data points along with the results of the MCSM calculations are presented in Fig. 4. At the top of the condenser, the heat transfer coefficient was high but decreased further down the condensing surface. This decrease, seen in both the theory and experiment, was due to the growing boundary layer which generated a diffusion layer barrier to mass transfer. The magnitude of the heat transfer coefficient was somewhat higher in the model than in the experiment. In the middle of the condensing section the heat transfer

coefficient plateaud somewhat, possibly a result of the competing effects of a growing boundary layer offset by an accelerating, unstable flow which tended to augment mass transfer. Ultimately, the large scale recirculation regions near the bottom of the condensing section served to disrupt the boundary layer, alternately carrying vapor rich regions toward and away from the wall resulting in a sharp rise in the heat transfer followed again by a decrease. Near the end of the condensing section the theory underpredicted the experiments somewhat, possibly due to the truly three dimensional effects coupled with increased numerical diffusion at higher flow velocities. However, the general character as well as the numerical values were in reasonably good agreement.

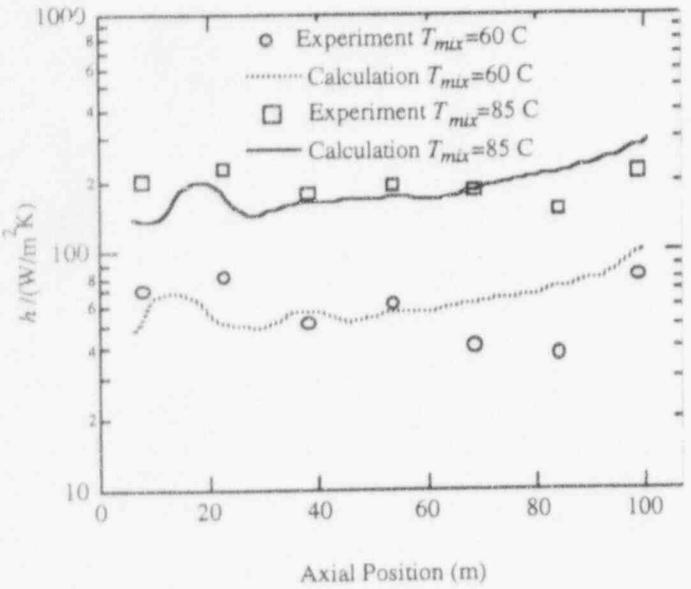

Figure 4 Local Heat Transfer Coefficient - Experiment and MCSM

Figure 5 is a plot of overall heat transfer coefficient for the experiment and the three different mist models used in the calculations. Comparison of the overall heat transfer coefficient tends to average out the differences somewhat in the local heat transfer coefficient, resulting in unusually good agreement in Figure 5 between the MCSM model and experiment. The traditional nonequilibrium or supersaturated model tended to overpredict the heat transfer coefficient. Conversely, the full equilibrium model tended to underpredict the overall heat transfer coefficient by about the same fraction. The Modified Critical Saturation Model (MCSM) used here resulted in excellent agreement between the two extremes, indicating that the real system probably lies somewhere in between full equilibrium and nonequilibrium. The differences between the three curves are do primarily to the liberation of latent heat caused by the formation of mist. As mist is generated the temperature increases, in turn increasing T_{mix} and lowering the heat transfer coefficient for a constant q''. Moreover, the curves generally predict higher heat transfer coefficients for increasing mixture temperatures. If the temperature is increased due to the liberation of latent heat, the curve is shifted to the right, further reducing the heat transfer coefficient compared with the ideal nonequilibrium, supersaturated case. The dual effect of shifting the curve to the right for increasing equilibrium along with lowering the heat transfer coefficient by changing the reference temperature resulted in a strong variation of the heat transfer coefficient between the full equilibrium and nonequilibrium cases.

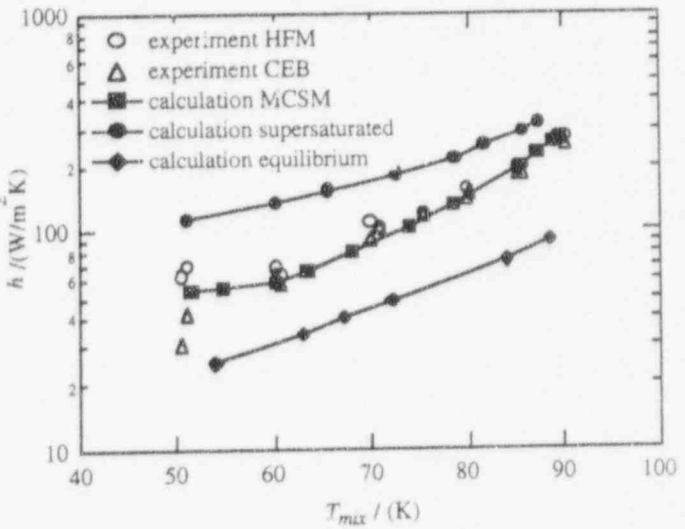

Figure 5 Overall Heat Transfer Coefficient - Experiment and Model

Table 2 provides the results for each calculation performed. Each data point represents at least 20 hours of CPU time on a Sparc 10. Each data point is taken at an instant in time, with averaging too costly to perform for every point. However, the numbers do not fluctuate significantly in time and represent reasonably stable values for use in comparison with one another. The table gives values for the average mass fraction of water (liquid and vapor), $\overline{\omega}_{vl}$; the average mass fraction of water vapor alone, $\overline{\omega}_v$; the mixture temperature, T_{mix} (K); the average gas density (gas loading), $\overline{\rho}_g$(kg/m^3); the latent and sensible heat fluxes, q''_{lat} and q''_{sen}(W/m^2); the average heat transfer coefficient, $\overline{h}$(W/m^2-K); and the maximum absolute and relative liquid mass fractions, $\omega^{abs}_{l,max}$ and $\omega^{rel}_{l,max}$. The last two terms are defined as

$$\omega^{abs}_{l,max} = \left.\frac{\rho_l}{\rho_l + \rho_v + \rho_g}\right|_{max} \tag{30}$$

$$\omega_{l,max}^{rel} = \left.\frac{\rho_l}{\rho_l + \rho_v}\right|_{max} \tag{31}$$

Equation (30) represents the maximum mass fraction of liquid based on the total density, whereas Eq. (31) represents the maximum mass fraction of liquid based on the amount of local water (vapor and liquid but not gas) and is usually interpreted as the quality in two phase mixture calculations.

The first six entries in Table 2 employed the equilibrium model (inverse supersaturation $1/S$=1.0). The latent heat transfer increased significantly as the vapor mass fraction increased. Similarly, the sensible heat transfer increased as the mixture temperature increased. The result gave rise to an average heat transfer coefficient that increased sharply over the mixture and temperature range. The maximum absolute mass fraction of liquid was just under 20% at the highest mixture temperature. The maximum relative mass fraction of mist (quality) was almost 80%. In some locations the vapor fraction was found to drop by up to 80% due to the mist formation. The total amount mist formed in the condenser is given by the difference between $\overline{\omega}_{vl}$ and $\overline{\omega}_v$. The difference results in a maximum of 6%. In addition the latent heat transfer (mass transfer) at $\overline{\rho}_g = 0.42$ kg/m^3, was reduced appreciably compared to the MCSM and supersaturated models, owing to a reduction in the gradient of the vapor mass fraction near the condensing surface.

The next nine entries in Table 2 employed the MCSM model. The inverse saturation ratio varies from 0.54 (towards nonequilibrium) up to 0.70 (towards equilibrium). The variance in $1/S$ is a function of the temperature dependence of Eq. (9). For the same gas loading ($\overline{\rho}_g = 0.42$ kg/m^3), the MCSM model resulted in a lower mixture temperature, owing to the reduction in the amount of mist formed. As in the equilibrium model, the heat flux and heat transfer coefficient increased sharply as the mixture temperature and vapor mass fraction increased. The MCSM model, however, resulted in far less mist formation compared with the equilibrium model. The highest absolute liquid fraction is under 10% while the highest relative liquid fraction (quality) is only 50%.

The last eight entries in Table 2 employed the nonequilibrium or supersaturated model. The supersaturated model resulted in the same trends as before but in this case no mist is formed. Again, by comparing the same gas loading ($\overline{\rho}_g = 0.42$kg/m^3) the supersaturated model showed a much lower mixture temperature than for the MCSM and equilibrium model, owing to the complete lack of mist formation that would liberate latent heat and a much higher latent heat transfer rate due to the increased vapor concentration near the wall (mist was not allowed to form).

The relative contribution of latent and sensible heat transfer to the overall heat flux demonstrated the important effect of mist formation on the heat and mass transfer. For the supersaturated model, the sensible heat flux was a small fraction of the combined total of latent and sensible heat transfer. Closer to equilibrium, the MCSM model yielded a higher fraction of sensible heat transfer to the total heat flux and a corresponding decrease in the latent heat flux due to the reduced species gradient. At full equilibrium the latent heat flux was reduced further and the increased sensible heat transfer was an appreciable fraction of the total heat transfer. In the equilibrium cases, since up to 25% of the heat transfer was by sensible heat and all the entering steam was removed at the condensing surface (as both vapor and mist), up to 25% of the incoming steam was removed in the form of mist. This competition between latent and sensible heat transfer generally served to offset each other. Figure 6 is a plot of the overall heat flux as a function of the vapor plus liquid mass fraction for the three models. Figure 6 removes the dependence on mixture temperature since the bulk mass fraction is independent of the mixture temperature. The data indicates that the total heat transfer was not altered significantly by the formation of mist. This result is consistent with previous investigations which found the net result on the total heat transfer to be negligible, owing the trade off between the reduction in latent heat to an increase in sensible heat as more mist is formed (Legay-Desequelles, 1986 and Toor, 1971). In other words, the total heat input is constant, and since energy conservation dictates that the energy must be removed somewhere, the system is not sensitive to the actual mode of heat transfer, be it latent or sensible.

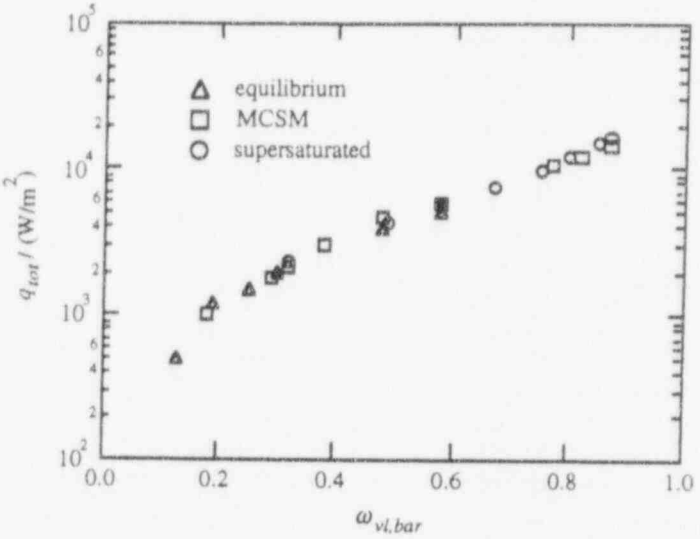

Figure 6 Total Heat Flux for Different Models

Table 2 Results of Steam-Air Calculations

Model	$1/S$	$\bar{\omega}_{vl}$	$\bar{\omega}_v$	T_{mix}	$\bar{\rho}_g$	q''_{lat}	q''_{sen}	$\bar{h}$	$\omega^{abs}_{l,max}$	$\omega^{rel}_{l,max}$
equilibrium	1	0.13	0.10	54.5	0.88	389	102	20	0.04	0.59
equilibrium	1	0.19	0.16	63.0	0.80	961	228	36	0.05	0.59
equilibrium	1	0.25	0.20	67.7	0.73	1187	285	40	0.10	0.75
equilibrium	1	0.30	0.25	72.6	0.65	1524	356	45	0.10	0.75
equilibrium	1	0.48	0.44	83.9	0.42	3231	632	73	0.14	0.67
equilibrium	1	0.58	0.52	87.9	0.33	4327	777	90	0.17	0.79
MCSM	0.54	0.18	0.18	50.8	0.81	944	49	48	0.007	0.08
MCSM	0.58	0.29	0.28	61.5	0.65	1688	105	58	0.019	0.17
MCSM	0.59	0.32	0.31	63.5	0.61	1971	147	65	0.026	0.27
MCSM	0.61	0.38	0.36	67.9	0.54	2710	267	80	0.044	0.41
MCSM	0.64	0.48	0.47	74.0	0.42	4003	443	104	0.058	0.50
MCSM	0.66	0.58	0.56	78.2	0.32	5005	566	120	0.083	0.47
MCSM	0.69	0.77	0.76	85.6	0.15	9668	897	201	0.090	0.33
MCSM	0.69	0.82	0.81	86.9	0.12	11060	959	225	0.081	0.27
MCSM	0.70	0.87	0.87	88.6	0.08	12995	1038	258	0.074	0.23
supersaturated	0	0.32	0.32	51.3	0.62	2194	68	110	0	0
supersaturated	0	0.49	0.49	59.2	0.42	4036	121	138	0	0
supersaturated	0	0.58	0.58	65.7	0.33	5304	157	154	0	0
supersaturated	0	0.67	0.67	72.6	0.24	7098	210	180	0	0
supersaturated	0	0.75	0.75	78.3	0.17	9456	280	213	0	0
supersaturated	0	0.80	0.80	81.7	0.14	11423	337	245	0	0
supersaturated	0	0.85	0.85	85.7	0.10	14234	421	286	0	0
supersaturated	0	0.87	0.87	86.9	0.08	15680	462	308	0	0

Although the vapor mass transfer was altered by the presence of mist, the total heat transfer remained nearly the same because of the increased sensible heat transfer. The balance between latent and sensible heat transfer can be understood as follows. When $1-\omega_{v,i} \approx 0$ (true for the calculations presented here), the total heat flux without mist formation can be written as:

$$q_o = -\rho D h_{fg} \nabla \omega_v^o - k \nabla T^o \tag{32}$$

Eq. (32) assumes that the specific heats are equal. The total heat flux with mist formation can be written similarly as (ignoring the effect of liquid on the diffusion):

$$q = -\rho D h_{fg} \nabla \omega_v - k \nabla T \tag{33}$$

The enthalpy comes from Eq. (7) and is set equal to same value with and without mist formation:

$$H = c_p\left(T^o - T_0\right) + h_{fg}\omega_v^o = c_p\left(T - T_0\right) + h_{fg}\omega_v \tag{34}$$

Taking the gradient of Eq. (34) results in the following:

$$c_p \nabla T^o + h_{fg} \nabla \omega_v^o = c_p \nabla T + h_{fg} \nabla \omega_v \tag{35}$$

The gradient of the vapor mass fraction given in Eq. (35) can be inserted into Eq. (33) yielding the total heat flux with mist formation:

$$q = -\rho D h_{fg} \nabla \omega_v^o - \frac{k}{Le}\left(\nabla T^o + (Le-1)\nabla T\right) \tag{36}$$

For Le approaching unity, Eq. (36) reduces to Eq. (32) indicating that the total heat flux with and without mist formation is the same. The condition that Le be identical to unity is not entirely necessary so long as Le is near unity the relationship between latent and sensible heat energy transfer will be the similar, resulting in similar overall heat transfer as shown in Fig. 6; thus although the overall heat transfer remains the same the mode of heat transfer is altered depending on the degree to which mist is formed.

5. CONCLUSIONS

Steam-air mixtures contained in a vertical reflux thermosyphon were studied using the numerical model and compared with existing experiments. The qualitative and quantitative agreement was good. The experimental data for the overall heat transfer coefficient was found to lie somewhere between the full equilibrium and nonequilibrium models. The MCSM model was used to match the experimental data with the numerical model by postulating that some fraction of equilibrium is attained everywhere in the condenser rather than full equilibrium at just the condensing surface only. The MCSM model contains one variable parameter and can be used to investigate the effect of mist formation on the heat and mass transfer by varying the equilibrium fraction.

Although mist formation may reduce the vapor mass transfer rate by up to 20%, the total mass transfer and heat flux are not largely impacted by the presence of mist, owing to the balance between latent and sensible heat transfer. For closed systems, however, the temperature rise of the bulk due to the formation of mist may result in large changes in the predicted heat transfer coefficients. For open systems, the reference state at infinity is not affected by the formation of mist and the impact of mist formation on the overall heat transfer coefficient is small. The vast majority of condensation calculations assume nonequilibrium behavior to generate heat fluxes for use in research and design work. This study points out that, though the nonequilibrium assumption may often be incorrect, the error does not impact the heat transfer coefficient in open systems with a fixed reference temperature. The difference, however, for closed systems is important and must be kept in mind. In fact, this study suggests that mass transfer coefficients may be superior to heat transfer coefficients for use in characterizing and correlating heat transfer data in closed, condensing systems. Unfortunately, vapor concentrations are are often difficult to measure experimentally, particularly when mist formation is present. Nevertheless, significant changes in system temperature may accompany mist formation and this fact should be kept in mind when performing experimental investigations.

REFERENCES

[1] W. J. Minkowycz and E.M. Sparrow,, "Condensation heat transfer in the presence of noncondensables, interfacial resistance, superheating, variable properties, and diffusion," International Journal of Heat and Mass Transfer 9, 1125-1142 (1966).

[2] E. M. Sparrow, W. J. Minkowycz, and M. Saddy, "Forced convection condensation in the presence of non-condensable and interfacial resistance," International Journal of Heat and Mass Transfer 10, 1829-1845 (1966).

[3] K. Hijikata and Y. Mori, "Forced convective condensation heat transfer with noncondensable gas on a vertical flat plate," International Journal of Heat and Mass Transfer 16, 2229-2240 (1973).

[4] K. Hijikata and Y. Mori, "Forced Convective Condensation Heat Transfer of a Gas with Condensing Vapour Around a Flat Plate," Heat Transfer - Japanese Research 2, 81-101 (1973).

[5] F. Legay-Desequelles and B. Prunet-Foch, "Heat and mass transfer with condensation in laminar and turbulent boundary layers along a flat plate," International Journal of Heat and Mass Transfer 29, 95-105 (1986).

[6] W.P. Jones and U. Renz, "Condensation from a turbulent stream onto a vertical surface," International Journal of Heat and Mass Transfer 17, 1019-1028 (1974).

[7] H.L. Toor, "Fog formation in boundary value problems," AIChE Journal 17, 5-14 (1971).

[8] H.J.H. Brouwers, "Film models for transport phenomena with fog formation: The classical film model," International Journal of Heat and Mass Transfer 35, 1-11 (1992).

[9] H.J.H. Brouwers, "Film models for transport phenomena with fog formation: The fog film model," International Journal of Heat and Mass Transfer 35, 13-28 (1992).

[10] D.E. Rosner, "Enhancement of diffusion-limited vaporization rates by condensation within the thermal boundary layer 1. The critical supersaturation approximation," International Journal of Heat and Mass Transfer 10, 1267-1279 (1967).

[11] M. Epstein and D.E. Rosner, "Enhancement of diffusion-limited vaporization rates by condensation within the thermal boundary layer 2. Comparison of homogenous nucleation theory with the critical supersaturation model," International Journal of Heat and Mass Transfer 13, 1393-1414 (1970).

[12] Y. Hayashi, A. Takimoto, and M. Kanbe, "Mechanism of mist formation based on a critical supersaturation model in a turbulent convective field," Heat Transfer - Japanese Research 7, 14-25 (1978).

[13] D.P. Sekulic, "Irreversible condensation conditions near the cryosurface," International Journal of Heat and Mass Transfer 28, 1205-1214 (1985).

[14] P.D. Dunn and D.A. Reay, Heat Pipes, Pergamon Press, New York (1982).

[15] P.F. Peterson and C.L. Tien, "Numerical and analytic solutions for two-dimensional gas distribution in gas-loaded heat pipes," Journal of Heat Transfer 111, 598-604 (1989).

[16] P. F. Peterson, N. Elkouh, K.W. Lee, and C.L. and Tien, "Flow instability and bifurcation in gas-loaded reflux thermosyphons," Journal of Heat Transfer 113, 158-165 (1991).

[17] Y. Mori, Y., K. Hijikata, and K. Utsunomiya, "The effect of noncondensable gas on film condensation along a vertical plate in an enclosed chamber," Journal of Heat Transfer 99, 257-262 (1977).

[18] R.J. Fox, T. Nagasaki, K. Hijikata, and P.F. Peterson, "Reflux condensation of binary mixtures in a two-phase thermosyphon," HTD-Vol. 262. ASME Winter Annual Meeting, 65-73 (1993).

[19] R.J. Fox, Mixed Convective Condensation in Enclosures with Noncondensable Gases, Ph.D. Dissertation - Nuclear Engineering, University of California at Berkeley (1994).

[20] F. Issacci, I. Catton, and N.M. Ghoniem, "Vapor dynamics of heat pipe start-up," ASME Journal of Heat Transfer 113, 985-994 (1991).

[21] B.R. Bird, W.E. Stewart, and E.N. Lightfoot, Transport Phenomena, Wiley, New York, (1960).

[22] W.M Kays and M.E. Crawford, Convective Heat and Mass Transfer, McGraw-Hill, New York (1993).

[23] K. Hijikata, T. Nagasaki, J. Yashioka, and Y. Mori, "A study on flow characteristics and heat transfer in countercurrent water and air flows," JSME International Journal 31, No. 3, 429-436 (1988).

[24] V.P. Carey, Liquid-Vapor Phase Change Phenomena, Hemisphere, Washington (1992).

[25] J.I. Yellott, "Supersaturated steam," Transactions of the ASME 56, 411-430 (1934).

[26] A. Huser, and S. Biringen, "Calculation of two-dimensional shear-driven cavity flows at high reynolds numbers," International Journal of Numerical Methods in Fluids 14, 1087-1109 (1992).

[27] P.M. Gresho, "On the theory of semi-implicit projection methods for viscous incompressible flow and its implementation via a finite element method that also introduces a nearly consistent mass matrix, part I: Theory," International Journal of Numerical Methods in Fluids 59, 587-620 (1990).

[28] C.A.J. Fletcher, Computational Techniques for Fluid Dynamics, Vol. II, Springer-Verlag, New York (1988).

[29] B. van Leer, "Towards the ultimate conservative difference scheme. IV. A new approach to numerical convection," Journal of Computational Physics 23, 276-299 (1977).

[30] E. Dick, and J. Linden, "A multigrid method for steady state incompressible Navier-Stokes equations based on flux difference splitting," International Journal of Heat and Mass Transfer 14, 1311-1323 (1992).

NOMENCLATURE

C	MCSM model constant or spectral power of
c_p	specific heat (J/kg)
D	binary diffusion coefficient (m^2/s)
F_B	buoyancy force (N), $F_B = (\rho - \overline{\rho})g$
Fr	Froude number
g	gravitational acceleration (m/s^2)
H	enthalpy (J/kg)
H	condenser height (cm)
h_{fg}	latent heat of vaporization (J/kg)
J	total flux
J	mist nucleation rate
Ja	Jakob number, $Ja = c_p(T_e - T_w) / h_{fg}$
k	thermal conductivity (W/m-K)
Le	Lewis number, $Le = \alpha / D$
$\dot{m}$	condensation rate in the vapor phase (kg/m^3-s)
$\dot{m}_c$	film condensation rate (kg/m^2-s)
M	molecular weight (g/mol)
P	system pressure (Pa)
P_m	motion pressure (Pa)
Q'	linear heat rate (W/m)
P_h	hydrostatic pressure (Pa)
q_w	wall heat flux (W/m^2-s)
R	ideal gas constant ($R = 8.314$ J / mol - K)
S	source term or supersaturation ratio
t	time (s)
T	temperature (K)
u	horizontal velocity (m/s)
v	vertical velocity (m/s)
v_{in}	inlet velocity
W	condenser width (cm)
x	horizontal coordinate (m)
y	vertical coordinate (m)

α_l volume fraction of liquid droplets $\alpha_l = V_l/V$
Γ diffusive flux
Δt time step (s) (Eq. 3-26)
μ dynamic viscosity (kg/m-s)
ν kinematic viscosity (m^2/s)
ω_i species mass fraction $\omega_i = \rho_i/\overline{\rho}$
ϕ conserved quantity
ρ density (kg/m^3)
$\overline{\rho}$ average density

Superscripts
* first guess velocity field
' velocity or pressure correction
n time step n
0 initial
1 final

Subscripts
e evaporator
g gas phase
i index or interface
in inlet
l liquid phase (mist)
sat saturation
u velocity
v vapor phase
vl vapor+liquid
w wall
0 initial

Condensation in the Presence of Noncondensible Gases: AP600 Containment Simulation

M.H. Anderson, M.L. Corradini
Department of Nuclear Engineering and Engineering Physics
University of Wisconsin, WI 53706

Abstract

The Westinghouse Electric Corporation has designed an advanced pressurized light water reactor, AP600. This reactor is designed with a passive cooling system to remove sensible and decay heat from the containment. The heat removal path involves condensation heat transfer, aided by natural convective forces generated by buoyancy effects. A one-twelfth scale rectangular slice of the proposed reactor containment was constructed at the University of Wisconsin to simulate conditions anticipated from transients and accidents that may occur in a full scale containment vessel under a variety of conditions. Similitude of the test facility was obtained by considering the appropriate dimensionless group for the natural convective process (modified Froude number) and the aspect ratio (H/R) of the containment vessel.

An experimental investigation to determine the heat transfer coefficients associated with condensation on a vertical and horizontal cooled wall (located in the scaled test section) at several different inlet steam flow rates and test section temperatures was conducted. In this series of experiments, the non-condensible mass fraction varied between (0.9-0.4) with corresponding mixture temperatures between 60-90°C . The heat transfer coefficients of the top horizontal surface varied from (82-296)W/m^2K and the vertical side heat transfer coefficients varied form (70-268)W/m^2K. The results were then compared to boundary layer heat and mass transfer theory by the use of the McAdams correlation for free convection.

Introduction:

A primary concern involved in the safety of nuclear power generation is the prevention or mitigation of an accident occurring in which radioactive byproducts may be released into the atmosphere One such event is a primary system pipe break, in which a large amount of primary system water discharges and flashes into steam. This will cause an increase in pressure and temperature in the containment atmosphere. This increase in the pressure and temperature must be controlled by some mechanism before the containment structural integrity is compromised. The mechanisms which are currently in use for operating light water reactors rely principally on active safety systems to spray cold water into the containment to condense the steam. These active safety systems require the use of AC power to drive the injection pumps, which must be supplied by either backup diesel generators or off-site power. This not only adds further cost to the plant construction but also adds more mechanical components whose reliability must be considered in

the event of an accident. New advanced reactor designs have included the use of passive cooling techniques which seek to take advantage of the natural circulation process within containment, eliminating costly mechanical components and adding improved reliability. The Westinghouse Electric Corporation has designed a 600 MWe pressurized light water reactor (AP600) that utilizes these concepts integrated into the passive safety system.

The AP600 utilizes a passive containment cooling system (PCCS) to transfer sensible and core decay heat from within the reactor containment to the atmosphere, during an accident, without compromising the containment vessel. The PCCS incorporates large water reservoirs situated above the containment vessel that are opened allowing water to flow by gravity over the containment shell. This assists natural circulation in removing heat primarily during the initial hours of an accident when the core decay heat is high. A water film develops from the flow of water over the outer shell of the steel containment which provides an evaporative cooling mechanism which increases the heat transfer coefficient on the outside of the containment. This heat sink causes the steam inside the containment to condense on the inner surface. This results in an overall increase in the heat removal capability of the containment structure. The energy removal rate is therefore governed by the evaporation of the water film on the outside of the containment and the energy transferred by condensation of the steam in the presence of non-condensible gases on the inside of the containment [1].

A series of experiments investigating the condensation of steam in the presence of noncondensible gas was conducted to measure the resulting heat transfer coefficients. Several tests were performed with differing ratios of air, helium, and steam to quantify the effects of non-condensible gases that may be present in the containment during an accident. The introduction of helium was used to model the possible presence of hydrogen gas in the containment atmosphere due to clad oxidation. This light non-condensible gas could have a variety of different effects. It could alter the effective diffusion coefficient and may also preferentially collect near the top of containment, due to the small molecular weight of the gas, which would increase the noncondensible gas barrier.

The set of experiments described in this paper differ from most previous studies [7, 3] due to a similar aspect ratio to the AP600. In past tests this was not the case and some of the important aspects of the heat transfer phenomena may have been overlooked, so that specific separate effects could be studied. For example; Huhtiniemi [3] investigated the effects of orientation of a cooled surface on condensation along with differing forced flow convection studies and Pernsteiner [4] considered the effects of helium concentrations. These studies were similar to the current tests except that they lacked the similar aspect ratios between the AP600 and there facilities. One of the major factors that we wished to resolve with our current study is the possible enhancement of the overall heat transfer rate due to mixed convection effects as the length scale increases. Our facility was designed to account for these effects by maintaining proper aspect ratios, while still being able to make precise measurements.

Experimental Facility

Our facility for testing the effectiveness of the AP600's PCCS heat removal capabilities is shown in Fig [1]. It consists of a rectangular shaped test section 243.8 cm tall, 1*2.9 cm wide and 31.8 cm in depth with a horizontal and vertical aluminum condensing surface located in the upper right hand corner of the apparatus. A Sussman model ES-7L boiler is used to provide the steam flow into the test section. The energy removal takes place on horizontally and vertically oriented condensing surfaces, which are held at a constant temperature of approximately 30°C by cooling plates bolted to the back side. Coolant water, supplied by a Neslab HX-150 constant temperature bath was passed through a series of Dwyer RMC-141 flow meters into the cooling plates. The steam flow rate was measured with an ASME spec. orifice flow meter, and throttled to a mass flow rate sufficient to produce a steady state test section temperature of 60,70,80,85, or 90°C.

Figure [2] is a schematic diagram of the test section. It consists of a front and back sheet of 1/2" thick ploycarbonate (Lexan^{TM}). The two 1.5" thick aluminum condensing plates are located in the upper right hand corner of the test section. Each plate is 36" long and 12" wide, which yields a total surface area of 864 sq.in. The test section was constructed to minimize the thermal conduction from the cold condensation plates to the rest of the test section. This would minimize any secondary conduction effects.

The two condensing plates were constructed from 2024t351 aluminum plate machined to 3'x1'x1.5". Thermophysical properties of the aluminum, needed in the heat transfer coefficient calculation were determined at TPRL (Thermo-physical Properties Research Laboratory) [2]. A surface finish similar to that of the proposed AP600 containment was obtained by sand blasting and coating the aluminum plates with a 3.75 mil thick coat of inorganic zinc paint. A set of three probe holes were drilled into the back side of the condensing plates every six inches to allow for the insertion of thermocouple heat flux meters Fig [3].

Measurement Techniques

The heat flux meters (HTFM's) mentioned above were one of the two independent means of measuring the heat transfer coefficient. The HTFM's provided a local measure of the heat transfer coefficient. The second method, an energy balance on the coolant fluid (CEB), provided an average heat transfer coefficient over the area of a 6"x12" coolant plate. The HTFM's consisted of a set of four E-type thermocouples encased in a 3/16" O.D. stainless steel tube separated by a distance of 5/16". (E-type thermocouple grade wire was used because both elements have a low thermal conductivity, good resistance to corrosion and high Seebeck coefficients). The heat transfer coefficient was determined by recording the temperature at each thermocouple location in the probe. By knowing the temperature gradient in the plate we could find the heat transfer coefficient with the equation:

$$h = \frac{k\frac{dT_{plate}}{dx}}{T_{mix} - T_{surf}} \tag{1}$$

Where h is the heat transfer coefficient, k is the thermal conductivity of the aluminum plate, T_{mix} is the local test section mixture temperature and T_{surf} is the plate surface temperature. Assuming a linear temperature dependence the plate temperature is given by the equation:

$$T_{alum}(x) = \frac{dT_{alum}}{dx}x + T_{back} \tag{2}$$

The second method of determination of the heat transfer coefficient was a coolant energy balance. Temperature controlled water was passed through a flow meter and then through coolant channels in the coolant plates. As the coolant flows through the channel the temperature increases due to the removal of energy from the test section. The temperature difference between the incoming water and the exiting water was measured with a series of E-type thermocouples. An energy balance on the liquid would then result in the heat flux which in turn could be used to calculate the heat transfer coefficient.

$$q_i'' = \frac{\rho_{cool} C(V'\Delta T)}{A_i} \tag{3}$$

$$h = \frac{q_i''}{T_{mix} - T_{surf}} \tag{4}$$

Where ρ_{cool} is the density of the coolant (water), C is the specific heat, V' is the volume flow rate and A_i is the area of the cooling plate. T_{mix} is the bulk gas temperature measured at a distance of about 3 inches from the cooling surface and T_{surf} is the coolant plate surface temperature. This method of the determination of the heat transfer coefficient is different than the HTFM's because this methodology measures the heat flux as an area average over the surface area of the coolant plate. The HTFM's measure the heat flux in the vicinity surrounding the probes. Although these are two different types of measurements they should yield similar results and they were found to agree to within 10% for the tests considered.

Scaling Consideration

The experiments were designed to represent a two-dimensional slice of the upper dome of the AP600 containment; i.e., from the radial center to the wall of the relatively open region above the operating deck in the containment. This representation assumes that any flow patterns are axisymmetric along the center of the containment. In addition, the size of the experiment is small enough (1:12 linear scale) that we must consider how the governing dimensionless groups are affected by these geometric distortions. In the past, our method of investigation of the condensation heat transfer upon the cooled surfaces similar to the AP600 walls indicated that for a large number of conditions a mixed convection regime may be present in the containment for low forced convective velocities; i.e., less than 1-3 m/s [3, 4]. Based on this analysis it seems that the most appropriate dimensionless group to preserve in our experiments is a modified Froude Number given by the expression:

$$Fr = \frac{\rho v^2}{\Delta\rho g L} \tag{5}$$

where ρ is the density of the gas mixture, $\Delta\rho$ is the difference in density between the bulk gas and the gas mixture near the interface at the cold wall, v is the bulk gas velocity, g is the gravitational acceleration and L is the characteristic length. For our analysis we have assumed that the gas velocity can be represented by the steam velocity entering the upper-dome containment from a compartment below the operating deck. This dimensionless group is felt to be the most important because it is the ratio of the natural convection forces to the forced convection forces in the volume.

Experimental Results

A series of experiments were conducted to categorize the effects of condensation in the presence of noncondensible gases. It was first necessary to investigate the effects of the test section walls. The test section was designed to mimic a two dimension slice of the upper portion of the containment, as described previously. The test section width was only about 1 foot, therefore it was necessary to document the effect that these walls had on the heat transfer coefficient in the y-component (width) of the test section. To investigate any significant gradients we took measurements of the heat flux in the aluminum plate in three different positions in the y-direction 1.5", 6", and 11.5" as measured from the front of the test section. The results of this investigation showed that the variation of the heat transfer coefficient in the y-direction were less than the error in the measurements. This does not preclude any wall effects on the velocity field , however it does suggest that the test section can be considered as two-dimensional at least in respect to the heat transfer coefficients. Since the heat transfer coefficient is a function of the bulk velocity this would also suggest that there is little change in the y-direction velocity close to the condensing plate.

The remainder of investigations discussed in this paper consider condensation in the presence of differing noncondensible concentrations, including the effects of the presence of helium in molar amounts between 0 and 30 %. The tests were conducted by filling the test section with either air or a known gas mixture of air and helium. This was accomplished by passing a stream of compressed air and a stream of compressed helium through separate flow meters. By adjusting the flow rates of the two different gases we could obtain an approximate air/helium ratio. After the gases were injected local gas samples were collected in the bulk of the test section and analyzed, to determine the true mass fractions of air and helium, on a mass spectrometer. Then steam was injected into the atmosphere at mass flow rates sufficient to raise the test section bulk atmosphere to a quasi-steady state temperature of 60,70,80,85, or 90 $^{\circ}C$ as measured by a thermocouple positioned as shown in Figure [2]. The test section was allowed to exhaust the air helium mixture to the surroundings in order to maintain a test section pressure of 1 atm. therefore setting the non-condensible mass fraction for a given temperature. The gas in the test section was exhausted into a reservoir of water to prevent outside air from entering the test section as the steam was injected. When one of the above temperatures was reached another gas sample was taking to determine the exact mass fractions of the relevant gases for that particular text. Figures [4,5] are graphs of typical heat transfer coefficients that result from a test section bulk

temperature of $80°C$. Figure [4] gives the heat transfer coefficients measured on the horizontal condensing plate and Figure [5] gives the heat transfer coefficients on the vertical plate. The dotted line depicts the heat transfer coefficient measured with the HTFM and the bar graph indicates the heat transfer coefficient measured with the CEB method. The errors calculated from sample and error analysis techniques are shown for both methods with corresponding error bars. A definite trend in the heat transfer coefficient was observed. As we move along the vertical plate from the top of the test section down, the heat transfer coefficients decrease fairly steadily until reaching a vertical distance of approximately 40 cm from the corner of the test section. At this point there is a slight increase in the heat transfer coefficients which usually continues across the rest of the condensing plate length. The behavior of the top (horizontal) plate seems to be more sporadic than the vertical side plate. The top plate consistently has a higher heat transfer coefficient than the vertical plate. There also appears to be a slightly higher discrepancy between the HTFM's and the CEB measurements of heat transfer coefficients of the horizontal plate, however they still lie within the error of the measurements. The effects of the increased heat transfer rate and the discrepancy in the two methods of measurement may be a result of droplet formation and the presence of rain from the top surface.

The inorganic zinc coating of the condensing surface promotes film-wise condensation, however as noted by Huhtiniemi [3] (who used a similar coating) at angles of less than 1° and with velocities less than 1 m/s droplets will form on the surface. Visual observation of the horizontal plate confirmed the presence of droplet formation along with a liquid film, while the vertical plate was observed to have pure film-wise condensation. The droplets on the top plate varied in size from approximately 0.2 cm to 0.5 cm. The presence of the droplets could have many effects on the heat transfer coefficient. They tend to effectively increase the heat transfer surface area and perhaps increase the heat transfer coefficient due to the enhancement of turbulent mixing caused by the droplet departure.

The procedure used in the introduction of helium slightly differs from what would occur in a actual accident scenario. We supply an initial concentration of air/helium mixture then enter steam. In an actual LOCA the steam entering the containment atmosphere would have reacted with the zircaloy cladding in the reactor pressure vessel. This oxidation reaction would replace some of the steam with hydrogen gas. In our experiments the amount of helium to air ratio stays constant while the total noncondensible gas mass fraction decreases with test section bulk temperature. This difference does not alter the experimental findings however, a correction of the amount of noncondensible gas introduced in the experiment may have to be made to compare this data to an actual accident scenario. Figures [6, 7] show the effects of increasing the helium molar concentration of the total non-condensible gas. There appears to be a degradation in the heat transfer coefficient in the horizontal plate a distance of approximately 23 cm from the right hand corner and on the vertical plate approximately 68 cm from the top corner of the condensing plate. This usually occurred when the helium concentrations were above approximately 4% however some tests with helium concentrations above this value did not always exhibit this phenomena. The origin of this degradation is not known, it may be some sort of random flow phenomena caused by the light helium gas accumulation, or it may be some yet undetected systematic error. Other than this unexplained local reduction in the heat transfer coefficient the introduction of

helium seems to have little effect. This was also observed by Pernsteiner [4]. He attempted to explain this by considering that the increase in the diffusion coefficient of steam through helium was offset by a stratification of additional noncondensible gas near the condensing surface thus creating little change in the resulting mass transfer.

Modeling Analysis

In an effort to compare the experimental results to boundary layer heat and mass transfer theory we used the McAdams correlation for free convection. This correlation relates the Nusselt Number to the Grashoff and Prandlt Numbers as follows:

$$Nu = 0.13 Gr^{\frac{1}{3}} Pr^{\frac{1}{3}} \tag{6}$$

To obtain a similar correlation for mass transfer, which accounts for the majority of the total energy transfer, the McAdams correlation was used with the momentum heat and mass transfer analogy. Thus, the Nusselt Number is replaced with the Sherwood Number and the Prandlt Number with the Schmidt Number. In the development of the McAdams correlation it was assumed that the flow across the plate was tangential thus the normal flow was neglected. In our situation there is a superimposed effect due to the normal component of the velocity, which will result in an increase in the total heat transfer coefficient. To account for this normal flow Bird et.al [6] suggests a multiplication factor be added in addition to the change of dimensionless numbers.

$$Sh = 0.13 Gr^{\frac{1}{3}} Sc^{\frac{1}{3}} \theta \tag{7}$$

where θ is the correction factor and is given by:

$$\theta = \frac{ln(R+1)}{R} \tag{8}$$

$$R = \frac{x_i - x_b}{1 - x_i} \tag{9}$$

The above equations which were developed from similarity arguments are dimensionless and independent of the length scale (Peterson et.al.) [8, 9]. They were also arrived at considering the Grashoff number based on a temperature difference rather than the Grashoff Number based on the total density difference. In our experiment the density is a function of both temperature and steam concentration. To include the effects of the concentration gradients it was felt more appropriate to use the Grashoff Number based on the total density difference, rather than just the temperature differences.

$$Gr = \frac{\rho \Delta \rho g L^3}{\mu^2} \tag{10}$$

The mixture properties of the bulk along with the properties at the condensing wall were used in the calculation of the convective heat transfer coefficient and

Bulk Temperature $^{\circ}C$	60 $^{\circ}C$	70 $^{\circ}C$	80 $^{\circ}C$	85 $^{\circ}C$	90 $^{\circ}C$
HTFM Horizontal plate $W/m^{2\circ}C$	88.23	115.24	209.50	229.84	295.28
CEB Horizontal Plate $W/m^{2\circ}C$	82.32	112.04	195.32	238.15	303.17
HTFM Vertical Plate $W/m^{2\circ}C$	70.53	95.24	168.40	178.02	230.66
CEB Vertical Plate $W/m^{2\circ}C$	71.07	99.79	173.32	201.74	267.45
McAdams Correlation $W/m^{2\circ}C$	71.06	106.28	162.61	206.46	273.13
m_{st}/m_{air}	0.133	0.218	0.355	0.455	0.586
D_0	$4.147e^{-5}$	$4.062e^{-5}$	$3.977e^{-5}$	$3.809e^{-5}$	$3.644e^{-5}$

Table 1: Comparison between Experimental Data and McAdams Correlation

the condensation heat transfer coefficient. The convection heat transfer coefficient can be determined directly by the definition of the Nusselt Number. In order to calculate the condensation heat transfer coefficient it is first necessary to calculate the mass transfer coefficient κ_m from the definition of the Sherwood Number. An approximation of the diffusion coefficient of steam in air was calculated from the following equation recommended by Rohsenow et.al [5].

$$D_0 = 0.0069 \frac{T^{3/2}}{P(V_a^{1/3} + V_b^{1/3})^2} \sqrt{\frac{1}{M_a} + \frac{1}{M_b}} \tag{11}$$

where T is the temperature in $^{\circ}R$, V_a and V_b are atomic volumes given in table 14.1 of reference [5], and P is the pressure in atmospheres. The mass flow rate is then given by the expression:

$$m = \kappa_m (C_g - C_w) \tag{12}$$

where C_g and C_w are the local vapor concentrations of the bulk gas and the wall respectively. The condensation heat transfer coefficient is then found by substituting the previous equation into the expression:

$$h_{cond} = \frac{m(i_{v,bulk} - i_{f,wall})}{T_{bulk} - T_{wall}} \tag{13}$$

The total heat transfer coefficient from the bulk to the wall is the sum of the contributions of the convective heat transfer and the condensation heat transfer ($h_{tot} = h_{conv} + h_{cond}$). The results of this analysis are compared with selected data in table [1].

Conclusions

Experiments were conducted to determine the heat transfer coefficient of steam in the presence of non-condensible gases, on horizontal and vertical cooled condensing plates with a similar surface finish to the Westinghouse AP600 containment. The aspect ratio of the experiment to the proposed containment was maintained to allow investigation of mixed convection effects. The results were found to yield heat transfer coefficients similar to those found by Huhtiniemi and Pernsteiner which suggest that there is not much effect of mixed convection. It was found that the heat transfer coefficient on the top (horizontal) surface was higher than that on the vertical plate by 10-20 %. This observation was possibly due to the presence of droplets on the upper surface as compared to a film on the vertical surface. Further work is needed to attempt to quantify the effects of the differing modes of condensation. Huhtiniemi [3] noted that at increasing angles of an inclined plate or increasing velocities across the plate surface the presence of the droplets diminish and a film forms on the plate surface. This suggests that one could study the effects of the presence of these droplets by inclining the horizontal condensing plate at differing angles.

Comparison of air/helium/steam tests with differing molar fractions of helium were found to have little effect on the overall heat transfer coefficients. This is consistent with the findings of Pernsteiner [4], however other investigators Dehbi [7] have noticed some effect in the HTC for large mole fractions of helium. The test conditions in our apparatus were limited to bulk temperatures ranging between 60-90 °C with pressures of one atmosphere. In this range of test conditions the McAdams Correlation for heat and mass transfer was found to predict the experimental results to well within 10% for the vertically cooled surface.

It is not yet known if the correlation will correctly predict the average heat transfer coefficients outside the range of tests. Actual containment pressures are usually in the range of 2-4 bar therefore the effects of higher pressures on the HTC need to be investigated. The current tests were conducted with a uniform steam injection system, whereas in accidental situations there may be a significant plume of steam from a particular location in the containment; e.g., the steam generator compartment. The effects of this more realistic distribution of steam injection could change the velocity field inside the test section thus alter the HTC. To obtain a more realistic energy removal rate the above mentioned factors will be investigated in future experiments.

Acknowledgments

We gratefully acknowledge Mr. Fred Peters and Mr. Dan Spencer for their invaluable consultation and the Westinghouse Electric Corporation and the Department of Energy for their continued financial support.

References

[1] Private Communication Dan Spencer Westinghouse Electric Corporation, Aug. 1994

[2] M. H. Anderson, M. L. Corradini, "Condensation in the Presence of Noncondensible Gases: AP600 Containment Simulation," Prelim, Aug. 1994

[3] I. K. Huhtiniemi, Condensation in the Presence of a Non-condensible Gas: The Effects of Surface Orientation, PhD Thesis, University of Wisconsin, (1991)

[4] A. P. Pernsteiner, Condensation in the Presence of a Non-condensible Gas: Effects of Helium Concentration, MS Thesis, University of Wisconsin, (1993)

[5] W. M. Rohsenow, Heat, Mass and Momentum Transfer, Prentice-Hall, (1961)

[6] R. B. Bird, W. E. Stewart, E. D. Lightfoot, Transport Phenomena, John Wiley, (1960)

[7] A. A. Dehbi, Analytical and Experimental Investigation of the Effects of Noncondensible Gases on Steam Condensation under Turbulent Natural Convection Conditions, PhD Thesis, Dept. of Nuclear Engineering, MIT, Jan. 1991

[8] P.F. Peterson, V.E. Schrock, T. Kageyama, "Diffusion Layer Theory for Turbulent Vapor Condensation with Noncondensible Gases," National Heat Transfer Conference, 1992

[9] P.F. Peterson, V.E. Schrock, T. Kageyama, "Diffusion Layer Theory for Turbulent Vapor Condensation with Noncondensible Gases," *Journal of Heat Transfer, Vol.115, pp. 998-1003, 1993*

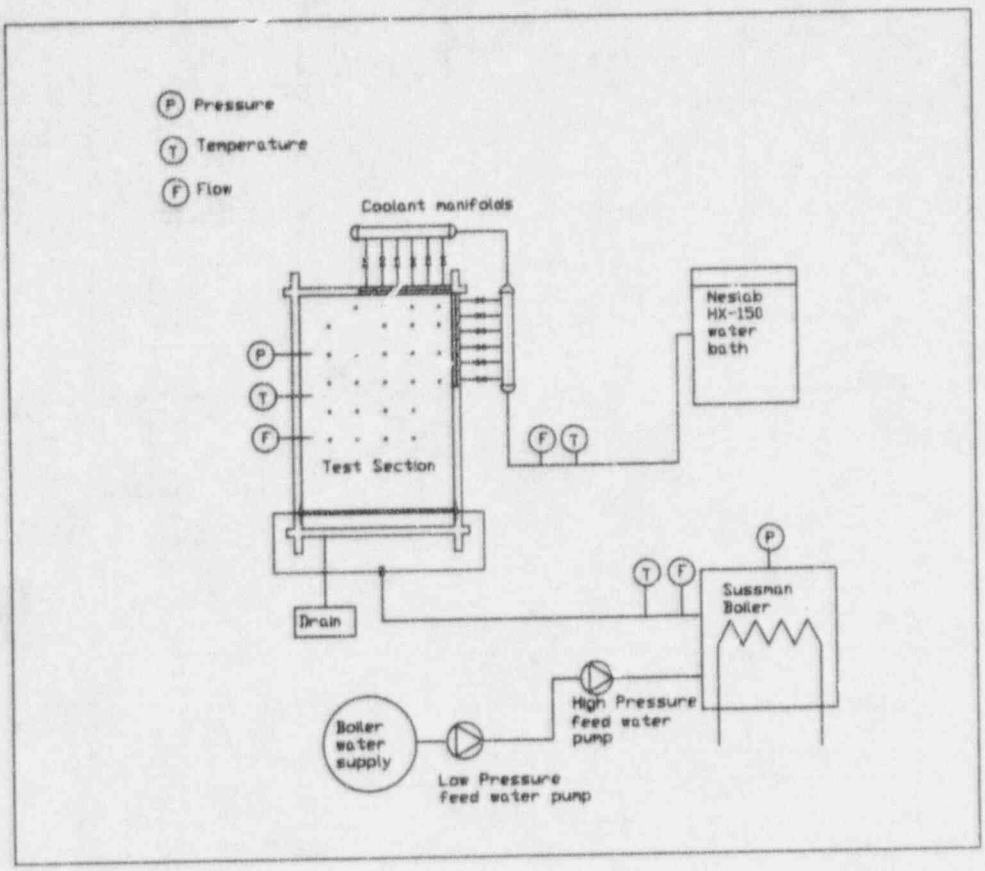

Figure 1: Schematic of Experimental Facility

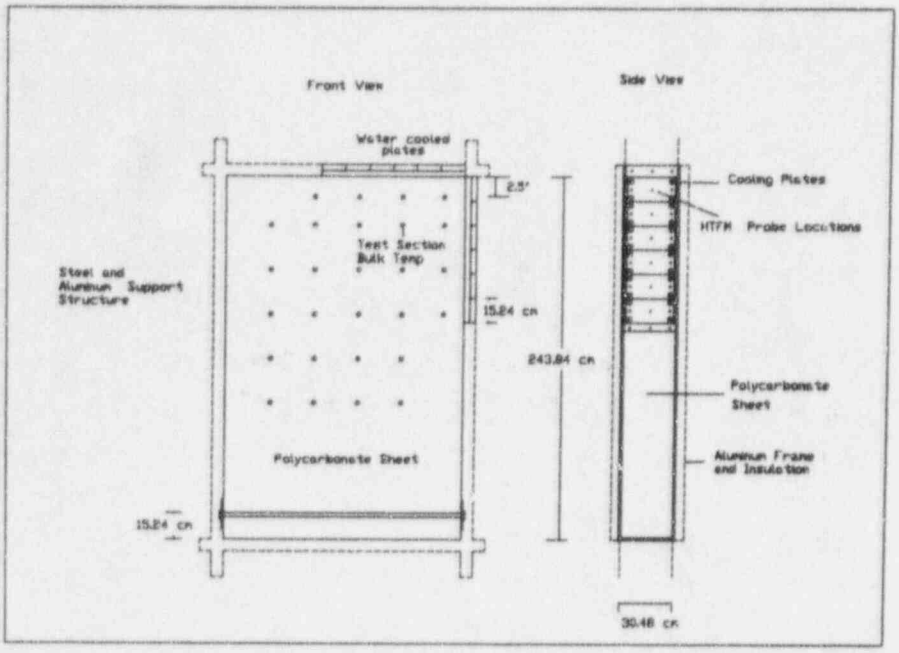

Figure 2: Schematic of test section

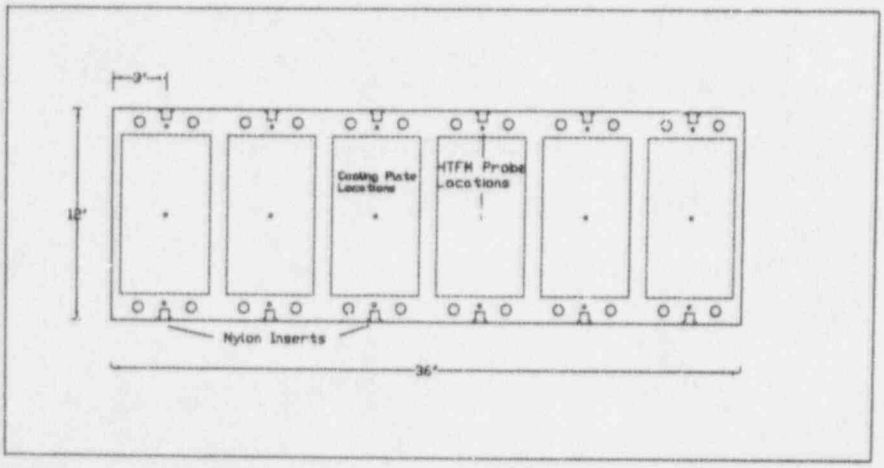

Figure 3: Condensing Plate

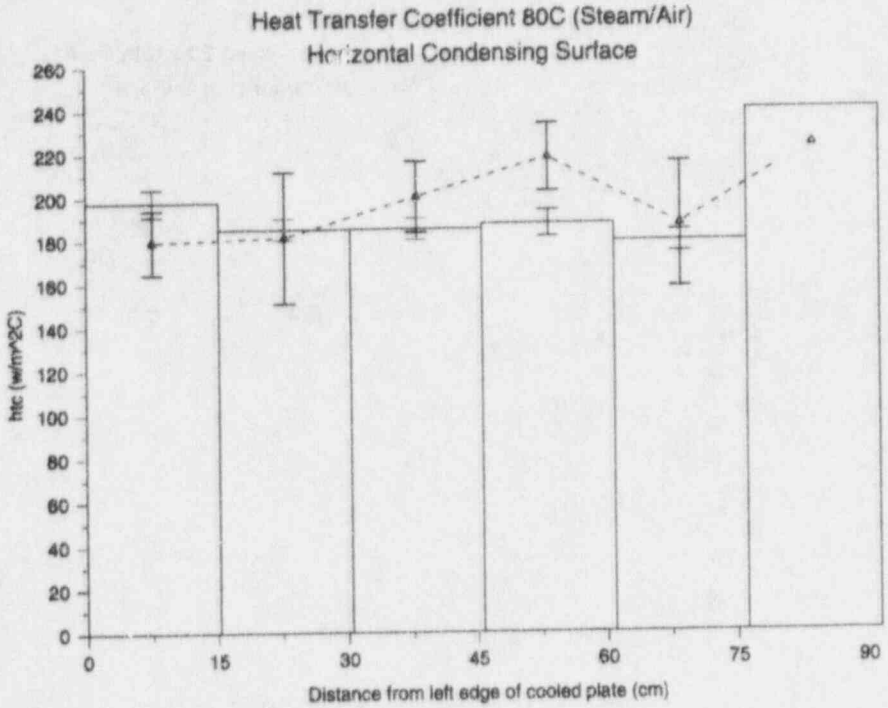

Figure 4: Air/Steam Mixture at $80°C$ Saturated ($m_{st}m_{air} = 0.355$)

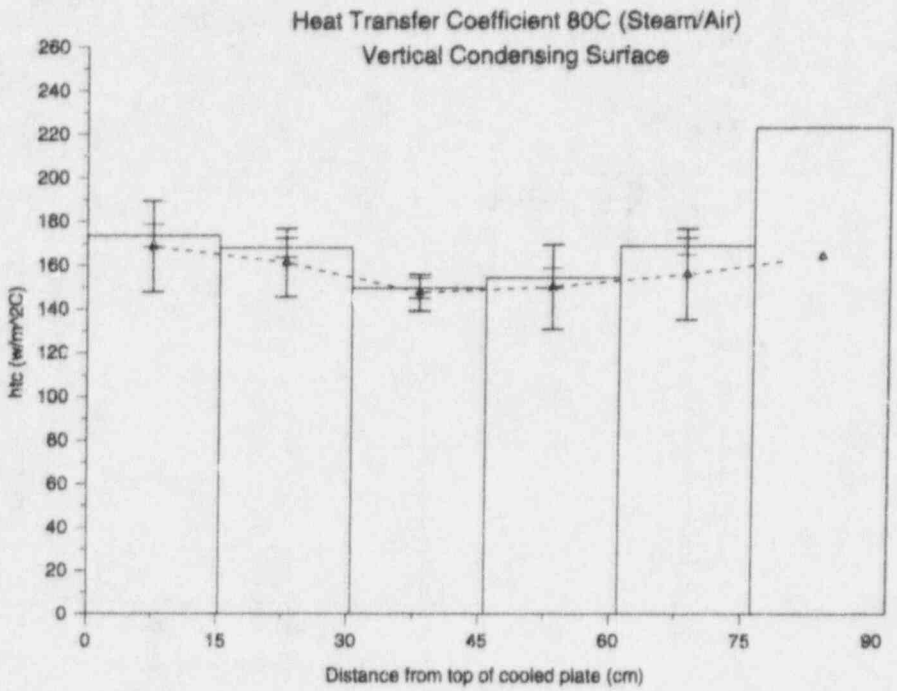

Figure 5: Air/Steam Mixture at $80°C$ Saturated ($m_{st}/m_{air} = 0.355$)

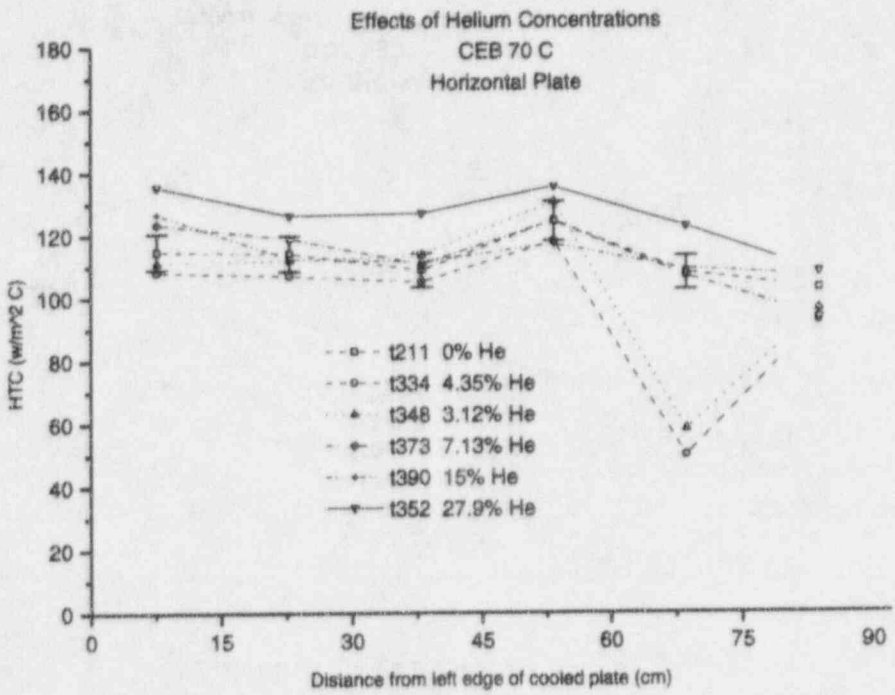

Figure 6: Effects of Helium ($m_{st}/m_{noncond} = 0.218$)

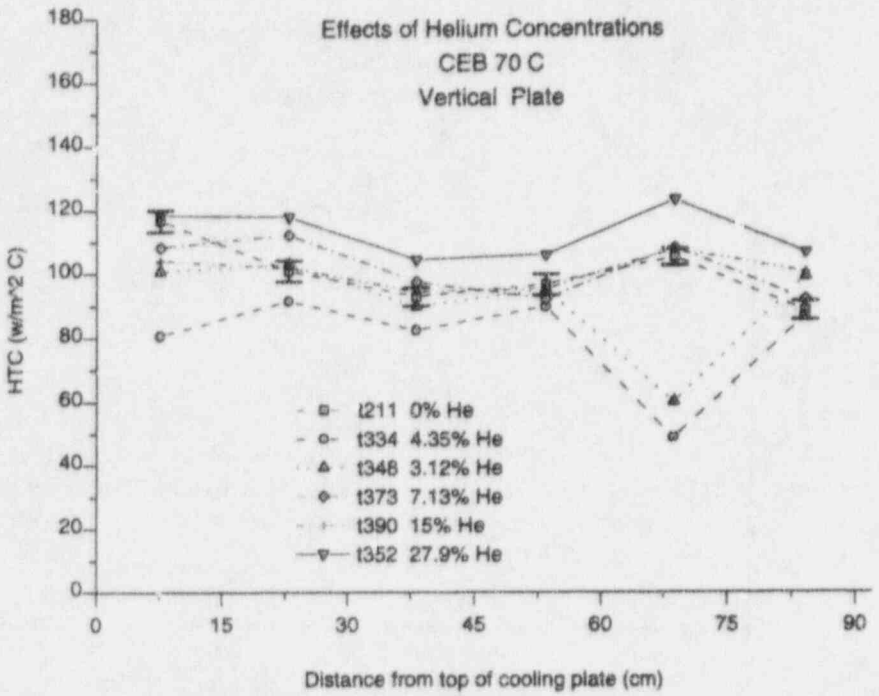

Figure 7: Effects of Helium ($m_{st}/m_{noncond} = 0.218$)

Hydrogen Behavior in Ice Condenser Containments

Petra Lundström, Peter Gango, and Harri Tuomisto
IVO International Ltd
01019 IVO, Finland

Olli Hongisto
Power Plant Laboratory
Imatran Voima Ltd
Viikintie 3, 00560 Helsinki, Finland

T.G. Theofanous
Center for Risk Studies and Safety
Department of Chemical and Nuclear Engineering
University of California, Santa Barbara
Santa Barbara, California 93106, USA

ABSTRACT

A new hydrogen management strategy is being developed for the Loviisa ice condenser containment. The strategy relies on containment-wide natural circulations that develop, once the ice condenser doors are forced open, to effectively produce a well-mixed behavior, and a correspondingly slow rise in hydrogen concentration. Levels can then be kept low by a distributed catalytic recombiner system, and (perhaps) an igniter system as a backup, while the associated energy releases can be effectively dissipated in the ice bed. Verification and fine-tuning of the approach is carried out experimentally in the VICTORIA facility and by associated scaling/modelling studies. VICTORIA represents an 1/15th scale model of the Loviisa containment, hydrogen is simulated by helium, and local concentration measurements are obtained by a newly developed instrument specifically for this purpose, called SPARTA. This paper is focused on experimental results from several key experiments that provide a first delineation of key behaviors.

1 INTRODUCTION

The Loviisa nuclear power plant is a two-unit VVER-440 owned and operated by Imatran Voima Ltd (IVO). The reactor containment has a free volume of 57 000 m^3, a design pressure of 1.7 bar(a) and an ultimate failure pressure of 3.25 bar(a). The containment was equipped with a Westinghouse-type ice condenser containing 835 000 kg ice in two sections. Ice condensers are very efficient heat sinks during the initial phase of the accident (lasting at least 5-10 hours from the beginning of the accident, depending on the scenario), which is the reason why the containment design pressure is rather low.

The containment features described above cause the Loviisa containments to be somewhat sensitive to pressure loads resulting from hydrogen combustion. The failure pressure can be exceeded in global deflagrations of mixtures containing rather moderate hydrogen molar fractions. The ice bed is not necessarily efficient in moderating these loads. The steam component of a hydrogen-steam-air mixture is removed through efficient condensation in the ice bed, which results in local hydrogen enrichment of the gas mixture. Therefore ice condensers add a new dimension of complexity to the hydrogen management problem compared to e.g. a large dry containment.

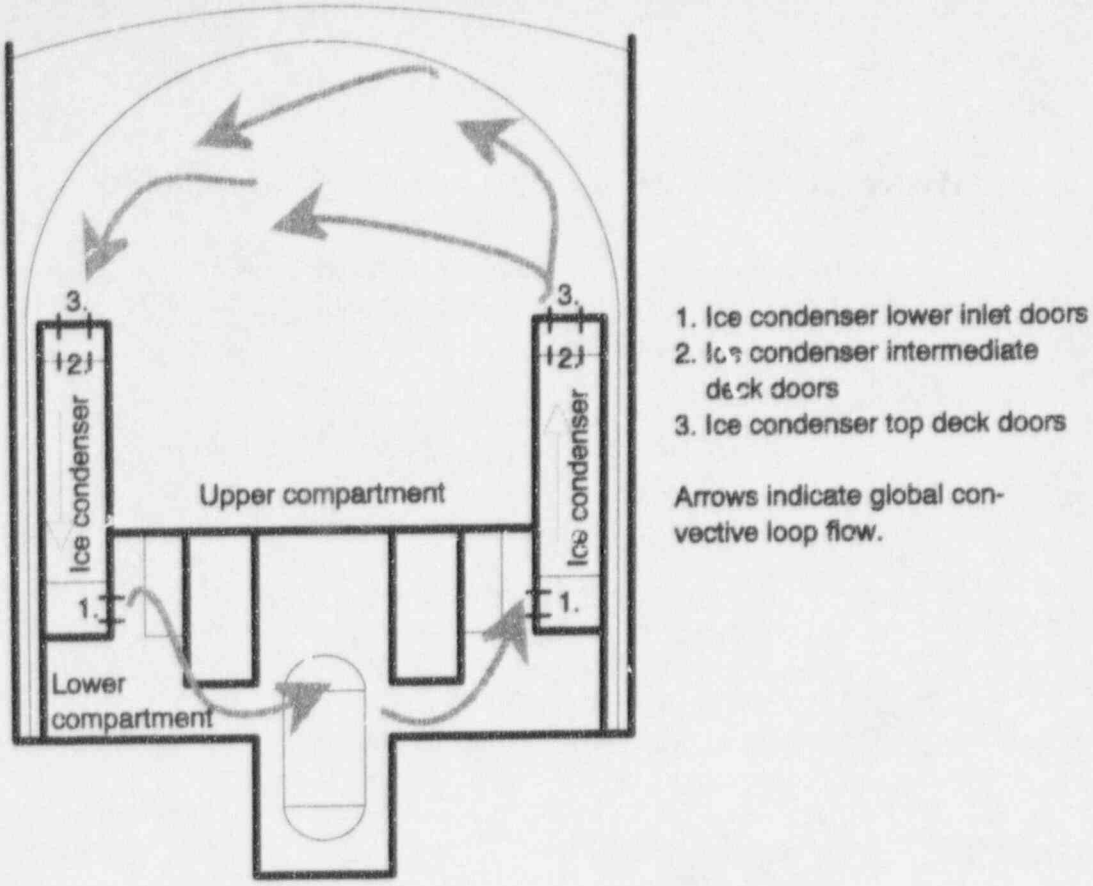

Figure 1 Ice condenser containment with global convective loop

In the early 80's, severe accident scenarios with substantial hydrogen generation (assuming 75% core zirconium oxidation) were analyzed. As a result of that work, glow plugs powered from the emergency diesel generators were installed into the different compartments of the containment. At the moment, we are developing a new severe accident management (SAM) strategy for the Loviisa NPP. The philosphy behind this work was described in [1]. A key aspect of this plant-specific approach is consistency in considering all significant containment-threatening phenomena, and in dealing with phenomenological uncertainties. We use accident management to reduce or eliminate many of these uncertainties. Hydrogen combustion is one possible hazard to containment integrity, and therefore the hydrogen issue is being analyzed anew within this framework of developing a consistent SAM strategy for the plant.

The objective of our hydrogen management strategy can be formulated as the aspiration to **avoid any hydrogen combustion mode or event that would cause a loss of containment integrity**. This obviously implies excluding the possibility of detonation. Our criteria are actually more limiting than so, since we should also avoid global deflagrations. High temperature diffusion flames could also cause a loss of containment integrity, if they occurred close to a containment wall penetration.

To achieve the strategic goal there are certain accident management options available. One important measure to avoid steep local hydrogen concentration gradients (risking local detonability) and to cause hydrogen concentrations in compartments to increase gradually (ensuring possible deflagrations are local and facilitating hydrogen removal without ignition) is providing sufficient mixing of the containment atmosphere. To provide mixing, either forced convection, i.e. installing fans, or natural convection due to existing density gradients could be considered. Controlled removal of hydrogen from the containment is another necessary accident management measure in the Loviisa containment. As mentioned above, currently around 70 glow plugs are installed in each

containment. Today, also battery-fed 'passive' spark igniters are available. The use of passive catalytic recombiners is a rather new, attractive method to safely remove hydrogen from the containment atmosphere. The most convincing way to achieve our goal would be to create non-flammable conditions in the containment. Different post-accident inerting or dilution approaches have been studied in [2].

We have determined the most promising accident management measures from the above list to be studied more extensively for the Loviisa plant. The presence of ice creates large density differences in the containment atmosphere. Therefore, forcing the ice condenser lower inlet doors, intermediate deck doors, and top deck doors open at an early stage of the accident would enable a global convective loop to be created in the containment, see Fig.1. The driving force behind this loop is completely passive and independent of power availability. The use of catalytic recombiners for hydrogen removal is also an attractive option in the Loviisa containment. This method is appealing since it is passive in start-up and operation, it recombines hydrogen far below the lower flammability limit, it operates also in a steam-inerted atmosphere, and since it constitutes an additional mixing mechanism in the containment. Glow plugs or igniters would act as a back-up safety measure in case of any unanticipated hydrogen releases into the containment. Post-accident inerting cannot be considered feasible to a containment with a low design pressure but lacking an efficient venting capability. Therefore, the proposed hydrogen management strategy is a **combination of convective loop mixing and hydrogen removal by means of catalytic recombination and deliberate ignition**. Validation of the loop mixing concept and dimensioning of the hydrogen removal system (also determining recombiner and igniter locations) are goals of the ongoing hydrogen analysis work at IVO.

Having determined the approach to hydrogen management above, several issues can be raised as to the feasibility of this concept. Does the convective loop stop functioning when all the ice has melted? What happens if hydrogen is released into the containment before start-up of the convective loop? Could we encounter strong stratification of gases while the convective loop is operating? Could we otherwise encounter local enrichment of the gas mixture while the loop is operating? Do we have scenarios where all the ice has melted before hydrogen is released into the containment? A comprehensive experimental/analytical effort is underway in pursuing these issues. The experiments, which are the subject of this paper, are carried out in an 1/15th-scale model of the Loviisa containment (the VICTORIA facility), with helium as the hydrogen simulant.

The experimental facility will be described in Section 2.1. We have also modelled the convective loop analytically to be able to scale the experiments to reactor dimensions. This model is now being extended into a containment zonal model, which will be our tool to demonstrate the feasibility of the proposed hydrogen management strategy, and the dimensioning and location of hydrogen removal capacity. We have studied the availability of ice in different accident scenarios by means of energy balance calculations. We have also studied the mechanisms of hydrogen generation of the Loviisa core geometry, since the hydrogen generation and release rate is an important parameter when catalytic recombiners are used for controlled removal of hydrogen.

This paper is focused on experimental results from several key experiments (in VICTORIA) that provide a first delineation of key behaviors. In particular, these three experiments, and the results/discussion include: (a) mixing behavior in the containment dome (experiment 43), (b) stratification in the lower compartment, and mixing in the upper dome under nearly isothermal conditions (experiment 44), and (c) mixing behavior when hydrogen is released "early", before the ice beds have been penetrated-through by steam i.e. before the inception of the global natural circulation loop (experiment 45). Velocity measurements are made using an LDA system, and helium concentrations are measured on-line, and locally at 10 positions in the containment, using a new instrument especially developed for this purpose, the SPARTA (Spark Transient Analyzer). The principle of this instrument and an initial demonstration of it in VICTORIA have been presented previously [3]. The present paper provides the first data from a full implementation in VICTORIA (10 measuring points) for the intented experimental program. For convenience, we

include here brief descriptions of VICTORIA and SPARTA.

2 VICTORIA TEST RIG AND MEASUREMENT TECHNIQUES

2.1 VICTORIA

The experimental facility, VICTORIA, was constructed at the IVO Power Plant Laboratory for studying containment thermal-hydraulics during small-break LOCAs and severe accidents [4]. The facility is a scale model of the Loviisa containment with a linear scaling factor of 1:15, see Fig. 2. The height of the vessel is 4.6 m and the diameter is 3.14 m. The model and the Loviisa ice condenser containment are geometrically similar. Concrete structures in the containment are made of concrete in VICTORIA, too. There are six different release locations (four of them into the lower compartment, one into the RCP room dead-ended compartment, and one into the cavity) to select from. Steam, water, and helium are released through a common, adjustable nozzle directed

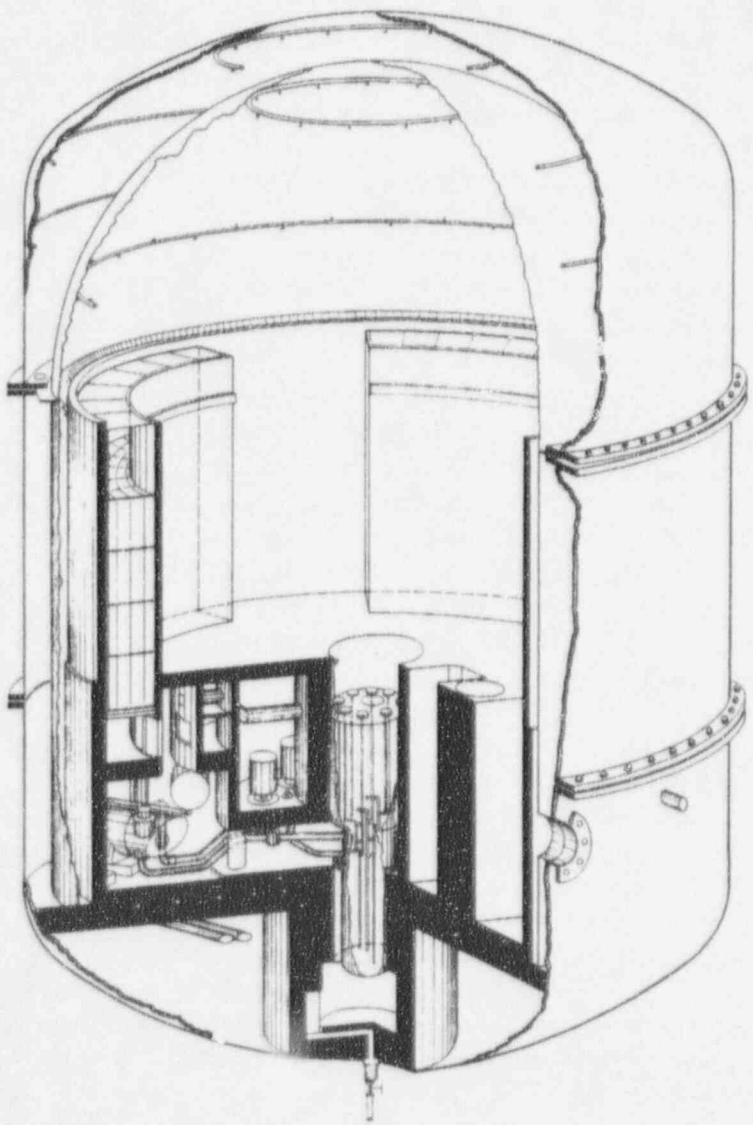

Figure 2 The VICTORIA facility

either downwards or upwards. The ice condenser model was built so that one of the ice condenser sections at a time can be moved into or out from the model. The section consists of four levels of ice handling baskets, with a total of 12 baskets in each section. In one basket there are 15 lattice cases, and in each case there are 6 ice batons. Ice condenser lower, intermediate deck, and top deck doors and bypasses are modelled. Containment internal and external spray systems are also modelled. The external spray system is the long-term residual heat removal system in a severe accident, cooling the containment through the dome steel shell.

The data acquisition system is based on a 386-processor micro computer with two PC TO S-NET-adapters and S-NET network to IMP (Isolated Measuring Pads) data collectors in which the collection is controlled by the computer program. This IMP system is very flexible. Temperatures are measured inside the vessel in about 300 points. Humidities are measured in 10 different locations. Total pressure, pressure differences between compartments, and water level height are also measured.

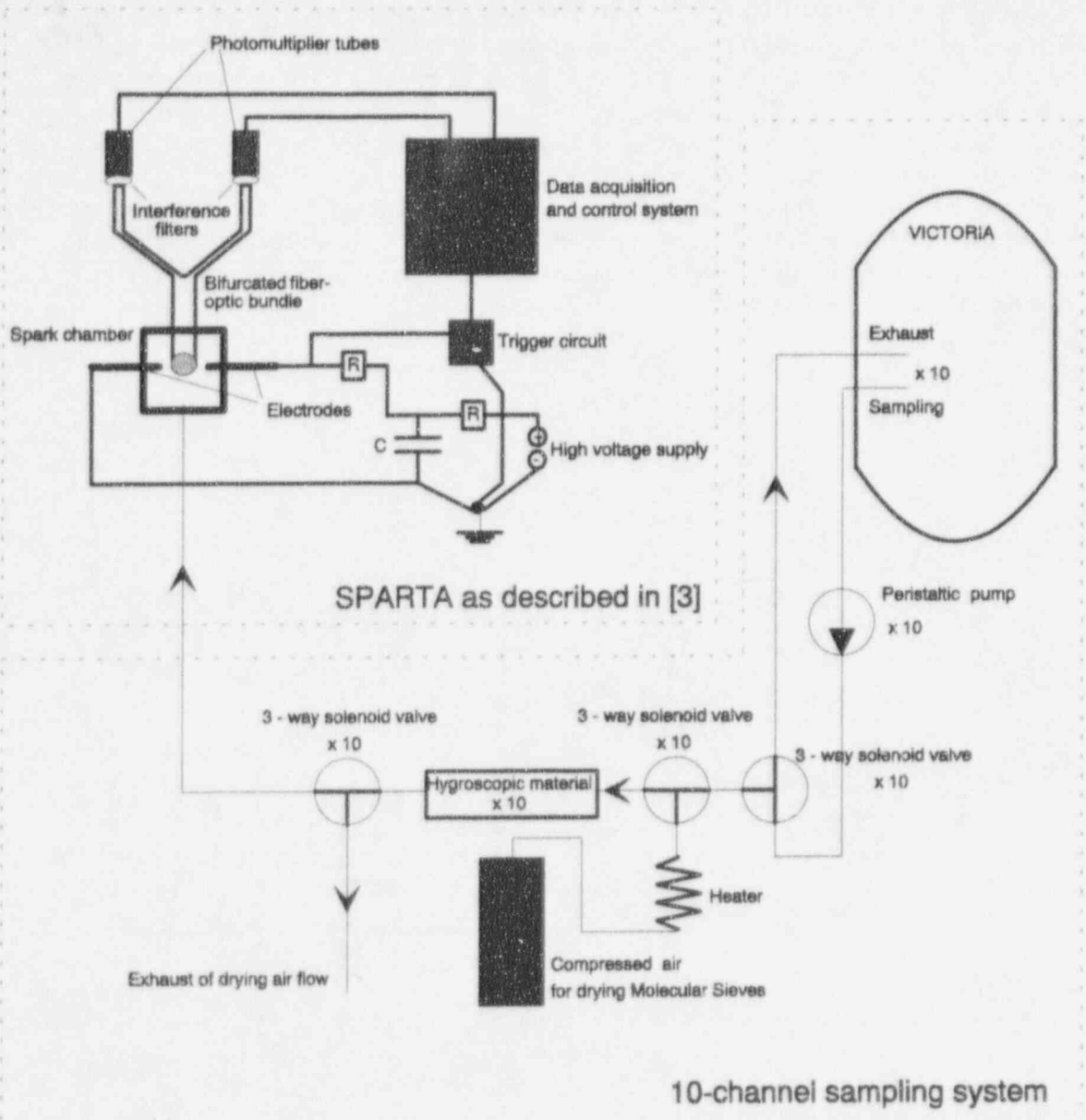

Figure 3 Extended SPARTA for helium concentration measurements in VICTORIA

2.2 HELIUM CONCENTRATION MEASUREMENT

As mentioned in the introduction, helium concentrations in the VICTORIA vessel are measured with a new technique, with an instrument called SPARTA. The method being applied is based on emission spectroscopy, where a high-voltage spark is created between two electrodes in the gas mixture. The appearance of the emission spectrum depends on the composition of the gas mixture. Even a low helium molar fraction shows as growing peaks at certain wavelengths of the spectrum. By measuring the intensity of those peaks, one can derive the helium concentration of the gas mixture. The instrument and its different modes of operation are described in detail in [3].

We noticed during the first test runs with SPARTA, at that time using only 3 to 5 sampling points, that sparking/detecting can be carried out quite frequently. A frequency of 10 sparks each minute was quite feasible. Therefore we decided to extend SPARTA by improving the sampling arrangement. In this way, we were able to have 10 measurement points in VICTORIA, without having to use several spark chambers. Fig. 3 is a schematic of the extended SPARTA. The pumping rate of the 10-channel peristaltic pump can be adjusted. In experiments 44 and 45 we used a sampling flow rate of 40 ml/min per line. Ten lines are continuously pumped, and the exhaust is close to the sampling point. This way we avoid a net flow out of the VICTORIA vessel, which is important since its free volume is rather small (about 21 m^3). The sampling lines are plastic tubes with a diameter of 2 mm. The sampling and exhaust nozzles are expanded to have diameters of about 5 mm. Therefore, sampling gives rise to a flow velocity at the nozzle of only a few centimeters per second, which is a low velocity compared to typical gas velocities due to the convective loop in the vessel. One channel at a time is selected for sampling into the spark chamber. The distance and volume between the large circulation loop and the spark chamber is miniaturizd. This way we ensure that the sampling delay between these two points is only a few seconds, and sparking can take place frequently.

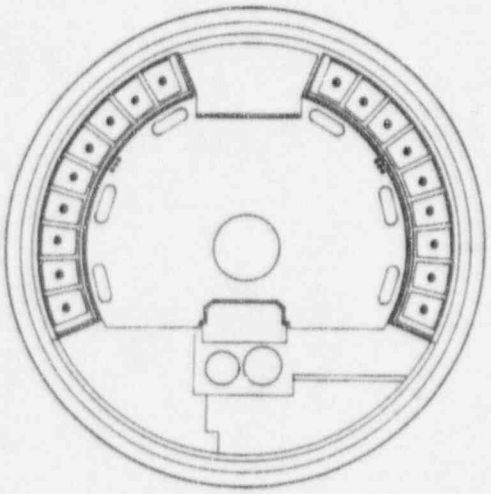

Figure 4 LDA measurement points indicated by dots (•)

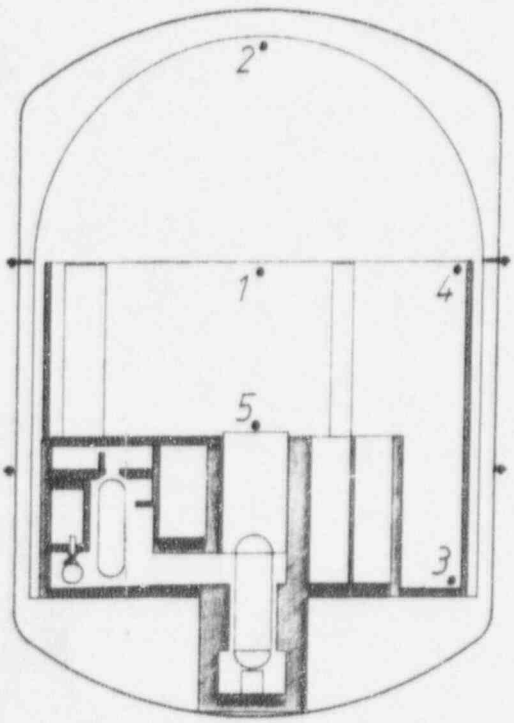

Figure 5 Sampling points in experiment 43, x = release location

As explained in [3], the sampled gas mixture has to be dried of steam before entering the spark gap. For this purpose we have a hygroscopic material holder containing a color indicator and Molecular Sieves in each line. A new feature of extended SPARTA is the heated air flow through the hygroscopic material holder at all times when that particular channel is not being sampled into the spark chamber. The air flow serves to regenerate (dry) Molecular Sieves, and has proved to be quite a useful feature of the new arrangement.

2.3 LOCAL GAS VELOCITY MEASUREMENTS

Local gas velocities in the upper compartment have been measured in experiments 43 and 44 with a fiber-optics laser-doppler anemometer (LDA) system. The measurement points are shown in Fig. 4. Measurements were made close to the ice condenser top decks. They also enable us to quantify the volumetric flow rate of the global convective loop. The top deck doors were removed (in accordance with the accident management strategy), but the flow area was restricted to 1/3 of the total top deck door area to produce a better defined flow profile. The LDA probe was moved by means of a light rotating steel wheel between the different measure-ment points. In experiment 45 the LDA measurements were omitted to make sure mixing is not caused by the measuring procedure itself.

3 PROCEDURE OF EXPERIMENTS 43-45

3.1 EXPERIMENT 43

Experiment 43 was carried out with original SPARTA using 5 channels. The results will be reported here, because the experiment is an interesting demonstration of the mixing behavior in the upper compartment. The sampling points are shown in Fig. 5. Another objective was to see how a configuration with only a small fraction of the ice present in the ice condensers at the onset of the experiment would affect the convective loop. We started the experiment with only 25% of the ice left in each ice condenser section, that is, one layer out of four the (ice layers are shown in Fig. 2). The ice configuration was symmetric, which means that both sections contained the third ice layer from the top. At t=0 the ice condenser lower inlet doors were forced open. Intermediate deck

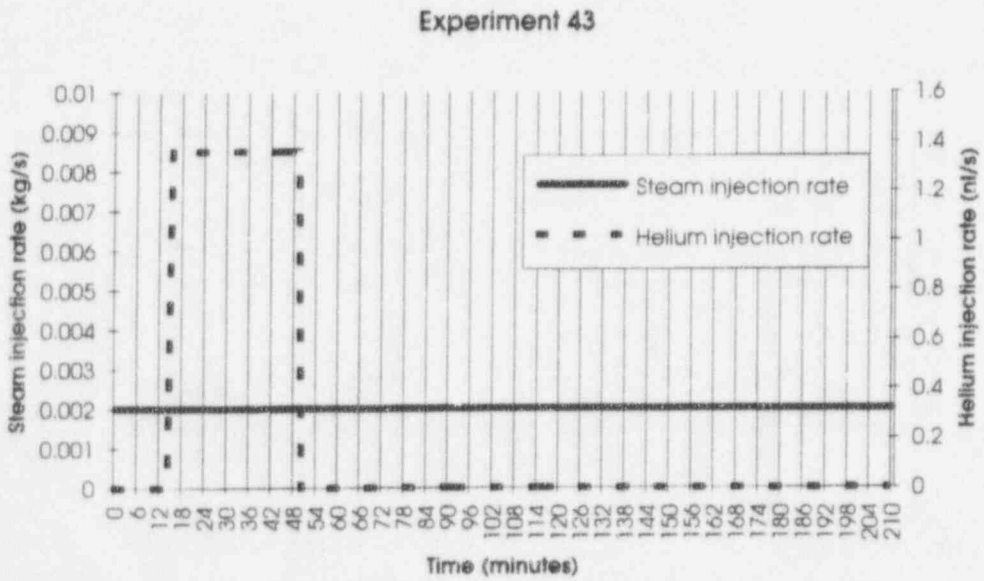

Figure 6 Steam and helium injection rates in experiment 43

and top deck doors were removed. The top deck flow area was restricted as explained in Section 2.3.

Fig. 6 shows the steam and helium injection history of experiment 43 (the unit nl/s, normal litres per second, expressed in 273K and 1.013 bar). Distributed uniformly in the VICTORIA vessel this injection history would eventually cause a helium molar fraction of about 12.7% on a dry atmospheric basis. This is actually a substantial amount of helium corresponding to 108% in-core zirconium oxidation. Helium injection started at 15 minutes. At that time the LDA-measurements confirmed steam had penetrated the ice bed, and initiated the global convective loop flow (indicated in Fig. 1) with upflow of gases through one ice condenser and downflow through the other one. The release location in the lower compartment was symmetric with respect to the ice condensers, between the two ice condenser sections, see Fig. 5. In the containment it would correspond to the location of the quench tank. The small nozzle with a diameter of 5 mm was directed downwards. Another important feature of the experiment was pre-heating of the lower compartment concrete structures to about 50°C before the experiment. If this were not done, a significant scaling deviation would occur. The structure areas are scaled as 1/225, and in this experiment energy input is scaled as 1/3375. This implies the concrete structures would act as too efficient heat sinks in the short term.

3.2 EXPERIMENT 44

This was the first experiment using the extended SPARTA 10-point-system. The sampling points are shown in Fig. 7.

Fig. 8 shows the steam and helium injection history of experiment 44. The new feature of this experiment was to discontinue steam injection when helium was injected. The reason for this was to study how well density differences due to helium only are able to drive the loop and to study mixing behavior in the upper compartment (dome) in more isothermal conditions than in our previous experiments. It is also a scenario motivated by the most probable hydrogen generation mode in the Loviisa core. Since the hydrogen generation rate can be assumed to be limited by the availablility of steam, almost all produced steam is consumed by zirconium oxidation. After some time most of what is released from the primary system into the containment should indeed be

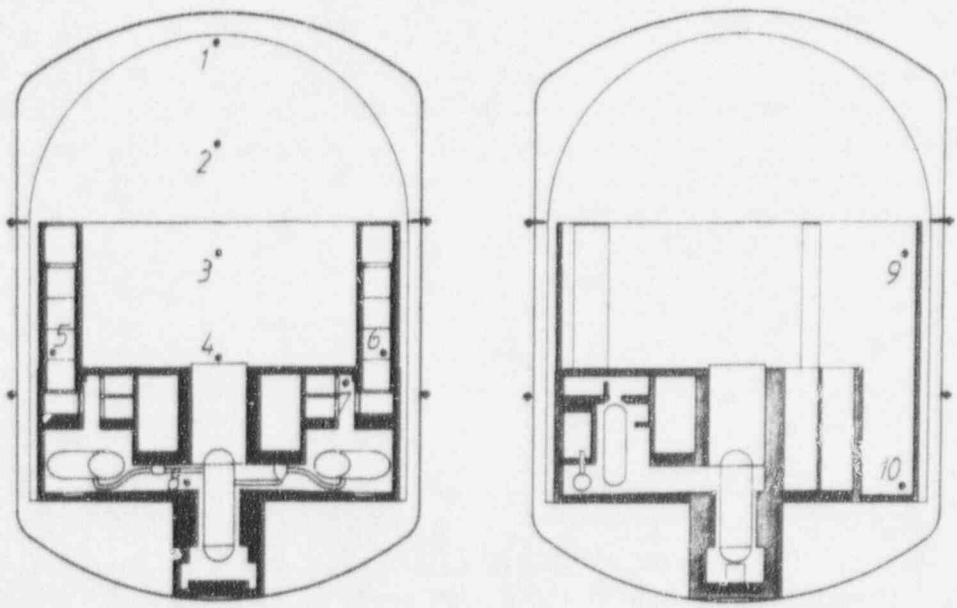

Figure 7 Sampling points in experiment 44

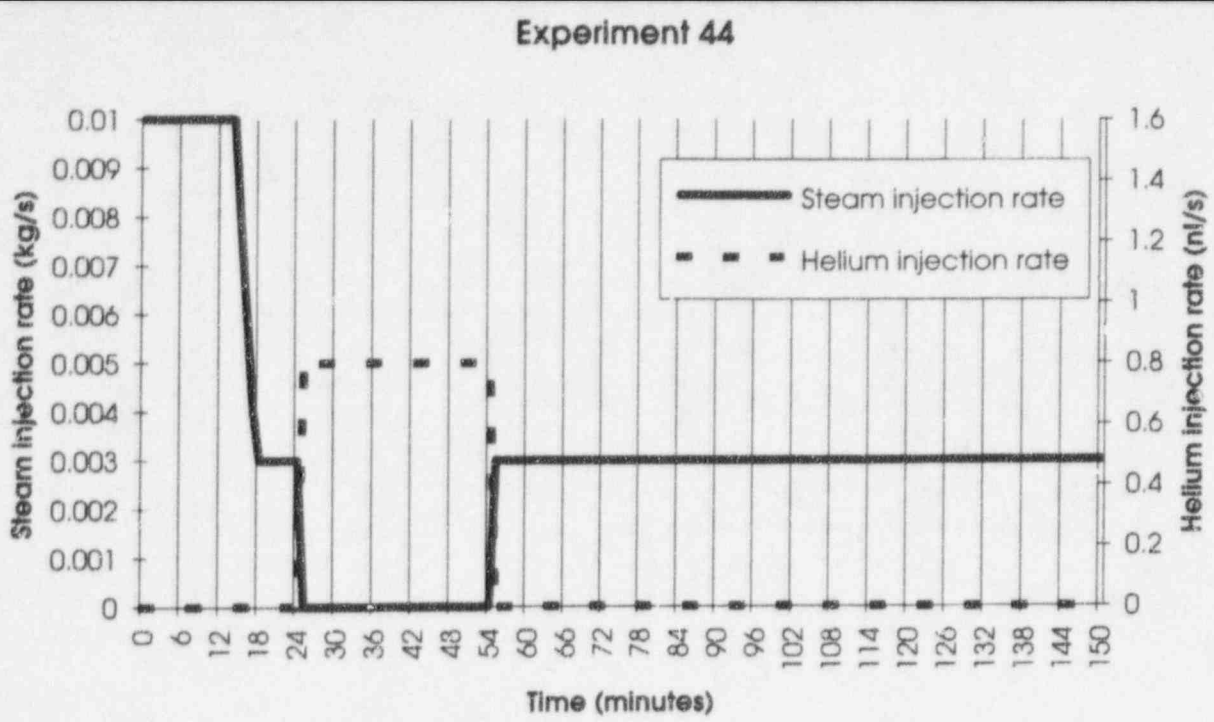

Figure 8 Steam and helium injection rates in experiment 44

hydrogen. The ice condenser door configuration was the same as in experiment 43. The helium injection rate was 0.8 nl/s during 30 minutes. Distributed uniformly in the VICTORIA vessel this injection history would eventually cause a helium molar fraction of about 6.9% on a dry atmospheric basis. This corresponds to a 54% in-core zirconium oxidation in the reactor. Another interesting feature of this experiment was creating stratifying conditions in the lower compartment. This was done by slowing down the release jet and directing it upwards. The nozzle diameter was here 12 mm. This way we attempted to maintain the Froude number of a release through the quench tank rupture disk, which in the reactor has a diameter of 0.31 m.

The experiment was started with 50% of the ice in place in the ice condensers. The ice configuration was again symmetric with the two middle ice condenser layers filled in each section. The reason for selecting symmetric ice beds in the experiments reported here is conservatism. If ice happens to melt in an asymmetric fashion during the initial stages of an accident, the driving force to the convective loop flow will be larger. Also, if ice condenser lower inlet doors are allowed to function as they are designed to (with four springs attached to each door causing a closing torque as soon as the pressure difference across it is reduced) before they are forced open, the initial melting behavior should be rather uniform and symmetric.

The lower compartment structures were again pre-heated to be as neutral as possible during the experiment.

3.3 EXPERIMENT 45

Experiment 45 was also run with 10 concentration measurement points. The sampling points are shown in Fig. 9.

The objective of experiment 45 was to inject helium before steam had had a chance to penetrate the ice bed. Therefore the global convective loop was not yet operating when helium injection was started. To achieve this situation, we started the experiment with 75% of the ice left in the ice condensers. The sections were loaded in a symmetric fashion having three bottom layers filled with ice. The ice condenser door configuration was the same as in experiments 43 and 44.

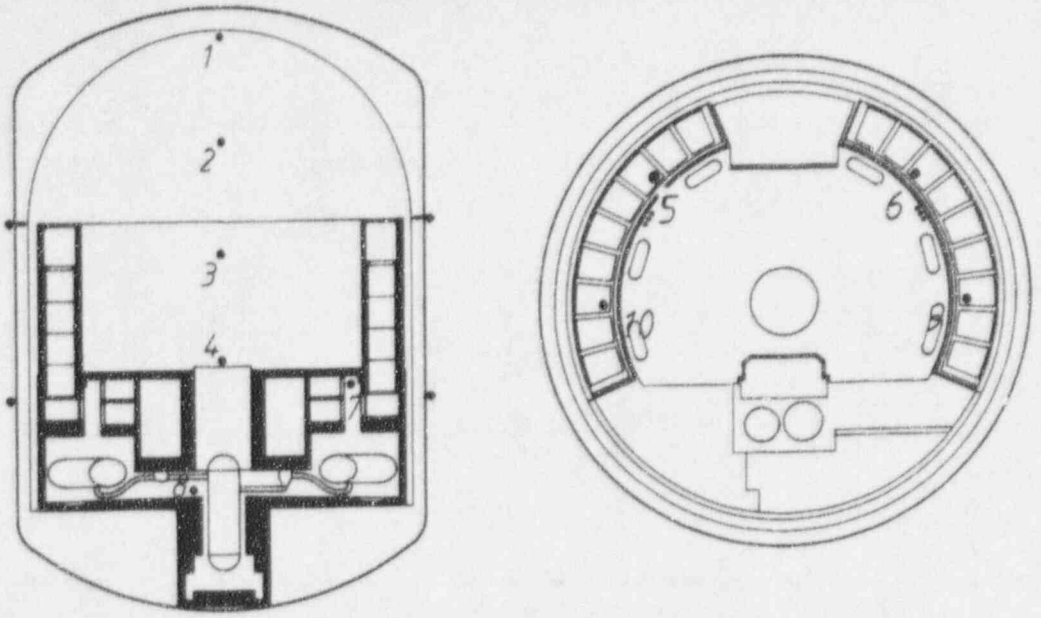

Figure 9 Sampling points in experiment 45

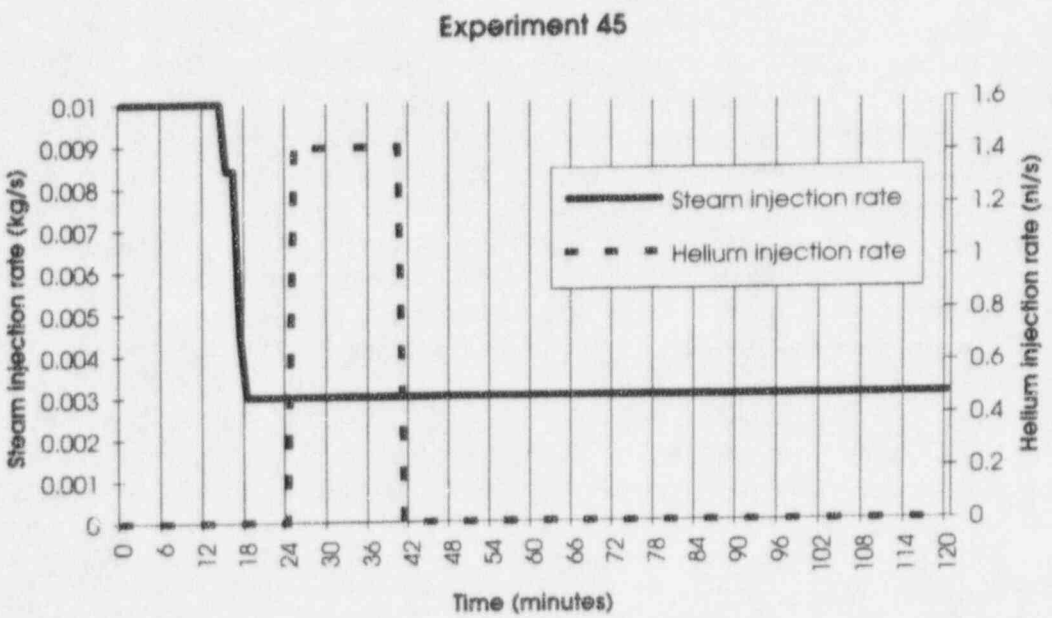

Figure 10 Steam and helium injection rates in experiment 45

The initial steam injection was determined to be small enough not to penetrate the ice bed during the first 25 minutes of the experiment. Prior to this experiment we were not sure about what kind of behavior to expect, whether the helium injection would promptly initiate the convective loop or not. If this didn't happen, one would expect to see rather fast concentration transients in the lower compartment.

Fig. 10 shows the steam and helium injection history of experiment 45. Another difference from previous experiments (in addition to attempting a "cold breakthrough" of the ice bed) was the release scaling principle. In most previous experiments the release molar flow rates of steam and helium have been scaled from an accident scenario with a factor of $1/15^3$ (1/3375). Volumetric

scaling causes the time scale of the accident scenario to be preserved in the experiment. In experiment 45 we decided to preserve the Froude number, which means scaling the release molar flow rates with a factor of $1/15^{2.5}$ (=1/871). This way the Froude number ($U^2/(g \cdot D \cdot \Delta\rho/\rho)$) using a typical compartment dimension D (scaled according to 1/15) will be preserved in the experiment. This is important, since it causes the balance between inertia and buoyancy forces to be correct. The time scale, however, will be accelerated with a factor of $15^{0.5}$ in the experiment.

The helium injection rate was 1.43 nl/s during 15.5 minutes. Distributed uniformly in the VICTORIA vessel this injection history would eventually cause a helium molar fraction of about 6.4% on a dry atmospheric basis. This corresponds to a 50% in-core zirconium oxidation in the reactor. According to the Froude scaling principle the release mass flow rate of hydrogen would be 0.111 kg H_2/s during 3600 s in containment dimensions. The release nozzle arrangement was the same as in experiment 43.

The lower compartment structures were again pre-heated to be as neutral as possible during the experiment.

4 RESULTS AND INTERPRETATION

4.1 EXPERIMENT 43

Experiment 43 is an illustration of the mixing behavior in the upper compartment, since all five sampling points are situated there. Fig. 11 shows the results of the helium concentration measurements. The molar fractions are here shown on a dry atmospheric basis. This doesn't cause a large error to real concentrations, since temperatures are quite low in the upper compartment throughout this experiment. At 49 minutes lapse time, when the highest dome point shows a helium molar fraction of 21%, the corresponding temperature is 35°C. Since the relative humidity is 100%, the steam molar fraction is about 4.8% (steam partial pressure of 0.056 bar by total pressure of 1.163 bar). Thus, the maximum helium molar fraction is corrected to 20%.

In this experiment there is a very distinct density interface around the ice condenser top deck level in the upper compartment. The density interface is caused by a temperature and a helium concentration gradient, as shown in Fig. 12. Fig. 13 shows the temperature profile.Temperatures are uniform in the dome region above the interface, and in the lower part of the upper compartment below the interface. It is interesting to see that the helium concentration below the interface rises to the equilibrium value at about 120 minutes, while temperatures hardly rise at all. There is a pronounced steam molar fraction (or temperature) gradient even as the experiment is finished after 3.5 hours, as can be seen in Fig. 13, whereas the helium is well mixed in the containment atmosphere.

The concentration curves between the dome point (helium channel 2) and the deck point (helium channel 5) are located right in the interface region, somewhat below the ice condenser top deck level. Channel 1 is in the middle between the dome and the deck, whereas channel 4 is on approximately the same elevation, but close to the wall. Since those points are in the interface region, even a small difference in vertical elevation causes a clear difference in the measured helium molar fraction.

Channel 3 is situated below channel 4 in the segment space. This is the lowest point of the upper compartment, and it seems to follow the concentrations of channel 5 with a rather short delay.

Ice condenser temperature measurements indicate all ice has melted after 90 minutes.

Fig. 14 shows our measurements of the volumetric flow rate of the convective loop, as measured on top of the hot side ice condenser. There is a maximum flow while helium injection takes place. Towards the end of the experiment, the flow rate stabilizes around 35 l/s. Melting the ice does not tend to slow down the loop, which is now being driven by temperature differences due

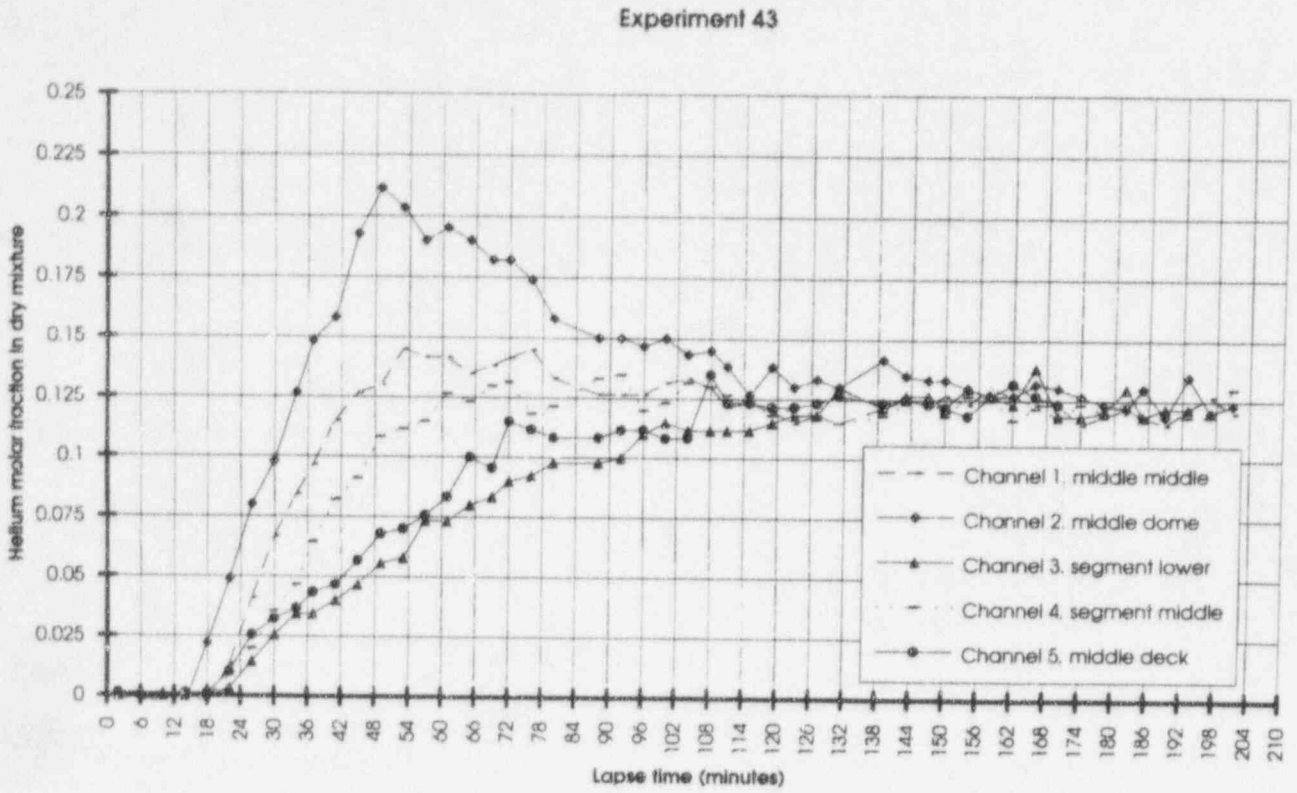

Figure 11 Helium molar fractions in experiment 43

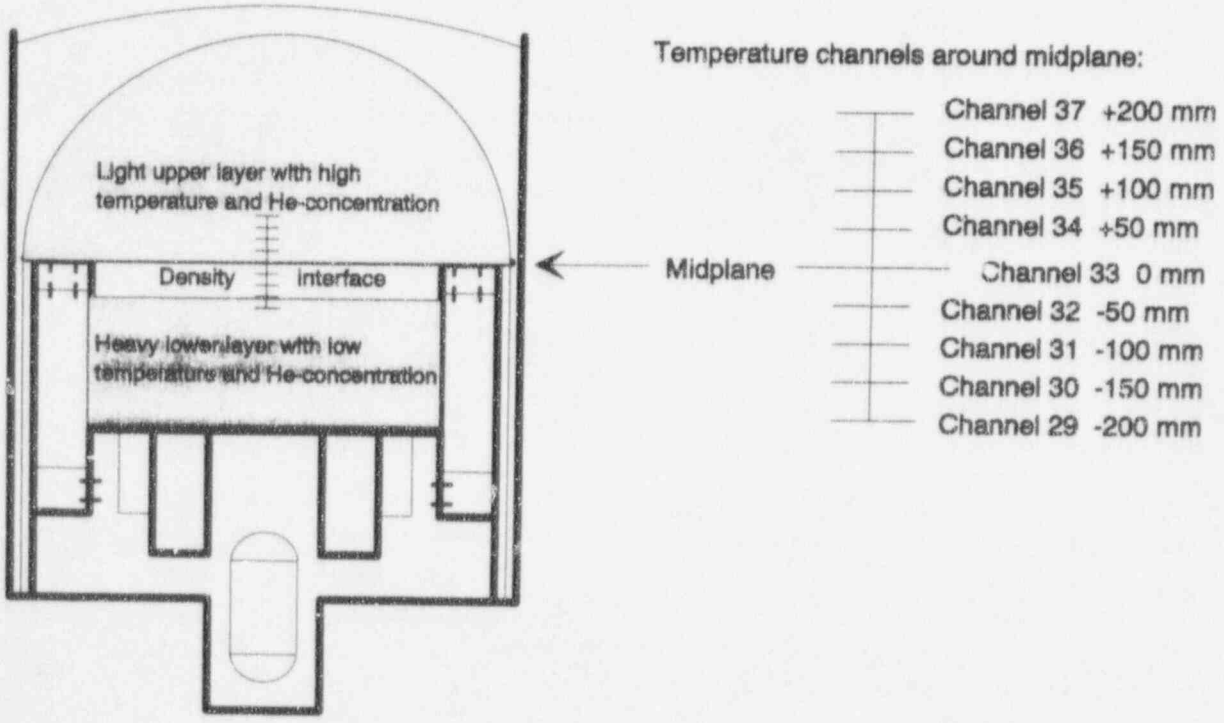

Figure 12 Stratification of upper compartment

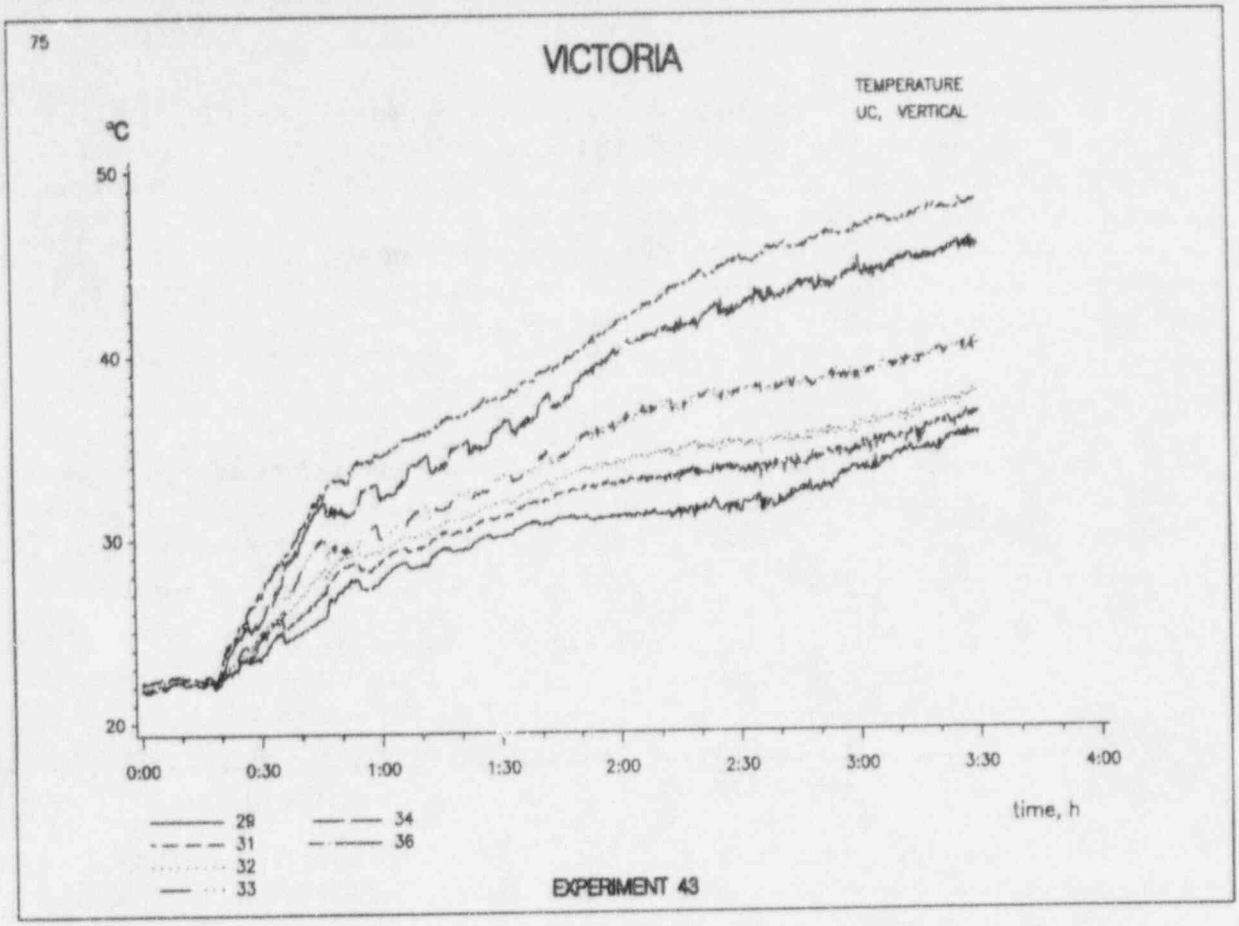

Figure 13 Temperature profile around midplane in experiment 43

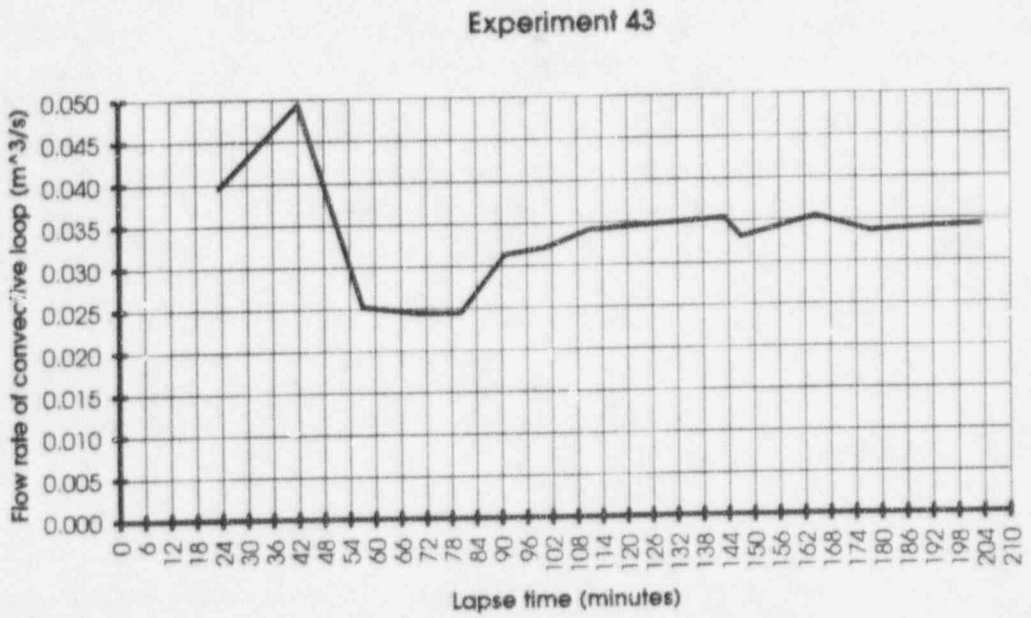

Figure 14 Volumetric flow rate in experiment 43

to heat losses to containment structures. With a continuing steam injection into the lower compartment there are still sufficient density differences to drive the loop.

The upper compartment mixing behavior is typical to all experiments of this kind. We have run several experiments where steam has penetrated the ice bed before helium was injected, thus heating up the upper dome part of the upper compartment. The first experiment of this kind was

used as an example in [3]. A stable temperature stratification is created quickly and maintained thoughout the experiment. Initially, there is a large helium concentration gradient across the interface, but it decreases and vanishes as the experiment continues. It seems puzzling that helium is able to mix across this obviously very stable interface.

The first idea that comes to mind is that there is, despite the apparent stability of the stratification, turbulent diffusion of species across the interface. Therefore we calculated the Richardson number (Ri) across the interface. Ri is defined as

$$Ri = g \cdot \Delta\rho/\rho \cdot L / (U_{char})^2 \qquad (1)$$

where L = the thickness of the interface, U_{char}= the velocity difference across the interface, and $\Delta\rho$ = the density step across the interface. Looking at the situation in the upper compartment at 49 minutes lapse time (see Fig. 11 and Fig. 13), and using the following assumptions

T_{upper} = 34°C $X_{He,upper}$ = 20.0% (helium molar fraction above interface)
T_{lower} = 28°C $X_{He,lower}$ = 6.8% (helium molar fraction below interface)
L = 0.2 m (the distance from point 32 to 36 in Fig. 13)
P_{tot} = 1.163 bar
U_{char} = 0.5 m/s (the maximum local gas velocity measured at the hot side ice condenser outlet at that time)

we arrive at a Richardson number larger than unity (1.3). As explained in [5], this implies a stable situation. Turbulence produced by the shear flow along the interface should not be able to diffuse through this layer. Therefore, turbulent entrainment cannot explain mixing across this density interface. The characteristic velocity is an uncertain parameter, since we do not have local velocity measurements along the density interface. The ice condenser upflow velocity, however, can be considered an upper limit. The conclusion regarding stability of stratification is therefore valid.

Thereafter we tested whether molecular diffusion of helium in air could account for transport of helium across the interface. Assuming the molar fraction of steam insignificant (it is 4.6% above the interface and 3.3% below it), we use the diffusion coefficient for helium in air in the given temperature and pressure, $D_{He\text{-}air} = 0.61 \cdot 10^{-4}$ m^2/s [6]. Assuming the diffusion process is stationary with absolute flux of species equal to the diffusive flux across the interface, we use as an approximation [7]

$$N_{He}'' = D_{He\text{-}air} \cdot (C_{He,upper} - C_{He,lower})/L \qquad (2)$$

where N_{He}'' = molar flux of helium through the interface, and C = is the molar concentration expressed as kmoles helium per unit volume of gas mixture. Inserting the parameters, and assuming that helium is diffusing into a volume of 8.5 m^3, we arrive at the result that diffusion at 49 minutes lapse time could account for a helium molar fraction increase in the lower part of the upper compartment of 0.003 %/s. From the slope of channel 5 at that time, we see the helium molar fraction increases by 1.5% in 12 minutes, that is, 0.002 %/s. Therefore molecular diffusion seems to be a plausible explanation for upper compartment mixing behavior in this experiment.

4.2 EXPERIMENT 44

Fig. 15 shows helium molar fractions in the real gas mixture (including steam) during experiment 44. In this experiment steam fractions are significant for the measurement points in the lower compartment.

The result shows we indeed succeeded in producing a strong stratification of the lower compartment, since channel 7 shows high helium molar fractions during the helium injection phase.

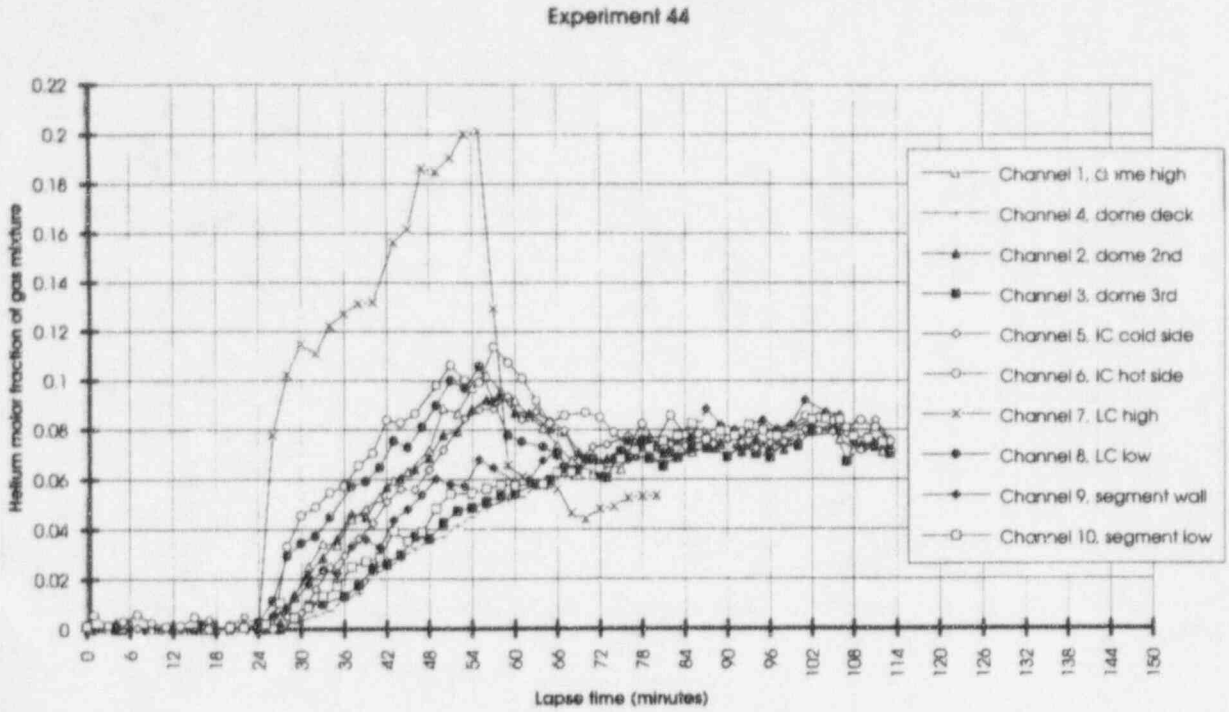

Figure 15 Helium molar fractions in experiment 44

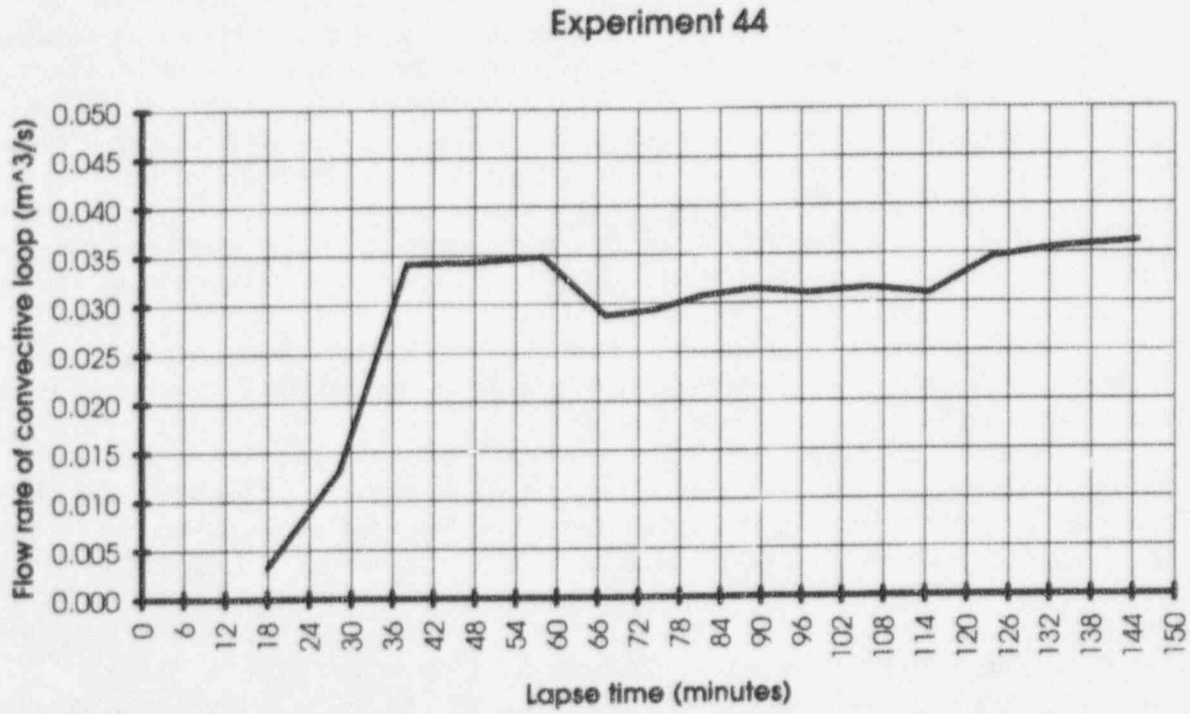

Figure 16 Volumetric flow rate in experiment 44

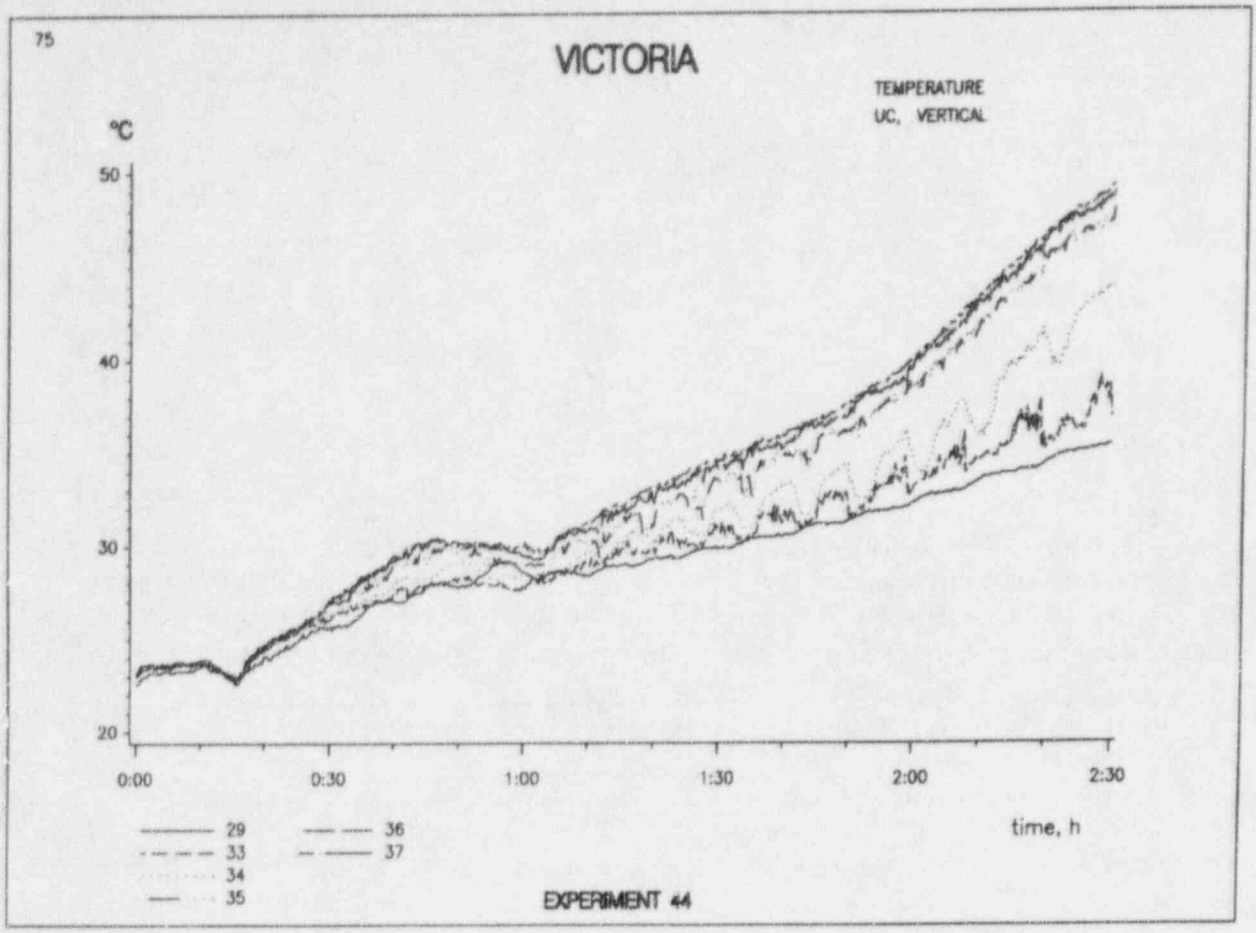

Figure 17 Temperature profile of midplane in experiment 44

Stratification was broken up immediately as helium injection stopped and steam injection continued. The stratified layer is located above the main loop flow in the lower compartment, that is, above the ice condenser lower inlet doors. The volume of this space is quite small (see Fig. 7), which is why this layer is not able to hold any significant fraction of the total amount of injected helium. This spatially limited stratification is also indicated by the measurement results of channel 6, which is located in the ice bed of the ice condenser through which the global convective loop flows upwards. This point sees approximately the same concentrations as the lower compartment floor point (channel 8). When stratification is broken up, this point measures higher helium molar fractions than the rest, until the entire vessel is well mixed. The possibility to stratify the containment lower compartment should be considered when the hydrogen management strategy is developed. One possibility to deal with the problem is to install passive catalytic recombiners in the lower compartment, since they have been shown to produce very efficient mixing of compartments.

Fig. 16 shows the volumetric flow rates of the convective loop during this experiment. Disruption of steam injection while helium was injected does not slow down the loop. Most of the ice has melted after 105 minutes. This does not slow down the loop in this experiment, either.

The mixing behavior in the upper compartment is again interesting. Helium channels 1 and 2, above the ice condenser outlet level, show nearly identical helium molar fraction during most part of the experiment. Channels 3 and 4, below the ice condenser outlet level, are also right on top of each other. The behavior of the wall points (9 and 10) is less well determined. The mixing behavior in this case looks somewhat different from what we saw in experiment 43. The helium molar fraction increase rate of channels 3 and 4 in Fig. 15 is clearly higher than that of channel 5 in experiment in Fig. 11, despite the very slow helium injection rate in experiment 44. Channels 3 and 4 in Fig. 15 are approaching the equilibrium molar fraction in a nearly linear way, whereas the slope of channel 5 in Fig. 11 is decreasing with time. An important difference compared to experiment 43 is the nearly isothermal upper compartment during the helium injection phase, see

Fig. 17.

Next we will study the mixing mechanisms in this experiment using the same methods as for experiment 43. From Fig. 15 one can see that the constant helium molar fraction increase rate at channels 3 and 4 between 27 and 57 minutes is approximately 0.003 %/s. Let us look at 40 minutes lapse time. From the measurements we get

$T_{upper} = T_{lower} = 28$°C
$X_{He,upper} = 5.0$ %
$X_{He,lower} = 2.0$ %
$P_{tot} = 1.071$ bar
= 0.4 m/s (the maximum local gas velocity measured at the hot side ice condenser outlet at that time)

If there exists a stable stratification, the Richardson number based on the above parameters should exceed some critical value. Let us assume $Ri_{crit} = 0.25$, which is the limit for onset of Kelvin-Helmholtz instabilities in this kind of a situation [5]. For Ri to exceed this limit the dimension of the interface has to exceed a certain value L_{crit}. Carrying out the calculation results in

$$L_{crit} = 0.15 \text{ m}$$

If the situation were the same as in the previous experiment, helium would diffuse across that interface and mix into the lower part of the upper compartment. The diffusion calculation can now be carried out, and results in the following instantaneous dX/dt (molar fraction increase rate)

$$dX/dt = 0.001 \text{ %/s}$$

Thus, it is not obvious that molecular diffusion alone would explain mixing in this case. The calculated increase rate is clearly less than the observed 0.003 %/s. In addition, when gases are left to stratify under the effect of a shear flow, the observed Richardson number for a stable situation is usually somewhat higher than the used critical value of 0.25 [5]. This results in a larger L_{crit}, and an even slower molar fraction increase rate from molecular diffusion. However, one should be cautious to draw conclusions in this situation. If the characteristic velocity (being an uncertain parameter) is reduced while the Richardson number assumption is maintained, a thinner interface will suffice to produce that Ri. In that case the molar fraction increase rate from molecular diffusion approaches what was observed in the experiment.

Thus, the hypothesis that the mixing mechanism in experiment 44 is different than in experiment 43 can be neither confirmed nor rejected based on available information from this experiment. We decided to run experiments with a flow visualization system in the upper compartment to see whether flow across midplane of the upper compartment is important to mixing in certain accident scenarios.

4.3 EXPERIMENT 45

Figures 18 - 20 (a) show helium molar fractions in the real gas mixture (inlcuding steam) and Figures 18 - 20 (b) show the temperatures of the sampling points in experiment 45. The objective here was to see how transport and mixing of species is affected by the fact that helium injection is initiated before the global convective loop had started.

Helium injection starts at 25 minutes. At that point of time no steam has reached the upper compartment, as indicated by Fig. 18 (b). The lower compartment (channels 7 and 8) experiences a fast helium concentration transient between 25 and 28 minutes. Also channel 6, on top of the second ice condenser detects helium immediately. What then seems to happen is a "cold

breakthrough" of the ice bed - a cold helium-air mixture with virtually no steam content reaches the upper compartment. This gas mixture is actually colder than the upper compartment atmosphere. Therefore, no stratification occurs on top, but the gas mixture is efficiently mixed into the entire volume of the upper compartment. Note that channels 3 and 4 measure the same helium molar fractions as channels 1 and 2 between 28 and 32 minutes. The breakthrough also initiates the convective loop, which is indicated (among other things) by the sudden change of slope of the

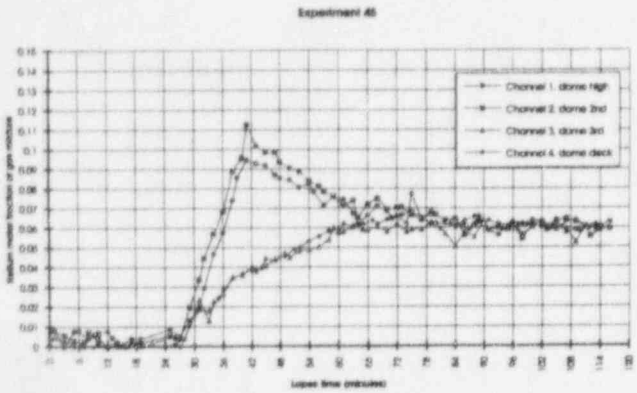

Figure 18(a) Upper compartment molar fractions

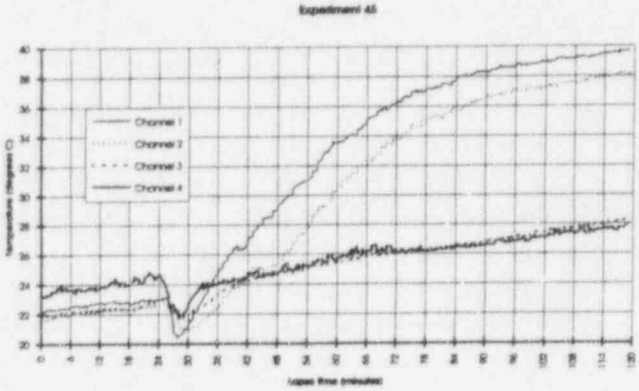

Figure 18(b) Upper compartment temperatures

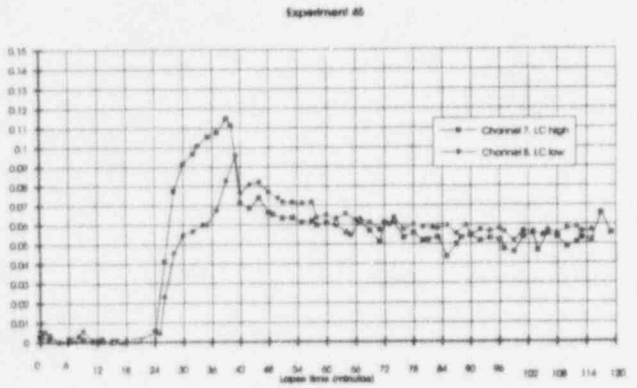

Figure 19(a) Lower compartment molar fractions

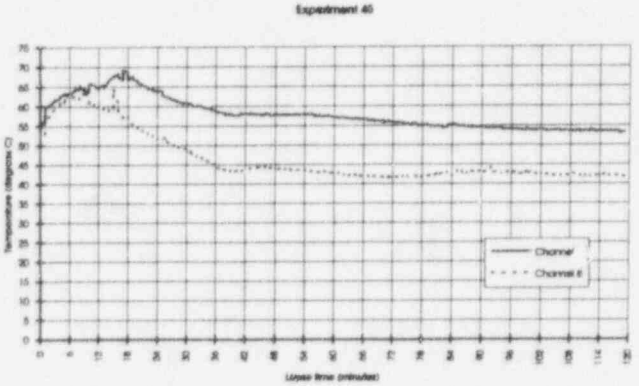

Figure 19(b) Lower compartment temperatures

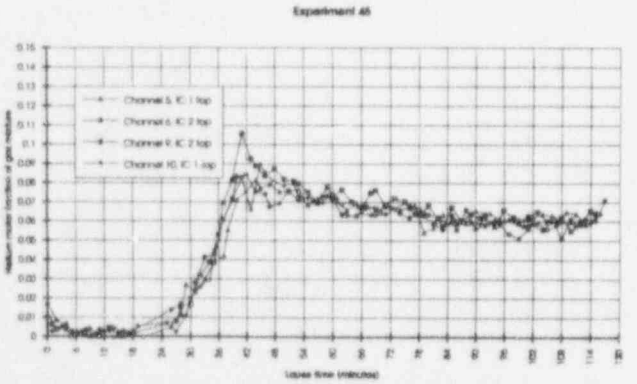

Figure 20(a) Molar fractions on top of IC's

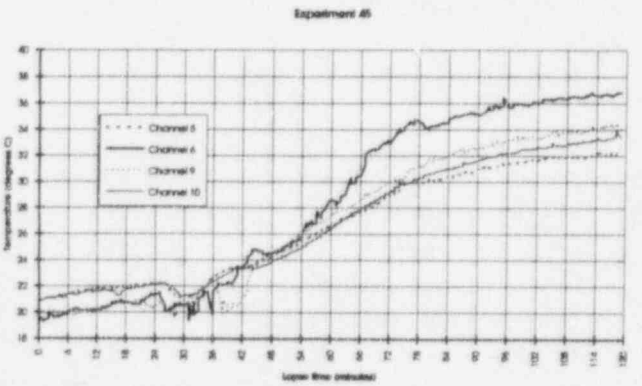

Figure 20(b) Temperatures on top of IC's

lower compartment concentration measurements.

At 32 minutes the temperature distribution of the upper compartment is stabilizing, since the temperature of channel 1 (the dome point) is now exceeding that of channel 2. This means steam is now also finding its way through the ice bed into the upper compartment. What is very interesting to see, however, is that channel 2 in the upper compartment consistently measures higher helium concentrations than channel 1. This means that there continues to be a local colder gas flow containing helium into the upper compartment. The temperature of point 2 doesn't exceed that of channel 3 until at 41 minutes. This assumption is confirmed by observations of the behavior of channel 9. Channel 9 has the highest helium concentrations of the ice condenser points in combination with a low temperature until 41 minutes.

After termination of helium injection at about 41 minutes, the vessel atmosphere is quickly approaching the equilibrium molar fraction of helium, to be reached at about 65 minutes (see Fig. 18 (a)).

There was plenty of ice left in the ice condensers even when helium concentration measurements were terminated at 120 minutes.

The fairly complex behavior of this experiment will require thorough analysis and modelling in the future. One important observation was the fact that the convective loop was promptly initiated by the cold breakthrough of the ice condensers.

5 DISCUSSION

VICTORIA hydrogen distribution experiments have been run in order to illuminate the hydrogen behavior in an ice condenser containment. Several important phenomena were demonstrated in these experiments. Since scaling is always difficult in a small scale test facility, modelling efforts are going on in parallel with the experimental work. We are currently developing a zonal model, in which the different mixing zones of the containment are modelled in a phenomenologically sound way. Special attention has been paid to modelling the convective loop behavior, which is an important feature of our proposed hydrogen management strategy for the plant. The model will be a tool for demonstrating the feasibility of the hydrogen management strategy, and in determining the number of passive catalytic recombiners needed, and recombiner location. The model will be used for blind pre-test calculations for VICTORIA experiments in early 1995.

6 CONCLUSIONS

A new hydrogen management strategy is being developed for the Loviisa ice condenser containment. The strategy relies on containment-wide natural circulations that develop, once the ice condenser doors are forced open, to effectively produce a well-mixed behavior, and a correspondingly slow rise in hydrogen concentration. Levels can then be kept low by a distributed catalytic recombiner system, and (perhaps) an igniter system as a backup, while the associated energy releases can be effectively dissipated in the ice bed. Verification and fine-tuning of the approach is carried out experimentally in the VICTORIA facility and by associated scaling/modelling studies. VICTORIA represents an 1/15th scale model of the Loviisa containment, hydrogen is simulated by helium, and local concentration measurements are obtained by a newly developed instrument specifically for this purpose, called SPARTA. This paper has been focused on experimental results from several key experiments that provide a first delineation of key behaviors. These include:

- A natural circulation loop develops with one ice condensor in upflow and the other one in downflow, even with an initially symmetric condition.
- The circulation loop is very effective in mixing the injected helium with volumes participat-

ing in the circulation; that is, all containment volumes bu. the lower portion of the upper compartment (from the ice condenser top deck level downwards).

- Molecular diffusion mechanisms are important in equalizing concentrations throughout the containment in a time frame of 1-2 hours at the VICTORIA scale.
- Under certain injection conditions - pure helium, low velocity, upwards directed jet - it is possible to create a stratified condition in the lower compartment. However, it breaks as soon as the injection stops, and overall mixing in the upper dome continues to be very effective throughout.
- Helium injection alone is able to start the natural circulation flow before steam has penetrated the ice beds.

REFERENCES

[1] Tuomisto, H. & Theofanous T.G. A Consistent Approach to Severe Accident Management. Nuclear Engineering and Design 148 (1994) 171-183.

[2] Tiltmann, M., et al. Post-Inerting of a Large Dry Containment in Beyond-Design-Basis Accidents in PWR Plants. A Survey of Existing Studies with an Initial Assessment. Report GRS-104, Gesellschaft für Anlagen- und Reaktorsicherheit (GRS)mbH, December 1993.

[3] Lundström, P., Tuomisto, H., Salmassi, T., & Theofanous T.G. Local/ Instant Measurement of Helium Concentrations in a Gaseous Atmosphere. Proceedings International Conference on "New Trends in Nuclear System Thermohydraulics", Volume II, May 30th-June 2nd, 1994, Pisa Italy.

[4] Hongisto, O., Tuomisto, H., & Lundström, P. Hydrogen Distribution Experiments for Loviisa Ice Condenser Containments. Proceedings Workshop on Hydrogen Behaviour and Mitigation in Water-Cooled Nuclear Power Reactors, March 4-8, 1991, Brussels, Belgium.

[5] Turner, J.S. Buoyancy Effects in Fluids. Cambridge University Press, 1973.

[6] Perry, R.H. & Green, D. Perry's Chemical Engineers' Handbook Sixth Edition International Student Edition. McGraw-Hill Books, 1984.

[7] Incropera, F.P. & De Witt, D.P. Fundamentals of Heat and Mass Transfer. Third Edition. John Wiley & Sons, 1990.

AERODYNAMICS, HEAT AND MASS TRANSFER IN STEAM-AEROSOL TURBULENT FLOWS IN CONTAINMENT

Nigmatulin B.I., Pershukov V.A., Ris V.V., Smirnov E.M., Zaichik L.I., Vinberg A.A., Sidenkov D.V., Belov V.A.

Research & Engineering Centre of Nuclear Plants Safety,
Electrogorsk, Moscow Region, Russia

ABSTRACT

In this report an analysis of aerodynamic and heat transfer processes at the blowdown of gas-dispersed mixture into the containment volume is presented. A few models for description of the volume averaged and local characteristics are analyzed. The mathematical model for description of the local characteristics of the turbulent gas-dispersed flows was developed. The calculation of aerodynamic, heat and mass transfer characteristics was based on the Navier-Stokes, energy and gas mass fractions conservation equations. For calculation of dynamics and deposition of the aerosols the original diffusion-inertia model is developed. The pulsating characteristics of the gaseous phase were calculated on the base (k-ε) model of turbulence with modification to account thermogravitational force action and influence of particle mass loading. The appropriate boundary conditions using the "near-wall function" approach was obtained. Testing of the mathematical models and boundary conditions has shown a good agreement between computation and data of comparison. The described mathematical models were applied to two- and three dimensional calculations of the turbulent flow in containment at the various stages of the accident.

INTRODUCTION

In the elements of containment there is motion of heat-transport medium in both forced and free convection modes. So during accident the forced convection flow realizes when the process is beginning as a result of throw out of steam into the containment volume. Free convection flow forms at the last stage of the accident development when the system approaches to quasi steady state. For high rate of flowing out of steam-gas mixture and large linear scale, the flow inside containment is turbulent and characterized by the large Reynolds and Grashof numbers. Steam is removed from the containment atmosphere as a result of its condensation and film draining off the structures, walls and equipment. Moving matter in the containment is a heterogeneous (two-phase or three-phase) system consisting of steam-gas mixture, water and solid aerosols made by steam condensation, spray systems and destroying of concrete and other surfaces.

In containment, the following types of heat and mass transfer takes place: heat transfer at forced and natural convection in the volume, heat transfer at phase transitions, steam condensation on the containment walls, evaporation of liquid droplets, radiation heat transfer, heat transfer at the hydrogen combustion, heat conductivity through condense film and the containment walls. In the present paper, the first stage of a scientific program for numerical simulation of the thermophysics processes is presented. As the first stage, the predictions of the three-dimensional turbulent single phase flow in the containment volume are carried out. For calculation of dynamics and deposition of aerosols, the original diffusion-inertia model is developed. This model is tested for various cases of the simple flows (jets and channels and etc.). The problem of film condensation of steam-gas mixture on the containment walls is considered.

1. MODELING OF TURBULENT FLOW IN CONTAINMENT

Calculation of the hydrodynamic characteristics of turbulent flows formed in the containment volume is the main elaboration of the numerical code. In contrast to the well known and widely used numerical codes GOTHIC, CONTAIN, CONTEMPT, MELCOR, WAVCO [1,2] based on hydraulic schemes, information, obtained using hydrodynamics codes, allows us with essential accuracy to determine the convection and diffusion fluxes. These fluxes not only form the temperature and concentration fields but also determine the rates of the physical and chemical processes. Equally with the averaged characteristics of the flow, the pulsating structure significantly affects the running processes.

For describing averaged and pulsating characteristics of the flow, the averaged Reynolds' equations are applied together with the well-known two-parametric "k-ε" model of turbulence. In spite of its simplicity this model allows to obtain satisfactory reliable data for broad spectrum of problems. The hydrodynamic computations are carried out for forced convection in the framework of a weak-compressible inert one-phase medium.

The averaged equations of continuity and momentum are

$$\frac{\partial \rho}{\partial \tau} + \frac{\partial \rho U_k}{\partial x_k} = 0, \tag{1.1}$$

$$\frac{\partial \rho U_i}{\partial \tau} + \frac{\partial \rho U_i U_k}{\partial x_k} = -\frac{\partial P}{\partial x_i} + \frac{\partial}{\partial x_k}[-\rho\langle u_i' u_k'\rangle + \mu(\frac{\partial U_i}{\partial x_k} + \frac{\partial U_k}{\partial x_i} - \frac{2}{3}\frac{\partial U_n}{\partial x_n}\delta_{ik})] + \rho g_i. \tag{1.2}$$

In the framework of "k-ε" turbulent model, it is assumed that Boussinesq's hypothesis of isotropic representation of the turbulent viscosity ν_T can be used for definition of the Reynolds' stress tensor

$$\langle u_i' u_k'\rangle = \frac{2}{3}k\delta_{ik} \quad \nu_T(\frac{\partial U_i}{\partial x_k} + \frac{\partial U_k}{\partial x_i} - \frac{2}{3}\frac{\partial U_n}{\partial x_n}\delta_{ik}). \tag{1.3}$$

In expression (1.3) the turbulent viscosity is defined by the Kolmogorov-Prandtl's formula

$$\nu_T = C_\mu k^2 / \varepsilon, \tag{1.4}$$

where C_μ is a constant.

The equations

$$\frac{\partial \rho k}{\partial \tau} + \frac{\partial \rho U_k k}{\partial x_k} = \frac{\partial}{\partial x_k}[(\mu + \frac{\mu_T}{\sigma_k})\frac{\partial k}{\partial x_k}] - \rho\langle u_i' u_k'\rangle\frac{\partial U_i}{\partial x_k} - \rho\varepsilon, \tag{1.5}$$

$$\frac{\partial \rho \varepsilon}{\partial \tau} + \frac{\partial \rho U_k \varepsilon}{\partial x_k} = \frac{\partial}{\partial x_k}[(\mu + \frac{\mu_T}{\sigma_\varepsilon})\frac{\partial \varepsilon}{\partial x_k}] - \rho\frac{\varepsilon}{k}(C_{1\varepsilon}\langle u_i' u_k'\rangle\frac{\partial U_i}{\partial x_k} + C_{2\varepsilon}\varepsilon). \tag{1.6}$$

are used to determine the turbulent energy k and the rate of its dissipation ε.

The values of the constants in equations (1.4)-(1.6) are picked out in accordance with [3]: C_μ =0.09, $C_{1\varepsilon}$=1.44, $C_{2\varepsilon}$=1.92, σ_k =1.0, σ_ε=1.3.

Equations (1.5), (1.6) can be written without the molecular viscosity terms for the areas of the flow far from the solid surfaces, where the viscous layer is formed. This formulation is correct for large-sized objects (e.g. the containment volume), therefore it is practically impossible to use the calculation grids including areas of the wall viscous flow.

In accordance to the above described high Reynolds' turbulence model (1.1)-(1.6) the wall function method is used for setting boundary conditions. Applying this method makes possible both decreasing the amount of numerical cells and using results of modeling compound physical processes carried out in objects with simple geometric properties (e.g. boundary layers on plate surfaces, flows in long pipes etc.). Moreover, on further developing mathematical models for more general cases (mixed convection, multiphase flows, liquid film presence) the authors will develop a methodology of specifying wall function as boundary conditions. At the present moment there exist only a few studies on wall functions in more general cases than usual situations (e.g. for forced convection on a plate [3]); however they are beginning to appear in the literature [4,5].

In the framework of this approach it is assumed that the boundary conditions can be defined not on the wall, but at some distance from it. Location of this point in the logarithmic layer (i.e. $30<y_+<100$) is a necessary condition. In this layer, the expressions of velocity vector, turbulent energy and dissipation rate are [3]

$$\frac{|\mathbf{U}-\mathbf{U}_w|}{u_*}=\frac{1}{æ}\ln(y_+)+A,\quad u_*=\sqrt{\tau_w/\rho},\quad y_+=\frac{yu_*}{\nu},$$
$$k=u_*^2/C_\mu^{1/2},\quad \varepsilon=u_*^3/æy, \tag{1.7}$$

where τ_w is the turbulent friction on the wall.

Values of the empirical constants are picked out in accordance with experimental data of turbulent boundary layer on smooth surface: æ=0.41, A=5.5. Placing the velocity $\mathbf{U}_w$ into expression (1.7) we take into account the motion on the surface, e.g. of the condense film. An extension of (1.7) to the possible mass fluxes to the wall as well from the wall (condensation or evaporation) is done in [6]. The account of wall roughness or film waviness may be carried out by varying the constant A.

Below we present the results of numerical modeling of hydrodynamics processes in the containment volume. For the accident affected by the tearing of the circulated pipeline, the steam-gas jets run through the floor holes into the containment volume. From under the dome of the containment, the steam-gas mixture goes into the outside circular split where steam condensation and water draining take place on the cylindrical part of the protection shell. So a closed circulation of medium is established. As the calculations using integral balance codes show, after the first 100 seconds of the accident, a state with almost constant pressure in the volume and quasi-steady circulation are realized. These regimes are characterized by slow variation of summed up steam and droplet flow rates with time. These rates are approximately equal. They can be estimated at a value of the order of 10 kg/s, that matches the volumetric steam flow rate of 2500 m^3/s under the pressure of 4 bars and at the temperature of 120°C.

The pattern of steam-gas mixture in containment is determined by the location of injection jets, by the irregularity of distribution of steam velocity and by the hydraulic resistance of circular split steam outlets from the considered area.

Let us consider the geometric size of the containment (fig.1). The dome diameter is 41 m, the cylinder diameter is 36.4 m, cylinder height is 31.1 m. Between the cylinder and the dome there are a circular split of width 1 m and a impenetrable ring of width 1.3 m. Every jet in floor is of area 3.4 m^2. Two configurations of jet inlets of steam were considered. In the first one (case 1) steam with equal velocities flowed through 12 jets, situated in groups of three jets symmetrically about two perpendicular diametrical planes. The initial velocities of stream were taken equal 60 m/s. In the second configuration (case 2) the steam was injected through 8 jets of group situation that was symmetrical about only one diametrical plane. The velocities in

these two cases were equal 140 and 70 m/s respectively . The Reynolds' number was of order 10^8. The grid generated for computations had total sizes 21x21x21. However in order to reduce the computation time, calculations were made only on half of the containment space with reflection about one of the diametric planes. So the computation grid was reduced to sizes 21x11x21. The grid had singular lines on the surface of the cylinder.

Fig. 2 shows the pattern of flow circulation that formed in the volume for case 1. The distributions of the velocity vectors indicates a very complex pattern of circulation in space. In the bigger part of the containment volume that includes the bottom layer, the movement has velocities in the region of 20%-30% of the initial ones. At the top of the containment dome zones with recirculated flow are formed, but the size of these zones are not considerable. Meantime, in the lower part of the space, a zone of low-velocity circulation forms. As a whole, the flow is symmetrical not only about the plane of symmetry, but also about the perpendicular one, which passes through the middle of the group jets. A sophisticated treatment of the values of outlet velocity in the split indicates variation of flow rate around the perimeter. This velocity nonuniformity is stipulated by the three-dimension effects due to the adopted scheme of stream medium inlet. For the considered configuration, the variation of the flow rate is ±20% from the mean value.

Fig. 3 shows the pattern of circulation in the case of the essentially non-symmetrical medium flowing into containment volume. It is shown by means of a section passed through the axis of jet that local influence of jet stream continues up to the dome top. A notable fact is that impulse of one single strong jet is 30% greater than summed up impulses of three jets in neighboring sector. It determines the direction of medium circulation in the plane of reflection and in the whole space. Zones with low intensity motion do not stand out. The flow rate in the bottom layer is faster in comparison with the earlier configuration and the flow rate variation around the perimeter of the outlet circulate split increases to 30%. The essential irregularity of the velocity field governs the high intensity of the turbulent energy that provides a high rate diffusive mixing. The distribution of normalized turbulent energy of the gas phase are presented by fig 4.

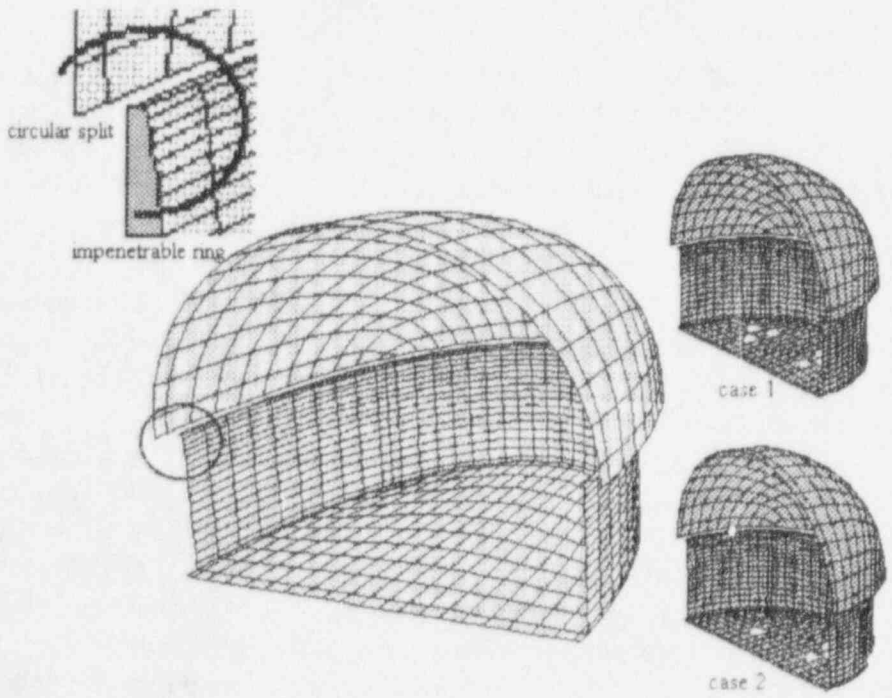

Fig. 1. Scheme of the containment and computation grid

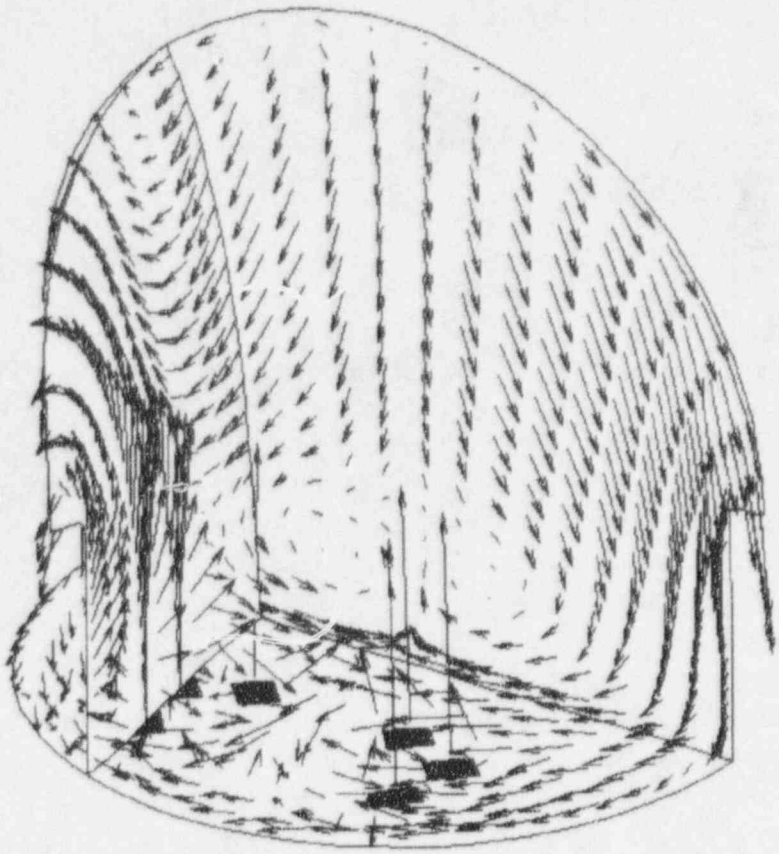

Fig. 2. Velocity vectors in the containment volume (case 1)

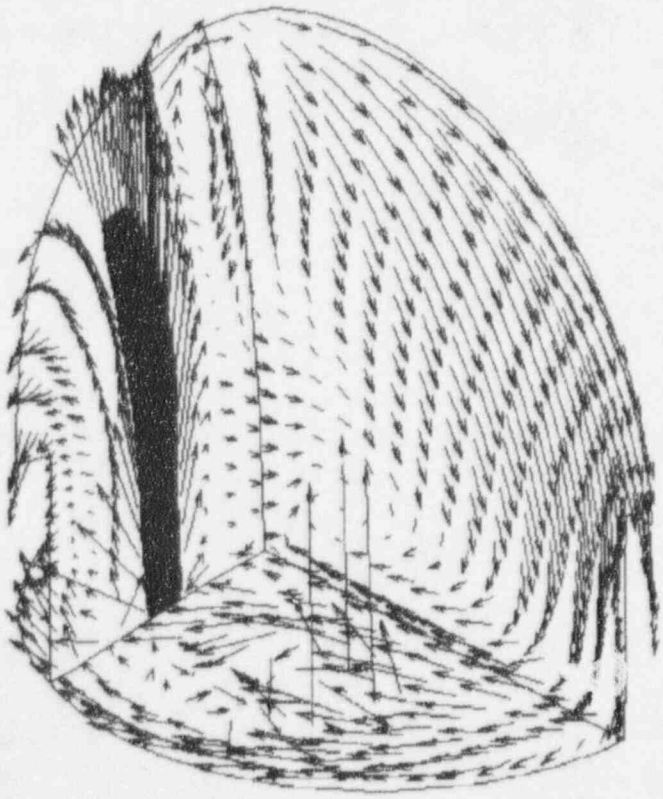

Fig. 3. Velocity vectors in the containment volume (case 2)

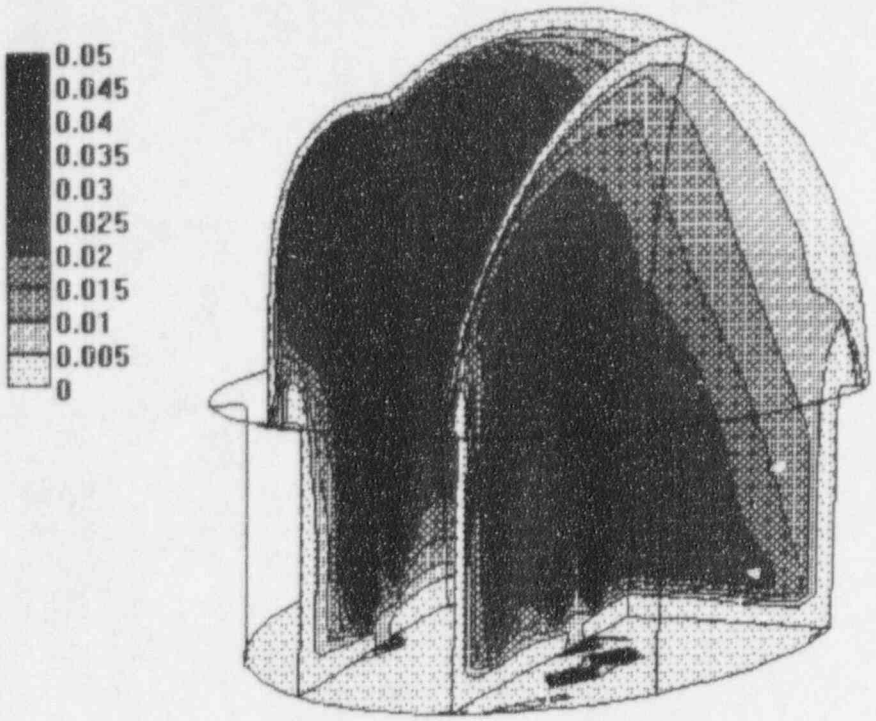

Fig. 4. Distribution of pulsation energy $\bar{k} = k / |\mathbf{U}|^2$ inside the containment volume (case 2)

2. MODELING OF DYNAMICS AND DEPOSITION OF AEROSOLS IN TWO-PHASE TURBULENT FLOWS

Description of the processes of dynamics and deposition of aerosols in turbulent flows is very important for various technical applications such as nuclear systems, fouling/erosion of turbine blades, steam generators, etc. In this paper, the diffusion-inertia mathematical model is presented. This model is based on the kinetic equation of probability density function (PDF) of distribution of aerosols in phase space of coordinates and velocities.

The equation for PDF of particles ensemble in turbulent flow is derived from the equations of motion of an individual particle

$$\frac{d\mathbf{R}_p}{d\tau} = \mathbf{v}_p, \quad \frac{d\mathbf{v}_p}{d\tau} = \frac{\mathbf{u} - \mathbf{v}_p}{\tau_u} + \mathbf{F} + \mathbf{f}_B. \tag{2.1}$$

Expressions (2.1) are the equations of Langevin type since the velocity of gas flow $\mathbf{u}$ and Brownian force $\mathbf{f}_B$ are considered to be random functions. In order to pass over from dynamic stochastic equations (2.1) to statistic description of droplets distribution according to velocities, the PDF in six-dimensional phase space $\mathbf{x}$, $\mathbf{v}$ is introduced

$$P = \langle p \rangle = \langle \delta(\mathbf{x} - \mathbf{R}_p(\tau)) \delta(\mathbf{v} - \mathbf{v}_p(\tau)) \rangle, \tag{2.2}$$

where P is obtained by averaging with respect to ensembles of realizations of random turbulent fields of $\mathbf{u}$ and $\mathbf{f}_B$.

The equation for PDF (2.2) can be derived using the technique of functional derivatives and assuming that the turbulent field of gas velocity is a Gaussian random process with known autocorrelation function. The closure equation for PDF will be [7-9]

$$\frac{\partial P}{\partial \tau}+v_k\frac{\partial P}{\partial x_k}+\frac{\partial}{\partial v_k}[(\frac{U_k-v_k}{\tau_u}+F_k)P]=\frac{f_u}{\tau_u}\langle u_i'u_k'\rangle\frac{\partial^2 P}{\partial v_i\partial v_k}+$$
$$+\frac{D_B}{\tau_u^2}\frac{\partial^2 P}{\partial v_k\partial v_k}+g_u\langle u_i'u_k'\rangle(\frac{\partial^2 P}{\partial x_i\partial v_k}+\frac{\partial V_n}{\partial x_k}\frac{\partial^2 P}{\partial v_i\partial v_n}). \qquad (2.3)$$

The coefficients of droplet entraining by the macropulsation continuous flow motion are obtained using a step approximation for two-time correlation function of the gas velocities pulsations [7,10]

$$f_u=1-\exp(-T_u/\tau_u)\,,\ g_u=T_u/\tau_u-f_u=T_u/\tau_u-1+\exp(-T_u/\tau_u)\,. \qquad (2.4)$$

The equations for calculation of mass and impulse transfer in dispersed phase are deduced as a result of integration of the equation for PDF (2.3)

$$\frac{\partial\Phi}{\partial\tau}+\frac{\partial\Phi V_k}{\partial x_k}=0, \qquad (2.5)$$

$$\frac{\partial\Phi V_i}{\partial\tau}+\frac{\partial\Phi V_iV_k}{\partial x_k}=-\frac{\partial}{\partial x_k}(\Phi\langle v_i'v_k'\rangle)+\Phi(\frac{U_i-V_i}{\tau_u}+F_i)-g_u\langle u_i'u_k'\rangle\frac{\partial\Phi}{\partial x_k}. \qquad (2.6)$$

The equation for second moments of velocity pulsations of dispersed phase $\langle v_i'v_j'\rangle$ will be

$$\Phi(\frac{\partial\langle v_i'v_j'\rangle}{\partial\tau}+V_k\frac{\partial\langle v_i'v_j'\rangle}{\partial x_k})=-\frac{\partial}{\partial x_k}(\Phi\langle v_i'v_j'v_k'\rangle-\Phi(\langle v_i'v_k'\rangle\frac{\partial V_j}{\partial x_k}+$$
$$+\langle v_j'v_k'\rangle\frac{\partial V_i}{\partial x_k})+\frac{2\Phi}{\tau_u}(f_u\langle u_i'u_j'\rangle+\frac{D_B}{\tau_u}\delta_{ij})-\frac{2\Phi}{\tau_u}\langle v_i'v_j'\rangle. \qquad (2.7)$$

For small particles the local-homogeneous approximation of equation (2.7) can be used

$$\langle v_i'v_j'\rangle=f_u\langle u_i'u_j'\rangle+\frac{D_B}{\tau_u}\delta_{ij}. \qquad (2.8)$$

From the equation of motion (2.6) with account of the expression (2.8) we can express the droplets velocity using the method of iteration according to relaxation time τ_u

$$V_i=U_i-(D_B\delta_{ik}+D_{ik})\frac{\partial\ln\Phi}{\partial x_n}+\tau_u(F_i-\frac{\partial f_u<u_i'u_k'>}{\partial x_k}-\frac{\partial U_i}{\partial\tau}-U_k\frac{\partial U_i}{\partial x_k}). \qquad (2.9)$$

The equation (2.9) shows that velocity interphase slip (dynamic non-equilibrium state of phases) is induced by the presence of a concentration gradient, mass forces effect, droplet turbulent migration from the field of high flow turbulence to one where the level of turbulent pulsations is low, and also by inertia transfer due to droplet trajectory deviations from the lines of gas stream due to curvature and as a result of flow unsteadiness.

Substituting (2.9) into the mass balance equation (2.5) we obtain the diffusion equation for droplet concentration

$$\frac{\partial\Phi}{\partial\tau}+\frac{\partial}{\partial x_i}\{\Phi[U_i+\tau_u(F_i-\frac{\partial f_u<u_i'u_k'>}{\partial x_k}-\frac{\partial U_i}{\partial\tau}-U_k\frac{\partial U_i}{\partial x_k}]\}=$$
$$=\frac{\partial}{\partial x_i}[(D_B\delta_{ik}+D_{ik})\frac{\partial\Phi}{\partial x_k}]. \qquad (2.10)$$

At $\tau_u \to 0$ the eq. (2.10) transforms into usual turbulent diffusion equation of inertialess admixture

$$\frac{\partial \Phi}{\partial \tau} + \frac{\partial \Phi U_i}{\partial x_i} = \frac{\partial}{\partial x_i}[(D_B \delta_{ik} + D_{ik}) \frac{\partial \Phi}{\partial x_k}]. \qquad (2.11)$$

Terms, proportional to τ_u in the equation (2.10), determine inertia effects induced by mass forces, migration transfer due to non-homogeneity of turbulent pulsations field of carrying flow velocity and inertia transfer as a result of flow unsteadiness and deviation of droplets trajectories from the lines of gas stream due to curvature. Thus, the equation (2.10) in contrast to the standard diffusion equation (2.11) allows to computation of small-dispersed droplet transport including of a number of inertia mechanisms of transfer.

For solving the system of equations which describes motion of dispersed phase, it is necessary to formulate the boundary conditions on solid or liquid (if there is film) surfaces bounding the flow. In order to create the boundary conditions for the equations of dispersed phase motion, as well as in the theory of rarefied gas, it is necessary to have the information on PDF of the droplet velocity distribution in the near-wall zone [9,11].

We assume that the PDF of particle transition from a situation before an impact with the wall 1 into a situation after an impact with the wall 2 can be determined as

$$P_w(2/1) = \chi \delta(v_{x_2} - \phi_v v_{x_1}) \delta(v_{y_2} + v_{y_1}). \qquad (2.12)$$

If the distribution of the normal particle velocity in the near-wall space is quasinormal, the boundary condition for averaged velocities and second moments of velocity pulsations are [9]

$$V_y = -\frac{1-\chi}{1+\chi}\sqrt{\frac{2\langle v_y'^2 \rangle}{\pi}}, \left(\frac{1-\phi_v \chi}{1+\phi_v \chi} - \frac{1-\chi}{1+\chi}\sqrt{\frac{2\langle v_y'^2 \rangle}{\pi}}\right) V_x = -\langle v_x' v_y' \rangle. \qquad (2.13)$$

For small particles, when the concentration is calculated by the equation (2.10), the boundary condition is presented in the form

$$D_{yy} \frac{\partial \Phi}{\partial y} = \left(\frac{1-\chi}{1+\chi}\sqrt{\frac{2\langle v_y'^2 \rangle}{\pi}} - \frac{\partial q D_{yy}}{\partial y} + U_y + \tau_u F_y\right) \Phi, \qquad (2.14)$$

where $q = \tau_u f_u / T_u$ is the factor of turbulent migration.

To simplify the computation procedure when carrying out real calculations, the boundary conditions can be given not on the wall, but at some distance from it beyond the zone of the viscous sublayer. In order to obtain the near-wall function it is necessary to find the droplet concentration distribution in the near-wall zone and to determine the deposition rate on the wall $G_w = \Phi_w V_w$. The characteristics of the liquid dispersed phase in the near-wall zone are determined from the solution of the system of standard difference equations for concentration (2.5), averaged velocity (2.6) and the second moments of velocity pulsations (2.7) [11]. On the basis of obtained solutions the following relation is proposed

$$G_w = \frac{(0{,}115/B^{3/4}\tau_+^{3/8} + 2{,}5 \cdot 10^{-4}\tau_+^{2,5}) u_* \Phi_1}{\max[0{,}61; \min(1{,}32 - 0{,}27 \ln \tau_+; 1)]}. \qquad (2.15)$$

Formula (2.15) is valid for relatively small particles (at $\tau_+ < 100$) when choosing concentration of Φ_1 in the range of distance variance from the wall $20 < y_+ < 100$, where Φ slightly varies with varying of y.

For testing of the diffusion-inertia model the calculations for various simple two-phase turbulent flows (flow in the round jets and pipes) are carried out.

Let us consider fine-dispersed admixture flow in axisymmetrical jet. Flows conditions correspond to experimental research represented in [12,13]. These works deal with the experimental research in the field of small particles propagation in horizontal turbulent jet, bleeding from the nozzle, the radius of which is R_0=17.5 mm, with velocity equal to U_0=45m/s. The dispersed phase was monodispersed system of particles with diameter d_p=7 μm or 17 μm and density ρ_p=4500 kg/m^3.

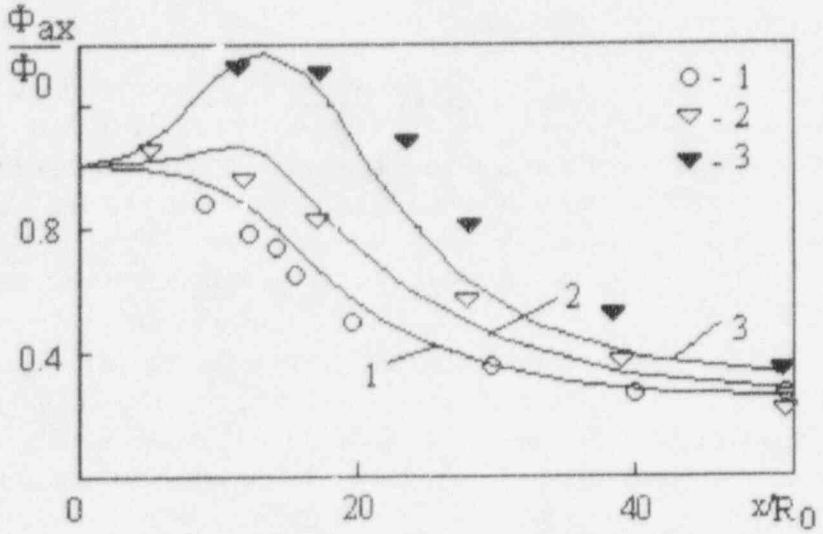

Fig.5. Fine-dispersed admixture concentration distribution along jet axis
1- single-phase jet, experiment [14]; 2 - d_p=7 μm; 3 - 17 μm, experiment [13]

Comparison between calculation and experimental data on variation of the admixture concentration along the jet axis at different values of particles diameter d_p is shown on Fig.5. In case of inertialess admixture (d_p = 0) monotonous concentration reduction with increase of the distance from the nozzle is observed. When injecting a fine-dispersed admixture into the flow, its concentration increases in the beginning of the flow (so-called "lacing up" effect) and then particles as well as inertialess admixture concentration decreases according to $\Phi_{ax} \sim 1/x$ law. The admixture concentration increase is explained by the non-monotonous character of turbulent energy alteration in axial and radial directions at high turbulence level in the initial part of jet. This phenomena evidences the considerable effect of interaction between particles and carrier flow turbulent pulsations on the admixture propagation character. As it is obvious from Fig.5, as the particles size increases the concentration maximum becomes more strongly pronounced which is explained by growth of turbulent migration importance. Thus, the "lacing up" effect, discovered in the experiments and lying in non-monotonous change of particles concentration, is reproduced sufficiently well for the fine-dispersed admixture in the framework of the approximation under consideration owing to turbulent migration process taken into account.

Admixture concentration variations in the jet cross-section at different distances from nozzle are given on Fig.6. The figure shows the non-monotonous character of concentration change on the section in the initial part of jet as well as in axial direction. This effect is determined by the displaced against jet axis maximum in turbulent energy radial distribution [14]. With increase of distance from nozzle the value of maximum in turbulent energy profile reduces and particles

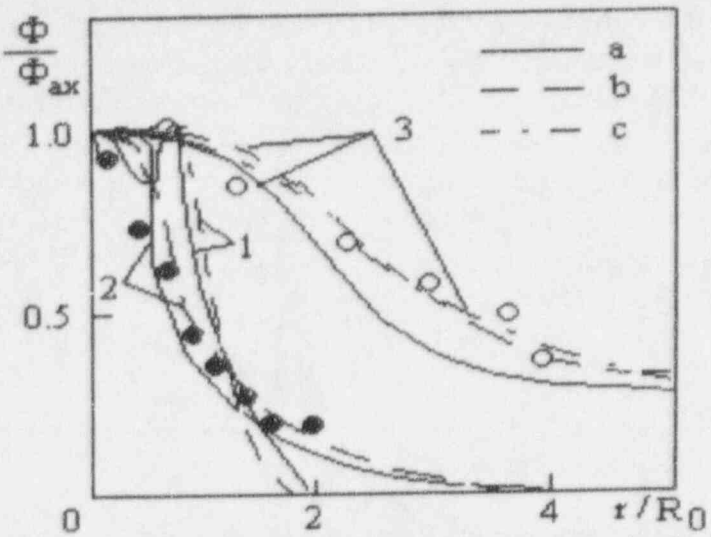

Fig.6. Radial distributions of fine-dispersed admixture concentrationin various jet cross-sections

1 - x/R_0=4; 2 - 12; 3 - 40; a - d_p=7 μm, b - 17 μm, experiment [12];
c- single-phase jet, experiment [14]

concentration lateral distribution becomes monotonous. In the particle size range under analyses, the concentration radial distribution profile is more sloping as compared with that of axial velocity; this phenomena evidences that the effective Schmidt number is more than one. This effect was often emphasized in research works devoted to two-phase jet flows (for instance [14]). However, in contrast with [14], in the present model, the above mentioned effect is accounted not by means of the Sc_T value increasing but as a result of viewing turbulent migration. It should be noted that at large distances from nozzle inertia admixture distributions differ slightly from those of the inertialess one, which is explained by the low level and smooth distribution of turbulent energy, and consequently by the fact that turbulent migration is negligible.

Along with the "lacing-up" effect in a number of experimental works (for instance [15]) there was discovered the effect of wave type particle concentration changing along jet axis. The most pronounced character of wave forming is revealed in a definite range of flow initial velocity change in the nozzle. The authors [15] explain the wave forming process by different initial averaged slip between phases. Calculations of flow characteristics at different initial values of carrier flow velocity were carried out on the diffusion-inertia model basis. The results obtained gave the evidence that despite practical absence of slip between phases at relatively high flow velocity values, the wave type character of admixture concentration change along axis is realized (Fig.7). The available effect is explained by non-monotonous variance of the coefficient of particle entrainment into gas pulsation motion along the jet induced by turbulence time integral scale change T_u and become pronounced at flow high velocities. In this case as well as in the case of pure gas jet, with increasing of U_0 velocity, the jet becomes more long-range and dispersed phase concentration on jet axis damps more slowly.

Let us consider the problem of diffusion-inertia model application for calculation of inner flows in pipes. The essential distinction between confined and free flows is the possibility for particles to deposit on the walls under the action of different physical nature forces: turbulent and Brownian diffusion, inertia, turbulent migration and mass forces. Droplet deposition processes under the action of turbulent and Brownian diffusion as well as turbulent migration shall be considered.

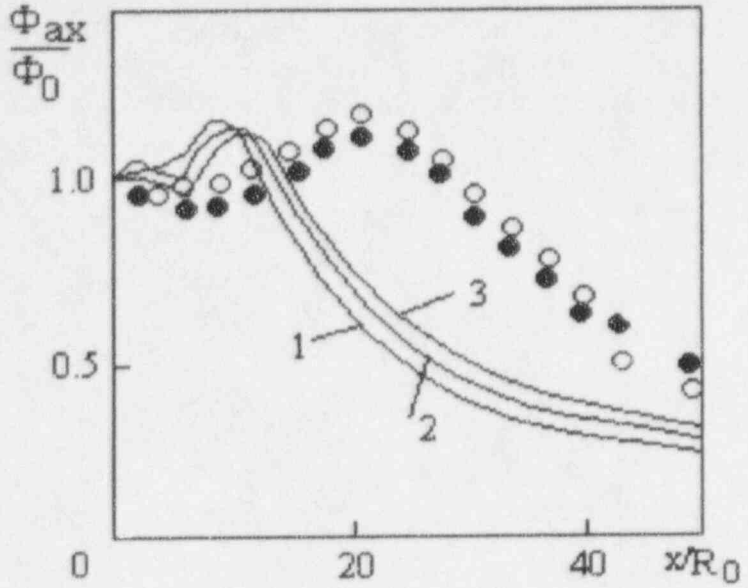

Fig.7. Flow initial velocity effect on particles concentration variation (d_p=23 μm) along jet axis
1 - U_0=20 m/s; 2 - 35 m/s; 3 - 70 m/s; 4, 5 - experiment [15]

Computations of droplet deposition processes in pipes with completely absorbing walls were carried out on the basis of the given model. Computation were made for turbulent steam-droplet flow at P=1 bars and T=100°C in the channel with the diameter D_0=0.1 m. Reynolds number variation was defined by means of varying steam velocity from U_0=5 m/s to U_0=50 m/s. Droplet sizes changed in the range between d_p=0.1 μm and d_p=50 μm.

Comparison of computation results of the deposition coefficient j_+ dependence upon the particle dimensionless relaxation time τ_+ with the experimental data collected in [16] is represented on Fig.7. Given computation results correspond to the self-similar part of the flow in the pipe at x/D_0=100 and are obtained at different Reynolds number values of the main flow. The coefficient of deposition upon the wall is computed on the basis of the following expression

$$j_+ = \frac{G_w}{\Phi_m u_*}, \quad \Phi_m = \int_0^{R_0} \Phi U_x r\,dr \Big/ \int_0^{R_0} U_x r\,dr$$

where Φ_m is the mean discharge value of the droplet concentration in pipe cross-sections.

Dependence of B upon the dynamic velocity u_* and consequently upon the Reynolds number Re accounts for calculation data differentiation at small values of τ_+. For high inertia droplets (τ_+>1), when the importance of Brownian diffusion becomes negligibly small, the deposition coefficient is determined only by the parameter of τ_+. Reduction of deposition coefficient with increase of τ_+ for very small droplets is induced by decrease of the Brownian diffusion coefficient, while for relatively high inertia droplets this phenomenon is connected with increase of the role of turbulent migration.

Solid lines on Fig.8 correspond to the formula

$$j_+ = \frac{0{,}115 / B^{3/4} \tau_+^{3/8} + 2{,}5 \cdot 10^{-4} \tau_+^{2{,}5}}{1 + 10^{-3} \tau_+^{2{,}5}},$$

which generalizes the results of numeric and analytic solutions of the combined equations for dispersed phase characteristics, closed at the level of equations for the second moments of velocity pulsations, in turbulent flow near-wall field including viscous sublayer.

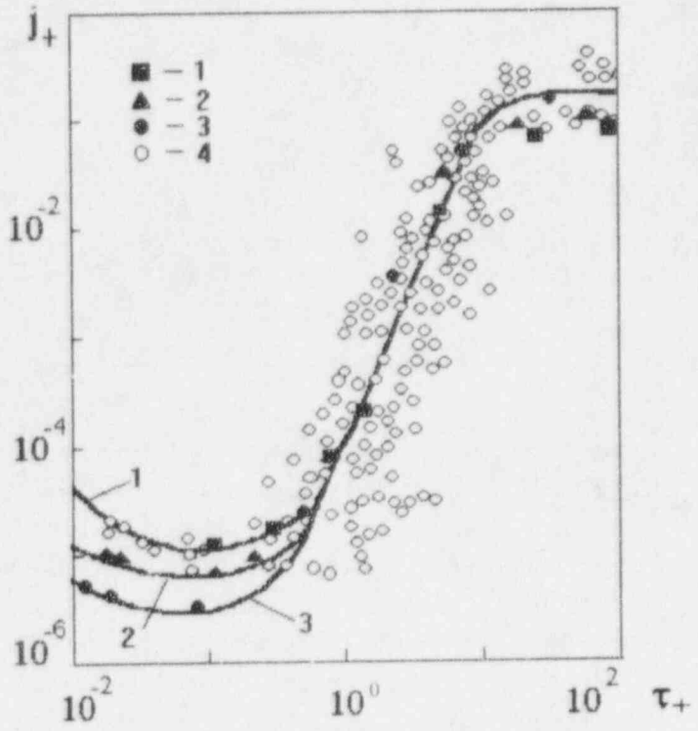

Fig.8. Deposition coefficient dependence upon droplets inertia
1 - calculation at $Re=1.5\cdot10^5$ ($B=5.0\cdot10^5$), 2 - $6{,}0\cdot10^4$ ($1.2\cdot10^6$); 3 - $1.5\cdot10^4$ ($4.2\cdot10^6$);
4 - experiment [16]

Proceeding from the following condition $\tau_u/T_u<1$ it is rather simple to obtain evaluation of diffusion-inertia model applicability range for turbulent flow in pipe. In the near-wall field of turbulent flow the integral time scale of pulsations with high energy consumption is equal to $T_u\approx10\nu/u_*^2$ [11,17], which leads to $\tau_+<10$, determining diffusion-inertia model validity range for particles deposition calculation. Turbulence mean integral time scale on the pipe cross section can be $T_u\approx L/u_*\approx0.1R_0/u_*$. The condition $\tau_u u_*/R_0<0.1$ derives from the evaluation given above for the turbulence time scale. These conditions restrict the range of application of the diffusion-inertia model for description of droplets concentration on pipe cross-section. Fig.8 shows that the represented model describes well enough the droplet deposition process even in some wider range of particle inertia variation ($\tau_+<100$).

Thus, the results obtained prove the possibility of diffusion-inertia model application for description of small droplet dynamics and deposition in two-phase turbulent flows.

3. MODELING OF FILM CONDENSATION IN CONTAINMENT

One of the main mechanisms of heat removal from the containment is the heat transfer due to condensation. Consider film condensation of the steam-gas mixture on the walls of the containment structures on the base of the model operated with integral characteristics of medium inside the containment during the unsteady heat transfer process [18]. The main goal is to determine boundary conditions (heat and mass fluxes) for multidimensional calculations

(via wall-function formulation) in description of condensation process. The initial conditions are known - values from the previous time step (pressure, temperature, concentration, etc.). These values may be local (nodal) parameters for the case of multidimensional formulation or an averaged parameters for "lumped" formulation.

In film condensation process there are convective and condensation heat fluxes on the inner surface.

$$q_{conv} = \alpha_{conv}\left(T_{bulk} - T_s\right) \tag{3.1}$$

$$q_{cond} = j \cdot r \tag{3.2}$$

The radiation heat transfer mechanism is not considered due to its negligible value. Sum of the inside heat fluxes must be in equlibrium with conductivity heat flux through the wall (q_w) (fig.9).

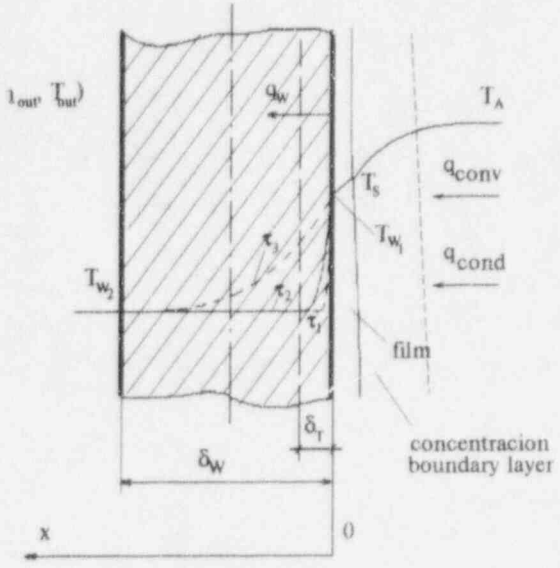

Fig.9 Heat and mass transfer in condensation
δ_T - temperature front depth, $\tau_1 < \tau_2 < \tau_3$

Presence of noncondensables leads to necessity of liquid film temperature (T_s) determination by mean of the partial pressure (concentration) of steam at interphase surface. Aditional difficulty concerned with unknown wall temperature (T_{w_1} at fig.9) at the current time step. To overcome these difficulties, the iteration technique for concordance of heat and mass fluxes in a near-wall boundary layer and through the liquid film developed in [18] was adopted. Two variants of the numerical algorithms are presented at fig.10.

The numerical procedure for the transient heat flux calculation includes the following steps:

. Guess the value of interphase temperature, $T_{out} < T_s < T_{bulk}$.

. Calculate interphase parameters (concentration, mixture density etc.) using the relation $P_{vap} = f(T_s)$.

. Calculate convective heat flux using the difference approximation for multidimensional case and eq.3.1 for the integral formulation, where h_{conv} is calculated using the well-known formulas for free and forced convection in enclosures with account of their directions (see [19] for more details).

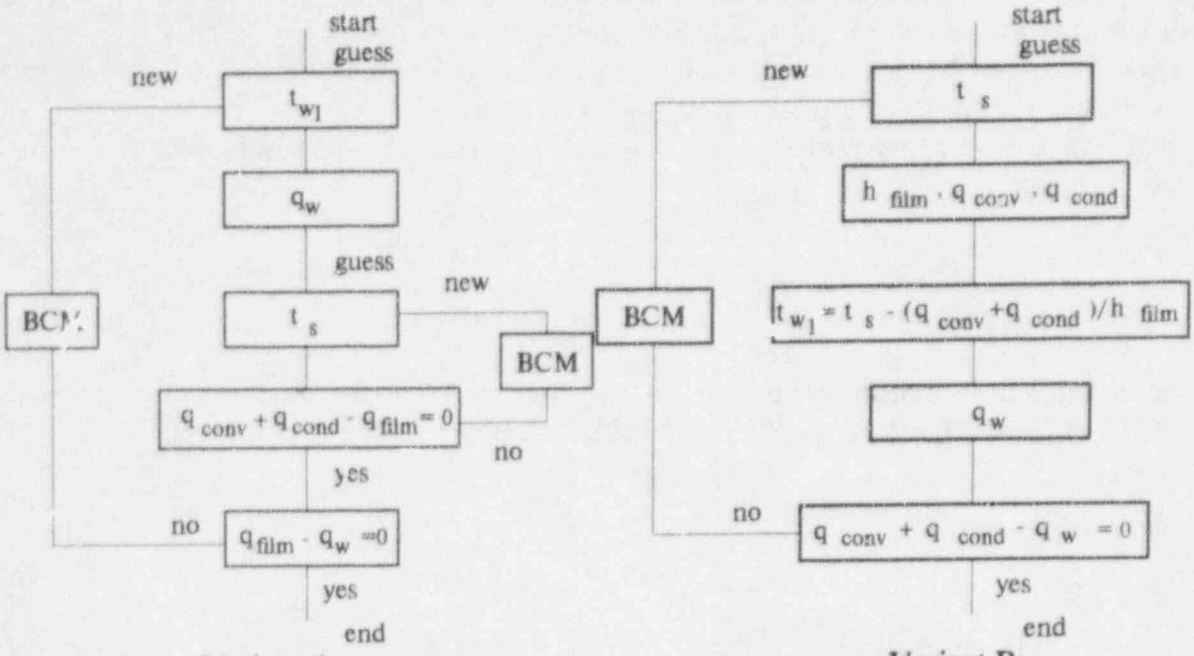

Fig.10 Algorithms for calculation of interphase and wall temperatures
BCM - bisection/chord method

4. Calculate heat flux due to condensation (3.2), where the condensation rate j is evaluated as follows [20]

$$j = \rho_a \cdot \beta^* \psi_D^m \cdot B \cdot C^n, \tag{3.3}$$

where $C = C_{g,a} / C_{g,s}$, $B = 1 - C$;

$$\beta^* = \beta_0 \gamma_s \tag{3.4}$$

and β_0 - mass transfer coefficient, which is calculated using heat and mass transfer analogy;

$$\gamma_s = 2.12 Sc_T^{2/3} / \left(1 + 0.66 Sc_T\right), \tag{3.5}$$

modification used to account for film motion;

$$\psi_D = 4 \cdot (1 - \sqrt{C})^2 \cdot B^2, \tag{3.6}$$

modification used to account cross-mass flux, and for laminar boundary layer: m=0.5, n=-0.5, for turbulent - m=0.8, n=-0.2.

. Calculate heat flux through the wall (q_w), using T_{w_1} as the inner boundary condition and, for the outer boundary, $q_{out} = h_{out}(T_{w_2} - T_{out})$.

Numerical solution of the unsteady heat conductivity equation was obtained using an implicit scheme and Tri-diagonal matrix algorithm (TDMA). For the walls with low thermal conductivity, the following formula for the heat transfer rate was used

$$q_w = \frac{T_{w_1} - T_{out}}{R_w + R_{out}}, \tag{3.7}$$

where

$$R_w = \frac{\delta_T}{k_w} \cdot \frac{1}{1+e^{-\pi^2 \alpha_w \tau_1 / \delta_w^2}}, R_{out} = \frac{1}{h_{out}} \cdot \frac{1-e^{-\pi^2 \alpha_w \tau_1 / \delta_w^2}}{1+e^{-\pi^2 \alpha_w \tau_1 / \delta_w^2}}, \quad (3.8)$$

and $\tau_1 = \tau - \tau_T$, where τ_T - time when $\delta_T = \delta_w$ (fig.9).

Compare $q_{conv} + q_{cond}$ and q_w. If residual is greater than the exit criterion, use bisection/chord algorithm logic to calculate a new value of T_s and return to step 2.

The calculation of the heat transfer through the film was done as follows

$$q_{film} = h_{film}(T_s - T_{w_1}) \quad (3.9)$$

The formulas for h_{film} in the considered geometry (cylinder with hemisphere dome) were obtained using the Nusselt assumption:

- hemisphere

$$h_\varphi = \sqrt[3]{\frac{1}{3} k_{film}^3 \frac{r}{q_w} \frac{\rho_{film} g}{R \nu_{film}} \frac{\sin^2 \varphi}{1-\cos\varphi}}, \bar{h} = 0.787 \sqrt[3]{k_{film}^3 \frac{r}{q_w} \frac{\rho_{film} g}{R \nu_{film}}} \quad (3.10)$$

- cylinder

$$h_x = \sqrt[3]{\frac{k_{film}^3}{3\nu_{film}} \rho_{film} g \frac{r}{q_w} \frac{1}{R+x}}, \bar{h} = 1{,}04\left(1/H\right)\left[(R+H)^{2/3} - R^{2/3}\right] \cdot \sqrt[3]{\frac{k_{film}^3}{\nu_{film}} \rho_{film} g \frac{r}{q_w}} \quad (3.11)$$

where φ - angle from the vertical, x - vertical coordinate from the top of cylinder, R, H - cylinder radius and height.

To account for aditional features (e.g. nonunifomity of properties, waviness etc.) the correction to formulas (3.10, 3.11) for film heat transfer coefficient was made

$$h = h_{Nu} \cdot \varepsilon, \quad (3.12)$$

where ε - correction factor which is determined in accordance with [21].

Testing of the described procedure was made against experimental data by Uchida [22] obtained for free convection steam-air mixture condensation on the cooled vertical plate 14cm x 30cm in the pressure range 0.101 MPa to 0.3 MPa and air concentration 0.1 to 0.96. Comparison was also made with the analytic correlation by Whitley [23] for total heat transfer coefficient

$$h = 0.037 r \rho_a \nu_a^{0.2} U_a^{0.8} L^{-0.2} Sc_T^{-0.4} \ln(1+B) * \left(T_s - T_{w_1}\right)^{-1} \quad (3.13)$$

where r - heat of vaporization, L - length , U_a- velocity at the ambient conditions, $B = \left(C_{g,a} - C_{g,s}\right) / \left(C_{g,s} - 1\right)$ - mass potential.

Calculation results for the case of p_a = 0.101 MPa and U_a = 0.1 m/sec are compared against data in fig.11. As shown in the figure, a good agreement is observed. At the same time, correlation (3.13) gives lower values of heat transfer coefficient (fig.12) than the procedure described above. The reason for this is the Couette approximation used to derive this correlation.

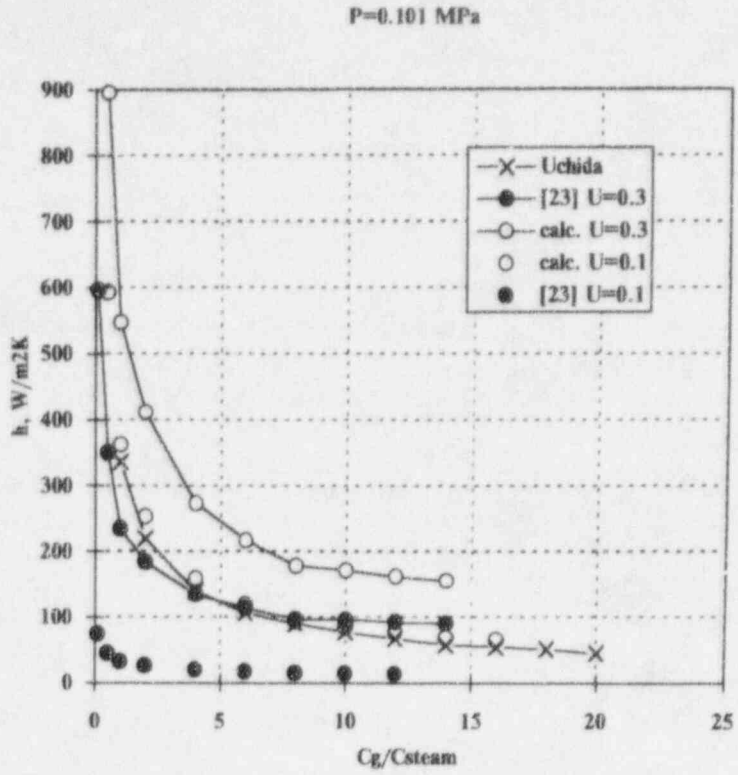

Fig.11. Comparison calculation results against data.
x - axis, ratio of ambient air and steam concentration

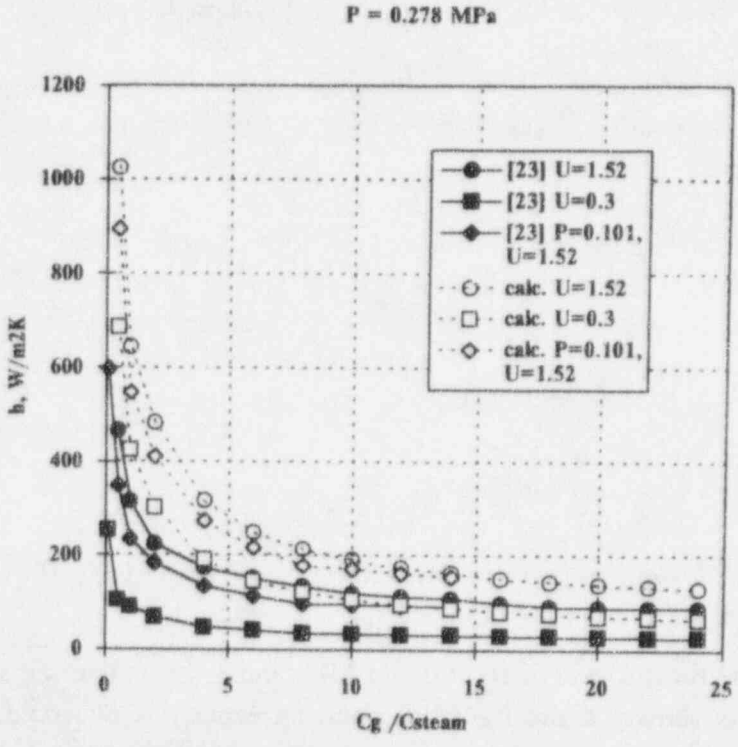

Fig.12. Comparison calculated results with correlation (3.13)

SUMMARY AND CONCLUSIONS

1. For hydrodynamic calculation of turbulent flow in containment elements the mathematic model is presented. Calculations of averaged and pulsating characteristics of three dimensional flow formed at both symmetric and non-symmetric localized steam-gas mixture throwing were carried out. In both cases it is shown that great non uniformity of gas flow distribution around the circular slip perimeter (as much as 30%) takes place.

2. A diffusion-inertia model for description of dynamics and deposition of the small aerosols in turbulent flows is proposed. The model includes the diffusion-like equation for concentrations and the boundary condition for the deposition rate of droplets in the form of wall-functions. Performed tests demonstrate applicability of this model for calculation of two-phase turbulent free and confined flows.

3. The film condensation of steam-gas mixture on containment walls surface is considered. On the basis of an integral parameters model, the boundary conditions calculation procedure for steam-gas condensation is described.

Table of Nomenclature

τ - time;
$\mathbf{x}$ - spatial coordinates;
$\mathbf{R}_p$, $\mathbf{v}_p$ - coordinate and velocity of particle;
$\mathbf{v}$,$\mathbf{V}$,$\mathbf{v}'$ - actual, averaged and pulsation velocity of dispersed phase;
$\mathbf{u}$,$\mathbf{U}$,$\mathbf{u}'$ - actual, averaged and pulsation velocity of dispersed phase;
$\mathbf{F}$ - external mass force;
$\mathbf{g}$ - gravitational force;
$\mathbf{f}_B$ - Brownian force acceleration;
P - gas pressure and probability density function;
Φ - volume aerosols concentration;
T - gas temperature;
k - turbulent energy of gas; heat conductivity coefficient;
ε - rate of turbulent energy dissipation;
τ_u - dynamic relaxation time of aerosols;
$\tau_+ = \tau_u u_*^2 / \nu$ - dimensionless time of aerosols relaxation;
T_u - integral time scale of turbulence;
L - integral spatial scale of turbulence
d_p - diameter of particles;
ρ, ρ_p - density of gas and dispersed phases;
μ, ν - coefficients of kinematic and dynamic viscosity of gas;
μ_T, ν_T - coefficients of kinematic and dynamic turbulent viscosity of gas;
D_B - Brownian diffusion coefficient;
$D_{ij} = T_u \langle u_i' u_j' \rangle$ - diffusion tensor of inertialess admixture;
M - molecular mass;
u_* - friction velocity;
x - longitudinal spatial coordinate;
y - transverse;
$Sc_T = \nu_T / D_T$ - Schmidt turbulent number;
$Sc_B = \nu / D_B$ - Schmidt Brownian number;

$B = Sc_B / \tau_+^{1/2}$ - dimensionless Brownian diffusion parameter;

R_0 - universal gas constant;

C_α - mass concentration of component α in the gas mixture;

χ_α - mole concentration of component α in the gas mixture;

$\delta(x)$ - Dirac delta-function;

h - heat transfer coefficient.

REFERENCES

[1] M. Merilo and T.L. George, "Thermalhydraulic analyze of containments," Proc. Third Int. Conf. on Simulation Methods in Nuclear Engineering , 716-736 (1990).

[2] L. Wolf, H. Holzbauer and T. Cron, "Detailed assessment of the HDR-hydrogen mixing experiments E11," Int. Conf. New Trends in Nuclear System Thermohydraulics of Containment and Severe Accidents, 91-103 (1992).

[3] B.E. Launder and D.B. Spalding, "The numerical computation of turbulent flows," Comput. Methods Appl. Mech. Eng. 3, 269-289 (1974).

[4] S. Abuzeid, A.A. Busnaina and G. Ahmadi, "Deposition of fine particle from turbulent flow on the channel wall," Particl. Sci. and Technol. 10, 209-225 (1992).

[5] X. Yuan, A. Moser, and P. Suter "Wall functions for numerical simulation of turbulent natural convection along vertical plates," Int. J. Heat Mass Transfer. 36, 4477-4485 (1993).

[6] V.M. Eroshenko and L.I. Zaichik, Hydrodynamics and Heat-Mass Transfer on the Penetrable Surfaces, Nauka, Moscow (1984).

[7] I.V. Derevich and L.I. Zaichik, "An equation for the probability density, velocity, and temperature of particles in a turbulent flow modelled by a random Gaussian field," Appl. Math. and Mech. 54, 631-638 (1990).

[8] L.I. Zaichik and A.A.Vinberg, "Modelling of particle dynamics and heat transfer in turbulent flows using equations for first and second moments of velocity and temperature fluctuations," Proc. 8th Symp. on Turbulent Shear Flows 10.2.1-10.2.6 (1991)

[9] L.I. Zaichik and V.A. Pershukov, "Mathematical models for simulation of dynamics, heat and mass transfer and combustion in two-phase turbulent flows," Proc. 10th Int. Conf. Heat Transfer 2, 171-176 (1994).

[10] I.V. Derevich, V.M. Yeroshenko and L.I. Zaichik, "Hydrodynamics and heat transfer of turbulent gas suspension flows in tubes. 1.Hydrodynamics," Int. J. Heat and Mass Transfer. 32, 2329-2339 (1989).

[11] I.N. Gusev, E.I. Gusev and L.I. Zaichik, "Model of particle deposition from turbulent gas-solid flow in channels with adsorbent walls," Fluid Dynamics 27, 43-48 (1992).

[12] M.K. Laats and F.A. Frishman, "Assumption used in calculating the two-phase jet," Fluid Dynamics, 5, 333-338 (1970).

[13] M.K. Laats and F.A. Frishman, "Development of technique and study of the intensity of turbulence on the axis two-phase turbulent jet," Fluid Dynamics, 8, 304-307 (1973).

[14] Theory of Turbulent Jets /Editor G.N.Abramovich, Nauka, Moscow (1984).

[15] S.I. Navoznov, A.A. Paveliev, A.C. Mulgi and M.K. Laats, "Influence of initial velocity slip on the propagation of admixture in two0phase jet," Turbul. Two-Phase Flows, Tallinn, 149-154 (1979).

[16] D.D. McCoy and D.D. Hanratty, "Rate of deposition of droplets in annular two-phase flow," Int. J. Multiphase Flow, 3, 319-331 (1977).

[17] G.A. Kallio and M.W. Reeks, "A numerical simulation of particle deposition in turbulent boundary layers," Int. J. Multiphase Flow, 15, 433-446 (1989).

[18] A.P.Solodov, D.V. Sidenkov and I.I. Kutakov, "Predicting of unsteady parameters in safety system of NPP", Moscow Power Engineering Institute (MPEI) Report, Gos. reg. N01900014222 (1989).
[19] D.V.Sidenkov, "Numerical simulation of thermohydrodynamic fields in complex geometries of NPP's safety system using finite element technique", Ph.D. Thesis, Moscow Technical University (MPEI), (1994).
[20] A.P.Solodov, "Development of experimentally proved calculation models for heat mass transfer in jet condensation", Sc.D. Thesis, MPEI, (1987)
[21] V.P.Isachenko, Heat Transfer in Condensation, Energy, Moscow (1976).
[22] H.Uchida, A.Oyama and Y.Togo, Proc. of the Int. Conf. of the Peaceful Uses of Atomic Energy., UN, New York, 13, 93-104 (1965).
[23] R.H.Whitley, C.K.Chan and D.Ckrent, "On the Analysis of Containment Heat Transfer Following LOCA", Annals of Nuclear Energy, 3, 515-525 (1976).

GEYSER/TONUS : a coupled multi-D lumped parameter code for reactor thermal hydraulics analysis in case of severe accidents

M. Petit, M. Durin* , J. Gauvain
Commissariat à l'Energie Atomique
DMT/SEMT/TTMF
91191 Gif sur Yvette Cedex
France

ABSTRACT

In many countries, the safety requirements for future light water reactors include accounting for severe accidents in the design process.

As far as the containment is concerned, the design must now include mitigation features to limit the pressure and temperature inside the building. Hydrogen concentration is also a major issue for severe accidents.

In this context, new needs appear for the modeling of the thermal hydraulics inside the containment. It requires the description of complex phenomena such as condensation, stratification, transport of gases and aerosols, heat transfers. Moreover, the effect of mitigation systems will increase the heterogeneities in the building, and most of those phenomena can be coupled, as for example hydrogen stratification and condensation.

To model such a complex situation, the use of multi-dimensional computer codes seems to be necessary in case of large volumes. The aim of the GEYSER/TONUS computer code is to fulfill this need. This code is currently under development at CEA in Saclay. It will allow the coupling of parts of the containment described in a lumped parameter manner, together with meshed parts.

Emphasis is put on the numerical methods used to solve the transient problem, as the objective is to be able to treat complete scenarios. Physical models of classical lumped parameters codes will adapted for the spatially described zones.

The code is developed in the environment of the CASTEM 2000/TRIO EF system which allows, thanks to its modular conception, to construct sophisticated applications based upon it.

---

* Presently at : Commissariat à l'Energie Atomique, IPSN/DPEI, CE Fontenay, BP 6, 92265 Fontenay aux Roses Cedex, France

INTRODUCTION

The first studies of PWR containment behavior during a severe accident were performed in the seventies. At that time, the main objective was to insure that no significant release of fission products could occur during and after a core-melt accident. Then, containment structure studies required the knowledge of the mechanical loading, that is the evolution with respect to time of the mean pressure and the mean temperature of the internal atmosphere. These evolutions were computed by codes developed with a « single node » approach based on a global mass and energy balance. In this category, one can find, for example, the CONTEMPT-LT [1] or MARCH2 [2] codes. This approach was sufficient because of the main characteristics of concrete containment (high thermal inertia and low thermal leakages) and because thermal exchanges are very efficient in case of steam condensation.

During the eighties, hydrogen risk became more and more a concern. Then, modeling activities have gone in two directions. On the one hand, multi-compartment codes have been developed, based on the previous approach with additional coupling relationships between compartments. Examples of those codes are CONTAIN [3], JERICHO [4], MAAP [5] or RALOC [6]. This approach give good results with respect to pressure evolution, but it underestimates the possible stratifications and is also sensitive to the domain nodalization.

On the other hand, general purpose multi-dimensional codes were used for solving mass, energy and momentum equations with a spatial discretization. In this category one can find codes as GASFLOW / HMS [7] and GOTHIC / WGOTHIC [8]. This approach yields good representation of stratification in large volumes but typically requires very large computation times.

Lumped parameter codes are still likely to be used for safety analysis. But mechanistic codes will be more and more required in order to justify some assumptions made in studies performed with lumped parameter codes. With this objective in mind, the « Département de Mécanique et Technologie » (DMT) of CEA has undertaken the development of a coupled multidimensional and lumped parameter code named GEYSER/TONUS. The multidimensional representation is intended to be used in volumes in which hydrogen concentration heterogeneities (e.g. stratification), that cannot be easily described by lumped parameter codes, are likely to occur. The lumped parameter type of description, which will be comparable to what already exist in codes like CONTAIN or JERICHO, is introduced in order to limit the computational efforts for parts of the containment in which detailed description is not required. Anyway, the user will have the possibility to model each volume in one way or the other.

PHYSICAL MODELS

There are different physical models to be included in the code in order to have a good representation of the phenomenons involved in the evolution of the containment atmosphere in case of a severe accident. These models are listed below.

For all the physical models presented, the computations can be carried out either in 2D or 3D.

Compressible two-phase flow

The main model to implement in the code was for computing flows composed of steam with non-condensable gases (air, hydrogen, ...). The model must be able to treat compressible flows because of the injection of mass inside the containment (essentially steam and hydrogen) which leads to a general raise in the pressure. It is also expected that the pressure level in the containment will remain quite low (typically less than five bars in French PWRs). Thus, apart from the condensate on walls and inner structures, only a very limited amount of water will exist as a liquid phase. If bulk condensation is willing to occur, the droplets will be of micrometric size and will follow the gaseous flow. These arguments have driven us to choose a homogeneous model for representing the compressible two phase flows.

In the present model, the gases are assumed to be perfect (state equation). The physical parameters of the mixture depends on the composition but not yet on the temperature.

Turbulence is accounted for by a constant eddy viscosity, but it is planned to incorporate, in a near future other turbulence models, in particular a K-ε model.

An implicit time integration scheme had been developed in order to be able to treat long transients.

Condensation on walls and structures

The mass transfer by condensation on walls is modeled using the Chilton-Colburn approach and an analogy between heat and mass transfer. This correlation is used because more suitable local correlations are not available now. Furthermore, an experimental program named COPAIN [9] exists in order to establish such correlations which could be later included in the code. Also, the condensation rate is expected to be high in the initial phase of the computed transients during which the rate of steam injection is large, and so the situation will be one of mixed convection.

The computation procedure is the following :

- The heat exchange coefficient by convection is calculated using a semi-empirical correlation on the Nusselt number Nu [10] :

$$Nu = 3.656 + 0.021\ Pr^{0.6}\ Re^{0.8}$$

- Using the analogy between heat and mass transfer, the Sherwood number Sh is written as [11] :

$$Sh = 3.656 + 0.021\ Sc^{0.6}\ Re^{0.8}$$

- The mass condensation rate j_s is evaluated by the following expression :

$$j_s = \frac{\alpha}{D} Sh (\rho_v - \rho_{ve}(T_w)),$$

- The heat flux rate by condensation φ_c is then :

$$\varphi_c = j_s L$$

In these expressions, Pr is the Prandtl number, Re is the Reynolds number, Sc is the Schmidt number, α is the vapor diffusion coefficient, D is the containment diameter, ρ_v is the vapor density, $\rho_{ve}(T_w)$ is the density of the saturated vapor at the wall temperature and L is the latent heat of phase change.

Spray

An important mitigation system used in containment buildings is the spray system. The main characteristic of such a system is to bring a great amount of water in a liquid phase inside the containment building. Due to the sizes of the droplets being generated (roughly between 100 and 1000 μm) , the homogeneous two phase flow model is not adequate for modeling such an event. Rather, it is important to take into account the difference between the movements of the gaseous phase and of the liquid phase. For these situations, a two fluid model has been developed. The formalism used for deriving the equations is as exposed by ISHII [12].

In this formulation, the first fluid is composed of the gases (vapor and non-condensibles) plus the small droplets generated by bulk condensation if any. This fluid is the same as the one described by the model for compressible two phase flows. Fluid number two is the collection of droplets generated by spray. For the moment, the spray model does not take into account the possible presence of aerosols. The effects which are modeled are the pressure reduction and the mixing of the gaseous athmosphere, but not yet the removal of aerosols by spray.

For the mixture, the supplementary assumptions as compared to the homogeneous model are the following :

- if present, the small droplets generated by bulk condensation are not affected by the spray droplets, because bulk condensation is expected to be very limited if any ;
- the volume fraction of the mixture is equal to unity, because the volume fraction of the spray droplets is always less than 0.001.

For the spray droplets, the main assumptions are :

- the droplets do not interact with one another, because for a typical spray system, the mean number of droplets per unit volume is low (around 2 droplets per cubic centimeter) ;
- the temperature is uniform inside a droplet and is equal to the interfacial temperature ;
- when injected in the computational domain, all the droplets have the same size ;
- the viscosity is neglected compared to inertia because the droplets have a density much larger than the one of the gaseous mixture and their concentration is low.

With this model, condensation can occur on the droplets, and their size is computed. For each fluid, local conservation equations for mass, momentum and energy are solved.

Also added are equations for the conservation of water and for the volume fraction of the droplets. Thus, a total of eight partial differential equations are solved, with additional constraints being the state equation for both the vapor and air. For each non-condensible gas to be added in the computation (for example hydrogen), another conservation equation is to be solved in addition to the previous ones.

When deriving the complete set of equations, heat, momentum and mass transfer terms appear. They are detailed below.

Mass Transfer : The mass transfer is generated by condensation of vapor on the droplets. The model used is a Chilton-Colburn approach as described above, but in this case droplet Nusselt number Nu_{dro} is evaluated as [13] :

$$Nu_{dro} = 2.0 + 0.6\, Pr^{1/3}\, Re_{dro}^{1/3}$$

with $Re_{dro} = \dfrac{D|V_{mix} - V_{dro}|}{\nu}$ the Reynolds number of the droplets, D the diameter of the droplets, V_{mix} the velocity of the mixture, V_{dro} the velocity of the droplets, ν the kinematic viscosity of the mixture.

Momentum Transfer : The momentum transfer is the result of friction of the gas on the droplets. Assuming that the shape of the droplets is spherical, the drag force F_d is expressed as [14] :

$$F_d = C_d \frac{\pi}{8} \rho_{mix} D^2 |V_{mix} - V_{dro}| (V_{mix} - V_{dro})$$

with C_d the friction coefficient being $C_d = 24\left(0.1103 + \dfrac{1}{\sqrt{Re_{dro}}}\right)^2$.

Heat Transfer : The heat transfer is the sum of two contributions. The first one is due to convection and is computed using the Nusselt number Nu_{dro} correlation. The second term is the result of condensation on the droplets and is calculated as for condensation on walls.

Other models

To complete the description, other physical models are to be included in the capabilities of the code.

For some of them, a first version has already been included in the TRIO-EF code [15, 16]. This is the case for **aerosols transport** [17]. Two approaches have already been investigated. In the first one, the Navier-Stokes equations are solved for a gas mixture. Then, a velocity field is computed for aerosols which is a combination of the gas velocity, the particles weight and the Stokes drag force. Aerosols concentration is calculated by solving a convection-diffusion equation, using a turbulent dispersion coefficient for the particles. The second approach consist in applying a two fluid modeling in a similar manner to what was done for spray. Work has also been performed on wall functions for aerosols deposition in a turbulent flow.

The model which is anticipated to be included in the code is the first one because the typical size of aerosols generated in the containment is small (around 1 to 5 μm). The

agglomeration will not be modeled for this phenomenon takes place very rapidly at the beginning of the transient [18, 19]. Thus, we feel it is sufficient to consider that at the beginning of the calculation, the aerosols have a size equal to the mean size of the particules and that will remain constant. If necessary, the initial size spectrum could be divided into classes, with a convection-diffusion equation solved for each class in order to compute the aerosols concentration. In any case, deposition has to be accounted for.

As far as **thermal radiation** is concerned, intensive work has been done in the past to model this phenomenon in transparent media [20]. For the last few years, focus has been put on modeling thermal radiation in participating media. This model is relevant for the containment because the atmosphere contains vapor and particles. Thermal radiation can possibly modify the flows if high temperatures are reached, for example in case of hydrogen combustion.

The chosen approach rely on a spherical harmonics decomposition with a P1 approximation. This method as proved to be efficient for coupling radiation equations with other conservation equations (momentum equation in the case of the containment) [21]. In a first phase, the radiative properties will be considered constant and will be determined by correlations as in the CONTAIN code. Then, if necessary, the model could be extended to take into account the spectral variation of the radiative properties, using the « Weighted Sum of Gray Gases » method.

Other models as **combustion** and **engineered safety systems** are currently under development. The work is also ongoing for both multi-D to 0-D and lumped parameter types of elements. For the latter, the physics included is not expected to be different from what already exist in the JERICHO code that was initially developed at CEA/DMT in Saclay.

CODE CONSTRUCTION AND STRUCTURE

One of the main characteristics of the containment modeling under severe accident conditions is to couple different physical phenomenons of various nature, as for example turbulent convection, thermics, aerosols transport, combustion, ...

We also wish to be able to couple different types of spatial discretization :

- multi-dimensional for large volumes ;
- nodes for compartments.

These two constraints imply to develop original algorithms. This in turn induces to achieve a modular and versatile conception of the software. Also requested are advanced capabilities in terms of language for manipulating data structures and implementing algorithms logic.

We chose to use CASTEM2000 [22] and its user data manipulating language called GIBIANE. The code has an object-oriented conception. One can manipulate *objects* (data) by applying to them elementary operations defined in *operators* which are independent from one another. Examples of operators are matrices construction, linear system resolution and so on. Some operators implement loops and test conditions. They are used to build algorithms such as time integration of the spray model.

The development of the physical models described above have then been carried out in two phases. The first phase was the transcription in CASTEM2000 of thermal hydraulics of TRIO-EF. This phase provided basic operators for computing flows. The second phase consisted in the writing of algorithms for two phase flows, condensation or spray.

The advantages of this structure are the following :

- it is possible to develop in parallel different physical models in different, independent operators with a specified interface (objects read, objects written) ;
- it is easy to develop and test rapidly new algorithms written with the help of the data language that will induce possible reduction of the execution time ;
- the user has the ability to redefine operators, in order, for example, to test the effect of different correlation.

This allowed us to build, in a limited amount of time, tools for computing complex flow situations.

Finally, CASTEM2000 gives the possibility to encapsulate the algorithms in generic data sequences called *procedures*. These procedures present to the user a simplified interface with only a limited number of parameters to define. The GEYSER/TONUS code consists in a set of procedures dedicated to the containment modeling.

CODE VALIDATION

The validation of the code can be divided in several steps. The first step will be to validate the lumped parameter part. This will be achieved by comparison to other already qualified codes that use the same approach, for example JERICHO or CONTAIN. The second step is to validate the multi-dimensional part on analytical tests. There already exist in the literature results for the different physical processes (condensation, combustion, ...). Then, the last step is to validate the code in a global manner, in particular the coupling of the different phenomenons. Global tests, at large scale, have already been performed (Battelle, HEDL, HDR, NUPEC). They are suitable for verifying only mean values, because they are not heavily instrumented and because the boundary conditions are not always well known.

Between both types of tests, there is a need for medium scale experiments with well defined boundary limits and with an instrumentation designed to assist in the modeling and validate this modeling. CEA/DMT has proposed to build an experimental facility called MISTRA [23] to fulfill this need for medium scale experiments.

APPLICATIONS

An application of the code has already been performed on a typical severe accident situation. The aim of the computation was to evaluate the evolution of the atmosphere in

the free volume of a 900 MWe PWR containment after a small break LOCA. This application is discussed in details in a companion paper presented at the same conference [24].

An extended presentation of the spray model applications have already been presented elsewhere [25].

In this paper, we will only present an application about the dynamic effect of spray on a stratification. This application is intended to be only an illustration of the capabilities and the results of the computation have not been checked against experimental data yet. However the validation of the model is planned to take place in the future on both existing and future experiments performed at CEA.

The studied geometry is that of the large dry volume of a 900 MWe PWR. It is 44 meter large and the maximum height is 36 meters. The computational domain is composed of about 2000 elements and the computations are carried out with a 2D plane model. There is a vertical symmetry plane so only one half is represented. The computation is isothermal.

It is assumed that there is a spray system of length 3.4 meters located at the top of the building on the symmetry plane. The diameter of the spray droplets is 500 μm. They are injected with a velocity of 2 m/s.

The atmosphere is initially composed of air at the bottom and a mixture of 44% air, 47.5% vapor and 8.5% hydrogen at the top. There is a stratification front located at an elevation of about 20 meters (see figure 1a). The atmosphere, initially at rest, is at 3 bars pressure.

After 35s (figure 1b), there is little interaction between the two zones. mixing is more efficient in the upper part (lighter gas) than at the bottom.

After 180s (figure 1c), there exist a jet of light gas that start from the top and goes to the bottom. The mixing now reaches also the heavier gas initially at the bottom.

After 270s (figure 1d), a general recirculation has taken place inside the containment, and the gases tends to become quasi homogeneous.

CONCLUSION

The basic physical models of the GEYSER/TONUS code have been presented. It is already possible to compute flows in reactors containment under severe accident conditions. Thanks to a spatial discretization, precise local informations can be obtained, in particular for hydrogen concentration which is a major concern nowadays. By use of an implicit method, the calculation of long transients can be achieved at a reasonable cost.

Further steps in the development will include improvements in the existing models, implementation of new ones for other phenomenons, and validation on both separate effects and global tests. The user interface will also have to be improved.

REFERENCES

[1] R.E. Deem, K.S. Rousseau, « The CONTEMPT containment analysis code », Proc. 2nd Int. Conf. on the impact of hydrogen on reactor safety, Albuquerque, USA, (1982)

[2] R.O. Wooton and al., « MARCH2 code description and user's manual », Battelle Colombus Laboratory BMI2063-R3, NRC Report, NUREG/CR-3988

[3] K.K. Murata and al., « User's Manual for CONTAIN 1.1 : A Computer Code for Severe Nuclear Reactor Accident Containment Analysis », Sandia National Laboratories SAND87-2309, NRC Report, NUREG/CR-2309, (1989)

[4] J. Gauvain, J.P. L'Hériteau, « JERICHO, a code for computation of containment thermal hydraulic behaviour during a severe accident in a NPP », Proc. Int. Conf. NURETH 4, 909-914, Karlsruhe, Germany, October 10-13, (1989)

[5] M. Plys and al., « MAAP4 model and validation status », Proc. 2nd Int. Conf on Nuclear Engineering, San Francisco, USA, March 21-24, (1993)

[6] H. Jahn and al., « Description of the RALOC/FIPLOC family - Part 2 : physical modeling of thermal hydraulics and integration methods », GRS Report, GRS-A-1426, (1988)

[7] J. R. Travis, « HMS : a computer program for transient three dimensional fluid flows with chemical reactions and fuel sprays », NRC Report, NUREG/CR-4020, (1984)

[8] T. L. Georges and al., « Containment Analysis with GOTHIC », Proc. 27th Nat. Heat Transfer Conf., Minneapolis, Minnesota, USA, (1991)

[9] J.C. Micaelli and al, « Steam Condensation Modelling », Technical Workshop on Containment Integrity and Energetic Threats, Saclay, France, October 13-14, (1994)

[10] W. M. Kays, Convective Heat and Mass Transfer, Mc Graw-Hill Book Co., (1966)

[11] R. B. Bird, W. E. Stewart, E. N. Ligtfoot, Transport Phenomena, John Wiley, (1960)

[12] M. Ishii, Thermo-fluid Dynamic Theory of Two-Phase Flows, Eyrolles, (1975)

[13] J. Taine, J. P. Petit, Transferts Thermiques, Mécanique des Fluides Anisothermes, Dunod, (1989)

[14] R. Comolet, Mécanique Expérimentale des Fluides, Masson, (1963 & 1982)

[15] J.P. Magnaud, S. Goldstein, « The Finite Element Version of the TRIO Code », Proc. 7th Intl. Conf. in Fluid Mechanics, Huntsville, USA, April 3-7, (1989)

[16] J.P. Magnaud and al., « TRIO-EF : A General Thermal Hydraulics Code Applied to the AVLIS Process », Proc. Intl. Symp. on Laser Isotope Separation, Los Angeles, USA, January 19-20, (1993)

[17] P. Armand, P. Cornet, A. Monavon, M. Durin, « Order of Magnitude Analysis of Motion Equations of a Particule in a Non Uniform Unsteady Flow. Application to a Turbulent Diphasic Jet », Proc. 4th Intl. Symp. on Ventilation for Contaminant Control, Stockholm, Sweden, September 5-9, (1994)

[18] D. A. Powers, S. B. Burson, « A Simplified Model of Aerosol Removal by Containment Sprays », Sandia National Laboratories SAND92-2689, NRC Report, NUREG/CR-5966, (1993)

[19] J. Gauvain, G. Lhiaubet, « Influence of Structural Insoluble Aerosols in Severe Accident Scenarios With and Without Steam Condensation onto Soluble Aerosols Fission Products », Joint NEA/CEC Workshop on Water-Cooled Reactor Aerosol Code Evaluation and Uncertainty Assessment, Bruxelles, Belgium, September 9-11, (1987)

[20] N. Coulon, « Computation of 3D Form Factors in Complex Environments », Proc. of ANS Topical Meeting on Advances in Nuclear Engineering and Radiation Shielding, Santa Fe, USA, April 9-13, (1989)

[21] J. R. Howell, « Thermal Radiation in Participating Media : The Past, the Present and Some Possible Futures », Transactions of the ASME, vol 110, 1220-1229, November, (1988)

[22] P. Verpeaux, A. Millard, T. Charras, A. Combescure, « A Modern Approach of Computer Codes for Structural Analysis », Proc. of the 10th Conf. on Structural Mechanics in Reactor Technology, Anaheim, USA, August 14-18, (1989)

[23] J.M. Humbert, A. Méjane, « MISTRA : an Experimental Program about the Thermodynamical Behaviour of Reactors Containments in Case of Severe Accidents », Technical Workshop on Containment Integrity and Energetic Threats, Saclay, France, October 13-14, (1994)

[24] L. V. Benet, C. Caroli, P. Cornet, N. Coulon, J. P. Magnaud, « Modelling of Local Steam Condensation on Walls in Presence of Noncondensable Gases. Application to a LOCA Calculation in Reactor Containment Using the Multidimensional GEYSER/TONUS Code », Proc. of the 7th Conf. on Nuclear Reactors Thermalhydraulics, Saratoga Springs, USA, September 10-15, (1995)

[25] P. Cornet, « A Two Fluid Model Applied to Spray Systems », Technical Workshop on Containment Integrity and Energetic Threats, Saclay, France, October 13-14, (1994)

ACKNOLEDGMENTS

The work described in this paper, initially started in the GEYSER code is now sponsored by the french « Institut de Protection et de Sûreté Nucléaire » (IPSN) in order to build the TONUS code that will also include hydrogen detonation and its consequences on the structures.

droplets

Figure 1a : 0 s

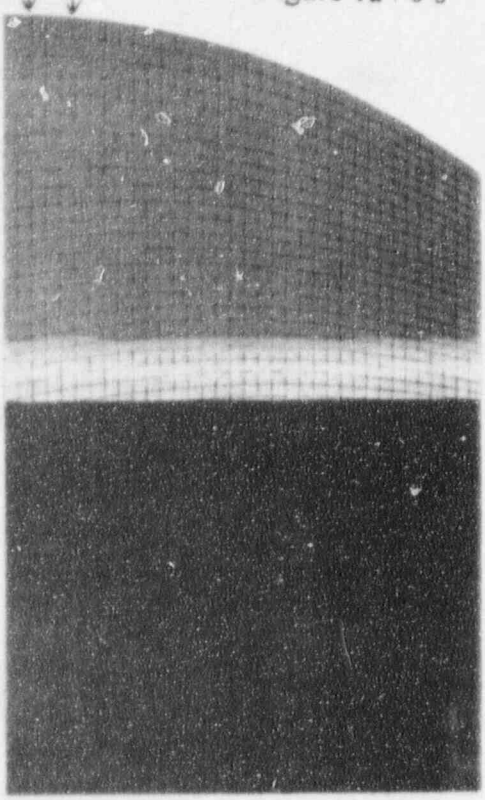

Figure 1b : 35 s

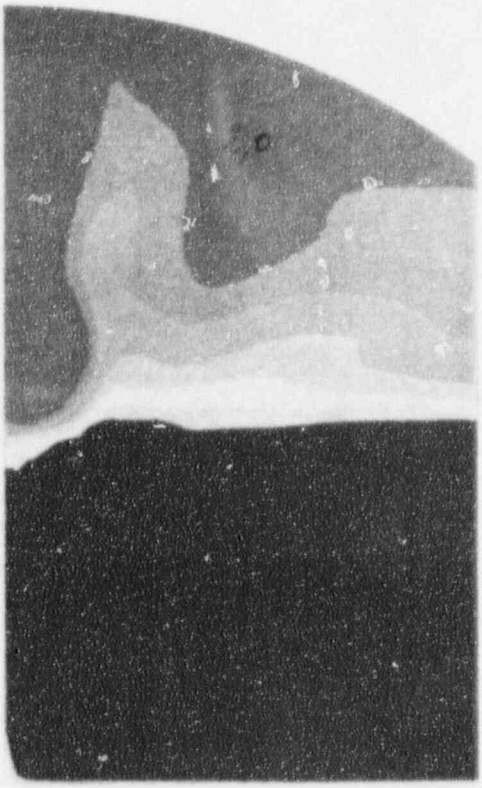

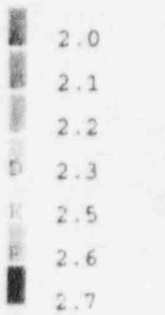

Figure 1c : 180 s

Figure 1d : 270 s

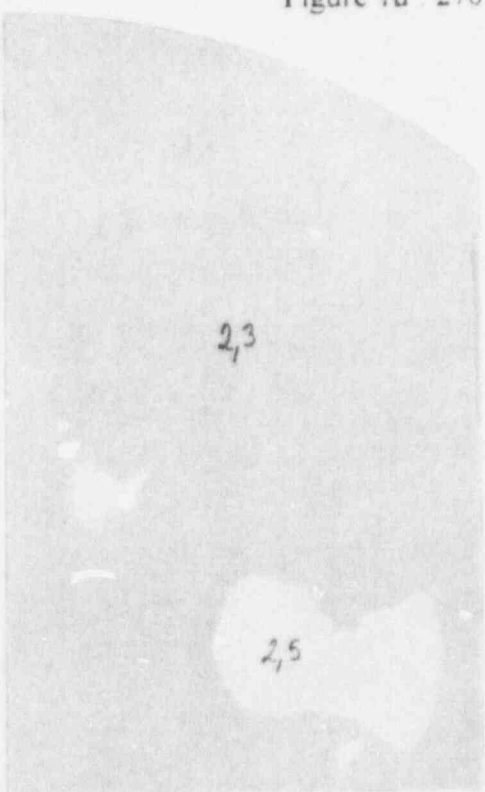

DENSITY IN THE CONTAINMENT AT DIFFERENT TIMES

AUTHORS INDEX

A

Abdelmessih, A.H. 264
Addabbo, C. 2159
Adomaitis, E. 3083
Akagane, K. 2994
Akiyama, M. 1653
Aksan, N. 2079, 2280, 2303
Aksan, S. N. 2904
Aksenova, A.E. 865
Aktas, B. 2035
Alemberti, A. 2869
Al-Falahi, S. 2263
Almenas, K. 1418
Allison, C.M. 1851
Analytis, G.Th. , 2011, 2067, 2079, 2654
Anderson, M. 1519
Andersson, N. G. 2895
Andreani, M. 1249, 2079
Angelini, S. 1754
Anghaie, S. 1997
Anglart , H. 673
Annunziato, A. 2159
Araya, F. 1169
Arnoux-Guisse, F. 2250
Aritomi, M. 875

B

Babelli, I. 947, 1272
Bacchiani, M. 2869
Balasubramaniam, V. 1380
Balino, J. 462
Banas, A.O. 284
Banati, J. 1116
Bang, K.H. 1677
Banerjee, S. 434
Baratta, A.J. 978
Barthel, V. 1456
Bartkus, G. 3083
Bartsoen, L. 2704
Barre, F. , 750, 2045
Baytas, A.C. 720
Bazin, P. 815
Beckjord, E. 1
Belov, V. A. 1555
Benet, L. V. 1443
Bengaouer, A. 815
Bertrand, C. 2250
Bertodano, M.L. 1272
Bestion, D. 2222
Blinkov, V.N. 967
Boatwright, W.J. 1083
Bobkov, V.P. 2539
Boldyrev, A. V 1914
Bonnet, J. M. 1958
Bonnin, O 2250
Boyack, B.E. , 1100, 1153
Boyer, B. D. 2185
Brauner, N. 192
Briere, E. 736
Brockmeir, U. 1830
Brown, N.W. 2470
Brun, P. 1351
Bui, V.A. 1809

C

Camelo, E. 111
Caroli, C. 1443
Carpentino, F.L. 21
Carrica, P. 462, 2453, 3218
Caruso, A. 1489
Carver, M.B. 284
Centner, B. 2704
Chae, H. T. 2786
Chaigne, G. 1351
Chang, J.S. 574
Chang, S. K. 2428
Chen, G. 1997
Chen, N. C. J. 2335
Chen, X. 1586
Chen, X.M. 377, 933

Cheng, X. 846
Cheng, S.C. 2583
Cheng, Z. 3093
Cherbonnel, C. 1489
Chetal, S. C. 1361, 1380
Chiang, J-H 875
Cho, J.H. 336
Choe, W.G. 1083
Chu, C. C. 2359
Chudanov, V.V. 865
Chun, M.-H. 93
Chung, B. J. 1477
Chung, M.K. 986
Cizek, J. 2112, 2636
Clausse, A. 231, 2453, 2762, 3218, 3232
Coddington, P. 1249
Cognet, G. 1797
Conway, L.E. 2869
Cornet, P. 1443
Corradini, M.L. 1501, 1519, 1637, 1728, 1743, 1779, 2240
Coste, P. 1456, 2222
Coulon, N. 1443

D

Dasaradhi, S. 2924
Daubert, O. 2250
D'Auria, F. 2146, 2303, 2904
Davis, K.L. 1851
Dehbi, A. 402
de Cachard, F. 166
de Crecy, F., 2045, 2480
Deguchi, A. 2721
Delgadino, G. 462
Delmastro, D.F. 3232
Deryugin, A. I. 1914
Deslandes, H. 1456
DeVore, C.V. 1083
DiMarco, P. 3218
Dinh, T.N. 827, 1809
Doerffer, S. 2583
Domoradov, A. 1090
Dor, I. 750
Dorning, J.J. 2677
Doubek, M. 2815
Dougherty, T.J. 3197
Dowlati, R. 1272
Driscoll, M.J. 1224
Durin, M. 1574

E

El-Genk, M.S. 353
Elkassabgi, Y. 2924
Elia, Jr., F.A. 336
Erbacher, F.J. 846
Ezsol, Gy. 2102

F

Fakory, M.R. 1982
Falkov, A. A. 2384
Farahani, A.A. 1728, 1779
Feltus, M.A. 1127
Finjakin, A. 1090
Firnhaber, M. 1830
Flour, I. 1489
Forsyth, D.R. 696
Fox, R. J. 1501
Franchello, G. 648
Fraser, D.W.H. 264
Frogheri, M. 2146
Frohlich, G. 1607
Fukahori, T. 2994
Fuketa, T. 2957
Fukuda, K. 554
Fujii, Y. 804, 1663
Furuya, M. 923

G

Gabrianovich, B.N. 711
Gango, P. 1535, 3120
Garnier, J. 2519
Gautier, G.M. 1196
Gauvain, J. 1574
Geffraye, G. 815
Georgevich, V. 2957, 2977, 3028, 3052
Glaeser, H. 2203, 2303, 2904
Glebov, A.G. 353

Gracyalny, E. 2240
Grassi, W. 3218
Green, J. 1418
Groeneveld, D.C. 2583
Gu, C-Y 3153
Guentay, S. 402
Guellouz, M.S. 2738
Gu[illegible]-Lavalle, G., 231, 2762

H

Haapelehto, T. 770, 2806
Hadaller, G.I. 2608
Hagen, S. 1830
Hama, K. 1333
Hamaguchi, H. 212
Han, J.T. 1272
Hanninen, M. 2263
Harkins, C.K. 2003
Harmony, S.C. 1100
Harrison, J.F. 1083
Harvel, G.D. 574
Hassan, Y.A. 434, 497, 591, 3073
Hata, K. 1333
Hayes, R.C. 2608
Hecker, M. 2250
Hejzlar, P. 1224
Hemstrom, B. 2895
Henderson, P. 1797
Herer, C. 2519
Herrero, V.A. 2762
Hiltbrand, D.W. 1083
Hochreiter, L.E. 43
Hofmann, F. 2250
Hofmann, P. 1830
Hohmann, H. 1688, 1712
Hohorst, J.K. 1851
Hongisto, O. 1535
Hori, K. 574
Hosokawa, S. 804
Huang, H. C. 2428
Huhtiniemi, I.K. 1712
Hwang, S. T. 2169

I

Ibrahim, W. A. 3073
Ieda, Y. 1313
Ikeda, T. 1972
Inada, F. 923
Inoue, A. 1663
Ishida, N. 487
Ishii, M. 947, 1272
Ishijima, K. 2957
Iwamura, T. 1169
Iwashige, K. 1972

J

Jacob, M.C. 21
Jacobson, S. 2895
Jafri, T. 3197
Juanico, L.E. 3232
Juhel, D. 2480
Jun, B. J. 2786

K

Kainulainen, S. 854
Kajiwara, H. 2021
Kalli, H. 299, 2146, 2834
Kamide, H. 1313
Kang, C. S. 1477
Kao, S. P. 2428
Karasulu, M. 911
Karlsson, R. 2895
Karoutas, Z. 3153
Karve, A.A. 2677
Karwat, H. 248
Kasinathan, N. 1361
Kawahara, A. 2721
Kawaji, M. 478
Kawanishi, K. 574
Kelly, A.E. 2003
Khodjaev, I.D. 1139
Kim, H. 2786
Kim, M.H. 1677
Kim, S. 2773
Kim, S.H. 2957, 2977, 3028, 3052
Kim, S.W. 1889

Kim, Y.-S. 93
Kiso, Y. 2994
Kisselev, A.E. 1914
Kirillov, P.L. 2558, 2916
Klingenfus, J. 1069
Klingenfus, J.A. 2410
Knebel, J. U. 1407
Kobayashi, J. 1313
Kodama, J. 804
Kodaira, T. 2957
Kok, H. V. 2884
Kondo, S. 1302
Korsun, A.S. 711
Kortenienni, V. 770
Kouhia, J. 299, 854, 2806, 2834
Kozina, N.V. 2539
Kramerov, A.J. 967
Krauss, T. , 603
Kuhn, S.Z. 312
Kurul, N. 673, 1889
Kuul, V. S. 2384

L

Lahey, Jr., R.T. 49, 1889, 1930
Larrauri, D. 736
Laugier, E. 2119
Laurinat, J.E. 514
Leduc, C. 1456
Lee, B.-R. 93
Lee, J. B. 2786
Lee, K-W 2489
Lee, S. J. 1863
Lee, S-Y 2489
Lemekha, A.V. 1914
Lemonnier, H. 111
Leonardi, M. 2146
Lepekhin, A.N. 2384
Levin, A.E. (2) 1231, 1291
Lider, S. 978
Lillington, J. 2904
Lime, J.F., 1100, 1153
Linca, A. 1607
Lischer, D.J. 336
Lombardi, C. 2506
Lorencez, C. 478
Lu, D. 1302
Lucas, A. T. 2941
Lundstrom, P. 1535

Mc

McDonald, J.M. 532
McDuffey, J. 131
McPherson, G.D. 1291

M

Macian, R. 2669
Madni, I. K. 2349
Magallon, D. 1688, 1712
Magnaud, J. P. 1443
Mahaffy, J.H. 2035, 2669
Majed, M. 2608
Maron, D.M. 192
Marshall, T.D. 532
Masson, V. 3218
Matsui, G. 3142
Matuszkiewicz, A. 781
Matsuzaki, M. 1663
Medich, C. 2841, 2869
Menant, B. 1324
Menna, J.D. 514
Melnikov, V. 508
Meyer, L. , 603
Midvidy, W. 781
Miettinen, A. 2146
Minagawa, H. 804
Monji, H. 3142
Moreau, G. -M. 1881
Moraga, F. 1930
Mori, M. 875
Morii, T. 1653
Moskalev, A. 1090
Mudde, R. F. 2884
Muftuoglu, A.K. 1127
Munther, R. 299
Murao, Y., 478, 1169

N

Nair, S 947

Nakamori, N. 804
Nam, H.-Y. 93
Neitzel, H.J. 846
Nguyen, T. Q. 2112
Nigmatulin, B.I. 508, 967, 1555
Nigmatulin, R.I., 49, 141
Nik, N. 911
Nimokata, H. 1398
Ninokata, H. 2721
Nithianandan, C.K. 2410
No, H.C. 986
Noe, H. 1324
Norback, G. 2608
Nourbakhsh, H.P. 3093
Nourgaliev, R.R. 827, 1809
Nylund, O. 673

O

Ochterbeck, J. 111
Ogura, K. 2021
Ohashi, H. 1653
Okamoto, K 497, 591
Ohshima, H. 1313
Okkonen, T. 1809
Olive, J. 736
Ousaka, A.
Ozawa, M. 487

P

Palagin, A.V. 1914
Palazov, V.V. 423
Park, G-C 2169, 2773
Park, H.S. 1743
Park, J.-W. 76
Park, R.J. 1863
Parlatan, Y. 2185
Perneczky, L. 2102
Pernsteiner, A.P. 1501
Parrish, K.R. 1046
Paul, P.K. 514
Pernica, R. 2636
Perret, C. 2045
Pershukov, V.A. 1555
Peterson, P.F., 312, 933, 1501
Petit, M. 1574
Petry, A. 1090
Pichon, P. 815
Pigny, S. 1881
Piplica, E.J. 43
Philip, O.G. 497, 591
Po, L-C 2438
Pochard, R. 2303, 2904
Podowski, M.Z. 673, 1003, 1889, 1930
Pokharna, H. 1272
Pokusaev, B.G. 1032
Polyansky, G.N. 2384
Porkholm, K. 2263
Poskas, P. 3083
Pribaturin, N.A 1032
Purhonen, H. 2146, 2834
Puustinen, M. 770

Q

R

Radet, J. 2119
Rajakumar, A. 1361
Rajan, S.R. 911
Ransom, V.H. 1272
Raussi, P. 854
Raymond, P. 2621
Refling, J.G. 978
Reilly, S.S. 2410
Revankar, S.T. 1272
Richards, C. 2303
Rigamonti, M. 2869
Ris, V.V. 1555
Ritterbusch, S.E. 21
Rizwan-uddin 2677
Robinson, G.E. 978
Rohatgi, U.S. 2185
Rosa, M. 1003
Rouge, S. 1949
Rovinsky, Y. 192
Ruan, Y.Q. 248
Ruggles, A.E. 131, 2470

S

Saarenpaa, T. 2438
Sakaguchi, T. 212, 804
Sakurai, A. 554, 1333
Samoilov, O.B. 2384
Sanz, D. 231
Saphier, D. 2621
Sawada, T. 1398
Schindler, M. 1607
Schmidl, W.D. 497, 591
Schmitt, B. 1022
Schneider, R.E. 21
Schoen, B. 2856
Scholin, B. 3153
Schrock, V.E. 312, 377, 933
Schwirian, R.E. 696
Sehgal, B.R. 827
Seo, J.K. 2169
Selmer-Olsen, S. 111
Selivanov, Y.F. 2916
Sencar, M. 2280
Shamoun, B.I. 1637
Shimizu, A. 1398
Shiotsu, M. 554, 1333
Shoukri, M. 3175
Sidenkov D.V. 1555
Siefken, L.J. 1851
Sienicki, J. J. 2359
Sim, S. K. 1863
Simoneau, J. P. 1324
Simonin, O. 1489
Sjoberg, A. 2303, 2904
Smirnov, E.M. 1555
Smith, R.J. 2003
Smogalev, I.P. 2558
Souyri, A. 2519
Solvik, G.C. 2185
Song, C.H. 986
Sonnenburg, H.G. 423
Soyama, K. 2957
Spencer, B.W. 2359
Spindler, B. 1881
Stadtke, H. 648
Steiner, J.L. 1100
Steinhoff, F. 2203
Stekelenburg, A.J.C. 2785
Stern, F. 2608
Strizhov, V.F. 865
Stumpf, H.J. 1100
Sulfredge, C.D. 3003
Sun, C. 750
Sung, Y. 2112
Syri, .S. 627
Szabados, L. 2102

T

Tabata, H. 875
Takaguchi, M. 3142
Takahashi, M. 1663
Takemoto, T. 875
Takeuchi, Y. 1333
Takizawa, A. 1302, 2021
Taleyarkhan, R.P. 2957, 2977, 3028, 3052
Tapucu, A. 781
Tavoularis, S. 2738
Tarantini, M. 2841
Teresaka, H. 2021
Teschendorff, V. 2203
Teyssedou, A. 781
Theofanous, T.G. 627, 1535, 1586, 1754
Tikhonenko, L.K. 967
Tirkkonen, H. 2438
Todreas, N.E. 1224
Trambauer, K. 1830
Tsiklauri, G. 1022
Tucker, R. F. 2924
Tuomisto, H. 1535
Tuunanen, J. 423
Tye, P. 781
Tyler, T.N. 2669

U

Ubra, O. 2815
Ueda, H. 2021
Ueno, T. 804
Umekawa, H. 487
Umminger, K. J. 2856
Unrau, D. 284

Ushakov, P.A. 711

V

Vabishchevich, P.N. 865
Vaidyanathan, G. 1361, 1380
Valenti, S. N. 2957, 2977, 3028, 3052
Valentin, B. 1351
Vanhoenacker, L. 2704
van der Hagen, T.H.J.J. 2785, 2884
Van Hove, W. 2704
Van Laeken, K. 2704
Vasil'ev, A.D. 2470
Velusamy, K. 1380
Vescovi, O. 2869
Veshchunov, M.S. 1914
Vilemas, J. 3083
Vinberg, A.A. 1555
Vinogradov, V.N. 2539
Virtanen, E. 2806
Viskanta, R. 1272
Vitruk, S.G. 711
Volchek, A M. 1914

W

Weber, P. 2856
Wang, W. 1272
Watson, R.D. 532
Wendel, M.W. 2335, 2470
Williams, P.T. 2941
Wiman, P. 2608
Wissinger, G. 1069
Worth, B. 648

X

Xiang, J. Y. 2977

Y

Yacout, A.M. 2394
Yamshchikov, N.Y. 1914
Yang, B.W. 3197
Yang, Y.H. 1653
Yang, J.Y. 2169
Yang, W.S. 2394
Yasuo, A. 923
Yefanov, A.D. 2916
Yegorova, L. 1830
Yoder, G.L. 2335, 2924
Yoo, K. J. 1863
Yoshino, M. 2994
Youchison, D.L. 532
Yuann, R.Y. 377
Yuen, W.W. 1586, 1754

Z

Zalchik, L.I. 1555
Zabiego, M. 1797
Zeitoun, O. 3175
Zhou, Z. 888
Zyatnina, A.O. 2539

NRC FORM 335 (2-89) NRCM 1102, 3201, 3202

U.S. NUCLEAR REGULATORY COMMISSION

BIBLIOGRAPHIC DATA SHEET

(See instructions on the reverse)

1. REPORT NUMBER (Assigned by NRC. Add Vol., Supp., Rev., and Addendum Numbers, if any.)
NUREG/CP-0142
Vol. 2

2. TITLE AND SUBTITLE
Proceedings of the 7th International Meeting on Nuclear Reactor Thermal-Hydraulics
NURETH-7

Sessions 6 - 11

3. DATE REPORT PUBLISHED
MONTH: September | YEAR: 1995

4. FIN OR GRANT NUMBER

5. AUTHOR(S)
Compiled by R. C. Block and F. Feiner, Northeastern New York Chapter, American Nuclear Society

6. TYPE OF REPORT
Conference Proceedings

7. PERIOD COVERED *(Inclusive Dates)*

8. PERFORMING ORGANIZATION – NAME AND ADDRESS *(If NRC, provide Division, Office or Region, U.S. Nuclear Regulatory Commission, and mailing address; if contractor, provide name and mailing address.)*
Compiled by Northeastern New York Chapter, American Nuclear Society

9. SPONSORING ORGANIZATION – NAME AND ADDRESS *(If NRC, type "Same as above"; if contractor, provide NRC Division, Office or Region, U.S. Nuclear Regulatory Commission, and mailing address.)*

American Nuclear Society
555 N. Kensington Avenue
La Grange Park, IL 60525

American Institute of Chemical Engineers
345 East 47th Street
New York, NY 10017-2392

American Society of Mechanical Engineers
345 East 47th Street
New York, NY 10017-2392

Canadian Nuclear Society
144 Front Street West
Suite 725
Toronto, Ontario, Canada M5J2L7

European Nuclear Society
Secretariat: Monbijoustrasse 5
P.O. Box 5032
CH-3001 Berne, Switzerland

Atomic Energy Society of Japan
No. 1-13, 1-chome
Shimbashi, Minato-ku
Tokyo 105, Japan

Japan Society of Multiphase Flow
Prof. Akimi Serizawa
Department of Nuclear Engineering
Yoshida, Sakyo, Kyoto 606-01
Japan

Division of Systems Technology
Office of Nuclear Regulatory Research
U.S. Nuclear Regulatory Commission
Washington, DC 20555-0001

10. SUPPLEMENTARY NOTES

11. ABSTRACT *(200 words or less)*

This volume includes papers presented at the 7th International Meeting on Nuclear Reactor Thermal-Hydraulics (NURETH-7) September 10-15, 1995 at Saratoga Springs, N.Y. The following subjects are discussed: progress in analytical and experimental work on the fundamentals of nuclear thermal-hydraulics, the development of advanced mathematical and numerical methods, and the application of advancements in the field in the development of novel reactor concepts. Also combined issues of thermal-hydraulics and reactor/power-plant safety, core neutronics and/or radiation.

12. KEY WORDS/DESCRIPTORS *(List words or phrases that will assist researchers in locating the report.)*
thermal-hydraulics, reactor/power-plant safety, core neutronics and/or radiation

13. AVAILABILITY STATEMENT
unlimited

14. SECURITY CLASSIFICATION
(This Page)
unclassified
(This Report)
unclassified

15. NUMBER OF PAGES

16. PRICE

Federal Recycling Program

UNITED STATES
NUCLEAR REGULATORY COMMISSION
WASHINGTON, D.C. 20555-0001

OFFICIAL BUSINESS
PENALTY FOR PRIVATE USE, $300

SPECIAL FOURTH CLASS RATE
POSTAGE AND FEES PAID
USNRC
PERMIT NO. G-67